Edited by

Katrin Schroeder | Jacopo Chiggiato

OCEANOGRAPHY OF THE MEDITERRANEAN SEA

An Introductory Guide

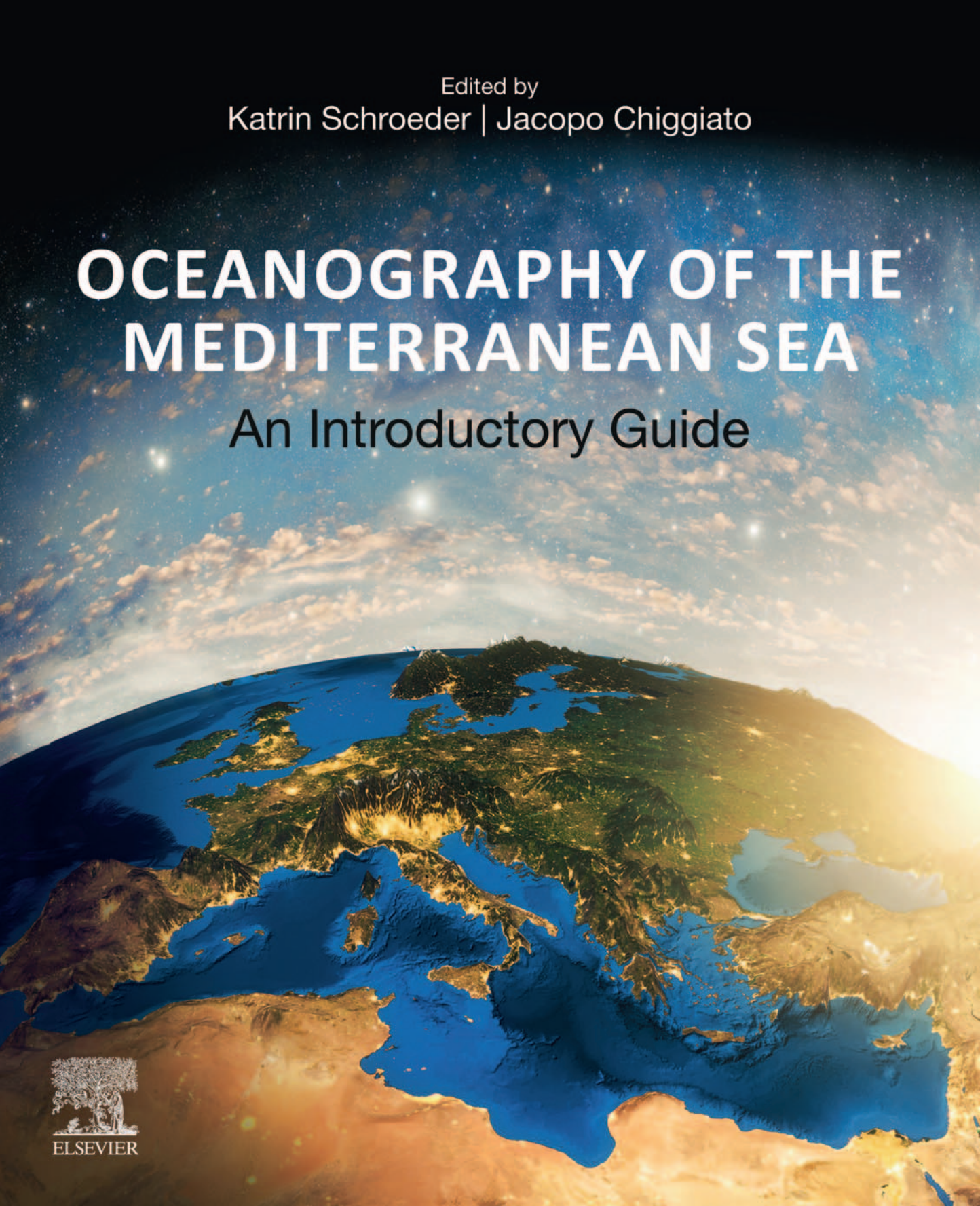

ELSEVIER

Oceanography of the Mediterranean Sea

This page intentionally left blank

Oceanography of the Mediterranean Sea

An Introductory Guide

Edited by

Katrin Schroeder
Consiglio Nazionale delle Ricerche-Istituto di Scienze Marine (CNR-ISMAR), Venezia, Italy

Jacopo Chiggiato
Consiglio Nazionale delle Ricerche-Istituto di Scienze Marine (CNR-ISMAR), Venezia, Italy

ELSEVIER

Elsevier
Radarweg 29, PO Box 211, 1000 AE Amsterdam, Netherlands
The Boulevard, Langford Lane, Kidlington, Oxford OX5 1GB, United Kingdom
50 Hampshire Street, 5th Floor, Cambridge, MA 02139, United States

Notices

Knowledge and best practice in this field are constantly changing. As new research and experience broaden our understanding, changes in research methods, professional practices, or medical treatment may become necessary.

Practitioners and researchers must always rely on their own experience and knowledge in evaluating and using any information, methods, compounds, or experiments described herein. In using such information or methods they should be mindful of their own safety and the safety of others, including parties for whom they have a professional responsibility.

To the fullest extent of the law, neither the Publisher nor the authors, contributors, or editors, assume any liability for any injury and/or damage to persons or property as a matter of products liability, negligence or otherwise, or from any use or operation of any methods, products, instructions, or ideas contained in the material herein.

ISBN: 978-0-12-823692-5

Publisher: Candice Janco
Acquisitions Editor: Peter Llewellyn
Editorial Project Manager: Sara Valentino
Production Project Manager: Kumar Anbazhagan
Cover Designer: Christian J. Bilbow

Typeset by TNQ Technologies

Contents

This page intentionally left blank

List of contributors

Enrique Alvarez-Fanjul
Puertos del Estado, Madrid, Spain; Mercator Ocean International, Toulouse, France

Marta Álvarez
Instituto Español de Oceanografía (IEO), CSIC, A Coruña, Spain

Angel Amores
Mediterranean Institute for Advanced Studies (IMEDEA, UIB-CSIC), Esporles, Spain

Vincenzo Artale
Consiglio Nazionale delle Ricerche-Istituto di Scienze Marine (CNR-ISMAR), Roma, Italy

Bàrbara Barceló-Llull
IMEDEA, Esporles, Mallorca, Spain

Francisco M. Calafat
Department of Marine Physics and Ocean Climate, National Oceanography Centre, Liverpool, United Kingdom

Daniele Casalbore
Dipartimento di Scienze Della Terra, Università di Roma, Sapienza Rome, Italy; Consiglio Nazionale delle Ricerche (CNR), Istituto di Geologia Ambientale e Geoingegneria (IGAG), Rome, Italy

Teresa S. Catalá
Institute for Chemistry and Biology of the Marine Environment (ICBM), University of Oldenburg, Oldenburg, Germany; Organization for Science, Education and Global Society, Stuttgart, Germany

Paola Cessi
Scripps Institution of Oceanography, San Diego, CA, United States

Domenico Chiarella
Clastic Sedimentology Investigation (CSI), Department of Earth Sciences, Royal Holloway, University of London, Egham, United Kingdom

Jacopo Chiggiato
Consiglio Nazionale delle Ricerche-Istituto di Scienze Marine (CNR-ISMAR), Venezia, Italy

Giuseppe Civitarese
National Institute of Oceanography and Applied Geophysics - OGS, Trieste, Italy

Emanuela Clementi
CMCC, Centro Euro-Mediterraneo sui Cambiamenti Climatici, Ocean Modelling and Data Assimilation, Bologna, Italy

Giovanni Coppini
CMCC, Centro Euro-Mediterraneo sui Cambiamenti Climatici, Ocean Predictions and Applications, Lecce, Italy

Laurent Coppola
Sorbonne Université, CNRS, Laboratoire d'Océanographie de Villefranche, France; Sorbonne Université, CNRS, Laboratoire d'Océanographie de Villefranche, Villefranche-sur-Mer, France; Sorbonne Université, CNRS, OSU STAMAR, Paris, France

Eugenio Cutolo
IMEDEA, Esporles, Mallorca, Spain

Pierre Daniel
Météo-France, Toulouse, France

Antoine Delepoulle
CLS: Parc Technologique du Canal, Ramonville-Saint-Agne, France

Jacques Déverchère
Univ Brest, CNRS, Ifremer, Geo-Ocean, Plouzane, France

Stephanie Dupré
Ifremer, CNRS, Univ Brest, Geo-Ocean Plouzane, France

Xavier Durrieu de Madron
Centre National de la Recherche Scientifique (CEFREM, CNRS-UPVD), Perpignan, France

Romain Escudier
Mercator Ocean, Toulouse, France

Claude Estournel
CNRS, LEGOS, Toulouse, France

Fedra Francocci
Consiglio Nazionale delle Ricerche (CNR), Istituto per lo studio degli Impatti Antropici e Sostenibilità in ambiente marino (IAS), Rome, Italy

Jesús García Lafuente
Grupo de Oceanografía Física, Instituto de Biotecnología y Desarrollo Azul (IBYDA), Universidad de Málaga, Málaga, Spain

Filippo Giorgi
International Centre for Theoretical Physics (ICTP), Trieste, Italy

Abed E.R. Hassoun
GEOMAR Helmholtz Centre for Ocean Research Kiel, Kiel, Germany; National Council for Scientific Research, National Center for Marine Sciences, Beirut, Lebanon

Valeria Ibello
Middle East Technical University, Institute of Marine Sciences (METU-IMS), Erdemli-Mersin, Turkey

Simon A. Josey
National Oceanography Centre, Southampton, United Kingdom

Gerasimos Korres
Hellenic Centre for Marine Research, Attiki, Greece

Paolo Lazzari
National Institute of Oceanography and Applied Geophysics - OGS, Trieste, Italy

Dominique Lefevre
Aix Marseille Université, Université de Toulon, CNRS, IRD, MIO, UM 110, Marseille, France

Piero Lionello
University of Salento, Lecce, Italy

Vladyslav Lyubartsev
Centro EuroMediterraneo sui Cambiamenti Climatici, Bologna, Italy

Diego Macías
Instituto de Ciencias Marinas de Andalucía (ICMAN), CSIC, Cádiz, Spain

Marta Marcos
Mediterranean Institute for Advanced Studies (IMEDEA, UIB-CSIC), Esporles, Spain; Department of Physics, University of the Balearic Islands, Palma, Spain

Evan Mason
IMEDEA, Esporles, Mallorca, Spain; Mediterranean Institute for Advanced Studies (IMEDEA, UIB-CSIC), Esporles, Spain

Elda Miramontes
Faculty of Geosciences, University of Bremen, Bremen, Germany; MARUM-Center for Marine Environmental Sciences, University of Bremen, Bremen, Germany

Baptiste Mourre
SOCIB, Balearic Islands Coastal Observing and Forecasting System, Palma, Spain

Antonio Novellino
ETT Solutions, Genova, Italy

Ananda Pascual
IMEDEA, Esporles, Mallorca, Spain

Claudio Pellegrini
Consiglio Nazionale delle Ricerche (CNR), Istituto di Scienze Marine (ISMAR), Italy

Nadia Pinardi
Alma Mater Studiorum University of Bologna, Department of Physics and Astronomy, Bologna, Italy

Maurizio Ribera d'Alcalà
Stazione Zoologica Anton Dohrn, Napoli, Italy; Consiglio Nazionale delle Ricerche (CNR), Istituto per lo studio degli Impatti Antropici e Sostenibilità in ambiente marino (IAS), Campobello di Mazara, Trapani, Italy

Daniel Rodríguez-Tarry
IMEDEA, Esporles, Mallorca, Spain

Eelco Rohling
Australian National University, Canberra, Australia

Simón Ruiz
IMEDEA, Esporles, Mallorca, Spain

Gianmaria Sannino
ENEA, Rome, Italy

Chiara Santinelli
Consiglio Nazionale delle Ricerche, Istituto di Biofisica (CNR-IBF), Pisa, Italy

Katrin Schroeder
Consiglio Nazionale delle Ricerche-Istituto di Scienze Marine (CNR-ISMAR), Venezia, Italy

Richard Seager
Columbia University, New York, United States

Mario Sprovieri
Consiglio Nazionale delle Ricerche (CNR), Istituto per lo studio degli Impatti Antropici e Sostenibilità in ambiente marino (IAS), Campobello di Mazara, Trapani, Italy

Antonio Sánchez-Román
IMEDEA, Esporles, Mallorca, Spain

Toste Tanhua
GEOMAR Helmholtz Centre for Ocean Research Kiel, Kiel, Germany

Isabelle Taupier-Letage
Institut Méditerranéen d'Océanologie (MIO), La Seyne, France

Joaquín Tintoré
SOCIB, Balearic Islands Coastal Observing and Forecasting System, Palma, Spain; IMEDEA, CSIC-UIB, Carrer de Miquel Marquès, Esporles, Spain

Marta Álvarez
Instituto Español de Oceanografía (IEO), CSIC, A Coruña, Spain

Fabio Trincardi
Consiglio Nazionale delle Ricerche (CNR), Dipartimento di Scienze del Sistema Terra e Tecnologie per l'Ambiente (DSSTTA), Rome, Italy; Consiglio Nazionale delle Ricerche (CNR), Dipartimento di Scienze del Sistema Terra e Tecnologie per l'Ambiente (DSSTTA), Rome, Italy

Caroline Ulses
Laboratoire d'Etudes en Géophysique et Océanographie Spatiales (LEGOS), Université de Toulouse, CNES, CNRS, IRD, UPS, Toulouse, France

Matteo Vacchi
Dipartimento di Scienze Della Terra, Università di Pisa, Pisa, Italy

Manuel Vargas-Yáñez
Insituto Español de Oceanografía, IEO-CSIC Málaga, Spain; Insituto Español de Oceanografía, IEO-CSIC, Málaga, Spain

Dimitris Velaoras
Hellenic Centre for Marine Research (HCMR), Institute of Oceanography, Anavyssos, Greece

Ivica Vilibić
Ruđer Bošković Institute, Zagreb, Croatia

Guy Wöppelmann
LIENSs, La Rochelle University – CNRS, La Rochelle, France

George Zodiatis
ORION Joint Research and Development Center, Nicosia, Cyprus

This page intentionally left blank

About the editors

Katrin Schroeder is a Senior Scientist at the Institute of Marine Sciences (CNR-ISMAR). She holds an MSc and a PhD in Environmental Science (2003 and 2008), University of Venice. Her major research interests are experimental studies in physical and biogeochemical oceanography of the Mediterranean Sea. She represents CNR at the European Marine Board (EMB), is the Italian National Delegate at the International Association for the Physical Sciences of the Oceans (IAPSO), and is Chair of the Committee "Physics and Climate of the Ocean" of the Mediterranean Science Commission (CIESM). In 2019 she was selected as the recipient of the IUGG Early Career Scientist Award, while in 2015 she was presented the Outstanding Young Scientists Award by the EGU. In 2011 she received the MedClivar Young Scientist Award. She has authored or coauthored more than 60 peer-reviewed scientific papers and participated in several oceanographic cruises in the Mediterranean Sea. She is the Associate Editor for *Frontiers in Marine Science* (Frontiers Media) and acted as Guest Editor for *Marine Geology* (Elsevier) and *Ocean Science* (Copernicus Publications).

Jacopo Chiggiato holds an MSc in Environmental Science (1998), University of Venice, and a PhD in Numerical Modeling for Environmental Protection (2004), University of Bologna. Among several experiences after PhD, he was a Scientist at the NATO Undersea Research Centre (2009−2011). He is currently the Senior Scientist at the Institute of Marine Sciences (CNR-ISMAR), Member of the Advisory Board of the Institute, and Member of the Scientific Council of the Department of Earth System Science and Environmental Technologies (CNR-DSSTTA). His research interests are data analysis and numerical modeling in coastal meteorology and oceanography, air−sea interactions, atmosphere-ocean coupled systems, climate variability of regional oceans, and R&D in operational oceanography. He has authored and coauthored more than 60 papers in refereed International Journals JCR and participated in several sea trials in the Mediterranean Sea. He received the Scientific Achievement Award in 2014 issued by the Science and Technology Organization of the NATO. He is the Associate Editor for the *Journal of Operational Oceanography* (Taylor & Francis), *Frontiers in Marine Science* (Frontiers Media), and acted as Guest Editor for *Marine Geology* (Elsevier) and *Ocean Science* (Copernicus Publications).

This page intentionally left blank

CHAPTER

Introduction 1

Jacopo Chiggiato[1], Katrin Schroeder[1], Baptiste Mourre[2], Elda Miramontes[3,4], Piero Lionello[5], Marta Marcos[6,7], Nadia Pinardi[8], Evan Mason[6], Marta Álvarez[9], Fabio Trincardi[10]

[1]Consiglio Nazionale delle Ricerche-Istituto di Scienze Marine (CNR-ISMAR), Venezia, Italy; [2]SOCIB, Balearic Islands Coastal Observing and Forecasting System, Palma, Spain; [3]Faculty of Geosciences, University of Bremen, Bremen, Germany; [4]MARUM-Center for Marine Environmental Sciences, University of Bremen, Bremen, Germany; [5]University of Salento, Lecce, Italy; [6]Mediterranean Institute for Advanced Studies (IMEDEA, UIB-CSIC), Esporles, Spain; [7]Department of Physics, University of the Balearic Islands, Palma, Spain; [8]Alma Mater Studiorum University of Bologna, Department of Physics and Astronomy, Bologna, Italy; [9]Instituto Español de Oceanografía (IEO), CSIC, A Coruña, Spain; [10]Consiglio Nazionale delle Ricerche (CNR), Dipartimento di Scienze del Sistema Terra e Tecnologie per l'Ambiente (DSSTTA), Rome, Italy

1.1 The Mediterranean Sea, a "miniature ocean"

The Mediterranean Sea (Fig. 1.1) is a source of biodiversity, food, and recreation, resulting in human well-being and health benefits. It represents a privileged and inspiring environment where important civilizations have emerged, with noteworthy contributions to the development of arts and science in particular. But today, with around 160 million people living along its coastline (UNEP/MAP and Plan Bleu, 2020), very high touristic concentration in the summer months and very busy regular shipping activity all across the region, the Mediterranean Sea is exposed to an extreme human pressure ("a sea under siege" as portrayed by Lajeusne et al., 2010). At the same time, it is in the frontline of climate change, being defined as a global hot spot (Giorgi, 2006), with significant expected impacts on its average temperature, which will likely lead to an increased occurrence of heatwaves, droughts and extreme storms, with effects such as sea level rise, ocean acidification, oxygen depletion or changes in the water masses and associated ocean circulation and distribution of nutrients. As a result of these human and climatic stressors, water mass modifications have been observed over the recent years (e.g., Schroeder et al., 2016, 2017; Margirier et al., 2020), together with a degradation of the marine and coastal ecosystems (Piroddi et al., 2017). Overfishing, marine litter, oil spills, contaminants, and invasive species are important threats to the present and future health of the Mediterranean Sea, with direct impacts on ecosystem services and human lives. The full understanding of the oceanography of the Mediterranean Sea and the detection of the changes affecting the circulation and ecosystems is of utmost

Oceanography of the Mediterranean Sea. https://doi.org/10.1016/B978-0-12-823692-5.00002-9

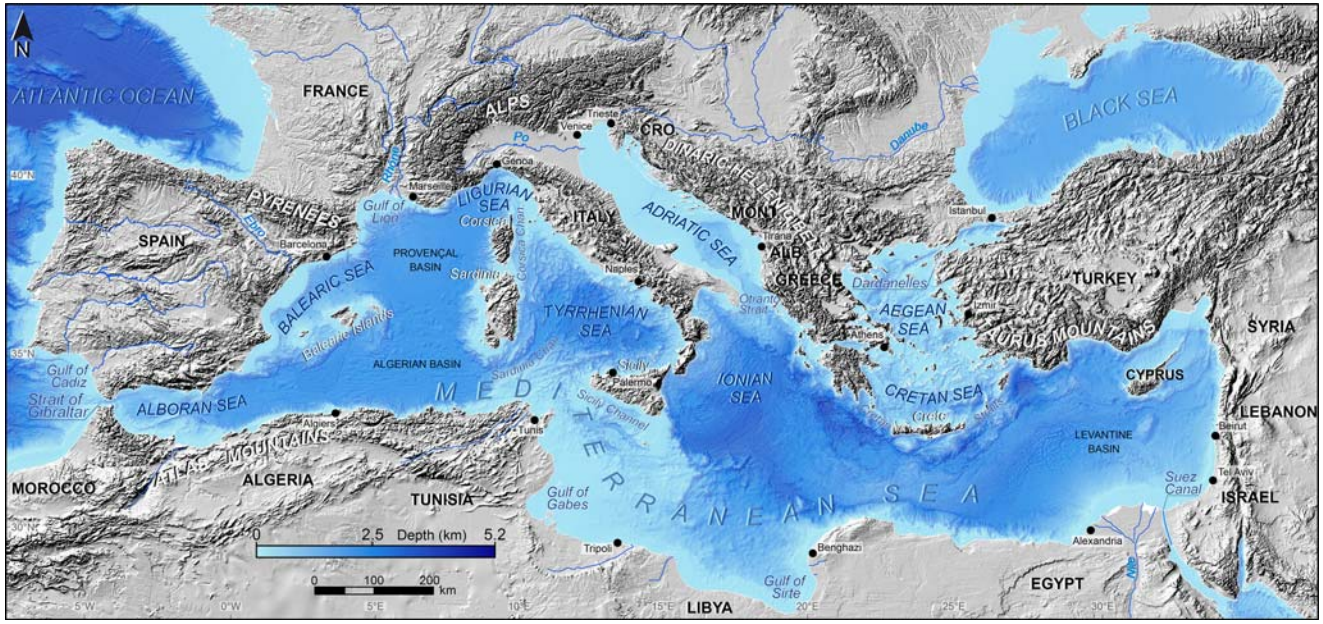

FIGURE 1.1

Map of the Mediterranean Sea, where the main geographical names mentioned in the book are indicated. Background: bathymetry and topography with blue and gray scales, respectively. The topographic data set used is the GEBCO Compilation Group (2020) GEBCO 2020 Grid (https://doi.org/10.5285/a29c5465-b138-234d-e053-6c86abc040b9) and the bathymetric data set corresponds to the EMODnet Digital Bathymetry (EMODnet Bathymetry Consortium (2018), https://doi.org/10.12770/18ff0d48-b203-4a65-94a9-5fd8b0ec35f6).

Image courtesy of Claudio Pellegrini.

importance to preserve this environmental treasure, biodiversity, coastal, and deep sea environments and to provide roots for an efficient response to threats to sea-facing urban areas and endangered heritage sites (e.g., Reimann et al., 2018), contributing to enabling appropriate mitigation and adaptation strategies.

The Mediterranean Sea can be considered as a laboratory basin. Robinson and Golnaraghi (1994) highlighted that many of the processes that are occurring in the world ocean also occur in the Mediterranean Sea, "either identically or analogously" and, in addition, the reduced size of the Mediterranean Sea also implies lower resources in carrying out oceanographic campaigns. Water mass formation and dispersion, eddies, meanders and frontal activity, unstable slope currents interacting with the topography, eddy-mean flow interactions, air-sea interplays, coastal upwellings or dynamic exchanges through straits, are all processes that occur in the Mediterranean Sea, generating rich dynamics over a wide range of interacting scales. What makes the Mediterranean Sea particularly useful is that it indeed behaves like a miniature ocean but with time scale much shorter than for the global ocean, with a turnover time of the order of decades (Bethoux et al., 1999), instead of centuries, that is, at the scale of a human lifetime. Under intensifying climatic stressors, the Mediterranean Sea is therefore also a potential model for patterns that might be soon experienced globally (Lejeusne et al., 2010). In addition, the relatively salty Mediterranean outflow is known to affect the global circulation once flowing within the North Atlantic Ocean, with direct impacts on the water mass properties and the associated circulation (e.g., Rahmstorf, 1998). Thus, despite its semienclosed characteristics, changes of the Mediterranean Sea circulation do also have a direct influence on the global ocean.

While the very first referred ocean density measurements were collected back in the 17th century (Pinardi et al., 2018), the comprehensive oceanographic exploration of the Mediterranean Sea really started at the beginning of the 20th century. The Danish Oceanographic Expeditions (Schmidt, 1912; Mavraki, 2016) carried out between 1908 and 1910 were the first exploratory surveys covering the whole Mediterranean basin, with several hundreds of hydrographic sampling stations. This expedition led to delineate the initial picture of the summer Mediterranean Sea circulation (Nielsen et al., 1912), already properly depicting the cyclonic circulation in the Western Mediterranean Sea and the eastward flow along the southern Mediterranean coast from the Strait of Gibraltar toward the Levantine Basin. Later on, Russian expeditions in the 1960s led to a refined description of the average general circulation during winter (Ovchinnikov and Fedoseyev, 1965). In the same years, Wüst (1961) probed into the vertical circulation structure, highlighting as the Mediterranean is a remarkable example of ocean-atmosphere interaction. Some regular monitoring programs at fixed stations also started to be established in the following years (Bougis and Carré, 1960; Cavaleri, 1999; Salat et al., 2019). But it is only in the 1980s that very significant developments of Mediterranean monitoring activities occurred with several international collaborations, leading to major experiments such as the Western Mediterranean Circulation Experiment (WMCE, La Violette, 1990), the Gibraltar Experiment (Lacombe and Richez, 1982), or the Physical

Oceanography of the Eastern Mediterranean (POEM, Özsoy et al., 1989; Robinson et al., 1992). These experiments, focusing on regional scales and specific ocean processes, were based on the deployment over several weeks of different and complementary instruments, providing a first evidence of the importance of current instabilities and mesoscale variability. At the same time, satellite remote sensing of surface temperature in the 1980s (Champagne-Philippe and Harang, 1982; Arnone and La Violette, 1986) and sea level altimetry in the 1990s (Larnicol et al., 1995) represented major breakthroughs, leading to tremendous advances in our understanding of the Mediterranean Sea surface mesoscale variability. Long time-series programs of repeated CTD transects or fixed stations were also further organized in the 1990s in specific areas of the western and eastern basins. After multiple "revolutions" in oceanography (Le Traon, 2013), nowadays several large programmes of Earth observation and modeling are fully settled (the most prominent for the Mediterranean, among several, probably being the EU COPERNICUS program) and vast amount of new data and knowledge is accessible. Yet, this "vast amount" may stun, at the beginning, students and scientists approaching for the first time to the oceanography of the Mediterranean Sea. This book is meant to convey, in a synthetic way, the pillars of the current understanding, so as to provide solid foundations to deepen the knowledge on the Physical Oceanography of the Mediterranean Sea, including Geology, Climate, and Chemical Oceanography.

1.2 Book structure and contents

The opening chapters of the book set the boundaries: bottom and lateral (origin, evolution, shape and dimensions of the basin, Chapter 2) and surface (Climate, Chapter 3). In particular, the tectonic processes at the origin of the Mediterranean Sea are described, as well as a particular paleo-environmental event (the Messinian salinity crisis) that resulted in the almost complete desiccation of the Mediterranean Sea. The morphological characteristics of the basin floor and the tectonic and climatic processes that control sedimentation and thus the evolution of the seafloor are introduced to the reader. The climate is then described: the Mediterranean region exhibits a large seasonal cycle of mean temperature and total precipitation, as well as a large spatial variability. Most of the region is characterized by mild winters, though small areas with mean winter temperature below zero exist in the Alps and Caucasus, and warm or hot summers. Most areas in the central Mediterranean rely on the wet season (October to March) for precipitation to provide water resources for the rest of the year, and large areas close to the north African and Middle East coasts are dry all over the year.

The next chapters discuss forcings and water mass characteristics as well as general circulation, in a classical steady-state approach (Chapter 4), the air-sea interface (Chapter 5 on sea level and Chapter 6 on surface waves) and one of the most prominent examples of ocean-atmosphere interaction, the generation of new water masses and overturning circulation (Chapter 7). In particular, the reader is introduced to

general concepts about the main forcings of the Mediterranean Sea, that are responsible for the peculiar characteristics of Mediterranean water masses. A general explanation on water mass analysis is given, and then the properties and vertical and horizontal distributions of the main Mediterranean water masses are described. The concept of mean sea level is introduced as well as its variability at low frequency time scales in the Mediterranean Sea. Ancillary geodetic measurements are also described, as these are relevant for coastal monitoring and sea level impacts. In addition, the past evolution of Mediterranean sea level, since the Holocene up to the late 19th century, are illustrated in detail. An overview is then given of a wide range of free and forced long oceanic waves (Chapter 6) that are relevant to disentangle major ocean processes and associated coastal risk in the Mediterranean Sea: this includes tides, seiches, wind waves, storm surges, tsunamis. The physical processes, characteristics, and risks posed by the different phenomena are described. Chapter 7 points out the main characteristics of the dense/deep water formation processes occurring in the Mediterranean Sea and the basin-wide vertical circulation is drawn. These processes are key elements of the circulation dynamics in the Mediterranean basin. The waters are formed by open ocean convection processes and dense shelf water cascading. The meridional and zonal overturning circulation of the Mediterranean Sea are driven to a large extent by these formation and spreading processes.

The Mediterranean Sea features a wide range of temporal and spatial scales (basin, subbasin, and mesoscale) that interact to force a complex, highly variable general circulation. While Chapter 8 inspects mesoscale features, increasing the "spatial resolution" of the general description provided in Chapter 4, Chapter 9 discusses the recent changes and variability over time of this general picture, abandoning the steady-state view of Chapter 4. Over recent decades, many oceanographic campaigns have been carried out with the goal to further understand the variability at the basin scale, as well as to investigate sharp fronts and mesoscale eddies. Multiplatform experiments are being complemented with instruments able to look beyond the mesoscale, into the submesoscale. General concepts about temporal changes of water mass properties in the Mediterranean Sea are then given to the reader, focusing in particular on the second half of the 20th century and the beginning of the 21st century, and situating them in the context of the global changes occurring in the oceans. After that, Chapter 10 overviews our ever-increasing ability to observe and predict the ocean linked to the recent advancements in operational oceanography. Sustained observations and forecasting systems provide a source of invaluable new information to advance the current knowledge and understanding of the functioning of the Mediterranean Sea and its ecosystems, and to efficiently respond to maritime emergencies, societal needs and preservation threats. The concepts behind ocean observing and forecasting systems are introduced, the present status of the systems operating in the Mediterranean Sea is described and some recent applications are illustrated.

The concluding three Chapters are devoted to the description of the major biogeochemical cycles (Chapter 11), the active geological processes in the basin (Chapter 12) and to the impact of the humans on the physical environment in the

last epoch, the Anthropocene, and its most recent part, the so-called Great Acceleration (Chapter 13). An overview of the general biogeochemistry is given, explaining the particularities of the main biogeochemical variables and the physical, biological and geochemical processes driving their distribution (dissolved oxygen, inorganic nutrients, dissolved organic carbon, the CO_2 system). Also a brief overview on the utility of those biogeochemical variables to identify water masses is given. Future projections and threats on biogeochemistry in the Mediterranean Sea under different future climate change scenarios are discussed. Then, the geological processes that resulted in the formation of the Mediterranean Sea are described, focusing on those that control recent sedimentation at the seafloor in coastal areas and in the deep sea, on how submarine volcanoes are formed and evolve and how fluid escape at the seafloor form cold seeps and related deposits. The last Chapter follows a slightly different philosophy behind the story-telling, excluding climate change that is, by editorial choice, tackled in a distributed way throughout the book. This chapter illustrates the major anthropic impacts shaping the geological, biological and biogeochemical dynamics of the Mediterranean Sea. A synthetic description of the main modifications of deep sea floor integrity and coastal landscapes is complemented by an in-depth picture of critical changes in the biogeochemical dynamics of major nutrients and pollutants (including a detailed paragraph on plastics) at Mediterranean scale.

1.3 Learning objectives at a glance

At the beginning of each chapter the reader is instructed about what are the specific learning objectives that the authors had in mind while writing the text. Here these objectives are highlighted for the whole book, to facilitate the reading and to give a general overview.

Chapter	In this chapter you will learn about ....
Chapter 2 Mediterranean Sea evolution and present-day physiography	- When the Mediterranean Sea started to form and which geological processes have controlled its formation and development - What are the morphology and dimensions of the Mediterranean Sea and which processes control them - How tectonic processes control sedimentation and affect straits, with a focus on the Messinian salinity crisis - How climate and oceanographic changes affect sedimentation along continental margins
Chapter 3 Mediterranean climate: Past, present and future	- What are the morphological characteristics of the Mediterranean region and their evolution since 30 My BP

Chapter	In this chapter you will learn about ....
Chapter 4 The forcings of the Mediterranean Sea and the physical properties of its water masses	- What are the characteristics of the climate of the Mediterranean region and how they have evolved in the past - which are the main processes and factors determining the regional climate conditions - What are the effects of anthropogenic climate change at regional scale - Which are the main forcings of the Mediterranean Sea - What are the heat and freshwater budgets of the Mediterranean Sea - How to identify Mediterranean water masses on a T-S diagram - How the Mediterranean water masses are distributed on a basin scale - What are the typical thermohaline properties of the Mediterranean water masses - How we can use other tracers to identify and track water masses
Chapter 5 Mediterranean Sea level	- The concept of mean sea level - Which are the driving physical mechanisms underlying mean sea level changes at different temporal scales - What are the instrumental and proxy measurements of past mean sea level changes with a focus on Mediterranean observations - By how much and at which rates mean sea level has been rising in the Mediterranean Sea - What are the future projected mean sea level changes in the Mediterranean Sea during the 21st century, according to climate models and climate scenarios
Chapter 6 Surface wave and sea surface dynamics in the Mediterranean	- What are the basic information on sinusoidal waves and their characteristics in seas and oceans - What are the basic information on astronomical tides and their causes - How the tides behave in the Mediterranean Sea - Which are the characteristics, dynamics and causes of marine storms in the Mediterranean Sea including waves and surges that they produce - What is the past and expected future evolution of Mediterranean coastal floods and of their causes

Continued

Chapter	In this chapter you will learn about ....
	- Which tools are available for predictions of waves and sea level extremes in the Mediterranean Sea - What are the characteristics of tsunamis in the Mediterranean Sea: Major past events, their causes (including meteorological factors) and their prediction
Chapter 7 Dense and deep water formation processes and Mediterranean overturning circulation	- What are the characteristics of Mediterranean dense and deep waters and their formation rates - Where and when dense water formation processes have been observed in the Mediterranean - What are the main formation areas - What is the difference between dense shelf water cascading and open ocean convection - What is the theoretical framework of these processes - How can these processes be represented by numerical models - What is the structure of the Mediterranean overturing cells
Chapter 8 Fronts, eddies, and mesoscale circulation	- How satellite altimetry can be used to investigate oceanic mesoscale features in the Mediterranean - About the different in situ instruments that oceanographers use to complement the satellite data - The wide range of advanced sampling instruments available to oceanographers in the Mediterranean Sea - The role of eddy identification and tracking codes in support of multiplatform experiments
Chapter 9 Recent changes in the Mediterranean Sea	- What are the factors that lead to changes over time in Mediterranean water mass properties - How the water masses of the eastern Mediterranean have changed over time - How the water masses of the western Mediterranean have changed over time - How these changes are transferred to the Atlantic ocean
Chapter 10 Mediterranean observing and forecasting systems	- What are the characteristics of the observing systems deployed in the Mediterranean Sea - Which are the associated international coordination programs

Chapter	In this chapter you will learn about ....
	- Where are the regional multi-platform observatories - What are the concepts behind and examples of ocean forecasting systems - How do the data management and distribution procedures work - Which are some of the recent applications of these integrated observing and forecasting systems
Chapter 11 Mediterranean Sea general biogeochemistry	- What are the peculiarities of the Mediterranean Sea biogeochemical variables and their physical and biological controlling processes - Why dissolved oxygen and inorganic nutrient ratios are high in the basin - What makes the CO_2 system so complex, how the storage of anthropogenic CO_2works and induces ocean acidification - Why dissolved organic matter in the Mediterranean Sea differs from that in the global ocean - How to identify and track water masses using biogeochemical variables - Which biogeochemical changes might be expected in the basin under different future scenarios
Chapter 12 Active geological processes in the Mediterranean Sea	- Which sedimentary processes are active in coastal and deep-water environments - How submarine volcanoes form and which processes contribute to the collapse of their flanks - How fluid escape forms cold seeps and related deposits - How sedimentary processes and fluid seepage can become geohazards and affect ecosystems
Chapter 13 The Mediterranean Sea in the Anthropocene	- What are the anthropic impacts on the deep seafloor and coastal landscapes in the Mediterranean basin - What are the main human impacts on the water budget and the biogeochemistry of nutrients at basin scale - What are the biogeochemical dynamics of contaminants (organic and inorganic) in the Mediterranean basin - What are the characteristics (sources, fluxes, etc.) of plastic input in the Mediterranean

References

Arnone, R., La Violette, P.E., 1986. Satellite definition of the bio-optical and thermal variation of the coastal eddies associated with the African current. J. Geophys. Res. 91, 2351−2364.

Bethoux, J.P., Gentili, B., Morin, P., Nicolas, E., Pierre, C., Ruiz-Pino, D., 1999. The Mediterranean Sea: a miniature ocean for climatic and environmental studies and a key for the climatic functioning of the North Atlantic. Prog. Oceanogr. 44, 131−146, 10.1016/S0079-6611(99)00023-3.

Bougis, P., Carré, C., 1960. Conditions hydrologiques à Villefranche sur Mer pendant les années 1957 et 1958. Cah. Oceanogr. 12 (6), 392−408.

Cavaleri, L., 1999. The oceanographic tower Acqua Alta: more than a quarter of a century of activity. Il Nuovo Cimento 22C (1), 1−111.

Champagne-Philippe, M., Harang, L., 1982. Fronts superficiels en Méditerranée d'après les télé-mesures AVHRR Note de travail n°31 de l'Etablissement d'Etudes et de Recherches Météorologiques, p. 172.

Giorgi, F., 2006. Climate change hot-spots. Geophys. Res. Lett. 33, L08707.

Lacombe, H., Richez, C., 1982. The regime of the Strait of Gibraltar. In: Nihoul, J.C.J. (Ed.), Hydrodynamics of Semi-enclosed Seas, vol 34. Elsevier Oceanogr. Ser., pp. 13−73

Larnicol, G., Le Traon, P.-Y., Ayoub, N., De Mey, P., 1995. Sea level variability in the Mediterranean Sea from two years of Topex/Poseidon data. J. Geophys. Res. 100, 25163−25177.

La Violette, P.E., 1990. The western Mediterranean circulation experiment (WMCE): introduction. J. Geophys. Res. 95, 1511−1514.

Lejeusne, C., Chevaldonné, P., Pergent-Martini, C., Boudouresque, C., Pérez, T., 2010. Climate change effects on a miniature ocean: the highly diverse, highly impacted Mediterranean Sea. Trends Ecol. Evol. 25, 250−260.

Le Traon, P.Y., 2013. From satellite altimetry to Argo and operational oceanography: three revolutions in oceanography. Ocean Sci. 9, 901−915. https://doi.org/10.5194/os-9-901-2013.

Margirier, F., Testor, P., Heslop, E., Mallil, K., Bosse, A., Houpert, L., et al., 2020. Abrupt warming and salinification of intermediate waters interplays with decline of deep convection in the Northwestern Mediterranean Sea. Sci. Rep. 10, 20923.

Mavraki, D., Fanini, L., Tsompanou, M., Gerovasileiou, V., Nikolopoulou, S., Chatzinikolaou, E., Plaitis, W., Faulwetter, S., 2016. Rescuing biogeographic legacy data: the "Thor" Expedition, a historical oceanographic expedition to the Mediterranean Sea. Biodivers. Data J. 4, e11054. https://doi.org/10.3897/BDJ.4.e11054.

Nielsen, J.N., 1912. Hydrography of the Mediterranean and adjacent waters. In: Report on the Danish Oceanographical Expeditions 1908−1910 to the Mediterranean and adjacent seas, vol 1, pp. 77−191.

Ovchinnikov, I.M., Fedoseyev, A.F., 1965. The horizontal circulation of the water of the Mediterranean Sea during the summer and the winter seasons. In: Fomin, L.M. (Ed.), Basic Features of the Geologic Structure, Hydrological Regime, and Biology of the Mediterranean. Translation of the Institute for Modern Languages of the US Navy Oceanographic Office, pp. 185−201.

Özsoy, E., Hecht, A., Ünlüata, Ü., 1989. Circulation and hydrography of the Levantine Basin. Results of POEM coordinated experiments 1985−1986. Prog. Oceanogr. 22, 125−170. Pergamon Press.

Pinardi, N., Özsoy, E., Latif, M.A., Moroni, F., Grandi, A., Manzella, G., 2018. Measuring the sea: Marsili's Oceanographic Cruise (1679−80) and the Roots of Oceanography. J. Phys. Oceanogr. 48, 845−860.

Piroddi, C., Coll, M., Liquete, C., Macías, D., et al., 2017. Historical changes of the Mediterranean Sea ecosystem: modelling the role and impact of primary productivity and fisheries changes over time. Sci. Rep. 7, 44491.

Rahmstorf, S., August 1998. Influence of Mediterranean outflow on climate. Eos Trans. 79 (24), 281−282. https://doi.org/10.1029/98EO00208.

Reimann, L., Vafeidis, A.T., Brown, S., et al., 2018. Mediterranean UNESCO World Heritage at risk from coastal flooding and erosion due to sea-level rise. Nat. Commun. 9, 4161.

Robinson, A.R., Golnaraghi, M., 1994. The physical and dynamical oceanography of the Mediterranean Sea. In: Malanotte-Rizzoli, P., Robinson, A.R. (Eds.), Ocean Processes in Climate Dynamics: Global and Mediterranean Examples. NATO ASI Series, vol 419. Springer, Dordrecht. https://doi.org/10.1007/978-94-011-0870-6_12.

Robinson, A.R., Malanotte-Rizzoli, P., Hecht, A., Michelato, A., Roether, W., Theocharis, A., Ünlüata, U., Pinardi, N., Artegiani, A., Bergamasco, A., et al., 1992. General circulation of the eastern Mediterranean Earth. Sci. Rev. 32 (4), 285−309.

Salat, J., Pascual, J., Flexas, M., et al., 2019. Forty-five years of oceanographic and meteorological observations at a coastal station in the NW Mediterranean: a ground truth for satellite observations. Ocean Dynam. 69, 1067−1084.

Schmidt, J., 1912. Introduction. Report on the Danish Oceanographical Expeditions 1908−1910 to the Mediterranean and Adjacent Seas. Høst & Son, Copenhagen, pp. 1−49.

Schroeder, K., Chiggiato, J., Bryden, H.L., Borghini, M., Ben Ismail, S., 2016. Abrupt climate shift in the western Mediterranean Sea. Sci. Rep. 6, 23009. https://doi.org/10.1038/srep23009.

Schroeder, K., Chiggiato, J., Josey, S.A., Borghini, M., Aracri, S., Sparnocchia, S., 2017. Rapid response to climate change in a marginal sea. Sci. Rep. 7, 4065. https://doi.org/10.1038/s41598-017-04455-5.

United Nations Environment Programme/Mediterranean Action Plan and Plan Bleu, 2020. State of the Environment and Development in the Mediterranean: Summary for Decision Makers. Nairobi.

Wust, G., 1961. On the vertical circulation of the Mediterranean Sea. J. Geophys. Res. 66, 3261−3271.

This page intentionally left blank

CHAPTER

Mediterranean Sea evolution and present-day physiography

2

Elda Miramontes[1,2], Jacques Déverchère[3], Claudio Pellegrini[4], Domenico Chiarella[5]

[1]*Faculty of Geosciences, University of Bremen, Bremen, Germany;* [2]*MARUM-Center for Marine Environmental Sciences, University of Bremen, Bremen, Germany;* [3]*Univ Brest, CNRS, Ifremer, Geo-Ocean, Plouzane, France;* [4]*Consiglio Nazionale delle Ricerche (CNR), Istituto di Scienze Marine (ISMAR), Italy;* [5]*Clastic Sedimentology Investigation (CSI), Department of Earth Sciences, Royal Holloway, University of London, Egham, United Kingdom*

Learning objectives

In this chapter you will learn:

- When the Mediterranean Sea started to form and which geological processes have controlled its formation and development.
- What are the morphology and dimensions of the Mediterranean Sea and which processes control them.
- How tectonic processes control sedimentation and affect straits, with a focus on the Messinian Salinity Crisis (MSC).
- How climate and oceanographic changes affect sedimentation along continental margins.

2.1 Origin of the Mediterranean Sea

2.1.1 Kinematic and geodynamical overview

The relative convergence of the Africa (Nubia) and the Eurasia plates began in Late Cretaceous time (Dercourt et al., 1986) and is still occurring today at a slow rate of less than 1 cm year^{-1} (Fig. 2.1), as for much of the past 20 million years (e.g., DeMets et al., 2015). During this long-term convergence history, the Mesozoic oceanic lithosphere located between these two land masses (the "Tethyan ocean", in dark blue in Fig. 2.2) was involved in a process of north-directed subduction absorbing most of the relative plate motion through time. Because the downgoing Tethyan slab is highly sensitive to changes in absolute plate motion, and because the geodynamic forces exerted from the Gibraltar arc to the Middle East (northern Arabia) have significantly changed since ~65 Ma in relation to the progressive plate collision, a process of Tethyan slab retreat started at ~35–30 Ma in the Mediterranean (black arrows, Fig. 2.2). This process triggered a lithospheric back-arc extension in the upper plate both in the western (Liguro-Provençal, Algero-Balearic),

Oceanography of the Mediterranean Sea. https://doi.org/10.1016/B978-0-12-823692-5.00006-6

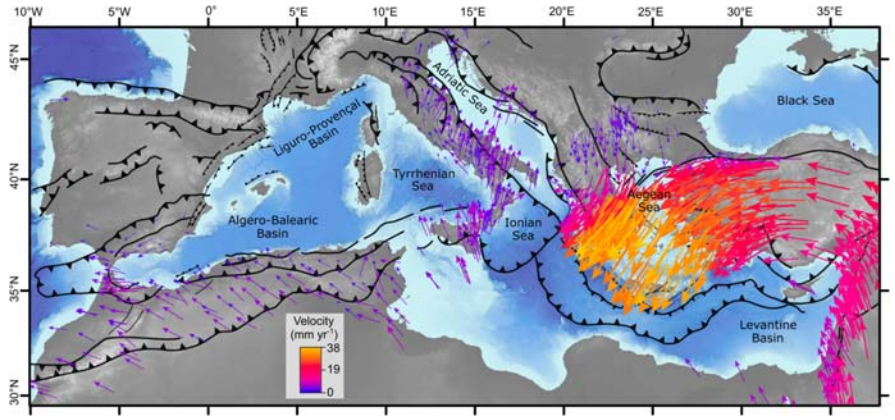

FIGURE 2.1

Velocity field of the Mediterranean realm from GPS measurements after Nocquet (2012), Bougrine et al. (2019) and Bahrouni et al. (2020). Vectors are plotted in a Eurasia fixed reference frame. Tectonic features (*black lines*) are based on Faccenna et al. (2014). Background: bathymetry (EMODnet) and topography (GEBCO) with blue and gray scales, respectively.

central (Tyrrhenian) and eastern (Aegean) domains (Jolivet and Faccenna, 2000), thus giving birth to newly-formed, relatively deep and thick sedimentary basins (Figs. 2.1 and 2.2).

In the western and central Mediterranean Sea, the slab retreat was large enough to promote not only a widespread continental rifting but also the birth of a new oceanic lithosphere forming the basement of the deep Liguro-Provençal basin as early as 18−20 Ma and of the Tyrrhenian basin in the last 5 million years (Jolivet and Faccenna, 2000). Meanwhile, the Tethyan slab was almost entirely subducted below Eurasia (Figs. 2.2 and 2.3). The early collision (docking) of Eurasian continental fragments with continental Africa to the south (namely, the Kabylian and Alboran blocks) induced a process of slab break-off: the Tethyan oceanic lithosphere detached from the African continent and slab tears propagated westward and eastward from the longitude of Lesser Kabylia, thus enhancing the birth of the narrow Algero-Balearic basin between 7 and 12 Ma and the triangular-shape Tyrrhenian basin between 5 and 0 Ma, respectively (Fig. 2.2). Note that in this evolution, the Corsica−Sardinia continental block is the largest fore-arc fragment left between two Neogene oceanic domains of different ages formed successively in response to the Tethyan slab roll-back toward the SE (Gueguen et al., 1998; Doglioni et al., 1999).

By comparison, the evolution of the eastern Mediterranean Sea appears to be strikingly different. The Tethyan slab roll-back (black arrow in Fig. 2.2) gave birth to a large area of stretched continental crust (namely, the Aegean Sea and surrounding areas), resulting from the combined effects of the south-westward retreat of the Hellenic trench and the westward displacement of the Anatolian plate along the

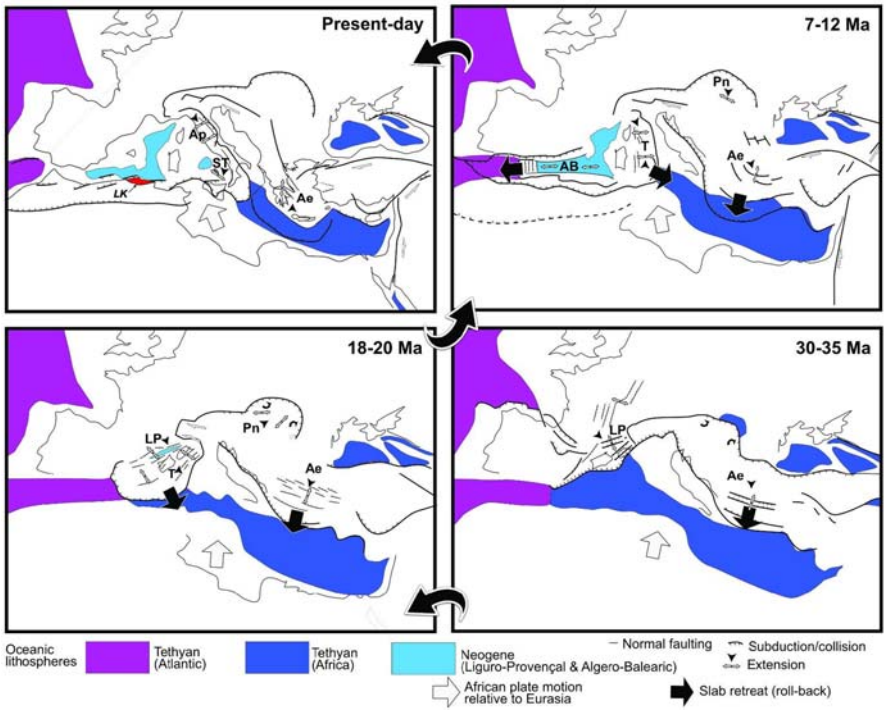

FIGURE 2.2

Reconstruction of the evolution of the Mediterranean area since Oligocene times, based on the paleotectonic reconstructions from Dercourt et al. (1986), Ricou (1994), and Jolivet and Faccenna (2000). *AB*, Algero-Balearic; *Ae*, Aegean; *LK*, Lesser Kabylia; *LP*, Liguro-Provençal; *Pn*, Pannonian; *ST*, South-Tyrrhenian *T*, Tyrrhenian.

North Anatolian Fault (Philippon et al., 2014). The Tethyan slab retreat has been a major process since Eocene times (45 Ma) that shaped the whole Aegean region and is still active today, accommodating about 700 km of trench retreat by crustal extension over a broad domain (Jolivet and Brun, 2010) and at a mean rate lower than 1 cm year^{-1} (Fig. 2.1). By contrast, the south-westward escape of the Anatolian plate started only in the Middle Miocene (ca. 13 million years ago) and has promoted the localization and propagation of the North Anatolian Fault during the last 5 Ma (Fig. 2.2), resulting into a much faster south-westward trench retreat in this last period of time (rates up to 3 cm year^{-1}; Fig. 2.1). However, the Eurasian and African plates have not reached a collisional stage yet, so that the basement of the eastern Mediterranean Sea is still today made of Tethyan oceanic lithosphere capped with a several kilometre-thick accretionary wedge, namely, the ~300 km wide and ~2000 km long Mediterranean Ridge (Kopf et al., 2003).

In summary, we emphasize that the main process responsible for shaping the whole Mediterranean area and for determining its strain distribution and style is

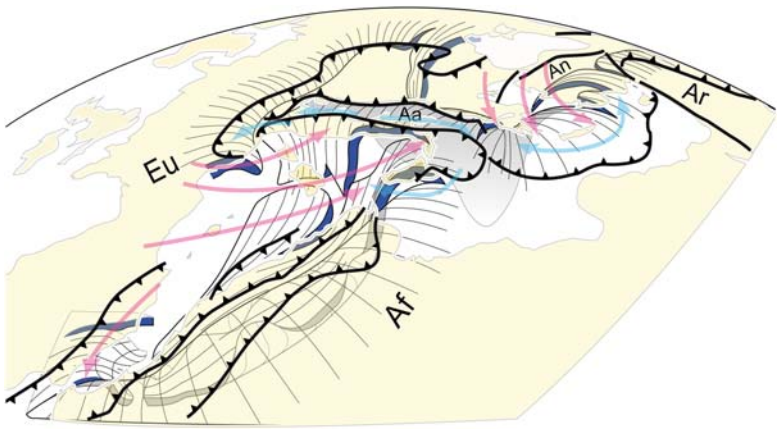

FIGURE 2.3

Schematic perspective view of the geometry at depth of Tethyan slabs under the Mediterranean area based on seismic tomography data and seismological strain indicators. Light red and blue arrows are assumed directions of mantle flow under the backarc domains and the sinking slabs, respectively. Thick black lines are main thrust faults between plates or blocks at the surface. Dark blue (or gray where hidden in the background) areas are slab slices resulting from lateral tearing (see text for details). Slab position and continuity may differ according to authors. Main plates or microplates: *Aa*, Apulo-adriatic; *Af*, Africa; *An*, Anatolia; *Ar*, Arabia; *Eu*, Eurasia.

Modified from Jolivet L., Faccenna C., Piromallo C., 2009. From mantle to crust: stretching the Mediterranean Earth Planet Sci. Lett. 198–209.

the dynamics of subduction, especially the retreat of the Tethyan slabs and the various tears that affected them (Fig. 2.3). During the last ~35 million years, the dynamics of the slabs has imposed fast (few million years) and large (several hundreds of kilometres) displacements of continental fragments, resulting into the formation of arcuate belts and deep basins. Similarly, this efficient slab dynamics also implies active asthenospheric mantle flows below the Mediterranean in the same time period (red and blue arrows in Fig. 2.3): this complex deep mantle pattern has a strong impact on the heat transfer and stress regimes, and therefore on the magmatic activity, strain distribution and location of mineral resources (Jolivet et al., 2019). Finally, it is worth to note that most of these slab motions were getting slower and slower in the last 8 million years owing to the continuation of Africa-Eurasia convergence and to the almost complete subduction of the slabs (Fig. 2.1), thus marking the increasing influence of compressional tectonics from the Gibraltar arc to the Black Sea (thick black lines, Fig. 2.3).

2.1.2 Messinian salinity crisis: an extraordinary event

For tens of millions of years, the slow convergence between the African and European plates progressively reduced the water exchange between the Atlantic Ocean and the Mediterranean Sea (Fig. 2.2). In Late Miocene (Tortonian-Messinian times), only two narrow connections remained, forming two corridors through southern Spain and northern Morocco, which are called the Betic and Rifian gateways, respectively (Benson et al., 1991). These gateways were getting narrower until they were closed about 6 million years ago, owing to the combination of tectonic contraction, westward slab retreat (Figs. 2.2 and 2.3) and glacio-eustatic sea-level fluctuations. Therefore, seawater exchange was reduced to the point that the Mediterranean waters became increasingly salty, leading to the precipitation of thick evaporite sequences (e.g., gypsum and halite) in the deep Mediterranean basin and the lower continental margins (Fig. 2.4; Roveri et al., 2014; de la Vara et al., 2015). This event is called-Messinian Salinity Crisis (MSC) and has attracted the attention of a wide community of earth and life scientists for the last 50 years (Hsü et al., 1973; Krijgsman et al., 1999; Roveri et al., 2014). The salt deposited during this event represents almost 5% of the salt volume of oceans (Ryan, 2008). This event was of short duration (5.96−5.33 Ma; Krijgsman et al., 1999) and had important biological, chemical and sedimentary consequences in the Mediterranean area (CIESM, 2008; Roveri et al., 2014). The North Atlantic hydrography and climate were also significantly impacted, and the exchange of water, heat, nutrients, and salt was deeply altered.

The onset of the MSC is dated at ca. 6.0 Ma and is synchronous over the entire Mediterranean Sea (Krijgsman et al., 1999; Roveri et al., 2014, Fig. 2.4A). A first modest fall in Mediterranean water level likely enhanced the deposition of marginal evaporites before ∼5.6 Ma (Clauzon et al., 1996). Between ∼5.6 and ∼5.3 Ma, the isolation from the Atlantic Ocean triggered a large sea-level fall followed by erosion and deposition of nonmarine sediments in a "Lago Mare" (Lake Sea) basin (Krijgsman et al., 1999). This succession of paleo-environmental changes, although occurring in a short time span (less than 700,000 years), left impressive imprints in the geological record both onshore and offshore, such as various types of evaporites (the Messinian "trilogy," Fig. 2.4A) or other specific sedimentary units, large erosional surfaces over long distances across and along the continental margins, and numerous stratigraphic relationships reflecting sea-level fluctuations and isostatic adjustments (CIESM, 2008; Govers et al., 2009; Lofi et al., 2011; Andreetto et al., 2021). Since the 70s, numerous seismic reflection profiles shot in the whole Mediterranean Sea have evidenced in a spectacular way the importance of the footprint of the MSC and the peculiar behavior of the Messinian salt, which tends to deform by ductile flow under differential tectonic or sedimentary loadings (Fig. 2.4B; Lofi et al., 2011, 2018, and references therein). However, the lack of deep drilling throughout the evaporites deposited in the deep basins and of complete and geometrically connected stratigraphic records has hampered until now a fully acknowledged assessment of land-sea correlations. Consequently, many scenarios about the causes, the progression or the timing of the MSC still remain controversial.

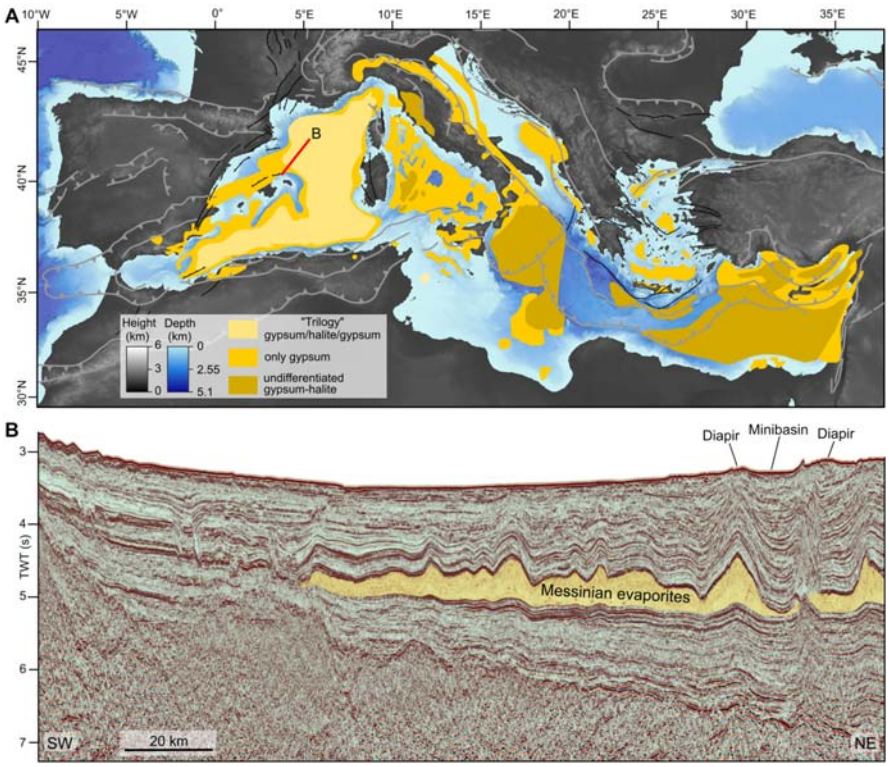

FIGURE 2.4

(A) Distribution of Messinian evaporites from the compilation by Roveri et al. (2014); modified from Rouchy and Caruso (2006) and Manzi et al. (2012). Tectonic features are based on Jolivet et al. (2020). Background: bathymetry (EMODnet) and topography (GEBCO) with blue and gray scales, respectively. (B) Seismic reflection profile along the Provencal basin (NW Mediterranean Sea) showing the Messinian evaporites (yellow polygon), which is a mobile unit and generated diapirs that are still visible at the present-day seafloor.

2.2 Dimensions and seafloor topography

The Mediterranean Sea has an area of about 2,470,000 km^2, an average depth of approximately 1500 m and a maximum depth of 5267 m at the Calypso Deep, in the Hellenic trench (Fig. 2.5). To the west, the Mediterranean Sea is connected to the Atlantic Ocean through the Strait of Gibraltar, which is 14.4 km wide at its narrowest zone and has a minimum depth of 170 m at the Camarinal Sill (Fig. 2.6). It is connected to the Marmara Sea in its NE part through the Dardanelles Strait, which has a minimum width of 1.2 km and an average depth of 55 m. The Mediterranean Sea is bounded in its northern part by southern Europe and Anatolia, to the south by North Africa, to the east by the Levant region and to west by the Iberian Peninsula (Fig. 2.5).

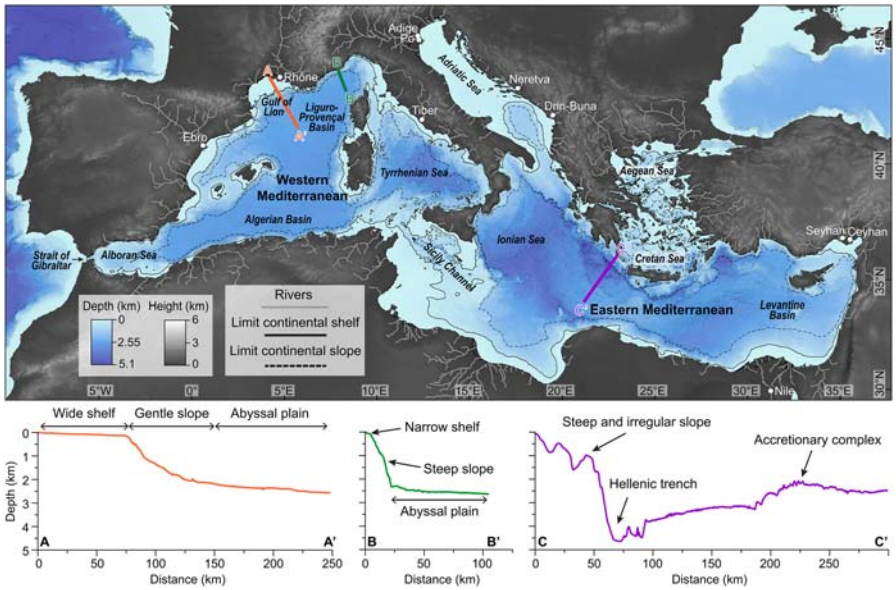

FIGURE 2.5

Bathymetric and topographic map of the Mediterranean Sea showing the main basins, subbasins, straits, main rivers flowing into the Mediterranean Sea (FAO GeoNetwork derived from HydroSHEDS), and the main morphology of continental margins represented by three bathymetric profiles. The *black solid line* indicates the limit between the continental shelf and the continental slope, while the *black dashed lines* indicate the limit between the continental slope and the abyssal plain (from Harris et al., 2014). The datasets used for the bathymetry and the topography are EMODnet and GEBCO, respectively.

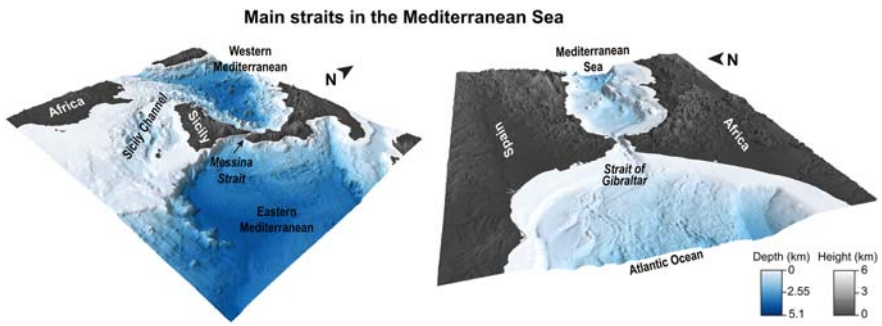

FIGURE 2.6

3D bathymetric and topographic maps of the main straits in the Mediterranean Sea (EMODnet bathymetry and GEBCO topography). Vertical exaggeration x10.

The Mediterranean Sea can be divided into two basins, the Western Mediterranean Sea and the Easter Mediterranean Sea, separated by the Sicily Channel and the Messina Strait (Figs. 2.5 and 2.6). The Sicily Channel is located between Tunisia and Sicily and has a minimum width of 145 km. The Adventure Bank is located in the NE part of the strait and has depths often above 200 m. The minimum depth at the narrowest part of the strait is about 600 m. In contrast, the Messina Strait is narrower and shallower separating Sicily from the continent. The Messina Strait is ca. 3 km wide at its narrowest point and has a minimum depth of 60 m at its sill.

Both Western and Eastern Mediterranean basins can be subdivided into different subbasins (Fig. 2.5). The main subbasins of the Western Mediterranean Sea are the Alboran Sea at its westernmost part, the Algero-Balearic Basin in the southern central part, the Gulf of Lion and the Liguro-Provençal Basin in the northern part, and the Tyrrhenian Sea in the eastern part (Fig. 2.5). The main subbasins of the Eastern Mediterranean Sea are the Adriatic Sea in the north western part, the Aegean Sea in the north-eastern part, the Ionian Sea to the Southwest and the Levantine Basin to the Southeast (Fig. 2.5).

The complex geological history of the Mediterranean Sea resulted in a very heterogeneous morphology of the seafloor. In general, continental margins are composed of: (i) a continental shelf that is a relatively flat surface gently dipping basinwards, (ii) the abyssal plain that corresponds to the deepest part of the basin, and (iii) the continental slope that is the steep zone that connects the continental shelf and the abyssal plain (Fig. 2.5). In the zones with passive continental margins (i.e., not in an active plate margins), such as in the Western Mediterranean Sea, the transition from the slope to the abyssal plain is gentle and continuous (Fig. 2.5).

Continental shelves represent a total area of 549,066 km^2 in the Mediterranean Sea. They have an average water depth of 88 m and an average slope of 0.6 degrees. The width of the continental shelf is very variable, in some areas such as in the Ligurian margin (SE France), along Algeria, Calabria, Creta or SW Anatolia, the continental shelf is almost absent and the continental slope practically reaches the coastline (Fig. 2.5). In contrast, other areas present wide continental shelves, for instance, reaching up to 70 km in the eastern Iberian Peninsula, up to 90 km in the Gulf of Lion, up to about 200 km off eastern Tunisia, and covering most part of the Adriatic Sea (Fig. 2.5).

Continental slopes in the Mediterranean Sea cover a total surface of 780,749 km^2, with a mean depth of 989 m and a mean slope of 3.6 degrees. The extension, morphology, and steepness of the slope are very variable, and it depends on the structure of the margin that is controlled by tectonic processes and on sediment accumulation. These processes will be explained more in detail in the next section. In zones with relatively abundant sediment supply from the coast through sedimentary gravity-driven processes, continental slopes are typically graded (sensu Mosher et al., 2017) and present a smooth exponential decay shape. This shape corresponds to the long-term equilibrium between erosional and depositional sedimentary processes (Mosher et al., 2017; Prather et al., 2017). This type of slope is, for example, characteristic of the Gulf of Lion, where sediment has been transported

downslope through submarine canyons over time (Fig. 2.5). In zones dominated by mass-wasting processes and sediment by-pass, little sediment is deposited on the slope. As a consequence, the slope is steep and typically characterized by an out-of-grade profile, as for instance in the Ligurian margin (Fig. 2.5). In areas where currents preferentially accumulate sediment, continental slopes can have an above-grade slope, which corresponds to a convex morphology. This type of slope profile can be observed in many areas of the Mediterranean Sea, such as in the Alboran Sea (Ercilla et al., 2016), the northern Tyrrhenian Sea (Miramontes et al., 2019), the Messina Strait (Viana et al., 1998), the Sicily Channel (Gauchery et al., 2021a, b), and the southern Adriatic Sea (Pellegrini et al., 2016).

Abyssal plains of the Mediterranean Sea correspond to a total area of 1,159,644 km^2 and have a mean depth of 2534 m and a mean slope of 2.6 degrees. In areas where abyssal plains are mainly covered by sediment, they correspond to very flat surfaces with slopes usually below 1 degree, such as in the Liguro-Provençal and Algerian Basins (Fig. 2.5). However, topographic changes are also common in abyssal plains. The Tyrrhenian Sea contains abundant seamounts that can elevate up to 2500 m from the seafloor and have steep slopes, often of more than 20 degrees (Fig. 2.7). Particular rounded topographic highs can be found in the abyssal plain of the Liguro-Provençal Basin. They have diameters of several kilometres and they can elevate more than 100 m from the seafloor (Figs. 2.4 and 2.7). These features correspond to salt diapirs that originate from the evaporites deposited during the MSC (Fig. 2.4B).

In contrast to continental slopes of passive margins, in active continental margins such as in the Hellenic Arc, the morphology of the seafloor is much rougher and is mainly controlled by tectonic processes. In this area, the slope is very steep (commonly above 20 degrees) and irregular (Fig. 2.5). In the Hellenic Arc, the subduction of the African Plate below the Aegean Sea Plate results in the formation of the Hellenic trench (Kopf et al., 2003) that is a topographic depression that corresponds to the deepest part of the Mediterranean Sea with maximum water depths of about 5100 m (Figs. 2.5 and 2.7). In the zone located basinward of the oceanic trench, the seafloor becomes shallower and presents a mounded morphology with an arcuate shape in plain view that corresponds to the Mediterranean Ridge accretionary complex and that formed from sediments accreted onto the Aegean Plate during the subduction (Kopf et al., 2003). The water depth of this area oscillates between 1500 and 3500 m (Figs. 2.5 and 2.7).

2.3 Sedimentation on continental margins

Continental margins comprise the interface between land and deep-ocean systems. The sediments deposited in oceanic basins are mainly originated by weathering and erosion of rocks on land that are transported by different processes (wind, water, or ice), and that end their transport and are finally deposited in the ocean floor (Fig. 2.8). Rivers deliver 84% of the total sediment load that reaches the oceans

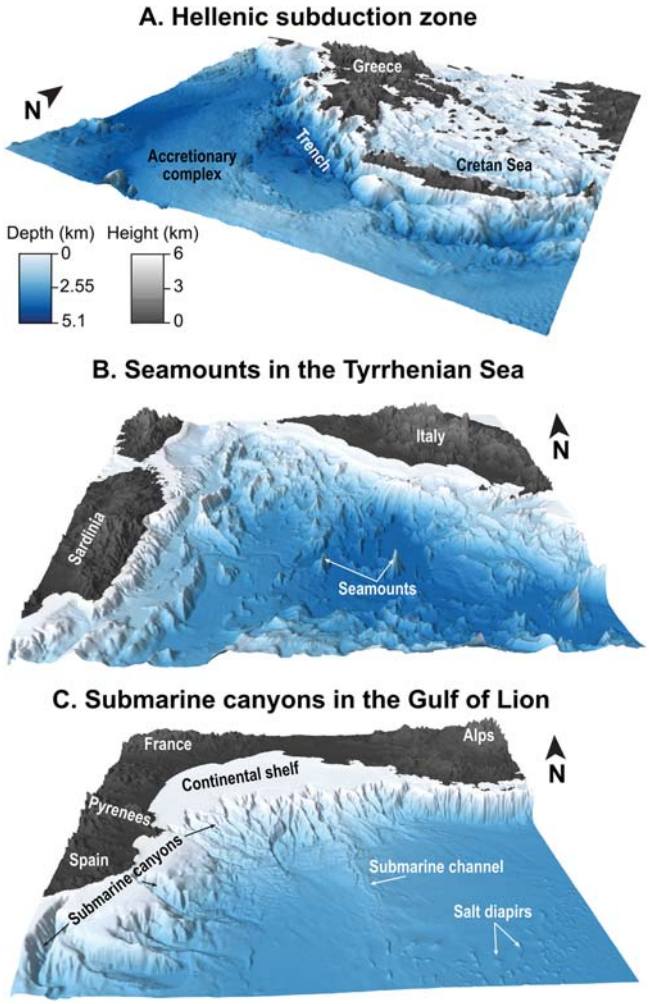

FIGURE 2.7

3D bathymetric and topographic maps showing three different seafloor morphologies: (A) Hellenic subduction zone; (B) Seamounts in the Tyrrhenian Sea; (C) Submarine canyons in the Gulf of Lion. The datasets used for the bathymetry and the topography are EMODnet and GEBCO, respectively. Vertical exaggeration $\times 10$.

(Milliman and Meade, 1983) and are the dominant means by which clastic sediments are transported to continental margins worldwide. The drainage basin of the Mediterranean rivers stretches over ca. two million km^2 (Struglia et al., 2004), and up to five million km^2 when considering the Nile catchment (Ludwig et al., 2009). In terms of discharge, the 10 largest rivers in the Mediterranean Basin are the Rhône, Po, Drin-Buna, Nile, Neretva, Ebro, Tiber, Adige, Seyhan and Ceyhan rivers

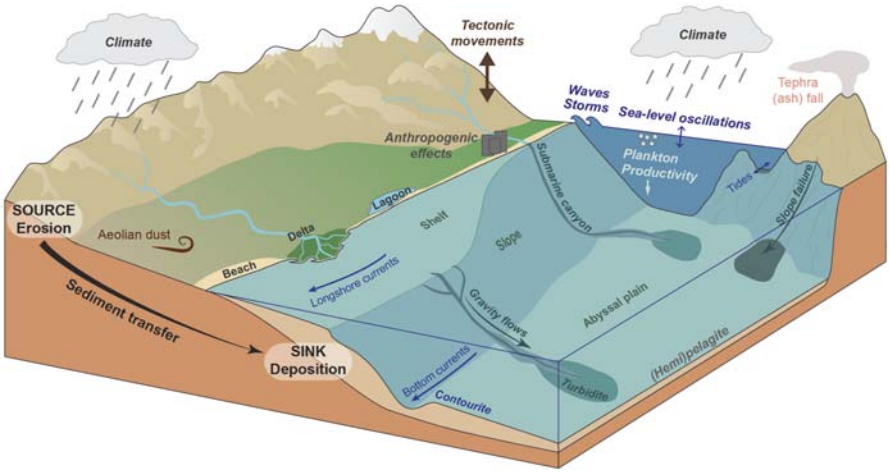

FIGURE 2.8

Schematic representation of a source-to-sink system, indicating the main depositional coastal and marine environments and processes controlling sedimentation.

(Fig. 2.5; Ludwig et al., 2009). Seven of these rivers are located in the northern Mediterranean countries, two in the eastern Mediterranean (Turkey) and one (the Nile) in the southern part of the Mediterranean area (Fig. 2.5). Large individual Mediterranean rivers often deliver the sediment in combination with smaller rivers: where multiple rivers feed a margin, they combine to form a line source sediment input (sensu Jaeger and Nittrouer, 2000). Examples of depositional systems nourished by line source sediment inputs are the Iberian margin with the Ebro River and the Iberian rivers (e.g., Fernández-Salas et al., 2003; Liquete et al., 2009), the Gulf of Lion with the Grand and Petit Rhône, Marti and Herault rivers (Palanques et al., 2006), the Adriatic margin, with the Po River and the Appennine rivers (Cattaneo et al., 2003; Pellegrini et al., 2015). In these systems, steep rivers with relatively small extent can deliver large quantities of sediment into the sea (e.g., Pellegrini et al., 2021). Total riverine freshwater flux into the Mediterranean is about 450 km^3 $year^{-1}$ (Vörösmarty et al., 1998; Jaoshvili, 2002), corresponding to an average sediment load of 1×10^9 t $year^{-1}$ (Poulos and Collins, 2002). The seasonal distribution of discharge is highly variable depending on the climate of the river basins. Due to the Mediterranean climate, precipitation is mostly available for river discharge during autumn, winter and spring. Some Mediterranean rivers have an ephemeral or intermittent character (Struglia et al., 2004; Argyroudi et al., 2009). Dam construction since the post II Global War has strongly reduced the flux of sediment reaching the Mediterranean coasts with the retention in reservoirs (Syvitski and Kettner, 2011).

Part of the sediment carried by rivers is deposited in coastal environments (e.g., beaches, deltas and lagoons) and on the continental shelf (Fig. 2.8), and part of it is

transported further into the basin floor defining an overall irregular profile of the continental margin characterized by the presence of multiple rollover points (Fig. 2.9; Pellegrini et al., 2020). These rollover points are morphological breaks in slope formed at depths that are governed by the sediment supply and the oceanographic regime (e.g., wave and storm wave base, ocean currents; Gamberi et al., 2020; Patruno et al., 2020). Most important rollover points on the shelf are those related to river delta clinoforms deposits and governed by wave- and fair weather wave-base (Fig. 2.9; Swenson et al., 2005). The depth of rollover points is assumed to reflect the seaward limit beyond which wave-current shear stress decreases allowing

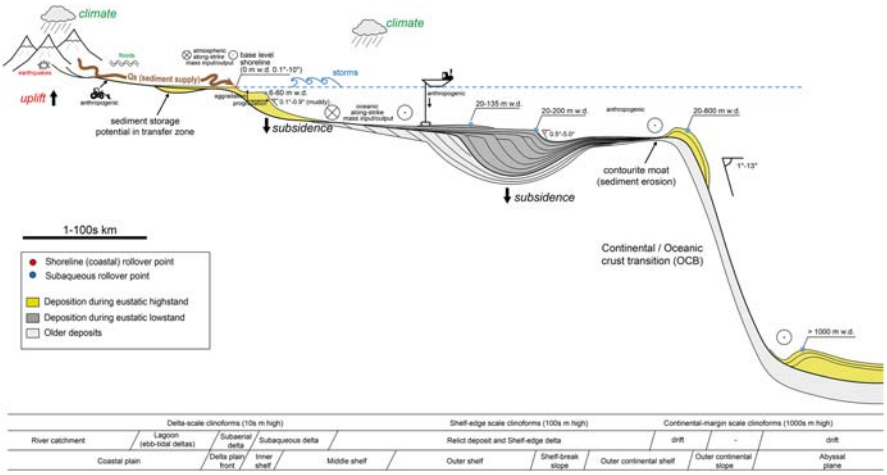

FIGURE 2.9

Sketch of sediment transport from the catchment area to the deepest part of an idealized continental margin . Climate, tectonic and anthropogenic forcing determines the fate of sedimentary particles both onshore and offshore. Bottom currents reshape margin deposits, such as delta and drift deposits at different water depths. Yellow lithosomes represent sectors where sedimentation is operating, whereas gray liposomes were deposited during earlier glacio-eustatic cycles. The water depth of the several breaks in slope (or rollover-points) is mainly governed by the interplay between tectonic, sediment supply and oceanographic regime.

Modified after Romans, B.W., Castelltort, S., Covault, J.A., Fildani, A., Walsh, J.P., 2016. Environmental signal propagation in sedimentary systems across timescales. Earth Sci. Rev. 153, 7–29 and based on Pellegrini, C., Bohacs, K. M., Drexler, T. M., Gamberi, F., Rovere, M., Trincardi, F., 2017. Identifying the sequence boundary in over-and under-supplied contexts: the case of the late Pleistocene adriatic continental margin. In: Sequence Stratigraphy: The Future Defined, Proceedings of the 36th Annual Perkins-Rosen Research Conference, pp. 160–182, Pellegrini, C., Asioli, A., Bohacs, K. M., Drexler, T. M., Feldman, H. R., Sweet, M. L., Trincardi, F., 2018. The late Pleistocene Po River lowstand wedge in the Adriatic Sea: controls on architecture variability and sediment partitioning. Mar. Petrol. Geol. 96, 16–50, Pellegrini, C., Patruno, S., Helland-Hansen, W., Steel, R. J., Trincardi, F., 2020. Clinoforms and clinothems: fundamental elements of basin infill. Basin Res. 32, 187–205.

finer-grained sediment deposition (e.g., Trincardi et al., 2020). Beside, at the outer shelf, the main rollover point coincides with the shelf-break usually swift by bottom currents (currents flowing near the seafloor; e.g., Pellegrini et al., 2017, 2018; Rovere et al., 2019) (Fig. 2.9), and in the Mediterranean Sea, present between 120 m and 180 m water depth (Fig. 2.5).

In addition to the terrigenous sediment transported from land by rivers, other types of sediments are also relevant in the Mediterranean Sea: biogenic sediments, evaporites, aeolian dust, and volcanic ash (Fig. 2.8). Moreover, at present anthropogenic particles, such as microplastics are also very common within the Mediterranean Sea at all water depths, from coastal areas (Constant et al., 2019) to the deep sea (Woodall et al., 2014; Kane et al., 2020), with physiographic elements (e.g., gateways and straits) potentially playing a key role in their distribution (Chiarella and Hernández-Molina, 2021). In the Mediterranean Sea, the carbonate production in coastal areas is dominated by red algae and seagrass-derived bioclastic grains (Michel et al., 2018). Biogenic production also occurs in the water column and is carried out by planktonic organisms (e.g., coccolithophorids, foraminifera, pteropods). In the zones far from the coast, these organisms can be accumulated at the seafloor in high proportions, and when the biogenic material constitutes >75% of the total sediment, the deposit is considered pelagic sediment (Hüneke and Henrich, 2011). Locally, terrigenous and biogenic production can accumulate together forming compositional or stratigraphic mixing (sensu Chiarella et al., 2017). Although no major evaporitic deposits are being formed at present in the Mediterranean Sea, these sediments are common in the Mediterranean Basin and were mainly formed during the MSC (5.96−5.33 Ma ago), as explained in detail above. Aeolian dust can be transported to the Mediterranean Sea directly from source areas in North Africa during occasional dust storms, but most of the dust supply occurs more continuously by indirect transport (Tomadin and Lenaz, 1989). In areas of the seafloor with low direct sediment supply from the continent, such as in the central Tyrrhenian Sea, aeolian dust can constitute a significant component of the seafloor sediments (Tomadin and Lenaz, 1989). Accumulation of volcanic ashes (tephra layers) in the seafloor of the Mediterranean Sea is also common due to the high abundance of active volcanoes, especially in the Italian and Aegean volcanic provinces (Fig. 2.8; Narcisi and Vezzoli, 1999). The explosive character of the volcanic activity and the distinctive composition of the volcanic ashes from the different volcanic provinces permits to identify the origin of the tephra layers deposited on the Mediterranean seafloor. When the age of the tephra deposits is dated, these distinct deposits can be used as an age marker in stratigraphic sections, a technique named *tephrochronology* (Narcisi and Vezzoli, 1999).

Two of the main factors controlling the evolution of sedimentation are tectonic processes and climate (Fig. 2.8). These processes affect weathering and erosion, and thus the production of sediment at the source, but also the transport of sediment and its final deposition. Tectonic movements and climate act at different time-scales and we will discuss them here separately.

2.3.1 Tectonic movements and sedimentation

As we briefly introduced in the previous section, the topography of the seafloor is affected by tectonic processes that control the main structure of the basin, but seafloor topography also strongly changes spatially and temporally with sedimentation. Sediments can be accumulated in zones where there is enough accommodation available. The term accommodation refers to the volume that can be potentially filled by sediment until it reaches the maximum theoretical surface in which no more sediment can be accumulated because this limit-surface is in equilibrium between sediment deposition and erosion. In marine environments, this limit mainly corresponds to the wave-base in clastic systems and the sea level in carbonate ones (Pomar and Kendall, 2008). The accommodation in shallow marine environments is affected by relative sea-level fluctuations, including eustatic sea-level changes and changes related to tectonic processes (i.e., reduction due to tectonic uplift and increase due to subsidence).

Tectonic activities might control the morphology and position of continental margins, as well as, the formation and evolution of straits. In tectonically controlled straits (e.g., Gibraltar, Korinthos and Messina), margins are typically characterized by high-gradient scarps. Along the scarps, gravity-controlled systems (e.g., base-of-scarp, Gilbert- and/or Shelf-deltas) represent the main entry-points for sediment, producing wedge-shaped deposits that can be reworked by tidal-currents (Fig. 2.10; Chiarella et al., 2020; Longhitano et al., 2021a).

Tidal currents are commonly locally amplified due to the restriction of the hydraulic cross section controlling sedimentation even in microtidal environments such as the Mediterranean Sea (Fig. 2.10; Longhitano and Chiarella, 2020). Recent studies (Chiarella et al., 2012, 2016; Longhitano, 2013; Longhitano et al., 2014, 2021b; de Weger et al., 2021) on ancient and present-day Mediterranean straits provide a good understanding of sediment distribution. In particular, four main depositional zones (strait-margin, strait-center, dune-bedded, and strait-end) have been recognized and described based on tidal current velocity, bed-shear stress and grain-size (see Longhitano and Chiarella, 2020 for further information; Fig. 2.11).

The shallowest area of straits (i.e., sill) corresponds to the narrowest strait cross section and the point of tidal maxima (i.e., the point where tidal currents reach their peak velocity) (Harris et al., 1995; Holleman and Stacey, 2014). Accordingly, the strait-center zone is the most energetic environment and the ones mainly characterized by erosion with sediments deposited in slightly deeper areas of the strait. Bedforms, such as ripples and dunes are commonly formed by tidal currents within straits in the dune-bedded and strait-end zones, respectively (Fig. 2.11; Longhitano et al., 2014; Longhitano and Chiarella, 2020). It has also been suggested that internal solitary waves formed in the Messina Strait could be also responsible for the formation of sand dunes (Droghei et al., 2016).

Since the Late Miocene, tectonic movements have induced large changes in the physiography, position and opening/closure of Mediterranean Sea straits. For example, during the Late Miocene the Atlantic-Mediterranean connection consisted

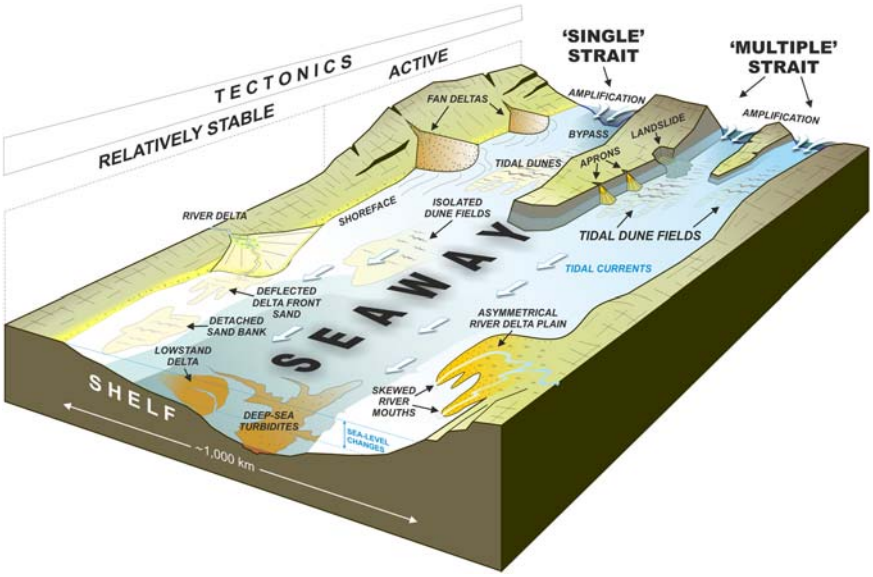

FIGURE 2.10

Sketch summarizing the typical sedimentary deposits found on straits, including tidal deposits.

From Longhitano, S.G. and Chiarella, D. (2020). Tidal straits: basic criteria for recognizing ancient systems from the rock. In: Regional Geology and Tectonics, Vol 1: Principles of Geologic Analysis (Eds Scarselli, N., Adam, J., Chiarella, D., Roberts, D.G. and Bally, A.W.). Elsevier, Amsterdam, Netherlands, Ch. 15, 365–415. https://doi.org/10.101/B978-0-444-64134-2.00014-6.

of a multiple-strait system composed by the "Betic Corridor" in the zone now located in SE Spain, the Gibraltar Strait and the "Rifian Corridor" located in the present-day northern Morocco (Krikgsman et al., 2018). The deposits formed in this palaeo-gateway exhibit sand dunes and coarse-grained sediments that indicate that they have been formed under intense currents (Martín et al., 2014; de Weger et al., 2020, 2021). Similarly, during the Quaternary multiple tectonically controlled straits (i.e., Catanzaro, Siderno, and Messina straits) related to an extensional phase interesting the Calabrian Arc (southern Italy) connected the Tyrrhenian and Ionian seas. Today, only the Messina Strait is still open while the uplift of the Calabrian Arc closed the Catanzaro and Siderno connections exposing the deposits of these ancient straits as well as the ancient counterpart of the Messina Strait (Chiarella et al., 2012; Longhitano et al., 2014; Rossi et al., 2017; Longhitano, 2018). Deposits pertaining to these ancient straits represent the analogues to the modern Messina Strait deposits and contain abundant sand dunes related to tidal processes (Longhitano and Chiarella, 2020 and references therein).

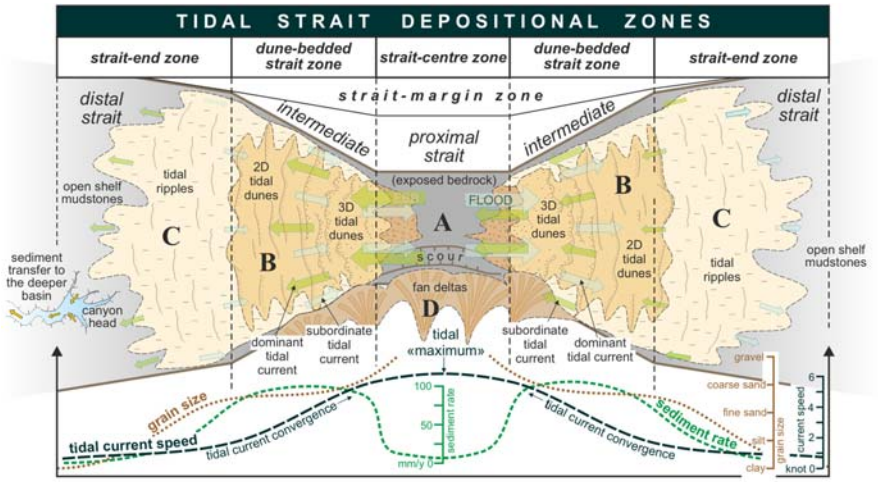

FIGURE 2.11

Schematic representation of tidal Straits depositional zones.

From Longhitano, S.G. and Chiarella, D. (2020). Tidal straits: basic criteria for recognizing ancient systems from the rock. In: Regional Geology and Tectonics, Vol 1: Principles of Geologic Analysis (Eds Scarselli, N., Adam, J., Chiarella, D., Roberts, D.G. and Bally, A.W.). Elsevier, Amsterdam, Netherlands, Ch. 15, 365–415. https://doi.org/10.101/B978-0-444-64134-2.00014-6.

In zones of relatively intense tectonic activity, earthquakes can often destabilize the seafloor and trigger sediment failures. Urgeles and Camerlenghi (2013) showed that in the Mediterranean Sea slope failures are smaller but more abundant in tectonically active margins (e.g., Algeria, Liguria, Gulf of Corinth, Aegean, and Northern Anatolian margins) than in passive margins (e.g., NW Mediterranean Sea). Earthquakes and submarine landslides can also trigger tsunamis producing peculiar deposits along the coast and in the basin floor. Although geological evidence of tsunamis has been observed in most of the Mediterranean margins, the main tsunamigenic structures are found around Sicily and in the Hellenic Arc (Scardino et al., 2020). Tsunami events in the Mediterranean Sea can be identified on coastal environments by washover fans and mega-boulder accumulations, anomaly coarse sediments in coastal plain and shelf deposits (Scardino et al., 2020). Tsunamis have also been suggested to be at the origin of large deposits found in abyssal plains of the Mediterranean Sea and known as homogenites (Cita, 2021). Homogenites are structureless homogeneous accumulations of silty clay without microfossils and are suggested to be formed by the liquefaction hemipelagic sediments or by turbidites triggered by tsunami waves (Cita, 2021). Turbidites are deposits related to turbidity currents that are gravity-driven flows in which sediment suspension is supported by turbulence (Middleton, 1993).

2.3.2 Climate and sedimentation

Climate can directly affect sediment generation and sedimentary processes, for instance, by controlling the humidity and the vegetation cover, which have strong implications for mechanical and chemical weathering, and erosion. It thus directly controls the production and transport of sediment by glaciers, rivers and wind. For instance, centennial to millennial scale fluctuation of sediment accumulated in the basin during the Last Glacial Maximum have been linked to high frequency fluctuations of glacier advance and retreat in the Alpine and Apennine catchments (Pellegrini et al., 2018). In the Mediterranean Sea, aeolian transport was enhanced during cold and arid periods of time (Dinarès-Turell et al., 2003). Climate can also affect oceanographic conditions and relative sea level, and thus alter marine primary productivity, the capacity of erosion and transport of currents and waves, and change the position of the shoreline and relative connection with the sources of sediment located onshore.

Changes in past climatic and oceanographic conditions are registered in the marine sedimentary record. For instance, a very particular phenomenon of the Mediterranean Sea is the periodic development of anoxic events that resulted in the formation of organic rich sediment layers, known as sapropels (Rohling et al., 2015). The high amount of organic carbon present in these layers gives them their characteristic dark color (Fig. 2.12). Sapropels occurred periodically in the Mediterranean Sea during the last 13.5 million years and were more abundant and often more developed in the Eastern Mediterranean Sea than in the Western Mediterranean Sea (Rohling et al., 2015). Sapropels formed during periods characterized by a strong surface buoyancy gain that resulted in a reduction of deep-water ventilation, that is, in a decrease in oxygen content near the seafloor. These episodes corresponded to periods of monsoon intensification that resulted in higher river runoff from North Africa and thus in a decrease in the density of surface waters (Fig. 2.12). The frequency of these events is approximately 21,000 years because the Earth's precession cycles have a strong influence on the African monsoon. Other factors such as regional precipitation, relative sea-level rise or the input of meltwater during deglaciations (especially in the Western Mediterranean Sea) were also important for a progressive surface-water buoyancy gain and for preconditioning the deposition of sapropels. The extension and frequency of sedimentation under anoxic conditions was not homogeneous, and it depended on basin physiography, regional properties of the oceanic circulation, local ecology, and biogeochemistry (Rohling et al., 2015; Tesi et al., 2017). Changes in the circulation of the Mediterranean Sea influenced by the African monsoon also affected the intensity of the Mediterranean Outflow Water (MOW) and the circulation in the Atlantic Ocean. The MOW was weaker during periods of summer insolation maxima due to enhanced runoff into the Mediterranean Sea and the reduction of the formation of Levantine Intermediate Water (Bahr et al., 2015).

Climate does not only affect the ventilation of deep waters in the Mediterranean Sea, but it also controls circulation and sedimentation at all water depths. During

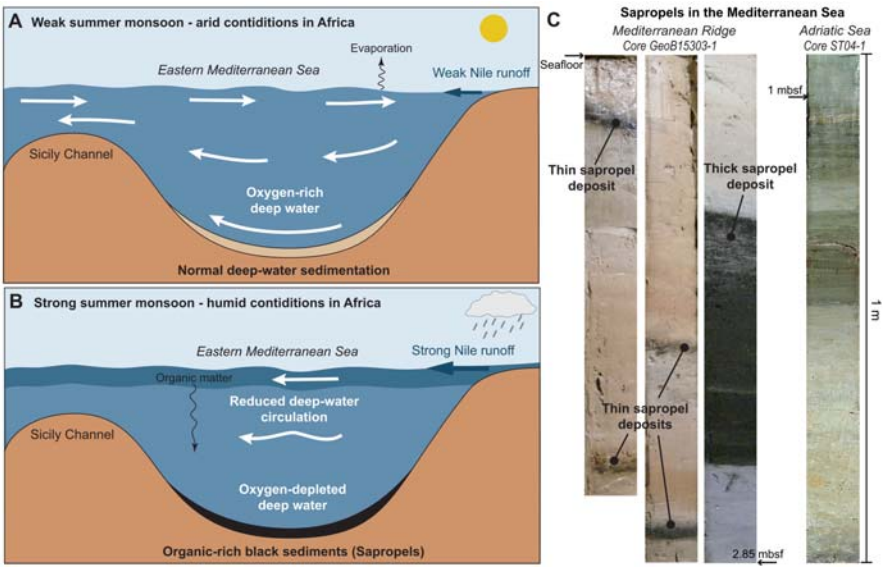

FIGURE 2.12

Effects of climate on sedimentation in the Eastern Mediterranean Sea: (A) Deposition of normal deep-water sediments during periods of weak summer monsoon and arid conditions in Africa (present-day situation); (B) Deposition of organic rich black sediments (sapropels) during periods of strong summer monsoon and humid conditions in Africa. (C) Photos of sediment cores showing the presence of sapropels that are characterized by dark color: GeoB15303-1 collected during the POS410 cruise in the Eastern Mediterranean Sea, on the Mediterranean Ridge accretionary wedge south of Creta (Kopf and Cruise Participants, 2012), and ST04-1 collected in the SW Adriatic Sea (Tesi et al., 2017).

(B) Adapted from Ruddiman, W.F., 2013. Earth's Climate: Past and Future, third ed. W. H. Freeman and Company, New York, p. 445.

cold periods, stronger north-westerlies wind enhanced deep-water formation in the Western Mediterranean Sea, favoring the degradation of organic matter in well-ventilated deep waters (Cacho et al., 2000). Intermediate waters were also faster and better ventilated during cold periods and resulted in the deposition of coarser sediments on the seafloor of the northern Tyrrhenian Sea and Sicily Channel related to the Levantine Intermediate Water and in the Gulf of Cadiz related to the MOW (Toucanne et al., 2012; Bahr et al., 2014; Miramontes et al., 2016; Gauchery et al., 2021b).

Sedimentation along continental margins is the result of a complex interaction between different processes and does not always only depend on oceanographic conditions. Sediment accumulation rates and the architecture of the sediment deposits are mainly the result of a balance between sediment supply and intensity of currents. In zones with high sediment input, gravitational processes usually dominate

sedimentation. Nevertheless, these processes are not continuous over geological time scales and are strongly affected by relative sea-level fluctuations (Fig. 2.13). The effect of sea level is especially evident on continental margins with a large continental shelf. During sea-level lowstands, the coast is located close to the shelf-edge promoting the delivery of high amounts of terrigenous sediment to the slope and deep-sea sectors (Fig. 2.13). This sediment commonly feeds submarine canyons and is transported downslope by gravitational processes, such as turbidity currents. Many turbidite systems of the Mediterranean Sea were active during sea-level lowstands because the continent was closer to the slope, favoring the downslope transport of terrigenous sediments by gravity-driven processes. On the contrary, during sea-level highstands, most of the terrigenous sediment stays on the continental shelf and does not reach the slope, and thus the activity in many turbidite systems decreases, especially in zones with wide continental shelves (Fig. 2.13). This relationship between sea level and frequency of turbidites was for instance observed in the Rhône turbidite system in the Gulf of Lion (Lombo Tombo et al., 2015), in the Golo turbidite system in the northern Tyrrhenian Sea (Calvès et al., 2013; Sweet et al., 2020), as well as in the central Adriatic Basin (Pellegrini et al., 2017, 2018). In zones of narrow continental shelves, the transfer of sediment from the continent to the deep sea is more continuous. In these cases, since sea level has a weaker effect on the activity of turbidite systems, the sediments carried downslope by turbidity currents may reflect better climatic changes. The Var turbidite system located in the Ligurian margin and fed by the Var River that transports sediment from the Southern French

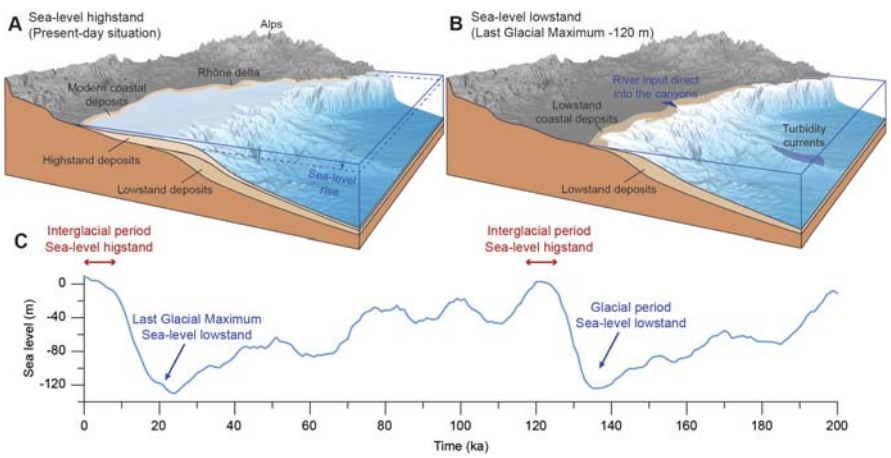

FIGURE 2.13

Simplified sketch of the changes in the position of the coastline and of the sedimentary deposits in the Gulf of Lion during sea-level highstand (A) and lowstand (B), showing the effect of sea-level changes on sedimentation. (C) Global sea-level curve for the last 200 ka (Spratt and Lisiecki, 2016). Note that during sea-level low-stands the shore line is close to the continental slope, favoring the transfer of sediment directly to the deep sea.

Alps recorded higher sediment fluxes during the Last Glacial Maximum because glaciers induced higher denudation rates than rivers. Therefore, the amount of sediment reaching the basinal depositional areas can strongly depend on the presence of glaciers in the mountain region (Bonneau et al., 2017).

2.4 Concluding remarks

The Mediterranean Sea formed after the closure of the Tethys Ocean and by the collision between the Africa (Nubia) and the Eurasia plates that began in the Late Cretaceous time. The collision between both plates is still active at present, with the fastest movements at the Hellenic arc and Anatolia. In contrast, other zones of the Mediterranean Sea, such as the NW Mediterranean Sea, are at present almost tectonically inactive. These differences in the tectonic setting result in an important diversity of seafloor physiography in the Mediterranean Basins. Continental slopes along active margins are typically steeper and deeper than in passive margins. In active margins, an accretionary wedge can be found in the abyssal plain, generating a convex topographic high that is separated from the continental slope by the trench.

Sedimentation in the Mediterranean Sea is mainly controlled by tectonic processes that affect the long-term deposition, and by climate, which can influence sedimentation at different time-scales. Climate also affects the circulation and thus the sedimentation related to currents (e.g., contourites). Some particular events that affected the circulation in the Mediterranean Sea were recorded in sediments. During the Messinian (from 5.96 to 5.33 Ma, Late Miocene), the Mediterranean Sea was almost desiccated due to the closure of the Strait of Gibraltar, resulting in the deposition of large amounts of evaporites in the Mediterranean basins. Another particular deposit of the Mediterranean Sea are sapropels, which are marine sediments that contain large amounts of organic matter. These sediments were formed during periods of limited ocean circulation and ventilation that resulted in the reduction of oxygen availability in the deep waters. They occurred with a frequency of 21,000 years and were related to changes in the freshwater inputs to the Mediterranean Sea.

Additional resources

- EMODnet Bathymetry https://www.emodnet-bathymetry.eu/
- EMODnet Geology https://www.emodnet-geology.eu/
- CIESM, The Mediterranean Science Commission, https://www.ciesm.org/
- EMODnet, https://emodnet.ec.europa.eu/en/portals
- The topographic data set used in this chapter is the GEBCO Compilation Group (2020) GEBCO 2020 Grid (https://doi.org/10.5285/a29c5465-b138-234d-e053-6c86abc040b9) and the bathymetric data set corresponds to the EMODnet Digital Bathymetry (EMODnet Bathymetry Consortium (2018), https://doi.org/10.12770/18ff0d48-b203-4a65-94a9-5fd8b0ec35f6)

References

Andreetto, F., Aloisi, G., Raad, F., Heida, H., Flecker, R., Agiadi, K., Krijgsman, W., 2021. Freshening of the Mediterranean Salt Giant: controversies and certainties around the terminal (Upper Gypsum and Lago-Mare) phases of the Messinian Salinity Crisis. Earth-Science Reviews 216, 103577.

Argyroudi, A., Chatzinikolaou, Y., Poirazidis, K., Lazaridou, M., 2009. Do intermittent and ephemeral Mediterranean rivers belong to the same river type? Aquat. Ecol. 43, 465−476.

Bahr, A., Jiménez-Espejo, F.J., Kolasinac, N., Grunert, P., Hernández-Molina, F.J., Röhl, U., Voelker, A.H.L., Escutia, C., Stow, D.A.V., Hodell, D., Alvarez-Zarikian, C.A., 2014. Deciphering bottom current velocity and paleoclimate signals from contourite deposits in the Gulf of Cádiz during the last 140 kyr: an inorganic geochemical approach. Geochem. Geophys. Geosyst. 15 (8), 3145−3160.

Bahr, A., Kaboth, S., Jiménez-Espejo, F.J., Sierro, F.J., Voelker, A.H., Lourens, L., Röhl, U., Reichart, G.J., Escutia, C., Hernández-Molina, F.J., Pross, J., Friedrich, O., 2015. Persistent monsoonal forcing of Mediterranean outflow water dynamics during the late Pleistocene. Geology 43 (11), 951−954.

Bahrouni, N., Masson, F., Meghraoui, M., Saleh, M., Maamri, R., Dhaha, F., Arfaoui, M., 2020. Active tectonics and GPS data analysis of the Maghrebian thrust belt and Africa-Eurasia plate convergence in Tunisia. Tectonophysics 785, 228440.

Benson, R.H., Rakic-El Bied, K., Bonaduce, G., 1991. An important current reversal (influx) in the Rifian Corridor (Morocco) at the Tortonian-Messinian boundary: the end of the Tethys ocean. Paleoceanography 6 (1), 165−192.

Bonneau, L., Toucanne, S., Bayon, G., Jorry, S.J., Emmanuel, L., Jacinto, R.S., 2017. Glacial erosion dynamics in a small mountainous watershed (Southern French Alps): a source-to-sink approach. Earth Planet Sci. Lett. 458, 366−379.

Bougrine, A., Yelles-Chaouche, A.K., Calais, E., 2019. Active deformation in Algeria from continuous GPS measurements. Geophys. J. Int. 217 (1), 572−588.

Cacho, I., Grimalt, J.O., Sierro, F.J., Shackleton, N., Canals, M., 2000. Evidence for enhanced Mediterranean thermohaline circulation during rapid climatic coolings. Earth Planet Sci. Lett. 183 (3−4), 417−429.

Calvès, G., Toucanne, S., Jouet, G., Charrier, S., Thereau, E., Etoubleau, J., Marsett, T., Droz, L., Bez, M., Abreu, V., Jorry, S., Mulder, T., Lericolais, G., 2013. Inferring denudation variations from the sediment record; an example of the last glacial cycle record of the Golo Basin and watershed, East Corsica, western Mediterranean sea. Basin Res. 25 (2), 197−218.

Cattaneo, A., Correggiari, A., Langone, L., Trincardi, F., 2003. The late-Holocene Gargano subaqueous delta, Adriatic shelf: sediment pathways and supply fluctuations. Mar. Geol. 193 (1−2), 61−91.

Chiarella, D., Capella, W., Longhitano, S.G., Muto, F., 2020. Fault-controlled base-of-scarp deposits. Basin Res. 33 (2), 1056−1075. https://doi.org/10.1111/bre.12505.

Chiarella, D., Hernández-Molina, F.J., 2021. Go with the flow: the role of gateway and straits on plastic distribution. Geol. Today 37 (2), 66−69.

Chiarella, D., Longhitano, S.G., Muto, F., 2012. Sedimentary Features of the Lower Pleistocene Mixed Siliciclastic-Bioclastic Tidal Deposits of the Catanzaro Strait (Calabrian Arc, South Italy). Rend. Online Soc. Geol. Italy, pp. 919−920.

Chiarella, D., Moretti, M., Longhitano, S.G., Muto, F., 2016. Deformed cross-stratified deposits in the early pleistocene tidally-dominated Catanzaro strait-fill succession, Calabrian Arc (Southern Italy): triggering mechanisms and environmental significance. Sedimentary Geol 344, 277–289.

Chiarella, D., Longhitano, S.G., Tropeano, M., 2017. Type of mixing and heterogeneities in mixed siliciclastic-carbonate sediments. Mar. Petrol. Geol. 88, 617–627.

CIESM, 2008. The Messinian Salinity Crisis from Mega-Deposits to Microbiology - a Consensus Report. No:33 in CIESM Workshop Monographs, p. 168.

Cita, M.B., 2021. In: Tsunamiites, S., Minoura, K., Yamazaki, T. (Eds.), Deep-sea Homogenites: Sedimentary Expression of a Prehistoric Megatsunamic in the Eastern Mediterranean. Elsevier, Amsterdam, pp. 207–224.

Clauzon, G., Suc, J.-P., Gautier, F., Berger, A., Loutre, M.-F., 1996. Alternate interpretation of the Messinian salinity crisis: controversy resolved? Geology 24 (4), 363–366.

Constant, M., Kerhervé, P., Mino-Vercellio-Verollet, M., Dumontier, M., Vidal, A.S., Canals, M., Heussner, S., 2019. Beached microplastics in the northwestern Mediterranean Sea. Mar. Pollut. Bull. 142, 263–273.

de la Vara, A., Topper, R.P.M., Meijer, P.T., Kouwenhoven, T.J., 2015. Water exchange through the Betic and Rifian corridors prior to the Messinian salinity crisis: a model study. Paleoceanography 30, 548–557.

de Weger, W., Hernández-Molina, F.J., Flecker, R., Sierro, F.J., Chiarella, D., Krijgsman, W., Manar, M.A., 2020. Late Miocene contourite channel system reveals intermittent overflow behavior. Geology 48 (12), 1194–1199.

de Weger, W., Hernández-Molina, F.J., Miguez-Salas, O., de Castro, S., Bruno, M., Chiarella, D., Sierro, F.J., Blackbourn, G., Amine Manar, M., 2021. Contourite depositional system after the exit of a strait: case study from the late Miocene South Rifian Corridor, Morocco. Sedimentology. https://doi.org/10.1111/sed.12882.

DeMets, C., Merkouriev, S., Sauter, D., 2015. High-resolution estimates of Southwest Indian Ridge plate motions, 20 Ma to present. Geophys. J. Int. 203 (3), 1495–1527.

Dercourt, J., Zonenshain, L.P., Ricou, L.E., Kazmin, V.G., Le Pichon, X., Knipper, A.L., Grandjacquet, C., Sbortshikov, I.M., Geyssant, J., Lepvrier, C., Pechersky, D.H., Boulin, J., Sibuet, J.-C., Savostin, L.A., Sorokhtin, O., Westphal, M., Bazhenov, M.L., Lauer, J.P., Biju-Duval, B., 1986. Geological evolution of the Tethys belt from the Atlantic to the Pamirs since the Lias. Tectonophysics 123 (1–4), 241–315.

Dinarès-Turell, J., Hoogakker, B.A., Roberts, A.P., Rohling, E.J., Sagnotti, L., 2003. Quaternary climatic control of biogenic magnetite production and eolian dust input in cores from the Mediterranean Sea. Palaeogeogr. Palaeoclimatol. Palaeoecol. 190, 195–209.

Doglioni, C., Gueguen, E., Harabaglia, P., Mongelli, F., 1999. On the origin of west-directed subduction zones and applications to the western Mediterranean. Geol. Soc. Spec. Publ. 156 (1), 541–561.

Droghei, R., Falcini, F., Casalbore, D., Martorelli, E., Mosetti, R., Sannino, G., Santoreli, R., Chiocci, F.L., 2016. The role of internal solitary waves on deep-water sedimentary processes: the case of up-slope migrating sediment waves off the Messina Strait. Sci. Rep. 6 (1), 1–8.

Ercilla, G., Juan, C., Hernandez-Molina, F.J., Bruno, M., Estrada, F., Alonso, B., Casas, D., Farran, M., Llave, E., García, M., Vázquez, J.T., D'Acremont, E., Gorini, C., Palomino, D., Valencia, J., El Moumni, B., Ammar, A., 2016. Significance of bottom currents in deep-sea morphodynamics: an example from the Alboran Sea. Mar. Geol. 378, 157–170.

Faccenna, C., Becker, T.W., Auer, L., Billi, A., Boschi, L., Brun, J.P., Capitanio, A., Funiviello, F., Horvàth, F., Jolivet, L., Piromallo, C., Royden, L., Rossetti, F., Serpelloni, E., 2014. Mantle dynamics in the Mediterranean. Rev. Geophys. 52 (3), 283−332.

Fernández-Salas, L.M., Lobo, F.J., Hernández-Molina, F.J., Somoza, L., Rodero, J., del Rıo, V.D., Maldonado, A., 2003. High-resolution architecture of late Holocene highstand prodeltaic deposits from southern Spain: the imprint of high-frequency climatic and relative sea-level changes. Continent. Shelf Res. 23 (11−13), 1037−1054.

Gamberi, F., Pellegrini, C., Dalla Valle, G., Scarponi, D., Bohacs, K., Trincardi, F., 2020. Compound and hybrid clinothems of the last lowstand Mid-Adriatic Deep: processes, depositional environments, controls and implications for stratigraphic analysis of prograding systems. Basin Res. 32, 363−377 (Clinoforms and Clinothems: Fundamental Elements of Basin Infill).

Gauchery, T., Rovere, M., Pellegrini, C., Cattaneo, A., Campiani, E., Trincardi, F., 2021a. Factors controlling margin instability during the plio-quaternary in the Gela Basin (Strait of Sicily, Mediterranean Sea). Mar. Petrol. Geol. 123, 104767.

Gauchery, T.T., Rovere, M., Pellegrini, C., Asioli, A., Tesi, T., Cattaneo, A., Trincardi, F., 2021b. Post-LGM multi-proxy sedimentary record of bottom-current variability and downslope sedimentary processes in a contourite drift of the Gela Basin (Strait of Sicily). Mar. Geol. 106564.

Govers, R., Meijer, P., Krijgsman, W., 2009. Regional isostatic response to Messinian salinity crisis events. Tectonophysics 463 (1−4), 109−129.

Granado, P., Urgeles, R., Sàbat, F., Albert-Villanueva, E., Roca, E., Muñoz, J.A., Mazzuca, N., Gambini, R., 2016. Geodynamical framework and hydrocarbon plays of a salt giant: the NW Mediterranean Basin. Petrol. Geosci. 22 (4), 309−321.

Gueguen, E., Doglioni, C., Fernandez, M., 1998. On the post-25 Ma geodynamic evolution of the western Mediterranean. Tectonophysics 298 (1−3), 259−269.

Harris, P.T., Pattiaratchi, C.B., Collins, M.B., Dalrymple, R.W., 1995. What is a bedload parting? In: Flemming, B.W., Bartholoma, A. (Eds.), Tidal Signatures in Modern and Ancient Sediments, vol. 24. International Association of Sedimentologists Special Publication, p. 318.

Harris, P.T., Macmillan-Lawler, M., Rupp, J., Baker, E.K., 2014. Geomorphology of the oceans. Mar. Geol. 352, 4−24.

Holleman, R.C., Stacey, M.T., 2014. Coupling of sea level rise, tidal amplification, and inundation. J. Phys. Oceanography 44, 1439−1455.

Hsü, K.J., Ryan, W.B.F., Cita, M.B., 1973. Late Miocene desiccation of the Mediterranean. Nature 242, 240−244.

Hüneke, H., Henrich, R., 2011. Pelagic sedimentation in modern and ancient oceans. In: Hüneke, H., Mulder, T. (Eds.), Deep-sea Sediments. Elsevier, Amsterdam, pp. 215−352.

Jaeger, J.M., Nittrouer, C.A., 2000. The formation of point- and multiple-source deposits on continental shelves. In: Henrichs, N.B., Garvine, R., Kineke, G., Lohrenz, S. (Eds.), Coastal Ocean Processes (CoOP): Transport and Transformation Processes over Continental Shelves with Substantial Freshwater Inflows. Technical Report TS-237-00. Center for Environmental Science, University of Maryland, Cambridge, MD, pp. 78−89.

Jaoshvili, S., 2002. The Rivers of the Black Sea. EEA Technical Report 71. European Environmental Agency, p. 58. https://www.eea.europa.eu/ds_resolveuid/d8f389e054210b1b8fad2fb5e9e0941f. (Accessed 27 September 2021).

Jolivet, L., Brun, J.-P., 2010. Cenozoic geodynamic evolution of the Aegean. Int. J. Earth Sci. 99, 109−138.

Jolivet, L., Faccenna, C., 2000. Mediterranean extension and the Africa-Eurasia collision. Tectonics 19 (6), 1095−1106.

Jolivet, L., Faccenna, C., Piromallo, C., 2009. From mantle to crust: stretching the Mediterranean. Earth Planet Sci. Lett. 285 (1−2), 198−209.

Jolivet, L., Romagny, A., Menant, A., 2019. Géodynamique de la Méditerranée. Geochronique 149, 14−19. ISSN:0292-8477.

Jolivet, L., Romagny, A., Gorini, C., Maillard, A., Thinon, I., Couëffé, R., Ducoux, M., Séranne, M., 2020. Fast dismantling of a mountain belt by mantle flow: late-orogenic evolution of Pyrenees and Liguro-Provençal rifting. Tectonophysics 776, 228312.

Kane, I.A., Clare, M.A., Miramontes, E., Wogelius, R., Rothwell, J.J., Garreau, P., Pohl, F., 2020. Seafloor microplastic hotspots controlled by deep-sea circulation. Science 368 (6495), 1140−1145.

Kopf, A., Mascle, J., Klaeschen, D., 2003. The Mediterranean Ridge: a mass balance across the fastest growing accretionary complex on Earth. J. Geophys. Res. Solid Earth 108 (B8).

Kopf, A., Cruise Participants, 2012. Heraklion/Greece, 12.03.2011 - Taranto/Italy, 01.04.2011. Report and preliminary results of RV Poseidon Cruise P410: MUDFLOW (Mud volcanism, Faulting and Fluid Flow on the Mediterranean Ridge Accretionary Complex), vol. 284. Department of Geosciences, Bremen University, Berichte aus dem Fachbereich Geowissenschaften der Universität Bremen. urn:nbn:de:gbv:46-00103061-12.

Krijgsman, W., Hilgen, F., Raffi, I., Sierro, F.J., Wilson, D.S., 1999. Chronology, causes and progression of the Messinian salinity crisis. Nature 400, 652−655.

Krijgsman, W., Capella, W., Simon, D., Hilgen, F.J., Kouwenhoven, T.J., Meijer, P.T., Sierrom, F.J., van den Berg, M.A., van der Schee, B.C.J., Flecker, R., 2018. The Gibraltar corridor: watergate of the Messinian salinity crisis. Mar. Geol. 403, 238−246.

Liquete, C., Canals, M., Ludwig, W., Arnau, P., 2009. Sediment discharge of the rivers of Catalonia, NE Spain, and the influence of human impacts. J. Hydrol. 366 (1−4), 76−88.

Lofi, J., Déverchère, J., Gaullier, V., Gillet, H., Gorini, C., Guennoc, P., Loncke, L., Maillard, A., Sage, F., Thinon, I., 2011. Seismic Atlas of the Messinian Salinity Crisis Markers in the Mediterranean and Black Seas - Vol. 1. Mém. Soc. Géol. France & Commission for the Geological Map of the World, t. 179, ISBN 2-85363-097-8, p. 72, 1CD.

Lofi, J., et al., 2018. Seismic Atlas of the Messinian Salinity Crisis Markers in the Mediterranean Sea - Vol. 2. Mém. Soc. Géol. France & Commission for the Geological Map of the World, t. 181, p. 72, 1CD, ISBN 2-97829-173-10373.

Lombo Tombo, S., Dennielou, B., Berné, S., Bassetti, M.A., Toucanne, S., Jorry, S.J., Jouet, G., Fontanier, C., 2015. Sea-level control on turbidite activity in the Rhone canyon and the upper fan during the Last Glacial Maximum and Early deglacial. Sediment. Geol. 323, 148−166.

Longhitano, S.G., 2013. A facies-based depositional model for ancient and modern, tectonically-confined tidal straits. Terra. Nova 25, 446−452.

Longhitano, S.G., 2018. Between Scylla and Charybdis (part 2): the sedimentary dynamics of the ancient, Early Pleistocene Messina Strait (central Mediterranean) based on its modern analogue. Earth Sci. Rev. 179, 248−286.

Longhitano, S.G., Chiarella, D., 2020. Tidal straits: basic criteria for recognizing ancient systems from the rock. In: Scarselli, N., Adam, J., Chiarella, D., Roberts, D.G., Bally, A.W. (Eds.), Regional Geology and Tectonics, Vol 1: Principles of Geologic Analysis. Elsevier,

Amsterdam, Netherlands, pp. 365–415. Ch. 15, https://doi.org/10.101/B978-0-444-64134-2.00014-6.

Longhitano, S.G., Chiarella, D., Muto, F., 2014. Three-dimensional to two-dimensional cross-strata transition in the lower Pleistocene Catanzaro tidal strait transgressive succession (southern Italy). Sedimentology 61, 2136–2171.

Longhitano, S.G., Chiarella, D., Gugliotta, M., Ventra, D., 2021a. Coarse-grained deltas approaching shallow-water canyon heads: a case study from the Lower Pleistocene Messina Strait. Southern Italy. Sedimentology 68, 2523–2562.

Longhitano, S.G., Rossi, V.M., Chiarella, D., Mellere, D., Tropeano, M., Dalrymple, R.W., Steel, R.J., Nappi, A., Olita, F., 2021b. Anatomy of a mixed bioclastic–siliciclastic regressive tidal sand ridge: facies-based case study from the lower Pleistocene Siderno Strait, southern Italy. Sedimentology 68, 2293–2333.

Ludwig, W., Dumont, E., Meybeck, M., Heussner, S., 2009. River discharges of water and nutrients to the Mediterranean and Black Sea: major drivers for ecosystem changes during past and future decades? Prog. Oceanogr. 80 (3–4), 199–217.

Manzi, V., Gennari, R., Lugli, S., Roveri, M., Scafetta, N., Schreiber, B.C., 2012. High-frequency cyclicity in the Mediterranean Messinian evaporites: evidence for solar–lunar climate forcing. J. Sediment. Res. 82, 991–1005.

Martín, J.M., Puga-Bernabéu, A., Aguirre, J., Braga, J.C., 2014. Miocene Atlantic-Mediterranean seaways in the Betic Cordillera (southern Spain). Rev. Soc. Geol. Esp. 27, 175186.

Michel, J., Borgomano, J., Reijmer, J.J., 2018. Heterozoan carbonates: when, where and why? A synthesis on parameters controlling carbonate production and occurrences. Earth Sci. Rev. 182, 50–67.

Middleton, G.V., 1993. Sediment deposition from turbidity currents. Annu. Rev. Earth Planet Sci. 21, 89–114.

Milliman, J.D., Meade, R.H., 1983. World-wide delivery of river sediment to the oceans. J. Geol. 91 (1), 1–21.

Miramontes, E., Cattaneo, A., Jouet, G., Thereau, E., Thomas, Y., Rovere, M., Cauquil, E., Trincardi, F., 2016. The Pianosa contourite depositional system (northern Tyrrhenian Sea): drift morphology and Plio-Quaternary stratigraphic evolution. Mar. Geol. 378, 20–42.

Miramontes, E., Garreau, P., Caillaud, M., Jouet, G., Pellen, R., Hernández-Molina, F.J., Clare, M.A., Cattaneo, A., 2019. Contourite distribution and bottom currents in the NW Mediterranean Sea: coupling seafloor geomorphology and hydrodynamic modelling. Geomorphology 333, 43–60.

Mosher, D.C., Campbell, D.C., Gardner, J.V., Piper, D.J.W., Chaytor, J.D., Rebesco, M., 2017. The role of deep-water sedimentary processes in shaping a continental margin: the Northwest Atlantic. Mar. Geol. 393, 245–259.

Narcisi, B., Vezzoli, L., 1999. Quaternary stratigraphy of distal tephra layers in the Mediterranean—an overview. Global Planet. Change 21 (1–3), 31–50.

Nocquet, J.M., 2012. Present-day kinematics of the Mediterranean: a comprehensive overview of GPS results. Tectonophysics 579, 220–242.

Palanques, A., de Madron, X.D., Puig, P., Fabres, J., Guillén, J., Calafat, A., Bonnin, J., 2006. Suspended sediment fluxes and transport processes in the Gulf of Lions submarine canyons. The role of storms and dense water cascading. Mar. Geol. 234 (1–4), 43–61.

Patruno, S., Scisciani, V., Helland-Hansen, W., D'Intino, N., Reid, W., Pellegrini, C., 2020. Upslope-climbing shelf-edge clinoforms and the stepwise evolution of the northern

European glaciation (lower Pleistocene Eridanos Delta system, UK North Sea): when sediment supply overwhelms accommodation (Clinoforms and Clinothems: Fundamental Elements of Basin Infill). Basin Res. 32, 224–239.

Pellegrini, C., Maselli, V., Cattaneo, A., Piva, A., Ceregato, A., Trincardi, F., 2015. Anatomy of a compound delta from the post-glacial transgressive record in the Adriatic Sea. Mar. Geol. 362, 43–59.

Pellegrini, C., Maselli, V., Trincardi, F., 2016. Pliocene–Quaternary contourite depositional system along the south-western Adriatic margin: changes in sedimentary stacking pattern and associated bottom currents. Geo Mar. Lett. 36 (1), 67–79.

Pellegrini, C., Bohacs, K.M., Drexler, T.M., Gamberi, F., Rovere, M., Trincardi, F., 2017. Identifying the sequence boundary in over-and under-supplied contexts: the case of the late Pleistocene adriatic continental margin. In: Sequence Stratigraphy: The Future Defined, Proceedings of the 36th Annual Perkins-Rosen Research Conference, pp. 160–182.

Pellegrini, C., Asioli, A., Bohacs, K.M., Drexler, T.M., Feldman, H.R., Sweet, M.L., Trincardi, F., 2018. The late Pleistocene Po River lowstand wedge in the Adriatic Sea: controls on architecture variability and sediment partitioning. Mar. Petrol. Geol. 96, 16–50.

Pellegrini, C., Patruno, S., Helland-Hansen, W., Steel, R.J., Trincardi, F., 2020. Clinoforms and clinothems: fundamental elements of basin infill. Basin Res. 32, 187–205.

Pellegrini, C., Tesi, T., Schieber, J., Bohacs, K.M., Rovere, M., Asioli, A., Trincardi, F., 2021. Fate of terrigenous organic carbon in muddy clinothems on continental shelves revealed by stratal geometries: insight from the Adriatic sedimentary archive. Global Planet. Change 103539.

Philippon, M., Brun, J.P., Gueydan, F., Sokoutis, D., 2014. The interaction between Aegean back-arc extension and Anatolia escape since Middle Miocene. Tectonophysics 631, 176–188.

Pomar, L., Kendall, C.G., 2008. Architecture of carbonate platforms: a response to hydrodynamics and evolving ecology. SEPM (Soc. Sediment. Geol.) Spec. Publ. 89, 187–216.

Poulos, S.E., Collins, M.B., 2002. Fluviatile sediment fluxes to the Mediterranean Sea: a quantitative approach and the influence of dams. London, Special Publications Geol. Soc. 191 (1), 227–245.

Prather, B.E., O'Byrne, C., Pirmez, C., Sylvester, Z., 2017. Sediment partitioning, continental slopes and base-of-slope systems. Basin Res. 29 (3), 394–416.

Ricou, L.E., 1994. Tethys reconstructed: plates, continental fragments and their boundaries since 260 Ma from Central America to South-eastern Asia. Geodin. Acta 7 (4), 169–218.

Rohling, E.J., Marino, G., Grant, K.M., 2015. Mediterranean climate and oceanography, and the periodic development of anoxic events (sapropels). Earth Sci. Rev. 143, 62–97.

Romans, B.W., Castelltort, S., Covault, J.A., Fildani, A., Walsh, J.P., 2016. Environmental signal propagation in sedimentary systems across timescales. Earth Sci. Rev. 153, 7–29.

Rossi, V.M., Longhitano, S.G., Mellere, D., Dalrymple, R.W., Steel, R.J., Chiarella, D., Olariu, C., 2017. Interplay of tidal and fluvial processes in an early Pleistocene, delta-fed, strait margin (Calabria, Southern Italy. Mar. Petrol. Geol. 87, 14–30.

Rouchy, J.M., Caruso, A., 2006. The Messinian salinity crisis in the Mediterranean basin: a reassessment of the data and an integrated scenario. Sediment. Geol. 188, 35–67.

Rovere, M., Pellegrini, C., Chiggiato, J., Campiani, E., Trincardi, F., 2019. Impact of dense bottom water on a continental shelf: an example from the SW Adriatic margin. Mar. Geol. 408, 123–143.

Roveri, M., Flecker, R., Krijgsman, W., Lofi, J., Lugli, S., Manzi, V., Sierro, F.J., Bertini, A., Camerlenghi, A., De Lange, G., Govers, R., Hilgen, F.J., Hübscher, C., Meijer, P.T.,

Stoica, M., 2014. The Messinian Salinity Crisis: past and future of a great challenge for marine sciences. Mar. Geol. 352, 25−58.
Ruddiman, W.F., 2013. Earth's Climate: Past and Future, third ed. W. H. Freeman and Company, New York, p. 445.
Ryan, W.B.F., 2008. Modeling the magnitude and timing of evaporative drawdown during the Messinian salinity crisis. Stratigraphy 5 (3−4), 227−243.
Scardino, G., Piscitelli, A., Milella, M., Sansò, P., Mastronuzzi, G., 2020. Tsunami fingerprints along the Mediterranean coasts. Rendiconti Lincei. Scienze Fisiche e Naturali 31 (2), 319−335.
Spratt, R.M., Lisiecki, L.E., 2016. A late Pleistocene sea level stack. Clim. Past 12 (4), 1079−1092.
Struglia, M.V., Mariotti, A., Filograsso, A., 2004. River discharge into the Mediterranean Sea: climatology and aspects of the observed variability. J. Clim. 17 (24), 4740−4751.
Sweet, M.L., Gaillot, G.T., Jouet, G., Rittenour, T.M., Toucanne, S., Marsset, T., Blum, M.D., 2020. Sediment routing from shelf to basin floor in the quaternary Golo system of eastern Corsica, France, western Mediterranean Sea. Bulletin 132 (5−6), 1217−1234.
Swenson, J.B., Paola, C., Pratson, L., Voller, V.R., Murray, A.B., 2005. Fluvial and marine controls on combined subaerial and subaqueous delta progradation: Morphodynamic modeling of compound-clinoform development. J. Geophys. Res.: Earth Surf. 110 (F2).
Syvitski, J.P., Kettner, A., 2011. Sediment flux and the anthropocene. Phil. Trans. Math. Phys. Eng. Sci. 369 (1938), 957−975.
Tesi, T., Asioli, A., Minisini, D., Maselli, V., Dalla Valle, G., Gamberi, F., Langone, L., Cattaneo, A., Montagna, P., Trincardi, F., 2017. Large-scale response of the Eastern Mediterranean thermohaline circulation to African monsoon intensification during sapropel S1 formation. Quat. Sci. Rev. 159, 139−154.
Tomadin, L., Lenaz, R., 1989. Eolian dust over the Mediterranean and their contribution to the present sedimentation. In: Leinen, M., Sarnthein, M. (Eds.), Paleoclimatology and Paleometeorology: Modern and Past Patterns of Global Atmospheric Transport, vol. 282. Springer, Dordrecht, pp. 267−282.
Toucanne, S., Jouet, G., Ducassou, E., Bassetti, M.A., Dennielou, B., Minto'o, C.M.A., Lahmi, M., Touyet, N., Charlier, K., Lericolais, G., Mulder, T., 2012. A 130,000-year record of Levantine intermediate water flow variability in the Corsica trough, western Mediterranean Sea. Quat. Sci. Rev. 33, 55−73.
Trincardi, F., Amorosi, A., Bosman, A., Correggiari, A., Madricardo, F., Pellegrini, C., 2020. Ephemeral rollover points and clinothem evolution in the modern Po Delta based on repeated bathymetric surveys (Clinoforms and Clinothems: Fundamental Elements of Basin Infill). Basin Res. 32, 402−418.
Urgeles, R., Camerlenghi, A., 2013. Submarine landslides of the Mediterranean Sea: trigger mechanisms, dynamics, and frequency-magnitude distribution. J. Geophys. Res.: Earth Surf. 118 (4), 2600−2618.
Viana, A.R., Faugères, J.-C., Stow, D.A.V., 1998. Bottom-current controlled sand deposits: a review from modern shallow to deep water environments. Sediment. Geol. 115, 53−80.
Vörösmarty, C.J., Fekete, B.M., Tucker, B.A., 1998. Global River Discharge 1807−1991, RivDIS v1.1. Available from: http://www.daacsti.ornl.gov//RIVDIS/guides/rivdis_guide.html. Last update: June 2004.
Woodall, L.C., Sanchez-Vidal, A., Canals, M., Paterson, G.L., Coppock, R., Sleight, V., Calafat, A., Rogers, A.D., Narayanaswamy, B.E., Thompson, R.C., 2014. The deep sea is a major sink for microplastic debris. R. Soc. Open Sci. 1 (4), 140317.

This page intentionally left blank

CHAPTER

Mediterranean climate: past, present and future

3

Piero Lionello[1], Filippo Giorgi[2], Eelco Rohling[3], Richard Seager[4]

[1]*University of Salento, Lecce, Italy;* [2]*International Centre for Theoretical Physics (ICTP), Trieste, Italy;* [3]*Australian National University, Canberra, Australia;* [4]*Columbia University, New York, United States*

Learning objectives

In this chapter you will learn:

- What are the morphological characteristics of the Mediterranean region and their evolution since 30 My ago
- What are the characteristics of the climate of the Mediterranean region and how they have evolved in the past
- Which are the main processes and factors determining the regional climate conditions
- What are the effects of anthropogenic climate change at regional scale

3.1 General climate and morphological characteristics of the Mediterranean basin

The definition of the Mediterranean region in climate studies is not univocal and several criteria can be proposed. It is commonly accepted that it comprises the Mediterranean Sea and the land areas around it, but its boundaries are ambiguous. A strict criterion of homogeneous climate conditions would exclude a large fraction of the Mediterranean shoreline itself, as will become apparent later in this section. A geographical criterion based on the catchment basins of rivers that discharge into the Mediterranean Sea would paradoxically imply, on the one hand, the inclusion of parts of tropical Africa that belong to the Nile basins, and on the other hand the exclusion of large parts of Iberia, western North Africa and the Middle East, in spite of their proximity to the Mediterranean shoreline. Furthermore, it is debatable whether the Black Sea, with its rather peculiar water masses and the surrounding land areas should be considered as part of the Mediterranean region. In general, the pragmatic solution of considering a rectangular box including the Mediterranean Sea has been adopted in the scientific literature, with different choices for its boundaries. The domain considered in this chapter (Figs. 3.1–3.7) is slightly larger than most available examples, such as the Intergovernmental Panel on Climate Change

Oceanography of the Mediterranean Sea. https://doi.org/10.1016/B978-0-12-823692-5.00011-X

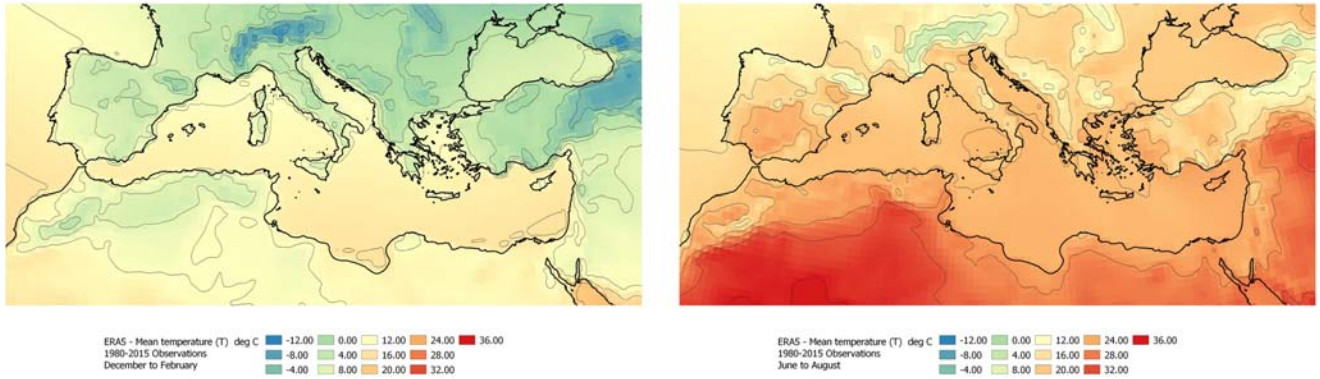

FIGURE 3.1

Winter (left) and summer (right) near surface air temperature (°C, based on ERA5, 1980–2015).

Data extracted from the IPCC WG1-AR6 Interactive Atlas Gutiérrez, J.M., Jones, R.G., Narisma, G.T., Alves, L.M., Amjad, M., Gorodetskaya, I.V., Grose, M., Klutse, N.A.B., Krakovska, S., Li, J., Martínez-Castro, D., Mearns, L.O., Mernild,S. H., Ngo-Duc, S.H., van den Hurk, B., Yoon, J.H., 2021. Atlas. In: Masson-Delmotte, V., Zhai, P., Pirani, A., Connors, S.L., Péan, C., Berger, S., Caud, N., Chen, Y., Goldfarb, L., Gomis, M.I., Huang, M., Leitzell, K., Lonnoy, E., Matthews, J.B.R., Maycock,T.K., Waterfield, T., Yelekçi,O., Yu, R., Zhou, B., (Eds.).Climate Change 2021: The Physical Science Basis. Contribution of Working Group I to the Sixth Assessment Report of the Intergovernmental Panel on Climate Change, Cambridge University Press; Iturbide, M., Fernández, J., Gutiérrez, J.M., Bedia, J., Cimadevilla, E., Díez-Sierra, J., Manzanas, R., Casanueva, A., Baño-Medina, J., Milovac, J., Herrera, S., Cofiño, A.S., San Martín, D., García-Díez, M., Hauser, M., Huard, D., Yelekci, Ö., 2021. Repository supporting the implementation of FAIR principles in the IPCC-WG1 Atlas. Zenodo. https://doi.org/10.5281/zenodo.3691645. Available from: https://github.com/IPCC-WG1/Atlas.

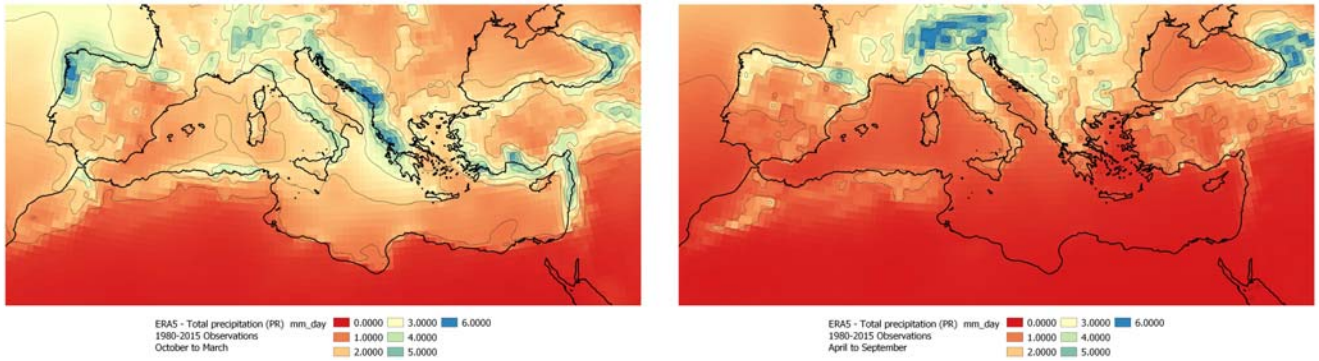

FIGURE 3.2

Wet season (October to March, left) and dry (April to September, right) mean daily precipitation (mm/day, based on ERA5, 1980–2015).

Data extracted from the IPCC WG1-AR6 Interactive AtlasGutiérrez, J.M., Jones, R.G., Narisma, G.T., Alves, L.M., Amjad, M., Gorodetskaya, I.V., Grose, M., Klutse, N.A.B., Krakovska, S., Li, J., Martínez-Castro, D., Mearns, L.O., Mernild,S. H., Ngo-Duc, S.H., van den Hurk, B., Yoon, J.H., 2021. Atlas. In: Masson-Delmotte, V., Zhai, P., Pirani, A., Connors, S.L., Péan, C., Berger, S., Caud, N., Chen, Y., Goldfarb, L., Gomis, M.I., Huang, M., Leitzell, K., Lonnoy, E., Matthews, J.B.R., Maycock,T.K., Waterfield, T., Yelekçi,O., Yu, R., Zhou, B., (Eds.).Climate Change 2021: The Physical Science Basis. Contribution of Working Group I to the Sixth Assessment Report of the Intergovernmental Panel on Climate Change, Cambridge University Press; Iturbide, M., Fernández, J., Gutiérrez, J.M., Bedia, J., Cimadevilla, E., Díez-Sierra, J., Manzanas, R., Casanueva, A., Baño-Medina, J., Milovac, J., Herrera, S., Cofiño, A.S., San Martín, D., García-Díez, M., Hauser, M., Huard, D., Yelekci, Ö., 2021. Repository supporting the implementation of FAIR principles in the IPCC-WG1 Atlas. Zenodo. https://doi.org/10.5281/zenodo.3691645. Available from: https://github.com/IPCC-WG1/Atlas.

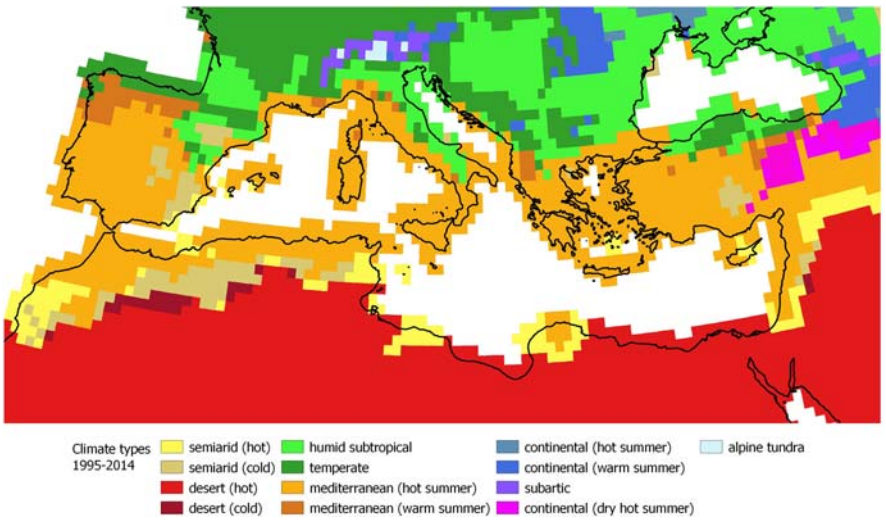

FIGURE 3.3

Köppen–Geiger climate classification in the Mediterranean region.

Data based on based on Rubel, F., Kottek, M., 2010. Observed and projected climate shifts 1901–2100 depicted by world maps of the 16 Köppen-Geiger climate classification. Meteorol. Z. 19 (2), 135–141 for the 1985–2014 period.

(IPCC) definition of MED region in its sixth assessment report (Iturbide et al., 2021), the MedECC domain considered in the first Mediterranean Assessment report (Cherif et al., 2020), and instead is very similar to the domain adopted in the MedCLIVAR books (Lionello et al., 2006a; Lionello, 2012).

The Mediterranean region exhibits a large seasonal cycle of mean temperature (Fig. 3.1) and total precipitation (Fig. 3.2), as well as a large spatial variability. Most of the region is characterized by mild winters, although small areas with mean winter temperatures below zero exist in the Alps and Caucasus, and warm or hot summers (see Section 3.4.1). During the dry part of the year, there is no or minimal precipitation in the south of the Mediterranean, but annual precipitation maxima occur in several mountainous areas of the north. Most areas in the central Mediterranean rely on the wet season (October to March) for precipitation to provide water resources for the rest of the year, and large areas close to the North African and Middle East coasts are dry all over the year. The characteristics of the annual cycle of precipitation are discussed in Section 3.4.2.

The large variability of precipitation and temperature regimes determines large geographical environmental gradients, which are shown by applying the Köppen–Geiger climate classification to the Mediterranean region (Fig. 3.3). The characterization of Mediterranean climate proper (with mild winters and dry summers) is valid only for the central areas and for a large fraction of the coastlines. In North Africa, the eastern parts of the coastline and most land areas have a semiarid or

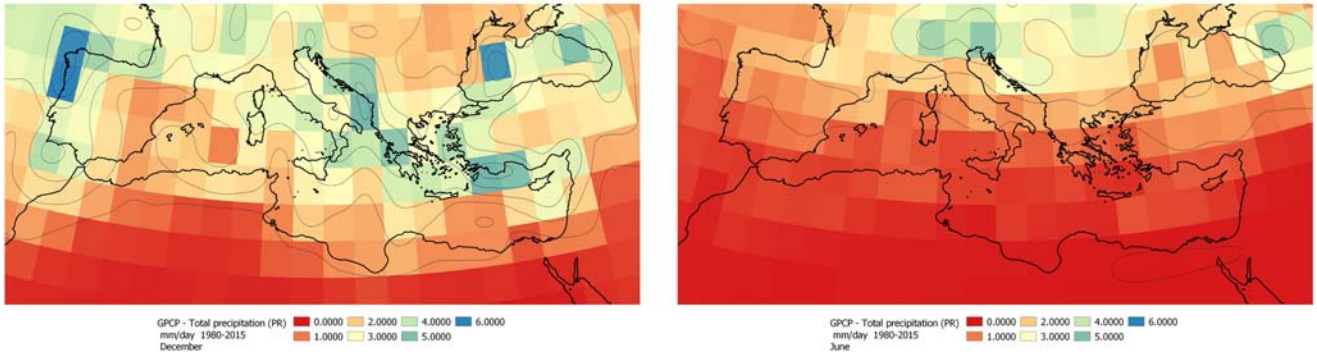

FIGURE 3.4

GPCP precipitation data (mm/day) for December (left panel) and June (right panel) based on combination of satellite and in situ observations.

Data extracted from the IPCC WG1-AR6 Interactive AtlasGutiérrez, J.M., Jones, R.G., Narisma, G.T., Alves, L.M., Amjad, M., Gorodetskaya, I.V., Grose, M., Klutse, N.A.B., Krakovska, S., Li, J., Martínez-Castro, D., Mearns, L.O., Mernild,S. H., Ngo-Duc, S.H., van den Hurk, B., Yoon, J.H., 2021. Atlas. In: Masson-Delmotte, V., Zhai, P., Pirani, A., Connors, S.L., Péan, C., Berger, S., Caud, N., Chen, Y., Goldfarb, L., Gomis, M.I., Huang, M., Leitzell, K., Lonnoy, E., Matthews, J.B.R., Maycock,T.K., Waterfield, T., Yelekçi,O., Yu, R., Zhou, B., (Eds.).Climate Change 2021: The Physical Science Basis. Contribution of Working Group I to the Sixth Assessment Report of the Intergovernmental Panel on Climate Change, Cambridge University Press; Iturbide, M., Fernández, J., Gutiérrez, J.M., Bedia, J., Cimadevilla, E., Díez-Sierra, J., Manzanas, R., Casanueva, A., Baño-Medina, J., Milovac, J., Herrera, S., Cofiño, A.S., San Martín, D., García-Díez, M., Hauser, M., Huard, D., Yelekci, Ö., 2021. Repository supporting the implementation of FAIR principles in the IPCC-WG1 Atlas. Zenodo. https://doi.org/10.5281/zenodo.3691645. Available from: https://github.com/IPCC-WG1/Atlas.

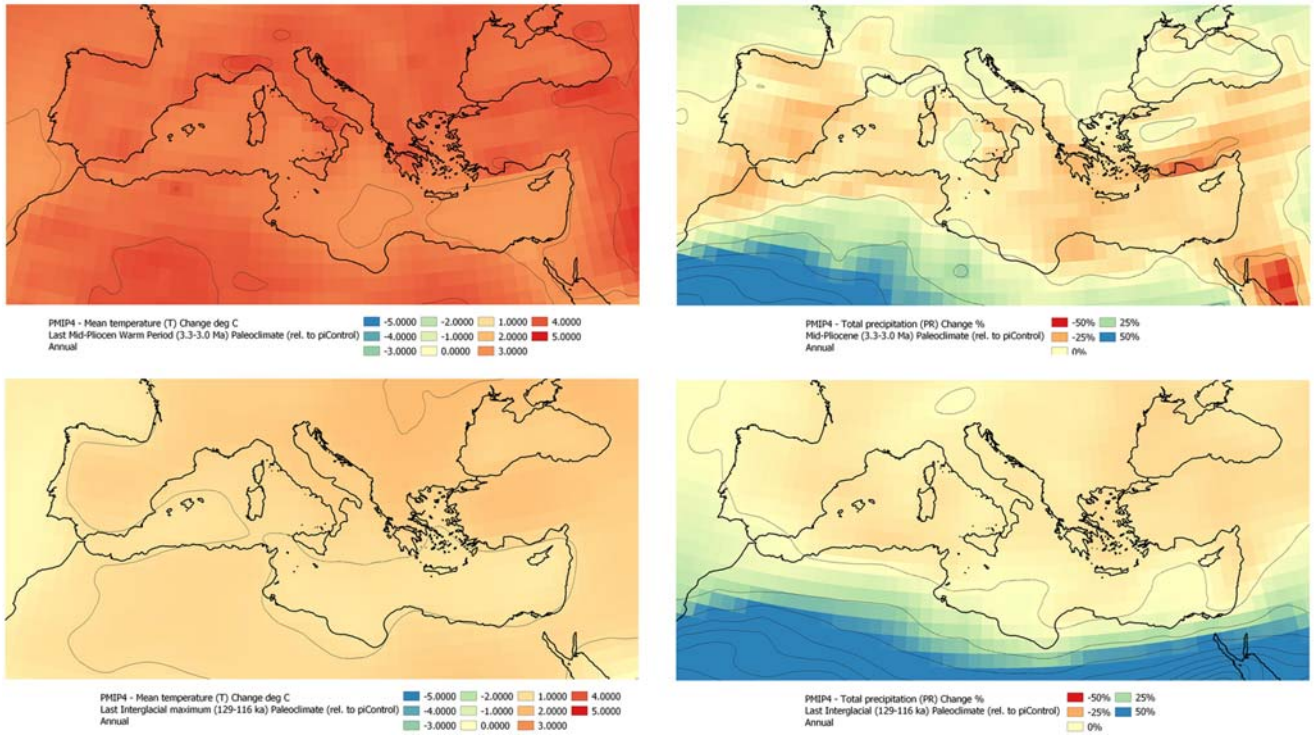

FIGURE 3.5

Mean annual temperature (°C) and total annual precipitation (%) change with respect to preindustrial conditions for (from top to bottom) Mid-Pliocene warm period (3.3—3.0 Ma), Last Interglacial (129-116ka), Last Glacial Maximum (21 ka), Mid-Holocene (6.5-5-5ka).

Data extracted from the IPCC WG1-AR6 Interactive Gutiérrez, J.M., Jones, R.G., Narisma, G.T., Alves, L.M., Amjad, M., Gorodetskaya, I.V., Grose, M., Klutse, N.A.B., Krakovska, S., Li, J., Martínez-Castro, D., Mearns, L.O., Mernild,S. H., Ngo-Duc, S.H., van den Hurk, B., Yoon, J.H., 2021. Atlas. In: Masson-Delmotte, V., Zhai, P., Pirani, A., Connors, S.L., Péan, C., Berger, S., Caud, N., Chen, Y., Goldfarb, L., Gomis, M.I., Huang, M., Leitzell, K., Lonnoy, E., Matthews, J.B.R., Maycock,T.K., Waterfield, T., Yelekçi,O., Yu, R., Zhou, B., (Eds.).Climate Change 2021: The Physical Science Basis. Contribution of Working Group I to the Sixth Assessment Report of the Intergovernmental Panel on Climate Change, Cambridge University Press; Iturbide, M., Fernández, J., Gutiérrez, J.M., Bedia, J., Cimadevilla, E., Díez-Sierra, J., Manzanas, R., Casanueva, A., Baño-Medina, J., Milovac, J., Herrera, S., Cofiño, A.S., San Martín, D., García-Díez, M., Hauser, M., Huard, D., Yelekci, Ö., 2021. Repository supporting the implementation of FAIR principles in the IPCC-WG1 Atlas. Zenodo. https://doi.org/10.5281/zenodo.3691645. Available from: https://github.com/IPCC-WG1/Atlas.

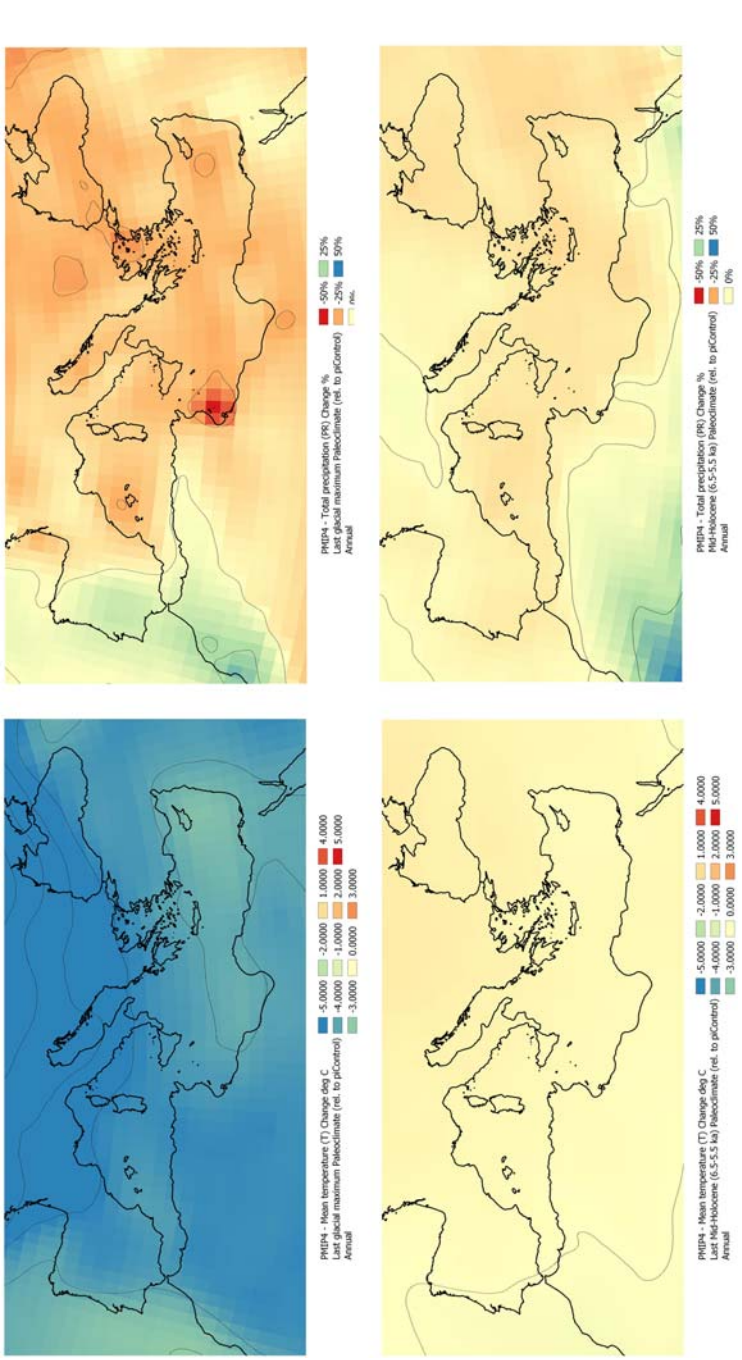

FIGURE 3.5 cont'd.

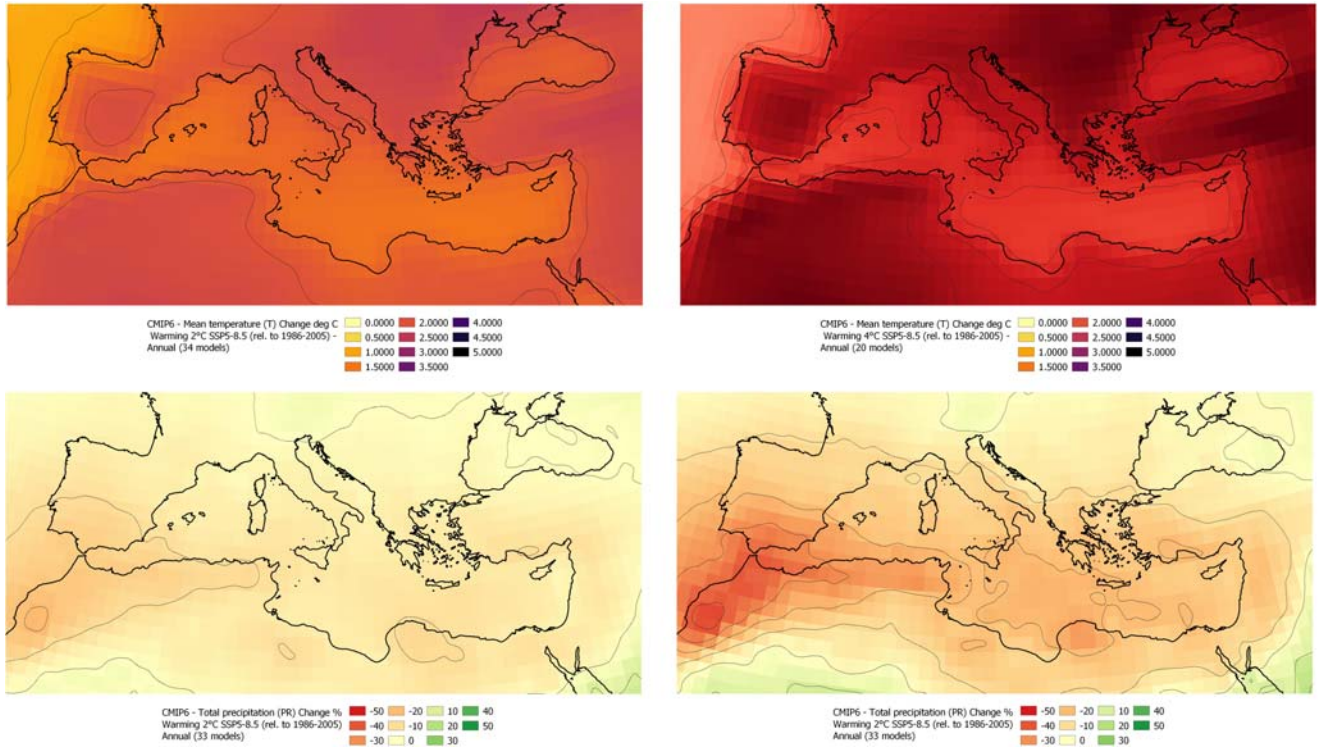

FIGURE 3.6

Change of mean annual temperature (top row, °C) and total annual precipitation (bottom row, %) with respect to the 1986–2005 period for 2°C (left column) and 4°C (right column) global warming level, based on CMIP6 simulations.

Data extracted from the IPCC WG1-AR6 Interactive Atlas Gutiérrez, J.M., Jones, R.G., Narisma, G.T., Alves, L.M., Amjad, M., Gorodetskaya, I.V., Grose, M., Klutse, N.A.B., Krakovska, S., Li, J., Martínez-Castro, D., Mearns, L.O., Mernild,S. H., Ngo-Duc, S.H., van den Hurk, B., Yoon, J.H., 2021. Atlas. In: Masson-Delmotte, V., Zhai, P., Pirani, A., Connors, S.L., Péan, C., Berger, S., Caud, N., Chen, Y., Goldfarb, L., Gomis, M.I., Huang, M., Leitzell, K., Lonnoy, E., Matthews, J.B.R., Maycock,T.K., Waterfield, T., Yelekçi,O., Yu, R., Zhou, B., (Eds.).Climate Change 2021: The Physical Science Basis. Contribution of Working Group I to the Sixth Assessment Report of the Intergovernmental Panel on Climate Change, Cambridge University Press; Iturbide, M., Fernández, J., Gutiérrez, J.M., Bedia, J., Cimadevilla, E., Díez-Sierra, J., Manzanas, R., Casanueva, A., Baño-Medina, J., Milovac, J., Herrera, S., Cofiño, A.S., San Martín, D., García-Díez, M., Hauser, M., Huard, D., Yelekci, Ö., 2021. Repository supporting the implementation of FAIR principles in the IPCC-WG1 Atlas. Zenodo, https://doi.org/10.5281/zenodo.3691645. Available from: https://github.com/IPCC-WG1/Atlas.

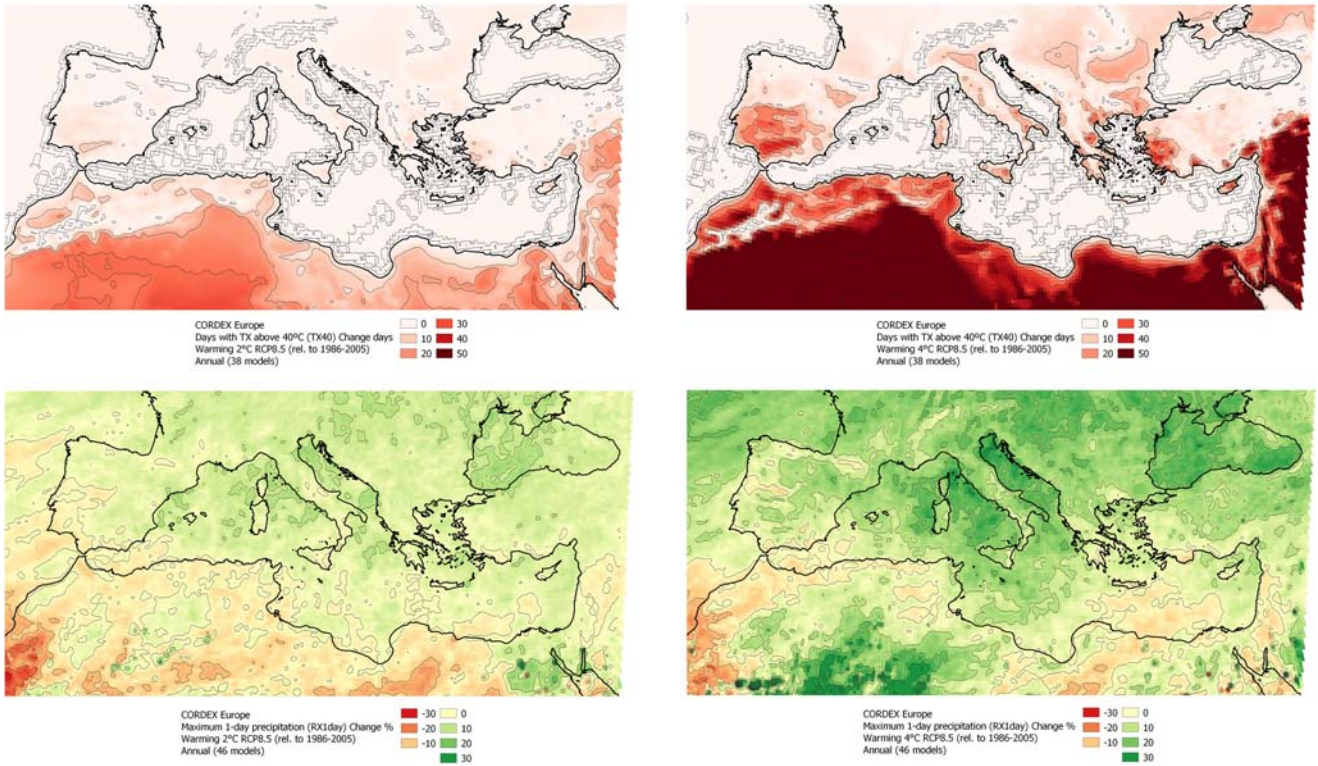

FIGURE 3.7

Annual mean change of number of days with maximum temperature above 40°C (top row, number of days) and of maximum 1-day precipitation (bottom row, %) with respect to the 1986–2005 period for 2°C (left column) and 4°C (right column) global warming level, based on EURO-CORDEX simulations.

Data extracted from the IPCC WG1-AR6 Interactive Atlas Gutiérrez, J.M., Jones, R.G., Narisma, G.T., Alves, L.M., Amjad, M., Gorodetskaya, I.V., Grose, M., Klutse, N.A.B., Krakovska, S., Li, J., Martínez-Castro, D., Mearns, L.O., Mernild,S. H., Ngo-Duc, S.H., van den Hurk, B., Yoon, J.H., 2021. Atlas. In: Masson-Delmotte, V., Zhai, P., Pirani, A., Connors, S.L., Péan, C., Berger, S., Caud, N., Chen, Y., Goldfarb, L., Gomis, M.I., Huang, M., Leitzell, K., Lonnoy, E., Matthews, J.B.R., Maycock,T.K., Waterfield, T., Yelekçi,O., Yu, R., Zhou, B., (Eds.).Climate Change 2021: The Physical Science Basis. Contribution of Working Group I to the Sixth Assessment Report of the Intergovernmental Panel on Climate Change, Cambridge University Press; Iturbide, M., Fernández, J., Gutiérrez, J.M., Bedia, J., Cimadevilla, E., Díez-Sierra, J., Manzanas, R., Casanueva, A., Baño-Medina, J., Milovac, J., Herrera, S., Cofiño, A.S., San Martín, D., García-Díez, M., Hauser, M., Huard, D., Yelekci, Ö., 2021. Repository supporting the implementation of FAIR principles in the IPCC-WG1 Atlas. Zenodo. https://doi.org/10.5281/zenodo.3691645. Available from: https://github.com/IPCC-WG1/Atlas.

desertic climate. Large parts of the Italian and Balkan peninsulas have humid subtropical and temperate climates. Continental climate types occur in the interior of the Balkans and Anatolia. Finally, subarctic and alpine tundra characterize the Alps and parts of the Caucasus.

3.2 Instrumental observations, satellites, and reanalyses

The Mediterranean area has some of the longest time series of instrumental temperature, precipitation and atmospheric pressure observations. In fact, the basic instruments for meteorological observations (thermometer, barometer, rain gauge, and hygrometers) were invented or improved in Italy in the first half of the 17th century (Camuffo et al., 2010). The oldest time series of temperature in the Mediterranean date back to the second half of the 17th century in Italy and began to be available in the 18th century in southern France, Spain, and Portugal. Regular observations of precipitation are available since the early 18th century in northern Italy, since late 18th century in Spain, southern France and southern Italy, since mid-19th century in Portugal (Camuffo et al., 2013). In spite of being instrumental observations, their use for producing homogeneous time series, which are suitable for assessing climate trends and significantly different climate conditions, requires specific adjustment accounting for the instrumental practices, the units and the technical specificities of ancient instruments (Middleton and Spilhaus, 2019). Accuracy has to be sufficient to assess trends that are of the order of a fraction of degree per decade and to allow a correct comparison between different periods, whose length is compliant with the 30-year long period recommended by the World Meteorological Organization (WMO) for the computation of the so-called climate normals. These data have been used for reconstructions of temperature and precipitation evolution in the western Mediterranean region, eventually combining them with historical documentations for obtaining time series extending beyond the availability of instrumental records (Camuffo et al., 2010, 2013; Luterbacher et al., 2006).

The spatial coverage of meteorological stations has become sufficient for basin-wide reconstructions only in the second half of the 19th and the beginning of the 20th century. The period 1871−1900 has been often used for approximating "preindustrial" conditions, as a compromise between a small anthropogenic effect and a number of observations that is sufficient to estimate the global mean temperature. The period 1961−1990 has been suggested by WMO, and adopted in early IPCC reports, to estimate reference climatological means because it was considered the earliest period with the density of observations needed to explore spatial variability at regional scales. For the Mediterranean region there is a strong imbalance between the amount of data in North European areas and the rest of the region, which is a major problem when assessing past differences at the subregional scale. Particularly for precipitation, the lack of data prevents an estimate of the preindustrial climatological values over a large fraction of the region. The production of gridded data sets requires mainly three steps: computations of anomalies, quality control

and interpolation of data to a regular latitude-longitude grid. Data for each station are usually first transformed to anomalies with respect to a reference period (often 1961−1990). Quality of data needs to be checked in terms of internal consistency and, when possible, consistency across variables and stations. Quality checks may also involve statistical tests to identify unlikely data (outliers) or discontinuities in the time series caused by instrumental problems or relocation of the station. Flawed stations could be either directly removed from the dataset or, if possible, corrected (New et al., 1999, 2000; Klein Tank et al., 2002; Haylock et al., 2008). Actual values at grid points result from interpolation that may be carried out with different methodologies, such as weighted averages of valid stations within a given distance (Hulme, 1994; New et al., 1999, 2001, New et al., 2000; New et al., 2001). These methodologies allowed the production of global gridded datasets at relatively high resolution (0.5 degrees) for the whole 20th century (Harris et al., 2020), from which monthly mean meteorological variables in the Mediterranean region can be extracted. Datasets of near surface air temperature are available at various resolutions, in some cases including part of the 19th century (Jones et al., 1999; Menne et al., 2018; Lenssen et al., 2019) and of monthly total precipitation for the whole 20th century (New et al., 2001; Schneider et al., 2016).

Satellite observations have the huge advantage of being able to provide a regular global coverage of many meteorological and oceanographic variables. Initiated with the launch of TIROS-1 in 1960 (Davies, 2007), satellite observations have had a revolutionary impact on weather forecast. For many variables and sensors, the length of available time series has now become sufficiently long for estimating climatological mean values and multidecadal trends. Satellite observations are particularly relevant for estimating precipitation over sea, where scarcity of in-situ platforms and technical difficulties of instrumentations mounted on ships and buoys (affected by pitching and rolling) are a strong limitation for acquiring reliable climatologies. Merged products, combining different data sources provide the overall best results (Adler et al., 2001). Fig. 3.4 is an example showing the annual mean precipitation field over the Mediterranean produced by the GPCP project (Huffman et al., 2009).

Reanalyses are long sequences of simulations carried out with the models used for weather forecast and covering multidecadal periods. They are meant to provide optimal reconstructions of past weather, by merging observations and model dynamics. They are called reanalyses because they imitate the operational procedure used for creating the optimal initial condition for weather forecast (the so-called analysis), by merging data and model dynamics. These reconstructions are homogeneous as model system used for the numerical computation (the atmospheric circulation model with all other modules and the data assimilation system) are kept constant during the whole considered period, while available operational analyses have been made with models that evolved in time becoming progressively more precise and with higher resolution. Further reanalyses can be carried out also for past decades when no operational forecasts were available. However, they are not actually homogeneous because type, quality, and quantity of the assimilated observations have changed during the period simulated in the reanalyses. A long list of

reanalyses has been produced by the European Center for Medium Range Weather Forecasts (ECMWF): ERA40 (Uppala et al., 2005), ERA-Interim (Dee et al., 2011), ERA-20C (Poli et al., 2016), ERA 5 (Hersbach et al., 2020). Other re-analyses are NCEP/NCAR (Kalnay et al., 1996), NCEP/NDOE (Kanamitsu et al., 2002), MERRA (Rienecker et al., 2011), 20CR (Compo et al., 2011). Reanalyses are widely used sources of data for climate studies (e.g., they have been used for producing Figs. 3.1 and 3.2).

3.3 Climate models and their evolution

Climate models are powerful tools to study physical processes that affect climate phenomena, to describe past climate conditions and to assess possible future evolutions of the climate system in response to external forcings and internal variability. Today, a wide range of climate models of increasing complexity, and operating from the global to the regional and local scale, has been developed (e.g., Washington and Parkinson 2005; McGuffie and Henderson-Sellers, 2014; Giorgi 2019). The models can be used for different purposes, often in a combined way, so that they are complementary tools to understand climate processes. Climate models are based on the fundamental equations that regulate the physics and biogeochemistry of the different components of the climate system, e.g., atmosphere, oceans and land surface, but with different degrees of approximation. The model equations are differential in time and space and their integration in time describes the evolution of the climate system (Washington and Parkinson 2005; McGuffie and Henderson-Sellers, 2014). In general, these highly nonlinear equations are not resolvable analytically in realistic cases, and thus they are integrated using numerical approximations on three dimensional grids or spectral elements. The result of this process is a set of millions of numerical equations that provides the temporal evolution of the climate fields at each point of the model grid. The distance between grid points determines the model resolution. Processes that occur at scales finer than the grid point distance cannot be explicitly described by the model and need to be parameterized in terms of resolved variables.

3.3.1 Components of climate models and model hierarchy

Today's most advanced climate models are composed by a number of components interactively coupled with each other: the atmosphere, the oceans, the land surface, the cryosphere and, in a particular type of models, a biogeochemistry module (e.g., Flato et al., 2013). As already mentioned, the equations of each component are discretized on three-dimensional grids and integrated in time at each grid point, thereby providing the evolution of all model variables.

The atmospheric component is a good example. Its equations are essentially the conservation of momentum, energy, mass, and water vapor, along with the equation of state of air. These equations in turns include two general components, referred to

as the "dynamics" and the "physics" of the model. The dynamical component, usually referred to as "dynamical core" includes all terms that regulate the diabatic evolution of an air parcel, while the physics includes the description of processes such as radiative transfer, cloud formation and precipitation, convection, boundary layer processes, and interactions with the land and ocean surface. There are many different ways to numerically solve the dynamics of a model and to represent its physics, especially processes that occur at subgrid scale (e.g., clouds and convection) and thus need to be parameterized. This is the reason why different models tend to behave in different ways and, in particular, can show different responses to the same radiative forcing (e.g., greenhouse gases). The different behavior of climate models is indeed an important element that determines, for example, the uncertainty in future climate projections. Similar considerations are valid for the other components of a climate model.

The complexity of climate models has considerably grown in the last decades (e.g., Edwards, 2011). In the 1970s, climate models were essentially atmospheric models with fixed surface conditions at the lower boundary. The first interactive land components were introduced in the 1980s, while the first fully coupled atmosphere-ocean-sea ice global models were developed and applied to climate change projection in the 1990s. In the 2000s some models started to include the carbon cycle and the effects of atmospheric aerosols, until present day models, also referred to as Earth System Models (ESMs) also include full chemistry and interactive biosphere components. Likewise, the resolution of the models has increased constantly over the years, with the increase in computing power. In fact, while the resolution of early global climate models (GCMs) was of the order of several hundred km, at the beginning of the 2020s it has generally reached 50−100 km and it continues to increase. With the increase of resolution and better representation of physics processes, the performance of GCMs has steadily improved. Today's GCMs can reproduce quite well the basic features of the general circulation, as well as the synoptic scale characteristics of weather systems and some modes of natural variability, such as the El Nino Southern Oscillation (ENSO) or the North Atlantic Oscillation (NAO) (Flato et al., 2013).

However, a resolution of 50−100 km cannot yet adequately capture the effects of complex physiographical features characterizing the Mediterranean region, such as complex mountain chains, coastlines and islands. In order to address this resolution problem and enhance climate information at regional to local scales, different downscaling techniques have been developed since the 1990s, broadly falling into the categories of "dynamical" (Giorgi, 2019) and "empirical-statistical" (e.g., Hewitson et al., 2014) downscaling (DS and ESD, respectively).

DS consists of running limited area models, or regional climate models (RCMs) only over selected areas of interest, which allows an increase of resolution of up to an order of magnitude. RCMs require boundary conditions for the model prognostic variables, e.g., wind components, temperature, pressure and water vapor, which are provided by a GCM, referred to as "driving" GCM. ESD employs observations of model data to produce statistical relationships between large scale predictors and

regional to local scale predictands (e.g., temperature and precipitation), and then applies these relationships to the output of GCM simulations. An additional approach to RCMs and ESD is the use of global variable resolution or high-resolution atmospheric models driven at the lower boundary by conditions derived from coupled GCM experiments (e.g., McGregor, 2015). All these techniques have different advantages and limitations and should be seen as complimentary tools for a better understanding of regional climate processes and for producing climate change information at regional to local scales for application to impact studies and climate service activities.

RCMs have proven to be successful in enhancing the GCM climate information, for example, by better representing the fine scale structure of mesoscale systems, the effects of complex topographical features and the simulation of extreme events (e.g., Giorgi, 2019). The use of RCMs is especially useful for the Mediterranean region, where local forcings play a major role in modulating the climate of the region. In fact, similarly to GCMs, RCMs are now evolving into fully coupled regional ESMs (or RESMs, Giorgi and Gao, 2018) including atmosphere, ocean, land, aerosol, and biogeochemistry (including marine) components (e.g., Reale et al., 2020). In particular, a number of RESM systems have been developed specifically for the Mediterranean region as part of the MED-CORDEX program (Ruti et al., 2016) and have already been applied to the production of 21st century climate projections (Ruti et al., 2016).

RCMs running at very high resolutions, of the order of a few km (Prein et al., 2015), are usually referred to as "convection permitting" RCMs, or CP-RCMs, because their resolution allows the direct simulation of cumulus convection without the use of cumulus parameterization schemes, which have known drawbacks such as the failure to reproduce the observed diurnal cycle of precipitation (e.g., Dai et al., 1999). CP-RCMs are very computationally demanding, however relatively large multi-model ensembles of decadal simulations have already been completed for a greater Alpine region encompassing a good portion of the central Mediterranean (Ban et al., 2021), also in a climate change context (Pichelli et al., 2021).

3.3.2 Climate modeling international programs

The process of producing regional climate projections is affected by a number of uncertainty sources (e.g., Hawkins and Sutton, 2009; Giorgi, 2020), namely, the presence of different emission scenarios, the use of climate models with varying global climate sensitivities and regional scale responses, and eventually the use of different downscaling techniques and different models within the same techniques (e.g., different RCMs; Giorgi et al., 2008). In order to characterize these uncertainties to the best possible extent, it is necessary to produce large multimodel ensembles of projections. This is a challenging task that can be achieved only through large international programs, which in fact have been established during the last decades.

On the GCM side, the primary international program aiming at producing large ensembles of projections is the Climate Model Intercomparison project (CMIP). As part of this project, different coupled GCMs are used to produce 21st century projections, using a common set of scenario forcings (GHGs, aerosols). These ensembles of simulations have typically provided the basic climate change information for the assessment report of the IPCC. For example, the fifth phase of the project, CMIP5 (Taylor et al., 2012) provided data for the fifth assessment report, while the sixth phase, CMIP6 (Eyring et al., 2016) provided the basis for the sixth IPCC report.

On the RCM side, the main reference international program is the Coordinated Regional Downscaling EXperiment (CORDEX, Giorgi et al., 2009; Gutowski et al., 2016). CORDEX aims at producing large multimodel ensembles of downscaled projections over domains covering most continental regions of the globe, using a common simulation and data production protocol. In the CORDEX program, 14 regional domains were identified. In the first phase the model resolution was set at ∼50 km and ensembles of projections were produced for all domains, but with varying ensemble sizes. In the second phase of CORDEX, homogeneous sets of projections for all CORDEX domains with a CORE set of RCMs downscaling a core set of GCMs over nine CORDEX domains at a horizontal grid spacing of ∼25 km, that is, doubled compared to the first phase (Giorgi et al., 2022), and, further, specific downscaling and regional climate issues have been addressed in the so called "Flagship Pilot Studies" or FPS (Gutowski et al., 2016; Coppola et al., 2020).

The most relevant projects concerning projections for the Mediterranean region are EURO-CORDEX (Jacob et al., 2014, 2020) and MED-CORDEX (Ruti et al., 2016). As part of EURO-CORDEX, a large ensemble of projections at grid spacing of ∼12 km is being produced, with an unprecedented GCM-RCM simulation matrix. The EURO-CORDEX domain encompasses the entire Mediterranean basin, so that it can be used to produce comprehensive assessments of high-resolution climate change projections over the region. The MED-CORDEX program instead focuses on the development of fully coupled Mediterranean RESMs and on the study of how the interactions across components can affect the climate characteristics over the region. Results have already indicated that land-sea coupling (e.g., Somot et al., 2008) and atmospheric aerosols of natural and anthropogenic origin can indeed have an important impact on the simulated climate change signals (Nabat et al., 2015).

Today a range of modeling tools is available, from GCMs to RESMs and CP-RCMs, and international coordinated programs, such as CMIP and CORDEX, which can be used to study climate processes in the Mediterranean basin in a comprehensive manner. In this respect, the Mediterranean is probably one of the most advanced regions, for which a wealth of information is already available, or will be produced in the next few years, to study the impacts of global warming toward the design of suitable response strategies.

3.4 Heat and moisture balance at Mediterranean regional scale and relation to surface climate

3.4.1 Heat budget

The mild temperatures in winter are largely due to the presence of the Atlantic Ocean and the Mediterranean Sea. Because of the high heat capacity of water, substantial heat absorbed during summer by these water bodies is gradually released back to the atmosphere in winter. This means that during winter the Mediterranean land areas that have onshore winds from the Atlantic Ocean or the Mediterranean Sea will have milder climates than other areas further inland that are shielded from maritime influence. In addition, due to flow around the Icelandic Low, the eastern North Atlantic is warmer in mid-latitudes than the western- North Atlantic (Seager et al., 2003). Furthermore, prevailing winds are from the southwest and hence from warmer latitudes. Consequently, mean southwesterlies bring a mild, maritime, winter climate to western Europe. The westerlies are, however, strongest over north-western Europe, so this effect is actually not very strong over the Mediterranean. Instead, in winter, augmenting the maritime influence, the Mediterranean comes under the warming influence of subsidence within the boreal Hadley Cell. Offsetting this, transient eddies cool the Mediterranean region in winter, as heat is moved poleward and upward.

In summer, the Mediterranean region is warm to hot, sitting between the cooler continent to the north and the extreme heat of the Sahara to the south. Heat in this season is maintained by subsidence warming within the eastward extension of the North Atlantic Subtropical High (NASH). Since the flow around the NASH is anticyclonic, there is cold northerly advection over the Mediterranean that partly offsets the subsidence warming.

3.4.2 Moisture budget

As already mentioned, a large part of the Mediterranean region is characterized by a marked seasonal cycle in precipitation with a maximum in winter and a minimum in summer. In contrast, evapotranspiration over land has a minimum in the cool winter season and a maximum in the warm summer season. Seager et al. (2014) have analyzed the moisture budget of the Mediterranean region within the ECMWF Interim Reanalysis (ERA-Interim). Evaporation from the Mediterranean Sea is larger in winter than in summer, sustained by mean flow and transient eddy moisture flux divergence over the sea and convergence over the surrounding land (Mariotti et al., 2002a; Seager et al., 2014). As such, for the land regions, there is a positive P-E (difference between precipitation and evaporation), a net supply of moisture to the surface, in winter and a negative P-E, a net deficit of moisture for the surface in summer, which shows the coupling across seasons of the land and atmospheric branches of the hydrological cycle. For the Mediterranean Sea, the phasing of P and E is similar, meaning that the net surface freshwater flux, P-E, is negative

throughout the year. The freshwater loss has to be balanced by a net inflow of water through the Strait of Gibraltar (see Chapter 4). The net flow through the Strait is the sum of a larger inflow than outflow. Negative P-E over the Mediterranean Sea induces the formation of water masses that are saltier and denser than those found in the North Atlantic, which therefore outflow into the Atlantic below the inflowing Atlantic water (see Chapters 4 and 7; Lacombe and Richez, 1982; Criado-Aldeanueva et al., 2012).

On the atmospheric side, the net surface flux P-E has to be balanced by the convergence (with P-E>0) or divergence (with P-E<0) of moisture by atmospheric motions. Atmospheric reanalyses can be used to determine how the atmosphere accomplishes this (Seager et al., 2014). In winter, the striking pattern of negative P-E over the Mediterranean Sea and positive P-E over southern Europe, Fertile Crescent in the Middle East and northwest Africa, is maintained in two ways. The atmospheric mean flow diverges moisture from almost this entire region as a consequence of subsidence, which can be thought of as the descending branch of the winter Hadley Cell. Furthermore, transient eddies extract moisture from the Mediterranean Sea and converge it over northern Africa and southern Europe. The western part of the Fertile Crescent is an exception where the mean flow moisture convergence sustains positive P-E and transient eddies diverge moisture. The net effect in winter is that over the Mediterranean Sea, both the mean flow and the transient eddies sustain negative P-E, while over land the transient eddy moisture convergence overwhelms the mean flow moisture divergence and sustains positive P-E. The transient eddy moisture convergences are associated with the Mediterranean storm track, a well-defined maximum of low-level cyclone activity over the Mediterranean Sea itself (e.g., Trigo et al., 1999; Campins et al., 2011; Lionello et al., 2006b; Flocas et al., 2010; Lionello et al., 2016). In summer, the negative P-E that covers the entire Mediterranean Sea and land areas to the north and south is sustained by mean flow moisture divergence due to widespread subsidence. An interesting exception is that the Alps have positive P-E in summer as well as winter. The alpine summer positive P-E is caused by a seasonal precipitation maximum (Frei and Schär, 1998), which is associated with intense and frequent mesoscale convective systems (Morel and Senesi, 2002) that are supported by a strong recycling of moisture at subregional scale with a large contribution from the local land areas (Sodemann and Zubler, 2010).

3.5 The atmospheric circulation of the subtropics and mid-latitudes

3.5.1 The Mediterranean basin as a transitional region

The Mediterranean basin is in a transitional zone that includes the subtropical zone between the desert climate of North Africa to the south and the humid midlatitude climate to the north. This is also a transitional zone between the semiarid to arid

climate to the south and the wet climate to the north. In winter the Mediterranean is located on the equatorward flank of the mid-latitude westerlies and storm track and on the poleward flank of the zonally oriented subtropical high-pressure belt that underlies the subsiding branch of the Hadley Cell. In summer the zonal mean circulation characteristic is replaced by a zonally asymmetric circulation dividing up into monsoons over the continents and subtropical anticyclones over the oceans (Rodwell and Hoskins 1996, 2001). The Mediterranean is on the eastern flank of the North Atlantic oceanic subtropical high. However, unlike other summer subtropical highs that are purely oceanic, this anticyclone extends eastward from the ocean to cover the entire Mediterranean region. There is no analogue of this in other Mediterranean climate regions of the world (Rodwell and Hoskins, 2001). While Portugal and Morocco are proper analogues of, e.g., California, Chile, Cape Town and southwest Australia, the summer high over the Mediterranean Sea is due to subsidence within a Rossby wave forced by the vast Asian monsoon system to the east (Rodwell and Hoskins, 1996, 2001). The detailed locations of the subsidence depend on the interaction of this wave with the complex topography of the Middle East (Simpson et al., 2015). Hence, the Mediterranean is unique among Mediterranean type climate regions.

3.5.2 The Mediterranean storm track

The Mediterranean is also unique in winter because of the existence of the Mediterranean storm track, a highly localized region of low-level transient eddy activity over the Mediterranean Sea itself (Trigo et al., 1999; Lionello et al., 2006b; Campins et al., 2011; Flocas et al., 2010, Lionello et al., 2016). The Mediterranean storm track is key to bring winter precipitation over land areas, to the north and to the south, and to determine the negative P-E over the sea in winter. According to Lionello et al. (2016), the majority of the Mediterranean winter cyclones are generated in the Mediterranean basin. However, their genesis is typically due to a "parent cyclone" from the Atlantic, Europe, Africa, or from the Red Sea trough. Hence, the Mediterranean storm track, although of local origin, is influenced by the North Atlantic storm track. Once generated, the cyclones tend to track eastward. The Mediterranean is highly cyclogenic in the cooler months, because of the strong meridional temperature gradient between the Sahara and the Mediterranean, and between the sea and the land to the north, and also because much of the area is in the lee of mountain ranges (see review by Lionello et al., 2006b; Ulbrich et al., 2012). The Ligurian Sea is the main center of cyclogenesis. Weaker centers can also be found in the eastern Mediterranean. Using cyclone tracking methodologies, it has been calculated that a considerable amount of precipitation within the region occurs within Mediterranean cyclones (Hawcroft et al., 2012; Reale and Lionello, 2013). Mediterranean cyclones are different from cyclones over the Pacific, North America, Atlantic, and north-western Europe. For those, heavy precipitation occurs in the warm sector of the depression where a southwesterly flow causes warm, moist advection, ascent, condensation, and precipitation. For Mediterranean cyclones,

the warm sector often advects warm but dry air from North Africa and, instead, heavy precipitation tends to occur in the cold sector with westerly flow over the Mediterranean Sea (Ulbrich et al., 2012, and references therein).

3.5.3 Remote factors affecting the Mediterranean climate

The NAO exerts a strong influence on the Mediterranean climate variability on subseasonal to decadal timescales during the cool season (Xoplaki et al., 2004). The NAO is an oscillation in mass between the Icelandic Low and the Azores High, first analyzed by Walker and Bliss (1932). In its positive phase, the Low is deeper than normal and the High is higher than normal and there are strong south-westerly wind anomalies into north-western Europe and weaker westerlies to the south. Walker and Bliss (1932) noted that the western-to-central Mediterranean region was drier than normal during the positive phases and wetter than normal during the negative phase. Recently, Seager et al. (2020) have analyzed the physical mechanisms of NAO-associated precipitation variability, using reanalysis data. In the Mediterranean region east of the Azores High, the wind anomalies tend to be northerly during the positive NAO phase when the Azores High is strong. This causes subsidence and mean flow moisture divergence and, hence, drying. During the negative NAO phase, the flow is southerly and ascending and, hence, precipitation anomalies are positive. Despite the influence of the NAO on both the North Atlantic and Mediterranean storm tracks, Seager et al. (2020) found that the drivers of the precipitation variability were the mean flow anomalies and not the transient eddy moisture convergence anomalies. During the positive phase of the NAO in winter, the western Mediterranean tends to be warmer than normal, but the eastern Mediterranean, under the influence of anomalous flows with a northerly component, tends to be cooler than normal (Hurrell, 1995).

The NAO is primarily a mode of internal atmosphere variability (Feldstein, 2000). However, it has been argued that to some extent it is influenced by surface boundary conditions including sea surface temperature (SST) and sea ice coverage (Scaife et al., 2014). Critically it is the leading mode of variability contributing to Mediterranean region climate variability on both interannual and decadal timescales (Xoplaki et al., 2004; Kelley et al., 2012; Mariotti and Dell'Acquila, 2012). A decadal scale upward trend in the winter NAO from the 1960s to the late 1990s induced a similarly long winter drying trend. As the winter NAO has shifted to more neutral values in the current century, so too has winter precipitation recovered.

In the warm season, the leading mode of variability in circulation and precipitation in the Euro-Mediterranean region is the so-called summer NAO (Folland et al., 2009). The southern center of action of the summer NAO is over north-western Europe and the North Sea, considerably further north than its winter realization, while the opposite signed northern center of action is over Greenland. During its positive phase, with anomalous high pressure over north-western Europe, the Mediterranean is under an anomalous northwesterly flow, but is nonetheless anomalously wet in summer in its central region and the Balkans on both interannual and decadal

timescales (Folland et al., 2009; Mariotti and Dell'Acquila, 2012). The wet/dry conditions for a positive/negative summer NAO appear to be related to zonal convergence/divergence of moisture fluxes caused by the specific longitudinal location of the pressure anomalies cantered north of the Mediterranean (Mariotti and Arkin, 2007). A positive summer NAO also causes a cool anomaly in the central to eastern Mediterranean, which is aided by increased cloud cover (Folland et al., 2009).

The globally dominant mode of natural climate variability is the ENSO, originating in the tropical Pacific (Deser et al., 2010). Although ENSO exerts strong controls on seasonal to interannual climate variability in the Americas, Asia, and Africa, its influence on Europe and the Mediterranean has been the subject of much conjecture. This indicates that, if it is present at all, the regional ENSO influence is not coherent across space and seasons and can be quite variable in time, due to the influence of other modes of variability, or depending on the exact location of the ENSO SST anomalies (e.g., Mariotti et al., 2002b; Lopez-Parages and Rodriguez-Fonseca, 2012; Lopez-Parages et al., 2015, 2016). However, Shaman (2014) was able to find a consistent El Niño/La Niña wet/dry signal in Iberia in summer to fall. The relative weakness of the ENSO influence (compared to the NAO) is because Rossby waves forced by convection anomalies in the tropical Pacific are quite damped by the time they reach the Mediterranean, after having propagated across the North Pacific, North America, and the North Atlantic.

A decadal timescale warming and cooling of the entire North Atlantic Ocean is referred to as the Atlantic Multidecadal Oscillation (AMO) (Kushnir, 1994). Whether the AMO arises from changes in Atlantic Ocean overturning that are internal to the ocean or coupled to the atmosphere, or from changes in surface heat fluxes with an important role for natural (volcanic and solar) and anthropogenic (aerosols and greenhouse gases) driving, remains debated (for contrasting views see Clement et al., 2015; Zhang et al., 2019; Mann et al., 2021). Regardless of its origin, Mariotti and Dell'Aquila (2012) found that the warm phase of the AMO is associated with warm anomalies in the western and central Mediterranean in summer.

3.6 Evolution of Mediterranean climate

Long-term Mediterranean climate changes as recorded in the region's sedimentary record are dominated by global climate trends, the influences of large-scale plate tectonics and associated regional tectonics, and astronomical forcing. Global plate-tectonic processes are implicated in the rise and fall of CO_2 concentrations and associated long-term multimillion year cycles of warming and cooling, causing the World to fluctuate between warm, ice-free climate states, and colder climate states with unipolar or bipolar glaciations (e.g., Wallmann and Aloisi, 2012; Foley, 2015; Rohling, 2019; and references therein). Tectonic influences on regional Mediterranean climate also dominate on multi-million year timescales, especially related to mountain-range formation in the wider Alpine belt and opening and closure of subbasins and sea straits. On time-scales of tens to hundreds of thousands of years,

with amplitude modulations of the order of 1.2 and 2.4 million years, climate changes are dominated by astronomical processes (e.g., Larrasoaña et al., 2003; Laskar et al., 2004; Pälike, 2005; DeConto et al., 2012; Westerhold et al., 2020; Grant et al., 2022), which are described more in detail in the following section.

3.6.1 Astronomical forcing

The influences of astronomical (also known as orbital) cycles on the intensity and distribution of insolation received by Earth were calculated by Milankovitch (1941). There are three important cycles of astronomical climate forcing. These are the cycles of eccentricity of Earth's orbit around the Sun, precession of the equinoxes, and obliquity (or tilt) of Earth's axis (for introductions, see Imbrie and Imbrie, 1986; Rohling, 2019). Of these, orbital eccentricity is the only orbital parameter that controls the total annual-mean amount of solar radiation received by Earth (albeit by a small amount, see below); the other parameters predominantly affect the seasonal and/or spatial distribution of insolation on Earth (Loutre et al., 2004; Pälike, 2005).

The eccentricity cycle relates to changes in the shape of the Earth's orbit around the Sun. An ellipse has two focal points, and as the ellipse transforms to a circle, the two focal points approach one another; the eccentricity parameter is defined as

$$e = \frac{\left(a^2 + b^2\right)^{0.5}}{a} \tag{3.1}$$

where a is the semimajor axis of the ellipse and b its semiminor axis (Pälike, 2005). Earth's orbital eccentricity varies in a cyclic manner between e values of 0 to about 0.06 (today, $e \approx 0.01671$) (Pälike, 2005), with a largest-amplitude period of about 400,000 years (400 ky) known as "long" eccentricity, and additional periods at around 95 and 123 ky, that are known as "short" eccentricity (Pälike, 2005; Berger et al., 2006). The Sun occupies one of the orbital focal points of Earth's orbit, so that, through one annual revolution around the Sun, Earth passes a point nearest to the Sun (perihelion) and one furthest from the Sun (aphelion); the difference in the distance from Earth to the Sun between these points is about 2e. The annual variation of solar insolation due to eccentricity between aphelion and perihelion is roughly 4e; today it is about 6.8% versus about 24% at maximum eccentricity. Eccentricity causes (small) variations in the total annual-mean amount of solar radiation received by Earth (by less than 0.5 Wm^{-2}; Loutre et al., 2004) through its influence on the mean distance between Earth and the Sun; i.e., as a function of $(1 - e^2)^{-0.5}$ (Berger and Loutre, 1994; Loutre et al., 2004). Eccentricity's main influence is that it modulates the amplitude of the precession cycle (Loutre et al., 2004).

The precession cycle arises from a "wobble" in Earth's rotational axis relative to the plane of the Earth's orbit, similar to the wobble of a spinning top. This wobble causes cyclical change in the direction of Earth's axis in space. A full cycle of axial precession takes about 26 ky. However, other complications in the Earth-Sun motions come into play; notably, the entire Earth orbit itself slowly rotates around the Sun in about 112 ky (so-called apsidal precession). As a result of the various

complex interactions, precession of the equinoxes and its manifestation in insolation received by Earth shows two dominant periodicities; one centered on about 23 ky and one on about 19 ky (Pälike, 2005). As a first-order approximation, an average periodicity of 22 ky is often used.

Precession affects climate by causing a slow shifting of the dates of the solstices and equinoxes along the orbit. Today, in its slightly elliptical orbit, perihelion occurs near to the northern winter (southern summer) solstice (3 January and 21 December, respectively), while aphelion occurs near to the northern summer (southern winter) solstice (4 July and 21 June, respectively). Given that some eccentricity applies today (albeit weak), insolation on illuminated places of the globe is somewhat more intense in northern winter (southern summer) than in northern summer (southern winter). This weakens the northern hemisphere seasonal contrast and intensifies that on the southern hemisphere. Half a cycle (about 11 ky) ago, perihelion occurred near to the northern summer (southern winter) solstice, and aphelion near to the northern winter solstice. This enhanced northern hemisphere seasonal contrasts, and weakened southern hemisphere seasonal contrasts. A full cycle ago, the configuration was similar to that of today. Importantly, the climatic impacts of precession and eccentricity need to be viewed together. When the orbit approaches a circle, the distance differences have negligible effects, while the distance effects are maximized during eccentricity maxima. While precession governs the seasonal insolation contrast, the amplitude of its impact depends on orbital eccentricity; precession has negligible impact when the orbit is near circular, and reaches maximum impact at times of maximum eccentricity.

The third astronomical cycle concerns the gradually changing angle (tilt, or obliquity) of Earth's spin axis relative to the perpendicular to the plane of Earth's orbit. This angle varies between just over 22 and 24.5 degrees, with a strong period of about 41 ky and additional periods of 29 and 54 ky. Today, the angle is about 23.45 degrees (Pälike, 2005). Increasing obliquity increases the amplitude of the seasonal insolation cycle (increasing summer insolation and decreasing winter insolation). Obliquity influences on the total annual insolation received per latitude show a change of sign at around 40 degrees latitude (for illustration, Loutre et al., 2004; Rohling et al., 2012). The influence of obliquity on total insolation received with latitude is strongest at high latitudes. Obliquity also determines the maximum latitudes where the Sun reaches a directly overhead position; i.e., the latitudes of the Tropics of Cancer and Capricorn, which shift between about 22.04 and 24.45 degrees through an obliquity cycle.

Orbital forcing has resulted in several key impacts on climate in the wider Mediterranean watershed areas. Most notably, the precession cycle has strongly affected the Mediterranean moisture balance over at least the past 15 million years (My), through its influence on especially the North African monsoon, and also on the Indian/East African monsoon. Because of the precession influence on seasonal contrasts and the different heat capacities of land and ocean, northern hemisphere monsoons are weaker during precession maxima (configurations similar to today), and intensified during precession minima (configurations similar to that of half a

precession cycle ago), while monsoon expansions during the latter phases are likely to have been amplified by feedbacks that include evaporation and transpiration from lakes, wetlands, and vegetation (e.g., Braconnot et al., 2008; Krinner et al., 2012; Bosmans et al., 2015; Rachmayani et al., 2015; Kutzbach et al., 2020). The periodic recurrence of precession minima drives a regular recurrence of 6 to 10-ky North African and Indian/East African monsoon maxima, which cause enhanced freshwater flooding into the Mediterranean Sea via the Nile and other (currently dry) rivers along the African margin of the basin (see below). In addition, regional precipitation over the Mediterranean and immediately surrounding lands may have been intensified during precession minima (see below). Because the amplitude of precession influences is modulated by orbital eccentricity into 100- and 400-ky clusters, intervals of high-amplitude precession minima with strong associated monsoon flooding alternate with intervals of lower-amplitude precession minima with weaker monsoon flooding.

Northern hemisphere monsoons, including the monsoon system over North Africa, were not only intensified during monsoon maxima, but had also spatially expanded (e.g., Fig. 3.5, Last Interglatial). The Sahara desert greened as savanna and woodland environments expanded in northerly and easterly directions. This resulted in so-called Green Sahara Periods (GSPs) with rivers, major lakes, and widespread presence of animals and early humans (e.g., Pachur and Braun, 1980; Pachur, 2001; Osborne et al., 2008; Paillou et al., 2009, 2012; Drake et al., 2011, 2013; Whiting-Blome et al., 2012; Coulthard et al., 2013; Larrasoaña et al., 2013; Rohling et al., 2015). The (currently dry) rivers along the African margin were fed by this abundance of water, especially as the monsoon front expanded across the central Saharan watershed, which lies at about 21 degrees N (Rohling et al., 2002a, 2004; Osborne et al., 2008; Coulthard et al., 2013; Amies et al., 2019). Monsoon penetrations to the north of this watershed mainly resulted from precession minimum conditions-assisted by feedbacks over the more humid, more vegetated, and less dusty North African landmass (Pausata et al., 2016; Hopcroft et al., 2017)-with a potential secondary influence of further northward displacement of the Tropic of Cancer during obliquity maxima (although modeling suggests a strong precession dominance; Bosmans et al., 2015). Resultant monsoon-driven freshwater flooding into the Mediterranean Sea caused deep-water ventilation crises and associated productivity changes, which together resulted in deposition of remarkable organic-carbon enriched marine sediments, known as sapropels, since at least ~14 My ago (e.g., Rossignol-Strick et al., 1982; Rossignol-Strick, 1983, 1985; Rohling and Gieskes, 1989; Howell and Thunell, 1992; Béthoux, 1993; Castradori, 1993; Rohling, 1994; Thomson et al., 1995, 1999; Emeis et al., 1998, 2000a, 2000b, 2003; Béthoux and Pierre, 1999; Jorissen, 1999; Kemp et al., 1999; Casford et al., 2002, 2003; Rohling et al., 2004, 2015; Bianchi et al., 2006; De Lange et al., 2008; Larrasoaña et al., 2013; Amies et al., 2019).

An early synthesis regarding climate over the Mediterranean basin itself at times of sapropel deposition suggested an increase in Mediterranean depression activity (Rohling and Hilgen, 1991), and some pollen-based reconstructions suggested

that this activity was focused on summer (Rossignol-Strick, 1987; Wijmstra et al., 1990). However, subsequent palynological, lake isotopic, lake-level, and climate modeling studies instead suggest that summers were arid, and that the regional signals of precipitation increase relate to increased Mediterranean storm-track activity in winter (e.g., Tzedakis, 2007, 2009; Brayshaw et al., 2011; Kutzbach et al., 2014; Bosmans et al., 2015).

Global glacial-interglacial (G-IG) cycles are another key expression of orbital climate forcing with considerable impact on the Mediterranean. Between ~34 and ~2.5 My ago, only the southern hemisphere (Antarctica) experienced large glacial expansion and contractions (e.g., Rohling et al., 2021, and references therein). About 2.5 million years ago, major ice ages appeared also in the northern hemisphere, so that global G-IG cycles became of a markedly bipolar nature. From ~8 to ~1 My ago, G-IG cycles had a dominant period governed by the ~41 ky cycle of obliquity or tilt of the Earth's rotational axis. Over a 500 ky interval centered on ~1 My ago (the so-called Mid-Pleistocene Transition, MPT), this shifted to G-IG cycles with a period of ~100 ky (Shackleton and Opdyke, 1973, 1976, 1977; Pisias and Moore, 1981; Ruddiman et al., 1986, 1989; Chalk et al., 2017; Willeit et al., 2019). The amplitude of these ~100 ky G-IG cycles became markedly amplified at around 500 ky ago. For further details of these changes, see Miller et al. (2020), Westerhold et al. (2020) and Rohling et al. (2021).

G-IG cycles have influenced the Mediterranean directly (e.g., Fig. 3.5, contrast between Last Glacial Maximum and Last Interglacial or Holocene), through modifications in atmospheric conditions and circulation patterns over the basin. This imprint is evident in records of extensive cooling and glacier equilibrium line lowering (e.g., Hayes et al., 2005; Kuhlemann et al., 2008), and in the presence of variations at precession, obliquity, and eccentricity frequencies in productivity and Saharan wind-blown dust fluxes into the Mediterranean basin (e.g., Lourens et al., 1992; Wehausen et al., 2000; Larrasoaña et al., 2003, 2013; Konijnendijk, 2014; Grant et al., 2017). Specifically, dust fluxes are high during ice ages and precession maxima (African monsoon minima), indicating more arid conditions with sparse vegetation cover and consequent enhanced ablation from the Sahara desert. With respect to the long-term trends, the early development of substantial northern hemisphere ice ages led to increasing seasonal contrasts in the Mediterranean region, with very dry summers (Suc, 1984; Thunell, 1986). The modern alternation between cool wet winters and hot dry summers first developed around 3.2 My ago during the Mid-Pliocene Warm Period (see Fig. 3.5); summer drought then intensified from ~2.8 My ago, culminating in periodic appearance of steppe vegetation in the Mediterranean region from ~2.3 My ago (Suc, 1984). The MPT at around 1 My ago is also well expressed in Mediterranean stable isotope, faunal, and floral records (e.g., Zachariasse et al., 1989, 1990; Thunell et al., 1991; Lourens et al., 1992; Vergnaud-Grazzini et al., 1993).

G-IG cycles have also influenced the Mediterranean in an indirect manner, through sea-level variations that over the last million years ranged between about +10 and −130 m, relative to present. These variations drove cycles of

shelf-sea emergence and flooding, which have been especially notable in regions with large shelf areas, such as the Adriatic Sea, the Aegean Sea, and the Gulf of Sirte. Even more importantly, sea-level cycles affected water exchange through important sea straits; for example, the Bosporus/Dardanelles to the Black Sea (Lane-Serff et al., 1997; Myers et al., 2003 and references therein), and the Strait of Gibraltar (e.g., Rohling, 1999; Rogerson et al., 2005, 2006; Rohling et al., 2014).

The Black Sea gets disconnected from the Sea of Marmara when sea level drops below the sill in the Bosporus Strait, which is today found at ~35 m depth, and the Sea of Marmara, in turn, gets disconnected from the Mediterranean when sea level drops below the sill in the Dardanelles Strait, which today resides at ~80 m depth (Ryan et al., 1997; Myers et al., 2003). This means that for much of the Pleistocene, when ice ages caused more than 35 m of sea-level lowering (e.g., Rohling et al., 2009a; Grant et al., 2012, 2014; Spratt and Lisiecki, 2016), the Black Sea was a fresh-water basin (Black Lake) that was isolated from Mediterranean water inflow (Badertscher et al., 2011).

Sea-level impacts on the Strait of Gibraltar have been notable as well, even though, since the Strait of Gibraltar opened up in the earliest Pliocene, Plio-Pleistocene G-IG sea-level variations never became large enough to isolate the Mediterranean from the Atlantic Ocean. This is because the Camarinal Sill, Strait of Gibraltar, has a maximum depth of 284 m, which considerably exceeds the greatest ice-age sea-level drop. Yet, the sea-level variations still resulted in severe restrictions in the water exchange through the Strait of Gibraltar (Rohling, 1999; Rohling et al., 2014). These restrictions caused increases in the water residence time within the highly evaporative Mediterranean, and thus enhanced water salinities and stable oxygen isotope ratios. Time-series of this influence on stable isotope ratios can be measured using microfossils, and these records can then be translated into sea-level time series (Rohling et al., 2014). In addition, the changes in Mediterranean outflow volume and salinity (density) had considerable impacts on the nature of subsurface Mediterranean Outflow and thus on subsurface oceanography in the eastern North Atlantic (Rogerson et al., 2005, 2006) (see Chapters 2 and 4).

3.6.2 The formation of the Mediterranean and geophysical forcing of Mediterranean climate

The Mediterranean is a final, closing remnant of the ancient Tethys Ocean, which began closing via subduction along its northern margin from ~150 My ago (Rohling, 2017). The thrust zone currently winds from the Strait of Gibraltar through the Rif-Maghreb range of northernmost Morocco and Algeria, then winds northward through Sicily, Italy, the Alps, and south-eastward again through the Dinarides down to Albania. From there, it passes offshore around Greece, winding eastward to the south of Crete and along Cyprus, from where it continues along the south of the Anatolian highlands (van Hinsbergen et al., 2020). The trust processes, with associated lateral movements, extension regions, and adjustment processes, were responsible for the formation of the mountain ranges along this entire trajectory (both on

land and below the sea), which started roughly around 150 My ago and is still ongoing in many places (van Hinsbergen et al., 2020). Formation and uplift of these ranges (including also the Pyrenees) would have accentuated the isolation of the Mediterranean region from temperate mid-latitude climates, and amplified regionality of these climate impacts downstream of gaps in the mountain chains.

Van Hinsbergen et al. (2020) also indicate that deep basins in the northern and western Mediterranean sectors are relatively young features, which formed through various extension phases between 30 and 11 My ago. As such, the Mediterranean predominantly represents Tethys Ocean remnants in the south and east, and more recent elements to the north and west.

At the eastern end, connection of the proto-Mediterranean with the Indian Ocean, via the so-called Mesopotamian Seaway, was lost in two stages: first, water mass exchange was reduced by ~90% at ~20 My ago; second, terminal closure of the seaway occurred close to 13.8 My ago (Bialik et al., 2019). The proto-Mediterranean from that time onward was connected only with the Atlantic Ocean, via two Straits: the Betic Strait through today's Southern Spain, and the Rifian Corridor through today's northern Morocco. The Rifian corridor closed at 6.08 My ago, and the Betic Strait at 5.96 My ago (Krijgsman et al., 1999a, 1999b, 2001; Hilgen et al., 2007; CIESM, 2008).

From 5.96 until 5.33 My ago, the Mediterranean underwent a phase of evaporite deposition, known as the Messinian Salinity Crisis (MSC). An estimated total of $\sim 7 \times 10^{18}$ kg of evaporites was deposited during this event (Blanc, 2000, 2006). Traditionally, three phases (the "trilogy") have been recognized within the MSC (Krijgsman et al., 1999a; Krijgsman et al., 2001; Van Assen et al., 2006; Hilgen et al., 2007; and references therein). The first phase comprises the Lower Evaporites, with massive selenite gypsum deposits in shallower regions (5.96–5.59 My ago). Then followed a widespread erosive phase, which marks the apex of the MSC with widespread basin desiccation (5.59–5.50 My ago) (Hilgen et al., 2007; Krijgsman et al., 1999a; CIESM, 2008). The final phase comprises the Upper Evaporites (5.50–5.33 My ago); a peculiar mix of evaporites and alternating marine and lacustrine deposits ("Lago Mare"; Hsü et al., 1973; Ruggieri and Sprovieri, 1976; McCulloch and De Deckker, 1989; Flecker et al., 2002; Hilgen et al., 2007; CIESM, 2008).

During the culmination of evaporative drawdown, Mediterranean sea levels stood ~1300 – ~2700 m below global sea level (Meijer and Krijgsman, 2005; Blanc, 2006; Gargani and Rigollet, 2007; Urgeles et al., 2011). Based on a moist adiabatic lapse rate of ~6.5 °C km^{-1} (within the ranges given by Alpert and Shafir, 1989; Vardavas et al., 1997; Dayan et al., 2002) and typical modern summer temperatures of ~30 °C at global sea level, this suggests typical Mediterranean surface temperatures during the maximum MSC desiccation phase(s) between roughly 38 and 48 °C. Add to this a high surface reflectivity because of light-colored evaporites and limited (salt-impaired) vegetation, as well as the generally corrosive nature of evaporite salts and highly concentrated brines, and both surface climate and environment in the partially desiccated Mediterranean must have been rather hostile, except

perhaps along river channels. The MSC ended at ~5.33 My ago, when the partially desiccated basin abruptly filled as the Gibraltar Strait opened up. It is estimated that the basin filled catastrophically, within a few years (Garcia-Castellanos et al., 2009, 2020; Micallef et al., 2018).

Clearly, intense tectonics (initially mainly compression and later also dominant extension) until ~11 My ago, and subsequent rapid uplift that continues even today (e.g., km-scale Plio-Pleistocene uplift in Italy: Galadini et al., 2003; Olivetti et al., 2012) have continuously affected landmasses bordering the (proto-)Mediterranean Sea. These processes were spatially highly variable (van Hinsbergen et al., 2020), and have significantly impacted micro- and meso-climate differentiations across the basin, as well as larger-scale processes such as cyclogenesis within the basin. Superimposed, the MSC presents an interval with exceptional oceanographic and climatic responses.

To summarize, palaeoceanographic conditions reveal a remarkably consistent variability through the last ~14 million years, both before and after the MSC, with respect to the alternation between sapropel and nonsapropel deposition. Throughout this period, this African monsoon driven rhythm seems to represent the dominant (first-order) climate forcing and oceanographic response in the Mediterranean (Rohling and Thunell, 1999; and references therein). Superimposed development of typical Mediterranean summer versus winter contrasts, and desertification of the Sahara region took place in response to long-term, secular, global cooling from the warm Miocene to the Late Pleistocene, with likely additional adjustments that were more related to the region's tectonic history. Also superimposed were the G-IG cycles over 10^4 to 10^5year timescales, ultimately driven by astronomical climate forcing, which modulated amplitude variations of the African monsoon events and imposed alternations of more intense (weaker) northern continental/polar influences during glacials (interglacials).

More details on the tectonic processes at the origin of the Mediterranean Sea and the particular paleo-environmental event known as the Messinian salinity crisis have been described in the dedicated Chapter 2.

3.6.3 The last million years: the glacial cycles

The duration of G-IG cycles changed from ~41- to ~100-ky over the MPT, which was centered on ~1 My ago, and the G-IG cycle amplitude became markedly amplified at around 0.5 My ago. Before the MPT, glacial and interglacial conditions alternated in a temporally roughly symmetrical pattern (similar durations), whereas the world spent much more time in glacial conditions than interglacial conditions after the MPT. Glacials are in general characterized by more wind-blown dust input into the Mediterranean Sea than interglacials (Larrasoaña et al., 2003), likely because vast expansion of northern hemisphere ice sheets suppresses northward penetration and intensification of the monsoon system over North Africa during precession-driven insolation maxima. Consistent with the MPT change in G-IG cycles, wind-blown dust input into the Mediterranean increased dramatically by ~1

My ago, and eccentricity-related 400- and 100-ky periodicities gained importance in the windblown input records (Larrasoaña et al., 2003).

However, the story of dust transport into the Mediterranean is not a simple G-IG story; there remains a notable imprint of the precession-driven monsoon cycles, and intriguingly also a clear expression of obliquity. Larrasoaña et al. (2003) report that reduced dust input occurred during periods of high obliquity throughout their record, even after the MPT. They hypothesize that this results partly from obliquity-driven changes in the southern hemisphere meridional temperature gradient in southern winter, creating cross-equatorial, northward "push" on northern hemisphere monsoons (high obliquity ==> enhanced temperature gradient ==> stronger cross-equatorial "push" ==> stronger monsoons ==> reduced dust); and partly from the aforementioned slight obliquity-related latitudinal shift of the tropic of Cancer, which may have assisted monsoon penetration to the north of the central Saharan watershed. Thus, dust variations show generally enhanced input during glacials, but no straightforward glacial <==> dusty relationship. There are substantial superimposed complications because monsoon variations are not just (or even dominantly) affected by G-IG cycles.

G-IG cycles are, at their core, primarily characterized by variations in global ice-volume (and, thus sea-level), and global temperature. During the last glacial maximum (LGM; ~30 to ~19 ky ago), global mean temperature was between 4 and 7 °C lower than today, and global mean sea level stood between about 120 and 130 m lower than today (e.g., Grant et al., 2012, 2014; Rohling et al., 2012, 2017; Spratt and Lisiecki, 2016; Snyder, 2016; Hibbert et al., 2016, 2018; Yokoyama et al., 2018; Sherwood et al., 2020; Tierney et al., 2020). This implies that, relative to the present, an extra continental ice volume existed that was equivalent to about 2 times the size of the Antarctic ice sheet. Most of this additional ice was located on the North American and Eurasian continents (for an overview, see Rohling et al., 2017).

Annual mean Mediterranean SSTs during the LGM reveal strong cooling over the entire western Mediterranean (more than −4 °C, up to −8 °C) and over the Aegean Sea (about −6 °C), and moderate cooling only over the open Ionian and Levantine basins (less than −2 °C, up to −4 °C) (Hayes et al., 2005; Kuhlemann et al., 2008). In the western Mediterranean, LGM reduction in SST was almost equally pronounced in summer and winter, but in the eastern Mediterranean cooling was predominantly focused in summer while winter temperatures were only ~1 °C lower than today (Hayes et al., 2005).

LGM atmospheric conditions in the Mediterranean region have been inferred from glacier equilibrium line lowerings on landmasses bordering the basin, and on islands with high topography (Kuhlemann et al., 2008). This reveals strong indications for frequent, topographically channeled, cold polar air incursions over the north-western Mediterranean Combined with the SST patterns (Hayes et al., 2005), this suggests a preferentially meridional circulation, a configuration favored by northward extension of the Azores High toward Iceland or Greenland, blocking westerly moisture supply. This configuration may have been further enhanced by

expansion and intensification of the Siberian High in winter (Rohling et al., 2002b). Kuhlemann et al. (2018) also find evidence for anomalously steep vertical temperature gradients in the central Mediterranean, which imply local convective precipitation. They infer that the topographically channeled polar air incursions drove more frequent cyclogenesis in the Ligurian Sea, which in turn enhanced precipitation along storm tracks in eastward directions from the Ligurian Sea.

3.6.4 The last millennia: the historical period

Throughout the last 11,000 years (Holocene), the Mediterranean region has been affected by centennial-to millennial-scale cool events; especially at 8.6−8.0 (or 7.8) ky ago, 6−5.2 kyrago, 3.1−2.9 ky ago, and during the Little Ice Age (LIA) at 0.6−0.15 ky ago (e.g., Rohling et al., 1997; Casford et al., 2003; Mercone et al., 2001; Rohling et al., 2002a,b, 2009b, 2019; Clare et al., 2008; Marino et al., 2009; Gogou et al., 2016). These were strongly related to episodes of intensified cold outbreaks through gaps in the northern rim of mountain ranges around the basin (Rohling et al., 2002b, 2019). The episode of 8.6−8.0 (or 7.8) ky ago caused interruption of sapropel formation, and that of 6−5.2 ky ago coincided with the termination of Holocene sapropel formation (e.g., Rohling et al., 1997, 2002b; Mercone et al., 2001; Casford et al., 2003; Kuhnt et al., 2007; Abu-Zied et al., 2008). This attests to the profound cooling influence of these events, which was sufficient to overcome long-lasting water-column stratification, resulting in ventilation that drove a return of bio-available oxygen to the deep sea. But similar-magnitude surface cooling was observed for the other Holocene events, and a model-based case history for the Aegean Sea found that the observed magnitudes of cooling agree with the expected evaporative cooling impacts of enhanced-frequency outbreaks of cold northerly airflows (Rohling et al., 2019).

The major events noted above, spaced ∼2400 years apart (Rohling et al., 2002b; Mayewski et al., 2004), are not alone in eastern Mediterranean records: there are many smaller/shorter fluctuations in ecosystem responses, which may be related to hydrological variations. Besides the ∼2400-year period, spectral analyses reveal an ∼1600-year period, as well as periods around ∼1000 and ∼800 years (Hennekam et al., 2014; Le Houedec et al., 2020). A link with solar output changes is sometimes inferred for the variations in Holocene records, based on agreement with variations in cosmogenic isotope series (^{10}Be and radiocarbon residuals) (e.g., Beer et al., 2000; Haigh, 2003; Maasch et al., 2005; Hennekam et al., 2014), although some periods may also reflect internal oscillators (Le Houedec et al., 2020 and references therein).

Based on modern and historical observations and accounts, we here summarize first the "on the ground" expressions of modern northerly polar/continental (NPC) air outbreaks, and next the consequences of a period of enhanced-frequency NPC air outbreaks based on the LIA. This summary draws heavily on that given in Rohling et al. (2019).

Individual wintertime NPC air outbreaks have been well documented during the instrumental era (Mariolopoulos, 1961; Theocharis, 1989; Roether et al., 1996; Poulos et al., 1997; Maheras et al., 1999; Lolis et al., 2002; Tolika et al., 2014; Anagnostopoulou et al., 2017). NPC air outbreaks do not occur during summer (Saaroni et al., 1996), but southward displacement of North African subtropical conditions in winter (Lionello et al., 2006a; Rohling et al., 2015) allows both southward expansion of westerly, moist temperate airflows, and occasional atmospheric blocking patterns that result in cold and dry NPC outbreaks (e.g., Tolika et al., 2014). The outbreaks play a key role in cyclogenesis over the Mediterranean, as cold air masses gain moisture and become conditionally unstable over the warmer waters (Tarolli et al., 2012). At the same time, there is intense evaporation and cooling of Mediterranean surface waters (e.g., Leaman and Schott, 1991; Saaroni et al., 1996; Poulos et al., 1997; Maheras et al., 1999; Casford et al., 2003; Josey et al., 2011; Velaoras et al., 2017). In the late 1980s—early 1990s, frequent events over the Aegean contributed to profound changes in eastern Mediterranean deep-water circulation (Theocharis, 1989; Roether et al., 1996). Casford et al. (2003) reported that the impacts of prolonged episodes with high event intensity/frequency substantially affected deep-water circulation in the Aegean-Levantine region throughout the Holocene, and Incarbona et al. (2016) found further compelling evidence for such a relationship within the past 500 years.

Between December 2001 and January 2002, a high-intensity (eight to nine Beaufort) and freezing (down to $-2\,^{\circ}C$) north-northeasterly outbreak occurred over the Aegean Sea (Casford et al., 2003; Clare et al., 2008). It was associated with exceptional snowfall around the Aegean region, leading to $\sim$30 cm in Istanbul and Athens. Temperatures in Bulgaria and northern and central-eastern Greece dropped to $-20\,^{\circ}C$, and there was widespread disruption of infrastructure and services (see summary in Clare et al., 2008). More than 300 villages in central and northern Greece became isolated, and there were many deaths from exposure (Rohling et al., 2019). In earlier years, 1929 and 1954, conditions were even more severe, causing much of the Bosporus to freeze over (Yavuz et al., 2007).

These instrumentally documented phenomena can be compared with documentary/anecdotal evidence for the LIA, illustrating the impacts of sustained cold NPC air outbreaks over the Aegean-Levantine region (e.g., Xoplaki et al., 2001; Yavuz et al., 2007; Clare et al., 2008; Clare, 2016). LIA accounts indicate more cold/severe winters and springs; a significant tendency to more winter precipitation; and also significantly more winter drought (Xoplaki et al., 2001; Clare, 2016). In other words, a significant increase in winter extremes, being either very cold, very wet/snowy, or very dry. Development/expansion of glaciers occurred in many Mediterranean mountain locations, and (semi-) permanent snowfields became established in the mountains of Greece (Hughes, 2014). In the Pirin Mountains of SW Bulgaria, mean summer temperatures dropped by $2-3^{\circ}C$ at around 1600 AD; soil formation processes came to a halt, the snowline descended, the vegetation period became shortened, and snow cover persisted for longer (Grunewald and Scheithauer, 2010). Frequent widespread freezing occurred in the Black Sea,

Bosporus, Golden Horn, and Istanbul region (Yavuz et al., 2007), and mean surface mixed-layer temperatures dropped by ~2 °C in the northern Aegean Sea (Gogou et al., 2016). There were increased flooding frequencies and fluvial discharge around the Aegean (see overview in Gogou et al., 2016). Conversely, high-altitude (1363 m) central Anatolia seems to have experienced increased aridity (Dean et al., 2013). This suggests increased vertical contrasts, possibly due to specific local conditions over the Anatolian highlands (Rohling et al., 2019).

Overall, the main synoptic situations responsible for the region's winter cold and snowfalls during the LIA were found to involve northerly airflow, with high pressure over northern Europe and lower pressure over the central or eastern Mediterranean (Xoplaki et al., 2001). This pattern is very similar to that associated with individual cold outbreaks during the instrumental era. The spatial distribution of impacts also bears strong similarity to that reconstructed (in more intense form) for the LGM mean state of climate over the Mediterranean (Kuhlemann et al., 2008).

In between the Holocene cold events, conditions were relatively warm. For example, stable isotope data from the Gulf of Taranto revealed a succession from a relatively wet and warm Roman Warm Period (RWP; 2.5−2.0 ky ago) , which changed via the Roman Classical Period (RCP; 2.0−1.8 ky ago) to the wetter Dark Ages Cold Period (DCP; 1.5−1.25 ky ago), to the Medieval Warm Period, which was more humid and warm at first and which then gradually become more arid toward an arid LIA (Grauel et al., 2013). Over the latter 2000 years or so, anthropogenic landscape influences may have played a role in climate change over the Mediterranean. Pollen and vegetation data indicate that the RWP-RCP interval was characterized by denser vegetation that led to a lower albedo (Reale and Shukla, 2000). Applied in a high-resolution GCM, this resulted (relative to the present) in "a northward shift of the ITCZ over the African continent and a coupled circulation between north-western Africa and the Mediterranean Sea. A large increase of precipitation occurs over the Sahel, the Nile valley and north-western Africa. A smaller increase of precipitation occurs also over the Iberian Peninsula and the region corresponding to the south of the Caucasus range (Armenia)" (Reale and Shukla, 2000). The authors concluded that current aridity around the Mediterranean region was substantially accentuated by deforestation over the last 2000 years.

3.6.5 Anthropogenic climate change

The massive use of fossil fuels by human activities has caused an artificial increase of the concentration of greenhouse gases, mainly of CO_2 from 280 ppm in the second half of the 19th century to more than 400 ppm at the beginning of the 21st century (Prentice et al., 2001). This level was never reached in the past two million years (IPCC 2021). There are indications that this increase is occurring at a rate unprecedented in the last 66 million years (Zeebe et al., 2016) and in absence of successful climate change mitigation policies might determine the doubling of CO_2 concentration with respect to preindustrial time within the next decades. The increase of CO_2 and of other anthropogenic greenhouse gases has important consequences on the

energy budget of the atmosphere leading to the ongoing global warming and climate change (Ramanathan and Feng, 2008). The Mediterranean region is impacted by this process through changes of temperatures, precipitation and other climate variables, with important effects on the environment and sectors important to society (Gutiérrez et al., 2021; MedECC, 2020).

Though variability at subregional scale plays an important role, the overall evolution of the temperature of the Mediterranean region in response to the anthropogenic climate change can be understood in terms of some basic conceots: the important role of the heat capacity of the Mediterranean Sea, the poleward intensification of the anthropogenic warming, the relevance of regional dimming produced by anthropogenic aerosols, and the amplification produced by regional circulation changes in summer. In fact, warming is not uniform across the Mediterranean region and it has not occurred at the same rate in all seasons and in all periods. Interior continental areas warm faster than coastal areas, consistently with the mitigation effect caused by the large capacity of the Mediterranean Sea. This attenuation is present in general for the whole Mediterranean region, which at annual scale tends to warm less than other regions in the same range of latitudes (Lionello and Scarascia, 2018). Global warming is not uniform and is characterized by an amplification of the temperature increase with latitude, with tropical areas warming significantly less than the high latitudes, particularly those of the northern hemisphere. This effect is evident at the latitudes of the Mediterranean region, which is warming approximately 20% faster than the global mean (Lionello and Scarascia, 2018; Cherif et al., 2020). Anthropogenic aerosols tend to concentrate over industrial areas of the northern hemisphere. Their prevalent effect on the energy balance of the surface is to decrease solar radiation (global dimming, Wild et al., 2012), both directly by reflecting it and indirectly by affecting cloud formation. In fact, anthropogenic aerosols have had a negative effect on surface temperature until the 1980s, when regulation of industrial pollution has successfully reduced them over many areas. This reduction of the warming rate has been observed also in the Mediterranean region and is consistent with the pause of warming from the 1950s to early 1980s (Nabat et al., 2013, 2015). Summer appears to be the season with the largest warming, up to 50% larger than the global mean. Explanations could be linked to changes of the atmospheric circulation and of the land atmosphere coupling. The role of the latter appears particularly relevant as, particularly during dry spells and the semiarid summer period, the absence of moisture in the soil to support surface cooling by evapotranspiration provides a positive feedback to regional warming processes.

In conclusion, the Mediterranean region at the end of the 2020s is about 1.5°C warmer than during the preindustrial period (Cherif et al., 2020), while the global mean temperature has increased approximately by 1.1°C (IPCC, 2021). The mean summer temperature in the 3 decades around the end of the 20th century has been warmer than in any previous 30-year long period since Roman times (Luterbacher et al., 2016). Warming is expected to continue as global warming will increase (Lionello and Scarascia, 2018) at a rate larger than the global mean, particularly

in summer with a spatial variability reflecting the considerations presented above (see Fig. 3.6).

The increase in the mean temperature is associated with a shift toward higher values of the whole temperature probability distribution, so that both its upper and lower tails move to higher values. This implies that the frequency of days with high and low temperatures increases and decreases, respectively, and intensity and duration of heat waves increases, with hotter extremes and more days above high temperature thresholds (Lionello and Scarascia, 2020). Fig. 3.7 shows the increase in the frequency of the number of days with maximum temperature above 40°C in case of global warming levels of 2 and 4°C.

As the atmosphere becomes warmer, the Clausius-Clapeyron law, which describes the dependence of saturation pressure of water vapor on temperature, predicts that the moisture content of the atmosphere increases. This physical law has been used as a basic guideline for understanding the intensification of the hydrological cycle and increasing precipitation in response to global warming (Trembert et al., 2003; Held and Soden, 2006; O'Gorman and Muller, 2010). An associated consequence is the increase in horizontal water vapor transport within the atmosphere and the enhancement of the P-E pattern, which is commonly described as that the wet-get-wetter and dry-get-drier paradigm (Held and Soden, 2006). The Mediterranean region drying in future climates is conceptually consistent with this concept. However changes of precipitation at regional scale are strongly modulated by atmospheric circulation and its role in humidity advection. Especially in summer heat lows develop over continental areas (such as over Iberia and Sahara) and corresponding circulation tends to isolate these areas from the sources of humidity (Drobinski et al., 2020). Winter precipitation is determined by cyclonic activity with the strength of the Mediterranean branch of the mid-latitude storm track whose northward shift and attenuation in future climate conditions contributes to decreasing precipitation in the Mediterranean region (Lionello and Giorgi, 2007; Zappa et al., 2015). Global model simulations project a decrease of total annual precipitation at a rate of about 4%/°C as a function of global warming (Fig. 3.6, Lionello and Scarascia, 2018).

Increase in low level moisture driven by the Clausius Clapeyron relation provides also the basis for expecting an increase in extreme precipitation driven by moisture convergence as the atmosphere warms (Allan and Solden, 2008). As for total precipitation, however, also this mechanism is strongly mediated by atmospheric circulation, moisture transport and availability (Drobinski et al., 2018). In fact the Mediterranean region appears to have a different behavior in its northern part, where extreme precipitation increases, and southern parts, where no significant change is evident in model projections (Lionello and Scarascia, 2020).

Observations show uncertain changes of total precipitation and precipitation extremes, comparing the evolution of those variables from the preindustrial time until the beginning of the 21st century (Lionello et al., 2012). In fact, the large interannual and spatial variability of the precipitation fields in the Mediterranean region makes it difficult to identify statistically significant changes of an emerging climate

change signal. This difficulty is further enhanced by lack of observations, allowing identification of changes with respect to the preindustrial period particularly in the southern part of the Mediterranean region. The inclusion of new time series in the currently available databases is required to reach a robust conclusion on the observed long term trends of precipitation in the Mediterranean region.

Additional resources

- IPCC Interactive Atlas https://interactive-atlas.ipcc.ch
- The Med-CORDEX and EURO-CORDEX regional climate data: https://www.medcordex.eu, https://euro-cordex.net
- The datasets of the Climate Research Unit of the University of East Anglia https://www.uea.ac.uk/groups-and-centres/climatic-research-unit

References

Abu-Zied, R.H., Rohling, E.J., Jorissen, F.J., Fontanier, C., Casford, J.S.L., Cooke, S., 2008. Benthic foraminiferal response to changes in bottom water oxygenation and organic carbon flux in the eastern Mediterranean during LGM to Recent times. Mar. Micropaleontol. 67, 46–68.

Adler, R.F., Kidd, C., Petty, G., Morissey, M., Goodman, H.M., 2001. Intercomparison of global precipitation products: the third Precipitation Intercomparison Project (PIP-3). Bull. Am. Meteorol. Soc. 82 (7), 1377–1396.

Allan, R.P., Soden, B.J., 2008. Atmospheric warming and the amplification of precipitation extremes. Science 321 (5895), 1481–1484.

Alpert, P., Shafir, H., 1989. Meso-scale distribution of orographic precipitation: numerical study and comparison with precipitation derived from radar measurements. J. Appl. Meteorol. 28, 1105–1117.

Amies, J.D., Rohling, E.J., Grant, K.M., Rodríguez-Sanz, L., Marino, G., 2019. Quantification of African monsoon runoff during last interglacial sapropel S5. Paleoceanogr. Paleoclimatol. 34, 1487–1516, 2019.

Anagnostopoulou, C., Tolika, K., Lazoglou, G., Maheras, P., 2017. The exceptionally cold January of 2017 over the Balkan Peninsula: a climatological and synoptic analysis. Atmosphere 8, 252.

Badertscher, S., Fleitmann, D., Cheng, H., Edwards, R.L., Göktürk, O.M., Zumbühl, A., Leuenberger, M., Tüysüz, O., 2011. Pleistocene water intrusions from the mediterranean and Caspian seas into the Black Sea. Nat. Geosci. 4, 236–239.

Ban, N., Caillaud, C., Coppola, E., Pichelli, E., Sobolowski, S., et al., 2021. The first multi-model ensemble of regional climate simulations at km scale resolutions. Part I: evaluation of precipitation. Clim. Dyn. 57, 275–302.

Beer, J., Wende, W., Stellmacher, R., 2000. The role of the sun in climate forcing. Quat. Sci. Rev. 19, 403–415.

Berger, A., Loutre, M.F., 1994. Precession, eccentricity, obliquity, insolation and paleoclimates. In: Long-Term Climatic Variations. Springer, Berlin, Heidelberg, pp. 107–151.

Berger, A., Loutre, M.F., Mélice, J.L., 2006. Equatorial insolation: from precession harmonics to eccentricity frequencies. Clim. Past 2, 131−136.

Béthoux, J.P., 1993. Mediterranean sapropel formation, dynamic and climatic viewpoints. Oceanol. Acta 16, 127−133.

Béthoux, J.P., Pierre, C., 1999. Mediterranean functioning and sapropel formation: respective influences of climate and hydrological changes in the Atlantic and the Mediterranean. Mar. Geol. 153, 29−39.

Bialik, O.M., Frank, M., Betzler, C., Zammit, R., Waldmann, N.D., 2019. Two-step closure of the Miocene Indian ocean Gateway to the mediterranean. Sci. Rep. 9, 8842.

Bianchi, D., Zavatarelli, M., Pinardi, N., Capozzi, R., Capotondi, L., Corselli, C., Masina, S., 2006. Simulations of ecosystem response during the sapropel S1 deposition event. Palaeogeogr. Palaeoclimatol. Palaeoecol. 235, 265−287.

Blanc, P.-L., 2000. Of sills and straits: a quantitative assessment of the Messinian salinity crisis. Deep-Sea Res. I 47, 1429−1460.

Blanc, P.-L., 2006. Improved modelling of the Messinian salinity crisis and conceptual implications. Palaeogeogr. Palaeoclimatol. Palaeoecol. 238, 349−372.

Bosmans, J.H.C., Drijfhout, S.S., Tuenter, E., Hilgen, F.J., Lourens, L.J., Rohling, E.J., 2015. Precession and obliquity forcing of the freshwater budget over the Mediterranean. Quat. Sci. Rev. 123, 16−30.

Braconnot, P., Marzin, C., Grégoire, L., Mosquet, E., Marti, O., 2008. Monsoon response to changes in Earth's orbital parameters: comparisons between simulations of the Eemian and of the Holocene. Clim. Past 4, 281−294.

Brayshaw, D.J., Rambeau, C.M.C., Smith, S.J., 2011. Changes in Mediterranean climate during the Holocene: insight from global and regional climate modelling. Holocene 21, 15−31.

Campins, J., Genovés, A., Picornell, M.A., Jansà, A., 2011. Climatology of Mediterranean cyclones using the ERA-40 dataset. Int. J. Climatol. 31, 1596−1614.

Camuffo, D., Bertolin, C., Barriendos, M., et al., 2010. 500-year temperature reconstruction in the Mediterranean Basin by means of documentary data and instrumental observations. Climatic Change 101, 169−199.

Camuffo, D., Bertolin, C., Diodato, N., Cocheo, C., Barriendos, M., Dominguez-Castro, F., et al., 2013. Western Mediterranean precipitation over the last 300 years from instrumental observations. Climatic Change 117 (1), 85−101.

Casford, J.S.L., Rohling, E.J., Abu-Zied, R., Cooke, S., Fontanier, C., Leng, M., Lykousis, V., 2002. Circulation changes and nutrient concentrations in the Late Quaternary Aegean Sea: a non-steady state concept for sapropel formation. Paleoceanography 17, 2000PA000601.

Casford, J.S.L., Rohling, E.J., Abu-Zied, R.H., Jorissen, F.J., Leng, M., Thomson, J., 2003. A dynamic concept for eastern Mediterranean circulation and oxygenation during sapropel formation. Palaeogeogr. Palaeoclimatol. Palaeoecol. 190, 103−119.

Castradori, D., 1993. Calcareous nannofossils and the origin of eastern Mediterranean sapropels. Paleoceanography 8, 459−471.

Chalk, T.B., Hain, M.P., Foster, G.L., Rohling, E.J., Sexton, P.F., Badger, M.P.S., Cherry, S.G., Hasenfratz, A.P., Haug, G.H., Jaccard, S.L., Martínez-García, A., Pälike, H., Pancost, R.D., Wilson, P.A., 2017. Causes of ice-age intensification across the mid-Pleistocene transition. Proceedings of the National Academy of Sciences of the USA 114, 13114−13119.

Cherif, S., Doblas-Miranda, E., Lionello, P., Borrego, C., Giorgi, F., Iglesias, A., Jebari, S., Mahmoudi, E., Moriondo, M., Pringault, O., Rilov, G., Somot, S., Tsikliras, A.,

Vila, M., Zittis, G., 2020. Drivers of change. In: Cramer, W., Guiot, J., Marini, K. (Eds.), Climate and Environmental Change in the Mediterranean Basin − Current Situation and Risks for the Future. First Mediterranean Assessment Report. Union for the Mediterranean, Plan Bleu, UNEP/MAP, Marseille, France, pp. 59−180.

CIESM, 2008. In: Briand, F. (Ed.), The Messinian Salinity Crisis from Mega-Deposits to Microbiology — A Consensus Report, vol. 33. CIESM Workshop Monographs, Monaco, p. 168.

Clare, L., 2016. Culture change and continuity in the eastern Mediterranean during rapid climate change. Assessing the vulnerability of late Neolithic communities to a Little Ice Age. In: The seventh millennium cal B.C. Kölner Studien zur Prähistorischen Archäologie, vol. 7. Verlag Marie Leidorf.

Clare, L., Rohling, E.J., Weninger, B., Hilpert, J., 2008. Warfare in Late Neolithic/Early Chalcolithic Pisidia, southwestern Turkey. Climate induced social unrest in the late 7th millennium calBC. In: Budja, M. (Ed.), Documenta Praehistorica XXXV, pp. 65−92.

Clement, A., Bellomo, K., Murphy, L.N., Cane, M.A., Mauritsen, T., Rädel, G., Stevens, B., 2015. The Atlantic Multidecadal Oscillation without a role for ocean circulation. Science 350, 320−324.

Compo, G.P., Whitaker, J.S., Sardeshmukh, P.D., Matsui, N., Allan, R.J., Yin, X., Gleason, B.E., Vose, R.S., Rutledge, G., Bessemoulin, P., Brönnimann, S., Brunet, M., Crouthamel, R.I., Grant, A.N., Groisman, P.Y., Jones, P.D., Kruk, M., Kruger, A.C., Marshall, G.J., Maugeri, M., Mok, H.Y., Nordli, Ø., Ross, T.F., Trigo, R.M., Wang, X.L., Woodruff, S.D., Worley, S.J., 2011. The twentieth century reanalysis project. Quarterly J. Roy. Meteorol. Soc. 137, 1−28.

Coppola, E., Sobolowski, S., Pichelli, E., Raffaele, F., Ahrens, B., et al., 2020. A first-of-its-kind multimodal convection permitting ensemble for investigating convective phenomena over Europe and the Mediterranean. Clim. Dyn. 55, 3−34.

Coulthard, T.J., Ramirez, J.A., Barton, N., Rogerson, M., Brücher, T., 2013. Were rivers flowing across the Sahara during the last interglacial? Implications for human migration through Africa. PLoS One 8, e74834.

Criado-Aldeanueva, F., Soto-Navarro, F.J., García-Lafuente, J., 2012. Seasonal and interannual variability of surface heat and freshwater fluxes in the Mediterranean Sea: budgets and exchange through the Strait of Gibraltar. Int. J. Climatol. 32, 286−302.

Dai, A., Giorgi, F., Trenberth, K., 1999. Observed and model simulated diurnal cycles of precipitation in the contiguous United States. J. Geophys. Res. 104, 6377−6402.

Davis, G.K., 2007. History of the NOAA satellite program. J. Appl. Remote Sens. 1 (1), 012504.

Dayan, U., Lifshitz-Goldreich, B., Pick, K., 2002. Spatial and structural variation of the atmospheric boundary layer during summer in Israel—profiler and rawinsonde measurements. J. Appl. Meteorol. 41, 447−457.

Dean, J.R., Jones, M.D., Leng, M.J., Sloane, H.J., Roberts, C.N., Woodbridge, J., Swann, G.E.A., Metcalfe, S.E., Eastwood, W.J., Yigitbasioglu, H., 2013. Palaeo- seasonality of the last two millennia reconstructed from the oxygen isotope composition of carbonates and diatom silica from Nar Golu, central Turkey. Quat. Sci. Rev. 66, 35−44.

DeConto, R.M., Galeotti, S., Pagani, M., Tracy, D., Schaefer, K., Zhang, T., et al., 2012. Past extreme warming events linked to massive carbon release from thawing permafrost. Nature 484 (7392), 87−91.

Dee, D.P., Uppala, S.M., Simmons, A.J., Berrisford, P., Poli, P., Kobayashi, S., Andrae, U., Balmaseda, M.A., Balsamo, G., Bauer, P., Bechtold, P., Beljaars, A.C.M., van de

Berg, L., Bidlot, J., Bormann, N., Delsol, C., Dragani, R., Fuentes, M., Geer, A.J., Haimberger, L., Healy, S.B., Hersbach, H., Hólm, E.V., Isaksen, L., Kållberg, P., Köhler, M., Matricardi, M., McNally, A.P., Monge-Sanz, B.M., Morcrette, J.-J., Park, B.-K., Peubey, C., de Rosnay, P., Tavolato, C., Thépaut, J.-N., Vitart, F., 2011. The ERA-Interim reanalysis: configuration and performance of the data assimilation system. Q. J. R. Meteorol. Soc. 137, 553−597.

De Lange, G.J., Thomson, J., Reitz, A., Slomp, C.P., Speranza Principato, M., Erba, E., Corselli, C., 2008. Synchronous basin-wide formation and redox-controlled preservation of a Mediterranean sapropel. Nat. Geosci. 1, 606−610.

Deser, C., Alexander, M.A., Xie, S.P., Phillips, A.S., 2010. Sea surface temperature variability: patterns and mechanisms. Ann. Rev. Mar. Sci 2, 115−143.

Drake, N.A., Blench, R.M., Armitage, S.J., Bristow, C.S., White, K.H., 2011. Ancient watercourses and biogeography of the Sahara explain the peopling of the desert. Proc. Natl. Acad. Sci. U.S.A. 108, 458−462.

Drake, N.A., Breeze, P., Parker, A., 2013. Palaeoclimate in the Saharan and Arabian deserts during the middle palaeolithic and the potential for hominin dispersals. Quat. Int. 300, 48−61.

Drobinski, P., et al., 2018. Scaling precipitation extremes with temperature in the Mediterranean: past climate assessment and projection in anthropogenic scenarios. Clim. Dyn. 51, 1237−1257. https://doi.org/10.1007/s00382-016-3083-x.

Drobinski, P., Da Silva, N., Bastin, S., et al., 2020. How warmer and drier will the Mediterranean region be at the end of the twenty-first century? Reg. Environ. Change 20, 78.

Edward, P.M., 2011. History of climate modeling. WIREs Climate Change 2, 128−139.

Emeis, K.C., Schulz, H.M., Struck, U., Sakamoto, T., Doose, H., Erlenkeuser, H., Howell, M., Kroon, D., Paterne, M., 1998. Stable isotope and temperature records of sapropels from ODP Sites 964 and 967: constraining the physical environment of sapropel for- mation in the Eastern Mediterranean Sea. In: Robertson, A.H.F., Emeis, K.C., Richter, C., Camerlenghi, A. (Eds.), Proceedings of the Ocean Drilling Program, vol. 160. ODP, College Station, TX, pp. 309−331. Scientific Results.

Emeis, K.C., Sakamoto, T., Wehausen, R., Brumsack, H.J., 2000a. The sapropel record of the eastern Mediterranean sea—results of ocean drilling program leg 160. Palaeogeogr. Palaeoclimatol. Palaeoecol. 158, 371−395.

Emeis, K.C., Struck, U., Schulz, H.M., Bernasconi, S., Sakamoto, T., Martinez-Ruiz, F., 2000b. Temperature and salinity of Mediterranean Sea surface waters over the last 16,000 years: constraints on the physical environment of S1 sapropel formation based on stable oxygen isotopes and alkenone unsaturation ratios. Palaeogeogr. Palaeoclimatol. Palaeoecol. 158, 259−280.

Emeis, K.C., Schulz, H., Struck, U., Rossignol-Strick, M., Erlenkeuser, H., Howell, M.W., Kroon, D., Mackensen, H., Ishizuka, S., Oba, T., Sakamoto, T., Koizumi, I., 2003. Eastern Mediterranean surface water temperatures and δ18O composition during deposition of sapropels in the late Quaternary. Paleoceanography 18. https://doi.org/10.1029/2000PA000617.

Eyring, V., Bony, S., Meehl, G.A., Senior, C.A., Stevens, B., et al., 2016. Overview of the coupled model Intercomparison project phase 6 (CMIP6) experimental design and organization. Geosci. Model Dev. (GMD) 9, 1937−1958.

Feldstein, S.B., 2000. The timescale, power spectra, and climate noise properties of teleconnection patterns. J. Clim. 13, 4430−4440.

Flato, G., Marotzke, J., et al., 2013. Evaluation of climate models. In: Stocker, T.F., et al. (Eds.), Chapter 9 of Climate Change 2013: The Physical Science Basis. Contribution of Working Group I to the Fifth Assessment Report of the Intergovernmental Panel on Climate Change (IPCC). Cambridge University press, Cambridge, U.K., pp. 741−866

Flecker, R., de Villiers, S., Ellam, R.M., 2002. Modelling the effect of evaporation on the salinity−87Sr/86Sr relationship in modern and ancient marginal-marine systems: the Mediterranean Messinian salinity crisis. Earth Planet Sci. Lett. 203, 221−233.

Flocas, H.A., Simmonds, I., Kouroutzoglou, J., Keay, K., Hatzaki, M., Bricolas, V., Asimakopoulos, D., 2010. On cyclonic tracks over the eastern Mediterranean. J. Clim. 23, 5243−5257.

Foley, B.J., 2015. The role of plate tectonic−climate coupling and exposed land area in the development of habitable climates on rocky planets. Astrophys. J. 812 (1), 36.

Folland, C.K., Knight, J., Linderholm, H.W., Fereday, D., Ineson, S., Hurrell, J.W., 2009. The summer North Atlantic Oscillation: past, present, and future. J. Clim. 22, 1082−1103, 2009.

Frei, C., Schär, C., 1998. A precipitation climatology of the Alps from high-resolution rain-gauge observations. Int. J. Climatol.: A Journal of the Royal Meteorological Society 18 (8), 873−900.

Galadini, F., Messina, P., Sposato, A., 2003. Early uplift history of the Abruzzi Apennines (central Italy): available geomorphological constraints. Quat. Int. 101−102, 125−135.

Garcia-Castellanos, D., Estrada, F., Jiménez-Munt, I., Gorini, C., Fernàndez, M., Vergés, J., De Vicente, R., 2009. Catastrophic flood of the Mediterranean after the Messinian salinity crisis. Nature 462, 778−781.

Garcia-Castellanos, D., Micallef, A., Estrada, F., Camerlenghi, A., Ercilla, G., Periáñez, R., Abril, J.M., 2020. The Zanclean megaflood of the Mediterranean—searching for independent evidence. Earth-Science Rev. 201, 103061.

Gargani, J., Rigollet, C., 2007. Mediterranean Sea level variations during the Messinian salinity crisis. Geophys. Res. Lett. 34, L10405.

Giorgi, F., Diffenbaugh, N.S., Gao, X.J., Coppola, E., Dash, S.K., et al., 2008. Exploring uncertainties in regional climate change. The regional climate change hyper-matrix framework. EOS Trans 89, 445−446.

Giorgi, F., Jones, C., Asrar, G., 2009. Addressing climate information needs at the regional level: the CORDEX framework. WMO Bull 58, 175−183.

Giorgi, F., Gao, X.J., 2018. Regional Earth System modeling: review and future directions. Atmos. Oce. Sci. lett. 11, 189−197.

Giorgi, F., 2019. Thirty years of regional climate modeling: where are we and where are we going? J. Geophys. Res. Atmos. 124, 5696−5723.

Giorgi, F., 2020. Producing actionable climate information for regions: the distillation paradigm and the 3R framework. Europ. Phys. J. Plus 135, 435.

Giorgi, F., Coppola, E., Jacob, D., Teichmann, D., Abba-Omar, S., et al., 2022. The CORDEX-CORE EXP-I initiative: description and highlight results from the initial analysis. Bull. Am. Meteorol. Soc. 103 (2), E293−E310.

Gogou, A., Triantaphyllou, M., Xoplaki, E., Izdebski, A., Parinos, C., Dimiza, M., Bouloubassi, I., Luterbacher, J., Kouli, K., Martrat, B., Toreti, A., Fleitmann, D., Rousakis, G., Kaberi, H., Athanasiou, M., Lykousis, V., 2016. Climate variability and socio-environmental changes in the northern Aegean (NE Mediterranean) during the last 1500 years. Quat. Sci. Rev. 136, 209−228.

Grant, K.M., Amarathunga, U., Amies, J.D., Hu, P., Qian, Y., Penny, T., et al., 2022. Organic carbon burial in Mediterranean sapropels intensified during Green Sahara Periods since 3.2 Myr ago. Communications Earth and Environment 3 (1), 1−9.

Grant, K.M., Rohling, E.J., Bar-Matthews, M., Ayalon, A., Medina-Elizalde, M., Bronk Ramsey, C., Satow, C., Roberts, A.P., 2012. Rapid coupling between ice volume and polar temperature over the past 150 kyr. Nature 491, 744−747.

Grant, K.M., Rohling, E.J., Bronk Ramsey, C., Cheng, H., Edwards, R.L., Florindo, F., Heslop, D., Marra, F., Roberts, A.P., Tamisiea, M.E., Williams, F., 2014. Sea-level variability over five glacial cycles. Nat. Commun. 5, 5076.

Grant, K.M., Rohling, E.J., Westerhold, T., Zabel, M., Heslop, D., Konijnendijk, T., Lourens, L.J., 2017. A 3 million year index for North African humidity/aridity and the implication of potential pan-African Humid periods. Quat. Sci. Rev. 171, 100−118.

Grauel, A.L., Goudeau, M.L.S., de Lange, G.J., Bernasconi, S.M., 2013. Climate of the past 2500 years in the Gulf of Taranto, central Mediterranean Sea: a high-resolution climate reconstruction based on δ18O and δ13C of Globigerinoides ruber (white). Holocene 23 (10), 1440−1446.

Grunewald, K., Scheithauer, J., 2010. Europe's southernmost glaciers: response and adaptation to climate change. J. Glaciol. 56, 129−142.

Gutiérrez, J.M., Jones, R.G., Narisma, G.T., Alves, L.M., Amjad, M., Gorodetskaya, I.V., Grose, M., Klutse, N.A.B., Krakovska, S., Li, J., Martínez-Castro, D., Mearns, L.O., Mernild, S.H., Ngo-Duc, T., van den Hurk, B., Yoon, J.-H., 2021. Atlas. In: Masson-Delmotte, V., Zhai, P., Pirani, A., Connors, S.L., Péan, C., Berger, S., Caud, N., Chen, Y., Goldfarb, L., Gomis, M.I., Huang, M., Leitzell, K., Lonnoy, E., Matthews, J.B.R., Maycock, T.K., Waterfield, T., Yelekçi, O., Yu, R., Zhou, B. (Eds.), Climate Change 2021: The Physical Science Basis. Contribution of Working Group I to the Sixth Assessment Report of the Intergovernmental Panel on Climate Change. Cambridge University Press.

Gutowski, W.J., Giorgi, F., Timbal, B., Frigon, A., Jacob, B., 2016. WCRP coordinated regional downscaling experiment (CORDEX): a diagnostic MIP for CMIP6. Geosci. Model Dev. (GMD) 9, 4087−4095.

Haigh, J.D., 2003. The effects of solar variability on the Earth's climate. Phil. Trans. R. Soc. A. 361, 95−111.

Harris, I., Osborn, T.J., Jones, P., Lister, D., 2020. Version 4 of the CRU TS monthly high-resolution gridded multivariate climate dataset. Sci. Data 7 (1), 1−18.

Hawcroft, M.K., Shaffrey, L.C., Hodges, K.I., Dacre, H.F., 2012. How much Northern Hemisphere precipitation is associated with extratropical cyclones? Geophys. Res. Lett. 39, L24809.

Hawkins, E., Sutton, R., 2009. The potential to narrow uncertainty in regional climate projections. Bull. Am. Meteorol. Soc. 90, 1095−1108.

Hayes, A., Kucera, M., Kallel, N., Sbaffi, L., Rohling, E.J., 2005. Glacial Mediterranean sea surface temperatures reconstructed from planktonic foraminiferal assemblages. Quat. Sci. Rev. 24, 999−1016.

Haylock, M.R., Hofstra, N., Klein Tank, A.M.G., Klok, E.J., Jones, P.D., New, M.A., 2008. European daily high-resolution gridded data set of surface temperature and precipitation for 1950−2006. J. Geophys. Res. Atmos. 113 (D20).

Held, I.M., Soden, B.J., 2006. Robust responses of the hydrological cycle to global warming. J. Clim. 19 (21), 5686−5699.

Hennekam, R., Jilbert, T., Schnetger, B., de Lange, G.J., 2014. Solar forcing of Nile discharge and sapropel S1 formation in the early to middle Holocene eastern Mediterranean. Paleoceanography 29, 343−356.

Hersbach, H., Bell, B., Berrisford, P., et al., 2020. The ERA5 global reanalysis. Q. J. R. Meteorol. Soc. 146, 1999−2049.

Hewitson, B.C., Daron, J., Crane, R.G., Zermoglio, M.F., Jack, C., 2014. Interrogating empirical-statistical downscaling. Clim. Change 122, 539−554.

Hibbert, F.D., Rohling, E.J., Dutton, A., Williams, F.H., Cutcharavan, P.H., Zhao, C., Tamisiea, M.A., 2016. Corals as indicators of past sea-level change: a global repository of U-series dated benchmarks. Quat. Sci. Rev. 145, 1−56.

Hibbert, F.D., Williams, F.H., Fallon, S., Rohling, E.J., 2018. Last deglacial sea level: a database of biological and geomorphological sea-level markers. Sci. Data 5, 180088.

Hilgen, F., Kuiper, K., Krijgsman, W., Snel, E., van der Laan, E., 2007. Astronomical tuning as the basis for high resolution chronostratigraphy: the intricate history of the Messinian salinity crisis. Stratigraphy 4, 231−238.

Hopcroft, P.O., Valdes, P.J., Harper, A.B., Beerling, D.J., 2017. Multi vegetation model evaluation of the Green Sahara climate regime. Geophys. Res. Lett. 44, 6804−6813.

Howell, M.W., Thunell, R.C., 1992. Organic carbon accumulation in Bannock Basin: evaluating the role of productivity in the formation of eastern Mediterranean sapropels. Mar. Geol. 103, 461−471.

Hsü, K.J., Ryan, W.B.F., Cita, M.B., 1973. Late Miocene desiccation of the mediterranean. Nature 242, 240−244.

Huffman, G.J., Adler, R.F., Bolvin, D.T., Gu, G., 2009. Improving the global precipitation record: GPCP version 2.1. Geophys. Res. Lett. 36 (17).

Hughes, P.D., 2014. Little Ice Age glaciers in the mediterranean mountains. Méditerranée 122, 63−97.

Hulme, M., 1994. Validation of large-scale precipitation fields in general circulation models. In: Global Precipitations and Climate Change. Springer, Berlin, Heidelberg, pp. 387−405.

Hurrell, J.W., 1995. Decadal trends in the north Atlantic oscillation: regional temperatures and precipitation. Science 269, 676−679.

Imbrie, J., Imbrie, K.P., 1986. Ice Ages − Solving the Mystery. Harvard University Press, Cambridge, Massachusetts, p. 224.

Incarbona, A., Martrat, B., Mortyn, P.G., Sprovieri, M., Ziveri, P., Gogou, A., Jorda, G., Luterbacher, J., Lagnone, L., Marino, G., Rodríguez-Sanz, L., Triantaphyllou, M., Di Stefano, E., Grimalt, J.O., Tranchida, G., Sprovieri, R., Mazzola, S., 2016. Mediterranean circulation perturbations over the last five centuries: relevance to past Eastern Mediterranean Transient-type events. Sci. Rep. 6, 29623.

IPCC, 2021. Summary for policymakers. In: Masson-Delmotte, V., Zhai, P., Pirani, A., Connors, S.L., Péan, C., Berger, S., Caud, N., Chen, Y., Goldfarb, L., Gomis, M.I., Huang, M., Leitzell, K., Lonnoy, E., Matthews, J.B.R., Maycock, T.K., Waterfield, T., Yelekçi, O., Yu, R., Zhou, B. (Eds.), Climate Change 2021: The Physical Science Basis. Contribution of Working Group I to the Sixth Assessment Report of the Intergovernmental Panel on Climate Change.

Iturbide, M., Fernández, J., Gutiérrez, J.M., Bedia, J., Cimadevilla, E., Díez-Sierra, J., Manzanas, R., Casanueva, A., Baño-Medina, J., Milovac, J., Herrera, S., Cofiño, A.S., San Martín, D., García-Díez, M., Hauser, M., Huard, D., Yelekci, Ö., 2021. Repository supporting the implementation of FAIR principles in the IPCC-WG1 Atlas. Zenodo.

https://doi.org/10.5281/zenodo.3691645. Available from: https://github.com/IPCC-WG1/Atlas.

Jacob, D., Pedersen, J., Eggert, B., Alias, A., Christensen, O.B., et al., 2014. EURO-CORDEX: new high resolution climate change projections for European impact research. Reg. Environ. Change 14, 563–578.

Jacob, D., Teichmann, C., Sobolowski, S., Katragkou, E., Anders, I., et al., 2020. Regional climate downscaling over Europe: perspectives from the EURO-CORDEX community. Reg. Environ. Change 20, 51.

Jones, P.D., New, M., Parker, D.E., Martin, S., Rigor, I.G., 1999. Surface air temperature and its variations over the last 150 years. Rev. Geophys. 37, 173–199.

Jorissen, F.J., 1999. Benthic foraminiferal successions across late quaternary Mediterraenan sapropels. Mar. Geol. 153, 91–101.

Josey, S.A., Somot, S., Tsimplis, M., 2011. Impacts of atmospheric modes of variability on Mediterranean Sea surface heat exchange. J. Geophys. Res. Oceans 116, C02032.

Kalnay, E., Kanamitsu, M., Kistler, R., Collins, W., Deaven, D., Gandin, L., Iredell, M., Saha, S., White, G., Woollen, J., Zhu, Y., Chelliah, M., Ebisuzaki, W., Higgins, W., Janowiak, J., Mo, K.C., Ropelewski, C., Wang, J., Leetmaa, A., Reynolds, R., Jenne, R., Joseph, D., 1996. The NCEP/NCAR 40-year reanalysis project. Bull. Amer. Meteor. Soc. 77, 437–471.

Kanamitsu, M., Ebisuzaki, W., Woollen, J., Yang, S.-K., Hnilo, J.J., Fiorino, M., Potter, G.L., 2002. NCEP-DOE AMIP-II reanalysis (R-2). Bull. Amer. Meteor. Soc. 83, 1631–1643.

Kelley, C., Ting, M., Seager, R., Kushnir, Y., 2012. Mediterranean precipitation climatology, seasonal cycle, and trend as simulated by CMIP5. Geophys. Res. Lett. 39, L21703.

Kemp, A.E.S., Pearce, R.B., Koizumi, I., Pike, J., Rance, S.J., 1999. The role of mat-forming di- atoms in the formation of Mediterranean sapropels. Nature 398, 57–61.

Klein Tank, A.M.G., Wijngaard, J.B., Können, G.P., Böhm, R., Demarée, G., Gocheva, A., et al., 2002. Daily dataset of 20th-century surface air temperature and precipitation series for the European Climate Assessment. Int. J. Climatol.: A Journal of the Royal Meteorological Society 22 (12), 1441–1453.

Konijnendijk, T., Ziegler, M., Lourens, L., 2014. Chronological constraints on Pleis- tocene sapropel depositions from high-resolution geochemical records of ODP sites 967 and 968. Newsletters Stratigr 47, 263–282.

Krijgsman, W., Hilgen, F.J., Raffi, I., Sierro, F.J., Wilson, D.S., 1999a. Chronology, causes and progression of the Messinian salinity crisis. Nature 400, 652–655.

Krijgsman, W., Langereis, C.G., Zachariasse, W.J., Boccaletti, M., Moratti, G., Gelati, R., Iaccarino, S., Papani, G., Villa, G., 1999b. Late Neogene evolution of the Taza-Guercif basin (Rifian corridor, Morocco) and implications for the Messinian salinity crisis. Mar. Geol. 153, 147–160.

Krijgsman, W., Fortuin, A.R., Hilgen, F.J., Sierro, F.J., 2001. Astrochronology for the Messinian Sorbas Basin (SE Spain) and orbital (precessional) forcing for evaporite cyclicity. Sediment. Geol. 140, 43–60.

Krinner, G., Lezine, A.-M., Braconnot, P., Sepulchre, P., Ramstein, G., Grenier, C., Gouttevin, I., 2012. A reassessment of lake and wetland feedbacks on the North African Holocene climate. Geophys. Res. Lett. 39, L07701.

Kuhlemann, J., Rohling, E.J., Kumrei, I., Kubik, P., Ivy-Ochs, S., Kucera, M., 2008. Regional synthesis of mediterranean atmospheric circulation during the last glacial maximum. Science 321, 1338–1340.

Kuhnt, T., Schmiedl, G., Ehrmann, W., Hamann, Y., Hemleben, C., 2007. Deep-sea ecosystem variability of the Aegean Sea during the past 22 kyr as revealed by benthic foraminifera. Mar. Micropaleontol. 64, 141–162.

Kushnir, Y., 1994. Interdecadal variations in North Atlantic sea surface temperature and associated atmospheric conditions. J. Clim. 7, 141–157.

Kutzbach, J.E., Chen, G., Cheng, H., Edwards, R.L., Liu, Z., 2014. Potential role of winter rainfall in explaining increased moisture in the Mediterranean and Middle East during periods of maximum orbitally-forced insolation seasonality. Clim. Dyn. 42, 1079–1095.

Kutzbach, J.E., Guan, J., He, F., Cohen, A.S., Orland, I.J., Chen, G., 2020. African climate response to orbital and glacial forcing in 140,000-y simulation with implications for early modern human environments. Proceedings of the National Academy of Sciences of the USA 117, 2255–2264.

Lacombe, H., Richez, C., 1982. The regime of the Strait of Gibraltar. Elsevier Oceanogr. Ser. 34, 13–73 (Elsevier).

Lane-Serff, G.F., Rohling, E.J., Bryden, H.L., Charnock, H., 1997. Post-glacial connection of the Black Sea to the Mediterranean and its relation to the timing of sapropel formation. Paleoceanography 12, 169–174.

Larrasoaña, J.C., Roberts, A.P., Rohling, E.J., 2013. Dynamics of green Sahara periods and their role in hominin evolution. PLoS One 8, e76514.

Larrasoaña, J.C., Roberts, A.P., Rohling, E.J., Winklhofer, M., Wehausen, R., 2003. Three million years of monsoon variability over the northern Sahara. Clim. Dynam. 21 (7), 689–698.

Laskar, J., Robutel, P., Joutel, F., Gastineau, M., Correia, A.C.M., Levrard, B., 2004. A long-term numerical solution for the insolation quantities of the Earth. Astron. Astrophys. 428, 261–285.

Le Houedec, S., Mojtahid, M., Bicchi, E., de Lange, G.J., Hennekam, R., 2020. Suborbital hydrological variability inferred from coupled benthic and planktic foraminiferal-based proxies in the southeastern Mediterranean during the last 19 ka. Paleoceanogr. Paleoclimatol. 35 e2019PA003827.

Leaman, K.D., Schott, F.A., 1991. Hydrographic structure of the convection regime in the gulf of lions: winter 1987. J. Phys. Oceanogr. 21, 575–598.

Lenssen, N., Schmidt, G., Hansen, J., Menne, M., Persin, A., Ruedy, R., Zyss, D., 2019. Improvements in the GISTEMP uncertainty model. J. Geophys. Res. Atmos. 124 (12), 6307–6326.

Lionello, P. (Ed.), 2012. The Climate of the Mediterranean Region: From the Past to the Future. Elsevier.

Lionello, P., Malanotte-Rizzoli, P., Boscolo, R., 2006a. Mediterranean Climate Variability, vol. 4. Elsevier, p. 438.

Lionello, P., Bhend, J., Buzzi, A., Della-Marta, P.M., Krichak, S.O., Jansa, A., et al., 2006b. Cyclones in the Mediterranean region: climatology and effects on the environment. In: Developments in Earth and Environmental Sciences, vol. 4, pp. 325–372 (Elsevier).

Lionello, P., Giorgi, F., 2007. Winter precipitation and cyclones in the Mediterranean region: future climate scenarios in a regional simulation. Advances in Geosciences 12, 153–158.

Lionello, P., Abrantes, F., Congedi, L., Dulac, F., Gacic, M., Gomis, D., et al., 2012. Introduction: mediterranean climate—background information. In: The Climate of the Mediterranean Region: From the Past to the Future. Elsevier Inc, pp. xxxv–xc.

Lionello, P., Trigo, I.F., Gil, V., Liberato, M.L., Nissen, K.M., Pinto, J.G., et al., 2016. Objective climatology of cyclones in the Mediterranean region: a consensus view among

methods with different system identification and tracking criteria. Tellus Dyn. Meteorol. Oceanogr. 68 (1), 29391.
Lionello, P., Scarascia, L., 2018. The relation between climate change in the Mediterranean region and global warming. Reg. Environ. Change 18 (5), 1481–1493.
Lionello, P., Scarascia, L., 2020. The relation of climate extremes with global warming in the Mediterranean region and its north versus south contrast. Reg. Environ. Change 20 (1), 1–16.
Lolis, C.J., Bartzokas, A., Katsoulis, B.D., 2002. Spatial and temporal 850 hPA air temperature and sea-surface temperature covariances in the Mediterranean region and their connection to atmospheric circulation. Int. J. Climatol. 22, 663–676.
López-Parages, J., Rodríguez-Fonseca, B., 2012. Multidecadal modulation of El Niño influence on the Euro-mediterranean rainfall. Geophys. Res. Lett. 39, L02704.
López-Parages, J., Rodríguez-Fonseca, B., Terray, L., 2015. A mechanism for the multidecadal modulation of ENSO teleconnection with Europe. Clim. Dynam. 45, 867–880.
López-Parages, J., Rodríguez-Fonseca, B., Dommenget, D., Frauen, C., 2016. ENSO influence on the North Atlantic European climate: a non-linear and non-stationary approach. Clim. Dynam. 47, 2071–2084.
Lourens, L.J., Hilgen, F.J., Gudjonsson, L., Zachariasse, W.J., 1992. Late Pliocene to early Pleistocene astronomically forced sea surface productivity and temperature variations in the Mediterranean. Mar. Micropaleontol. 19, 49–78.
Loutre, M.F., Paillard, D., Vimeux, F., Cortijo, E., 2004. Does mean annual insolation have the potential to change the climate? Earth Planet Sci. Lett. 221 (1–4), 1–14.
Luterbacher, J., Xoplaki, E., Casty, C., Wanner, H., Pauling, A., Küttel, M., et al., 2006. Mediterranean climate variability over the last centuries: a review. In: Developments in Earth and Environmental Sciences, vol. 4, pp. 27–148.
Luterbacher, J., Werner, J.P., Smerdon, J.E., Fernández-Donado, L., González-Rouco, F.J., Barriopedro, D., et al., 2016. European summer temperatures since Roman times. Environ. Res. Lett. 11 (2), 024001.
Maasch, K.A., Mayewski, P.A., Rohling, E.J., Stager, J.C., Karlén, W., Meeker, L.D., Meyerson, E.A., 2005. A 2000-year context for modern climate change. Geogr. Ann. 87 A, 7–15.
Maheras, P., Xoplaki, E., Davies, T., Martin-Vide, J., Bariendos, M., Alcoforado, M.J., 1999. Warm and cold monthly anomalies across the Mediterranean basin and their relationship with circulation; 1860-1990. Int. J. Climatol. 19, 1697–1715.
Mann, M.E., Steinman, B.A., Brouillette, D.J., Miller, S.K., 2021. Multidecadal climate oscillations during the past millennium driven by volcanic forcing. Science 371, 1014–1019.
Marino, G., Rohling, E.J., Sangiorgi, F., Hayes, A., Casford, J.L., Lotter, A.F., Kucera, M., Brinkhuis, H., 2009. Early and middle Holocene in the Aegean Sea: interplay between high and low latitude climate variability. Quat. Sci. Rev. 28, 3246–3262.
Mariolopoulos, E.G., 1961. An Outline of the Climate of Greece, vol. 6. Publications of the Meteorological Institute of the University of Athens, p. 51.
Mariotti, A., Arkin, P., 2007. The North Atlantic Oscillation and oceanic precipitation variability. Clim. Dynam. 28, 35–51.
Mariotti, A., Dell'Aquila, A., 2012. Decadal climate variability in the Mediterranean region: roles of large-scale forcings and regional processes. Clim. Dynam. 38, 1129–1145.
Mariotti, A., Struglia, M.V., Zeng, N., Lau, K.M., 2002. The hydrological cycle in the Mediterranean region and implications for the water budget of the Mediterranean Sea. J. Clim. 15, 1674–1690.

Mariotti, A., Zeng, N., Lau, K.M., 2002. Euro-Mediterranean rainfall and ENSO—a seasonally varying relationship. Geophys. Res. Lett. 29, 59-1.

Mayewski, P.A., Rohling, E.J., Stager, J.C., Karlén, W., Maasch, K., Meeker, L.D., Meyerson, E., Gasse, F., Van Kreveld, S., Holmgren, K., Lee-Thorp, J., Rosqvist, G., Rack, F., Staubwasser, M., Schneider, R.R., Steig, E., 2004. Holocene climate variability. Quaternary Research 62, 243−255.

McCulloch, M.T., DeDecker, P., 1989. Sr isotope constraints on the Mediterranean environment at the end of the Messinian salinity crisis. Nature 342, 62−65.

McGregor, J.L., 2015. Recent developments in variable resolution global climate modeling. Clim. Change 129, 369−380.

McGuffie, K., Henderson-Sellers, A., 2014. The Climate Modeling Primer, fourth ed. John Wiley and Sons, NY, p. 432.

MedECC, 2020. Climate and environmental change in the Mediterranean basin − current situation and risks for the future. First mediterranean assessment report. In: Cramer, W., Guiot, J., Marini, K. (Eds.), Union for the Mediterranean, Plan Bleu. UNEP/MAP, Marseille, France, p. 632pp.

Meijer, P.T., Krijgsman, W., 2005. A quantitative analysis of the desiccation and re-filling of the Mediterranean during the Messinian salinity crisis. Earth Planet Sci. Lett. 240, 510−520.

Menne, M.J., Williams, C.N., Gleason, B.E., Rennie, J.J., Lawrimore, J.H., 2018. The global historical climatology network monthly temperature dataset, version 4. J. Clim. 31 (24), 9835−9854.

Mercone, D., Thomson, J., Abu-Zied, R.H., Croudace, I.W., Rohling, E.J., 2001. High-resolution geochemical and micropalaeontological profiling of the most recent eastern Mediterranean sapropel. Mar. Geol. 177, 25−44.

Micallef, A., Camerlenghi, A., Garcia-Castellanos, D., Cunarro Otero, D., Gutscher, M.-A., Barreca, G., Spatola, D., Facchin, L., Geletti, R., Krastel, S., Gross, F., Urlaub, M., 2018. Evidence of the Zanclean megaflood in the eastern Mediterranean basin. Sci. Rep. 8, 1−8.

Middleton, W.E.K., Spilhaus, A.F., 2019. Meteorological Instruments. University of Toronto Press.

Milankovitch, M., 1941. Kanon der Erdbestrahlung und seine Anwendung auf das Eiszeitenproblem. Special Publication 133, Mathematics and Natural Sciences Section. Royal Serbian Academy, Belgrade, 1941.

Miller, K.G., Browning, J.V., Schmelz, W.J., Kopp, R.E., Mountain, G.S., Wright, J.D., 2020. Cenozoic sea-level and cryospheric evolution from deep-sea geochemical and continental margin records. Sci. Adv. 6, eaaz1346.

Morel, C., Senesi, S., 2002. A climatology of mesoscale convective systems over Europe using satellite infrared imagery. II: characteristics of European mesoscale convective systems. Q. J. R. Meteorol. Soc. J. Atmos. Sci. Appl. Meteorol. & Phys. Oceanogr. 128 (584), 1973−1995.

Myers, P.G., Wielki, C., Goldstein, S.B., Rohling, E.J., 2003. Hydraulic calculations of post-glacial connections between the mediterranean and the Black Sea. Mar. Geol. 201, 253−267.

Nabat, P., Somot, S., Mallet, M., Chiapello, I., Morcrette, J.J., et al., 2013. A 4-D climatology (1979-2009) of the monthly tropospheric aerosol optical depth distribution over the Mediterranean region from a comparative evaluation and blending of remote sensing and model products. Atmos. Meas. Tech. 6. https://doi.org/10.5194/amt-6-1287-2013.

Nabat, P., Somot, S., Mallet, M., Sevault, F., Chiacchio, M., et al., 2015. Direct and semi-direct aerosol radiative effect on the Mediterranean climate variability using a coupled regional climate system model. Clim. Dyn. 44, 1127–1155.

New, M., Hulme, M., Jones, P., 1999. Representing twentieth-century space–time climate variability. Part I: development of a 1961–90 mean monthly terrestrial climatology. J. Clim. 12 (3), 829–856.

New, M., Hulme, M., Jones, P., 2000. Representing twentieth-century space–time climate variability. Part II: development of 1901–96 monthly grids of terrestrial surface climate. J. Clim. 13 (13), 2217–2238.

New, M., Todd, M., Hulme, M., Jones, P., 2001. Precipitation measurements and trends in the twentieth century. Int. J. Climatol. J. R. Meteorolog. Soc. 21 (15), 1889–1922.

O'Gorman, P.A., Muller, C.J., 2010. How closely do changes in surface and column water vapor follow Clausius–Clapeyron scaling in climate change simulations? Environ. Res. Lett. 5 (2), 025207.

Olivetti, V., Cyr, A.J., Molin, P., Faccenna, C., Granger, D.E., 2012. Uplift history of the Sila Massif, southern Italy, deciphered from cosmogenic 10Be erosion rates and river longitudinal profile analysis. Tectonics 31, TC3007.

Osborne, A.H., Vance, D., Rohling, E.J., Barton, N., Rogerson, M., Fello, N., 2008. A humid corridor across the Sahara for the migration "Out of Africa" of early modern humans 120,000 years ago. Proceedings of the National Academy of Sciences of the USA 105, 16444–16447.

Pachur, H.J., 2001. Holozäne Klimawechsel in den nördlichen subtropen. Nova Acta Leopold. NF88 (331), 109–131.

Pachur, H.J., Braun, G., 1980. The paleoclimate of the central Sahara, Libya and the Libyan Desert. Palaeoecol. Afr. 12, 351–363.

Paillou, P., et al., 2009. Mapping of a major paleodrainage system in eastern Libya using orbital imaging radar: The Kufrah River. Earth Planet. Sci. Lett. 277, 327–333.

Paillou, P., Tooth, S., Lopez, S., 2012. The Kufrah paleodrainage system in Libya: a past connection to the Mediterranean Sea? C. R. - Geosci. 344, 406–414.

Pälike, H., 2005. EARTH; orbital variation (including Milankovitch cycles). Encyclopedia of Geology 410–421.

Pausata, F.S.R., Messori, G., Zhang, Q., 2016. Impacts of dust reduction on the northward expansion of the African monsoon during the Green Sahara period. Earth Planet Sci. Lett. 434, 298–307.

Pichelli, E., Coppola, E., Sobolowski, S., Ban, N., Giorgi, F., et al., 2021. The first multi-model ensemble of regional simulations at km scale resolutions. Part II: historical and future simulations of precipitation. Clim. Dyn. 56, 3581–3602.

Pisias, N.G., Moore, T.C., 1981. The evolution of Pleistocene climate: a time series approach. Earth Planet Sci. Lett. 52, 450–458.

Poli, P., Hersbach, H., Dee, D.P., Berrisford, P., Simmons, A.J., Vitart, F., Laloyaux, P., Tan, D.G.H., Peubey, C., Thépaut, J., Trémolet, Y., Hólm, E.V., Bonavita, M., Isaksen, L., Fisher, M., 2016. ERA-20C: an atmospheric reanalysis of the twentieth century. J. Clim. 29 (11), 4083–4097.

Poulos, S.E., Drakopoulos, P.G., Collins, M.B., 1997. Seasonal variability in sea surface oceanographic conditions in the Aegean Sea (Eastern Mediterranean): an overview. J. Mar. Syst. 13, 225–244.

Prein, A.F., Langhans, W., Fosser, G., Ferrone, A., Ban, N., et al., 2015. A review on regional convection-permitting climate modeling: demonstrations, prospects and challenges. Rev. Geophys. 53, 323−361.

Prentice, I., Farquhar, G., Fasham, M., Goulden, M., Heinmann, M., et al., 2001. The carbon cycle and atmospheric carbon dioxide. In: Houghton, J.T., Ding, Y., Griggs, D.J., Noguer, M., van der Linden, P.J., et al. (Eds.), Climate Change 2001: The Scientific Basis. Contributions of Working Group I to the Third Assessment Report of the Intergovernmental Panel on Climate Change. Cambridge University Press, Cambridge, UK, pp. 183−238.

Rachmayani, R., Prange, M., Schulz, M., 2015. North African vegetation-precipitation feedback in early and mid-Holocene climate simulations with CCSM3-DGVM. Clim. Past 11, 175−185.

Ramanathan, V., Feng, Y.A.N., 2008. On avoiding dangerous anthropogenic interference with the climate system: formidable challenges ahead. Proc. Natl. Acad. Sci. U.S.A. 105 (38), 14245−14250.

Reale, M., Lionello, P., 2013. Synoptic climatology of winter intense precipitation events along the Mediterranean coasts. Nat. Hazards Earth Syst. Sci. 13 (7), 1707−1722.

Reale, M., Giorgi, F., Solidoro, C., Di Biagio, V., Di Sante, F., et al., 2020. The regional Earth system model RegCM-ES: evaluation of the mediterranean climate and marine biogeochemistry. J. Adv. model Earth Sys 12 e2019MS001812.

Reale, O., Shukla, J., 2000. Modeling the effects of vegetation on mediterranean climate during the Roman Classical Period: Part II. Model simulation. Global Planet. Change 25 (3−4), 185−214.

Rienecker, M.M., Suarez, M.J., Gelaro, R., Todling, R., Bacmeister, J., Liu, E., Bosilovich, M.G., Schubert, S.D., Takacs, L., Kim, G., Bloom, S., Chen, J., Collins, D., Conaty, A., da Silva, A., Gu, W., Joiner, J., Koster, R.D., Lucchesi, R., Molod, A., Owens, T., Pawson, S., Pegion, P., Redder, C.R., Reichle, R., Robertson, F.R., Ruddick, A.G., Sienkiewicz, M., Woollen, J., 2011. MERRA: NASA's modern-era retrospective analysis for research and applications. J. Clim. 24 (14), 3624−3648.

Rodwell, M.J., Hoskins, B.J., 1996. Monsoons and the dynamics of deserts. Q. J. R. Meteorol. Soc. 122, 1385−1404.

Rodwell, M.J., Hoskins, B.J., 2001. Subtropical anticyclones and summer monsoons. J. Clim. 14, 3192−3211.

Roether, W., Manca, B.B., Klein, B., Bregant, D., Georgopoulos, D., Beitzel, V., Kovacevic, V., Luchetta, A., 1996. Recent changes in eastern Mediterranean deep waters. Science 271, 333−335.

Rogerson, M., Rohling, E.J., Weaver, P.P.E., Murray, J.W., 2005. Glacial to interglacial changes in the settling depth of the Mediterranean outflow plume. Paleoceanography 20, PA3007.

Rogerson, M., Rohling, E.J., Weaver, P.P.E., 2006. Promotion of meridional overturning by Mediterranean-derived salt during the last deglaciation. Paleoceanography 21, PA4101.

Rohling, E.J., 1994. Review and new aspects concerning the formation of Mediterranean sapropels. Mar. Geol. 122, 1−28.

Rohling, E.J., 1999. Environmental controls on Mediterranean salinity and δ18O. Paleoceanography 14, 706−715.

Rohling, E.J., 2017. The Oceans: A Deep History. Princeton University Press, p. 272, 2017.

Rohling, E.J., 2019. The Climate Question: Natural Cycles, Human Impact, Future Outlook. Oxford University Press, p. 162.

Rohling, E.J., Gieskes, W.W.C., 1989. Late quaternary changes in mediterranean intermediate water density and formation rate. Paleoceanography 4, 531–545.

Rohling, E.J., Hilgen, F.J., 1991. The eastern Mediterranean climate at times of sapropel formation: a review. Geol. Mijnbouw 70, 253–264.

Rohling, E.J., Thunell, R.C., 1999. Five decades of Mediterranean paleoclimate and sapropel studies. Mar. Geol. 153, 7–10.

Rohling, E.J., Cane, T.R., Cooke, S., Sprovieri, M., Bouloubassi, I., Emeis, K.C., Schiebel, R., Kroon, D., Jorissen, F.J., Lorre, A., Kemp, A.E.S., 2002a. African monsoon variability during the previous interglacial maximum. Earth Planet Sci. Lett. 202, 61–75.

Rohling, E.J., Mayewski, P.A., Hayes, A., Abu-Zied, R.H., Casford, J.S.L., 2002b. Holocene atmosphere-ocean interactions: records from Greenland and the Aegean Sea. Clim. Dynam. 18, 587–593.

Rohling, E.J., Foster, G.L., Grant, K.M., Marino, G., Roberts, A.P., Tamisiea, M.E., Williams, F., 2014. Sea-level and deep-sea-temperature variability over the past 5.3 million years. Nature 508, 477–482.

Rohling, E.J., Grant, K., Bolshaw, M., Roberts, A.P., Siddall, M., Hemleben, C., Kucera, M., 2009a. Antarctic temperature and global sea level closely coupled over the past five glacial cycles. Nat. Geosci. 2, 500–504.

Rohling, E.J., Hayes, A., Mayewski, P.A., Kucera, M., 2009b. Holocene climate variability in the eastern mediterranean, and the end of the Bronze age. In: Bachhuber, C., Roberts, R.G. (Eds.), Forces of Transformation: the End of the Bronze Age in the Mediterranean. BANEA Publication Series 1, Oxbow Books, Oxford, pp. 2–5.

Rohling, E.J., Hibbert, F.D., Williams, F.H., Grant, K.M., Marino, G., Foster, G.L., Hennekam, R., de Lange, G.J., Roberts, A.P., Yu, J., Webster, J.M., Yokoyama, Y., 2017. Differences between the last two glacial maxima and implications for ice-sheet, δ18O, and sea-level reconstructions. Quat. Sci. Rev. 176, 1–28.

Rohling, E.J., Jorissen, F.J., DeStigter, H.C., 1997. 200 year interruption of Holocene sapropel formation in the Adriatic Sea. J. Micropalaeontol. 16, 97–108.

Rohling, E.J., Marino, G., Grant, K.M., 2015. Mediterranean climate and oceanography, and the periodic development of anoxic events (sapropels). Earth Sci. Rev. 143, 62–97.

Rohling, E.J., Marino, G., Grant, K.M., Mayewski, P.A., Weninger, B.A., 2019. Model for archaeologically relevant Holocene climate impacts in the Aegean-Levantine region (easternmost Mediterranean). Quat. Sci. Rev. 208, 38–53.

Rohling, E.J., Medina-Elizalde, M., Shepherd, J.G., Siddall, M., Stanford, J.D., 2012. Sea surface and high-latitude temperature sensitivity to radiative forcing of climate over several glacial cycles. J. Clim. 25, 1635–1656.

Rohling, E.J., Sprovieri, M., Cane, T.R., Casford, J.S.L., Cooke, S., Bouloubassi, I., Emeis, K.C., Schiebel, R., Hayes, A., Jorissen, F.J., Kroon, D., 2004. Reconstructing past planktic foraminiferal habitats using stable isotope data: a case history for Mediterranean sapropel S5. Mar. Micropaleontol. 50, 89–123.

Rohling, E.J., Yu, J., Heslop, D., Foster, G.L., Opdyke, B., Roberts, A.P., 2021. Sea level and deep-sea temperature reconstructions suggest quasi-stable states and critical transitions over the past 40 million years. Sci. Adv. 7 (26), eabf5326.

Rossignol-Strick, M., 1983. African monsoons, an immediate climate response to orbital insolation. Nature 30, 446–449.

Rossignol-Strick, M., 1985. Mediterranean quaternary sapropels, an immediate response of the African monsoon to variations of insolation. Palaeogeogr. Palaeoclimatol. Palaeoecol. 49, 237–263.

Rossignol-Strick, M., 1987. Rainy periods and bottom water stagnation initiating brine accumulation and metal concentrations: 1. The Late Quaternary. Paleoceanography 2, 333−360.

Rossignol-Strick, M., Nesteroff, V., Olive, P., Vergnaud-Grazzini, C., 1982. After the deluge; Mediterranean stagnation and sapropel formation. Nature 295, 105−110.

Rubel, F., Kottek, M., 2010. Observed and projected climate shifts 1901−2100 depicted by world maps of the 16 Köppen-Geiger climate classification. Meteorol. Z. 19 (2), 135−141.

Ruddiman, W.F., Raymo, M., McIntyre, A.M., 1986. 41,000-year cycles: north Atlantic Ocean and northern hemisphere ice sheets. Earth Planet Sci. Lett. 80, 117−129.

Ruddiman, W.F., Raymo, M., Martinson, D., Clement, B., Backman, J., 1989. Pleistocene evolution: northern hemisphere ice sheets and North Atlantic Ocean. Paleoceanography 4, 353−412.

Ruggieri, G., Sprovieri, R., 1976. Messinian salinity crisis and its palaeogeographical implications. Palaeogeogr. Palaeoclimatol. Palaeoecol. 20, 13−21.

Ruti, P.M., Somot, S., Giorgi, F., Dubois, C., Flaounas, E., et al., 2016. MED-CORDEX initiative for Mediterranean climate studies. Bull. Am. Metoprolol. Soc. 97, 1187−1208.

Ryan, W.B.F., Pitman III, W.C., Major, C.O., Shimkus, K., Moskalenko, V., Jones, G.A., Dimitrov, P., Gorur, N., Sakinc, M., Yuce, H., 1997. An abrupt drowning of the Black Sea shelf. Mar. Geol. 138, 119−126.

Saaroni, H., Bitan, A., Alpert, P., Ziv, B., 1996. Continental polar outbreaks into the Levant and eastern Mediterranean. Int. J. Climatol. 16, 1175−1191.

Scaife, A.A., Arribas, A., Blockley, E., Brookshaw, A., Clark, R.T., Dunstone, N., Eade, R., Fereday, D., Folland, C.K., Gordon, M., Hermanson, L., 2014. Skillful long-range prediction of European and North American winters. Geophys. Res. Lett. 41, 2514−2519.

Schneider, U., Ziese, M., Meyer-Christoffer, A., Finger, P., Rustemeier, E., Becker, A., 2016. The new portfolio of global precipitation data products of the Global Precipitation Climatology Centre suitable to assess and quantify the global water cycle and resources. Proc. IAHS 374, 29−34.

Seager, R., Murtugudde, R., Naik, N., Clement, A., Gordon, N., Miller, J., 2003. Air−sea interaction and the seasonal cycle of the subtropical anticyclones. J. Clim. 16, 1948−1966.

Seager, R., Liu, H., Henderson, N., Simpson, I., Kelley, C., Shaw, T., Kushnir, Y., Ting, M., 2014. Causes of increasing aridification of the Mediterranean region in response to rising greenhouse gases. J. Clim. 27, 4655−4676.

Seager, R., Liu, H., Kushnir, Y., Osborn, T.J., Simpson, I.R., Kelley, C.R., Nakamura, J., 2020. Mechanisms of winter precipitation variability in the European−mediterranean region associated with the north Atlantic oscillation. J. Clim. 33, 7179−7196.

Shackleton, N.J., Opdyke, N.D., 1973. Oxygen isotope and paleomagnetic stratigraphy of equatorial Pacific core V28-238: oxygen isotope temperatures and ice volume on a 105 and 106 year time scale. Quat. Res. 3, 39−55.

Shackleton, N.J., Opdyke, N.D., 1976. Oxygen isotope and pa- leomagnetic stratigraphy of equatorial Pacific core V28−238, late Pliocene to latest Pleistocene. In: Cline, R.M., Hays, J.D. (Eds.), Investigations of Late Quaternary Palaeoceanography and Palaeoclimatology, vol. 145. Mem. Geol. Soc. Am., pp. 449−464

Shackleton, N.J., Opdyke, N.D., 1977. Oxygen isotope and pale- omagnetic evidence for early northern hemisphere glaciation. Nature 270, 216−219.

Shaman, J., 2014. The seasonal effects of ENSO on European precipitation: observational analysis. J. Clim. 27, 6423−6438.

Sherwood, S., Webb, M.J., Annan, J.D., Armour, K.C., Forster, P.M., Hargreaves, J.C., Hegerl, G., Klein, S.A., Marvel, K.D., Rohling, E.J., Watanabe, M., Andrews, T., Braconnot, P., Bretherton, C.S., Foster, G.L., Hausfather, Z., von der Heydt, A.S., Knutti, R., Mauritsen, T., Norris, J.R., Proistosescu, C., Rugenstein, M., Schmidt, G.A., Tokarska, K.B., Zelinka, M.D., 2020. An assessment of Earth's climate sensitivity using multiple lines of evidence. Rev. Geophys. 58 e2019RG000678.

Simpson, I.R., Seager, R., Shaw, T.A., Ting, M., 2015. Mediterranean summer climate and the importance of Middle East topography. J. Clim. 28, 1977−1996.

Snyder, C.W., 2016. Evolution of global temperature over the past two million years. Nature 538, 226−228.

Sodemann, H., Zubler, E., 2010. Seasonal and inter-annual variability of the moisture sources for Alpine precipitation during 1995−2002. Int. J. Climatol. J. R. Meteorol. Soc. 30 (7), 947−961.

Somot, S., Sevault, F., Deque, M., Crepon, M., 2008. 21st century climate change scenario for the Mediterranean using a coupled atmosphere-ocean regional climate model. Glob. Planet. Change 63, 112−126.

Spratt, R.M., Lisiecki, L.E., 2016. A Late Pleistocene sea level stack. Clim. Past 12, 1079−1092.

Suc, J.P., 1984. Origin and evolution of the Mediterranean vegetation and climate in Europe. Nature 307, 429−432.

Tarolli, P., Borga, M., Morin, E., Delrieu, G., 2012. Analysis of flash flood regimes in the North-Western and South-Eastern Mediterranean regions. Nat. Hazards Earth Syst. Sci. 12, 1255−1265.

Taylor, K.E., Stouffer, R.J., Meehl, G.A., 2012. An overview of CMIP5 and the experiment design. Bull. Am. Meteorol. Soc. 93, 485−498.

Theocharis, A., 1989. Deep water formation and circulation in the Aegean Sea. In: Charnock, H. (Ed.), Reports in Meteorology and Oceanography, vol. 40, pp. 335−359 (I).

Thomson, J., Higgs, N.C., Wilson, T.R.S., Croudace, I.W., De Lange, G.J., Van Santvoort, P.J.M., 1995. Redistribution and geochemical behaviour of redox-sensitive elements around S1, the most recent eastern Mediterranean sapropel. Geochim. Cosmochim. Acta 59, 3487−3501.

Thomson, J., Mercone, D., de Lange, G.J., van Santvoort, P.J.M., 1999. Review of recent advances in the interpretation of eastern Mediterranean sapropel S1 from geochemical evidence. Mar. Geol. 153, 77−89.

Thunell, R.C., 1986. Pliocene−Pleistocene climatic changes: evidence from land-based and deep-sea marine records. Mem. Soc. Geol. Ital. 31, 135−143.

Thunell, R.C., Rio, D., Sprovieri, R., Vergnaud-Grazzini, C., 1991. An overview of the post-Messinian paleoenvironmental history of the western Mediterranean. Paleoceanography 6, 143−164.

Tierney, J.E., Zhu, J., King, J., Malevich, S.B., Hakim, G.J., Poulsen, C.J., 2020. Glacial cooling and climate sensitivity revisited. Nature 584, 569−573.

Tolika, K., Maheras, P., Pytharoulis, I., Anagnostopoulou, C., 2014. The anomalous low and high temperatures of 2012 over Greecedan explanation from a meteorological and climatological perspective. Nat. Hazards Earth Syst. Sci. 14, 501−507.

Trenberth, K.E., Dai, A., Rasmussen, R.M., Parsons, D.B., 2003. The changing character of precipitation. Bull. Am. Meteorol. Soc. 84, 1205−1217.

Trigo, I.F., Davies, T.D., Bigg, G.R., 1999. Objective climatology of cyclones in the Mediterranean region. J. Clim. 12, 1685−1696.

Tzedakis, P.C., 2007. Seven ambiguities in the Mediterranean palaeoenvironmental narrative. Quat. Sci. Rev. 26, 2042−2066.

Tzedakis, P., 2009. Cenozoic climate and vegetation change. In: Woodward, J. (Ed.), The Physical Geography of the Mediterranean. Oxford University Press, Oxford, pp. 89−137.

Ulbrich, U., Lionello, P., Belusic, D., Jacobeit, J., Knippertz, P., Kuglitsch, F.G., Leckebusch, G.C., Luterbacher, J., Maugeri, M., Maheras, P., Nissen, K.M., 2012. Climate of the Mediterranean: synoptic patterns, temperature, precipitation, winds and their extremes. In: Climate of the Mediterranean Region-From the Past to the Future. Elsevier, pp. 301−346.

Uppala, S.M., Kållberg, P.W., Simmons, A.J., Andrae, U., Bechtold, V.D.C., Fiorino, M., et al., 2005. The ERA-40 re-analysis. Q. J. R. Meteorol. Soc.: A journal of the atmospheric sciences, applied meteorology and physical oceanography 131 (612), 2961−3012.

Urgeles, R., Camerlenghi, A., Garcia-Castellanos, D., De Mol, B., Garcés, M., Vergés, J., Haslam, I., Hardman, M., 2011. New constraints on the Messinian sealevel drawdown from 3D seismic data of the Ebro Margin, western Mediterranean. Basin Res. 23, 123−145.

Van Assen, E., Kuiper, K.F., Barhoun, N., Krijgsman, W., Sierro, F.J., 2006. Messinian astrochronology of the Melilla basin: stepwise restriction of the mediterranean− Atlantic connection through Morocco. Palaeogeogr. Palaeoclimatol. Palaeoecol. 238, 15−31.

van Hinsbergen, D.J.J., Torsvik, T.H., Schmid, S.M., Matenco, L.C., Maffione, M., Vissers, R.L.M., Gürer, D., Spakman, W., 2020. Orogenic architecture of the Mediterranean region and kinematic reconstruction of its tectonic evolution since the Triassic. Gondwana Res. 81, 79−229.

Vardavas, I.M., Papamastorakis, J., Fountoulakis, A., Manousakis, M., 1997. Water resources in the desertification-threatened Messara Valley of Crete: estimation of potential lake evaporation. Ecol. Model. 102, 363−374.

Velaoras, D., Papadopoulos, V.P., Kontoyiannis, H., Papageorgiou, D.K., Pavlidou, A., 2017. The response of the Aegean sea (eastern Mediterranean) to the extreme 2016−2017 winter. Geophys. Res. Lett. 44, 9416−9423.

Vergnaud-Grazzini, C., Capotondi, L., Lourens, L.J., 1993. A refined Pliocene to early Pleistocene chronostratigraphic frame at ODP Hole 653A (west mediterranean). Mar. Geol. 117, 329−349.

Walker, G.T., Bliss, E.W., 1932. World weather V. Memoirs Royal Meteorogical Society, vol. 4, pp. 53−84.

Wallmann, K., Aloisi, G., 2012. The global carbon cycle: geological processes. Fundamentals of Geobiology 20−35.

Washington, W.M., Parkinson, C.L., 2005. An Introduction to Three-Dimensional Climate Modeling, second ed. University Science Books, Millway, CA, p. 353.

Wehausen, R., Brumsack, H.J., 2000. Chemical cycles in Pliocene sapropel-bearing and sapropel-barren eastern Mediterranean sediments. Palaeogeogr. Palaeoclimatol. Palaeoecol. 158, 325−352.

Westerhold, T., Marwan, N., Drury, A.J., Liebrand, D., Agnini, C., Anagnostou, E., Barnet, J.S.K., Bohaty, S.M., De Vleeschouwer, D., Florindo, F., Frederichs, T., Hodell, D.A., Holbourn, A.E., Kroon, D., Lauretano, V., Littler, K., Lourens, L.J., Lyle, M., Pälike, H., Röhl, U., Tian, J., Wilkens, R.H., Wilson, P.A., Zachos, J.C., 2020. An astronomically dated record of earth's climate and its predictability over the last 66 million years. Science 369, 1383−1387.

Whiting-Blome, M., Cohen, A.S., Tyron, C.A., Brooks, A., Russell, J., 2012. The environmental context for the origins of modern human diversity: a synthesis of regional variability in African climate 150,000−30,000 years ago. J. Hum. Evol. 62, 563−592.

Wijmstra, T.A., Young, R., Witte, H.J.L., 1990. An evaluation of the climatic conditions during the Late Quaternary in northern Greece by means of multivariate analysis of palynological data and comparison with recent phytosociological and climatic data. Geol. Mijnbouw 69, 243−251.

Wild, M., 2012. Enlightening global dimming and brightening. Bull. Am. Meteorol. Soc. 93, 27−37.

Willeit, M., Ganopolski, A., Calov, R., Brovkin, V., 2019. Mid-Pleistocene transition in glacial cycles explained by declining CO2 and regolith removal. Sci. Adv. 5, eaav7337.

Xoplaki, E., Maheras, P., Luterbacher, J., 2001. Variability of climate in meridional Balkans during the periods 1675−1715 and 1780−1830 and its impact on human life. Clim. Change 48, 581−615.

Xoplaki, E., González-Rouco, J.F., Luterbacher, J., et al., 2004. Wet season Mediterranean precipitation variability: influence of large-scale dynamics and trends. Clim. Dynam. 23, 63−78.

Yavuz, V., Akcar, N., Schlüchter, C., 2007. The frozen Bosphorus and its paleoclimatic implications based on a summary of the historical data. In: Yanko-Hombach, V., Gilbert, A.S., Panin, N., Dolukhanov, P.M. (Eds.), The Black Sea Flood Question: Changes in Coastline, Climate, and Human Settlement. Springer, Dordrecht, pp. 633−649.

Yokoyama, Y., Esat, T.M., Thompson, W.G., Thomas, A.L., Webster, J.M., Miyairi, Y., Sawada, C., Aze, T., Matsuzaki, H., Okuno, J., Fallon, S., Braga, J.-C., Humblet, M., Iryu, Y., Potts, D.C., Fujita, K., Suzuki, A., Kan, H., 2018. Rapid glaciation and a two-step sea level plunge into the Last Glacial Maximum. Nature 559, 603−607.

Zachariasse, W.J., Zijderveld, J.D.A., Langereis, C.G., Hilgen, F.J., Verhallen, P.J.J.M., 1989. Early Late Pliocene biochronology and surface water temperature variations in the Mediterranean. Mar. Micropaleontol. 14, 339−355.

Zachariasse, W.J., Gudjonsson, L., Hilgen, F.J., Langereis, C.G., Lourens, L.J., Verhallen, P.J.J.M., Zijderveld, J.D.A., 1990. Late Gauss to Early Matuyama invasions of Neogloboquadrina atlantica in the Mediterranean and associated record of climatic change. Paleoceanography 5, 239−252.

Zappa, G., Hawcroft, M.K., Shaffrey, L., Black, E., Brayshaw, D.J., 2015. Extratropical cyclones and the projected decline of winter Mediterranean precipitation in the CMIP5 models. Clim. Dynam. 45 (7), 1727−1738.

Zeebe, R.E., Ridgwell, A., Zachos, J.C., 2016. Anthropogenic carbon release rate unprecedented during the past 66 million years. Nat. Geosci. 9 (4), 325−329.

Zhang, R., Sutton, R., Danabasoglu, G., Kwon, Y.O., Marsh, R., Yeager, S.G., Amrhein, D.E., Little, C.M., 2019. A review of the role of the Atlantic meridional overturning circulation in Atlantic multidecadal variability and associated climate impacts. Rev. Geophys. 57, 316−375.

This page intentionally left blank

CHAPTER

4 The forcings of the Mediterranean Sea and the physical properties of its water masses

Katrin Schroeder[1], Toste Tanhua[2], Jacopo Chiggiato[1], Dimitris Velaoras[3], Simon A. Josey[4], Jesús García Lafuente[5], Manuel Vargas-Yáñez[6]

[1]*Consiglio Nazionale delle Ricerche-Istituto di Scienze Marine (CNR-ISMAR), Venezia, Italy;* [2]*GEOMAR Helmholtz Centre for Ocean Research Kiel, Kiel, Germany;* [3]*Hellenic Centre for Marine Research (HCMR), Institute of Oceanography, Anavyssos, Greece;* [4]*National Oceanography Centre, Southampton, United Kingdom;* [5]*Grupo de Oceanografía Física, Instituto de Biotecnología y Desarrollo Azul (IBYDA), Universidad de Málaga, Málaga, Spain;* [6]*Insituto Español de Oceanografía, IEO-CSIC, Málaga, Spain*

Learning objectives

In this Chapter you will learn:
- Which are the main forcings of the Mediterranean Sea
- What are the heat and freshwater budgets of the Mediterranean Sea
- How to identify Mediterranean water (MW) masses on a T-S diagram
- How the MW masses are distributed on a basin scale
- What are the typical thermohaline properties of the MW masses
- How we can use other tracers to identify and track water masses

4.1 The forcings of the Mediterranean Sea

The forcings of the Mediterranean Sea are responsible for driving the circulation and determining the water mass (WM) properties. The most important ones are the exchanges at the Strait of Gibraltar (discussed in Section 4.1.1) and the air-sea exchanges of momentum, heat, and freshwater (discussed in Section 4.1.2). Other drivers are river inputs and exchanges with the Black Sea.

4.1.1 Exchanges through the strait of Gibraltar

The net freshwater deficit of the Mediterranean Sea (positive E-P, where E = evaporation, P = precipitation plus river runoff) requires a compensating flow

Oceanography of the Mediterranean Sea. https://doi.org/10.1016/B978-0-12-823692-5.00005-4

to maintain its volume, which takes place through the Strait of Gibraltar, the only connection with the world ocean. The bathymetry shown in the middle panels of Fig. 4.1 thus plays a determining role in the exchanged flows and, hence, in the bulk properties of the Mediterranean Sea. The compensating flow is the outcome of a two-way flow, a surface inflow (Q_1) into the Mediterranean Sea and an outflow (Q_2) at depth toward the Atlantic Ocean. As the reader will learn also later, the fact that the outflow occurs below the inflow is also of utmost importance from the biogeochemical point of view.

In addition to forcing the compensating flow, the net evaporation transforms relatively light Atlantic Water (AW) into denser Mediterranean Water (MW) that sinks to intermediate and great depths to fill progressively the basin. Once this water reaches the depth of the main sill of the Strait (i.e., Camarinal sill, about 300 m depth; see CS in Fig. 4.1), it flows out to the Atlantic Ocean as a deep undercurrent, thus establishing the two-way flow (Fig. 4.1 bottom panel). A simple model to get insight in the process is a two-layer system in which homogeneous AW of salinity S_1 flows at a constant rate Q_1 (>0) into the Mediterranean Sea, where the net evaporation (E-P) transforms it into MW of salinity S_2 ($S_1<S_2$), forcing an outflow Q_2 (<0). In an ideal steady state, two equations hold (the so-called Knudsen relations, Knudsen, 1900):

$$Q_1 + Q_2 = (E - P); \quad Q_1 S_1 = -Q_2 S_2 \tag{4.1a, 4.1b}$$

which establish volume and salt conservation in the basin. Assuming that water salinities and net evaporation were known, the unknown flows Q_1 and Q_2 are given by

$$Q_1 = \frac{S_2(E - P)}{(S_2 - S_1)}; \quad Q_2 = -\frac{S_1(E - P)}{(S_2 - S_1)} \tag{4.2a, 4.2b}$$

These equations were used by Nielsen (1912) to estimate the size of the exchanged flows from estimations of (E-P) over the basin and measurements of S_1 and S_2 at the Strait. Eq. (4.2) highlight the crucial role of the salinity difference (S_2-S_1): the smaller the difference, the greater the exchanged flows. However, whereas (E-P) and S_1 can be considered as known inputs in the model, the salinity S_2 (and, hence, S_2-S_1) is unknown since it is a result of (E-P) itself. Dynamically, the flows are proportional to the density difference of MW and AW, since this difference provides the potential energy that drives the currents through the Strait. As the density difference is mainly due to salinity, large flows require large salinity differences, which is just the opposite of what Eq. (4.2) indicate.

Bryden and Stommel (1984) addressed this point by arguing that mixing in the Mediterranean basin makes the salinity difference as small as possible (overmixing), but that the hydrodynamics forced by the restrictive topography of the Strait imposes a lower limit to this difference. Thus, the Strait bathymetry determines not only the intensity of the flows but also the salinity S_2 of the MW. Since the Mediterranean Sea behaves like an inverse estuary, they used the theory developed for estuaries by

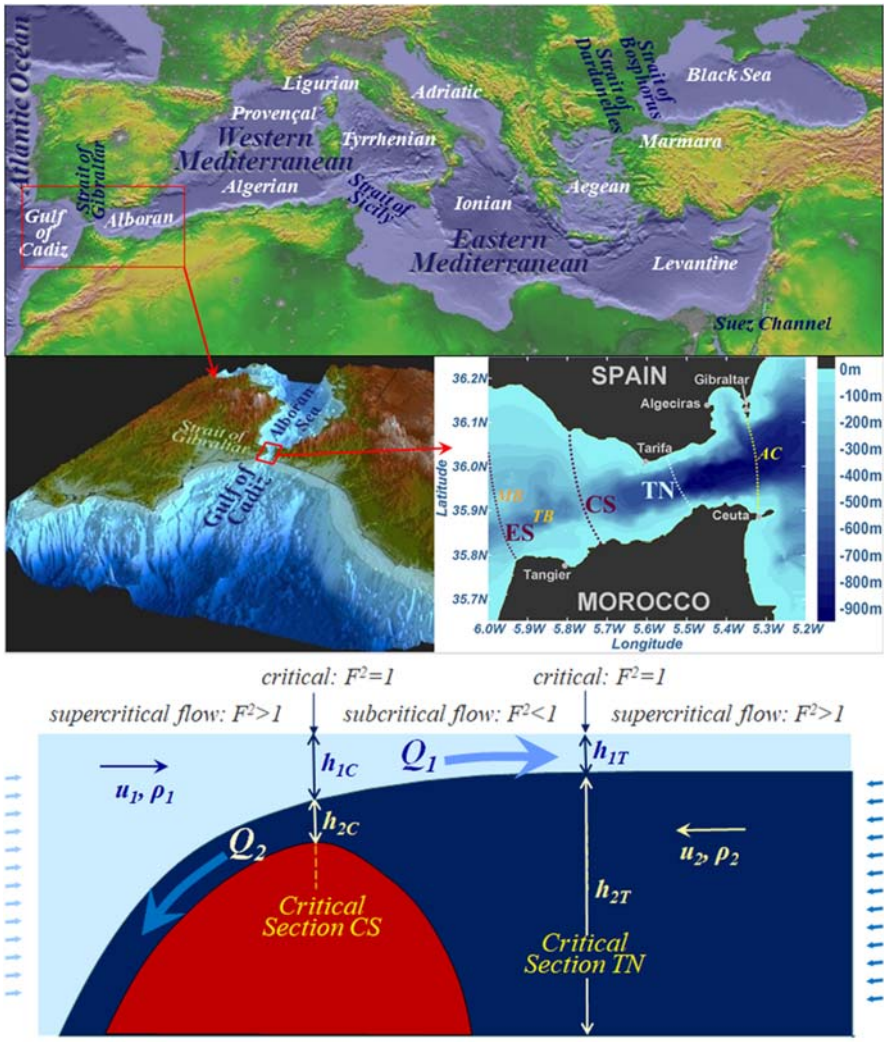

FIGURE 4.1

Top panel: map of the Mediterranean and Black seas. Left-middle panel: 3D bathymetry of the Gulf of Cadiz and Alboran Sea. Right-middle panel: detailed bathymetry of the Strait of Gibraltar where ES and CS stand for Espartel and Camarinal sills, respectively, and the dotted lines are the associated cross-sections; TN is Tarifa Narrows, the minimum-width section, and AC specifies the eastern entrance of the Strait; TB indicates the relatively deep Tangier Basin between the two main sills; MB is a submarine mountain that shapes the channel linked to ES (see also Chapter 2 about the physiography of the sea). Bottom panel: Sketch of the exchange illustrating the maximal exchange situation. Control sections exist at CS and TN, which are connected by a region of subcritical flow.

Stommel and Farmer (1953) and applied the concept of hydraulic control, where the composite Froude number, defined as

$$F^2 = F_1^2 + F_2^2 = \frac{u_1^2}{g'h_1} + \frac{u_2^2}{g'h_2} \tag{4.3}$$

reaches the critical value $F = 1$. Here, $g' = g(\rho_2 - \rho_1)/\rho_2$ is the reduced gravity, and ρ_i, h_i and u_i are density, thickness and velocity of layer $i = 1,2$, respectively (see sketch in Fig. 4.1 bottom panel).

Bryden and Kinder (1991) applied the theory of the double hydraulic control at the shallowest (CS) and narrowest (TN) sections, elaborated by Armi and Farmer (1985, 1986) and Farmer and Armi (1986), and derived formulas for Q_2 and $(S_2 - S_1)$ in terms of (E-P). They found $Q_2 = -1.1(\text{E-P})^{1/3}$ and $(S_2 - S_1) = 2.7(\text{E-P})^{2/3}$ with Q_2 in Sv (Sverdrup; 1 Sv $= 10^6$ m^{3}s^{-1}), $(S_2 - S_1)$ in practical salinity scale units, and (E-P) in m yr^{-1}. For (E-P) $= 0.7$ m yr^{-1}, typical of the Mediterranean basin, $Q_2 = -0.98$ Sv and $(S_2 - S_1) = 2.13$ (or $S_2 = 38.33$ for an Atlantic salinity $S_1 = 36.2$ in the Strait area), which are slight overestimation and underestimation, respectively, of the observed values.

The attempts to provide reliable estimates of the exchange are traced back to the beginning of the 20$^{\text{th}}$ century and include theoretical approaches and observation-based estimations (Sammartino et al., 2015; Jordá et al., 2017). Hydraulic models disclose the fundamentals of the functioning of the Mediterranean Sea and Strait of Gibraltar system, but cannot provide accurate values of the exchange A continuous monitoring of the velocity field with good spatial resolution would result in more accurate estimates. However, the collection of suitable velocity data sets is not easy in this region, which has marked spatial and temporal variability linked to the tides and to the abrupt bathymetry. The tidal current - topography interaction causes intermittent flow reversals and large vertical oscillations of the Atlantic-Mediterranean interface (Farmer and Armi, 1988; Bryden et al., 1994; García Lafuente et al., 2000, 2007; Sannino et al., 2004; Sánchez Garrido et al., 2008, 2011; Sammartino et al., 2015; see the surface signature of these internal waves in https://www.eumetsat.int/internal-waves-eastern-strait-gibraltar, for instance), which hampers the straightforward estimation of the long-term exchanged flows, even if the difficulty of accomplishing a suitable monitoring is overcome. Despite the difficulties, observational attempts to address the issue have been carried out. One of them is the monitoring station deployed at Espartel sill (ES, see Fig. 4.1; García Lafuente et al., 2007). Fig. 4.2 shows a time series of the outflow (Sammartino et al., 2015; García-Lafuente et al., 2021), where tidal variability has been removed but meteorologically-driven and seasonal fluctuations have not. The mean value, computed as the mean ($\pm$ standard deviation) is $Q_2 = -0.858 \pm 0.028$ Sv . Eddy-fluxes, a typical an unwelcome process to compute flows, which arises from the positive correlation of the interface oscillations and the tidal currents (Bryden et al., 1994; García Lafuente et al., 2000), are shown in light blue to illustrate their limited importance (4.8% of the total Q_2). The large fluctuations in Fig. 4.2 (deep blue line) are the response of the outflow to meteorological forcing (Sánchez-

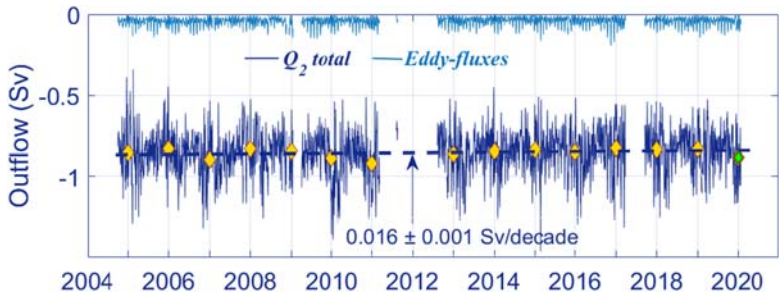

FIGURE 4.2

Mediterranean outflow computed from the data collected at ES (*deep blue line*). Yellow diamonds indicate each year-averaged value (year n spanning from October year n−1 to September year n). The last diamond is filled in green because year 2020 is incomplete (data finish in January 2020). Eddy-fluxes are shown in light blue. *Dashed line* is the linear trend.

Garrido et al., 2011): when the basin is under high (low) atmospheric pressure, the sea level is forced downwards (upwards). Since the basin is not large enough to allow for internal adjustment, a net outflow (inflow) across the Strait of Gibraltar, which adds to the long-term exchange, is the result.

No similarly long time series are currently available for a direct computation of the inflow. It must be indirectly estimated from the outflow through conservation (Eq. 4.1a).

In addition to water exchange, heat, and salt fluxes are important to the bulk balance of properties in the Mediterranean basin. Heat (QH in W) and salt (QS in kg s^{-1}) fluxes are computed as indicated by Eq. (4.4):

$$QH_i = \int_{LS}^{US} \rho_i c_{p,i} \theta_i u_i ds_i \quad QS_i = \int_{LS}^{US} \rho_i S_i u_i ds_i, \quad \text{where } i = 1, 2 \qquad (4.4a, 4.4b)$$

where subscript i refers to layers, ρ_i, θ_i, S_i and u_i are layer density, potential temperature, salinity, and velocity, and $c_{p,i}$ is the specific heat of seawater at constant pressure, which depends slightly on temperature and salinity. Computing these transports from observations require the simultaneous availability of time series of vertical profiles of u, θ and S, where the latter two are usually reduced to discrete observations at fixed depths, from which the profile is inferred. This method was used by Macdonald et al. (1994), who found a positive heat flux[1] of 5.2 ± 1.3 W m^{-2}, in agreement with reported values of the Mediterranean Sea heat budgets (Jordá et al., 2017). No observation-based estimates of salt transports have yet been done.

[1] It is usual to transform heat transport (W) into equivalent heat flux (Wm^{-2}) across the surface of the Mediterranean Sea by dividing by its area (2.51×10^{12} m^2) in order to provide a magnitude comparable with air-sea heat exchanges.

4.1.2 Climatological mean surface flux fields

In this section, climatological mean fields of the key air-sea transfers are introduced and discussed. First, the wind stress which is equivalent to the air-sea momentum flux and is proportional to the product of the drag coefficient (C_D) and the wind speed (u) squared,

$$\tau = \rho C_D u^2 \tag{4.5}$$

where ρ is the density of air. Second, the net heat flux which is the sum of four individual components: the latent and sensible turbulent fluxes, and the longwave (thermal) and shortwave (solar) radiative fluxes. Third, the net evaporation or air-sea freshwater flux (E-P) which is determined by the difference between evaporation (E) and precipitation (P).

4.1.2.1 Wind stress

The wind stress field is similar to the wind field which in turn is primarily set by the sea level pressure (SLP). In the Mediterranean, SLP tends to be lower in summer than winter as higher temperatures favor atmospheric convection. Particularly intense low pressure (Fig. 4.3, blue colors, bottom panel) is evident in the far Eastern

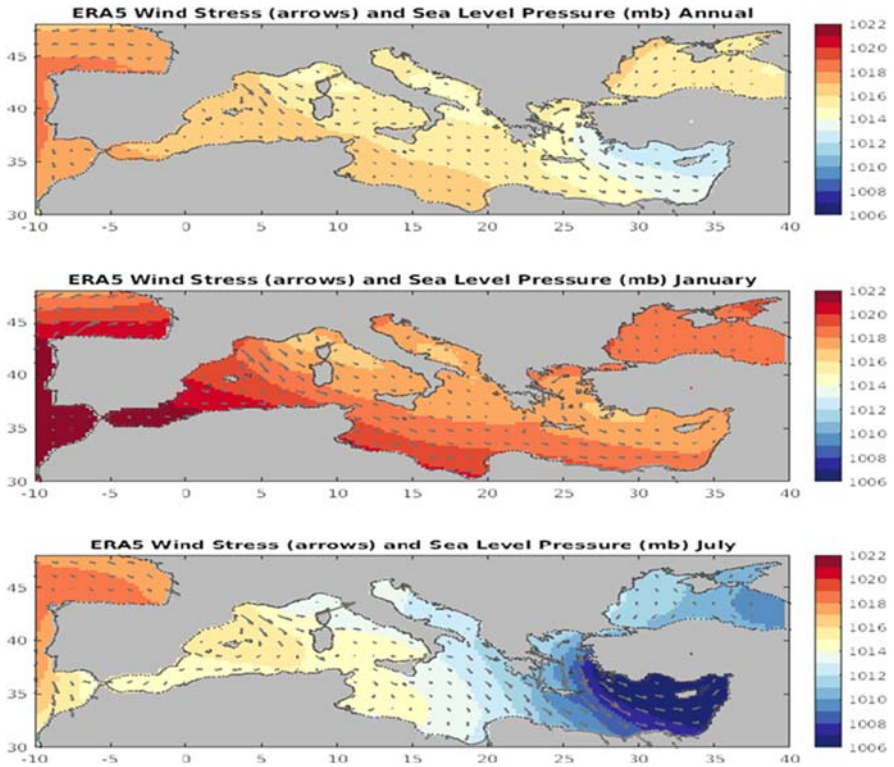

FIGURE 4.3

Climatological mean wind stress (*arrows*) and seal level pressure (color) determined from the ERA5 reanalysis for the period 1981–2010. Top panel-annual mean, middle—January, bottom—July.

Mediterranean region termed the Levantine Basin in July, this results in strong winds from the north to north-east. In January, the strongest winds are found in the north-west of the basin particularly in the Gulf of Lion which is recognized to be a region of dense water formation resulting from wind driven surface heat loss (see also Chapter 7).

4.1.2.2 Heat flux

The net heat flux, Q_n, is the sum of the turbulent (latent, Q_e, sensible, Q_h) and radiative (shortwave, Q_{sw}, longwave, Q_{lw}) terms:

$$Q_n = Q_e + Q_h + Q_{lw} + Q_{sw} \tag{4.6}$$

The sign convention employed here is for heat gain by the ocean to be positive. The turbulent terms are primarily dependent on the near surface gradients of humidity (for the latent) and temperature (for the sensible) together with the wind speed. This dependence can be seen in the following equations used for their estimation which are usually termed "bulk formulae":

$$Q_e = \rho L C_e u(q_s - q_a) \tag{4.7}$$

$$Q_h = \rho c_p C_h u(T_s - T_a) \tag{4.8}$$

In the above, ρ is the density of air; L, the latent heat of vaporization; C_e and C_h, the stability and height dependent transfer coefficients for latent and sensible heat, respectively; u, the wind speed; q_s, 98% of the saturation specific humidity at the sea surface temperature to allow for the salinity of sea water, and q_a, the near surface atmospheric specific humidity; c_p, the specific heat capacity of air at constant pressure; T_s, the sea surface temperature; T_a, the near surface air temperature.

The annual mean het heat flux field (Fig. 4.4) has a balance between ocean heat loss as strong as -30 W m^{-2} in the northern half of the basin and heat gain in the southern half which is particularly strong (50 W m^{-2}) in the Alboran Sea and Strait of Gibraltar. Over the basin as a whole, the heat exchange has to average to a small net heat loss of about -4 W m^{-2} to match the ocean heat transported into the Mediterranean at Gibraltar. Strong seasonal variations are evident with January heat loss over the entire basin which approaches -220 W m^{-2} in the Aegean Sea; this region being strongly influenced by the intense winds noted above. In July, the whole basin experiences heat gain reflecting the dominant role for solar heating at this time of year. The individual heat flux components are shown in Fig. 4.5.

The two dominant terms are the latent heat loss which is most intense in the regions with strong wind forcing (as it is proportional to the product of the wind speed and sea-air humidity difference) and the shortwave gain which increases as latitude decreases due to the greater mean solar elevation. The sensible heat (proportional to the product of the wind speed and sea-air temperature difference) and longwave contributions are minor in comparison.

4.1.2.3 Freshwater flux

The net evaporation is positive over virtually the entire Mediterranean consistent with its role as a concentration basin. This reflects the dominance of evaporation over precipitation with the latter small over most of the region with the exception of a few coastal regions (principally the Eastern Adriatic) where P approaches E in magnitude (Fig. 4.6).

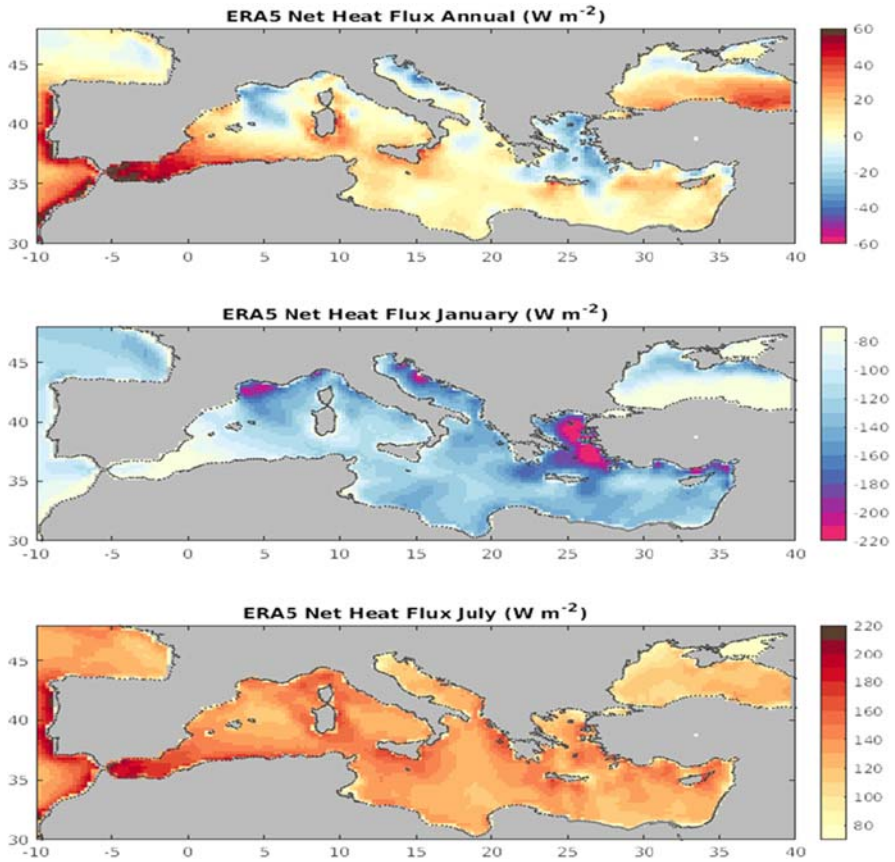

FIGURE 4.4

Climatological mean net heat flux (ERA5, 1981–2010). Top panel shows the annual mean, middle panel shows January, bottom panel shows July. Negative values indicate ocean surface heat loss, positive heat gain.

4.1.3 Temporal variability

The climatological fields discussed above present a static view of air-sea interaction. This approach is useful for characterizing the long term mean state but conceals a rich range of short time scale variability. This is illustrated in Fig. 4.7 by time series of the daily mean net heat flux at an example site (42.4°N, 4°E) in the Gulf of Lion dense water formation region. The latent heat flux shows particularly notable variations at daily time scales with extreme values in winter approaching -600 W m^{-2}. Similar variability is evident in the sensible heat flux with smaller extremes of about -250 W m^{-2}. These events are generated by intense winds and cold, dry air masses associated with the passage of severe atmospheric cyclones. They combine on occasion to produce very large daily turbulent (latent + sensible) heat

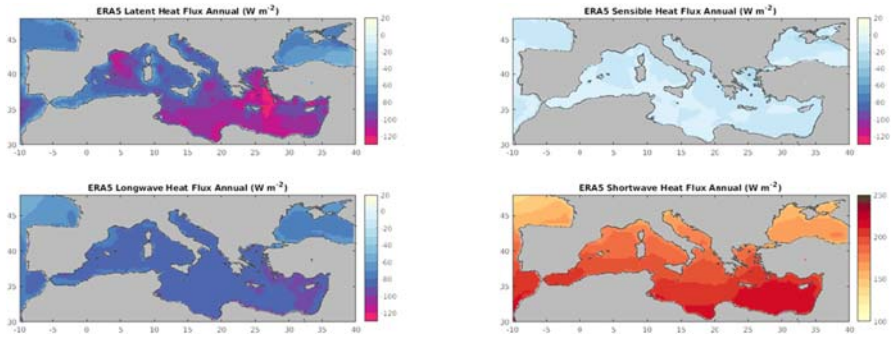

FIGURE 4.5

Climatological annual mean heat flux components (ERA5, 1981–2010). Top left panel shows latent, top right panel shows sensible, bottom left panel shows longwave, bottom right panel shows shortwave.

losses stronger than -800 W m^{-2}. In comparison, the longwave day to day variability (determined principally by changing cloud amount) is small at the level of tens of W m^{-2} while the shortwave can vary by 100–150 W m^{-2} from day to day in summer. The net heat flux variability reflects the combination of the individual components and is dominated by the turbulent heat flux contribution with extremes of daily heat loss exceeding -900 W m^{-2} in winter.

Large scale atmospheric modes of variability (see also Chapter 3), particularly the North Atlantic Oscillation (NAO) and the East Atlantic Pattern (EAP) have a significant impact on the pattern of heat loss across the basin in a given winter (and to a lesser extent summer). Of the two, the EAP has the biggest influence on the basin averaged heat flux tending to either increase or reduce the heat loss over much of the Mediterranean Sea depending on whether the EAP is in a negative or positive state (Josey et al., 2011). When these modes are in a particularly strong state, they can give rise to airflows driving intense heat loss, for example in winter 2004/05 in the North-western Mediterranean (Schroeder et al., 2010). However, it is not always possible to link winter heat loss to established modes of variability, for example, the severe winter heat loss in the Aegean Sea in winters 1991/92 and 1992/93, that gave rise to the Eastern Mediterranean Transient was not a simple response to the NAO or EAP (Josey, 2003).

4.2 The thermohaline properties of the Mediterranean water masses

The driving forces presented in Section 4.1 are largely responsible for the (thermohaline) properties that are typically found in the water column of the Mediterranean Sea. These properties trigger the movements of WMs, that is, the so-called

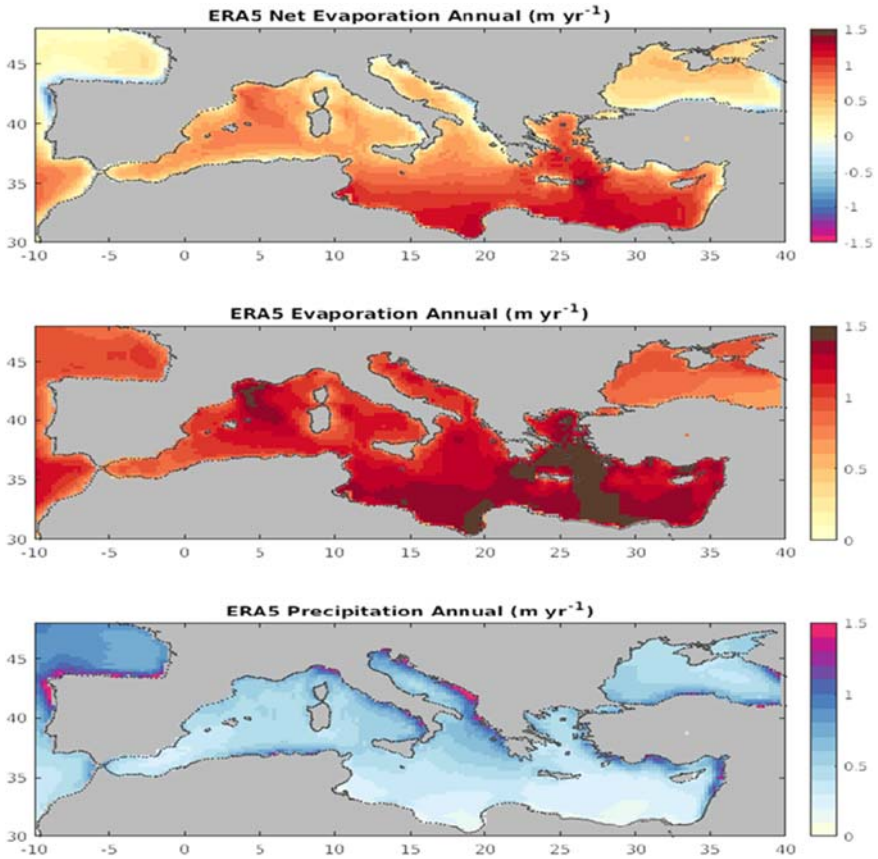

FIGURE 4.6

Climatological annual mean E-P and components (ERA5, 1981–2010). Top panel shows E-P, middle panel shows E, bottom panel shows P.

thermohaline circulation. And indeed, much of our early and present knowledge about the movement of water in the ocean, especially those at great depths, has been inferred from investigations about the distribution of water properties such as temperature, salinity, and density, but also dissolved oxygen and nutrients. This subchapter reviews the mean properties of the Mediterranean Sea, focusing on the distributions of its major WMs and their relationships to the main current pathways.

Our knowledge about the properties of the WMs of the Mediterranean Sea and their circulation has evolved since the end of the 19th century and the beginning of the 20th. This evolution has run in parallel to the development and improvement of the measurement techniques and the increasing data availability (see Chapter 10 where the Mediterranean Observing and Forecasting Systems are explained in detail). Furthermore, our understanding about the functioning of the Mediterranean

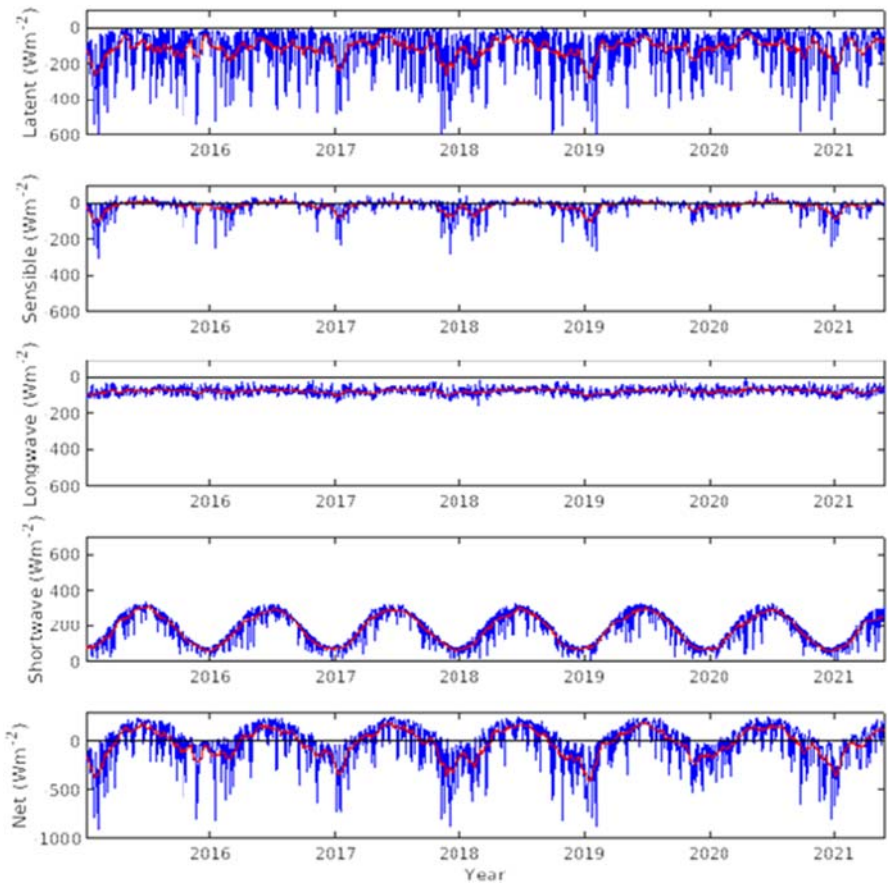

FIGURE 4.7

Time series of ERA5 daily (blue) and 30 day running mean (red) heat flux at an example site (42.4°N, 4°E) in the Gulf of Lion.

has changed at the same time that the functioning of the Mediterranean Sea has been changing because of climate change, or other anthropogenic alterations, or simply because of the internal variability of the ocean-atmosphere system (see Chapter 9).

4.2.1 Water masses, water types, and their representation

The concept of "WMs" derives from the meteorological concept of "air masses," to differentiate between volumes of air with specific characteristics. Although sometimes they are treated as such, WMs are not real, objective physical entities. Here we will rather talk about "core" WM properties. The vertical structure, or stratification, of the ocean is the result of mixing of the various WMs that have been advected at one specific location. This mixing can occur both horizontally and vertically. Each

core WM has acquired its basic and distinctive characteristics in a specific "formation region" (Iselin, 1939).

Before going into detail on how the MW masses are distributed, we will briefly introduce the basic tools that are used by oceanographers to describe them. The diagram where (potential) temperature (y-axis) and salinity (x-axis) data of each water sample are shown, is called TS diagram (first introduced by Helland-Hansen, 1918), and allows to relate density to the observed thermohaline properties. Furthermore it is easy to locate relative and absolute maxima and minima. As density increases with increasing salinity and decreasing temperature, in the TS diagram the density-isolines (or isopycnals) are shown as diagonal curves going from the upper right corner to the lower left one, and where density increases going from the upper left corner to the lower right corner of the plot (Fig. 4.8 left). An interesting feature that can be easily understood by looking at a TS diagram, is the cabbeling effect (Fig. 4.8 right), which occurs when two separate water parcels of equal density (A and B) mix linearly (i.e., along the red lines) to form a third one (C): the combined water parcel is denser than the original two water parcels, and sinks below both parents.

It appears now easy to understand the difference between a WM, that is, "a body of water with a common formation history, having its origin in a particular region of the ocean" (Tomczak, 1999), and a water type (WT), that is, a point in an n-dimensional parameter space, thus a combination of temperature, salinity (and other

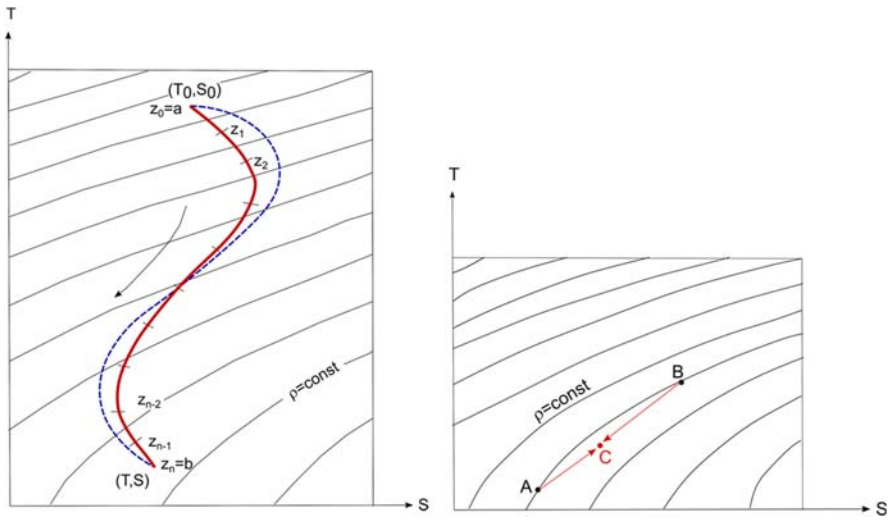

FIGURE 4.8

(left) T-S curve of an oceanographic station, where z values denote the depths of the corresponding levels (a<b); (right) representation of the cabelling effect.

Adapted from Mamayev, O.I., 1975. Temperature-Salinity Analysis of World Ocean Waters, vol. 11, first ed., Elsevier Science, 373 pp.

tracer values, such as nutrients, dissolved oxygen, transient tracers). A different but related concept is the Source Water Type (SWT), that is the original properties of a particular WM in its formation area. A WM has a physical extent, i.e., a volume, while WT and SWT are defined values of properties without any physical extent. While we are often interested in the pathways, residence times, volume, transformation, and ventilation of WM, we tend to describe the properties in terms of (source) WTs. WM formation occurs generally in contact with the atmosphere (this topic is explained more in detail in Chapter 7), while its spreading from the formation region generally occurs without atmospheric contact. A WM can then be followed during the spreading and mixing phase, and its mixing with other WM quantified, by analyzing the distribution of thermohaline (and chemical) properties.

4.2.2 Water mass analysis and the interpretation of the TS diagram

Temperature and salinity are so-called conservative properties (i.e., they can only change at the sea surface, by air-sea interactions). Thus as long as the WM remains isolated from the surface, where heat or fresh water can be gained or lost, these properties would slowly change only due to mixing with adjacent WMs. The TS diagram is the basic tool for WM classification and analysis, in which the two conservative properties are plotted against each other. Isopycnals are drawn on the same diagram to give additional insights. Deep WMs retain their TS characteristics for long periods of time, and can be identified readily on a TS plot. Furthermore, the TS diagram also allows to investigate mixing patterns between WMs. In Fig. 4.9A a schematized TS diagram of the deep waters in the Western Mediterranean Sea (WMED) during the so-called Western Mediterranean Transition (see Chapter 9) is shown. Three end-members can be identified (A, B, and C), that in this case correspond to old and resident deep water (A), newly formed convective deep water (B) and newly formed cascading water (C) (see Chapter 9 and Schroeder et al., 2006 for details). These three WMs can mix with each other along mixing lines, that is, the lines in the TS diagram connecting the three WTs: the closer a sample is found to a certain endmember, the higher is the fraction of this WT in the sample. In Fig. 4.9A this is exemplified by three colored WTs, that are a mixing product, at different mixing fractions, of the three source WTs considered in the example: the blue dot represents a water parcel that is composed of 50% of WM A and 50% of WM B; the red dot represents a water parcel that is composed of 70% of WM B and 30% of WM C; the green dot represents a water parcel that is composed of 30% of WM A, 20% of WM B and 50% of WM C. This originally called "core-layer" method has been a systematic attempt to describe the waters of the ocean, developed by Wüst (1935), and was crucial in early studies of ocean WMs (some examples for the Mediterranean can be found in Wüst, 1961, see also Fig. 4.11; Font, 1987; Millot, 1987). In this method Wüst (1935) distinguished between different core layers characterized by maxima or minima in their oxygen, salinity or temperature fields.

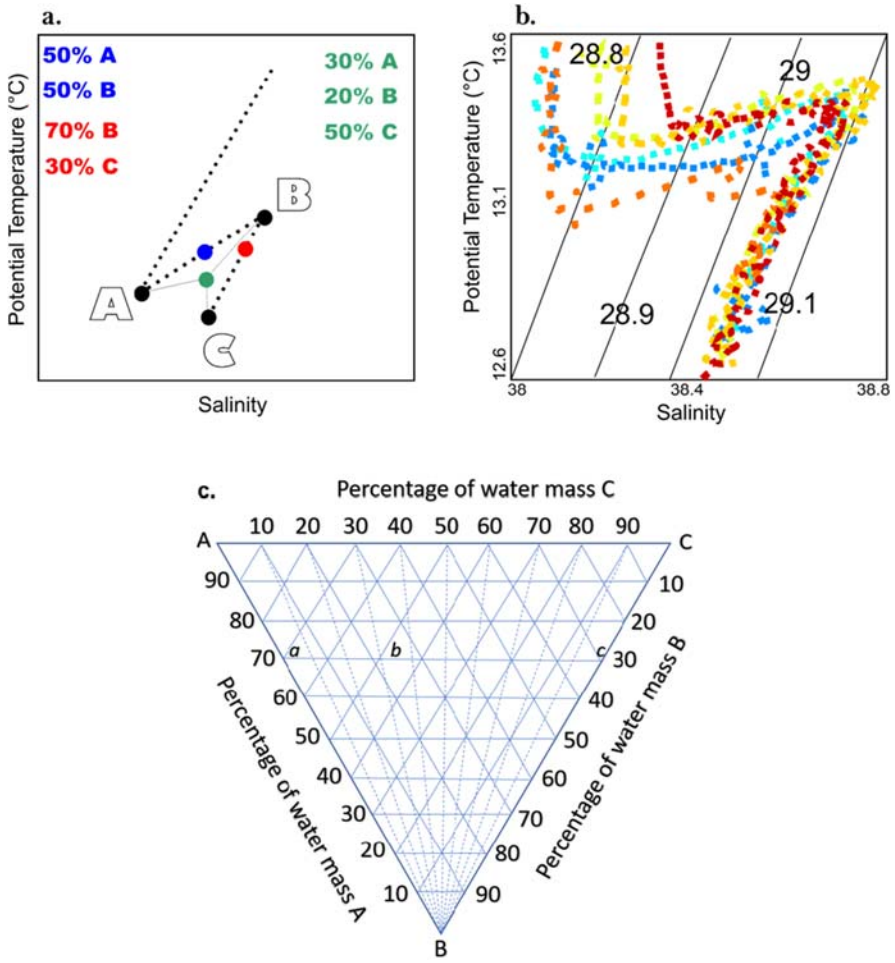

FIGURE 4.9

(A) Representation of mixing lines, fractions and products between three different deep water masses; (B) a typical TS diagram in the Mediterranean Sea (below the mixed layer), density is expressed as potential density anomaly ($\sigma = \rho - 1000$); (C) generic mixing triangle, where the broken lines plot the isolines of percentage content of waters CB on their mixing with waters AB.

Redrawn from Mamayev, O.I., 1975. Temperature-Salinity Analysis of World Ocean Waters, vol. 11, first ed., Elsevier Science, 373 pp.

The "core-layer" method has been further developed in a multivariate mathematical model to include other tracers (both conservative and nonconservative), and is often referred to as Optimum Multiparametric Analysis (OMP, see e.g., Tomczak, 1981; Tomczak and Large, 1989; Mackas et al., 1987; for Mediterranean applications see e.g., Vilibic and Orlic, 2001; Hainbucher et al., 2014; Carracedo et al.,

2016; Jullion et al., 2017; Schroeder et al., 2008, 2020; Kovacevic et al., 2012). Briefly, according to this simple linear mixing method, a water sample can be described as a set of linear mixing equations of different predefined SWTs that contributed to its characteristics. All data points should therefore be located "downstream," on the spreading path, of the unmixed source water. The fractions of the SWTs for each sample are then computed by determining the best linear mixing combination in the parameter spaces that allows to minimize the residuals in a nonnegative least squares sense. In addition, OMP analysis conserve mass, and so add an additional constraint to the WM analysis. To get a physically realistic result, two constraints are included, that is, the contributions of all SWTs must add up to 100% and all need to be nonnegative. The OMP can also be extended to include biogeochemical WM tracers (see Section 4.3).

The TS curve shown in Fig. 4.9B is a sketch of typical features that can be found below the mixed layer in any profile taken in the Mediterranean Sea, with each color representing one vertical CTD profile. The definition and identification of WMs can be done by locating extremes in salinity and/or potential temperature. In the Mediterranean Sea, the salinity maximum in the TS curves (in Fig. 4.9B it is at about 38.7) generally identifies the core of the Intermediate Water (IW), which forms in the Eastern Mediterranean Sea (EMED) and flows toward the WMED, eventually exiting toward the Atlantic Ocean (see also Chapters 7 and 9). A general mixing triangle is shown in Fig. 4.9C, and illustrates well how the percentages of up to three WMs are combined in any of their mixing products.

It is to be noted that the extremes associated with a particular WM, may not remain at the same TS values: as a WM moves away from its formation region, the sharp edges (maxima or minima) that mark it, start to erode, broadening the range of the extreme. However, the shape of the TS diagram for a given region where certain WMs reside tends to be maintained.

One particularly instructive variant of a TS diagram is a "volumetric TS curve," where it can be seen how much volume is associated with a particular bin of T-S values in a three-dimensional relationship (in Fig. 4.10 this is shown using numerical model data). It is evident from this plot that a rather small region of TS values is representative for most of the water volume of the basin. This is explained by the fact that the WMs that sit close to the surface have the largest property ranges, but occupy a relatively small fraction of the ocean volume, while the intermediate and deep WMs, which occupy a large portion of the ocean, exhibit a quite restricted property range, due to the absence of air−sea interactions (Emery, 2003).

One difficulty in WM analysis is the definition of the source WTs that often require access to data from a large region and ideally over a time-span. A recent study provides an overview of the characteristics and distribution of the main WMs in the Atlantic Ocean (Liu and Tanhua, 2021). The level of detail and granularity of a WM study must reflect the study area and the problem at hand. One example is the Labrador Sea Water that can, in a basin wide view, be considered

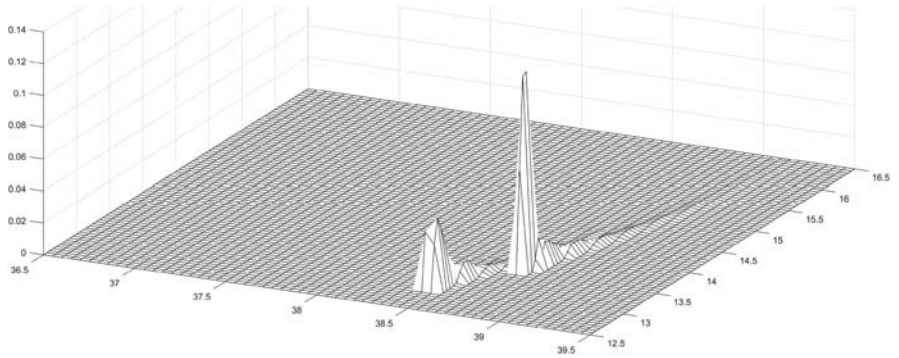

FIGURE 4.10

Volumetric TS diagram in the Mediterranean Sea, where the z-axis defines the volume fractions represented by the T and S bins (all volume fractions add up to 1).

Data used to plot this diagram come from CMEMS reanalysis of the year 2019 (product MEDSEA_MULTIYEAR_PHY_006_004).

as a well-defined WM, but for studies looking into detail of formation rates and processes is often looked at as different WMs (e.g., Rhein et al., 2011). In the Mediterranean Sea, this is particularly important as WMs tend to change properties due to variability in ventilation (e.g., Li and Tanhua, 2020), and to climate change induced trends (Box 4.1).

Box 4.1 Double diffusion in the Mediterranean Sea

A particular mixing mechanism, which is common in certain oceanic regions, including some parts of the Mediterranean Sea (Ferron et al., 2021), is the so-called double diffusion. This arises when the overall density stratification of the water column is statically stable, but the contribution of either temperature or salinity is toward instability. There are two distinct double diffusion regimes: the salt-finger regime is characterized by a destabilizing salinity stratification (saltier and warmer water over fresher and cooler water), and the diffusive-convective regime is characterized by destabilizing temperature stratification (fresher and cooler water over saltier and warmer water). The typical WM distribution in the Mediterranean is prone to the salt-finger regime, which occurs between the halocline-thermocline connecting the IW at about 400 m depth with the WMDW below 1500 m depth (Bryden et al., 2014). In this halocline-thermocline salt finger, mixing processes are thought to be active and produce thermohaline staircases with layers of order 50−100 m thickness containing nearly constant properties separated by sharp steps of order 5−10 m thickness with jumps in properties between the layers (Fig. 4.1.1). The release of potential energy stored in the stratification of the unstable component drives the double-diffusive mixing, resulting in a countergradient buoyancy flux that restratifies the water column. In the Mediterranean, the Tyrrhenian Sea is the most susceptible basin to saltfenger occurrences (Meccia et al., 2016), where staircases observations have been reported since the 1970s (Johannessen and Lee, 1974; Molcard and Tait, 1977; Zodiatis and Gasparini, 1996; Durante et al., 2019).

Box 4.1 Double diffusion in the Mediterranean Sea—cont'd

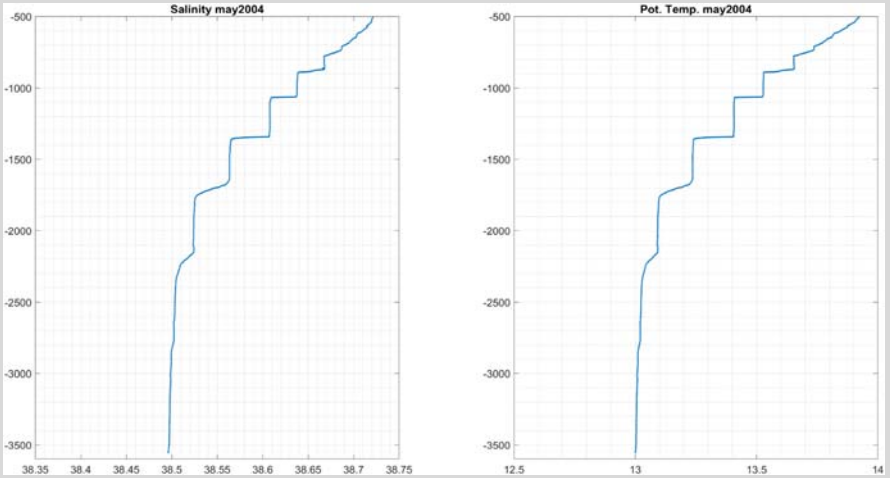

FIGURE 4.1.1

Profiles of salinity and potential temperature below 500 dbar in the southern Tyrrhenian Sea.

Data from an Italian cruise in 2004 on RV Urania.

4.2.3 Water mass properties and distribution in the Mediterranean Sea

The expeditions of the Danish oceanographic vessel Thor in 1908 and 1910, and the pioneering work by Nielsen (1912) can be considered as the starting point for the modern oceanography of the Mediterranean Sea. This work and those that followed along the 20th century until the beginning of the 1990s considered that the Mediterranean Sea was in an equilibrium state forced by the net evaporation and the net heat loss to the atmosphere through the sea surface. As depicted in Figs 4.11 and 4.12, the AW spreads through the basin and is modified: in the EMED it is transformed into salty and warm Intermediate Water (IW), called Levantine Intermediate Water (LIW) or Cretan Intermediate Water (CIW), depending on the specific formation location (in the area of the Rhodes Gyre in the Levantine basin, or in the Cretan Sea, see Schroeder et al., 2017). Both WMs, AW and IW, are involved in the formation of deep water (DW), specifically of Western Mediterranean Deep Water (WMDW) in the north-western part of the basin (offshore the Gulf of Lion), and the Eastern Mediterranean Deep Water (EMDW) in the Adriatic Sea (Adriatic Deep Water, AdDW) and/or in the Aegean Sea (Aegean Deep Water, AeDW). For more details on these water formation processes, the reader is referred to Chapter 7. Here we will focus on the main WMs, although it is noteworthy that there is a number of other local WMs, at surface, intermediate and deep layers (Chapter 7).

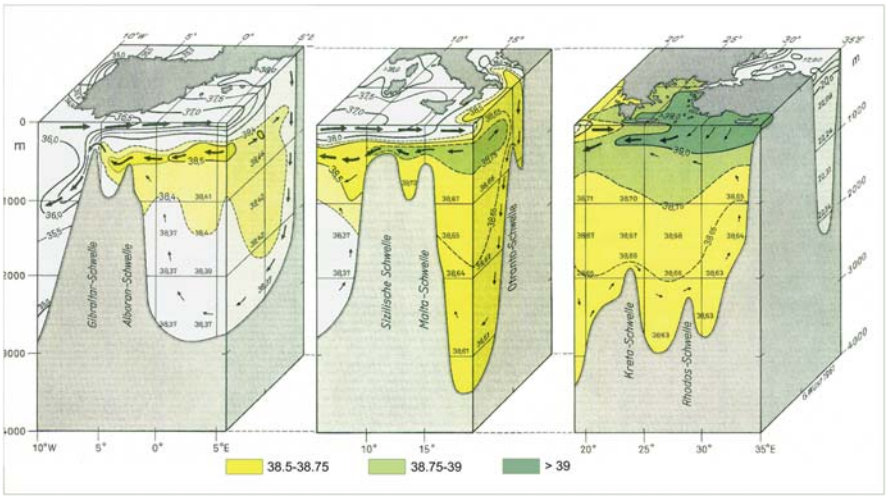

FIGURE 4.11

Schematic block diagram of vertical circulation and distribution of salinity in the Mediterranean Sea during winter.

Adaptation from Wüst, G., 1961. On the vertical circulation of the Mediterranean Sea. J. Geophys. Res. 66 (10), 3261–3271.

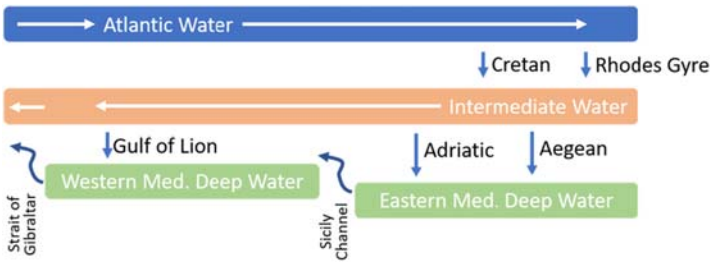

FIGURE 4.12

Schematic of overturning circulation (surface, intermediate, and deep layers); *curved arrows* indicate that only the lighter part of the layer can flow over the sill.

Modified from Talley, L.D., Pickard, G.L., Emery, W.J., Swift, J.H., 2011. Chapter S8 - gravity waves, tides, and coastal oceanography: Supplementary materials. In: Talley, L.D., Pickard, G.L., Emery, W.J., Swift, J.H. (Eds.), Descriptive Physical Oceanography, sixth ed., Academic Press, 1–31.

The high temperatures and salinities of the deep water in this semienclosed sea are surpassed only in the Red Sea. Salinity ranges from 36.1 in entering AW, to 39.1 at the surface in the EMED, while bottom temperatures may are higher than 12.5°C, even as deep as 4000 m (Wüst, 1961, see also Fig. 4.11) and have even become warmer over the past decades (see Chapter 9). Due to the high salinity, the density of bottom water can exceed $\sigma_\theta = 29.25$ kg m^{-3}. These values diverge

considerably from those that can be found at the same depth in the North Atlantic, where at 4000 m the typical values are 2.4°C, 34.9 and 29.25 kg m^{-3}, for temperature, salinity and density respectively (Talley et al., 2011). Oceanographic investigations starting from the beginning of the 90s began to reveal that the ocean is not in a steady state at all, and that its properties and circulation features are subject to marked variabilities across multiple scales (see Chapter 8 about mesoscale variability). However the aim of this subchapter is to give the reader a flavor of the bulk distribution, using average or climatological values of the WM tracers, while the changes that have been observed in the properties of MW masses are discussed in Chapter 9.

To start a concise description of the WMs that are present in the Mediterranean Sea and how they are distributed, we will introduce each one in terms of its peculiar thermohaline characteristics and in terms of the oceanic processes that lead to its formation.

In terms of vertical structure, as can be seen in Fig. 4.13, at midlatitudes the water column is generally divided into three major zones: (1) the mixed layer (ML), (2) the thermocline (and halocline), and (3) the abyssal layer. In general near the surface, the water properties are very well mixed (especially during winter, when its depth may reach 100−150 m or much more in the case of open ocean deep convection, see Chapter 7), because of wind and buoyancy loss. The layer where the properties are homogenized in the vertical is thus called ML. The layer restratifies and becomes less thick by the action of warming (and to a lesser extent by precipitation), and in the absence of wind (usually in summer, when its depth is a small as 1−2 m). Below

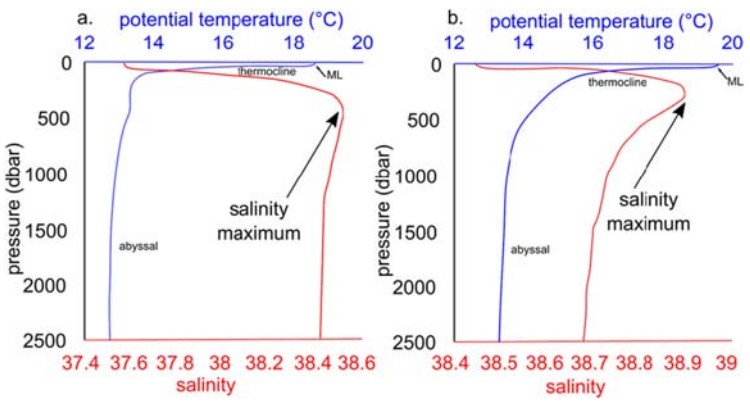

FIGURE 4.13

Climatological potential temperature and salinity profiles for (A) the WMED and (B) the EMED. The minimum salinity is at the sea surface and the maximum salinity corresponds to the core of the LIW.

Redrawn from Garcia-Martinez, M. C., Vargas-Yáñez, M., Moya, F., Zunino P., Bautista, B., 2018. The effects of climate change and rivers Damming in the Mediterranean Sea during the Twentieth century. Res. J. Environ. Sci. 8, https://dx.doi.org/10.19080/IJESNR.2018.08.555741.

this layer, temperature begins to decrease at a very high rate with depth, and this strong vertical gradient defines the zone called thermocline (and/or pycnocline and halocline, depending on the region). There are regions in the Mediterranean Sea, where the vertical profiles of temperature and salinity assume peculiar shapes, with well evident staircases. These are due to a particular mixing regime, called double diffusion, which is described more in detail in Box 4.1.

However, for the scope of this chapter, in the following we will rather describe the vertical structure of the sea by referring to the three main WMs, that are found in the Mediterranean Sea, that is, the AW, which occupies the ML and the thermocline, the IW and the DW, which both occupy the abyssal layer (below the thermocline). These are described in detail hereafter.

4.2.3.1 Atlantic water

The core of the AW can be traced, in the whole Mediterranean Sea, as a near-surface salinity minimum (its temperature mainly depends on the season). Very schematically, after its entrance through the Strait of Gibraltar, the AW flow follows the North-African coast and when it reaches the Sardinia Channel it splits into two main branches: (i) one circulates cyclonically through the Tyrrhenian Sea, exits it and eventually continues along the northern shores of the WMED (where it is known as the Northern Current), and (ii) one enters the EMED crossing the Sicily Channel, and then continues eastward along a tortuous path, characterized by a variable number of mesoscale eddies (see also Chapter 8).

During its journey across the basin, AW is continuously modified, due to air-sea interactions (e.g., evaporation) and its mixing with other WMs. This is well evident when plotting the TS diagram of the surface layer at CTD stations that are located along an east-west transect (Tanhua et al., 2013b). In Fig. 4.14A the data within the pressure range 20−250 dbar is plotted, and longitude is color-coded, to put the gradual warming and salinification of the AW along a west-east gradient into evidence. The temperature and salinity ranges vary from 13 to 17°C and 36.4−38.2, respectively, in the WMED (blueish data points) to 15−18°C and 38.5−39.1 in the EMED (yellow-reddish data points).

These modifications eventually lead to its transformation into a very warm and salty surface water (the Levantine Surface Water, LSW) in the easternmost parts of the basin. The LSW is then directly involved in the formation of the LIW/CIW.

These along-path changes are also very evident in the horizontal maps of surface characteristics. The basin-wide distribution of temperature and salinity at the surface is shown in Fig. 4.15A and B, respectively. The climatological Sea Surface Temperature (SST) shows curves of constant temperature (isotherms) moving roughly from north-west (15−16°C) to south-east (23−24°C). The coldest patches correspond to the dense water formation areas (Gulf of Lion, North-Adriatic, Aegean, see Chapter 7). The climatological Sea Surface Salinity (SSS) shows the influence of the relatively fresh AW inflowing through the Strait of Gibraltar, as well as of the major rivers (Po, Rhone and Nile) and of the Dardanelles (the connection with the Black Sea). The regions with the highest net evaporation are clearly located in the

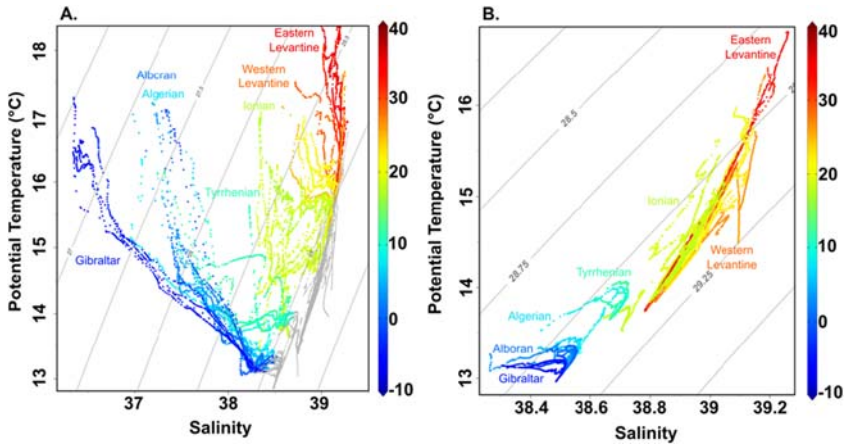

FIGURE 4.14

TS diagrams of the layers (A) 20–250 dbar (deeper data in light gray) and (B) 250–600 dbar. Longitude is color coded (data along the transect shown in Fig. 4.17, collected in spring 2011, see Tanhua et al., 2013a).

south-east. In general, the patterns of both SST and SSS reflect the cyclonic circulation that dominates at the basin scale.

4.2.3.2 Intermediate water

The distinctive characteristic of the IW, throughout the whole Mediterranean, is a subsurface salinity maximum (to which a relative temperature maximum is generally associated) in an average depth range of 250–600 m (Figs. 4.11 and 4.13). At its formation area(s), i.e., the Levantine and the Cretan seas, the salinity of LIW/CIW is the highest (>39.1), with a θ of about 15–16°C. These extremes then slowly erodes while the WM moves westward, and when it crosses the Sicily Channel the core of IW is significantly colder (<14.5°C), fresher (38.8) and slightly less dense. Part of the IW return flow, instead of crossing directly the Channel, is diverted into the Cretan Sea and the Adriatic Sea, where it may take part in the formation of AeDW or AdDW, respectively (see Chapter 7). When the IW enters the WMED, bathymetric constraints force it into the Tyrrhenian Sea, where it follows a cyclonic path, until it exits to the south (across the Sardinia Channel) or to the north (across the Corsica Channel). In the northern WMED, IW takes part in the formation of WMDW. Eventually IW forms the bulk of the Mediterranean Outflow Water across the Strait of Gibraltar.

In the same manner as AW, also the erosion of IW properties along its journey across the basin can be highlighted with a TS diagram (within the pressure range 250–600 dbar) where longitude is color-coded (Fig. 4.14B), to put the gradual cooling and freshening of the IW along an east-west gradient into evidence. The temperature and salinity ranges vary from 13.8 to 16.8°C and 38.8–39.3, respectively, in

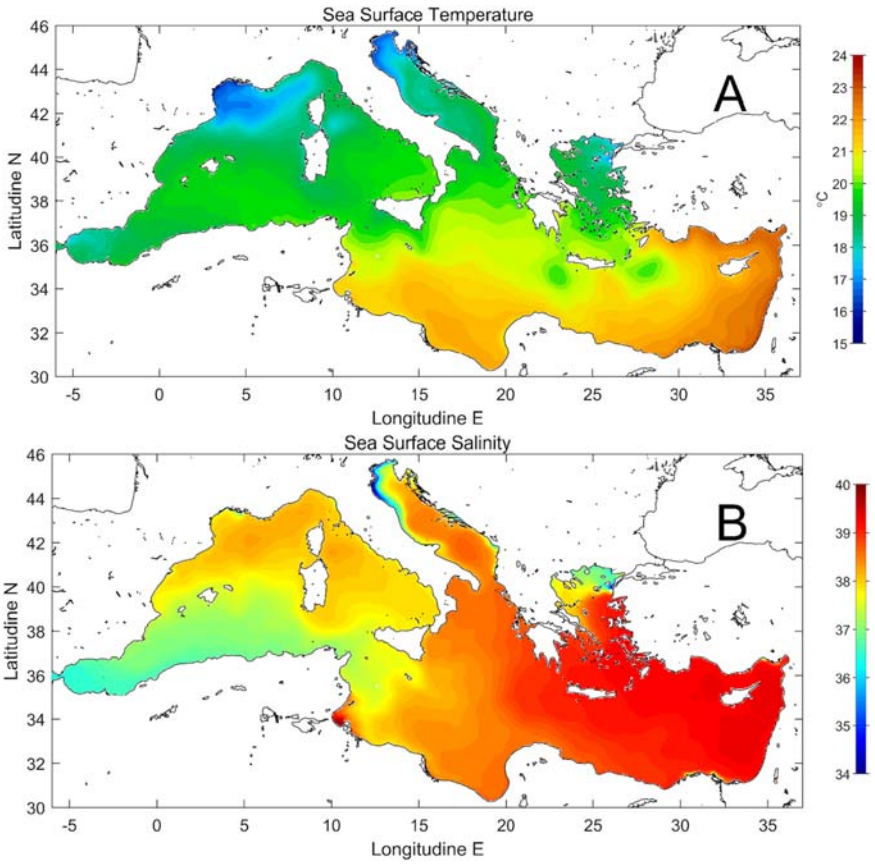

FIGURE 4.15

Distribution at the surface of the Mediterranean Sea of (A) temperature and (B) salinity (average fields of the period 1987–2021 CMEMS reanalysis, product MEDSEA_MULTIYEAR_PHY_006_004).

the EMED (yellow-reddish data points) to 13–14°C and 38.2–38.7 in the WMED (blueish data points).

These along-path changes are also very evident in the horizontal maps of the characteristics at the IW core depth. The basin-wide distribution of temperature and salinity at the depth of the salinity maximum (computed excluding the first 100 m) is shown in Fig. 4.16A and B, respectively. The temperature distribution shows the isotherms moving roughly from east (17–18°C) to west (13–14°C). The warmest patches correspond to the IW formation areas (Cretan Sea and in the proximity of the Rhodes Gyre, see Chapter 7). The salinity distribution shows a similar patter, and goes from >39.2 in the IW formation areas to <38.5 in the

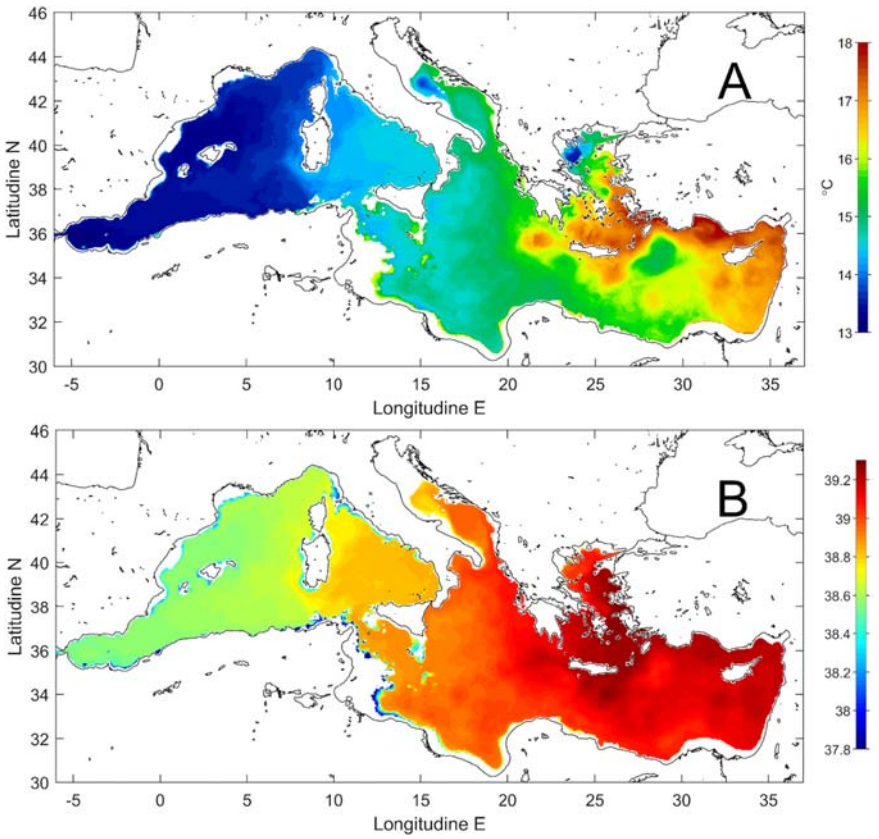

FIGURE 4.16

Distribution at the depth of the salinity maximum (the first 100 m were excluded) of (A) potential temperature and (B) salinity (average fields of the year 2019, CMEMS reanalysis, product MEDSEA_MULTIYEAR_PHY_006_004).

westernmost parts of the basin. Also here, the patterns of Fig. 4.16 reflect the cyclonic circulation that dominates at the basin scale.

4.2.3.3 Deep water

The DW is obviously the densest WM, with temperature and salinity slightly decreasing toward the bottom (see Figs. 4.11 and 4.13). As already mentioned and as it will be explained in more detail in the dedicated Chapter 7, the Mediterranean DWs originate at different locations along the northern shores during late winter-early spring (Aegean Sea, Adriatic Sea, Gulf of Lion), due to the presence of cold and dry winter winds (Bora, Mistral). The MEDOC Group (1970) did the first measurements ever of deep convection in 1969 in the Gulf of Lion. Marshall and Schott (1999) described the WMDW properties as 12.8°C, 38.45, and

29.1 kg m^{-3}, respectively, for potential temperature, salinity and potential density. Among others, Gacic et al. (2001) described the AdDW properties (13°C, 38.6, 29.24 kg m^{-3}) and Theocharis et al. (1999) those of the AeDW (14.25°C, 39.1 and up to 29.36 kg m^{-3}). These are just bulk values for the reader to get the general picture, but since then, these values have changed over time, as explained in Chapter 9.

As shown in the volumetric TS diagram (Fig. 4.10) the DW occupies a very large volume of the basin, but is represented only by a very narrow range of TS values. This is why it will not be represented here in a similar manner as AW and IW in Figs. 4.14–4.16, since only minor differences would be visible. Instead, to identify common and typical features, as well as the differences in DWs (but also of AW and IW) in the various regions, it is useful to view a zonal cross-section of thermohaline properties along an east-west transect covering the whole basin, from the Levant to Gibraltar (Fig. 4.17). Potential temperature and salinity both decrease downward through the thermocline and halocline into much more uniform, colder and fresher water at depth. The most striking feature is the well evident differences between the WMDW and the EMDW, the latter being much warmer, saltier, and denser. In fact, while AW and IW occupy depth ranges from which they can overflow through the Sicily Channel, the two deep water circulation cells are separated by bathymetric constraints and confined within the WMED and EMED, respectively.

4.3 Other water mass tracers

As explained above, physical oceanographers use mainly temperature and salinity (i.e., density) to trace WM pathways, but a variety of other dissolved matter in seawater can be used for the scope. These properties can have a conservative behavior, which means that below the surface they change only due to mixing (such as some transient tracers), or a nonconservative behavior, which means that they change also because of biochemical processes (such as dissolved oxygen, dissolved inorganic nutrients).

In particular, the concentration of various tracers and biogeochemical variables has proven to be useful to define WMs. It is beneficial to add variables to the WM analysis (such as OMP, see above), as more WMs have to be resolved simultaneously, i.e., where salinity and temperature alone is not sufficient to solve the system of linear equations. Although a range of biogeochemical tracers can be used in this context, normally one would choose variables that are commonly measured during oceanographic campaigns, in order to have a large enough database to work with. However, there are chemicals that are particularly good at characterizing particular WMs, so there are certainly possibilities to target those for specific studies. Ideally a chemical tracer for WM definition should be feasible to measure (i.e., a good database of accurate measurements) and be conservative. However, most biogeochemical WM tracers, that are routinely measured, tend to be nonconservative.

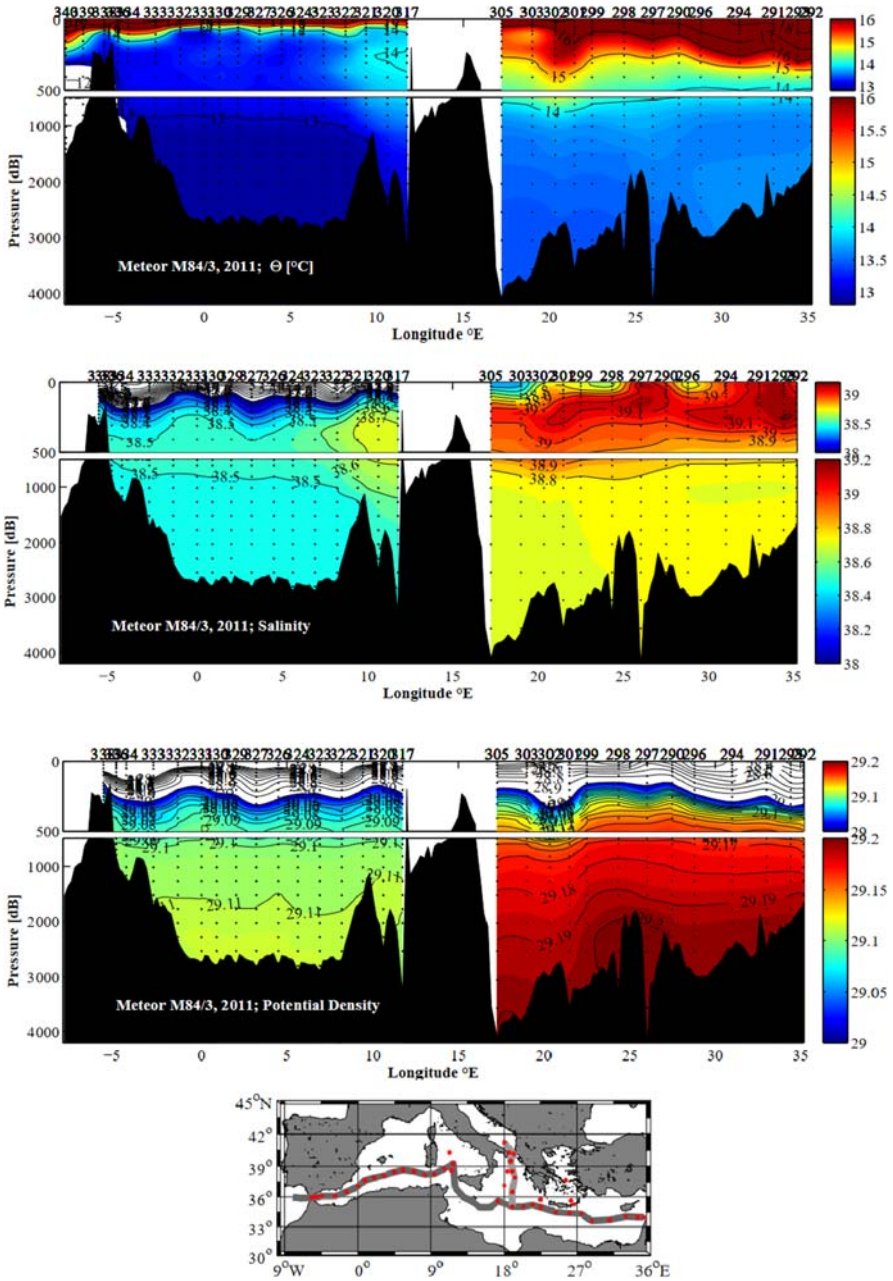

FIGURE 4.17

Sections of potential temperature, salinity and potential density in the Mediterranean Sea from the Meteor cruise M84/3 in April of 2011 along the section highlighted in gray in the map. To be compared with Fig. 4.11.

Redrawn from Tanhua, T., Hainbucher, D., Schroeder, K., Cardin, V., Álvarez, M., Civitarese, G., 2013b. The Mediterranean Sea system: a review and an introduction to the special issue. Ocean Sci. 9, 789–803.

The most commonly used biogeochemical tracers for WM studies are dissolved inorganic nutrients (nitrate, phosphate and silicate) and dissolved oxygen. Although relatively easy to measure, these are all nonconservative in the marine environment, as organic matter is remineralized in the ocean interior, oxygen is consumed and nutrients are released. Furthermore, in low oxygen environments, nitrate can be removed from the water by reduction (in the Mediterranean Sea this is mostly happening in abyssal salt-brines). The nonconservative behavior can be compensated for the effect of remineralization by using the Redfield ratios (Redfield, 1963). The globally averaged ratio of P:N: O_2:C_{org} is usually set to 1:16:170:117 (Anderson and Sarmiento, 1994), although it is well known that the N:P ratio in the Mediterranean is different (see Chapter 11), and appears to change with time as well (Moon et al., 2016). To do so, the variables NO ($NO = 9*NO_3 + O_2$) and PO ($PO = 170*PO_4 + O_2$) are constructed, so that increasing nutrient concentration and decreasing oxygen concentration are compensated for, and thereby creating quasi-conservative variables.

Applying WM analysis to more than 3 WMs, using more than two variables (i.e., in addition to S and θ) creates a multidimensional problem that is more difficult to illustrate in a 2D figure. The multivariate concept behind the OMP Analysis (Tomczak, 1981), or its variations, is therefore commonly used. For instance, in a study of dissolved Barium dynamics, Jullion et al. (2017) used four variables (S, θ, NO, and PO) to distinguish four WMs in the EMED and the WMED, using a variation called Parametric OMP. OMP analysis can be applied with fewer variables too. In a study by Hainbucher et al. (2014) the three variables available for the continuous measurements from a CTD probe (S, θ, O_2) were used to distinguish between WMs with a high vertical resolution that is normally not possible to achieve for variables where water samples are needed (and taken only at discrete depths).

Other tracers of WMs exist, for instance, trace metals, isotopes of rare earth elements, and transient tracers or other anthropogenic compounds. These can sometimes be powerful WM tracers offering a detailed view of distribution and pathways of WMs, in particular if there is a well-defined source of the compound. One example of WM tracer is the radioactive isotopes ^{236}U and ^{129}I, that for the Mediterranean have the main source from the Rhone river and the Marcoule reprocessing plant, although there are also contributions from other sources, such as "global fallout" from nuclear bomb testing in the 1960s and from the Chernobyl accident, that may complicate the data interpretation (Castrillejo et al., 2017).

The WM context is useful for biogeochemical and biological studies as it offers a concept in which biogeochemical and/or biological transformation can be studied and separated from the effect of ocean circulation and mixing. For instance, when Jullion et al. (2017) used a WM framework on dissolved Barium data, they found how underwater ridges and mountains affect its concentration by dissolving particulate biologic barium. Another example is a study by Rusiecka et al. (2018), in which a WM framework was used to identify Mediterranean Overflow Water as a source of anthropogenic lead in the Celtic Sea, where the transport times suggest the source is from the previous century prior to restrictions in leaded gasoline.

Transient tracers such as CFCs provide information on ventilation time-scales, that is, the time since the water was in contact with the atmosphere, and can as such be used to identify "old" or "recently ventilated" waters (the age of a WM defined as the last time it was in contact with the atmosphere). For instance, deep water formation is a transient phenomenon, where newly formed deep water carries a signal of high transient tracer concentration. This can be seen in Fig. 4.18: the new deep water formed in the Adriatic Sea carries a high CFC-12 signal, that clearly distinguishes it from the old EMDW, even though the S-θ signature is similar. Repeat measurements of transient tracers over time allows for the possibility to identify temporal changes in ventilation, a process that is relevant for the Mediterranean Sea where deep water formation is known to be variable over time (e.g., Li and Tanhua, 2020, see also Chapters 7 and 9). The draw-back of transient tracers is that they change over time by definition, so that it is difficult to compare data from different years, but they are powerful tracers to resolve WM distribution for one cruise, or several campaigns during a limited time period (e.g., Tanhua et al., 2005).

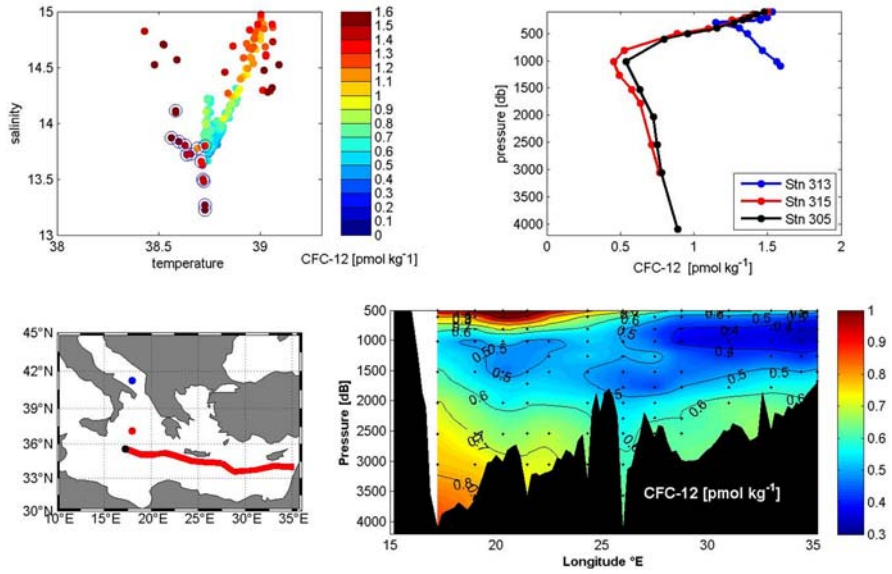

FIGURE 4.18

Using CFC-12 as a water mass tracer: Upper left panel shows a T/S diagram for the eastern Mediterranean from cruise M84/3 in 2011, the CFC-12 concentrations are color coded, dots with a circle are deep water samples from the Adriatic Sea. Upper right panel shows CFC-12 profiles for three stations in the Adriatic and Ionian Seas; color code for position in the map (lower left panel). The section (lower right panel, red line on the map) of deep CFC-12 clearly show the Adriatic Deep Water in the deep western part of the EMED.

Additional resources

- https://www.geotraces.org/.
- https://www.ncei.noaa.gov/products/world-ocean-atlas.

References

Anderson, L.A., Sarmiento, J.L., 1994. Redfield ratios of remineralization determined by nutrient data analysis. Global Biogeochem. Cycles 8 (1), 65−80.

Armi, L., Farmer, D., 1985. The internal hydraulics of the Strait of Gibraltar and associated sill and narrows. Oceanol. Acta 8, 37−46.

Armi, L., Farmer, D., 1986. Maximal two-layer exchange through a contraction with net barotropic flow. J. Fluid Mech. 164, 27−51.

Bryden, H.L., Stommel, H., 1984. Limiting processes that determine basic features of the circulation in the Mediterranean Sea. Oceanol. Acta 7, 289−296.

Bryden, H.L., Kinder, T.H., 1991. Steady two-layer exchange through the Strait of Gibraltar. Deep-Sea Res. 38S, S445−S463.

Bryden, H.L., Candela, J., Kinder, T.H., 1994. Exchange through the Strait of Gibraltar. Prog. Oceanogr. 33 (3), 201−248.

Bryden, H.L., Schroeder, K., Sparnocchia, S., Borghini, M., Vetrano, A., 2014. Thermohaline staircases in the western Mediterranean Sea. J. Mar. Res. 73 (1), 1−18.

Carracedo, L.I., Pardo, P.C., Flecha, S., Pérez, F.F., 2016. On the Mediterranean water composition. J. Phys. Oceanogr. 46 (4), 1339−1358.

Castrillejo, M., Casacuberta, N., Christl, M., Garcia-Orellana, J., Vockenhuber, C., Synal, H.A., Masqué, P., 2017. Anthropogenic ^{236}U and ^{129}I in the Mediterranean Sea: first comprehensive distribution and constrain of their sources. Sci. Total Environ. 593−594, 745−759.

Durante, S., Schroeder, K., Mazzei, L., Pierini, S., Borghini, M., Sparnocchia, S., 2019. Permanent thermohaline staircases in the Tyrrhenian Sea. Geophys. Res. Lett. 46, 1562−1570.

Emery, W.J., 2003. Ocean circulation - water types and water masses. In: Holton, J.R. (Ed.), Encyclopedia of Atmospheric Sciences. Academic Press, pp. 1556−1567.

Farmer, D., Armi, L., 1986. Maximal two-layer exchange over a sill and through the combination of a sill and contraction with barotropic flow. J. Fluid Mech. 164, 53−76.

Farmer, D., Armi, L., 1988. The flow of Mediterranean water through the Strait of Gibraltar. Prog. Oceanogr. 21 (1), 1−103.

Ferron, B., Bouruet-Aubertot, P., Schroeder, K., Bryden, H.L., Cuypers, Y., Borghini, M., 2021. Contribution of thermohaline staircases to deep water mass modifications in the western Mediterranean Sea from microstructure observations. Front. Mar. Sci. 8, 664509.

Font, J., 1987. The path of the Levantine intermediate water to the Alboran sea. Deep Sea Res. A. Oceanogr. Res. Papers 34 (10), 1745−1755.

Gačić, M., Lascaratos, A., Manca, B.B., Mantziafou, A., 2001. Adriatic deep water and interaction with the eastern Mediterranean Sea. In: Cushman-Roisin, B., Gačić, M., Poulain, P.M., Artegiani, A. (Eds.), Physical Oceanography of the Adriatic Sea. Springer, Dordrecht.

García Lafuente, J., Vargas, J.M., Plaza, F., Sarhan, T., Candela, J., Bascheck, B., 2000. Tide at the eastern section of the Strait of Gibraltar. J. Geophys. Res. Oceans 105 (C6), 14197−14213.

García-Lafuente, J., Sánchez-Román, A., Díaz del Río, G., Sannino, G., Sánchez-Garrido, J.C., 2007. Recent observations of the seasonal variability of the Mediterranean outflow in the Strait of Gibraltar. J. Geophys. Res. 112, C10005.

García Lafuente, J., Sammartino, S., Huertas, E.I., Flecha, S., Sánchez-Leal, R.F., Naranjo, C., Nadal, I., Bellanco, M.J., 2021. Hotter and weaker Mediterranean outflow as a response to basin-wide alterations. Front. Mar. Sci. 8, 613444.

Garcia-Martinez, M.C., Vargas-Yáñez, M., Moya, F., Zunino, P., Bautista, B., 2018. The effects of climate change and rivers damming in the Mediterranean Sea during the twentieth century. Res. J. Environ. Sci. 8. https://doi.org/10.19080/IJESNR.2018.08.555741.

Hainbucher, D., Rubino, A., Cardin, V., Tanhua, T., Schroeder, K., Bensi, M., 2014. Hydrographic situation during cruise M84/3 and P414 (spring 2011) in the Mediterranean Sea. Ocean Sci. 10, 669−682.

Helland-Hansen, B., 1918. Nogen hydrografisk metoder. Forhandelingen ved de skandinaviske Naturforskeres 16 de mote 357−359.

Iselin, C.O.'D., 1939. The influence of vertical and lateral turbulence on the characteristics of the waters at middepths. Trans. Am. Geophys. Union 20, 414−417.

Johannessen, O.M., Lee, O.S., 1974. A deep stepped thermo-haline structure in the Mediterranean. Deep Sea Res. A21, 629−639.

Jordà, G., Von Schuckmann, K., Josey, S.A., Caniaux, G., García-Lafuente, J., Sammartino, S., Özsoy, E., Polcher, J., Notarstefano, G., Poulain, P.M., Adloff, F., Salat, J., Naranjo, C., Schroeder, K., Chiggiato, J., Sannino, G., Macías, D., 2017. The Mediterranean Sea heat and mass budgets: estimates, uncertainties and perspectives. Prog. Oceanogr. 156, 174−208.

Josey, S.A., 2003. Changes in the heat and freshwater forcing of the eastern Mediterranean and their influence on deep water formation. J. Geophys. Res. 108 (C7), 3237.

Josey, S.A., Somot, S., Tsimplis, M., 2011. Impacts of atmospheric modes of variability on Mediterranean Sea surface heat exchange. J. Geophys. Res. Oceans 116, C02032.

Jullion, L., Jacquet, S.H.M., Tanhua, T., 2017. Untangling biogeochemical processes from the impact of ocean circulation: first insight on the Mediterranean dissolved barium dynamics. Global Biogeochem. Cycles 31, 1256−1270.

Ein hydrographischer Lehrsatz, Hydrogr. Mar. Meteorol., 28 (7), 316−320 (in German; an English translation of this article can be seen in appendix 1 of Burchard et al., 2018) Knudsen, M., 1900. The Knudsen theorem and the total exchange flow analysis framework applied to the Baltic Sea. Prog. Oceanogr. 165.

Kovačević, V., Manca, B.B., Ursella, L., Schroeder, K., Cozzi, S., Burca, M., Mauri, E., Gerin, R., Notarstefano, G., Deponte, D., 2012. Water mass properties and dynamic conditions of the Eastern Mediterranean in June 2007. Prog. Oceanogr. 104, 59−79.

Li, P., Tanhua, T., 2020. Recent changes in deep ventilation of the Mediterranean Sea: evidence from long-term transient tracer observations. Front. Mar. Sci. 7, 10−3389.

Liu, M., Tanhua, T., 2021. Water masses in the Atlantic Ocean: characteristics and distributions. Ocean Sci. 17, 463−486.

Macdonald, A.M., Candela, J., Bryden, H.L., 1994. An estimate of the net heat transport through the Strait of Gibraltar. In: LaViolette, P. (Ed.), Seasonal and Interannual Variability of the Western Mediterranean Sea, vol. 46. Coastal and Estuarine Studies, pp. 13−32.

Mackas, D.L., Denman, K.L., Bennett, A.F., 1987. Least-square multiple tracer analysis of water mass composition. J. Geophys. Res. 92, 2907–2918.

Mamayev, O.I., 1975. Temperature-Salinity Analysis of World Ocean Waters, first ed., vol. 11. Elsevier Science, p. 373.

Marshall, J., Schott, F., 1999. Open-ocean convection: observations, theory, and models. Rev. Geophys. 37 (1), 1–64.

Meccia, V.L., Simoncelli, S., Sparnocchia, S., 2016. Decadal variability of the Turner angle in the Mediterranean Sea and its implications for double diffusion. Deep-Sea Res. Part I 114, 64–77.

MEDOC Group, 1970. Observation of the formation of deep water in the Mediterranean Sea, 1969. Nature 227 (5262), 1037–1040.

Millot, C., 1987. The circulation of the levantine intermediate water in the Algerian basin. J. Geophys. Res. 92 (C8), 8265–8276.

Molcard, R., Tait, R.I., 1977. The steady state of the step structure in the Tyrrhenian Sea. In: Angel, M.V. (Ed.), A Voyage of Discovery. Pergamon Press, Amsterdam, pp. 221–233.

Moon, J.-Y., Lee, K., Tanhua, T., Kress, N., Kim, I.-N., 2016. Temporal nutrient dynamics in the Mediterranean Sea in response to anthropogenic inputs. Geophys. Res. Lett. 2016GL068788.

Nielsen, J.N., 1912. Hydrography of the Mediterranean and Adjacent Waters. Report on the Danish Oceanographical Expeditions 1908-1910, 1, pp. 77–191.

Redfield, A.C., Ketchum, B.H., Richards, F.A., 1963. The influence of organism on the composition of sea water. In: Hill, M.N. (Ed.), The Sea, vol. 2. Interscience, NewYork, pp. 26–77.

Rhein, M., Kieke, D., Hüttl-Kabus, S., Roessler, A., Mertens, C., Meissner, R., Klein, B., Böning, C.W., Yashayaev, I., 2011. Deep water formation, the subpolar gyre, and the meridional overturning circulation in the subpolar North Atlantic. Deep Sea Res. Part II Top. Stud. Oceanogr. 58, 1819–1832.

Rusiecka, D., Gledhill, M., Milne, A., Achterberg, E.P., Annett, A.L., Atkinson, S., Birchill, A., Karstensen, J., Lohan, M., Mariez, C., Middag, R., Rolison, J.M., Tanhua, T., Ussher, S., Connelly, D., 2018. Anthropogenic signatures of lead in the Northeast Atlantic. Geophys. Res. Lett. 45, 2734–2743.

Sammartino, S., García Lafuente, J., Naranjo, C., Sánchez-Garrido, J.C., Sánchez-Leal, R.F., Sánchez-Roman, A., 2015. Ten years of marine current measurements in Espartel Sill, Strait of Gibraltar. J. Geophys. Res. Oceans 120, 6309–6328.

Sánchez-Garrido, J.C., García Lafuente, J., Criado Aldeanueva, F., Baquerizo, A., Sannino, G., 2008. Time-spatial variability observed in velocity of propagation of the internal bore in the Strait of Gibraltar. J. Geophys. Res. 113, C07034.

Sánchez-Garrido, J.C., Sannino, G., Liberti, L., García Lafuente, J., Pratt, L., 2011. Numerical modeling of three-dimensional stratified tidal flow over Camarinal Sill, Strait of Gibraltar. J. Geophys. Res. Oceans 116 (C12), C12026.

Sannino, G., Bargagli, A., Artale, V., 2004. Numerical modeling of the semidiurnal tidal exchange through the Strait of Gibraltar. J. Geophys. Res. 109 (C5), C05011.

Schroeder, K., Gasparini, G.P., Tangherlini, M., Astraldi, M., 2006. Deep and intermediate water in the western Mediterranean under the influence of the eastern Mediterranean transient. Geophys. Res. Lett. 33, L21607.

Schroeder, K., Borghini, M., Cerrati, G., Difesca, V., Delfanti, R., Santinelli, C., Gasparini, G.P., 2008. Multiparametric mixing analysis of the deep waters in the Western Mediterranean Sea. Chem. Ecol. 24 (Suppl. 1), 47–56.

Schroeder, K., Josey, S.A., Herrmann, M., Grignon, L., Gasparini, G.P., Bryden, H.L., 2010. Abrupt warming and salting of the Western Mediterranean Deep Water: atmospheric forcings and lateral advection. J. Geophys. Res. 115, C08029.

Schroeder, K., Chiggiato, J., Josey, S.A., Borghini, M., Aracri, S., Sparnocchia, S., 2017. Rapid response to climate change in a marginal sea. Sci. Rep. 7, 4065.

Schroeder, K., Cozzi, S., Belgacem, M., Borghini, M., Cantoni, C., Durante, S., Petrizzo, A., Poiana, A., Chiggiato, J., 2020. Along-path evolution of biogeochemical and carbonate system properties in the intermediate water of the western Mediterranean. Front. Mar. Sci. 7, 375.

Stommel, H., Farmer, H.G., 1953. Control of salinity in an estuary by a transition. J. Mar. Res. 12, 13−20.

Talley, L.D., Pickard, G.L., Emery, W.J., Swift, J.H., 2011. Chapter S8 - Gravity waves, tides, and coastal oceanography: supplementary materials. In: Talley, L.D., Pickard, G.L., Emery, W.J., Swift, J.H. (Eds.), Descriptive Physical Oceanography, sixth ed. Academic Press, pp. 1−31.

Tanhua, T., Olsson, K.A., Jeansson, E., 2005. Formation of Denmark strait overflow water and its hydro-chemical composition. J. Mar. Syst. 57, 264−288.

Tanhua, T., Hainbucher, D., Cardin, V., Álvarez, M., Civitarese, G., McNichol, A.P., Key, R.M., 2013a. Repeat hydrography in the Mediterranean Sea, data from the meteor cruise 84/3 in 2011. Earth Syst. Sci. Data 5, 289−294.

Tanhua, T., Hainbucher, D., Schroeder, K., Cardin, V., Álvarez, M., Civitarese, G., 2013b. The Mediterranean Sea system: a review and an introduction to the special issue. Ocean Sci. 9, 789−803.

Theocharis, A., Balopoulos, E., Kioroglou, S., Kontoyiannis, H., Iona, A., 1999. A synthesis of the circulation and hydrography of the south Aegean Sea and the straits of the Cretan Arc (March 1994−January 1995). Prog. Oceanogr. 44 (4), 469−509.

Tomczak, M., Large, D.G.B., 1989. Optimum multiparameter analysis of mixing in the thermocline of the eastern Indian Ocean. J. Geophys. Res. 94, 16141−16149.

Tomczak, M., 1981. A multi-parameter extension of temperature/salinity diagram techniques for the analysis of non isopycnal mixing. Progr. Oceanogr. 10, 147−171.

Tomczak, M., 1999. Some historical, theoretical and applied aspects of quantitative water mass analysis. J. Mar. Res. 57, 275−303.

Vilibić, I., Orlić, M., 2001. Least-squares tracer analysis of water masses in the South Adriatic (1967−1990). Deep Sea Res. Oceanogr. Res. Pap. 48 (10), 2297−2330.

Wüst, G., 1935. Die Stratosphaere des Atlantischen Ozeans. Wiss. Ergebn. Dr. Atlant. Exped. „Meteor" 1925-1927, gI (Text), 1. Tell, 2. Lfg., Berlin.

Wüst, G., 1961. On the vertical circulation of the Mediterranean Sea. J. Geophys. Res. 66 (10), 3261−3271.

Zodiatis, G., Gasparini, G.P., 1996. Thermohaline staircase in the Tyrrhenian Sea. Deep Sea Res. 43, 655−678.

This page intentionally left blank

CHAPTER

Mediterranean Sea level

5

Marta Marcos[1,2], Guy Wöppelmann[3], Francisco M. Calafat[4], Matteo Vacchi[5], Angel Amores[1]

[1]*Mediterranean Institute for Advanced Studies (IMEDEA, UIB-CSIC), Esporles, Spain;* [2]*Department of Physics, University of the Balearic Islands, Palma, Spain;* [3]*LIENSs, La Rochelle University – CNRS, La Rochelle, France;* [4]*Department of Marine Physics and Ocean Climate, National Oceanography Centre, Liverpool, United Kingdom;* [5]*Dipartimento di Scienze Della Terra, Università di Pisa, Pisa, Italy*

Learning objectives

In this chapter, you will learn:

- The concept of mean sea level
- Which are the driving physical mechanisms underlying mean sea level changes at different temporal scales
- What are the instrumental and proxy measurements of past mean sea level changes with a focus on Mediterranean observations
- By how much and at which rates mean sea level has been rising in the Mediterranean Sea
- What are the future projected mean sea level changes in the Mediterranean Sea during the 21st century, according to climate models and climate scenarios.

5.1 General concepts about sea level

Sea level is the position of the sea surface after being time-averaged to filter out the high-frequency variations due to, for example, wind-waves (Pugh and Woodworth, 2014). The term mean sea level is used to indicate a time-mean value of sea level over a period that is long enough to remove short-term meteorological effects (Gregory et al., 2019). Depending on the averaging period, which should be specified, mean sea level may or may not include tidal oscillations or other longer term signals. This chapter is about the low-frequency variability of mean sea level, including interannual, decadal, and longer time scales. High-frequency sea level changes related to tides, storm surges, and waves are addressed in Chapter 6.

Sea level is an integrated variable that responds to a variety of underlying physical processes, including ocean thermal expansion, ocean density and circulation changes, atmospheric forcing, ground-based ice melting, variations in the hydrological reservoirs and geoid changes due to glacial isostatic adjustment and to

Oceanography of the Mediterranean Sea. https://doi.org/10.1016/B978-0-12-823692-5.00012-1

present-day surface mass redistribution (Fig. 5.1). All these processes act on a wide range of spatial and temporal scales. Thus, disentangling the drivers of mean sea level changes is a challenging task that requires accurate sea level and other ancillary observations as well as a good understanding of the mechanistic principles that shape such changes. Despite the inherently complicated nature of sea level changes, involving a complex interplay between processes and spatiotemporal scales, much of their observed structure can be explained by appealing to basic dynamical concepts. Perhaps the most fundamental of such concepts is the fact that the ocean is almost always and everywhere hydrostatically balanced in the vertical in the sense that gravitational and pressure gradient forces balance one another (only in small-scale systems involving large vertical accelerations may this balance break down). In fact, all climate models make the hydrostatic approximation to the vertical momentum equation. The hydrostatic equation allows us, by integration, to decompose sea level changes into the sum of three contributions, namely changes in ocean bottom pressure, changes in ocean density (also called steric changes), and changes in atmospheric pressure (also called inverse barometer effect). Such decomposition is common practice in sea level research because it turns out that the effect of many drivers is often limited to only one of these three contributions, thus enabling us to relate sea level changes to processes. For example, sea level changes due to geographical mass redistribution, such as that caused by contemporary land-ice melting, primarily reflect changes in ocean bottom pressure. As another example, the thermal expansion caused by ocean heat uptake is a manifestation of density changes, as are sea level changes arising from changes in ocean circulation induced by heat and salt redistribution. The relationship between ocean circulation and sea level is largely a reflection of another basic dynamical concept known as geostrophic balance in which pressure gradient forces associated with sea surface height variations balance Coriolis forces. Indeed, on the time scales relevant to mean sea level, the ocean is not only hydrostatically balanced but is also often close to geostrophic balance in the horizontal.

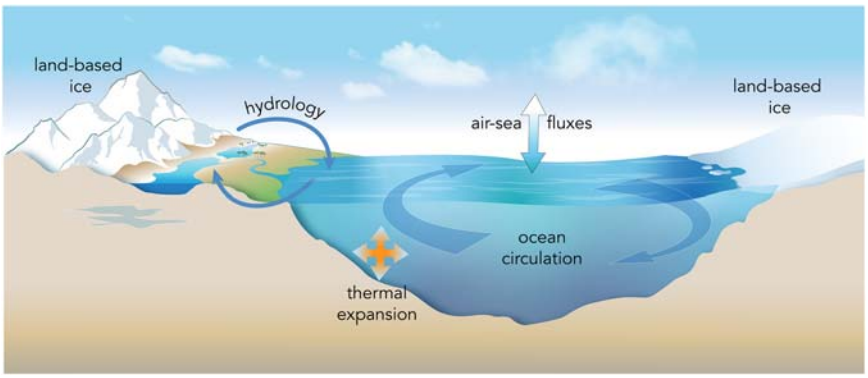

FIGURE 5.1

Physical mechanisms that contribute to mean sea level changes.

Courtesy of Thierry Guyot.

There is compelling evidence from instrumental records that mean sea level has been rising globally in response to increased atmospheric concentrations of greenhouse gases derived from human activities since the early 20th century (Oppenheimer et al., 2019, and references therein). Likewise, proxy-based estimates of sea level changes indicate that these rates are unprecedented in the late Holocene (Kopp et al., 2016). Estimates of rates of global mean sea level rise over the recent decades and since the early 20th century and their contributors are summarized in Oppenheimer et al. (2019). Since 1900, observed mean sea level rise has been estimated at 1.4 ± 0.6 mm yr^{-1} (5-95% confidence level) globally. However, there is significant spatial variability at interannual, decadal, and longer time scales driven by heat and momentum air-sea fluxes and differential thermal expansion (Meyssignac et al., 2017). In the Mediterranean Sea, as in the entire north Atlantic region, patterns of mean sea level change are linked to large-scale climate modes, the dominant of which is the North Atlantic Oscillation. This chapter reviews the indirect, or proxy, sea level observations in the Mediterranean Sea, the instrumental records, including in-situ and satellite-based, and complementary geophysical measurements that are crucial to interpret the observed sea level changes. Regional sea level changes are then described for the periods from the Holocene to the recent decades. Finally, future projections of regional mean sea level for the 21st century are also shown.

5.2 Techniques for measuring sea level

5.2.1 Tide gauges

Tide gauges (also referred to as sea or water level gauges in the literature) are instruments that measure coastal sea level relative to the land on which they are grounded (Fig. 5.2); hence, their recording quantity is termed as relative sea level (Gregory et al., 2019). Because of their relevance for maritime navigation and harbor operation and safety, sea level measurements from tide gauges are among the longest geophysical instrumental records. The first systematic coastal sea level measurements were visual observations on tide poles, that is, a vertical graduated staff attached to the coast from which readings of the height of the sea surface were taken, typically at high and low water levels. This type of sea level record dates back as far as the 17th century (1679 at Brest, France; Wöppelmann et al., 2006). Self-recording tide gauges were developed in the mid-19th century (Palmer, 1831), and consisted in a floating device at the sea surface, connected to an automatic chart recorder through wires and pulleys (Palmer, 1831). The floating component is installed inside a stilling well to guide its vertical displacement and to filter out high-frequency fluctuations due to wind-waves. Floating tide gauges have been widely used until the 1980s (IOC, 1985; Pugh and Woodworth, 2014). Other types of tide gauges, developed, and deployed since the mid-20th century, include pressure gauges and acoustic gauges. Pressure gauges measure the hydrostatic pressure at a given depth below the sea surface and, therefore, must be combined with measurements of atmospheric pressure to isolate the oceanic contribution (provided that water density is known).

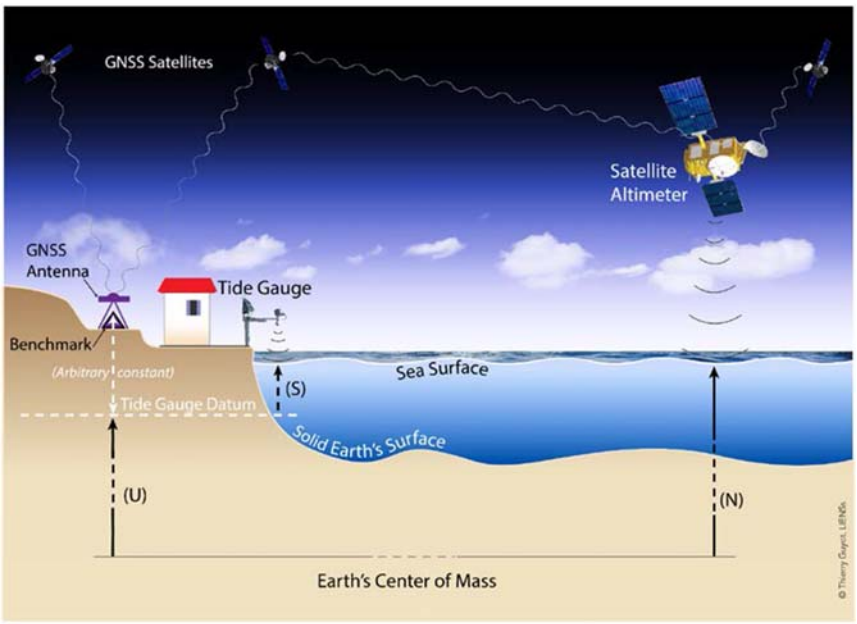

FIGURE 5.2

Basic observational quantities and techniques associated with sea level measurement, either in-situ (tide gauge) or space-borne (satellite altimeter). GPS (the best known of the GNSS techniques) enables the link between tide gauge (S) and satellite altimetry (N) data via the monitoring of the tide gauge datum or benchmark height (U).

Courtesy of Thierry Guyot.

Acoustic gauges are installed a few meters above the sea surface and measure the time of travel of an acoustic signal reflected by the sea surface. More recently, in the early 21st century, radar gauges have become the most extended technology in new and upgraded tide gauge stations. Similarly to the acoustic instruments, radar gauges are placed above the sea surface and measure the time of arrival of the echo of an electromagnetic signal, thus with different propagation characteristics that make these gauges more robust than the acoustic ones. These radar tide gauges are relatively inexpensive instruments, easy to install and to observe sea level changes at very high sampling frequencies. The interested reader is referred to Pugh and Woodworth (2014) and references therein for details on the different types of tide gauges and observations and to the IOC manuals that encompass all mentioned technologies (https://www.psmsl.org/train_and_info/training/manuals/). Finally, it is worth mentioning the current development of promising sea level observational technologies based on Global Navigation Satellite System (GNSS) reflectometry (Larson et al., 2013).

Irrespective of the type of instrument, tide gauges provide data on changes in the height of the sea surface above the solid Earth surface (Fig. 5.2). This is to say that

tide gauge observations reflect a combination of changes in sea surface height and solid Earth surface or vertical land movement. This is highlighted in Fig. 5.2 where the tide gauge datum or reference level is tied to an external benchmark, so-called tide gauge benchmark (TGBM). The knowledge, stability (in terms of vertical ground displacement) and maintenance of the TGBM is essential to build a consistent time series, in spite of sea level gauges that could supersede one another at a given location. The tide gauge datum continuity and stability is thus crucial to describe, interpret, and unravel the source and mechanisms of sea level variations. Consequently, the vertical position of the tide gauge (more precisely of its datum) should be monitored through high-precision leveling and space techniques (Woodworth et al., 2017b). In addition, field work has demonstrated that the manufacture zero changes once the instrument is installed in a specific environment; thus, the best practical procedure is then a field calibration via comparison of two simultaneous measurements which have been connected to each other through leveling (Martin Miguez et al., 2008). Nonreported or unidentified changes in the vertical position of the datum or its TGBM compromise the interpretation of changes in sea levels, for instance due to datum redefinition, offsets, or drifts (Zerbini et al., 2017), that can hardly be characterized a posteriori. Furthermore, GNSS positioning techniques, of which GPS is the best known, enable to express tide gauge data in the same geocentric reference as satellite altimetry by measuring the height of the tide gauge benchmark (Fig. 5.2).

Tide gauges are deployed, maintained, and operated by national and subnational agencies and research institutions. Most frequently, every institution now distributes the observations of their tide gauge network through their own website and data servers with varying formats, quality standards, and requirements. In addition to these individual data providers, a number of international data assembly centers exist that collect, store, control, standardizes, and distribute tide gauge data and metadata. One of the most prominent data centers is the Permanent Service for Mean Sea Level (PSMSL), founded in 1933 and currently hosted by the National Oceanography Center in Liverpool (UK). The PSMSL website (www.psmsl.org) distributes monthly and yearly mean sea level time series from more than 2300 tide gauge stations worldwide for which datum information is available (Holgate et al., 2013). Low-frequency data are calculated by filtering high-frequency measurements to hourly values and these to daily means, prior to computing the monthly and annual averages.

Tide gauge records available in the Mediterranean Sea are mapped in Fig. 5.3A and B. A total of 217 mean sea level records from PSMSL are located here (Fig. 5.3A), with lengths up to 146 years and a median time span of 15 years. Here only tide gauge records are considered for which changes in the vertical datum are documented at the PSMSL data set, the so-called revised local reference (RLR) records. A second global tide gauge data base is the Global Extreme Sea Level Analysis data set (GESLA, Woodworth et al., 2017a) that freely distributes high-frequency (from hourly up to 1 min) tide gauge time series in a unique user-friendly text format through its web site www.gesla.org. 72 tide gauge records are

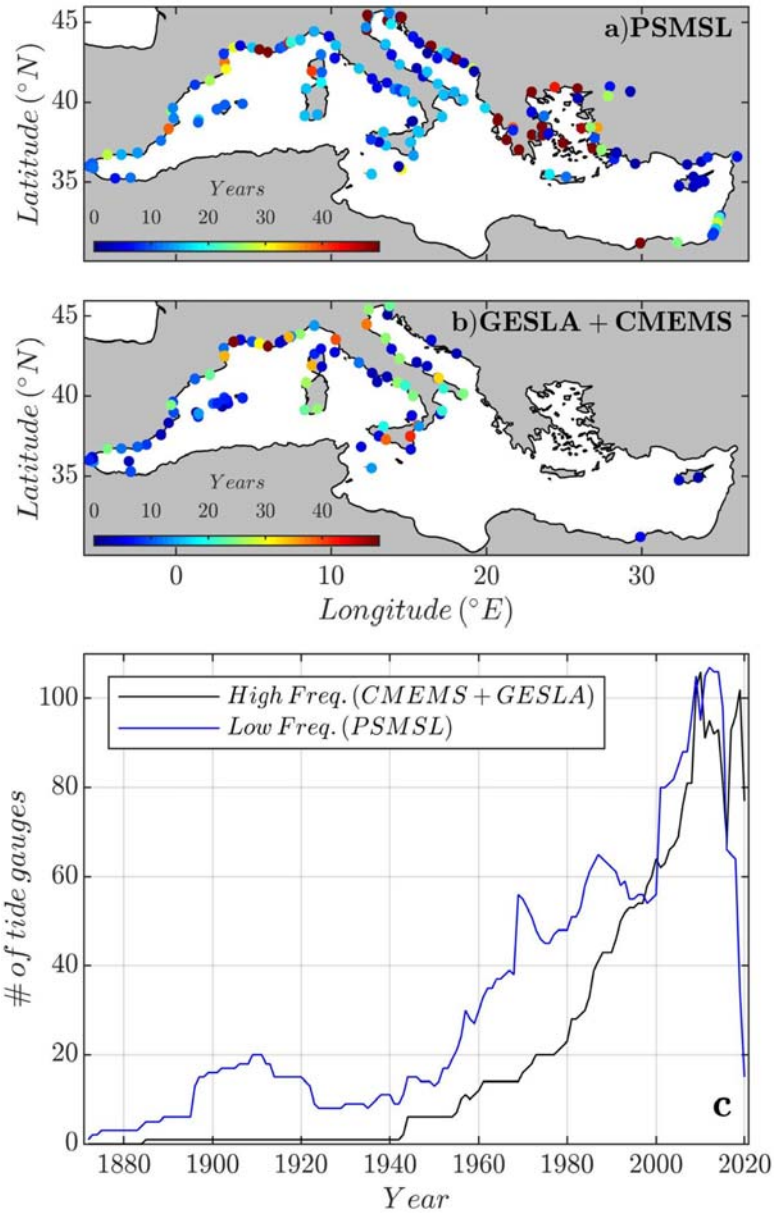

FIGURE 5.3

Location and length of tide gauge records from different data bases: monthly records from PSMSL (A) and high-frequency records from GESLA and CMEMS (B) are mapped. In (C) the number of stations with data every year since the late 19th century for both the low- and the high-frequency data sets is shown.

available in the Mediterranean basin in the current version 2 of GESLA (Fig. 5.3B), spanning periods of operation up to 70 years, with a median length of 21.5 years. At the European scale, the Copernicus Marine Environment Monitoring Service (CMEMS) includes tide gauge records among its comprehensive catalog of oceanographic data. CMEMS provides in situ high-frequency sea level observations from 136 tide gauge stations in the Mediterranean Sea (Fig. 5.3B). Note that many of the tide gauge stations are duplicated in these international data centers, with the major differences being the update frequency and the format. The most recent observations are found in CMEMS data server as it is aimed at providing near real-time information, while both PSMSL and GESLA distribute delayed mode data.

In the Mediterranean, there is a clear geographical bias in coastal sea level monitoring with almost all tide gauge stations located in the northern European coasts. This pattern has long been identified (Marcos et al., 2019) in spite of historical records (e.g., Algiers 1843) yet to be rescued through a data archaeology study. The oldest available sea level records are located in Genova (starting in 1884), Marseille (1849), Porto Corsini (1873), Trieste (1875) and Venice (1872). One more tide gauge record has recently been rescued in Alicante (Marcos et al., 2021), starting in 1870. It completes the subset of Mediterranean tide gauge observations that have data back in the 19th century. This latter time series is one of the latest tide gauge data rescue efforts that have been undertaken aimed at recovering ancient measurements from archives in nonelectronic format. Details on tide gauge data archaeology study in Alicante and Marseille are provided in Box 5.1. The temporal distribution of the

Box 5.1 Sea level data archaeology

The Mediterranean Sea is home of some of the oldest sea level measurements. Coastal observatories such as those in Marseille and Alicante were established in the 19th century with the purpose of defining the datum for the geodetic leveling of mainland France and Spain, respectively (Wöppelmann et al., 2014; Marcos et al., 2021). Likewise, sea level observations in Trieste , Porto Corsini and Venice date back to the late 19th century for geodetic and hydrographic applications (Raicich et al., 2007; 2020; Bruni et al., 2019; Zanchettin et al., 2021). Ancient observations from these historical floating gauges were recorded as either tidal charts (continuous paper bands) or in handwritten logbooks or both. Fig. 5.1.1 displays pictures of some of the historical instruments that were originally located in Alicante (A,B), Marseille (D) and Trieste (C), while panels (E), (F) show scanned copies of original data sets that have been recovered. Data archaeology encompasses the activities undertaken to search for historical sea level records and metadata documentation in archives, transform them into digital form for computer processing, quality control the rescued data sets, analyzes, and tie their datum to modern datum via benchmark information and leveling ties. When successful, long-term changes in sea levels can be appraised. The documentation search in archives and field work to identify benchmarks are activities that are worth the "archaeology" attribute. The outcome of data archaeology exercises is especially relevant for studies of mean sea level changes, tidal variability, extreme events, etc. These exercises are relatively recent. They are motivated by the need for improving our knowledge on climate-related changes. Fortunately, sea level records of more than a century old are now readily available.

The tide gauge of Marseille is a rather iconic case of an ancient, but still well maintained sea level station (Wöppelmann et al., 2014). Working almost continuously since 1885, the structure and the original float tide gauge are still operational, especially its unique mechanical integrator, which enables the direct recording of mean values over a given interval between two readings, whether a day or a week or longer duration.

Continued

Box 5.1 Sea level data archaeology—cont'd

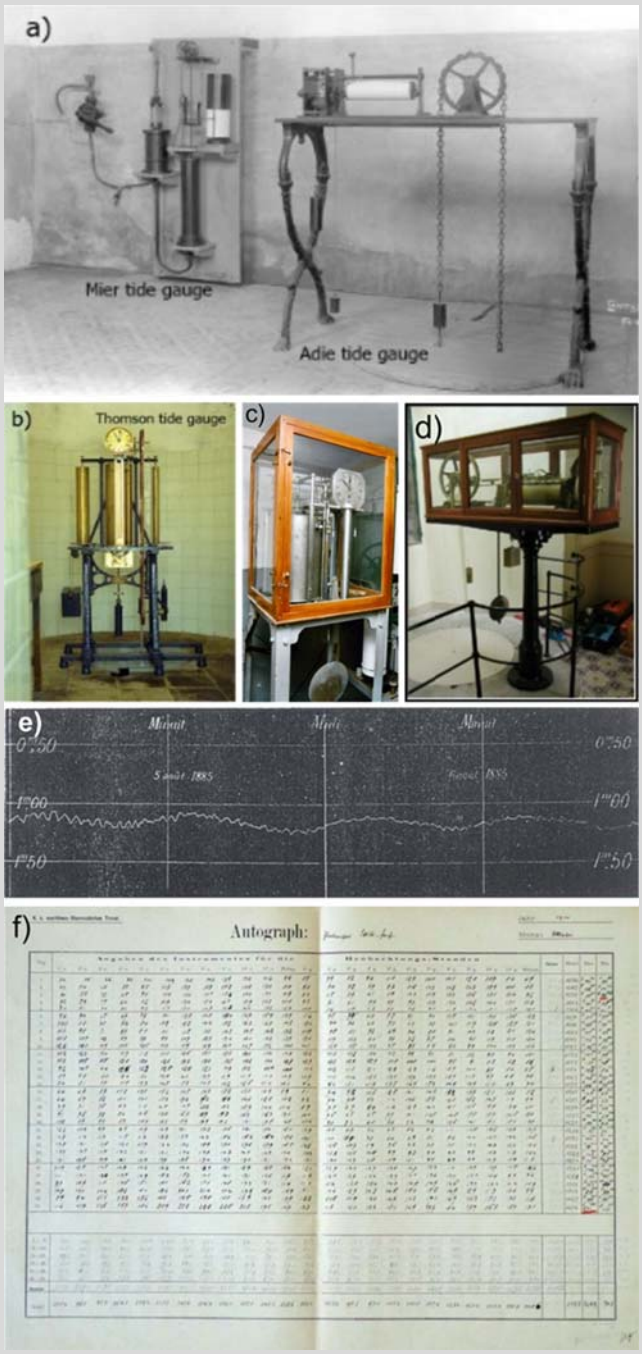

FIGURE 5.1.1

Ancient tide gauges installed in (A, B) Alicante (C) Trieste, (D) the mechanical integrator in Marseille. Scanned copies of (E) a tidal chart from the tide gauge in Marseille, (F) a page of a logbook from the Trieste tide gauge.

(C) Courtesy of F. Raicich; (D) courtesy of A. Coulomb; (F) Courtesy of F. Raicich.

tide gauge set is highly variable (Fig. 5.3C). Out of 217 time series in PSMSL RLR data set, only 26 started before 1940. The vast majority of the current monitoring tide gauge stations (60%) have been deployed after 1980. The increase in the number of records during the most recent decades is more evident for the high-frequency measurements, associated with the development of new technologies (e.g., upgrade of floating gauges to incorporate digital recorders) and typologies of instruments (e.g., radar tide gauges which are more robust than acoustic ones). Technological developments facilitate the installation and operation of tide gauge stations, including real-time monitoring and data transfer as well as very high-frequency measurements (minutes to seconds) able to detect tsunamis and even wind-waves. One notable difference between the temporal availability of monthly and high-frequency observations is that the former decays rapidly in recent years. The reason is because, generally, national and subnational operators of tide gauge networks transfer quality-controlled monthly data to international repositories with some delay, whereas high-frequency measurements are provided near real time as they serve operational purposes.

5.2.2 Satellite altimetry

Altimeters on board of satellites are the major source of quasi-global sea surface height observations. The first satellite altimetry missions date from the 1970s and 1980s, but it was not until 1992 with the launch of the TOPEX/POSEIDON satellite that the high-precision (centimetre-level) satellite altimetry era began. Radar altimeters determine the distance between the orbiting satellite and the sea surface (called the range) at regular time intervals (of the order of days) at a given point on the sea surface and along tracks by measuring the time of travel of a reflected radar pulse (Fig. 5.2). The height of the sea surface is then calculated with respect to a reference surface (typically the reference ellipsoid) by subtracting the range from the satellite's height (the distance between the satellite and the reference surface). This calculation requires a precise determination of the position of the satellite with respect to the Earth center of mass, obtained using techniques such as Satellite Laser Ranging or GNSS. Also, a set of geophysical and environmental corrections, linked to processes that may alter the timing and path of the reflected signal, must be applied. These include tropospheric and ionospheric corrections associated with the state of the atmosphere and a sea state bias correction representing the roughness of the sea surface due to the presence of wind-waves (Nerem and Mitchum, 2001). The temporal sampling of altimeters at a given ground track typically ranges from 10 to 35 days, depending on orbit inclination and other factors, implying that high frequency signals are aliased into the observed records. For example, the main tidal constituent M_2 with a period of 12.42 h appears as a signal of 62 days in the records of TOPEX/POSEIDON altimeter owing to a repeat cycle of 9.9 days (Nerem and Mitchum, 2001). The same applies to sea level fluctuations driven by atmospheric

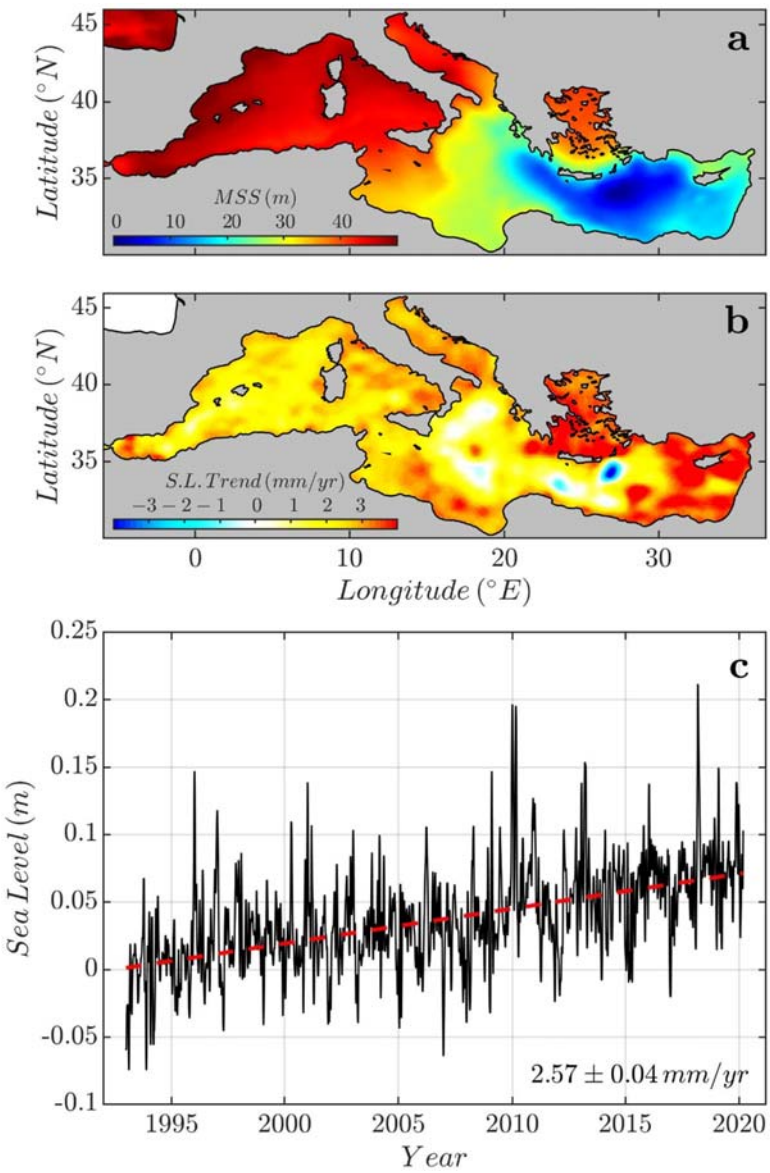

FIGURE 5.4

(A) Mean sea surface as observed from satellite altimetry; (B) Linear trends in mean sea level computed from satellite altimetry observations for the period 1993 to 2020 and (C) mean sea level anomalies averaged over the basin with indication of the linear trend.

pressure and wind variations, with temporal scales of the order of hours. These high-frequency signals are generally removed from the altimetry measurements to prevent aliasing errors. In the case of tides, the tidal oscillations, which can reach several meters in some ocean regions and are thus one of the largest signals in sea surface oscillations, are removed from altimetric measurements using ocean tidal models. Likewise, the effects of atmospheric pressure and wind variations on sea level at high frequencies (periods <20 days) can be estimated through a hydrodynamic ocean model forced with reanalyzed atmospheric data (e.g., Carrère and Lyard, 2003). For periods longer than 20 days, only atmospheric pressure effects are generally removed, typically by assuming an inverse barometer adjustment (i.e., an increase in 1 mbar of atmospheric pressure over the ocean surface translates into a decrease of 1 cm in sea level). These important corrections are to be taken into account when in-situ sea level measurements from tide gauges are compared to altimetric observations, since the former include the tidal and atmospherically-induced signals.

Satellite altimetry provides measurements of geocentric (sometimes termed absolute, which actually is ambiguous and geocentric should be preferred, see Gregory et al., 2019) sea surface height above a reference ellipsoid, a theoretical surface that approximates the geoid and is easier to work with. The geoid is an equipotential surface of the Earth's gravity field that is defined such that the volume between this geopotential surface and the sea floor coincides with the time-mean volume of ocean water (Gregory et al., 2019). This surface would be equivalent to mean sea surface in absence of external forces (Pugh and Woodworth, 2014). In reality, sea level can deviate locally from the geoid by up to a few meters due to ocean currents and other perturbing phenomena in what is termed the ocean dynamic sea level (Gregory et al., 2019) and often referred to as absolute dynamic topography in the literature. The time-mean component of the ocean dynamic sea level primarily reflects the imprint of prevailing ocean currents on sea surface height. Neither the geoid nor the mean ocean dynamic sea level can be directly obtained from satellite altimetry data, only their sum (the mean sea surface—MSS) can. Accurate measurements of the time-mean of ocean dynamic sea level (also termed mean dynamic topography, although this is a deprecated term) are difficult to achieve, partly due to the limited knowledge of the geoid, especially at small (on the order of km to tens of km) spatial scales; thus, sea level changes from satellite altimetry are computed as anomalies with respect to the MSS over a reference period. Fig. 5.4A maps the MSS in the Mediterranean Sea, relative to the referenced ellipsoid and with respect to the period 1993–99. There is significant spatial variation in the MSS with values ranging between 50 m in the western basin to 20 m in the eastern basin. These large spatial variations are mostly attributed to changes in the geoid, while the time-mean ocean dynamic sea level in this region has a spatial variation of only 10–20 cm (Woodworth et al., 2015).

Since 1992, successive and continuous high-precision satellite missions have been intercompared and intercalibrated to provide a homogeneous and consistent sea level record of nearly global coverage. Each satellite mission is monitored

and validated against in-situ data from tide gauges (Mitchum, 2000), improving the characterization of uncertainties, and allowing estimates of global and regional mean sea level changes with accuracies of 0.5 mm yr^{-1} and 2–3 mm yr^{-1} in the open ocean, respectively (Ablain et al., 2019). In regions close to the coast (within about 20 km), satellite altimetry observations tend to be less reliable due to land contamination in the altimeter footprint and less accurate geophysical corrections (Cipollini et al., 2017). In recent years, however, several international projects (e.g., COASTALT and the Sea Level Climate Change Initiative, both funded by the European Space Agency) have aimed to address these limitations and improve the quality of altimetry data in the coastal zone. These recent efforts have led to better geophysical corrections as well as new processing algorithms (i.e., retracking) that are able to greatly reduce the effects of land contamination, such as the Adaptive Leading Edge Subwaveform (ALES) retracker (Passaro et al., 2014). These recent advances have enabled accurate altimetry observations, on average, up to 4 km from the coast (The Climate Change Initiative Coastal Sea Level Team, 2020; Birol et al., 2021). More recently, new technologies, such as the Synthetic Aperture Radar (SAR) altimeters onboard CryoSat-2 (launched in 2010) and the Sentinel-3 satellites (launched in 2016), can provide reliable observations of sea level closer than 1 km from the coast (Fenoglio et al., 2020), albeit only in the along-track direction.

Multi-mission satellite altimetry observations are nowadays available in standardized formats through different national and international agencies and initiatives. Together with along-track observations for every individual satellite mission, gridded sea level fields are also derived using measurements from simultaneous missions (e.g., Le Traon et al., 1998; Legeais et al., 2018). The process of combining measurements from different satellites requires minimizing the intermission bias and computing sea level values over a regular grid through objective analysis (Ablain et al., 2017). Gridded sea level fields are particularly useful for regional sea level analyses, research of mesoscale variability, or model data assimilation. Both along-track and gridded global and regional products are distributed through data repositories such as the CMEMS or international programmes as Climate Change Initiative of the European Space Agency.

Regional mean sea level anomalies computed for the Mediterranean Sea are provided through CMEMS over a regular grid with a spatial resolution of 0.125 degrees in latitude and longitude. Linear trends fitted at each grid point using the least squares method for the period between January 1993 and June 2020 are mapped in Fig. 5.4B. Positive trends dominate over the entire basin, with the exception of the Ionian Sea and some particular areas in the Eastern Mediterranean that display negative values, corresponding to the Ierapetra gyre located at the south of Crete. These features are the surface signal of dynamical mesoscale structures and reflect changes in the ocean circulation. Although for slightly different periods, these results are in agreement with similar analyses of linear trends in the Mediterranean basin (e.g., Calafat et al., 2012a; Marcos et al., 2015; Bonaduce et al., 2016). The overall positive mean sea level rise is evidenced in Fig. 5.4C where mean sea level anomalies have been averaged over the basin. The averaged record has been

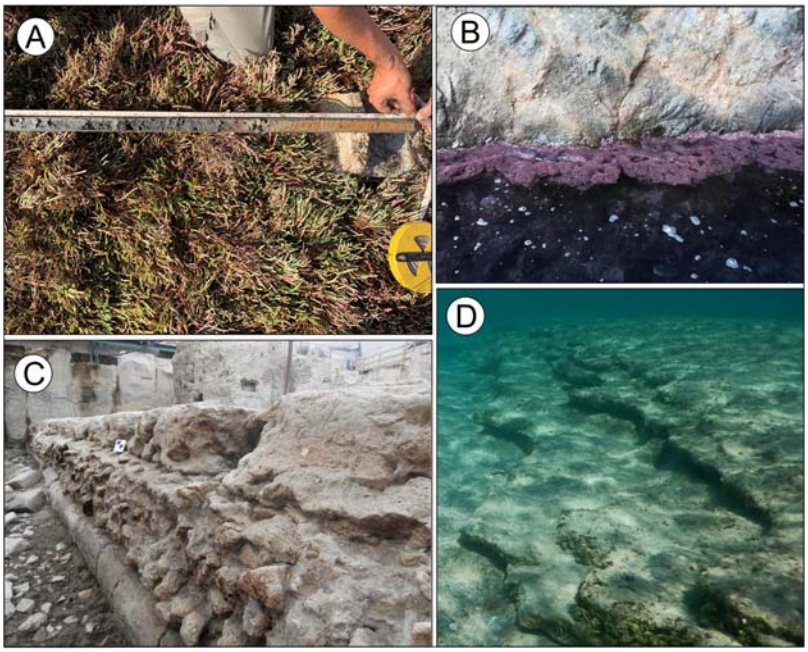

FIGURE 5.5

Common sea level proxies used to reconstruct the paleo sea-level in the Mediterranean: (A) sedimentary core extracted from a Mediterranean saltmarsh (Sardinia, Italy); (B) *Lithophyllum byssoides* rim in Capraia Island (Italy); (C) archaeological harbor structure from the Roman period (Naples, Italy, Vacchi et al., 2020b); (D) underwater beachrock outcrop in Corsica Island (France).

deseasoned by fitting an annual and a semiannual cycle using least squares. Mediterranean mean sea level has risen at a rate of 2.57 ± 0.04 mm yr^{-1}, which amounts to nearly 7 cm since 1993 (note that the quoted uncertainty refers to 1-sigma error without accounting for temporal autocorrelation).

Relative in situ sea level observations from tide gauges and geocentric observations from satellite altimetry in the vicinity of the tide gauges displays high coherence. Correlations between the two sources reach, on average, a value over 0.7 using monthly deseasoned time series (Marcos et al., 2015), while root mean square differences range between 2.5 and 5 cm (Bonaduce et al., 2016). The coherence of remote and in situ measurements may extend spatially, reaching long distances in the along-coast direction, especially in regions over continental shelves due to the barotropic nature of sea level changes in these regions (Marcos, 2015). In terms of linear trends, tide gauge and altimetry observations differ in the nonclimate contribution of vertical motion of the ground upon which the tide gauge is attached. This motion of the solid Earth surface can be either determined through leveling or monitored using space geodesy techniques (see Section 5.2.4). Alternatively, some

authors have exploited the synergies between both sources of sea level observations during their overlapping periods to quantify the contribution of vertical land motion to relative sea level, complementing the still scarce observations from GNSS at tide gauges, with the aim of identifying areas where land subsidence may increase the coastal exposure to mean sea level rise. Wöppelmann and Marcos (2012) used this approach to calculate the long-term contribution of vertical land motion to Mediterranean tide gauge linear sea level trends and, after this correction, they revisited the magnitude of geocentric rates of mean sea level change in the basin that resulted in 1.7 mm yr^{-1} for the period 1940–2010. Oelsmann et al. (2021) have recently refined the approach with the use of coastal altimetry along-track products, although they only included one station in the Mediterranean Sea.

5.2.3 Sea level proxies

The reconstruction of the sea-level evolution following the end of the last glaciation (Last Glacial Maximum, ca, 21000 years ago) is relevant to gauge how climatic forcing may influence the rates of future sea-level change. The production of sea-level proxy data has facilitated the quantification of the response of the solid Earth and gravity field to ice-mass redistribution and provided constraints for statistical and geophysical models used to project future sea-level rise (Peltier, 2004; Khan et al., 2019). The Mediterranean region has been a major focus for sea-level studies since the 60s (Fleming, 1969; Lambeck and Bard, 2000; Vacchi et al., 2016). These studies analyzed a wide range of proxies which allowed to robustly define the variability of the Mediterranean sea-level evolution over the last 12,000 years.

The largest amount of data was derived from sediment cores extracted from coastal lagoons and salt marshes (Melis et al., 2017; Brisset et al., 2018, Fig. 5.5A). The coupled analysis of grain size and the fossil faunal assemblages (foraminifera; ostracods and malacofauna) found within the cores was largely used to produce sea-level data which are generally dated with radiocarbon techniques on fossil shells, organic matter and vegetal remains (Vacchi et al., 2016). Another major source of Mediterranean sea-level data is represented by fossil remains of intertidal bioconstructed reefs. In particular, the fossil rims of *Lithophyllum byssoides* (Fig. 5.5B) were used for a high-resolution sea-level reconstruction along the coast of mainland France and Corsica (Laborel et al., 1994) and along the Adriatic coasts (Faivre et al., 2019). Fossil reefs of vermetid gastropods (*Dendropoma petraeum* and *Vermetus triquetrus*) yielded important insights into the sea-level changes in the southern and eastern Mediterranean basin (Sisma-Ventura et al., 2020). These proxies are dated with radiocarbon techniques and their age did not exceed the last 4000 years.

Beachrocks (i.e., cemented fossil beach deposits, Mauz et al., 2015, Fig. 5.5D) are a widespread feature of the Mediterranean coastlines occurring down to −40 m depth. They can be used as sea-level proxy even if their accuracy is strongly dependent on the degree of preservation of the sediment bedding information and on the accurate analysis of the intertidal cement (Mauz et al., 2015). Beachrocks allowed

to reconstruct the millennial sea-level evolution in several sites of the Aegean Sea (Desruelles et al., 2009; Karkani et al., 2017) and along the Corsican and Sardinian coasts (Demuro and Orrù, 1998; Vacchi et al., 2020a). The age of Mediterranean beachrocks was mostly obtained by radiocarbon dating on bioclasts found in the beach body and on the intertidal cements as well as from Optically Stimulated Luminescence techniques performed on the grains of the paleo beach.

Finally, the large abundance of archaeological remains along the Mediterranean coasts provided many insights into the sea-level evolution, notably since the Bronze Age (5000−3000 BP). In the last 2500 years, the precision of archaeological paleo-sea level reconstructions increased significantly thanks to the maritime archaeological structures from the Hellenistic and the Roman periods (Lambeck et al., 2004; Mattei et al., 2022).These structures (e.g., piers, slipways, breakwaters, fishtanks) can be used as sea-level proxy because their functioning is robustly related to the former mean sea level notably when found covered by fossil biological encrustations (Morhange and Marriner, 2015, Fig. 5.5C).

5.2.4 Supplementary techniques for understanding sea level changes

Since relative sea level changes result from a combination of physical processes (from ocean, ice, atmosphere and solid Earth), the use of supplementary observing techniques has become essential to understand the observed changes, and interpret these changes in terms of forcing factors. Some are now highly recommended or mandatory to upgrade observing sea level stations to international standards (IOC, 2012). For instance, the geodetic monitoring of tide gauge benchmarks using permanent GNSS stations (Fig. 5.2) is crucial to disentangle ocean-related changes from solid Earth surface changes at the coast. Once the importance of vertical land motion is accurately assessed in a geocentric reference frame (i.e., relative to the Earth's center of mass), this knowledge can be used, either from the ocean-climate perspective or the coastal management perspective. In the first perspective, tide gauge records are corrected using the GNSS-determined vertical land motion, and hence contribute to estimate sea level changes due to land-ice melting and ocean thermal expansion at regional scale (e.g., Wöppelmann and Marcos, 2012) or at global scale (e.g., Dangendorf et al., 2017). In the second perspective, the vertical land motion knowledge from GNSS can be used to assess the relative importance of the ocean and solid Earth contributions to relative sea level change along a given coastline, and hence enable anticipating future relative sea levels which requires an understanding of both contributions (Ballu et al., 2019) for coastal management. In this latter perspective, Fig. 5.2 highlights that satellite altimetry data is blind to the vertical land motion component, and thus needs to be corrected or supplemented with vertical land motion information to obtain the relevant quantity of relative sea level (S quantity in Fig. 5.2).

The first perspective or application corresponds to adding U (GNSS) to S (tide gauge) quantities in Fig. 5.2, whereas the second application corresponds to

subtracting U (GNSS) from N (satellite altimetry). Whatever the application, the GNSS monitoring of vertical land motion at the coast is crucial (Wöppelmann and Marcos, 2016). Note that due to its high-precision positioning performances in a geocentric reference frame, but also to the relatively low cost of the equipment, availability, easy implementation, and maintenance, GNSS is the recommended space geodetic technique for monitoring tide gauge benchmarks today (IOC, 2012). However, obtaining precise GNSS estimates of vertical land motion at better than the millimeter per year level is not that straightforward (Box 5.2). What is more, the GNSS information is pointwise. That is, strictly speaking, it is valid only at the GNSS antenna location. Fortunately, there are geodetic techniques which can provide the relative information between two distant points on the solid Earth surface. For decades, spirit leveling has been the classical way of obtaining the relative heights between two nearby points with millimeter level precision. Unfortunately, with the advent of GNSS techniques, many groups have progressively lost the skills and resources needed to carry out precise leveling surveys at the millimeter level, resulting in an important lack of key information associated with the local geodetic ties between tide gauges and nearby permanent GNSS stations (Woodworth et al., 2015, 2017b). Note that here the geodetic surveys need to be repeated at regular time intervals (annually or more frequently) to infer height changes, which can ultimately be costly, whether using leveling or episodic GNSS surveys.

The alternative option is to install a dedicated permanent GNSS station at the very tide gauge location, and consider the GNSS antenna as an additional tide gauge benchmark. This colocation setting has a couple of additional advantages, if the GNSS antenna is installed with an unobstructed view of the sea and the signal-to-noise ratio (SNR) of the GNSS signals are recorded.First, Larson et al. (2013) have demonstrated the promising perspective of GNSS-reflectometry as a new tide gauge technology, whereby sea level heights are estimated from the sea surface reflections of GNSS signals, recorded as oscillations in SNR. Second, Santamaria-Gomez et al. (2015) have used GNSS-reflectometry to estimate the leveling tie between the GNSS antenna reference point and the tide gauge zero. In one of their case studies, they were able to identify an unreported tide gauge change of 1.5 cm, which was later on confirmed by the operating agency.

Another important limitation with local geodetic surveying is that the outcome is essentially a collection of point measurements that are sparse compared to the short spatial scales of vertical land motion along many coastlines. For instance, Raucoules et al. (2013) reported large (centimeter per year level) vertical land motion within a distance of a few kilometers from the Manila (Philippines) tide gauge using Interferometric Synthetic Aperture Radar (InSAR) over the 1993−2010 period. A similar conclusion was reached in the area of Venice (Italy) tide gauge by Tosi et al. (2013) using a Persistent Scatterer InSAR (PSI) approach, although the observed vertical land motion in Venice city was found smaller than in Manila, ranging between 0 and 3 mm yr^{-1} subsidence over the period 1992−2010. In the Mediterranean, Wöppelmann et al. (2013) applied the PSI technique along the coastline of Alexandria including the tide gauge, and found a moderate land subsidence of 0.4 mm yr^{-1} on average, up to 2 mm yr^{-1} locally over the period 2002−10.

Box 5.2 GNSS measurements and estimates of vertical land motion

The process of estimating vertical land motion from GNSS measurements (i.e., from propagation delays of electromagnetic GNSS signals) at better than 1-mm yr^{-1} accuracy (the order of magnitude of vertical land motion is often close to the order of magnitude of sea level rise) is not straightforward, involving several steps such as (i) computing daily positions from GNSS measurements (in which many other parameters such as orbits, clocks, and atmospheric delays are also adjusted), (ii) referencing these positions in a geocentric reference frame, and (iii) modeling and inverting the position time-series to obtain the quantity of interest (trends, cycles, step discontinuities, etc.). From this complex multistep procedure, one should understand that GNSS positions are not direct measurements of position but rather estimates of a position or a series of positions from GNSS delay signals (inverse problem), which can be correlated with some other estimated parameters (e.g., atmospheric parameters). In addition to position time series, most GNSS data analysis centers provide linear trend estimates of vertical land motion (even though the actual vertical land motion at a given station can be more complicated than a linear trend). It is thus a good practice to first display the GNSS position time series to assess whether a linear trend is adequate and adopt its estimate, or devise a more complex model that best describes the time evolution of the station positions (Bevis and Brown, 2014). In any case, never assume that someone has concluded about this issue of time series modeling, especially if the analysis center deals with thousands, or sometimes more, GNSS stations (Blewitt et al., 2018).

Ballu et al. (2019) raise the issue of how to deal with and/or choose between the multiple high-precision GNSS solutions easily and freely available from various renowned analysis centers, and explain the significant differences in the estimates of vertical land motion that can be observed from one solution to the other at a number of stations in a given region with application to the Southwest and Central Pacific. The authors have indeed noted differences between the rate (linear trend) estimates that can be larger than the error bars provided by the analysis centers. Part of the differences arises from different choices in the above-mentioned data analysis steps (modeling, adjustment strategy, alignment to the reference frame), even though the highest international standards were adopted. For instance, they note that different sets of position offset discontinuities in the time series modeling identified and adopted by analysis centers from different expert eyeball or automatic procedures (Fig. 4 in Ballu et al., 2019), ultimately led to significant differences in rate estimates (Fig. 5 in Ballu et al., 2019). One direct implication of this outcome is that equipment changes in GNSS stations must be minimized and reported (metadata) when targeting high accuracy positioning.

Thus, each of the GNSS data analysis steps involves analyst choices which can significantly affect the estimated values of the quantity of interest, for example, the value of a linear trend representing a steady land motion or the amplitude of offset discontinuities representing sudden displacements due, for instance, to earthquakes (coseismic displacements). Moreover, differences between GNSS estimates of vertical land motion can be statistically significant, even for solutions produced by highly skilled and experienced groups following the state-of-the-art models and corrections adopted by the International GNSS Service (IGS).

Comparison experiments of GNSS products are organized at regular intervals within IGS to assess the performance of cutting-edge data analysis strategies, but Ballu et al. (2019) point out that these comparisons are carried out on a global scale that can hide regional issues. For instance, the alignment to the reference frame and its errors is known to map differently depending on the region considered (Collilieux and Wöppelmann, 2011), meaning that errors due to referencing issues that are minimized at the global scale, may be more significant at the regional scale. Accordingly, the final uncertainty on the vertical land motion estimates stems from a combination of the uncertainty due to the GNSS data processing itself and the uncertainty due to the stability of the reference frame in which the GNSS estimates are expressed (Santamaria-Gomez et al., 2017). The latter uncertainty component is beyond the GNSS technique as the practical realization of an accurate terrestrial reference frame involves a multi-technique approach including other high-precision space geodetic techniques than GNSS (Altamimi et al., 2016). In addition to the global geographic extent of the network of stations considered, the use of a consistent GNSS data analysis

Continued

Box 5.2 GNSS measurements and estimates of vertical land motion—cont'd

strategy across the data time span (reprocessing with the latest internationally agreed modeling) has also proven to be a key factor in obtaining consistent results, especially in the vertical component (Wöppelmann et al., 2007).

Ballu et al. (2019) study also demonstrates the interest of having multiple analysis centers processing the data for each station, as different and reasonable assumptions can provide different results, which should be a red flag to the user against using any one solution, without knowing the assumptions behind an individual solution. By contrast, when the estimates provided by different analysis centers agree within their error bars, they increase confidence in the results and their geophysical interpretation. Besides obtaining an agreed best estimate of linear trend from multiple high-precision GNSS solutions, one relevant question for the perspective of adaptation to future sea level rise and coastal management planning is the following: is the fairly steady behavior of a position time-series and the absence of significant nonlinear phenomena (e.g., earthquake-induced discontinuities) over several years or even decades a sufficient criterion for extrapolation into the future? The same question is posed for the climate-related perspective, where the estimate of vertical land motion is applied to correct longer-term tide gauge records dating back several decades to centuries in the past before the advent of GNSS. Moreover, a minimum record length (typically 3 years) is also critical for accurate determination of vertical land motion rates, due to seasonal variations and correlated noise. In addition, one should keep in mind the possible contribution of error sources other than GNSS data processing (e.g., the GNSS equipment and antenna monumentation).

Considering the complexity and high-level of expertise required in GNSS data analysis to achieve vertical land motion estimates at better than 1-mm yr^{-1} accuracy, the latest implementation plan of the Global sea level observing (GLOSS) program calls for the upgrade of permanent tide gauges with continuous GNSS stations, and that their measurements and metadata be provided to its dedicated data assembly center (SONEL, http://www.sonel.org) so that the measurements and generated products (position time series and linear trends) be public and free to anyone, in line with the IOC/UNESCO oceanographic data exchange policy (IOC, 2012), and particularly to those groups with the knowledge and expertise to analyze the data using state-of-the art data analysis strategies. Accordingly, SONEL assembles, archives, and distributes GNSS measurements and metadata from ca 950 stations at or nearby tide gauges, (https://www.sonel.org/-GPS-.html) from 67 countries and 120 agencies around the world, provided these are publicly available and free.

In terms of GNSS products, SONEL considers only state-of-the-art GNSS solutions; the minimum prerequisites being the adoption of the latest IGS-agreed models and corrections applied consistently across the data time span (reprocessing) based on a global network of stations and loosely constrained data analysis strategy. As of July 2021, the GNSS solutions distributed on SONEL portal are produced by La Rochelle university (ULR, Santamaria-Gomez et al., 2017), Nevada Geodetic Laboratory (NGL, Blewitt et al., 2018), Jet Propulsion Laboratory (JPL, Heflin et al., 2019), and (GFZ, Deng et al., 2015).

Fig. 5.2.1 shows the GNSS solution webpage, which includes a clickable map with the GNSS vertical velocities from a group (here, it displays the latest solution from NGL). The arrows are clickable to obtain a small popup window with the station name, its vertical velocity (a minimum of three continuous years is required), the associated time span, data completeness, and a link to the station web-page with full information on the station and its position time series. Fig. 5.2.2 illustrates an excerpt from a station web-page example and how the user may choose a particular GNSS solution (the analysis centers that have processed the station measurements are displayed on the top panel as tabs). The reader is encouraged to visit SONEL portal and explore its web-pages for further details.

Box 5.2 GNSS measurements and estimates of vertical land motion—cont'd

FIGURE 5.2.1

GNSS vertical velocities from NGL group, displayed on a web-based clickable map.

Online version at: http://www.sonel.org/-Vertical-land-movement-estimate-.html.

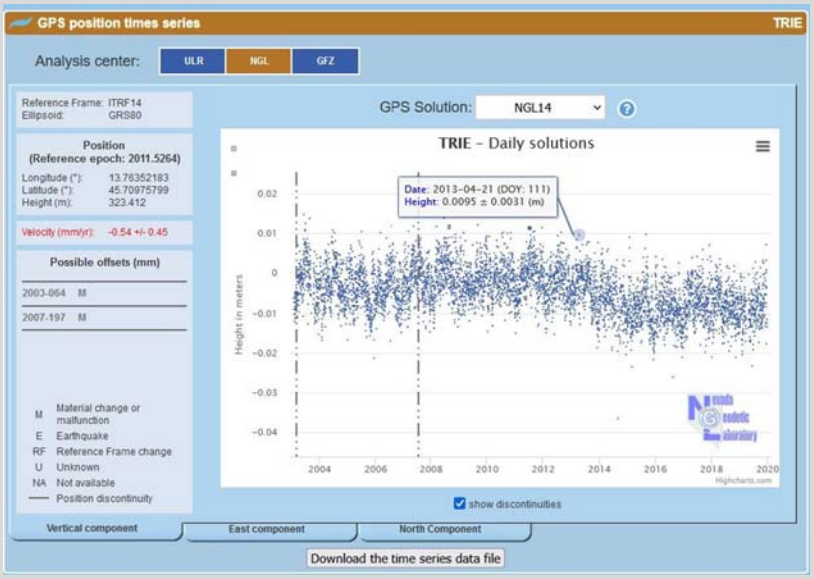

FIGURE 5.2.2

An example of products for the station near Trieste tide gauge in Italy.

Online version at: https://www.sonel.org/spip.php?page=gps&idStation=2042&solCentre=NGL.

A major implication of the above case studies is that data from nearby GNSS stations can be affected by a distinct land motion than that affecting the tide gauge, even at short distances, suggesting that the best GNSS installation is at the very tide gauge location, unless differential vertical land motion data (e.g., from InSAR) are available to assess the relative stability of a distant GNSS location. However, it is worth noting that coastal management studies are interested in the coastline beyond the tide gauge location. From these considerations, a comprehensive multitechnique approach emerges that combines pointwise but accurate geocentric measurements from GNSS with spatially dense but relative (to an arbitrary point on land) measurements from InSAR. The combined GNSS and InSAR products could yield deeper physical understanding and predictive power to determine relative sea level changes along the coastline beyond a tide gauge location (Poitevin et al., 2019). A final note is that GNSS and InSAR, as most space geodetic techniques (e.g., satellite radar altimetry) are not operational (at the required level of precision) before the 1990s, compromising any attempt to apply their results further back in time, as longer-term phenomena can have a nonlinear behavior.

This section has focused on supplementary techniques to understand the solid Earth surface component of relative sea level. Marcos et al. (2019) extend this discussion to techniques that can provide insights into the ocean-climate component of relative sea level at the coast. These include satellite gravimetry to identify the water mass redistribution from the land into the oceans, or vice-versa, and water density measurements (temperature, salinity) to assess the contribution from ocean water expansion. Ponte et al. (2019) further discuss the observational gaps and priorities for the development of an optimal and integrated coastal sea level observing system.

5.3 Past evolution of Mediterranean Sea level

5.3.1 Holocene sea-level changes and the role of isostatic-related subsidence

The comprehensive assessment of the geological and archaeological sea-level proxies described in Section 5.2.3 allowed us to have a basin-scale picture of the millennial sea-level evolution in the Mediterranean Sea. This dataset is particularly robust in the western Mediterranean Sea (Lambeck and Bard, 2000; Vacchi et al., 2016) which is relatively less influenced by neotectonics than the eastern one (Faccenna et al., 2014). The Mediterranean sea-level record (Fig. 5.6) indicates that sea-level rose by ca. 45 m within the Holocene period (last 11,700 years). However, the rates of this rise were not uniform throughout the whole Holocene. Rising rates were faster (up to 8.5 mm yr^{-1}) between 12,000 BP to 7500 years BP. In this period, the rise of Mediterranean sea level is largely controlled by the rapid melting of

the polar ice-sheets with consequent redistribution of melted water in the oceans (Lambeck et al., 2014; Roy and Peltier, 2018). The final phase of the North American deglaciation triggered a general sudden reduction in the meltwater input after 7500 years BP (Peltier, 2004). This major change in the oceanic setting is observable in the Mediterranean sea-level record which shows a significant stabilization between 7500 and 4000 years BP with average rising rates which did not exceed 1.5 mm yr^{-1}.

In the late Holocene period (last 4000 years), the global ice-equivalent meltwater input was minimal (Peltier, 2004; Milne et al., 2005) and the sea-level evolution was primarily controlled by Glacio-hydro Isostatic (GIA) adjustment. GIA processes are related to the large redistributions of mass between the ice-sheets and oceans during glacial and interglacial cycles and to the time-dependent response of the Earth's lithosphere to surface loads (Roy and Peltier, 2018).

GIA-related deformation in the Mediterranean basin is mainly controlled by water loading, which has resulted in widespread subsidence throughout much of the basin with average rates 0.5 mm yr^{-1} in the last 4000 years. Maximum values

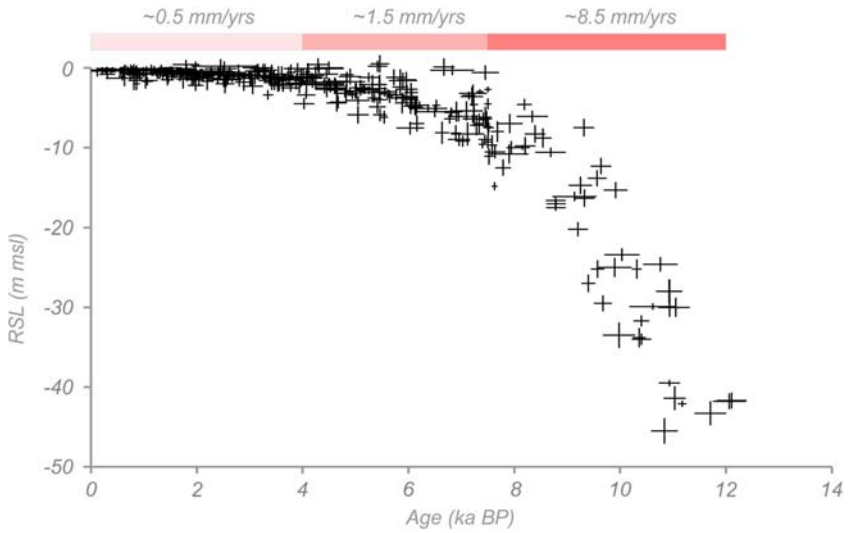

FIGURE 5.6

Anatomy and rising rates of the sea-level evolution in the central and western Mediterranean Sea in the last 12.0 ka. Black crosses indicate the position in time and space of the sea-level data used to reconstruct the sea-level evolution.

Modified after Vacchi, M., Ghilardi, M., Melis, R.T., Spada, G., Giaime, M., Marriner, N.,Morhange, C., Rovere, A., 2018. New relative sea-level insights into the isostatic history of the Western Mediterranean. Quat. Sci. Rev. 201, 396–408.

of GIA-related subsidence are predicted by GIA geophysical models in the sector of the basin comprising Sardinia and Balearic Islands and in the Ionian Sea (Lambeck and Purcell, 2005; Roy and Peltier, 2018, Fig. 5.7). However, recent investigations performed in Mallorca (Vacchi et al., 2018) indicate a significant misfit between data in models in this sector of the Mediterranean Sea. This calls for a refinement of the GIA models in the Mediterranean which represent a fundamental tool to produce robust predictions of future sea-level rise.

Furthermore, other vertical components played a major role in controlling the Mediterranean sea-level evolution in the late Holocene. In tectonically active portions of the Mediterranean coasts such as in Lebanon (Morhange et al., 2006), along the Greek and Turkish coasts (e.g., Pirazzoli et al., 1991, 1994; Stiros et al., 2000) in the volcanic district of Naples (e.g., Mattei et al., 2020; Vacchi et al., 2020b) and along the Calabrian arc and eastern Sicily (e.g., Ferranti et al., 2008; Scicchitano et al., 2011) seismic and aseismic ground movements have significantly controlled the sea-level evolution in the last millennia. Finally, late-Holocene sea-level rising rates were faster than the Mediterranean average in the large deltas such as the Nile (Stanley and Clemente, 2017), the Ebro (Sornoza et al., 1998) and in large coastal plains such the Venice lagoon (Tosi et al., 2013). In these cases, a significant part of the late-Holocene sea-level rise is the result of sediment compaction processes which induced a widespread subsidence.

5.3.2 Decadal to centennial sea level trends since the late 19th century

Decadal to centennial relative mean sea-level changes can be computed from tide gauge records. Fig. 5.8 represents 10 of the longest tide gauge annual time series in the Mediterranean Sea that are archived in the PSMSL data repository (note that only those classified as RLR—see Section 5.2.1—have been included in this set as their vertical leveling is known). The longest records, corresponding to the tide gauges in Marseille and Genova, allow quantifying the rates of relative mean sea-level rise in the Mediterranean in 1.3−1.4 mm yr^{-1} since the late 19th century. However, the rates are not constant in time. Decadal rates of mean sea level changes vary between −5 mm yr^{-1} and 7 mm yr^{-1} on average when all available tide gauges are used after correction for GIA (Marcos and Tsimplis, 2008). It is notable that between the 1960s and the 1990s mean sea level in the Mediterranean Sea dropped on average, mainly in response to an increase of the long-term atmospheric pressure over the basin (Tsimplis and Josey, 2001). In consequence, some of the longest tide gauge records display negative mean sea level accelerations for the 20th century (Marcos and Tsimplis, 2008). Long-term rates of relative mean sea level may differ among stations due to the presence of vertical land movements (Wöppelmann and Marcos, 2012), which can account for a significant fraction of the observed linear

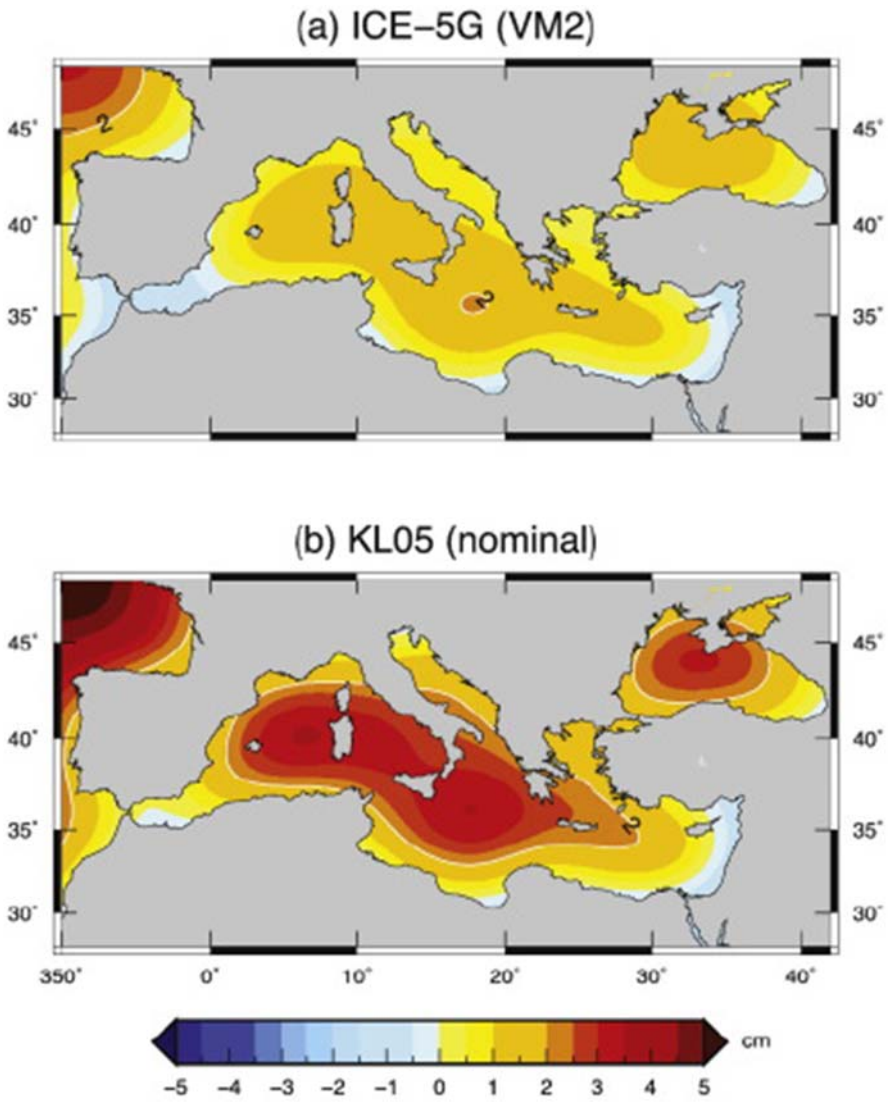

FIGURE 5.7

Modeled Glacio and hydro-isostatic adjustment (GIA) sea-level fingerprints in the Mediterranean Sea. Predictions were obtained using two models ICE-5G (VM2, Peltier, 2004) and KL05 (Lambeck et al., 2011) which were largely used in the Mediterranean region.

Modified after Vacchi, M., Ghilardi, M., Melis, R.T., Spada, G., Giaime, M., Marriner, N.,Morhange, C., Rovere, A., 2018. New relative sea-level insights into the isostatic history of the Western Mediterranean. Quat. Sci. Rev. 201, 396–408.

trends. The paradigmatic case is the city of Venice, unique because of its historic and cultural heritages, that is subsiding due to natural causes and, mostly, due to anthropogenic activities. Larger rates of subsidence have been reported for the period 1930–70 due to gas and groundwater extraction (Zanchettin et al., 2021). From Fig. 5.8, the comparison between relative sea level trends in Venice and in the nearby Trieste reveal subsidence rates in excess of 1 mm yr^{-1} on average, in agreement with earlier findings (Wöppelmann and Marcos, 2012).

At decadal and multi-decadal time scales, the Mediterranean sea level responds to variations in mean sea level in the nearby Northeast Atlantic Ocean. Calafat et al. (2012b) identified coherent decadal sea level variations in the Mediterranean Sea and along the European coasts. These are controlled by boundary trapped waves generated by longshore winds that propagate northwards from 25°N along the European continental shelf and induce mass exchanges between the Mediterranean basin and the Atlantic Ocean that dominate the sea level signal at decadal time scales. The result is a basin-wide coherent signal, supported by decadal changes in tide gauge observations within the basin.

At interannual time scales, nearby tide gauges display consistency in mean sea level changes (Fig. 5.8). Atmospheric forcing through heat and, mostly, momentum flux exchanges are the driving mechanisms of sea level variations at these time scales. Thus, interannual mean sea level changes present strong correlations with large-scale atmospheric climate patterns over the region, the dominant of which is the North Atlantic Oscillation (NAO). The NAO has a strong influence on Mediterranean sea level, mostly during the winter season, due to its effect on the atmospherically-induced sea level changes (in response to changes in atmospheric pressure and winds), reflected in significant negative correlations (Tsimplis and Josey, 2001). To a lesser extent the NAO also affects the thermosteric sea level component (Tsimplis and Rixen, 2002; Tsimplis et al., 2006). Martínez-Asensio et al. (2014) explored the influence of the NAO but also of other climate modes, namely East Atlantic (EA), East Atlantic/Western Russian (EA/WR) and the Scandinavian (SCAN) patterns, on Mediterranean sea level and its atmospherically induced and thermosteric components. They concluded that the correlation with NAO, that reaches a value of −0.9, is the result of two effects: the local and direct forcing on the sea surface of atmospheric pressure and wind and its relationship with winds near Gibraltar Strait that induce water mass exchanges between the Mediterranean and the nearby Atlantic Ocean. The EA/WR acts on Mediterranean sea level through its pressure signature, whereas the EA pattern influences winter thermosteric sea level through its effects on heat fluxes.

At seasonal time scales, thermal expansion and contraction and, to a lesser extent, the seasonal variations in the atmospheric pressure and winds are the mechanisms that explain the differences in mean sea level during summer and winter seasons (Marcos and Tsimplis, 2007).

Tide gauges provide only pointwise information at stations along the coasts. To overcome this limitation, statistical techniques have been proposed that combine the temporal sea level variability observed by tide gauges at decadal and longer time

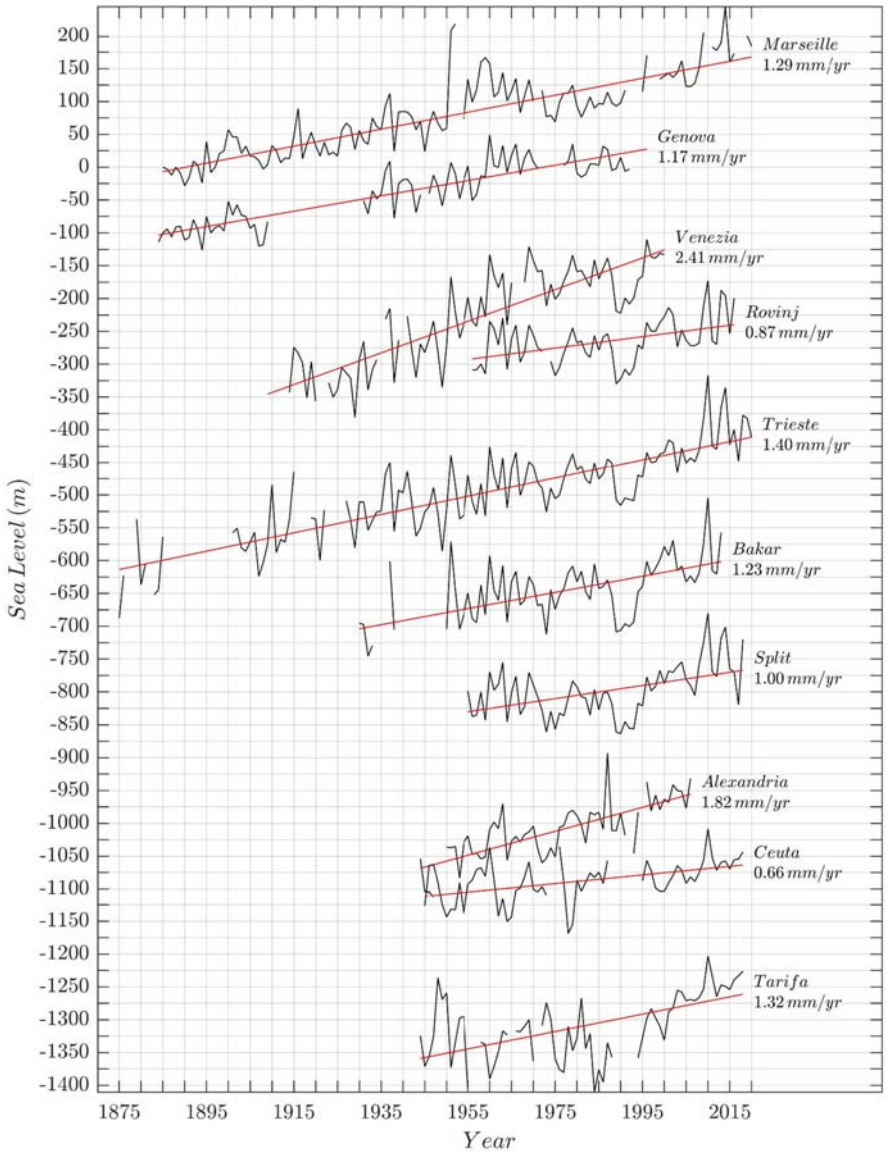

FIGURE 5.8

Ten tide gauge annual sea level records, sorted by proximity. Note that time series have been offset for a better visualization.

scales with the spatial patterns obtained from satellite altimetry or from numerical models with a shorter time span. In Calafat and Gomis (2009), the authors used a reduced space optimal interpolation analysis to reconstruct sea level changes in

the Mediterranean Sea for the period 1945–2000. The technique, based on Church et al. (2004), consisted on calculating empirical orthogonal functions from gridded altimetry data and combining the main patterns obtained with tide gauge records. Their sea level reconstruction reproduced dynamical features of Mediterranean circulation and the spatial distribution of sea level trends over the basin. Nevertheless, this method, although powerful, also has shortcomings such as its poor performance in regions of strong mesoscale activity (Calafat and Gomis, 2009) and the inability to simultaneously capture long-term trends and variability (Calafat et al., 2014). Other methods to reconstruct sea level fields exist and have been applied globally (Hay et al., 2015; Dangendorf et al., 2019), in some cases also providing solutions at the regional scales.

5.4 Future projections of Mediterranean Sea level

Future sea level projections for the 21st century and beyond can be obtained from coupled atmosphere-ocean climate models. Coordinated climate model experiments are designed within the Climate Model Intercomparison Project, currently in its phase 6, that establishes a set of standard model simulations that allow the model intercomparisons for historical periods and future projections under a predefined set of climate change scenarios. Climate models provide a comprehensive list of climate variables, including sea surface height that represents the sterodynamic contributions to sea level changes, that is, the variations in sea level due to ocean heat redistribution and ocean circulation changes (Church et al., 2013). Model outputs also provide global mean thermosteric sea level caused by global ocean heat uptake that must be combined with sea surface height in order to calculate the overall contribution of ocean density and circulation changes (Slangen et al., 2014). Other contributions such as atmospheric loading (the effects of atmospheric pressure on sea level), land-ice melting, groundwater depletion and glacial isostatic adjustment can be computed offline and added to the models' outputs to obtain regional maps of total projected mean sea level (Slangen et al., 2014). A major shortcoming of the available climate models is their relatively coarse spatial resolution of around 1 degree in latitude and longitude. This prevents their regional results from being applied directly to the Mediterranean Sea, since the water exchanges through the Strait of Gibraltar are misrepresented. Therefore, to assess regional mean sea level projections in the Mediterranean from coupled climate models, the sterodynamic contributor must be modified and taken from a region in the nearby Atlantic Ocean, since the long-term Mediterranean mean sea level follows sea level changes in the nearby Atlantic (Jordà and Gomis, 2013). This procedure is illustrated, for example, in Sayol and Marcos (2018) for a location in the western Mediterranean Sea.

Alternatively to the use of the process-based models for projected mean sea level as described above, other approaches, such as expert elicitation assessments (e.g., Bamber et al., 2019) or probabilistic projections (e.g., Kopp et al., 2014), are also available. A complete discussion on these alternatives is provided in Oppenheimer

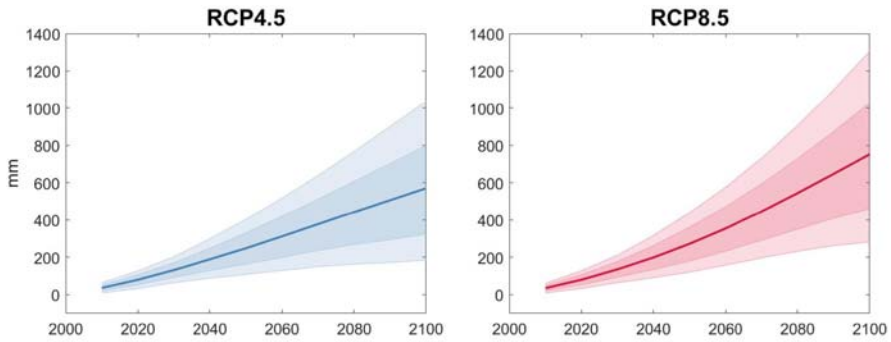

FIGURE 5.9

Mean sea level projections representative of the Mediterranean Sea under two climate change scenarios for the 21st century. Shaded areas indicate the 17%–83% and the 5%–95% probability intervals and solid lines represent the multimodel ensemble median.

Obtained from Kopp, R.E. et al., 2014. Probabilistic 21st and 22nd century sea-level projections at a global network of tide-gauge sites. Earth's Fut. 2 (8), 383–406.

et al. (2019). Fig. 5.9 displays an example of mean sea level projections for the 21st century in the Mediterranean Sea derived from Kopp et al. (2014) under the two climate change scenarios RCP4.5 and RCP8.5, together with estimated uncertainties. Median values indicate a rise in mean sea level of 54 and 72 cm under RCP4.5 and RCP8.5, respectively, by 2100.

Additional Resources

- CMEMS https://marine.copernicus.eu/
- Climate Change Initiative of the European Space Agency https://climate.esa.int/en/
- Climate Model Intercomparison Project, phase 6 https://www.wcrp-climate.org/wgcm-cmip/wgcm-cmip6
- Global Extreme Sea Level Analysis www.gesla.org/
- Permanent Service for Mean Sea Level https://www.psmsl.org/
- Système d'Observation du Niveau des Eaux Littorales (SONEL) https://www.sonel.org/

References

Ablain, M., Legeais, J.F., Prandi, P., Fenoglio-Marc, L., Marcos, M., Benveniste, J., Cazenave, A., 2017. Satellite altimetry based sea level at global and regional scales. Surv. Geophys. 38, 9–33. https://doi.org/10.1007/s10712-016-9389-8.

Ablain, M., Meyssignac, B., Zawadzki, L., Jugier, R., Ribes, A., Spada, G., Benveniste, J., Cazenave, A., Picot, N., 2019. Uncertainty in satellite estimates of global mean sea-level changes, trend and acceleration. Earth Syst. Sci. Data 11, 1189–1202. https://doi.org/10.5194/essd-11-1189-2019.

Altamimi, Z., Rebischung, P., Métivier, L., Collilieux, X., 2016. ITRF2014: a new release of the International Terrestrial Reference Frame modeling nonlinear station motions. J. Geophys. Res. Solid Earth 121, 6109–6131. https://doi.org/10.1002/2016JB013098.

Ballu, V., Gravelle, M., Wöppelmann, G., de Viron, O., Rebischung, P., Becker, M., Sakic, P., 2019. Vertical land motion in the Southwest and Central Pacific from available GNSS solutions and implications for relative sea levels. Geophys. J. Int. 218, 1537–1551. https://doi.org/10.1093/gji/ggz247.

Bamber, J.L., et al., 2019. Ice sheet contributions to future sea level rise from structured expert judgment. Proc. Natl. Acad. Sci. Unit. States Am. 116 (23), 11195–11200.

Bevis, M., Brown, A., 2014. Trajectory models and reference frames for crustal motion geodesy. J. Geodes. 88, 283–311. https://doi.org/10.1007/s00190-013-0685-5.

Birol, F., Léger, F., Passaro, M., Cazenave, A., Niño, F., Callafat, F., Shaw, A., Legeais, J.-F., Gouzenes, Y., Schwatke, C., Benveniste, J., 2021. The X-TRACK/ALES multi-mission processing system: new advances in altimetry towards the coast. Adv. Space Res. 67 (8), 2398–2415.

Blewitt, G., Kreemer, C., Hammond, W.C., 2018. Harnessing the GPS data explosion for interdisciplinary science. EOS 99. https://doi.org/10.1029/2018EO104623.

Bonaduce, A., Pinardi, N., Oddo, P., Spada, G., Larnicol, G., 2016. Sea-level variability in the Mediterranean Sea from altimetry and tide gauges. Clim. Dynam. 47, 2851–2866. https://doi.org/10.1007/s00382-016-3001-2.

Brisset, E., Burjachs, F., Navarro, B.J.B., de Pablo, J.F.L., 2018. Socio-ecological adaptation to Early-Holocene sea-level rise in the western Mediterranean. Global Planet. Change 169, 156–167.

Bruni, S., Zerbini, S., Raicich, F., Errico, M., 2019. Rescue of the 1873-1922 high and low waters of the Porto Corsini/Marina di Ravenna (Northern Adriatic, Italy) tide gauge. J. Geodes. 93, 1227–1244. https://doi.org/10.1007/s00190-019-01238-w.

Calafat, F.M., Gomis, D., 2009. Reconstruction of Mediterranean sea level fields for the period 1945–2000. Global Planet. Change 66 (3–4), 225–234. https://doi.org/10.1016/j.gloplacha.2008.12.015.

Calafat, F.M., Jordà, G., Marcos, M., Gomis, D., 2012a. Comparison of Mediterranean sea level variability as given by three baroclinic models. J. Geophys. Res. 117, C02009. https://doi.org/10.1029/2011JC007277.

Calafat, F.M., Chambers, D.P., Tsimplis, M.N., 2012b. Mechanisms of decadal sea level variability in the eastern North Atlantic and the Mediterranean Sea. J. Geophys. Res. 117, C09022. https://doi.org/10.1029/2012JC008285.

Calafat, F.M., Chambers, D.P., Tsimplis, M.N., 2014. On the ability of global sea level reconstructions to determine trends and variability. J. Geophys. Res. Oceans 119, 1572–1592. https://doi.org/10.1002/2013JC009298.

Carrère, L., Lyard, F., 2003. Modeling the barotropic response of the global ocean to atmospheric wind and pressure forcing—comparisons with observations. Geophys. Res. Lett. 30 (6), 1275.

Church, J.A., White, N.J., Coleman, R., Lambeck, K., Mitrovika, J.X., 2004. Estimates of the regional distribution of sea level rise over the 1950–2000 Period. J. Clim. 17, 2609–2625.

Church, J.A., Clark, P.U., Cazenave, A., Gregory, J.M., Jevrejeva, S., Levermann, A., et al., 2013. Sea level change. In: Stocker, T.F., et al. (Eds.), Climate Change 2013: The Physical Science Basis, Contribution of Working Group I to the Fifth Assessment Report of the Intergovernmental Panel on Climate Change. CUP, Cambridge, UK.

Cipollini, P., Calafat, F.M., Jevrejeva, S., Melet, A., Prandi, P., 2017. Monitoring sea level in the coastal zone with satellite altimetry and tide gauges. Surv. Geophys. 38, 33–57. https://doi.org/10.1007/s10712-016-9392-0.

Collilieux, X., Wöppelmann, G., 2011. Global sea-level rise and its relation to the terrestrial reference frame. J. Geodes. 85, 9–22. https://doi.org/10.1007/s00190-010-0412-4.

Dangendorf, S., Marcos, M., Wöppelmann, G., Conrad, C.P., Frederikse, T., Riva, R., 2017. Reassessment of 20th century global mean sea level rise. Proc. Nat. Acad. Sci. of USA 114 (23), 5946–5951. https://doi.org/10.1073/pnas.1616007114.

Dangendorf, S., Hay, C., Calafat, F.M., Marcos, M., Piecuch, C.G., Berk, K., Jensen, J., 2019. Persistent acceleration in global sea-level rise since the 1960s. Nat. Clim. Change. https://doi.org/10.1038/s41558-019-0531-8.

De Muro, S., Orrù, P., 1998. Il contributo delle beach rock nello studio della risalita del mare olocenico. Le beach rock post-glaciali della Sardegna nord-orientale. Il Quat. 11 (1), 19–39.

Deng, Z., Gendt, G., Schöne, T., 2015. Status of the IGS-TIGA tide gauge data reprocessing at GFZ. In: Rizos, C., Willis, P. (Eds.), IAG 150 Years, 143. International Association of Geodesy Symposia, Springer, pp. 33–40. https://doi.org/10.1007/1345_2015_156.

Desruelles, S., Fouache, É., Ciner, A., Dalongeville, R., Pavlopoulos, K., Kosun, E., et al., 2009. Beachrocks and sea level changes since Middle Holocene: comparison between the insular group of Mykonos–Delos–Rhenia (Cyclades, Greece) and the southern coast of Turkey. Global Planet. Change 66 (1–2), 19–33.

Faccenna, C., Becker, T.W., Auer, L., Billi, A., Boschi, L., Brun, J.P., Capitanio, F., Funiciello, F., Horvat, F., Jolivet, L., Piromallo, C., Royden, L., Rossetti, F., Serpelloni, E., 2014. Mantle dynamics in the mediterranean. Rev. Geophys. 52 (3), 283e332.

Faivre, S., Bakran-Petricioli, T., Barešić, J., Horvatić, D., Macario, K., 2019. Relative sea-level change and climate change in the Northeastern Adriatic during the last 1.5 ka (Istria, Croatia). Quat. Sci. Rev. 222, 105909.

Fenoglio, L., Dinardo, S., Uebbing, B., Buchhaupt, C., Gärtner, M., Staneva, J., Becker, M., Klos, A., Kusche, J., 2020. Advances in NE-Atlantic coastal sea level change monitoring by Delay Doppler altimetry. Adv. Space Res. https://doi.org/10.1016/j.asr.2020.10.041. ISSN: 0273-1177.

Ferranti, L., Monaco, C., Morelli, D., Antonioli, F., Maschio, L., 2008. Holocene activity of the Scilla Fault, Southern Calabria: insights from coastal morphological and structural investigations. Tectonophysics 453 (1–4), 74–93.

Flemming, N.C., 1969. Archaeological Evidence for Eustatic Change of Sea Level and Earth Movements in the Western Mediterranean during the Last 2000 Years, 109. Geological Society of America.

Gregory, J.M., Griffies, S.M., Hughes, C.W., Lowe, J.A., Church, J.A., Fukimori, I., et al., 2019. Concepts and terminology for sea level: mean, variability and change, both local and global. Surv. Geophys. 40, 1251–1289. https://doi.org/10.1007/s10712-019-09525-z.

Hay, C.H., Morrow, E., Kopp, R.E., Mitrovica, J.X., 2015. Probabilistic reanalysis of twentieth-century sea level rise. Nature 517, 481–484.

Heflin, M., Moore, A., Murphy, D., Desai, S., Bertiger, W., Haines, B., Kuang, D., Sibthorpe, A., Sibois, A., Ries, P., Hemberger, D., Dietrich, A., 2019. Introduction to JPL's GNSS Time Series. https://sideshow.jpl.nasa.gov/post/tables/GNSS_Time_Series.pdf.

Holgate, S.J., Matthews, A., Woodworth, P.L., Rickards, L.J., Tamisiea, M.E., Bradshaw, E., Foden, P.R., Gordon, K.M., Jevrejeva, S., Pugh, J., 2013. New data systems and products at the permanent Service for mean sea level. J. Coast Res. 29 (3), 493–504. https://doi.org/10.2112/JCOASTRES-D-12-00175.1.

IOC, 1985. Manual on Sea Level Measurement and Interpretation. Intergovernmental Oceanographic Commission, Manuals and Guides, 14, vol. I. Basic procedures, p. 75. Available online at: https://www.psmsl.org/train_and_info/training/manuals/.

IOC, 2012. The Global Sea Level Observing System Implementation Plan 2012, 100. Intergovernmental Oceanographic Commission Technical Series.

Jorda, G., Gomis, D., 2013. On the interpretation of the steric and mass components of sea level variability: the case of the Mediterranean basin. J. Geophys. Res. Oceans 118, 953–963. https://doi.org/10.1002/jgrc.20060.

Karkani, A., Evelpidou, N., Vacchi, M., Morhange, C., Tsukamoto, S., Frechen, M., Maroukian, H., 2017. Tracking shoreline evolution in central Cyclades (Greece) using beachrocks. Mar. Geol. 388, 25–37.

Khan, N.S., Horton, B.P., Engelhart, S., Rovere, A., Vacchi, M., Ashe, E.L., et al., 2019. Inception of a global atlas of sea levels since the Last Glacial Maximum. Quat. Sci. Rev. 220, 359–371.

Kopp, R.E., et al., 2014. Probabilistic 21st and 22nd century sea-level projections at a global network of tide-gauge sites. Earth's Fut. 2 (8), 383–406.

Kopp, R.E., et al., 2016. Temperature-driven global sea level variability in the Common Era. Proc. Natl. Acad. Sci. Unit. States Am. 113 (11), E1434–E1441.

Laborel, J., Morhange, C., Lafont, R., Le Campion, J., Laborel-Deguen, F., Sartoretto, S., 1994. Biological evidence of sea-level rise during the last 4500 years on the rocky coasts of continental southwestern France and Corsica. Mar. Geol. 120 (3–4), 203–223.

Lambeck, K., Bard, E., 2000. Sea-level change along the French Mediterranean coast for the past 30 000 years. Earth Planet Sci. Lett. 175 (3–4), 203–222.

Lambeck, K., Purcell, A., 2005. Sea-level change in the Mediterranean Sea since the LGM: model predictions for tectonically stable areas. Quat. Sci. Rev. 24 (18–19), 1969–1988.

Lambeck, K., Anzidei, M., Antonioli, F., Benini, A., Esposito, A., 2004. Sea level in Roman time in the Central Mediterranean and implications for recent change. Earth Planet Sci. Lett. 224 (3–4), 563–575.

Lambeck, K., Antonioli, F., Anzidei, M., Ferranti, L., Leoni, G., Scicchitano, G., Silenzi, S., 2011. Sea level change along the Italian coast during the Holocene and projections for the future. Quat. Int. 232 (1–2), 250–257.

Lambeck, K., Rouby, H., Purcell, A., Sun, Y., Sambridge, M., 2014. Sea level and global ice volumes from the last glacial maximum to the Holocene. Proc. Natl. Acad. Sci. Unit. States Am. 111 (43), 15296–15303.

Larson, K.M., Ray, R.D., Nievinski, F.G., Freymueller, J., 2013. The accidental tide gauge: a GPS reflection case study from Kachemak Bay, Alaska. Geosci. Rem. Sens. Lett. IEEE 10, 1200–1204. https://doi.org/10.1109/LGRS.2012.2236075.

Le Traon, P.Y., Nadal, F., Ducet, N., 1998. An improved mapping method of multisatellite altimeter data. J. Atmos. Ocean. Technol. 15 (2), 522–534. https://doi.org/10.1175/1520-0426(1998)015<0522:AIMMOM>2.0.CO;2.

Legeais, J.-F., Ablain, M., Zawadzki, L., Zuo, H., Johannessen, J.A., Scharffenberg, M.G., Fenoglio-Marc, L., Fernandes, M.J., Andersen, O.B., Rudenko, S., Cipollini, P., Quartly, G.D., Passaro, M., Cazenave, A., Benveniste, J., 2018. An improved and

homogeneous altimeter sea level record from the ESA Climate Change Initiative. Earth Syst. Sci. Data 10, 281−301. https://doi.org/10.5194/essd-10-281-2018.

Marcos, M., 2015. Ocean bottom pressure variability in the Mediterranean Sea and its relationship with sea level from a numerical model. Global Planet. Change 124, 10−21.

Marcos, M., Tsimplis, M.N., 2007. Variations of the seasonal sea level cycle in southern Europe. J. Geophys. Res. 112, C12011. https://doi.org/10.1029/2006JC004049.

Marcos, M., Tsimplis, M.N., 2008. Coastal sea level trends in southern Europe. Geophys. J. Int. 175, 70−82. https://doi.org/10.1111/j.1365-246X.2008.03892.x.

Marcos, M., Pascual, A., Pujol, I., 2015. Improved satellite altimeter mapped sea level anomalies in the Mediterranean Sea: a comparison with tide gauges. Adv. Space Res. 56, 596−604. https://doi.org/10.1016/j.asr.2015.04.027.

Marcos, M., Wöppelmann, G., Matthews, A., Ponte, R.M., Birol, F., Ardhuin, F., Coco, G., Santamaria-Gomez, A., Ballu, V., Testut, L., Chambers, D., Stopa, J.E., 2019. Coastal sea level and related fields from existing observing systems. Surv. Geophys. 40, 1293−1317. https://doi.org/10.1007/s10712-019-09513-3.

Marcos, M., Puyol, B., Amores, A., Pérez Gómez, B., Fraile, M.A., Talke, S.A., 2021. Historical tide-gauge sea-level observations in Alicante and Santander (Spain) since the 19th century. Geosci. Data J. https://doi.org/10.1002/gdj3.112.

Martin Miguez, B., Testut, L., Wöppelmann, G., 2008. The Van de Casteele test revisited: an efficient approach to tide gauge error characterization. J. Atmos. Ocean. Technol. 25, 1238−1244. https://doi.org/10.1175/2007JTECHO554.1.

Martínez-Asensio, A., Marta, M., Tsimplis, M.N., Gomis, D., Simon, J., Gabriel, J., 2014. Impact of the atmospheric climate modes on Mediterranean sea level variability. Global Planet. Change 118 (2014), 1−15. https://doi.org/10.1016/j.gloplacha.2014.03.007.

Mattei, G., Aucelli, P.P., Caporizzo, C., Rizzo, A., Pappone, G., 2020. New geomorphological and historical elements on morpho-evolutive trends and relative sea-level changes of naples coast in the last 6000 years. Water 12 (9), 2651.

Mattei, G., Caporizzo, C., Corrado, G., Vacchi, M., Stocchi, P., Pappone, G., Schiattarella, M., Aucelli, P.P., 2022. On the influence of vertical ground movements on Late-Quaternary sea-level records. A comprehensive assessment along the mid-Tyrrhenian coast of Italy (Mediterranean Sea). Quat. Sci. Rev. 279, 107384.

Mauz, B., Vacchi, M., Green, A., Hoffmann, G., Cooper, A., 2015. Beachrock: a tool for reconstructing relative sea level in the far-field. Mar. Geol. 362, 1−16.

Melis, R.T., Depalmas, A., Di Rita, F., Montis, F., Vacchi, M., 2017. Mid to late Holocene environmental changes along the coast of western Sardinia (Mediterranean Sea). Global Planet. Change 155, 29−41.

Meyssignac, B., et al., 2017. Causes of the regional variability in observed sea level, sea surface temperature and ocean colour over the period 1993− 2011. Surv. Geophys. 38, 187−215.

Milne, G.A., Long, A.J., Bassett, S.E., 2005. Modelling Holocene relative sea-level observations from the Caribbean and South America. Quat. Sci. Rev. 24, 1183−1202. https://doi.org/10.1016/j.quascirev.2004.10.005.

Mitchum, G.T., 2000. An improved calibration of satellite altimetric heights using tide gauge sea levels with adjustment for land motion. Mar. Geodes. 23, 145−166. https://doi.org/10.1080/014904100501285 91.

Morhange, C., Marriner, N., 2015. Archeological and biological relative sea-level indicators. In: Handbook of Sea-Level Research, pp. 146−156.

Morhange, C., Pirazzoli, P.A., Marriner, N., Montaggioni, L.F., Nammour, T., 2006. Late Holocene relative sea-level changes in Lebanon, eastern mediterranean. Mar. Geol. 230 (1−2), 99−114.

Nerem, S., Mitchum, G., 2001. Observations of sea level change from satellite altimetry. In: Douglas, B.C., Kearney, M.S., Leatherman, S.P. (Eds.), Sea Level Rise: History and Consequences. Academic Press, San Diego, CA, USA, pp. 121−164.

Oelsmann, J., Passaro, M., Dettmering, D., Schwatke, C., Sánchez, L., Seitz, F., 2021. The zone of influence: matching sea level variability from coastal altimetry and tide gauges for vertical land motion estimation. Ocean Sci. 17, 35−57. https://doi.org/10.5194/os-17-35-2021.

Oppenheimer, M., Glavovic, B.C., Hinkel, J., van de Wal, R., Magnan, A.K., Abd-Elgawad, A., Cai, R., Cifuentes-Jara, M., DeConto, R.M., Ghosh, T., Hay, J., Isla, F., Marzeion, B., Meyssignac, B., Sebesvari, Z., 2019. sea level rise and implications for low-lying Islands, coasts and communities supplementary material. In: Pörtner, H.-O., Roberts, D.C., Masson-Delmotte, V., Zhai, P., Tignor, M., Poloczanska, E., Mintenbeck, K., Alegría, A., Nicolai, M., Okem, A., Petzold, J., Rama, B., Weyer, N.M. (Eds.), IPCC Special Report on the Ocean and Cryosphere in a Changing Climate (in press).

Palmer, H.R., 1831. Description of graphical register of tides and winds. Phil. Trans. Roy. Soc. Lond. 121, 209−213.

Passaro, M., Cipollini, P., Vignudelli, S., Quartly, G., Snaith, H., 2014. ALES: a multi-mission subwaveform retracker for coastal and open ocean altimetry. Remote Sens. Environ. 145, 173−189. https://doi.org/10.1016/j.rse.2014.02.008.

Peltier, W.R., 2004. Global glacial isostasy and the surface of the ice-age Earth: the ICE-5G (VM2) model and GRACE. Annu. Rev. Earth Planet Sci. 32, 111−149.

Permanent Service for Mean Sea Level (PSMSL), 2020. Tide Gauge Data. Retrieved 07 Dec 2020 from. http://www.psmsl.org/data/obtaining/.

Pirazzoli, P.A., Laborel, J., Saličge, J.F., Erol, O., Kayan, I., Person, A., 1991. Holocene raised shorelines on the Hatay coasts (Turkey): palaeoecological and tectonic implications. Mar. Geol. 96 (3−4), 295−311.

Pirazzoli, P.A., Stiros, S.C., Arnold, M., Laborel, J., Laborel-Deguen, F., Papageorgiou, S., 1994. Episodic uplift deduced from Holocene shorelines in the Perachora Peninsula, Corinth area, Greece. Tectonophysics 229 (3−4), 201−209.

Poitevin, C., Wöppelmann, G., Raucoules, D., Le Cozannet, G., Marcos, M., Testut, L., 2019. Vertical land motion and relative sea level changes along the coastline of Brest (France) from combined space-borne geodetic methods. Remote Sens. Environ. 222, 275−285. https://doi.org/10.1016/j.rse.2018.12.035.

Ponte, R.M., Carson, M., Cirano, M., Domingues, C.M., et al., 2019. Towards comprehensive observing and modeling systems for monitoring and predicting regional to coastal sea level. Front. Mar. Sci. 6. https://doi.org/10.3389/fmars.2019.00437. Article 437.

Pugh, D., Woodworth, P.L., 2014. Sea-level Science: Understanding Tides, Surges, Tsunamis and Mean Sea-Level Changes. Cambridge University Press, ISBN 978-1-107-02819-7.

Raicich, F., 2007. A study of early Trieste Sea level data (1875−1914). J. Coast Res. 234, 1067−1073. https://doi.org/10.2112/04-0325.1.

Raicich, F., 2020. A 1782−1794 sea level record at Trieste (northern Adriatic), Hist. Geo Space. Sci. 11, 1−14. https://doi.org/10.5194/hgss-11-1-2020.

Raucoules, D., Le Cozannet, G., Wöppelmann, G., De Michele, M., Gravelle, M., Daag, A., Marcos, M., 2013. High nonlinear urban ground motion in Manila (Philippines) from 1993 to 2010 observed by DInSAR: implications for sea-level measurement. Remote Sens. Environ. 139, 386–397. https://doi.org/10.1016/j.rse.2013.08.021.

Roy, K., Peltier, W.R., 2018. Relative sea level in the Western Mediterranean basin: a regional test of the ICE-7G_NA (VM7) model and a constraint on Late Holocene Antarctic deglaciation. Quat. Sci. Rev. 183, 76–87.

Santamaria-Gomez, A., Watson, C., Gravelle, M., King, M., Wöppelmann, G., 2015. Levelling co-located GNSS and tide gauge stations using GNSS reflectometry. J. Geodes. 89, 241–258. https://doi.org/10.1007/s00190-014-0784-y.

Santamaria-Gomez, A., Gravelle, M., Dangendorf, S., Marcos, M., Spada, G., Wöppelmann, G., 2017. Uncertainty of the 20th century sea-level rise due to vertical land motion errors. Earth Planet Sci. Lett. 473, 24–32. https://doi.org/10.1016/j.epsl.2017.05.038.

Sayol, J.M., Marcos, M., 2018. Assessing flood risk under sea level rise and extreme sea levels scenarios. application to the Ebro Delta (Spain). J. Geophys. Res. Oceans 123. https://doi.org/10.1002/2017JC013355.

Scicchitano, G., Spampinato, C.R., Ferranti, L., Antonioli, F., Monaco, C., Capano, M., Lubritto, C., 2011. Uplifted Holocene shorelines at Capo Milazzo (NE Sicily, Italy): evidence of co-seismic and steady-state deformation. Quat. Int. 232 (1–2), 201–213.

Sisma-Ventura, G., Antonioli, F., Silenzi, S., Devoti, S., Montagna, P., Chemello, R., et al., 2020. Assessing vermetid reefs as indicators of past sea levels in the Mediterranean. Mar. Geol. 429, 106313.

Slangen, A.B.A., Carson, M., Katsman, C.A., van de Wal, R.S., Kohl, W.A., Vermeersen, L.L.A., Stammer, D., 2014. Projecting twenty-first century regional sea-level changes. Climatic Change 124, 317–332. https://doi.org/10.1007/s10584-014-1080-9.

Sornoza, L., Barnolas, A., Arasa, A., Maestro, A., Rees, J.G., Hernandez-Molina, F.J., 1998. Architectural stacking patterns of the Ebro delta controlled by Holocene high-frequency eustatic fluctuations, delta-lobe switching and subsidence processes. Sediment. Geol. 117 (1–2), 11–32.

Stanley, J.D., Clemente, P.L., 2017. Increased land subsidence and sea-level rise are submerging Egypt's Nile Delta coastal margin. GSA Today (Geol. Soc. Am.) 27 (5), 4–11.

Stiros, S.C., Laborel, J., Laborel-Deguen, F., Papageorgiou, S., Evin, J., Pirazzoli, P.A., 2000. Seismic coastal uplift in a region of subsidence: Holocene raised shorelines of Samos Island, Aegean Sea, Greece. Mar. Geol. 170 (1–2), 41–58.

The Climate Change Initiative Coastal Sea Level Team, Benveniste, J., Birol, F., Calafat, F.M., Cazenave, A., Dieng, H., Gouzenes, Y., Legeais, J.F., Nino, F., Passaro, M., Schwatke, C., Shaw, A., 2020. Coastal sea level anomalies and associated trends from Jason satellite altimetry over 2002-2018. Sci. Data 7, 357. https://doi.org/10.1038/s41597-020-00694-w.

Tosi, L., Teatini, P., Strozzi, T., 2013. Natural versus anthropogenic subsidence of Venice. Sci. Rep. 3 (1), 1–9.

Tsimplis, M.N., Josey, S., 2001. Forcing the Mediterranean Sea by atmospheric oscillations over the North Atlantic. Geophys. Res. Lett. 28 (5), 803–806.

Tsimplis, M.N., Rixen, M., 2002. Sea Level in the Mediterranean Sea: the contribution of temperature and salinity changes. Geophys. Res. Lett. 29 (23), 2136–2140.

Tsimplis, M., Shaw, A., Flather, R., Woolf, D., 2006. The influence of the North Atlantic Oscillation on the sea level around the northern European coasts reconsidered: the thermosteric effects. Phil. Trans. R. Soc. A 364 (1841), 845–856.

Vacchi, M., Marriner, N., Morhange, C., Spada, G., Fontana, A., Rovere, A., 2016. Multiproxy assessment of Holocene relative sea-level changes in the western Mediterranean: Sea-level variability and improvements in the definition of the isostatic signal. Earth Sci. Rev. 155, 172–197.

Vacchi, M., Ghilardi, M., Melis, R.T., Spada, G., Giaime, M., Marriner, N., Morhange, C., Rovere, A., 2018. New relative sea-level insights into the isostatic history of the Western Mediterranean. Quat. Sci. Rev. 201, 396–408.

Vacchi, M., Ghilardi, M., Stocchi, P., Furlani, S., Rossi, V., Buosi, C., Rovere, A., De Muro, S., 2020a. Driving mechanisms of Holocene coastal evolution in the Bonifacio Strait (Western Mediterranean). Mar. Geol. 427, 106265.

Vacchi, M., Ermolli, E.R., Morhange, C., Ruello, M.R., Di Donato, V., Di Vito, M.A., et al., 2020b. Millennial variability of rates of sea-level rise in the ancient harbour of Naples (Italy, western Mediterranean Sea). Quat. Res. 93 (1), 284–298.

Woodworth, P.L., Gravelle, M., Marcos, M., Wöppelmann, G., Hughes, C.W., 2015. The status of measurement of the Mediterranean mean dynamic topography by geodetic techniques. J. Geodes. 89, 811–827. https://doi.org/10.1007/s00190-015-0817-1.

Woodworth, P.L., Hunter, J.R., Marcos, M., Caldwell, P., Menendez, M., Haigh, I., 2017a. Towards a global higher-frequency sea level data set. Geosci. Data J. 3, 50–59. https://doi.org/10.1002/gdj3.42.

Woodworth, P.L., Wöppelmann, G., Gravelle, M., Marcos, M., Bingley, R.M., 2017b. Why we must tie satellite positioning to tide gauge data. EOS 98, 13–15. https://doi.org/10.1029/2017eo064037.

Wöppelmann, G., Marcos, M., 2012. Coastal sea level rise in southern Europe and the non-climate contribution of vertical land motion. J. Geophys. Res. 117, C01007. https://doi.org/10.1029/2011JC007469.

Wöppelmann, G., Marcos, M., 2016. Vertical land motion as a key to understanding sea level change and variability. Rev. Geophys. 54, 64–92. https://doi.org/10.1002/2015RG000502.

Wöppelmann, G., Pouvreau, N., Simon, B., 2006. Brest sea level record: a time series construction back to the early eighteenth century. Ocean Dynam. 56, 487–497. https://doi.org/10.1007/s10236-005-0044-z.

Wöppelmann, G., Martín Míguez, B., Bouin, M.-N., Altamimi, Z., 2007. Geocentric sea-level trend estimates from GPS analyses at relevant tide gauges world-wide. Global Planet. Change 57, 396–406. https://doi.org/10.1016/j.gloplacha.2007.02.002.

Wöppelmann, G., Le Cozannet, G., De Michele, M., Raucoules, D., Cazenave, A., Garcin, M., Hanson, S., Marcos, M., Santamaria-Gomez, A., 2013. Is land subsidence increasing the exposure to sea level rise in Alexandria, Egypt? Geophys. Res. Lett. 40, 2953–2957. https://doi.org/10.1002/grl.50568.

Wöppelmann, G., Marcos, M., Coulomb, A., Martin Miguez, B., Bonnetain, P., Boucher, C., Gravelle, M., Simon, B., Tiphaneau, P., 2014. Rescue of the historical sea level record of Marseille (France) from 1885 to 1988 and its extension back to 1849–1851. J. Geodes. 88, 869–885. https://doi.org/10.1007/s00190-014-0728-6.

Zanchettin, D., Bruni, S., Raicich, F., Lionello, P., Adloff, F., Androsov, A., Antonioli, F., Artale, V., Carminati, E., Ferrarin, C., Fofonova, V., Nicholls, R.J., Rubinetti, S., Rubino, A., Sannino, G., Spada, G., Thiéblemont, R., Tsimplis, M., Umgiesser, G., Vignudelli, S., Wöppelmann, G., Zerbini, S., 2021. Review article: sea-level rise in Venice: historic and future trends. Nat. Hazards Earth Syst. Sci. https://doi.org/10.5194/nhess-2020-351.

Zerbini, S., Raicich, F., Prati, C.M., Bruni, S., Del Conte, S., Errico, M., Santi, E., 2017. Sea-level change in the Northern Mediterranean Sea from long-period tide gauge time series. Earth Sci. Rev. 167, 72−87. https://doi.org/10.1016/j.earscirev.2017.02.009.

This page intentionally left blank

CHAPTER

Surface wave and sea surface dynamics in the Mediterranean

6

Piero Lionello[1], **Gianmaria Sannino**[2], **Ivica Vilibić**[3]
[1]*University of Salento, Lecce, Italy;* [2]*ENEA, Rome, Italy;* [3]*Ruđer Bošković Institute, Zagreb, Croatia*

Learning Objectives

In this chapter, you will learn:
- What are the basic information on sinusoidal waves and their characteristics in seas and oceans
- What are the basic information on astronomical tides and their causes
- How the tides behave in the Mediterranean Sea
- Which are the characteristics, dynamics and causes of marine storms in the Mediterranean Sea including waves and surges that they produce
- What is the past and expected future evolution of Mediterranean coastal floods and of their causes
- Which tools are available for prediction of waves and sea level extremes in the Mediterranean Sea
- What are the characteristics of tsunamis in the Mediterranean Sea: major past events, their causes (including meteorological factors) and their prediction

6.1 General concepts about waves, definitions and phenomenology

This chapter provides an overview of a wide range of free and forced oceanic waves that are relevant to disentangle major ocean processes and associated coastal risks in the Mediterranean Sea. It includes tides, seiches, wind waves, storm surges, tsunamis. It describes physical processes, characteristics and risks posed by the different phenomena. It also includes for each topic a basic introduction for readers not familiar with the subject.

Wave is a quite generic concept describing processes where a signal travels across a medium. The basic and simplest approach to wave dynamics is based on the concept of sinusoidal wave (Fig. 6.1) propagating along a fixed direction:

$$a(x,t) = A\ \cos(kx - \omega t + \phi), \quad \omega = 2\pi/T \tag{6.1}$$

where A is the amplitude of the wave, which is the maximum deviation of the signal from the equilibrium level. The amplitude has the physical units of the wave, that is

Oceanography of the Mediterranean Sea. https://doi.org/10.1016/B978-0-12-823692-5.00007-8

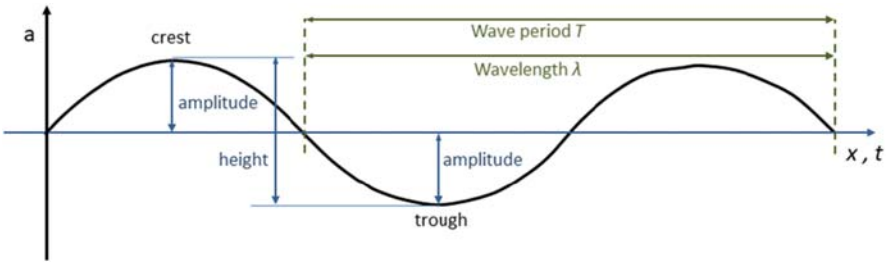

FIGURE 6.1

Representation of a sinusoidal wave: amplitude, wavelength, and period.

the unit of the oscillating quantity. The space coordinate along which the wave propagates is x, t is time, ϕ is a phase constant (which is often neglected in idealized condition by properly selecting the origin of the x axis). The period T is the time (in seconds) for one complete oscillation of the wave at a fixed point. The frequency $f = 1/T$ is the number of periods per unit time (in Hz). The angular frequency ω represents the frequency in radians per second: $\omega = 2\pi f$. The wavelength λ measures the distance (in meters) between two sequential crests or troughs (or any other successive points along the propagation direction with the same phase). The wavenumber k is related to the wavelength by a relation analogous to that relating the circular frequency to the period: $k = 2\pi/\lambda$.

Wavenumber and circular frequency are linked by the dispersion relation, which is presented by a functional dependence of the frequency on the wavenumber: $\omega = \omega(k)$. This implies that having fixed k, the frequency is fixed. In general k should be described as a vector, because the direction is generally important, and the product kx in Eq. (6.1) should be replaced with the scalar product $\vec{k}\vec{x}$. However, in many simple case, for teaching purposes, considering one-dimensional sinusoidal waves is sufficient.

The dispersion relation $\omega = \omega(k)$ describes fully the behavior of a linear wave, because using the Fourier decomposition any arbitrary signal shape can be described as the superposition of sinusoidal components of different wavenumber, each of them with the frequency prescribed by the dispersion relation. The overall signal at any arbitrary time t can be obtained by recombining the individual sinusoidal components.

Two speeds characterize a wave: the phase speed and the group velocity. In formulas:

$$\omega = \omega(k), \qquad c_{ph} = \frac{\omega}{k} = \frac{\lambda}{k}, \qquad c_g = d\omega/dk \tag{6.2}$$

The phase speed c_{ph} describes how the phase of the wave propagates, which can be immediately represented as the speed at which crests progress. The group

velocity c_g describes how the wave energy propagates, that is how the amplitude of the wave propagates. This is shown in Fig. 6.2, representing a propagation of a wave group, that is the region where the wave energy is concentrated. The crests inside the group travel at c_{ph}, but the group itself travels with c_g. Fig. 6.2 shows the wave packet propagation in different cases: nondispersive wave ($c_{ph} = c_g$; $\omega = c_0 k$, case A) dispersive wave ($c_{ph} > c_g$, case B and $c_p h < cg$ case C). In case A, wave crests and packet move at the same speed and the shape of the packet is fixed in time. In cases B and C, the crests propagate faster and slower, respectively, than the packet. In the former (latter) case the wave moves toward the front (back) of the packet, progressively diminishing its amplitude, until it disappears.

Waves occur in the ocean in a very wide range of wavelengths and periods, from the ripples (wavelengths and periods of order 10^{-2} m and 10^{-1} s, respectively) to the planetary waves (wavelengths of thousands of kilometers and monthly periods). Across such a large range the restoring force producing the oscillation change is shown in Fig. 6.3.

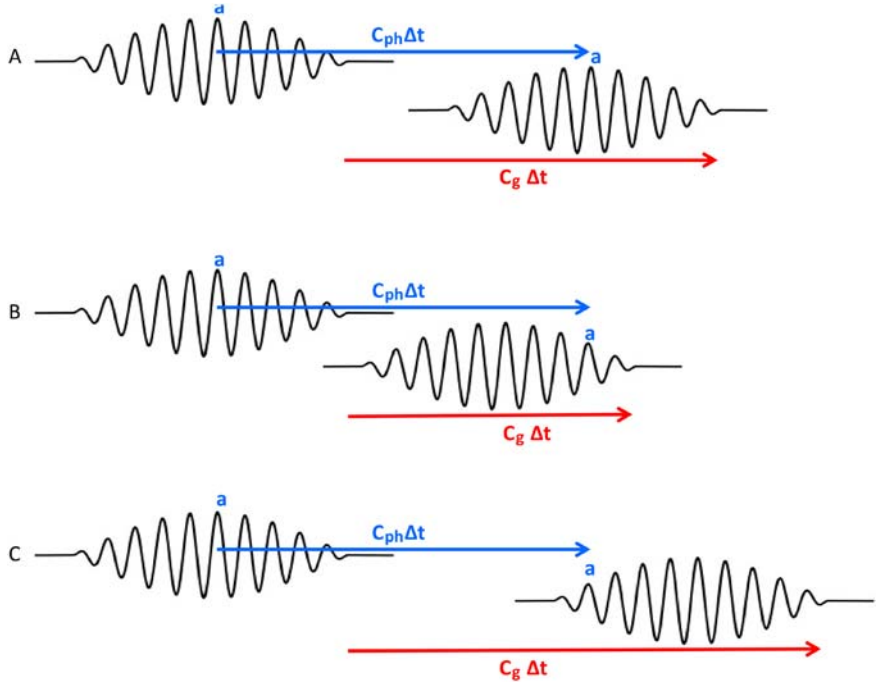

FIGURE 6.2

Wave packet propagation during the time Δt in different cases: nondispersive waves ($c_{ph} = c_g = c_0$; $\omega = c_0 k$, case A); dispersive waves (with the two alternatives: $c_{ph} > c_g$, case B and $c_{ph} < c_g$ case C). The red arrow denotes the space traveled by the front of the packet, the label "a" is used to denote a fixed crest inside the packet and the blue arrow the space traveled by it.

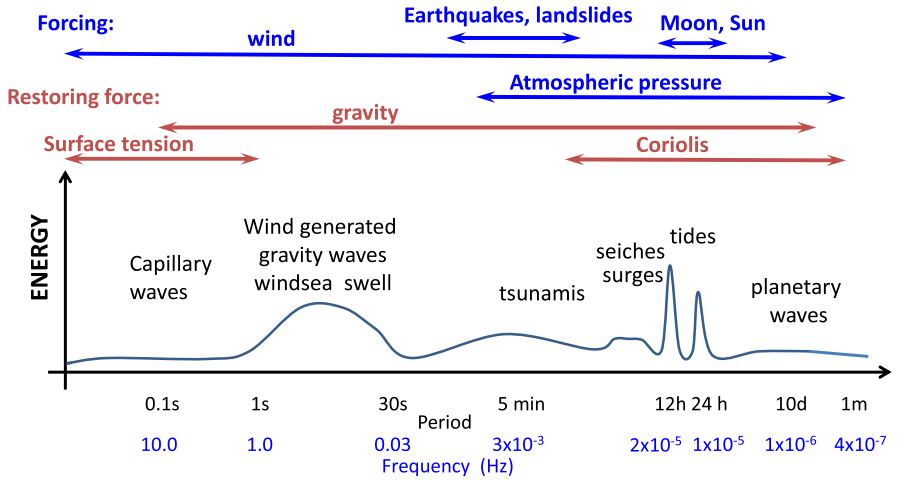

FIGURE 6.3

Qualitative diagram showing the energy (arbitrary scale) distribution as a function of the oscillation period (frequency) of surface waves in the ocean.

At the small spatial scales of ripples the restoring force is the capillary tension, which tends to minimize the area of the surface and bring it back to a flat condition. As wavelength increases, the mass of water displaced from the horizontal unperturbed position increases and so the relative importance of gravity. The transition wavelength at which the two forces are comparable is 1.7 cm. The dispersion relation combining both mechanisms is shown in Table 6.1, together with the two limits of purely capillary and gravity waves in deep water.

Gravity is the dominant force over a broad range of scales, and it is also responsible for waves propagating along the interface between two layers with different water density. In this case, in the dispersion relation, g should be replaced with the reduced gravity g' which accounts for the buoyancy effect of the Archimedean force (Table 6.1).

Gravity waves as they propagate in shallow water are affected by the limitation of water depth. The dispersion relation has two limits for deep and shallow water depending whether the product $\left|\overrightarrow{k}\right|D$ is very large or small. Note that the shallow water limit applies also in the open ocean when the wavelength is larger than a few tens of kilometers, which is typical for the tsunamis produced by earthquakes.

As the space and time scale of the time scale of the motion increase, the Coriolis force contribution becomes progressively large. The criterion for assessing its importance with respect to that of gravity is comparing the wavelength to the Rossby $R_R = \sqrt{gD}/f_c$ deformation radius, where $f_c = 2\Omega_e \sin\phi$ is the Coriolis parameter (Ω_e is the angular rotation speed of the Earth and ϕ is latitude). If λ/R_R is large

(small) the effect of Coriolis is large (small) with respect to gravity. The dispersion relation combining for a shallow water wave the effect of Coriolis force and gravity is the Poincaré-Sverdrup wave. Its limit in case of an infinite wavelength describes the inertial wave, rather frequent in reality, in which the Coriolis force would move uniformly the water mass in circular loops with frequency $f/2\pi$.

A very special case is the Kelvin wave, in which water moves parallelly to the coastline with the gravity (the hydrostatic pressure) and Coriolis forces in exact balance in the cross-shore direction. The Kelvin wave has a fundamental role in the propagation of tides.

Table 6.1 also reports the case of topographic and planetary Rossby waves whose basic dynamics is produced by the conservation of angular momentum accounting for the variation of the Coriolis parameter with latitude and/or of the depth of the water.

Table 6.1 Dispersion relation for ocean waves. $\omega\ \vec{k}\ g\sigma\rho\Delta\rho Df\phi R_e\gamma N\Theta$.

Deep water gravity capillary waves,	$\omega^2 = g\lvert\vec{k}\rvert + \frac{\sigma}{\rho}\lvert\vec{k}\rvert^3$
Deep water gravity waves,	$\omega^2 = g\lvert\vec{k}\rvert;\ \lvert\vec{k}\rvert D \gg 1$
Deep water interfacial gravity waves,	$\omega^2 = g'\lvert\vec{k}\rvert;\ g' = g\Delta\rho/\rho_0$
Capillary waves	$\omega^2 = \frac{\sigma}{\rho}\lvert\vec{k}\rvert^3$
Gravity waves (general)	$\omega^2 = g\lvert\vec{k}\rvert\tanh\left(\lvert\vec{k}\rvert D\right)$
Shallow water gravity waves and Kelvin waves	$\omega = \lvert\vec{k}\rvert\sqrt{gD};\ \lvert\vec{k}\rvert D \ll 1$
Poincaré-Sverdrup waves	$\omega^2 = f^2 + gD\lvert\vec{k}\rvert^2$
Topographic and planetary Rossby waves [a]	$\omega = -\frac{\beta_T k}{f^2/gD + \lvert\vec{k}\rvert^2};\ \beta_T = \frac{df}{R_e d\phi} - \frac{\gamma f}{D}$
Planetary Rossby waves (long)	$\omega = -\frac{\beta_T k}{\lvert\vec{k}\rvert^2};\ \frac{\lambda}{R_R} \gg 1$
Rossby waves (short)	$\omega = -\frac{gD\beta_T\lvert\vec{k}\rvert}{f^2};\ \frac{\lambda}{R_R} \ll 1$
Internal waves	$\omega^2 = f^2\sin\Theta + N^2\cos\Theta\ ;\ N^2 = -\left(\frac{g}{\rho}\frac{d\rho}{dz} + \frac{g^2}{c_s^2}\right)$

Meaning of symbols: ω *circular frequency,* $\vec{k}$ *wavenumber,* g *acceleration of gravity,* σ *surface tension,* ρ *water density,* $\Delta\rho$ *density contrast and density average of upper and lower layer,* D *water depth,* f *Coriolis parameter,* ϕ *Latitude,* R_e *radius of Earth,* γ *slope of sea bottom,* N *Brunt-Väisälä (buoyancy) frequency,* Θ *wave propagation angle with respect to the horizontal plane.*

[a] *for algebraic simplicity the bottom slope is assumed in the north-south direction.*

The interfacial gravity waves are a special case of internal waves when a discontinuity on the vertical profile of density is present. In the case in which the stratification is continuous, waves can propagate at an arbitrary angle Θ with respect to the horizontal plane ($\Theta = 0$ and $\Theta = \pi/2$ corresponding to horizontally and vertically propagating waves).

While the restoring force is responsible for the dynamics producing the oscillation, the energy of waves is produced by an external source. Wind is the source of energy for capillary and wind waves, which grow by the transfer of momentum and energy from the air flow. Tsunamis are produced by sudden motions of the sea floor or of the coastal slope with different extension, from submarine landslides (producing generally only small tsunamis) to explosions of oceanic calderas and earthquakes. Synoptic and mesoscale atmospheric perturbations can trigger large-scale waves (such as inertial waves) and meteotsunamis. The periodic variation of the strength of the astronomical attraction exerted by the Moon and the Sun on a water mass at the Earth's surface causes astronomical tides. Internal waves can be triggered by tidal currents in the presence of sharp features of the bottom topography.

Fig. 6.3 also includes surges and seiches. Generally, storm surge denotes the positive anomaly produced by a storm and it is the result of superposition of a static response, forced waves (e.g., forced Kelvin waves) and free wave propagation. Seiches are standing waves that represent the normal oscillation modes of water bodies such as gulfs and basins. Their frequencies depend on the depth, shape and extension of the basin and range from minutes (for small water bodies) to around 1 day for large, elongated basins such as the Adriatic Sea. They result from the superposition of long shallow water waves that propagates across the basin under the effect of the gravity and Coriolis forces when, after a storm, the large-scale surface anomaly is not anymore sustained by the mechanical action of wind and atmospheric pressure.

6.2 Tides and seiches

6.2.1 Generalities and basic definitions

Though the periodic rise and fall of the sea level is evident to most observers, tidal currents, among the strongest in the world ocean, are the fundamental phenomenon, whose convergence or divergence at the shore produces the vertical motion of the sea surface. Tidal currents are caused by the gravitational pull of celestial bodies, specifically the Sun and the Moon, because the other planets in the solar system exert tidal forces that are so small in comparison that they are quite negligible. Tidal movements occur in the atmosphere as well as in the solid earth, but here we consider exclusively the oceanic and sea.

Due to the relative motion of the Moon and Sun with respect to a fixed point at the Earth's surface, their force of attraction changes with time and it is not uniform in space. For local tide prediction, the temporal response of the ocean is very linear, so

the tide recordings can be interpreted as a superposition of periodic components with frequencies associated with the motions of the celestial bodies. The spatial response is influenced by the presence of continents and by the seabed topography. Ocean tides, especially in closed sea areas such as the Mediterranean Sea, due to unequal water depths and to the fact that the complex coastlines prevent the free movement of water masses, deviate substantially from the theoretical values that would be computed for an Earth with no continents and covered by an ocean with uniform depth.

The tide generating force is given by the sum of gravitational and centrifugal forces. The computation of the forces producing the tides can be considered in a reference frame revolving with the Earth around the gravitational center of the Moon-Earth (or Sun-Earth) system. The geometry of the Moon-Earth and the Sun-Earth systems differ in that the former has its center of mass in the Earth interior (at about 4600 km from the Earth center), while the center of mass of the latter practically coincides with that of the Sun. However, this difference is not relevant for understanding the mechanism producing the tides. In this noninertial reference frame, the gravitation exerted by the celestial body (either the Sun or the Moon) and the centrifugal force balance exactly each other in the center of Earth. However, gravity is larger than the centrifugal force in all points of the hemisphere facing the celestial body. The difference has a maximum at the point crossing the Earth's surface along the line joining the centers of the two bodies (Zenith). Conversely, gravity is smaller than the centrifugal force in all points of the opposite hemisphere with the maximum at the point opposite to the Zenith (Nadir) (Fig. 6.4). The difference is always parallel to the direction joining the center of the Earth and of the celestial body. The component orthogonal to the Earth's surface (vertical component) is negligibly smaller than gravity and its effect on the ocean can be disregarded. The magnitude

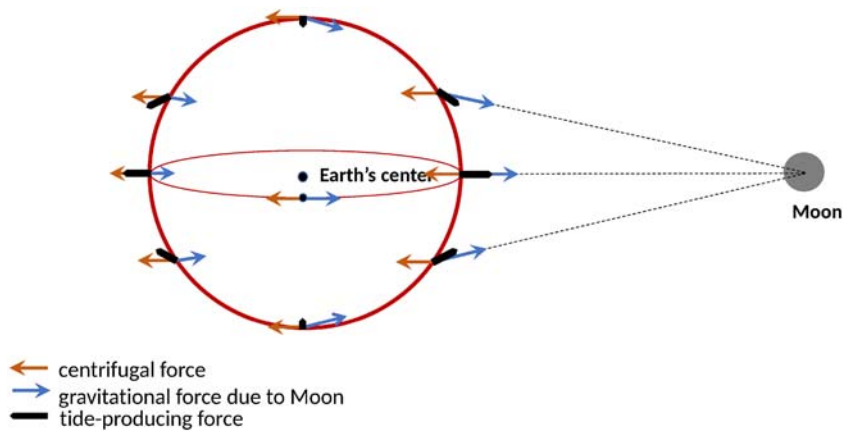

FIGURE 6.4

The tide generating force as the resultant of centrifugal and gravitational forces for the Earth-Moon system.

and direction of component parallel to the Earth's surface vary depending on its position (Fig. 6.5) and produces the tides. In fact, it would move water masses along the Earth's surface until when it would be balanced by the hydrostatic pressure caused by a nonuniform sea level. This is the concept of equilibrium tide, consisting of bulges of water, with maxima at the Zenith and Nadir.

The Earth daily rotation does not affect the results of the balance of gravitational and centrifugal forces. Its only effect on the tides is that it shifts the entire tidal force field (Fig. 6.5) around the Earth once a day, introducing the semidiurnal periodicity of the tides as the two bulges circle daily around the Earth. The tilt of the Earth rotation axis would imply that the two bulges would circle around the surface at different latitudes, producing an asymmetry that causes the diurnal periodicity of tides.

Since tides are not generated by the absolute gravitational force exerted by the Sun and the Moon, but rather by the differences in their gravitational fields on the Earth's surface, as the Moon is closer to the Earth, the variations of gravitational force field is larger for the Moon than for the Sun. A quantitative analysis shows that the differences in gravitational forces on the Earth's surface are proportional to the inverse of the cube of the Sun-Earth and Earth-Moon distances. This effect prevails over that of the larger mass of the Sun, and consequently, the tidal force of the Sun is only about 46% of that of the Moon. Other celestial bodies do not exert a significant tidal force.

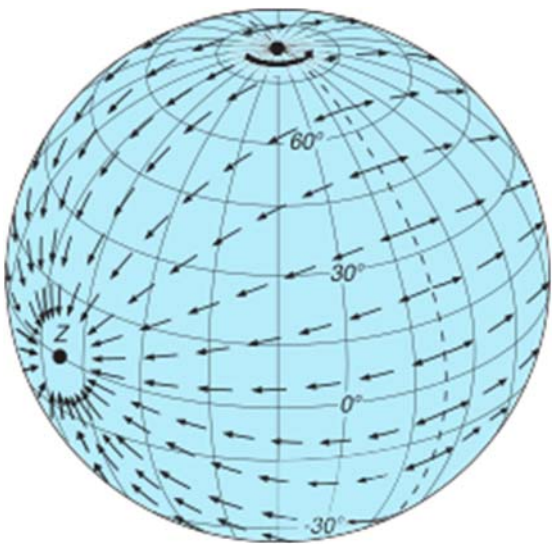

FIGURE 6.5

A snapshot of the horizontal component of the tidal force on Earth when the Moon is above the Equator at Z ('zenith'). This field rotates daily around the Earth with the Moon.

From Dietrich G., Kalle, K., Krauss, W., Siedler, G., 1980. General Oceanography, second ed. Translated by Susanne and Hans Ulrich Roll. John Wiley and Sons (Wiley- Interscience), New York.

This basic reasoning leads to immediate understanding of basic tidal oscillations, those produced by the Moon, i.e.,

- M2 (semidiurnal lunar), period: 1/2 lunar day = 12 h 25 min
- O1 (diurnal lunar), period: 1 lunar day = 24 h 50 min

by the Sun, i.e.,

- S2 (semidiurnal solar), period 1/2 solar day = 12 h

and jointly by the two celestial bodies, i.e.,

- K1 (diurnal lunisolar), period, 1 sidereal day = 23 h 56 min.

The tides can be expressed as the sum of the harmonic oscillations with these periods, plus the harmonic oscillations of all other combination periods. This classification is due to Thomson in the late 19th century (Thomson, 1898) and the table of the Tidal Committee of the International Hydrographic Organization reports 409 constituents. Each oscillation, known as a tidal constituent, has its own amplitude, period and phase, which can be extracted from observations by means of harmonic analysis. Hundreds of these oscillations have been identified and are used for tidal tables, mainly for navigation purposes. The number of components needed for an accurate description depends on the location. In the Mediterranean Sea, tides are low in comparison with most ocean basins and a good accuracy is obtained using few components.

The form factor F is adopted for classifying tides:

$$F = (K1 + O1)/(M2 + S2) \tag{6.3}$$

where the symbols of the tidal constituents indicate their respective amplitudes. Four categories are distinguished:

- $0 < F < 0.25$ semidiurnal
- $0.25 < F < 1.5$ mixed, mainly semidiurnal
- $1.5 < F < 3$ mixed, mainly diurnal
- $F > 3$ diurnal

Only in the largest water bodies tides are forced directly by the action of the tidal forces inside the basin. Marginal seas and gulfs are forced also by the periodic variations of sea level along their open boundaries. As the size of the basin decreases, the relative importance of the internal forcing decreases, becoming negligible for small gulfs. Already at the size of the Adriatic Sea, tides are mostly forced by the oscillation at the Otranto Strait connecting it to the rest of the Mediterranean Sea.

If the tidal range resonates with a seiche period of a sea or bay, the tidal range will increase dramatically, becoming very large in some places. This is the case of the Bay of Fundy on the east coast of Canada, where the tidal range is 14 m, St. Malo in France with 10 m. The tidal range is, in general, maximum at the inner end of the bay, which is consistent with the tidal dynamics of open basins. The Adriatic Sea is a very good example of tides in an elongated marginal sea and of resonance with the diurnal and semidiurnal tides, whose period is very close to 22 and 11 h periods of its main seiches (Lionello et al., 2005).

Tides exhibit a back-and-forth movement of water through lines of no vertical movement called nodes, and the wave can become a movement around points of no vertical motion inside the ocean, called amphidromic points on the rotating Earth, where the tidal range is zero. Tidal charts are a traditional representation of tides (Fig. 6.6). They include two sets of lines: co-range lines (constant tidal amplitude), which run around the amphidromic points almost circularly, and co-phase lines (constant phase lines, or lines connecting all places where high/low water level occurs simultaneously), which emanate from the amphidromic points like the spokes of a wheel.

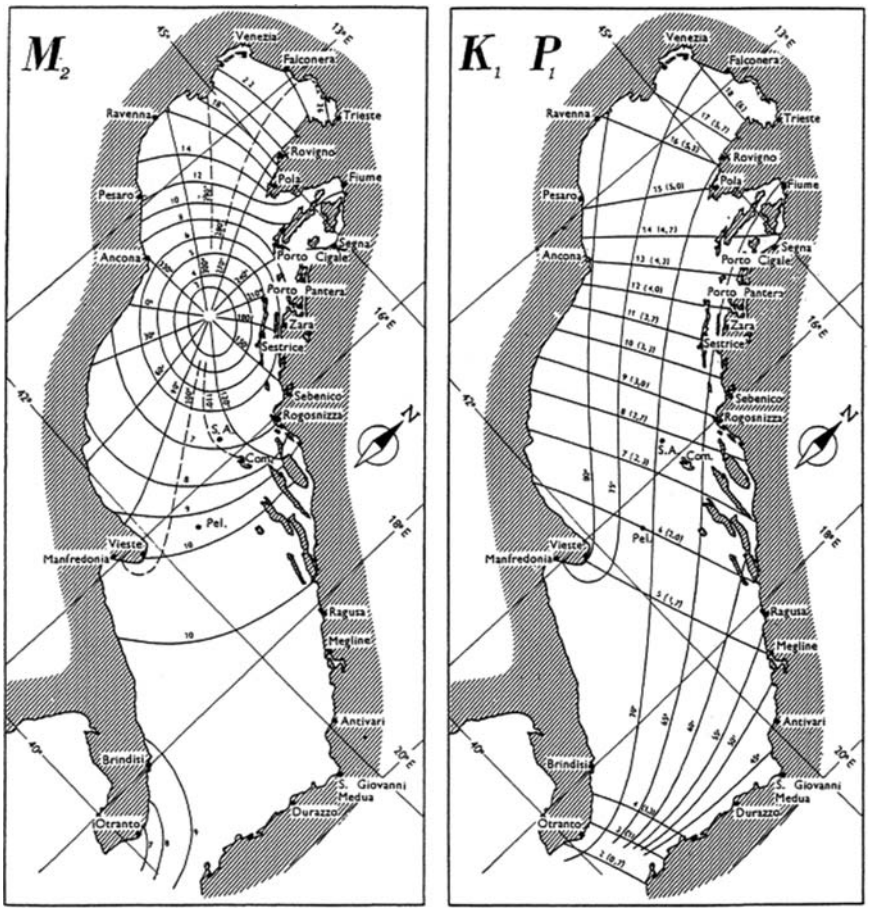

FIGURE 6.6

Tidal chart with corange and cophase line describing the M2 semidiurnal and K1 diurnal tides in the Adriatic Sea.

From Cushman-Roisin, B., Naimie, C.E., 2002. A 3D finite-element model of the Adriatic tides. J. Mar. Syst. 37 (4), 279–297 after original from Polli, 1960 La propagazione delle maree nell'Alto Adriatico. Publications of the Istituto Sperimentale Talassografico-Trieste 370. 1960

The details of the shape of the tidal wave depend on the configuration of the ocean basin and are challenging to assess. A computer-based model can describe the behavior of tides. Its results need to be validated against observations of tidal levels and the time of occurrence of high and low tides. Tidal models can be categorized into three groups: hydrodynamic, empirical, and assimilation models. Hydrodynamic models are derived by solving the Laplace Tidal Equations and using bathymetry data as boundary conditions. Empirical models are derived by extracting ocean tidal signals from satellite altimetry and they describe the total geocentric ocean tides, which include the ocean loading effect. Those models can be used directly in altimetry applications such as ocean tide corrections. Assimilation models are derived by solving the hydrodynamic equations with altimetric and tide gauges data assimilation.

6.2.2 Tides in the Mediterranean Sea

The Mediterranean Sea has a complex topography with deep basins separated by sills and islands and circumvented for the most part by narrow shelves, with the important exceptions of the Tunisian shelf and the relatively shallow Adriatic and Aegean Seas. The Mediterranean basin itself can be seen as a composite of semienclosed basins, the largest being the Western and Eastern basins separated by the Sicily Channel (and the minor Strait of Messina). This complex topography, which has been extensively described in Chapter 2, drives the tidal structure of the basin.

Tidal amplitudes in the Mediterranean Sea are generally small compared with the adjacent Atlantic Ocean. Bathymetric features locally amplify tides in several areas, such as the Strait of Gibraltar, where Atlantic water and tides enter in the basin and propagate, and the Sicily. Tidal effects are also relevant in the Strait of Messina, the narrow passage separating Sicily from the continental part of Italy, where very strong tidal currents occur, and in the northern part of the Adriatic Sea.

In the Strait of Gibraltar and the Strait of Messina, spectacular effects of the tides have been evidenced by remote observations. Synthetic Aperture Radar images acquired by American and European satellites have revealed the signatures of trains of internal solitary waves generated by the interaction of tidal currents with shallow topographic features (see, e.g., the book by Barale and Gade, 2008, and references therein). In the Strait of Gibraltar, the identical signatures have also been reproduced by a high-resolution, nonhydrostatic simulation performed by Sanchez-Garrido et al. (2011).

The tides of the Mediterranean Sea are semidiurnal, according to Eq. (6.3), with an important diurnal component (Fig. 6.7). They result from the combination of internal gravitational forcing and of the Atlantic tides that penetrate through the Strait of Gibraltar (Tsimplis et al., 1995). A barotropic model (single layer) model can reproduce the tidal parameters derived from tide gauges with very good accuracy (Tsimplis et al., 1995) and many practical management purposes are effectively served by simply considering the linear superposition of tides and wind-driven surges (e.g., high water events in the Lagoon of Venice). However, impact evaluation

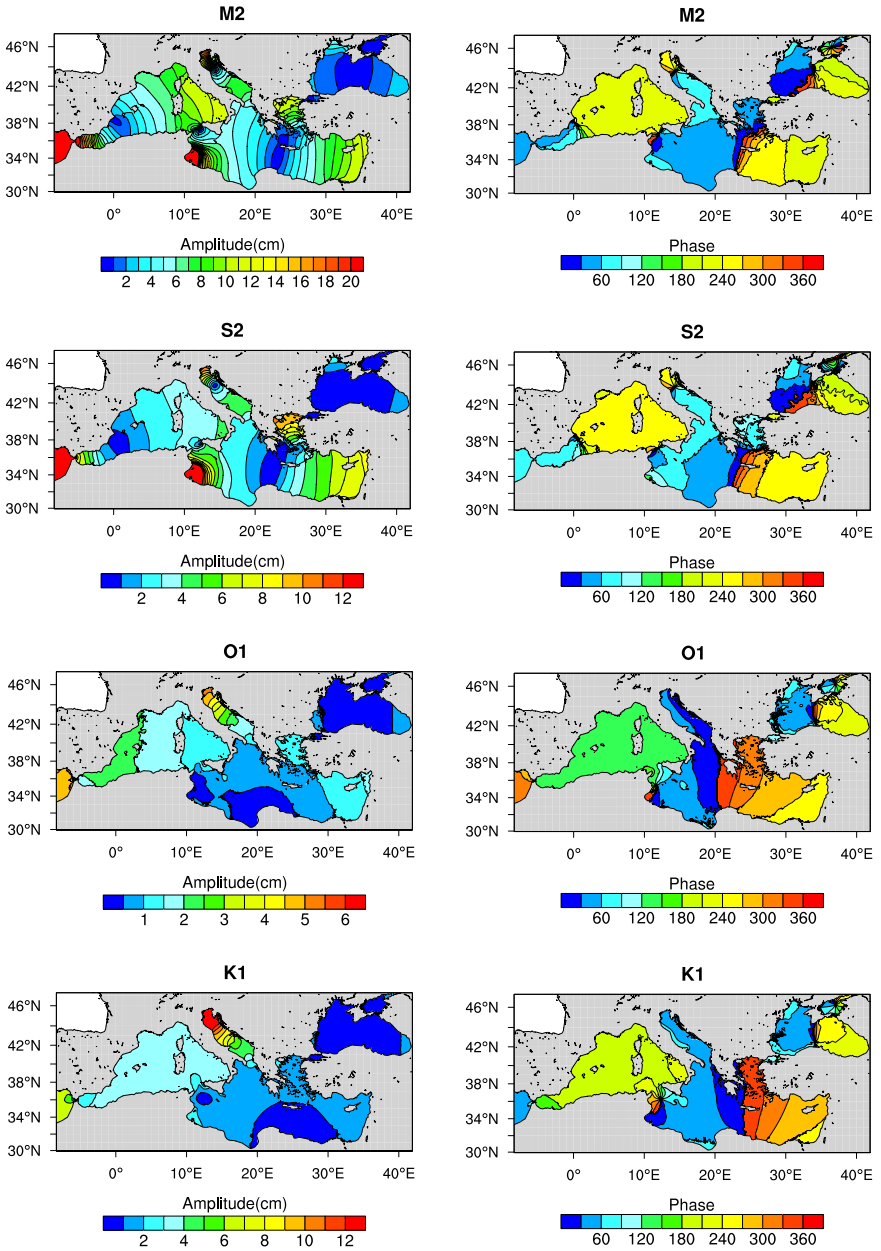

FIGURE 6.7

Spatial distributions of amplitude (left column) and phase (right column) of the main semidiurnal (M2 and S2) and diurnal (K1 and O1) tidal constituents, based on model simulation validated against tide gauges.

From Palma, M., Iacono, R., Sannino, G., Bargagli, A., Carillo, A., Fekete, B.M., et al., 2020. Short-term, linear, and non-linear local effects of the tides on the surface dynamics in a new, high-resolution model of the Mediterranean Sea circulation. Ocean Dynam. 70, 935–963.

in complex and sensitive coastal areas require a modeling framework capable of simultaneously describing all the relevant processes, including the residual circulation originating from the interaction of the density field, river flow, and the nonlinear rectification of the periodic tides (Maas and Zimmermann, 1989). Eddy-resolving three-dimensional Mediterranean tidal models, with high horizontal resolution in the region of the Strait of Gibraltar, simulate the propagation of the tidal signal from the north Atlantic Ocean and show the role of tidal forcing on main features of the Mediterranean thermohaline circulation, with intensification of local mixing processes, and consequences on critical processes, such as deep water formation in the Gulf of Lion and intermediate water recirculation (Sannino et al., 2015).

Eddy-resolving three-dimensional models (Palma et al., 2020) have shown that tidal effects in the Mediterranean cannot be linearly superimposed on the basin circulation. Tides significantly modulate water transports across the Strait of Gibraltar, the Sicily Channel, the Corsica Channel and the Otranto Strait. In addition, tidal effects induce local modulations of some of the main currents exciting topographic waves over the Adventure Bank and the Malta Plateau, in the Sicily Channel, in the eastern portions of the Corsica Channel and the Otranto Strait. Furthermore, in several locations (Sicily Channel, Corsica Channel, Strait of Messina, North Adriatic Sea), the spectral analysis of the mean kinetic energy reveals the presence of spectral peaks corresponding to periods of about 8 and 6 h, which can only be interpreted as harmonics (overtides and compound tides) of the diurnal and semidiurnal tidal components, generated through nonlinear interactions.

6.3 Marine storms and coastal floods in the Mediterranean Sea

Marine storms are a severe weather phenomenon. They generate high waves, strong currents, and large sea level anomalies resulting in hazards that pose risks at the coastlines. Coastal impacts are mostly caused by storm surges (the abnormal rise of sea level during a storm) with consequent floods. In compound events, where multiple factors such as severe winds, high waves, and intense precipitation combine their impacts on the coast, the hazard can be nonlinearly amplified.

Marine storms have a strong impact on a number of sectors: (1) navigation, as they affect its safety and cause shipwrecks, victims and accidents (Abaei et al., 2018), (2) port operations, as they prevent regular traffic in the ports and interrupt supply lines, in particular along the major routes (Adam et al., 2016), (3) coastal infrastructures, as they endanger buildings, roads, transportation and defense structures (Sutton-Grier et al., 2015), (4) human security, as they might cause victims and threaten the health of coastal populations (Adelekan, 2010; Lane et al., 2013).

In the Mediterranean, there are many examples of marine storms that produced very severe damages and victims. Events are well documented along the northern coasts, where coastal infrastructures are exposed to the severe storms coming

from west to northwest. Examples of devastating storms in recent times is the Vaia Storm (Cavaleri et al., 2020a; Davolio et al., 2020), which hit northern Italy and the Adriatic Sea at the end of October 2018, causing around three billion euros in damage and death of 11 people, and the storm that on November 12, 2019 caused an exceptional flood in Venice (Ferrarin et al., 2021), second only to the highest flood that occurred on November 4, 1966 (De Zolt et al., 2006). Another example is the Storm Gloria (Amores et al., 2020), which in 2020 devastated the Mediterranean Spanish coastlines and southern France, lasting for several days. These extreme marine storms are typical for the Mediterranean Sea, where in some cases storms develop quickly and intensely, having a relatively rapid transit time over the coastal areas, with gale winds and heavy precipitation, while in other cases storms are blocked in their motion by the stationarity of the planetary processes with negative consequences in the area where they persist.

6.3.1 Storm surges

Storm surges are produced by the combined mechanical action of wind and the atmospheric sea level pressure gradient. In steady condition, the slope of the sea surface elevation is given by the equation:

$$\rho g \frac{\partial \eta}{\partial x} = -\frac{\partial p_a}{\partial x} + \frac{\tau_x^w}{H} \tag{6.4}$$

with η the vertical displacement of free surface, p_a the atmospheric sea level pressure and τ_x^w the wind stress and H water depth, complemented by the analogous expression for the y-direction. Although the temporal behavior including the transient response and the action of the Coriolis force and friction can be much different from this steady condition, Eq. (6.4) shows two important characteristics. The action of the atmospheric pressure is described as the inverse barometer effect, meaning that a negative pressure anomaly causes a positive sea level anomaly. The equation shows that this effect is linear and 1 hPa pressure anomaly determines approximately 1 cm sea level anomaly. The wind stress, which is approximately proportional to the square of the wind speed ($\tau_x^w = \rho C_D U_{10}^2$, where C_D itself is a linear function of the wind speed) produces a sea slope, which is inversely proportional to the water depth. The slope is typically of the order of 10^{-5}. If the fetch (i.e., the extension of the sea under the action of the wind) is of the order of 100 km, the resulting contribution, called wind set-up, to the surge is of the order of meters. The comparison wind set-up and inverse barometer effect shows that the action of the wind is the main factor producing storm surges in shallow seas and explain the large values of the storm surge extremes shown in Fig. 6.8 in the northern Adriatic and the Gulf of Gabes, where during a storm strong winds blow toward the shore over a shallow sea.

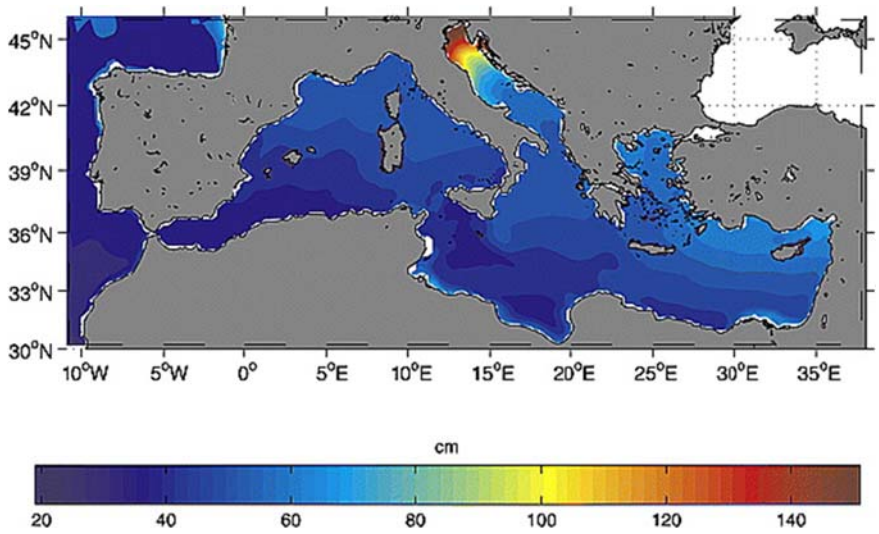

FIGURE 6.8

Extreme sea level with an average return period of 50 years. Values have been produced by a sea level hindcast of tides and storm surges.

From Marcos, M., Tsimplis, M.N., Shaw, A.G.P., 2009. Sea level extremes in southern Europe. J. Geophys. Res. 114, C010017.

6.3.2 Planetary scale forcing of storm surges

The flood of Venice in November 2019 (Cavaleri et al., 2020b) shows that storm surges, particularly in areas prone to coastal flooding like the northern Adriatic, may occur in sequences lasting some weeks (Godin and Trotti, 1975). There is a variety of processes that, occurring over time scale from weeks to a few months, may generate persisting positive sea level variations creating the conditions for repeated floods. Some of them are partially connected with the planetary atmospheric wave forcing (Pasarić et al., 2000), others with changes in heat and water budget, variability in freshwater coming from rivers, and changes in ocean circulation.

Planetary atmospheric waves, or Rossby waves (Rossby, 1939) owe their existence to the change of planetary vorticity with latitude. They can encompass a large portion of a hemisphere, depending on their maturity—zonal circulation versus blocking omega circulation—spanning over tens of degrees with longitudinal wavelengths of 6000–8000 km. They can propagate both eastward and westward, depending on their wavelength and mean zonal wind speed. They can persist over the same area for periods ranging from a few days to months, when the zonal wind speed balances their phase velocity. The latter case may cause so-called blocking situations in the atmosphere and may precondition long-lasting severe weather phenomena (e.g., heat and cold waves, Ruti et al., 2014).

The atmospheric convection and the cyclogenesis normally occur ahead of a planetary wave trough due to convergence (Davis and Emanuel, 1991), while the wave crest front is characterized by an anticyclone, with consequences on surface air pressure and wind regimes that are forcing the variations of the sea surface. Therefore, planetary waves can cause sea level variations at scales from a week to a few months that contribute significantly during flooding events, particularly where the tides are not large (Šepić et al., 2012). In regions prone to large coastal flooding, the magnitude of the contribution of planetary atmospheric waves forcing to sea level extremes and coastal flooding is generally similar to the tidal and synoptic-scale contributions (Fig. 6.9, Pasarić and Orlić, 2001). However, synoptic-scale forcing is the dominant contributor to sea level extremes during extreme events in the northernmost regions, e.g., the northwestern Adriatic Sea (Lionello et al., 2021a). In the Mediterranean, the planetary atmospheric wave contribution increases from the south toward the north coasts, having maxima at its northernmost enclosed and shallow regions, like the northern Adriatic Sea, the Gulf of Lion and the northern Aegean Sea (Šepić et al., 2012, Fig. 6.10).

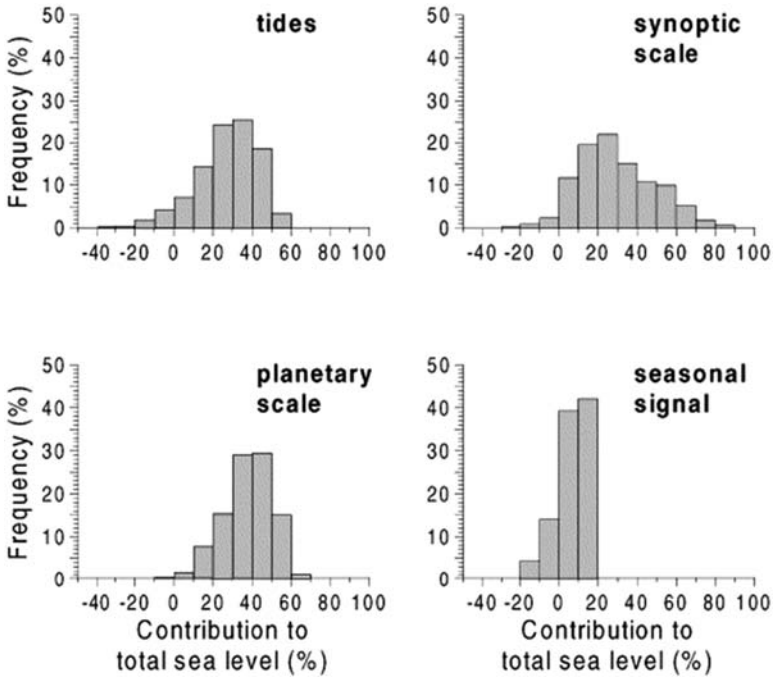

FIGURE 6.9

Distributions of different sea level contributors for coastal floods at the Bakar tide gauge. Coastal floods are defined as hourly sea level heights surpassing the 99.5 percentile in the period between November 1, 1983 and December 31, 1997.

From Pasarić, M., Orlić, M., 2001. Long-term meteorological preconditioning of the North Adriatic coastal floods. Cont. Shelf Res. 21, 263–278.

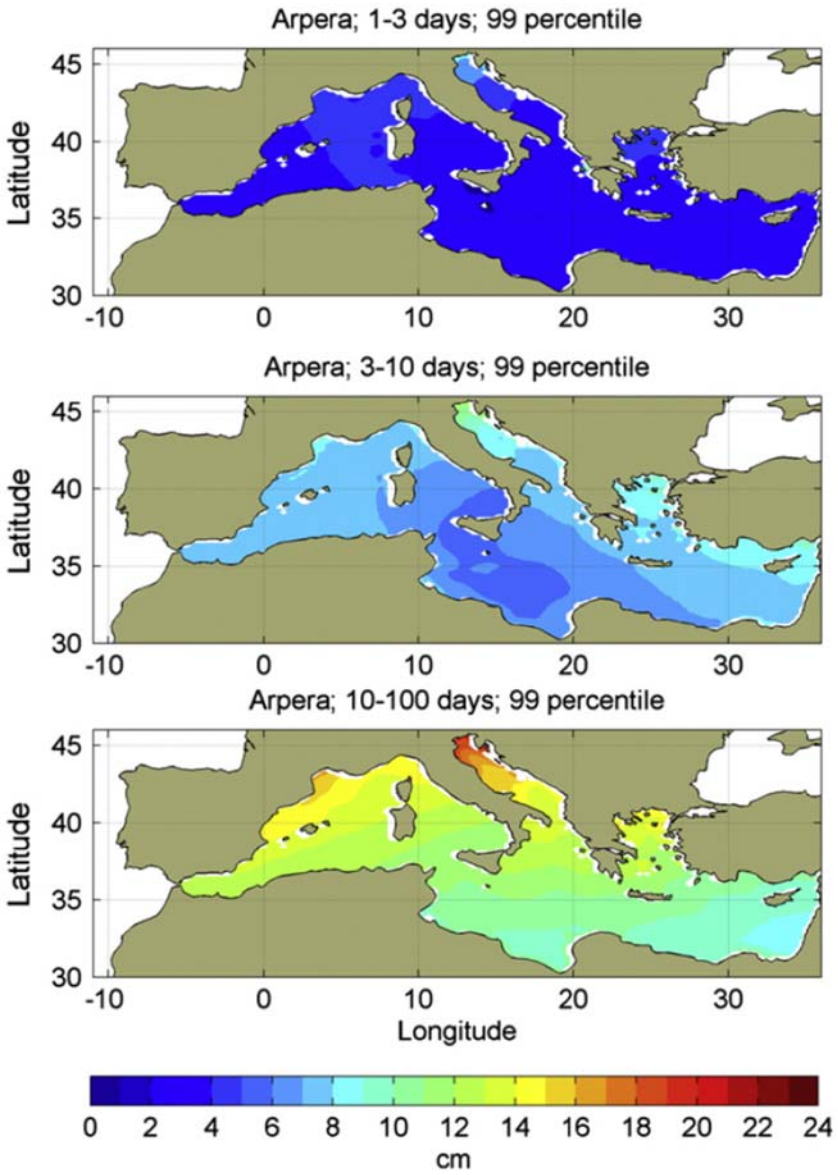

FIGURE 6.10

Distribution of the 99th percentile of sea level variability values obtained from a hindcast model run (1958–2008) for three period bands. The contribution of planetary waves is most relevant in the 10–100 days band.

From Šepić, J., Vilibić, I., Jordà, G., Marcos, M., 2012. Mediterranean sea level forced by atmospheric pressure and wind: variability of the present climate and future projections for several period bands. Global Planet. Change 86–87, 20–30.

6.3.3 Synoptic scale forcing of storm surges

Synoptic scale forcing is a major contributor to sea level extremes, as coastal floods occur most frequently during the storm peak, which is often associated with the frontal zones within cyclones. The synoptic-scale weather systems—cyclones and anticyclones—range in size from some hundreds of kilometres to a few thousand of kilometers and move with a speed that is prevalently determined by the planetary atmospheric wave dynamics. Thus, they might move fast, crossing a whole Mediterranean subbasin in a single day, or be stuck for a week or longer in an extreme blocking situation. Fast moving cyclonic systems tend to cause extreme sea levels and coastal flooding mostly in the northern midlatitudes (e.g., North Sea, Ross et al., 2018), while the blocking weather situations and slow moving cyclones are frequent in the Mediterranean Sea (Lionello et al., 2016).

Sea level extremes in the Mediterranean are frequently produced by a cyclogenesis occurring inside the basin that is driven by the midlatitude storm track (Lionello et al., 2019). The interaction of Atlantic cyclones crossing central and northern Europe with the sharp orography around the Mediterranean Sea is further reinforced by air-sea interaction and result in strong cyclogenesis at certain regions like the Ligurian Sea, lee of the Atlas Mountains and the Aegean Sea (Trigo et al., 1999). Fig. 6.11 shows the average evolution of cyclones producing storm surges at various cities along the Mediterranean coasts. As mentioned in Section 6.3.1, the wind set-up produced by cyclones is amplified over wide shelves (Dodet et al., 2019), so that highest sea level extremes are found in the shallow northern Adriatic Sea and Gulf of Gabes (Marcos et al., 2009), where winds accumulate water toward the closed end of the basin.

The Sirocco wind is the major generator of coastal flooding in the northern Adriatic, in particular in the Lagoon of Venice, where substantial floods are recorded with a dominant contribution of synoptic-scale forcing. The level of the Sirocco-driven sea level surge is extremely sensitive to the wind intensity, duration and spatial extent (Lionello et al., 2021a), as well as wind direction (Međugorac et al., 2018). Small differences of cyclone path, intensity, and speed may result in significant differences of the storm surge setup in the most sensitive areas. This was particularly relevant for the 2019 flood of Venice, where an improper forecast of near-shore processes resulted in about 40 cm underestimation of the surge (Ferrarin et al., 2021). In general, strong winds at the front sections of cyclones, blowing toward the northern Mediterranean coastlines, rise sea level, often in synergy with the air pressure forcing, and are normally connected with sea level extremes, whose values depend on the orientation of the coastline, intensity and duration of the wind (Wakelin and Proctor, 2002; Ullmann and Moron, 2008; Letetrel et al., 2010; Krestenitis et al., 2011; Androulidakis et al., 2015; Cid et al., 2016; Pérez Gómez et al., 2021).

Synoptic-scale forcing has a substantial interannual variability, which is strongly reflected in the intensity of sea level extreme and coastal floods between years (see the case of the northern Adriatic in Fig. 6.12). During extreme coastal flooding, this contribution may be substantially larger, like during the record-breaking flood of Venice on November 4, 1966, when the synoptic-scale contribution was 25% larger than for any other recorded modern flood (Lionello et al., 2021a; Ferrarin et al., 2022).

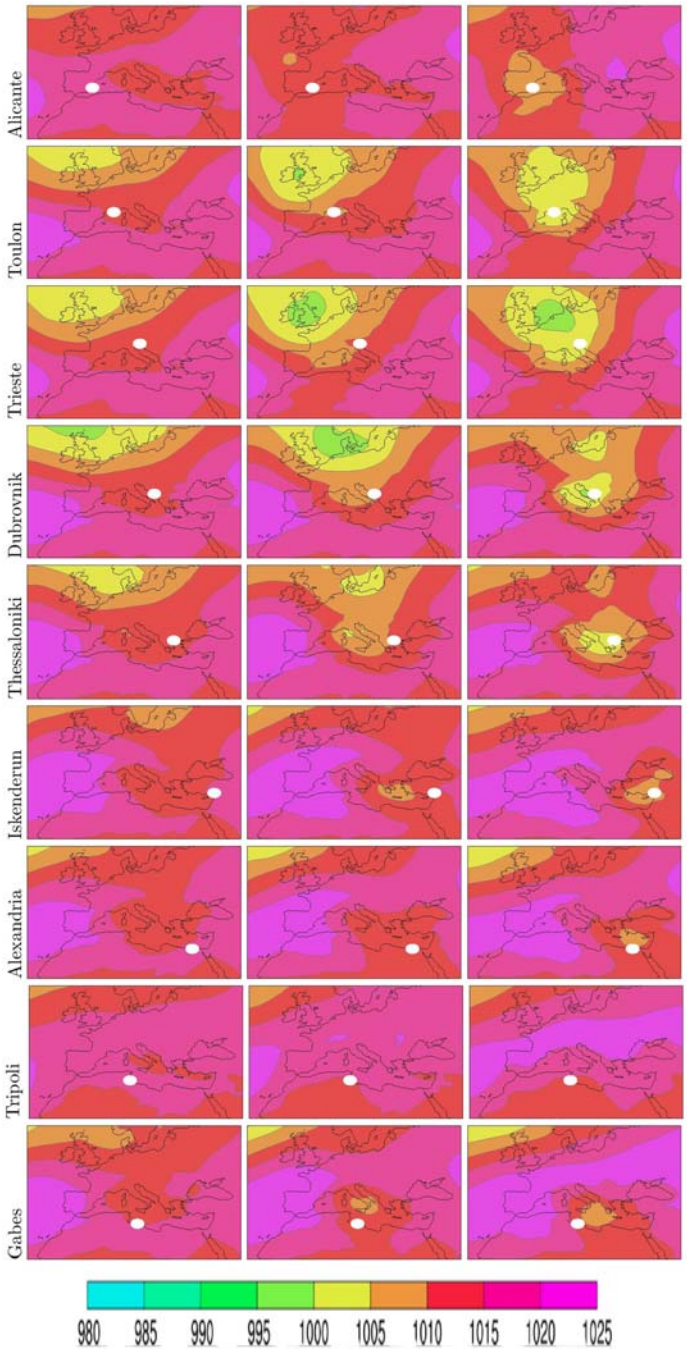

FIGURE 6.11

Composites of ERA-Interim MSLP fields (in hPa) associated with the values of large positive sea level anomalies 48 h before (left column), 24 h before (middle column) and at the peak (right column) of the event in Alicante, Toulon, Trieste, Dubrovnik, Thessaloniki, Iskenderun, Alexandria, Tripoli, and Gabès, denoted with white circles in the maps.

From Lionello, P., Conte, D., Reale, M., 2019. The effect of cyclones crossing the Mediterranean region on sea level anomalies on the Mediterranean Sea coast. Nat. Hazards Earth Syst. Sci., 19, 1541–1564.

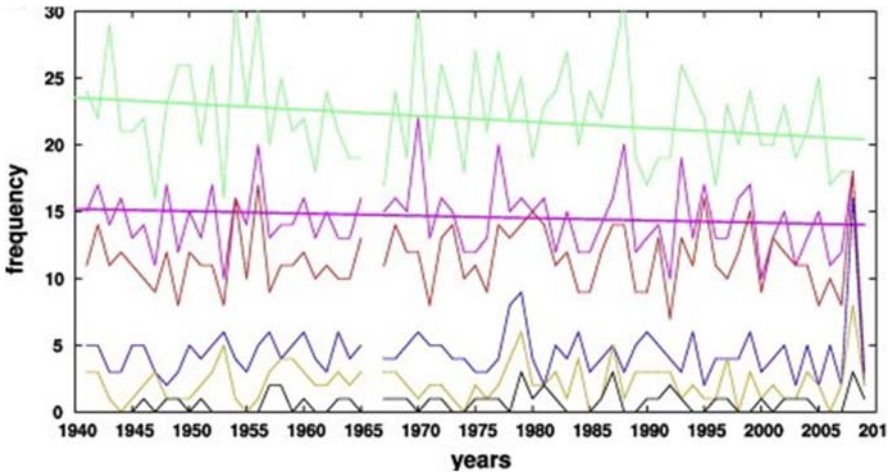

FIGURE 6.12

Time series (1940–2009) of annual frequency (y-axis, number of events per year) of storm surges in Venice. The panel shows the total frequency (green) and that of events above the 35th (pink), 50th (red), 80th (blue), 90th (yellow) and 97th (black) long-term percentile thresholds. These results have been obtained after subtracting the effect of the relative mean sea level rise.

From Lionello, P., Cavaleri, L., Nissen, K. M., Pino, C., Raicich, F., Ulbrich, U., 2012a. Severe marine storms in the Northern Adriatic: characteristics and trends. Phys. Chem. Earth 40–41, 93–105.

6.3.4 Mesoscale forcing of storm surges

High-frequency sea level changes (with periods in the range up to a few hours, Fig. 6.13) have been recently recognized to significantly contribute to the Mediterranean sea level extremes, particularly in bays and harbors characterised by seiches having such short periods. Flooding at these frequencies occur quite rapidly, in a few minutes, destroying coastal structures, endangering local inhabitants and, particularly in the Mediterranean, tourists. Coastal flooding and high-frequency sea level oscillations can be caused by a variety of atmospheric processes and phenomena, such as mesoscale convective systems, squall lines, atmospheric internal gravity waves and tropical/extratropical mesoscale storms. The latter occur in the Mediterranean in the form of the medicanes (Mediterranean hurricanes), which are troposphere-wide formations resembling some characteristics of hurricanes, being recognized by a clearly developed eye in their center (Tous and Romero, 2013).

Medicanes are rare events occurring about 15 times per decade (Cavicchia et al., 2014; Nastos et al., 2018). They mostly develop in the middle of the western and central Mediterranean and hit a land area in a few days at maximum. Their diameter does

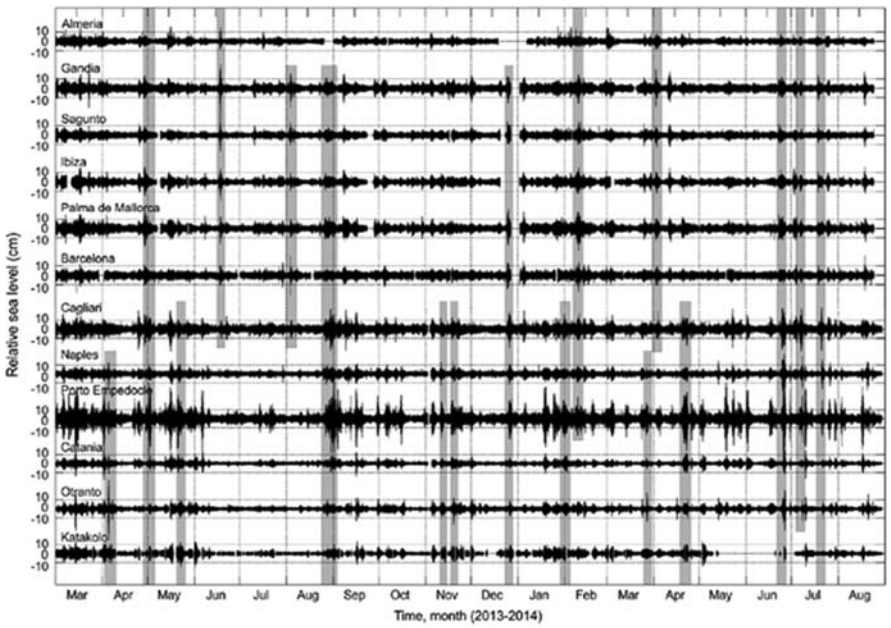

FIGURE 6.13

High-frequency (cut-off period at 6 h) sea level series from selected Mediterranean tide gauges for the period between March 2013 and August 2014, with coherent oscillations marked by gray bars.

From Šepić, J., Vilibić, I., Lafon, A., Macheboeuf, L., Ivanović, Z., 2015a. High-frequency sea level oscillations in the Mediterranean and their connection to synoptic patterns. Prog. Oceanogr. 137, 284–298.

not exceed 300 km, due to the size of the basin, and their strength is limited to category two in the Saffir-Simpson hurricane wind scale. In spite of this, their impact can be destructive: for example, in 22–27 September 1969 a medicane killed almost 600 people in North Africa and produced a substantial destruction to the coastal infrastructure in the western and central Mediterranean (Nastos et al., 2018). Storm surge levels caused by medicanes have been reported to have reached 1 m (Scicchitano et al., 2021) and they can flood coastal areas of the microtidal Mediterranean Sea.

High-frequency surges can also be driven by meteotsunamis (see Section 6.5.3) and local storms. As measured by tide gauges, these oscillations contribute to less than 10% to the sea level variability in the Mediterranean, yet their amplitude may surpass 10 cm or more, being equal to other coastal flood contributors (Šepić et al., 2015a). Summer storms and meteotsunamis contribute differently to coastal floods. Meteotsunamis produce most of the floods in funnel-shaped bays and harbors, but have a small magnitude in the open sea. Summer mesoscale storms usually

hit open waters and unprotected coasts, where they can produce substantial damage and victims by coastal flooding and waves, which can surpass the significant height of 5 m during some events (e.g., medicanes, Lagouvardos et al., 2021).

6.3.5 Prediction of storm surges

A reliable prediction of storm surges is essential to reduce the risks posed by coastal floodings. Therefore, a great effort has been invested in accurate operational forecasting tools, particularly in sensitive locations, such as Venice in the northern Adriatic (Umgiesser et al., 2021).

The accuracy of the meteorological forcing is a fundamental issue for the accuracy of sea level forecast systems in regions with a complex morphology such as the Mediterranean Sea. The action of the orography surrounding the Mediterranean Sea has often posed problems for the forecast and high spatial resolution is important for producing wind fields with a realistic intensity and structure (e.g., Cavaleri and Bertotti, 2004). Predicting accurately mesoscale features is challenging also with nonhydrostatic high resolution meteorological models. For example, during the flood of November 12, 2019 (Fig. 6.14) the intensity of the secondary mesoscale storm that brought additional 40 cm of water in the Venice lagoon was underestimated in the operational forecast, resulting in a substantial underestimation of the flood (Ferrarin et al., 2021). Fig. 6.14 shows that using the nonhydrostatic regional atmospheric model MOLOCH with horizontal resolution of 1.25 km improves the reproduction

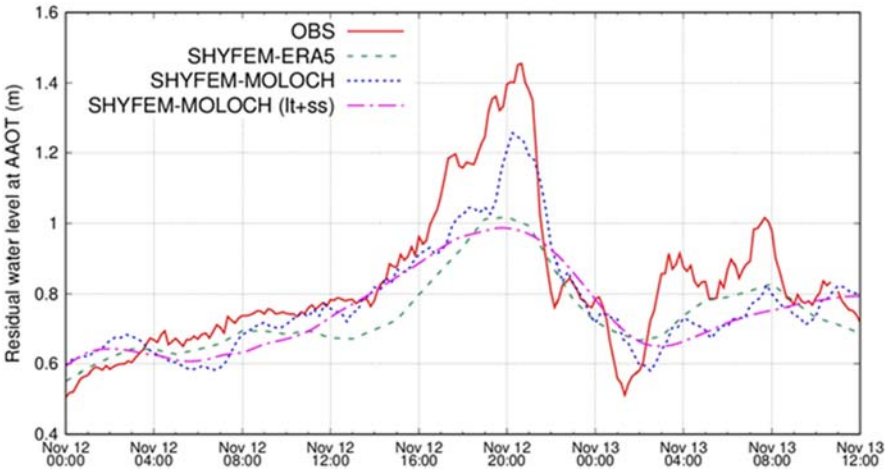

FIGURE 6.14

Observed and simulated (using ERA5 and MOLOCH forcing, total and long-term + storm surge components only) residual water level (after the subtraction of the astronomical tide) at Aqua Alta Oceanographic Tower in the northern Adriatic Sea.

From Ferrarin, C., Bajo, M., Benetazzo, A., Cavaleri, L., Chiggiato, J., Davison, S., et al., 2021. Local and large-scale controls of the exceptional Venice floods of November 2019. Prog. Oceanogr. 197, 102628.

of the surge with respect to the low-resolution global ERA5 reanalysis, but does not prevent the underestimation of the event. The limits of the atmospheric models for forecasting mesoscale phenomena is recognized also for the modeling of meteotsunamis in the Adriatic Sea (Denamiel et al., 2019a) and the Balearic Islands, in spite of the 4 km resolution adopted by the present model (BRIFS, Balearic Rissaga Forecasting System, Mourre et al., 2021, see also Section 10.4.2.2).

Assimilation of sea level observations and ensemble modeling can improve the quality and the informative content in the forecasts of storm surges and other processes contributing to coastal floods. The assimilation of ocean and atmospheric observations in the storm surge model, specifically tide gauge data and in situ wind observations, have been shown to improve the reliability of the sea level forecast for Venice at daily time scales (Lionello et al., 2008; Bajo et al., 2019). Ensembles of simulations allow to estimate the probability of exceeding given sea level thresholds and to assign an uncertainty range of the prediction. The ensemble can be obtained using the same model driven by different meteorological forcings (Mel and Lionello, 2014) or using different models (Ferrarin et al., 2020). Also a surrogate stochastic approach, through the extraction of key features and parameters, can quantify the uncertainty of the forecast (Yildirim and Karniadakis, 2015) and develop a reliable forecast (Fig. 6.15, Denamiel et al., 2021). This technique is used for hurricanes, which can be characterized using landfall location, track direction, translational speed, central pressure, radius of maximum winds, maximum wind speed and density of the air. The evolution of these parameters can be associated with a predefined distribution to add a location-specific probabilistic hazard estimate to a forecast. Further, this technique has been used for integrating a single model forecast of the sea level in Venice with the uncertainty caused by the meteorological forcing (Mel and Lionello, 2016).

Local effects can be important for forecasting storm surges in the Western Mediterranean, when operational systems (such as NIVMAR, Fanjul et al., 2001) tend to underestimate sea level extremes at the coast, like these observed during Storm Gloria (Pérez Gómez et al., 2021). The inclusion of waves, and of the associated contribution to the sea level at the coast, wave set up, can be significant along coastlines with a long offshore fetch. Numerical ocean forecasting is further discussed in Chapter 10.

6.3.6 Coastal floods in future climates

Changes of the coastal hazard level depend on the combination of the trend and variability of marine storminess with the ongoing sea level rise (see Chapter 5). Relative mean sea level rise increases the severity and frequency of floods, while the increase or decrease in the storm surge can reinforce or attenuate it.

The observation of marine storms in the recent decades do not show large significant trends, with mild indication of decreasing intensity (Šepić et al., 2012; Lionello et al., 2012a; Androulidakis et al., 2015). However, mean sea level rise and local subsidence have contributed to increase the frequency of floods in sensitive locations (Lionello et al., 2021b).

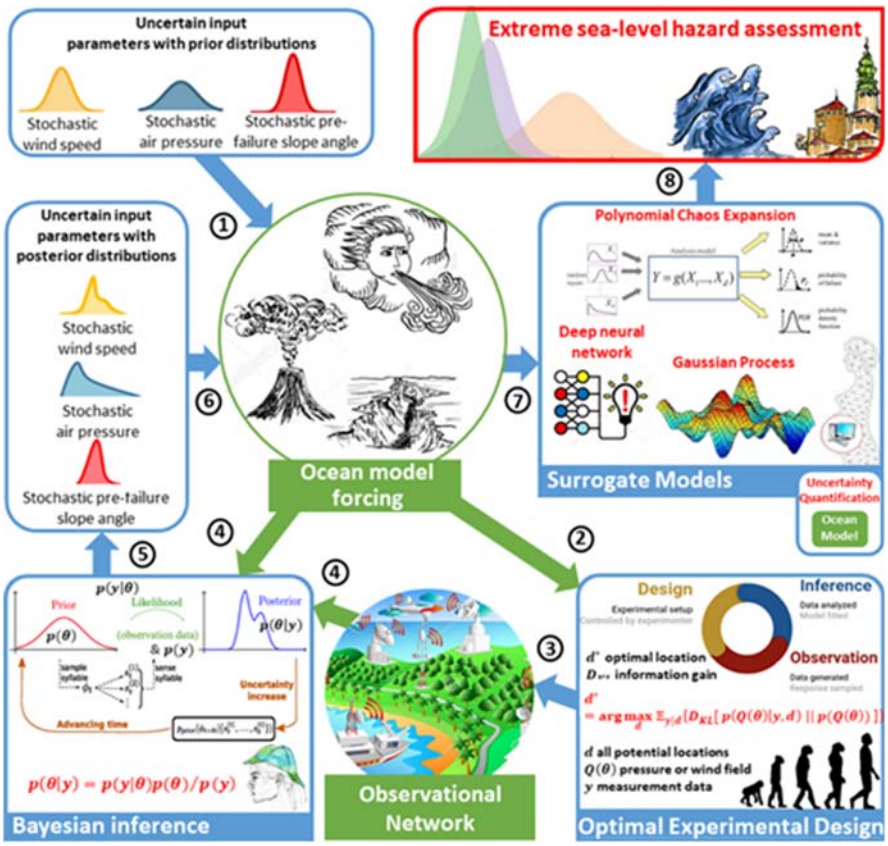

FIGURE 6.15

Extreme sea-level hazard assessments based on uncertainty quantification and optimization engineering methods: (1) uncertain input parameters with prior distribution are used to create stochastic ocean model forcing which are both (2 and 3) used to optimize the observational network with optimal experimental design strategies and (4) modified with the assimilation of observational data via Bayesian inference in order to (5) create the posterior distributions of the input parameters. Finally, (6) new stochastic ocean forcing based on these parameters are used to force (7) the surrogate models, and produce (8) extreme sea-level hazard assessments.

From Denamiel, C., Huan, X., Vilibić, I., 2021. Conceptual design of extreme sea-level early warning systems based on uncertainty quantification and engineering optimization methods. Front. Mar. Sci. 8, 650279.

The future mean sea level rise in the Mediterranean is linked to the global mean sea level and is modulated by regional processes of warming and salinification (see Chapters 3 and 9), exchanges with the Atlantic across the Gibraltar strait and atmospheric circulation. The projected values depend on scenario in a range from 0.3 to 1.1 m at the end of the 21st century (IPCC WG2-AR6, CCP4). This expected increase plays the most important role in future increase in coastal floods and it is much more relevant than any change of regional storminess.

The projection of storm surge is generally based on a storm surge prediction model that adopts the atmospheric forcing (mean sea level pressure and surface wind) of a climate model projection. Therefore, the evolution of the frequency and intensity of storm surges in climate projections is driven by the changes of strength and intensity of the atmospheric circulation simulated by climate models. First studies were based on individual model projections (Lionello et al., 2003, 2012b; Marcos et al., 2011; Šepić et al., 2012; Mel et al., 2013; Androulidakis et al., 2015; Međugorac et al., 2021). Further studies have used ensembles of model projections allowing to estimate the uncertainty of results (Conte and Lionello, 2013; Lionello et al., 2017). In general, as a consequence of the poleward shift of the midlatitude storm track in climate projections, the number of cyclones is expected to somewhat be lower in the future than in the present climate (e.g., Reale et al., 2021) and, therefore, the storm surges are expected to decrease in the majority of the Mediterranean, mostly related to the frequency of local peaks and the duration and spatial coverage of the storm surges. Fig. 6.16 shows the values of the storm surge index (which is the mean value of the three highest surges per year) along the coast of the Mediterranean Sea (the sequence of points is ordered clockwise, along the x axis, starting from the Strait of Gibraltar) that is produced by the model for the end of the 20th century. The sequence evidences the large values of storm surges in the northern Adriatic and in the Gulf of Gabes. The bottom panel shows projected changes for the mid of the 21st century and the expected decrease (ca. −5%) of storm surges.

Meteotsunamis involve mesoscale processes that require a dedicated modeling effort and could evolve differently from storm surges produced by midlatitude cyclone. For the Balearic Islands Vilibić et al. (2018) and for the Adriatic Sea Denamiel et al. (2022) suggest that in the model projections the hazard level posed by meteotsunamis increases for the regions that are presently most affected (such as the central Adriatic), in particular for the RCP 8.5 scenario with a 35% increase. In the central Adriatic this tendency is driven by the more frequent occurrence of an intense midtroposphere jet stream directed north-eastward, favoring the generation of meteotsunamis in an extreme greenhouse gas emission scenario. Ensembles of simulations, which are an essential tool for assessing the mesoscale processes responsible for rapid changes of sea levels along the coasts and changes of planetary-scale forcing, are not yet documented in the scientific literature.

6.4 Wind generated waves

6.4.1 Generalities and basic definitions

Surface gravity waves in the range up to periods of several tens of seconds are generated by the wind. The initial phase of wave growth is produced by random surface pressure fluctuations that are present in the wind flow (Phillips, 1957). This slow and linear growth is very soon overwhelmed by a nonlinear mechanism caused by the

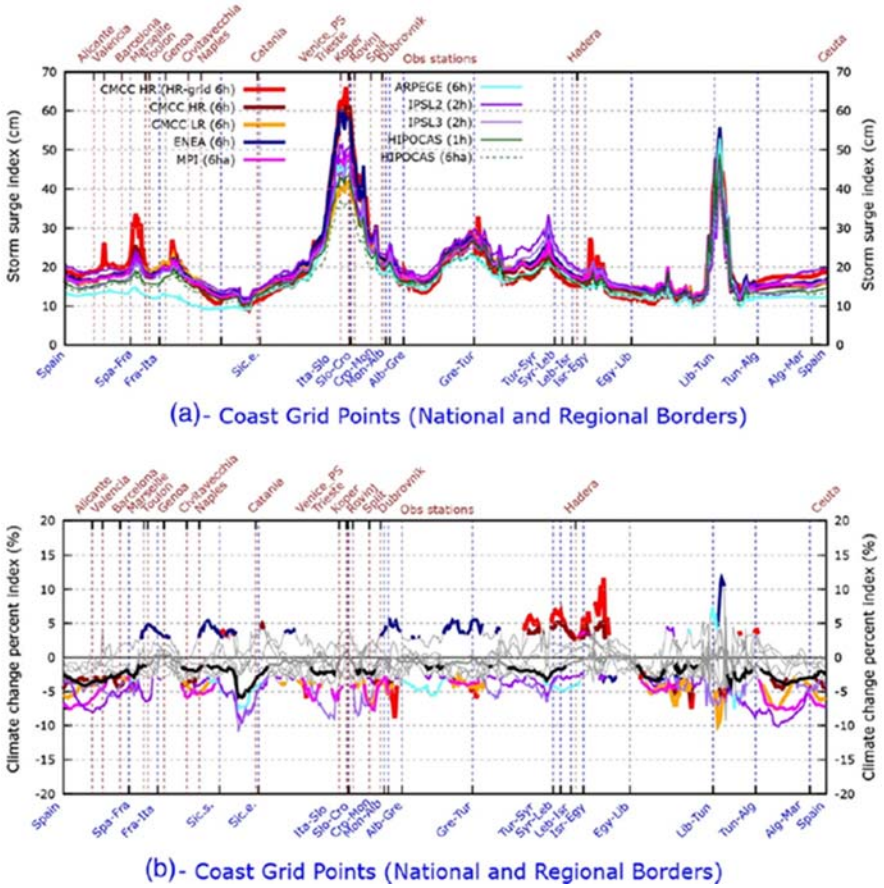

FIGURE 6.16

Storm surge index for positive surges at the end of 20th century in model simulations (top panel) and its variation (%) in mid 21st century (bottom panel), expressed using the climate change index. Each line represents a different model simulation (annotated in the figure). Bold lines in the bottom panel denote statistically significant changes.

From Conte, D., Lionello, P., 2013. Characteristics of large positive and negative surges in the Mediterranean Sea and their attenuation in future climate scenarios. Glob. Planet. Change 111, 159–173.

perturbations introduced by the wave itself in the wind flow, which, being locked to the phase of the wave, produces an exponential growth (Miles, 1957). This mechanism is responsible for most of the growth of waves whose phase speed is lower than the wind velocity. Waves with higher phase velocity grow by nonlinear mechanisms, involving exchange of energy among different components (Phillips, 1960; Hasselmann, 1967). The energy input is contrasted by energy dissipation, which in deep water is caused by the breaking of the waves (white capping, Hasselmann, 1974).

These different mechanisms produce waves with different frequencies propagating in different directions whose random superposition and growth is described by the two-dimensional wave spectrum.

The wave spectrum represents the distribution of the wave energy (actually of the variance, which is proportional to the energy) as a function of frequency and direction. During the generation phase the evolution of the wave spectrum is characterized by a dominant component, propagating along the wind direction, whose frequency decreases (wavelength increases) and energy increases as the action of the wind continues. Consequently, the aspect of the sea surface is characterized by waves becoming progressively longer and higher. This has been described using a prescribed spectral shape, the JONSWAP spectrum (Hasselman et al., 1973), whose parameters depend on the fetch and the wind speed The JONSWAP spectrum describes the evolution of the wave field under the action the wind until an ideal final condition is reached, in which energy input and output balance each other's (the Pierson-Moskowitz spectrum, Pierson and Moskowitz, 1964). These ideas are very effective in describing the evolution of the wind-sea (the waves under the direct action of the wind), but their application in the realistic spatial patterns of an actual storm is complicated. Further, they cannot be applied to the propagation of the waves when the storm ceases or waves are radiated out of the storm areas (swell waves). Swell can propagate for very long distances (thousands of kilometers in wide oceanic basins) with long waves propagating faster than short waves (see dispersion relation in Table 6.1) and can have important implications for harbor operations. A model capable of describing with a single approach the full evolution of the wave field from the deep sea to the shallow water (but excluding the surf zone) has been proposed in the late 1980s (WAMDI, 1988) and it is based on the solution of the wave energy equation

$$\frac{DF\left(\overrightarrow{x}, t, \omega, \vartheta\right)}{Dt} = S_{in} + S_{nl} + S_{ds} + S_{bf} \tag{6.5}$$

where F in the wave spectrum, which is a function of space $\overrightarrow{x}$, time t, frequency ω, propagation direction ϑ, and D/Dt is the total derivative. The right term is composed of complicated functions describing the sources of energy due to the wind S_{in}, nonlinear interactions S_{nl}, white capping S_{ds} and bottom friction S_{bf}, when wave motion in attenuated by the friction exerted by the bottom before waves enter in the surf zone. Note that wind waves in deep water travel at a speed depending in the frequency (long and low-frequency waves travel faster than short high-frequency waves), while in shallow water the speed does not depend on the frequency and decreases with the water depth D.

Integrating the wave spectrum across all directions and frequencies provides the total energy (per unit surface) of the waves:

$$E = \frac{1}{2}\rho g \int F\left(\overrightarrow{x}, t, \omega, \vartheta\right) d\omega d\vartheta \tag{6.6}$$

However, the quantity that is generally used to represent the strength of the wave field is the significant wave height H_s, which is a statistically quantity representing the mean value of the uppermost tertile of the waves crests and is linked to the total energy by a simple relation

$$H_s = 4\sqrt{E/\rho g} \tag{6.7}$$

H_s approximates the visual estimate of the wave height provided by experienced sailors. Note that the square root is consistent with the basic physical law that the energy of a sinusoidal wave is proportional to the square of its amplitude.

The behavior of waves in shallow water and in the presence of complicated geometry, such as in harbors or bays is complex and other modeling tools are required for its description.

On a gently sloping bottom the dependence of the wave speed on the water depth has a strong effect on the wave propagation toward the shore. As waves approach the shore in progressively shallower water, the decrease in their speed shortens the wavelength and increases the wave height (shoaling), while crests tend to align with the isobaths. In general, variations in offshore water depth tend to focus wave crests toward shallow areas and deviate them from deep areas. This evolution is a special case of the general process called refraction, affecting all waves propagating in a medium where their speed in not uniform. Wave breaking in the surf zone generates strong currents, both in the longshore and crossshore direction whose convergence can produce local very intense current, such as the rip currents. This complicate system is associated with sediment transports that change the coast profile. The behavior of wave in shallow water is modeled using the wave action $N(\omega, \vartheta) = F(\omega, \vartheta)/\omega$ and its conservation (the SWAN—Simulating Wave Nearshore model, Booij et al., 1999). Further, waves contribute to coastal floodings because of the wave set-up and run-up. The wave set-up is the increase of the mean sea level associated to the reduction of their height as they break when reaching the shore and, in some situations, it can be an important addition to the storm surge during severe events. The run-up is the maximum elevation reached by the waves as they collapse on a beach and affects the safety of the structures along the shore. In harbors and in the presence of structures and obstacles the behavior of waves is further complicated by reflection and diffraction when they interact with features whose size if comparable to the wavelength. In these cases, the actual computation traditionally requires phase-resolving models explicitly describing the response of the water level and currents to the wave motion penetrating in the area.

6.4.2 Wind and waves regimes in the Mediterranean Sea

The annual mean wind field in the Mediterranean Sea reflects the prevalent role of north westerly winds across the basin, whose effect is modulated by the presence of complicated coastlines and islands, which limit the fetch of the wind and shield parts of the basins from its action (Lionello and Sanna, 2005). Annual mean wave height

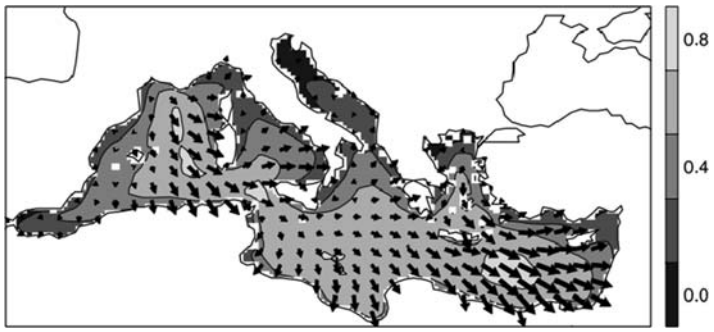

FIGURE 6.17

Mean wave field in the Mediterranean Sea. Arrows show the mean wave propagation direction and contour levels the mean significant wave height value.

From Lionello, P., Sanna, A., 2005. Mediterranean wave climate variability and its links with NAO and Indian Monsoon. Clim. Dynam. 25, 611–623.

maxima are located in the north-western part of the basin, in the Ionian Sea and in the Levantine basin. This annual mean condition results from the superposition of two different regimes: the winter "Mistral" regime, where waves are largest in the western areas of the basin, mainly caused by the strong winds produced by the cyclones that cross the basing along the Mediterranean winter storm track (see Chapter 3); the summer "Etesian" regime with strong northerly winds in the Aegean Sea and the Levantine Basin (Lionello and Sanna, 2005) caused by a persistent surface pressure gradient. Figs. 6.17 and 6.18 represent the annual mean condition and the contrast between winter (December) and summer (July), respectively. The maps in these two figures adopt the usual representation of waves using arrows whose size represent the significant wave height and point to the mean wave propagation direction (contour lines or other techniques are usually used for increasing graphic effectiveness).

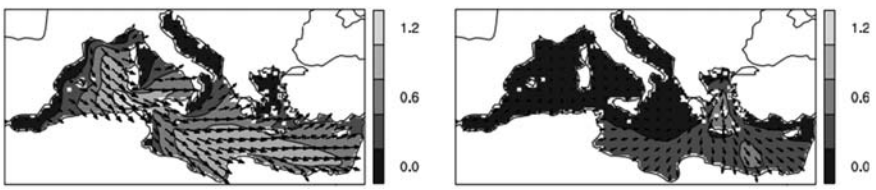

FIGURE 6.18

Mean monthly wave field in December and July, representative of the winter "Mistral" and summer "Etesian" wave regimes, respectively. Arrows show the mean wave propagation direction and contour levels the mean significant wave height value.

From Lionello, P., Sanna, A., 2005. Mediterranean wave climate variability and its links with NAO and Indian Monsoon. Clim. Dynam. 25, 611–623.

The instantaneous aspect of the wave field as a cyclone crosses the Mediterranean Sea does not reflect the mean wave condition, but a complex pattern that approximately matches the wind direction and fetch, progressively growing from the coastline that is located upwind toward the opposite side of the basin. In these situations the mean wave propagation direction may not be representative of the actual sea conditions, because as the cyclone move, the wind-sea and the swell produced during former phases overlap and the wave spectrum may exhibit two or more peaks. Fig. 6.19 shows the mean sea level pressure, and the wave field at the peak of the destructive storm of November 4, 1966. Ahead of the very elongated pressure minimum the south-easterly wind, channeled and veered by the orography, produced high waves propagating north-westwards, whose presence is not detectable in the annual mean wave field.

6.4.3 Waves forecasts in the Mediterranean Sea

The Mediterranean Sea with its complicated shape and the strong mesoscale features of the winds blowing over it has been a have made it a testbed for wave model developments. It has been used for crucial validations of the WAM model in the late 1980s and early 1990s, to show its capability to perform well in different environmental conditions (Cavaleri et al., 1989a; 1989b, 1991), These studies have led to the implementation of operational prediction systems at ECMWF (Cavaleri and Bertotti, 1993) and at several national weather services (e.g., Gómez Lahoz and Carretero Albiach, 2005; Bertotti et al., 2013; Ravdas et al., 2018). Some of these systems have multiple components to predict simultaneously surges, tides and wind waves and their interactions in unstructured grids (Ferrarin et al., 2013). Further, ensemble forecast systems with multiple mode runs have been developed for estimating uncertainties and provide a probabilistic prediction of wave evolution (Pezzuto et al., 2016).

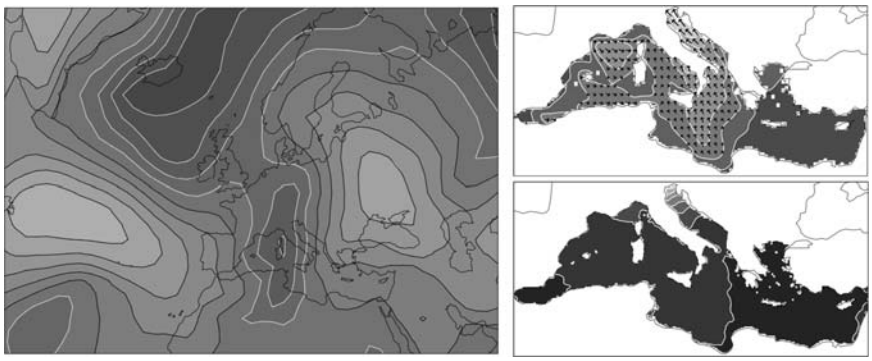

FIGURE 6.19

Mean sea level pressure, wave field and sea level anomaly on November 4, 1966 at 12 UTC.

From De Zolt, S., Lionello, P., Nuhu, A., Tomasin, A., 2006. The disastrous storm of 4 November 1966 on Italy. Nat. Hazards Earth Syst. Sci. 6 (5), 861–879.

The wave forecasts uses the wind forcing produced by a meteorological model for computing the corresponding wave forecast, using models such as WAM, SWAN, WAVEWATCH (WAVE-height, WATer depth and Current Hindcasting, Tolman, 1991) developed in the 1990s at NOAA/NCEP, following the approach of the WAM model. The wave forecast is characterized as a boundary problem depending of the input of energy from the atmosphere via the action of the wind. The memory of past sea states gets lost as waves reaches the coastline represented at large scale as fully absorbing boundaries. Consequently, the wave forecast does not present any chaotic behavior and its predictability is connected to that of the atmospheric forcing. Therefore, the quality of the wind field, connected with the resolution of the meteorological model, is a key issue for the reliability of the model forecast, whose accuracy diminishes with the length of the forecast window together with the accuracy of the weather forecast.

The prediction of waves in a partial area of the basin requires the specification of the wave field along the open boundary of the model domain. The relative importance of the wind forcing inside the domain and of the boundary condition increases with the extension of the domain. In the case of gulfs or small bays, the boundary forcing plays the most important role, but its relevance decreases with the distance from the open boundary and the size of the domain.

The ensemble prediction approach has been mostly used for wave modeling to translate the uncertainty in the evolution of the meteorological forcing in different realization of wave fields. This allows to produce a range of significant wave heights and directions, and to integrate a single model deterministic prediction with a probabilistic estimate.

6.4.4 Past and future evolution of wind-generated waves

The observation of wind waves requires dedicated instrumentations and few long time series are available. The longest record is available in the northern Adriatic Sea, where a wave gauge has been operational since 1979. In this location, the analysis of the period 1979–2015 shows an increase in the average storm frequency and a decrease of the maximum significant wave height values (Pomaro et al., 2017). However, a single time series cannot be used to represent trends valid for the whole Mediterranean Sea, with its complicated division in subbasins and the heterogenous winds affecting them.

Hindcast studies are the alternative tool to compute past trends when observations are not available. They consist in running a wave model adopting the meteorological forcing produced by a meteorological reanalysis project. The quality of the results of a wave model hindcast depends on the quality of the meteorological forcing, with issues that are similar to those concerning the wind fields required for accurate simulation of storm surges, particularly in terms of the high spatial resolution needed for producing surface wind fields with correct intensity and spatial structure (e.g., Cavaleri and Bertotti, 2004). The available hindcast studies (e.g., Lionello and Sanna, 2005; Musić and Nicković; 2008; De Leo et al., 2020) suggest negative trends during the second half of the 20th century and a modest increase, mostly in the central Mediterranean, when a more recent period is considered (1979–2018).

The projection of waves is based on an approach that is methodologically similar to the hindcast studies: a wave model is operated for simulating future wave conditions using the forcing wind field provided by a climate model projection. The first wave projection study was based on a single climate model and a relatively low resolution (0.5 degs, Lionello et al., 2008). A following study adopted a small model ensemble, but it was limited to the western Mediterranean (Casas-Prat and Sierra, 2013). Later studies considered the whole Mediterranean and an ensemble of simulations (Lionello et al., 2017; De Leo et al., 2021). Though studies differ because they consider different time slices and emission scenarios, a consensus emerges in terms of negative trends of mean significant wave height. The interpretation of these variations is analogues to the corresponding attenuation of storm surges that is expected in the future, both being driven by the decreasing number of cyclones crossing the Mediterranean.

6.5 Tsunamis

Tsunami (tsu—harbor, nami—wave, from Japanese) is an oceanic long wave generated by an impulse force that causes a displacement of a large amount of water. The impulsive force can be exerted by submarine earthquakes, coastal or submarine landslides, volcanic eruptions, atmospheric mesoscale disturbances, asteroid impact, and others. Once displaced, the gravitational instability causes a generation of waves that are normally propagating through the whole water column with the speed of a nondispersive barotropic wave $\sqrt{gD}$, where D is the depth of the ocean, while g is the gravity acceleration. Thus, the tsunami waves travel fast in the deep ocean (about 200 m s^{-1} over 4000 m depth) and reduce their speed on the continental shelf and nearshore (about 30 m s^{-1} over 100 m depth). As the tsunami wavelength can reach a few hundreds of kilometres, the front side of the wave travels with much lower speed that its rear side when approaching the coastline, shortening the wavelength and increasing dramatically the wave height. The actual evolution is made complicated by the interacting with the topography (reflection, refraction) as it breaks nearshore and inundates the coastal areas.

Most tsunamis—more than 80%—are seismic ones (NOAA, 2022), generated by earthquakes, in particular by those that cause vertical movements of the seabed. The most destructive events are generated by the interplate thrust fault, in particular along the tectonic plates that surround the Pacific Ocean (the so-called Pacific Ring of Fire), which generated the two recent most destructive seismic tsunamis: the Sumatra-Andaman earthquake in 2004 (Titov et al., 2005) and the Tohoku earthquake in 2011 (Fujii et al., 2011), with a magnitude of Mw = 9.1−9.3 and Mw = 9.0−9.1, respectively. These two events generated tsunami waves which reached several tens of meters at some location, overtopping the coastal protection barriers (if any), destroying coastal cities and causing the death of about 230.000 and 20,000 people, respectively.

Landslide tsunamis are generated by submarine or coastal landslides propagating beneath the sea surface (see also Chapter 12). Landslides are often triggered by earthquakes or volcanic explosions, but can be also due to a pure instability of a large volume of sediment at shelf breaks. The effects of these tsunamis are normally localized unless they are generated by massive submarine landslides, like the Storegga landslide (Bondevik et al., 2005), or volcano collapses (Ward and Day, 2001).

Meteorological tsunamis or meteotsunamis consist of atmospherically-generated long ocean waves in the tsunami frequency band. They are the least frequent events among those documented in tsunami catalogs (Maramai et al., 2014), but may occur quite frequently at some particular coastlines. Their magnitude does not reach that of seismic and landslide tsunamis, but they can cause victims and destructions in the coastal strip, in particular where the tidal range is small. This section provides an overview of tsunamis in the Mediterranean Sea. It includes a description of major events and of their sources, and of the development and operational capabilities of tsunami early warning systems (EWS).

6.5.1 Historical events in the Mediterranean Sea

Destructive tsunamis, generating widespread damages on large scales and causing the death of tens of thousands of people, occur every few decades. The Mediterranean Sea coastline has been hit by several destructive tsunamis. The explosive eruption of the Santorini volcano generated tsunami waves with a height of several tens of meter that destroyed Minoan coastal settlements in Crete (Lespez et al., 2021). The Cretan earthquake of 365 BCE generated a tsunami that destroyed cities and drowned thousands of people in coastal regions from the Nile Delta to modern-day Dubrovnik (Shaw et al., 2008). Recently, the Messina (Sicily) earthquake and tsunami in 1908 caused around 80,000 casualties, a lot of them by the tsunamis waves that surpassed a 5 m height in some locations (Billi et al., 2008). The destruction of the city of Dubrovnik in 1667 by the earthquake was accompanied with several meters high tsunami waves (Pasarić et al., 2012). A sequence of tsunamis has also been documented in the Gargano area (south Italy) in 2430 BP, 1550 BP, 493 CE, 1527 CE and 1627 CE (Tinti et al., 1995; Gianfreda et al., 2001). Concerning tsunamis generated by submarine landslides, a severe event occurred in the Western Mediterranean around 9500 BC along the slopes of the Iberian Peninsula, when about 26 km^3 of debris moved down to 2000 m of depth in less than an hour producing 10 m high waves along the coasts of the Balearic Islands and the Iberian Peninsula (Iglesias et al., 2012). Submarine landslides have been recorded also along the slopes of the southern Adriatic Pit and associated with significant tsunamis (Valle et al., 2015). Finally, tsunami waves generated by rapid atmospheric disturbances caused the flood of Vela Luka (Adriatic Sea) in 1978 and of Ciutadella (Balearic Islands) in 1984, when 4−6 m high waves were observed (Monserrat et al., 2006).

6.5.2 Source, propagation and tsunami models

In the Mediterranean, the largest tsunamis are generated along the Hellenic Arc, where the African plate creates the strongest tensions and subducts to the Euro-Asian plate (Fig. 6.20). Tsunamis can be generated also along microplates, like the Adriatic microplate, and the fault lines connected with the subduction zones. Landslide tsunamis are not frequent in the Mediterranean Sea, although slope failures may occur at shelf breaks, mostly triggered by earthquakes and volcano collapses and flows (De Girolamo et al., 2014; Lovholt et al., 2014).

Modeling of seismic tsunamis has been, in addition to the real-time observations, the most important tool for providing the estimates of wave arrival time, wave height and inundation area immediately after a submarine earthquake. Numerical models, like MOST (Method of Splitting Tsunami) or TUNAMI (Tohoku University's Numerical Analysis Model for Investigation of Near field tsunamis) solve the shallow water adopting different types of meshes. Some meshes reach a resolution of a few meters near the coastlines, to allow the reproduction of the complex dynamics of tsunamis over bottom topography and the effect of local morphological features of scales of tens or hundreds of meters (Samaras et al., 2015). The largest source of uncertainty for the reproduction and prediction of a seismic tsunami comes from the initial conditions, as the precise seafloor deformation during earthquakes cannot be measured in real-time. Analogously, the speed, volume and density of the sliding

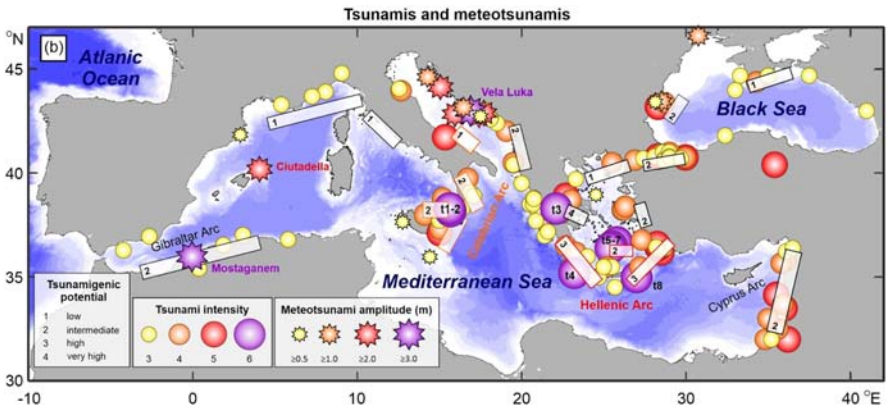

FIGURE 6.20

Epicentres of earthquakes that resulted in tsunamis having intensities of three or higher at the Sieberg-Ambraseys tsunami intensity scale (colored circles, after Maramai et al., 2014); white rectangles show tsunamigenic fault areas with annotation indicating their tsunamigenic potential; locations where historic meteotsunamis surpassed an amplitude of 0.5 m are marked with colored stars.

From Pérez Gómez, B., Vilibić, I., Šepić, J., Međugorac, I., Ličer, M., Testut, L., et al., 2022. Coastal sea level monitoring in the Mediterranean and black seas. Ocean Sci. Discuss. https://doi.org/10.5194/os-2021-125 (accepted).

material (for the landslide tsunamis) and the speed, direction, and intensity of the atmospheric disturbance (for meteotsunamis) are required for proper quantification of the generated tsunamis, but real time observation to monitor them are not available (Denamiel et al., 2019b; Paris et al., 2021).

6.5.3 Meteotsunamis

Meteorological tsunamis or meteotsunamis (Monserrat et al., 2006) are generated by traveling atmospheric disturbances through a resonant transfer of energy toward the sea, dominantly through either Proudman resonance, in which the speed of the disturbance is equal to the speed of the shallow water waves (Proudman, 1929), or Greenspan resonance, in which the speed of the disturbance is equal to the speed of edge waves (Greenspan, 1956). Once generated, meteotsunami can travel both as forced or free waves, being reflected and refracted on their travel as "ordinary" tsunami waves. When they hit the coastline, they are amplified through coastal or harbor resonance (Rabinovich, 2009), reaching heights of several meters and penetrating for hundreds of meters inside the coastal areas.

The traveling disturbances that generate meteotsunamis can be identified in surface air pressure or wind observations taken at short intervals (typically 1 minute). The air pressure rapid changes—which may range up to 10 hPa in some tens of minutes—act as a primary generation mechanism in deeper waters, while wind forcing is important in very shallow areas. The processes leading to the meteotsunamigenic disturbances have spatial scales from O($\sim$100 m) to O($\sim$10 km). They might be associated to upper-troposphere "storms," squall lines, mesoscale convective storms and hurricanes. Key issues are the propagation speed, direction and sustainability of the disturbances over long, that is, O($\sim$100 km), distances, preserving their form through wave-ducting in the lower troposphere (Monserrat and Thorpe, 1996), mesoscale instabilities of the second kind (so-called wave-CISK, Belušić et al., 2007) or other dynamic. Fig. 6.21 illustrates both atmospheric and ocean processes involved in meteotsunamis.

Meteotsunamis and high-frequency sea level oscillations contribute significantly to the sea level extremes in the microtidal Mediterranean Sea. In some bays or harbors, meteotsunami waves can reach the height of 6 m (Orlić, 2015), as eyewitnessed during the Great Flood of Vela Luka in 1978, or during the event (called rissaga in Catalan) of 1984 and 2006 that hit Ciutadella, a small town on the island of Menorca, Spain (Fig. 6.22, Vilibić et al., 2021). Exceptionally strong currents produced by meteotsunamis at harbor and gulf constrictions have killed people on coasts and boats, like during the 2007 in Mostaganem, Algeria, when 12 people were killed by a 7−10 m unexpected run-up (Okal, 2021). A meteotsunami wave hit the beaches near Odessa just a few weeks after deadly clashes in that city, frightening the population and placing different maladaptive explanations in the media in spite of its clear meteorological origin (Šepić et al., 2018). In general, records show that destructive meteotsunamis occur once in a few years in the Mediterranean basins, from the Balearic Islands, through the Sicily Channel and the Adriatic Sea, till the north-western Black Sea shelf. They damage coastal infrastructure, buildings and boats, sometimes injuring people and, sometimes, causing deaths.

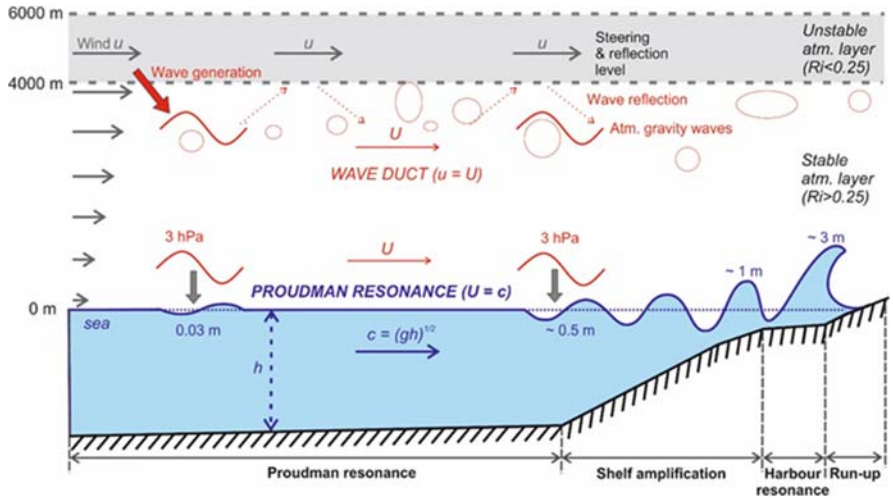

FIGURE 6.21

Illustration of meteotsunami generation processes. A strong wind shear produces atmospheric gravity waves (represented by bubbles) at the interface between unstable and stable atmospheric layers. The atmospheric gravity waves (marked in red), which propagate with a speed U that is equal to wind speed (u) of the unstable layer, gets trapped in the stable layer and propagates as a "duct wave." The atmospheric gravity wave manifest itself as an air pressure change that generates long-ocean waves, which can be amplified through (1) Proudman resonance (when the speed of long-ocean waves speed matches the speed of the atmospheric gravity wave), (2) shelf amplification (due to shoaling and focusing of wave crests), and (3) harbor resonance (when the frequency of the incoming long-ocean waves matches that of the seiches of harbor or gulfs). During these processes, the initial ocean wave height can be amplified more than 100 times and hit the coast as a destructive meteotsunami. Numbers shown in figure are for illustration only and are highly dependent on properties of atmospheric gravity wave, bathymetry, and topography of the area.

From Šepić, J., Vilibić, I., Rabinovich, A. B., Monserrat, S., 2015b. Widespread tsunami-like waves of 23–27 June in the Mediterranean and Black Seas generated by high-altitude atmospheric forcing. Sci. Rep. 5, 11682.

6.5.4 Early warning systems

A reliable Early Warning System (EWS) of height and timing of tsunami waves is a fundamental tool for reducing the related risks. Tsunami EWSs are based on the real time detection of the source, through seismic networks, and of the tsunami waves, through coastal sea level stations, tide gauges and open ocean tsunami detection devices. The latter are pressure sensors located at the sea bottom that are capable of detecting waves that are only few centimeters high in the open sea and are connected to a buoy that transmits the signal to a station on land. They are fundamental for detecting a tsunami when it is far from the coast allowing to compute its propagation and issue a warning with an anticipation sufficient to evacuate the areas at risk. The

FIGURE 6.22

Locations (red circles) and photographs of large meteotsunami events in the Mediterranean Sea: the Balearic meteotsunami of (A) the June 21, 1984 and (B) the June 15, 2006, (C) the middle Adriatic meteotsunami of June 21, 1978, (D) the Mali Lošinj meteotsunami of August 15, 2008, (E) the Mazara del Vallo meteotsunami of June 25, 2014, and (F) the Odessa meteotsunami of June 27, 2014.

From Vilibić, I., Denamiel, C., Zemunik, P., Denamiel, C., 2021. The Mediterranean and Black Sea meteotsunamis: an overview. Nat. Hazards 106, 1223–1267.

systems include the use of a mathematical model computing the evolution of the tsunami and the inundation area in the short time from the detection of the tsunami and its arrival time at the coast. The first tsunami warning systems in the Pacific Ocean (Pacific Tsunami Warning System) has been developed after the great Chilean earthquake and tsunami of 1960, while regional tsunami warning systems in other oceans were developed after the Sumatra-Andaman tsunami of 2004 (Fujii and Satake, 2007). The most known network is the DART (Deep-ocean Assessment and Reporting of Tsunamis, Mungov et al., 2013) stretching along most of the Pacific coastlines.

In the Mediterranean Sea, efforts coordinated by the UNESCO Intergovernmental Oceanographic Commission (IOC) initiated in 2005 and have led to the formal establishment of the North-eastern Atlantic, Mediterranean, and Connected Seas Tsunami Warning System (NEAMTWS; UNESCO-IOC, 2017). The efficiency requirements of such a warning system are very high in the Mediterranean, as the limited extension of the basin implies tsunami arrival times of the order of an

hour or less for most of the coastlines. Fig. 6.23 shows the Decision Matrix for real-time assessment of a potential tsunamis after a seismic event (Tinti et al., 2012). It relies on the assessment of the characteristics that are known to be connected with past tsunamis (depth, magnitude and epicentre location in relation to the coastline of an earthquake), taking into account the distance between the tsunami source and the potentially endangered locations. Beside seismometers, coastal measurements of rapid sea level oscillations like these available in real-time at the IOC Sea Level Station Monitoring Facility portal (VLIZ/IOC, 2022, http://www.ioc-sealevelmonitoring.org/) are useful for assessment of tsunami related risks (Pérez Gómez et al., 2022). Recently, new methods for the assessment of tsunami potential have been developed, for example, Probabilistic Tsunami Forecast (Selva et al., 2021), while measurements of ionospheric processes have been considered appropriate for real-time detection of large tsunamis (Artru et al., 2005).

Meteotsunami EWSs rely on the proper forecasting of the meteotsunamigenic disturbances in the atmosphere. The oldest EWS in the Mediterranean was developed for the Balearic Islands, 1 year after the destructive event in 1984, and is based on the assessment of the synoptic conditions that are favourable for a meteotsunami (Jansà and Ramis, 2021). This system is reliable for the forecast of weak and moderate events, but it underestimates the intensity of the strongest and most destructive events. The recently established EWS for meteotsunamis in the Balearic Islands, the BRIFS system (available through the SOCIB pages at www.socib.eu/, see also Chapter 10), is based on a coupled high-resolution atmosphere-ocean modeling system

<table>
<tr><th rowspan="2">Depth</th><th rowspan="2">M</th><th rowspan="2">Epicenter Location</th><th rowspan="2">Tsunami Potential</th><th colspan="3">ALERT LEVEL VS DISTANCE</th></tr>
<tr><th>Δeq ≤ 100 km</th><th>100 km < Δeq ≤ 400 km</th><th>Δeq > 400 km</th></tr>
<tr><td rowspan="6">< 100 km</td><td>5.5 ≤ M ≤ 6.0</td><td>Offshore or Inland ≤ 100 km</td><td>Nil</td><td colspan="3">Information Bulletin</td></tr>
<tr><td rowspan="2">6.0 < M ≤ 6.5</td><td>Inland (40 km < Inland ≤ 100 km)</td><td>Nil</td><td colspan="3">Information Bulletin</td></tr>
<tr><td>Offshore or near the coast (Inland ≤ 40 km)</td><td>Potential of weak local tsunami Δeq < 100 km</td><td>LOCAL Tsunami ADVISORY</td><td colspan="2">Information</td></tr>
<tr><td>6.5 < M ≤ 7.0</td><td rowspan="3">Offshore or Inland ≤ 100 km</td><td>Potential of destructive local tsunami Δeq < 100 km | 400 km</td><td>LOCAL Tsunami WATCH</td><td>REGIONAL Tsunami ADVISORY</td><td>Information</td></tr>
<tr><td>7.0 < M ≤ 7.5</td><td>Potential of destructive regional tsunami Δeq < 400 km | basin</td><td colspan="2">REGIONAL Tsunami WATCH</td><td>BASIN-WIDE Tsunami ADVISORY</td></tr>
<tr><td>M > 7.5</td><td>Potential of destructive tsunami in the whole basin any Δeq</td><td colspan="3">BASIN-WIDE Tsunami WATCH</td></tr>
<tr><td>≥100 km</td><td>M ≥5.5</td><td>Offshore or Inland ≤100 km</td><td>Nil</td><td colspan="3">Information Bulletin</td></tr>
<tr><td>any</td><td>any</td><td>Inland > 100 km</td><td>Nil</td><td colspan="3">Nil</td></tr>
<tr><td colspan="4"></td><td>LOCAL</td><td>REGIONAL</td><td>BASIN-WIDE</td></tr>
</table>

FIGURE 6.23

Decision Matrix of the tsunami warning system operational at Istituto Nazionale di Geofisica e Vulcanologia.

Source: https://www.ingv.it/cat/en/tsunami-alert/alert-procedures/decision-matrix.

and provides a forecast of meteotsunamigenic conditions 48 h in advance. A similar system, with a higher resolution, has been set up for the Adriatic (Denamiel et al., 2019a). However, underestimation of severe meteotsunamis remains an issue together with the sensitivity of the forecast to spatial shifts in the trajectories of the atmospheric disturbances. Operational consequences of this shortcoming can be compensated by a stochastic surrogate model providing probabilistic information based on large ensemble of model simulations for propagating the uncertainties from the meteorological input to the meteotsunami forecast (Fig. 6.24, Denamiel et al., 2019b). Such an approach is found to increase the reliability of the meteotsunami forecast.

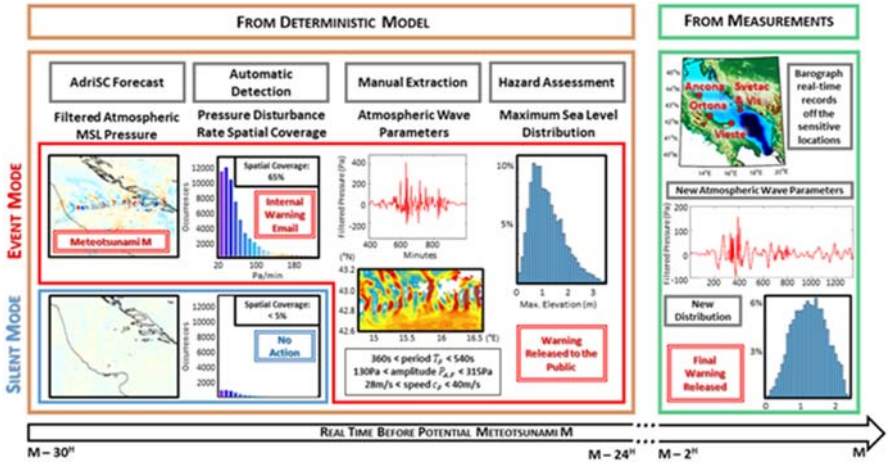

FIGURE 6.24

Operational meteotsunami hazard forecast within the Croatian Meteotsunami Early Warning System, based on atmospheric pressure field input from both (1) the deterministic model results (brown box) and (2) the measurements (green box). The high-pass filtered pressure is extracted from the AdriSC forecast and used to automatically detect meteotsunamis. The criterion is based on the spatial coverage of large rate of variations of sea level pressure (larger than 20 Pa per 4 minutes). If this coverage is small (less than 5% of the sea surface), then no meteotsunami is forecasted (blue box) —"silent" warning mode, otherwise a potential meteotsunami is foreseen to occur (red box)—"event" warning mode, and a warming is sent to the AdriSC team to start the production of the tsunami forecast using a stochastic surrogate model. When the real-time observations become available, the hazard assessment is updated with new parameters extracted from the measurements.

After Denamiel, C., Šepić, J., Huan, X., Bolzer, C., Vilibić, I., 2019b. Stochastic surrogate model for meteotsunami early warning system in the eastern Adriatic Sea. J. Geophys. Res. Oceans 124, 8485–8499.

Additional resources

- NOAA: Why does the ocean have waves?, https://oceanservice.noaa.gov/facts/wavesinocean.html
- Smithsonian: Currents, Waves and Tides, https://ocean.si.edu/planet-ocean/tides-currents/currents-waves-and-tides
- WHOI, https://www.whoi.edu/know-your-ocean/did-you-know/what-causes-ocean-waves/
- Copernicus Marine Environment Monitoring Service (CMEMS) https://marine.copernicus.eu/

References

Abaei, M.M., Arzaghi, E., Abbassi, R., Garaniya, V., Chai, S.H., Khan, F., 2018. A robust risk assessment methodology for safety analysis of marine structures under storm conditions. Ocean. Eng. 156, 167–178.

Adam, E.F., Brown, S., Nicholls, R.J., Tsimplis, M., 2016. A systematic assessment of maritime disruptions affecting UK ports, coastal areas and surrounding seas from 1950 to 2014. Nat. Hazards 83, 691–713.

Adelekan, I.O., 2010. Vulnerability of poor urban coastal communities to flooding in Lagos, Nigeria. Environment and Urbanisation 22, 433–450.

Amores, A., Marcos, M., Carrio, D.S., Gomez-Pujol, L., 2020. Coastal impacts of storm Gloria (january 2020) over the North-western Mediterranean. Nat. Hazards Earth Syst. Sci. 20, 1955–1968.

Androulidakis, Y.S., Kombiadou, K.D., Makris, C.V., Baltikas, V.N., Krestenitis, Y.N., 2015. Storm surges in the Mediterranean Sea: variability and trends under future climatic conditions. Dynam. Atmos. Oceans 71, 56–82.

Artru, J., Ducic, V., Kanamori, H., Lognonne, P., Murakami, M., 2005. Ionospheric detection of gravity waves induced by tsunamis. Geophys. J. Int. 160, 840–848.

Bajo, M., Međugorac, I., Umgiesser, G., Orlić, M., 2019. Storm surge and seiche modelling in the Adriatic Sea and the impact of data assimilation. Quarterly Journal of the Royal Meteorological. Society 145, 2070–2084.

Barale, V., Gade, M., 2008. Remote Sensing of the European Seas. Springer Science & Business Media.

Belušić, D., Grisogono, B., Klaić, Z.B., 2007. Atmospheric origin of the devastating coupled air-sea event in the east Adriatic. J. Geophys. Res. 112, D17111.

Bertotti, L., Cavaleri, L., Loffredo, L., Torrisi, L., 2013. Nettuno: analysis of a wind and wave forecast system for the Mediterranean Sea. Mon. Weather Rev. 141 (9), 3130–3141.

Billi, A., Funiciello, R., Minelli, L., Faccenna, C., Neri, G., Orecchio, B., et al., 2008. On the cause of the 1908 Messina tsunami, southern Italy. Geophys. Res. Lett. 35, L06301.

Bondevik, S., Lovholt, F., Harbitz, C., Mangerud, J., Dawson, A., Svendsen, J.I., 2005. The Storegga Slide tsunami—comparing field observations with numerical simulations. Mar. Petrol. Geol. 22, 195–208.

Booij, N.R.R.C., Ris, R.C., Holthuijsen, L.H., 1999. A third-generation wave model for coastal regions: 1. Model description and validation. Journal of geophysical research. Oceans 104 (C4), 7649–7666.

Casas-Prat, M., Sierra, J.P., 2013. Projected future wave climate in the NW Mediterranean Sea. J. Geophys. Res. Oceans 118 (7), 3548–3568.

Cavaleri, L., Bertotti, L., Lionello, P., 1989a. Shallow water application of the third-generation WAM wave model. J. Geophys. Res.: Oceans 94 (C6), 8111−8124.
Cavaleri, L., Bertotti, L., Luis, J.E., Lionello, P., 1989b. The wams model applied to the Mediterranean sea. Coast. Eng. 1988, 566−577.
Cavaleri, L., Bertotti, L., Lionello, P., 1991. Wind wave cast in the Mediterranean sea. J. Geophys. Res.: Oceans 96 (C6), 10739−10764.
Cavaleri, L., Bertotti, L., 1993. The Mediterranean Sea wave forecasting system. Coast. Eng. 1992, 116−128.
Cavaleri, L., Bertotti, L., 2004. Accuracy of the modelled wind and wave fields in enclosed seas. Tellus Dyn. Meteorol. Oceanogr. 56 (2), 167−175.
Cavaleri, L., Bajo, M., Barbariol, F., Bastianin, M., Benetazzo, A., Bertotti, L., Chiggiato, J., Davolio, S., Ferrarin, C., Magnusson, L., Papa, A., Pezzutto, P., Pomaro, A., Umgeisser, G., 2020a. The October 29, 2018 storm in Northern Italy—an exceptional event and its modeling. Prog. Oceanogr. 178, 102178.
Cavaleri, L., Bajo, M., Barbariol, F., Bastianini, M., Benetazzo, A., Bertotti, L., Chiggiato, J., et al., 2020b. The 2019 flooding of Venice and its implications for future predictions. Oceanography 33, 42−49.
Cavicchia, L., von Storch, H., Gualdi, S., 2014. A long-term climatology of medicanes. Clim. Dynam. 43 (5), 1183−1195.
Cid, A., Menéndez, M., Castanedo, S., Abascal, A.J., Méndez, F.J., Medina, R., 2016. Long-term changes in the frequency, intensity and duration of extreme storm surge events in southern Europe. Clim. Dynam. 46 (5), 1503−1516.
Conte, D., Lionello, P., 2013. Characteristics of large positive and negative surges in the Mediterranean Sea and their attenuation in future climate scenarios. Global Planet. Change 111, 159−173.
Cushman-Roisin, B., Naimie, C.E., 2002. A 3D finite-element model of the Adriatic tides. J. Mar. Syst. 37 (4), 279−297.
Davolio, S., Della Fera, S., Laviola, S., Miglietta, M.M., Levizzani, V., 2020. Heavy precipitation over Italy from the Mediterranean storm "Vaia" in October 2018: assessing the role of an atmospheric river. Mon. Weather Rev. 148, 3571−3588.
Davis, C.A., Emanuel, K.A., 1991. Potential vorticity diagnostics of cyclogenesis. Mon. Weather Rev. 119, 1929−1953.
De Girolamo, P., Di Risio, M., Romano, A., Molfetta, M.G., 2014. Landslide tsunami: physical modeling for the implementation of tsunami early warning systems in the Mediterranean Sea. Procedia Eng. 70, 429−438.
De Leo, F., De Leo, A., Besio, G., Briganti, R., 2020. Detection and quantification of trends in time series of significant wave heights: an application in the Mediterranean Sea. Ocean. Eng. 202, 107155.
De Leo, F., Besio, G., Mentaschi, L., 2021. Trends and variability of ocean waves under RCP8. 5 emission scenario in the Mediterranean Sea. Ocean Dynam. 71 (1), 97−117.
Denamiel, C., Šepić, J., Ivanković, D., Vilibić, I., 2019a. The Adriatic Sea and coast modelling suite: evaluation of the meteotsunami forecast component. Ocean Model. 135, 71−93.
Denamiel, C., Šepić, J., Huan, X., Bolzer, C., Vilibić, I., 2019b. Stochastic surrogate model for meteotsunami early warning system in the eastern Adriatic Sea. J Geophys Res Oceans 124, 8485−8499.

Denamiel, C., Huan, X., Vilibić, I., 2021. Conceptual design of extreme sea-level early warning systems based on uncertainty quantification and engineering optimization methods. Front. Mar. Sci. 8, 650279.

Denamiel, C., Tojčić, I., Vilibić, I., 2022. Meteotsunamis in orography-free, flat bathymetry and warming climate conditions. J. Geophy Res Oceans 127 e2021JC017386.

De Zolt, S., Lionello, P., Nuhu, A., Tomasin, A., 2006. The disastrous storm of 4 November 1966 on Italy. Nat. Hazards Earth Syst. Sci. 6 (5), 861–879.

Dietrich, G., Kalle, K., Krauss, W., Siedler, G., 1980. Translated by Susanne and Hans Ulrich Roll. General Oceanography, second ed. John Wiley and Sons, New York. (Wiley-Interscience).

Dodet, G., Bertin, X., Bouchette, F., Gravelle, M., Testut, L., Wöppelmann, G., 2019. Characterization of sea-level variations along the metropolitan coasts of France: waves, tides, storm surges and long-term changes. J. Coast Res. 88 (sp1), 10–24.

Fanjul, E.A., Gomez, B.P., Sanchez-Arevalo, I.F., 2001. Nivmar: a storm surge forecasting system for Spanish waters. Sci. Mar. 65, 145–154.

Ferrarin, C., Roland, A., Bajo, M., Umgiesser, G., Cucco, A., Davolio, S., Drofa, O., 2013. Tide-surge-wave modelling and forecasting in the Mediterranean Sea with focus on the Italian coast. Ocean Model. 61, 38–48.

Ferrarin, C., Valentini, A., Vodopivec, M., Klaric, D., Massaro, G., Bajo, M., De Pascalis, F., Fadini, A., Ghezzo, M., Menegon, S., Bressan, L., Unguendoli, S., Fettich, A., Jerman, J., Ličer, M., Fustar, L., Papa, A., Carraro, E., 2020. Integrated sea storm management strategy: the 29 October 2018 event in the Adriatic Sea. Nat. Hazards Earth Syst. Sci. 20, 73–93. https://doi.org/10.5194/nhess-20-73-2020.

Ferrarin, C., Bajo, M., Benetazzo, A., Cavaleri, L., Chiggiato, J., Davison, S., et al., 2021. Local and large-scale controls of the exceptional Venice floods of November 2019. Prog. Oceanogr. 197, 102628.

Ferrarin, C., Lionello, P., Orlic, M., Raicich, F., Salvadori, G., 2022. Venice as a paradigm of coastal flooding under multiple compound drivers. Sci. Rep. 12, 5754. https://doi.org/10.1038/s41598-022-09652-5.

Fujii, Y., Satake, K., 2007. Tsunami source of the 2004 Sumatra-Andaman earthquake inferred from tide gauge and satellite data. Bull. Seismol. Soc. Am. 97, S192–S207.

Fujii, Y., Satake, K., Sakai, S., Shinohara, M., Kanazawa, T., 2011. Tsunami source of the 2011 off the Pacific coast of Tohoku earthquake. Earth Planets Space 63, 815–820.

Gianfreda, F., Mastronuzzi, G., Sansò, P., 2001. Impact of historical tsunamis on a sandy coastal barrier: an example from the northern Gargano coast, southern Italy. Nat. Hazards Earth Syst. Sci. 1 (4), 213–219.

Godin, G., Trotti, L., 1975. Trieste, water levels 1952–1971: a study of the tide, mean level and seiche activity. Fisheries and Marine Service in Ottawa. Miscellaneous Special Publication 28, 1–24.

Gómez Lahoz, M., Carretero Albiach, J.C., 2005. Wave forecasting at the Spanish coasts. J. Atmos. Ocean Sci. 10 (4), 389–405.

Greenspan, H.P., 1956. The generation of edge waves by moving pressure distributions. J. Fluid Mech. 1, 574–592.

Hasselmann, K., 1967. Nonlinear interactions treated by the methods of theoretical physics (with application to the generation of waves by wind). In: Proceedings of the Royal Society of London. Series A. Mathematical and Physical Sciences, 299, pp. 77–103, 1456.

Hasselmann, K., 1974. On the spectral dissipation of ocean waves due to white capping. Boundary-Layer Meteorol. 6 (1), 107–127.

Hasselmann, K., Barnett, T.P., Bouws, E., Carlson, H., Cartwright, D.E., Enke, K., Walden, H., 1973. Measurements of wind-wave growth and swell decay during the joint North Sea wave project (JONSWAP). Ergaenzungsheft zur Deutschen Hydrographischen Zeitschrift, Reihe A.

Iglesias, O., Lastras, G., Canals, M., Olabarrieta, M., González, M., Aniel-Quiroga, Í, et al., 2012. The BIG'95 submarine landslide-generated tsunami: a numerical simulation. J. Geol. 120, 31−48.

Jansà, A., Ramis, C., 2021. The Balearic rissaga: from pioneering research to present-day knowledge. Nat. Hazards 106, 1269−1297.

Krestenitis, Y.N., Androulidakis, Y.S., Kontos, Y.N., Georgakopoulos, G., 2011. Coastal inundation in the north-eastern Mediterranean coastal zone due to storm surge events. J. Coast Conserv. 15 (3), 353−368.

Lagouvardos, K., Karagiannidis, A., Dafis, S., Kalimeris, A., Kotroni, V., 2021. Ianos-a hurricane in the Mediterranean. Bull. Am. Meteorol. Soc. https://doi.org/10.1175/BAMS-D-20-0274.1.

Lane, K., Charles-Guzman, K., Wheeler, K., Abid, Z., Graber, N., Matte, T., 2013. Health effects of coastal storms and flooding in urban areas: a review and vulnerability assessment. J. Environ. Public Health 2013. https://doi.org/10.1155/2013/913064, 913064.

Lespez, L., Lescure, S., Saulnier-Copard, S., Glais, A., Berger, J.-F., Lavigne, F., et al., 2021. Discovery of a tsunami deposit from the Bronze Age Santorini eruption at Malia (Crete): impact, chronology, extension. Sci. Rep. 11, 15487.

Letetrel, C., Marcos, M., Míguez, B.M., Woppelmann, G., 2010. sea Level extremes in Marseille (NW Mediterranean) during 1885−2008. Cont. Shelf Res. 12, 1267−1274.

Lionello, P., Nizzero, A., Elvini, E., 2003. A procedure for estimating wind waves and storm-surge climate scenarios in a regional basin: the Adriatic Sea case. Clim. Res. 23 (3), 217−231.

Lionello, P., Sanna, A., 2005. Mediterranean wave climate variability and its links with NAO and Indian Monsoon. Clim. Dynam. 25, 611−623.

Lionello, P., Mufato, R., Tomasin, A., 2005. Sensitivity of free and forced oscillations of the Adriatic Sea to sea level rise. Clim. Res. 29 (1), 23−39.

Lionello, P., Cogo, S., Galati, M.B., Sanna, A., 2008. The Mediterranean surface wave climate inferred from future scenario simulations. Global Planet. Change 63 (2−3), 152−162.

Lionello, P., Cavaleri, L., Nissen, K.M., Pino, C., Raicich, F., Ulbrich, U., 2012a. Severe marine storms in the Northern Adriatic: characteristics and trends. Phys. Chem. Earth 40−41, 93−105.

Lionello, P.G.M.E.E., Galati, M.B., Elvini, E., 2012b. Extreme storm surge and wind wave climate scenario simulations at the Venetian littoral. Phys Chem Earth 40, 86−92.

Lionello, P., Trigo, I.F., Gil, V., Liberato, M.L.R., Nissen, K.M., Pinto, J.G., et al., 2016. Objective climatology of cyclones in the Mediterranean region: a consensus view among methods with different system identification and tracking criteria. Tellus 68, 29391.

Lionello, P., Conte, D., Marzo, L., Scarascia, L., 2017. The contrasting effect of increasing mean sea level and decreasing storminess on the maximum water level during storms along the coast of the Mediterranean Sea in the mid 21st century. Global Planet. Change 151, 80−91.

Lionello, P., Conte, D., Reale, M., 2019. The effect of cyclones crossing the Mediterranean region on sea level anomalies on the Mediterranean Sea coast. Nat. Hazards Earth Syst. Sci. 19, 1541−1564.

Lionello, P., Barriopedro, D., Ferrarin, C., Nicholls, R.J., Orlić, M., Raicich, F., et al., 2021a. Extreme floods of Venice: characteristics, dynamics, past and future evolution (review article). Nat. Hazards Earth Syst. Sci. 21, 2705–2731.

Lionello, P., Nicholls, R.J., Umgiesser, G., Zanchettin, D., 2021b. Venice flooding and sea level: past evolution, present issues, and future projections (introduction to the special issue). Nat. Hazards Earth Syst. Sci. 21 (8), 2633–2641.

Lovholt, F., Harbitz, C.B., Vanneste, M., De Blasio, F.V., Urgeles, R., Iglesias, O., et al., 2014. Modeling potential tsunami generation by the BIG'95 Landslide. Adv. Nat Technol Hazards Res 37, 507–515.

Maas, L.R.M., Zimmerman, J.T.F., 1989. Tide-topography interactions in a stratified shelf sea I. Basic equations for quasi-nonlinear internal tides. Geophys. Astrophys. Fluid Dynam. 45 (1–2), 1–35.

Maramai, A., Brizuela, B., Graziani, L., 2014. The Euro-Mediterranean tsunami catalogue. Ann. Geophys. 57, S0435.

Marcos, M., Tsimplis, M.N., Shaw, A.G.P., 2009. Sea level extremes in southern Europe. J. Geophys. Res. 114, C010017.

Marcos, M., Jorda, G., Gomis, D., Perez, B., 2011. Changes in storm surges in southern Europe from a regional model under climate change scenarios. Global Planet. Change 77, 116–128.

Međugorac, I., Orlić, M., Janeković, I., Pasarić, Z., Pasarić, M., 2018. Adriatic storm surges and related cross-basin sea-level slope. J. Mar. Syst. 181, 79–90.

Međugorac, I., Pasarić, M., Güttler, I., 2021. Will the wind associated with the Adriatic storm surges change in future climate? Theor. Appl. Climatol. 143, 1–18.

Mel, R., Lionello, P., 2014. Verification of an ensemble prediction system for storm surge forecast in the Adriatic Sea. Ocean Dynam. 64, 1803–1814.

Mel, R., Lionello, P., 2016. Probabilistic dressing of a storm surge prediction in the Adriatic Sea. Adv. Meteorol. 2016.

Mel, R., Sterl, A., Lionello, P., 2013. High resolution climate projection of storm surge at the Venetian coast. Nat. Hazards Earth Syst. Sci. 13 (4), 1135–1142.

Miles, J.W., 1957. On the generation of surface waves by shear flows. J. Fluid Mech. 3 (2), 185–204.

Monserrat, S., Thorpe, A.J., 1996. Use of ducting theory in an observed case of gravity waves. J. Atmos. Sci. 53, 17242–21736.

Monserrat, S., Vilibić, I., Rabinovich, A.B., 2006. Meteotsunamis: atmospherically induced destructive ocean waves in the tsunami frequency band. Nat. Hazards Earth Syst. Sci. 6, 1035–1051.

Mourre, B., Santana, A., Builds, A., Gautreau, L., Ličer, M., Jansà, A., et al., 2021. On the potential of ensemble forecasting for the prediction of meteotsunamis in the Balearic Islands: sensitivity to atmospheric model parameterizations. Nat. Hazards 106, 1315–1336.

Mungov, G., Eble, M., Bouchard, R., 2013. DART® tsunameter retrospective and real-time data: a reflection on 10 years of processing in support of tsunami research and operations. Pure Appl. Geophys. 170, 1369–1384.

Musić, S., Nicković, S., 2008. 44-year wave hindcast for the Eastern Mediterranean. Coast. Eng. 55 (11), 872–880.

Nastos, P.T., Papadimou, K.K., Matsangouras, I.T., 2018. Mediterranean tropical-like cyclones: impacts and composite daily means and anomalies of synoptic patterns. Atmos. Res. 208, 156–166.

NOAA, 2022. NCEI/WDS global historical tsunami database, 2100 BC to present. NOAA National Centers for Environmental Information. https://doi.org/10.7289/V5PN93H7.
Okal, E.A., 2021. On the possibility of seismic recording of meteotsunamis. Nat. Hazards 106, 1125−1147.
Orlić, M., 2015. The first attempt at cataloguing tsunami-like waves of meteorological origin in Croatian coastal waters. Acta Adriat. 56, 83−95.
Palma, M., Iacono, R., Sannino, G., Bargagli, A., Carillo, A., Fekete, B.M., et al., 2020. Short-term, linear, and non-linear local effects of the tides on the surface dynamics in a new, high-resolution model of the Mediterranean Sea circulation. Ocean Dynam. 70, 935−963.
Paris, A., Heinrich, P., Abadie, S., 2021. Landslide tsunamis: comparison between depth-averaged and Navier-Stokes models. Coast. Eng. 170, 104022.
Pasarić, M., Orlić, M., 2001. Long-term meteorological preconditioning of the North Adriatic coastal floods. Cont. Shelf Res. 21, 263−278.
Pasarić, M., Pasarić, Z., Orlić, M., 2000. Response of the Adriatic Sea level to the air pressure and wind forcing at low frequencies (0.01−0.1 cpd). J. Geophys. Res. 105, 11423−11439.
Pasarić, M., Brizuela, B., Graziani, L., Maramai, A., Orlić, M., 2012. Historical tsunamis in the Adriatic Sea. Nat. Hazards 61, 281−316.
Pérez-Gómez, B., García-León, M., García-Valdecasas, J., Clementi, E., Mösso Aranda, C., Pérez-Rubio, S., et al., 2021. Understanding Sea Level processes during western Mediterranean storm Gloria. Front. Mar. Sci. 8, 647437.
Pérez Gómez, B., Vilibić, I., Šepić, J., Međugorac, I., Ličer, M., Testut, L., et al., 2022. Coastal sea level monitoring in the Mediterranean and black seas. Ocean Sci. Discuss. https://doi.org/10.5194/os-2021-125 (in review).
Pezzutto, P., Saulter, A., Cavaleri, L., Bunney, C., Marcucci, F., Torrisi, L., Sebastianelli, S., 2016. Performance comparison of meso-scale ensemble wave forecasting systems for Mediterranean sea states. Ocean Model. 104, 171−186.
Phillips, O.M., 1957. On the generation of waves by turbulent wind. J. Fluid Mech. 2 (5), 417−445.
Phillips, O.M., 1960. On the dynamics of unsteady gravity waves of finite amplitude Part 1. The elementary interactions. J. Fluid Mech. 9 (2), 193−217.
Pierson Jr., W.J., Moskowitz, L., 1964. A proposed spectral form for fully developed wind seas based on the similarity theory of SA Kitaigorodskii. J. Geophys. Res. 69 (24), 5181−5190.
Polli, S., 1960. La propagazione delle maree nell'Alto Adriatico. Publications of the Istituto Sperimentale Talassografico-Trieste 370.
Pomaro, A., Cavaleri, L., Lionello, P., 2017. Climatology and trends of the Adriatic Sea wind waves: analysis of a 37-year long instrumental data set. Int. J. Climatol. 37 (12), 4237−4250.
Proudman, J., 1929. The effects on the sea of changes in atmospheric pressure. Mon. Not. R. Astron. Soc. 2 (4), 197−209.
Rabinovich, A.B., 2009. Seiches and harbor oscillations. In: Kim, Y.C. (Ed.), Handbook of Coastal and Ocean Engineering. World Scientific Publishing, pp. 193−236. https://doi.org/10.1142/9789812819307_0009.
Ravdas, M., Zacharioudaki, A., Korres, G., 2018. Implementation and validation of a new operational wave forecasting system of the Mediterranean monitoring and forecasting centre in the framework of the Copernicus marine environment monitoring service. Nat. Hazards Earth Syst. Sci. 18 (10), 2675−2695.

Reale, M., Cabos Narvaez, W.D., Cavicchia, L., Conte, D., Coppola, E., Flaounas, E., et al., 2021. Future projections of Mediterranean cyclone characteristics using the Med-CORDEX ensemble of coupled regional climate system models. Clim. Dynam. 58, 2501–2524. https://doi.org/10.1007/s00382-021-06018-x.

Ross, E., Sam, S., Randell, D., Feld, G., Jonathan, P., 2018. Estimating surge in extreme North Sea storms. Ocean. Eng. 154, 430–444.

Rossby, C.-G., 1939. Relation between variations in the intensity of the zonal circulation of the atmosphere and the displacements of the semi-permanent centers of action. J. Mar. Res. 2 (1), 38–55.

Ruti, P.M., Dell'Aquila, A., Giorgi, F., 2014. Understanding and attributing the Euro-Russian summer blocking signatures. Atmos. Sci. Lett. 15, 204–210.

Samaras, A.G., Karambas, T.V., Archetti, R., 2015. Simulation of tsunami generation, propagation and coastal inundation in the Eastern Mediterranean. Ocean Sci. 11, 643–655.

Sánchez-Garrido, J.C., Sannino, G., Liberti, L., García Lafuente, J., Pratt, L., 2011. Numerical modeling of three-dimensional stratified tidal flow over Camarinal Sill, Strait of Gibraltar. J. Geophys. Res. Oceans 116 (C12).

Sannino, G., Carillo, A., Pisacane, G., Naranjo, C., 2015. On the relevance of tidal forcing in modelling the Mediterranean thermohaline circulation. Prog. Oceanogr. 134, 304–329.

Scicchitano, G., Scardino, G., Monaco, C., Piscitelli, A., Milella, M., De Giosa, F., et al., 2021. Comparing impact effects of common storms and Medicanes along the coast of south-eastern Sicily. Mar. Geol. 439, 106556.

Selva, J., Lorito, S., Volpe, M., Romano, F., Tonini, R., Perfetti, P., et al., 2021. Probabilistic tsunami forecasting for early warning. Nat. Commun. 12, 5677.

Šepić, J., Vilibić, I., Jordà, G., Marcos, M., 2012. Mediterranean sea level forced by atmospheric pressure and wind: variability of the present climate and future projections for several period bands. Global Planet. Change 86–87, 20–30.

Šepić, J., Vilibić, I., Lafon, A., Macheboeuf, L., Ivanović, Z., 2015a. High-frequency sea level oscillations in the Mediterranean and their connection to synoptic patterns. Prog. Oceanogr. 137, 284–298.

Šepić, J., Vilibić, I., Rabinovich, A.B., Monserrat, S., 2015b. Widespread tsunami-like waves of 23–27 June in the Mediterranean and Black Seas generated by high-altitude atmospheric forcing. Sci. Rep. 5, 11682.

Šepić, J., Rabinovich, A.B., Sytov, V.N., 2018. Odessa tsunami of 27 June 2014: observations and numerical modelling. Pure Appl. Geophys. 175, 1545–1572.

Shaw, B., Ambraseys, N.N., England, P.C., Floyd, M.A., Gorman, G.J., Higham, T.F.G., 2008. Eastern Mediterranean tectonics and tsunami hazard inferred from the AD 365 earthquake. Nat. Geosci. 1, 268–276.

Sutton-Grier, A.E., Wowk, K., Bamford, H., 2015. Future of our coasts: the potential for natural and hybrid infrastructure to enhance the resilience of our coastal communities, economies and ecosystems. Environ. Sci. Pol. 51, 137–148.

Thomson, A.S., 1898. Periodic tides. Nature 59 (1519), 125–126.

Tinti, S., Maramai, A., Favali, P., 1995. The Gargano promontory: an important Italian seismogenic-tsunamigenic area. Mar. Geol. 122 (3), 227–241.

Tinti, S., Graziani, L., Brizuela, B., Maramai, A., Gallazzi, S., 2012. Applicability of the decision Matrix of north eastern Atlantic, Mediterranean and connected seas tsunami warning system to the Italian tsunamis. Nat. Hazards Earth Syst. Sci. 12, 843–857.

Titov, V., Rabinovich, A.B., Mofjeld, H.O., Thomson, R.E., González, F.I., 2005. The global reach of the 26 December 2004 Sumatra tsunami. Science 309, 2045–2048.

Tolman, H.L., 1991. A third-generation model for wind waves on slowly varying, unsteady, and inhomogeneous depths and currents. J. Phys. Oceanogr. 21 (6), 782−797.

Tous, M., Romero, R., 2013. Meteorological environments associated with medicane development. Int. J. Climatol. 33, 1−14.

Trigo, I.F., Davies, T.D., Bigg, G.R., 1999. Objective climatology of cyclones in the Mediterranean region. J. Clim. 12, 1685−1696.

Tsimplis, M.N., Proctor, R., Flather, R.A., 1995. A two-dimensional tidal model for the Mediterranean sea. J. Geophys. Res. Oceans 100 (C8), 16223−16239.

Ullmann, A., Moron, V., 2008. Weather regimes and sea surge variations over the Gulf of Lions (French Mediterranean coast) during the 20th century. Int. J. Climatol. 28 (2), 159−171.

Umgiesser, G., Bajo, M., Ferrarin, C., Cucco, A., Lionello, P., Zanchettin, D., et al., 2021. The prediction of floods in Venice: methods, models and uncertainty (review article). Nat. Hazards Earth Syst. Sci. 21, 2679−2704.

UNESCO-IOC, 2017. Ten years of the north-eastern Atlantic, the Mediterranean and connected seas tsunami warning and mitigation system (NEAMTWS) − accomplishments and challenges in preparing for the next tsunami. In: Guymer, T., Santoro, F. (Eds.), Paris. IOC Information Document, 1340.

Valle, G.D., Gamberi, F., Foglini, F., Trincardi, F., 2015. The Gondola slide: a mass transport complex controlled by margin topography (South-Western Adriatic Margin, Mediterranean sea). Mar. Geol. 366, 97−113.

Vilibić, I., Šepić, J., Dunić, N., Sevault, F., Monserrat, S., Jordà, G., 2018. Proxy-based assessment of strength and frequency of meteotsunamis in future climate. Geophys. Res. Lett. 45, 10501−10508.

Vilibić, I., Denamiel, C., Zemunik, P., Denamiel, C., 2021. The Mediterranean and Black Sea meteotsunamis: an overview. Nat. Hazards 106, 1223−1267.

VLIZ/IOC, 2022. Sea level station monitoring facility. Flanders Marine Institute (VLIZ); Intergovernmental Oceanographic Commission (IOC). https://doi.org/10.14284/482. Accessed at. http://www.ioc-sealevelmonitoring.org. on 2022-02-22 at VLIZ.

Wakelin, S.L., Proctor, R., 2002. The impact of meteorology on modelling storm surges in the Adriatic Sea. Global Planet. Change 34, 97−119.

WAMDI, Hasselmann, S., Hasselmann, K., Bauer, E., Janssen, P.A.E.M., Komen, G.J., Bertotti, L., et al., 1988. The WAM model—a third generation ocean wave prediction model. J. Phys. Oceanogr. 18, 1775−1810.

Ward, S.N., Day, S., 2001. Cumbre Vieja volcano—potential collapse and tsunami at La Palma, Canary Islands. Geophys. Res. Lett. 28, 3397−3400.

Yildirim, B., Karniadakis, G.E., 2015. Stochastic simulations of ocean waves: an uncertainty quantification study. Ocean Model. 86, 15−35.

This page intentionally left blank

CHAPTER

7 Dense and deep water formation processes and Mediterranean overturning circulation

Nadia Pinardi[1], Claude Estournel[2], Paola Cessi[3], Romain Escudier[4], Vladyslav Lyubartsev[5]

[1]*Alma Mater Studiorum University of Bologna, Department of Physics and Astronomy, Bologna, Italy;* [2]*CNRS, LEGOS, Toulouse, France;* [3]*Scripps Institution of Oceanography, San Diego, CA, United States;* [4]*Mercator Ocean, Toulouse, France;* [5]*Centro EuroMediterraneo sui Cambiamenti Climatici, Bologna, Italy*

Learning Objectives

In this chapter, you will learn:
- What are the characteristics of Mediterranean dense and deep waters and their formation rates
- Where and when dense water formation processes have been observed in the Mediterranean
- What are the main formation areas
- What is the difference between dense shelf water cascading and open ocean convection
- What is the theoretical framework of these processes
- How can these processes be represented by numerical models
- What is the structure of the Mediterranean overturning cells

7.1 General concepts

The first scientific investigations into dense/deep water formation (DWF) events were conducted in the Mediterranean Sea, and were inspired by the early attempts of the oceanographic community to work together on common and critical science issues related to oceanographic processes. Henry Stommel et al. (1971) wrote in his inspiring article "Submarine clouds in the Deep Ocean" that: "Boyhood readers of Jules Verne will remember [.] the great funnel-shaped vortex that sucks ships down to the bottom of the ocean. [.] Nothing like that portrayed by Verne [.] occurs in the open sea. In fact nearly everywhere there is a permanent density stratification in the ocean [.] that affects a buoyant stability against vertical displacement of volumes of water and inhibits vertical displacement of large amplitude." Thus, the scientific

Oceanography of the Mediterranean Sea. https://doi.org/10.1016/B978-0-12-823692-5.00009-1

questions formulated were that if water buoyancy only changes at the surface, how and where does surface-transformed water reach the bottom? How is it possible to capture an event of large vertical velocities and sinking to the ocean bottom? What arrays of measurements are required, where should they be placed, and for what duration? An international group of oceanographers (MEDOC Group, 1970) from the US, UK, France and Italy conducted the first observational experiment into how DWF events occur. This took place in the offshore area of the Gulf of Lion in January to March 1969. Between February 7 and 11, this MEDOC Group (1970) gathered the first complete and undisputable evidence of water homogenization from the surface to a depth of 1000 m. The original data were published 1 year after the experiment and are shown in Fig. 7.1, showing a water column that is completely homogeneous in terms of temperature and salinity down to approximately 1500 m, which was not observed during the January investigations (not shown, see Anati and Stommel (1970) for more details). The Mediterranean remains an important area for investigations about water mass transformations.

The World Ocean Database 2018 (WOD18, Boyer et al., 2018) retains the stations from this initial experiment, although they have been redrawn with modern computer mapping algorithms and displayed similarly to those in Fig. 7.2. The station metadata are given in Table 7.1 and, although there are some omissions, the emerging picture is similar to the original. A lens of high-salinity water at the bottom

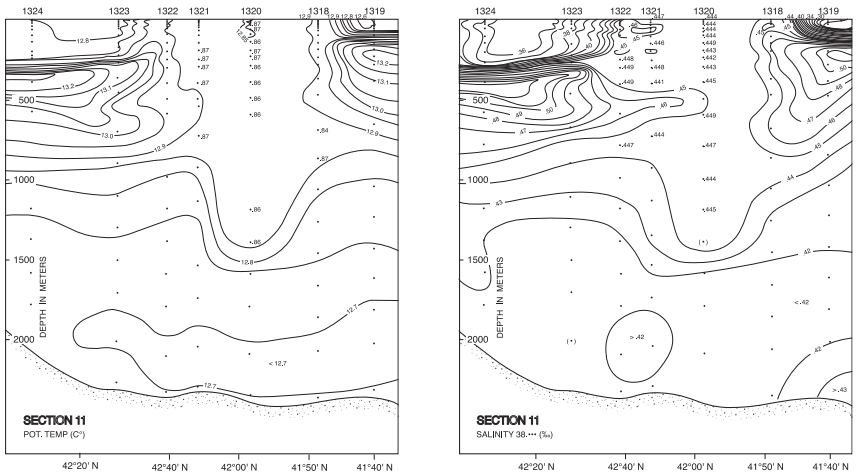

FIGURE 7.1

The stations are indicated by the numbers at the top. Data were collected between February 7–11, 1969 by the RV Atlantis II. Left panel: the potential temperature is shown in $^\circ C$°C and, in the region of the mixed patch, as any departure from 12°C of 2 decimal digits. Right panel: the salinity is shown as the departure from the reference value of 38 of 2 significant digits and with 3 in the mixed patch.

Reproduced from MEDOC Group, 1970. Observation of formation of deep water in the Mediterranean Sea, 1969. Nature, 227.

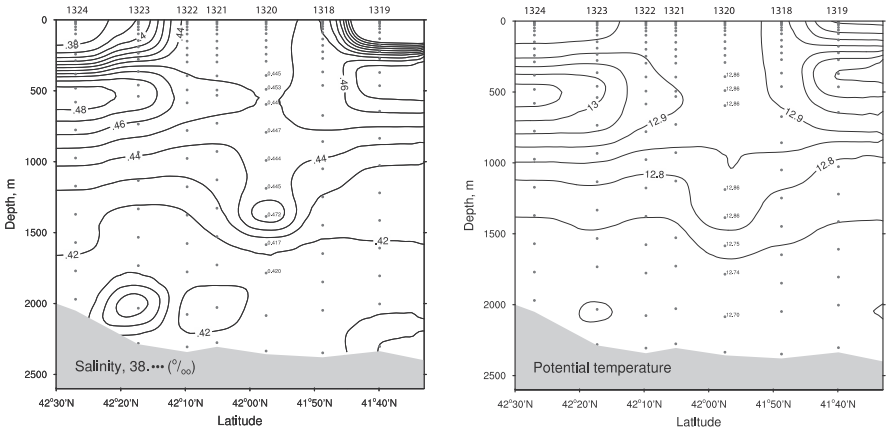

FIGURE 7.2

The objectively mapped stations corresponding to the original section represented in Fig. 7.1. Station data were retrieved from the WOD18 database and are described in Table 7.1.

of the unstratified dense water patch is now evident, which was not present in the original section. This highlights the interplay between stratification conditions, buoyancy losses, and homogenization of the water column in the process of open ocean DWF.

In the following sections, an overview of the dense/deep water characteristics and the formation rates in the Mediterranean Sea is given, with a focus on areas where dense/deep waters are formed and providing evidence for their interannual variability. In addition, the observations over the past 40 years that have followed the MEDOC's experiment are summarized. The theory of open ocean convection and shelf dense water cascading is then described, along with realistic numerical modeling of the water mass formation processes. Finally, the vertical circulation structure of the Mediterranean Sea is discussed.

7.2 Dense/deep water characteristics and formation rates

The antiestuarine character of the Mediterranean Sea is due to the specific buoyancy and momentum fluxes at the air-sea interface and determines the transformation of the entering Atlantic water (AW) into intermediate, dense and deep Mediterranean Waters (MW). These intense, diabatic, and spatially widespread water transformations occur in both the open ocean and on the shelf. The cascading of the dense waters from the shelf contributes to the intermediate water volume and to DWF in several regions of the Mediterranean.

The basic mechanism of DWF in the upper water column is through water transformation processes due to buoyancy exchanges. These dense waters can ventilate

Table 7.1 The MEDOC stations metadata shown in Fig. 7.1 by the MEDOC Group (1970) and in 8.2 with modern visualization methods.

Transect station	MEDOC station ID	WOD cast ID	Date	Time	Longitude	Latitude	Bottom depth, m
1	1324	560959	1969.02.11	00:00	5.15	42.45	2050
2	1323	6694504	1969.02.10	00:00	5.355	42.288	2287
3	1322	6694505	1969.02.10	00:00	5.363	42.162	2342
4	1321	6694500	1969.02.10	00:00	5.398	42.085	2305
5	1320	6694501	1969.02.10	00:00	5.45	41.958	2357
6	1318	6694415	1969.02.07	13:06	5.38	41.812	2329
7	1319	560605	1969.02.08	00:02	5.38	41.665	2336

the intermediate depths or become deep waters, depending on the specific mixing and spreading mechanisms, which are discussed later. Here the "source" regions of various dense water types throughout the Mediterranean Sea are examined.

The dense water masses of the Mediterranean have been classified by several authors, and an overview is given in Table 7.2. Their formation areas are located in nine regions, as indicated by the boxes in Fig. 7.3. All of the DWF areas are located in the northern part of the basin, where buoyancy fluxes may reach critical values, break the basin stratification and convect waters to the bottom. The red boxes indicate the shelf DWF areas, while the blue boxes indicate the open ocean convection areas, for both intermediate and deep waters. The shelf dense waters are characterized by cooled and well mixed waters, which then cascade into the open ocean areas at various depths. The shelf dense waters can directly affect the DWF processes, as described in Sections 7.4 and 7.5. In the areas where deep waters are formed by open ocean convection processes, the water may be convected down to the bottom, reaching $>$1200 m in the Adriatic and $>$2000$-$3000 m in the Rhodes Gyre area, Cretan Sea, and Gulf of Lion area. Such deep waters directly renew the abyssal waters of the formation area. Note that the literature sometimes refers to Eastern Mediterranean Deep Water (EMDW), which is not present in the table. This generic term is applied to deep waters in the Eastern Mediterranean Sea (EMED) that can originate from the AdDW, the CDW, the LDW, or combinations of these.

First the different estimation methods for the water mass formation rates are described, as well as the associated vertical circulation. Methods that estimate the volume formed per unit of time include that firstly described by Speer and Tziperman (1992), which computes the water mass formation rate from surface buoyancy fluxes. These give an upper limit for water transformed from light surface to denser intermediate and deep waters. This method is effective if the atmospheric conditions and surface densities are known. Second, the method described by Lascaratos (1993) estimates the formation rate from the maximum volume of the water mass in the mixed layer, which is then divided by one year. Recent papers such as those of Pinardi et al. (2015) and Simoncelli et al. (2018) apply this method, as reported in Fig. 7.4. Somot et al. (2018) recently evaluated the formation rate by comparing the maximum water mass volume in the whole water column within the formation area in one year with the minimum of this volume in the previous year, as illustrated in Fig. 7.5. The rates indicate that water mass formation occurs continuously over three- to five-year periods and then stops, which is a phenomenon yet to be fully understood. It may be connected to year-to-year preconditioning and other yet unidentified remote effects.

Fig. 7.6 illustrates the formation rate of the WMDW, as computed from the daily outputs of the latest Mediterranean Sea reanalysis products by all three of the methods described (Escudier et al., 2021). The estimations of the formation rate are similar, despite the different approaches. Selecting one method over another depends on the data available and their accuracy.

Table 7.2 Dense, Deep and Intermediate water mass characteristics in the Mediterranean Sea at the area of formation indicated in Fig. 7.3.

Water Mass name	Acronym	T-S range	Area of formation	Reference literature
Adriatic Deep Water	AdDW	T = 13 S = 38.6	4	Artegiani et al. (1997) Gacic et al. (2001) Mantziafou and Lascaratos (2004) Theocharis et al. (2014) Verri et al. (2018) Manca et al. (2003)
Northern Adriatic Dense Water	NAdDW	T = 9 −11.3 S = 38.3 −38.5	6	Artegiani et al. (1997) Orlić et al. (1992) Supić and Vilibić (2006) Wang et al. (2006) Marini et al. (2010) Theocharis et al. (2014)
Mid-Adriatic Dense Water	MAdDW	T = 11 −12.3 S = 38.2 −38.6	5	Cushman-Roisin et al. (2001) Artegiani et al. (1997) Marini et al. (2010)
Aegean Dense Water	AgDW	T = 10 S = 38.4	3	Gertman et al. (2006) Zervakis et al. (2000)
Cretan Deep Water	CDW	T = 14 −14.5 S = 38.9 −39.1	2	Theocharis et al. (1999) Theocharis et al. (2014) Velaoras et al. (2014) Velaoras et al. (2021)
Cretan Intermediate Water	CIW	T = 14.5 −15.5 S = 38.95 −39.1	2	Schlitzer et al. (1991) Theocharis et al. (1999)
Levantine Deep Water	LDW	T = 13.5 −14 S = 38.7 −38.8	1	Lascaratos (1993) Gertman et al. (1994)

Table 7.2 Dense, Deep and Intermediate water mass characteristics in the Mediterranean Sea at the area of formation indicated in Fig. 7.3.—*cont'd*

Water Mass name	Acronym	T-S range	Area of formation	Reference literature
				Theocharis et al. (2014)
Levantine Intermediate Water	LIW	T = 15 −16 S = 38.95 −39.05	1	Wüst (1961) Lascaratos (1993)
Tyrrhenian Intermediate Water	TIW	T = 13.2 −14 S = 38 −38.2	7	Napolitano et al. (2019)
Western Intermediate Water	WIW	T = 13 S = 37.7 −38.3	9	López-Jurado et al. (1995) Juza et al. (2019) Fuda et al. (2000)
Western Mediterranean Deep Water	WMDW	T = 12.70 S = 38.40	8	Pinardi et al. (2015) Somot et al. (2018)

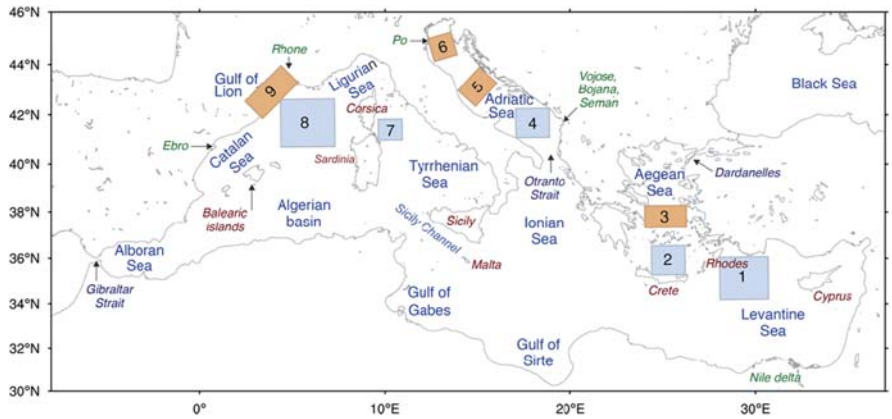

FIGURE 7.3

The nine areas where dense/deep and intermediate water formation occurs, as documented in observational and modeling studies over the past 40 years. Area 1 is the Levantine Intermediate (LIW) and Deep Water (LDW) formation area, Area 2 the Cretan Intermediate Water (CIW) and Deep Water (CDW) formation area, Area 3 the Cyclades Plateau where Aegean shelf Dense Water (AgDW) is formed, Area 4 the DWF area of the Southern Adriatic Sea (AdDW), Areas 5 and 6 are shelf DWF areas in the Middle (MAdDW) and Northern Adriatic Sea (NAdDW), respectively, Area 7 is the Tyrrhenian Intermediate Water (TIW) formation area, Area eight the Western Mediterranean Deep Water (WMDW) formation area, Area 9 is the shelf DWF area in the Gulf of Lion. Western Intermediate Water (WIW) is formed in Areas 8 and 9. Blue boxes indicate open ocean convection areas, red boxes shelf dense cascading areas.

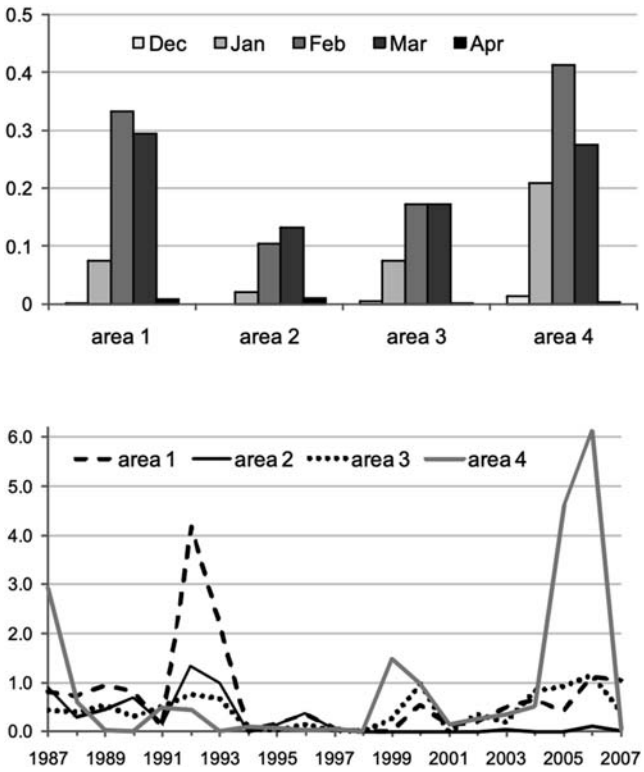

FIGURE 7.4

DWF rates in areas 1, 2, 3 and 4 of (Pinardi et al., 2015) that correspond to areas 1, 2, 4 and 8 of Fig. 7.3

Modified from Pinardi, N., Zavatarelli, M., Adani, M., Coppini, G., Fratianni, C., Oddo, P., Simoncelli, S., Tonani, M., Lyubartsev, V., Dobricic, S., Bonaduce, A., 2015. Mediterranean Sea large-scale low-frequency ocean variability and water mass formation rates from 1987 to 2007: a retrospective analysis. Prog. Oceanogr. 132, 318–332.

7.3 Observations of deep/dense water formation in the Mediterranean Sea

In the following, the DWF observations over the past 50 years in the Mediterranean Sea will be discussed. In the first part, the focus is on the Gulf of Lion because it is the most studied formation area in the region. Subsequently, observations from other dense, deep, and intermediate water formation regions of the basin will be described.

7.3.1 Convection and deep water formation in the Gulf of Lion: five decades of observations

Repeated measurements before the 1960s in the northern part of the western Mediterranean Sea (WMED) along north-south hydrographic sections revealed a permanent doming of the isopycnal surfaces associated with a cyclonic circulation.

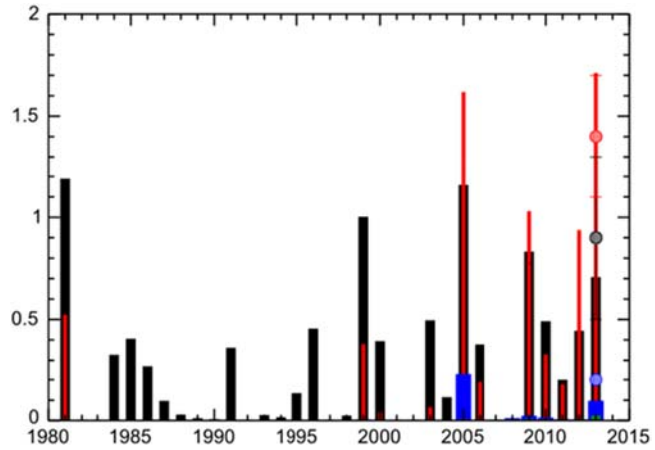

FIGURE 7.5

Interannual time series of the yearly DWF rate for WMDW area (in Sv) for the model (thick bars) and for the observation-based indicators with error bars (dotted circles Waldman et al., 2016). DWF rates using different density thresholds are shown: 29.10 kg m^{-3} (black), 29.11 kg m^{-3} (red), 29.12 kg m^{-3} (blue) and 29.13 kg m^{-3} (green).

From Somot, S., Houpert, L., Sevault, F., Testor, P., Bosse, A., Taupier-Letage, I., Bouin, M.N., Waldman, R., Cassou, C., Sanchez-Gomez, E., Durrieu de Madron, X., Adloff, F., Nabat, P., Herrmann, M., 2018. Characterizing, modelling and understanding the climate variability of the deep water formation in the North-Western Mediterranean Sea. Clim. Dynam. 51, 1179–1210.

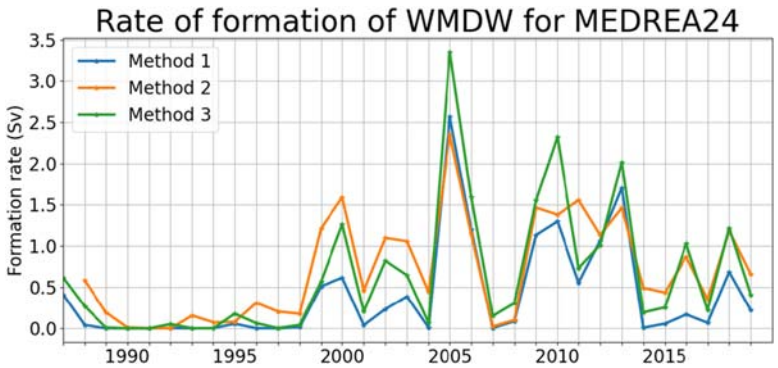

FIGURE 7.6

DWF rates for WMDW computed from the outputs of a Mediterranean Sea Reanalysis (Escudier et al., 2021) over the past 32 years. The yearly rates are estimated differently in the three methods. Method 1 is based on the air-sea fluxes (Speer and Tziperman, 1992), Method 2 uses the yearly maximum of the volume of dense water in the mixed layer (Lascaratos et al., 1993) and Method 3 the evolution of the total volume of dense water (e.g., Somot et al., 2018). For all methods, the density threshold used is 29.11 kg m^{-3}.

Tchernia (1960) noted that this doming should favor the formation of deep water. During the cold winter of 1963 (Sankey, 1973), hydrographic measurements conducted along the 6°E meridian revealed homogeneous profiles over the entire water column (0−2500 m). These measurements were repeated over the winter and a significant spatial and temporal variability was observed. At the beginning of the cold period, a station characterized by deep mixing was located less than 10 km from those where the stratification followed the classical three-layer structure of this region, consisting of AW, LIW and WMDW (see Table 7.2 for water mass names). After a month of severe cold weather, the vertically homogenized zone extended over a much wider area and occupied portions of the explored section for as far as 75 km. However, during the following much milder winter, no rupture of the three-layer structure was observed. These pioneering observations indicated the geographical area occupied by convection and also revealed that a dense network of measurements was necessary to accurately describe such a rapid oceanic process in space and time. The international measurement campaign MEDOC69 was thus conducted in 1969, using six oceanographic vessels (MEDOC Group, 1970) and samples were taken in the Gulf of Lion and the Ligurian Sea over 3 months.

The observations obtained through MEDOC69 have led to major advances in the general understanding of the processes associated with DWF, and the specific processes in the northern WMED formation area. First, this region is exposed to the Mistral in the Rhone valley and the Tramontane between the Massif Central and the Pyrenees, the dominant northerly winds that are channeled and intensified by the continental orography. In winter, these winds can be associated with cold and dry (<5°C) polar air masses blowing over the sea surface, which can be as cold as 13°C. The sea surface undergoes strong cooling through evaporation, which increases its water density. This results in an unstable vertical stratification that produces convective mixing between the surface layer and the underlying layers. Low stratification of the deep waters characterizes the northern WMED, and thus the erosion of the stratification of surface and intermediate waters by winter storms represents the critical point for deep convection (Anati and Stommel, 1970).

The extreme homogeneity of the temperature profile measured at some stations in 1969 (Fig. 7.1) reflected the intensity of the vertical mixing. In the horizontal direction, the mixing affected an area of about 50 km in the north-south direction and 130 km in the west-east direction. Unlike the vertical direction, the properties of the mixed water mass were not homogeneous horizontally within this patch of dense water (or "chimney"), because of the nonuniform thickness of the mixing. Current measurements were also conducted, which revealed increasing velocities at the cessation of the wind, with typical values of 15−20 cm s^{-1} at the surface. The horizontal structure of the current was not discerned as the number of measurements was limited, although a series of measurements carried out three weeks after the cessation of the wind showed the presence of at least three eddies of about 20 km in diameter (Sankey, 1973). Neutrally buoyant floats equipped with inclined vanes so they rotated in a vertical current were used to measure the vertical velocity (Stommel et al., 1971), and measured intensities of up to 2.5 cm s^{-1}.

The understanding of the development of open ocean convection and the processes at work increased significantly after these early observations, but some questions remained unanswered. The vertical structure of the currents, the horizontal structure of the dense water patch and the quantity of water formed were not fully understood. In the 1980 and 1990s, new observations provided further insights into the structure of currents. First, Millot (1987) identified hourly averaged current bursts near the bottom of up to 0.5 m s^{-1} during winter storms (compared to summer near-bottom currents of the order of 0.03 m s^{-1}). Further advances in current measurements were achieved through the second MEDOC experiment, the so-called MEDOC87 (Leaman and Schott, 1991; Schott and Leaman, 1991). In this experiment, Acoustic Doppler Current Profilers (ADCP) were positioned on three moorings within the center of the convection zone. These observations confirmed the presence of vertical shear in the horizontal currents, which were organized in a surface-cyclonic circulation. They also revealed the presence of relatively strong barotropic currents ($\sim$0.4 m s^{-1}) in the mixed patch zone. Finally, the ADCPs enabled vertical velocities to be characterized much more systematically than before. Downward velocities of 5−10 cm s^{-1} were recorded (Fig. 7.7A), separated by lower upward velocities (Schott and Leaman, 1991). Schott et al. (1994) used ADCP data from a new experiment in 1992 (the THETIS experiment), and found that the diameter of these cells or plumes was around 300−500 m.

Schott and Leaman (1991) summarized these observations and proposed classifying the horizontal scales during convection into three regimes: first, the scale of an homogeneous dense water patch or chimney enclosing the convection zone, which is typically of the order of 100 km; second, the scale of eddies detached from the front, which are of the order of the Rossby deformation radius (5 km); and third, the scale of convective plumes of less than 1 km.

In 2012−13, a series of campaigns was conducted using glider paths through the convection zone (Estournel et al., 2016a; Testor et al., 2018). These autonomous platforms have provided extensive information about small-scale vertical velocity structures in the dense water patch (Fig. 7.7B). Margirier et al. (2017) provided a 3D description of these plumes and a statistical description of their distribution. They have typical vertical velocities of 10−20 cm s^{-1}, a mean radius of 350 m, and are spaced apart about 2 km, covering about 30% of the convection area. The upward velocities are three times lower than the downward velocities and cover the remainder of the area. The glider observations also revealed the presence of different types of Submesoscale Coherent Vortices (SCV, McWilliams, 1985). Some of these SCV are cyclonic and others anticyclonic eddies of 5−8 km in radius and are composed of newly formed water expelled from the convection patch. Their vertical extension can reach that of the entire water column for cyclones (Bosse et al., 2016). These SCV can survive until the following winter and disperse dense water while preserving its characteristics (temperature and salinity). SCV can also encourage local convection the following winter.

The convection zone is illustrated in detail in Fig. 7.8. A complex pattern of currents develop at the edge of the zone, in the form of alternating patterns of downward/

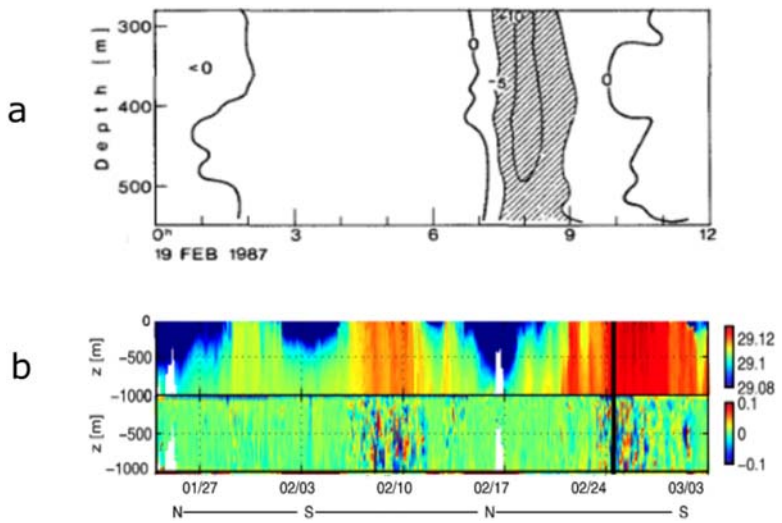

FIGURE 7.7

Characterization of vertical velocity during convective events in the Gulf of Lion with two experiments, 25 years apart. (A) ADCP observations (cm s^{-1}) in February 1987, with the horizontal axis indicating a distance (km) along a measurement section. (B) North-south glider transects in February 2013, where (top panel) shows potential density anomaly (σ_θ, kg m^{-3}) and (bottom panel) shows vertical velocity (m s^{-1}), with the horizontal axis indicating time (mm/dd). Vertical velocities associated with the dense and well-mixed water column correspond to two convective episodes of approximately 3 days following buoyancy losses, on 8–11 and 24–27 February 2013. N and S represent the northern and southern limits of the glider transects.

(A) From Schott, F., Leaman, K.D., 1991. Observations with moored acoustic Doppler current profilers in the convection regime in the Golfe du Lion. J. Phys. Oceanogr. 21 (4), 558–574, © American Meteorological Society, used with permission. (B) From Margirier, F., Bosse, A., Testor, P., L'Heveder, B., Mortier, L., Smeed, D., 2017. Characterization of convective plumes associated with oceanic deep convection in the northwestern Mediterranean from high-resolution in situ data collected by gliders. J. Geophys. Res. Oceans 122, 9814–9826.

outward cold water and upward/inward warm water. Bosse et al. (2021) proposed that symmetric instability is a major vertical and horizontal mixing process that particularly develops along fronts where wind and currents flow in the same direction.

Schroeder et al. (2010) analyzed the anomalous WMDW formation in 2004 and 2005 winter periods and deduced from observations that the contributions of atmospheric forcing and LIW lateral advection were equally important in setting the new deep water properties. Margirier et al. (2020) also documented an interplay between LIW warming and salting trends and the occurrence of deep ocean convection in the Gulf of Lion. Annual open ocean DWF events characterized the period between

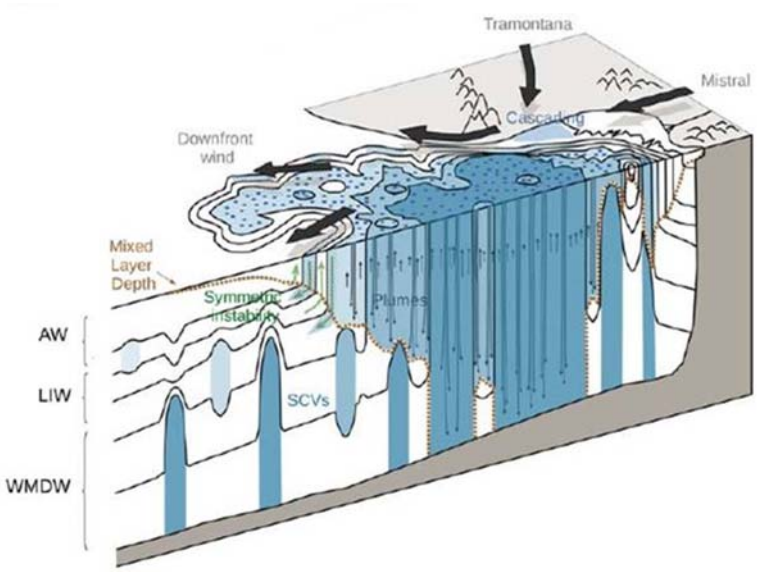

FIGURE 7.8

Scheme of the different processes at work during a major convection event in the Gulf of Lion in 2013: the inside of the dense water patch with narrow downward plumes and larger upward motions, submesoscale coherent cyclonic vortices that locally favor and/or disperse dense water, and symmetric instability along the downwind fronts.

From Testor, P., Bosse, A., Houpert, L., Margirier, F., Mortier, L., Legoff, H., Dausse, D., Labaste, M., Karstensen, J., Hayes, D., Olita, A., Ribotti, A., Schroeder, K., Chiggiato, J., Onken, R., Heslop, E., Mourre, B., D'ortenzio, F., Mayot, N., Lavigne, H., de Fommervault, O., Coppola, L., Prieur, L., Taillandier, V., Durrieu de Madron, X., Bourrin, F., Many, G., Damien, P., Estournel, C., Marsaleix, P., Taupier-Letage, I., Raimbault, P., Waldman, R., Bouin, M.N., Giordani, H., Caniaux, G., Somot, S., Ducrocq, V., Conan, P., 2018. Multiscale observations of deep convection in the northwestern Mediterranean Sea during winter 2012–2013 using multiple platforms. J. Geophys. Res. Oceans 123, 1745– 1776.

2009 and 2013, in which the LIW properties were transferred to the deep layers. During the following years (2014−18), the lack of convection produced a warming and salinification of the intermediate layers in the convection zone and the deep waters restratified making it increasingly difficult for convection to develop.

7.3.2 Deep water formation in the eastern Mediterranean

7.3.2.1 The Adriatic Sea as a main contributor to Eastern Mediterranean deep waters

The Adriatic Sea was previously identified as the largest source of the bottom water of the EMED (Pollak, 1951; Wüst, 1961; Schlitzer et al., 1991). The South Adriatic pit reaches a depth of 1200 m, is connected to the EMED through the Strait of Otranto at a depth of 800 m, and is a typical open sea DWF site. Fewer studies of

the physical processes in the Adriatic have been conducted than in the Gulf of Lion, but numerous observations reveal the interactions between the different water masses and enable us to evaluate the quantities of water formed and the dispersal pathways to the EMED.

Manca et al. (2003) analyzed hydrographic and current measurements taken during the period from March 1997 to March 1999 in the Southern Adriatic and in the Otranto Strait. During winter, the Adriatic is subject to violent north-easterly dry winds (Bora) that produce intense heat loss. Convective mixing involves surface waters and intermediate waters entering from the Otranto Strait as part of the cyclonic circulation of the Adriatic Sea. Mixing down to 800 m was observed during the winter of 1999, with a density in the range of about 29.16−29.17 kg m^{-3} (Manca et al., 2003). Below this layer of locally formed AdDW (Table 7.2), a denser water layer reached 29.34 kg m^{-3}, corresponding to NadDW (Table 7.2). A mixture of the newly formed AdDW and NAdDW exits the Adriatic through the Otranto Strait as a 200 m thick vein at a maximum velocity of 12 cm s^{-1} down-sloping in the Ionian Sea as a deep western boundary current and plunging to the bottom of the EMED (Robinson et al., 1992). Roether and Schlitzer (1991) found a mean formation rate of AdDW of 0.3 Sv using tracers. Over 3 years, the dense water outflow rate was estimated to vary from about 0.1 to 0.4 Sv (Manca et al., 2003).

The southern Adriatic appears to have much more variable water mass characteristics than the Gulf of Lion, which reflects the specific combination of lateral advective and surface buoyancy forcings, producing an open ocean convection of weaker intensity. Malanotte-Rizzoli and Robinson (1994) and Kokkini et al. (2020) investigated the impact of the Ionian circulation on the salinity of surface and intermediate waters in the southern Adriatic. During Ionian cyclonic periods (see also Chapter 9, Pinardi et al., 1997; Demirov and Pinardi, 2002; Vigo et al., 2005) high-salinity surface and intermediate water masses from the Levantine and Aegean areas enter the southern Adriatic, thus leading to dense water preconditioning, while an Ionian anticyclonic circulation leads to the advection of fresher AW.

As will be explained more in detail in Chapter 9, Adriatic winter convection produces saltier and warmer or fresher and colder dense waters, depending on the sign of this circulation (Bensi et al., 2013). Kokkini et al. (2020) showed that during a rainy year/season, high river discharges from the North Adriatic and from the Po can lead to a significant amount of fresher water being advected into the South Adriatic, which prevents DWF (the topography of the Gulf of Lion does not allow for rivers to have a significant impact in the convection zone). The combination of variable low-salinity water volumes from the northern Adriatic, high salinity inflow from Otranto, and variable buoyancy fluxes at the sea surface can lead to complex stratifications in the Southern Adriatic preconditions, such as the presence of a salinity double maximum in 2015 and 2016 (Fig. 7.9). Bensi et al. (2013) demonstrated that the arrival of very dense NAdDW in the South Adriatic pit could contribute to the deep waters of the EMED, with anomalous properties. In addition, the Adriatic Sea is a semienclosed basin, which distinguishes it from the open ocean DWF processes of the Gulf of Lion, and thus creates specific conditions for DWF.

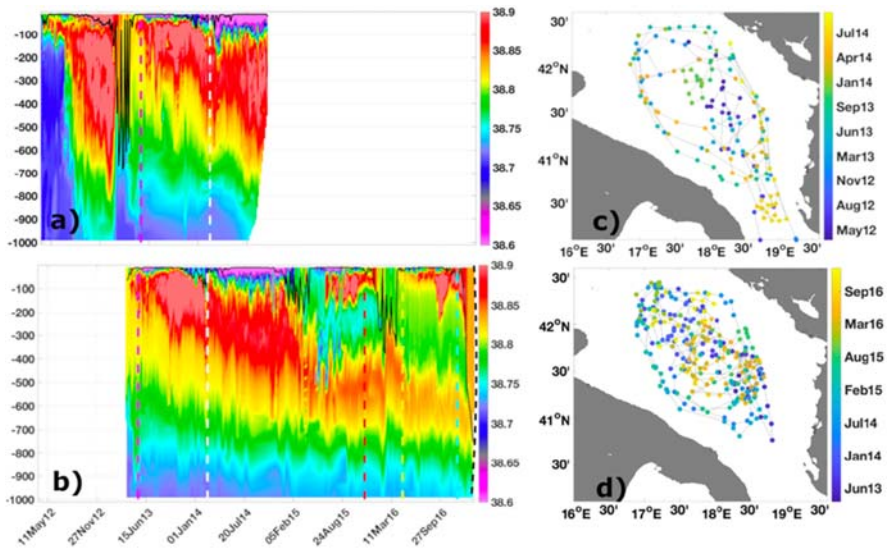

FIGURE 7.9

Hovmöller diagrams of salinity data from Argo floats (A) 6901040 and (B) 6901822 in the southern Adriatic Sea. The corresponding float trajectories are color-coded by time and shown in (C) and (D), respectively. The colored vertical dashed lines depict the time of glider campaigns. The black line indicates the mixed layer depth in (A) and (B).

From Kokkini, Z., Mauri, E., Gerin, R., Poulain, P.M., Simoncelli, S., Notarstefano, G.,n 2020. On the salinity structure in the South Adriatic as derived from float and glider observations in 2013–2016. Deep-Sea Res. Part II 171, 104625.

7.3.2.2 The Aegean Sea as an intermittent deep water source to the eastern Mediterranean

The Aegean Sea has been proposed as a possible source of deep waters for the EMED since the 1950s (Pollak, 1951). However, before 1987 the Aegean Sea was found to be only an occasional and minor contributor to the deep and bottom waters of the EMED (Lascaratos et al., 1999). The Eastern Mediterranean Transient (EMT) event, occurred after 1987, unambiguously defined the Aegean Sea as a source of EMDW. The changes that occurred during the EMT are the subject of Chapter 9, and thus here it is only noted that very cold and dry winds marked the winters of 1991–92 and 1992–93, with heat losses exceeding climatology by about 40% (Josey, 2003). These heat losses are the main cause of the massive formation of dense waters in the Aegean Sea, in particular those in the deep basin of the Cretan Sea. Cretan Deep Water (CDW) underwent a continuous increase in density throughout the 1987–95 period (0.2 kg m^{-3}, Gertman et al., 2006), leading to its overflow through the Cretan Arc Straits, filling the deep and bottom layers of the EMED. Observations demonstrated that by 1996 the CDW signal had penetrated

the Western Ionian Sea. The CDW outflow averaged nearly 3 Sv between mid-1992 and late 1994, and was at its largest during 1993, when Aegean-influenced deep waters extended from the bottom upwards to 400 m depth to the south and west of Crete (Roether et al., 2007).

The Aegean Sea DWF processes have similar characteristics to those of the Adriatic Sea. The Cretan Sea pits are areas of dense, open ocean convection at ∼2000 m, and thus slightly deeper but comparable to the Southern Adriatic pit. The northern Aegean and the Cyclades plateau DWF processes (see Table 7.2) may also contribute to the bottom waters of the Cretan Sea (Velaoras et al., 2021). The Black Sea waters entering from the Dardanelles have approximately the same influence as the river runoff in the Northern Adriatic Sea (Verri et al., 2018), that is, they can shut off the water densification processes.

As Ozer et al. (2020) noted, the Adriatic became again the main source of EMDW in the 2000s, as confirmed in other studies (Manca et al., 2006; Rubino and Hainbucher, 2007; Bensi et al., 2013). Manca et al. (2006) estimated that in 2002 the dense water of Adriatic origin again replenished the volume of the deep Ionian basin by more than 50%.

7.3.3 Formation of intermediate water masses

7.3.3.1 Levantine intermediate water

The LIW water mass is ubiquitous in the Mediterranean basin, and is characterized by a relative maximum in potential temperature and an absolute maximum in salinity in the TS diagram (see Chapter 4). LIW is also known to be a major contributor to the Mediterranean outflow in Gibraltar. LIWEX Group (2003) noted that the DWF in the Rhodes Gyre follows the "recipe" proposed by the MEDOC Group (1970), i.e., the phases of open ocean convection, preconditioning, mixing and spreading. In the preconditioning, the cyclonic circulation is associated with the doming of isopycnals, and the strong increase of surface salinity in summer and fall through evaporation is associated with the northern Etesian winds, which thus explains the high salinity of LIW. This surface increase in salinity is specific to the Levantine Sea area preconditioning. The "violent mixing" phase most frequently occurs in January/February during strong episodes of cold and dry winds. At the end of the mixing phase, the spreading of the newly formed water mass occurs along isopycnal surfaces from the periphery of the convection site toward the various parts of the basin. Although also the formation of deep water (Levantine Deep Water, LDW) has been documented (Sur et al., 1992; Ozsoy et al., 1993; Gertman et al., 1994; LIWEX Group, 2003), the Rhodes Gyre is mainly known to be the main source of the LIW. Other regions of the Levantine basin have also been identified as LIW sources, leading to extensive scatter in the LIW TS characteristics. These include the Antalya Bay in the northern Levantine (LIWEX Group, 2003) and the Turkish coastline to the west of Cyprus in general (Ovchinnikov, 1984), the southern Levantine basin (Hecht et al., 1988) and the Cilician basin. The formation

mechanism in these regions differs from that of the open sea, as it corresponds to the shelf water formation described in the next section.

7.3.3.2 Cretan intermediate water

Schlitzer et al. (1991) identified the CIW mass in the Aegean, which is formed both on the Aegean continental shelves and by open ocean convective mixing in the Cretan Sea (Velaoras et al., 2021). This water mass has variable characteristics although it is close to the LIW and is probably formed in smaller amounts. Millot (2013) reported that the density of CIW compared to that of LIW can depend on the period. In the western Cretan Straits, the intermediate water mass can be extremely variable, which reflects the varying mix of LIW and CIW. Following on from Manca et al. (2006), Millot (2013) estimated that LIW could represent two-thirds to three-quarters of the intermediate waters found at the Sicily Channel, with CIW responsible for the remainder.

7.3.3.3 Western intermediate water

WIW is a cold, low-salinity water mass formed in winter in the WMED and located in the layer between the surface AW and the intermediate LIW/CIW. WIW has a wide range of temperature and salinity, reflecting the different formation zones. This water mass has been commonly observed in the Ligurian Sea and the Gulf of Lion and has been extensively documented in the Balearic Sea. Millot (1999) identified two formation mechanisms, one in the open sea corresponding to winter winds where the cooling is too weak to trigger deep convection, and the other on the Gulf of Lion shelf and the Balearic Sea, which is associated with lower salinities. Pinot and Ganachaud (1999) deduced from a 1993 hydrographic survey that WIW formation could take place on the slope at the edge of the density dome, where convection cannot penetrate deeply because of stratification. Fuda et al. (2000) explained that WIW present near the surface in winter is progressively mixed with warmer AW, while Gasparini et al. (1999) suggested its subduction below the Liguro-Provencal Current. Cold WIW is expected to mainly follow the path of AW along the Spanish coast and across the Algerian Basin (Millot, 1999) but Fuda et al. (2000) proposed another pathway directly southward from the Gulf of Lion to the Algerian basin. Pinot and Ganachaud (1999) noted the recurrent presence of WIW in mesoscale eddies (or Weddies) in the Balearic Sea that strongly affect the general circulation, such as the recurrent obstruction of the Ibiza Channel by a large anticyclonic eddy. WIW was identified by Gascard and Richez (1985) in the Strait of Gibraltar, while Allen et al. (2008) conducted a detailed analysis of a Weddy and speculated that eddy transport toward the Alboran Sea may prove to be the ultimate fate for a significant proportion of WIW. Ben Ismail et al. (2014) observed that WIW is also able to penetrate the EMED through the Sicily Channel. WIW changes have recently been examined (Juza et al., 2019), and positive trends in both temperature and salinity have been found for the WIW, indicating a decrease in density in the most recent period from 2011 to 2015.

7.3.3.4 Tyrrhenian intermediate water

Another intermediate water mass formation area, the Bonifacio cyclonic gyre (Artale et al., 1994), has only recently been proposed (Napolitano et al., 2019). This WIW is called TIW, it sits above the LIW, in the layer between 100 and 200 m, and is characterized by a relative minimum of temperature and salinity in the TS diagram (Napolitano et al., 2019). Fuda et al. (2002) examined observations of Tyrrhenian deep waters and argued that local open ocean DWF can also occur in the Bonifacio cyclonic gyre. However, the evidence is not strong enough and no conclusions about this open ocean DWF region are drawn.

7.3.4 Dense shelf water formation and cascading

Dense waters formed over shelves by cooling and evaporation is a common process in the world ocean (Ivanov et al., 2004). Once it is denser than its surroundings, shelf water sinks and overflows off shelves, a process known as dense shelf water cascading (DSWC). This develops into a near-bottom gravity current that is able to reach the ocean bottom or to form intermediate waters. Cascading is a major contribution to shelf-deep ocean exchange.

These processes have been extensively documented for the Gulf of Lion shelf and the Adriatic, and in various regions of the Aegean Sea. The water masses formed are cold and have low salinity, due to fluvial inputs. They can interact with convection by sinking into deep basins in the open sea and thus change the composition of the bottom waters.

7.3.4.1 Gulf of Lion

Winters with strong cascading in the Gulf of Lion are less numerous than those producing deep convection. The dense shelf water formation in the Gulf of Lion appears to be linked to an anticyclonic atmospheric anomaly in the North Atlantic and a cyclonic atmospheric anomaly over the Baltic Sea, which provides particularly favorable conditions for strong, cold, and dry northerly winds over the Gulf of Lion (Durrieu de Madron et al., 2013, see also Chapter 9). Several years of strong cascading reaching the seafloor have been documented through observations at sea (Canals et al., 2006; Durrieu de Madron et al., 2013) as shown in Fig. 7.10.

The Cap de Creus Canyon located at the southwestern extremity of the Gulf of Lion shelf has been found to be the main conduit for cascading, with near-bottom gravity currents approaching 1 m s^{-1}. In the Gulf of Lion, the volume of dense water reaching the open sea ($\sim$1000 km^3) is one order of magnitude below that produced by open-sea convection. However, cascading can play a more important role in the transfer of matter (carbon, sediment, and pollutants). Durrieu de Madron et al. (2013) estimated the large volume of dense shelf water formed during the winter of 2012 and suggested that a significant proportion of the Gulf of Lion open ocean deep water was composed of dense shelf water cascading, which was entrained in the open ocean convection event that occurred at the same time.

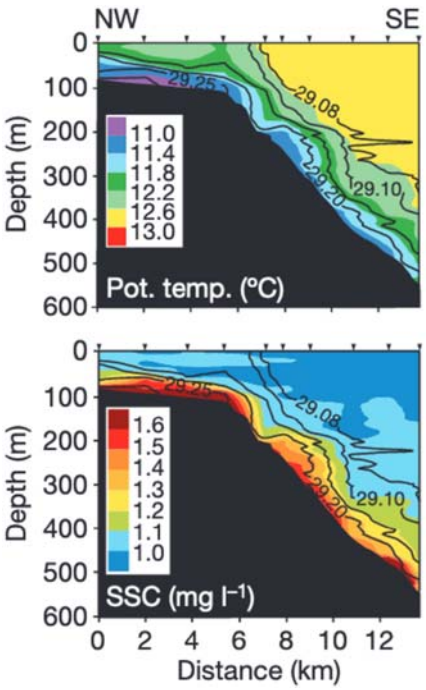

FIGURE 7.10

Potential temperature and suspended sediment concentration measured along the upper part of the Cap de Creus Canyon (potential density anomaly superimposed with black lines). The plume of dense cold water loaded with sediment cascades along the canyon seafloor.

From Canals, M., Puig, P., Durrieu de Madron, X., Heussner, S., Palanques, A., Fabres, J., 2006. Flushing submarine canyons. Nature 444, 354–357.

7.3.4.2 Adriatic Sea

The formation of very dense waters (Northern Adriatic Dense Water - NadDW) on the broad shallow shelf of the Northern Adriatic was identified many years ago (Zore-Armanda, 1963; Artegiani et al., 1997), and Mihanovic et al. (2013) recently reported high-density anomalies in 2012 along the entire eastern Adriatic coastal area, north-west of Split, all of which were above 29.55 kg m^{-3}. They concluded that at least during this exceptional winter, the Croatian shelf areas may be important for DWF and follow the same processes that occur in the Northern Adriatic Sea and other Mediterranean shelf areas. A NAdDW density of up to 30 kg m^{-3} (Vilibic, 2003; Mihanovic et al., 2013) was recorded during severe winters with outbreaks of the cold and dry northeast Bora winds. This is the highest density ever recorded in the whole Mediterranean Sea. NadDW flows as a dense vein along the western Adriatic shelf and escarpment area at a depth of around 50–150 m, cascading in the Middle Adriatic pit, where it rapidly renews old bottom waters (Artegiani

et al., 1997), and in the Southern Adriatic depression (Vilibic and Supic, 2005; Bensi et al., 2013). Turchetto et al. (2007) showed that the Bari Canyon is an efficient conduit for this water mass and associated sediment into the deep Southern Adriatic basin. The NAdDW can occupy the deepest part of the South Adriatic pit with density anomalies of >29.3 kg m^{-3}. Manca et al. (2003) concluded that outflow through the Otranto Strait can be sustained by the contribution of the NAdDW, which fills up the Southern Adriatic dense water reservoir even when deep convection does not occur.

7.4 Theory of dense/deep water formation processes: general concepts

In the following, the conceptual and theoretical models of DWF processes and spreading in the Mediterranean Sea are examined. All symbols in the equations are described in Table 7.3.

DWF processes are associated with a surface increase of water density, due to diabatic exchanges with the atmosphere. Air-sea interactions change the water buoyancy $\left(b = -g\frac{\rho-\rho_0}{\rho_0}\right)$ by buoyancy fluxes, B, written as:

$$B = \frac{g\alpha_T}{\rho_0 C_w} Q_H - \beta_S S_0 g(E - P - R) \tag{7.1}$$

The sign convention in this formulation is that buoyancy fluxes are positive when heat enters the ocean ($Q_H > 0$) and freshening occurs through precipitation and river runoff. DWF is associated with negative buoyancy fluxes that produce "new" waters that have lower buoyancy (higher densities) than those of the underlying layers. Dense waters can become deep waters if several conditions are met, such as if they are dense enough to be gravitationally unstable and force convection.

If only heat losses are considered, and if it is assumed that they are distributed in a layer Δz balanced by turbulent diffusivity, then the following is obtained:

$$K_v\frac{\Delta\rho}{\Delta z} = \frac{-\alpha_T}{C_W} Q_H \text{ or } Q_H = -K_v\frac{\Delta\rho}{\Delta z}\frac{C_W}{\alpha_T} \tag{7.2a, 7.2b}$$

By using (7.2) for a change of density of $\Delta\rho = 0.2$ kg m^{-3} in a layer of 100 m and with a vertical diffusivity of 0.01 m^2 s^{-1}, a heat loss of about -390 W m^{-2} is required, which is a typical winter-time heat loss in several DWF regions of the Mediterranean. Thus, dense waters are "winter waters" that in the subsequent seasons are found either at the bottom or at intermediate depths or disappear due to positive buoyancy gains. At least eight areas of DWF occur in the Mediterranean Sea, as previously described (including four shelf areas).

The question of how dense waters reach the sea bottom is more challenging. Dense waters can become deep or bottom waters through different processes. First, in open ocean convection, newly formed dense waters directly reach the bottom

Table 7.3 Symbols, units, and values of the parameters used in the text.

Symbol	Units	Description	Typical value in the Mediterranean sea
ρ	kg m^{-3}	Seawater potential density	[1027.5 – 1029.3]
ρ_o	kg m^{-3}	Reference constant density value	1000
f	s^{-1}	Coriolis parameter at 40N	9.410^{-5}
β	$m^{-1}s^{-1}$	Beta parameter at 40N	1.810^{-11}
H	m	Depth of open ocean convection	[1000 –2500]
B	m^2s^{-3}	Buoyancy flux	$[5.10^{-9} – 30.10^{-8}]$
$\vec{\tau}_w$	N m^{-2}	Wind stress	[0.02 – 0.1] for module
C_W	J $kg^{-1}K^{-1}$	Specific heat at constant pressure	3900
α_T	K^{-1}	Coefficient of thermal expansion	2.10^{-4}
β_S	−1	Coefficient of haline contraction	7.610^{-4}
K_v	m^2s^{-1}	Turbulent diffusion coefficient during the violent mixing phase	0.1 – 10
Q_H	W m^{-2}	Heat flux during winter in DWF areas	[−100, −1000]
$\text{curl}\left(\vec{\tau}_w\right)$	N m^{-3}	Curl of the wind stress	$[2 – 710^{-7}]$
g′	m s^{-2}	Reduced gravity	10^{-4} for almost unstratified plume
L_ρ	m	Reduced gravity Rossby radius of deformation	10^4
N	s^{-1}	Brunt-Vaisala frequency	$[0.8 – 4\ 10^{-3}]$
u_{rim}	m s^{-1}	Rim velocity	0.1

layer in the region where they are formed. Second, through down-sloping or cascading from the shelf area dense waters can reach the abyssal regions as bottom currents. These two different processes must be separately examined.

7.4.1 Theory of dense/deep water formation in the open ocean

Theories regarding the DWF processes in the open ocean regions were proposed immediately after the previously described MEDOC Group (1970) mission in the WMED. The early works of Anati (1971), Killworth (1976), and Gascard (1973, 1978) identified the different phases of the process before the idealized numerical models were developed in the 1990s (Legg and Marshall, 1993; Send and Marshall, 1995; Madec et al., 1996; Marshall and Schott, 1999; Straneo and Kawase, 1999). Here the study by Marshall and Schott (1999) (hereafter MS99) is considered, to provide the main overview of theories about the DWF processes in the open sea.

MS99 subdivided the processes of open ocean DWF into three phases (Fig. 7.11): (a) preconditioning occurs at the scale of a cyclonic gyre circulation (the order of 100 km), where a "dense water patch" (what was previously referred to as the

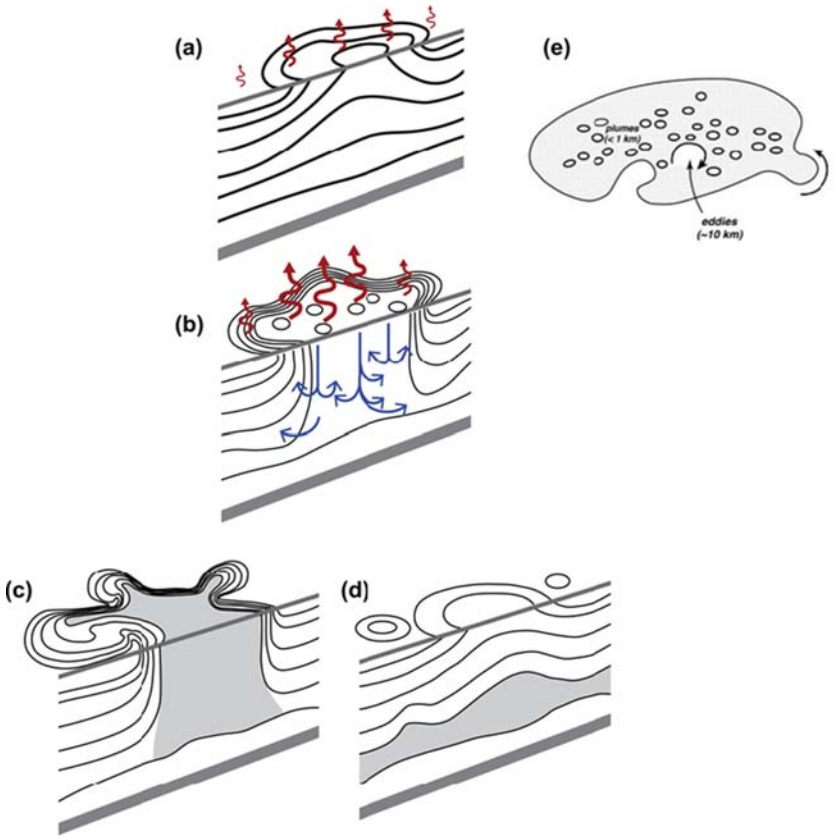

FIGURE 7.11

Phases of the dense/deep water open ocean formation processes and scales of relevance for the overall mechanism of formation of open ocean convection: (A) preconditioning with the isopycnals outcropping in the center of a cyclonic gyre with an intense rim current; (B) violent mixing phase where large buoyancy losses occur and mix the water column; (C) the patch of dense water formed (gray area), the instabilities of the rim current (meanders) that stop convection by fluxing heat inside the area, and with the isopycnals slanted laterally with a net downward motion at the periphery and dense water exiting at depth from the convection area; (D) stratification is reestablished and the newly formed dense water (gray area) is now separated from the surface, ventilating the deep layers; (E) shows the different horizontal scales of motion during the violent mixing phase (the patch of dense water in gray is populated by plumes <1 km and mesoscale eddies of ~ 10 km, originated by the instabilities of the rim current or entrained from outside the patch).

Redrawn from Marshall, J., Schott, F., 1999. Open-ocean convection: observations, theory, and models. Rev. Geophys. 37 (1), 1–64.

"chimney" area, but after the discovery that the net vertical velocity is zero at the center of the dense water area, it is preferable to use "patch" to indicate the newly formed dense water area) can form by convection; (b) the violent mixing phase or deep convection is characterized by scales of "plumes" (the order of 1 km) inside the patch; and (c–d) the lateral exchange and spreading phase occurs at the mesoscale (the order of 10 km or more in the Mediterranean Sea) produced by instabilities of the rim current at the border of the patch.

The preconditioning phase at the cyclonic gyre circulation scale characterizes all of the dense/deep water open ocean areas. This was examined in detail by Madec et al. (1996) (hereafter MLDC96) in the northern WMED formation area, by taking a mechanistic numerical modeling approach. The simulation was conducted with specific air-sea forcing and simplified geometry. No equivalent process study has been conducted on other open ocean DWF areas in the Mediterranean Sea. MLDC96 established that the wind-driven circulation in the northern WMED produces a preconditioning cyclonic gyre that is not necessarily of the same size as the dense water patch, and that in the open ocean is dominated by the Sverdrup balance, that is,

$$\beta vH = \frac{1}{\rho_0} \mathrm{curl}\left(\vec{\tau}_w\right) \tag{7.3}$$

Given that the winds of this area have an important northerly component, $\vec{\tau}_w \sim \left(0, \tau_w^{(y)}\right)$ and using the barotropic velocity stream function $vH = \frac{\partial \psi}{\partial x}$, it is possible to estimate the maximum value of the barotropic stream function field in the preconditioning gyre as:

$$\psi_{max} = \frac{1}{\rho_0 \beta} \max\left(\tau_w^{(y)}\right) \approx 5 - 10 \text{ Sv} \tag{7.4}$$

The value is slightly higher than those calculated using complex realistic models (Pinardi et al., 2015), but is of the correct order of magnitude. Thus, in the Mediterranean the dense water preconditioning gyre is a wind stress curl forced gyre, as suggested by MLDC96 and Pinardi and Navarra (1993). The buoyancy forcing has little or no impact on the preconditioning gyre strength.

This preconditioning gyre is characterized by a rim current of the order of few tens of cm s^{-1}, as implied by Eq. (7.3) for the maximum wind stress curl values of the Mediterranean Sea given by Pinardi et al. (2015) and reported in Table 7.3. MLCD96, noted that the buoyancy forcing and the thermohaline structure of the gyre add two other important factors: weak stratification at the center of the gyre and the baroclinic instability process of the rim current, which is active during the third phase of the process, that is, the lateral exchange phase.

MLCD96 also demonstrate the importance of the "Rhone fan," which is a bathymetric feature that constrains the local flow, as shown in the realistic bathymetry of Fig. 7.12.

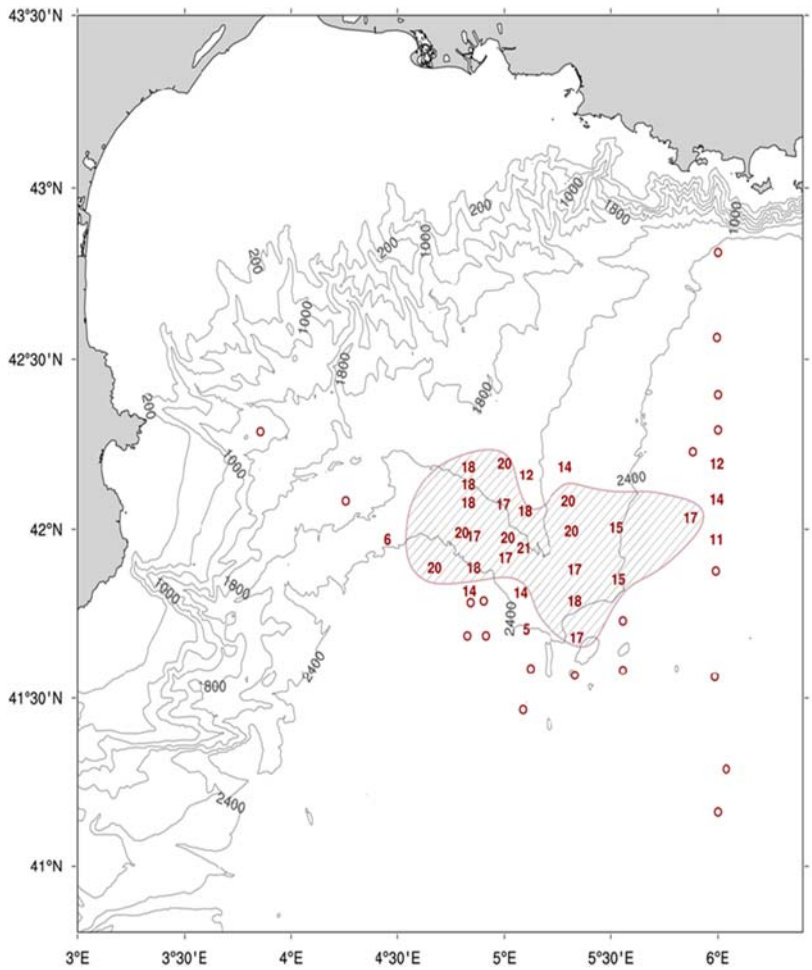

FIGURE 7.12

The "Rhone fan" geometry in the area of DWF in the northern WMED. The fan is characterized by the shape of the bathymetric isoline of 2400 m. The numbers on the shaded patch indicate the depth of the temperature mixed layer in units of 100 meters. The stations were collected between 16 and 21 February 1969.

Redrawn from Swallow, J.C., Caston, G.F., 1973. The preconditioning phase of MEDOC 1969. Part I. Observations. Deep-Sea Res. 20, 429–448.

The cyclonic preconditioning gyre within the Rhone fan is smaller and closely resembling the final dense water patch (Fig. 7.13). Thus, both wind stress curl and bathymetry are important in controlling the preconditioning gyre for open ocean DWF. This basic preconditioning feature appears to be valid (Lascaratos et al., 1993)

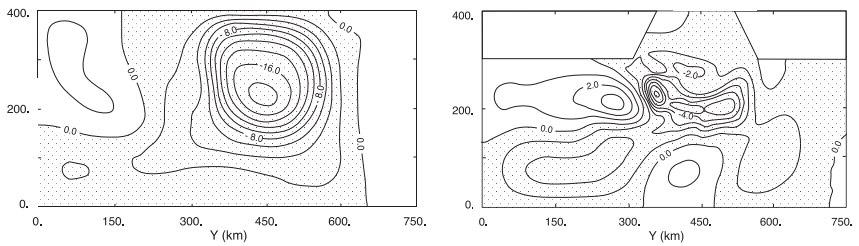

FIGURE 7.13

The wind driven cyclonic circulation for the north-western Mediterranean: left panel, the barotropic streamfunction for the flat bathymetry case; right panel, the barotropic streamfunction for an idealized bathymetry with the Rhone fan. Units are Sv. From MLDC96.

for the other open ocean areas of DWF, i.e., areas 4, 2 and 1 in Fig. 7.3, although no similar studies have been conducted in these regions.

Send and Marshall (1995) (hereafter SM95) described in detail the deep convection/violent mixing phase dynamics in the Mediterranean open ocean areas. This phase is characterized by downward water motion, that is, a negative vertical velocity w, which has been measured to be as much as 10 cm s^{-1} (Schott and Leaman, 1991) as shown in Fig. 7.7. How can such a high vertical velocity occur in this deep convective patch? If net downward motions of this intensity were created in the mixed patch, the induced vorticity and rim current speed would be several orders of magnitude larger than that found through laboratory and numerical experiments. The explanation given by SM95 provides some insights. The space scale of the convection inside the patch is connected to "plumes" that can be understood as 1 km diameter cylinders that mix water vertically. Plumes are very rapid overturning cells with upward and downward vertical velocities that almost compensate for each other, with each having both descending and ascending branches. The vertical velocity associated with the plumes was found by Jones and Marshall (1993) to be:

$$w_{plume} = \sqrt{\frac{B}{f}} \tag{7.5}$$

where B is the buoyancy flux and f is the Coriolis parameter. With $B = 5\ 10^{-7}$ m^2 s^{-3}, corresponding to heat losses of 1000 W m^{-2}, 7 cm s^{-1} is obtained. This is consistent with the measured downward vertical velocities, but there are equivalent upward vertical velocities in the plumes, so that in the area of the mixed patch the net vertical velocity is close to zero. Margirier et al. (2017), shown in Fig. 7.7, found in the northern WMED a prevalence of downward velocities in the mixed patch, but this may be due to the limited observational sampling of the area. Waldman et al. (2018) examined the sampling error to estimate the volume of water formed in the northern WMED and found it to be of the order of 20% −25%, which can also apply to the distribution of upward and downward vertical

velocities. Spall (2003) conducted a theoretical study of DWF in a marginal sea, and found that a net downwelling motion was only present at the periphery of the cyclonic preconditioning gyre. Thus, the dense water patch does not have a uniform downward vertical velocity. The vertical velocity is in the plumes and the net is almost zero.

MS99 developed the scaling for the diameter of the plumes as:

$$L_{plumes} = \sqrt{\frac{B}{f^3}} \tag{7.6}$$

which then amounts to 600 m for the largest values of B given in Table 7.3. This value has recently been verified by the glider experiment of Margirier et al. (2017), who also reported that the plumes were separated by about 2 km.

The plumes containing dense waters reach the bottom and then collapse under gravity and rotation, giving rise to a geostrophically adjusted well-mixed patch. This collapse has been extensively examined in idealized and laboratory experiments, such as in the studies of Dewar and Killworth (1990) and Maxworthy and Narimousa (1994). The dense water cylinders formed by convection in the chimney slump the interface laterally over a Rossby radius distance $L_\rho = \frac{\sqrt{g'H}}{f}$, that is, the baroclinic Rossby radius of deformation (g' is the reduced gravity and H is the scale height of the stratification). The chimney area then looks like a "cone" with bottom waters moving outwards.

At this point the third phase of the process starts and the baroclinic rim current, enclosing the patch of dense well-mixed waters, becomes unstable and forms mesoscale eddies that contain "dense water cones" and spread apart with time. The dense water at the bottom of these eddies attempts to spread out even further and is only contained by rotation. The eddies are markedly cyclonic at the surface (less at depth), and are efficient at exchanging heat laterally, thus restratifying the cold-water mixed patch in about one week. Straneo (2006) detailed the final process of lateral heat exchange through eddies, which balance the heat loss during the violent mixing phase, fluxing heat laterally into the well mixed patch. In this phase, the restratification of the mixed patch is mediated by the eddies.

SM95 treated the instability of the rim current as an Eady instability problem, and examined continuous buoyancy loss over 6 days. They analyzed the development time of eddies along the rim current. They found that the time scale corresponding to the rim current wave amplification was approximately 3−5 days. The Eady wave along the rim becomes nonlinear and eddies pinch off the patch. The spreading phase continues for months, as eddies propagate away from the mixed patch where vertical stratification is restored. Each region of formation in the Mediterranean Sea has different eddy pathways (this will be discussed in Section 7.5, focused on numerical modeling).

The southern Adriatic Sea is a special case of open ocean convection. This is a deep marginal sea (maximum depth of ~1200 m) connected to the Ionian Sea by the relatively narrow Strait of Otranto (Fig. 7.3). Unlike other open ocean convection

areas that are unbounded in the horizontal direction, the preconditioning cyclonic circulation is constrained by the geometry of the coasts and by the inflow/outflow system at the Strait of Otranto. In this marginal sea the net buoyancy loss is ultimately balanced by advection through the Strait of Otranto. Spall (2003, 2004) (S04 hereafter) and Iovino et al. (2008) (ISS08 hereafter) investigated a dense/deep water mass transformation process in a marginal sea with the inflow/outflow system at the Strait and a sill, which is very similar to the southern Adriatic Sea convection problem.

S04 confirmed that the net vertical velocity in the patch of well-mixed, dense water formed by buoyancy losses was zero, and that downwelling was present at the boundaries of the domain, where boundary currents sit along the bathymetry slope. The ratio of the isopycnal slope to the bathymetry slope is the key parameter for quantifying the exchange between the well mixed patch and the unstable boundary current during the last phase of convection. Thus, fully open ocean dense/deep convection differs from marginal sea open ocean deep water convection in the last phase of the process, during the lateral exchange and restratification, and during spreading. ISS08 examined the effect of the addition of a sill in the marginal sea and found that the temperature of the well-mixed patch of water was lower than without a sill, as the inflow of warm waters by the boundary currents around the basin is affected (Fig. 7.14). The greater density of the deep waters of the EMED compared to the WMED may be due to this, and the deep waters of the Adriatic and Aegean Seas may be denser than the WMDW because they are formed in deep marginal seas with sills.

7.4.2 Dense water formation on the shelf and their cascading into the deep ocean

Dense waters on the shelf are formed as in the open ocean through extensive buoyancy losses during winter. The process of dense water preconditioning for the shelf areas differs from that of the open ocean due to lateral and vertical geometrical constraints. The nearby land-derived runoff and precipitation are also important factors that can modify the preconditioning processes and the final dense water volume. The spreading phase is also very different because it involves cascading: this is a specific type of buoyancy-driven current in which the dense water formed over the continental shelf descends along the continental slope to a greater depth.

Shapiro et al. (2003) (SHI03 hereafter) proposed a three-stage process of dense water cascading from shelves: the dense waters form on the shelf; they are transported to greater depths (plumes and bottom density currents); and finally the cascading waters mix with the ambient waters.

In the first phase, a homogeneous patch of dense water forms on the shelf directly down to the bottom because the convection depth is typically greater than the shelf depth, and thus the dense water occupies the whole shelf volume. With the same level of cooling and evaporation at the surface, the shelf waters will be heavier

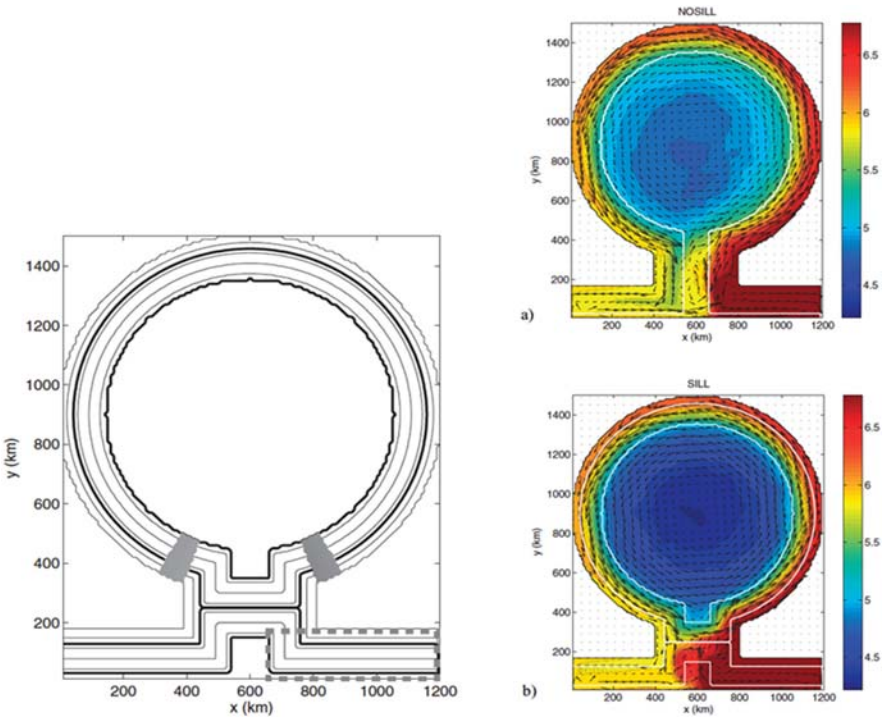

FIGURE 7.14

Left panel: the idealized geometry of the dense/water formation numerical simulation domain for a marginal sea with a sill at the entrance but with a deep basin in the semienclosed area. The center of the marginal sea is cooled to produce the well-mixed patch while the boundary current entering and outflowing is baroclinic and produces eddies. (a) and(b) panels on the right: temperature field in the basin with (b) and without (a) sill

From ISS08.

than the offshore waters. The density difference between the shelf and the offshore waters is:

$$\frac{d\rho}{\rho_o} = \frac{\rho_c - \rho_s}{\rho_o} = \left(\beta_S \frac{dS}{dz} - \alpha_T \frac{dT}{dz}\right) \frac{(H_c - H_s)^2}{2H_s} \tag{7.7}$$

Some of the symbols are explained in Fig. 7.15. This theory is valid without considering the advection of salinity on the shelf. The dense waters are transported from the shelf after the first phase of dense water and density gradient formation. The cross-shelf distance over a slope S is indicated by L, and thus SHI03 find that

$$R_H = \frac{d\rho}{\rho_0} \frac{S\, g}{L\, f^2} > 1 \tag{7.8}$$

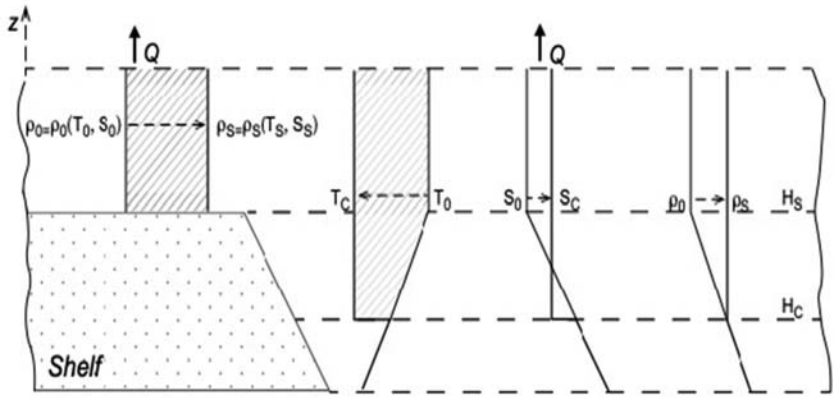

FIGURE 7.15

Scheme of formation of horizontal density contrast between shelf and slope waters under identical outward heat flux. Subscripts 0, S and C denote the initial state, shelf water and slope water, respectively.

From SHI03.

is the necessary condition for the start of the time-dependent shelf-water cascading process. If the density gradient is not strong enough or if the slope is too small compared to the across-shelf density contrast distance L, cascading will not occur. Several regimes of dense water downslope transport have been observed, from a broad and thick plume dominated by geostrophy to an unstable along-slope current that will transport the waters away by eddies. The bottom Ekman layer thickness is also a controlling factor for the shape of the downsloping plume, and if the plume is thicker than twice the bottom Ekman layer depth $H_E = \sqrt{\frac{2K_v}{f}}$, the plume has a nose and a complex shape. The cascading process can last several months and have been estimated to be 6–7 months in some conditions, and thus remnants of shelf dense waters plumes can be found during the summer. In the Mediterranean Sea, dense water cascading occurs from the areas in the Cyclades Plateau, the Northern and North-Eastern Adriatic and the Gulf of Lion shelves (areas 3, 5, 6, and 8 in Fig. 7.3).

After the initiation of cascading, the density and volume of the plume are modified by mixing with the ambient waters, thus entering the third phase. During this phase the plume finds its buoyant layer and it detaches from the bottom, intruding into the ambient waters. An interesting outcome of (7.7) is that the maximum depth of intrusion H_{max} of dense waters can be written as (the symbols are defined in Fig. 7.15):

$$H_{max} = H_c + \frac{H_s}{2}\left(\frac{H_c}{H_s} - 1\right)^2 \tag{7.9}$$

For the northern WMED, assuming the depth of open ocean convection to be 1000 m and the shelf depth to be 200 m, the maximum depth of intrusion will be

2600 m, that is, the bottom of the Gulf of Lion area. For the northern Adriatic, assuming a shelf of 30 m and a convective process in the Middle Adriatic of 100 m, the dense water plume will descend only to 180 m. For the Cyclades Plateau, assuming a depth of the shelf of 200 m and an offshore convection depth of up to 500 m, the depth of cascading is 725 m. These estimates are only valid if during the first phase of cascading there is no advection of ambient waters on the shelf. Dense water cascading is thus an efficient method of ventilating the deep layers of the ocean in the offshore areas of the Mediterranean Sea, even below the depth of the open ocean convection process.

7.5 Numerical modeling of deep/dense water formation

In this section, the reconstruction of DWF events and processes in the Mediterranean Sea using numerical models with realistic geometry is presented. In the previous section, it was noted that the geometry of the subbasins in the Adriatic and Aegean Seas is important for DWF in semienclosed seas, as it differs from that in the open ocean. The WMDW may also depend on continental escarpment structures such as the "Rhone fan" (Fig. 7.12) that affect the preconditioning phase of DWF. As previously discussed, the DWF on the shelf depends on the shelf bathymetry. Finally, the spreading phase of dense/deep waters depends on the specific bathymetry, such as the funneling effect of canyons in dense shelf water cascading. Thus it is important to use realistic bathymetry and geometry to understand and reproduce the observations.

Attempts at realistic modeling first began in the 1990s, when numerical models based on primitive equations first achieved eddy resolution and included adequate physical representations of mixing. These models were mainly aimed at characterizing the buoyancy forcing that triggers the DWF processes, the interactions between water masses formed in different parts of the basin, the spreading phase of deep convection and the climate trends in water formation rates. First the open ocean convection will be discussed, and then the shelf dense water cascading simulations.

7.5.1 Dense/deep water formation numerical modeling in the open ocean

The first numerical DWF simulations in the WMED were conducted by Madec et al. (1991) within an idealized context. A realistic geometry and bathymetry simulation throughout the Mediterranean was then conducted by Castellari et al. (1998, 2000). The air-sea buoyancy fluxes required to obtain the heat and water losses favorable for DWF to occur were taken particularly into account in these simulations. Several numerical artifacts were required to produce the observed features of the formed deep water (particularly for the salinity boundary conditions) because the primitive equation model and the atmospheric forcing variables were of relatively coarse resolutions in both the horizontal and the vertical (0.25° lat $\times$ 0.25° long and 31

vertical levels for the ocean model). The atmospheric forcing variables were also coarse in space and time (12 h atmospheric forcing analyses on a 1° lat × 1° long grid). The results confirmed that open ocean convection could be simulated in a realistic basin-scale ocean general circulation model of the Mediterranean Sea with calibrated buoyancy fluxes.

These early results also indicated the importance of salinity in the preconditioning of the convection depth, but raised the question of how salt accumulates in the dense/deep ocean areas and whether it affects the formation process. In the Mediterranean Sea, surface salinity increases locally through basin-scale summer and event-intense winter evaporation events, and also through the advected subsurface salinity maximum corresponding to LIW. Wu and Haines (1996) investigated the problem of connecting the advection of intermediate, salty waters to the DWF mechanisms in the Mediterranean Sea. They indicated that the advection of LIW partially drives the specific DWF processes in the Adriatic and WMED by increasing the density, thus leading to convection at greater depths. Thus, it is concluded that salinity not only increases locally through summer evaporation and winter buoyancy fluxes, but it is also advected from remote regions, thus affecting the local DWF processes.

Around the same time, the EMT (Roether et al., 1996 and Chapter 9) captured the attention of the numerical modeling community who examined the EMT phenomenon. Wu et al. (2000) performed realistic numerical simulations of the entire Mediterranean Sea and found that the CDW was associated with a salinity redistribution process and was triggered by intense cooling events over the Aegean Sea. The salinity redistribution process is connected to changes in LIW path that lead to the accumulation of salt at the subsurface in the Cretan Sea, but the intense and repeated large buoyancy losses in the Aegean Sea are the final trigger of the deep water convection in the Cretan Sea. Nittis et al. (2003) obtained numerical simulations for the EMED realistic geometry for a period of ∼15 years and demonstrated not only the significance of buoyancy losses over the Aegean Sea, but also the uniqueness of this event, which formed 0.2−0.3 Sv of dense and deep waters. The latest numerical simulations of the EMT (Beuvier et al., 2012) confirmed the triggering effect of atmospheric forcing conditions using a much higher resolution model of the Mediterranean Sea and more accurate atmospheric forcing.

The latest attempt to simulate the open ocean convection processes in the Adriatic Sea with a realistic general circulation model was conducted by Verri et al. (2018), encompassing the entire central Mediterranean Sea. They addressed the effect of the large river runoff of the Adriatic Sea basin on the DWF in the southern basin. They found that the open ocean DWF processes were marginally affected by river runoff changes and that wind and buoyancy fluxes were the dominant controlling factors for AdDW formation processes, in addition to the semienclosed basin geometry. While the southern Adriatic DWF process may also occur in years of large river runoff, the amount of deep water formed was found to be affected by the freshwater inputs and by dense water cascading from the middle and northern Adriatic regions.

For most of the water masses shown in Table 7.2, Pinardi et al. (2015) examined the rate of formation through the first reanalysis of the Mediterranean Sea (Adani et al., 2011). The reanalysis data-sets are the basis of the study of realistic deep water simulations, as they encapsulate the observations and the dynamic numerical model interpolation/extrapolation. The analysis showed that in the various open ocean DWF regions shown in Fig. 7.3, the formation processes occur over 3−5 years, after which they remain low for a comparable length of time, suggesting that there is multiyear memory in the process, which is yet to be fully understood. This is also shown in Fig. 7.6, which illustrates the most recent reanalysis of the Mediterranean Sea climate (Escudier et al., 2021).

The latest attempt to simulate the complex dynamics of WMDW processes over a long time period (1980−2013) was conducted by Somot et al. (2018) using a combined ocean-atmosphere model. They found that the model reported deep convection (deeper than 1000 m) in 22 of the 33 winters over this period, corresponding to an average DWF rate of $\sim$0.3 Sv, with a strong interannual variability and a maximum value of $\sim$1.7 Sv in 2013 and 2005.

Estournel et al. (2016b) focused on specific large formation events, like that of 2012−13, and demonstrated that with precise initial conditions and atmospheric flux time series, oceanic convection is predictable over several months. However, they focused on two key processes that affect the buoyancy budget of the convection zone during the preconditioning and convective phases, such as the direction of the wind with respect to the frontal area in the ocean. When the wind blows in the same direction as the current associated to the front (downfront wind), destratification is produced at the submesoscale through the Ekman buoyancy flux, which is the product of the Ekman transport and the horizontal surface buoyancy gradient. Seyfried et al. (2019) showed that = in the Gulf of Lion the stratification variations in the vicinity of the Northern Balearic front (separating the warm and fresh AW from the colder and saltier water present in the center of the Gulf of Lion cyclonic gyre) are principally driven by the Ekman buoyancy flux. Bosse et al. (2021) examined this process in winter, and they identified remarkable layers of negative potential vorticity in the upper 100 m on the dense side of fronts surrounding the deep convection area along the Northern Current. During winter, and particularly during the convection phase, lateral advection tends to restratify surface waters. Estournel et al. (2016b) used a 1-km horizontal resolution model and suggested that during convection, much of the buoyancy forcing works against the restratification effects of the lateral advection intensified by the intermittencies of surface forcing (wind and associated surface buoyancy fluxes). Waldman et al. (2017) evaluated the significance of ocean internal variability (mesoscales) in the water mass formation area extension and DWF rate in 2012−13 through a comprehensive numerical simulation study. They identified a relatively low impact during the preconditioning and violent mixing phases, but as expected, the impact was greater in the spreading phase.

The spreading phase of open ocean DWF events has only been examined using numerical simulations, as newly formed waters must be followed for several months after their formation. Demirov and Pinardi (2007) analyzed the relationship between

eddy transport and pathways for the 1987 and 1992 WMDW events. They found that in the 6 months following the convection event in 1987, a large amount of newly formed deep water remained confined to the Gulf of Lion gyre. At the end of summer, the southern rim of the Gulf of Lion gyre begins to break down and forms eddies (diameter $\sim$ 100 km) that transport the deep waters away from the formation regions. Such eddies interact and merge later with other eddies of the Algerian basin. Demirov and Pinardi (2007) concluded that the spreading of the WMDW is dominated by the eddy processes of the Algerian basin, which disperse the newly formed deep waters westward toward the Gibraltar Strait.

Beuvier et al. (2012) recently conducted another numerical modeling study of deep water spreading for the WMDW event of 2005. They again found that at the end of summer several deep cyclones were mainly responsible for the rapid spreading of the WMDW southwards in the WMED. These cyclones also encourage the propagation of the WMDW toward the Channel of Sardinia and possibly decrease the volume of WMDW that can reach the Strait of Gibraltar.

Finally, Damien et al. (2017) conducted a realistic simulation of intermediate and deep convection events in the Gulf of Lion, and identified for the first time the formation of Submesoscale Coherent Vortices with a radius of $\sim$6 km. The long lifetimes (several months) of these anticyclonic and cyclonic eddies reflect a slow diffusive process between their core and the surroundings. These SCVs help to spread a significant proportion (from 15% to 35%) of the convected waters in the Gulf of Lion and contribute to the ventilation of the deep basin.

7.5.2 Dense/deep water cascading numerical modeling

In the following an overview of the numerical modeling of dense water cascading from the Gulf of Lion shelves (area 9 in Fig. 7.3) and the Northern Adriatic shelf areas (areas 5 and 6 in Fig. 7.3) is provided.

Dufau-Julliand et al. (2004) simulated area 9, where dense coastal water form. Their analysis demonstrated that the down-slope motion of the plume is only partially explained by the friction effects and Ekman drainage. Local effects, such as the sharp bottom topography or coastline shape, also lead to the nonnegligible forcing of the down-slope motion. The presence of the Lacaze-Duthiers and Cap Creus canyons in the study area probably causes the breaking of the geostrophic constraint. Ulses et al. (2008) analyzed the 2005 cascading event and provided the reproduction of the water mass properties and the amount of water transported off the shelf, showing that it contributes to the renewal of the WMDW.

Wang et al. (2006) modeled the NAdDW cascading into the southern Adriatic Sea. They showed that the NAdDW bottom density plume cascades from the Gargano peninsula (located approximately at 42° N on the Italian coastlines) arrive there along the western Italian shelf, with a propagation speed of 0.1 m s^{-1} and a down-slope component of the order of 0.05 m s^{-1} at the Gargano peninsula. The connection between the interannual variability in the Gargano bottom density plume and the production of NAdDW constitutes an important finding in this work. The

numerical study demonstrated that a continuous heat loss of 175 W m^{-2} from November to January is required to produce an adequate volume of NAdDW, so that the density anomaly is strong enough to drive a density current that reaches the Gargano Peninsula in the spring and then cascades into the southern Adriatic deep basin .

7.6 The Mediterranean overturning circulation: structure and dynamics

Like the overturning circulation of the global ocean, which plays a key role in setting the stratification of different basins and transporting oxygen and other tracers from the surface to the deep ocean, the Mediterranean overturning circulation is key to provide low salinity waters to the Mediterranean as it balances the salt increase associated with the net evaporation inside the basin and determines the basin's stratification.

The Mediterranean overturning circulation is fed by the two-layer flow at the Gibraltar Strait. The potential energy associated with the Gibraltar Strait flow balances the surface wind-work and buoyancy flux (Cessi et al., 2014), thus providing energy to the overturning cells. The geometry of the Mediterranean Sea (Fig. 7.3), reveals several sills shallower than 500 m that divide the basin into several subbasins. The major subdivision occurs at the Sicily Channel, which separates the WMED from the EMED.

The zonal overturning cell that connects the two-layer flow at the Strait of Gibraltar to the EMED is limited to the surface and intermediate waters exchanged at the shallow Sicily Channel (Pinardi et al., 2019). However, within the EMED there are deeper circulations associated with DWF in the Adriatic and the Aegean Seas. The geometry of the basins and the large winter buoyancy losses in these semi-enclosed seas enables DWF, as explained earlier.

In addition to the zonal overturning cell that spans the Mediterranean from the Gibraltar Strait to the eastern end of the EMED, two primarily meridional deep cells occupy the WMED and the EMED. The WMED overturning circulation is connected to the DWF areas of the Gulf of Lion. The EMED meridional overturning is connected to the Rhodes Gyre, Aegean Sea, and Adriatic Sea DWF areas (Pinardi et al., 2019).

7.6.1 Zonal overturning

Wüst (1961) mapped the zonal overturning circulation (ZOC) by following water masses in the basin using the "core method", that is, tracking the positions of extremes in temperature, salinity and oxygen (see more on this in Chapter 4). A tongue of high salinity was identified along a longitudinal section spanning from the eastern end of the EMED to the Gibraltar Strait, which emanated from the EMED below a low-salinity tongue from the Gibraltar Strait.

A modern dataset supplemented by a dynamically consistent eddy-resolving model that assimilates observations (Simoncelli et al., 2017) can provide a quantitative estimate of the ZOC. The ZOC can be calculated in either vertical-longitudinal or density-longitudinal space. The transport of volume is quantified in the vertical-longitudinal space, which is the zonal equivalent of the classical Eulerian Meridional Overturning Circulation (MOC).

The overturning in density space quantifies the transport of buoyancy and is associated with the residual circulation, defined as:

$$\psi^{*}_{zon}\left(x,\widetilde{\sigma}\right)=\frac{1}{T}\int_{t_0}^{t_1}\int_{y_{B1}}^{y_{B2}}\int_{-H}^{0}\mathscr{H}\left[\widetilde{\sigma}-\sigma(x,y,z,t)\right]u(x,y,z,t)dzdydt \tag{7.10}$$

where $\mathscr{H}$ is the Heaviside function and σ is the potential density (Young, 2012). The zonal circulation is illustrated in Fig. 7.16 (Pinardi et al., 2019). The Eulerian overturning (upper panel) shows a shallow clockwise cell spanning the whole basin in longitude, corresponding to the circulation identified by Wüst using the "core method." Additionally, a counterclockwise cell dominates the WMED below 700 m, while multi-centred clockwise cells extend to the bottom in the EMED. These clockwise cells are associated with deep water outflow in the Aegean and with DWF in the Rhodes gyre.

The WMED deep counterclockwise residual overturning (see the lower panel of Fig. 7.16) is stronger than its Eulerian counterpart, indicating that transport by stationary gyres and eddies reinforces the mean abyssal vertical circulation. The residual cross-isopycnals flow indicates that diapycnal mixing is important for the maintenance of this cell. In the Tyrrhenian Sea, the residual overturning circulation mainly flows along isopycnals, thus indicating a more adiabatic balance.

However, the main differences between Eulerian and residual zonal overturning appear in the EMED. The residual circulation is weaker at depth than the Eulerian circulation, and a detectable residual counterclockwise circulation emerges. The large and deep Eulerian clockwise cell is broken into two parts in the residual representation: the deep overturning at 22° E is along isopycnals, while the circulation around the secondary maxima located approximately in the Rhodes gyre area of 28° E is across-isopycnals. The deep to abyssal ZOC of the EMED is strongly influenced by the transport due to the eddy/permanent gyres component. This analysis covers the period of the EMT event, and the Aegean deep water source is apparent in the zonal overturning cell of the Mediterranean Sea.

7.6.2 Western Mediterranean overturning

The Mediterranean has multiple subbasins and an opening at the Gibraltar Strait, and thus its geometry does not easily fit the traditional zonal integration associated with meridional overturning circulation.

Integrating over a subsection of longitudes is thus more informative, as it separates the meridional overturning of the WMED and the EMED. Again, the overturning

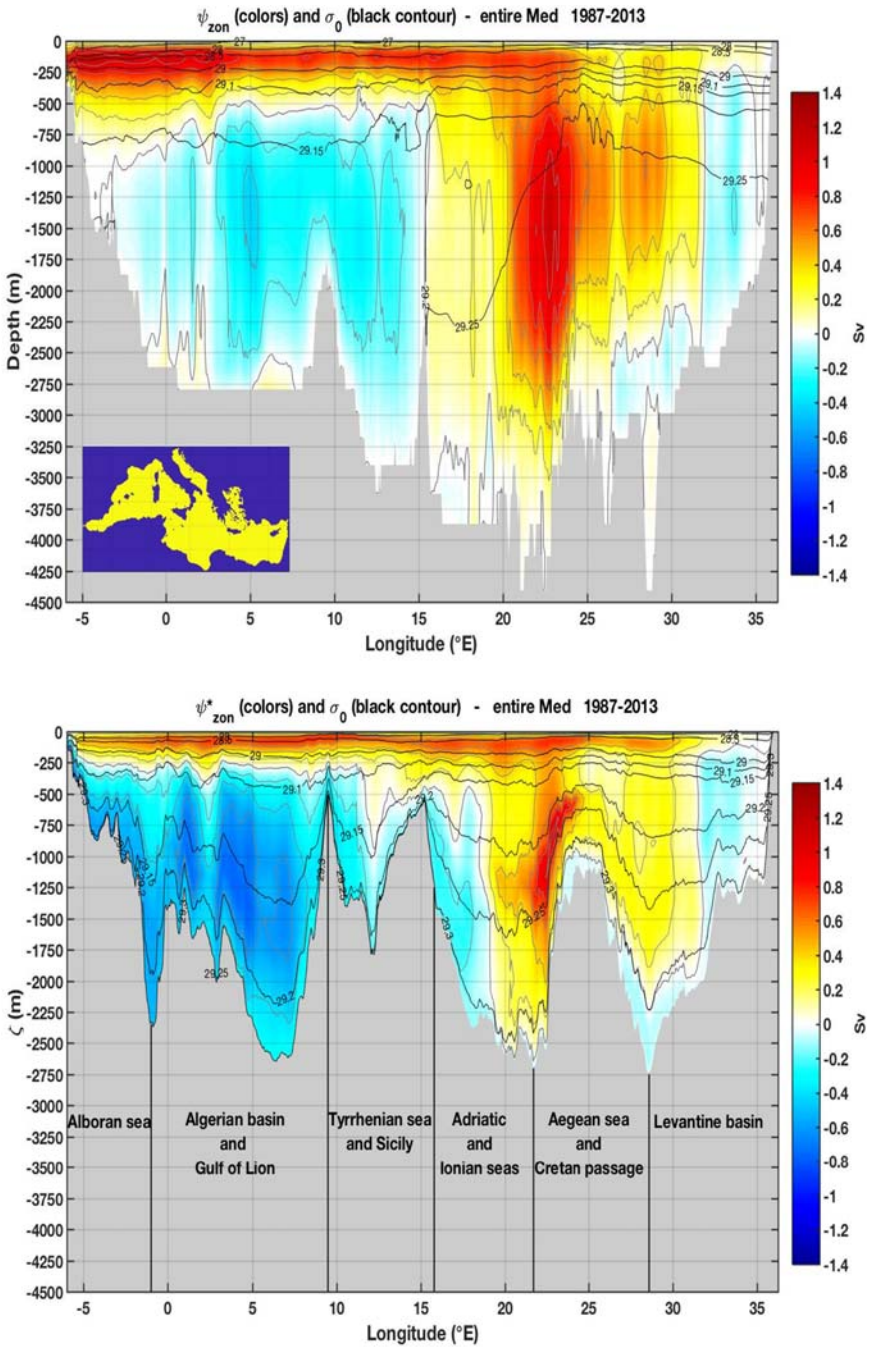
ψzon (colors) and σ0 (black contour) - entire Med 1987-2013
Depth (m)
Longitude (°E)
Sv
ψ*zon (colors) and σ0 (black contour) - entire Med 1987-2013
ζ (m)
Alboran sea
Algerian basin and Gulf of Lion
Tyrrhenian sea and Sicily
Adriatic and Ionian seas
Aegean sea and Cretan passage
Levantine basin
Longitude (°E)
Sv

FIGURE 7.16

streamfunction is shown with either depth (Eulerian streamfunction) or density (residual streamfunction) as a vertical coordinate, and with latitude as the horizontal coordinate.

The Eulerian streamfunction (Fig. 7.17, top panel) consists of a clockwise cell with multiple maxima from 100 m down to 2000 m. Counterclockwise cells, with maximum transport in the deep Algerian basin, occupy the abyssal Mediterranean region (the large positive values are above 500 m, just south of 37° N, and are associated with the Gibraltar Strait inflow). The residual WMED (bottom panel) meridional overturning shows only two well-separated counter-rotating cells, which are both stronger than their Eulerian counterparts. The clockwise streamfunction has a maximum volume transport of approximately 0.36 Sv, while the residual streamfunction reaches 0.88 Sv. For the counterclockwise cells, the minimum of −0.22 Sv in the Eulerian framework increases to −0.7 Sv in the residual streamfunction. The strengthening of the residual flow compared to the Eulerian flow is consistent with the WMED spreading of deep water being dominated by eddies, and their transport is only captured by the integration in the density coordinates. The boundary between the two residual cells is at approximately 39° N, i.e., the latitude marking the division between the permanent cyclonic gyre of the Gulf of Lion and the eddy-dominated anticyclonic area of the Algerian current, as described by Pinardi et al. (2015) and Demirov and Pinardi (2007). The clockwise northern cell is associated with the DWF areas in the northern basin, which are typically centered around 41−42° N.

7.6.3 Eastern Mediterranean overturning

Capturing the DWF areas in marginal seas such as the Adriatic and the Aegean allows to resolve the meridional overturning of the EMED. The Eulerian overturning (Fig. 7.18, top panel) is complex, with a shallow clockwise circulation in the Adriatic, Ionian, and Aegean Seas associated with the respective DWFs (Verri et al., 2018). This deepens south of the Rhodes gyre and Levantine Seas areas and is associated with their respective DWFs processes (Velaoras et al., 2014). The near-surface anticlockwise cell south of the Sicily Channel is associated with the Ekman transport and its shallow return flow. The deep counterclockwise Eulerian cell below 1000 m

Eulerian (top) and residual (bottom) zonal streamfunction, integrated over the latitudinal extension of the basin and averaged in time from 1987 to 2013. The gray contour lines and the colors show values at 0.2 Sv intervals. The black contours are isopycnal surfaces of σ (in kg m^{-3}) latitudinally and time averaged (top), calculated as described in Pinardi et al. (2019) (bottom). The gray areas mark the deepest bathymetry level (top) and the highest density layer depth (bottom) found over each latitudinal section of the basin. The different regions of the Mediterranean considered in the latitudinal averaging are described on the gray area of the bottom panel.

From Pinardi, N., Cessi, P., Borile, F., Wolfe, C.L., 2019. The Mediterranean Sea overturning circulation. J. Phys. Oceanogr. 49 (7), 1699–1721.

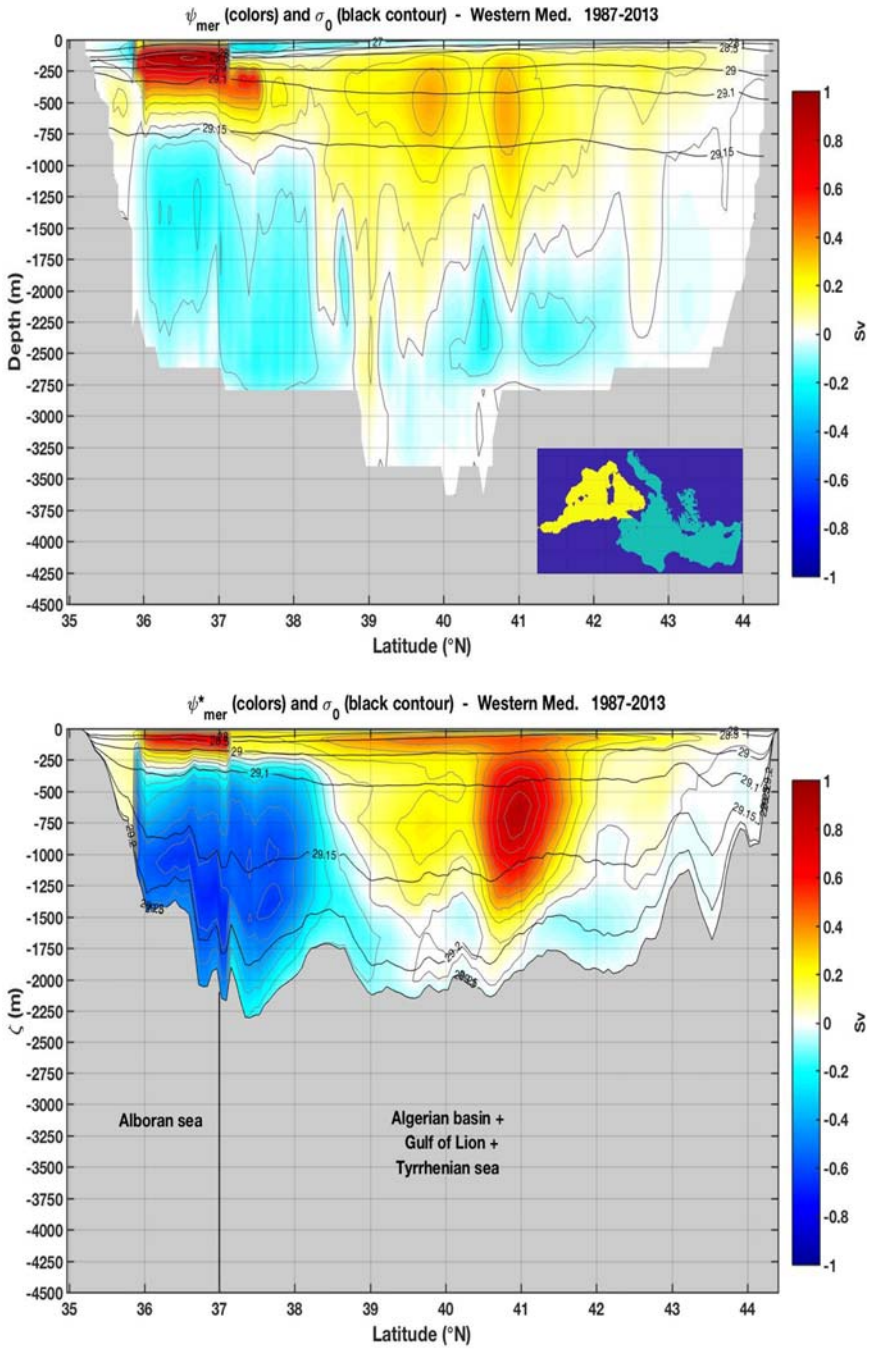
ψ_{mer} (colors) and σ_0 (black contour) - Western Med. 1987-2013
Depth (m)
Latitude (°N)
Sv
ψ^*_{mer} (colors) and σ_0 (black contour) - Western Med. 1987-2013
ζ (m)
Alboran sea
Algerian basin +
Gulf of Lion +
Tyrrhenian sea
Latitude (°N)
Sv

FIGURE 7.17

has been previously described (Zavatarelli and Mellor, 1995; Pisacane et al., 2006; Verri et al., 2018). The deep counterclockwise circulation is reduced in the residual framework (Fig. 7.18, bottom panel), while the clockwise circulation is enhanced relative to the Eulerian measure. The southern maximum of the clockwise residual cell corresponds to the region of dense Aegean Sea water outflows and the Rhodes gyre southern areas.

7.6.4 Comparison of the Mediterranean with the North Atlantic overturning

The Mediterranean Sea has been referred to as a miniature ocean in climate studies (Bethoux et al., 1999; Tsimplis et al., 2006) because it is a basin with deep and intermediate water mass formation processes that generate a vigorous overturning circulation. In this section, the similarities and differences between the Atlantic meridional overturning circulation (AMOC), the global overturning circulation (GOC) and the Mediterranean overturning are discussed.

The AMOC and GOC are primarily visualized in terms of meridional cells. The Atlantic sector is dominated by an interhemispherical clockwise mid-depth cell (Fig. 7.19, top panel), i.e., the AMOC, with downwelling in the high latitudes of the North Atlantic and upwelling in the global ocean. The GOC is characterized by the clockwise mid-depth circulation associated with the AMOC and an abyssal clockwise cell with downwelling in the high latitudes of the southern hemisphere. Most of the abyssal cell occurs in the Indo-Pacific sector (Fig. 7.19, bottom panel). The longitudinal integration gives the impression that the mid-depth and abyssal cells are separated, but these 2 cells are interconnected in three dimensions. A proportion of the water in the lower branch of the AMOC circulates in the abyssal cell before rejoining the upper branch of the AMOC, and becomes denser before it upwells. Estimates of this proportion range from 50% to 100% (Lumpkin and Speer, 2007; Talley, 2013; Rousselet et al., 2021). The mid-depth cell primarily "feeds" the abyssal cell in the Weddell Sea gyre and at the Campbell Plateau-Chatham Rise, just east of New Zealand, where the deep western boundary current of the South Pacific enters the abyssal Pacific basin.

Eulerian (top) and residual (bottom) meridional streamfunctions for the WMED, integrated in longitude over the yellow region shown in the inset and averaged in time over the years 1987–2013. The gray contour lines and the colors show values at 0.1 Sv intervals. The black contours are isopycnal surfaces of σ (in kg m^{-3}) longitudinally and time averaged (top), calculated as described in Pinardi et al. (2019) (bottom). The gray areas mark the deepest bathymetry level (top) and the highest density layer depth (bottom) found over each longitudinal section of the basin. The different regions of the Mediterranean considered in the longitudinal averaging are described over the gray area of the bottom panel.

From Pinardi, N., Cessi, P., Borile, F., Wolfe, C.L., 2019. The Mediterranean Sea overturning circulation. J. Phys. Oceanogr. 49 (7), 1699–1721.

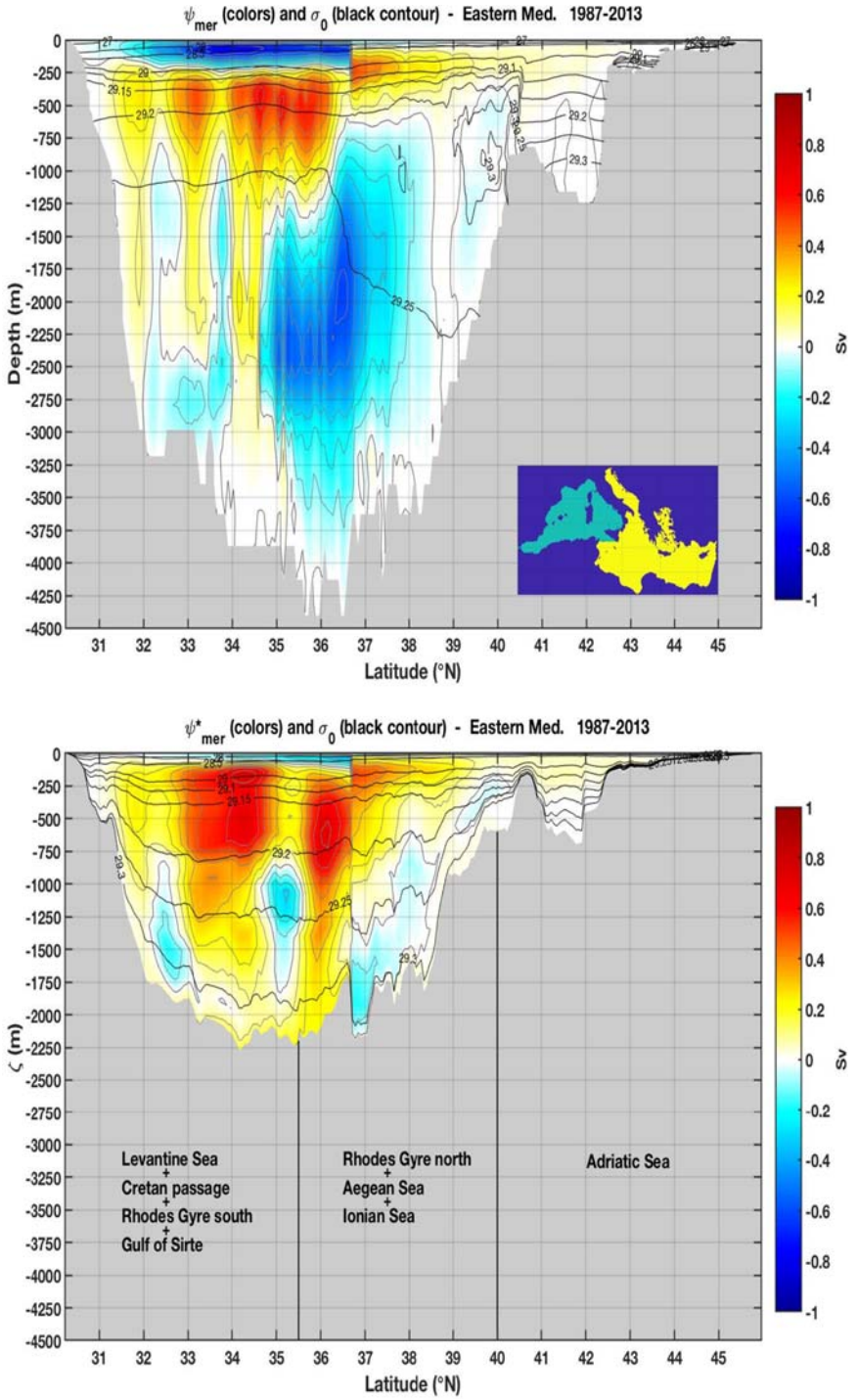
ψmer (colors) and σ0 (black contour) - Eastern Med. 1987-2013
Depth (m)
Latitude (°N)
Sv
ψ*mer (colors) and σ0 (black contour) - Eastern Med. 1987-2013
ζ (m)
Levantine Sea
+
Cretan passage
+
Rhodes Gyre south
+
Gulf of Sirte
Rhodes Gyre north
+
Aegean Sea
+
Ionian Sea
Adriatic Sea
Latitude (°N)
Sv

FIGURE 7.18

Eulerian (top) and residual (bottom) meridional streamfunctions of the EMED, integrated in longitude over the yellow region shown in the inset and averaged in time over the years 1987–2013. The gray contour lines and the colors show values at 0.1 Sv intervals. The black contours are isopycnal surfaces of σ (in kg m^{-3}) longitudinally and time averaged (top), calculated as described in Pinardi et al. (2019) (bottom). The gray areas mark the deepest bathymetry level (top) and the highest density layer depth (bottom) found over each longitudinal section of the basin. The different regions of the Mediterranean considered in the longitudinal averaging are described over the gray area of the bottom panel.

FromPinardi, N., Cessi, P., Borile, F., Wolfe, C.L., 2019. The Mediterranean Sea overturning circulation. J. Phys. Oceanogr. 49 (7), 1699–1721.

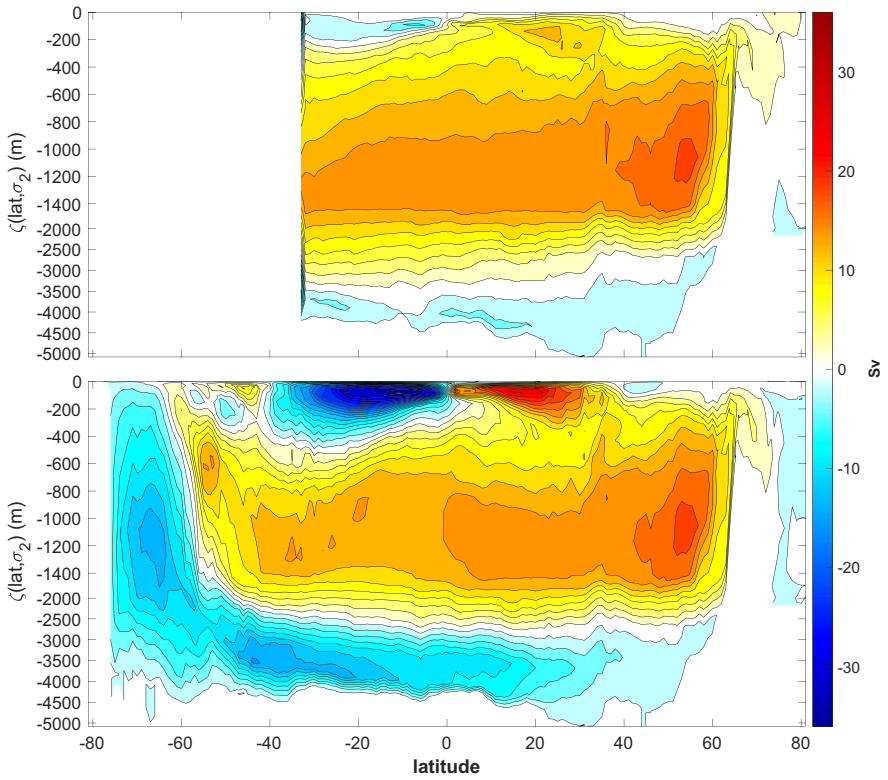

FIGURE 7.19

Residual meridional streamfunction integrated over the Atlantic sector north of 33° S (top) and the global ocean (bottom), and averaged in time over the years 1992–2015, using the Estimating the Circulation and Climate of the Ocean (ECCO) assimilated model. The black contour lines and the colors show values at 2 Sv intervals.

The mid-depth AMOC is powered by the winds of the Antarctic circumpolar region and is enabled by surface high density in the high latitudes of the North Atlantic (Toggweiler and Samuels, 1993). The AMOC mainly flows along isopycnals, except at the endpoints where strong diapycnal upwelling and downwelling occurs (Wolfe and Cessi, 2011). In contrast, the abyssal circulation is powered by diapycnal upwelling associated with the breaking of internal gravity waves near rough topography and balances the near-surface negative buoyancy flux in the downwelling regions, primarily in the Southern Ocean.

The Mediterranean ZOC or Wüst cell can be regarded as analogous to the mid-depth AMOC, although the ZOC is visualized as a zonal circulation and the AMOC as a meridional circulation. In Fig. 7.18 the mean pathways of the zonal and meridional vertical circulation are shown: between the surface and 150 m for the AW; between 150 and 1000 m for LIW/CIW; and below 1000 m for deep waters. The upper branch of the ZOC enters from Gibraltar and feeds the intermediate and deep waters following a two-step process. It is first converted into intermediate waters in the Eastern Levantine basin and then to deep waters in the four open ocean DWF areas 1,2, 4 and 8 (Fig. 7.3).

The zonal predominance of the Wüst cell is not only due to the geometrical differences between the Mediterranean and the Atlantic, but also to its energy source. The ZOC is powered by the inflow/outflow at the Gibraltar Strait, which in turn is balanced by the wind-stress work and the buoyancy flux in the basin (Cessi et al., 2014). Thus, the Mediterranean ZOC is locally powered, while the AMOC is powered remotely by wind-stress outside the Atlantic basin. Both the AMOC and the Mediterranean ZOC mainly flow along isopycnals, indicating that mixing is not the main driver of these cells.

Similarly, the deep clockwise circulation in the WMED can be viewed as analogous to the anticlockwise global abyssal circulation (which is primarily confined to the southern hemisphere). Both these cells are primarily driven by diapycnal mixing and reach the deepest part of the basins they flow into.

Similar to the feeding of the abyssal cell of the GOC by the AMOC, the Wüst cell return flow (150−1000°m) is an essential component of the WMED and EMED deep overturning. In Fig. 7.20 this effect is illustrated through the contribution of the LIW to DWF in the four areas of the Aegean, the Adriatic and the Gulf of Lion. The inflowing LIW in these areas increases the salinity of the local intermediate waters and preconditions the deep convection of the EMED and WMED cells. Another path flows directly to the Gibraltar Strait, providing a direct closure of the lower branch of the Wüst cell. The densification of LIW as it enters the abyssal waters of the Mediterranean before exiting at the Gibraltar Strait (at a shallower and lighter level than the abyss) is analogous to the interconnection between the mid-depth and abyssal cells in the global ocean.

Modern computations with and without assimilated data also indicate LIW eddy-dominated transport connecting the western Sardinia to the Balearic slopes, which merges with the LIW flowing from the Gulf of Lion (Pinardi et al., 2019; Estournel et al., 2021). However, this path is not depicted in Fig. 7.20 as its relative transport

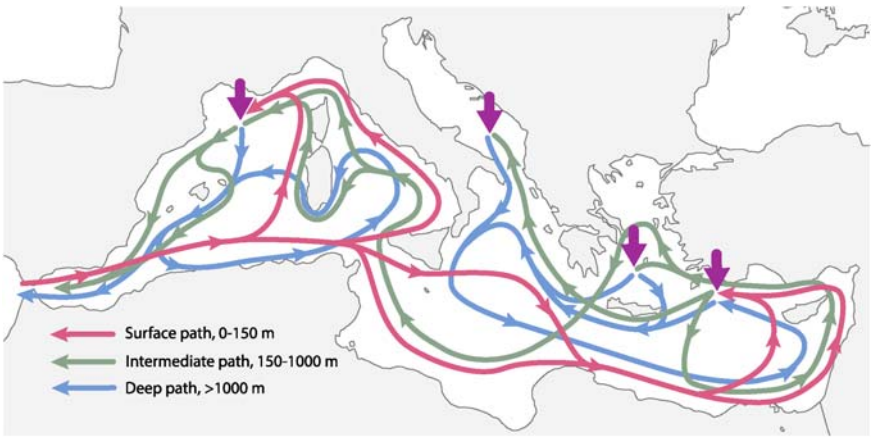

FIGURE 7.20

The vertical pathways at three different depths. The surface to upper ocean circulation is denoted by the red ribbon, the intermediate to deep is green and the abyssal circulation blue. DWF occurs where one color joins a different color and the four locations are denoted by downward purple arrows. Shelf DWF and cascading is not considered.

with respect to the other paths over multidecadal time scales is not yet clear. Similarly, the surface path from the Malta shelf escarpment toward the Adriatic Sea is also omitted as it was part of the EMT and it is not a persistent feature (Malanotte-Rizzoli et al., 1997).

In a recent work, Amitai et al. (2021) shows that the two deep water sources of the EMED, the Adriatic and the Aegean Seas, largely influence the WMED intermediate water pathways and finally the DWF occurring in the Gulf of Lion. If the Adriatic Sea source is depressed (as shown in Fig. 7.4 during the EMT), smaller volumes of deep waters are exchanged at the Sicily Channel. Furthermore, when the Adriatic is depressed, the intermediate and deep waters coming from the Sicily Channel reach the Gulf of Lion region more frequently. On the contrary, when the Adriatic is active, the water flowing along the eastern Tyrrhenian is diluted with deep Tyrrhenian water; hence, less water mass trajectories arrive to the Gulf of Lion area.

The abyssal pathways for the EMED were simulated by (Curchitser et al., 2001) and those of the WMED by Send and Testor (2017) with average drifting float trajectories. In both basins, the abyssal circulation is cyclonic and is connected to the four open ocean deep water sources previously described.

7.7 Concluding remarks

This chapter reviewed the observational, theoretical and numerical scientific studies of the past 50 years that examined the complex DWF and redistribution processes occurring in the Mediterranean Sea.

Several DWF areas have been detected and at least nine areas of DWF have been identified, with four of them involving open ocean DWF processes. These pervasive dense water transformation processes occur at submesoscales and on the shelf, with bathymetric-specific structures and with the semienclosed nature of DWF subbasins having significant effects (Aegean and Adriatic Seas). The interannual variability of formation rates is now well-established for both the EMED and the WMED, with 3–5 year-long periods in which formation rates are high, intertwined with low formation rate periods of equivalent length. The EMT (see Chapter 9) is a key dense/deep water event of the past 30 years and has affected the vertical circulation of the basin.

The Mediterranean Sea vertical circulation is vigorous both in the EMED and WMED. The Gibraltar Strait inflow waters are converted into intermediate waters, forming the ZOC of the basin: its lower branch is composed of LIW/CIW, which partially become denser in the open ocean DWF areas before exiting through the Gibraltar Strait into the Atlantic. The meridional overturning is different in the Eulerian and Lagrangian frameworks, indicating the importance of eddy transport and diabatic mixing processes. Lyubartsev et al. (2020) devises an index that shows the interannual variability of the WMED and EMED meridional clockwise cells: the preliminary findings show that in a 32 year period (1987–2018), the EMED has larger index values than the WMED indicating larger vertical transports. Furthermore, the index maxima coincide with the EMT and the 2004–05 WMDW formation events.

A significant connection between intermediate depth and the meridional component of the vertical circulation is likely similar to the situation in the global ocean between the AMOC and the abyssal circulation of the global ocean. A schematic of the surface, intermediate, and abyssal circulations of the Mediterranean Sea demonstrates the interconnections between the zonal and meridional overturning cells.

Much remains to be understood, including the eddy-driven intermittent transport of waters in various basin subportions, the effective contribution of the shelf DWF mechanisms in the meridional circulation, the long-term trends due to climate and hydrological changes, and the links between the Atlantic and Mediterranean Seas.

Additional resources

- CMEMS, https://marine.copernicus.eu/

References

Adani, M., Dobricic, S., Pinardi, N., 2011. Quality assessment of a 1985–2007 Mediterranean Sea reanalysis. J. Atmos. Ocean. Technol. 28 (4), 569–589.

Allen, J.T., Painter, S.C., Rixen, M., 2008. Eddy transport of western Mediterranean intermediate water to the Alboran Sea. J. Geophys. Res. C Oceans Atmos. 113, C04024.

Amitai, Y., Ashkenazy, Y., Gildor, H., 2021. The effect of the source of deep water in the eastern Mediterranean on western Mediterranean intermediate and deep water. Front. Mar. Sci. 7, 615975.

Anati, D., Stommel, H., 1970. The initial phase of deep water formation in the northwest Mediterranean, during MEDOC69, on the basis of observations made by Atlantic II, January 25−February 12, 1969. Cah. Oceanogr. XXII (4), 343−351.

Anati, D.A., 1971. On the mechanism of the deep mixed layer formation during Medoc 69. Cah. Oceanogr. 23 (4), 427−443.

Artale, V., Astraldi, M., Buffoni, G., Gasparini, G., 1994. Seasonal variability of gyre-scale circulation in the northern Tyrrhenian Sea. J. Geophys. Res. 991, 14127−14138.

Artegiani, A., Bregant, D., Paschini, E., Pinardi, N., Raicich, F., Russo, A., 1997. The Adriatic Sea General Circulation. Part I: air-sea interactions and water mass structure. J. Phys. Oceanogr. 27, 1492−1514.

Ben Ismail, S., Schroeder, K., Sammari, C., Gasparini, G.P., Borghini, M., Aleya, L., 2014. Interannual variability of water mass properties in the Tunisia−Sicily Channel. J. Mar. Syst. 135, 14−28.

Bensi, M., Cardin, V., Rubino, A., Notarstefano, G., Poulain, P.M., 2013. Effects of winter convection on the deep layer of the Southern Adriatic Sea in 2012. J. Geophys. Res. Oceans 118, 6064−6075.

Bethoux, J.P., Gentili, B., Morin, P., Nicolas, E., Pierre, C., Ruiz-Pino, D., 1999. The Mediterranean Sea: a miniature ocean for climatic and environmental studies and a key for the climatic functioning of the North Atlantic. Prog. Oceanogr. 44 (1−3), 131−146.

Beuvier, J., Béranger, K., Lebeaupin Brossier, C., Somot, S., Sevault, F., Drillet, Y., Bourdallé-Badie, R., Ferry, N., Lyard, F., 2012. Spreading of the western Mediterranean deep water after winter 2005: time scales and deep cyclone transport. J. Geophys. Res. 117, C07022.

Bosse, A., Testor, P., Houpert, L., Damien, P., Prieur, L., Hayes, D., Taillandier, V., Durrieu de Madron, X., d'Ortenzio, F., Coppola, L., Karstensen, J., Mortier, L., 2016. Scales and dynamics of submesoscale coherent vortices formed by deep convection in the northwestern Mediterranean Sea. J. Geophys. Res. Oceans 121, 7716−7742.

Bosse, A., Testor, P., Damien, P., Estournel, C., Marsaleix, P., Mortier, L., Prieur, L., Taillandier, V., 2021. Wind-forced submesoscale symmetric instability around deep convection in the northwestern Mediterranean Sea. Fluid 6 (3), 123.

Boyer, T.P., Baranova, O.K., Coleman, C., Garcia, H.E., Grodsky, A., Locarnini, R.A., Mishonov, A.V., Paver, C.R., Reagan, J.R., Seidov, D., Smolyar, I.V., Weathers, K., Zweng, M.M., 2018. World ocean database 2018. In: Mishonov, A.V., Technical (Eds.), NOAA Atlas NESDIS, vol. 87.

Canals, M., Puig, P., Durrieu de Madron, X., Heussner, S., Palanques, A., Fabres, J., 2006. Flushing submarine canyons. Nature 444, 354−357.

Castellari, S., Pinardi, N., Leaman, K., 1998. A model study of air-sea interactions in the Mediterranean Sea. J. Mar. Syst. 18, 89−114.

Castellari, S., Pinardi, N., Leaman, K., 2000. Simulation of water mass formation processes in the Mediterranean Sea: influence of the time frequency of the atmospheric forcing. J. Geophys. Res. 105 (C10), 24157−24181.

Cessi, P., Pinardi, N., Lyubartsev, V., 2014. Energetics of semienclosed basins with two-layer flows at the Strait. J. Phys. Oceanogr. 44, 967−979.

Curchitser, E.N., Haidvogel, D.B., Iskandarani, M., 2001. Transient adjustment of circulation in a midlatitude abyssal ocean basin with realistic geometry and bathymetry. J. Phys. Oceanogr. 31 (3), 725−745.

Cushman-Roisin, B., Poulain, P.M., Gacic, M., Artegiani, A., 2001. Physical Oceanography of the Adriatic Sea. Springer, Dordrecht. https://doi.org/10.1007/978-94-015-9819-4.

Damien, P., Bosse, A., Testor, P., Marsaleix, P., Estournel, C., 2017. Modeling postconvective submesoscale coherent vortices in the northwestern Mediterranean Sea. J. Geophys. Res. Oceans 122, 9937−9961.

Demirov, E., Pinardi, N., 2002. The Simulation of the Mediterranean Sea circulation from 1979 to 1993. Part I: the interannual variability. J. Mar. Syst. 33−34, 23−50.

Demirov, E.K., Pinardi, N., 2007. On the relationship between the water mass pathways and eddy variability in the Western Mediterranean Sea. J. Geophys. Res. 112, C02024.

Dewar, W.K., Killworth, P.D., 1990. On the cylinder collapse problem, mixing, and the merger of isolated eddies. J. Phys. Oceanogr. 20, 1563−1575.

Dufau-Julliand, C., Marsaleix, P., Petrenko, A., Dekeyser, I., 2004. Three-dimensional modeling of the Gulf of Lion's hydrodynamics (northwest Mediterranean) during January 1999 (MOOGLI3 Experiment) and late winter 1999: western Mediterranean Intermediate Water's (WIW's) formation and its cascading over the shelf break. J. Geophys. Res. 109, C11002.

Durrieu de Madron, X., Houpert, L., Puig, P., Sanchez-Vidal, A., Testor, P., Bosse, A., Estournel, C., Somot, S., Bourrin, F., Bouin, M.N., Beauverger, M., Beguery, L., Calafat, A., Canals, M., Cassou, C., Coppola, L., Dausse, D., D'Ortenzio, F., Font, J., Heussner, S., Kunesch, S., Lefevre, D., Le Goff, H., Martín, J., Mortier, L., Palanques, A., Raimbault, P., 2013. Interaction of dense shelf water cascading and open-sea convection in the northwestern Mediterranean during winter 2012. Geophys. Res. Lett. 40, 1379−1385.

Escudier, R., Clementi, E., Cipollone, A., Pistoia, J., Drudi, M., Grandi, A., Lyubartsev, V., Lecci, R., Aydogdu, A., Delrosso, D., Omar, M., Masina, S., Coppini, G., Pinardi, N., 2021. A high resolution reanalysis for the Mediterranean Sea. Front. Earth Sci. 9, 702285.

Estournel, C., Testor, P., Taupier-Letage, I., Bouin, M.-N., Coppola, L., Durand, P., Conan, P., Bosse, A., Brilouet, P.-E., Beguery, L., Belamari, S., Béranger, K., Beuvier, J., Bourras, D., Canut, G., Doerenbecher, A., Durrieu de Madron, X., D'Ortenzio, F., Drobinski, P., Ducrocq, V., Fourrié, N., Giordani, H., Houpert, L., Labatut, L., Brossier, C.L., Nuret, M., Prieur, L., Roussot, O., Seyfried, L., Somot, S., 2016a. HyMeX-SOP2: the field campaign dedicated to dense water formation in the northwestern Mediterranean. Oceanography 29 (4), 196−206.

Estournel, C., Testor, P., Damien, P., D'Ortenzio, F., Marsaleix, P., Conan, P., Kessouri, F., Durrieu de Madron, X., Coppola, L., Lellouche, J.M., Belamari, S., Mortier, L., Ulses, C., Bouin, M.N., Prieur, L., 2016b. High resolution modeling of dense water formation in the north-western Mediterranean during winter 2012−2013: processes and budget. J. Geophys. Res. Oceans 121, 5367−5392.

Estournel, C., Marsaleix, P., Ulses, C., 2021. A new assessment of the circulation of Atlantic and intermediate waters in the eastern Mediterranean. Prog. Oceanogr. 198, 102673.

Fuda, J.L., Millot, C., Taupier-Letage, I., Send, U., Bocognano, J.M., 2000. XBT monitoring of a meridian section across the western Mediterranean Sea. Deep-Sea Res. I 47, 2191−2218.

Fuda, J.-L., Etiope, G., Millot, C., Favali, P., Calcara, M., Smriglio, G., Boschi, E., 2002. Warming, salting and origin of the Tyrrhenian deep water. Geophys. Res. Lett. 29 (19), 1898.

Gačić, M., Lascaratos, A., Manca, B.B., Mantziafou, A., 2001. Adriatic deep water and interaction with the eastern Mediterranean Sea. In: Cushman-Roisin, B., Gačić, M.,

Poulain, P.M., Artegiani, A. (Eds.), Physical Oceanography of the Adriatic Sea. Springer, Dordrecht.
Gascard, J.C., 1973. Vertical motions in a region of deep water formation. Deep-Sea Res. Oceanogr. Abstr. 20 (11), 1011−1027.
Gascard, J.C., 1978. Mediterranean deep-water formation baroclinic instability and oceanic eddies. Oceanol. Acta 1 (3), 315−330.
Gascard, J.-C., Richez, C., 1985. Water masses and circulation in the western Alboran Sea and in the Straits of Gibraltar. Prog. Oceanogr. 15, 157−216.
Gasparini, G.P., Zodiatis, G., Astraldi, M., Galli, C., Sparnocchia, S., 1999. Winter intermediate water lenses in the Ligurian Sea. J. Mar. Syst. 20, 319−332.
Gertman, I.F., Ovchinnikov, I.M., Popov, Y.I., 1994. Deep convection in the eastern basin of the Mediterranean Sea. Oceanology 34 (1), 19−25.
Gertman, I., Pinardi, N., Popov, Y., Hecht, A., 2006. Aegean Sea water masses during the early stages of the eastern Mediterranean climatic transient (1988−1990). J. Phys. Oceanogr. 36 (9), 1841−1859.
Hecht, A., Pinardi, N., Robinson, A., 1988. Currents, water masses, eddies and jets in the Mediterranean Levantine Basin. J. Phys. Oceanogr. 18, 1320−1353.
Iovino, D., Straneo, F., Spall, M., 2008. On the effect of a sill on dense water formation in a marginal sea. J. Mar. Res. 66 (3), 325−345.
Ivanov, V.V., Shapiro, G.I., Huthnance, J.M., Aleynik, D.L., Golovin, P.N., 2004. Cascades of dense water around the world ocean. Prog. Oceanogr. 60, 47−98.
Jones, H., Marshall, J., 1993. Convection with rotation in a neutral ocean: a study of open-ocean deep convection. J. Phys. Oceanogr. 23 (6), 1009−1039.
Josey, S.A., 2003. Changes in the heat and freshwater forcing of the eastern Mediterranean and their influence on deep water formation. J. Geophys. Res. 108 (C7), 3237.
Juza, M., Escudier, R., Vargas-Yáñez, M., Mourre, B., Heslop, E., Allen, J., Tintoré, J., 2019. Characterization of changes in Western Intermediate Water properties enabled by an innovative geometry-based detection approach. J. Mar. Syst. 191, 1−12.
Killworth, P.D., 1976. The mixing and spreading phases of MEDOC.I. Prog. Oceanogr. 7 (2), 59−90.
Kokkini, Z., Mauri, E., Gerin, R., Poulain, P.M., Simoncelli, S., Notarstefano, G., 2020. On the salinity structure in the South Adriatic as derived from float and glider observations in 2013−2016. Deep-Sea Res. Part II 171, 104625.
Lascaratos, A., 1993. Estimation of deep and intermediate water mass formation rates in the Mediterranean Sea. Deep-Sea Research II 40 (6), 1327−1333.
Lascaratos, A., Roether, W., Nittis, K., Klein, B., 1999. Recent changes in deep water formation and spreading in the eastern Mediterranean Sea: a review. Prog. Oceanogr. 44, 5−36.
Leaman, K.D., Schott, F.A., 1991. Hydrographic structure of the convection regime in the Gulf of Lions: winter 1987. J. Phys. Oceanogr. 21 (4), 575−598.
Legg, S., Marshall, J., 1993. A heton model of the spreading phase of open-ocean deep convection. J. Phys. Oceanogr. 23 (6), 1040−1056.
LIWEX Group, 2003. The Levantine Intermediate Water Experiment (LIWEX) Group: Levantine basin—a laboratory for multiple water mass formation processes. J. Geophys. Res. 108, 8101.
López-Jurado, J., Lafuente, J.M.G., Lucaya, N.C., 1995. Hydrographic conditions of the Ibiza Channel during November 1990, March 1991 and July 1992. Oceanol. Acta 18 (2), 235−243.

Lumpkin, R., Speer, K., 2007. Global ocean meridional overturning. J. Phys. Oceanogr. 37 (10), 2550–2562.

Lyubartsev, V., Borile, F., Clementi, E., Masina, S., Drudi, M., Coppini, G., Cessi, P., Pinardi, N., 2020. Interannual variability in the eastern and western Mediterranean overturning index. Copernicus marine service ocean state report, issue 4. J. Oper. Oceanogr. 13, S1–S172.

Madec, G., Delecluse, P., Crepon, M., Chartier, M., 1991. A three-dimensional numerical study of deep-water formation in the northwestern Mediterranean Sea. J. Phys. Oceanogr. 21 (9), 1349–1371.

Madec, G., Delecluse, P., Crépon, M., Lott, F., 1996. Large-scale preconditioning of deep-water formation in the northwestern Mediterranean Sea. J. Phys. Oceanogr. 26 (8), 1393–1408.

Malanotte-Rizzoli, P., Robinson, A.R., 1994. Ocean processes in climate dynamics: global and Mediterranean examples. In: Proceedings of NATO-ASI. Kluwer Academic Publishers, Dordrecht, The Netherlands, p. 437.

Malanotte-Rizzoli, P., Manca, B.B., Ribera D'Alcalà, M., Theocharis, A., Bergamasco, A., Bregant, D., Budillon, G., Civitarese, G., Georgopoulos, D., Michelato, A., Sansone, E., Scarazzato, P., Souvermezoglou, E., 1997. A synthesis of the Ionian Sea hydrography, circulation and water mass pathways during POEM-Phase I. Prog. Oceanogr. 39 (3), 153–204.

Manca, B.B., Budillon, G., Scarazzato, P., Ursella, L., 2003. Evolution of dynamics in the eastern Mediterranean affecting water mass structures and properties in the Ionian and Adriatic Seas (1995–1999). J. Geophys. Res. Oceans 108, C9.

Manca, B.B., Ibello, V., Pacciaroni, M., Scarazzato, P., Giorgetti, A., 2006. Ventilation of deep waters in the Adriatic and Ionian Seas following changes in thermohaline circulation of the Eastern Mediterranean. Clim. Res. 31, 239–256.

Mantziafou, A., Lascaratos, A., 2004. An eddy resolving numerical study of the general circulation and deep-water formation in the Adriatic Sea. Deep Sea Res. Oceanogr. Res. Pap. 51, 921–952.

Margirier, F., Bosse, A., Testor, P., L'Heveder, B., Mortier, L., Smeed, D., 2017. Characterization of convective plumes associated with oceanic deep convection in the northwestern Mediterranean from high-resolution in situ data collected by gliders. J. Geophys. Res. Oceans 122, 9814–9826.

Margirier, F., Testor, P., Heslop, E., Mallil, K., Bosse, A., Houpert, L., Mortier, L., Bouin, M.N., Coppola, L., D'Ortenzio, F., Durrieu de Madron, X., Mourre, B., Prieur, L., Raimbault, P., Taillandier, V., 2020. Abrupt warming and salinification of intermediate waters interplays with decline of deep convection in the Northwestern Mediterranean Sea. Sci. Rep. 10, 20923.

Marini, M., Grilli, F., Guarnieri, A., Jones, B.H., Klajic, Z., Pinardi, N., Sanxhaku, M., 2010. Is the southeastern Adriatic Sea coastal strip an eutrophic area? Estuar. Coast Shelf Sci. 88, 395–406.

Marshall, J., Schott, F., 1999. Open-ocean convection: observations, theory, and models. Rev. Geophys. 37 (1), 1–64.

Maxworthy, T., Narimousa, S., 1994. Unsteady, turbulent convection into a homogeneous, rotating fluid, with oceanographic applications. J. Phys. Oceanogr. 24 (5), 865–887.

McWilliams, J.C., 1985. Submesoscale, coherent vortices in the ocean. Rev. Geophys. 23 (2), 165–182.

MEDOC Group, 1970. Observation of formation of deep water in the Mediterranean Sea, 1969. Nature 227.

Mihanović, H., Vilibić, I., Carniel, S., Tudor, M., Russo, A., Bergamasco, A., Bubić, N., Ljubešić, Z., Viličić, D., Boldrin, A., Malačič, V., Celio, M., Comici, C., Raicich, F., 2013. Exceptional dense water formation on the Adriatic shelf in the winter of 2012. Ocean Sci. 9, 561−572.

Millot, C., 1987. Circulation in the western Mediterranean Sea. Oceanol. Acta 10 (2), 143−149.

Millot, C., 1999. Circulation in the western Mediterranean Sea. J. Mar. Syst. 20, 423−442.

Millot, C., 2013. Levantine Intermediate Water characteristics: an astounding general misunderstanding! Sci. Mar. 77 (2), 217−232.

Napolitano, E., Iacono, R., Ciuffardi, T., Reseghetti, F., Poulain, P.-M., Notarstefano, G., 2019. The Tyrrhenian intermediate water (TIW): characterization and formation mechanisms. Prog. Oceanogr. 170, 53−68.

Nittis, K., Lascaratos, A., Theocharis, A., 2003. Dense water formation in the Aegean Sea: numerical simulations during the eastern Mediterranean transient. J. Geophys. Res. 108 (C9), 8120.

Orlić, M., Gacic, M., La Violette, P., 1992. The currents and circulation of the Adriatic Sea. Oceanol. Acta 15 (2), 109−124.

Ovchinnikov, I.M., 1984. the formation of intermediate water in the Mediterranean Sea. Oceanology 24, 168−173.

Ozer, T., Gertman, I., Gildor, H., Goldman, R., Herut, B., 2020. Evidence for recent thermohaline variability and processes in the deep water of the Southeastern Levantine Basin, Mediterranean Sea. Deep-Sea Res. Part II 171, 104651.

Özsoy, E., Hecht, A., Ünlüata, Ü., Brenner, S., Sur, H.I., Bishop, J., Latif, M.A., Rozentraub, Z., Oğuz, T., 1993. A synthesis of the Levantine Basin circulation and hydrography, 1985−1990. Deep Sea Res. Part II Top. Stud. Oceanogr. 40 (6), 1075−1119.

Pinardi, N., Navarra, A., 1993. Baroclinic wind adjustment processes in the Mediterranean Sea. Deep Sea Res II 40 (6), 1299−1326.

Pinardi, N., Korres, G., Lascaratos, A., Roussenov, V., Stanev, E., 1997. Numerical simulation of the interannual variability of the Mediterranean Sea upper ocean circulation. Geophys. Res. Lett. 24 (4), 425−428.

Pinardi, N., Zavatarelli, M., Adani, M., Coppini, G., Fratianni, C., Oddo, P., Simoncelli, S., Tonani, M., Lyubartsev, V., Dobricic, S., Bonaduce, A., 2015. Mediterranean Sea large-scale low-frequency ocean variability and water mass formation rates from 1987 to 2007: a retrospective analysis. Prog. Oceanogr. 132, 318−332.

Pinardi, N., Cessi, P., Borile, F., Wolfe, C.L., 2019. The Mediterranean Sea overturning circulation. J. Phys. Oceanogr. 49 (7), 1699−1721.

Pinot, J.-M., Ganachaud, A., 1999. The role of winter intermediate waters in the spring-summer circulation of the Balearic Sea: 1. Hydrography and inverse box modelling. J. Geophys. Res. 104 (C12), 29843−29864.

Pisacane, G., Artale, V., Calmanti, S., Rupolo, V., 2006. Decadal oscillations in the Mediterranean Sea: a result of the overturning circulation variability in the eastern basin? Clim. Res. 31 (2−3), 257−271.

Pollak, M.I., 1951. The sources of the deep water in the eastern Mediterranean. J. Mar. Res. 10 (1), 128−152.

Robinson, A.R., Malanotte-Rizzoli, P., Hecht, A., Michelato, A., Roether, W., Theocharis, A., Ünlüata, U., Pinardi, N., Artegiani, A., Bergamasco, A., Bishop, J., Brenner, S.,

Christianidis, S., Gacic, M., Georgopoulos, D., Golnaraghi, M., Hausmann, M., Junghaus, H.-G., Lascaratos, A., Latif, M.A., Leslie, W.G., Lozano, C.J., Oguz, T., Özsoy, E., Papageorgiou, E., Paschini, E., Rozentroub, Z., Sansone, E., Scarazzato, P., Schlitzer, R., Spezie, G.-C., Tziperman, E., Zodiatis, G., Athanassiadou, L., Gerges, M., Osman, M., 1992. General circulation of the eastern Mediterranean. Earth Sci. Rev. 32 (4), 285−309.

Roether, W., Schlitzer, R., 1991. Eastern Mediterranean deep water renewal on the basis of chlorofluoromethane and tritium data. Dynam. Atmos. Oceans 15 (3−5), 333−354.

Roether, W., Manca, B.B., Klein, B., Bregant, D., Georgopoulos, D., Beitzel, V., Kovačević, V., Luchetta, A., 1996. Recent changes in eastern Mediterranean deep waters. Science 271 (5247), 333−335.

Roether, W., Klein, B., Manca, B.B., Theocharis, A., Kioroglou, S., 2007. Transient Eastern Mediterranean deep waters in response to the massive dense-water output of the Aegean Sea in the 1990s. Prog. Oceanogr. 74, 540−571.

Rousselet, L., Cessi, P., Forget, G., 2021. Coupling of the mid-depth and abyssal components of the global overturning circulation according to a state estimate. Sci. Adv. 7 (21) eabf5478.

Rubino, A., Hainbucher, D., 2007. A large abrupt change in the abyssal water masses of the eastern Mediterranean, Geophys. Res. Lett. 34, L23607.

Sankey, T., 1973. The formation of deep water in the northwestern Mediterranean. Prog. Oceanogr. 6, 159−179.

Schlitzer, R., Roether, W., Oster, H., Junghans, H.-G., Hausmann, M., Johannsen, H., Michelato, A., 1991. Chlorofluoromethane and oxygen in the eastern Mediterranean. Deep-Sea Res. 38 (12), 1531−1551.

Schott, F., Leaman, K.D., 1991. Observations with moored acoustic Doppler current profilers in the convection regime in the Golfe du Lion. J. Phys. Oceanogr. 21 (4), 558−574.

Schott, F., Visbeck, M., Send, U., 1994. open ocean deep convection, Mediterranean and Greenland seas. In: Malanotte-Rizzoli, P., Robinson, A.R. (Eds.), Ocean Processes in Climate Dynamics: Global and Mediterranean Examples, NATO ASI Series (Series C: Mathematical and Physical Sciences), vol. 419. Springer, Dordrecht.

Schroeder, K., Josey, S.A., Herrmann, M., Grignon, L., Gasparini, G.P., Bryden, H.L., 2010. Abrupt warming and salting of the western Mediterranean deep water after 2005: atmospheric forcings and lateral advection. J. Geophys. Res. 115, C08029.

Send, U., Testor, P., 2017. Direct observations reveal the deep circulation of the western Mediterranean Sea. J. Geophys. Res. Oceans 122, 10091−10098.

Send, U., Marshall, J., 1995. Integral effects of deep convection. J. Phys. Oceanogr. 25, 855−872.

Seyfried, L., Estournel, C., Marsaleix, P., Richard, E., 2019. Dynamics of the North Balearic Front during an autumn tramontane and mistral storm: air−sea coupling processes and stratification budget diagnostic. Ocean Sci. 15, 179−198.

Shapiro, G.I., Huthnance, J.M., Ivanov, V.V., 2003. Dense water cascading off the continental shelf. J. Geophys. Res. 108, 3390.

Simoncelli, S., Fratianni, C., Pinardi, N., Grandi, A., Drudi, M., Oddo, P., Dobricic, S., 2017. Mediterranean Sea Physical Reanalysis (MEDREA 1987-2015). Copernicus Monitoring Environment Marine Service. https://doi.org/10.25423/medsea_reanalysis_phys_006_004.

Simoncelli, S., Pinardi, N., Fratianni, C., Dubois, C., Notarstefano, G., 2018. Water mass formation processes in the Mediterranean sea over the past 30 years. In: Copernicus Marine

Service Ocean State Report, Issue 2, Copernicus Marine Service Ocean State Report, Journal of Operational Oceanography, vol. 11, pp. S1−S142. Suppl. 1.

Somot, S., Houpert, L., Sevault, F., Testor, P., Bosse, A., Taupier-Letage, I., Bouin, M.N., Waldman, R., Cassou, C., Sanchez-Gomez, E., Durrieu de Madron, X., Adloff, F., Nabat, P., Herrmann, M., 2018. Characterizing, modelling and understanding the climate variability of the deep water formation in the North-Western Mediterranean Sea. Clim. Dynam. 51, 1179−1210.

Spall, M.A., 2003. On the thermohaline circulation in flat bottom marginal seas. J. Mar. Res. 61, 1−25.

Spall, M.A., 2004. Boundary currents and water mass transformation in marginal seas. J. Phys. Oceanogr. 34, 1197−1213.

Speer, K., Tziperman, E., 1992. Rates of water Mass Formation in the north Atlantic ocean. J. Phys. Oceanogr. 22 (1), 93−104.

Stommel, H., Voorhis, A., Webb, D., 1971. Submarine Clouds in the Deep Ocean: surface cooling during late winter in the northwestern Mediterranean Sea causes large masses of water to sink to great depths. Am. Sci. 59 (6), 716−722.

Straneo, F., Kawase, M., 1999. Comparisons of localized convection due to a Localized forcing and to preconditioning. J. Phys. Oceanogr. 29, 55−68.

Straneo, F., 2006. Heat and freshwater transport through the central Labrador sea. J. Phys. Oceanogr. 36 (4), 606−628.

Supić, N., Vilibić, I., 2006. Dense water characteristics in the northern Adriatic in the 1967−2000 interval with respect to surface fluxes and Po river discharge rates. Estuar. Coast Shelf Sci. 66 (3−4), 580−593.

Sur, H.I., Ozsoy, E., Umluata, U., 1992. Simultaneous deep and intermediate depth convection in the Northern Levantine Sea, winter 1992. Oceanol. Acta 16 (1), 33−43.

Swallow, J.C., Caston, G.F., 1973. The preconditioning phase of MEDOC 1969. Part I. Observations. Deep-Sea Res. 20, 429−448.

Talley, L.D., 2013. Closure of the global overturning circulation through the Indian, Pacific, and southern oceans: schematics and transports. Oceanography 26 (1), 80−97.

Tchernia, P., 1960. Hydrologic d'hiver en Méditerranée occidentale. Cah. Oceanogr. 12 (3), 184−198.

Testor, P., Bosse, A., Houpert, L., Margirier, F., Mortier, L., Legoff, H., Dausse, D., Labaste, M., Karstensen, J., Hayes, D., Olita, A., Ribotti, A., Schroeder, K., Chiggiato, J., Onken, R., Heslop, E., Mourre, B., D'ortenzio, F., Mayot, N., Lavigne, H., de Fommervault, O., Coppola, L., Prieur, L., Taillandier, V., Durrieu de Madron, X., Bourrin, F., Many, G., Damien, P., Estournel, C., Marsaleix, P., Taupier-Letage, I., Raimbault, P., Waldman, R., Bouin, M.N., Giordani, H., Caniaux, G., Somot, S., Ducrocq, V., Conan, P., 2018. Multiscale observations of deep convection in the northwestern Mediterranean Sea during winter 2012−2013 using multiple platforms. J. Geophys. Res. Oceans 123, 1745−1776.

Theocharis, A., Balopoulos, E., Kioroglou, S., Kontoyiannis, H., Iona, A., 1999. A synthesis of the circulation and hydrography of the south Aegean Sea and the Straits of the Cretan Arc (March 1994−January 1995). Prog. Oceanogr. 44 (4), 469−509.

Theocharis, A., Krokos, G., Velaoras, D., Korres, G., 2014. An internal mechanism driving the alternation of the eastern Mediterranean dense/deep water sources. In: Borzelli, G.L.E., Gačić, M., Lionello, P., Malanotte-Rizzoli, P. (Eds.), The Mediterranean Sea. https://doi.org/10.1002/9781118847572.ch8.

Toggweiler, J.R., Samuels, B., 1993. Is the magnitude of the deep outflow from the Atlantic Ocean actually governed by Southern Hemisphere winds?. In: The Global Carbon Cycle. Springer, Berlin, Heidelberg, pp. 303–331.

Tsimplis, M.N., Zervakis, V., Josey, S.A., Peneva, E.L., Struglia, M.V., Stanev, E.V., Theocharis, A., Lionello, P., Malanotte-Rizzoli, P., Artale, V., Tragou, E., 2006. Changes in the oceanography of the Mediterranean Sea and their link to climate variability. In: Developments in Earth and Environmental Sciences, vol. 4. Elsevier, pp. 227–282.

Turchetto, M., Boldrin, A., Langone, L., Miserocchi, S., Tesi, T., Foglini, F., 2007. Particle transport associated with the Bari canyon (southern Adriatic Sea). Mar. Geol. 246, 231–247.

Ulses, C., Estournel, C., Puig, P., Durrieu de Madron, X., Marsaleix, P., 2008. Dense water cascading in the northwestern Mediterranean during the cold winter 2005. Quantification of the export through the Gulf of Lion and the Catalan margin. Geophys. Res. Lett. 35, L07610.

Velaoras, D., Krokos, G., Nittis, K., Theocharis, A., 2014. Dense intermediate water outflow from the Cretan Sea: a salinity driven, recurrent phenomenon, connected to thermohaline circulation changes. J. Geophys. Res. Oceans 119 (8), 4797–4820.

Velaoras, D., Zervakis, V., Theocharis, A., 2021. The physical characteristics and dynamics of the Aegean water masses. In: The Handbook of Environmental Chemistry. Springer, Berlin, Heidelberg.

Verri, G., Pinardi, N., Oddo, P., Ciliberti, S.A., Coppini, G., 2018. River runoff influences on the Central Mediterranean overturning circulation. Clim. Dynam. 50, 1675–1703.

Vigo, M.I., Garcia, D., Chao, B.F., 2005. Change of sea level trend in the Mediterranean and Black seas. J. Mar. Res. 63, 1085–1100.

Vilibic, I., 2003. An analysis of dense water production on the North Adriatic shelf. Estuar. Coast Shelf Sci. 56, 861–867.

Vilibić, T., Supić, N., 2005. Dense water generation on a shelf: the case of the Adriatic Sea. Ocean Dynam. 55 (5–6), 403–415.

Waldman, R., Somot, S., Herrmann, M., Testor, P., Estournel, C., Sevault, F., Prieur, L., Mortier, L., Coppola, L., Taillandier, V., Conan, P., Dausse, D., 2016. Estimating dense water volume and its evolution for the year 2012–2013 in the north-western Mediterranean Sea: an observing system simulation experiment approach. J. Geophys. Res. Oceans 121, 6696–6716.

Waldman, R., Somot, S., Herrmann, M., Bosse, A., Caniaux, G., Estournel, C., Houpert, L., Prieur, L., Sevault, F., Testor, P., 2017. Modeling the intense 2012–2013 dense water formation event in the northwestern Mediterranean Sea: evaluation with an ensemble simulation approach. J. Geophys. Res. Oceans 122, 1297–1324.

Waldman, R., Brüggemann, N., Bosse, A., Spall, M., Somot, S., Sevault, F., 2018. Overturning the Mediterranean thermohaline circulation. Geophys. Res. Lett. 45, 8407–8415.

Wang, X.H., Oddo, P., Pinardi, N., 2006. On the bottom density plume on coastal zone off Gargano (Italy) in the southern Adriatic Sea and its interannual variability. J. Geophys. Res. 111, C03S17.

Wolfe, C.L., Cessi, P., 2011. The adiabatic Pole-to-Pole overturning circulation. J. Phys. Oceanogr. 41 (9), 1795–1810. https://doi.org/10.1175/2011JPO4570.1.

Wu, P., Haines, K., 1996. Modeling the dispersal of Levantine Intermediate Water and its role in Mediterranean deep water formation. J. Geophys. Res. 101 (C3), 6591–6660.

Wu, P., Haines, K., Pinardi, N., 2000. Toward an understanding of deep-water renewal in the eastern Mediterranean. J. Phys. Oceanogr. 30, 443–458.

Wüst, G., 1961. On the vertical circulation of the Mediterranean Sea. J. Geophys. Res. 66, 3261−3271.

Young, W.R., 2012. An exact thickness-weighted average formulation of the Boussinesq equations. J. Phys. Oceanogr. 42 (5), 692−707.

Zavatarelli, M., Mellor, G.L., 1995. A numerical study of the Mediterranean Sea circulation. J. Phys. Oceanogr. 25 (6), 1384−1414.

Zervakis, V., Georgopoulos, D., Drakopoulos, P.G., 2000. The role of the North Aegean in triggering the recent Eastern Mediterranean climatic changes. J. Geophys. Res. 105 (C11), 103−116.

Zore-Armanda, M., 1963. Mixing of three water types in the south Adriatic. Rapp. Proces Verbaux Reunions Comm. Int. pour Explor. Sci. Mer Mediterr. 17 (3), 879−885.

This page intentionally left blank

CHAPTER

Fronts, eddies and mesoscale circulation in the Mediterranean Sea

8

Evan Mason[1], Bàrbara Barceló-Llull[1], Antonio Sánchez-Román[1], Daniel Rodríguez-Tarry[1], Eugenio Cutolo[1], Antoine Delepoulle[2], Simón Ruiz[1], Ananda Pascual[1]

[1]*IMEDEA, Esporles, Mallorca, Spain;* [2]*CLS: Parc Technologique du Canal, Ramonville-Saint-Agne, France*

Learning Objectives

In this Chapter you will learn:

- How satellite altimetry can be used to investigate oceanic mesoscale features in the Mediterranean.
- About the different in-situ instruments that oceanographers use to complement the satellite data.
- The wide range of advanced sampling instruments available to oceanographers in the Mediterranean Sea.
- The role of eddy identification and tracking codes in support of multiplatform experiments.

8.1 General concepts

Oceanic mesoscale features and processes can be compared to the "weather" of the sea. This implies that at any discrete location in the ocean, day-to-day changes in temperature, salinity, and current speeds and directions are influenced by a turbulent ever-evolving field of fronts, filaments, eddies and meandering currents. Just as meteorologists try to map and predict the weather, oceanographers have sampled the ocean, seeking to understand the movements of the currents and other ocean weather. This chapter describes major frontal and mesoscale features and their impact on the oceanography of the Mediterranean Sea. The description is mostly based on altimetry data but widens for several selected case studies of a multiplatform/multiparameter dataset approach that provides a 3D picture of the interactions between these dynamical processes.

In the Mediterranean Sea, mesoscale processes play a key role in determining the large-scale circulation, the distribution of water masses and their mixing. All these features do have important consequences on the whole ecosystem functioning

Oceanography of the Mediterranean Sea. https://doi.org/10.1016/B978-0-12-823692-5.00003-0

(Schroeder et al., 2012, and references therein). Meanders, eddies, and filaments mainly originate as instabilities of large-scale currents and fronts.

The length-scale associated with mesoscale-type features is the Rossby radius of deformation, LR (e.g., Gill, 1982). The Rossby radius is a parameter of fundamental importance, given that it provides a priori knowledge about the sizes of mesoscale features. Typical LR scales for the mid-latitudes of the global ocean range between ∼30 and 50 km (e.g., Chelton et al., 1998). However, in the Mediterranean Sea, LR is notably smaller and varies from 5 to 12 km in the whole Mediterranean and for the different seasons (Grilli and Pinardi, 1998). This is because the size of LR at any particular location is a function of several factors: the earth's rotation rate, latitude, the vertical density gradient, and water depth. More precise estimates of LR in the Western Mediterranean Sea (WMED) have recently been made by Escudier et al. (2016a) and Barceló-Llull et al. (2019). These authors reported meridional gradients of relatively small Rossby radii (∼8−15 km), with the smaller scales to the north. Kurkin et al. (2020), using a 0.1667 degrees observational dataset, made estimates of LR over the full Mediterranean Sea and concluded with a comparable range between ∼ 5 and 15 km. These values highlight the important differences that exist between the scales of mesoscale features in the Mediterranean Sea and in the global ocean (Fig. 8.1). Mediterranean Sea spatial scales are notably smaller, and this explains why the basin is sometimes described as "a small-scale laboratory" for the study of mesoscale processes.

As a provider of Sea Surface Height (SSH) observations over most of the globe, altimeters are perhaps the most revolutionary of the various sensors in the study of surface mesoscale dynamics (see also Chapter 10). Their signal is not interrupted by cloud cover, a problem that does affect the ocean color and some Sea Surface Temperature (SST) sensors (e.g., infrared SST). The near-synoptic views of the surface ocean obtained from these satellite-borne sensors have enabled major advances in our knowledge of mesoscale dynamics in the Mediterranean Sea (e.g., Send et al., 1999). The main surface currents are well mapped (e.g., Millot, 1987; Hamad et al., 2003; Millot and Taupier-Letage, 2005), and will be described later in the chapter, and our understanding of their variability is steadily increasing (e.g., Pinardi et al., 2000; Poulain et al., 2012; Escudier et al., 2013; Pascual et al., 2015; Juza et al., 2016; Menna et al., 2021). Through SSH observations from satellite altimetry, the mesoscale eddy field can be mapped and tracked on a daily basis using specialized eddy-identifying algorithms such as those developed by Chelton et al. (2011), Mason et al. (2014) and Le Vu et al. (2018), among others. These codes have led to the construction of a number of altimetry-based Mediterranean eddy atlases that are made available to users through platforms such as Copernicus Marine Environment Monitoring Service (CMEMS, see also Chapter 10). However, products that are derived from altimetric observations have the limitation of present-day satellite altimeter spatial resolution. In regions of the ocean with a small Rossby radius of deformation, such as the Mediterranean, this resolution does not allow the representation of the full range of mesoscale dynamics (Barceló-Llull et al., 2021). This gap in the altimetric observation of mesoscale features is expected to be filled by the

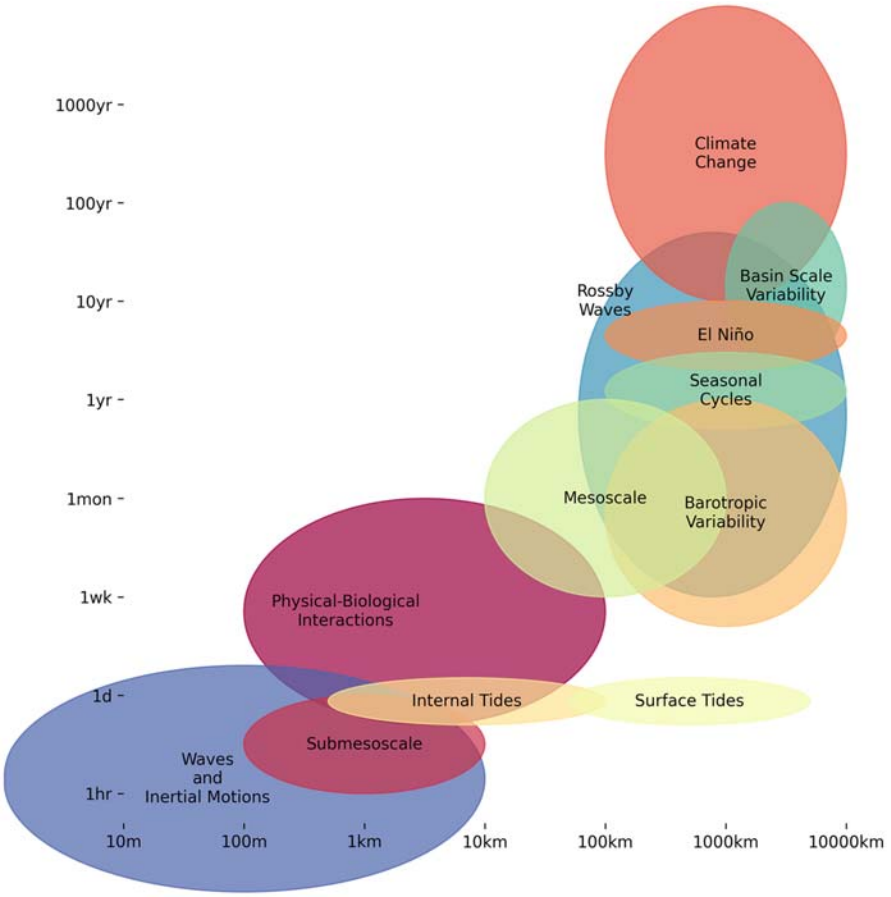

FIGURE 8.1

Schematic diagram showing the ranges of the temporal and spatial scales of oceanic processes and phenomena.

SWOT mission (see subchapter 8.4), planned to be launched in 2022 and offer a spatial resolution of one order of magnitude higher than present-day altimeters (Morrow et al., 2019; D'Ovidio et al., 2019). The last 2 decades have seen the emergence of so-called multi-platform approaches where, in addition to the above satellite data, information is retrieved from several sources, typically ships (CTD casts, towed instruments such as SeaSoar, etc.), gliders, surface drifters, Argo floats, among others (e.g., Marullo et al., 2003; Pascual et al., 2010, 2017; Ruiz et al., 2019; Tarry et al., 2021). This type of approach to data retrieval and analysis is expanded upon in Box 8.1.

Sustained and integrated multidisciplinary ocean observations are vital for a better understanding of the oceans' role in climate change (e.g., Tintoré et al., 2019;

Box 8.1 Multi-platform observations reveal mesoscale variability

Ocean observing platforms can be classified into three categories: Eulerian instruments, which remain stationary, Lagrangian instruments, which passively follow the currents, and self-propelled instruments such as ships, gliders or other autonomous underwater vehicles. So-called multiplatform experiments at sea attempt to utilize all of the above instruments in order to gather a diverse range of measurements (Fig. 8.1.1), including surface and subsurface data (see also Chapter 10). Further support would include data from a variety of remote sensing sources (e.g., altimetry, SST, chlorophyll, …) and 3D data from operational numerical models.

FIGURE 8.1.1

(Left) Rosette with sensors and water bottles during the PRE-SWOT multi-platform experiment; (right up) drifter release during PRE-SWOT; (right down) a Slocum glider at the surface in the Balearic Sea.

Credits: ICTS SOCIB.

Recent examples of these approaches include the projects ALBOREX (Pascual et al., 2017; Ruiz et al., 2018), CALYPSO (Mahadevan et al., 2020), MedClic (Aguiar et al., 2020) and PreSWOT (Barceló-Llull et al., 2021), which took place in the WMED between 2014 and 2020. The ALBOREX and CALYPSO campaigns were carried out in the Alboran Sea, while the PreSWOT and MedClic studies were located near the Balearic Islands. During ALBOREX CTDs, ADCPs, nutrient samples, gliders, drifters, Argo floats, satellite data and numerical models were employed. The CALYPSO and PreSWOT campaigns featured similar ranges of instruments but also introduced Lagrangian methods and vertical velocity estimates. The MedClic contribution aimed to use multi-platform methods and data to evaluate the progress of the WMOP operational modeling effort at SOCIB in the Balearic Islands (details can be found in Chapter 10). The EMED Eye of the Levantine project supported a multi-platform experiment that combined CTDs and gliders to

Box 8.1 Multi-platform observations reveal mesoscale variability—cont'd

sample the warm core Cyprus eddy (Hayes et al., 2011). Other experiments include those carried out in the northern WMED (Petrenko et al., 2017; Garreau et al., 2020), in the Adriatic Sea (Vilibić et al., 2018) or by the Recognized Environmental Picture (REP) or Long-Term Glider Mission for Environmental Characterization (LOGMEC) campaign series carried out by the NATO Center for Maritime Research and Experimentation in different areas of the Mediterranean Sea (Alvarez and Mourre, 2012; Onken et al., 2018; Storto et al., 2019). The different instruments and how they can contribute to these multiplatform experiments are briefly described in the following. Additional details can also be found in Chapter 10.

Drifters Surface drifting buoys, or drifters, are used in oceanographic and climate research. Drifters passively follow the ocean surface currents. Drifters have positive buoyancy and capture the two-dimensional flow at the ocean surface. Drifters are commonly used in oceanography as they are ideal for mapping the large-scale circulation (e.g., Poulain et al., 2013). In recent decades, improvements in GPS accuracy paired with production-cost reductions have opened the way for large-number drifter deployments. Examples of this are the projects LASER (e.g., Poje et al., 2014; D'Asaro et al., 2018) in the Gulf of Mexico and CALYPSO (Mahadevan et al., 2020) in the Mediterranean Sea. With incremental improvements in GPS accuracy, drifter observations provide sufficient temporal resolution and positional accuracy to resolve not only mesoscale but also submesoscale flows. Furthermore, different sensors can be mounted on the surface buoys thereby providing additional sources of data. Apart from measuring the large-scale ocean currents, drifters can be used to estimate subinertial wind-driven variability, inertial motions, surface dispersion and hydrographic data such as temperature and salinity.

Underwater Gliders Underwater gliders are buoyancy-driven platforms equipped with a range of sensors that measure physical and biological properties over the water column. Underwater gliders are deployed and recovered at the desired locations by qualified technicians. However, once released they only require human supervision from the laboratory as they complete their missions. Gliders communicate their position through an antenna each time they emerge at the sea surface, and the technicians communicate any necessary changes in the trajectory remotely from the laboratory. Data sampled by these autonomous platforms have a high spatial resolution, however, they are slower than traditional ship-based observational platforms. New methodologies for glider data processing have been developed to guarantee the quality of CTD data collected by autonomous vehicles (Garau et al., 2011). A novel first application of gliders was the use of these platforms in combination with altimetry to investigate the limitations and potential improvements of coastal altimetry data (e.g., Ruiz et al., 2009a; Bouffard et al., 2010; Troupin et al., 2015). Gliders have also been used to better characterize ocean mesoscale eddies, currents and their variability (e.g., Ruiz et al., 2009b, 2012; Cotroneo et al., 2016; Aulicino et al., 2018). An example of the unique high-resolution observational data that gliders can provide is the subduction of filaments with high chlorophyll concentration observed for the first time by Ruiz et al. (2009b) inside an Alboran Sea front. Gliders are also used to support multi-platform experiments that aim to sample a region of study over a specific period of time (e.g., Pascual et al., 2017; Barceló-Llull et al., 2018; Ruiz et al., 2019; Mahadevan et al., 2020), but they can also be used alone to periodically sample a given region in order to provide information about the temporal evolution of water properties (e.g., Heslop et al., 2012; Bosse et al., 2015; Barceló-Llull et al., 2019; Juza et al., 2019; Margirier et al., 2020).

Underway CTDs The Underway-CTD (UCTD) is an oceanographic tow-yo instrument used to measure seawater conductivity, temperature, and pressure from a moving vessel (Rudnick and Klinke, 2007). It consists of a probe attached to a shipboard winch. The tether line is spooled freely such that the velocity of the line through the water is close to zero, line drag is negligible and the probe can reach its desired depth. Additional sensors, such as optical sensors (i.e., chlorophyll, oxygen, backscatter, etc.), can be mounted onto the UCTD probe (Dever et al., 2019). The maximum depth that the UCTD probe can reach is 2000 m, although this may vary if extra sensors are also required.

Continued

Box 8.1 Multi-platform observations reveal mesoscale variability—cont'd

The underway CTD is mainly used for high-frequency sampling of the upper ocean (200 −250 m). With a steady ship speed of six knots, the time needed to complete a profile (including recovery time) is about 5 min, which corresponds to a horizontal resolution of one profile per kilometer. With such high resolution, the UCTD is a useful tool to characterise meso- and sub-mesoscale structures in the upper ocean, such as eddies or filaments of water subducting along narrow frontal regions.

Acoustic Doppler Current Profilers Acoustic Doppler Current Profilers (ADCP) are devices, mounted on ships or on moorings, that exploit the Doppler frequency shift from an acoustic ping to infer water velocity: they calculate an average velocity over a series of selected depth ranges (bins or cells). This averaging reduces the harmful effects of spatial aliasing. When an ADCP is mounted on a moving ship, it mainly measures the ship's speed. To obtain the net current speed the ship velocity must be subtracted. Ancillary sensors are recording simultaneously with the current measurements. At present, the ADCP is the most widely used instrument for observing ocean currents. Many studies have demonstrated its unique capabilities for mapping the space-time evolution of internal waves (e.g., Pinkel, 1983; Pinkel and Smith, 1992), small-scale nearshore circulation features (Smith, 1993; Smith and Largier, 1995) and detailed characterisations of stronger currents (Plaisted and Richardson 1970).

In the Adriatic Sea, a complete characterization of the tidal flow was possible through vessel-mounted ADCP measurements carried out from May 1995 through February 1996. This study was one of the first to exploit the very high horizontal resolution of the ADCP over a long sampling period of about one year. Such extensive measurements were needed to separate the tidal signal from the low-frequency one, in order to study the space-time variability of both of them. A common problem with ship-borne ADCPs is filtering, since both space and time variations are present in the data. In the abovementioned work, a detiding method developed by Candela et al. (1992) was used, but many others are available. Temporal-aliasing problems arise in many contexts where ADCP measurements are available, especially where rapid variations of submesoscale velocity fields occur (Shcherbina, 2013). This is why the total horizontal velocities provided by the ADCP are commonly used to improve the geostrophic velocity estimates. By assuming geostrophy we can exclude the unbalanced motions inevitably included in the ADCP measurements and, at the same time, take advantage of the frequently simultaneous hydrographic measurements (with CTD or similar). Even if it is easy to compute the geostrophic velocities from dynamic height, a so-called "reference level" is needed: using the ADCP data to define a certain no-motion level (NML), as deep as possible, in order to capture the full baroclinic contribution to the motion field, is thus a useful application. A more complex approach aims to fine a "level of *known* motion", rather than an NML as proposed by Rudnick (1996), and implemented by Buongiorno Nardelli et al. (2001), to study small mesoscale features along a meandering upper-ocean front in the western Ionian Sea. In this method, the "known motion" is obtained by minimising the vertical root-mean-square deviation (RMSD) between the geostrophic velocities and the rotational component of the ADCP. The rotational component of the ageostrophic part of the field is negligible compared with the geostrophic one. A further study in the Alboran Sea by Gomis et al. (2001) computed, instead, the hydrographic and ADCP analysis separately, using a multivariate interpolation technique based on optimal interpolation (OI). Compared to this last example, variational analysis commonly adopted in atmospheric physics is now being adopted even in the ocean community. Its main advantage is the simple way to integrate physical relations between different variables compared to the OI methods. For example, the vertical gradient of the rotational component from the ADCP velocities is used to constrain and reconstruct the density gradients (observed by a UCTD) according to the thermal wind equation. Looking to the upcoming multi-platform experiments that aim to overcome the single instrument limitations by combining different measurements, ADCPs play a crucial role in understanding ocean dynamics.

Juza and Tintoré, 2021). Ocean observations are also essential for the preservation of ocean health, and our responses to real-time societal needs at regional and local scales, in order to assure the preservation and sustainability of our natural resources and continuing science-based management of the marine and coastal environment. For more details, the reader is referred to Chapter 10. The importance of accurate and reliable observations of the ocean has always been recognised by the scientific community, and has been recently remarked upon by international expert committees such as the Intergovernmental Panel on Climate Change (IPCC; Pörtner et al., 2019), and the Committee on Earth Observation Satellites. Assuring their continuing availability is among the objectives of a number of international projects, e.g., the European Commission's Copernicus program, the European Space Agency, and the ESA Climate Change Initiatives. Ocean observations are also needed to support the Blue Economy, which is predicted to more than double its contribution to the global value-added economy.

8.2 Mediterranean Sea mesoscale variability derived from satellite altimetry

Satellite altimetry provides high-precision SSH measurements that complement in-situ observations from a variety of platforms (see Box 8.1). This contributes to a better understanding of both the ocean circulation and the response of the Earth system to climate change. A combination of different satellite missions is presently used to produce daily maps that allow us to resolve the ocean circulation at the meso- and global scale. Fig. 8.2 shows the mean circulation of the Mediterranean Sea derived from satellite absolute dynamic topography (ADT). At least two satellites are needed to resolve mesoscale signals from altimetry (Le-Traon et al., 2013). This minimum requirement was met for the first time in 1992 with the Topex/Poseidon

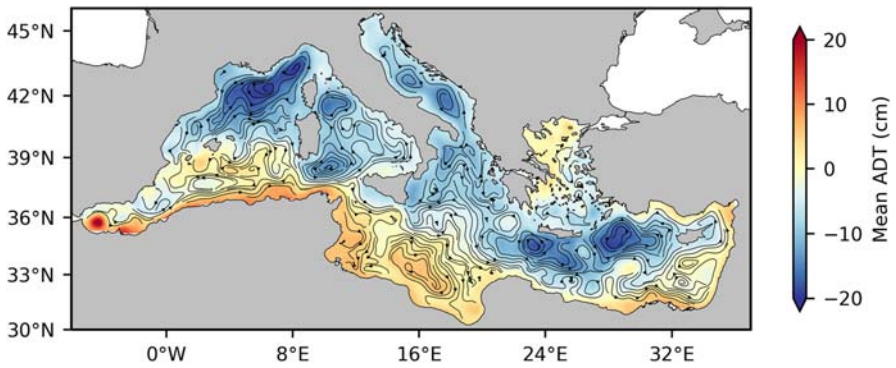

FIGURE 8.2

Mean ADT (cm) in the Mediterranean Sea for the period 1993–2020. Streamflow contours indicate the mean geostrophic velocity.

(T/P) and Jason-1 and ERS and ENVISAT missions. Since then, the constellations used to produce altimetric maps have been growing as new satellites are sent into orbit.

8.2.1 Mediterranean sea field dependency on the satellite constellation

Combinations of at least two satellite missions give improved estimates of mesoscale surface ocean circulation compared to results derived from only one altimeter (Pascual et al., 2006). In the Mediterranean Sea, the combination of T/P and ERS-1 and 2 satellite missions allowed the characterization of major changes in the sea-level variability over the basin for the 1993–99 period (Larnicol et al., 2002). However, the Mediterranean Sea is an area of complex spatial and temporal variability, where the mesoscale features have typical sizes of about 100 km; this scale is not fully resolved by two-satellite constellations (e.g., Pascual et al., 2007). These authors investigated the mesoscale features in the basin captured by four different satellite configurations, varying from one to four altimeters. They used, among others, the eddy kinetic energy (EKE), which is a common way to monitor mesoscale processes. EKE is the kinetic energy that is due to transient dynamics. It measures the degree of variability of the SSH, which then enables the identification of different regions with highly variable phenomena such as eddies, current meanders, fronts and/or filaments. According to Pascual et al. (2007), EKE is computed from sea level anomaly (SLA) (η') gridded maps by making the assumption of geostrophy as follows:

$$EKE = \frac{1}{2}\left[U'^2_g + V'^2_g\right] \tag{8.1}$$

$$U'^2_g = -\frac{g}{f}\frac{\delta\eta'}{\delta y} \tag{8.2}$$

$$V'^2_g = \frac{g}{f}\frac{\delta\eta'}{\delta x} \tag{8.3}$$

where U'_g and V'_g represent the zonal and meridional geostrophic velocity anomalies relative to the time period used in the computation of the gridded SLA maps, respectively; f is the Coriolis parameter, g is the acceleration of gravity, and $\frac{\delta\eta'}{\delta y}$ $\frac{\delta\eta'}{\delta x}$ are computed by finite differences with x and y being the distances in longitude and latitude. Pascual et al. (2007) demonstrated that the use of a single altimeter led to stronger signals being detected in the vicinity of the satellite passes, but further away from the tracks the signals dropped off rapidly, clearly indicating a sampling problem. Notable improvements in these EKE maps were seen as the number of satellites increased. The four-altimeter configuration contributed to the greatest intensification of all the structures, some of the weakest ones not detected with the other configurations, and increased the accuracy of detection of certain structures. This study concluded that at least three altimeter missions are required to effectively

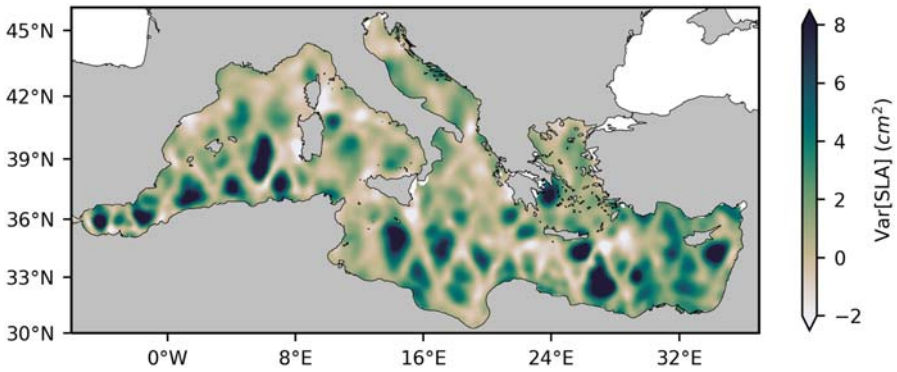

FIGURE 8.3

Difference between SLA variance (cm^2) calculated from a satellite configuration using all altimeters presently available and a satellite configuration of two altimeters.

monitor the surface mesoscale variability in the Mediterranean Sea. Pascual et al. (2006) investigated improvements in the estimation of the mesoscale surface circulation in the global ocean by merging data from four altimeter missions. They found root mean square (RMS) SLA differences of 10 cm between the two-satellite configurations and the merging of four missions in areas of intense variability, reaching EKE values of 0.04 $m^2\ s^{-2}$, which represent an important percentage of the signal variance.

Fig. 8.3 shows the differences of variance between the SLA computed for the Mediterranean basin from a satellite configuration using all altimeters presently available, and a satellite configuration of two altimeters. The satellite tracks for the common missions of the two configurations can be observed. The computation has been done over the time period from January 1993 through March 2020. Positive SLA values are observed throughout the basin indicating a larger variance in the SLA maps computed from the multi-satellite configuration. This configuration provides a clearer definition of the mesoscale structures in the basin contributing to their intensification, especially in regions of intense mesoscale activity such as the Alboran Sea and the Algerian and Levantine Basins, where improvements in the variance of $>20\ cm^2$ are observed. On the other hand, lower differences between both configurations are found in areas of weak mesoscale activity such as the northern WMED, and the Aegean and Adriatic Seas.

8.2.2 Quantifying spatial and temporal variability

The present 27-year time series of global daily altimetric (SLA) data allows us to study both the spatial and temporal variability of oceanic surface structure features. Juza et al. (2015) assessed the mean geostrophic circulation and EKE associated with mesoscale features in the WMED basin from altimetry products, using

combinations of up to four satellites. These authors characterised the Eastern and Western Alboran Gyres (EAG and WAG, respectively), located in the Alboran Sea, showing velocities of 0.6 m s^{-1} and 0.4 m s^{-1}, respectively; and the Algerian Current further east, close to the African co6ast, with mean values ranging from 0.25 m s^{-1} to 0.5 m s^{-1}. They found the highest energy and mesoscale activity in the Alboran Sea corresponding to the EAG and WAG, with a maximum EKE of 0.04 m^2 s^{-2}. These results are in agreement with the spatial distributions of mean EKE across the Mediterranean Sea obtained from the reprocessed gridded product presently available in the CMEMS catalog for the period 1993–2020 (Fig. 8.4). In this product, the SLA is estimated by optimal interpolation that merges the measurements from all available altimeter missions (CMEMS QUID, 2020). This product reveals some areas of intense mesoscale activity (EKE up to 0.05 m^2 s^{-2}) in the Alboran Sea, associated with the aforementioned EAG and WAG, the southern Algerian Basin, and the Levantine Basin (in the Eastern Mediterranean Sea, or EMED) associated with the Ierapetra Eddy (e.g., Ioannou et al., 2020). These three regions of higher energy are connected to other areas of high activity throughout the basin, showing clear continuity in all the EKE features. This is a well-known result already pointed out by e.g., Pascual et al. (2007). All these areas of high energy are located in the southern half of the basin, while the northern half has significantly weaker mesoscale activity with values below 0.01 m^2 s^{-2}.

Empirical Orthogonal Functions (EOF, e.g., Preisendorfer, 1988) are used to decompose ocean signals, in order to identify and quantify spatial and temporal variability. Fig. 8.5 shows the first EOF mode for the ADT over the period 1993–2020, accounting for 71.3% of the total variance. The spatial patterns reveal that the structures that vary the most during the year are the EAG in the Alboran Sea and the Ierapetra Eddy in the EMED. The temporal amplitude of the first mode is associated with the steric contribution to the seasonal cycle.

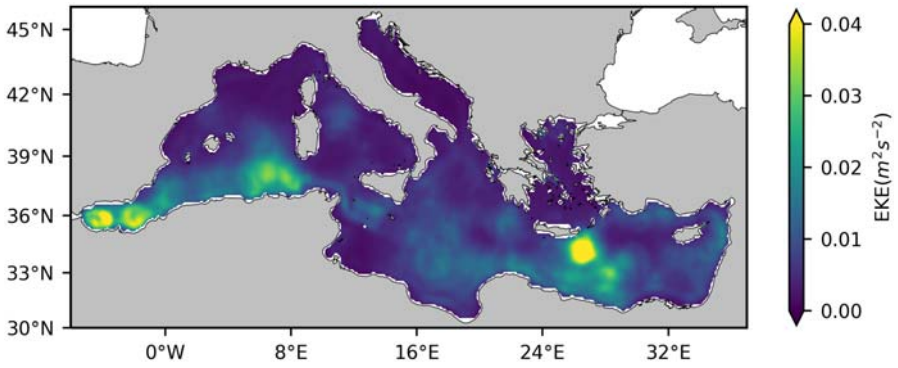

FIGURE 8.4

Mean eddy kinetic energy (m^2 s^{-2}) in the Mediterranean Sea for the period 1993–2020 was computed from the regional reprocessed gridded product presently available in the CMEMS catalog.

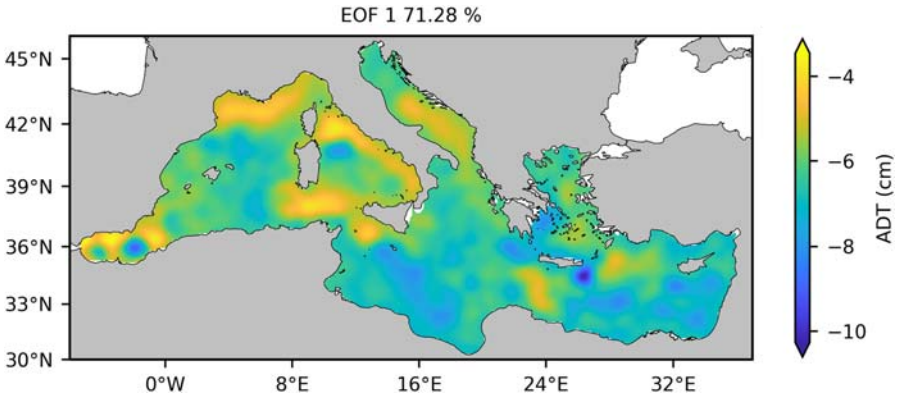

FIGURE 8.5

First EOF mode for ADT (cm) over the period 1993–2020.

8.3 Eddies, fronts and vertical velocity

8.3.1 Vertical velocity and fronts in the Mediterranean Sea

Vertical velocity associated with mesoscale and submesoscale features (eddies, fronts and filaments) triggers the vertical exchange of tracers between the upper layers of the ocean, which are nutrient-limited in the Mediterranean, and the deeper layers, which have high concentrations of nutrients but are light-limited. To understand the importance of vertical velocity it is necessary first to understand the importance of phytoplankton, the microscopic algae that are the base of the marine food chain and are key drivers of primary production. Phytoplankton is the primary producers of the ocean and obtain their energy through photosynthesis, hence they need sunlight and live in the euphotic (sunlit) layer. In the presence of light, phytoplankton assimilates carbon dioxide and dissolved nutrients (nitrogen, phosphorus, etc.) to produce carbohydrates and oxygen. However, the nutrients phytoplankton need are limited in the euphotic layer. Upward vertical velocities are responsible for the injection of these nutrients from deeper to sunlit layers, while downward vertical velocities subduct phytoplankton and organic carbon biomass, contributing to the sequestration of carbon into the deep ocean. These vertical velocities have very small orders of magnitude in comparison with horizontal velocities. At the mesoscale, vertical velocities are typically ~ 10 m day^{-1}, while at the submesoscale they can reach values of ~ 100 m day^{-1} (e.g., Mahadevan and Tandon, 2006; D'Asaro et al., 2011), which makes direct observations of vertical velocities difficult to obtain (most studies are limited to tracer release experiments and Lagrangian isopycnal drifter measurements, see Hansen and Paul, 1987; Lindstrom and Watts, 1994; Schultz Tokos et al., 1994; Harcourt et al., 2002; McGillicuddy et al., 2007; D'Asaro et al., 2011). These observational methods provide vertical velocity bulk estimates but are unable to characterize the 3D vertical velocity field and study

the forcing mechanisms. To achieve this, indirect approaches have been developed to calculate the vertical velocity field from observations of temperature, salinity, and horizontal velocity (Viúdez et al., 1996; Thomas et al., 2010). A widely used method in physical oceanography for calculating the vertical velocity field associated with mesoscale flows is the quasi-geostrophic omega equation. This equation was first developed to diagnose vertical velocity in the atmosphere by Hoskins et al. (1978), and then adapted to the ocean by Tintoré et al. (1991) and Pollard and Regier (1992), and has the advantage of requiring just the observed density field to integrate the vertical velocity, but is only valid for low Rossby number flows (Ro $<<$ 1). The Rossby number is defined as Ro = U/Lf, where U and L are characteristic velocity and length scales of the dynamical feature to be resolved, and f is the Coriolis parameter (see Cushman-Roisin and Beckers, 2011). Two other versions of the omega equation that include additional forcing terms and can be solved inflows with higher Ro are the semi-geostrophic (Hoskins and Draghici, 1977) and the generalised (Viúdez et al., 1996) omega equations. Viúdez and Dritschel (2004) evaluated the accuracy of these three versions of the omega equation and concluded that the generalized model was more accurate. However, the downside of this equation is that it requires the integration of both density and horizontal velocity observations.

In the energetic eastern and western Alboran Sea, quasi-synoptic physical and biochemical measurements collected over the last 20 years have revealed small-scale structures associated with mesoscale frontal zones (Ruiz et al., 2009a,b; Pascual et al., 2017; Olita et al., 2017; Ruiz et al., 2019). The results suggest that these small-scale features apparently modulate the distributions of biological parameters such as chlorophyll. In this area, the confluence of (fresher) Atlantic water and (more saline) resident Mediterranean water results in lateral density gradients of the order of 1 kg m^{-3} every 10 km (Ruiz et al., 2015) and, in turn, associated vertical velocities that range from $\pm$10 m day^{-1} to $\pm$50 m day^{-1}, based on the quasi-geostrophic omega equation (Gomis et al., 2001; Allen et al., 2001; Flexas et al., 2006; Ruiz et al., 2019) and modeling (Viúdez and Claret, 2009; Oguz et al., 2014).

In other regions of the WMED, horizontal density gradients are less intense, which induces smaller vertical velocities. An example is in the Balearic Sea, where a small anticyclonic eddy was sampled during the multiplatform experiment SINOCOP (Ruiz et al., 2018), which was carried out in 2009 to investigate mesoscale and submesoscale processes, using two gliders, seven drifters, a tide gauge and 24 standard CTDs, together with remote sensing images (altimetry, SST and ocean color). In this experiment, the quasi-geostrophic vertical velocity was around $\pm$2 m day^{-1} (Fig. 8.6), with sinking motions in the center of the eddy that may indicate an early stage of formation of the anticyclonic eddy.

8.3.2 Eddy detection, tracking and characterisation

In recent years several numerical codes have been developed to use digital SSH maps, be they from altimetry or numerical models, for the automated identification and tracking of mesoscale eddies (e.g., Isern-Fontanet et al., 2003; Chaigneau et al.,

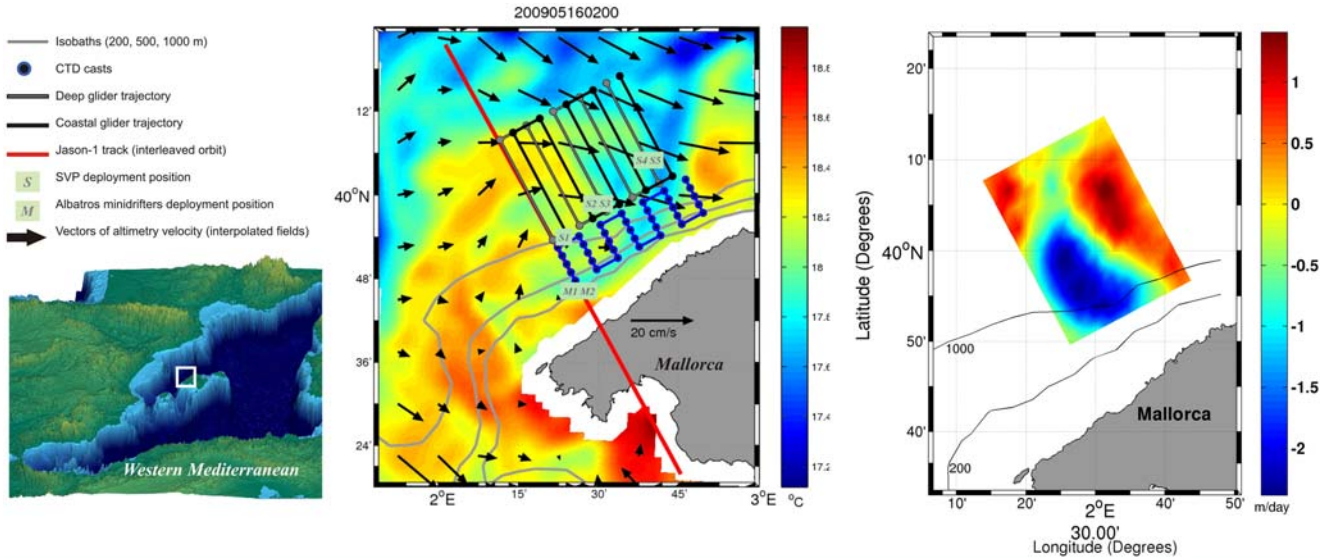

FIGURE 8.6

The Sinocop multi-platform experiment strategy and map of the region of study (left and middle); quasi geostrophic vertical velocity (m day^{-1}) field at 100 m depth estimated from hydrographic data (right), where blue colors reveal sinking motions at the center of the eddy.

From Ruiz, S., Mahadevan, A., Pascual, A., Claret, M., Tintoré, J., Mason, E., 2018. Multi-platform observations and numerical simulations to understand meso- and submesoscale processes: a case study of vertical velocities in the Western Mediterranean, 117–130, New Frontiers in Operational Oceanography, Publisher Godae OceanView, 811 pages, ISBN-10: 1720549974, ISBN-13: 978-1720549970, https://dx.doi.org/10.17125/gov2018.

2008; Nencioli et al., 2010; Chelton et al., 2011; Halo et al., 2014; Mason et al., 2014; Le Vu et al., 2018). Eddy identification and tracking are important because eddies are transporters of physical and biogeochemical tracers. The eddy core properties are typically anomalous with respect to the periphery of the eddy; furthermore, the core environment is conditioned by the sign of the eddy rotation, anticyclonic (clockwise in the northern hemisphere) or cyclonic (anticlockwise) (e.g., Mason et al., 2019). The eddy properties also change during an eddy's lifetime: the surface radii and amplitudes are initially small at birth, both ramping up after a month or two when the eddy is considered to be "mature". At some point later on, possibly a year or two in the enclosed Mediterranean, the eddy will dissipate and die (e.g., Pegliasco et al., 2021).

Identified eddies are typically mapped at the same frequency (usually daily) as the input SSH data. As well as recording the positions (longitude, latitude, time) of individual eddy instances, a series of eddy property variables such as the eddy radius, amplitude, rotational speed and polarity are saved, as these can be useful for later diagnostics. The most obvious application is the tracking of individual eddies over their lifetimes. This is based on the positional information but can be extended to all of the abovementioned properties. In the following, a number of examples of different applications of eddy identification and tracking codes across the Mediterranean will be provided.

Knowledge of eddy locations can be useful to oceanographers in a variety of ways. With a multi-decadal dataset, it is possible to make maps of a range of eddy properties such as, for example, the Mediterranean eddy frequency in Fig. 8.7, which is computed using altimetric SSH. The map clearly reveals the main hotspots of eddy presence over time: the WAG, the Ligurian Sea, the Algerian current, the Adriatic Sea, and several locations near Crete and Cyprus. For further recent examples across the Mediterranean and its sub-basins see Mason et al. (2019), Barboni et al. (2021), Bonaduce et al. (2021) and Pegliasco et al. (2021).

Although the data obtained from an eddy tracker is limited to the surface of the Mediterranean, it may also enable useful views into the subsurface. This can be achieved using both observational data, such as from the CTDs carried on Argo floats, and 3D model data. Over the period 2000−18 approximately 34,406 historical Argo profiles have been acquired in the Mediterranean (Barboni et al., 2021) and are available from the DYNED-Atlas-Med atlas (DYNED-Atlas-Med, 2019). As a certain percentage of these floats are entrained within eddies, the temperature and salinity profiles recorded by them are anomalous with respect to the surrounding waters. Examples of depth-averaged profiles of temperature, salinity and currents inside eddies identified by eddy tracking algorithms in the WMED, from both numerical models and altimetry, can be found in Escudier et al. (2016a,b) and Mason et al. (2019). Recent complementary work in the EMED has been documented by Ioannou et al. (2020) in the region of Crete. Another EMED example is an exhaustive investigation into individual eddies that undergo several splits and/or merges, as reported by Barboni et al. (2021).

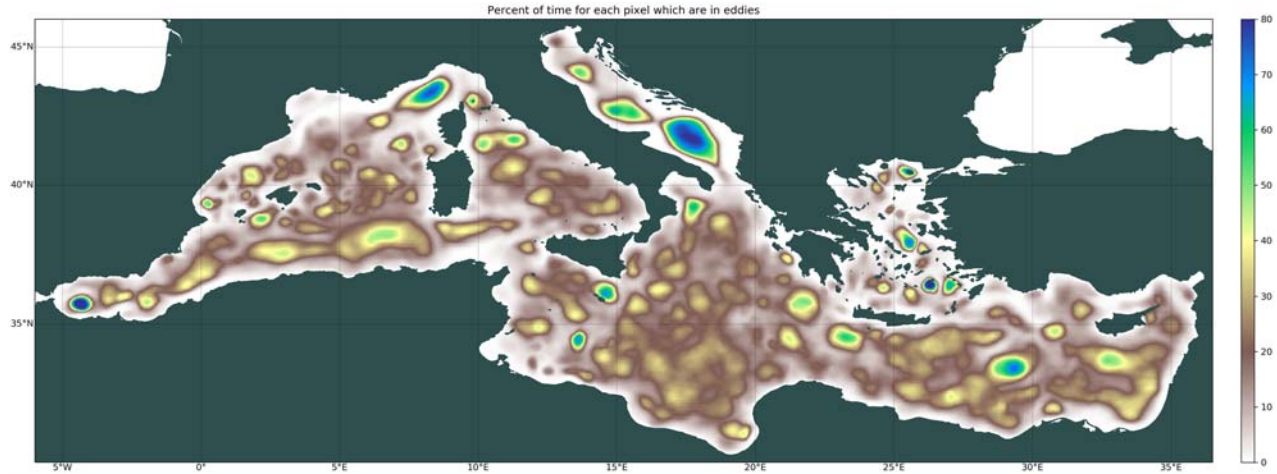

FIGURE 8.7

Eddy frequency (%) per grid point for anticyclones and cyclones from an eddy identification and tracking algorithm applied to altimeter SSH data over the period 1993–2018 (see https://py-eddy-tracker.readthedocs.io/en/stable/index.html for more diagnostic examples and related codes).

Oceanographers also use eddy tracker outputs to focus on particular eddies over their lifetimes, perhaps because they have in-situ data collected during an earlier oceanographic cruise that sampled part of the eddy trajectory. An example is the work of Pessini et al. (2020) in the WMED, who tracked an Algerian eddy that formed in 2004 near the Algerian coast, and was active for nearly 2 years south of the North Balearic Front. The authors used the eddy trajectory, and data collected from two short cruises (in October 2004 and June 2005) that allowed CTD sampling of portions of the subsurface fields. The in-situ data revealed the changes in subsurface water properties over the periods when sampling was within the eddy. Other data sets, such as SST or surface chlorophyll (from satellites or the surface fields of 3D model outputs), can also be incorporated into maps of the eddy positions. Examples include Escudier et al. (2016a,b) in the WMED, Mkhinini et al. (2014) in the central basin and in the EMED, and most recently Bonaduce et al. (2021) who consider the full Mediterranean using input data from a high-resolution numerical model. Additional useful applications of Mediterranean eddy datasets can be found in the work of Amores et al. (2019) and Pegliasco et al. (2021). Amores et al. (2019) point out that eddy trackers using the Mediterranean gridded SLA datasets detect fewer eddies in locations far from the satellite tracks than near them. They attribute this to an optimal interpolation algorithm that has a too restrictive temporal correlation scale. Going further, Stegner et al. (2021) identify a cyclone-anticyclone asymmetry of the eddy detection that arises from the Mediterranean Sea altimetry products. They found the detection of Mediterranean anticyclones to be more accurate than it is for cyclones. They also observed that the intensity of large-scale eddies is underestimated, and cautioned that these biases be accounted for when using AVISO/CMEMS SLA data. Pegliasco et al. (2021) assess the respective advantages of choosing SLA or ADT altimetric inputs for eddy identification in the Mediterranean Sea. They generally recommend ADT over SLA, but caution that SLA may be preferable in regions where there is uncertainty in the mean dynamic topography (MDT, see Chapter 5).

Anticipation is rising with the prospect of applying eddy identification algorithms to the high-resolution SSH outputs expected once the data stream from SWOT comes online in 2022 (see next section). The shorter spatial scales that SWOT is designed to resolve will enable the identification of eddy-like features extending for the first time into the submesoscale range.

8.4 Future perspectives

In general, the complexity of the mesoscale phenomena in the Mediterranean, and their interaction with the general circulation, make a full understanding and realistic modeling of the Mediterranean dynamics a challenge (Schroeder et al., 2012). Even after assimilating all available observations, the smaller-scale processes cannot be adequately reproduced in numerical models, so additional efforts will be required to fully understand the dynamics and role of mesoscale variability in the Mediterranean Sea.

Conceived as a major new diagnostic tool for climate studies, the Surface Water and Ocean Topography (SWOT) satellite mission will be launched in 2022 by the NASA (United States) and CNES (France) space agencies (Morrow et al., 2019). SWOT measurements will provide information on the dynamics of the upper ocean at an unprecedented resolution of $\sim$10 km; this is roughly one order of magnitude finer than contemporary measurements with conventional satellite altimetry.

The SWOT mission has been prioritised by the US National Research Council as a means to provide society with ongoing information about global climate and climate change. The improved spatial resolution of global ocean circulation observations is considered critical for a better understanding of a range of important climatic processes, including the ocean energy budget, export of organic matter, and fluxes of matter and energy at the ocean interfaces. The SWOT Science Team encourages the international community to coordinate future fine-scale in-situ oceanographic campaigns around the world during the calibration/validation phase. A new initiative, known as the SWOT Adopt-a-Crossover (D'Ovidio et al., 2019), has the objective to define common in-situ observing protocols adapted to the SWOT mission in order to perform the first global ocean survey of fine-scale ocean dynamics, over a wide range of latitudes and conditions with innovative and multi-focus approaches to study fine-scale ocean circulation and impacts at the climate scale.

The final goal is to improve the characterisation of oceanic mesoscale and submesoscale features (e.g., fronts, meanders, eddies and filaments) through the combined use of in-situ multi-platform and satellite data in synergy with numerical models and innovative computational techniques. The wide-swath SWOT altimeter will allow synoptic observations at scales shorter than 100 km for the first time. In anticipation of the 2D SSH fields that will be provided by SWOT, and to monitor and establish the vertical exchange associated with mesoscale and submesoscale features, multi-sensor synoptic observations must be acquired. In-situ observations from R/Vs (e.g., CTD, water samples, ADCP), gliders, moorings, and drifters should be used in coordination with satellite data for a full description of physical and biogeochemical variability. The observational approach must be integrated with numerical simulations, both realistic and process-oriented studies, in order to better understand the underlying processes. The area of study will be the WMED, a natural reduced-scale laboratory basin for the examination of processes of global importance and one of the zones in the global ocean that will be covered by SWOT at a daily resolution during the initial fast sampling phase.

Additional Resources

- https://resources.marine.copernicus.eu/products (Copernicus data)
- https://py-eddy-tracker.readthedocs.io/en/stable/ (*py-eddy-tracker* documentation)
- https://www.lmd.polytechnique.fr/dyned/data-base.html (DYNED-Atlas eddy database for the Mediterranean Sea)

References

Aguiar, E., Mourre, B., Juza, M., et al., 2020. Multi-platform model assessment in the Western Mediterranean Sea: impact of downscaling on the surface circulation and mesoscale activity. Ocean Dynam. 70, 273–288. https://doi.org/10.1007/s10236-019-01317-8.

Allen, J.T., Smeed, D.A., Tintoré, J., Ruiz, S., 2001. Mesoscale subduction at the Almeria–Oran front: Part 1: ageostrophic flow. J. Mar. Syst. 30 (3–4), 263–285.

Alvarez, A., Mourre, B., 2012. Oceanographic field estimates from remote sensing and glider fleets. J. Atmos. Ocean. Technol. 29, 1657–1662.

Aulicino, G., Cotroneo, Y., Ruiz, S., Sánchez-Román, A., Pascual, A., Fusco, G., Tintoré, J., Budillon, G., 2018. Monitoring the Algerian Basin through glider observations, satellite altimetry and numerical simulations along a SARAL/AltiKa track. J. Mar. Syst. 179, 55–71. https://doi.org/10.1016/j.jmarsys.2017.11.006. ISBN: 0924-7963.

Amores, A., Jordà, G., Monserrat, S., 2019. Ocean eddies in the Mediterranean Sea from satellite altimetry: Sensitivity to satellite track location. Front. Mar. Sci. 703.

Barboni, A., Lazar, A., Stegner, A., Moschos, E., 2021. Lagrangian eddy tracking reveals the Eratosthenes anticyclonic attractor in the eastern Levantine Basin. Ocean Sci. 17, 1231–1250. https://doi.org/10.5194/os-17-1231-2021.

Barceló-Llull, B., Pascual, A., Díaz Barroso, L., Sánchez-Román, A., Casas, B., Muñoz, C., Torner, M., Alou, E., Cutolo, E., Mourre, B., Allen, J., Aulicino, G., Cabornero, A., Calafat, N., Capó, E., Cotroneo, Y., Cyr, F., Doglioli, A., d'Ovidio, F., Dumas, F., Fernández, J.-G., Gómez- Navarro, L., Gregori, G., Hernández-Lasheras, J., Mahadevan, A., Mason, E., Miralles, A., Roque, D., Rubio, M., Ruiz, I., Ruiz, S., Ser-Giacomi, E., Toomey, T., 2018. PRE-SWOT Cruise Report. Mesoscale and submesoscale vertical exchanges from multi-platform experiments and supporting modeling simulations: anticipating SWOT launch (CTM2016-78607-P). Tech. Rep. CSIC. 138. https://doi.org/10.20350/digitalCSIC/8584.

Barceló-Llull, B., Pascual, A., Ruiz, S., Escudier, R., Torner, M., Tintoré, J., 2019. Temporal and spatial hydrodynamic variability in the Mallorca channel (western Mediterranean Sea) from 8 years of underwater glider data. J. Geophys. Res.: Oceans 124. https://doi.org/10.1029/2018JC014636.

Barceló-Lull, B., Pascual, A., Sánchez-Román, A., Cutolo, E., d'Ovidio, F., Fifani, G., Ser-Giacomi, E., Ruiz, S., Mason, E., Cyr, F., Doglioli, A., Mourre, B., Allen, J.T., Alou-Font, E., Casas, B., Díaz-Barroso, L., Dumas, F., Gómez-Navarro, L., Muñoz, C., 2021. Fine-scale ocean currents derived from in situ observations in anticipation of the upcoming SWOT altimetric mission. Front. Mar. Sci. 8, 1070.

Bonaduce, A., Cipollone, A., Johannessen, J.A., Staneva, J., Raj, R.P., Aydogdu, A., 2021. Ocean Mesoscale Variability: A Case Study on the Mediterranean Sea from a Reanalysis Perspective.

Bosse, A., Testor, P., Mortier, L., Prieur, L., Taillandier, V., d'Ortenzio, F., Coppola, L., 2015. Spreading of Levantine Intermediate Waters by submesoscale coherent vortices in the northwestern Mediterranean Sea as observed with gliders. J. Geophys. Res.: Oceans 120, 1599–1622. https://doi.org/10.1002/2014JC010263.

Bouffard, J., Pascual, A., Ruiz, S., Faugère, Y., Tintoré, J., 2010. Coastal and mesoscale dynamics characterization using altimetry and gliders: a case study in the Balearic Sea. J. Geophys. Res. 115, C10029. https://doi.org/10.1029/2009JC00608.

Buongiorno Nardelli, B., Santoleri, R., Sparnocchia, S., 2001. Small mesoscale features at a meandering upper-ocean front in the western IonianSea (Mediterranean Sea): vertical motion and potential vorticity analysis. J. Phys. Oceanogr. 31, 2227–2250.

Candela, J., Beardsley, R.C., Limeburner, R., 1992. Separation of tidal and subtidal currents in ship-mounted acoustic Doppler current profiler observations. J. Geophys. Res.: Oceans 97 (C1), 769–788.

Chaigneau, A., Gizolme, A., Grados, C., 2008. Mesoscale eddies off Peru in altimeter records: identification algorithms and eddy spatio-temporal patterns. Prog. Oceanogr. 79 (2–4), 106–119. https://doi.org/10.1016/j.pocean.2008.10.013.

Chelton, D.B., deSzoeke, R.A., Schlax, M.G., El Naggar, K., Siwertz, N., 1998. Geographical variability of the first-baroclinic Rossby radius of deformation. J. Phys. Oceanogr. 28, 433–460.

Chelton, D.B., Schlax, M.A., Samelson, R.M., 2011. Global observations of nonlinear mesoscale eddies. Prog. Oceanogr. 91, 167–216. https://doi.org/10.1016/j.pocean.2011.01.002.

CMEMS, 2020. QUID for Sea Level TAC DUACS Products. Available online: http://marine.copernicus.eu/documents/QUID/CMEMS-SL-QUID-008-032-062.pdf (Accessed 4 January 2021).

Cotroneo, Y., Aulicino, G., Ruiz, S., Pascual, A., Budillon, G., Fusco, G., Tintoré, J., 2016. Glider and satellite high resolution monitoring of a mesoscale eddy in the Algerian Basin: effects on the mixed layer depth and biochemistry. J. Mar. Syst. 162, 73–88.

Cushman-Roisin, B., Beckers, J.-M., 2011. Introduction to Geophysical Fluid Dynamics In: International Geophysics Series, second ed., 101. Academic Press.

D'Asaro, E., Lee, C., Rainville, L., Harcourt, R., Thomas, L., 2011. Enhanced turbulence and energy dissipation at ocean fronts. Science 332 (6027), 318–322.

D'Asaro, E.A., Shcherbina, A.Y., Klymak, J.M., Molemaker, J., Novelli, G., Guigand, C.M., Haza, A.C., Haus, B.K., Ryan, E.H., Jacobs, G.A., Huntley, H.S., Laxague, N.J.M., Chen, S., Judt, F., McWilliams, J.C., Barkan, R., Kirwan, A.D., Poje, A.C., Özgökmen, T.M., 2018. Ocean convergence and the dispersion of flotsam. Proc. Natl. Acad. Sci. Unit. States Am. 115 (6), 1162–1167. https://doi.org/10.1073/pnas.1718453115.

Dever, M., Freilich, M., Hodges, B., Farrar, T., Lanagan, T., Mahadevan, A., 2019. Uctd and ecoctd observations from the Calypso pilot experiment. In: 2018 Cruise and Data Report (Tech. Rep.). Woods Hole Oceanographic Institution Technical Report. https://doi.org/10.1575/1912/23637. WHOI-2019-01.

d'Ovidio, F., Pascual, A., Wang, J., Doglioli, A., Jing, Z., Moreau, S., Gregori, G., Swart, S., Speich, S., Cyr, F., Legresy, B., Chao, Y., Fu, L., Morrow, R.A., 2019. Frontiers in fine scale in-situ studies: opportunities during the SWOT fast sampling phase. Front. Mar. Sci. Section Ocean Observ. https://doi.org/10.3389/fmars.2019.00168.

Stegner, A., Le Vu, B., Pegliasco, C., Faugere, Y., DYNED-Atlas-Med, 2019. Dynamical Eddy Atlas of the Mediterranean-Sea 2000–2018. https://doi.org/10.14768/2019130201.2. MISTRALS (data set).

Escudier, R., Bouffard, J., Pascual, A., Poulain, P.M., Pujol, M.I., 2013. Improvement of coastal and mesoscale observation from space: application to the northwestern Mediterranean Sea. Geophys. Res. Lett. 40 (10), 2148–2153.

Escudier, R., Renault, L., Pascual, A., Brasseur, P., Chelton, D., Beuvier, J., 2016a. Eddy properties in the Western Mediterranean Sea from satellite altimetry and a numerical

simulation. J. Geophys. Res. Oceans 121, 3990–4006. https://doi.org/10.1002/2015JC011371.

Escudier, R., Mourre, B., Juza, M., Tintoré, J., 2016b. Subsurface circulation and mesoscale variability in the Algerian subbasin from altimeter-derived eddy trajectories. J. Geophys. Res. Oceans 121, 6310–6322. https://doi.org/10.1002/2016JC011760.

Flexas, M.M., Gomis, D., Ruiz, S., Pascual, A., León, A., 2006. In situ and satellite observations of the eastward migration of the Western Alboran sea gyre. Prog. Oceanogr. 70, 486–509.

Garau, B., Ruiz, S., Zang, G.W., Pascual, A., Heslop, E., Kerfoot, J., Tintoré, J., 2011. Thermal lag correction on Slocum CTD glider data. J. Atmos. Ocean. Technol. 28 (9), 1065–1071. https://doi.org/10.1175/JTECH-D-10-05030.1.

Garreau, P., Dumas, F., Louazel, S., Correard, S., Fercocq, S., Le Menn, M., et al., 2020. PROTEVS-MED field experiments: very high resolution hydrographic surveys in the Western Mediterranean Sea. Earth Syst. Sci. Data 12 (1), 441–456.

Gill, A.E., 1982. Atmosphere-ocean dynamics. In: International Geophysics Series, 30. Academic Press, 662pp.

Gomis, D., Ruiz, S., Pedder, M.A., 2001. Diagnostic analysis of the 3D ageostrophic circulation from a multivariate spatial interpolation of CTD and ADCP data. Deep Sea Res. Oceanogr. Res. Pap. 48 (1), 269–295.

Grilli, F., Pinardi, N., 1998. The computation of Rossby radii of deformation for the Mediterranean Sea. MTP News 6 (4).

Halo, I., Backeberg, B., Penven, P., Ansorge, I., Reason, C., Ullgren, J., 2014. Eddy properties in the Mozambique Channel: a comparison between observations and two numerical ocean circulation models. Deep-Sea Res. II 100, 38–53. https://doi.org/10.1016/j.dsr2.2013.10.015.

Hamad, N., Millot, C., Taupier-Letage, I., 2003. The surface circulation in the eastern basin of the Mediterranean Sea. Sci. Mar. 70, 457–503.

Hansen, D.V., Paul, C.A., 1987. Vertical motion in the eastern equatorial Pacific inferred from drifting buoys. Oceanol. Acta. Special issue.

Harcourt, R.R., Steffen, E.L., Garwood, R.W., D'Asaro, E.A., 2002. Fully Lagrangian floats in Labrador Sea deep convection: comparison of numerical and experimental results. J. Phys. Oceanogr. 32 (2), 493–510.

Hayes, D.R., Zodiatis, G., Konnaris, G., Hannides, A.K., Solovyov, D.M., Testor, P., 2011. Glider Transects in the Levantine Sea: Characteristics of the Warm Core Cyprus Eddy. OCEANS 2011 IEEE, Spain, pp. 1–9.

Heslop, E., Ruiz, S., Allen, J.T., López-Jurado, J.L., Renault, L., Tintoré, J., 2012. Autonomous underwater gliders monitoring variability at "choke points" in our ocean system: a case study in the Western Mediterranean Sea. Geophys. Res. Lett. 39, L20604. https://doi.org/10.1029/2012GL053717.

Hoskins, B.J., Draghici, I., 1977. The forcing of ageostrophic motion according to the semi-geostrophic equations and in an isentropic coordinate model. J. Atmos. Sci. 34 (12), 1859–1867.

Hoskins, B.J., Draghici, I., Davies, H.C., 1978. A new look at the ω-equation. Q. J. R. Meteorol. Soc. 104 (439), 31–38.

Ioannou, A., Stegner, A., Dumas, F., Briac, L.V., 2020. Three-dimensional evolution of mesoscale Anticyclones in the lee of Crete. Front. Mar. Sci. 7. https://doi.org/10.3389/fmars.2020.609156.

Isern-Fontanet, J., García-Ladona, E., Font, J., 2003. Identification of marine eddies from altimetric maps. J. Atmos. Ocean. Technol. 20, 772−778. https://doi.org/10.1175/1520-0426(2003)20<772:IOMEFA>2.0.CO;2.

Juza, M., Tintoré, J., 2021. Multivariate sub-regional ocean indicators in the Mediterranean Sea: from event detection to climate change estimations. Front. Mar. Sci. 8, 233. https://doi.org/10.3389/fmars.2021.610589.

Juza, M., Mourre, B., Lellouche, J.-M., Tonani, M., Tintoré, J., 2015. From basin to sub-basin scale assessment and intercomparison of numerical simulations in the Western Mediterranean Sea. J. Mar. Syst. 149, 36−49. https://doi.org/10.1016/j.jmarsys.2015.04.010.

Juza, M., Escudier, R., Pascual, A., Pujol, M.I., Taburet, G., Troupin, C., et al., 2016. Impacts of reprocessed altimetry on the surface circulation and variability of the Western Alboran Gyre. Adv. Space Res. 58 (3), 277−288.

Juza, M., Escudier, R., Vargas-Yez, M., Mourre, B., Heslop, E., Allen, J., Tintoré, J., 2019. Characterization of changes in western inter-mediate water properties enabled by an innovative geometry-based detection approach. J. Mar. Syst. 191, 1−12. https://doi.org/10.1016/j.jmarsys.2018.11.003.

Kurkin, A., Kurkina, O., Rybin, A., Talipova, T., 2020. Comparative analysis of the first baroclinic Rossby radius in the Baltic, Black, Okhotsk, and Mediterranean seas. Russ. J. Earth Sci. 20.

Larnicol, G., Ayoub, N., Le Traon, P.-Y., 2002. Major changes in Mediterranean Sea level variability from 7 years of TOPEX/POSEIDON and ERS-1/2 data. J. Mar. Syst. 33−34, 63−89.

Le Vu, B., Stegner, A., Arsouze, T., 2018. Angular momentum eddy detection and tracking algorithm (AMEDA) and its application to coastal eddy formation. J. Atmos. Ocean. Technol. 35, 739−762. https://doi.org/10.1175/JTECH-D-17-0010.1.

Le-Traon, P.Y., 2013. From satellite altimetry to Argo and operational oceanography: three revolutions in oceanography. Ocean Sci. 9, 901−915. https://doi.org/10.5194/os-9-901-2013.

Lindstrom, S.S., Pandolph Watts, D., 1994. Vertical motion in the Gulf stream near 68 W. J. Phys. Oceanogr. 24 (11), 2321−2333.

Mahadevan, A., Tandon, A., 2006. An analysis of mechanisms for submesoscale vertical motion at ocean fronts. Ocean Model. 14 (3−4), 241−256.

Mahadevan, A., Pascual, A., Rudnick, D.L., Ruiz, S., Tintoré, J., D'Asaro, E., 2020. Coherent pathways for vertical transport from the surface ocean to interior. Bull. Am. Meteorol. Soc. 101, E1996−E2004. https://doi.org/10.1175/BAMS-D-19-0305.1.

Margirier, F., Testor, P., Heslop, E., et al., 2020. Abrupt warming and salinification of intermediate waters interplays with decline of deep convection in the Northwestern Mediterranean Sea. Sci. Rep. 10, 20923. https://doi.org/10.1038/s41598-020-77859-5.

Marullo, S., Napolitano, E., Santoleri, R., Manca, B., Evans, R., 2003. Variability of rhodes and Ierapetra gyres during levantine intermediate water experiment: observations and model results. J. Geophys. Res. 108, 8119. https://doi.org/10.1029/2002JC001393,C9.

Mason, E., Pascual, A., McWilliams, J.C., 2014. A new sea surface height−based code for oceanic mesoscale eddy tracking. J. Atmos. Ocean. Technol. 31 (5), 1181−1188. https://journals.ametsoc.org/view/journals/atot/31/5/jtech-d-14-00019_1.

Mason, E., Ruiz, S., Bourdalle-Badie, R., Reffray, G., García-Sotillo, M., Pascual, A., 2019. New insight into 3-D mesoscale eddy properties from CMEMS operational models in the western Mediterranean. Ocean Sci. 15 (4), 1111−1131.

McGillicuddy Jr., D.J., Anderson, L.A., Bates, N.R., Bibby, T., Buesseler, K.O., Carlson, C.A., et al., 2007. Eddy/wind interactions stimulate extraordinary mid-ocean plankton blooms. Science 316 (5827), 1021−1026.

Menna, M., Gerin, R., Notarstefano, G., Mauri, E., Bussani, A., Pacciaroni, M., Poulain, P.M., 2021. On the circulation and thermohaline properties of the eastern Mediterranean Sea. Front. Mar. Sci. 903.

Millot, C., 1987. Circulation in the western Mediterranean Sea. J. Mar. Syst. 20, 423−442.

Millot, C., Taupier-Letage, I., 2005. Circulation in the Mediterranean Sea. In: Saliot, A. (Ed.), The Mediterranean Sea. Handbook of Environmental Chemistry, 5K. Springer, Berlin, Heidelberg. https://doi.org/10.1007/b107143.

Mkhinini, N., Coimbra, A.L.S., Stegner, A., Arsouze, T., Taupier-Letage, I., Béranger, K., 2014. Long-lived mesoscale eddies in the eastern Mediterranean Sea: analysis of 20 years of AVISO geostrophic velocities. J. Geophys. Res. Oceans 119 (12), 8603−8626.

Morrow, R., Fu, L.-L., Ardhuin, F., Benkiran, M., Chapron, B., Cosme, E., et al., 2019. Global observations of fine-scale ocean surface topography with the Surface Water and Ocean Topography (SWOT) mission. Front. Mar. Sci. 6. https://doi.org/10.3389/fmars.2019.00232.

Nencioli, F., Dong, C., Dickey, T.D., Washburn, L., McWilliams, J.C., 2010. A vector geometry−based eddy detection algorithm and its application to a high-resolution numerical model product and high-frequency radar surface velocities in the Southern California Bight. J. Atmos. Ocean. Technol. 27, 564−579. https://doi.org/10.1175/2009JTECHO725.1.

Oguz, T., Macias, D., Garcia-Lafuente, J., Pascual, A., Tintoré, J., 2014. Fueling plankton production by a meandering frontal jet: a case study for the Alboran Sea (Western Mediterranean). PLoS One 9 (11), 1−14.

Olita, A., Capet, A., Claret, A.M., Mahadevan, A., Poulain, P.-M., Ribotti, A., Ruiz, S., Tintoré, J., Tovar-Sánchez, A., Pascual, A., 2017. Frontal dynamics boost primary production in the summer stratified Mediterranean Sea. Ocean Dynam. 67, 767−782. https://doi.org/10.1007/s10236-017-1058-z.

Onken, R., Fiekas, H.V., Beguery, L., Borrione, I., Funk, A., Hemming, M., et al., 2018. High-resolution observations in the western Mediterranean Sea : the REP14-MED experiment. Ocean Sci. 14, 321−335.

Pascual, A., Faugère, Y., Larnicol, G., Le Traon, P.-Y., 2006. Improved description of the ocean mesoscale variability by combining four satellite altimeters. Geophys. Res. Lett. 33, L02611. https://doi.org/10.1029/2005GL024633.

Pascual, A., Pujol, M.-I., Larnicol, G., Le Traon, P.-Y., Rio, M.-H., 2007. Mesoscale mapping capabilities of multisatellite altimeter missions: first Results with real data in the Mediterranean Sea. J. Mar. Syst. 65, 190−211. https://doi.org/10.1016/j.jmarsys.2004.12.004.

Pascual, A., Ruiz, S., Tintoré, J., 2010. Combining new and conventional sensors to study the Balearic Current. Sea Technol. 51 (7), 32−36.

Pascual, A., Ruiz, S., Buongiorno Nardelli, B., Guinehut, S., Iudicone, D., Tintoré, J., 2015. Net primary production in the Gulf Stream sustained by quasi-geostrophic vertical exchanges. Geophys. Res. Lett. 42 (2), 441−449.

Pascual, A., Ruiz, S., Olita, A., Troupin, C., Claret, M., Casas, B., Mourre, B., Poulain, P.-M., Tovar-Sanchez, A., Capet, A., et al., 2017. A multiplatform experiment to unravel meso- and submesoscale processes in an intense front (AlborEx). Front. Mar. Sci. 4, 39. https://doi.org/10.3389/fmars.2017.00039.

Pegliasco, C., Chaigneau, A., Morrow, R., Dumas, F., 2021. Detection and tracking of mesoscale eddies in the Mediterranean Sea: a comparison between the sea level anomaly and the absolute dynamic topography fields. Adv. Space Res. 68 (2), 401−419.

Pessini, F., Cotroneo, Y., Olita, A., Sorgente, R., Ribotti, A., Jendersied, S., Perilli, A., 2020. Life history of an anticyclonic eddy in the Algerian basin from altimetry data, tracking algorithm and in situ observations. J. Mar. Syst. 207, 103346. https://doi.org/10.1016/j.jmarsys.2020.103346.

Petrenko, A.A., Doglioli, A.M., Nencioli, F., et al., 2017. A review of the LATEX project: mesoscale to submesoscale processes in a coastal environment. Ocean Dynam. 67, 513−533.

Pinardi, N., Masetti, E., 2000. Variability of the large scale general circulation of the Mediterranean Sea from observations and modelling: a review. Palaeogr., Paleoclimatol. Palaeoecol. 158 (3−4). https://doi.org/10.1016/S0031-0182(00)00048-1.

Pinkel, R., 1983. Doppler sonar observations of internal waves: wavefield structure. J. Phys. Oceanogr. 13, 804−815.

Pinkel, R., Smith, J.A., 1992. Repeat-sequence coding for improved precision of Doppler sonar and sodar. J. Atmos. Ocean. Technol. 9, 149−163.

Plaisted, R.O., Richardson, W.S., 1970. Current fine structure in the Florida current. J. Mar. Res. 28 (3), 359−363.

Poje, A.C., Özgökmen, T.M., Lipphardt Jr., B.L., Haus, B.K., Ryan, E.H., Haza, A.C., et al., 2014. Submesoscale dispersion in the vicinity of the Deepwater Horizon spill. Proc. Natl. Acad. Sci. U.S.A. 111, 12693−12698. https://doi.org/10.1073/pnas.1402452111.

Pollard, R.T., Regier, L.A., 1992. Vorticity and vertical circulation at an ocean front. J. Phys. Oceanogr. 22, 609−625.

Pörtner, H.O., Roberts, D.C., Masson-Delmotte, V., Zhai, P., Tignor, M., Poloczanska, E., Weyer, N.M., 2019. The Ocean and Cryosphere in a Changing Climate. IPCC Special Report on the Ocean and Cryosphere in a Changing Climate.

Poulain, P.M., Menna, M., Mauri, E., 2012. Surface geostrophic circulation of the Mediterranean Sea derived from drifter and satellite altimeter data. J. Phys. Oceanogr. 42 (6), 973−990.

Poulain, P.-M., Bussani, A., Gerin, R., Jungwirth, R., Mauri, E., Menna, M., Notarstefano, G., 2013. Mediterranean surface currents measured with drifters: from basin to subinertial scales. Oceanography 26 (1), 38−47. https://doi.org/10.5670/oceanog.2013.03.

Preisendorfer, R.W., 1988. Principal Component Analysis in Meteorology and Oceanography. Elsevier Science and Technology, 444pp.

Rudnick, D.L., 1996. Intensive surveys of the Azores Front: 2. Inferring the geostrophic and vertical velocity fields. J. Geophys. Res.: Oceans 101 (C7), 16291−16303.

Rudnick, D.L., Klinke, J., 2007. The underway conductivity−temperature−depth instrument. J. Atmos. Ocean. Technol. 24 (11), 1910−1923. https://doi.org/10.1175/JTECH2100.1.

Ruiz, S., Pascual, A., Garau, B., Faugere, Y., Alvarez, A., Tintoré, J., 2009a. Mesoscale dynamics of the Balearic front integrating glider, ship and satellite data. J. Mar. Syst. 78, S3−S16. https://doi.org/10.1016/j.jmarsys.2009.01.007.

Ruiz, S., Pascual, A., Garau, B., Pujol, I., Tintoré, J., 2009b. Vertical motion in the upper ocean from glider and altimetry data. Geophys. Res. Lett. 36, L14607. https://doi.org/10.1029/2009GL038569.L14607.

Ruiz, S., Renault, L., Garau, B., Tintoré, T., 2012. Glider observations and modelling of an abrupt mixing event in the Western Mediterranean. Geophys. Res. Lett. 39, L01603. https://doi.org/10.1029/2011GL050078.

Ruiz, S., Pascual, A., Casas, B., Poulain, P.-M., Olita, A., Troupin, C., et al., 2015. Report on Operation and Data Analysis for Multi-Platform Synoptic Intensive Experiment (AlborEx) (Technical Report). Available at. https://nimbus.imedea.uib-csic.es/index.php/s/ABxQC8xwiYN9gaY.

Ruiz, S., Mahadevan, A., Pascual, A., Claret, M., Tintoré, J., Mason, E., 2018. Multi-platform observations and numerical simulations to understand meso- and submesoscale processes: a case study of vertical velocities in the Western Mediterranean, 117-130. In: New Frontiers in Operational Oceanography. Publisher Godae OceanView, p. 811. https://doi.org/10.17125/gov2018. ISBN-10: 1720549974, ISBN-13: 978-1720549970.

Ruiz, S., Claret, M., Pascual, A., Olita, A., Troupin, C., Capet, Tovar-Sánchez, A., Allen, J., Poulain, P.-M., Tintoré, J., Mahadevan, A., 2019. Effects of oceanic mesoscale and submesoscale frontal processes on the vertical transport of phytoplankton. J. Geophys. Res. Oceans 124. https://doi.org/10.1029/2019JC015034.

Shcherbina, A.Y., D'Asaro, E.A., Lee, C.M., Klymak, J.M., Molemaker, M.J., McWilliams, J.C., 2013. Statistics of vertical vorticity, divergence, and strain in a developed submesoscale turbulence field. Geophys. Res. Lett. 40 (17), 4706−4711.

Schroeder, K., Garcìa-Lafuente, J., Josey, S.A., Artale, V., Buongiorno Nardelli, B., Carrillo, A., Gačić, M., Gasparini, G.P., Herrmann, M., Lionello, P., Ludwig, W., Millot, C., Özsoy, E., Pisacane, G., Sánchez-Garrido, J.C., Sannino, G., Santoleri, R., Somot, S., Struglia, M., Stanev, E., Taupier-Letage, I., Tsimplis, M.N., Vargas-Yáñez, M., Zervakis, V., Zodiatis, G., 2012. Chapter 3: Circulation of the Mediterranean Sea and its variability. In: Lionello, P. (Ed.), The Climate of the Mediterranean Region, from the Past to the Future. Elsevier Insights, Amsterdam.

Schultz Tokos, K.L., Hinrichsen, H.H., Zenk, W., 1994. Merging and migration of two meddies. J. Phys. Oceanogr. 24 (10), 2129−2141.

Send, U., Font, J., Krahmann, G., Millot, C., Rhein, M., Tintoré, J., 1999. Recent advances in observing the physical oceanography of the western Mediterranean Sea. Prog. Oceanogr. 44 (1−3), 37−64.

Stegner, A., Le Vu, B., Dumas, F., Ghannami, M.A., Nicolle, A., Durand, C., Faugere, Y., 2021. Cyclone-anticyclone asymmetry of eddy detection on gridded altimetry product in the Mediterranean Sea. J. Geophys. Res. Oceans 126. https://doi.org/10.1029/2021JC017475.

Smith, J.A., 1993. Performance of a horizontally scanning Doppler sonar near shore. J. Atmos. Ocean. Technol. 10 (5), 752−763. https://doi.org/10.1175/1520-0426(1993)010<0752:POAHSD>2.0.CO;2.

Smith, J.A., Largier, J.L., 1995. Observations of nearshore circulation: rip currents. J. Geophys. Res. 100 (C6), 10967−10975.

Storto, A., Oddo, P., Cozzani, E., Ferreira Coelho, E., 2019. Introducing along-track error correlations for altimetry data in a regional ocean prediction system. J. Atmos. Ocean. Technol. 36, 1657−1674.

Tarry, D.R., Essink, S., Pascual, A., Ruiz, S., Poulain, P.M., Özgökmen, T., et al., 2021. Frontal convergence and vertical velocity measured by drifters in the Alboran Sea. J. Geophys. Res. Oceans 126 (4) e2020JC016614.

Thomas, L.N., Joyce, T.M., 2010. Subduction on the northern and southern flanks of the Gulf Stream. J. Phys. Oceanogr. 40 (2), 429−438.

Tintoré, J., Gomis, D., Alonso, S., Parrilla, G., 1991. Mesoscale dynamics and vertical motion in the Alborán Sea. J. Phys. Oceanogr. 21 (6), 811−823.

Tintoré, J., Pinardi, N., Álvarez-Fanjul, E., Aguiar, E., Álvarez-Berastegui, D., Bajo, M., Balbin, R., Bozzano, R., Nardelli, B.B., Cardin, V., Casas, B., Charcos-Llorens, M., Chiggiato, J., Clementi, E., Coppini, G., Coppola, L., Cossarini, G., Deidun, A., Deudero, S., D'Ortenzio, F., Drago, A., Drudi, M., El Serafy, G., Escudier, R., Farcy, P., Federico, I., Fernández, J.G., Ferrarin, C., Fossi, C., Frangoulis, C., Galgani, F., Gana, S., García Lafuente, J., Sotillo, M.G., Garreau, P., Gertman, I., Gómez-Pujol, L., Grandi, A., Hayes, D., Hernández-Lasheras, J., Herut, B., Heslop, E., Hilmi, K., Juza, M., Kallos, G., Korres, G., Lecci, R., Lazzari, P., Lorente, P., Liubartseva, S., Louanchi, F., Malacic, V., Mannarini, G., March, D., Marullo, S., Mauri, E., Meszaros, L., Mourre, B., Mortier, L., Muñoz-Mas, C., Novellino, A., Obaton, D., Orfila, A., Pascual, A., Pensieri, S., Pérez Gómez, B., Pérez Rubio, S., Perivoliotis, L., Petihakis, G., de la Villéon, L.P., Pistoia, J., Poulain, P.M., Pouliquen, S., Prieto, L., Raimbault, P., Reglero, P., Reyes, E., Rotllan, P., Ruiz, S., Ruiz, J., Ruiz, I., Ruiz-Orejón, L.F., Salihoglu, B., Salon, S., Sammartino, S., Sánchez Arcilla, A., Sannino, G., Sannino, G., Santoleri, R., Sardá, R., Schroeder, K., Simoncelli, S., Sofianos, S., Sylaios, G., Tanhua, T., Teruzzi, A., Testor, P., Tezcan, D., Torner, M., Trotta, F., Umgiesser, G., von Schuckmann, K., Verri, G., Vilibic, I., Yucel, M., Zavatarelli, M., Zodiatis, G., 2019. Challenges for sustained observing and Forecasting systems in the Mediterranean Sea. Front. Mar. Sci. 6. https://doi.org/10.3389/fmars.2019.00568.

Troupin, C., Pascual, A., Valladeau, G., Pujol, I., Lara, A., Heslop, E., Ruiz, S., Torner, M., Picot, N., Tintoré, J., 2015. Illustration of the emerging capabilities of SARAL/AltiKa in the coastal zone using a multi-platform approach. Adv. Space Res. 55, 51−59. https://doi.org/10.1016/j.asr.2014.09.011.

Vilibić, I., Mihanović, H., Janeković, I., Denamiel, C., Poulain, P.-M., Orlić, M., et al., 2018. Wintertime dynamics in the coastal northeastern Adriatic Sea: the NAdEx 2015 experiment. Ocean Sci. 14, 237−258.

Viúdez, Á., Dritschel, D.G., 2004. Optimal potential vorticity balance of geophysical flows. J. Fluid Mech. 521, 343−352.

Viúdez, A., Claret, M., 2009. Numerical simulations of submesoscale balanced vertical velocity forcing unsteady nutrient-phytoplankton-zooplankton distributions. J. Geophys. Res. 114, C04023. https://doi.org/10.1029/2008JC005172.

Viúdez, Á., Haney, R.L., Tintoré, J., 1996. Circulation in the Alboran See as determined by quasi-synoptic hydrographic observations. Part II: mesoscale ageostrophic motion diagnosed through density dynamical assimilation. J. Phys. Oceanogr. 26 (5), 706−724.

This page intentionally left blank

CHAPTER

Recent changes in the Mediterranean Sea

9

Jacopo Chiggiato[1], Vincenzo Artale[6], Xavier Durrieu de Madron[2], Katrin Schroeder[1], Isabelle Taupier-Letage[3], Dimitris Velaoras[4], Manuel Vargas-Yáñez[5]

[1]Consiglio Nazionale delle Ricerche-Istituto di Scienze Marine (CNR-ISMAR), Venezia, Italy; [2]Centre National de la Recherche Scientifique (CEFREM, CNRS-UPVD), Perpignan, France; [3]Institut Méditerranéen d'Océanologie (MIO), La Seyne, France; [4]Hellenic Centre for Marine Research (HCMR), Institute of Oceanography, Anavyssos, Greece; [5]Insituto Español de Oceanografía, IEO-CSIC Málaga, Spain; [6]Consiglio Nazionale delle Ricerche-Istituto di Scienze Marine (CNR-ISMAR), Roma, Italy

Learning Objectives

In this chapter, you will learn:

- What are the factors that lead to changes over time in Mediterranean water mass properties
- How the water masses of the Eastern Mediterranean have changed over time
- How the water masses of the Western Mediterranean have changed over time
- How these changes are transferred to the Atlantic Ocean

9.1 General concepts about Mediterranean water masses and their circulation

The following concepts have been already addressed in earlier chapters, and are only briefly recalled here for clarity and as an introduction to the main topic of this chapter. The upper branch of the Mediterranean Sea circulation is composed by the Atlantic Water (AW) that extends over the Western Mediterranean (WMED) and the Eastern Mediterranean (EMED). This layer is characterized by a rather complex pattern that is a superposition of interacting large and mesoscale features (more details on this have been given in Chapter 8), with each of them displaying their own scales of variability (see Schroeder, 2019). Very schematically, east of the Strait of Gibraltar the AW follows the African coast and once it has reached the Sardinian Channel, it divides in two branches, one entering the Tyrrhenian Sea, where it forms a basin-wide cyclonic boundary current, and one entering the EMED through the Sicily Channel. In the WMED, AW continues along the northern shore, while the

Oceanography of the Mediterranean Sea. https://doi.org/10.1016/B978-0-12-823692-5.00008-X

AW that has entered the EMED is transported further eastward. In the whole basin, one can identify the AW by a near-surface salinity minimum, which is, however, modified by mixing with surrounding water masses and air–sea interactions, along the path of the water mass. In the EMED, AW is transformed into salty and warm Intermediate Water (IW), called Levantine Intermediate Water (LIW) or Cretan Intermediate Water (CIW), depending on the specific formation location (Levantine or Cretan Sea, respectively), as a consequence of strong wind-induced evaporation and heat loss during winter. The layer of LIW/CIW can be identified in the whole basin by a subsurface local salinity maximum, associated to a relative temperature maximum (easily seen in TS diagrams, as explained in Chapter 4). The IW flows back toward the west, partly being diverted into the Adriatic, and partly crossing the Sicily Channel, and along this path it gradually dilutes with adjacent waters, becoming less salty, less warm, and less oxygenated (Schroeder et al., 2020). The IW flows cyclonically across the Tyrrhenian Sea eventually exiting through the Corsica Channel or the Sardinia Channel. The IW then reaches the northern WMED where it plays a crucial role in dense water formation (DWF, see Chapter 7). Finally, it outflows into the Atlantic Ocean, across the Strait of Gibraltar.

The deep water circulation cells of the EMED and the WMED are separated by the topography of the Sicily Channel (see Chapter 2) and mainly confined within these subbasins and are driven by DWF processes occurring in the Adriatic/Aegean Seas and in the north-WMED Sea where Eastern Mediterranean Deep Water (EMDW) and Western Mediterranean Deep Water (WMDW) are formed, respectively.

While Chapter 4 was mainly devoted to the description of the climatological properties of the Mediterranean water masses, the present chapter deals more specifically with how these properties and the circulation have changed over time. The changes observed in the EMED are described in Section 9.2, those in the WMED in Section 9.3. Current long-term trends and the role of climate change are discussed in Section 9.4, while the implications for the Mediterranean-Atlantic connected system are detailed in Section 9.5.

9.2 Changes observed in the Eastern Mediterranean water masses

9.2.1 Formation of dense waters and the Eastern Mediterranean Transient (EMT)

As already mentioned, the WMED and the EMED are separated by the Sicily Channel which blocks the direct advection of water masses at depths deeper than the IW masses. Thus, LIW/CIW are the only water masses, of Mediterranean origin, that is ubiquitous in both Mediterranean subbasins. LIW is formed in the north-western part of the Levantine Basin within the Rhodes cyclonic Gyre (RG), south of the Rhodes Island. Its formation area may extend up to the eastern Cretan straits. The

formation process takes place over the RG when winter buoyancy losses lead to direct convection over the isopycnal dome of the cyclonic center (Malanotte-Rizzoli et al., 2003; see also Chapter 7), or within mesoscale eddies in the RG center as well as over boundary currents along the coastline north of the RG (Kubin et al., 2019; Waldman et al., 2018). LIW formation rate varies between $\sim$0.6−1 Sv depending on the strength of the winter forcing (Nittis and Lascaratos, 1998). Sporadic deep water formation has also been reported in the RG area under strong atmospheric forcing, with a mixed layer depth $>$600 m (Kubin et al., 2019) or even $>$1000−2000 m in extreme cases (Gertman et al., 1994; Kontoyiannis et al., 1999; Sur et al., 1992). IW masses in the EMED are also formed inside the Cretan Sea (Cardin et al., 2003; Georgopoulos et al., 1989; Theocharis et al., 1993; Velaoras et al., 2013; Zodiatis, 1991), which Schlitzer et al. (1991) first identified as CIW. This water mass is usually slightly colder and denser compared to LIW (Theocharis et al., 1999a; Velaoras et al., 2019), thus settling at deeper depths. Nonetheless, there are reported cases in the literature where warmer CIW was found at shallower depths than LIW (Manca et al., 2006). Although it is generally considered that CIW is formed in lesser quantities compared to LIW, the intermediate layer in the Ionian Sea is a mixture of LIW and CIW and it is this mixture that penetrates into the Adriatic Sea providing salt to that basin (Manca et al., 2006; Millot, 2013).

As extensively described in Chapter 7, two DWF areas dominate the deep thermohaline cell of the EMED (Pollak, 1951; Robinson et al., 2001): the Adriatic Sea is considered as the main deep water source, while the Aegean Sea has been reported as a sporadic deep water contributor. Dense water production in the Adriatic occurs both on the northern shelf and by open-ocean convection in the south. According to Mantziafou and Lascaratos (2004), about 82% of the Adriatic Deep Water (AdDW) is formed by open ocean convection. The convection processes are strongly influenced by the local presence and characteristics of the saline IW mass. The reader is referred to Gačić et al. (2002), Manca et al. (2002), Mantziafou and Lascaratos (2004), Mihanović et al. (2013), Vilibić et al. (2020), Zore-Armanda (1963), and references therein, for further information on the Adriatic Sea functioning. The DWF rate in the south Adriatic Sea has been estimated to be $\sim$0.3 Sv (Artegiani et al., 1997; Mantziafou and Lascaratos, 2004). Following its formation, AdDW outflows through the western bottom layer of the Otranto Strait, while a compensatory inflow of IW enters the basin through the eastern part of the Strait (Astraldi et al., 1999; Kovačević et al., 1999; Orlić et al., 2007). Outflowing AdDW then plunges from the Otranto strait following a mostly cyclonic flow pattern to the abyssal plains of the Ionian Sea (Rubino and Hainbucher, 2007) and thereon continues toward the Levantine Basin. The mixture of newly produced AdDW and preexisting deep water masses accumulated in the deep EMED forms the EMDW. The most important DWF regions in the Aegean Sea are the shallow shelf areas either close to the shore or between the various islands. Also open-sea convection has been reported in both the central and the southwestern Aegean (Gertman et al., 2006; Nittis et al., 2003; Theocharis and Georgopoulos, 1993; Sayin et al., 2011; Theocharis et al., 1999b; Velaoras et al., 2014).

The belief that the only DWF site of the EMED was the Adriatic Sea and that the hydrological properties of the basin were stable, which persisted since the early 20th century when the first oceanographic cruise in the Mediterranean Sea took place (Nielsen, 1912), dissolved during the early 1990s when the event known as the Eastern Mediterranean Transient (EMT) occurred, i.e., the abrupt switch of the DWF source of the EMED from the Adriatic Sea to the Aegean Sea. The production of deep water in the Aegean Sea during the peak of the EMT event was so massive that an estimated deep water volume of $\sim 2.8 \times 10^{14}$ m^3 at an average rate of ~ 3 Sv was exported between 1992 and 1994 through the Cretan straits into the deep EMED. This amounted to about 75% of the total Aegean Sea outflow during the whole EMT period, while the remaining portion was exported during 2001–02 (Klein et al., 1999; Lascaratos et al., 1999; Roether et al., 1996, 2007; Theocharis et al., 1999a, 2002). The evolution of the event can be separated into three phases:

i. the EMT-onset phase (1987–1991), when the extreme winter of 1987 over the Aegean Sea (Lagouvardos et al., 1998) raised the deep water potential density (σ_θ) of both north and south Aegean basins and the consequent dense water outflow through the Cretan straits was compensated by the intrusion of high salinity surface/IWs from the Levantine Basin that increased the Aegean Sea salinity (Theocharis et al., 1999a); this acted as a salinity preconditioning that facilitated DWF during the next phase (Velaoras and Lascaratos, 2010);
ii. the EMT-peak phase (1992–95). The very cold winters of 1992 and 1993 increased even more the σ_θ of the deep Aegean water masses which inside the Cretan Sea exceeded 29.35 kg m^{-3} while at the same time the 29.20 kg m^{-3} isopycnal was uplifted to 30 m. During this period the Aegean deep water outflow toward the EMED was at its maximum (Theocharis et al., 1999a; Zervakis et al., 2000). During this phase, the convection depth in the RG area reached $\sim$2000 m (Gertman et al., 1994; Kontoyiannis et al., 1999; Sur et al., 1992);
iii. the EMT-relaxation phase lasted up to the early 2000s, during which there was no significant new DWF episodes; dense water continued to outflow through the Cretan straits, but with decreasing σ_θ values (Theocharis et al., 2002).

During the EMT-onset phase, the dense ($\sigma_\theta < 29.20$ kg m^{-3}) waters exported from the Aegean Sea were settling at depths of less than 2000 m south of Crete, while during the EMT-peak even denser ($\sigma_\theta > 29.20$ kg m^{-3}) waters flowed in large quantities through the Cretan straits and filled the abyssal reservoirs of the EMED. It was this massive outflow of deep Aegean waters that altered the characteristics of the EMDW. Without new formation episodes, after the early 2000s, the dense outflow did not reach the bottom of the EMED, but reached its equilibrium depth at $\sim$1500–2000 m (Theocharis et al., 2002; Velaoras et al., 2014). Fig. 9.1 shows a vertical salinity transect south of Crete before the EMT (left panel, 1987) and at the end of the EMT-peak phase (right panel, 1995). The warm and saline deep waters in 1995 are of Aegean origin (Aegean Deep Water, AeDW). After the event, the EMDW is a mixture of deep waters of Aegean origin and new AdDW produced

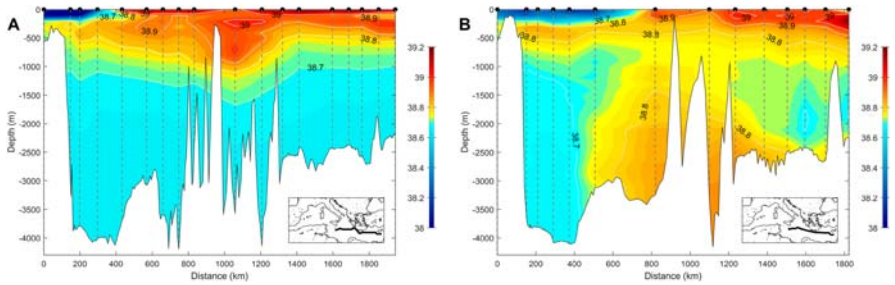

FIGURE 9.1

Salinity transect south of Crete (A) before the EMT, in 1987 and (B) after the EMT-peak phase, in 1995. Data are from the R/V METEOR cruises M5/6 (1987) and M31/1 (1995), and are the same data that were used by Roether et al. (1996).

in the Adriatic after the EMT and exported to the EMED (Roether et al., 2007; Theocharis et al., 2002). In general, since the EMT, the EMDW is now warmer and saltier than ever before.

Various causes and mechanisms acting in synergy, both external (atmospheric) and internal (oceanic) have been proposed as being responsible for the EMT (Josey, 2003; Klein et al., 1999; Lascaratos et al., 1999; Malanotte-Rizzoli et al., 1997, 1999; Theocharis et al., 1999a). The most commonly referenced are: (a) local atmospheric forcing including extremely cold winters and a synchronous increase in the evaporation—precipitation (E-P) water budget deficit, (b) alteration of circulation patterns leading to a blocking of the normal AW and LIW pathways in the EMED that increased the salt content of the Aegean Sea and Levantine Basin, as well as an internal redistribution of salt, and (c) a decrease of the brackish, low-density Black Sea Water (BSW) inflow into the North Aegean Sea through the Dardanelles during 1992 and 1993, which facilitated local DWF.

The changes caused by the EMT did radically modify the well-established scientific perception regarding the thermohaline functioning of the EMED. Following the event, the dominant role of the Aegean Sea in triggering the formation and export of deep water masses to the EMED has been fully acknowledged. The EMT did not exclusively alter the thermohaline status of the EMED, but also affected the hydrology of the thermohaline conveyor belt of the whole Mediterranean Sea by altering the properties of the IW outflow toward the WMED through the Sicily Channel. It has been suggested (Herrmann et al., 2010; Schroeder et al., 2006) that following the EMT the export of warmer and more saline LIW/CIW toward the WMED has been a major contributing factor for the onset of an abrupt change that occurred there in 2005 (the Western Mediterranean Transition, or WMT), that will be discussed in Section 9.3. This warming and salinification of LIW/CIW, which has been attributed partly to the EMT (Schroeder et al., 2006; Gasparini et al., 2005) is well evident in Fig. 9.2, where the time series of potential temperature (θ) and salinity (S) from a mooring at 400 m in the Sicily Channel between 1993 and 2020 is shown.

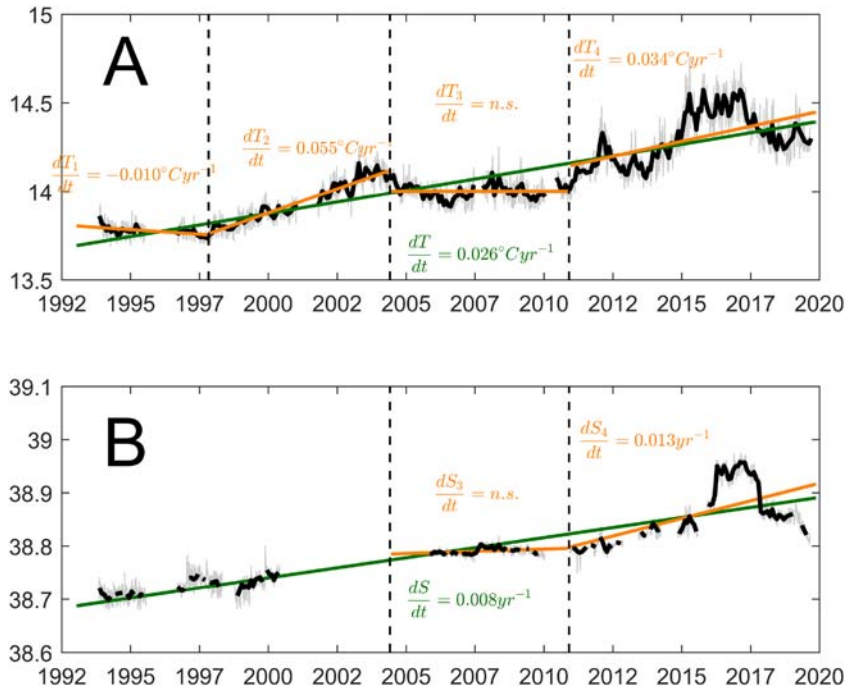

FIGURE 9.2

Timeseries of potential temperature (A) and salinity (B) from a mooring at 400 m in the Sicily Channel (gray data). Monthly mean time series is shown in black. The green line represents the long-term trend line while short-term trends are shown in orange.

From von Schuckmann, K., Le Traon, P.-Y., Smith, N., Pascual, A., Djavidnia, S., Gattuso, J.-P., Grégoire, M. (Eds.). 2021. Copernicus Marine Service Ocean State Report, Issue 5, Journal of Operational Oceanography, vol. 14, Suppl. 1, s1–s185; https://doi.org/10.1080/1755876X.2021.1946240. updated from Schroeder, K., Chiggiato, J., Josey, S.A., Borghini, M., Aracri, S., Sparnocchia, S., 2017. Rapid response to climate change in a marginal sea. Sci. Rep. 7, 4065. https://doi.org/10.1038/s41598-017-04455-5.

9.2.2 Decadal oscillations of the upper thermohaline circulation in the EMED

As early as the 1950s, evidences of strong decadal variability in the salinity of the south Adriatic Sea were observed (Buljan, 1953) and attributed to the variable intensity of the water inflow into it, the so-called "Adriatic ingression." This decadal variability, either linked to the intensity of the inflow or the changing properties of the inflowing water mass, is necessarily connected to some sort of variability of the northern Ionian Sea circulation. Indeed, the vorticity of the upper thermohaline circulation in the northern Ionian Sea has been depicted in the past as being either cyclonic (Ovchinikov, 1966) or anticyclonic (Malanotte-Rizzoli et al., 1999).

The studies of Malanotte-Rizzoli et al. (1997, 1999) pointed out that during the EMT-onset phase (1987–91) the north-eastward branch of the AW in the western part of the EMED followed a large anticyclonic meander in the Ionian Sea interior, replacing the cyclonic circulation pattern observed in 1987, the latter being considered as the typical upper thermohaline circulation mode. This anticyclonic behavior resulted in the freshening of the upper layers of the northern Ionian Sea while at the same time IW masses recirculated in the Levantine Basin, further increasing their salinity and consequently the salt content of the Levantine and Aegean Seas. By studying in situ data collected during and after the EMT, Manca et al. (2003) reached to the same conclusion as the previous authors, i.e., that the upper thermohaline Ionian Sea circulation during the whole EMT period (1987–95) favored the advection of AW toward the northern Ionian and the Adriatic Seas. Additionally, Theocharis et al. (2002) and Manca et al. (2003) observed that in 1999, during the EMT-relaxation phase, the typical cyclonic upper thermohaline circulation mode was re-established and hence the AW pathway was mainly directed toward the Levantine Basin. The same authors suggested that the Adriatic and Aegean Seas as potential sources of DWF are influenced by these changes of the upper thermohaline circulation in the EMED, which is able to regulate, intensify or weaken, the transport of AW and LIW masses toward each basin.

Using numerical simulations, Pisacane et al. (2006) suggested that the EMED presents self-sustained variability on a decadal time scale. Their results showed that there exist internal oscillations in the EMED that weaken or strengthen the zonal overturning circulation cell as a result of the alternation of DWF between the Adriatic and the Aegean Sea sources. Further studies using in situ data (Borzelli et al., 2009; Poulain et al., 2012) have confirmed that in 1997 and again in 2006 the Ionian Sea upper circulation reversed, suggesting that the upper layer circulation pattern changes in the Ionian Sea are a recurrent phenomenon on an quasi-decadal time scale. Gačić et al. (2010, 2011) proposed a new concept for the observed circulation oscillations of the Ionian Sea, based on the assumption that the oscillations are driven by internal dynamics. They postulated a feedback mechanism, which they called the Adriatic—Ionian Bimodal Oscillating System (BiOS), between the observed northern Ionian upper layer circulation inversions and the water mass redistributions in the basin related to variations of the thermohaline properties of waters formed in the southern Adriatic Sea. According to these authors, the north Ionian circulation reversals constitute inversions of the Northern Ionian Gyre (NIG). During the cyclonic NIG mode, AdDW of high density spreads along the western Ionian Sea continental slope, thus lowering the sea level along its path. The induced surface pressure gradient results in a surface geostrophic flow toward the north, gradually reversing the surface flow from cyclonic to anticyclonic. This enhances the import of low salinity AW into the Adriatic Sea, resulting in the decrease of AdDW density. Due to this density reduction, the sea level along the AdDW path in the western Ionian Sea rises locally, producing a surface pressure gradient and a southward geostrophic flow eventually reestablishing the cyclonic NIG mode. The proposed BiOS theory can thus explain the so called “Adriatic

ingressions" and the variability of the AW path inside the Ionian basin. According to Gačić et al. (2011) the NIG mode can also affect the hydrology of the Levantine and Aegean Seas. The cyclonic NIG mode enhances advection of saline masses toward the Adriatic, thus favoring local winter convection, while at the same time the Aegean/Levantine Seas gains buoyancy due to enhanced low salinity AW inflow toward them. On the contrary, the anticyclonic NIG mode favors winter convection in the Aegean/Levantine Seas, as in this case the more intense AW flow into the Adriatic Sea makes the latter more buoyant.

In an alternative interpretation of the observed quasi-decadal upper thermohaline circulation variability of the EMED, Theocharis et al. (2014) used both in situ data and a numerical simulation for a 40-year period (1960–2000) in the EMED to show the existence of a rather permanent and almost decadal anti-correlated oscillation between the Adriatic and the Aegean Seas, acting as competitive DWF sources. They proposed that the competitive functioning of these two dense water sources is controlled by an internal oceanic process they called the "thermohaline pump" mechanism. The production and consequent outflow of dense water from these marginal seas during their active DWF phases is compensated by inflow from the upper layers. This convection-advection scheme activates the pump mechanism which then disturbs the upper thermohaline cell of the whole EMED, modifying the hydrological structure which alternatively preconditions each DWF source. In particular, the Adriatic Sea DWF activation causes the gradual compensatory deflection of the AW pathway toward the northern Ionian Sea, limiting at the same time its eastward flow, thus resulting in the recirculation of the LIW/CIW in the Levantine Sea and the consequent increase of the Aegean/Levantine upper thermocline salinities. This acts as a preconditioning factor that eventually activates the Aegean Sea DWF process. The following DWF and export from the Aegean Sea reestablishes the eastward pathway of the AW, while the westward flow of LIW/CIW is restored, again favoring the Adriatic DWF capacity. According to Theocharis et al. (2014), the reversals of the northern Ionian upper circulation are not related to the NIG but reflect the disturbance of the upper thermohaline cell in the Ionian Sea caused by this advection-convection "pumping" mechanism. Notably, Pisacane et al. (2006) in their work on the internal oscillations in the EMED, related the EMT to an advection-convection feedback mechanism, similar to the later work of Theocharis et al. (2014).

Other hypotheses, supported by numerical simulation studies (Nagy et al., 2019; Pinardi et al., 2015), highlight the wind-driven nature of the mechanisms underlying the observed northern Ionian circulation inversions, or the excursion of the Atlantic-Ionian Stream (AIS) from the middle to the northern parts of the basin. According to Nagy et al. (2019), the wind influences the reversals, with a positive wind stress curl sign being responsible for cyclonic motion, and a negative one being responsible for anticyclonic motion. According to Pinardi et al. (2015), prior to 1997, the AIS was occupying the northern Ionian Sea, producing an overall anticyclonic circulation structure, while after 1997 the AIS remains in the middle of the Ionian basin and a cyclonic gyre develops at its the northern limits. These authors also showed that

the Ionian reversal mechanism is evident in the streamfunction, thus giving further evidence of the wind-driven nature of the mechanisms underlying the northern Ionian reversal.

A schematic representation of the two upper thermohaline circulation modes is shown in Fig. 9.3. The upper panel depicts mode 1, with the outflowing dense masses from the Adriatic Sea following local DWF, causing the compensatory deflection of the AW pathway (cyan) toward the northern Ionian and the reduced eastward flow which then results in the recirculation of the LIW/CIW (red) in the Levantine, local salinity preconditioning and finally DWF and outflow (blue) in the Aegean Sea. The lower panel depicts mode 2, with the outflowing dense masses from the Aegean Sea causing the re-establishment of the AW eastward flow (cyan), which results in the restoration of the LIW/CIW westward return flow (red), local salinity preconditioning and finally DWF and outflow (blue) in the Adriatic Sea. The yellow dotted circles show the respective NIG reversals in both modes.

Further numerical studies (Amitai et al., 2017) have suggested that the EMED overturning circulation is subject to decadal variability and abrupt transients showing multiple equilibria under the same atmospheric conditions. Two steady states have been recognized: one of an active DWF and export from the Adriatic Sea and a second, passive one, when the Adriatic exports water masses that are

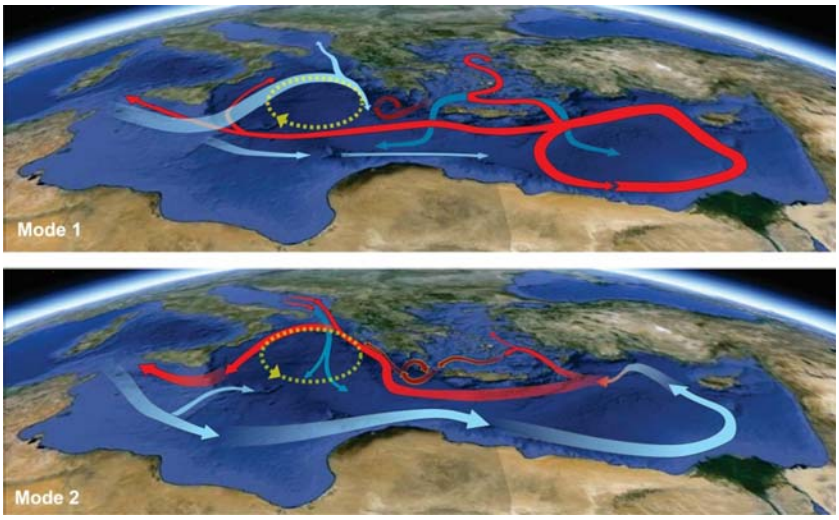

FIGURE 9.3

Schematic representation of the two upper thermohaline circulation modes. Cyan color shows AW pathway, red color shows LIW/CIW pathway, blue color shows dense water outflow and yellow circles show the different NIG modes.

From Velaoras, D., Krokos, G., Nittis, K., Theocharis, A., 2014. Dense intermediate water outflow from the Cretan Sea: a salinity driven, recurrent phenomenon, connected to thermohaline circulation changes. J. Geophys. Res. Oceans, 119 (8), 4797–4820. https://doi.org/10.1002/2014JC009937.

less dense than those it imports. The same authors demonstrated a strong correlation between the Adriatic and Aegean Seas functioning, where changes over each basin induce variations to the other. The link of this interaction is established by horizontal advection, where warm and saline water of Aegean origin can either enter the Adriatic Sea, activating DWF in that basin by increasing its salinity, or the Aegean water may limit its presence solely in the deeper layers of the Ionian and Levantine Seas thus switching off the DWF in the Adriatic Sea. These results are close to those presented by Pisacane et al. (2006) and Theocharis et al. (2014). Reale et al. (2016) used numerical simulations in order to evaluate the relative importance of various forcings on the vorticity and energy budget of the Ionian Sea. They concluded that the wind forcing can strengthen or weaken the circulation in the Ionian Sea but it is not able to reverse its polarity. The observed reversals in the upper layer circulation of the Ionian Sea can only be explained if the role of the Aegean Sea is taken into consideration in the presence of an active boundary between the Aegean - Levantine and Ionian Seas. Moreover, Reale et al. (2017) showed through numerical simulations that the covariant behavior between the Ionian and Aegean Seas is linked to an interactive zonal exchange of water masses with different salinity characteristics. They concluded that the observed circulation reversals in the Ionian Sea reflect the existence of multiple equilibrium states in the EMED thermohaline circulation and that a thorough evaluation of the observed variability demands the recognition of a fully coupled Adriatic-Ionian-Aegean system as suggested by Theocharis et al. (2014).

The variability of the EMED upper thermohaline circulation has been well documented during the last decade by a number of papers mostly focusing on sea surface height/dynamic topography observations. The reader is referred to Bessières et al. (2013), Borzelli et al. (2009), Gačić et al. (2010, 2011), Menna et al. (2019), Poulain et al. (2012), von Schuckmann et al. (2019), among others.

The cyclonic upper circulation in the Ionian Sea observed in 1987 changed to anticyclonic in 1991, a change that directly impacted the EMT, and thereon further reversals have been observed in 1997 (cyclonic), 2006 (anticyclonic), 2011 (cyclonic) while recently (2017) a new anticyclonic reversal was observed. Fig. 9.4 shows the time series of surface current vorticity in the northern Ionian Sea between 1993 and 2018. The disturbance observed in 2012−13 is attributed by Gačić et al. (2014) to the extreme winter 2012 cold spell in the Adriatic Sea and the consequent formation of very dense AdDW (Mihanović et al., 2013; Chiggiato et al., 2016a; 2016b), which clearly showed that the periodicity of the circulation variability can be disturbed by strong atmospheric forcing events.

9.2.3 Post-EMT status in the EMED

An abrupt event like the EMT drastically changed the thermohaline properties of the EMED. Since then, the hydrological status of the basin has been slowly relaxing toward pre-EMT conditions. However data show that until recently the EMED is still far from the pre-EMT status (Cardin et al., 2015; Velaoras et al., 2019). The Aegean

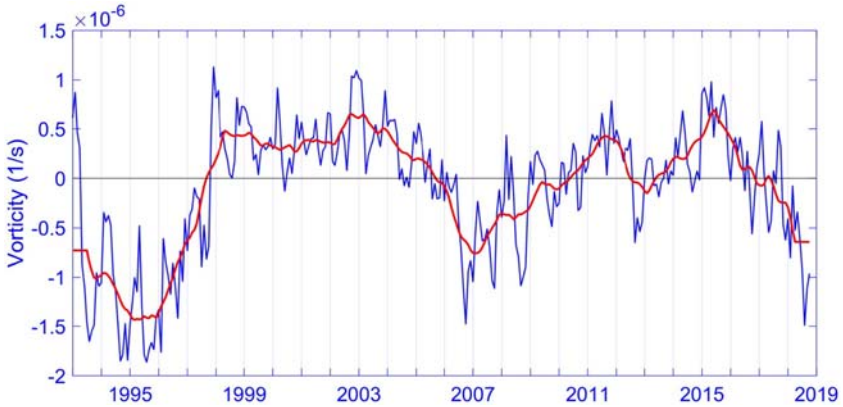

FIGURE 9.4

Time Series of surface current vorticity in the northern Ionian Sea between 1993 and 2018. Red line shows the low-pass filtered time series. Positive values denote cyclonic and negative values anticyclonic vorticity.

From von Schuckmann et al. (2019).

Sea stopped exporting deep waters by the late 1990s (Theocharis et al., 2002) and the Adriatic Sea gradually regained its role as the main DWF site since the early 2000s (Manca et al., 2003, 2006). However, during the anticyclonic circulation phase between 2006 and 2011, the salinity values in the Aegean Sea increased again as expected. Moreover, Krokos et al. (2014) and Velaoras et al. (2014) showed that a salinity preconditioning is necessary for DWF, as described in Theocharis et al. (2014), and reported that, at that period, the Cretan Sea exported IW masses denser that typical CIW. This water settled below the LIW layers and as deep as ∼1000 m.

The idea that the observed circulation oscillations are mostly driven by internal oceanic processes has been generally accepted. However, the role of the atmospheric forcing must not be neglected, as the winter of 2012 with the major DFW formation event in the Adriatic Sea has undoubtedly. The EMT event was a result of an internal mode that provoked salinity preconditioning in the Aegean/Levantine Seas as well as of extreme atmospheric forcing. In case both factors act concomitantly, a new EMT—like event may be possible again in the future.

The salinity evolution in the south Aegean (Cretan) Sea can be seen in Fig. 9.5, a Hovmöller diagram of in situ salinity between 1986 and 2020 in the central-eastern Cretan Sea from 100 to 2000 dbar. The salinification of the whole water column can be seen in the early 1990s due to the EMT event, followed by the intrusion of less saline Transitional Mediterranean Water (TMW, see Theocharis et al., 1999a). This intrusion gradually reached a core depth of ∼700 dbar as densities relaxed inside the basin after the event. Most interestingly, two phases of salinification can be observed after the early 2000s: (a) between 2008 and 2011 and (b) after 2017. During these phases the salinity increase extended down to depths below the

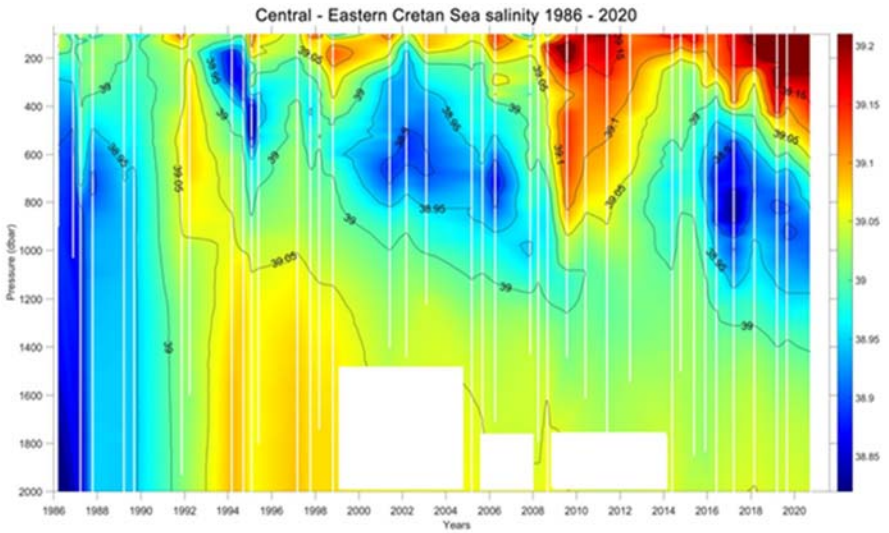

FIGURE 9.5

Hovmöller diagram of salinity evolution inside the south Aegean (Cretan) Sea between 1986 and 2020. Data have been truncated between the 100–2000 dbar layer. White lines show in-situ profiles.

Updated from Velaoras, D., Krokos, G., Theocharis, A., 2015. Recurrent intrusions of transitional waters of Eastern Mediterranean origin in the Cretan Sea as a tracer of Aegean Sea dense water formation events. Prog. Oceanogr. 135, 113–124. https://doi.org/10.1016/j.pocean.2015.04.010.

intermediate layer, and they coincided with the respective periods of an anticyclonic NIG, when the eastern part of the EMED receives less AW, with a consequent salinity increase. As already mentioned, the first period led to the formation and export of dense CIW from the Aegean Sea. Concerning the period which begun after 2017, it is not yet clear which implications this might have had. Finally, it can be observed that during these two periods the salinity in the first hundreds of meters inside the basin was much higher ($\Delta S > 0.15$) than even during the peak-EMT phase. The reason why there was not a similar EMT event may lay in the fact that the atmospheric forcing was not strong enough during that period (Velaoras et al., 2014).

As already mentioned, after the EMT (i.e., after the early 2000s) the Adriatic Sea was reactivated as DWF site. However, the new AdDW that was found in the abyssal Ionia Sea layers between 2003 and 2007 was warmer and saltier than in the past (Bensi et al., 2013; Rubino and Hainbucher, 2007). The extreme winter in 2012 (Mihanović et al., 2013; Chiggiato et al., 2016a; 2016b) led the Adriatic to export very dense water toward the Ionian Sea, causing an abrupt but temporal reversion of the Ionian circulation, from cyclonic to anticyclonic one (Gačić et al., 2014). In general, the situation of the Ionian abyssal layer has changed after the EMT, since

the intrusion of AeDW during the event has increased both temperature and salinity of this part of the water column, from typical pre-EMT properties of 13.26°C and 38.66 to ~13.42°C and ~38.73, respectively for θ and S (Artale et al., 2018). Indeed, the post-EMT EMDW is a mixture of old AeDW and new AdDW. As new AdDW is advected toward the Levantine Basin, a west-to-east gradient of hydrological properties develops in the bottom layers, with an eastward increase in θ and S, associated with a decrease in dissolved oxygen (Cardin et al., 2015; Velaoras et al., 2019). The first signal of AdDW after the EMT period was identified south of Cyprus in 2012–13 (Gertman et al., 2016) and close the Levantine continental slope in 2018 (Ozer et al., 2020). These latter authors also report the warming and salinification of the 600–1200 dbar layer in the south-eastern Levantine Basin between 2012 and 2017, signifying the general salinification trend at shallow and intermediate levels of the region and possibly the effect of CIW advection to the area.

Although the observed circulation oscillations may be the most important aspect in our recent understanding of the EMED functioning, the gradual changes and trends in water mass properties are also strongly affected by climatic change. This will be addressed in Section 9.4 in more detail.

9.3 Changes observed in the Western Mediterranean water masses

9.3.1 The twentieth century: gradual warming and salinification

Studies since the first half of the 20th century and up to the late-1980s–early 1990s describing the "steady state" of the Mediterranean Sea, show θ and S values that are clearly lower than those observed at present. During the early stages of Mediterranean oceanography, there were no monitoring programs devoted to the systematic and periodic sampling of the water mass properties. Nevertheless, as the number of oceanographic campaigns and the amount of data increased, a comparison of the existent information became possible. Lacombe et al. (1985) reviewed the works by Nielsen (1912) and Sverdrup (1942), and data from several campaigns carried out from the early 1950s to the late 1970s. They realized that θ and S of the deep waters in the WMED had increased from 12.66°C and 38.38 to 12.71°C and 38.41, respectively. The study by Béthoux et al. (1990) was the first to invoke global warming to explain the warming and salinification of the WMDW (which these authors estimated as 0.004°C yr^{-1} and 0.0008 yr^{-1}). Leaman and Schott (1991) compared the properties of WMDW during the periods 1969–77 and 1977–89 and estimated an increase of θ and S at rates of 0.0027°C yr^{-1} and 0.0019 yr^{-1}. Both Béthoux et al. (1990) and Leaman and Schott (1991) found that the changes in θ and S compensated each other, and that the σ_θ remained constant at a value around 29.11 kg m^{-3}, even though they disagreed about the causes. The latter authors considered that the warming of the deep waters was caused by the S increase of LIW, as saltier IWs would reach the deep water density at higher temperatures.

This hypothesis was also supported by Rohling and Bryden (1992), who analyzed the θ and S of the WMDW from 1909 to 1989 and calculated positive trends for both variables. Such trends accelerated from 1955 with a value of 0.0021°C yr^{-1} for θ. They also analyzed the θ and S at the salinity maximum corresponding to the LIW, and found that only S experienced a positive trend that once again was accelerated after 1955 (0.0025 yr^{-1}). The salinification of LIW would be linked to the damming of the River Nile and those rivers that drain into the Black Sea, as also reported in the previous subchapter. The warming and salinification of WMDW were also reported by Krahmann and Schott (1998) for the period 1960–95 (0.0016 ± 0.0005°C yr^{-1}, 0.0008 ± 0.0001 yr^{-1}). Also these authors attributed the changes to the S increase in the water masses contributing to the deep water formation. In opposition to Rohling and Bryden (1992), they showed no changes for the LIW salinity. They attributed the warming and salinification of WMDW to the S increase in AW, linked to the damming of Ebro River, and the precipitation reduction in the WMED associated with a persistent positive phase of the North Atlantic Oscillation (NAO) index from 1960 to 1994. According to these authors, the θ of the AW did not change.

The preceding paragraph shows that many different works are in agreement about the existence of positive trends for the θ and S of the WMDW during the twentieth century, with an acceleration of such trends during its second half. Nevertheless, there are many contradictions concerning the changes experienced by the upper and intermediate layers of the WMED. Béthoux et al. (1998) and Sparnocchia et al. (1994) also supported the warming and salinification of the LIW, whereas Rixen et al. (2005) only found an increase of S, but not of θ. Painter and Tsimplis (2003) studied the evolution of the θ and S at the same geographical area analyzed by Rohling and Bryden (1992), and concluded that the positive S trends estimated by those authors were not consistent. According to Rixen et al. (2005, their Fig. 1), the θ of the upper 150 m of the water column increased in the WMED during the second half of the twentieth century, but with two distinctive periods. A first one when the upper 150 m of the WMED cooled until the mid-1980s, and a second period of warming until the end of the century. Vargas-Yáñez et al. (2009) concluded that the discrepancies between different works could be caused by the data scarcity, which makes trend estimations very sensitive to data processing or interpolation methods (Vargas-Yáñez et al., 2012), the use of bathythermographs (Vargas-Yáñez et al., 2010a), or slight variations in the time period considered. Similar results were obtained by Llasses et al. (2015) and Jordá and Gomis (2013), who found that the estimations of long term trends depend on the data base used. Finally, Vargas-Yañez et al. (2010b) accepted as robust results the warming and salinification of the WMDW (0.002 ± 0.001°C yr^{-1}, 0.0009 ± 0.0001 yr^{-1}) and the S increase of LIW (0.001 ± 0.0004 yr^{-1}).

The discrepancies concerning the warming of the AW vanish when satellite data are considered. All the works reviewed show positive and intense warming trends (~ 0.02°C yr^{-1}), but it should be noted that the period analyzed is different from those dealing with in situ data, as satellite sea surface temperature (SST) time series

started between the late 1970s and the mid-1980s (Nykjaer, 2009; Skliris et al., 2012; Skliris and Lascaratos, 2004; López-García, 2015, Pisano et al., 2020). These long-term trends, also beyond the twentieth century, will be addressed more in detail in Section 9.4.

9.3.2 Changes during the 21st century: the Western Mediterranean Transition (WMT)

The changes observed in the properties of the WMED water masses during the twentieth century took place in a more or less gradual manner. Both θ and S have increased, but, except for some specific episodes, the shape of the θ-S diagram remained invariant. This fact indicates that the same water masses have been present in the WMED during the last century, only with slightly different θ and S values. The classical shape of the θ-S diagram in the WMED during the 20th century shows an absolute salinity maximum and a relative temperature maximum located between 200 and 600 m, associated with the LIW. The σ_θ of LIW ranges between 29.05 and 29.1 kg m^{-3}. Below this water mass, the water column is weakly stratified and temperature and salinity smoothly decrease until a relative minimum associated with the WMDW (core deeper than 2000 m), with σ_θ slightly higher than 29.1 kg m^{-3} (see Fig. 9.6).

The situation has changed since the winter of 2004/2005, although the alterations described in the following are likely the result of processes that initiated years before. Oceanographic surveys in the Balearic Sea, the Provençal and the Algerian Basins, revealed the presence of a "new" WMDW (nWMDW, hereafter), much warmer, saltier, and denser (>29.12 kg m^{-3}) than the "old" WMDW (oWMDW, hereafter, after López-Jurado et al., 2005; Schroeder et al., 2006; Smith et al., 2008). The nWMDW, formed by open sea convection, displaced the oWMDW

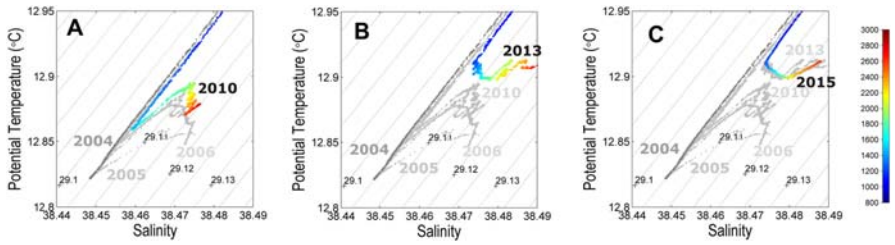

FIGURE 9.6

θ-S diagrams from 800 m depth to the bottom (2800 m), in a repeated station in the Algerian Basin (37.98°N, 4.65°E) (pressure is color coded) in (A) 2010 (light gray points refer to preceding years, i.e., 2005–09, dark gray points refer to 2004, the pre-WMT situation), (B) 2013 (light gray 2005–10, dark gray 2004) and (C) 2015 (light gray 2005–14, dark gray 2004).

Redrawn from Schroeder, K., Chiggiato, J., Bryden, H.L., Borghini, M., Ismail, S.B., 2016. Abrupt climate shift in the western Mediterranean Sea. Sci. Rep. 6, 23009. https://doi.org/10.1038/srep23009.

upwards, initially causing the freshening and cooling of intermediate layers. Very close to the bottom, just below this new warmer and saltier deep water, the new θ-S diagram revealed a cooler, fresher, and much denser water mass (>29.15 kg m^{-3}, see Fig. 9.6), which was the result of dense water formation on the continental shelf of the Gulf of Lion and the northern Catalan Sea, that cascaded to the bottom along the submarine canyons present in this region (Canals et al., 2006; Font et al., 2007, see also Box 9.1). These changes altered the heat and salt content of the whole water column. Schroeder et al. (2006) analyzed data from a campaign during May 2005 in the Central Mediterranean, and showed the presence of the nWMDW with θ, S and σ_θ of 12.9°C, 38.48 and 29.12 kg m^{-3}, respectively. They found a thin layer of cascading dense shelf waters below, with values around 12.76°C and 38.46. They argued that this abrupt warming and salting was the result of a heat and salt transfer from the intermediate layers. This is evidenced by the fact that while θ and S were found to increase in the layer 1400−2000 m, at the same time they decreased in the layer 200−1200 m (Schroeder et al., 2008). The changes in water mass properties and vertical structure, observed during this winter and in the following years, are the most dramatic ones currently reported in the literature of the WMED. They are known as the WMT. Since then, this anomaly started to spread from its formation region into the WMED interior, toward Gibraltar and the Tyrrhenian Sea, filling up the whole basin.

Schroeder et al. (2010, 2016) considered that the severe meteorological conditions during winter 2004/2005 could have been the cause of the anomalously large volume of WMDW that was formed. Nevertheless, just larger heat losses to the atmosphere would have produced cooler deep waters, instead of warmer and saltier waters. Therefore, at the origin of the WMT there must also be the accumulation of heat and salt in the intermediate layers during the previous years. This accumulation would be related to the arrival of the EMT signal into the WMED, which had already been evidenced by Astraldi et al. (2002) and Gasparini et al. (2005) by means of the analysis of θ-S time series in the Sicily Channel and the southern Tyrrhenian Sea. According to Schroeder et al. (2006) the influence of the EMT at the changes experienced by the WMED had two phases. During the first one (1992−2001), old EMDW was uplifted as AeDW filled the bottom layers of the EMED. This allowed the upper part of EMDW (transitional or tEMDW) to overflow through the Sicily Channel. A second phase (after 2001) was characterized by the arrival through the Sicily Channel of warmer and saltier IWs with a higher contribution by CIW.

Another hypothesis about the causes that triggered the WMT was presented by Herrmann et al. (2010). These authors conducted a series of numerical simulations under different atmospheric forcings and using different initial conditions and concluded that the origin of the WMT is certainly the accumulation of heat and salt in the intermediate layers of the WMED during the years preceding winter 2004/2005. However, this accumulation would have been caused by the quasi-absence of deep-water formation during the 1990s decade (Béthoux et al., 2002). The EMT would also have influenced this process, as it would have been responsible

for the large volume of deep water formed during this winter. These processes act on different temporal scales, with local air-sea interactions remaining the main driver (though modulated by larger scale atmospheric modes) for the Mediterranean circulation. However, the occurrence of extreme or abrupt events like the WMT would depend on the contemporary presence of the appropriate oceanic conditions (preconditioning), a consequence of processes acting on the interannual/interdecadal scale. It should be noted that this "nWMDW" is not unprecedented, as similar deep and bottom waters had already been detected by Lacombe et al. (1985) during the winters 1972/73 and 1981/82, and by Béthoux et al. (2002) in 1988/89 and 1999 (see Salat et al., 2009 for a complete review). Nevertheless, those episodes do not seem to have been as intense and persistent as the WMT.

After the major event in winter 2004/2005, also in winter 2005/2006 large volumes of anomalous WMDW formed, while the following winters 2006/2007 and 2007/2008 were relatively mild and no deep convection occurred. Dense waters started to be produced again in winters 2008/2009, 2009/2010, 2010/2011, 2011/2012 and 2018/2019. In particular, during winter 2011/2012, Europe and the Mediterranean Sea experienced an extreme cold spell that triggered the production of very dense water (Durrieu de Madron et al., 2013). Each winter a new warmer, saltier, and denser deep water is formed, leading to a stepwise increase of heat and salt contents in the deep layer and the deep θ-S diagrams became increasingly complex (Fig. 9.6). The new deep waters do exhibit such different properties than the old one, that they can straightforwardly be identified in deep CTD casts: a natural tracer in the form of warmer, saltier and denser deep water. Over time, the signature became visible in wider and wider regions, allowing a time scale estimate of the spreading. Schroeder et al. (2017) have followed the propagation of the anomaly throughout the WMED providing a chronological description of the uplifting of old deep water, replaced near the bottom by the new ones (Fig. 9.7): a near-bottom salty and warm vein intrudes in 2005 and this layer have become 600 m thick in 2006, almost 1000 m thick in 2008, more than 1200 m in 2010, 1400 m in 2013 and $>$ 1500 m in 2015. A more recent MedSHIP (Schroeder et al., 2015) cruise in 2018 (Hainbucher, 2020) along the east-west transect MED01 (a GO-SHIP line) has shown that the upper interface of nWMDW reached the lower LIW density horizon, thus nWMDW and oWMDW are no longer distinguishable, with the latter that flushed out through Gibraltar or mixed with the former.

The signature of the deep warm and salty anomaly spread both eastward (toward the Tyrrhenian Sea) and westward (toward Gibraltar). To the east, the Sardinia Channel (sill at 1930 m) allows exchanges of the upper part of the deep waters between the Algerian Basin and the Tyrrhenian Sea. Until 2005 only the "classical" oWMDW was found at the sill, while the denser nWMDW started to cross it since then, with the interface between old and new deep water becoming about 200 m shallower here between 2006 and 2009. By 2014, the whole layer below the LIW ($>$500 m, i.e., the halocline/thermocline and the deep water) has densified to values of 29.11−29.12 kg m^{-3}, becoming denser than the "classical" resident water found at $<$3000 m in the Tyrrhenian Sea (Zodiatis and Gasparini, 1996). In 2012−15,

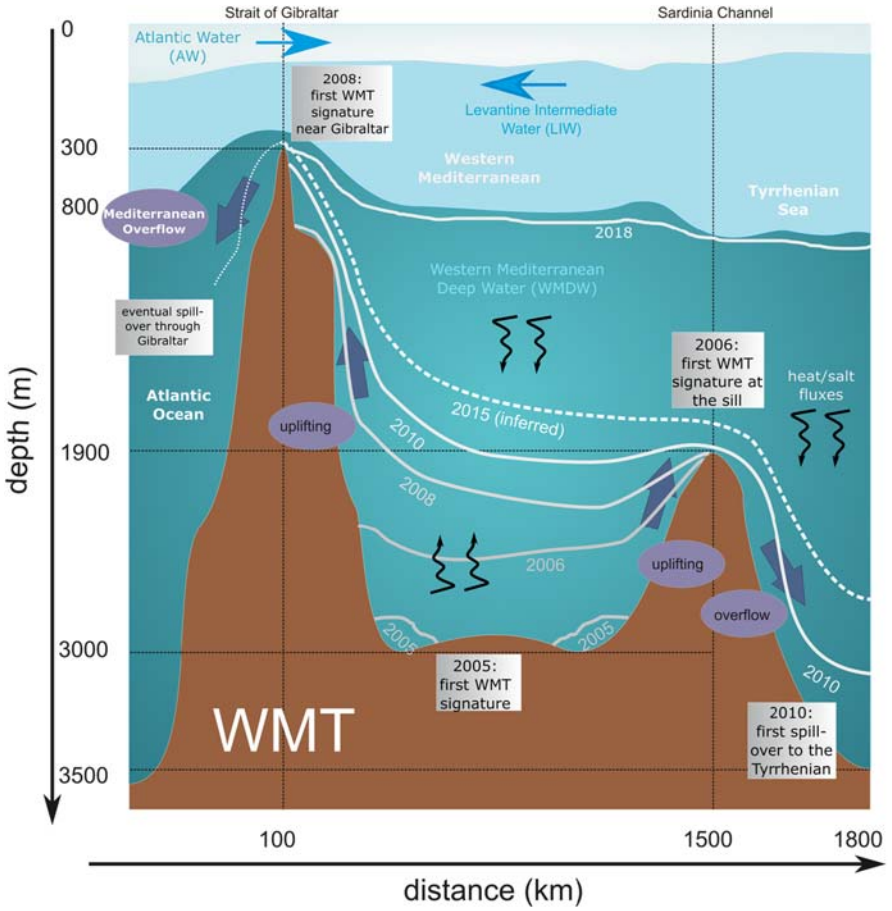

FIGURE 9.7

Temporal and geographical evolution of the processes associated with the WMT. The lines denoted by the years indicate the upper interface of the new WMDW. For 2015 a mean uplifting of this interface has been inferred from single stations (see Schroeder et al., 2016 for details), rather than from a whole transect.

Modified and updated from Schroeder, K., Chiggiato, J., Bryden, H.L., Borghini, M., Ismail, S.B., 2016. Abrupt climate shift in the western Mediterranean Sea. Sci. Rep. 6, 23009. https://doi.org/10.1038/srep23009.

the signature of the WMT in the Tyrrhenian Sea (typical hooks in the θ-S diagram) was clear in almost all stations in the interior (Schroeder et al., 2017). The nWMDW crossing the sill was dense enough to cascade down to the bottom of the Tyrrhenian Sea, and data collected in 2018 (Hainbucher, 2020) evidenced that also here the upper interface of nWMDW reached the lower LIW density horizon (Fig. 9.7).

On the western side of the WMED, early experiments in the Strait of Gibraltar (Stommel et al., 1973) have demonstrated the existence of a mechanism (called

Box 9.1 A closer look at the Gulf of Lion

Since 2007, extensive national observation systems have been in place in the north-WMED, based on multiple platforms (instrumented mooring lines, submarine glider endurance lines, profiling floats, annual campaigns, see Chapter 10), which make it possible to continuously monitor changes in the characteristics of water masses throughout the region. The high-frequency data in the intermediate and deep waters of the Gulf of Lion (Fig. Box 9.1.1) illustrate the high seasonal

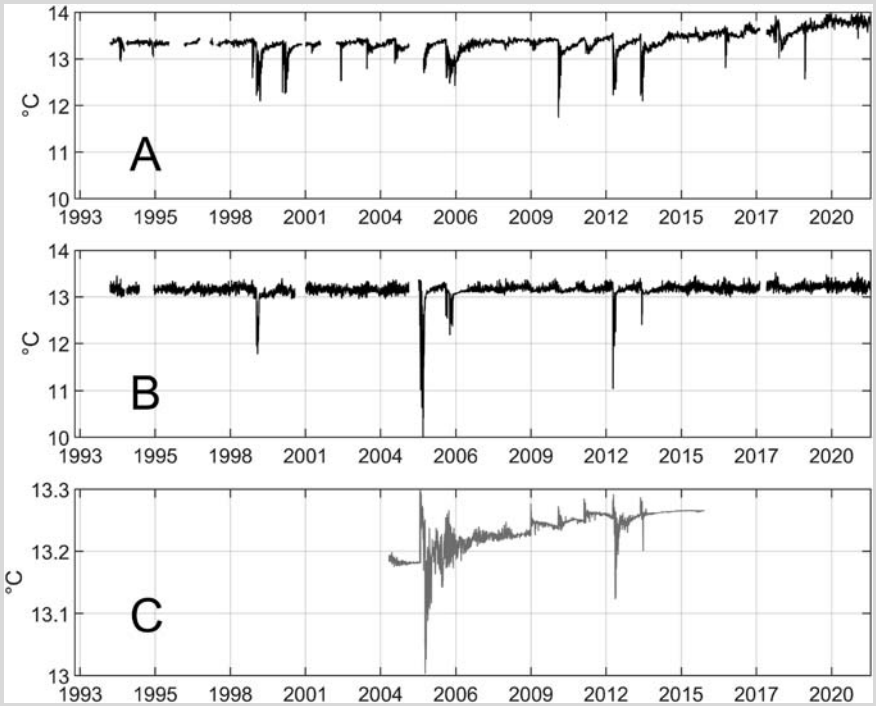

FIGURE BOX 9.1.1

Hourly time series of in situ temperature measured at 500m (A) and 1000 m (B) nominal depth in the southwestern part of the Gulf of Lion margin (Lacaze-Duthiers Canyon 42.43°N 3.54°E) from October 1993 to June 2021. The mooring line is positioned on a 1000m bottom. Hourly time series of in situ temperature measured near the bottom at ~2300m depth in the convection zone of Gulf of Lion (C) (LION: 42.04 N 4.69 E; HYDROCHANGE: 42 N 5 E).

Data from Durrieu de Madron, X., Heussner, S., Delsaut, N., Kunesch, S., Menniti, C., 2019. Billion Observatory Data. SEANOE. https://doi.org/10.17882/45980, Testor, P., Durrieu de Madron, X., Mortier, L., D'Ortenzio, F., Legoff, H., Dausse, D., Labaste, M., Houpert, L., 2020. LION Observatory Data. SEANOE. https://doi.org/10.17882/44411, and Schroeder, K., Millot, C., Bengara, L., Ben Ismail, S., Bensi, M., Borghini, M. , Budillon, G., Cardin, V. , Coppola, L., Curtil, C., Drago, A., El Moumni, B., Font, J., Fuda, J.L., García-Lafuente, J., Gasparini, G.P., Kontoyiannis, H., Lefevre, D., Puig, P., Raimbault, P., Rougier, G., Salat, J., Sammari, C., Sánchez Garrido, J.C., Sanchez-Roman, A., Sparnocchia, S., Tamburini, C., Taupier-Letage, I., Theocharis, A., Vargas-Yáñez, M., Vetrano, A., 2013. Long-term monitoring programme of the hydrological variability in the Mediterranean Sea: a first overview of the HYDROCHANGES network. Ocean Sci., 9, 301–324. https://doi.org/10.5194/os-9-301-2013.

Continued

Box 9.1 A closer look at the Gulf of Lion—cont'd

variability and the abrupt changes that occur in the winter period, superimposed on a visible warming trend over the long term. Along the continental slope, these fluctuations are the result of the overflow and cascading of cold and dense shelf water that penetrates the warmer IW layer (Fig. Box 9.1.1A) and may plunge during the strongest events down to the deep basin (Fig. Box 9.1.1B), as in 1999 (Béthoux et al., 2002), in 2005 (Canals et al., 2006), and in 2012 (Durrieu de Madron et al., 2013). Offshore, deep convection events are characterized by a sudden increase (between a few hundredths to more than a 10th of a degree) in bottom water temperature, followed by a gradual cooling resulting from heat losses from the entire water column under persistent atmospheric forcings (Fig. Box 9.1.1C). In 2005 and 2012, the arrival of dense shelf water was visible with a cooling of one to two tenths of a degree in the bottom water one to 2 months after the convection reached the bottom.

From 2009 to 2013, bottom-reaching open-ocean convection occurred every year in February (Houpert et al., 2016). The violent vertical mixing of the entire water column established the characteristics of the newly formed deep water. Each winter of deep convection has formed a new "vintage" of warmer and saltier deep water. These sudden additions of salt and heat to the ocean depths were responsible for the evolution of S ($3.3 \pm 0.2\ 10^{-3}$ yr^{-1}) and θ ($3.2 \pm 0.5\ 10^{-3}$°C yr^{-1}) observed from 2009 to 2013 for the 600−2300 m layer. Thanks to a high spatial coverage and temporal resolution of gliders up to 1000 m over the period 2007−17, Margirier et al. (2020) observed a warming (0.06°C yr^{-1}) and salinification (0.012 yr^{-1}) of the LIW in the Ligurian Sea. Further downstream, in the Gulf of Lion, intermediate heat and salt content was exported to the deep layers from 2009 to 2013 through deep convection. In 2014, a LIW step of +0.3°C in θ and +0.08 in S were observed concomitant with weak winter convection. Warmer and more saline LIW then accumulated in the northern WMED in the absence of deep and intense convective winters until 2018. Time series of θ measured at a depth of 500 m in the Planier and Lacaze-Duthiers canyons (i.e., within the LIW along the continental slope of the Gulf of Lion) even suggest that such an increase had not occurred since observations began in 1993 (Fig. Box 9.1.1). It is expected that the next intense bottom-reaching convection event will significantly change the thermohaline characteristics of the WMDW.

Bernoulli aspiration) by which high speed shallow flows within the strait are capable of sucking deep Mediterranean Water into the adjacent shallow Alboran Sea and then up and over the sill into the Atlantic. After the onset of the WMT the nWMDW has been brought to much shallower depths inside the Alboran Sea by this mechanism. In 2008 its interface with the overlying water was found at 900 m in the Alboran Sea, while in the WMED interior the same isopycnal was located 1000 m deeper (Fig. 9.7), but its signature was still too weak to resist the strong mixing at Gibraltar and hence could not be found at stations further west. In 2010, the signature of the new dense waters (σ_θ was even higher then, >29.11 kg m^{-3}) was found within the strait. As anticipated by Schroeder et al. (2016), the nWMDW was later found flowing through Gibraltar, escaping the Mediterranean Sea and feeding the Mediterranean Outflow Water (MOW): Naranjo et al. (2017) analyzing temperature and salinity time series near the sea floor at the Espartel Sill (within the Gibraltar Strait), between 2004 and 2016, showed positive trends which have

strongly accelerated after 2013 (an almost fourfold increase in the trend of the whole period), and related this to a possible footprint of the WMT at the Gibraltar Strait. Box 9.2 synthesises the recent changes discussed so far.

Box 9.2 Schematic of the recent changes in the Mediterranean deep ventilation

Li and Tanhua (2020) provided a nice and effective visual summary (Fig. Box 9.2.1) of the phases the Mediterranean Sea recently experienced in terms of deep ventilation: phase A, with the low salinity cold AdDW as the dominant source of ventilation for the EMED; phase B, with the EMT and massive production of CDW; phase C, post-EMT, with progressively decreasing ventilation depth by CDW and reactivation of the Adriatic Sea as the main source in the EMED, while the WMED is undergoing the WMT with renewal of the WMDW; phase D represents the current status, with slow-down of deep ventilation in the WMED as well as the Adriatic Sea as dominant source of ventilation in the EMED, yet weakened with respect to previous years.

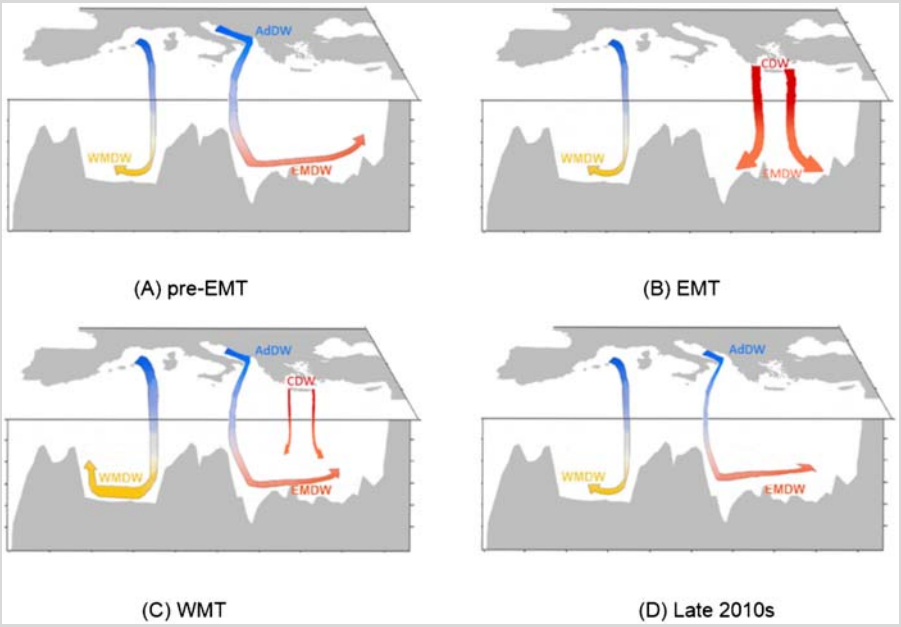

FIGURE BOX 9.2.1

Mediterranean deep overturning circulation phases. Colors highlight the approximate change in salinity (blue = low salinity and red = high salinity). Thickness of arrows represents the approximate change in source intensity (thick = high intensity and thin = low intensity).

From Li, P., Tanhua, T., 2020. Recent changes in deep ventilation of the Mediterranean Sea; evidence from long-term transient tracer observations. Front. Mar. Sci. 7, 1–23. https://doi.org/10.3389/fmars.2020.00594.

9.4 Long-term trends and climate change

There is increasing evidence that Mediterranean water masses are becoming warmer and saltier (see MedECC, 2020, for more details). Since the 1980s, upper layer temperature has increased (Rivetti et al., 2017; Vargas-Yáñez et al., 2017) as well as SST (Marullo et al., 2010; Pastor et al., 2018), with acceleration since the 1990s (Macías et al., 2013). The average Mediterranean SST (Fig. 9.8) increased by 0.29−0.44°C decade^{-1} since the early 1980s (Nabat et al., 2014; CEAM 2019; Darmaraki et al., 2019). Comparing the two periods 1980−99 and 2000−17, a positive SST anomaly of at least +0.2°C can be seen in all Mediterranean areas, but with stronger trends in the EMED (Fig. 9.8). More specifically in the EMED the SST trend has been estimated to be +0.042°C yr^{-1} (between 1985 and 2008, Skliris et al., 2012), +0.048°C yr^{-1} (in the Levantine/Aegean basins between 1982 and 2018, Pisano et al., 2020) and 0.04−0.06°C yr^{-1} (between 1988 and 2005, Romanou et al., 2010).

It is in indeed beyond doubt that SST, salinity and net evaporation have been constantly increasing, especially in the EMED, during the last decades. Future projections (Somot et al., 2006) predict a continuation of the SST increase throughout the Mediterranean Sea accompanied by a surface salinity increase in the Levantine Basin and in the Aegean Sea (see also Soto-Navarro et al., 2020).

Positive trends are reported also at depth (Fig. 9.9). As reported in the First Mediterranean Assessment Report (MAR1) prepared by the independent network of Mediterranean Experts on Climate and environmental Change (MedECC, 2020) changes in the Mediterranean water mass characteristics have a signature in the water outflowing from the Mediterranean Sea through the Strait of Gibraltar (Millot

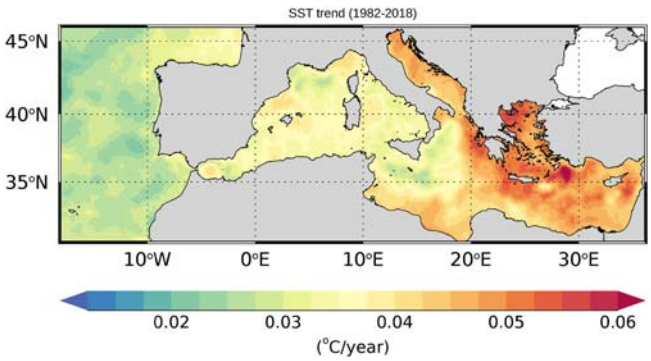

FIGURE 9.8

SST trend map (°C yr^{-1}) at the 95% significance level (i.e., $P \leq .05$) covering the 1982−2018 period. Trend ranges from the minimum of 0.019°C year^{-1} to the maximum of 0.066°C year^{-1}.

From Pisano, A., Marullo, S., Artale, V., Falcini, F., Yang, C., Leonelli, F., Santoleri, R., Nardelli, B.B., 2020. New evidence of mediterranean climate change and variability from sea surface temperature observations. Rem. Sens. 12 (1), 1−18. https://doi.org/10.3390/rs12010132.

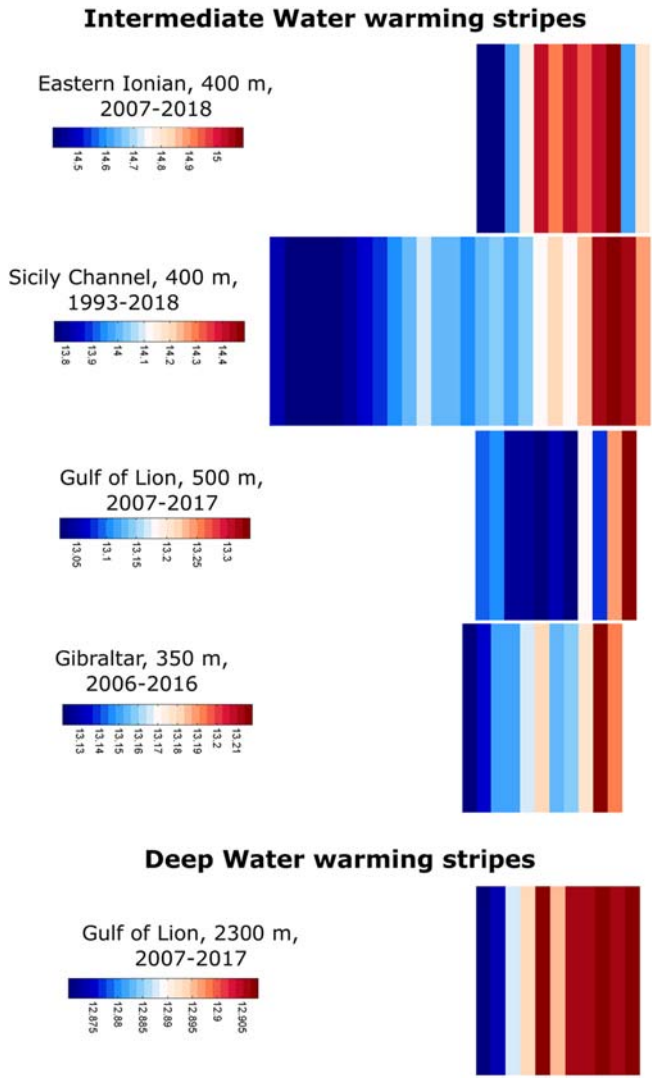

FIGURE 9.9

Warming stripes in the Intermediate Water (from east to west) and the Deep Water (in the Gulf of Lion). Each stripe refers to a single year and covered periods differ among sites. Values have been computed using yearly potential temperature averages in different locations where long-term mooring data are available at different depths. Data from the eastern Ionian come from the HCMR Pylos deep Observatory (Velaoras et al., 2013), and have been downloaded from CMEMS. Data from the Sicily Channel are those reported in Fig. 9.2 and in Schroeder et al. (2017) and can be downloaded from CMEMS. Data from the Gulf of Lion (500 and 2300 m) come from the LION Observatory of the MOOSE Network (Houpert et al., 2016) and can be downloaded from SEANOE (Testor et al., 2020). Data from the Gibraltar Strait come from the IEO (Spanish Oceanographic Institute) mooring (von Schuckmann et al., 2018) and can be downloaded from CMEMS. Note that color scales are different for each panel.

From MedECC. 2020. Climate and environmental change in the Mediterranean Basin – current situation and risks for the future. In: Cramer, W., Guiot, J., Marini, K. (Eds.), First Mediterranean Assessment Report, Union for the Mediterranean, Plan Bleu, UNEP/MAP, Marseille, France, 632 pp. https://doi.org/10.5281/zenodo.4768833.

et al., 2006; Naranjo et al., 2017). Mooring observations collected since 2004 (Fig. 9.9, "Gibraltar Strait" panel) show a positive trend in temperature and salinity of 7.7 10^{-3}°C yr^{-1} and 0.63 10^{-3} yr^{-1}, respectively (von Schuckmann et al., 2018). As reported above, since 2013 a noticeable increase of these trends is interpreted as the signal of the WMT (Naranjo et al., 2017).

Contrary to SST, a corresponding sea surface salinity evolution has not been reported (Rixen et al., 2005; Sevault et al., 2014), except for specific locations (Ozer et al., 2017; Vargas-Yáñez et al., 2017). Skliris et al. (2018) has estimated a salinity trend or the whole water column to be +0.009 $decade^{-1}$ (between 1950 and 2015). Long-term trends in the Mediterranean Sea intermediate and deep hydrology have been detected, though they are affected by marked variability on decadal time scales (as the previously described WMT, EMT, and BiOS). In the Levantine Sea, Ozer et al. (2017) examined a 30 years long (1979−2014) time series of hydrological properties and found an increasing trend of +0.12°C yr^{-1} in temperature and +0.008 yr^{-1} in salinity in the Levantine Surface Water (LSW) and +0.03°C yr^{-1} and +0.005 yr^{-1}, respectively, in the LIW. Correspondingly, the θ and S of the LIW/CIW crossing the Sicily Channel have increased at a rate of 0.028°C yr^{-1} and 0.008 yr^{-1}, respectively (as already reported above in Fig. 9.2; note that these are updated values with respect to those reported by Schroeder et al., 2017). Such trends are at least one order of magnitude greater than those reported for the global ocean intermediate layer (Schroeder et al., 2017).

The role of LIW/CIW is crucial in determining the characteristics of the deep waters. It also forms the bulk of the MOW exiting toward the Atlantic Ocean, where it settles down to 1000 m and where it caused a salinity increase. Indeed, warmer and drier regional climatic conditions over the eastern basin favor the formation of a warmer and saltier intermediate layer. LIW is the product of the transformation and sinking of LSW, which originates from the modification of AW in the Levantine Seas, where it becomes particularly warm and salty. The dramatic drought that lasts since the late 1990s in the Levantine area, and which has been reported to be the driest period in the past 500 years (Cook et al., 2016), is at the origin of a prolonged intensification of net evaporation that is affecting the region and is strongly modifying the LSW. This LSW will later on transform into a saltier and warmer LIW. Given that all processes of DWF involve AW and IW to some extent, the latter being the main contributor to the heat and salt contents of the newly formed waters, all Mediterranean water masses are intimately related to each other, so that significant modifications to one will also affect the others sooner or later.

As a side note, other nonclimatic factors come also into play, the most prominent example being the damming of the Nile River in the 1960s (the Aswan Dam was constructed in 1964) and the consequent dramatic reduction (>90%) of the river's freshwater input to the sea (Skliris and Lascaratos, 2004; Skliris et al., 2007, and references therein). This affected the salt budget of the EMED, and had an important role in the long-term salinity increase in the EMED surface and intermediate layers.

A numerical study by Skliris and Lascaratos (2004) suggested that the Nile River damming accounts for a salinity increase as high as 0.1 in the surface waters of the Levantine Basin, which could result in about 30% increase of the LIW formation rate. This salinity increase is considered as a long-term preconditioning factor that helped triggering the EMT. A lesser but important anthropogenic reduction in the freshwater input of the EMED has been the reduction in the brackish BSW export toward the Aegean Sea due to the damming of rivers flowing into the Black Sea. The major river damming started in the 1950s and gradually led to the reduction in BSW export by more than 50% until the end of the 20th century (Zervakis et al., 2000).

Concerning the changes during the last century, all previous studies show unambiguously that the WMDW increased its θ and S since the beginning of the twentieth century with an acceleration of these trends during the second half of the century. There is not a general agreement concerning the trends experienced by the intermediate and upper layers. Since WMDW is formed by the mixing of AW and LIW offshore the Gulf of Lion, its salinification must be caused by the salinification of one or both the contributing water masses: salinification of LIW (hypothesis of Leaman and Schott, 1991; Rohling and Bryden, 1992), and/or salinification of AW (hypothesis by Krahmann and Schott, 1998), or both. However, this could not justify the warming of WMDW. If none of the contributing water masses had changed its temperature, and the heat fluxes along the whole year, or during winter convection, had remained constant, WMDW would be formed with the same temperature and higher salinity values. A similar argument is proposed by Schroder et al. (2010) in relation to the formation of nWMDW during the WMT. Therefore, it is very likely that also AW and/or LIW have warmed during the twentieth century. It is clear that the Mediterranean Sea cannot be considered in an equilibrium state anymore. Changes have become clear during the beginning of the present century and, according to current projections, are expected to continue (Somot et al., 2006; Adloff et al., 2015).

9.5 Impact on the Mediterranean-Atlantic system

9.5.1 Mediterranean outflow water (MOW)

Within the present climate, the Mediterranean Sea is in an antiestuarine condition and therefore produces dense, warm and salty water that outflows through the Gibraltar Strait into the North Atlantic, while importing freshwater from the North Atlantic (Armi and Farmer, 1988). The outflow amounts to about 1 Sv of water that can be $> 5^{\circ}$C warmer and >1 saltier than any other water mass in the North Atlantic at the same latitude and depth. After mixing with the surrounding water masses, the MOW sinks reaching its neutrally buoyant at about 1000 m depth with a slight contribution of the cabbeling effect (see Chapter 4; Bashmachnikov et al., 2015;

Schmidtko et al., 2013). More on the exchanges between the Mediterranean Sea and the North−Atlantic is detailed in Chapter 4.

The Strait of Gibraltar plays the role of a salt valve generating a tipping point (Lenton et al., 2008) in the North Atlantic-Mediterranean connected system (Artale et al., 2006). The physics within the strait include a large spectrum of phenomena from tide-induced mixing (Sannino et al., 2007) to the interannual/multidecadal variability due to the external forcing and the north Atlantic circulation. They all eventually have an impact on the hydrological characteristics of the MOW (Fusco et al., 2008; Izquierdo and Mikolajewicz, 2019).

The spreading of the salinity anomaly in the North Atlantic associated with the presence of MOW ("Mediterranean tongue") has captured much attention in the past (Reid, 1979). Yet, major issues remain rather uncertain. In fact, a contribution to the average salinity of the world ocean equivalent to that of MOW would be achieved by distributing over the North Atlantic the net evaporation observed over the Mediterranean Sea. The present estimate of the freshwater budget of the North Atlantic (Ganachaud and Wunsch, 2003 and references therein) is rather uncertain, ranging from 0.2 to 0.8 Sv of net loss north of 30°N. The corresponding estimate of the Mediterranean freshwater deficit has also a large uncertainty (see Table 1 in Mariotti et al., 2002), ranging from 370 to 950 mm y^{-1} (see also Chapter 4). Assuming an area for the Mediterranean Sea of 2.5×10^{12} m^2, these values correspond to 0.03−0.08 Sv net evaporation. Therefore, the contribution of the MOW to the freshwater budget of the North Atlantic can be currently estimated between 4% and 40%.

In the following, three issues related to the dynamics of such a connected system will be discussed: the variability of water mass transformation processes inside the Mediterranean Sea and the time necessary for water masses formed within the Mediterranean Sea to spread into the North Atlantic; the physics that have an impact on the exchange of fluxes (mass, salt and heat) at the Strait of Gibraltar; the spreading of MOW in the North Atlantic and its relation with the variability and stability of the Atlantic Meridional Overturning Circulation (AMOC) of the global ocean.

The MOW that exits at depth through the Strait of Gibraltar is a salinity source for the DWF processes in the Norwegian Sea (Reid, 1979; Sarafanov et al., 2008). On the other hand, the changes affecting the North AW masses could also be transferred to the Mediterranean Sea, through the inflow of AW.

According to García-Lafuente et al. (2007), the main water masses contributing to the outflow are LIW and WMDW, with a larger contribution of the former. Nevertheless, the volume of WMDW seems to increase during late winter when the maximum outflow is observed (García-Lafuente et al., 2007). Naranjo et al. (2015) identified the different water masses outflowing in the eastern side of the Strait of Gibraltar: Western Intermediate Water (WIW), LIW, TDW and WMDW. All these water masses increased their salinity during the period 2004−14, although only the trends corresponding to WIW and WMDW were significant at the 95% confidence level (0.031 yr^{-1} and 0.003 yr^{-1}, respectively).

All the works referred above show that most of the MWs, overflowing the Strait of Gibraltar, are warmer and saltier as a result of the trends that these water masses have

experienced within the Mediterranean Sea. These changes would have an impact on the AWs affected by the MOW (see Fig. 9.10). In fact, also the MOW observed in the North Atlantic has experienced positive θ and S trends during the second half of the twentieth century (Fusco et al., 2008). Nevertheless, the relationship between the changes observed in the North Atlantic and those alterations described for the source waters within the Mediterranean Sea are not clear yet and, according to Lozier and Sindlinger (2009), a direct link between both changes cannot be established.

The relation between the warming and salinification of water masses has also been considered in the opposite direction, that is, from the Atlantic to the Mediterranean. Soto-Navarro et al. (2012) analyzed the θ and S of the upper 100 m of the water column to the west of Gibraltar and found that these waters had increased their S from 2004 to 2010 at a rate of 0.038 ± 0.009 yr^{-1}. No significant trends were observed for the θ. The layer between 100 and 600 m, occupied by Eastern North

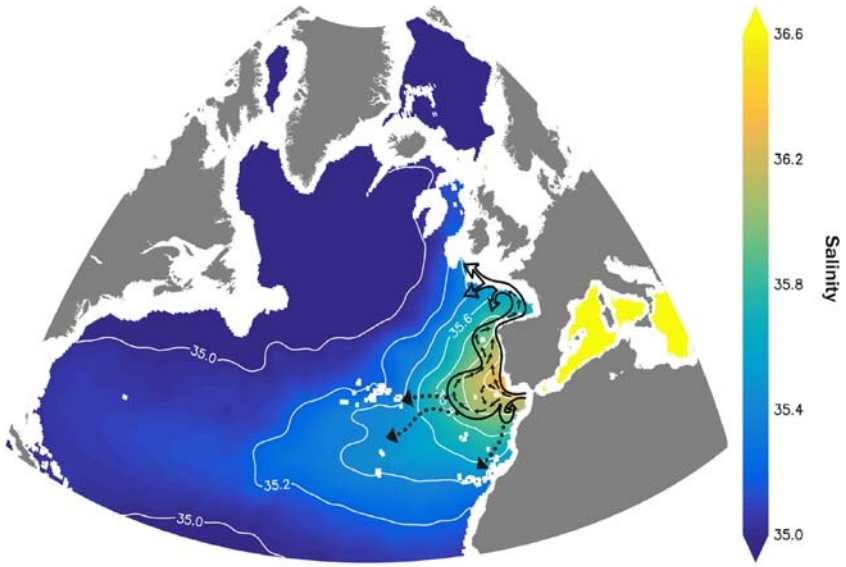

FIGURE 9.10

Mediterranean salt tongue representation on the World Ocean Atlas 2013 (WOA13, Zweng et al., 2013) salinity field at 1200 m depth. The overlaid scheme indicates the permanent MOW pathways (continuous arrows) and the preferred paths of Meddies (dotted arrows).

Modified after Iorga M.C., Lozier, M.S., 1999. Signatures of the Mediterranean outflow from a North Atlantic climatology 1. Salinity and density fields. J. Geophys. Res. 104, 25985–26009. https://doi.org/10.1029/1999JC900115. From Izquierdo A., Mikolajewicz, U., 2019. The role of tides in the spreading of Mediterranean Outflow waters along the southwestern Iberian margin. Ocean Model. 133, 27–43. https://doi.org/10.1016/j.ocemod.2018.08.003.

Atlantic Central Water (ENACW) also exhibited warming and salinification trends. Millot (2007) reported a strong salinity trend (0.047 yr^{-1}) for the AW flowing into the Mediterranean Sea for the period 2003–07. On the other hand, θ did not change during this period and therefore the density of AW increased. Millot (2007) suggested that the trends and changes that have been observed in the Mediterranean Sea during the last century and the beginning of the present one could be partially caused by the changes imported from the Atlantic Ocean.

9.5.2 Following the MOW signal: from the strait of Gibraltar to the North Atlantic

The spreading of MOW in the North Atlantic at intermediate depth follows two main paths (see Figs. 9.10 and 9.12A–H), the Westward Tongue (WT) and the Northward Undercurrent (NU).

The WT, extends from the Gulf of Cadiz toward the central North Atlantic at midlatitudes. This path is characterized by the presence of stable subsurface eddies containing Mediterranean Water (MW), so called Meddies, that are advected by the large-scale wind driven circulation (Nof, 1982; Hogg and Stommel, 1990) and play the role of heat and salt sources in the Mid-North Atlantic. The first accounts of the westward propagation of Meddies can be found in Worthington (1976) and Reid (1979). The strong mesoscale activity of the WT was first reported by McDowell and Rossby (1978) who first introduced the term *Meddy,* to indicate submesoscale coherent vortices containing water of Mediterranean origin. Armi and Zenk (1984) described the kinematics and hydrology of three individual Meddies. These are coherent structures about 50–140 Km wide and are observed to be stable over periods of many years. Richardson et al. (2000) observed Meddies as old as 5 years and estimated an average lifetime of 1.7 years. Along with a Meddy formation rate of 17 years, estimated by Bower et al. (1997), who examined the initial growth of Meddies off the coast of Portugal, this gives an expected number of 29 Meddies coexisting in the North–Atlantic.

The other path is the NU, off the Iberian Peninsula, driven by geostrophic balance of the ocean interior and mixing with the surrounding water masses (Spall, 1999). A quantitative description of these two flow branches is given by Sparrow et al. (2002) who analyzed float data and found, north of 36°N, a background northward flow, with an average velocity of 1.8 ± 0.6 cm s^{-1}, with peaks of 10.1 ± 3.7 cm s^{-1}, off the coast of Portugal. South of 36°N they found a weaker background flow (about 0.12 cm s^{-1}), and a strong mesoscale activity with peak energy as high as 89 cm^2 s^{-1}. The pictures of the MOW spreading described above were slightly modified by the contribution of Iorga and Lozier (1999), that valorized the significant spreading of the MW along the North African slope (see also Zweng et al., 2013), and by the study of Izquierdo and Mikolajewicz (2019) about the impact of tides on the spreading of MOW in the Gulf of Cadiz. The latter has shown through numerical experiments that without tides there is an excessive southwestward spreading of MW along the North African slope, whereas the numerical

run that included also tides gives results that are closer to climatology. A detailed analysis indicates that tidal residual currents in the Gulf of Cadiz are the main cause for these differences.

Further north, the MOW can be clearly tracked at 46°N in the central Bay of Biscay (see Fig. 9.10). Two different scenarios have been proposed for the way the MOW can affect the AMOC. The first one was proposed by Reid (1979) in which the MOW is directly advected to the Greenland-Iceland-Norwegian Sea on all the intermediate layers density horizons. Iorga and Lozier (1999) also support the so-called deep source hypothesis, whereby a substantial northward transport of MOW, way through the Rockall Channel, may directly affect the preconditioning in the Greenland-Iceland-Norwegian Sea.

A second scenario was originally proposed by Lozier (1995) in which the MOW progressively "peels off" interacting with the North Atlantic Current and modifying its water properties. More recently, the direct advection/deep source hypothesis has been severely criticized on the base of different hydrographical observations by McCartney and Mauritzen (2001), who strongly support the alternative shallow-source hypothesis, that is, the scenario proposed by Lozier (1995). In this case the warm, salty inflow in the Nordic Sea is attributed to the northward branching of the North Atlantic Current.

To summarize, different pictures of the MOW spreading in the North Atlantic have been described from the observations and no definitive agreement has been reached yet about any of them. Most importantly, very little is known about the variability of these pathways.

Finally, Lozier and Stewart (2008) using historical hydrographic data in the eastern North Atlantic suggest a connection between the northward penetration MOW and the location of the subpolar front, the latter of which is shown to vary with the NAO. During persistent high-NAO periods, when the subpolar front moves eastward, waters in the subpolar gyre essentially block the northward-flowing MOW, preventing its entry into the subpolar gyre. Conversely, during low NAO periods, the subpolar front moves westward, allowing MOW to penetrate past Porcupine Bank into the subpolar gyre. The impacts of an intermittent penetration of MOW into the subpolar gyre, including the possible effect on water mass transformations and its impact on the precondition phase of the deep-water formation in the GIS sea and Labrador Sea remain to be investigated.

However, numerical results, and specifically the Global Ocean Reanalyses Ensemble Products (ORAS5, Zuo et al., 2018 and 2019), and its five members, despite its coarse resolution of 0.25° precluding a detailed bathymetric representation of the Strait of Gibraltar, show that the MOW is correctly represented. In particular, Fig. 9.11 shows the ensemble spread of the climatological salinity at the Gibraltar Strait latitude, in which the maximum spread is concentrated along the main patterns of the Gulf Stream and the MOW. This result is determined by two, more likely independent, physical processes but both take part in the AMOC variability (Artale et al., 2006). The first spread is determined from the variability of the intensity of the Gulf Stream and to its horizontal decorrelation. The second

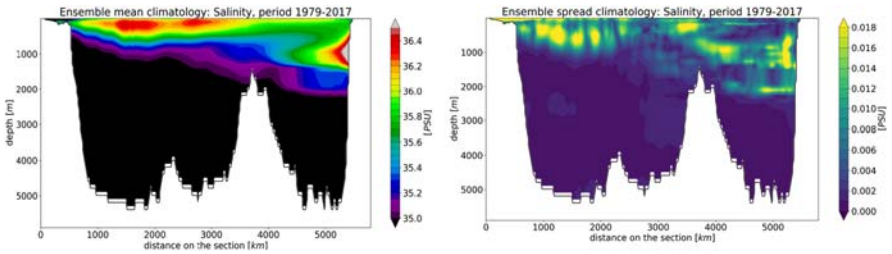

FIGURE 9.11

Ensemble mean of the climatological salinity along section 40°N (left panel), Ensemble spread of climatological salinity on section 40°N (right panel) from ORAS5 (Ocean ReAnalysis System 5), Copernicus Climate Change Service.

Courtesy of Vincenzo de Toma.

spread is due to the variability of the MOW induced by the nonlinear interaction between the hydraulic control and other physical mechanisms (tide, topographic stress, etc.) occurring within the Strait of Gibraltar (Sannino et al., 2002). More precisely, the observed variability of MOW can be considered as a "mediterranean climate index" correlated to the Mediterranean water deficit and/or E-P variability, but the transferring of this climate signal to the North Atlantic will happen in a complex and strongly nonlinear way, through a tipping point or salt valve, that is the Gibraltar Strait (see Artale et al., 2006; Lenton et al., 2008). Recent numerical simulations have also shown that the natural decadal variability of the Mediterranean Sea thermohaline cell is related to the amount of water that flows through all channel and straits, including the Strait of Gibraltar that makes a "synthesis" of all waters produced within the entire Mediterranean water column and finally evidenced in the MOW variability shown in Figs. 9.11 and 9.13A (Kinder and Bryden, 1990; Artale et al., 2006; Fusco et al., 2008).

9.5.3 MOW trends and variability

The Gulf of Cadiz is the transition subbasin where the MW undergoes, for the first time, a strong mixing and entrainment with the AW. Fusco et al. (2008) used θ and S data from Medar/Medatlas II and WODB to investigate possible changes in the thermohaline characteristics of the MOW in the eastern North Atlantic. Fig. 9.13A and B show a clear increase in the thickness of the layer occupied by the MOW for the period 1906–99, but not a shift of the depth at which the salinity maximum is found. However, it is necessary to consider that in the period 1906–48, there are measurement gaps of up to 20 years; therefore, Fig. 9.13C and D show S and θ at 1200 m, including the standard deviation of the data from 1948 to 1999. Here it is possible to note examples of high-frequency intradecadal variability as well as the long-term interdecadal trends. The standard deviation around the mean value can be quite variable. This is due to the fact that it is calculated by assembling monthly data, by combining different cruises and often from different parts of the basin. In the period

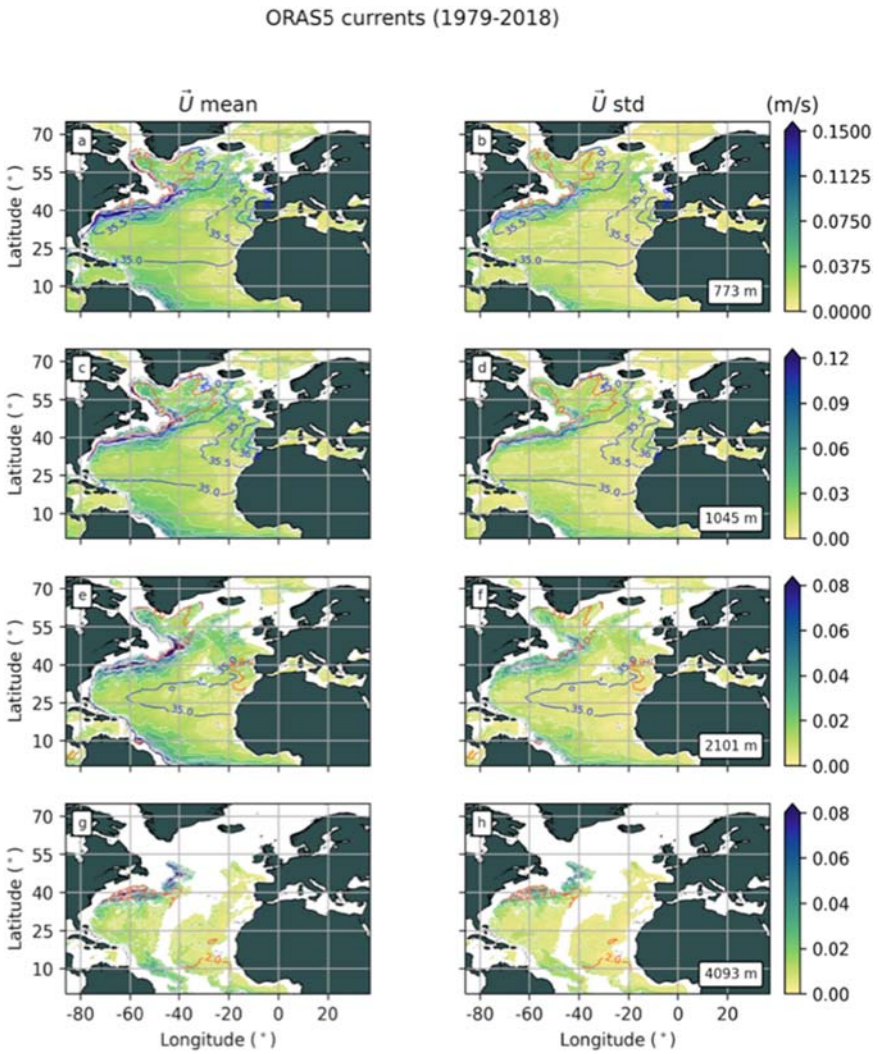

FIGURE 9.12

Mean velocity and standard deviation at four depths of the North Atlantic-Mediterranean system: 773 m (A–B), 1045 m (C–D), 2101 m (E–F) and 4093 m (G–H). Analysis based on ORAS5 made by Evan Mason (CSIC, Spain, personal communication, 2020).

1906–99 an increase in S and θ of 0.31 and 1.01°C, respectively, was estimated. In the 1948–99 period, the calculated variations in S and θ are based on a large number of measurements, with an average value of 0.05 and 0.16°C per decade, respectively. In the period 1970–99, the trend estimates of S and θ result to be 0.12 decade^{-1} and 0.38°C decade^{-1}, respectively. These trends are the highest observed values. Moreover, the continuing warming and salting of the MW source water seems confirmed from the analysis of the MW outflow measured at Espartel Sill (within the Strait of Gibraltar) from September 2004 to September 2016 (see Fig. 9.14, and Chapter 4).

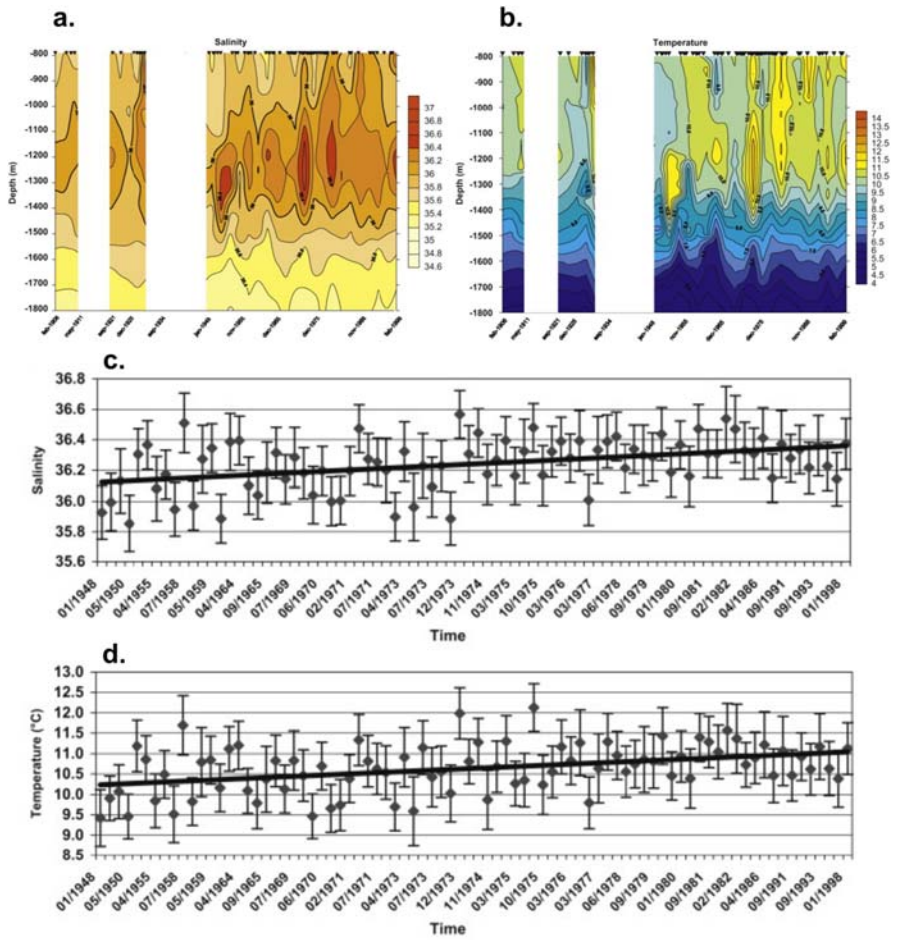

FIGURE 9.13

Properties of MW in the Gulf of Cadiz from 1906 to 99 (depth vs. time): monthly mean of (A) salinity and (B) potential temperature. Superimposed triangles show temporal distribution of monthly mean profiles. (C) salinity and (D) potential temperature trends from 1948 to 1999.

From Fusco, G., Artale V., Cotroneo Y., 2008. Thermohaline variability of mediterranean water in the Gulf of Cadiz over the last decades (1948–1999). Deep Sea Res. Part I 55, 12, 1624–1638. https://doi.org/10.1016/j.dsr.2008.07.009.

Concerning the relevance of the impact of the MOW on the strength of the overturning circulation of the North Atlantic, Rahmstorf (1998) observed a slight impact of MOW on AMOC, using numerical simulations, while Hecht et al. (1997) established that a stable AMOC is achieved only when a realistic MOW is present. Artale et al. (2002) have proposed a synthesis between these two rather different points of

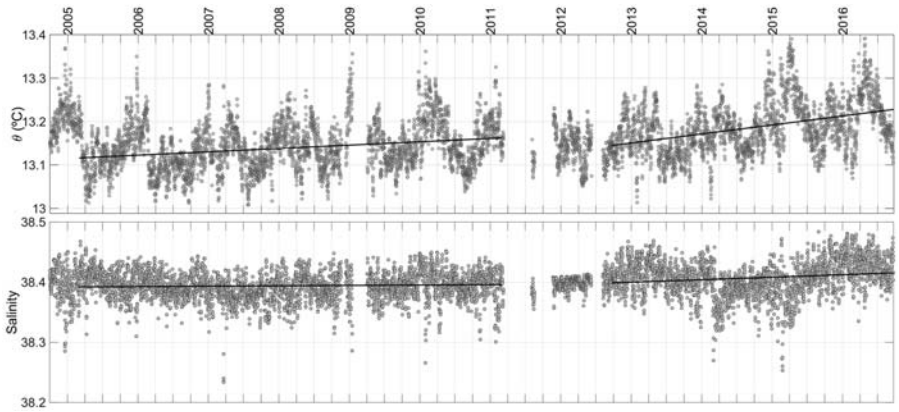

FIGURE 9.14

Observed (black dots) subtidal series of (A) potential temperature and (B) salinity at Espartel Sill at 348 m depth (15 m above the sea floor of the Strait of Gibraltar) from September 2004 to September 2016. For details on the data decimation refer to Naranjo et al. (2017).

Modified after von Schuckmann, K., Le Traon, P.Y., Smith, N., Pascual, A., Brasseur, P., Fennel, K., Djavidnia, S., et al., 2018. Copernicus marine Service ocean state report. J. Oper. Oceanogr. 11, Suppl. 1, S1–S142. https://doi.org/10.1080/1755876X.2018.1489208.

view, by showing that the MOW has only a slight influence on the strength of the AMOC but a considerable impact on the preference for certain patterns of circulation and their stability. More recently Ivanovic et al. (2014), using the same approach of Artale et al. (2002), suggested that although the effect remains relatively small, MOW had a greater influence on North Atlantic Ocean circulation and climate in the past than it does today (see also Hernández-Molina et al., 2014).

The importance of the heat and salt transport promoted by the MOW flow has implications beyond the boundaries of the close domain of the Gulf of Cadiz. Therefore, monitoring of MOW variability becomes decisive to have a proper understanding of the climate system and its evolution at least for the North Atlantic basin.

Additional Resources

- https://marine.copernicus.eu/
- https://climate.copernicus.eu/
- Scientific assessment of climate and environmental changes impacts in the Mediterranean Basin, https://www.medecc.org/
- The present state of marine ecosystems in the Spanish Mediterranean in a climate change context: https://digital.csic.es/handle/10261/189580
- https://climatedataguide.ucar.edu/climate-data
- https://www.cen.uni-hamburg.de/en/icdc.html
- https://www.seadatanet.org/
- https://www2.atmos.umd.edu/~ocean/index_files/soda3_readme.htm
- https://www.aoml.noaa.gov/phod/research/moc/samoc/sam/data_access.php;
- https://psl.noaa.gov/data/gridded/data.noaa.ersst.v5.html

References

Adloff, F., Somot, S., Sevault, F., Jordà, G., Aznar, R., Déqué, M., Herrmann, M., Marcos, M., Dubois, C., Padorno, E., Alvarez-Fanjul, E., Gomis, D., 2015. Mediterranean Sea response to climate change in an ensemble of twenty first century scenarios. Clim. Dynam. 45, 2775–2802. https://doi.org/10.1007/s00382-015-2507-3.

Amitai, Y., Ashkenazy, Y., Gildor, H., 2017. Multiple equilibria and overturning variability of the Aegean-Adriatic Seas. Global Planet. Change 151, 49–59. https://doi.org/10.1016/j.gloplacha.2016.05.004.

Armi, L., Zenk, W., 1984. Large lenses of highly saline Mediterranean Water. J. Phys. Oceanogr. 14, 1560.

Armi, L., Farmer, D., 1988. The flow of Mediterranean water through the Strait of Gibraltar. Prog. Oceanogr. 21, 41–82.

Artale, V., Calmanti, S., Sutera, A., 2002. Thermohaline circulation sensitivity to intermediate-level anomaly. Tellus A 54 (2), 159–174. https://doi.org/10.1034/j.1600-0870.2002.01284.x.

Artale, V., Calmanti, S., Malanotte-Rizzoli, P., Pisacane, G., Rupolo, V., Tsimplis, M., 2006. The Atlantic and Mediterranean Sea as connected systems. In: Lionello, P., Malanotte-Rizzoli, P., Boscolo, R. (Eds.), Mediterranean Climate Variability. Elsevier, Amsterdam, pp. 283–323.

Artale, V., Falcini, F., Marullo, S., Bensi, M., Kokoszka, F., Iudicone, D., Rubino, A., 2018. Linking mixing processes and climate variability to the heat content distribution of the Eastern Mediterranean abyss. Sci. Rep. 8 (1), 1–10. https://doi.org/10.1038/s41598-018-29343-4.

Artegiani, A., Bregant, D., Paschini, E., Pinardi, N., Raicich, F., Russo, A., 1997. The adriatic sea general circulation. Part II: baroclinic circulation structure. J. Phys. Oceanogr. 27 (8), 1515–1532. https://doi.org/10.1175/1520-0485.

Astraldi, M., Balopoulos, S., Candela, J., Font, J., Gacic, M., Gasparini, G., Manca, B., Theocharis, A., Tintoré, J., 1999. The role of straits and channels in understanding the characteristics of Mediterranean circulation. Prog. Oceanogr. 44 (1–3), 65–108. https://doi.org/10.1016/S0079-6611(99)00021-X.

Astraldi, M., Gasparini, G.P., Vetrano, A., Vignudelli, S., 2002. Hydrographic characteristics and interannual variability of water masses in the central Mediterranean: a sensitivity test for long-term changes in the Mediterranean Sea. Deep-Sea Res. I 49, 661–680. https://doi.org/10.1016/S0967-0637(01)00059-0.

Bensi, M., Rubino, A., Cardin, V., Hainbucher, D., Mancero-Mosquera, I., 2013. Structure and variability of the abyssal water masses in the Ionian Sea in the period 2003–2010. J. Geophys. Res. Oceans 118 (2), 931–943. https://doi.org/10.1029/2012JC008178.

Bashmachnikov, I., Neves, F., Calheiros, T., Carton, X., 2015. Properties and pathways of Mediterranean water eddies in the Atlantic. Prog. Oceanogr. 137 (Part A), 149–172. https://doi.org/10.1016/j.pocean.2015.06.001.

Bessières, L., Rio, M.H., Dufau, C., Boone, C., Pujol, M.I., 2013. Ocean state indicators from MyOcean altimeter products. Ocean Sci. 9 (3), 545–560. https://doi.org/10.5194/os-9-545-2013.

Béthoux, J.P., Gentili, B., Raunet, J., Taillez, D., 1990. Warming trend in the Western Mediterranean deep water. Nature 347, 660–662. https://doi.org/10.1038/347660a0.

Béthoux, J.P., Gentili, B., Tailliez, D., 1998. Warming and freshwater budget change in the Mediterranean since 1940s, their possible relation to the greenhouse effect. Geophys. Res. Lett. 25 (7), 1023−1026. https://doi.org/10.1029/98GL00724.

Béthoux, J.P., Durrieu de Madron, X., Nyffeler, F., Tailliez, D., 2002. Deep water in the western Mediterranean: peculiar 1999 and 2000 characteristics, shelf formation hypothesis, variability since 1970 and geochemical inferences. J. Mar. Syst. 33−34, 117−131. https://doi.org/10.1016/S0924-7963(02)00055-6.

Borzelli, G.L.E., Gačić, M., Cardin, V., Civitarese, G., 2009. Eastern mediterranean transient and reversal of the Ionian Sea circulation. Geophys. Res. Lett. 36 (15), L15108. https://doi.org/10.1029/2009GL039261.

Bower, A.S., Armi, L., Ambar, I., 1997. Lagrangian observation of Meddy formation during a Mediterranean undercurrent seeding experiment. J. Phys. Oceanogr. 27, 2545.

Buljan, M., 1953. Fluctuation of salinity in the adriatic. Acta Adriat. 2, 1−64.

Canals, M., Puig, P., Durrieu de Madron, X., Heussner, S., Palanques, A., Fabrès, J., 2006. Flushing submarine canyons. Nature 444, 354−357. https://doi.org/10.1038/nature05271.

Cardin, V., Gačić, M., Nittis, K., Kovačević, V., Perini, L., 2003. Sub-inertial variability in the Cretan Sea from the M3A buoy. Ann. Geophys. 21, 89−102. https://doi.org/10.5194/angeo-21-89-2003.

Cardin, V., Civitarese, G., Hainbucher, D., Bensi, M., Rubino, A., 2015. Thermohaline properties in the Eastern Mediterranean in the last three decades: is the basin returning to the pre-EMT situation? Ocean Sci. 11 (1), 53−66. https://doi.org/10.5194/os-11-53-2015.

CEAM 2019 Mediterranean Sea Surface Temperature Report, Summer 2019. https://doi.org/10.13140/RG.2.2.23375.23209.

Chiggiato, J., Schroeder, K., Trincardi, F., 2016a. Cascading dense shelf-water during the extremely cold winter of 2012 in the Adriatic, Mediterranean Sea: formation, flow, and seafloor impact. Mar. Geol. 375, 1−4. https://doi.org/10.1016/j.margeo.2016.03.002.

Chiggiato, J., Bergamasco, A., Borghini, M., Falcieri, F.M., Falco, P., Langone, L., Miserocchi, S., Russo, A., Schroeder, K., 2016b. Dense-water bottom currents in the southern Adriatic Sea in spring 2012. Mar. Geol. 375, 134−145. https://doi.org/10.1016/j.margeo.2015.09.005.

Cook, B.I., Anchukaitis, K.J., Touchan, R., Meko, D.M., Cook, E.R., 2016. Spatiotemporal drought variability in the Mediterranean over the last 900 years. J. Geophys. Res. 121. https://doi.org/10.1002/2015JD023929.

Darmaraki, S., Somot, S., Sevault, F., Nabat, P., 2019. Past variability of Mediterranean Sea marine heatwaves. Geophys. Res. Lett. 46, 9813−9823. https://doi.org/10.1029/2019gl082933.

Durrieu de Madron, X., et al., 2013. Interaction of dense shelf water cascading and open-sea convection in the northwestern Mediterranean during winter 2012. Geophys. Res. Lett. 40, 1379−1385. https://doi.org/10.1002/grl.50331.

Durrieu de Madron, X., Heussner, S., Delsaut, N., Kunesch, S., Menniti, C., 2019. Billion Observatory Data. SEANOE. https://doi.org/10.17882/45980.

Font, J., Puig, P., Salat, J., Palanques, A., Emelianov, M., 2007. Sequence of hydrographic changes in NW Mediterranean deep water due to exceptional winter of 2005. Sci. Mar. 71 (2), 339−346.

Fusco, G., Artale, V., Cotroneo, Y., 2008. Thermohaline variability of mediterranean water in the Gulf of Cadiz over the last decades (1948−1999). Deep Sea Res. Part I 55 (12), 1624−1638. https://doi.org/10.1016/j.dsr.2008.07.009.

Gačić, M., Civitarese, G., Miserocchi, S., Cardin, V., Crise, A., Mauri, E., 2002. The open-ocean convection in the Southern Adriatic: a controlling mechanism of the spring phytoplankton bloom. Continent. Shelf Res. 22 (14), 1897–1908. https://doi.org/10.1016/S0278-4343(02)00050-X.

Gačić, M., Eusebi Borzelli, G.L., Civitarese, G., Cardin, V., Yari, S., 2010. Can internal processes sustain reversals of the ocean upper circulation? The Ionian Sea example. Geophys. Res. Lett. 37 (9), 1–5. https://doi.org/10.1029/2010GL043216.

Gačić, M., Civitarese, G., Eusebi Borzelli, G.L., Kovačević, V., Poulain, P.M., Theocharis, A., Menna, M., Catucci, A., Zarokanellos, N., 2011. On the relationship between the decadal oscillations of the northern Ionian Sea and the salinity distributions in the eastern Mediterranean. J. Geophys. Res. Oceans 116 (12), 1–9. https://doi.org/10.1029/2011JC007280.

Gačić, M., Civitarese, G., Kovačević, V., Ursella, L., Bensi, M., Menna, M., Cardin, V., Poulain, P.-M., Cosoli, S., Notarstefano, G., Pizzi, C., 2014. Extreme winter 2012 in the Adriatic: an example of climatic effect on the BiOS rhythm. Ocean Sci. 10 (3), 513–522. https://doi.org/10.5194/os-10-513-2014.

Ganachaud, A., Wunsch, C., 2003. Large-scale ocean heat and freshwater transport during the world ocean circulation experiment. J. Clim. 16, 696–705. https://doi.org/10.1175/1520-0442(2003)016%3C0696:LSOHAF%3E2.0.CO;2.

García Lafuente, J., Sánchez Román, A., Díaz del Río, G., Sannino, G., Sánchez Garrido, J.C., 2007. Recent observations of seasonal variability of the Mediterranean outflow in the strait of Gibraltar. J. Geophys. Res. 112 (C10), C10005. https://doi.org/10.1029/2006JC003992.

Gasparini, G.P., Ortona, A., Budillon, G., Astraldi, M., Sansone, E., 2005. The effect of the eastern mediterranean transient on the hydrographic characteristics in the strait of Sicily and in the Tyrrhenian. Deep-Sea Res. I 52, 915–935. https://doi.org/10.1016/j.dsr.2005.01.001.

Georgopoulos, D., Theocharis, D., Zodiatis, G., 1989. Intermediate water formation in the Cretan Sea (south Aegean Sea). Oceanol. Acta 12, 353–359.

Gertman, I., Ovchinnikov, I., Popov, Y., 1994. Deep convection in the eastern basin of the Mediterranean Sea. Oceanology 34 (1), 19–25.

Gertman, I., Pinardi, N., Popov, Y., Hecht, A., 2006. Aegean Sea water masses during the early stages of the eastern mediterranean climatic transient (1988–90). J. Phys. Oceanogr. 36 (9), 1841–1859. https://doi.org/10.1175/JPO2940.1.

Gertman, I., Zodiatis, G., Ozer, T., Goldman, R., Herut, B., 2016. Renewal of deep water in vicinity of the Eastern Levantine slope. Rapport de la Commission Internationale de la Mer Méditerranée, 41, p. 124.

Hainbucher, D., 2020. Physical Parameters of the Mediterranean Sea, Cruise MSM72. https://doi.org/10.1594/PANGAEA.913613. March-April 2018. PANGAEA.

Hecht, M., Holland, W., Artale, V., Pinardi, N., 1997. North Atlantic model sensitivity to Mediterranean waters. In: Howe, W., Henderson-Sellers, A. (Eds.), Assessing Climate Change: Results from the Model Evaluation Consortium for Climate Assessment. Gordon and Breach, pp. 169–191.

Hernández-Molina, F.J., Stow, D.A., Alvarez-Zarikian, C.A., Acton, G., Bahr, A., Balestra, B., Ducassou, E., Flood, R., Flores, J.A., Furota, S., Grunert, P., 2014. Onset of mediterranean outflow into the north Atlantic. Science 344, 1244–1250.

Herrmann, M., Sevault, F., Beuvier, J., Somot, S., 2010. What induced the exceptional 2005 convection event in the northwestern Mediterranean basin? Answers from a modeling study. J. Geophys. Res. 115, C12051. https://doi.org/10.1029/2010JC006162.

Hogg, N.G., Stommel, H.M., 1990. How currents in the upper thermocline could advect meddies deeper down. Deep-Sea Res. 37 (4), 613–623. https://doi.org/10.1016/0198-0149(90)90093-B.

Houpert, L., Durrieu de Madron, X., Testor, P., Bosse, A., D'Ortenzio, F., Bouin, M.N., Dausse, D., Le Goff, H., Kunesch, S., Labaste, M., Coppola, L., Mortier, L., Raimbault, P., 2016. Observations of open-ocean deep convection in the Northwestern Mediterranean Sea seasonal and interannual variability of mixing and deep water masses for the 2007–2013 period. J. Geophys. Res. Oceans 121, 8139–8171. https://doi.org/10.1002/2016JC011857.

Iorga, M.C., Lozier, M.S., 1999. Signatures of the Mediterranean outflow from a North Atlantic climatology 1. Salinity and density fields. J. Geophys. Res. 104, 25985–26009. https://doi.org/10.1029/1999JC900115.

Ivanovic, R.F., Valdes, P.J., Flecker, R., Gutjahr, M., 2014. Modelling global-scale climate impacts of the late Miocene Messinian salinity Crisis. Clim. Past 10, 607–622. https://doi.org/10.5194/cp-10-607-2014.

Izquierdo, A., Mikolajewicz, U., 2019. The role of tides in the spreading of Mediterranean Outflow waters along the southwestern Iberian margin. Ocean Model. 133, 27–43. https://doi.org/10.1016/j.ocemod.2018.08.003.

Jordá, G., Gomis, D., 2013. Reliability of the steric and mass components of the Mediterranean Sea level as estimated from hydrographic gridded products. Geophys. Res. Lett. 40, 3655–3660. https://doi.org/10.1002/grl.50718.

Josey, S.A., 2003. Changes in the heat and freshwater forcing of the eastern Mediterranean and their influence on deep water formation. J. Geophys. Res. 108 (C7), 3237. https://doi.org/10.1029/2003JC001778.

Kinder, T., Bryden, H., 1990. Aspiration of deep waters through straits. In: Pratt, L.J. (Ed.), The Physical Oceanography of Sea Straits, vol. 295. Kluwer, Boston.

Klein, B., Roether, W., Manca, B.B., Bregant, D., Beitzel, V., Kovacevic, V., Luchetta, A., 1999. The large deep water transient in the Eastern Mediterranean. Deep-Sea Res. Part I Oceanogr. Res. Pap. 46 (3), 371–414. https://doi.org/10.1016/S0967-0637(98)00075-2.

Kontoyiannis, H., Theocharis, A., Nittis, K., 1999. Structures and characteristics of newly formed water masses in the NW Levantine during 1986, 1992, 1995. In: Malanotte-Rizzoli, P., Eremeev, V. (Eds.), The Eastern Mediterranean as a Laboratory Basin for the Assessment of Contrasting Ecosystems, NATO ASI Series, vol. 51. Kluwer Academic Publishers, Netherlands, pp. 465–473.

Kovačević, V., Gačić, M., Poulain, P.M., 1999. Eulerian current measurements in the strait of Otranto and in the southern adriatic. J. Mar. Syst. 20 (1–4), 255–278. https://doi.org/10.1016/S0924-7963(98)00086-4.

Krahmann, G., Schott, F., 1998. Long term increases in Western Mediterranean salinities and temperatures: anthropogenic and climatic sources. Geophys. Res. Lett. 25 (22), 4209–4212. https://doi.org/10.1029/1998GL900143.

Krokos, G., Velaoras, D., Korres, G., Perivoliotis, L., Theocharis, A., 2014. On the continuous functioning of an internal mechanism that drives the Eastern Mediterranean thermohaline circulation: the recent activation of the Aegean Sea as a dense water source area. J. Mar. Syst. 129, 484–489. https://doi.org/10.1016/j.jmarsys.2013.10.002.

Kubin, E., Poulain, P.-M., Mauri, E., Menna, M., Notarstefano, G., 2019. Levantine intermediate and Levantine deep water formation: an Argo float study from 2001 to 2017. Water 11 (9), 1781. https://doi.org/10.3390/w11091781.

Lacombe, H., Tchernia, P., Gamberoni, L., 1985. Variable bottom water in the Western Mediterranean basin. Prog. Oceanogr. 14, 319−338. https://doi.org/10.1016/0079-6611(85)90015-1.

Lagouvardos, K., Kotroni, V., Kallos, G., 1998. An extreme cold surge over the Greek peninsula. Q. J. R. Meteorol. Soc. 124 (551), 2299−2327. https://doi.org/10.1002/qj.49712455107.

Lascaratos, A., Roether, W., Nittis, K., Klein, B., 1999. Recent changes in deep water formation and spreading in the eastern Mediterranean Sea: a review. Prog. Oceanogr. 44 (1−3), 5−36. https://doi.org/10.1016/S0079-6611(99)00019-1.

Leaman, K.D., Schott, F., 1991. Hydrographic structure of the convection regime in the Gulf of Lions: winter 1987. J. Phys. Oceanogr. 21, 575−598. https://doi.org/10.1175/1520-0485(1991)021<0575:HSOTCR>2.0.CO;2.

Lenton, T.M., Held, H., Kriegler, E., Hall, J.W., Lucht, W., Rahmstorf, S., Schellnhuber, H.J., 2008. Tipping elements in the Earth's climate system. Proc. Natl. Acad. Sci. USA 105 (6), 1786−1793. https://doi.org/10.1073/pnas.0705414105.

Li, P., Tanhua, T., 2020. Recent changes in deep ventilation of the Mediterranean Sea; evidence from long-term transient tracer observations. Front. Mar. Sci. 7, 1−23. https://doi.org/10.3389/fmars.2020.00594.

Llasses, J., Jordà, G., Gomis, D., 2015. Skills of different hydrographic networks in capturing changes in the Mediterranean Sea at climate scales. Clim. Res. 63, 1−18. https://doi.org/10.3354/cr01270.

López García, M.J., 2015. Recent warming in the Balearic Sea and Spanish Mediterranean coast. Towards an earlier and longer summer. Atmósfera 28 (3), 149−160. https://doi.org/10.20937/ATM.2015.28.03.01.

López-Jurado, J.L., González-Pola, C., Vélez-Belchí, P., 2005. Observation of an abrupt disruption of the long-term warming trend at the Balearic Sea, Western Mediterranean, in summer 2005. Geophys. Res. Lett. 32, L24606. https://doi.org/10.1029/2005GL024430.

Lozier, M.S., Stewart, N.M., 2008. On the temporally varying northward penetration of Mediterranean Overflow Water and eastward penetration of Labrador Sea Water. J. Phys. Oceanogr. 38, 2097−2103.

Lozier, M.S., Sindlinger, L., 2009. On the source of Mediterranean Overflow water property changes. J. Phys. Oceanogr. 39. https://doi.org/10.1175/2009JPO4109.1.

Lozier, M.S., Owens, W.B., Curry, R.G., 1995. The climatology of the north Atlantic. Prog. Oceanogr. 36, 1.

Macías, D.M., García-Gorriz, E., Stips, A., 2013. Understanding the causes of recent warming of Mediterranean waters. How much could be attributed to climate change? PLoS One 8, e81591. https://doi.org/10.1371/journal.pone.0081591.

Malanotte-Rizzoli, P., Manca, B.B., Ribera D'Alcalà, M., Theocharis, A., Bergamasco, A., Bregant, D., Budillon, G., Civitarese, G., Georgopoulos, D., Michelato, A., Sansone, E., Scarazzato, P., Souvermezoglou, E., 1997. A synthesis of the Ionian Sea hydrography, circulation and water mass pathways during POEM-Phase I. Prog. Oceanogr. 39 (3), 153−204. https://doi.org/10.1016/S0079-6611(97)00013-X.

Malanotte-Rizzoli, P., Manca, B.B., D'Alcala, M.R., Theocharis, A., Brenner, S., Budillon, G., Ozsoy, E., 1999. The Eastern Mediterranean in the 80s and in the 90s: the

big transition in the intermediate and deep circulations. Dynam. Atmos. Oceans 29 (2−4), 365−395. https://doi.org/10.1016/S0377-0265(99)00011-1.

Malanotte-Rizzoli, P., Manca, B.B., Marullo, S., Ribera d'Alcalá, M., Roether, W., Theocharis, A., Bergamasco, A., Budillon, G., Sansone, E., Civitarese, G., Conversano, F., Gertman, I., Hernt, B., Kress, N., Kioroglou, S., Kontoyannis, H., Nittis, K., Klein, B., Lascaratos, A., Latif, M.A., Ozsoy, E., Robinson, A.R., Santoleri, R., Viezzoli, D., Kovacevic, V., 2003. The Levantine Intermediate Water Experiment (LIWEX) Group: Levantine basin—a laboratory for multiple water mass formation processes. J. Geophys. Res. Oceans 108 (C9). https://doi.org/10.1029/2002JC001643.

Manca, B.B., Kovaĉević, V., Gaĉić, M., Viezzoli, D., 2002. Dense water formation in the southern Adriatic Sea and spreading into the Ionian Sea in the period 1997−1999. J. Mar. Syst. 33 (34), 133−154. https://doi.org/10.1016/S0924-7963(02)00056-8.

Manca, B.B., Budillon, G., Scarazzato, P., Ursella, L., 2003. Evolution of dynamics in the eastern Mediterranean affecting water mass structures and properties in the Ionian and Adriatic Seas. J. Geophys. Res. Oceans 108 (C9). https://doi.org/10.1029/2002JC001664.

Manca, B.B., Ibello, V., Pacciaroni, M., Scarazzato, P., Giorgetti, A., 2006. Ventilation of deep waters in the Adriatic and Ionian Seas following changes in thermohaline circulation of the Eastern Mediterranean. Clim. Res. 31 (2−3), 239−256. https://doi.org/10.3354/cr031239.

Mantziafou, A., Lascaratos, A., 2004. An eddy resolving numerical study of the general circulation and deep-water formation in the Adriatic Sea. Deep Sea Res. Oceanogr. Res. Pap. 51 (7), 921−952. https://doi.org/10.1016/j.dsr.2004.03.006.

Margirier, F., Testor, P., Heslop, E., Mallil, K., Bosse, A., Houpert, L., Mortier, L., Bouin, M.-N., Coppola, L., D'Ortenzio, F., Mourre, B., Durrieu de Madron, X., Prieur, L., Raimbault, P., Taillandier, V., 2020. Abrupt warming and salinification of intermediate waters interplays with decline of deep convection in the Northwestern Mediterranean Sea. Sci. Rep. 10, 20923. https://doi.org/10.1038/s41598-020-77859-5.

Mariotti, A., Struglia, M.V., Zeng, N., Lau, K.M., 2002. The hydrological cycle in the Mediterranean region and implications for the water budget of the Mediterranean sea. J. Clim. 15, 1674−1690. https://doi.org/10.1175/1520-0442.

Marullo, S., Santoleri, R., Banzon, V., Evans, R.H., Guarracino, M., 2010. A diurnal-cycle resolving sea surface temperature product for the tropical Atlantic. J. Geophys. Res. 115, C05011. https://doi.org/10.1029/2009JC005466.

McCartney, M.S., Mauritzen, C., 2001. On the origin of the warm inflow in the Nordic Sea. Prog. Oceanogr. 51, 125.

McDowell, S.E., Rossby, H.T., 1978. Mediterranean water: an intensive mesoscale eddy off the Bahamas. Science 202, 1085−1087.

MedECC, 2020. Climate and environmental change in the Mediterranean Basin − current situation and risks for the future. First mediterranean assessment report. In: Cramer, W., Guiot, J., Marini, K. (Eds.), Union for the Mediterranean, Plan Bleu. UNEP/MAP, Marseille, France, p. 632. https://doi.org/10.5281/zenodo.4768833.

Menna, M., Suarez, N.C.R., Civitarese, G., Gačić, M., Rubino, A., Poulain, P.-M., 2019. Decadal variations of circulation in the Central Mediterranean and its interactions with mesoscale gyres. Deep Sea Res. Part II Top. Stud. Oceanogr. 164, 14−24. https://doi.org/10.1016/j.dsr2.2019.02.004.

Mihanović, H., Vilibić, I., Carniel, S., Tudor, M., Russo, A., Bergamasco, A., Bubić, N., Ljubešić, Z., Viličić, D., Boldrin, A., Malačič, V., Celio, M., Comici, C., Raicich, F.,

2013. Exceptional dense water formation on the Adriatic shelf in the winter of 2012. Ocean Sci. 9, 561–572. https://doi.org/10.5194/os-9-561-2013.

Millot, C., 2007. Interannual salinification of the Mediterranean inflow. Geophys. Res. Lett. 34. https://doi.org/10.1029/2007GL031179.

Millot, C., 2013. Levantine Intermediate Water characteristics: an astounding general misunderstanding! ; Las características de LIW: un malentendido asombroso. Sci. Mar. 77 (772), 217–232. https://doi.org/10.3989/scimar.03518.13A.

Millot, C., Candela, J., Fuda, J.L., Tber, Y., 2006. Large warming and salinification of the Mediterranean outflow due to changes in its composition. Deep-Sea Res. I 53, 656–665.

Nabat, P., Somot, S., Mallet, M., Senchez-Lorenzo, A., Wild, M., 2014. Contribution of anthropogenic sulfate aerosols to the changing Euro-Mediterranean climate since 1980. Geophys. Res. Lett. 41, 5605–5611. https://doi.org/10.1002/2014GL060798.

Nagy, H., Di Lorenzo, E., El-Gindy, A., 2019. The impact of climate change on circulation patterns in the Eastern Mediterranean Sea upper layer using Med-ROMS model. Prog. Oceanogr. 175, 226–244. https://doi.org/10.1016/j.pocean.2019.04.012.

Naranjo, C., Sammartino, S., García-Lafuente, J., Bellanco, M.J., Taupier-Letage, I., 2015. Mediterranean waters along and across the Strait of Gibraltar, characterization and zonal modification. Deep Sea Res. Part I 105, 41–52. https://doi.org/10.1016/j.dsr.2015.08.003.

Naranjo, C., García-Lafuente, J., Sammartino, S., Sánchez-Garrido, J.C., Sánchez-Leal, R., Jesús Bellanco, M., 2017. Recent changes (2004–2016) of temperature and salinity in the Mediterranean outflow. Geophys. Res. Lett. 44, 5665–5672. https://doi.org/10.1002/2017GL072615.

Nielsen, J.N., 1912. Hydrography of the Mediterranean and adjacent waters. Report on the Danish Oceanographical Expeditions 1908–1910 to the Mediterranean and Adjacent Seas, I, pp. 72–191.

Nittis, K., Lascaratos, A., 1998. Diagnostic and prognostic numerical studies of LIW formation. J. Mar. Syst. 18 (1–3), 179–195. https://doi.org/10.1016/S0924-7963(98)00011-6.

Nittis, K., Lascaratos, A., Theocharis, A., 2003. Dense water formation in the Aegean Sea: numerical simulations during the eastern mediterranean transient. J. Geophys. Res. Oceans 108 (C9). https://doi.org/10.1029/2002JC001352.

Nof, D., 1982. On the movement of deep mesoscale eddies in the North Atlantic. J. Mar. Res. 40, 57.

Nykjaer, L., 2009. Mediterranean Sea surface warming 1985–2006. Clim. Res. 39, 11–17. https://doi.org/10.3354/cr00794.

Orlić, M., Dadić, V., Grbec, B., Leder, N., Marki, A., Matić, F., Mihanović, H., Beg Paklar, G., Pasarić, M., Pasarić, Z., Vilibić, I., 2007. Wintertime buoyancy forcing, changing seawater properties, and two different circulation systems produced in the Adriatic. J. Geophys. Res. 112 (C3), C03S07. https://doi.org/10.1029/2005JC003271.

Ovchinikov, I., 1966. Circulation in the surface and intermediate layers of the Mediterrarean. Oceanology 6 (1), 48–58.

Ozer, T., Gertman, I., Kress, N., Silverman, J., Herut, B., 2017. Interannual thermohaline (1979–2014) and nutrient (2002–2014) dynamics in the Levantine surface and intermediate water masses, SE Mediterranean Sea. Global Planet. Change 151, 60–67. https://doi.org/10.1016/j.gloplacha.2016.04.001.

Ozer, T., Gertman, I., Gildor, H., Goldman, R., Herut, B., 2020. Evidence for recent thermohaline variability and processes in the deep water of the Southeastern Levantine Basin,

Mediterranean Sea. Deep Sea Res. Part II Top. Stud. Oceanogr. 171, 104651. https://doi.org/10.1016/j.dsr2.2019.104651.

Painter, S.C., Tsimplis, M.N., 2003. Temperature and salinity trends in the upper waters of the Mediterranean Sea as determined from MEDATLAS data set. Continent. Shelf Res. 23, 1507–1522. https://doi.org/10.1016/j.csr.2003.08.008.

Pastor, F., Valiente, J.A., Palau, J.L., 2018. Sea surface temperature in the Mediterranean: trends and spatial patterns (1982–2016). Pure Appl. Geophys. 175, 4017–4029. https://doi.org/10.1007/s00024-017-1739-z.

Pinardi, N., Zavatarelli, M., Adani, M., Coppini, G., Fratianni, C., Oddo, P., Simoncelli, S., Tonan, M.I., Lyubartsev, V., Dobricic, S., Bonaduce, A., 2015. Mediterranean Sea large-scale low-frequency ocean variability and water mass formation rates from 1987 to 2007: a retrospective analysis. Prog. Oceanogr. 132, 318–332. https://doi.org/10.1016/j.pocean.2013.11.003.

Pisacane, G., Artale, V., Calmanti, S., Rupolo, V., 2006. Decadal oscillations in the Mediterranean Sea: a result of the overturning circulation variability in the eastern basin? Clim. Res. 31 (2–3), 257–271. https://doi.org/10.3354/cr031257.

Pisano, A., Marullo, S., Artale, V., Falcini, F., Yang, C., Leonelli, F., Santoleri, R., Nardelli, B.B., 2020. New evidence of mediterranean climate change and variability from sea surface temperature observations. Rem. Sens. 12 (1), 1–18. https://doi.org/10.3390/rs12010132.

Pollak, M.J., 1951. The sources of the deep water of the eastern Mediterranean Sea. J. Mar. Res. 10 (1), 128–152.

Poulain, P.-M., Menna, M., Mauri, E., 2012. Surface geostrophic circulation of the Mediterranean Sea derived from drifter and satellite altimeter data. J. Phys. Oceanogr. 42 (6), 973–990. https://doi.org/10.1175/JPO-D-11-0159.1.

Rahmstorf, S., 1998. Influence of mediterranean outflow on climate. Eos Trans. AGU 79 (24), 281–282. https://doi.org/10.1029/98EO00208.

Reale, M., Crise, A., Farneti, R., Mosetti, R., 2016. A process study of the Adriatic-Ionian System baroclinic dynamics. J. Geophys. Res. Oceans 121 (8), 5872–5887. https://doi.org/10.1002/2016JC011763.

Reale, M., Salon, S., Crise, A., Farneti, R., Mosetti, R., Sannino, G., 2017. Unexpected covariant behavior of the aegean and Ionian seas in the period 1987–2008 by means of a nondimensional sea surface height index. J. Geophys. Res. Oceans 122 (10), 8020–8033. https://doi.org/10.1002/2017JC012983.

Reid, J., 1979. On the contribution of the Mediterranean Sea outflow to the Norwegian-Greenland sea. Deep Sea Res. 26, 1199.

Richardson, P.L., Bower, A.S., Zenk, W., 2000. A census of Meddies tracked by floats. Prog. Oceanogr. 45 (2), 209–250.

Rixen, M., Beckers, J.M., Levitus, S., Antonov, J., Boyer, T., Maillard, C., Fichaut, M., Balopoulos, E., Iona, S., Dooley, H., Grcía, M.J., Manca, B.B., Giorgetti, A., Manzella, G., Mikhailov, N., Pinardi, N., Zavatarelli, M., 2005. The western mediterranean deep water: a proxy for climate change. Geophys. Res. Lett. 32. https://doi.org/10.1029/2005GL022702.

Rivetti, I., Boero, F., Fraschetti, S., Zambianchi, E., Lionello, P., 2017. Anomalies of the upper water column in the Mediterranean Sea. Glob. Planet. Change 151, 68–79. https://doi.org/10.1016/j.gloplacha.2016.03.001.

Robinson, A.R., Leslie, W.G., Theocharis, A., Lascaratos, A., 2001. Mediterranean Sea Circulation. Encyclopedia of Ocean Sciences, pp. 1689–1705. https://doi.org/10.1006/rwos.2001.0376.

Roether, W., Manca, B.B., Klein, B., Bregant, D., Georgopoulos, D., Beitzel, V., Kovačević, V., Luchetta, A., 1996. Recent changes in eastern mediterranean deep waters. Science 271 (5247), 333–335. https://doi.org/10.1126/science.271.5247.333.

Roether, W., Klein, B., Manca, B.B., Theocharis, A., Kioroglou, S., 2007. Transient Eastern Mediterranean deep waters in response to the massive dense-water output of the Aegean Sea in the 1990s. Prog. Oceanogr. 74 (4), 540–571. https://doi.org/10.1016/j.pocean.2007.03.001.

Rohling, E.J., Bryden, H.L., 1992. Man-induced salinity and temperature increase in western mediterranean deep water. J. Geophys. Res. 97 (C7), 11191–11198. https://doi.org/10.1029/92JC00767.

Romanou, A., Tselioudis, G., Zerefos, C.S., Clayson, C.A., Curry, J.A., Andersson, A., 2010. Evaporation-precipitation variability over the mediterranean and the black seas from satellite and reanalysis estimates. J. Clim. 23 (19), 5268–5287. https://doi.org/10.1175/2010JCLI3525.1.

Rubino, A., Hainbucher, D., 2007. A large abrupt change in the abyssal water masses of the eastern Mediterranean. Geophys. Res. Lett. 34 (23), 1–5. https://doi.org/10.1029/2007GL031737.

Salat, J., Emelianov, M., Puig, P., 2009. From bottom water (Lacombe, 1985) to new-WMDW since 2005. Possible shifts on open sea deep convection. En CIESM, 2009. In: Briand, F. (Ed.), Dynamics of Mediterranean Deep Waters. CIESM Workshop Monographs, N°38. CIESM Publisher, Monaco, p. 132.

Sannino, G.M., Bargagli, A., Artale, V., 2002. Numerical modeling of the mean exchange through the Strait of Gibraltar. J. Geophys. Res. C 107 (C8). https://doi.org/10.1029/2001JC000929.

Sannino, G., Carillo, A., Artale, V., 2007. Three-layer view of transports and hydraulics in the Strait of Gibraltar: a three-dimensional model study. J. Geophys. Res. Oceans 112 (C3), C03010. https://doi.org/10.1029/2006JC003717.

Sarafanov, A., Falina, A., Sokov, A., Demidov, A., 2008. Intense warming and salinification of intermediate waters of southern origin in the eastern subpolar North Atlantic in the 1990s to mid-2000s. J. Geophys. Res. 113, C12022. https://doi.org/10.1029/2008JC004975.

Sayin, E., Eronat, C., Uçkaç, Ş., Beşiktepe, Ş.T., 2011. Hydrography of the eastern part of the aegean sea during the eastern mediterranean transient (EMT). J. Mar. Syst. 88 (4), 502–515. https://doi.org/10.1016/j.jmarsys.2011.06.005.

Schlitzer, R., Roether, W., Oster, H., Junghans, H.-G., Hausmann, M., Johannsen, H., Michelato, A., 1991. Chlorofluoromethane and oxygen in the eastern mediterranean. Deep Sea Res. Part A Oceanogr. Res. Pap. 38 (12), 1531–1551. https://doi.org/10.1016/0198-0149(91)90088-W.

Schmidtko, S., Johnson, G.C., Lyman, J.M., 2013. MIMOC: a global monthly isopycnal upper-ocean climatology with mixed layers. J. Geophys. Res. 118, 1658–1672. https://doi.org/10.1002/jgrc.20122.

Schroeder, K., et al., 2008. An extensive western Mediterranean Deep Water renewal between 2004 and 2006. Geophys. Res. Lett. 35, L18605.

Schroeder, K., 2019. Current systems in the Mediterranean Sea. In: Cochran, J.K., Bokuniewicz, J.H., Yager, L., Patricia (Eds.), Encyclopedia of Ocean Sciences, third ed., vol. 3. Elsevier, pp. 219–227. ISBN: 978-0-12-813081-0.

Schroeder, K., Gasparini, G.P., Tangherlini, M., Astraldi, M., 2006. Deep and intermediate water in the western mediterranean under the influence of the eastern mediterranean transient. Geophys. Res. Lett. 33 (21), L21607. https://doi.org/10.1029/2006GL027121.

Schroeder, K., Josey, S.A., Hermann, M., Grignon, L., Gasparini, G.P., Bryden, H.L., 2010. Abrupt warming and salting of the western mediterranean deep water after 2005: atmospheric forcing and lateral advection. J. Geophys. Res. 115, C08029. https://doi.org/10.1029/2009JC005749.

Schroeder, K., Millot, C., Bengara, L., Ben Ismail, S., Bensi, M., Borghini, M., Budillon, G., Cardin, V., Coppola, L., Curtil, C., Drago, A., El Moumni, B., Font, J., Fuda, J.L., García-Lafuente, J., Gasparini, G.P., Kontoyiannis, H., Lefevre, D., Puig, P., Raimbault, P., Rougier, G., Salat, J., Sammari, C., Sánchez Garrido, J.C., Sanchez-Roman, A., Sparnocchia, S., Tamburini, C., Taupier-Letage, I., Theocharis, A., Vargas-Yáñez, M., Vetrano, A., 2013. Long-term monitoring programme of the hydrological variability in the Mediterranean Sea: a first overview of the HYDROCHANGES network. Ocean Sci. 9, 301–324. https://doi.org/10.5194/os-9-301-2013.

Schroeder, K., Tanhua, T., Bryden, H.L., Álvarez, M., Chiggiato, J., Aracri, S., 2015. Mediterranean sea ship-based hydrographic investigations program (Med-SHIP). Oceanography 28 (3), 12–15. https://doi.org/10.5670/oceanog.2015.71.

Schroeder, K., Chiggiato, J., Bryden, H.L., Borghini, M., Ismail, S.B., 2016. Abrupt climate shift in the western Mediterranean Sea. Sci. Rep. 6, 23009. https://doi.org/10.1038/srep23009.

Schroeder, K., Chiggiato, J., Josey, S.A., Borghini, M., Aracri, S., Sparnocchia, S., 2017. Rapid response to climate change in a marginal sea. Sci. Rep. 7, 4065. https://doi.org/10.1038/s41598-017-04455-5.

Schroeder, K., Cozzi, S., Belgacem, M., Borghini, M., Cantoni, C., Durante, S., Petrizzo, A., Poiana, A., Chiggiato, J., 2020. Along-path evolution of biogeochemical and carbonate system properties in the intermediate water of the western mediterranean. Front. Mar. Sci. 7, 375. https://doi.org/10.3389/fmars.2020.00375.

Sevault, F., Somot, S., Alias, A., Dubois, C., Lebeaupin Brossier, C., Nabat, P., Adloff, F., Déqué, M., Decharme, B., 2014. A fully coupled Mediterranean regional climate system model: design and evaluation of the ocean component for the 1980–2012 period. Tellus 66. https://doi.org/10.3402/tellusa.v66.23967.

Skliris, N., Lascaratos, A., 2004. Impacts of the Nile River damming on the thermohaline circulation and water mass characteristics of the Mediterranean Sea. J. Mar. Syst. 52 (1–4), 121–143. https://doi.org/10.1016/j.jmarsys.2004.02.005.

Skliris, N., Sofianos, S., Lascaratos, A., 2007. Hydrological changes in the Mediterranean Sea in relation to changes in the freshwater budget: a numerical modelling study. J. Mar. Syst. 65, 400–416. https://doi.org/10.1016/j.jmarsys.2006.01.015.

Skliris, N., Sofianos, S.S., Gkanasos, A., Mantziafou, A., Versatis, V., Axaopoulos, P., Lascaratos, A., 2012. Decadal scale variability of sea surface temperature in the Mediterranean Sea in relation to atmospheric variability. Ocean Dynam. 62 (1), 13–30. https://doi.org/10.1007/s10236-011-0493-5.

Skliris, N., Zika, J.D., Herold, L., Josey, S.A., Marsh, R.A., 2018. Mediterranean sea water budget long-term trend inferred from salinity observations. Clim. Dynam. 51, 2857–2876. https://doi.org/10.1007/s00382-017-4053-7.

Smith, R.O., Bryden, H.L., Stansfield, K., 2008. Observations of new western Mediterranean deep water formation using Argo floats 2004–2006. Ocean Sci. 4, 133–149. https://doi.org/10.5194/os-4-133-2008.

Somot, S., Sevault, F., Déqué, M., 2006. Transient climate change scenario simulation of the Mediterranean Sea for the twenty-first century using a high-resolution ocean circulation model. Clim. Dynam. 27, 851–879. https://doi.org/10.1007/s00382-006-0167-z.

Soto-Navarro, J., Criado-Aldeanueva, F., Sánchez-Garrido, J.C., García-Lafuente, J., 2012. Recent thermohaline trends of the Atlantic waters inflowing to the Mediterranean Sea. Geophys. Res. Lett. 39 (1).

Soto-Navarro, J., Jordá, G., Amores, A., Cabos, W., Somot, S., Sevault, F., Macías, D., Djurdjevic, V., Sannino, G., Li, L., Sein, D., 2020. Evolution of Mediterranean Sea water properties under climate change scenarios in the Med-CORDEX ensemble. In: Climate Dynamics, vol. 54. https://doi.org/10.1007/s00382-019-05105-4.

Spall, M.A., 1999. A simple model of the large-scale circulation of Mediterranean water and Labrador Sea water. Deep-Sea Res. 46, 181.

Sparnocchia, S., Manzella, G.M.R., La Violette, P.E., 1994. The interannual and seasonal variability of the MAW and LIW core properties in the Western Mediterranean Sea. In: La Violette, P.E. (Ed.), Seasonal and Interannual Variability of the Western Mediterranean. Coastal and Estuarine Studies. American Geophysical Union, Washington.

Sparrow, M., Boebel, O., Zervakis, V., Zenk, W., Cantos-Figuerola, A., Gould, W.J., 2002. Two circulation regimes of the Mediterranean outflow revealed by Lagrangian measurements. J. Phys. Oceanogr. 32 (5), 1322–1330.

Stommel, H., Bryden, H., Mangelsd, P., 1973. Does some of Mediterranean outflow come from great depth? Pure Appl. Geophys. 105 (4), 879–889.

Sur, H.I., Ozsoy, E., Unluata, U., 1992. Simultaneous deep and intermediate depth convection in the northern Levantine Sea, winter 1992. Oceanol. Acta 16, 33–43.

Sverdrup, H.U., Johnson, M.W., Fleming, R.H., 1942. The Oceans, Their Physics, Chemistry, and General Biology. Prentice Hall, New York, p. 1087.

Testor, P., Durrieu de Madron, X., Mortier, L., D'Ortenzio, F., Legoff, H., Dausse, D., Labaste, M., Houpert, L., 2020. Lion Observatory Data. SEANOE. https://doi.org/10.17882/44411.

Theocharis, A., Georgopoulos, D., 1993. Dense water formation over the Samothraki and Limnos Plateaux in the North Aegean Sea (eastern Mediterranean Sea). Continent. Shelf Res. 13 (8), 919–939. https://doi.org/10.1016/0278-4343(93)90017-R.

Theocharis, A., Georgopoulos, D., Lascaratos, A., Nittis, K., 1993. Water masses and circulation in the central region of the Eastern Mediterranean. Deep-Sea Res. II 40 (6), 1121–1142.

Theocharis, A., Nittis, K., Kontoyiannis, H., Papageorgiou, E., Balopoulos, E., 1999a. Climatic changes in the Aegean Sea influence the eastern Mediterranean thermocline circulation (1986–1997). Geophys. Res. Lett. 26 (11), 1617–1620. https://doi.org/10.1029/1999GL900320.

Theocharis, A., Balopoulos, E., Kioroglou, S., Kontoyiannis, H., Iona, A., 1999b. A synthesis of the circulation and hydrography of the south Aegean Sea and the straits of the Cretan arc (March 1994–January 1995). Prog. Oceanogr. 44 (4), 469–509. https://doi.org/10.1016/S0079-6611(99)00041-5.

Theocharis, A., Klein, B., Nittis, K., Roether, W., 2002. Evolution and status of the eastern mediterranean transient (1997–1999). J. Mar. Syst. 33–34, 91–116. https://doi.org/10.1016/S0924-7963(02)00054-4.

Theocharis, A., Krokos, G., Velaoras, D., Korres, G., 2014. An internal mechanism driving the alternation of the eastern mediterranean dense/deep water sources. In: The Mediterranean

Sea: Temporal Variability and Spatial Patterns, pp. 113–137. https://doi.org/10.1002/9781118847572.ch8.

Vargas-Yáñez, M., Moya, F., Tel, E., García-Martínez, M.C., Guerber, E., Bourgeon, M., 2009. Warming and salting in the Western Mediterranean during the second half of the 20th century: inconsistencies, unknowns and the effect of data processing. Sci. Mar. 73 (1). https://doi.org/10.3989/scimar.2009.73n1007.

Vargas-Yáñez, M., Zunino, P., Benali, A., Delpy, M., Pastre, F., García-Martínez, M.C., Tel, E., 2010a. How much is the Western Mediterranean really warming and salting? J. Geophys. Res. 115, C04001. https://doi.org/10.1029/2009JC005816.

Vargas-Yáñez, M., Moya, F., García-Martínez, M.C., Tel, E., Zunino, P., Plaza, F., Salat, J., Pascual, J., López-Jurado, J.L., Serra, M., 2010b. Climate change in the western Mediterranean Sea 1900–2008. J. Mar. Syst. 82, 171–176. https://doi.org/10.1016/j.jmarsys.2010.04.013.

Vargas-Yáñez, M., Mallard, E., Rixen, M., Zunino, P., García-Martínez, M.C., Moya, F., 2012. The effect of interpolation methods in temperature and salinity trends in the Western Mediterranean. Mediterr. Mar. Sci. 13/1, 118–125. https://doi.org/10.12681/mms.28.

Vargas-Yáñez, M., García-Martínez, M.C., Moya, F., Balbín, R., López-Jurado, J.L., Serra, M., Zunino, P., Pascual, J., Salat, J., 2017. Updating temperature and salinity climatologies and trends in the Western Mediterranean: RADMED project. 2017. Prog. Oceanogr. 157, 27–46. https://doi.org/10.1016/j.pocean.2017.09.004.

Velaoras, D., Lascaratos, A., 2010. North-Central Aegean Sea surface and intermediate water masses and their role in triggering the Eastern Mediterranean Transient. J. Mar. Syst. 83 (1–2), 58–66. https://doi.org/10.1016/j.jmarsys.2010.07.001.

Velaoras, D., Kassis, D., Perivoliotis, L., Pagonis, P., Hondronasios, A., Nittis, K., 2013. Temperature and salinity variability in the Greek seas based on POSEIDON stations time series: preliminary results. Mediterr. Mar. Sci. 14 (3), 5–18. https://doi.org/10.12681/mms.446.

Velaoras, D., Krokos, G., Nittis, K., Theocharis, A., 2014. Dense intermediate water outflow from the Cretan Sea: a salinity driven, recurrent phenomenon, connected to thermohaline circulation changes. J. Geophys. Res. Oceans 119 (8), 4797–4820. https://doi.org/10.1002/2014JC009937.

Velaoras, D., Krokos, G., Theocharis, A., 2015. Recurrent intrusions of transitional waters of Eastern Mediterranean origin in the Cretan Sea as a tracer of Aegean Sea dense water formation events. Prog. Oceanogr. 135, 113–124. https://doi.org/10.1016/j.pocean.2015.04.010.

Velaoras, D., Papadopoulos, V.P., Kontoyiannis, H., Cardin, V., Civitarese, G., 2019. Water masses and hydrography during April and June 2016 in the Cretan Sea and Cretan passage (eastern Mediterranean Sea). Deep-Sea Res. Part II Top. Stud. Oceanogr. 164, 25–40. https://doi.org/10.1016/j.dsr2.2018.09.005.

Vilibić, I., Zemunik, P., Dunić, N., Mihanović, H., 2020. Local and remote drivers of the observed thermohaline variability on the northern Adriatic shelf (Mediterranean Sea). Continent. Shelf Res. 199. https://doi.org/10.1016/j.csr.2020.104110. December 2019.

von Schuckmann, K., Le Traon, P.Y., Smith, N., Pascual, A., Brasseur, P., Fennel, K., Djavidnia, S., et al., 2018. Copernicus marine Service ocean state report. J. Oper. Oceanogr. 11 (Suppl. 1), S1–S142. https://doi.org/10.1080/1755876X.2018.1489208.

von Schuckmann, K., Le Traon, P.Y., Smith, N., Pascual, A., Djavidnia, S., Gattuso, J.P., Zuo, H., 2019. Copernicus marine Service ocean state report, issue 3. J. Oper. Oceanogr. 12 (Suppl. 1), S1–S123. https://doi.org/10.1080/1755876X.2019.1633075.

von Schuckmann, K., Le Traon, P.-Y., Smith, N., Pascual, A., Djavidnia, S., Gattuso, J.-P., Grégoire, M. (Eds.), 2021. Copernicus Marine Service Ocean State Report, Issue 5, Journal of Operational Oceanography, vol. 14, pp. s1−s185. https://doi.org/10.1080/1755876X.2021.1946240. Suppl. 1.

Waldman, R., Brüggemann, N., Bosse, A., Spall, M., Somot, S., Sevault, F., 2018. Overturning the mediterranean thermohaline circulation. Geophys. Res. Lett. 45 (16), 8407−8415. https://doi.org/10.1029/2018GL078502.

Worthington, L.V., 1976. On the North Atlantic Circulation. Oceanographic Studies, vol. 6. The John Hopkins University, p. 110.

Zervakis, V., Georgopoulos, D., Drakopoulos, P.G., 2000. The role of the North Aegean in triggering the recent Eastern Mediterranean climatic changes. J. Geophys. Res. Oceans 105 (C11), 26103−26116. https://doi.org/10.1029/2000jc900131.

Zodiatis, G., 1991. Water masses and deep convection in the Cretan Sea during late winter 1987. Ann. Geophys. 9, 367−376.

Zodiatis, G., Gasparini, G.P., 1996. Thermohaline staircase formations in the Tyrrhenian Sea. Deep Sea Res. Part I 43 (5), 655−678. https://doi.org/10.1016/0967-0637(96)00032-5.

Zore-Armanda, M., 1963. Les masses d'eau de la mer Adriatique. Acta Adriat. 10 (3), 5−88.

Zuo, H., Balmaseda, M.A., Mogensen, K., Tietsche, S., 2018. OCEAN5: The ECMWF Ocean Reanalysis System and its Real-Time Analysis Component. European Centre for Medium Range Weather Forecasts, p. 44.

Zuo, H., Balmaseda, M.A., Tietsche, S., Mogensen, K., Mayer, M., 2019. The ECMWF operational ensemble reanalysis−analysis system for ocean and sea ice: a description of the system and assessment. Ocean Sci. 15, 779−808. https://doi.org/10.5194/os-15-779-2019.

Zweng, M.M., Reagan, J.R., Antonov, J.I., Locarnini, R.A., Mishonov, A.V., Boyer, T.P., Garcia, H.E., Baranova, O.K., Johnson, D.R., Seidov, D., Biddle, M.M., 2013. world ocean Atlas 2013, volume 2: salinity. In: Levitus, S., Mishonov Technical, A. (Eds.), NOAA Atlas NESDIS, vol. 74, p. 39.

CHAPTER

Mediterranean observing and forecasting systems 10

Baptiste Mourre[1], Emanuela Clementi[2], Giovanni Coppini[3], Laurent Coppola[4], Gerasimos Korres[5], Antonio Novellino[6], Enrique Alvarez-Fanjul[7,12], Pierre Daniel[8], George Zodiatis[9], Katrin Schroeder[10], Joaquín Tintoré[1,11]

[1]SOCIB, Balearic Islands Coastal Observing and Forecasting System, Palma, Spain; [2]CMCC, Centro Euro-Mediterraneo sui Cambiamenti Climatici, Ocean Modelling and Data Assimilation, Bologna, Italy; [3]CMCC, Centro Euro-Mediterraneo sui Cambiamenti Climatici, Ocean Predictions and Applications, Lecce, Italy; [4]Sorbonne Université, CNRS, Laboratoire d'Océanographie de Villefranche, France; [5]Hellenic Centre for Marine Research, Attiki, Greece; [6]ETT Solutions, Genova, Italy; [7]Puertos del Estado, Madrid, Spain; [8]Météo-France, Toulouse, France; [9]ORION Joint Research and Development Center, Nicosia, Cyprus; [10]Consiglio Nazionale delle Ricerche-Istituto di Scienze Marine (CNR-ISMAR), Venezia, Italy; [11]IMEDEA, CSIC-UIB, Carrer de Miquel Marquès, Esporles, Spain; [12]Mercator Ocean International, Toulouse, France

Learning Objectives

In this Chapter, you will learn about:

- What are the characteristics of the observing systems deployed in the Mediterranean Sea
- Which are the associated international coordination programs
- Where are the regional multi-platform observatories
- What are the concepts behind and examples of ocean forecasting systems
- How do the data management and distribution procedures work
- Which are some of the recent applications of these integrated observing and forecasting systems

10.1 The emergence of operational oceanography in the Mediterranean Sea

While the very first ocean density measurements at referred geographic positions and times were collected back in years 1679–80 along the route from Venice to Bosporus (Pinardi et al., 2018), the comprehensive oceanographic exploration of the Mediterranean Sea only really started at the beginning of the 20th century (Schmidt, 1912). After decades of significant developments of ocean observational programs including in situ campaigns, fixed station monitoring and satellite remote sensing (see Chapter 1), an important paradigm shift affected ocean observations at the beginning of the 21st century, coinciding with the emergence of the concept of

Oceanography of the Mediterranean Sea. https://doi.org/10.1016/B978-0-12-823692-5.00001-7

operational oceanography (i.e., a service of real-time ocean products similar to the meteorological services for the weather, Schiller et al., 2018). New ocean monitoring technologies combined with the development of internet network connections have allowed a transition from single-ship campaigns often collecting confidential data, to multiplatform systems including a variety of instruments providing open data with a near-real time availability (Tintoré et al., 2013, 2019). Data assembly centers constitute a new essential element of these systems, allowing to collect, standardize, archive and distribute the observations not only from satellites, but also from fixed stations, research vessel (RV), drifting buoys, autonomous profilers, or underwater gliders. This enabled new possibilities to characterize the ocean dynamics from the basin to the coastal scales. In 2002, the scientific community started to get organized to establish a Mediterranean Operational Oceanography Network (MOON) in order to join efforts and develop a strategic plan for the expansion of operational oceanography systems enabling improved environmental predictions. Regional observatories implementing long-term monitoring programs based on multiplatform systems were settled in the 2000s and early 2010s. POSEIDON in Greece, the Mediterranean Ocean Observing System for the Environment (MOOSE) in France and the Balearic Islands Coastal Observing and Forecasting System (SOCIB) in Spain provide three examples which will be described in more details in this chapter. Implemented and maintained in the framework of these new regional observatories, underwater glider endurance lines illustrate this observational breakthrough, providing new high-resolution and repeated sampling in key oceanic sections of the Mediterranean Sea (Heslop et al., 2012; Margirier et al., 2020). Since 2012, MOON coordination efforts are pursued in the framework of the Mediterranean Operational Network for the Global Ocean Observing System (MONGOOS[1]).

The development of observing systems was accompanied by that of numerical modeling and prediction systems. Numerical models are complementary tools for oceanographic research, allowing to better understand dynamical processes and generate predictions. From the 1980s, they have also been used to analyze the Mediterranean Sea circulation and its variability and identify the role of its different drivers including winds, topography, Gibraltar inflow or heat fluxes. Finizio et al. (1972), Tomasin (1973) and Robinson et al. (1973) developed the first prediction models for the flooding in Venice. A few years later, Hendershott and Rizzoli (1976) provided the first modeling results on the circulation of the Adriatic Sea, and Preller and Hurlburt (1982) started implementing models to investigate the dynamics of the Alboran Sea. The late 1980s and the 1990s were periods with significant advances in model developments, with both regionally-focused studies and whole basin representations. All this work paved the way for the development of the first basin-scale operational model. The first ocean forecast of the Mediterranean Forecasting System was produced in January 2000, providing for the first time regular and publicly available 10-day predictions of ocean conditions over the

[1] http://www.mongoos.eu/.

Mediterranean Sea with a spatial resolution of 7 km (Pinardi et al., 2003). The model was further developed incorporating different levels of complexity, and finally integrated into the Copernicus Marine Environment Monitoring Service (CMEMS[2]) in 2015. Through the provision of the necessary boundary conditions, it enabled the implementation of higher resolution relocatable predictive models in different areas of interest (e.g., Lermusiaux 1999; Onken et al., 2008), as well as other Mediterranean downscaled forecasting systems (Umgiesser et al., 2018), which also take advantage of the continuous increase of high-performance computing capabilities.

A common characteristic of these forecasting systems is their capacity to integrate the near-real-time information from multiplatform observations through so-called data assimilation techniques. These approaches allow to constrain the model initial states at regular intervals to be as consistent as possible with the available observations, preventing the model from undesirable drifts. The gain in the realism of high-resolution model simulations and predictions in the recent decades has been opening a new horizon for scientific and societal applications. The analysis of the dispersion of fish larvae, the response to oil spill emergencies, the evaluation of the risk associated with the deployment of offshore platforms, and the support of maritime search and rescue operations are among the most significant examples.

10.2 The framework for ocean observing and the essential ocean variables

The increasing demand of scientific information for ocean governance and management has pushed scientists to build international coordination frameworks for ocean observations so as to be able to meet the challenges of delivering ocean products and services deriving in societal benefit. During the 20th century, largely independent observing systems have evolved to meet the needs of particular disciplines and end users—the majority of these measuring ocean physics. It then became evident that the scopes of observing networks needed to be extended to include ocean geochemistry and biology, and to break down barriers between open-ocean and coastal observing systems. Over the 2010–2020 decade, the Global Ocean Observing System (GOOS, established in 1991 by the Member States of the IOC[3]-UNESCO) and its partners have worked in this direction (Tanhua et al., 2019), and eventually published the GOOS 2030 Strategy. This publication, expanding the concepts previously published in the Framework for Ocean Observing (FOO, Lindstrom et al., 2012), provides a guideline for requirements, readiness of technologies, and usefulness of data and data products for different kinds of end users (see the schematic in Fig. 10.1), also with the aim of supporting observations for operational forecasting systems.

[2] https://marine.copernicus.eu/.
[3] Intergovernmental Oceanographic Commission.

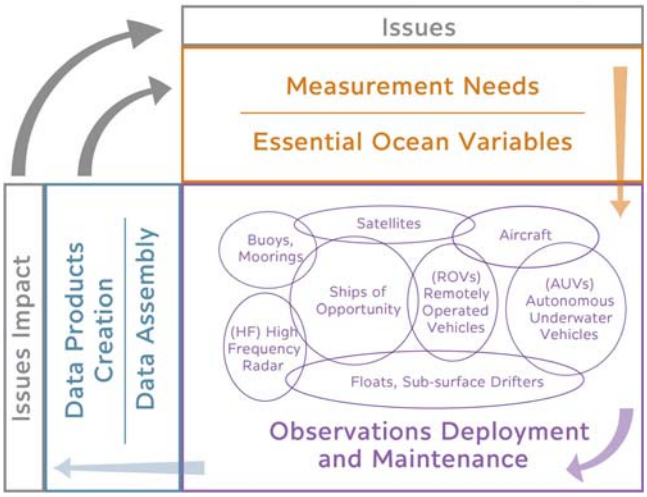

FIGURE 10.1

Overview of the key elements in the Framework of Ocean Observing (FOO), tracing the path from Inputs (e.g., Essential Ocean Variables), to Processes (observations and maintenance), to Outputs (data and data products).

From Tanhua, T., McCurdy, A., Fischer, A., Appeltans, W., Bax, N., Currie, K., et al., 2019. What we have learned from the framework for ocean observing: evolution of the Global Ocean observing system. Front. Mar. Sci. 6, 471. doi:10.3389/fmars.2019.00471.

Within this framework, Essential Ocean Variables (EOVs) have been identified to describe and communicate the "essential" requirements for sustained ocean observations (Sloyan et al., 2019). Three GOOS panels have been created to focus on the development of EOVs for Physics, Biogeochemistry and Biology and Ecosystems. The priority EOVs defined by these panels are listed in Table 10.1. While the technology for synoptic and/or automatic biological observations has lagged behind physical and biogeochemical measurements, the integration of these EOVs into sustained observing systems is now occurring following the FOO guidelines (Muller-Karger et al., 2018). Notice that the key ocean processes that need to be monitored by measuring the EOVs occur over a very wide range of spatial and temporal scales, thus requiring multiple observing platforms with different sampling characteristics.

10.3 Observing systems operating in the Mediterranean Sea

The Mediterranean Sea is presently regularly monitored by complementary systems combining satellite information, land-based remote sensing measurements and in-situ observations from field campaigns, fixed stations and autonomous platforms. Both global and regional observation programs have been necessary to implement these systems and will remain essential for their sustainability.

Table 10.1 GOOS Essential Ocean Variables (EOVs), which have been defined by using criteria of Relevance, Feasibility, and Cost-Effectiveness. The last column lists some of the key ocean processes that need to be captured by the EOVs.

Essential ocean variables			
Physics	**Biogeochemistry**	**Biology and ecosystems**	**Key ocean processes**
Sea state Ocean surface stress Sea ice Sea surface height Sea surface temperature Subsurface temperature Surface currents Subsurface currents Sea surface salinity Subsurface salinity Ocean surface heat flux	Oxygen Nutrients Inorganic carbon Transient tracers Particulate matter Nitrus oxide Stable C isotopes Dissolved organic C	Phytoplankton biomass and diversity Zooplankton biomass and diversity Fish abundance and distribution Marine turtles, birds, mammals abundance and distribution Hard coral cover and composition Seagrass cover and composition Macroalgal canopy cover and composition Mangrove cover and composition Microbe biomass and diversity (emerging) Invertebrate abundance and distribution (emerging)	Heat storage Salt storage Water mass properties Ocean circulation Sea level Fronts and eddies Stratification Mixed layer Sea ice Air-sea fluxes Upwelling Coastal processes Tides Riverine input Surface waves Near inertial oscillations Extreme events (i.e., marine heatwaves, tsunamis, cyclones, storms) Acidification Primary production Deoxygenation …
Cross-disciplinary (including human impact)			
Ocean sound Ocean color Marine debris (emerging)			

Adapted from Tanhua, T., McCurdy, A., Fischer, A., Appeltans, W., Bax, N., Currie, K., et al., 2019. What we have learned from the framework for ocean observing: evolution of the Global Ocean observing system. Front. Mar. Sci. 6, 471. doi:10.3389/fmars.2019.00471 and Sloyan, B.M., Wilkin, J., Hill, K.L., Chidichimo, M.P., Cronin, M.F., Johannessen, J.A., et al., 2019. Evolving the physical Global Ocean observing system for research and application services through international coordination. Front. Mar. Sci. 6, 449. doi:10.3389/fmars.2019.00449.

10.3.1 Satellites

Since the late 1970s, satellites have demonstrated to be an essential source of surface ocean observations providing very valuable contributions to understand ocean dynamics and constrain and validate numerical models. Taking advantage of the remote sensing capability of both passive radiometers and active radar sensors,

which either directly measure the radiation emitted by the ocean surface or the properties of the signals reflected on it, satellites provide routine measurements of the elevation, temperature, salinity and roughness of the sea surface, of the ocean color associated with the chlorophyll content of the upper meters of the sea, as well as of the wave and wind fields (Le Traon, 2018). The raw data (levels 0 and 1) are processed by dedicated data assembly centers to provide estimates of geophysical variables (levels 2), which are then projected on a map (level 3) and further merged with additional information from other sensors or models to generate higher level gap-free gridded products (level 4).

The Sea Surface Temperature (SST) is monitored with a high ($\sim$1 km) resolution by infrared radiometers since the late 1970s (Minnett et al., 2019) and the launch of the first Advanced Very High Resolution Radiometer (AVHRR) onboard an US National Oceanic and Atmospheric Administration (NOAA) operational environmental satellite. These data were soon used to characterize thermal fronts in the Gulf of Lion and Ligurian Sea (Albuisson et al., 1979; Crépon et al., 1982). They were also crucial to analyze the surface signature of eddies and currents in the Algerian and Balearic basins in particular (see Chapter 8). The diurnal warming, which in the Mediterranean Sea has one of the largest amplitude worldwide, was also object of specific attention in the Mediterranean Sea (Marullo et al., 2016). Since clouds are a main limitation for infrared measurements, several satellites were equipped with complementary microwave radiometers allowing to measure the SST even in the presence of clouds, yet with other limitations such as a much lower spatial resolution (around 50 km). Comparisons with in situ observations have shown that the accuracy of satellite SST estimates was of the order of 0.5 C, depending both on sensors and environmental conditions. Motivated by the advent of operational forecasting systems in the early 2000s, a specific effort was devoted to generate routine and consistent gap-free gridded SST estimates merging multi-sensor products over the Mediterranean Sea (Buongiorno-Nardelli et al., 2003, 2013). This consolidated product is now distributed through CMEMS, in the form of daily maps at ultrahigh resolution ($\sim$1 km).

Taking advantage of the sensitivity of the ocean surface brightness temperature to salinity, in addition to SST and surface roughness, L-band radiometers have also been launched onboard satellites in the 2010s with the objective to retrieve sea surface salinity from space. SMOS, Aquarius and SMAP are three missions providing SSS measurements with resolutions no lower than few tens or 100 km. While the limited resolution, the land contamination and radio frequency interferences prevent from detecting the fine-scale patterns of SSS variability in the Mediterranean Sea, these data have yet been demonstrated to be useful to monitor the relatively fresh salinity core of Algerian eddies (Isern-Fontanet et al., 2016; Aulicino et al., 2019) or the salinification of the Eastern Mediterranean Sea (Grodsky et al., 2019). The Barcelona Expert Center (BEC), a joint initiative between the Spanish Research Council (CSIC) and the Universitat Politècnica de Catalunya (UPC), provides a specific support to SMOS calibration and retrieval algorithms developments (Turiel et al., 2016).

Sea level measurements by satellite altimeters (Chelton et al., 2001) have provided an invaluable contribution to the monitoring of the Mediterranean Sea for several decades now (see also Chapter 5). In the early 1990s, the launch of altimeter satellites providing high-accuracy ($\sim$2 cm) repetitive sea level observations revolutionized our understanding of ocean dynamics, allowing an unprecedented description of the mesoscale ocean field (i.e., ocean variability with temporal scales between a few days and a few months and spatial scales between 50 km and a few hundred km; Le Traon and Morrow, 2001). Altimeters are active radars that measure the two-way travel time between the satellite and the sea surface. Precise orbit localization allows to meet the challenge of determining the sea level elevation with an accuracy of a few centimeters from a distance of the order of 1000 km. This allows to precisely monitor the sea surface bumps and troughs caused by Mediterranean mesoscale currents, which have magnitudes of the order of 10 cm. Conventional altimeters measure sea level anomalies with respect to a mean sea surface along the track of the satellites, with an along-track resolution around 7 km. The tracks are revisited every 10, 27 or 35 days depending on the orbit of the satellite. The longer the repeat period, the shorter the distance between two tracks (this distance is around 315 km at the equator for a 10 day repeat period, vs. 90 km for a 35-day repeat period). As for the SST, data processing is performed in specific assembly centers to filter and reduce the noise in along-track observations, merge the information from several satellites and generate higher level gridded products. TOPEX/Poseidon, ERS-1&2, Envisat, Cryosat-2, SARAL/AltiKa, HY-2, the Jason and Sentinel-3 series are among the historical and present satellite missions used to generate these products. After filtering, the smallest features resolved by along-track altimetry have diameters around 20−25 km depending on the satellite characteristics (Dufau et al., 2016). A specific regional gridded product is generated by CMEMS over the Mediterranean Sea, leading to a mean effective resolution of around 65 km in terms of eddy diameter (Ballarotta et al., 2019). Recently, the use of Synthetic Aperture Radar (SAR) techniques allowing much reduced footprints compared to traditional altimeters have led to a significant increase in the along-track resolution, down to 300 m. In the near future, interferometer instruments such as the Surface Water Ocean Topography (SWOT) project should provide 2D images of the sea level with an increased resolution over a swath cantered on the track of the satellite, allowing to refine our understanding of mesoscale and submesoscale dynamics (see Chapter 8).

In the Mediterranean Sea, altimeter data have allowed major discoveries about the mean circulation and dynamics of fronts and eddies. Larnicol et al. (1995), Vazquez-Cuervo et al. (1996), Iudicone et al. (1998) and Ayoub et al. (1998) were the first studies to analyze the variable circulation of the basin with these new instruments. Later, the availability of sufficiently long sea level time series has also allowed precise characterizations of the dynamics of Mediterranean subregions such as the eastern Levantine basin (Amitai et al., 2010), Alboran Sea (Renault et al., 2012a) or Balearic Sea (Mason and Pascual, 2013). Combined with new analysis approaches including eddy tracking methods, these data have more recently allowed to map the trajectory of eddies (see Chapter 8), identify their areas of formation and describe

their life cycle (Escudier et al., 2016a, 2016b; Pessini et al., 2018). It is also worth noticing that the Mediterranean Sea has been a place with continuous dedicated efforts to calibrate and improve the altimeter signals, especially in coastal areas where the signal contamination by land becomes problematic (Vignudelli et al., 2005; Bouffard et al., 2008; Escudier et al., 2013; Birol and Delebecque 2014). Notice that wave height and surface wind speed are complementary products provided by satellite altimetry through a careful analysis of the echo reflected by the sea surface. Scatterometers are another type of active radars taking advantage of the resonant Bragg scattering principle to deduce the surface wind speed and direction from the signals reflected by the sea surface (Vogelzang et al., 2011). The accuracy of scatterometer measurements is of the order of 1 m s^{-1} for the wind speed at a horizontal resolution of a few tens of km, depending on the sensor.

SAR satellites, which use the reflection of radio waves to measure sea surface roughness with high accuracy and resolution (down to a few meters for the instruments with the largest swaths), are another very valuable source of remotely sensed information. They present the advantage of working 24-hour under all weather conditions. They reveal the signature of surface and internal waves, currents, eddies and fronts, which all affect the roughness of the sea surface. A typical example in the Mediterranean Sea is the signature of internal waves generated in the Strait of Gibraltar by the interaction of the tides with the topography, and propagating into the western Alboran Sea (Alpers et al., 2008). SAR observations are also very valuable to detect and track oil slicks at the sea surface, with several examples in the Mediterranean Sea (Zodiatis et al., 2012; Pisano et al., 2016), or to provide high resolution maps of surface winds (Signell et al., 2010).

Biogeochemical measurements are also available from space from multispectral instruments (e.g., NASA/NOAA MODIS and VIIRS radiometers, Sentinel-3 Ocean and Land Colour Instrument). These allow to monitor the ocean color, which is affected by the absorption, scattering and reflection of the sunlight by phytoplankton and other suspended material in the upper meters of the ocean. Specific complex algorithms exploiting multispectral data and calibrated using in-situ measurements then allow to separate the impact of the different contributors and quantify the surface concentrations of chlorophyll or dissolved organic material. Benefitting from the relatively high number of cloud-free days in the Mediterranean basin, especially in the summer season, these ocean color satellites offer spectacular images of swirling patterns associated with eddies and filaments which either trap or advect phytoplankton at the surface of the ocean.

Finally, and as a more recent progress, the radiometers onboard the European Space Agency Sentinel-2 twin satellites, launched in 2015 and 2017, are offering open access images with a few tens of meters of resolution and a repetition period of 5 days, which provide unprecedented monitoring capabilities of coastal waters (Caballero et al., 2020). In the Mediterranean Sea, the very promising potential of these data has already been exploited to detect the impact of flooding during a storm event along the south-eastern Iberian coast (Caballero et al., 2019) or to study phytoplankton dynamics in the bays of Ebro delta (Soriano-González et al., 2019).

10.3.2 In-situ and land-based remote sensing observations: systems and international coordination programs

In situ observations are essential not only to validate satellite measurements, but also to provide increased spatiotemporal resolution in specific areas of interest, to monitor EOVs which are not measured by satellites, and inform about ocean conditions throughout the water column. At the same time, collecting in-situ observations which meet internationally agreed standards to be used for scientific purposes and to generate useful products for society is highly challenging, requiring a significant amount of human and economic resources, as well as international collaboration. Present observing systems in the Mediterranean Sea exploit the complementarity between global platform-centered observing networks and regional observatories providing local sustained multi-platform monitoring capabilities. International collaborative frameworks have been built to coordinate and support sustained observation efforts. Besides, dense observation campaigns are occasionally carried out to deploy a large number of platforms and sensors in specific areas, with the objective to focus on the understanding of specific ocean processes.

Regional observatories in the Mediterranean Sea deploy many different platforms to characterize the oceanic conditions at subbasin scales. These platforms include RVs, moorings, surface drifting buoys, profiling floats, gliders, tide gauges, high-frequency (HF) radars, FerryBox (FB) systems, animal tagging, video monitoring systems, etc (see Fig. 10.2).

10.3.2.1 Research vessels

RVs are a historical and essential pillar of ocean exploration, offering one of the most reliable means to access diverse marine environments, including extreme and hardly accessible locations (Nieuwejaar et al., 2019). They are platforms allowing the collection of a wide variety of data and samples from the atmosphere, the ocean surface, across the water column, the deep seafloor, and the subseafloor. Instrumented with thermosalinograph (TSG), fluorometer and Acoustic Doppler Current Profiler (ADCP), they allow to measure surface temperature, salinity and chlorophyll concentration along the vessel track, as well as ocean currents down to a few hundred meters. Equipped with a CTD[4]-rosette, which combines a conductivity and temperature sensor with a carousel of sampling bottles, they collect temperature and salinity profiles at specific locations, as well as water samples at different depths, which biogeochemical characteristics can be later analyzed in laboratory. Expendable Bathythermograph (XBT) probes can also be dropped over the side of the vessel, collecting temperature measurements as the probe falls through the water column, thus allowing to reconstruct the whole vertical temperature profile. Instrumented vehicles towed behind the moving RV are also frequently used to provide high resolution sections of hydrographic variables. RVs are used to deploy, service, maintain and recover fixed and mobile observation platforms.

[4] Instrument measuring ocean Conductivity (then converted into salinity), Temperature and Depth.

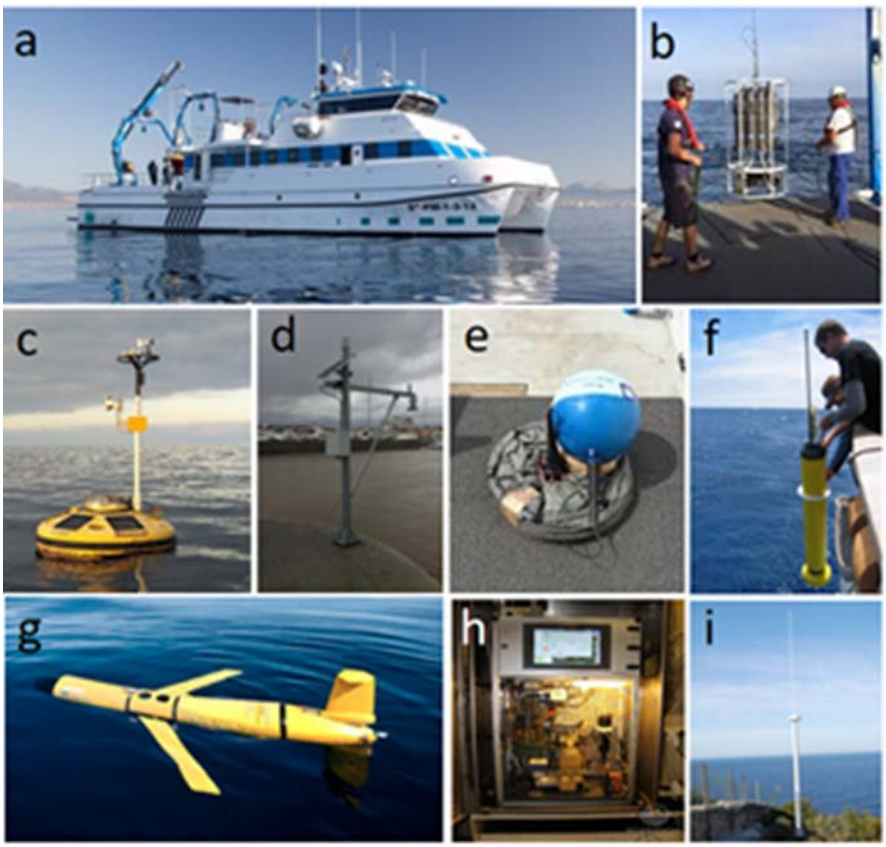

FIGURE 10.2

Observing platforms: (a) Research Vessel, (b) CTD-rosette, (c) mooring, (d) tide gauge, (e) surface drifter, (f) profiling float, (g) underwater glider, (h) FerryBox, (i) HF radar antenna.

Source: SOCIB, IMEDEA (CSIC-UIB), POSEIDON.

Finally, by furnishing high quality data, they provide the reference ground-truth for data collected by satellites and in situ autonomous platforms (Sloyan et al., 2019). The international effort called Global Ocean Ship-Based Hydrographic Investigations Program (GO-SHIP[5]), initiated in 2007, maintains the global survey of selected hydrographic sections (Sloyan et al., 2019). In the Mediterranean Sea, marine scientists elaborated the Med-SHIP plan (Schroeder et al., 2015) in 2012, with the aim to regularly measure physical and biogeochemical properties along two meridional composite transects in the eastern and western Mediterranean basins and one zonal

[5] https://www.go-ship.org.

transect from the Strait of Gibraltar to the easternmost Mediterranean. Since 2015, the Mediterranean zonal section has been included as a component of the global GO-SHIP program. At the European level, the EUROFLEETS[6] projects (on its way to become a permanent research infrastructure) are working toward an open and trans-national access to an integrated and advanced European RV fleet.

10.3.2.2 Moorings

Fixed buoys and submerged moorings have long been an essential Eulerian component of ocean observing systems. They consist of equipping a line between an anchor on the seafloor and a buoyant float at the sea surface or at a determined depth, with a wide range of different sensors (to measure e.g., temperature, conductivity, pressure, currents, oxygen, chlorophyll, nutrients, turbidity, carbon system). For moorings that reach the sea surface, wave recorders and weather stations can provide complementary data of winds, air temperature and pressure, solar radiation or wave characteristics. These data can be transmitted in real-time via satellite communications. Profilers can also be used to move sensors up and down along the mooring line and provide measurements throughout a determined ocean layer.

The EMSO[7] (European Multidisciplinary Seafloor and water column Observatory) ERIC (European Research Infrastructure Consortium) coordinates a number of sites in the northeast Atlantic Ocean, the Mediterranean Sea and the Black Sea while other European countries coordinate their observations via the OceanSITES,[8] OceanOPS, Jerico-RI[9] and Hydrochanges[10] network (Schroeder et al., 2013). Within the GOOS, OceanSites is a global network of Eulerian observatories covering the entire water column from air-sea interface to deep waters. EMSO ERIC comprises fixed-point multidisciplinary facilities in key deep seafloor and water column environmental sites, recording long-term time series of EOVs and marine hazards (Dañobeitia et al., 2020). The objective of OceanSites and EMSO networks is to ensure the optimal application of the time series technology for as much users as possible in the framework of a sustained GOOS. The main scientific goal is to help scientists to understand global environmental processes and stimulate the development of new technologies and knowledge. These networks also push toward the adoption of best practices, i.e., standards in sensors and measurement methodologies applied to increase their interoperability. In the Mediterranean Sea, the EMSO ERIC includes six regional facilities (Ligurian Sea, Western Mediterranean Sea, western Ionian Sea, South Adriatic Sea, Hellenic Arc and Cretan Sea) and one test site (OBSEA). They are composed of autonomous fixed platforms powered by submarine cables or stand-alone devices. The OceanSites network in the Mediterranean Sea includes most of EMSO regional facilities, with additional moorings

[6] https://www.eurofleets.eu/.
[7] http://emso.eu/.
[8] http://www.oceansites.org/.
[9] https://www.jerico-ri.eu/.
[10] https://www.ciesm.org/marine/programs/hydrochanges.htm.

located on both sides of the Mediterranean basin. Some other sites are included in Hydrochanges, mainly more simple moorings, devoted to the recording of deep temperature and salinity changes (see Chapter 9).

10.3.2.3 Tide gauges and coastal stations

Tide gauges are fixed instruments continuously recording sea level elevations at the coast. While the oldest models were measuring the vertical movement of floats with the water, modern tide gauges determine the water level by electronic measurements of the height of the water flowing through a pipe. Sea level measurements need to be carefully referenced to the global ellipsoid with collocated GPS positioning to remove the effect of local land movements and allow accurate climatic sea level rise analysis. Alternative instruments to deduce sea level variations are bottom-mounted barometers which measure water pressure variations and transmit data via a cable to the shore. Coastal fixed stations are also sometimes complemented by sea temperature and meteorological sensors. Further details are provided in Chapter 5.

10.3.2.4 Drifters

Surface drifting buoys are Lagrangian mobile autonomous platforms driven by ocean currents. They have been used from the first expeditions at sea: the IOC reports that Leonardo da Vinci (1452−1519) carried out the earliest recorded experiment measuring surface water velocity by tracking the downstream travel of a surface float (IOC/WMO, 1988). Several models of drifting buoys have been developed, some of them including a drogue of several meters which allows to measure the strength and direction of ocean currents at a specific depth below the surface (typically 15 m for the widely used Surface Velocity Program model, SVP,[11] Niiler et al., 1995). While the Coastal Ocean Dynamics Experiment (CODE) drifters were designed to follow the top 1-m average current (Poulain et al., 2019), the Consortium for Advanced Research on Transport of Hydrocarbon in the Environment (CARTHE) model is a compact and low-cost drifter including a drogue that extends 60 cm below the surface (Novelli et al., 2017). The position of the drifter is generally transmitted in real-time via satellite communication, providing useful information on the characteristics of ocean velocities. When deployed in clusters, their trajectories can be analyzed to provide estimates of ocean convergence, dispersion and stirring (e.g., Schroeder et al., 2012). Some drifters are also instrumented to record the sea temperature.

10.3.2.5 Profiling floats

Profiling floats (also often known as Argo floats due to the major associated international implementation program, see below) are autonomous platforms which sink to a parking depth (generally around 350 m in the Mediterranean Sea), drift with ocean currents at that depth during a specified period (generally five days in the Mediterranean Sea), before profiling the water column from a depth around 700 m up to the

[11] https://gdp.ucsd.edu/ldl/svp/.

surface, measuring pressure, temperature and salinity and other parameters. The data and position are then transmitted via satellite, allowing land-based data centers to provide the measurements in near real-time. The floats dive again after the few hours necessary for the data transmission and repeat the whole park-and-profile cycle. Since 2012, biogeochemical (BGC) floats have also been deployed, equipped with additional sensors measuring dissolved oxygen, pH, nitrate, chlorophyll fluorescence, particulate backscatter or incoming solar radiation. For BGC floats, the parking depth is usually set at 1000 m depth to prevent fouling issues.

Initiated in 1999, Argo[12] is an international network of approximately 4000 profiling floats that measure temperature and salinity worldwide (Wong et al., 2020). More than 30 countries participate to this program, deploying floats separately and distributing their data globally with common standards. Euro-Argo ERIC[13] is the European infrastructure for Argo floats allowing to monitor the floats after deployments, and ensure standardized data processing and delivery to users. As part of this program and at the time of writing this chapter, there were 77 Argo floats providing data in the Mediterranean Sea, 33 of them in the western basin and 44 in the eastern basin (real-time positions can be consulted in the MedArgo website[14]). These data have allowed an unprecedented monitoring of the evolution of the characteristics of surface and intermediate water masses and are today essential pillars of ocean observing and forecasting systems. BGC floats have been deployed also in the Mediterranean Sea (Le Traon et al., 2020), which was specifically selected to conduct the BGC-Argo pilot experiments due to its laboratory characteristics and the presence of a wide range of contrasting biogeochemical regimes, making it an ideal test site for such a basin-wide BGC-Argo and Argo-O_2 (oxygen) network pilot experiment. Since 2012, 32 BGC-Argo and 15 Argo-O_2 floats have been deployed, providing more than 6000 BGC and oxygen profiles, contributing to significantly improve our understanding of the impacts of convection and ventilation on Mediterranean biogeochemical and ecosystem dynamics (D'Ortenzio et al., 2021; Coppola et al., 2017). The new generation of Deep Argo autonomous floats is presently under development, including an enhanced capacity to sample the full water column down to 4000 m or 6000 m depth.

10.3.2.6 Gliders

Underwater gliders are selfpropelled autonomous vehicles taking advantage of small changes of their buoyancy to fly up and down throughout the water column. Their wings and tail permit an additional directed horizontal motion at a speed around 1 km h^{-1}. Gliders can be equipped with a variety of sensors (e.g., CTD, fluorometer, oxygen, turbulence probe, ADCP), providing high-resolution measurements along oceanic sections. Glider work in all weather conditions and can remain at sea for

[12] https://argo.ucsd.edu/about/.
[13] https://www.euro-argo.eu/.
[14] http://nettuno.ogs.trieste.it/sire/medargo/active/index.php.

several months, being limited only by battery duration or biofouling. Two-way communication is established via satellite during the glider regular surfacings, allowing to both transmit data and receive navigation and sampling instructions from glider pilots on land. These characteristics make them very valuable platforms for the sampling of the transition zone between coastal waters and the open ocean. The duration of a glider mission ranges from weeks to months depending on the type of battery (lithium or alkaline), the number of sensors and the sampling characteristics.

OceanGliders[15] is an international program associated with GOOS, which was initiated in 2016, focusing on glider observation activities (Testor et al., 2019). It is an international forum for marine scientists and engineers operating gliders, with the aims to observe the physical, biogeochemical, and biological ocean processes and deliver data through both real-time and delayed modes. The OceanGliders program is composed of national and regional observing systems and aims to harmonize best practices and improvement of glider data collection and analysis. In the Western Mediterranean and in the southeast Levantine basin, repeated transects have been conducted along glider endurance lines for over 10 years to monitor the variability of the main currents. Endurance lines have also been settled in the Cretan, Aegean and Ionian Seas since 2017. Several missions have been carried out between the Balearic Islands and Sardinian and African coasts.

10.3.2.7 HF radars

HF radars are coastal land-based instruments allowing to deduce surface currents by measuring the reflected echo of radio waves at the sea surface. More concretely, HF radars measure the radial velocities toward or away from a fixed antenna. Radar installations generally consist of two antennas allowing to reconstruct the zonal and meridional components of the surface ocean velocities in the area commonly covered by the two antennas. HF radars have a spatial range of several tens of km and provide hourly 2D gridded surface velocity maps with a resolution around 3 km after appropriate processing. They provide a unique continuous and high-resolution monitoring of surface ocean currents in coastal areas. Details of their implementation and use in the Mediterranean Sea can be found in Lorente et al. (2022) and Reyes et al. (2022).

10.3.2.8 FerryBox

FB is an automated instrument package installed on an RV or a ship of opportunity operating along regular ferry or shipping lines, and allowing a continuous monitoring of surface waters. Seawater is pumped into a measuring system composed of several sensors, which collects multivariate observations at intervals of a few seconds. Temperature, salinity, chlorophyll, turbidity and oxygen sensors are the most common sensors installed. A GPS receiver continuously monitors the position of the

[15] https://www.oceangliders.org/.

measurements. A debubbler system removes potential air bubbles in the incoming water, and automatic cleaning procedures are implemented to avoid sensor biofouling issues. The routes from Tunis to Marseille and Genova, from Algiers to Marseille, from Toulon to Corsica, from Livorno to Sardinia or from Athens to Heraklion are the main lines regularly monitored by FB in the Mediterranean basin.

10.3.2.9 Animal tagging

Specific programs have been implemented to instrument loggerhead marine turtles in the Mediterranean Sea to track the animal trajectories, understand their life habits and collect environmental information (e.g., Casale et al., 2007; Eckert et al., 2008; Revelles et al., 2007). Satellite tags measuring the animal position together with ocean temperature and pressure are fixed on the shell of the animal and transmit data in between the animal dives. Examples of turtle trajectories can be followed in near-real-time for instance on SOCIB web server.[16] Among the other marine species subject to instrumentation with telemetry, sea birds have also recently been used to infer information about surface currents during their rafting stages (Sanchez-Roman et al., 2019).

10.3.2.10 EuroGOOS and MONGOOS

EuroGOOS is the European component of the GOOS. It aims at enhancing cooperation to ensure sustained observations in European seas including the monitoring of identified EOVs. EuroGOOS provides a framework for the coordination of specific task teams and working groups constituting operational networks of observing platforms. The task teams are used to share experience, promote synergies, define best practices and common procedures for data acquisition and management and foster scientific and technological developments. EuroGOOS task teams have been constituted for FB, tide gauges, gliders, HF radars, Argo floats, fixed platforms, and animal-borne instruments. The European marine community is also working together in the European Ocean Observing System (EOOS[17]) under the guidance of EuroGOOS[18] and the European Marine Board (EMB[19]). EOOS aims to establish mechanisms for users to formulate and convey their needs to ocean observation systems, and further track and assess the implemented solutions (Tanhua et al., 2019).

Supported by EuroGOOS, MONGOOS was established in 2012 to specifically promote and develop synergies between the different observing networks in the Mediterranean Sea and to foster collaborations with a focus on operational oceanography. As part of this effort, the MONGOOS data center[20] provides user-friendly visualization of the real-time Mediterranean Sea in-situ observations from floats, drifting buoys, fixed stations, tide gauges, gliders, CTDs, and HF radars.

[16] http://apps.socib.es/dapp/.
[17] https://www.eoos-ocean.eu/.
[18] https://eurogoos.eu/.
[19] https://www.marineboard.eu/.
[20] www.mongoos.eu/data-center.

10.3.3 Multi-platform regional and coastal observing systems

The ocean varies over a wide range of spatial and temporal scales and no single instrument provides the appropriate spatial and temporal coverage to disentangle the complexity of ocean dynamics. A useful approach to face this difficulty is to implement and analyze multi-platform integrated monitoring systems. For instance, while moorings measurements provide high temporal resolution, they are limited to a single location. Satellite then provides complementary information about the overall surface variability, and glider can be deployed to describe the hydrographic conditions along a vertical section in the vicinity of the mooring. Several multiplatform ocean observatories have been developed over the past decade, both in the western and eastern basins. Some of them are described below as examples. The interested reader is referred to Tintoré et al. (2019) for a recent and more exhaustive description.

10.3.3.1 MOOSE

The MOOSE observing system[21] is an integrated and multidisciplinary network located in the north-western Mediterranean basin, which has been established in 2010 (Coppola et al., 2019). Its main objective is to monitor the regional long-term evolution of ocean conditions in the context of climate change and anthropogenic pressure in order to detect and identify trends and environmental anomalies of the marine ecosystem. The MOOSE network is supported by French institutes (CNRS-INSU, French Ministry of Higher Education and Research). It involves different partners (Universities, Météo France and IFREMER) and participates in the European and international infrastructures like Euro-Argo, EMSO/OceanSites, OceanGliders and the European Marine Biological Resource Center (EMBRC).

The MOOSE network includes multiscale measurement capabilities to observe trends and anomalies and accurately capture the broad spectrum of hydrodynamic processes (large-scale circulation, mesoscale, and submesoscale eddies) and their impacts on biogeochemical cycles (oxygen ventilation, nutrients supply, phytoplankton production, carbon export and acidification trends). The strategy of MOOSE is to include different platforms operating at different spatial and temporal scales: fixed open sea observatories (moorings, surface buoys and monthly ship visits), two gliders endurance lines, rivers and atmospheric monitoring sites, HF radar stations, annual large-scale RV campaigns and some Argo floats deployment.

Two key areas of the north-western basin have been selected to address the issues identified by MOOSE. The first one is the central and western part of the Ligurian Sea, where the Levantine Intermediate Water formed in the eastern basin flows before spreading into the north-western basin. It constitutes a homogeneous system isolated from direct coastal inputs by rivers, and with a predominant role of the atmospheric forcing. The second one is the Gulf of Lion, which is the most dynamic area of the western basin with intense vertical mixing in winter and episodic events of shelf water cascading (Houpert et al., 2016).

[21] https://www.moose-network.fr/.

10.3.3.2 SOCIB

SOCIB[22] Tintoré et al., 2013) is a marine research infrastructure initiated in 2008 and included since 2014 in the Spanish Large-Scale Infrastructure Map. In close collaboration with other Spanish institutions like the National Research Council (CSIC), the Spanish Institute of Oceanography (IEO) or Puertos del Estado, SOCIB has been developing an integrated network of multi-platform observing facilities in the Western Mediterranean Sea, with the objective to characterize the ocean state and variability from the nearshore to the open ocean, and from the short-term to longer climatic scales. SOCIB observing facilities include a 24 m-long catamaran coastal RV, a fleet of seven underwater gliders, two metocean moorings located in the Bay of Palma and in the Ibiza Channel, 16 fixed coastal stations around the coast of the Balearic Islands, two HF radar antennas in Ibiza and Formentera Islands, two beach monitoring stations in Mallorca and Menorca islands, and annual deployments of around eight satellite-tracked surface drifters and three Argo floats. Multidisciplinary seasonal RV oceanographic campaigns, high-resolution bathymetry surveys, sediment sampling and occasional tagging of sea turtles complement these routine observing systems. The Ibiza Channel, a key chokepoint in the Western Mediterranean Sea, is a privileged area of SOCIB monitoring activities. In addition to the fixed mooring and HF radar installation, a glider endurance line has been established to precisely monitor the meridional water mass exchanges and transports and understand their impact on ecosystems in this critical area. SOCIB observing capabilities are also used to support intensive process-oriented sea trial experiments in the Western Mediterranean Sea (Pascual et al., 2017; Mahadevan et al., 2020; Barcelo-Llull et al., 2021).

SOCIB follows an open-access data policy, strongly committed to the Findable, Accessible, Interoperable and Reusable (FAIR) principles and adhering to the international ocean Best Practices system. Data can be easily and interactively visualized and downloaded from SOCIB website and through European data distribution portals. SOCIB is also strongly engaged in outreach activities and Responsible Research and Innovation to facilitate the access to scientific results and foster the scientific education in the society.

10.3.3.3 POSEIDON

The POSEIDON system,[23] initiated in Greece in the late 1990s is one of the very first efforts in the Mediterranean Sea toward a comprehensive regional marine monitoring and forecasting system, that aims to improve environmental monitoring and support maritime activities, rescue and safety of life at sea, fishing and aquaculture and protection of the marine ecosystem. Over the last few years POSEIDON has adopted a multiplatform-multiparameter approach including open and coastal sea fixed platforms, deep-ocean observatories, an FB system, HF radar, and Argo

[22] www.socib.es.
[23] https://poseidon.hcmr.gr.

autonomous floats (Frangoulis et al., 2019). Since 2010, the list of biogeochemical-ecosystems parameters has been expanded by the addition of sediment traps, frequent RV visits for water-plankton sampling, and of an ADCP delivering information on macrozooplankton-micronekton vertical migration. Gliders and drifters are the platforms currently under integration to the existing system. Wavescan buoys are deployed in the South Aegean (E1-M3A, see Petihakis et al., 2006), North Aegean (Athos) and Ionian Sea (Pylos) to provide meteorological, physical and biochemical (oxygen, chlorophyll-a) data. Three additional Seawatch type buoys (Saronikos, Heraklion and Mykonos coastal buoys) have been deployed to monitor the coastal-open sea processes interaction.

The FB system operates on the route connecting the ports of Piraeus and Heraklion, collecting temperature, salinity, fluorescence, turbidity, and pH measurements. Sampling of seawater and plankton is also made regularly next to the fixed biochemical platforms and on-board the FB. R/V visits are made at a monthly frequency next to the E1-M3A site and the Heraklion buoy. They include CTD casts and seawater/plankton sampling which are analyzed following specific protocols adapted to the oligotrophic conditions of the area. Moreover, a total of 30 Argo floats including standard and BGC-Argo have been deployed in the period 2012−20 in the Aegean and Ionian Seas.

Finally, two SeaExplorer gliders were recently added to the monitoring platforms of the POSEIDON system aiming to establish at least two endurance lines in the Aegean and Ionian Seas. These systems are expected to significantly contribute to advance the knowledge of the seasonal variability of the flow field, to track the low salinity Black Sea water path and to characterize the intermediate and deep-water formation events that are known to occur in the area.

10.3.3.4 Other sustained multi-platform observing systems and intensive surveys

Other sustained observing programs have been implemented in Spanish coastal waters. One of them is the PORTUS system,[24] operated by the Puertos del Estado, the Spanish holding of harbors (Alvarez-Fanjul et al., 2018), operating several observing networks along the eastern coast of the Spanish peninsula and the Balearic Islands. PORTUS includes seven deep water buoys moored between 400 and 2000 m, six coastal buoys equipped with directional wave sensors, two HF radar systems in the Strait of Gibraltar and the Ebro Delta and 16 tide gauges as part of the REDMAR multi-propose network providing both long-term and HF sea level data to a large range of users. The PORTUS system complements the IEO monitoring system also deploying tide gauges and moorings, and maintaining long-term hydrographic sections for over 20 years along the Spanish coast through the RADMED monitoring program (Lopez-Jurado et al., 2015; Vargas Yañez et al., 2020). The RADMED program measures physical, chemical and biological variables, together with planktonic

[24] http://portus.puertos.es.

data, with the objectives to characterize shelf-slope gradients and their latitudinal changes, as well as the seasonal and long-term variability of water masses. The TUNIBAL program is another sustained IEO observing program which samples the waters surrounding the Balearic Islands every year during the spawning period of Bluefin tuna in early summer (Alemany et al., 2010).

In Italian waters, the RITMARE network[25] (Ravaioli et al., 2016) maintains 17 fixed point observatories and regularly deploys surface drifters, floats and gliders. RV transects are also carried out and several HF radars collect data in Italian coastal areas. In the eastern basin, the Center for Marine Ecosystems and Climate Research (DEKOSIM[26]) implements a network of observing systems to collect continuous and sustained physical and biogeochemical measurements in Turkish waters. It includes in particular fixed stations, Argo floats deployments and monthly RV trawl surveys. For over 20 years, data are also being collected routinely in the south-eastern Levantine basin from various Cyprus and Israeli institutions. The data are quality processed and archived by local data centers such as the Israel Marine Data Center ISRAMAR[27] and EastMedAtlas, both connected to the European data platforms, which are described later. The monitoring infrastructure in the south-eastern Levantine basin includes the Israeli biannual RV cruises collecting biophysical observations at several stations, coastal and deep moorings, coastal physico-biochemical surveys, gliders transects and sea level stations networks.

Complementary to these sustained monitoring systems, intensive observational campaigns deploying multiple sensors in reduced areas also allow scientists to focus on the understanding of specific ocean processes and test new observing technologies and data integration methods. Recent examples include specific experiments carried out in the western Mediterranean Sea (Pascual et al., 2017; Petrenko et al., 2017; Onken et al., 2018; Garreau et al., 2020; Mahadevan et al., 2020; Barceló-Llull et al., 2021) and in the Adriatic Sea (Vilibić et al., 2018). Fig. 10.3 illustrates the spatial distribution of all in-situ observations made available on CMEMS database during the first semester 2021.

10.4 Forecasting the Mediterranean Sea

10.4.1 General concepts

The knowledge of the state and short-term evolution of ocean waves, currents, temperature, sea level, and biogeochemical parameters such as carbon fluxes or phytoplankton concentration are required for a wide range of societal applications. While observations taken alone do not generally allow to reconstruct the full 3-dimensional multivariate ocean state and its temporal evolution, numerical models resolving the

[25] http://www.ritmare.it.
[26] https://ims.metu.edu.tr/ecosystem-and-climate-center.
[27] https://isramar.ocean.org.il.

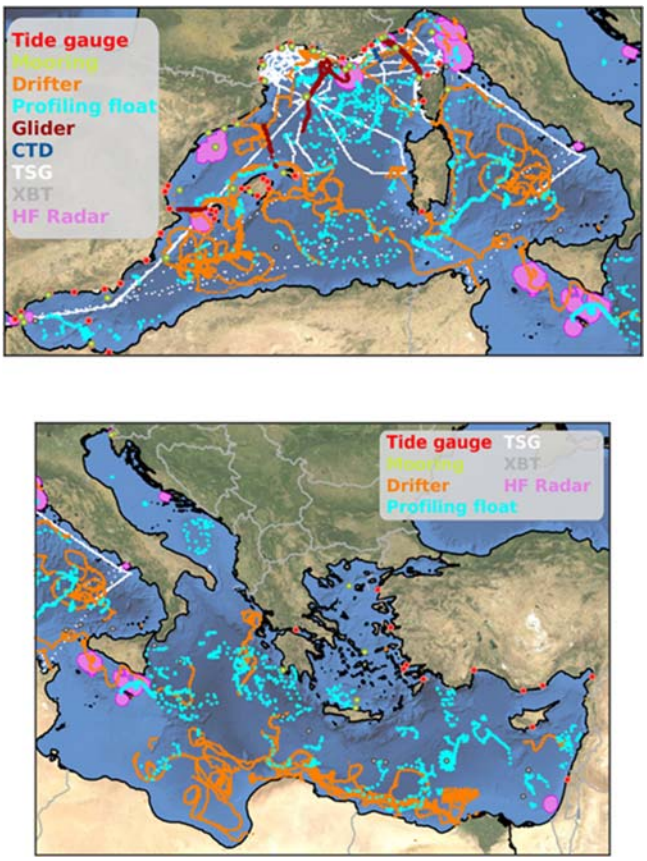

FIGURE 10.3

Map of observations compiled from the CMEMS data base during the period in the Mediterranean Sea during the first semester 2021.

equations of fluid dynamics do have this capacity, providing very valuable and complementary tools for the estimate and prediction of ocean conditions. However, due to computational resources, models can not represent all ocean processes. The variety and complexity of physical processes that take place in the Mediterranean Sea over a wide range of spatio-temporal scales (including interannually and seasonally variable wind driven and thermohaline circulation, intermediate and deep water formation, mesoscale and submesoscale processes, coastal upwellings, storm surges, extreme waves as a response to medicanes, or natural hazards such as meteotsunamis) generally require focusing on specific processes of interest, by developing models representing the evolution of specific variables at specific scales.

Overall, the modeling systems that have been developed as European, national or individual research centers initiatives, provide regular and systematic information

about the current and future (few days in advance or climate projections) physical state and dynamics of the Mediterranean Sea and its ecosystem at regional (3−5 km) or coastal scales (<1 km). The model products in retrospective analysis (reanalysis), analysis and forecast modes describe 3D currents, temperature, salinity, mixed layer thickness, wind waves, sea level, and biogeochemistry to support marine and maritime applications. The present chapter does not address the field of climate modeling involving simulation periods of several centuries and future emission scenarios. The interested reader is referred to Chapter 3 of this book for Mediterranean climate concerns at these scales.

10.4.1.1 Hydrodynamics

Hydrodynamic modeling relies on the numerical resolution of different approximations of the Navier−Stokes equations describing the motion of water. Scale considerations allow to simplify the equations and reduce computing times, considering for instance the very large ratio between the horizontal and vertical scales in the ocean (hydrostatic approximation) or neglecting density variations in momentum equations, with the only exception of the buoyancy terms (Boussinesq hypothesis) in the so-called primitive equations. The shallow water or Saint-Venant equations are obtained by integrating vertically the Navier−Stokes equations and provide accurate approximations for the representation of tidal, tsunami-like waves, storm surge or continental shelf dynamics. In all cases, the equations are discretized and resolved at the nodes of two- or three-dimensional grids.

In the Mediterranean Sea, state-of-the-art numerical models are used to provide the basin scale solution (Clementi et al., 2021) and implement nested systems that downscale this solution down to the kilometric scale in Mediterranean regions and local areas. Different models are used to solve the hydrodynamics including NEMO[28] (Nucleus European Model of the Ocean, Madec et al., 2019), POM[29] (Princeton Ocean Model, Blumberg and Mellor, 1987), ROMS[30] (Regional Ocean Modeling System, Shchepetkin and McWilliams, 2005), SHYFEM[31] (Ferrarin et al., 2019), MIT OGCM[32] (Marshall et al., 1997) and SYMPHONIE[33] (Marsaleix et al., 2008). The core of these models differs by their numerical resolution approaches or vertical discretization methods (vertical levels might be chosen to follow constant depth levels, density levels or adapt to the bottom topography). Hydrodynamics are driven by atmospheric parameters and fluxes of momentum, heat, and fresh water generally provided by the European Center for Medium-Range Weather Forecasts (ECMWF[34]) or by Limited Area Models that downscale the ECMWF or

[28] http://www.nemo-ocean.eu.
[29] http://www.ccpo.odu.edu/POMWEB.
[30] https://www.myroms.org.
[31] http://www.ismar.cnr.it/shyfem.
[32] http://mitgcm.org.
[33] https://sirocco.obs-mip.fr/ocean-models/s-model.
[34] https://www.ecmwf.int/.

the US National Centers for Environmental Prediction (NCEP[35]) global analyses and forecasts onto the Mediterranean basin.

10.4.1.2 Storm surges and meteotsunamis

The evolution of the sea level in the coastal areas of the Mediterranean Sea results from the influence of several processes acting from short (HF waves with periods of a seconds to minutes) to longer scales (seasonal and climatic variations). Among them, the storm surge phenomenon (see also Chapter 6) resulting in a water build-up due to winds and atmospheric pressure lows associated with storms can have a dramatic impact on coastal areas generating coastal flooding and erosion. Short term changes in sea level are usually simulated and forecasted by solving the shallow water equations forced with surface winds, sea level atmospheric pressure and astronomical tides at high spatial and temporal resolution. Uncertainties in meteorological forcing are often the main source of uncertainty in storm surge forecasts especially in the case of intense storms or medicanes (specific term used to identify Mediterranean hurricane-like storms). Some of the storm surge systems involve wind waves forecasting modules to account for the interaction between currents and waves while other solve the full 3D hydrodynamics to account for all the drivers controlling sea level variations, including steric effects and baroclinic processes.

The region of Venice in the north Adriatic Sea is the area where storm surges reach the highest values in the Mediterranean Sea (Marcos et al., 2009). Many storm surges forecasting systems have been developed in that area (Umgiesser et al., 2021), involving both deterministic and probabilistic forecasting approaches. Other storm surge forecasting systems have been developed over the western basin (Álvarez-Fanjul et al., 2001; Pérez-Gómez et al., 2012) and the whole Mediterranean Sea (Ferrarin et al., 2013).

Meteotsunamis, which are tsunami-like waves generated by atmospheric pressure disturbances (see also Chapter 6), are other natural hazards regularly affecting several coastal areas in the Mediterranean Sea (in particular the Balearic Islands, Croatian archipelago, southwestern Sicily, Malta shelf and Aegean Sea). They result in HF (periods of the order of a few minutes) sea level oscillations in harbors and bays with specific topographical characteristics. Dedicated prediction systems have been developed in the Balearic Islands (BRIFS, Renault et al., 2011; Mourre et al., 2021) and in Croatia (Denamiel et al., 2019). These systems are based on very high temporal resolution atmospheric models which provide the sea level pressure forcing to very high spatio-temporal resolution hydrodynamic models, so as to represent the different stages of the ocean wave amplification over the shelves and in the harbors.

10.4.1.3 Wind waves

Wind waves and their accurate prediction in the Mediterranean Sea are of great interest for many applications and activities ranging from offshore and tourism industry to navigation safety, sediment transport, shoreline erosion and coastal

[35] https://www.weather.gov/ncep/.

engineering. Waves interact with ocean currents (Bennis et al., 2011) and with the lower atmospheric boundary layer, thus affecting the fluxes at the air-sea interface (Cavaleri et al., 2012). Spectral (i.e., phase-averaged) models are generally employed for oceanic wave modeling, using the wave spectrum as the prognostic variable instead of treating waves individually (Cavaleri et al., 2007). They resolve the spectral wave energy balance equation, including source, and sink terms, nonlinear interactions between waves quadruplets and parameterizations of wave-bottom interactions and white capping dissipation.

Several forecasting systems have been developed in the Mediterranean Sea, operating at different scales and using WAM (WAMDI Group, 1988), WAVEWATCH III (Tolman and Hendrik, 1991) and SWAN (Booij et al., 1999) third generation phase average spectral models. Wave products generally include significant wave height, period and propagation direction for the total, wind sea and low-frequency wave spectrum. They are validated using available wave measurements from buoys and satellites. The interested reader is referred to Chapter 6 of the present book for an in-depth description of Mediterranean waves.

10.4.1.4 Biogeochemistry

Biogeochemical models are valuable tools to understand the dynamics of marine ecosystems and address management issues requiring an integrated approach of physical and biotic processes. They intend to represent the different interactions between the physical, biological and chemical processes in the ocean. BGC models usually consist of two coupled subsystems describing (i) the hydrodynamics and (ii) the biogeochemical component related to the pelagic and benthic ecosystems and their coupling in terms of biogeochemical processes affecting the fluxes of carbon, nitrogen, phosphorus and silicates. The biogeochemical cycles of these four chemical compounds are represented through the dissolved inorganic, living organic, and nonliving organic compartments including all the important physiological (ingestion, respiration, excretion, and egestion), and population (growth, migration, and mortality) processes described in terms of fluxes of carbon and nutrients. Different levels of complexity can be included in the BGC models by representing different numbers of plankton functional groups. No clear consensus exists on the appropriate level of complexity, and the choice of the model components and parameters ultimately depends on the area of study and specific processes targeted by the model.

Several biogeochemical models have been implemented to provide predictions over the whole Mediterranean Sea (Salon et al., 2019; Kalaroni et al., 2020) or within its subregions (Nagy et al., 2017; Mussap and Zavatarelli, 2017; Petihakis et al., 2012, 2014). They are validated routinely by satellite chlorophyll observations as well as Argo and glider biogeochemical measurements when available.

10.4.1.5 Data assimilation as a tool to integrate models and observations

The turbulent nature of the ocean most often prevents the atmospherically forced ocean models from properly representing ocean eddies and fronts at their exact positions and with an accurate timing. Constraining the model by the information

coming from available measurements is then necessary to represent the mesoscale oceanic features more realistically. Data assimilation is a commonly used approach to combine models and observations, allowing to interpolate the information provided by generally sparse and multivariate observations into dynamically consistent multivariate 3D fields (the so-called analysis) which can be used to initialize the subsequent simulation or model prediction. Model and observation errors are used in the data assimilation process to balance the respective weight of both sources of information in the final ocean field estimates. Sequential methods (Optimal Interpolation, Kalman filter, and its variants) and variational methods (4dVar) provide two different approaches to this problem, both based on error variance minimization algorithms. Satellite altimetry, SST and Argo profiles provide essential routine datasets to constrain both surface and subsurface hydrodynamic model fields at regular few-days intervals. They can be completed by complementary profiles from ship CTDs or gliders when available or HF radar measurements in specific coastal areas. Besides, satellite-derived significant wave height observations are assimilated in wave models. In BGC systems, the assimilation of satellite chlorophyll measurements is also used in the Mediterranean Sea, to improve model simulations and achieve more realistic estimates of chlorophyll, nitrate and phosphate concentrations (Fontana et al., 2010; Kalaroni et al., 2016; Teruzzi et al., 2018). During the data assimilation process, the information provided by the measurements is optimally propagated onto all model variables and grid-points, and accumulated over time along the repetition of assimilation cycles, leading to an overall reduction of the model errors. While real-time observations are generally incorporated in operational ocean forecasting systems, delayed reprocessed observations are used to generate reanalysis simulations of past periods.

Data assimilative models are also frequently used to help design observational systems. Observing System Experiments (OSEs) consist in comparing the performance of a data-assimilative simulation versus a non−data-assimilative counterpart to evaluate the impact of specific observations. Using a second and different high-resolution simulation considered as representing the ocean truth (called nature run), this approach can even be used in a simulated observation mode to assess the potential impact of future observations or evaluate different potential sampling strategies to help observation planning. This is the so-called Observing System Simulation Experiments (OSSEs) approach. When considering observations whose position and sampling is controllable in near real time (e.g., as in the case of underwater gliders), these data-assimilative models also enable real-time adaptive sampling strategies by guiding the vehicles at regular intervals into the areas where the evolving model errors are maximum. The Mediterranean Sea has been a demonstration area for many OSEs evaluating the impact of FB, CTDs, gliders, Fishery observing systems, HF radar measurements or satellite data (Dobricic et al., 2010; Korres et al., 2014; Hernandez−Lasheras and Mourre, 2018; Hayes et al., 2019; Storto and Oddo, 2019; Hernandez-Lasheras et al., 2021), as well as OSSEs supporting the design of future observing networks (Alvarez and Mourre, 2012, 2014; Aydogdu et al., 2016; Storto et al., 2020). The Mediterranean Sea has also been a

test bed for new data assimilation and ensemble forecasting approaches (Lenartz et al., 2010; Pinardi et al., 2011; Oddo et al., 2016), to compare data assimilation strategies (Mourre and Chiggiato, 2014; Storto et al., 2020) or evaluate the benefit of glider adaptive sampling on the model performance (Mourre and Alvarez, 2012). The concept of the integrative approach combining multiplatform ocean observing and modeling components through model assessment, data assimilation, support to the understanding of ocean processes and optimization of the design of observing systems is shown in Fig. 10.4.

10.4.1.6 Reaching coastal scales

Coastal areas are areas of specific interest since they concentrate a large number of human activities including fisheries, aquaculture, ports activity, tourism and recreation. They receive the discharge of continental waters, are regularly affected by contamination events and their dynamics determines the quality of coastal waters, with direct impacts on coastal populations. The realistic representation of shelf dynamics, characterized by smaller spatiotemporal scales compared to the open ocean under the impact of capes, embayments, small islands and variable wind forcing, requires an increased resolution in ocean models. A common approach to refine the solution of a large scale ocean model in regional and coastal zones of interest is the so-called dynamical downscaling. It consists in taking initial and boundary information from coarser models to generate refined solutions in specific areas using

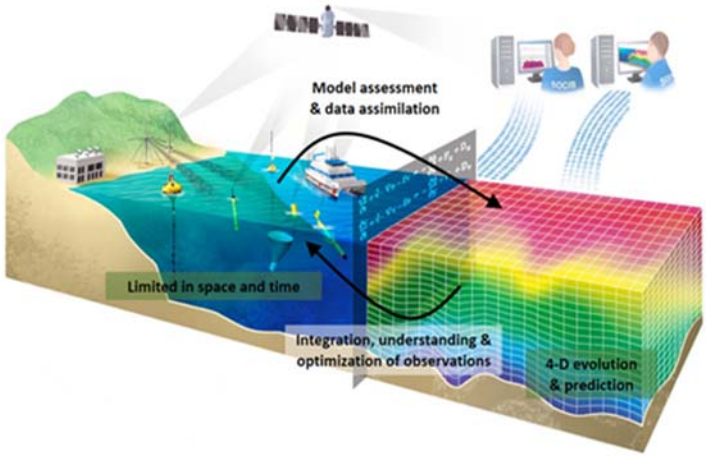

FIGURE 10.4

Illustration of the ocean observing and modeling integrated approach.

Adapted from Mourre B., Aguiar, E., Juza, M., Hernandez-Lasheras, J., Reyes, E., Heslop, E., et al., 2018. Assessment of high-resolution regional ocean prediction systems using muli-platform observations: illustrations in the Western Mediterranean Sea. In: Chassignet, E., Pascual, A., Tintoré, J., Verron, J. (Eds,.), New Frontiers in Operational Oceanography. GODAE Ocean View, 663–694. doi:10.17125/gov2018.ch24 and reproduced with permission of GODAE OceanView.

either multiple telescopic nested grid with increased resolution (this is the case for classical ocean models using regular Cartesian grids), or unstructured mesh methods allowing a spatially variable resolution suitable to represent both coarse processes over the open ocean and high-resolution dynamics closer to the coast and in estuaries. One-way and two-way nesting procedures can be implemented depending on whether the parent grid only provides or both provides and receives information for/from the child grid.

In the Mediterranean Sea, the CMEMS regional model provides a parent simulation for several downscaled models. Nested regular grid approaches have been used to better represent coastal processes in several areas. Even if still minoritarian due to the need for specific model developments, unstructured models using finite-elements or finite-volume discretisations allowing resolutions varying from several km to several tens of meters in the same simulation, have been successfully employed in the Venice lagoon (Umgiesser et al., 2004), Bonifacio Strait (Cucco et al., 2012), southern Adriatic and Ionian Sea (Federico et al., 2017), and in the middle Adriatic Sea, where the complex coastline geometry makes very high-resolution necessary to properly simulate the nearshore circulation and oceanic long waves amplifications (Denamiel et al., 2019). Relocatable platforms based on finite-elements models have also been developed to easily downscale the CMEMS predictions to any region of the Mediterranean Sea (Trotta et al., 2016).

10.4.1.7 Coupling hydrodynamics, wave, hydrology, and atmospheric components

In recent years, the increasing availability of computational resources has allowed substantial improvements in coupling the different components of the Earth's systems, addressing the need to better represent their multiple interactions. The complexity represented by these models can vary depending on the components involved in the coupling and on the coupling technique (i.e., offline, when data are read from external model outputs; or online one-way or two-way, when the different models are executed in parallel and exchange information on specific variables during the execution). First examples of coupled models refer to ocean-atmosphere coupling (Manabe and Bryan, 1969), developed to improve the representation of the high-resolution and HF air-sea interactions. Specifically, the sea surface temperature anomaly induces heating or cooling of the marine atmospheric boundary layer, thus altering the wind stress and heat fluxes at the sea surface which then produce variations in the ocean temperature and circulation. Air-sea coupling processes can thus improve model performance concerning, for example, the representation of extreme events (Renault et al., 2012b; Ličer et al., 2016) and the transfer of wind energy into the ocean (Byrne et al., 2016). Wind-current interactions have also recently been showed to impact the representation of the mean currents, eddying activity and wave energy in the ocean (Olita et al., 2015; Zodiatis et al., 2015; Renault et al., 2016).

Air-sea interaction processes are also influenced by surface waves, since waves modify the exchange of momentum, heat, and turbulent kinetic energy at the air-sea interface (Cavaleri et al., 2012). More precisely, wind waves modify the stress felt by

both the ocean and the atmosphere, the sea surface roughness affects the marine atmospheric boundary layer, wave breaking modifies the mixing of heat and momentum in the upper ocean layers, the shear of the Stokes drift can drive the generation of Langmuir turbulence and nonbreaking waves can also affect the upper ocean mixing.

In order to properly describe the freshwater cycle, the oceanic, atmospheric and hydrological components must also be connected at the sea surface and land interface by means of evaporation, precipitation and run-off. The hydrological cycle is further affected by currents in the ocean and winds in the atmosphere, which advect and redistribute the freshwater (Dey and Döös, 2019). The coupling between hydrological, atmospheric and oceanic models is presently still a research challenge (Verri et al., 2017) and has not yet been implemented in Mediterranean forecasting systems.

10.4.2 Illustration of some of the Mediterranean regional ocean prediction systems

10.4.2.1 Copernicus marine environment monitoring service

High resolution Mediterranean Sea prediction systems are developed and operationally delivered by the Mediterranean Monitoring Forecasting Center (Med-MFC[36]) in the framework of CMEMS. Med-MFC is a consortium implementing operational services that delivers reanalysis, analysis, and 10-day forecast products for the Mediterranean Sea dynamics, including hydrodynamics, biogeochemistry and waves through state-of-the-art modeling frameworks. These three modeling components are fully consistent in terms of resolution (1/24°, ∼3.5 km in the horizontal), bathymetry and atmospheric forcing fields (ECMWF analysis and forecasts at 1/10° resolution).

The hydrodynamic analysis and forecasting system is composed by the NEMO model 2-way coupled with the WAVEWATCH III wave model (Clementi et al., 2017). Ocean measurements from satellites (Sea Level Anomaly) and in-situ observations (temperature and salinity vertical profiles from Argo, CTD and XBT) are assimilated weekly by means of a 3D variational data assimilation system called OceanVar (Dobricic and Pinardi, 2008). Moreover a heat flux correction is performed using satellite SST data. The system is nested in the CMEMS global model with lateral open boundaries located in the Atlantic Ocean and in the Dardanelles strait. Moreover, 39 land river inputs are imposed by means of climatological runoff values. The system was upgraded in 2021 to represent the eight major Mediterranean tidal constituents. The skill of the near real-time system is continuously monitored through comparison to in situ and satellite observations.[37]

[36] https://marine.copernicus.eu/about/producers/med-mfc.
[37] https://medfs.cmcc.it/and https://marine.copernicus.eu/(Product Quality Dashboard).

The biogeochemical analysis and forecasting system (Salon et al., 2019) is composed by the BFM biogeochemical model[38] coupled with the OGSTM transport model (modified from Foujols et al., 2000). It includes a 3DVarBio assimilation scheme to assimilate surface chlorophyll retrieved from satellite sensors and chlorophyll and nitrate from BGC-Argo floats (Teruzzi et al., 2018; Cossarini et al., 2019). The system is off-line coupled with the hydrodynamic component, i.e., the ocean temperature, salinity, velocities, sea surface height, and vertical eddy diffusivity from the hydrodynamic model are used to force the OGSTM-BFM system.

Finally, the wave component (Ravdas et al., 2018) is based on a separate configuration of the WAM wave model, which allows independent and continuous upgrades in terms of data assimilation, ensemble forecasting capabilities and modeling developments. The system is also off-line coupled with the hydrodynamic component through the exchange of surface currents and sea level information.

10.4.2.2 SOCIB

SOCIB has developed three numerical operational forecasting systems[39] to respond to the regional needs in the Balearic Sea. These models predict the short-term evolution of (1) hydrodynamics and currents in the Western Mediterranean Sea, (2) wave conditions around the Balearic Islands, and (3) extreme sea level oscillations associated with meteotsunamis affecting the harbor of Ciutadella in Menorca Island.

The WMOP model (Juza et al., 2016; Mourre et al., 2018) is a regional configuration of the ROMS community model downscaling the conditions of the CMEMS Mediterranean model with a spatial resolution of 2 km and covering the Western Mediterranean basin from the Strait of Gibraltar to the longitude of the Sardinia Channel. It represents the variability from the coastal to the meso- and basin scale. It assimilates along-track satellite altimeter observations, satellite SST maps, Argo temperature and salinity profiles, surface moorings measurements, and HF radar surface currents in the Ibiza Channel, using a cost-effective local multi-model Ensemble Optimal Interpolation approach (Hernandez-Lasheras and Mourre, 2018; Hernandez-Lasheras et al., 2021). The WMOP outputs are evaluated by systematic comparisons of recent model forecasts to multiplatform observations. The system is used to generate daily predictions with a 72 h horizon, as well as multiyear free run hindcasts over past periods or data-assimilative reanalysis focusing on specific periods of interest.

The wave conditions are forecasted by the SAPO system in collaboration with the partner Spanish institution Puertos del Estado. SAPO generates predictions using the WAM model over the Western Mediterranean Sea, with several local implementations of the SWAN model for refined coastal predictions. SOCIB generates 500 m resolution predictions along the coast of the Balearic Islands.

[38] http://bfm-community.eu/.
[39] https://www.socib.es/?seccion=modelling.

SOCIB has developed a dedicated high-resolution atmosphere-ocean prediction system (BRIFS, Renault et al., 2011; Ličer et al., 2017; Mourre et al., 2021) to forecast the occurrence of meteotsunamis in Ciutadella, which is the place with the largest meteotsunamis in the region (and among the largest in the world, see also Chapter 6). BRIFS is able to represent both the HF atmospheric pressure variability and the associated oceanic response, including the generation of long oceanic waves, their amplification over the continental shelf and the final resonance in the harbor. Given the sensitivity of the magnitude of meteotsunamis to the small scale processes in the atmosphere, simulations starting with different initial states are used to generate small ensembles (Mourre et al., 2021), which allow to provide indications of the uncertainties in the prediction and associated rissaga risk warning level. The forecast horizon of BRIFS is presently 48 h.

10.4.2.3 Poseidon

The POSEIDON forecasting system includes a complete set of atmosphere and ocean prediction models (hydrodynamics, ecosystems, waves and oil spill). The atmospheric component produces high accuracy 5-day weather forecasts on a daily basis, covering the Mediterranean and the Black Sea regions with a horizontal resolution around 5 km and using boundary conditions from the NCEP global forecasts. It incorporates the nonhydrostatic version of the SKIRON/Eta model (Janjic et al., 2001), a state-of-the-art parameterization of all the major phases of the atmospheric dust life and a 3dVar data assimilation package to produce high resolution analysis fields.

The Mediterranean Sea hydrodynamic forecasting component (Fig. 10.5) is composed of a 1/20 degrees (∼5 km) resolution Mediterranean Sea implementation

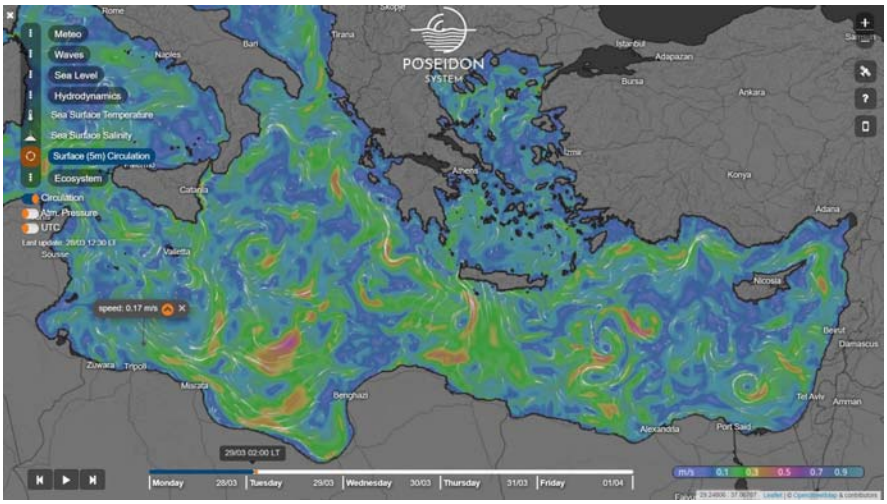

FIGURE 10.5

Surface currents forecast provided by the POSEIDON ocean prediction system in March 2022.

of the POM model with a data assimilation scheme based on the Singular Evolutive Extended Kalman (SEEK) filter operating at 1/10 degrees (Hoteit et al., 2002; Korres et al., 2007). The system produces hourly 5-day forecasts of sea level, 3D temperature salinity, and currents. The model is forced with hourly momentum, heat and freshwater fluxes derived from the POSEIDON weather prediction system. Boundary conditions at the western open boundary of the Mediterranean Sea hydrodynamic model is provided on a daily basis (daily averaged fields) by the CMEMS Mediterranean hydrodynamic model (Clementi et al., 2021). The model SST is relaxed toward the CMEMS Mediterranean near real-time satellite product (Buongiorno Nardelli et al., 2013). The SEEK assimilation scheme corrects the forecast state of a 1/10 degrees Mediterranean model on a weekly basis producing an analysis state that is further downscaled to 1/20 degrees using Gaussian 3D interpolation and variational initialization techniques (VIFOP, Auclair et al., 2000). The assimilated observational data set includes CMEMS satellite sea level height and SST, Argo profiles, XBT, FB, and gliders data whenever available.

The POSEIDON ecosystem forecasting tool couples the 1/10 degrees hydrodynamic model with a low-trophic biogeochemical component based on the European Regional Seas Ecosystem Model (ERSEM, Baretta et al., 1995; Petihakis et al., 2002). Three major functional groups are included (primary producers, heterotrophs and decomposers), providing all the necessary information for the description and analysis of carbon cycling processes, with each group further subdivided into a number of subgroups following size and/or feeding method differentiations creating a web of 10 state variables. Carbon flow in the web is governed by processes operating both at physiological and community levels such as growth, respiration, lysis, excretion, mortality, and grazing, while nutrients are loosely coupled to carbon.

The wave modeling component of POSEIDON was developed and implemented using state-of-the-art wave models like WAM Cycle 4.6.2 with a resolution of 1/10 degrees and WAVEWATCH III V6.06 with a resolution of 1/20 degrees, covering also the Black Sea. The wind inputs are provided by the POSEIDON meteorological component at hourly intervals. Finally, the POSEIDON Oil Spill fate and trajectory model (OSM) is used to simulate the drift of the oil along with the chemical transformations under the specific environmental conditions (evaporation, emulsification, beaching, and sedimentation).

10.4.2.4 Other prediction systems

Many other systems have been implemented and are routinely operated in different areas of the Mediterranean Sea. The Southern Adriatic Northern Ionian coastal Forecasting System (SANIFS[40], Federico et al., 2017) is for instance a coastal-ocean operational system based on the unstructured grid finite-element three-dimensional hydrodynamic SHYFEM model and provides short-term forecasts from the open sea to coastal areas in the Southern Adriatic and Northern Ionian

[40] http://sanifs.cmcc.it/.

Seas. The SANIFS horizontal resolution ranges from 3 km in the open sea, through 100 m in the coastal waters, to 20 m for the port and harbor areas. The Cyprus Coastal Ocean Forecasting System (CYCOFOS,[41] Zodiatis et al., 2018a) provides predictions of hydrodynamics over the Levantine Basin at a resolution of 2 km and over the Levantine Basin at a resolution of 600 m. Both models are nested in the CMEMS Mediterranean model. CYCOFOS provides also waves predictions over the entire Mediterranean Sea and the Black Sea including the Sea of Azov at a resolution of 5 km. CYCOFOS use the HF SKIRON atmospheric surface forcing for its hydrodynamics. ROSARIO (Drago et al., 2003) is an operational hydrodynamic forecasting system covering Malta continental shelf area with a resolution of around 1 km. It is part of the CAPEMALTA[42] forecasting system also including waves and atmospheric components. In France, the previous Previmer and now Marc[43] system developed by Ifremer provides daily predictions of hydrodynamics and waves in the northwestern Mediterranean Sea. As a service for Spanish ports, the SAMOA system (Sotillo et al., 2019) developed by Puertos del Estado provides a suite of 25 very coastal configurations of the ROMS model providing refined predictions with a resolution of 350 m in the vicinity of the main Spanish harbors. Several regional environmental agencies also implement their own ocean forecasting systems. This is the case for LAMMA[44] in Tuscany, ARPAE[45] in Emilia-Romagna or ARSO[46] in Slovenia. Finally, model intercomparisons tools such as the NARVAL validation system (Lorente et al., 2019) implemented over the Western Mediterranean Sea were proven useful to exploit the availability of multi-model predictions to compare model outputs and detect specific anomalies and biases.

10.5 Data management and distribution

The development of these observing and forecasting systems has generated a significant increase in the amount of oceanic data in the recent years, making specific data management strategies necessary, including defined procedures for data format harmonization, data quality control, data access, visualization and archiving. A wide range of applications involving both scientific and nonscientific users requires an automatic access to these marine data parameters. It is thus important to provide user-friendly discovery and access to multidisciplinary and aggregated data sets and data products. Associated metadata, which contain the descriptive information about the content of the dataset, are essential in this process to easily identify the data of interest. Over the three past decades, great progress has been done on data

[41] http://cycofos.orioncyprus.org/.
[42] http://www.capemalta.net.
[43] https://marc.ifremer.fr.
[44] https://www.lamma.rete.toscana.it.
[45] https://www.arpae.it.
[46] https://www.arso.gov.si.

management: national and international networks and projects progressively converged toward adoption of shared key concepts such as "measure once—use many times" (Tanhua et al., 2019), data management best practices (e.g., Pearlman et al., 2019), community standards, adoption of common vocabularies to improve the consistency, and guiding principles like FAIR advocating Findability, Accessibility, Interoperability, and Reusability of the data (Wilkinson et al., 2016). This has allowed that data from multiple sources, multiple platforms and sensors can be combined in reanalysis and forecast models, and so support services and the definition of paths toward sustainable uses of the oceans.

The international marine data management process was initiated in 1961 when the IOC-UNESCO started the International Oceanographic Data and Information Exchange (IODE) program, with the aim of enhancing marine research and meeting the needs of users for data and data products. The coordinated, decentralized and federated system GOOS collaborates with international partner infrastructures such as JCOMM (the Joint Technical Commission for Oceanography and Marine Meteorology of the World Meteorological Organization WMO and UNESCO's IOC), IODE, the International Science Council, and data centers worldwide for the planning and implementation of marine observations aimed ultimately at delivering data, products and services for both research and applications.

The key data management process cornerstones of MONGOOS include (i) provision of easy access to data through standard generic tools, preventing the user from being concerned about data source and processing, and availability of adequate metadata, (ii) integration of in situ observations with other information (e.g., satellite images or model outputs) in order to derive new products, build new services and enable better-informed decision-making, and (iii) reduction of duplication of effort among agencies.

Under this framework, the data flows through several structures and infrastructures including:

(i) Data Production Centers, i.e., primary data providers, which can be universities, oceanographic institutes or governmental agencies. There is a large number of data providers in the Mediterranean Sea. They apply as much as possible international standards of data formats and quality control to the data they collect, before distributing them through their own web servers and/or sending them directly to international data assembly centers. Specific visualization tools are often also developed for a quick and easy access to the marine information. POSEIDON,[47] SOCIB ,or PORTUS web applications are a few examples allowing easy discovery and data access to both real-time and past information.

(ii) National Oceanographic Data Centers (NODCs), which can apply a second level of standard harmonization and quality control over long-term time series

[47] https://poseidon.hcmr.gr/services/ocean-data/situ-data.

acquired by all ocean observation initiatives, missions, or experiments. NODCs were designed within the framework of IODE to manage the delayed-mode data from research cruises and research projects data. Data is delivered to NODCs to be validated and made available for secondary use. NODCs make data ready for long term stewardship by checking and completing metadata (controlled vocabularies), detecting duplicates and outliers and checking coherence with available climatologies.

(iii) Thematic Data Assembly or Regional Data Assembly Centers, which operate as data hubs to support and facilitate data sharing and interoperability at either platform specific or regional levels. Assembly centers process thematic ocean data to provide users with data and products needed by modeling and data assimilation systems. Data assembly centers collect data from providers or satellite, qualify and flag the observations and deliver them to the Global Data Assembly Centers and Integrators.

(iv) Integrators of marine data, which result from significant international collaboration and compile the maximum amount of available data.

Since the early 1990s, a wide range of initiatives have been funded and/or supported by different European Directorates-General (EU DG) such as EU DG RTD (Research and Innovation) and EU DG MARE (Maritime Affairs and Fisheries). These initiatives aimed at developing a European capacity for collecting and managing marine in situ and remote sensing data, while federating and interacting with national activities for developing data centers and data management systems. This has resulted in establishing leading European marine data management infrastructures, such as SeaDataNet[48] (physics, chemistry, geophysics, geology, and biology), EurOBIS[49] (marine biodiversity), Euro-Argo (ocean physics and marine biogeochemistry), EMODnet[50] (bathymetry, chemistry, geology, physics, biology, seabed habitats, and human activities), ICOS-Ocean[51] (carbon), and CMEMS (ocean analysis and forecasting).

These infrastructures are developed and operated by research, governmental, and industrial organizations from European states. Each of these data infrastructures is based on close links with data providers, facilitating supervision and engagement in the process that goes from data collection to validation, storage and distribution. Some of them are also increasingly involved in generating added-value data products and models. These blue data infrastructures are complementary to each other, focusing on specific databases or on different stages in the processing chains.

SeaDataNet develops the European infrastructure for managing, indexing and providing access to marine research data sets and research data products. SeaDataNet founding partners promote, develop and govern controlled vocabularies and

[48] https://www.seadatanet.org.
[49] https://www.eurobis.org/.
[50] https://www.emodnet.eu.
[51] https://otc.icos-cp.eu/.

common standards in order to facilitate data interoperability and long-term stewardship.

CMEMS, as the operational marine application service of the Copernicus Earth Observation program, is composed of three main service layers: the central information system (i.e., the catalog and the help desk), the dissemination unit (i.e., the cloud infrastructure that receives and disseminate the CMEMS products) and the production layers (composed by several production units that manage the production of observation and forecast products). The Copernicus Data and Information Access Services WEkEO[52] provides a digital platform to easily access and use data from the different Copernicus Services (marine, atmospheric, climate, and land) to facilitate innovation, science, development of new businesses and implementation of public policies.

EMODnet, the European Marine Observation and Data network, funded by the European Maritime and Fisheries Fund, was implemented in 2008 with the objective to advance toward the implementation of the European Marine Knowledge 2020 strategy, and to address seven thematic projects (bathymetry, geology, physics, chemistry, biology, seabed habitats and human activities) each aimed at developing the best methodology and standards to provide easy and free access to marine data. EMODnet turns marine data into maps, digital terrain models, time-series and statistics, dynamic plots, map viewers and other applications ready to support researchers, industries, and policymakers when tackling large societal challenges. In addition to the central portal and thematic portals and services, there is a specific ingestion portal dedicated to the uptake of data submissions from third parties which are not yet connected to the major European data infrastructures.

Focusing on the access to ocean physics parameters and products, EMODnet Physics is built on, combines and extends the scope of CMEMS and SeaDataNet. Available products are collections of in situ data, with possibilities of selection in both space and time. Data products are provided in near real-time or in the form of validated long term time series. The synchronization process is based on smart adapters connecting data from the different sources to the system and applying procedures to harmonize information (common standards, common vocabularies and metadata). Data quality is flagged according to an automatic procedure at the data source. EMODnet Physics is operationally processing this data flow to generate map layers (organized in the EMODnet GeoServer) and extract in situ trends, averages, and peak values of the parameters. Historical validated datasets are organized in collaboration with SeaDataNet and its network of NODCs, which are supplying EMODnet Physics with products (climatologies) of water column temperature and salinity. This huge amount of information is made available to users by means of several dissemination channels including map-viewers (Fig. 10.6), data servers and catalogs (Box 10.1).

[52] https://www.wekeo.eu/.

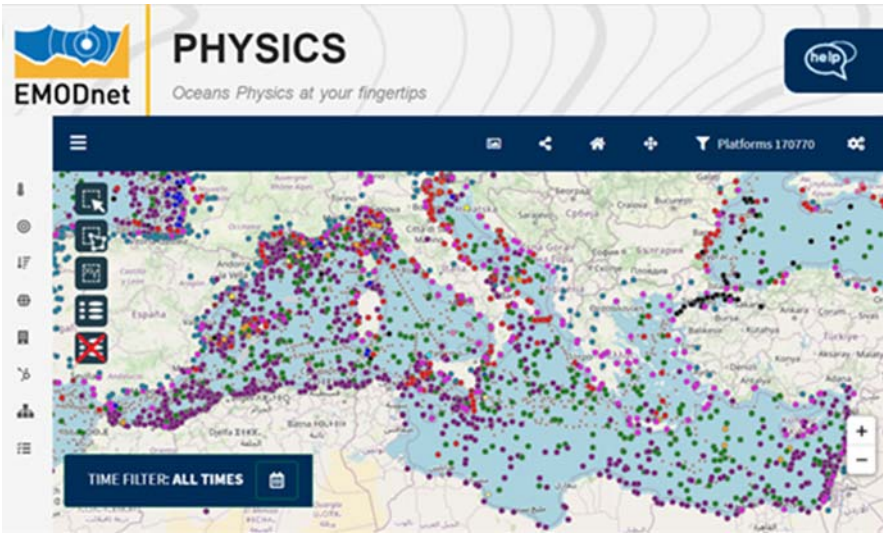

FIGURE 10.6

EMODNnet-physics map portal showing Mediterranean Sea observations from all times (https://www.emodnet-physics.eu/map).

Box 10.1 A new horizon of downstream applications: from data to products and services

These new integrated observing and forecasting systems not only have contributed to help improve our understanding of the functioning of the Mediterranean Sea, but have also opened new horizons to address sustainable development goals and provide solutions for the management and sustainable exploitation of the resources. Oceanographic products from the regional and subregional national forecasting services are transformed and provided to scientific users, administrations, private companies and citizens through added-value chains (downstreaming). Important steps forward have been taken in order to facilitate the dialogue among service providers and users for identifying requirements and needs and to co-develop and test the applications and solutions. Experiences like the Copernicus Users Uptake program, the international initiative of GeoBlue Planet, the GOOS Regional alliance downstream effort, the IOC and WMO expert teams, or SOCIB products and services approach (Heslop et al., 2019), illustrate these strategies. Communication of results and applications is also important to contribute to Ocean literacy for the dissemination of the knowledge provided by operational oceanography. As an example, capabilities and future challenges associated with larvae dispersion and fishery management, oil spills and marine litter dispersion modeling are briefly illustrated here. Notice that maritime navigation companies (Mannarini et al., 2016), ports (Sotillo et al., 2019), search and rescue agencies (Révelard et al., 2021; Ličer et al., 2020), or beach lifeguards (Heslop et al., 2019) are other important users of Mediterranean Sea marine prediction systems.

Fish larvae dispersion and fishery management During their early life, fish larvae are passively advected by ocean currents. Integrated ocean forecasting systems provide a very valuable source of information to study larvae dispersion, regional connectivity and their impact on the structure of species populations and fisheries. Lagrangian modeling (van Sebille et al., 2018) is generally used to analyze larval dispersal. It consists in computing trajectories of virtual particles

Continued

Box 10.1 A new horizon of downstream applications: from data to products and services—cont'd

moving in the ocean under the action of time-varying currents, winds, or other contributions linked to specific particle behaviors (e.g., swimming or vertical migration). Additional diffusion is often included to represent the effect of subgrid-scale processes which are not resolved in the model simulations. In the Mediterranean Sea, such approaches have been used to characterize ocean connectivity and its variability, with the objective to help design marine reserves (Di Franco et al., 2012; Andrello et al., 2013; Rossi et al., 2014; Ospina-Alvarez et al., 2020), understand correlations between genetic and oceanographic factors (Schunter et al., 2011), analyze recruitment patterns of specific species (Ospina-Alvarez et al., 2015) or investigate the role of ocean currents on the propagation of a disease at the origin of a mass mortality event (Cabanellas-Reboredo et al., 2019). Backward-in-time simulations from the settlement areas have also been analyzed to identify potential egg release zones (Calò et al., 2018; Kersting et al., 2020). Inclusion of swimming capabilities during specific larval stages allows to increase the complexity of the simulation and investigate the impact of early life traits on the larval dispersal (Torrado et al., 2021).

The study of the impact of environmental factors on larval growth and survival is also an active field of research due to their implication on the determination of species spawning grounds and recruitment all the way up to stock assessment and fisheries management. This is the case for instance for the emblematic Bluefin Tuna species, for which the Balearic Sea is one of the most important worldwide spawning grounds (Alemany et al., 2010). Oceanographic variables from integrated observing and forecasting systems can be used to define larval survival indices (Reglero et al., 2019) or to attempt modeling and predicting spawning areas according to the evolving hydrodynamic conditions (Alvarez-Berastegui et al., 2016).

Oil spills Despite the long-term decline in the total number of oil spills in the Mediterranean Sea, the risk of major accidents in the region is still high due to the increase of the hydrocarbon exploration and exploitation in the last decade and the increase of the maritime traffic following the enlargement of the Suez canal. The most advanced oil spill modeling systems are fully operational, meet the robustness and accuracy criteria, as well as the real-time requirements in terms of performance and dynamic service delivery (Zodiatis et al., 2016, 2018b; Cucco and Daniel, 2018). Oil spill models are coupled to up-to-date meteo-ocean monitoring and forecasting systems that provide the fields of ocean currents, wind and waves on a regular basis. This information not only allows computing the oil drift trajectories, but it also helps to simulate the oil weathering processes and interaction with sediments, both at the coast and on the seabed. The results are typically represented by oil mass balance time series delineating what fraction of the original spilled oil is expected to be kept afloat, evaporated, dispersed in the water column, beached or sedimented (Zodiatis et al., 2021). The predictive skills of these operational models have been evaluated during significant oil spill accidents in the Mediterranean Sea, for example, Lebanon crisis in 2006 (Coppini et al., 2011), Ulysse-Virginia oil spill in the Ligurian Sea in 2018 (Liubartseva et al., 2020).

Since oil transport is controlled by met-ocean conditions, the accuracy of oil spill simulations crucially depends on the resolution of the hydrodynamic models used, especially in coastal areas and in cases of subsurface oil leakages. To resolve coastal scale processes, downscaling techniques are being developed to reach fine scales with a resolution around 100 m. As examples, Cucco et al. (2012) developed a high-resolution system in the Strait of Bonifacio, and Sorgente et al. (2020) an operational decision supporting system for oil spill emergencies addressed to the Italian Coast Guard. Progress in downscaling led to operational oil spill modeling in harbor and port areas, such as the Port of Taranto in south Italy (Liubartseva et al., 2021) and the Port of Tarragona in Spain (Morell Villalonga et al., 2020). De Dominicis et al. (2014) developed a relocatable nested ocean model coupled to an oil spill module to provide a quick support to the Costa Concordia environmental emergency in the Tyrrhenian Sea in 2012. In these three examples, the MEDSLIK-II (De Dominicis et al., 2013) oil spill model was applied in various configurations.

Box 10.1 A new horizon of downstream applications: from data to products and services—cont'd

In France, the National Forecasting Center of Météo-France provides met-ocean support and drift forecasts to assist authorities in charge of accidental marine pollution and search and rescue operations. Forecasts are based on a drift system, called MOTHY (Daniel, 1996), consisting of an ocean model developed to best represent the surface current, and a slick or object model. In Italy, the WITOIL (Where Is The Oil) multimodel Decision Support System (DSS) was developed to provide forecast of transport and weathering of actual or hypothetical oil spills in the regional European Seas and selected coastal areas.

Along with operational oil drift forecasts in the Mediterranean, stochastic oil spill modeling has been developed for a wide variety of strategic management tasks. The approach employs a statistical analysis of model outputs composed of a large number of individual trajectories that represent the hypothetical spill scenarios from various initial locations selected randomly over a relatively long-time window. Ensemble simulations were used in the eastern Mediterranean Sea to assess the shoreline and offshore susceptibility to oil spills (Alves et al., 2014, 2015), evaluate the potential risk associated with the deployment of new offshore platforms (Alves et al., 2016; Zodiatis et al., 2021) or analyze the influence of atmospheric drivers on the evolution of the spills (Kampouris et al., 2021).

Marine litter Marine plastic pollution related to traditional human activities, such as plastic production and usage, shipping, fishing, solid-waste management, and waste water treatment, is increasingly recognized as an emerging threat to the Mediterranean environment, biodiversity, human health, and well-being. In spite of significant scientific efforts over the last decade, marine litter dispersion models have not yet reached the level of reliability of oil spill simulations. A major difficulty consists in properly initializing the model by determining the sources of plastics, including the geographic coordinates, time of release and number/mass of plastic items. Recently, an important shift has been conducted from the spatially-uniform distributions of plastic sources to a more realistic representation of land-based and offshore inputs (Liubartseva et al., 2018; Zambianchi et al., 2017; Macias et al., 2019; Soto-Navarro et al., 2020; Kaandorp et al., 2020). As an important development, the mass concentration units started to be used, which generates more practical outcomes than counting the numbers of virtual particles. Additionally, this allows the balance of plastic budget in terms of absolute units without any assumptions about the mass distribution of plastic items. The transport of floating plastic is controlled by ocean currents, waves, and wind, which redistribute plastics at sea until they eventually wash ashore or sink. The availability of long-term time series of high-resolution meteo-oceanographic model simulations have permitted major advances in marine litter simulations. Interaction with sediments, both at the coast and at the sea bottom, has been generally recognized as a relevant process for the landlocked Mediterranean Basin. At the coastline, the reflecting (Soto-Navarro et al., 2020) and absorbing boundary conditions or their combinations (Mansui et al., 2015, 2020; Liubartseva et al., 2016, 2018; Macias et al., 2019; Kaandorp et al., 2020) are usually imposed to simulate stranding of marine litter, washing off, and its stagnation near the shore. Sedimentation is mainly simulated for negatively buoyant plastics (Soto-Navarro et al., 2020; De La Fuente et al., 2021) or for those that change from positive to negative buoyancy due to biofouling (Liubartseva et al., 2018). In the Balearic Islands, the WMOP high-resolution ocean prediction system has been used to understand the observed plastic distribution in the Menorca Channel (Ruiz-Orejón et al., 2019) and to identify the origin of plastics ending up around the coasts (Compa et al., 2020) using backward-in-time trajectory simulations. With a similar approach, the evaluation of plastic pollution for two Marine Protected Areas in the Gulf of Taranto and south Adriatic Sea was carried out by Liubartseva et al. (2019). Although contemporary models are still far from covering all the processes related to marine litter at sea, they have already contributed to mutual progress in the monitoring paradigm (Galgani et al., 2019) and policy development, taking a significant step toward a robust risk assessment of plastic pollution in the Mediterranean.

10.6 Concluding remarks

A relatively large number of integrated multiplatform observing and forecasting systems have been successfully developed in the Mediterranean Sea, resulting from decades of technological developments, national and regional investments and fruitful international collaborations. Supported by established international data centers which facilitate the access to data, their visualization and archiving, these observations and model predictions have shown to be of high value to advance our understanding of the functioning of the Mediterranean Sea and its ecosystems, provide support to maritime emergencies related to search and rescue or contamination events, and build knowledge for a sustainable science-based management of coastal areas. The complementarity between prediction models and observations is exploited to optimize resources through sampling design evaluations and overall integration through data assimilation.

In the future, technological developments are expected to further enhance our monitoring capabilities. Saildrones, which are autonomous surface vehicles driven by winds and equipped with multiple sensors, are for instance presently providing new cost-effective opportunities for ocean sampling. The first pilot mission crossing the Western Mediterranean, Ionian and Adriatic Sea was carried out in 2020. In addition, time series of the sustained observation infrastructures will continue extending, delivering new knowledge on the decadal variability and trends in the Mediterranean Sea. As an example, Mediterranean glider endurance lines are reaching the 10 years of operation, providing new insights into the interannual variability in key oceanic sections.

The increased integration of biogeochemical measurements into added value products allowing to efficiently support the management and preservation of ecosystems is today among the important remaining challenges for Mediterranean observing and forecasting systems. It will also be important to reduce the north-south imbalance and help develop specific integrated systems on the southern Mediterranean coast to improve data coverage and reduce spatial gaps. Finally, the ability to exploit big data and machine learning approaches to take maximum benefit of the multiple observations now efficiently gathered in data assembly centers is certainly also an important working direction to better understand the changes occurring in the sea and be quickly adaptive in front of the present and forthcoming challenges associated with Mediterranean climate change.

References

Albuisson, M., Pontier, L., Wald, L., 1979. A comparison between sea surface temperature measurements from satellite NOAA 4 and from airborne radiometer ARIES. Oceanol. Acta 2, 1.

Alemany, F., Quintanilla, L., Velez-Belchi, P., Garcia, A., Cortés, D., Rodriguez, J.M., Fernández de Puelles, M.L., González-Pola, C., López-Jurado, L.J., 2010. Characterization of the spawning habitat of Atlantic bluefin tuna and related species in the Balearic Sea (western Mediterranean). Prog. Oceanogr. 86, 21−38.

Alpers, W., Brandt, P., Rubino, A., 2008. Internal waves generated in the straits of Gibraltar and Messina: observations from space. In: Barale, V., Gade, M. (Eds.), Remote Sensing of the European Seas. Springer, Dordrecht.

Alvarez, A., Mourre, B., 2012. Optimum sampling designs for a glider-mooring observing network. J. Atmos. Ocean. Technol. 29, 601−612.

Alvarez, A., Mourre, B., 2014. Cooperation or coordination of underwater glider networks ? an assessment from observing system simulation experiments in the Ligurian Sea. J. Ocean. Atmos. Technol. 31, 2268−2277.

Alvarez-Berastegui, D., Hidalgo, J.M., Tugores, M.P., Reglero, P., Aparicio-Gonzalez, A., Ciannelli, L., Juza, M., Mourre, B., Pascual, A., López-Jurado, J.L., García, A., Rodríguez, J.M., Tintoré, J., Alemany, F., 2016. Pelagic seascape ecology for operational fisheries oceanography: modeling and predicting spawning distribution of Atlantic bluefin tuna in Western Mediterranean. ICES (Int. Counc. Explor. Sea) J. Mar. Sci. 73 (7), 1851−1862.

Álvarez Fanjul, E., Pérez Gómez, B., Rodríguez Sánchez Arévalo, I., 2001. Nivmar: a storm surge forecasting system for Spanish waters. Sci. Mar. 65 (S1), 145−154.

Álvarez Fanjul, E., García Sotillo, M., Pérez Gómez, B., García Valdecasas, J.M., Pérez Rubio, S., Lorente, P., Rodríguez Dapena, A., Martínez Marco, I., Luna, Y., Padorno, E., Santos Atienza, I., Díaz Hernandez, G., López Lara, J., Medina, R., Grifoll, M., Espino, M., Mestres, M., Cerralbo, P., Sánchez Arcilla, A., 2018. Operational oceanography at the service of the ports. In: Chassignet, E., Pascual, A., Tintoré, J., Verron, J. (Eds.), New Frontiers in Operational Oceanography. GODAE OceanView, pp. 729−736. https://doi.org/10.17125/gov2018.ch27.

Alves, M.T., Kokinou, E., Zodiatis, G., 2014. A three-step model to assess shoreline and offshore susceptibility to oil spills: the South Aegean (Crete) as an analogue for confined marine basins. Mar. Pollut. Bull. 86, 443−457, 2014.

Alves, M.T., Kokinou, E., Zodiatis, G., Lardner, R., Panagiotakis, C., Radhakrishnan, H., 2015. Modelling of oil spills in confined maritime basins: the case for early response in the Eastern Mediterranean Sea. Environ. Pollut. 206, 390−399.

Alves, M.T., Kokinou, E., Zodiatis, G., Radhakrishnan, H., Panagiotakis, C., Lardner, R., 2016. Multidisciplinary oil spill modeling to protect coastal communities and the environment of the Eastern Mediterranean Sea. Sci. Rep. 6, 36882.

Amitai, Y., Lehahn, Y., Lazar, A., Heifetz, E., 2010. Surface circulation of the eastern Mediterranean Levantine basin: insights from analyzing 14 years of satellite altimetry data. J. Geophys. Res. 115, C10058.

Andrello, M., Mouillot, D., Beuvier, J., Albouy, C., Thuiller, W., Manel, S., 2013. Low connectivity between Mediterranean marine protected areas: a biophysical modeling approach for the Dusky grouper Epinephelus marginatus. PLoS One 8 (7), e68564.

Auclair, F., Casitas, S., Marsaleix, P., 2000. Application of an inverse method to coastal modeling. J. Atmos. Ocean. Technol. 17, 1368−1391.

Aulicino, G., Cotroneo, Y., Olmedo, E., Cesarano, C., Fusco, G., Budillon, G., 2019. In situ and satellite sea surface salinity in the Algerian basin observed through ABACUS glider measurements and BEC SMOS regional products. Rem. Sens. 11, 1361.

Aydoğdu, A., Pinardi, N., Pistoia, J., Martinelli, M., Belardinelli, A., Sparnocchia, S., 2016. Assimilation experiments for the fishery observing system in the Adriatic sea. J. Mar. Syst. 162, 126−136.

Ayoub, N., Pierre-Yves, L.T., de Mey, P., 1998. A description of the Mediterranean surface variable circulation from combined ERS-1 and TOPEX/POSEIDON altimetric data. J. Mar. Syst. 18 (1−3), 3−40.

Ballarotta, M., Ubelmann, C., Pujol, M.-I., Taburet, G., Fournier, F., Legeais, J.-F., et al., 2019. On the resolutions of ocean altimetry maps. Ocean Sci. 15, 1091−1109.

Barceló-Llull, B., Pascual, A., Sánchez-Román, A., Cutolo, E., d'Ovidio, F., Fifani, G., et al., 2021. Fine-scale ocean currents derived from in situ observations in anticipation of the upcoming SWOT altimetric mission. Front. Mar. Sci. 8, 679844.

Baretta, J.W., Ebenhöh, W., Ruardij, P., 1995. The European regional seas ecosystem model, a complex marine ecosystem model. Neth. J. Sea Res. 33, 233−246.

Bennis, A.C., Ardhuin, F., Dumas, F., 2011. On the coupling of wave and three-dimensional circulation models: choice of theoretical framework, practical implementation and adiabatic tests. Ocean Model. 40 (3−4), 260−272.

Birol, F., Delebecque, C., 2014. Using high sampling rate (10/20 Hz) altimeter data for the observation of coastal surface currents: a case study over the northwestern Mediterranean Sea. J. Mar. Syst. 129, 318−333.

Booij, N., Ris, R.C., Holthuijsen, L.H., 1999. A third-generation wave model for coastal regions, Part I, Model description and validation. J. Geoph. Res. 104 (C4), 7649−7666.

Blumberg, A.F., Mellor, G.L., 1987. A description of a three-dimensional coastal ocean circulation model. In: Heaps, N. (Ed.), Three-Dimensional Coastal Ocean Models, vol 4. American Geophysical Union, p. 208.

Bouffard, J., Vignudelli, S., Herrmann, M., Lyard, F., Marsaleix, P., Ménard, Y., Cipollini, P., 2008. Comparison of ocean dynamics with a regional circulation model and improved altimetry in the North-western Mediterranean. Terr. Atmos. Ocean Sci. 19, 117−133.

Buongiorno Nardelli, B., Larnicol, G., D'Acunzo, E., Santoleri, R., Marullo, S., Le Traon, P.Y., 2003. Near real time SLA and SST products during 2-years of MFS pilot project: processing, analysis of the variability and of the coupled patterns. Ann. Geophys. 21, 103−121.

Buongiorno Nardelli, B., Tronconi, C., Pisano, A., Santoleri, R., 2013. High and ultra-high resolution processing of satellite sea surface temperature data over Southern-European seas in the framework of MyOcean project. Remote Sens. Environ. 129, 1−16.

Byrne, D., Münnich, M., Frenger, I., et al., 2016. Mesoscale atmosphere ocean coupling enhances the transfer of wind energy into the ocean. Nat. Commun. 7 ncomms11867.

Caballero, I., Ruiz, J., Navarro, G., 2019. Sentinel-2 satellites provide near-real time evaluation of catastrophic floods in the west Mediterranean. Water 11, 2499.

Caballero, I., Fernández, R., Escalante, O.M., Mamán, L., Navarro, G., 2020. New capabilities of Sentinel-2A/B satellites combined with in situ data for monitoring small harmful algal blooms in complex coastal waters. Sci. Rep. 10, 8743.

Cabanellas-Reboredo, M., Vázquez-Luis, M., Mourre, B., Álvarez, E., Deudero, S., Amores, A., Addis, P., Ballesteros, E., Barrajón, A., Coppa, S., García-March, J.R., Giacobbe, S., Giménez Casalduero, F., Hadjioannou, l., Jiménez-Gutiérrez, S.V., Katsanevakis, S., Kersting, D., Mačić, V., Mavrič, B., Patti, F.P., Planes, S., Prado, P., Sánchez, J., Tena-Medialdea, J., de Vaugelas, J., Vicente, N., Zohra Belkhamssa, F., Zupan, I., Hendriks, I.E., 2019. Tracking the dispersion of a pathogen causing mass mortality in the pen shell Pinna nobilis: a collaborative effort of scientists and citizens. Sci. Rep. 9, 13355.

Calò, A., Lett, C., Mourre, B., Pérez-Ruzafa, A., García-Charton, J.A., 2018. Use of Lagrangian simulations to hindcast the geographical position of propagule release zones in a Mediterranean coastal fish. Mar. Environ. Res. 134, 16−27.

Casale, P., Mazaris, A.D., Freggi, D., Basso, R., Argano, R., 2007. Survival probabilities of loggerhead sea turtles (*Caretta caretta*) estimated from capture-mark-recapture data in the Mediterranean Sea. Sci. Mar. 71, 365−372.

Cavaleri, L., Alves, J., Ardhuin, F., Babanin, A., Banner, M., Belibassakis, K., Benoit, M., Donelan, M., Groeneweg, J., Herbers, T.H., Hwang, P., Janssen, P.A.E.M., Janssen, T., Lavrenov, I.V., Magne, R., Monbaliu, J., Onorato, M., Polnikov, V., Resio, D., Rogers, W.E., Sheremet, A., McKee Smith, J., Tolman, H.L., van Vledder, G., Wolf, J., Young, I., 2007. Wave modelling—the state of the art. Prog. Oceanogr. 75, 603−674.

Cavaleri, L., Fox-Kemper, B., Hemer, M., 2012. Wind waves in the coupled climate system. Bull. Am. Meteorol. Soc. 93 (11), 1651−1661.

Chelton, D., Ries, J.C., Haines, B., Fu, L.L., Callahan, P., 2001. Chapter 1 satellite altimetry. In: Satellite Altimetry and Earth Sciences—A Handbook of Techniques and Applications, vol 69. International Geophysics, pp. 1−131.

Clementi, E., Oddo, P., Drudi, M., Pinardi, N., Korres, G., Grandi, A., 2017. Coupling hydrodynamic and wave models: first step and sensitivity experiments in the Mediterranean Sea. Ocean Dynam. 67, 1293−1312.

Clementi, E., Aydogdu, A., Goglio, A.C., Pistoia, J., Escudier, R., Drudi, M., et al., 2021. Mediterranean Sea Analysis and Forecast (CMEMS MED-Currents, EAS6 System) (Version 1) [Data Set]. Copernicus Monitoring Environment Marine Service (CMEMS).

Compa, M., Alomar, C., Mourre, B., March, D., Tintoré, J., Deudero, S., 2020. Nearshore spatio-temporal sea surface trawls of plastic debris in the Balearic Islands. Mar. Environ. Res. 158, 104945.

Coppini, G., De Dominicis, M., Zodiatis, G., Lardner, R., Pinardi, N., Santoleri, R., Colella, S., Bignami, F., Hayes, D.R., Soloviev, D., Georgiou, G., Kallos, G., 2011. Hindcast of oil-spill pollution during the Lebanon crisis in the eastern Mediterranean, July-August 2006. Mar. Pollut. Bull. 62 (1), 140−153.

Coppola, L., Prieur, L., Taupier-Letage, I., Estournel, C., Testor, P., Lefevre, D., Belamari, S., Le Reste, S., Taillandier, V., 2017. Observation of oxygen ventilation into deep waters through targeted deployment of multiple Argo-O 2 floats in the north-western Mediterranean Sea in 2013. J. Geophys. Res. Oceans 122 (8), 6325−6341.

Coppola, L., Raimbault, P., Mortier, L., Testor, P., 2019. Monitoring the Environment in the Northwestern Mediterranean Sea. Eos, Transactions American Geophysical Union, American Geophysical Union (AGU), p. 100.

Cossarini, G., Mariotti, L., Feudale, L., Mignot, A., Salon, S., Taillandier, V., et al., 2019. Towards operational 3D-Var assimilation of chlorophyll Biogeochemical-Argo float data into a biogeochemical model of the Mediterranean Sea. Ocean Model. 133, 112−128.

Crépon, M., Wald, L., Monget, J.-M., 1982. Low-frequency waves in the Ligurian Sea during December 1977. J. Geophys. Res. Oceans 87, 595−600.

Cucco, A., Daniel, P., 2018. Numerical modeling of oil pollution in the western Mediterranean Sea. In: Barcelo, D., Kostianoy, A.G. (Eds.), The Handbook of Environmental Chemistry Volume 83, Oil Pollution in the Mediterranean Sea, Part I, International Context. Springer, p. 345.

Cucco, A., Ribotti, A., Olita, A., Fazioli, L., Sorgente, B., Sinerchia, M., Satta, A., Perilli, A., Borghini, M., Schroeder, K., Sorgente, R., 2012. Support to oil spill emergencies in the Bonifacio Strait, western Mediterranean. Ocean Sci. 8, 443−454.

Daniel, P., 1996. Operational forecasting of oil spill drift at Meteo-France. Spill Sci. Technol. Bull. 3 (1/2), 53−64.

Dañobeitia, J.J., Pouliquen, S., Johannessen, T., Basset, A., Cannat, M., Pfeil, B.G., Fredella, M.I., Materia, P., Gourcuff, C., Magnifico, G., Delory, E., del Rio Fernandez, J., Rodero, I., Beranzoli, L., Nardello, I., Iudicone, D., Carval, T., Gonzalez Aranda, J.M., Petihakis, G., Blandin, J., Kutsch, W.L., Rintala, J.-M., Gates, A.R., Favali, P., 2020. Toward a comprehensive and integrated strategy of the European marine research infrastructures for ocean observations. Front. Mar. Sci. 7, 180.

De Dominicis, M., Pinardi, N., Zodiatis, G., Lardner, R., 2013. MEDSLIK-II, a Lagrangian marine surface oil spill model for short term forecasting—Part 1: theory. Geosci. Model Dev. (GMD) 6, 1851−1869.

De Dominicis, M., Falchetti, S., Trotta, F., Pinardi, N., Giacomelli, L., Napolitano, E., Fazioli, L., Sorgente, R., Haley Jr., P.J., Lermusiaux, P.F.J., Martins, F., Cocco, M., 2014. A relocatable ocean model in support of environmental emergencies: the Costa Concordia emergency case. Ocean Dynam. 64 (5), 667−688.

De la Fuente, R., Drotos, G., Hernandez-Garcia, E., Lopez, C., van Sebille, E., 2021. Sinking microplastics in the water column: simulations in the Mediterranean Sea. Ocean Sci. 17, 431−453.

Denamiel, C., Šepić, J., Ivanković, D., Vilibić, I., 2019. The Adriatic Sea and coast modelling suite: evaluation of the meteotsunami forecast component. Ocean Model. 135, 71−93.

Dey, D., Döös, K., 2019. The coupled ocean−atmosphere hydrologic cycle. Tellus Dyn. Meteorol. Oceanogr. 71, 1.

Di Franco, A., Gillanders, B.M., de Benedetto, G., Pennetta, A., de Leo, G.A., Guidetti, P., 2012. Dispersal patterns of coastal fish: implications for designing networks of marine protected areas. PLoS One 7 (2), e31681.

Dobricic, S., Pinardi, N., 2008. An oceanographic three-dimensional variational data assimilation scheme. Ocean Model. 22 (3−4), 89−105.

Dobricic, S., Pinardi, N., Testor, P., Send, U., 2010. Impact of data assimilation of glider observations in the Ionian Sea (eastern Mediterranean). Dynam. Atmos. Oceans 50 (1), 78−92.

D'Ortenzio, F., Taillandier, V., Claustre, H., Coppola, L., Conan, P., Dumas, F., Durrieu du Madron, X., Fourrier, M., Gogou, A., Karageorgis, A., Lefevre, D., Leymarie, E., Oviedo, A., Pavlidou, A., Poteau, A., Poulain, P.M., Prieur, L., Psarra, S., Puyo-Pay, M., Ribera d'Alcalà, M., Schmechtig, C., Terrats, L., Velaoras, D., Wagener, T., Wimart-Rousseau, C., 2021. BGC-Argo floats observe nitrate injection and spring phytoplankton increase in the surface layer of Levantine sea (eastern Mediterranean). Geophys. Res. Lett. 48 e2020GL091649.

Drago, A.F., Sorgente, R., Ribotti, A., 2003. A high resolution hydrodynamic 3-D model simulation of the Malta shelf area. Ann. Geophys. 21, 323−344.

Dufau, C., Orsztynowicz, M., Dibarboure, G., Morrow, R., Le Traon, P.-Y., 2016. Mesoscale resolution capability of altimetry: present and future. J. Geophys. Res. Oceans 121, 4910−4927.

Eckert, S.A., Moore, J.E., Dunn, D.C., van Buiten, R.S., Eckert, K.L., Halpin, P.N., 2008. Modeling loggerhead turtle movement in the Mediterranean: importance of body size and oceanography. Ecol. Appl. 18, 290−308.

Escudier, R., Bouffard, J., Pascual, A., Poulain, P.-M., Pujol, M.-I., 2013. Improvement of coastal and mesoscale observation from space: application to the northwestern Mediterranean Sea. Geophys. Res. Lett. 40, 2148−2153.

Escudier, R., Renault, L., Pascual, A., Brasseur, P., Chelton, D., Beuvier, J., 2016a. Eddy properties in the Western Mediterranean Sea from satellite altimetry and a numerical simulation. J. Geophys. Res. Oceans 121, 3990−4006.

Escudier, R., Mourre, B., Juza, M., Tintoré, J., 2016b. Subsurface circulation and mesoscale variability in the Algerian basin from altimeter-derived eddy trajectories. J. Geophys. Res. Oceans 121 (8), 6310−6322.

Federico, I., Pinardi, N., Coppini, G., Oddo, P., Lecci, R., Mossa, M., 2017. Coastal ocean forecasting with an unstructured grid model in the southern Adriatic and northern Ionian seas. Nat. Hazards Earth Syst. Sci. 17, 45−59.

Ferrarin, C., Roland, A., Bajo, M., Umgiesser, G., Cucco, A., Davolio, S., et al., 2013. Tide-surge-wave modelling and forecasting in the Mediterranean Sea with focus on the Italian coast. Ocean Model. 61, 38−48.

Ferrarin, C., et al., 2019. Cross-scale operational oceanography in the Adriatic Sea. J. Oper. Oceanogr. 12, 86−103.

Finizio, C., Palmieri, S., Riccucci, A., 1972. A numerical model of the Adriatic for the prediction of high tides at Venice. Q. J. Roy. Meteorol. Soc. 98, 86−104.

Fontana, C., Grenz, C., Pinazo, C., 2010. Sequential assimilation of a year-long time-series of SeaWiFS chlorophyll data into a 3D biogeochemical model on the French Mediterranean coast. Continent. Shelf Res. 30, 1761−1771.

Foujols, M.-A., Lévy, M., Aumont, O., Madec, G., 2000. OPA 8.1 Tracer Model Reference Manual. Institute Pierre Simon Laplace, p. 39.

Frangoulis, C., Petihakis, G., Perivoliotis, L., Korres, G., Ballas, D., Pagonis, P., et al., 2019. The POSEIDON Supersite Observatory. A Technological Test-Bed for the Eastern Mediterranean. Oceans 2019-Marseille. IEEE, pp. 1−6.

Galgani, F., Deidun, A., Liubartseva, S., Gauci, A., Doronzo, B., Brandini, C., Gerigny, O., 2019. Monitoring and Assessment Guidelines for Marine Litter in Mediterranean MPAs. Technical Report of the Interreg/MED/AMARE Project. IFREMER/AMARE editor, p. 57.

Garreau, P., Dumas, F., Louazel, S., Correard, S., Fercocq, S., Le Menn, M., et al., 2020. PROTEVS-MED field experiments: very high resolution hydrographic surveys in the Western Mediterranean Sea. Earth Syst. Sci. Data 12 (1), 441−456.

Grodsky, S.A., Reul, N., Bentamy, A., Vandemark, D., Guimbard, S., 2019. Eastern Mediterranean salinification observed in satellite salinity from SMAP mission. J. Mar. Syst. 198, 103190.

Hayes, D.R., Dobricic, S., Gildor, H., Matsikaris, A., 2019. Operational assimilation of glider temperature and salinity for an improved description of the Cyprus Eddy. Deep-Sea Res. Part II 164, 41−53.

Hendershott, M.C., Malanotte-Rizzoli, P., 1976. The winter circulation of the Adriatic Sea. Deep-Sea Res. 23, 353−370.

Hernandez-Lasheras, J., Mourre, B., 2018. Dense CTD survey versus glider fleet sampling: comparing data assimilation performance in a regional ocean model West of Sardinia. Ocean Sci. 14, 1069−1084.

Hernandez-Lasheras, J., Mourre, B., Orfila, A., Santana, A., Reyes, E., Tintoré, J., 2021. Evaluating high-frequency radar data assimilation impact in coastal ocean operational modelling. Ocean Sci. 17, 1157−1175.

Heslop, E.E., Ruiz, S., Allen, J., López-Jurado, J.L., Renault, L., Tintoré, J., 2012. Autonomous underwater gliders monitoring variability at “choke points” in our ocean system: a case study in the Westerrn Mediterranean Sea. Geophys. Res. Lett. 39, L20604.

Heslop, E., Tintoré, J., Rotllan, P., Alvarez-Berastegui, D., Frontera, B., Mourre, B., et al., 2019. SOCIB integrated multi-platform ocean observing and forecasting: from ocean data to sector-focused delivery of products and services. J. Oper. Oceanogr. S67–S79.

Hoteit, I., Pham, D.T., Blum, J., 2002. A simplified reduced Kalman filtering and application to altimetric data assimilation in the Tropical Pacific. J. Mar. Syst. 36, 101–127.

Houpert, L., Durrieu de Madron, X., Testor, P., Bosse, A., D'Ortenzio, F., Bouin, M.N., et al., 2016. Observations of open-ocean deep convection in the northwestern Mediterranean Sea: seasonal and interannual variability of mixing and deep water masses for the 2007–2013 Period. J. Geophys. Res. Oceans 121, 8139–8171.

IOC (Intergov Oceanogr Comm), WMO (World Meterol Organ), 1988. Guide to Drifting Data Buoys. Man. Guides 20. UNESCO (United Nations Educational Scientific and Cultural Organization), Paris.

Isern-Fontanet, J., Olmedo, E., Turiel, A., Ballabrera-Poy, J., García-Ladonaía-Ladona, E., 2016. Retrieval of eddy dynamics from SMOS sea surface salinity measurements in the Algerian Basin (Mediterranean Sea). Geophys. Res. Lett. 43 (12), 6427–6434.

Iudicone, D., Santoleri, R., Marullo, S., Gerosa, P., 1998. Sea level variability and surface eddy statistics in the Mediterranean Sea from TOPEX/POSEIDON data. J. Geophys. Res. 103 (C2), 2995–3011.

Janjic, Z.I., Gerrity Jr., J.P., Nickovic, S., 2001. An alternative approach to nonhydrostatic modeling. Mon. Weather Rev. 129, 1164–1178.

Juza, M., Mourre, B., Renault, L., Gómara, S., Sebastián, K., Lora, S., et al., 2016. SOCIB operational ocean forecasting system and multi-platform validation in the Western Mediterranean Sea. J. Oper. Oceanogr. 9 (Suppl. 1), s155–s166.

Kaandorp, M., Dijkstra, H.A., Van Sebille, E., 2020. Closing the Mediterranean marine floating plastic mass budget: inverse modeling of sources and sinks. Environ. Sci. Technol. 54, 11980–11989.

Kalaroni, S., Tsiaras, K., Petihakis, G., Hoteit, I., Economou-Amilli, A., Triantafyllou, G., 2016. Data assimilation of depth-distributed satellite chlorophyll-a in two Mediterranean contrasting sites. J. Mar. Syst. 160, 40–53.

Kalaroni, S., Tsiaras, K., Petihakis, G., Economou-Amilli, A., Triantafyllou, G., 2020. Modelling the Mediterranean pelagic ecosystem using the POSEIDON ecological model. Part II: Biological dynamics. Deep-Sea Res. Part II 171, 104711.

Kampouris, K., Vervatis, V., Karagiorgos, J., Sofianos, S., 2021. Oil spill model uncertainty quantification using an atmospheric ensemble. Ocean Sci. 17, 919–934.

Kersting, D.K., Vázquez-Luis, M., Mourre, B., Belkhamssa, F.Z., Álvarez, E., Bakran-Petricioli, T., et al., 2020. Recruitment disruption and the role of unaffected populations for potential recovery after the Pinna nobilis mass mortality event. Front. Mar. Sci. 7, 594378.

Korres, G., Hoteit, I., Triantafyllou, G., 2007. Data assimilation into a Princeton Ocean model of the Mediterranean Sea using advanced Kalman filters. J. Mar. Syst. 1–4, 84–104.

Korres, G., Ntoumas, M., Potiris, M., Petihakis, G., 2014. Assimilating ferry box data into the Aegean sea model. J. Mar. Syst. 140, 59–72.

Larnicol, G., Le Traon, P.-Y., Ayoub, N., De mey, P., 1995. Mean sea level and surface circulation variability of the Mediterranean Sea from 2 years of TOPEX/POSEIDON altimetry. J. Geophys. Res. Oceans 100 (C12), 25163–25177.

Lenartz, F., Beckers, J.-M., Chiggiato, J., Mourre, B., Troupin, C., Vandenbulcke, L., Rixen, M., 2010. Super-ensemble techniques applied to wave forecast: performance and limitations. Ocean Sci. 6 (2), 595–604.

Lermusiaux, P.F.J., 1999. Estimation and study of mesoscale variability in the Strait of Sicily. Dynam. Atmos. Oceans 29, 255−303.

Le Traon, P.-Y., 2018. Satellites and operational oceanography. In: Chassignet, E., Pascual, A., Tintoré, J., Verron, J. (Eds.), New Frontiers in Operational Oceanography. GODAE OceanView, pp. 161−190. https://doi.org/10.17125/gov2018.ch07.

Le Traon, P.-Y., Morrow, R., 2001. Ocean currents and eddies (chapter 3). In: Fu, L.-L., Cazenave, A. (Eds.), A Handbook of Techniques and Applications.

Le Traon, P.-Y., D'Ortenzio, F., Babin, M., Leymarie, E., Marec, C., Pouliquen, S., et al., 2020. Preparing the new phase of Argo: scientific achievements of the NAOS project. Front. Mar. Sci. 7, 577408.

Ličer, M., Smerkol, P., Fettich, A., Ravdas, M., Papapostolou, A., Mantziafou, A., et al., 2016. Modeling the ocean and atmosphere during an extreme bora event in northern Adriatic using one-way and two-way atmosphere−ocean coupling. Ocean Sci. 12, 71−86.

Ličer, M., Mourre, B., Troupin, C., Krietemeyer, A., Jansá, A., Tintoré, J., 2017. Numerical study of Balearic meteotsunami generation and propagation under synthetic gravity wave forcing. Ocean Model. 111, 38−45.

Ličer, M., Estival, S., Reyes-Suarez, C., Deponte, D., Fettich, A., 2020. Lagrangian modelling of a person lost at sea during the Adriatic scirocco storm of 29 October 2018. Nat. Hazards Earth Syst. Sci. 20, 2335−2349.

Lindstrom, E., Gunn, J., Fischer, A., McCurdy, A., Glover, L.K., 2012. A framework for ocean observing. In: Proceedings of the Task Team for an Integrated Framework for Sustained Ocean Observing, UNESCO 2012 (Revised in 2017), IOC/INF-1284 Rev. 2, Venice.

Liubartseva, S., Coppini, G., Lecci, R., Cretì, S., 2016. Regional approach to modeling the transport of floating plastic debris in the Adriatic Sea. Mar. Pollut. Bull. 103, 115−127.

Liubartseva, S., Coppini, G., Lecci, R., Clementi, E., 2018. Tracking plastics in the Mediterranean: 2D Lagrangian model. Mar. Pollut. Bull. 129, 151−162.

Liubartseva, S., Coppini, G., Lecci, R., 2019. Are Mediterranean marine protected areas sheltered from plastic pollution? Mar. Pollut. Bull. 140, 579−587.

Liubartseva, S., Smaoui, M., Coppini, G., Gonzalez, G., Lecci, R., Creti, S., Federico, I., 2020. Model-based reconstruction of the Ulysse-Virginia oil spill, October−November 2018. Mar. Pollut. Bull. 154, 111002.

Liubartseva, S., Federico, I., Coppini, G., Lecci, R., 2021. Stochastic oil spill modeling for environmental protection at the Port of Taranto (southern Italy). Mar. Pollut. Bull. 171, 112744 (accepted).

López-Jurado, J.L., Balbín, R., Amengual, B., Aparicio-González, A., Fernández, de Puelles, M.L., et al., 2015. The RADMED monitoring program: towards an ecosystem approach. Ocean Sci. 11, 645−671.

Lorente, P., et al., 2019. The NARVAL software toolbox in support of ocean models skill assessment at regional and coastal scales. In: Rodrigues, J., et al. (Eds.), Computational Science − ICCS 2019. ICCS 2019. Lecture Notes in Computer Science, vol 11539. Springer.

Lorente, P., et al., 2022. Coastal high-frequency radars in the Mediterranean − Part 1: Status of operations and a framework for future development. Ocean Sci. 18, 761−795. https://doi.org/10.5194/os-18-761-2022.

Macias, D., Cózar, A., Garcia-Gorriz, E., González-Fernández, D., Stips, A., 2019. Surface water circulation develops seasonally changing patterns of floating litter accumulation in the Mediterranean Sea. A modelling approach. Mar. Pollut. Bull. 149, 110619.

Madec and NEMO System Team, 2019. NEMO Ocean Engine. Ocean Dynamics. Scientific Notes of Climate Modelling Center (27). Institut Pierre-Simon Laplace (IPSL). ISSN 1288-1619.

Mahadevan, A., et al., 2020. CALYPSO 2019 Cruise Report: Field Campaign in the Mediterranean. Woods Hole Oceanographic Institution.

Manabe, S., Bryan, K., 1969. Climate calculations with a combined ocean-atmosphere model. J. Atmos. Sci. 26, 786–789.

Mannarini, G., Turrisi, G., D'Anca, A., Scalas, M., Pinardi, N., Coppini, G., et al., 2016. VISIR: technological infrastructure of an operational service for safe and efficient navigation in the Mediterranean Sea. Nat. Hazards Earth Syst. Sci. 16, 1791–1806.

Mansui, J., Molcard, A., Ourmieres, Y., 2015. Modelling the transport and accumulation of floating marine debris in the Mediterranean basin. Mar. Pollut. Bull. 91, 249–257.

Mansui, J., Darmon, G., Ballerini, T., Van Canneyt, O., Ourmieres, Y., Miaud, C., 2020. Predicting marine litter accumulation patterns in the Mediterranean basin: spatio-temporal variability and comparison with empirical data. Prog. Oceanogr. 182, 102268.

Marcos, M., Tsimplis, M.N., Shaw, A.G.P., 2009. Sea level extremes in southern Europe. J. Geophys. Res. 144, 16. C01007.

Margirier, F., Testor, P., Heslop, E., Mallil, K., Bosse, A., Houpert, L., et al., 2020. Abrupt warming and salinification of intermediate waters interplays with decline of deep convection in the, Northwestern Mediterranean Sea. Sci. Rep. 10, 20923.

Marsaleix, P., Auclair, F., Floor, J.W., et al., 2008. Energy conservation issues in sigma-coordinate free-surface ocean models. Ocean Model. 20, 61–89.

Marshall, J., Adcroft, A., Hill, C., Perelman, L., Heisey, C., 1997. A finite-volume, incompressible Navier-Stokes model for studies of the ocean on parallel computers. J. Geophys. Res. 102 (C3), 5753–5766.

Marullo, S., Minnett, P.J., Santoleri, R., Tonani, M., 2016. The diurnal cycle of sea-surface temperature and estimation of the heat budget of the Mediterranean Sea. J. Geophys. Res. Oceans 121.

Mason, E., Pascual, A., 2013. Multiscale variability in the Balearic Sea: an altimetric perspective. J. Geophys. Res. Oceans 118 (6), 3007–3025.

Minnett, P.J., Alvera-Azcárate, A., Chin, T.M., Corlett, G.K., Gentemann, C.L., Karagali, I., et al., 2019. Half a century of satellite remote sensing of sea-surface temperature. Remote Sens. Environ. 233, 111366, 2019.

Morell Villalonga, M., Espino Infantes, M., Grifoll Colls, M., Mestres Ridge, M., 2020. Environmental management system for the analysis of oil spill risk using probabilistic simulations. J. Mar. Sci. Eng. 8, 277.

Mourre, B., Alvarez, A., 2012. Benefit assessment of glider adaptive sampling in the Ligurian Sea. Deep Sea Res. Oceanogr. Res. Pap. 68, 68–78.

Mourre, B., Chiggiato, J., 2014. A comparison of the performance of the 3-D super-ensemble and an ensemble Kalman filter for short-range regional ocean prediction. Tellus 66, 21640.

Mourre, B., Aguiar, E., Juza, M., Hernandez-Lasheras, J., Reyes, E., Heslop, E., et al., 2018. Assessment of high-resolution regional ocean prediction systems using muli-platform observations: illustrations in the Western Mediterranean Sea. In: Chassignet, E., Pascual, A., Tintoré, J., Verron, J. (Eds.), New Frontiers in Operational Oceanography", pp. 663–694. https://doi.org/10.17125/gov2018.ch24. GODAE Ocean View.

Mourre, B., Santana, A., Builds, A., Gautreau, L., Ličer, M., Jansà, A., Cases, B., et al., 2021. On the potential of ensemble forecasting for the prediction of meteotsunamis in the

Balearic Islands: sensitivity to atmospheric model parameterizations. Nat. Hazards 106, 1315–1336.

Muller-Karger, F.E., Miloslavich, P., Bax, N.J., Simmons, S., Costello, M.J., Sousa Pinto, I., et al., 2018. Advancing marine biological observations and data requirements of the complementary Essential Ocean variables (EOVs) and essential biodiversity variables (EBVs) frameworks. Front. Mar. Sci. 5, 211. https://doi.org/10.3389/fmars.2018.00211.

Mussap, G., Zavatarelli, M., 2017. A numerical study of the benthic–pelagic coupling in a shallow shelf sea (Gulf of Trieste). Reg. Stud. Mar. Sci. 9, 24–34, 2017.

Nagy, H., Elgindy, A., Pinardi, N., Zavatarelli, M., Oddo, P., 2017. A nested pre-operational model for the Egyptian shelf zone: model configuration and validation/calibration. Dynam. Atmos. Oceans 80, 75–96.

Nieuwejaar, P., Mazauric, V., Betzler, C., Carapuço, M., Cattrijsse, A., Coren, F., et al., 2019. Next generation European research vessels: current status and foreseeable evolution. In: Heymans, J.J., Kellett, P., Viegas, C., Alexander, B., Coopman, J., Muñiz Piniella, Á. (Eds.), Position Paper 25 of the European Marine Board, Ostend, Belgium, p. 140. https://doi.org/10.5281/zenodo.3477893. ISBN: 978-94-92043-79-5.

Niiler, P.P., Sybrandy, A.S., Bi, K., Poulain, P.M., Bitterman, D., 1995. Measurements of the water-following capability of holey-sock and TRISTAR drifters. Deep Sea Res. Oceanogr. Res. Pap. 42 (11–12), 1951–1964. https://doi.org/10.1016/0967-0637(95)00076-3.

Novelli, G., Guigand, C.M., Cousin, C., Ryan, E.H., Laxague, N.J.M., Dai, H., Özgökmen, T.M., 2017. A biodegradable surface drifter for ocean sampling on a massive scale. J. Atmos. Ocean. Technol. 34 (11), 7622509–7622532. https://doi.org/10.1175/JTECH-D-17-0055.1.

Oddo, P., Storto, A., Dobricic, S., Russo, A., Lewis, C., Onken, R., et al., 2016. A hybrid variational-ensemble data assimilation scheme with systematic error correction for limited-area ocean models. Ocean Sci. 12, 1137–1153.

Olita, A., Iermano, I., Fazioli, L., Ribotti, A., Tedesco, C., Pessini, F., et al., 2015. Impact of currents on surface flux computations and their feedback on dynamics at regional scales. Ocean Sci. 11, 657–666.

Onken, R., Alvarez, A., Fernandez, V., Vizoso, G., Basterretxea, G., Tintoré, J., et al., 2008. A forecast experiment in the Balearic Sea. J. Mar. Syst. 71 (1–2), 70–98.

Onken, R., Fiekas, H.V., Beguery, L., Borrione, I., Funk, A., Hemming, M., et al., 2018. High-resolution observations in the western Mediterranean Sea: the REP14-MED experiment. Ocean Sci. 14, 321–335.

Ospina-Alvarez, A., Catalán, I.A., Bernal, M., Roos, D., Palomera, I., 2015. From egg production to recruits: connectivity and inter-annual variability in the recruitment patterns of European anchovy in the northwestern Mediterranean. Prog. Oceanogr. 138, 431–447.

Ospina-Alvarez, A., de Juan, S., Alós, J., Basterretxea, G., 2020. MPA network design based on graph theory and emergent properties of larval dispersal. Mar. Ecol. Prog. Ser. 650, 309–326.

Pascual, A., Ruiz, S., Olita, A., Troupin, C., Claret, M., Mourre, B., et al., 2017. A multiplatform experiment to unravel meso- and submesoscale processes in an intense front (AlborEx). Front. Mar. Sci. 4, 39.

Pearlman, J., et al., 2019. Evolving and sustaining ocean Best practices and standards for the next decade. Front. Mar. Sci. 6, 277.

Pérez Gómez, B., Brouwer, R., Beckers, J., Paradis, D., Balseiro, C., et al., 2012. ENSURF: multi-model sea level forecast-implementation and validation results for the IBIROOS and Western Mediterranean regions. Ocean Sci. 8, 211–226.

Pessini, F., Olita, A., Cotroneo, Y., Perilli, A., 2018. Mesoscale eddies in the Algerian Basin: do they differ as a function of their formation site? Ocean Sci. 14, 669–688.

Petihakis, G., et al., 2006. M3A system (2000–2005) – operation and maintenance. Ocean Sci. Discuss. 3, 165–198.

Petihakis, G., Triantafyllou, G., Allen, I.J., Hoteit, I., Dounas, C., 2002. Modelling the spatial and temporal variability of the Cretan Sea ecosystem. J. Mar. Syst. 36 (3–4), 173–196.

Petihakis, G., Triantafyllou, G., Korres, G., Tsiaras, K., Theodorou, A., 2012. Ecosystem modelling: towards the development of a management tool for a marine coastal system part-II, ecosystem processes and biogeochemical fluxes. J. Mar. Syst. 94, S49–S64.

Petihakis, G., Tsiaras, K., Triantafyllou, G., Kalaroni, S., Pollani, A., 2014. A Sensitivity of the N. Aegean Sea ecosystem to black sea water inputs. Mediterr. Mar. Sci. 15 (4), 790–804.

Petrenko, A.A., Doglioli, A.M., Nencioli, F., et al., 2017. A review of the LATEX project: mesoscale to submesoscale processes in a coastal environment. Ocean Dynam. 67, 513–533.

Pinardi, N., Allen, I., Demirov, E., De Mey, P., Korres, G., et al., 2003. The Mediterranean ocean Forecasting System: first phase of implementation (1998-2001). Ann. Geophys. 21, 3–20.

Pinardi, N., Bonazzi, A., Dobricic, S., Milliff, R.F., Wikle, C.K., Berliner, L.M., 2011. Ocean ensemble forecasting. Part II: Mediterranean forecast system response. Q. J. R. Meteorol. Soc. 137, 879–893.

Pinardi, N., Özsoy, E., Latif, M.A., Moroni, F., Grandi, A., Manzella, G., 2018. Measuring the sea: Marsili's oceanographic cruise (1679–80) and the roots of oceanography. J. Phys. Oceanogr. 48, 845–860.

Pisano, A., De Dominicis, M., Biamino, W., Bignami, F., et al., 2016. An oceanographic survey for oil spill monitoring and model forecasting validation using remote sensing and in situ data in the Mediterranean Sea. Deep Sea Res. Part II Top. Stud. Oceanogr. 133.

Poulain, P.-M., Gerin, R., 2019. Assessment of the water-following capabilities of code drifters based on direct relative flow measurements. J. Atmos. Ocean. Technol. 36 (4), 621–633. https://doi.org/10.1175/JTECH-D-18801-0097.1.

Preller, R.H., Hurlburt, H.E., 1982. In: Nihoul, J.C.J. (Ed.), A Reduced Gravity Numerical Model of Circulation in the Alboran Sea. Hydrodynamics of Semi-enclosed Seas. Elsevier, pp. 75–89.

Ravaioli, M., Bergami, C., Riminucci, F., Langone, L., Cardin, V., Di Sarra, A., et al., 2016. The RITMARE Italian Fixed-Point Observatory Network (IFON) for marine environmental monitoring: a case study. J. Oper. Oceanogr. 9 (Suppl. 1), s202–s214. https://doi.org/10.1080/1755876X.2015.1114806.

Ravdas, M., Zacharioudaki, A., Korres, G., 2018. Implementation and validation of a new operational wave forecasting system of the Mediterranean monitoring and forecasting centre in the framework of the Copernicus marine environment monitoring service. Nat. Hazards Earth Syst. Sci. 18 (10), 2675–2695.

Reglero, P., Balbín, R., Abascal, F., Medina, A., Alvarez-Berastegui, D., et al., 2019. Pelagic habitat and offspring survival in the eastern stock of Atlantic bluefin tuna. ICES (Int. Counc. Explor. Sea) J. Mar. Sci. 76 (2), 549−558.

Renault, L., Vizoso, G., Jansà, A., Wilkin, J., Tintoré, J., 2011. Toward the predictability of meteotsunamis in the Balearic Sea using regional nested atmosphere and ocean models. Geophys. Res. Lett. 38, 10.

Renault, L., Oguz, T., Pascual, A., Vizoso, G., Tintore, J., 2012a. Surface circulation in the Alboran Sea (western Mediterranean) inferred from remotely sensed data. J. Geophys. Res. Ocean. 117, C8.

Renault, L., Chiggiato, J., Warner, J.C., Gomez, M., Vizoso, G., Tintoré, J., 2012b. Coupled atmosphere-ocean-wave simulations of a storm event over the Gulf of lion and Balearic Sea. J. Geophys. Res. 117, C09019.

Renault, L., Molemaker, M.J., McWilliams, J.C., Shchepetkin, A.F., Lemarié, F., et al., 2016. Modulation of wind work by oceanic current interaction with the atmosphere. J. Phys. Oceanogr. 46 (6), 1685−1704.

Révelard, A., Reyes, E., Mourre, B., Hernández-Carrasco, I., Rubio, A., et al., 2021. Sensitivity of skill score metric to validate Lagrangian simulations in coastal areas: recommendations for search and rescue applications. Front. Mar. Sci. 8, 630388.

Revelles, M., Cardona, L., Aguilar, A., San Felix, M., Fernandez, G., 2007. Habitat use by immature loggerhead sea turtles in the Algerian Basin (western Mediterranean): swimming behaviour, seasonality and dispersal pattern. Mar. Biol. 151, 1501−1515.

Reyes, E., et al., 2022. Coastal high-frequency radars in the Mediterranean − Part 2: Applications in support of science priorities and societal needs. Ocean Sci. 18, 797−837. https://doi.org/10.5194/os-18-797-2022.

Robinson, A.R., Tomasin, A., Artegiani, A., 1973. Flooding of Venice: phenomenology and prediction of the Adriatic storm surge. Q. J. Roy. Meteorol. Soc. 99, 688−692.

Rossi, V., Ser-Giacomi, E., Lõpez, C., Hernández-García, E., 2014. Hydrodynamic provinces and oceanic connectivity from a transport network help designing marine reserves. Geophys. Res. Lett. 41, 2883−2891.

Ruiz-Orejón, L.F., Mourre, B., Sarda, R., Tintoré, J., Ramis-Pujol, J., 2019. Quarterly variability of floating plastic debris in the marine protected area of the Menorca Channel (Spain). Environ. Pollut. 252, 1742−1754.

Salon, S., Cossarini, G., Bolzon, G., Feudale, L., Lazzari, P., Teruzzi, A., et al., 2019. Marine Ecosystem forecasts: skill performance of the CMEMS Mediterranean Sea model system. Ocean Sci. 15, 997−1022.

Sánchez-Román, A., Gómez-Navarro, L., Fablet, R., et al., 2019. Rafting behaviour of seabirds as a proxy to describe surface ocean currents in the Balearic Sea. Sci. Rep. 9, 17775.

Schiller, A., Mourre, B., Drillet, Y., Brassington, G., 2018. An overview of operational oceanography. In: Chassignet, E., Pascual, A., Tintoré, J., Verron, J. (Eds.), New Frontiers in Operational Oceanography", pp. 1−26. https://doi.org/10.17125/gov2018.ch01. GODAE Ocean View.

Schmidt, J., 1912. Report on the Danish oceanographical expeditions 1908−10 to the Mediterranean and adjacent seas. In: Introduction. Høst & Son, Copenhagen, pp. 1−49.

Schroeder, K., Chiggiato, J., Haza, A.C., Griffa, A., Ozgokmen, T.M., Zanasca, P., et al., 2012. Targeted Lagrangian sampling of submesoscale dispersion at a coastal frontal zone. Geophys. Res. Lett. 39 (11), L11608. https://doi.org/10.1029/2012GL051879.

Schroeder, K., Millot, C., Bengara, L., Ben Ismail, S., Bensi, M., Borghini, M., et al., 2013. Long-term monitoring programme of the hydrological variability in the Mediterranean Sea: a first overview of the HYDROCHANGES network. Ocean Sci. 9, 301–324. https://doi.org/10.5194/os-9-301-2013.

Schroeder, K., Tanhua, T., Bryden, H.L., Álvarez, M., Chiggiato, J., Aracri, S., 2015. Mediterranean Sea ship-based hydrographic Investigations program (Med-SHIP). Oceanography 28 (3), 12–15. https://doi.org/10.5670/oceanog.2015.71.

Schunter, C., Carreras-Carbonell, J., Macpherson, E., Tintoré, J., Vidal-Vijande, E., Pascual, A., et al., 2011. Matching genetics with oceanography: directional gene flow in a Mediterranean fish species. Mol. Ecol. 20, 5167–5181.

Shchepetkin, A.F., McWilliams, J.C., 2005. The regional oceanic modeling system (ROMS): a split-explicit, free-surface, topography-following-coordinate oceanic model. Ocean Model. 9, 347–404.

Signell, R.P., Chiggiato, J., Horstmann, J., Doyle, J.D., Pullen, J., Askari, F., 2010. High-resolution mapping of Bora winds in the northern Adriatic Sea using synthetic aperture radar. J. Geophys. Res. Oceans 115 (4), C04020. https://doi.org/10.1029/2009JC005524.

Sloyan, B.M., Wilkin, J., Hill, K.L., Chidichimo, M.P., Cronin, M.F., Johannessen, J.A., et al., 2019. Evolving the physical Global Ocean observing system for research and application services through international coordination. Front. Mar. Sci. 6, 449. https://doi.org/10.3389/fmars.2019.00449.

Sorgente, R., La Guardia, D., Ribotti, A., Arrigo, M., Signa, A., et al., 2020. An operational supporting system for oil spill emergencies addressed to the Italian coast guard. J. Mar. Sci. Eng. 8, 1035.

Soriano-González, J., Angelats, E., Fernández, M., Alcaraz, C., 2019. First results of phytoplankton spatial dynamics in two NW-Mediterranean bays from chlorophyll-a estimates using Sentinel 2: potential implications for aquaculture. Rem. Sens. 11 (15), 1756.

Sotillo, M.G., Cerralbo, P., Lorente, P., Grifoll, M., Espino, M., Sanchez-Arcilla, A., et al., 2019. Coastal ocean forecasting in Spanish ports: the Samoa operational service. J. Operat. Oceanogr. 13, 37–54.

Soto-Navarro, J., Jordá, G., Deudero, S., Alomar, C., Amores, Á., Compa, M., 2020. 3D hotspots of marine litter in the Mediterranean: a modeling study. Mar. Pollut. Bull. 155, 111159.

Storto, A., Oddo, P., 2019. Optimal assimilation of daytime SST retrievals from SEVIRI in a Regional Ocean prediction system. Rem. Sens. 11 (23), 2776.

Storto, A., Falchetti, S., Oddo, P., Jiang, Y.M., Tesei, A., 2020. Assessing the impact of different ocean analysis schemes on oceanic and underwater Acoustic predictions. J. Geophys. Res. Oceans 125, 7.

Tanhua, T., McCurdy, A., Fischer, A., Appeltans, W., Bax, N., Currie, K., et al., 2019. What we have learned from the framework for ocean observing: evolution of the Global Ocean observing system. Front. Mar. Sci. 6, 471. https://doi.org/10.3389/fmars.2019.00471.

Teruzzi, A., Bolzon, G., Salon, S., Lazzari, P., Solidoro, C., Cossarini, G., 2018. Assimilation of coastal and open sea biogeochemical data to improve phytoplankton simulation in the Mediterranean Sea. Ocean Model. 132, 46-6.

Testor, P., et al., 2019. OceanGliders: a component of the integrated GOOS. Front. Mar. Sci. 6, 422.

Tintoré, J., Vizoso, G., Casas, B., Heslop, E., Pascual, A., Orfila, A., Ruiz, S., et al., 2013. SOCIB: the Balearic Islands Coastal ocean observing and forecasting system, responding to science, technology and society needs. Mar. Technol. Soc. J. 47, 101–117.

Tintoré, J., et al., 2019. Challenges for sustained observing and forecasting systems in the Mediterranean Sea. Front. Mar. Sci. 6, 568.

Tolman, H., Hendrik, L., 1991. A third-generation model for wind waves on slowly varying, unsteady, and inhomogeneous depths and currents. J. Phys. Oceanogr. 21, 782−797.

Tomasin, A., 1973. A computer simulation of the Adriatic Sea for the study of its dynamics and for the forecasting of floods in the town of Venice, Comput. Phys. Commun. 5, 51−55.

Torrado, H., Mourre, B., Raventos, N., Carreras, C., Tintoré, J., Pascual, M., McPherson, E., 2021. Impact of individual early life traits in larval dispersal: a multispecies approach using backtracking models. Prog. Oceanogr. 192, 102518.

Trotta, F., Fenu, E., Pinardi, N., Bruciaferri, D., Giacomelli, L., Federico, I., Coppini, G., 2016. A structured and unstructured grid relocatable ocean platform for forecasting (SURF). Deep Sea Res. II 133, 54−75.

Turiel, A., Piles, M., González-Gambau, V., Ballabrera-Poy, J., Gabarró, C., Martinez, J., et al., 2016. 2000 days of SMOS at the Barcelona expert centre: a tribute to the work of Jordi font. Sci. Mar. 80S1, 173−193.

Umgiesser, G., Canu, D., Cucco, A., Solidoro, C., 2004. A finite element model for the Venice Lagoon. Development, set up, calibration and validation. J. Mar. Syst. 51, 123−145.

Umgiesser, G., Garreau, P., Arcilla, A.S., Clementi, E., Salon, S., et al., 2018. Modeling in the Mediterranean Sea: the MonGOOS contribution. In: Proceedings of the Eight EuroGOOS International Conference, 3-5 October 2017, Bergen, Norway. EuroGOOS, Brussels, Belgium, pp. 295−303. D/2018/14.040/1, ISBN 978-2-9601883-3-2.

Umgiesser, G., Bajo, M., Ferrarin, C., Cucco, A., Lionello, P., Zanchettin, D., et al., 2021. The prediction of floods in Venice: methods, models and uncertainty. Nat. Hazards Earth Syst. Sci. 21, 2679−2704.

Van Sebille, E., et al., 2018. Lagrangian ocean analysis: fundamentals and practices. Ocean Model. 121, 49−75.

Vargas-Yáñez, M., Juza, M., Balbín, R., Velez-Belchí, P., García-Martínez, M.C., et al., 2020. Climatological hydrographic properties and water mass transports in the Balearic channels from repeated observations over 1996−2019. Front. Mar. Sci. 7, 568602.

Vazquez-Cuervo, J., Font, J., Martinez-Benjamin, J.J., 1996. Observations on the circulation in the Alboran Sea using ERS1 altimetry and sea surface temperature data. J. Phys. Oceanogr. 26 (1996), 1426−1439.

Verri, G., Pinardi, N., Gochis, D., Tribbia, J., Navarra, A., Coppini, G., et al., 2017. A meteo-hydrological modelling system for the reconstruction of river runoff: the case of the Ofanto river catchment. Nat. Hazards Earth Syst. Sci. 17 (10), 1741−1761.

Vignudelli, S., Cipollini, P., Roblou, L., Lyard, F., et al., 2005. Improved satellite altimetry in coastal systems: case study of the Corsica channel (Mediterranean Sea). Geophys. Res. Lett. 32, 7.

Vilibić, I., Mihanović, H., Janeković, I., Denamiel, C., Poulain, P.-M., Orlić, M., et al., 2018. Wintertime dynamics in the coastal northeastern Adriatic Sea: the NAdEx 2015 experiment. Ocean Sci. 14, 237−258.

Vogelzang, J., Stoffelen, A., Verhoef, A., Figa-Saldaña, J., 2011. On the quality of high-resolution scatterometer winds. J. Geophys. Res. 116, C10033.

WAMDI Group, 1988. The WAM model—a third generation ocean wave prediction model. J. Phys. Oceanogr. 18, 1775−1810.

Wilkinson, M., Dumontier, M., Aalbersberg, I., et al., 2016. The FAIR Guiding Principles for scientific data management and stewardship. Sci. Data 3, 160018. https://doi.org/10.1038/sdata.2016.18.

Wong, A.P.S., et al., 2020. Argo data 1999−2019: two million temperature-salinity profiles and subsurface velocity observations from a global array of profiling floats. Front. Mar. Sci. 7, 700.

Zambianchi, E., Trani, M., Falco, P., 2017. Lagrangian transport of marine litter in the Mediterranean Sea. Front. Mar. Sci. 5, 5.

Zodiatis, G., Lardner, R., Solovyov, D., Panayidou, X., De Dominicis, M., 2012. Predictions for oil slicks detected from satellite images using MyOcean forecasting data. Ocean Sci. 8, 1105−1115.

Zodiatis, G., Galanis, G., Kallos, G., Nikolaidis, A., Kalogeri, C., Liakatas, A., Stylianou, S. 2015. The impact of sea surface currents in wave power potential modeling. Ocean Dynam. 65, 1547.

Zodiatis, G., et al., 2016. The Mediterranean decision support system for marine safety dedicated to oil slicks predictions. Deep Sea Res. II 133, 4−20.

Zodiatis, G., Galanis, G., Nikolaidis, A., Radhakrishnan, H., Emmanouil, G., Nikolaidis, G., et al., 2018a. Downscaling the Copernicus CMEMS Med-MFC in the Eastern Mediterranean: the new CYCOFOS forecasting systems at regional and sub-regional scales. In: Proceedings of the Eight EuroGOOS International Conference, 3−5 October 2017, Bergen, Norway. 305−310. EuroGOOS, Brussels, Belgium. D/2018/14.040/1, ISBN 978-2-9601883-3-2.

Zodiatis, G., Coppini, G., Perivoliotis, L., Lardner, R., Alves, T., Pinardi, N., et al., 2018b. Chapter: numerical modeling of oil pollution in the eastern Mediterranean Sea. In: Barcelo, D., Kostianoy, A.G. (Eds.), The Handbook of Environmental Chemistry Volume 83, Oil Pollution in the Mediterranean Sea, Part I, International Context. Springer, p. 345.

Zodiatis, G., Lardner, R., Spanoudaki, K., Sofianos, S., Radhakrishnan, H., Coppini, G., et al., 2021. Oil spill modelling assessment. In: Makarinskyy, O. (Ed.), Marine Hydrocarbon Spill Assessments. Elsevier, pp. 145−198p. ISBN: 978-0-128193549.

CHAPTER

Mediterranean Sea general biogeochemistry 11

Marta Álvarez[1], Teresa S. Catalá[2,3], Giuseppe Civitarese[4], Laurent Coppola[5,6], Abed E.R. Hassoun[7,8], Valeria Ibello[9], Paolo Lazzari[4], Dominique Lefevre[10], Diego Macías[11], Chiara Santinelli[12], Caroline Ulses[13]

[1]*Instituto Español de Oceanografía (IEO), CSIC, A Coruña, Spain;* [2]*Institute for Chemistry and Biology of the Marine Environment (ICBM), University of Oldenburg, Oldenburg, Germany;* [3]*Organization for Science, Education and Global Society, Stuttgart, Germany;* [4]*National Institute of Oceanography and Applied Geophysics - OGS, Trieste, Italy;* [5]*Sorbonne Université, CNRS, Laboratoire d'Océanographie de Villefranche, Villefranche-sur-Mer, France;* [6]*Sorbonne Université, CNRS, OSU STAMAR, Paris, France;* [7]*GEOMAR Helmholtz Centre for Ocean Research Kiel, Kiel, Germany;* [8]*National Council for Scientific Research, National Center for Marine Sciences, Beirut, Lebanon;* [9]*Middle East Technical University, Institute of Marine Sciences (METU-IMS), Erdemli-Mersin, Turkey;* [10]*Aix Marseille Université, Université de Toulon, CNRS, IRD, MIO, UM 110, Marseille, France;* [11]*Instituto de Ciencias Marinas de Andalucía (ICMAN), CSIC, Cádiz, Spain;* [12]*Consiglio Nazionale delle Ricerche, Istituto di Biofisica (CNR-IBF), Pisa, Italy;* [13]*Laboratoire d'Etudes en Géophysique et Océanographie Spatiales (LEGOS), Université de Toulouse, CNES, CNRS, IRD, UPS, Toulouse, France*

Learning Objectives

In this chapter, you will learn:

- What are the peculiarities of the Mediterranean Sea biogeochemical variables and their physical and biological controlling processes
- Why dissolved oxygen and inorganic nutrient ratios are high in the basin
- What makes the CO_2 system so complex, how the storage of anthropogenic CO_2works and induces ocean acidification
- Why dissolved organic matter in the Mediterranean Sea differs from that in the global ocean.
- How to identify and track water masses using biogeochemical variables
- Which biogeochemical changes might be expected in the basin under different future scenarios.

11.1 Dissolved oxygen distribution and ventilation

11.1.1 Introduction

Dissolved oxygen (DO) concentrations are the product of a complex equilibrium between exchanges at the ocean–atmosphere interface, thermodynamic solubility

Oceanography of the Mediterranean Sea. https://doi.org/10.1016/B978-0-12-823692-5.00004-2

equilibrium, physical (mixing and advection), and biogeochemical (photosynthesis, respiration, nitrification) fluxes in the water column, and exchanges at the sediment−water interface. The variations of DO concentrations integrate all these phenomena (Fig. 11.1). In the Mediterranean Sea, the dynamics of the convection cells (see Chapter 7) provide an important deep ventilation mechanism which limits the loss of oxygen in deep waters (Schneider et al., 2014). However, a minimum oxygen layer is located at intermediate depths with values close to 180 μmol kg^{-1}, above 70% of the saturation level (Tanhua et al., 2013a). It results from the stratification of the surface water, which limits the diffusion of oxygen into the underlying layers, and an input of organic matter from the productive layers above, fueling bacterial respiration and oxygen consumption. With the global warming that particularly affects the Mediterranean Sea (see Chapter 3), DO concentrations have become very sensitive and a global decrease in oxygen is predicted by climate and biogeochemical models, especially due to an increased water column stratification (Oschlies et al., 2008). In this context, sustained time-series and an integrated multi-platform approach capable of observing the DO variability in the Mediterranean Sea, as well as modeling, would help us to determine whether deoxygenation will be determinant and will have important implications for the carbon cycle and marine ecosystems in future climate scenarios. Further comments on the future evolution of biogeochemistry, and particularly DO, in the Mediterranean Sea is provided in subchapter 11.56.

11.1.2 Measurements of oxygen and models contribution

Measurements of DO concentrations in aquatic systems were made possible at the end of the 19th century, thanks to the implementation of the so-called Winkler

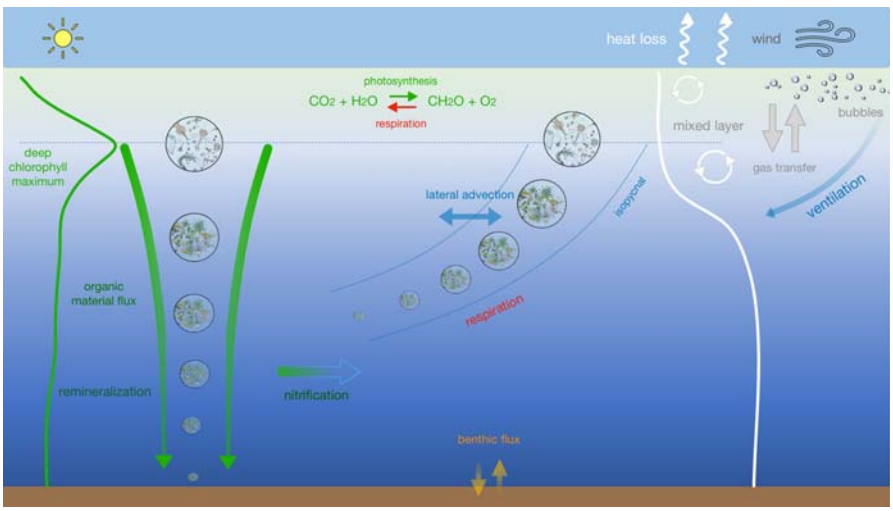

FIGURE 11.1

Processes affecting the general cycle of dissolved oxygen from the surface to deep waters.

method (Winkler, 1888). Since this method only allows discrete measurements on individual water samples, sensors were developed to estimate the concentration of DO in situ and continuously. Two families of sensors, based on two measurement principles, are used in oceanography: the electrochemical and the optical sensors.

For the electrochemical sensor, the detection technique is based on a Clark cell, in which oxygen diffuses through a membrane (permeable to gas) in contact with seawater and undergoes an amperometric reduction. The cathodic current measured is proportional to the diffusive flow of oxygen at the electrode and can be related to the concentration of DO in solution. For the optical sensor (or optode), the measurement principle is based on the *quenching* of the luminescence emitted by a luminophore immobilized on a sensitive membrane (a platinum-porphyrin complex on a silicone matrix). By the *quenching* effect, oxygen reduces the lifetime of luminescence emitted by this luminophore excited by a light pulse. In the optodes, the phosphor is modulated by a light generated by a blue Light Emitting Diode (LED). The luminescence quenching induces a phase difference in the luminescent response of the membrane. A reference phase reading is taken by a red LED. Thus the phase difference between the reference radiation and the luminescence of the membrane is related to the amount of oxygen diffusing into the membrane. In contact with seawater, the optodes provide an estimate of the DO concentration.

The electrochemical sensors developed over several decades are accurate and precise with a short response time. They are routinely coupled to a Conductivity Temperature and Depth (CTD) sensor performing profiles during oceanographic campaigns. A widely used sensor is the SBE43 sensor developed by the American company Sea-Bird Scientific. However, this sensor drifts strongly over time (biofouling effect) and has a high energy consumption, limiting its use on autonomous platforms using batteries. Optode sensors have been developed for in-water applications for about 2 decades and commercial optode sensors for measurements in the seawater column have been available for more than 10 years by different well-known marine instrument companies. Due to their small size, low power consumption and a priori good stability of the measurement over time (Körtzinger et al., 2005), optode type sensors are widely used on autonomous platforms (gliders, Argo floats, instrumented moorings, see Chapter 10).

The performance of electrochemical and optode sensors has greatly improved in recent years, yet the accuracy of DO measurements is still not optimal due to the large number of sources of uncertainty (Johnson et al., 2007). For example, in addition to the large drift over time of electrochemical sensors, these two families of sensors show a quasi-systematic bias during their deployment even if they have been correctly calibrated by the suppliers. This phenomenon is certainly largely related to the aging of the membranes. It is therefore necessary to apply systematic corrections of this bias. In this context, the Argo-DO community has developed validation and correction tools for DO data acquired on floats from optodes (Thierry et al., 2021). Recent studies have shown that measuring the partial pressure of oxygen in air by the optode (placed on a mast) when the Argo float is at the surface allows correcting for the drift of oxygen measurements and obtaining results with an

accuracy of 1% (Bittig and Körtzinger, 2015; Johnson et al., 2015). This method of correcting optode oxygen data on floats (and potentially on gliders) opens up new possibilities.

It remains true, however, that upstream (before sensor deployment) and downstream (once the data are transmitted) adjustment of the data with reference discrete measurements using the Winkler method will remain essential as the ultimate reference in any oxygen data validation/correction chain.

The dynamics of DO is simulated in coupled physical-biogeochemical models of the Mediterranean Sea (Cossarini et al., 2021; Friedland et al., 2021; Macías et al., 2018b; Moriarty et al., 2017; Ulses et al., 2021), which are complementary to the observations. In those models, the rate of change of DO concentration is the sum of biogeochemical and physical sources and sinks in the ocean interior, as well as of gas exchanges across the air-sea and sea-sediment interfaces (Fig. 11.1). The variation of DO due to physics is calculated using advection and mixing terms. The biogeochemical variation is composed of a gain term, representing the production of oxygen during photosynthesis, and sink terms representing (1) the respiration of living organisms (phytoplankton, zooplankton and bacteria that degrade organic matter) and (2) the oxidation of ammonium to nitrate (nitrification) (Fig. 11.1). When applied to areas and/or periods likely to be characterized by low concentrations, supplementary terms are added to account for anaerobic remineralization processes.

11.1.3 Dissolved oxygen distribution in the Mediterranean Sea

DO concentrations in the water column are a proxy for the physical and biological processes that affect the water masses (Fig. 11.1). DO integrates the history of these water masses since their formation in contact with the atmosphere, their passage through a bloom area, their sinking and mixing with other water masses, and the processes of mineralization of organic matter in the aphotic zone. The balance between those processes sets the DO concentration and evolution in the water column. The seasonal cycle of DO in the surface layer displays a mixing period in autumn-winter, with an increasing solubility due to a decrease in surface temperature, and an uptake of atmospheric oxygen (Coppola et al., 2018). In convective areas, undersaturation is intensified by a decrease in surface DO concentration induced by intense vertical mixing of surface DO-rich waters with the underlying DO-poorer waters (Coppola et al., 2017; Ulses et al., 2021). When sea surface temperature increases in spring, the solubility decreases, an oversaturation situation occurs, and the Mediterranean Sea starts to release oxygen to the atmosphere. During deep convection and in bloom areas during the peak of the spring bloom, oversaturation and, consequently, oxygen release to the atmosphere are maximum. Finally, the maximum DO concentration deepens with the formation of the Deep Chlorophyll Maximum (DCM) and the deepening of the biological production (Fig. 11.1).

In the Eastern Mediterranean (EMED), minimum values of DO ($\sim$180 μmol kg^{-1}) are observed in a transitional layer between the Levantine

Intermediate Water (or LIW, see Chapter 4) and the Eastern Mediterranean Deep Water (or EMDW, see Chapter 4) (Tanhua et al., 2013a; Mavropoulou et al., 2020). Here, DO concentrations in the LIW are slightly higher than in the Western Mediterranean (WMED), due to the low primary and export production (inducing a lower respiration) and the recent formation of the LIW (Fig. 11.2). In the WMED, outside the deep convection zone, LIW (300−800m) is marked by a stronger minimum of DO ($\sim$160−170 µmol kg^{-1}), due to the long time elapsed since the last contact with the atmosphere, demonstrating its older formation compared to the surrounding waters. In deep waters, i.e., the Western Mediterranean Deep Water (or WMDW, see Chapter 4) and the EMDW, the DO concentrations are higher than in intermediate layers. This reflects the formation of oxygen enriched or ventilated deep/dense water (a process that occurs in the Gulf of Lion, the Adriatic and the Cretan Seas, see Chapter 7) and its spreading in the deep subbasins (Schroeder et al., 2008; Schneider et al., 2014; Stöven and Tanhua, 2014). More information about water masses formation and distribution can be found in Chapters 4 and 7.

11.1.4 Ventilation mechanisms

The ventilation of the Mediterranean deep waters is known to be intermittent and associated with rates of dense water formation (see Chapter 7). It occurs regularly in the Gulf of Lion (and more episodically in the Ligurian Sea) and in the Adriatic or the Aegean and Cretan Seas, due to the atmospheric forcing and the preconditioning process (Testor et al., 2018). Two major recent events marked the variability of ventilation (Li and Tanhua, 2020) in the Mediterranean: the Eastern Mediterranean Transient (EMT) and the Western Mediterranean Transition (WMT). More details in these can be found in Chapters 7 and 9. Very briefly, the Adriatic Sea has been the major source

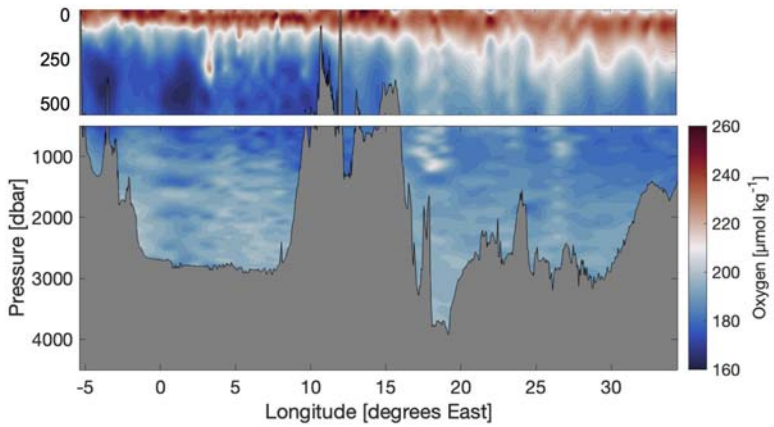

FIGURE 11.2

Mean vertical distribution of dissolved oxygen along the whole Mediterranean Sea over the last 30 years (from cruises and Argo floats data).

of dense water for the EMED before the EMT. The EMDW in the Ionian and Levantine Basins was mainly formed of relatively fresh and cold Adriatic Deep Water (AdDW). During the EMT, in the early 1990s, the dominant source of ventilation shifted to the high saline and warm Cretan Deep Water (CDW), with associated higher oxygen concentration (Mavropoulou et al., 2020). These new deep waters of Aegean origin and higher oxygen content propagated below the older and oxygen-poorer deep waters of Adriatic origin, leading to an uplift of the base of the oxygen minimum layer (OML) in the EMED. After the EMT, the Adriatic Sea restarted to be the major source of EMDW in the 2010 and 2020s (Li and Tanhua, 2020).

In the WMED, the deep DO concentration is higher than in the EMED, due to the higher rate of mixing and spreading processes. The major source of the WMDW is the deep convection area in the Gulf of Lion. Recent intense deep water formation events in the mid-2000s produced a large amount of new deep waters, ventilating much of the western deep layer. This has begun to alter the deep stratification of the entire basin causing abrupt increases in deep water temperature and salinity (Schroeder et al., 2008). This event, called WMT, induced a considerable ventilation and an increase of DO in the WMED (Coppola et al., 2018). Coppola et al. (2017) also observed a large increase in the oxygen content in the Gulf of Lion during the deep convection period in 2012−13. During the same period, Ulses et al. (2021) estimated that an amount of 20 mol m^{-2} of oxygen was captured from the atmosphere by the deep convection zone, exported toward the deep waters and then transferred laterally to the rest of the WMED in the intermediate and deep layers. They suggested that based on the rate of dense water formation (Somot et al., 2016), the ventilation due to deep convection in the north-western area in 2012/2013 may represent half of the ventilation observed in 2004/2005 by Schroeder et al. (2008).

Previous studies to estimate the dense water volume and ventilation rate are based on deep water density change criteria and numerical models from temperature and salinity data (Marty and Chiaverini, 2010; Smith et al., 2008; Schroeder et al. 2008, 2010; Béranger et al., 2010; Herrmann et al., 2010; Durrieu De Madron et al., 2013). Other ventilation studies are based on transient tracer measurements, such as CFCs and SF_6 from dedicated cruises in the Mediterranean Sea (Schneider et al., 2014; Stöven and Tanhua, 2014, see also Chapter 4). However, none of the approaches is certain and do not specifically constrain the ventilation process that involves oxygenation of the intermediate and deep waters (those using the potential density criterion), or they are complex to implement (those using models and involving water mass residence time) and benefit from only sparse data (those using CFC or SF_6 measurements). These caveats, in fact, can be overcome thanks to high-density coupled temperature, salinity, and DO data obtained from intensive deployments of autonomous systems as gliders and/or Argo-DO floats in already identified deep convection areas. As the quality of these data is increasing (e.g., the accuracy of sensor based DO data is close to 2 μmol kg^{-1} after quality control and offset and drift correction), it is now possible to use DO as a criterion to limit the volume of dense water ventilated in addition to the physical criterion of potential density (Coppola et al., 2017).

11.1.5 Long term trends: in situ observation and model contribution

Long-term DO data compiled from discrete and sensor-based measurements over the Mediterranean Sea (Fig. 11.3) show different situations depending on the depth range (surface, intermediate and deep), the time period (mixing vs. stratification), and the number of DO measurements, which has increased over time, thanks to technological advances and integration of sensors on autonomous platforms. The general trend in the surface layer (Fig. 11.3, top panel) is related to air-sea flux exchanges in winter, the spatial distribution of sea surface temperature that differs among subbasins, and the biomass production during the spring period that differs among

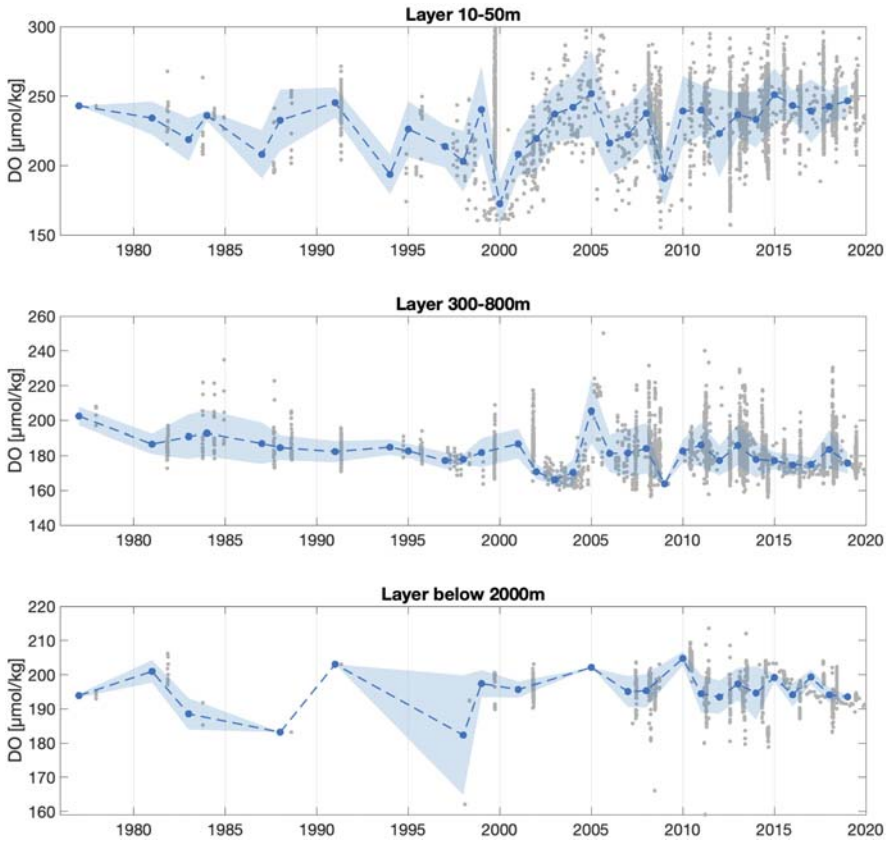

FIGURE 11.3

Trends of dissolved oxygen concentration in surface, intermediate and deep waters for the entire Mediterranean Sea from 1976 to 2019. Gathered discrete and sensor-based data are represented by gray dots, mean DO concentrations by blue dots and standard deviation by the blue patch.

bio-regions. Indeed, in the subsurface layer, biological activity is associated with a maximum at a depth of about 50−100 m (i.e., just above the DCM), and important spatial differences are associated with different levels of subbasin productivity (the western subbasins being more productive than eastern subbasins; D'Ortenzio and Ribera d'Alcalà, 2009). The trend in DO concentrations is particularly interesting in the intermediate waters (300−800 m), where an OML is typically observed (Fig. 11.3, middle panel). A negative trend has been observed from 1976 to 2000 which could be a signal of increasing deoxygenation in the intermediate waters, that goes in parallel with global warming, which might have serious impacts on the marine ecosystems. In the Mediterranean Sea, the OML is maintained by infrequent and weak convective events in regions of dense water formation (limiting DO input from surface layers) and active bacterial remineralization (responsible for DO consumption and nutrient regeneration). For example, in the Ligurian Sea, a decrease in DO was estimated to be about 5 $\mu mol\ kg^{-1}\ yr^{-1}$ during the period 1994−2005, due to the shallow mixed layer (Coppola et al., 2018). More recently, from 2014 to 2018, warmer and saltier LIW accumulated in the north-western basin, in the absence of intense deep convective winters (Margirier et al., 2020). Deep stratification beneath the LIW thus increased, which, along with the intensity of air-sea heat fluxes, constrained the depth of convection and thus oxygen ventilation. In this context, if such a scenario would be repeated, especially in the Ligurian Sea, which is less sensitive to winter mixing, the appearance of a hypoxic zone ($DO < 60\ \mu mol\ kg^{-1}$) could be expected for the next 25 years in the intermediate waters, which would be dramatic for marine life. In this context, coupled hydrodynamic-biogeochemical models will be useful tools to predict the DO trend in future periods. For example, a recent reanalysis implemented over the 20-year period (1999−2019) found a slightly negative trend in DO concentration, of the order of 0.05 and 0.10 $mmol\ m^{-3}\ yr^{-1}$ in the EMED and WMED, respectively (Cossarini et al., 2021).

In the intermediate and deep waters (Fig. 11.3, middle and bottom panels), interannual variability in DO concentrations is related to the intensity of the winter mixing layer in deep convection regions and to signals of ventilation change between the deep waters of the EMED and WMED. Rather than long-term trends, the variability of intermediate and deep DO mainly reflects the two major climatic events described above, the EMT in 1995 and 2001 and the WMT between 2004 and 2006 (Mavropoulou et al., 2020). During these periods, changes in deep DO concentrations (below 2000 m) have been reported for the Levantine Basin (Sisma-Ventura et al., 2021), the Gulf of Lion (Coppola et al., 2018), the southern Adriatic Sea (Lipizer et al., 2014), and the southern Aegean Sea (Velaoras et al., 2019), with large inputs of newly formed deep waters rich in oxygen (see Chapter 9 about abrupt changes in the Mediterranean Sea).

11.2 Dissolved nutrients: forms, sources, distribution, and dynamics

11.2.1 Introduction

The concentration of dissolved nutrients is a fundamental property of seawater, probably the most important (along with light) as far as life in the oceans is concerned. In fact, the trophic chain in the sea starts from phytoplankton and other microorganisms, which in order to grow and carry out their vital functions need to assimilate nutrients. Among nutrients, the most important species are nitrogen (N) and phosphorus (P) because, in addition to stimulating primary production (i.e., the process of incorporating inorganic nutrients by autotrophic algae), they can also be a limiting factor to growth: their deficiency makes it almost impossible for primary producers and the rest of the trophic chain to develop. Once the life cycle is completed, the produced organic matter leaves the surface production zone and is oxidized and degraded back into its initial components. This renewed bulk of nutrients will constitute a reservoir for the next production cycle.

The elemental composition of phytoplankton is relatively uniform in the ocean (on average, C:N:P = 106:16:1) reflecting the ratio of the common biochemical molecules from which they are made (Williams and Follows, 2011). As first noted by Alfred Redfield in 1958 (Redfield, 1958), in deep oceanic waters, the molar ratio between the dissolved forms of nitrate and phosphate is similar to the total N to total P ratio of marine phytoplankton (16:1), as a direct result of the equilibrium between processes of formation of living organic matter and its subsequent mineralization.

The Mediterranean Sea as a whole has long been known as an impoverished area both in terms of nutrient content (concentrations) and limited supply (fluxes) of nutrients to the surface water (McGill, 1969). Driven by the general antiestuarine circulation, the exchanges of nitrogen and phosphorus through the Strait of Gibraltar are characterized by a surface inflow of relatively nutrient-depleted water, and an intermediate outflow of nutrient-rich Mediterranean water, yielding to a large net loss of nitrate and phosphate from the Mediterranean Sea into the adjacent Atlantic Ocean. Within the Mediterranean Sea, a similar dynamic occurs at the Sicily Channel, where the exchange between the two main basins drives a net nutrient transport into the WMED, impoverishing the EMED.

As a consequence of the low nutrient concentration and the weak vertical dynamics enriching the euphotic layer, the Mediterranean is known as an oligotrophic sea and, within it, the EMED is even defined as ultraoligotrophic, with low biomass production.

The inorganic nutrient fluxes at the two straits, Gibraltar and Sicily, are highly unbalanced, the (deep) export being remarkably higher than the (surface) import. On the other hand, considering also the dissolved and particulate organic components, thus the total N and P flux across the straits, the unbalance is greatly reduced, suggesting that the WMED acts as site of mineralization for the Atlantic Ocean, while the EMED acts as a site of mineralization for the WMED. In other words,

the two basins import nutrients mostly in their organic form from the surface water of the adjacent oceanic and sea compartments, and export inorganic (mineralized) nutrients within the flux of LIW (Durrieu de Madron et al., 2009). However, this is not the only peculiarity of the Mediterranean Sea regarding inorganic nutrients. Indeed, in the deep Mediterranean, the molar ratio between NO_3^- and PO_4^{3-} concentrations (N:P hereafter) varies from 20 to 25 (Ribera d'Alcalà et al., 2003), which is significantly higher than the already mentioned Redfield ratio of 16. In other words, compared to the global ocean, the Mediterranean is poor in P, that is, it is phosphorus-limited, with an averaged N:P ratio deviating from the elemental composition of phytoplankton.

11.2.2 Nutrient forms and sources

Nutrients are crucial elements for life. In particular, nitrogen is essential for genetic material (DNA and RNA), proteins, and cell wall synthesis. Analogously, phosphorus plays a central role in genetic material (DNA and RNA), phospholipid membranes, and energetic molecular synthesis (adenosine triphosphate). Also silicon (Si) is an essential nutrient, which is required for the construction of the skeleton of peculiar phytoplankton cells, as, for example, diatoms and silicoflagellates. These three macronutrients, N, P, and Si, are needed in large amounts for the formation of organic matter in the ocean. Other nutrients, known as micronutrients (e.g., Fe, Zn, Co), are also required for life in lower concentrations, but they are not a matter of discussion in this chapter.

In the ocean, nitrogen is available for phytoplankton in different forms: inorganic (nitrate NO_3^-, nitrite NO_2^-, and ammonium NH_4^+) and organic (dissolved organic nitrogen, DON). Phosphorus is available in just one inorganic form (phosphate PO_4^{3-}) and multiple organic forms (dissolved organic phosphorus, DOP), while silicon is available as silicic acid (or dissolved silica $Si(OH)_4$) and biogenic silica (organic form bSi).

Organic nutrients differ from inorganic nutrients because they have chemical bonds with atoms of carbon, oxygen, and hydrogen, forming long chains of polymers. To make organic N bioavailable, the bonds with carbon need to be broken and this requires a certain amount of energy. Therefore, organic nutrients are generally not the first choice for phytoplankton uptake. Instead, algae prefer nutrients in an inorganic form, that require less energy for assimilation and the synthesis of organic matter. The different forms of N in the ocean are uptaken with a specific preference. NH_4^+ is preferred to NO_2^- and NO_3^-, which in turn is preferred to DON. The same happens for P, PO_4^{3-} is always preferred to DOP. Historically, organic forms were considered not accessible for the synthesis of organic matter. However, in the last decades, many studies demonstrated that in extreme oligotrophic conditions, primary production can be largely based on the organic forms of nutrients (Torres-Valdés et al., 2009). Organic forms, indeed present a continuum of availability, equivalent to a wide range of liability, i.e., the freshly produced

organic forms are more labile than the older ones, being known that many organic forms are also available for the synthesis of organic matter. Therefore, a more appropriate classification of nutrients should be done based on their bioavailability, instead of simply organic and inorganic forms. However, information about nutrient bioavailability is missing in the Mediterranean Sea, so in this section data on inorganic and organic nutrients will be used to assess the nutrient budget and distribution.

Dissolved silica is the key nutrient for building silica shells primarily of diatoms and silicoflagellates. The concentration of silica in the Mediterranean varies from one to about 10 μmol kg^{-1}. At the surface, the concentration is typically around 1 μmol kg^{-1} throughout the year, indicating that this nutrient is not limiting. Few studies have examined the silica budget in the Mediterranean Sea (Schink, 1967; Ribera d'Alcalà et al., 2003; Krom et al., 2014a), leaving some open questions as the balance of the fluxes, the real importance of diatoms, and others. Krom et al. (2014a) observed that the enrichment of the intermediate and deep water column in the EMED was due only in part to the dissolution of diatom frustules, the main internal source of silica in deep layers being the contribution of the dense water of Adriatic origin, and from in situ diagenetic weathering of aluminosilicate minerals fluxing out of the sediment (Krom et al., 2014a). The main external input for the Mediterranean Sea as a whole is the flux at the Strait of Gibraltar, estimated in the range of $51-127 \times 10^9$ mol yr^{-1} by Ribera d'Alcalà et al. (2003). The same authors estimated the Atmospheric and Terrestrial Inputs (ATI, rivers + submarine groundwater discharges + wastewaters) in the range of $12'000-42'000 \times 10^9$ mol yr^{-1}. However, they were not able to close the budget at the Strait of Gibraltar.

While the biogeochemical cycle of silicon is of great importance, it is mostly related to silica shell-building organisms, such as diatoms. Throughout the remainder of this chapter, we will focus on N and P, since the biogeochemical dynamics of these two elements involve and affect the entire marine ecosystem and determine the trophic characteristics of the Mediterranean Sea.

Both inorganic and organic N and P might have a marine or a terrestrial origin. Marine-derived nutrients can result from the mineralization of particulate organic matter (phytoplankton cells, fecal pellets, marine snow, etc.) or can be a by-product (as dissolved organic matter, DOM) from primary producers. On the other side, non-marine-derived nutrients can be originated by natural inputs (atmospheric deposition, river runoff, and submarine groundwater discharges) also impacted by anthropogenic pollution. In the Mediterranean Sea, marine-derived nutrients enter from the Atlantic Ocean: at the Strait of Gibraltar relatively fresh water enters at the surface and saltier Mediterranean waters exit at deeper layers. The nutrient inputs into the Mediterranean Sea are mainly in organic forms, while the outputs are inorganic (Fig. 11.4). The Mediterranean Sea also exchanges waters with the Black Sea through the Strait of Dardanelles and the Marmara Sea. However, here the nutrient inputs represent about 10% of the inputs from the Atlantic Ocean (Sempéré et al., 2002). Further, most of the inputs of dissolved phosphorus and

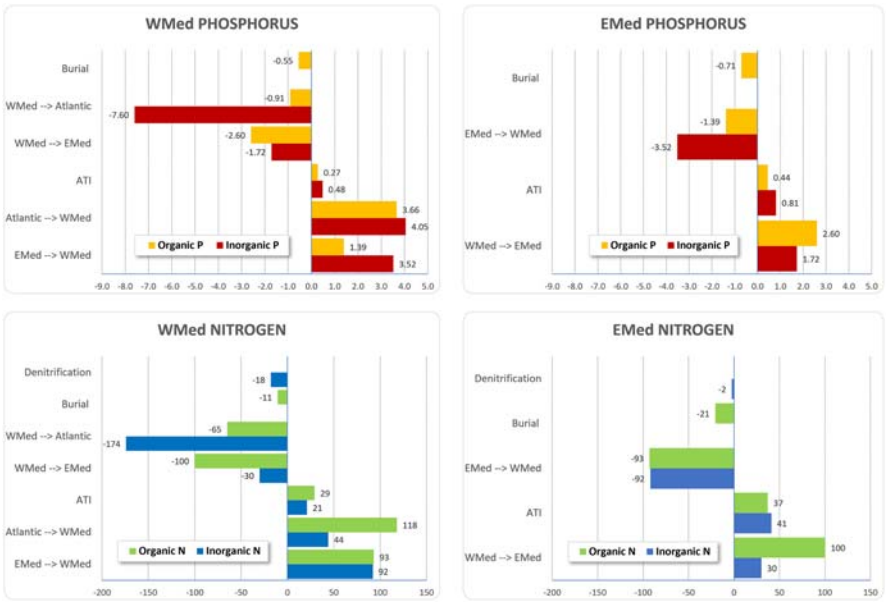

FIGURE 11.4

Transport of nutrients (organic and inorganic fraction) toward (positive) and outwards (negative) of the WMED and EMED.

Data have been extracted from P owley et al. (2017). Values are given in in 10^9 mol yr^{-1}.

dissolved inorganic nitrogen are processed within the Aegean Sea and therefore, are considered neglectable on a basin-scale (Krom et al., 2004; Sempéré et al., 2002). In addition to the surface waters entering from the adjacent seas, other sources significantly contribute to the total nutrient budget of the basin (Fig. 11.4). Inputs from the atmosphere, included within the term ATI, play an important role for both N and P, that is, more than 30% of the nonmarine-derived inputs (Markaki et al., 2010). Within ATI fluxes, submarine groundwater discharge has been underestimated for a long time, while it seems to have a crucial role for nitrogen, it seems less important for the phosphorus budget (Rodellas et al., 2015). Vice versa, river inputs contribute more to the phosphorus and less to the nitrogen budget (Ludwig et al., 2009). Wastewater discharges are comparable to riverine inputs, both for phosphorus and nitrogen (Powley et al., 2016). Note that in Fig. 11.4 the cumulative values of ATI fluxes are reported.

As commented before and summarized in Fig. 11.4, fluxes at the Strait of Gibraltar indicate that the Mediterranean exports inorganic N and P to the Atlantic, and imports organic N and P from the Atlantic. Therefore, the Mediterranean Sea acts as a site of mineralization of organic matter or, in other terms, it is heterotrophic, that is, more organic matter is consumed than produced (Powley et al., 2017).

11.2.3 Nutrients distribution

The Mediterranean Sea presents a clear east to west pattern, with the maximum concentrations of inorganic nutrients in the WMED (Fig. 11.5). In addition, the vertical distributions show two main differences (Fig. 11.6): (i) the horizon of maximum nutrient vertical gradient (nutricline) is deeper in the EMED than in the WMED; (ii) the layer of maximum nutrient concentration is deeper in the EMED than in the WMED. These two features are related to the marked oligotrophic character of the EMED and the different vertical mixing dynamics of the two basins. It is worth noticing that the upper 250 m are more stratified in the EMED, restricting upward diffusive mixing in the EMED compared to the WMED (Tanhua et al., 2013a). Fig. 11.5 depicts the large-scale open sea vertical distributions of nitrate and phosphate along a trans-Mediterranean section, showing the general and overall depletion in inorganic nutrients. However, not all Mediterranean subbasins are characterized by such a low level of nutrients: exceptions are observed in the Alboran Sea (east of the Strait of Gibraltar), the northern part of the Algero-Provençal Basin, and the northern Adriatic Sea. In this latter, due to particular dynamics (cyclonic circulation) and the terrestrial contributions to the nutrients pool (Rhone and Po rivers), respectively, a significant organic production develops and can even turn to eutrophication. On the contrary, the southern part of the Mediterranean Sea and especially the EMED are more markedly oligotrophic, because they are characterized by the Atlantic water stream (impoverished in inorganic nutrients) and the presence of permanent anticyclonic structures, respectively.

Vertically, along the water column, inorganic nutrients display the typical profile (Fig. 11.6) and the seasonality of subtropical gyres (Krom et al., 2014b). The surface euphotic layer (first $\sim$100 m) is depleted in nutrients for most of the year and shows the highest nutrient concentrations in winter, when the upper mixing is active and allows the nutrient vertical injection from the enriched intermediate layer.

In the WMED, the decrease in nutrients generally starts in spring and continues in summer—early autumn, when the water column is stratified in response to warming. In the EMED, spring blooms take place less frequently, but occur more often in late winter, due to recurrence of typical events of warming and lack of wind. During late winter, the stratification of the surface layer enriched in nutrients creates suitable conditions for phytoplankton to bloom. In late spring, when the warming drives higher stability of the water column, the blooms are weak or absent: the lack of nutrients, already consumed during the late winter production, prevents a new peak of phytoplankton (Krom et al., 2014b).

Coherently with the circulation and the trophism of the Mediterranean, nutrient content in the LIW of the EMED is lower than in the LIW of the WMED, due to its more recent formation history in the EMED (Fig. 11.6). This feature is further supported by the lower rates of primary production in the EMED, which leads to lower vertical export of organic matter and reduced mineralization of inorganic nutrients. Intermediate waters generally are characterized by the maximum concentration of nutrients (NML, Nutrient Maximum Layer), because of the mineralization of

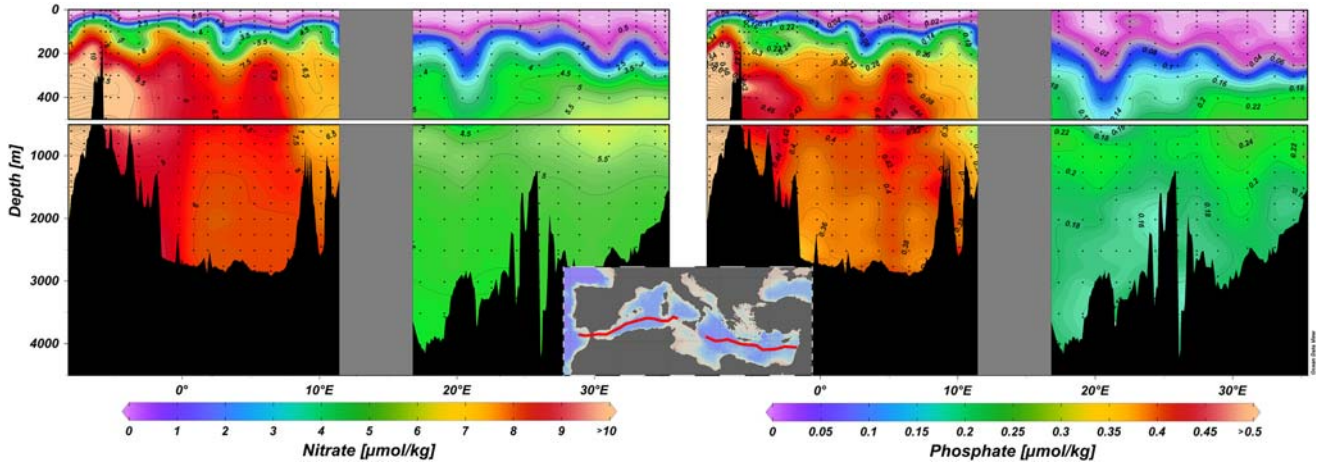

FIGURE 11.5

Vertical distribution of nitrate (left) and phosphate (right), in μmol kg^{-1}, along a trans-Mediterranean Sea section (RV METEOR cruise M84/3 in April 2011, see also Tanhua et al., 2013b).

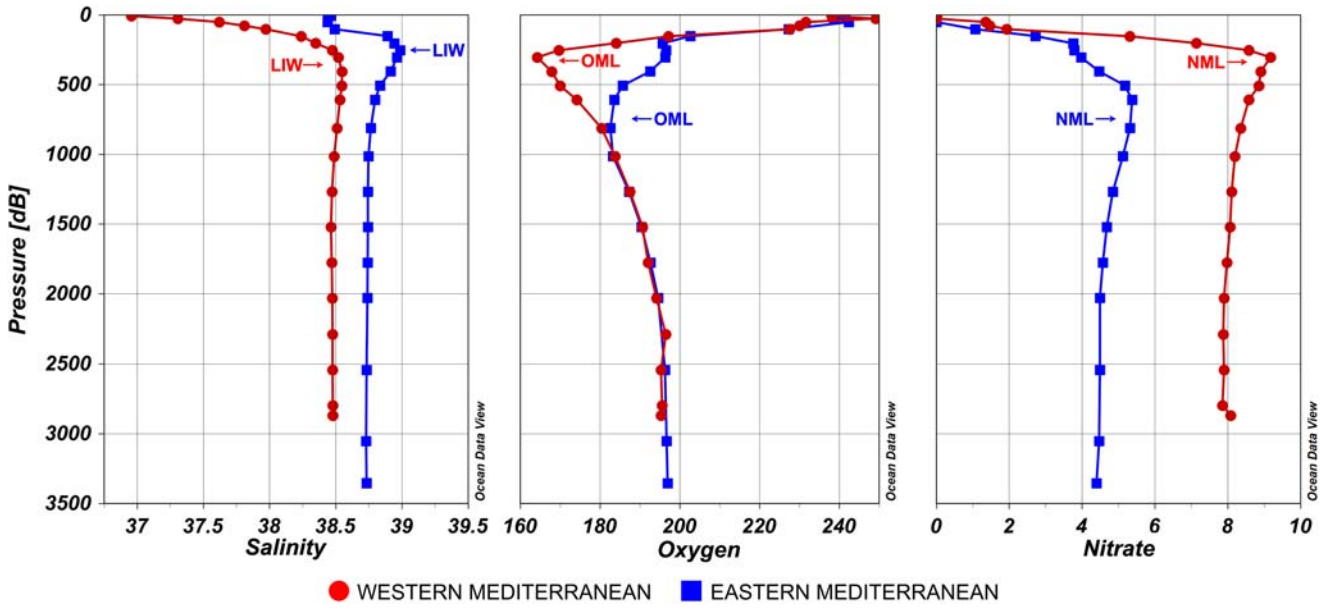

FIGURE 11.6

Vertical profiles of salinity, dissolved oxygen (μmol kg^{-1}) and nitrate (μmol kg^{-1}) in a station in the middle of the WMED (*red dots*) and in the central Ionian Sea (*blue dots*). *LIW*, Levantine Intermediate Water; *OML*, Oxygen Minimum Layer; *NML*, Nutrient Maximum Layer (RV METEOR cruise M84/3 in April 2011, see also Tanhua et al., 2013b).

organic matter that sinks from the surface layer, which is associated with a minimum oxygen concentration layer (OML). In the EMED, the NML is the result of two contrasting processes occurring along the water column: (i) the mineralization of organic matter which produces inorganic nutrients; (ii) the slight nutrient impoverishment from below because of the slow vertical mixing with deeper water of lower nutrient content. The deep layers, as in the global ocean, display a lower nutrient content than the intermediate layer, because of the reduced amount of organic matter reaching this layer and the contribution of newly formed waters, partly of surface origin.

The equilibrium between the processes of mineralization and upward mixing of deep waters determines the vertical position of the NML and the corresponding nutrient concentration. Similar considerations, but opposite, apply to DO (Fig. 11.6): the minimum of oxygen corresponds to the maximum of nutrients. In the WMED, similar features occur, but the vertical position of the NML and the corresponding OML coincide with the LIW (i.e., the salinity maximum, see Chapter 4 for a detailed description of physical properties of Mediterranean water masses), as indicated in Fig. 11.6. In that case, in the WMED there is a significant contribution of upward motion due to deep water formation processes, more pronounced than in the EMED, due to the different dynamics and spreading of dense water formation (Tanhua et al., 2013a).

11.2.4 Impact of the circulation on nutrients and biological dynamics

The oligotrophy of the Mediterranean Sea is anomalous when compared to other semienclosed basins. In the Mediterranean Sea, the special climatic conditions cause an excess of evaporation over precipitation. The saltier and denser waters formed in the basin are therefore the engine of the antiestuarine circulation, characterized by lower salinity waters entering the basin at the surface and saltier waters exiting in deep layers (see Chapter 4). In terms of nutrient dynamics, the antiestuarine circulation promotes the entrance of organic nutrients at the surface and the exit of inorganic nutrients in deep layers. However, as organic nutrients are, in respect to inorganic nutrients, less bioavailable for phytoplankton, this type of circulation determines the oligotrophy observed in the Mediterranean offshore waters.

When comparing the Mediterranean Sea with other semienclosed seas, like the Baltic Sea, it emerges that the peculiarities of the Mediterranean depend on the differences in the circulation and the bioavailability of nutrients in the surface layer (Fig. 11.7).

In the Baltic Sea, for example, rivers deliver to the basin a large amount of freshwater which stabilizes on top of the saltier waters coming from the North Sea in the subsurface layer. The euphotic layer of the basin receives a large amount of nutrients from two main sources: the rivers and the subsurface marine waters, which are naturally more enriched in nutrients with respect to the surface waters. Primary production in such conditions is highly favored and rarely limited by the

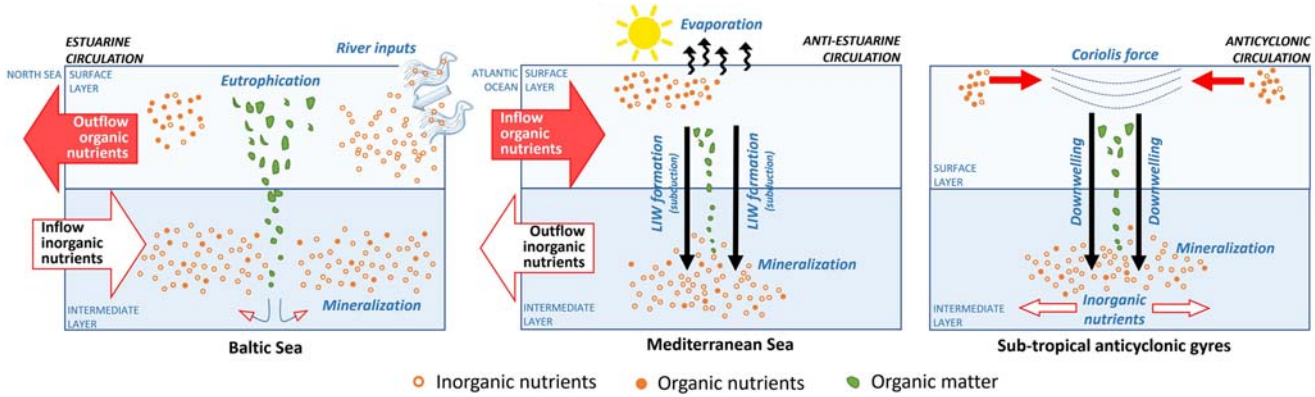

FIGURE 11.7

Infographic showing the general circulation patterns, organic, and inorganic nutrient dynamics in three different systems, from right to left: downwelling system (subtropical anticyclonic gyres), semienclosed basin with antiestuarine circulation (Mediterranean Sea) and semienclosed basin with estuarine circulation (Baltic Sea). See the text for further explanation.

availability of nutrients, which is the main reason behind the eutrophic conditions of the Baltic Sea. The chlorophyll concentration of the Mediterranean Sea is by far lower than the one recorded in the Baltic Sea and other semienclosed basins. Instead, chlorophyll concentration in the Mediterranean Sea is more comparable to the one observed in Subtropical anticyclonic gyres. In these latter, the nutrient dynamics presents a clear analogy with the antiestuarine circulation of the Mediterranean Sea: within an anticyclonic gyre, the surface water enriched in organic and depleted in inorganic nutrients is advected toward the center of the gyre; at the same time, subsurface waters enriched in inorganic nutrients are prevented from reaching the surface due to downwelling dynamics; instead, they are transported downward out of the gyre, constantly removing the most bioavailable forms of nutrients. Within the Mediterranean Sea and the anticyclonic gyres, new primary production is fueled by allochthonous nutrients, which are mainly supported by laterally advected organic forms (Letscher et al., 2016).

The above-mentioned oligotrophy is extreme in the EMED. The reasons are multiple: firstly, although the area of the two basins is comparable, the EMED receives far less nutrients from the surface waters advected through the Sicily Channel. The other source of nutrients (ATI in Fig. 11.4) does not compensate for this lack of nutrient inputs. Secondly, the mechanisms transferring nutrients from the deep layers to the surface (i.e., upwelling, winter mixing) are weaker in the EMED with respect to the WMED. Finally, due to the higher primary and bacterial production of the WMED, the nutrient content of the intermediate and deep water is higher in the WMED than in the EMED (Turley et al., 2000).

11.2.5 Anomalous N:P ratio

The so-called Redfield ratio is the stoichiometric ratio of essential elements (N:P) inside the phytoplankton cells and the ratio of inorganic nutrients in the deep ocean. As mentioned above, this convergence has been attributed to the interconnection between surface and deep ocean regulated by nutrient phytoplankton uptake, bacterial degradation, and release of nutrients back to the ocean interior (Redfield, 1958).

At the surface, nutrients are uptaken by phytoplankton with a relationship or ratio, N:P, of 16. At depth, the mineralization of organic matter sinking along the water column drives a release of inorganic nutrients in almost the same ratio. Phytoplankton is also able to uptake nutrients in different ratios, in case of excess or lack of some of the nutrients at the surface. In this case, they might accumulate more cellular growth machinery (at external N:$P < 16$, accumulated in ribosomal RNA) or more cellular resource-machinery (at external N:$P > 16$, accumulated in pigments, proteins, enzymes) depending on the limiting nutrients (Geider and LaRoche, 2002; Arrigo, 2005). The mineralization of organic matter resulting from such deviation will reflect the sources and, in the long term, will converge again toward the Redfield ratio. Other processes such as nitrogen fixation, introducing an excess of nitrogen into the ocean, might also drive a divergence from the Redfield ratio. However, on long timescales, the N surplus is equilibrated by

denitrification (Deutsch et al., 2007), a process occurring in absence of oxygen which releases molecular nitrogen gas, ultimately bubbled back to the atmosphere. In the global ocean, the combination of all these processes makes the average of N:P inside the phytoplankton cell and within the deep ocean prone to converge to the *magic* number of 16.

Using the Redfield N:P number 16 as a reference, the Mediterranean Sea receives a relatively larger amount of highly nitrogen-enriched ATI, with respect to the global ocean. The transfer of this signature to the intermediate and deep layers is carried out mainly by physical processes, while phytoplankton assimilates nutrients with an N:P = 16. Remineralization (from zooplankton and bacteria) of organic matter, which internal N:P ratio is 16, produces inorganic nutrients with N:P = 16. On the other hand, nitrogen fixation, a process where diazotrophs uptake nutrients with a highly unbalanced N:P ratio, is quite weak in the Mediterranean, while it is much stronger in the global ocean. The organic matter derived from diazotrophic production is more enriched in nitrogen than phosphorus, producing a high N:P ratio in inorganic nutrients. The nitrogen excess is reconciled by the anoxic denitrification process (from denitrifying bacteria), which consumes NO_3^- to mineralize organic matter. When denitrification rates are low, like in the Mediterranean Sea, the excess of nitrogen cannot be removed and remains as a signature of the extrainputs of N in the system.

In the Mediterranean Sea, deep waters do not present such a convergence. They display an N:P ratio of 20 and 25, respectively in the WMED and in the EMED (Ribera d'Alcalà et al., 2003). Many hypotheses have been proposed to explain such an anomaly: lack of denitrification (Krom et al., 2004), excess of nitrogen fixation (Pantoja et al., 2002), high atmospheric deposition rates (Markaki et al., 2010), the different uptake rate of nutrients by phytoplankton (Ribera d'Alcalà et al., 2003). However, none of these hypotheses, taken alone, could find a clear confirmation with field observations. Finally, a recent study combining processes and sources in a box model has disentangled the conundrum (Powley et al., 2017). Two main factors are responsible for the observed divergence: atmospheric deposition and denitrification. From one side, the Mediterranean Sea receives a large amount of N from the atmospheric deposition (Guerzoni et al., 1999), with an average N:P ratio of 100:1 (Krom et al., 2010) (Fig. 11.8). On the other hand, there is no mechanism for removing the nitrogen excess since denitrification is limited by the high content of oxygen in the basin. Therefore, the Mediterranean does not present any new or anomalous process. The anomalous N:P ratio is caused by a combination of two well-known processes presenting a different intensity in respect to the global ocean (Powley et al., 2017).

11.2.6 The anthropogenic impact

Recent studies have shown that the concentration of total N in the Mediterranean increased from 1958 to 2005 and then gradually decreased to reach the current values (Moon et al., 2016). Similarly, but with an anticipation of about 20 years, ATI have also increased. Since the 2000s, thanks to regulatory policies,

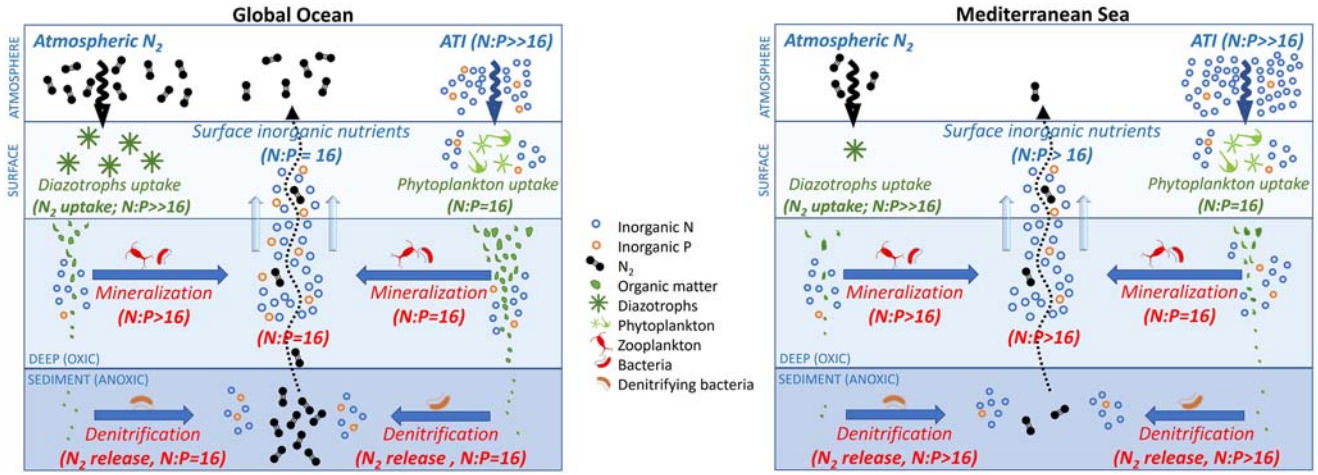

FIGURE 11.8

Infographic showing the processes (and their relative intensity) regulating the N:P ratio in the global ocean (left) and in the Mediterranean Sea (right).

anthropogenic impacts have decreased considerably, especially for air emissions (see also Chapter 13 for anthropogenic impacts on the biogeochemical cycles). Once again, it is interesting to consider how the Mediterranean reacts relatively quickly to changes in inputs, and how it can be a useful test case for policies addressed to mitigate anthropogenic impacts.

Similar results have been obtained by the model of Powley et al. (2018), where the authors have also shown that in response to a dramatic increase of anthropogenic N and P (16%−85%) emissions, primary production in the offshore waters has slightly increased (10%−20%). Powley et al. (2018) have attributed the relatively low intensity of the primary production increase to the unique thermohaline circulation within the Mediterranean Sea: thanks to the biological pump, nonmarine inputs of N and P uptaken by primary producers are transferred rapidly from surface waters into the intermediate and deep layers and then finally exported from the EMED and the WMED via the outflow through the Sicily Channel and the Strait of Gibraltar, respectively. In other words, on a longer timescales, thanks to the antiestuarine circulation and rapid overturning circulation, the amount of extranutrients introduced by anthropogenic sources is partly exported, limiting potential impacts on coastal and marine ecosystems.

This biogeochemical resilience to variations of nutrient inputs might possibly vary due to climate change. In a warmer ocean (IPCC AR6 2021), processes degrading organic matter would be favored and at the same time, less oxygen would be dissolved into the Mediterranean Sea due to the reduced solubility of gasses. Further, variations of the thermohaline circulation might lead to a decrease in the oligotrophic nature of the Mediterranean. In this regard, there is no consensus between researchers. According to IPCC AR6 (2021), the climate of the Mediterranean Sea is expected to become warmer and drier (see Chapter 3). It is therefore possible to assume some sort of balanced impact on density, the driving force behind the thermohaline circulation: the decrease of density due to the temperature increase could be compensated by the parallel reduction of freshwater input. The preservation of the current characteristics of the antiestuarine circulation in the Mediterranean will depend on the balance of these factors (see subchapter 11.6).

11.3 Dissolved organic matter: relevance, distribution, and dynamics

11.3.1 Introduction, definitions, and relevance

Marine DOM comprises a complex mixture of uncharacterized molecules in very low concentrations (Repeta, 2015, and references therein). At a mean concentration <1 mgC l^{-1}, marine DOM accounts for more than 660 PgC (Hansell et al., 2009), exceeding the carbon inventory of marine biomass by 200-fold (Hansell and Carlson, 2013) and being comparable to the CO_2 stored in the atmosphere.

DOM contains vast amounts of carbon, nitrogen, phosphorus, sulfur, iron and other essential elements, thus playing an important role in the biogeochemical cycles (Dittmar and Stubbins, 2014). According to stoichiometry rates, 93% of DOM is composed of carbon (Dissolved Organic Carbon, DOC). Being DOC a measure of DOM concentration, DOC and DOM can be used as synonymous. DOM has different key roles for marine ecosystems: (i) serves as substrate for heterotrophic microbial growth and/or nutrients recycling (Kujawinski, 2011; Cuss and Guéguen, 2015); (ii) influences the atmospheric chemistry exchanging CO_2, CO and dimethyl sulfide among other biogases; (iii) regulates the UV and visible light penetration into the water column (Blough and Del Vecchio, 2002; Nelson and Siegel, 2013); (iv) undergoes photochemical processes changing its biological lability (Mopper and Kieber, 2002); (v) acts as a trace metal ligand (Hirose, 2007); and (vi) shows antioxidant potential that counteracts the free radical negative effect on organisms (Romera-Castillo and Jaffé, 2015; Catalá et al., 2020).

Phytoplankton is the main DOM producer in the ocean epipelagic layer (0−150 m depth), as a result of photosynthesis (Hansell et al., 2009; Druffel et al., 1992). Contrary to terrestrial environments, little carbon is stored in living marine biomass, since marine organisms excrete compounds during their life cycle. Most of the released compounds are quickly turned over to CO_2 by marine microheterotrophs (i.e., labile DOM), but a minor fraction turns over very slowly and accumulates over several millennia to construct the measurable pool of DOM (i.e., recalcitrant DOM). DOM persistence in the ocean is one of the most pressing issues in marine science (Dittmar et al., 2021).

Two long-standing hypotheses have been postulated to explain the DOM persistence in the ocean: (1) the long-standing *intrinsic recalcitrance* paradigm suggests that some organic compounds are intrinsically hard to metabolize, while in (2) the *emergent recalcitrance* concept, DOM is continuously transformed by marine microheterotrophs, with recalcitrance emerging on an ecosystem level (Dittmar et al., 2021; Repeta, 2021; Zakem et al., 2021). Both concepts are integrated with the ecological and environmental context in the new overarching research strategy *ecology of molecules* (Dittmar et al., 2021). In such a term, individual DOM compounds and organisms interact within ecological networks, emerging new system properties as result of the synergy of the individual compounds (Mentges et al., 2019, 2020).

11.3.2 DOC distribution in the Mediterranean Sea, a basin scale view

In the Mediterranean Sea, DOC values and vertical profiles compare well with those observed in the open ocean, even if some differences can be highlighted. This is explained for each layer in detail in the following sections.

11.3.2.1 Surface layer

Most of the DOM production and release processes occur in the surface layer, where the highest values (53−128 μM) and the largest variability are observed. Surface distribution is strongly affected by external inputs (atmosphere, rivers, and ground waters) (Galletti et al., 2020; Retelletti Brogi et al., 2022); mesoscale activity, leading to DOC accumulation in the core of anticyclonic eddies; surface transport among basins (Santinelli et al., 2021); and stratification/homogenization patterns (Santinelli et al., 2013; Santinelli, 2015). The Mediterranean Sea shows an eastward increase in DOC, associated with a decrease in both heterotrophic prokaryote abundance and production. DOC values higher than 65 μM are usually observed in the easternmost part of the basin, with a stock of 9−13 mol m^{-2} accumulating in the surface layer (150−250 m) (Pujo-Pay et al., 2011; Santinelli et al., 2012; Santinelli, 2015). A different functioning of the microbial loop has been hypothesized for the Mediterranean. In the WMED, DOC shows low values, whereas both bacteria and their grazers are abundant, suggesting that the microbial loop is very active and works as a link of carbon to the food web. Going east, DOC concentration increases, but this accumulation does not fuel the bacterial production (Santinelli et al., 2012). DOM accumulation is usually due to a decoupling between its production and removal processes. In the EMED, the low bacterial production and abundance suggest that the main driver of DOC accumulation is the decrease in bacterial activity. We can therefore hypothesize that bacteria are limited by the availability of an essential nutrient (in particular P) or by the occurrence of recalcitrant DOC that cannot be used on the short temporal scale. No matter what is the main process responsible for DOC accumulation, the Levantine basin would be an ideal place to study DOM persistence in the ocean.

11.3.2.2 Seasonal variability

Information about DOM temporal variability in the Mediterranean Sea is scarce and limited to restricted coastal areas (Santinelli, 2015 and references therein; Álvarez-Salgado et al., 2020; Sánchez-Pérez et al., 2020). Though this basin is located at temperate latitudes and is characterized by an evident seasonal cycle, the DOM temporal variability shows some interesting differences depending on the area taken into consideration. In some areas, such as the Ligurian and the Adriatic Sea, DOM shows a seasonal cycle, similar to that observed in temperate regions of the oceans with maximum values in mid-to-late summer (August−September), followed by a gradual decrease until a minimum in winter (Santinelli et al., 2013; Avril, 2002; Sánchez-Pérez et al., 2020). In other areas, such as the Tyrrhenian Sea, where stratification never breaks and winter mixing rarely exceeds 150 m, DOM shows high values in the above-pycnocline layer throughout the year (Santinelli et al., 2013).

Interestingly, seasonality is also observed in DOC exchange at the Gibraltar Strait. DOC flux exhibits a marked bimodal distribution with minima in late June and late October and maxima in mid-April and late August. Net DOC input from the Atlantic is equivalent to 4.2 ± 1.5 TgC yr^{-1}, representing 53% of the external

DOC inputs, and contributes to supporting 32% of the net heterotrophy of the Mediterranean Sea (Álvarez-Salgado et al., 2020).

11.3.2.3 Intermediate layer

In the intermediate layer (LIW, between 200 and 500 m, where the salinity maximum occurs, see Chapter 4), the main process affecting DOC distribution is its removal by heterotrophic prokaryotes along with the LIW aging or evolution within the Mediterranean. Indeed, a gradual decrease in DOC (64−67 μM) and oxygen (180−200 μmol kg^{-1}) concentration is observed moving from the Levantine Basin (LIW formation site) to the WMED (Fig. 11.9), where LIW is characterized by a minimum in both DOC (34−44 μM) and oxygen (155−200 μmol kg^{-1}) (Santinelli, 2015). A large contribution of DOC to the oxygen demand during the LIW route from the Levantine to the Tyrrhenian Sea has been observed (30%−50%; Santinelli et al., 2010, 2012; Martínez-Pérez et al., 2017a), as compared to the open world ocean (10%−20%; Arístegui et al., 2002), with an estimated DOC mineralization rate of 2.3 μM yr^{-1} (Santinelli et al., 2012). This value is higher than the DOC decay rates reported for different water masses in the North Atlantic Ocean (0.13−0.93 μM yr^{-1}) (Carlson et al., 2010), indicating that the semilabile fraction of DOC is mineralized at a rate approximately twice as much as the highest values reported for the North Atlantic Ocean.

11.3.2.4 Deep layer

Below 500 m DOC shows almost constant values (34−45 μM), with a minimum usually observed around 1000 m and a slight increase in recently ventilated bottom waters (Santinelli et al., 2010; Santinelli, 2015). The average DOC concentration in the WMDW is around 42−43 μM and drops to 37−41 μM in the less ventilated EMDW (Catalá et al., 2018). Interestingly, deep DOC concentrations are equal to

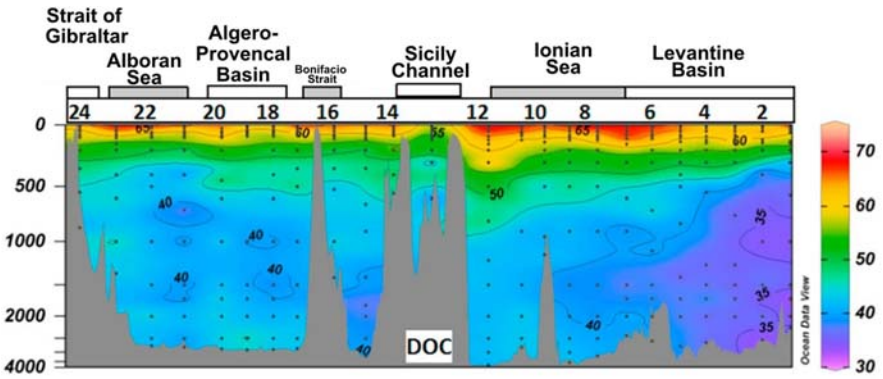

FIGURE 11.9

Distribution of DOC (μM) along a section covering the Mediterranean Sea (HotMix cruise in April 2014).

Modified from Catalá et al. (2018).

the lowest values found in the deep Atlantic and Pacific oceans (36–42 μM; Santinelli, 2015, and references therein). The very low DOC values in the deep Mediterranean Sea were unexpected since the renewal time of deep waters in the basin is only 60–220 years (Stöven and Tanhua, 2014). Over this short timescale, just a very small, nearly undetectable, fraction of recalcitrant DOC is expected to be removed. The first DOC isotope data show that DOC in deep Mediterranean water is more depleted in both $\Delta^{14}C$ and $\delta^{13}C$ than in the deep Atlantic Ocean, where waters have an estimated age of 4500–5100 years. These data suggest that at least 10% and up to 45% of the Atlantic refractory DOC entering the Mediterranean is removed and replaced by isotopically lighter DOC in less than 50–100 years, and that a substantial fraction (up to 45%) of *refractory* DOC in the oceans is instead labile, and that truly the *refractory* fraction could be only ~ 20–25 μM. The Mediterranean can thus be viewed as a reactor, where marine DOC coming from the Atlantic is replaced by terrestrial DOC, and the Mediterranean Outflow (MOW) through Gibraltar may be a source of terrestrial (atmospheric) DOC to the ocean. The mechanisms that lead to DOC replacement are unknown and these data open intriguing questions about DOC lability and cycling in the deep Mediterranean.

Another peculiarity of DOM cycling in the Mediterranean is the fast mineralization rate (1.4–14.4 μM yr^{-1}) estimated for the deep waters (Santinelli et al., 2010; Martínez-Pérez et al., 2017a), which is markedly faster than in the deep ocean (0.1–0.9 μM yr^{-1}; Carlson et al., 2010). The high DOC concentrations, along with the high DOC removal rates observed in recently ventilated deep waters, suggest that the DOC fraction exported to deeper layers is semilabile. It is also noteworthy that the lowest DOC values are located in areas affected by volcanic activities (e.g., Tyrrhenian Sea) or by the occurrence of hyperhaline anoxic lakes (Ionian Sea, see Chapter 2 for more details).

11.3.3 Properties of Mediterranean DOM

11.3.3.1 Optical properties

Optical properties (absorption and fluorescence) of DOM highlight the different composition of Mediterranean waters with respect to other ocean basins and suggest some differences with respect to other marginal basins. Full-depth distributions of optical parameters and their patterns in open waters from the two main Mediterranean basins have been reported recently in the literature (Catalá et al., 2018; Galletti et al., 2019; Martínez-Pérez et al., 2019) (Fig. 11.10).

The absorption of chromophoric DOM (CDOM) at different wavelengths (254 and 325 nm) is similar to that reported for the oceans (a254 = 0.56 to 1.54 m^{-1}; a325 = 0.05 to 0.28 m^{-1}). The vertical distribution of a254 strongly resembles the one of DOC concentration (Catalá et al., 2018; Galetti et al., 2019). The a325 vertical distribution shows a maximum in the surface layer and a minimum around 1500 m in the EMED (Catalá et al., 2018) (Fig. 11.10, top panel). In the surface layer, a325 decreases moving from the WMED to the EMED, as DOM progressively photodegrades. The spectral slope of absorption spectra (S275-295) is significantly

lower than in the global ocean for the same range of oxygen consumption (Catalá et al., 2018) suggesting that in the Mediterranean CDOM is characterized by molecules with an average molecular weight and aromaticity degree higher than in the open oceans. This observation supports the occurrence of a higher percentage of molecules with a terrestrial signature in this basin, as will be discussed later.

The fluorescent fraction of DOM (FDOM) is characterized by the presence of humic-like compounds both of terrestrial and marine origin, protein-like compounds, and a mixture of protein and polycyclic aromatic hydrocarbons (Galletti et al., 2019; Martínez-Pérez et al., 2019). As observed for the absorption, in the epipelagic layer, the humic-like fluorescence decreases eastwards (Martínez-Pérez et al., 2019) (Fig. 11.10). FDOM vertical profiles compare well with those observed

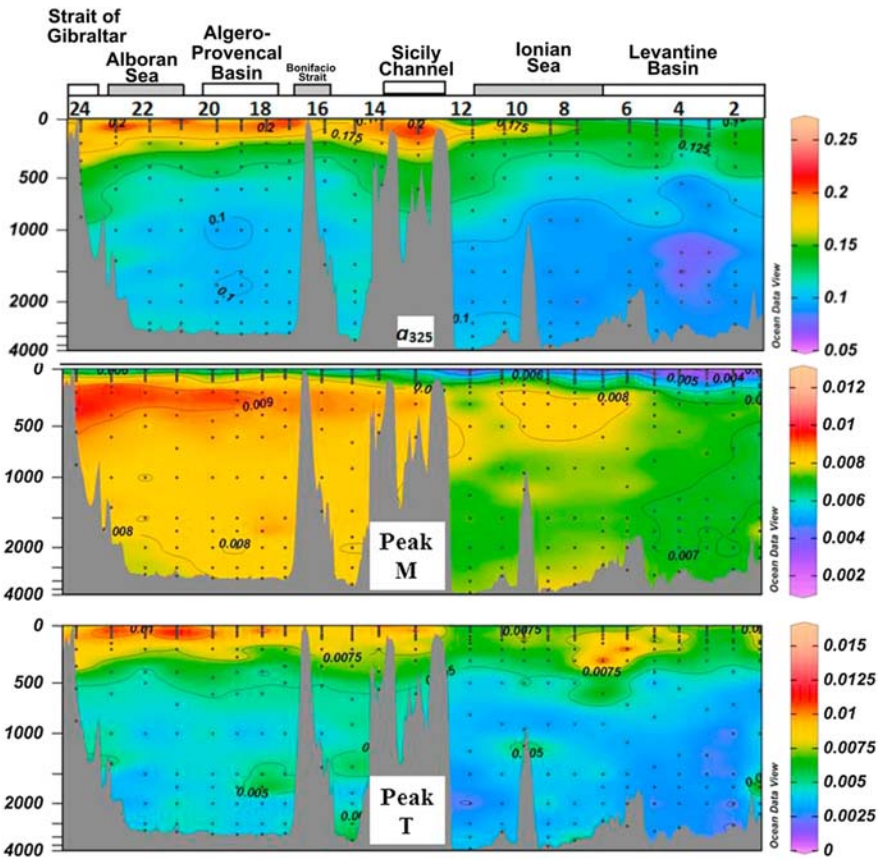

FIGURE 11.10

Distribution of optical parameters along a basin-wide section in the Mediterranean Sea (HotMix cruise in April 2014).

Modified from Catalá et al. (2018) and Martínez-Pérez et al. (2019).

in the major ocean basins (Jørgensen et al., 2011), with the minimum in humic−like fluorescence (Peak M in Fig. 11.10, middle panel), observed in the epipelagic waters, being explained by photobleaching (Kouassi and Zika, 1992; Pitta et al., 2019). Maximum fluorescence intensities are found in the intermediate layers related with the maximum oxygen consumption, which agrees with the production of microbial by-products during the mineralization of bioavailable organic matter (Kramer and Herndl, 2004; Jørgensen et al., 2014). Protein-like fluorescence (Peak T, Fig. 11.10, bottom panel) is high in the epipelagic layer (Martínez-Pérez et al., 2019; Galletti et al., 2019), where it is produced, and decreases with depth (Jørgensen et al., 2011).

In the surface layer, net community respiration is the main process affecting a254 distribution, whereas a325 is basically controlled by temperature (Catalá et al., 2018). Oxygen consumption, chlorophyll and temperature are the main environmental drivers of the humic−like peaks distribution, similar to the global ocean (Catalá et al., 2016), suggesting a dominant influence of the microbial food web respiration and photobleaching in the distribution of these compounds (Galletti et al., 2019; Martínez-Pérez et al., 2017a, 2019). In contrast, the variability of protein−like fluorescence is largely explained by prokaryotic heterotrophic abundance (Martínez-Pérez et al., 2019). In the intermediate and deep layers, water mass mixing and basin−scale mineralization contributed more substantially to explain the variability of DOC, a254, a325 and humic-like fluorescent peaks (>72%), than the variability of the spectral slopes and protein-like peaks (35% −64%) (Catalá et al., 2018; Martínez-Pérez et al., 2019).

11.3.3.2 Molecular composition

Even though the Mediterranean Sea behaves as a miniature ocean for DOM concentration and distribution, its composition shows some intriguing differences. Radiocarbon (Santinelli et al., 2015) and Fourier Transform Ion Cyclotron Resonance Mass Spectroscopy (FT-ICR-MS) (Martínez-Pérez et al., 2017b) data suggest that DOM in this sea is older, lighter, and with a higher degradation index than DOM coming from the Atlantic Ocean.

The very high level of molecular diversity is a key property of DOM (Dittmar et al., 2021). This fact challenges even the most advanced analytical techniques. In this regard, only a minor fraction of all the compounds present in DOM are analytically recognizable biomolecules (Ogawa et al., 2001). In the Mediterranean, carbohydrates are shown to be the main constituents of DOM in the surface layer by using 1H nuclear magnetic resonance, amino acid and neutral sugar analysis (Jones et al., 2013). A strong correlation between amino acid concentration, oxygen consumption, and picoplankton activity was also observed (Jones et al., 2013; Meador et al., 2010).

Martínez-Pérez et al. (2017b) pursued an exhaustive DOM molecular characterization using FT-ICR-MS. Besides, an overall estimation of the DOM molecular composition within the two Mediterranean basins and in different water masses was contrasted, as well as the DOM molecular transformation along the

Mediterranean overturning circulation. With the aging of water masses and DOM reworking, molecular weight, oxygenation, and degradation indices increase, whereas unsaturated aliphatic compounds decrease (Martínez-Pérez et al., 2017b). These authors also proved that DOM outflowing at the Strait of Gibraltar from the Mediterranean is more degraded than DOM in the Atlantic surface inflow. Molecular and optical signatures of DOM in the Mediterranean are also linked (Martínez-Pérez et al., 2017c): significant multiple linear regressions between optical and molecular indices were built, thus simplifying the acquisition of valuable, and cumbersome to obtain, molecular information from easier to measure optical properties.

11.3.4 External sources of DOM

11.3.4.1 River run-off

Rivers represent an important external source of DOM to the oceans, particularly in the Mediterranean Sea, where their contribution to the DOM pool is expected to be relevant because of its long coastline, high coastal population density, and small size. DOM concentrations found in river mouths are high and highly variable, ranging between 92 and 366 μM.

The total river input estimated for the Mediterranean Sea accounts for $0.708 \cdot 10^{12}$ gC yr^{-1} ($0.299 \cdot 10^{12}$ gC yr^{-1} into the WMED and $0.409 \cdot 10^{12}$ gC yr^{-1} into the WMED) (Santinelli, 2015). When this Mediterranean value is divided by the total water volume of the sea, the estimated flux ($0.17–0.19 \cdot 10^{6}$ gC yr^{-1} km^{-3}) is comparable to values estimated for the oceans ($0.14–0.18 \cdot 10^{6}$ gC yr^{-1} km^{-3}) (Dai et al., 2012). This estimate is affected by large uncertainty since it is based on snapshot samples collected sporadically in the rivers, whereas it is well known that DOM shows seasonal variability. For instance, a time-series of DOM data is available in the Arno river, where it has been observed that 80% of DOM flux is generally delivered during autumn/winter, with significant amounts ascribed to flood events (up to 26% in 2014) (Retelletti Brogi et al., 2020). Rivers also represent an important source of anthropogenic DOM that can enter into the Mediterranean (Retelletti Brogi et al., 2022).

11.3.4.2 Atmospheric input

The atmosphere represents an important and overlooked source of DOM to the Mediterranean. Recent studies estimate a DOM input from the atmosphere to the Mediterranean of 120.7 mmol DOC m^{-2} yr^{-1} ($3.64 \cdot 10^{12}$ gC yr^{-1}) taking into consideration both wet and dry deposition (Galletti et al., 2020; Djaoudi et al., 2018). DOM deposition rates are highly variable and do not show a clear seasonality. These studies stress that atmospheric input has a larger impact to the Mediterranean than to the global ocean and DOM fluxes from the atmosphere to the Mediterranean can be up to sixfold larger than the riverine inputs. They also show that the organic substances transported by Saharan dust at Lampedusa site are primarily of natural origin, especially from sea spray and that Saharan dust can be an important carrier of organic substances.

11.4 Inorganic carbon chemistry and acidification in the Mediterranean Sea: concepts, particularities, and distribution

11.4.1 General definitions and current challenges of the seawater CO_2 system

Seawater is about 96.5% water and 3.5% salt. Salt is mostly constituted by major strong cations and anions, conforming the ionic seawater media. Other minor constituents in salt are weak acids and bases, such as carbonic and boric acid species (Millero et al., 2008). The carbonic, carbonate or CO_2 system is an acid-base system, derived from the dissolution of carbon dioxide gas from the atmosphere into the ocean and the dissolution of carbonate minerals from the sediments into seawater (see Box 11.1). The relevance of the inorganic carbon chemistry in seawater stems from the fact that of the three major reservoirs where carbon is stored and exchanged on timescales of decades to centuries (atmosphere, ocean and biosphere), the ocean stores more than 90% of the total exchangeable carbon, 50 times more than the atmosphere. This carbon is mostly found as inorganic carbon dissolved in seawater. Therefore, understanding the complex CO_2 chemistry in seawater is essential for at least two reasons: (i) the ocean would control the CO_2 concentration in the atmosphere and probably control glacial-interglacial changes within an unaltered Earth system; and unfortunately, (ii) within the current anthropogenically perturbed Anthropocene era (see Chapter 13), the ocean is absorbing about 30% of the anthropogenic CO_2 emissions into the atmosphere, with the side effect of ocean acidification (OA), among other consequences (IPCC, 2019). Thus, oceanographers are trying to quantify and predict the role of the ocean in the altered carbon cycle, and to design adaptation and mitigation measures to preserve, and even recover, ocean ecosystems.

The CO_2 chemistry in seawater is highly complex. This is derived from the interactions between a myriad of organic and inorganic compounds within the ocean high ionic strength media, among them, the CO_2. A general introduction is given in Box 11.1. and the main definitions and equations in Box 11.2., with hints to measurement methods and software packages for the calculation of derived CO_2 variables. Recommended literature about chemistry is given in Box 11.2, most of them are publicly available.

Leaving aside the gaps in the observational capacity of CO_2 and other biogeochemical variables in the Mediterranean Sea surface and deep ocean waters (see subchapter 11.4.6), current challenges regarding CO_2 chemistry in the ocean, among others, relate with (i) the lack of intercomparability of pH measurements among different research groups, (ii) the common, and inherently required, use of

Box 11.1 CO_2 acid-base equilibria in seawater: general description

Gaseous CO_2 (g) enters the ocean from the atmosphere when the partial pressure of CO_2 (pCO_2) in this reservoir is higher than in the surface seawater (pCO_2 atm > pCO_2 sw). CO_2 is found in the ocean in three main forms, free aqueous CO_2 (CO_2 (aq)) bicarbonate $\left(HCO_3^-\right)$, carbonate $\left(CO_3^{2-}\right)$, a fourth form is carbonic acid (H_2CO_3) which is nearly negligible. In fact, the two neutral forms, H_2CO_3 and CO_2 (aq) are not separable and are usually abbreviated as CO_2^*, $H_2CO_3^*$ or just CO_2. Here we will use CO_2 as CO_2 (aq) + H_2CO_3

A closed parcel of seawater equilibrated with gaseous CO_2 (i.e., pCO_2 atm = pCO_2 sw) is governed by the Henry's law (Eq. (11.6), see Box 11.2.) which relates the pCO_2 in seawater with the CO_2 concentration by means of the CO_2 solubility in seawater, K_0. The speciation of carbonate species in seawater, that is, the dissolution of CO_2 in seawater, follows the equilibria in Eq. (11.7) (see Box 11.2.). Each equilibrium in Eqs. (11.6) and (11.7) is governed by the corresponding constants, K_0, K_1 and K_2, dependent on temperature, salinity and pressure of the seawater. Other important acid-base equilibria in seawater are the dissociation of boric acid and the ionization of water, also governed by the corresponding constants, K_B and K_w (Eqs. (11.8) and (11.9), Box 11.2.). Macronutrients such as silicate and phosphate also should be considered to constrain the carbonate system (Eq. 11.10 to Eq.11.13, Box 11.2.). Usually, equilibrium constants (K) are expressed as $pK = -\log_{10}(K)$. When the seawater pH (Eq. (11.1), Box 11.2.) equals the pK of the chemical equilibrium, the acid and base forms contribute equally in the solution. This is exemplified in the Bjerrum plot for carbonate and borate species as a function of pH in the inset of Fig. Box 11.1.1. This plot helps to understand why seawater is a natural buffer system where pH is kept nearly constant, mostly thanks to the CO_2 chemical equilibria in Eq. 11.7, Box 11.2): any strong acid added will be neutralized by carbonate and bicarbonate ions. In fact any constituent (acid-base equilibria) for which lines are curved in a Bjerrum plot within the pH range of the ocean 7–9 (therefore, with a pK between 7 and 9) can accept or donate protons and therefore contribute to the charge balance of the ocean, that is, the buffer capacity, which is directly linked to the troublesome concept of alkalinity.

Probably ocean CO_2 chemistry research started in the Carlsberg Brewery Copenhagen laboratory in 1909 when Sørensen created the pH (potential of hydrogen) scale to study the effect of hydrogen ions on enzymatic processes. He even made some dye-based measurements of seawater pH (Sørensen and Palitzsch, 1909). However, even as early as 1725, seawater was assigned to be basic, as detected with "eau de fleurs de mauve" (a dye that turns yellow-green in seawater) used by count Marsili (Marsili, 1725; Wallace, 1974). The reader might think that measuring pH, and other CO_2 variables, in the ocean is an easy task but in fact it is the opposite, as pH for example remains a challenge even in the 21st century, mostly due to the lack of a well-defined and established metrology (Dickson, 1993, 2016) and the evolution of the spectrophotometric pH method, where new dyes and corresponding characterization have changed (Álvarez et al., 2020). Methods for Total Alkalinity (TA) and Dissolved Inorganic Carbon (DIC) are well established, and except for their automatization, have remained as described in Dickson et al. (2007). The quality and common baseline reference of worldwide TA and DIC measurements rely on the availability of Certified Reference Materials (CRMs) (Dickson et al., 2003), used to control the quality of carbonate system measurements worldwide and currently produced in one single lab in the Scripps Institution of Oceanography (USA). However, the CRMs paramount relevance was evidenced during the COVID-related closure of the production laboratory, inducing a global shortage (Cathermane, 2021) that affected many biogeochemical laboratories around the globe. Currently, the risk is not overcome as the production of CRMs is not guaranteed and the CO_2 scientific community cannot rely on only one production and certification center. Consequently, the carbon community is searching now for alternatives in the US, Europe and other continents to avoid future shortages and sustain the good quality of the ocean carbon measurements.

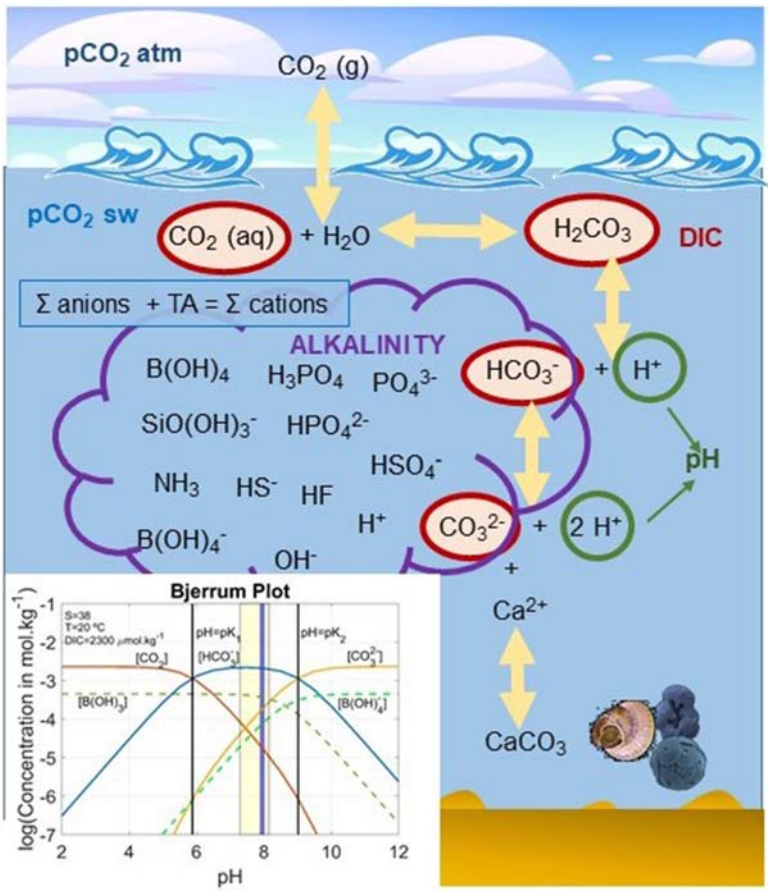

FIGURE BOX 11.1.1

Illustration showing general concepts of the acid-base CO_2 system in seawater.

CRMs as a unique calibration source for TA and DIC measurements, instead of using CRMs as an additional check for accuracy and precision, (iii) the lack of internal consistency between measured and calculated variables beyond the needed agreement to detect climate-derived trends. Those challenges[1] relate to the wide range of parameterizations for the dissociation constants (Eq. 11.7, Box 11.2.), analytical and sampling procedures (preservation of high CO_2 samples, automatization of analytical systems, detectors accuracy, unavailability, or cumbersome preparation of CO_2-free standard solutions), the evolution of methods as for pH or the

[1] see the "Ocean Carbonate System Intercomparison Forum": https://www.us-ocb.org/ocean-carbonate-system-intercomparison-forum/.

Box 11.2 CO_2 acid-base equilibria in seawater: definitions, equations and methodologies

Compared to TA, an easier concept is total inorganic carbon also named total dissolved CO_2 or DIC, and abbreviated as TIC, TCO_2, DIC, C_T or ΣCO_2, equivalent to the sum of all the CO_2 species in seawater (Eq. 11.2). These species are individually pressure, salinity (S) and temperature (T) dependent but the sum, DIC, is conservative in the sense that an isolated water sample when changed in physical conditions, keeps DIC constant but the contributors change. The concept of pH is easy as commonly known, but it complicates in seawater due to the existence of different scales to define it in seawater, the most commonly used is the Total scale (Eq. 11.1). The concept of TA, abbreviated as TA, A_T or ALK, relates to the charge balance in the ocean: positive cations in seawater excess anions, weak acids as CO_2 and borate contribute to balance the positive charge. In fact, the TA is defined as the capacity of the ocean to accept protons and is measured using a potentiometric titration. Other minor contributors to TA are those from silicate and phosphate equilibria (Eqs. 11.10 to 13) and many more as seen in Fig. Box 11.1.1, including minor and weak organic proton acceptors mostly in coastal regions. TA is usually measured by potentiometric titration and DIC by coulometry, both are considered as conservative parameters, and their CRMs are available for quality control purposes. On the other side, the other two measurable variables, pCO_2 and pH, are nonconservative, that is, pressure, T and S dependent. These latter parameters are measured by infrared detection after water equilibration with an airstream, and by spectrophotometric detection after dye addition to the seawater sample, respectively. Tris buffer solutions and calibrated mixtures of CO_2 gas are available to quality control these parameters, but no specific CRM. The formation and dissolution of calcite and aragonite carbonate minerals (Fig. Box 11.1.1) also affect the CO_2 system (Eq. 11.14). The solubility product, pKsp, for aragonite is lower than that of calcite, i.e., aragonite shells and skeletons (pteropods, corals) are more soluble than those containing calcite (coccolithophorids, foraminifera). The carbonate saturation state, Ω (Eq. 11.14), informs on the seawater saturation on calcite or aragonite. If seawater concentrations are higher than the saturation product, $\Omega > 1$, seawater is supersaturated, while if $\Omega < 1$, seawater is undersaturated in carbonate minerals and the dissolution process is prone to occur.

Equations regarding definitions

$$\text{pH Free} = -\log_{10}\left[H^+\right]_F$$

$$\text{pH} = -\log_{10}\left(H^+\right) \quad \text{pH Total} = -\log_{10}\left(\left[H^+\right]_F + \left[HSO_4^-\right]\right) \tag{11.1}$$

$$\text{pH Seawater} = -\log_{10}\left(\left[H^+\right]_F + \left[HSO_4^-\right] + [HF]\right)$$

$$\text{DIC} = [CO_2] + \left[HCO_3^-\right] + \left[CO_3^{2-}\right] \tag{11.2}$$

$$\text{TA} = \left[HCO_3^-\right] + 2\left[CO_3^{2-}\right] + [B(OH_4)^-] + [OH^-] - \left[H^+\right] + \text{minor components} \tag{11.3}$$

$\Omega > 1$ supersaturation

$$\Omega = \left[CO_3^{2-}\right]_{SW} \times \left[Ca^{2+}\right]_{SW}/\text{Ksp} \quad \Omega < 1 \text{ undersaturation} \tag{11.4}$$

$$\text{RF} = (\partial pCO_2 / \partial DIC) \times (DIC / pCO_2) = \partial \ln pCO_2 / \partial \ln DIC \tag{11.5}$$

As a thermodynamic system, knowing the constants, equations, physical conditions of pressure, S and T, from two measured variables, the other two can be calculated. There are several software packages which contain the available CO_2 constants in the literature and all combinations of input pairs (see the work of Orr et al., 2015, and the most recent CO_2 software written in Python by Humphreys et al., 2022). Calculated variables always have a higher uncertainty than the directly measured ones, and lower uncertainty is obtained when combining a conservative measured variable with a nonconservative one (pressure, S and T dependent), combinations as DIC and TA or pH and pCO_2 yield calculated variables that needs to be considered with caution, given the controversial current precision and accuracy of direct measurements.

Box 11.2 CO_2 acid-base equilibria in seawater: definitions, equations and methodologies—cont'd

Recommended general literature about the CO_2 chemistry in seawater is Zeebe and Wolf-Gladrow (2001) and Dickson (2010), specifically about the alkalinity concept in Middelburg et al. (2020) and Dickson (1992), about methods and uncertainty propagation in Dickson et al. (2007) and Orr et al. (2018).

Equations regarding reactions and pK values at S = 38, T = 20°C, 1 atm

$$[CO_2] = K_0 \times pCO_{2\ SW} \quad pK_0\ (1.49) \tag{11.6}$$

$$tCO_2 \leftrightarrow HCO_3^- + H^+ \leftrightarrow CO_3^{2-} + 2H^+ \quad pK_1(5.88) \quad pK_2(9.02) \tag{11.7}$$

$$B(OH)_3 + H_2O \leftrightarrow B(OH_4)^- + H^+ \quad pK_B(8.64) \tag{11.8}$$

$$H_2O \leftrightarrow H^+ + OH^- \quad pK_W(13.4) \tag{11.9}$$

$$H_4SiO_4 \leftrightarrow H_3SiO_4^- + H^+ \quad pK_{Si}(9.46) \tag{11.10}$$

$$H_3PO_4 \leftrightarrow H_2PO_4^- + H^+ \quad pK_{P1}(1.60) \tag{11.11}$$

$$H_2PO_4^- \leftrightarrow HPO_4^{2-} + H^+ \quad pK_{P2}(5.98) \tag{11.12}$$

$$HPO_4^{2-} \leftrightarrow PO_4^{3-} + H^+ \quad pK_{P3}(8.93) \tag{11.13}$$

Aragonite $pK_{sp}(6.13)$

$$CO_3^{2-} + Ca^{2+} + \leftrightarrow CaCO_3 \quad \text{Calcite } pK_{sp}(6.32) \tag{11.14}$$

introduction of new ones, as for ion carbonate and other aquatic chemistry issues (e.g., the chemical speciation model in seawater, currently revised by the SCOR working group 147,[2] also developing Tris buffers to calibrate pH measurements).

11.4.2 General processes affecting the CO_2 system with a Mediterranean overview

The main motivation to study the inorganic carbon cycle or CO_2 variability in the ocean stems from its relevance in controlling atmospheric CO_2 and consequently the Earth's climate system. The behavior of the sea surface as a CO_2 source or sink to the atmosphere is the consequence of the interplay of two pumps affecting the pCO_2 and therefore the complete CO_2 system. The physical (also called solubility or circulation) and the biological (soft and hard tissue) pumps comprise almost the same processes that are also affecting the DO (Fig. 11.1). Opposite to oxygen and other gasses dissolving in seawater, the fact that CO_2 is a weak acid reacting in seawater (Fig. Box 11.1.1) marks the difference and complexity in assessing, quantifying and modeling the carbon cycle in the ocean (Sarmiento and Gruber, 2006).

The physical pump is related to abiotic processes: water masses formed in the surface tend to equilibrate with atmospheric CO_2, dissolving more as they get colder. Denser waters sink afterward in the thermocline (intermediate waters) or to the

[2] http://marchemspec.org/.

ocean's interior (deep and bottom waters), and are transported within the general circulation of the basin (Chapters 4 and 7 explain these processes within the Mediterranean Sea more in detail). Moreover, the ocean is full of life, that is why its biological processes transforming inorganic carbon into organic carbon (photosynthesis and calcification) and vice versa (remineralization and dissolution) also affect the CO_2 system. The biological pump involves all biotic processes where inorganic carbon is involved: soft tissue pump and hard tissue pump. According to the soft tissue pump, organic matter is formed by primary producers with soft tissues (microscopic sea creatures called phytoplankton) in the euphotic zone and mostly decomposed in deep layers by remineralization. On the other hand, the primary producers of the hard tissue pump are formed by skeletons or shells of calcium carbonate, aragonite or calcite. So, when they die, these skeletons/shells sediment through the water column to the sediments, along this pathway carbonate is preserved or dissolved according to the carbonate saturation state.

The impact of these processes on the CO_2 system can be understood with the diagram in Fig. 11.11, where the conservative variables DIC and TA are used to calculate the two other carbonate system parameters, pH and pCO_2 (shown as isolines) at constant conditions (S = 38, 20°C and 1 atm). Processes are shown as arrows on the top left plot: an input of CO_2 from the atmosphere increases DIC, but TA keeps constant (blue arrow rightwards), while pH decreases and pCO_2 increases; N_2 fixation decreases TA, but keeps DIC constant (yellow arrow downwards), this biotic process has a higher impact on pCO_2 and pH; the carbon fixation by autotrophic production slightly increases TA and has a higher impact on DIC (green arrow leftwards), and finally the formation of carbonate ions drives a reduction in DIC and TA with a ratio of 1:2 (orange arrow downwards). The complementary processes, CO_2 outgassing from the ocean, denitrification, remineralization, and dissolution of carbonate ions, respectively, follow the corresponding arrows in opposite directions. Note that the two biological pumps have different impacts on pCO_2 and pH, calcification (hard tissue pump) induces a pCO_2 increase (pH decrease), while photosynthesis (soft tissue pump) drives the opposite. A detailed explanation about the stoichiometric coefficients modeling the impact of biological processes on TA can be found in Wolf-Gladrow et al. (2007) and Fraga and Álvarez-Salgado (2005), and on the impact on pCO_2 in Humphreys et al. (2018).

Other species of the carbonate system, such as CO_2, HCO_3^- or CO_3^{2-}, are nonconservative, that is, depending on temperature, salinity and pressure conditions (Box 11.1 and Box 11.2), and could be added as isolines in Fig. 11.11. Note that within the oceanic pH range, these carbon species are always distributed as follows: $[HCO_3^-] \gg [[CO_3^{2-}] \gg [CO_2]$, see Bjerrum plot in Fig. Box 11.1.1. For example, a typical water sample within the Mediterranean Sea with TA = 2600 μmol kg^{-1} and DIC = 2300 μmol kg^{-1} at 20°C and S = 38 at the surface would correspondingly have 89.9%, 9.5% and 0.6% of these nonconservative carbon species.

The right plot of Fig. 11.11 clearly shows the particular values of DIC and TA within the Mediterranean Sea compared to other oxygenated basins, for example,

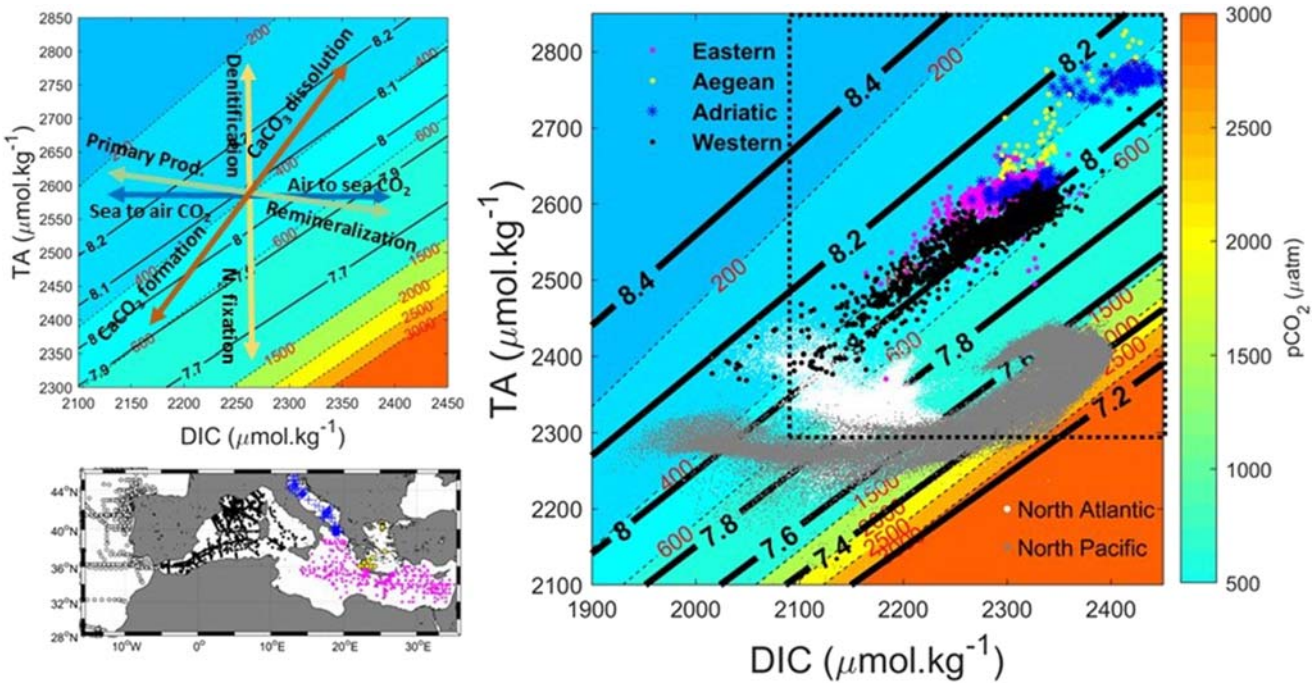

FIGURE 11.11

DIC and TA diagrams with pH isolines (*continuous lines*, at Total scale) and pCO_2 isolines (*dashed lines*, μatm) at S = 38, T = 20°C and 1 atm. The bottom left map shows the location of stations with CO_2 data for the Atlantic Ocean (*white dots*) and the Mediterranean Sea (color legend in the right plot). The top left plot shows the processes affecting CO_2 variables for the range of DIC and TA values found in the Mediterranean Sea, processes are identified with colored arrows: air-sea CO_2 exchange (*blue*), primary production/remineralization of organic matter (*green*), formation and dissolution of $CaCO_3$ (*orange*) and N_2 fixation and denitrification (*yellow*). The right plot is a DIC-TA diagram with real DIC and TA values for different Mediterranean Sea subbasins identified with the legend on the top, and the North Atlantic (*white dots*) and the North Pacific (*gray dots*) oceans. Atlantic and Pacific ocean data were taken from GLODAPv2.2021 (Lauvset et al., 2021) and Mediterranean values from CARIMED (Álvarez et al., in preparation).

the North Atlantic and the North Pacific oceans. Data from the anoxic Black Sea is not considered, as it has a completely different stoichiometry (Goyet et al., 1991; Kondratiev et al., 2017). Note that DIC values in Mediterranean waters are only comparable to those in the North Pacific Ocean, although the processes explaining them are different: Pacific waters have low salinity and are highly remineralized, while in the Mediterranean remineralization processes have lower impact but is a concentration basin with very high salinity, and consequently higher DIC (and TA). Mediterranean TA values are outstandingly high, compared to the adjacent North Atlantic waters. Within the Mediterranean, waters in the Aegean and Adriatic Seas present even higher TA values. Given the TA and DIC values, pH in the Mediterranean are high compared to the Atlantic and Pacific waters and with a narrow range of variability (sample points are distributed around the 8 pH isoline in the right plot of Fig. 11.11). The same reasoning is applied to pCO_2 values, which are comprised within the 400 and 600 μatm isolines.

Diagrams in Fig. 11.11 represent real DIC and TA values and calculated pH and pCO_2 values at constant physical conditions of S, T and pressure. The pressure effect will not be detailed here, as usually pCO_2 is measured at the surface ocean to study air-sea fluxes. This layer witnesses the greatest seasonal changes in S and T. The sensitivity of pCO_2 to those changes is attributed to the corresponding dependence of the solubility K_0 (Eq. 11.6, Box 11.2.), which is relatively insensitive to S, while its dependence on T can be approximated with the following relationship obtained by Takahashi et al. (1993) in a closed system: $\partial \ln(pCO_2)/\partial T = 0.0423^{\circ}C^{-1}$. This approximation assumes a closed system, where TA and DIC remain constant. However, when precipitation or evaporation occur, TA and DIC change accordingly, and the effect of these freshwater fluxes on pCO_2 increases in about 60% the sensitivity from the pure S effect on the constants (Sarmiento and Gruber, 2006).

11.4.3 Particularities and distribution of the CO_2 system in the Mediterranean Sea

The Mediterranean Sea can be considered as a thermodynamic machine that exchanges water and heat (and biogeochemical variables) with the Atlantic Ocean through the Strait of Gibraltar, as well as with the atmosphere (Sanchez-Gomez et al., 2011; see also Chapter 4). The Mediterranean Sea is a concentration basin where evaporation exceeds precipitation, transforming the relatively fresh and cool Atlantic water into salty and warm MOW (Chapter 4). This outflow also presents different biogeochemical signatures (high TA, DIC, and low pH and oxygen) compared to the surrounding Atlantic waters (Fig. 11.12). Surface waters locally affected by freshwater inputs present very high TA and DIC values ($TA > 2700$ µmol kg^{-1} and $DIC > 2400$ µmol kg^{-1}), such as in the Northern Adriatic Sea, influenced by the river Po discharges, and in the Aegean Sea, influenced by Black Sea inputs (Cossarini et al., 2015). The antiestuarine circulation is well evidenced by the TA distribution: the inflow of surface low salinity Atlantic water is also noted with low TA values in the WMED, which increase eastwards

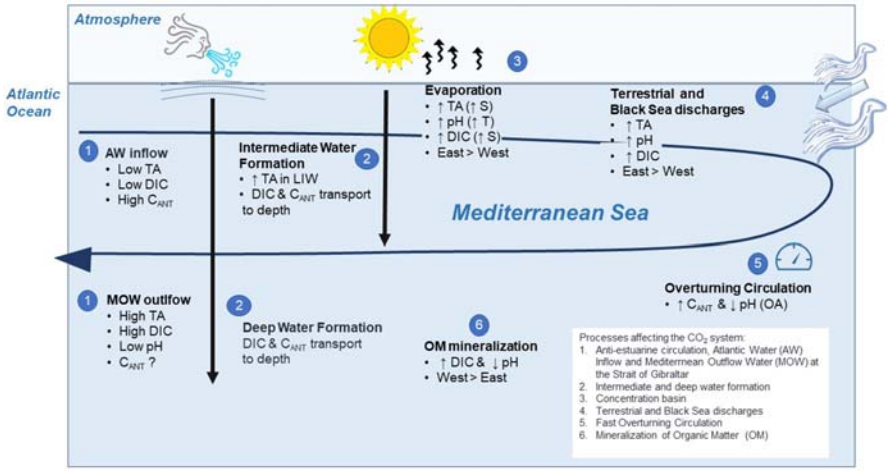

FIGURE 11.12

Infographic showing key processes and particularities of the CO_2 system in the Mediterranean.

concomitantly with the evaporation rate. A general overview of the CO_2 system particularities in the Mediterranean is given in Fig. 11.12. Another relevant general feature of the biogeochemistry of this basin is its oligotrophic and heterotrophic nature (subchapter 11.2), where mineralization processes dominate over organic matter formation processes. In addition, the freshwater inputs and exchanges with the Black Sea introduce particular signatures, both being a main input of TA into the Mediterranean. These facts explain the high DIC in Mediterranean waters compared to the rest of the oceanic compartments (Fig. 11.11). The oligotrophy increases eastwards and, therefore, DIC increases westwards: the less organic matter is produced at the surface, the lower remineralization occurs in deeper layers (i.e., less CO_2 is released back to the dark ocean). Furthermore, Mediterranean waters are characterized by short ventilation rates and residence times of ~60–220 years (Schneider et al., 2014; Stöven and Tanhua, 2014), relatively short compared to those of the large oceans where they vary from 100 to 1000 years (Khatiwala et al., 2012). This is the reason behind the high sensitivity (and vulnerability) of the whole basin to climate change and why the Mediterranean Sea is considered as a climate hotspot (Giorgi, 2006). The relatively short ventilation time along with the intense overturning circulation where deep and dense water is formed in several regions, as the northern WMED, the Adriatic, Levantine, and Aegean Seas (see Chapter 7), force the basin to keep pace with the CO_2 atmospheric increase, and therefore to accumulate higher inventories of anthropogenic carbon (C_{ANT}) compared to the adjacent North Atlantic Ocean (Lee et al., 2011).

The ability of the ocean to keep pace with the atmospheric CO_2 increase is governed by its buffer capacity, expressed by the Revelle Factor (RF in Eq. 11.5,

Box 11.2.). Roger Revelle was a visionary oceanographer who along with Hans Suess published a first paper stating that *human beings are now carrying out a large scale geophysical experiment of a kind that could not have happened in the past nor be reproduced in the future* (Revelle and Suess, 1957). In fact, they were the first in assessing the mitigation role of the ocean in slowing climate change, and they even estimated a 40% storage of atmospheric CO_2 originating from human activities in the ocean. More details on the history of oceanographic studies focused on CO_2 variables can be found in Brewer (2013). Quantitatively, the RF predicts the change in DIC for a given change in pCO_2 in the atmosphere, and can be calculated with CO_2 software packages.

The above-mentioned Mediterranean peculiarities (i.e., the high load of inputs of carbon and TA from rivers and the Black Sea, the predominance of mineralization processes, the antiestuarine and fast overturning circulation and the eastwards increase in evaporation and oligotrophy) influence the general patterns of the carbonate system (Fig. 11.12) explaining the vertical distribution of the different variables. Atlantic waters are clearly different from Mediterranean waters in Fig. 11.13, especially in DIC and TA, with values out of the color scale, being DIC <2250 μmol kg^{-1} and TA < 2550 μmol kg^{-1} west of the Strait of Gibraltar. In this latter, in situ pH and Omega Aragonite are much lower, while the Revelle Factor and the DIC/TA ratio are higher compared to the Mediterranean Sea. In the surface layer, all properties shown in Fig. 11.13 increase eastwards, with the exception of RF and the DIC/TA ratio, mainly associated with the salinification of the Atlantic water inflow. The lower branch of the antiestuarine circulation, associated with the LIW, is clearly identified by the TA and in situ pH maxima above 500 dbars, especially in the EMED, while in the WMED the intermediate DIC maxima is associated with a DO minimum (see subchapter 11.1), related to the layer of higher remineralization of organic matter. The deep layer below 500 dbars clearly shows the great differences between EMED and WMED. In the WMED, DIC is higher due to the higher organic matter production in the surface, which is decomposed at depth, in addition the formation of deep water is more active in this basin conveying DIC to depth. The outstanding feature of the EMED is the high TA of deep waters, and consequently the high in situ Omega Aragonite and low RF and DIC/TA ratio. Low RF values indicate that waters more easily follow the CO_2 increase in the atmosphere, they dissolve more DIC for a given CO_2 increase in the atmosphere. This fact in addition to the active overturning circulation drives an active C_{ANT} accumulation in the Mediterranean Sea, while the inherent acidification is hampered by the high TA content of the waters (Álvarez et al., 2014a; Hassoun et al., 2019).

More information on the distribution of DIC and TA over the Mediterranean Sea using regional and seasonal reconstructions can be found in Cossarini et al. (2021), Gemayel et al. (2015) and Lovato and Vichi (2015).

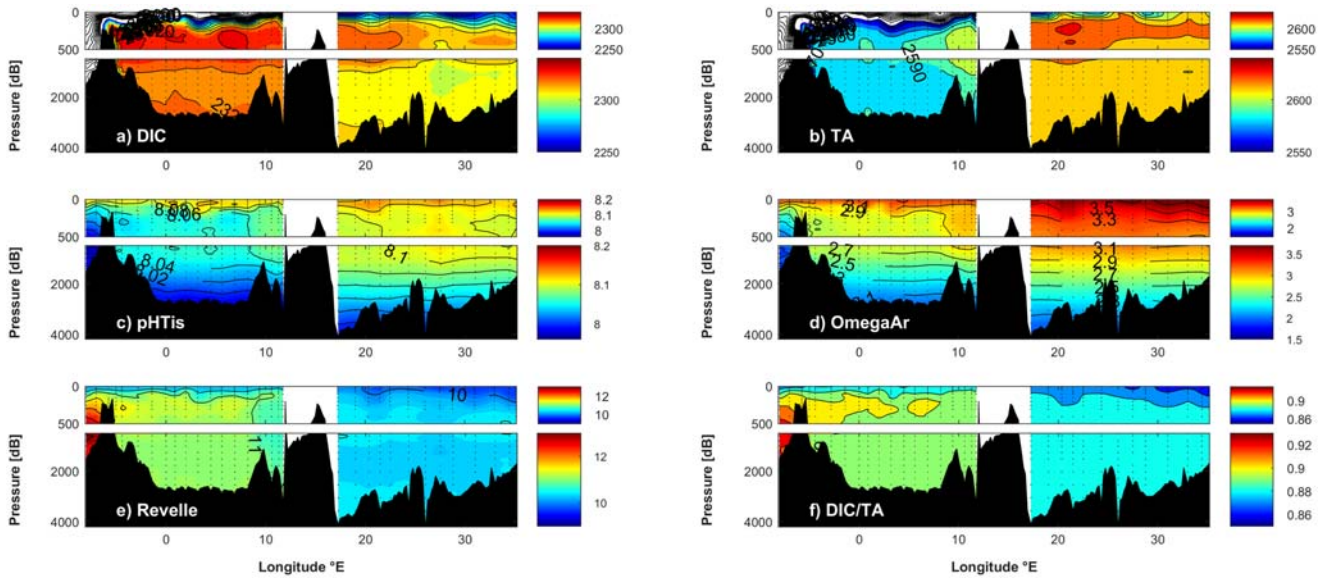

FIGURE 11.13

Vertical distribution of (a) DIC, μmol kg^{-1}, (b) TA, μmol kg^{-1}, (c) in situ pH on the Total scale, (d) in situ Omega Aragonite, (e) the Revelle Factor and (f) the DIC/TA ratio, along a trans-Mediterranean Sea section (RV METEOR cruise M84/3 in April 2011, see also Tanhua et al., 2013b).

11.4.4 Surface pCO_2 and air-sea CO_2 fluxes

The air-sea CO_2 exchange flux takes into account the solubility of CO_2 gas in seawater, the CO_2 gas transfer velocity which is parameterized as a function of the wind velocity, and the air-sea pCO_2 gradient (see the review by Wanninkhof, 2014, for more details). By convention, positive fluxes indicate outgassing, which means a release of CO_2 from the ocean toward the atmosphere, while negative fluxes reflect a sink of CO_2 from the atmosphere to the ocean. The direction of the flux is dominantly driven by the difference of pCO_2 between the ocean and the atmosphere, while the intensity of the flux is regulated by (i) the CO_2 solubility, dependant on T and S (maximum at low T and S) and (ii) the gas velocity transfer, dependant on the wind speed and the surface T (the higher the wind speed and temperature, the higher the gas transfer velocity).

The assessment of the Mediterranean as an overall source or sink of CO_2 from the atmosphere clearly suffers from a lack of surface ocean pCO_2 data with enough spatial and temporal coverage. This fact is evidenced in the Surface Ocean CO_2 Atlas data portal[3] (SOCAT, see Bakker et al., 2016), where large portions of the Mediterranean have no pCO_2 measurement at all. Consequently, basin-scale estimates of the air-sea CO_2 flux are very uncertain and rely on (i) closing the carbon budget from direct measurements in the Strait of Gibraltar, with contradicting results as a sink (Copin-Montegut, 1993) or a source (Huertas et al., 2009); or (ii) physical-biological-chemical coupled models developed for the Mediterranean, reconstructing available satellite or discrete biogeochemical data products. Basin scale modeling works present a longitudinal variation in surface pCO_2, where the WMED mainly behaves as a CO_2 sink, while the easternmost areas behave as a net CO_2 source, due to the higher temperature and lower productivity, causing a reduced uptake of atmospheric CO_2. Even more, those works show a shift in the net air-sea CO_2 fluxes from a sink in the 1960 and 1980s to a slight source in the 1990 and 2000s (D'Ortenzio et al., 2008; Louanchi et al., 2009; Taillandier et al., 2012), to a nearly fourfold sink in a future scenario SRES A2 or RCP8.5 (IPCC, 2014) were atmospheric CO_2 is expected to be about 575 and 870 ppm for the middle and the end of the 21st century, respectively (Solidoro et al., 2022). This switch relates to the increase in both, atmospheric CO_2 and surface temperature, and also to changes in the biological pump.

Specific regional and seasonal information on pCO_2 variability and air-sea fluxes relies on fixed time-series as DYFAMED and BOUSSOLE in the north-western Mediterranean (Bégovic and Copin-Montégut, 2002; Hood and Merlivat, 2001; Merlivat et al., 2018), the PALOMA (Cantoni et al., 2012) and VIDA (Turk et al., 2010) buoys, both in the northern Adriatic Sea, some offshore (e.g., PROSOPE, Claustre et al., 2002) or regional dedicated cruises in the Aegean Sea (Krasakopoulou et al., 2009) or the Levantine Basin (Sisma-Ventura et al., 2017;

[3] https://www.socat.info/index.php/data-access/.

Wimart-Rousseau et al., 2021). General patterns arise from those studies, with the highest values of pCO_2 are reported in surface waters during summer, due to the high temperature, which drives an increase of pCO_2 in seawater due to: (i) a decrease of the CO_2 solubility, (ii) a change in the thermodynamic equilibrium of DIC species in favor of CO_2, and (iii) an increase in the metabolic activity promoting higher mineralization rates, thus increasing DIC. The two prevailing ones are (ii) and (iii), and consequently, in summer a net outgassing of CO_2 from the ocean is reported. On the other hand, strong winds, heat loss and photosynthetic activity cause minimal pCO_2 values in winter, reversing the fluxes.

Modeling and data-based studies remark that the seasonal and spatial variations of pCO_2 are strongly dependent on the surface T. This relation may be masked in areas with important influence of river inputs, as the northern Adriatic Sea (Cantoni et al., 2012; Ingrosso et al., 2016; Urbini et al., 2020), intense phytoplankton blooms, and events of strong winds (Copin-Montégut et al., 2004; Turk et al., 2010). The continental shelf in the Mediterranean is estimated to be a net source of CO_2 to the atmosphere based on available SOCAT data and a regionalized CO_2 exchange budget (Laruelle et al., 2014). Specific works along the French coast, Bay of Villefranche-sur-Mer (De Carlo et al., 2013; Kapsenberg et al., 2017) and Bay of Marseille (Wimart-Rousseau et al., 2020), show a wide seasonal cycle in seawater pCO_2, but also in atmospheric pCO_2 near highly urbanized areas. In the former studies T is again the main driver of ocean pCO_2, but the impact of freshwater discharges affecting TA should be taken into account, as much as the strong seasonal TA change due to evaporation in the EMED (Hassoun et al., 2019; Wimart-Rousseau et al., 2021).

11.4.5 Anthropogenic carbon and ocean acidification in the Mediterranean Sea

Undoubtedly, the Mediterranean is an area of uptake and storage of anthropogenic carbon (C_{ANT}), mainly because of two reasons: the naturally high capacity to keep pace with the atmospheric CO_2 increase due to the low RF (subchapter 11.4.3) and the active overturning circulation (Chapter 7), which conveys the uptaken C_{ANT} to the interior of the sea (Lee et al., 2011; Schneider et al., 2010). Despite the general evidence, the quantification of the vertical and longitudinal distribution of C_{ANT}, and the inherent OA is still a matter of debate in the Mediterranean. The bulk C_{ANT} concentration is defined as the excess of CO_2 that any water mass dissolves when formed at the surface ocean at any time after the industrial revolution, compared to when formed in preindustrial times. As C_{ANT} cannot be directly measured, it is estimated using mainly three different approaches, and under several assumptions: (i) the back-calculation techniques; (ii) the Transient Time Distribution (TTD) methods; and (iii) using global ocean carbon models. The back-calculation techniques rely on CO_2 and ancillary variables measurements, for example the ΔC^* (Gruber et al., 1996) and the TrOCA (Touratier and Goyet, 2004) approaches, both try to correct the impact of remineralization of organic

matter on DIC as well as the DIC preformed conditions at preindustrial times. The TTD methods (Waugh et al., 2006) rely on transient tracer measurements (CFCs, SF_6, helium and tritium) to estimate the time since when the water mass was in contact with the atmosphere and therefore with a given atmospheric CO_2 level. Finally, the global ocean carbon models infer circulation and carbon uptake and storage (Orr et al., 2001; Wang et al., 2012). In the global open ocean, those approaches are in reasonable agreement (Khatiwala et al., 2013). However, this is not the case in the Mediterranean. The ΔC^* method was only applied in the area of the Gulf of Cádiz and Strait of Gibraltar (Flecha et al., 2012), while the TrOCA approach has been widely used at the basin scale (Rivaro et al., 2010; Touratier and Goyet, 2011; Hassoun et al., 2015), in the northern WMED (Touratier et al., 2016), in the Adriatic Sea (Ingrosso et al., 2017; Krasakopoulou et al., 2011), in the Algero-Provençal subbasin (Keraghel et al., 2020) and the Aegean Sea (Krasakopoulou et al., 2017). The TTD approach was applied in the EMED (Schneider et al., 2010) and a high resolution regional model for the Mediterranean was developed by Palmiéri et al. (2015). All methods show an invasion of C_{ANT} all over the water column, contrary to the open adjacent Atlantic Ocean (Vázquez-Rodríguez et al., 2009), with higher C_{ANT} accumulation in the WMED and lower values in the EMED and Tyrrhenian Sea (Hassoun et al., 2015). However, these methods yield great differences in the estimated C_{ANT} concentrations, with values distributed as follows: TrOCA > TTD > model, and with C_{ANT} differences between them of about 50% in some areas/water masses. Consequently, although their general patterns are comparable, C_{ANT} budget and the bulk acidification of the basin are in disagreement with modeling and observational studies (Palmiéri et al., 2015; Kapsenberg et al., 2017). Therefore, bulk estimates of the associated pH change since the preindustrial period for surface waters vary from −0.15, −0.1 to −0.08 pH units, using TrOCA, TTD and the high resolution model results, respectively (Schneider et al., 2010; Palmiéri et al., 2015; Hassoun et al., 2015).

Rates of change in the CO_2 chemistry can only be assessed from repeated observations in time and space. This sort of data is generally lacking in the Mediterranean, but the situation is changing (see subchapter 11.4.6). Although OA is primarily associated with the C_{ANT} storage in the ocean, other chemical additions or subtractions could lead to pH reductions,[4] for example, a reduction of ventilation leading to an increase of organic matter remineralization (Feely et al., 2010). Rates of OA documented from the published time series and bulk approaches previously commented were compiled by Kapsenberg et al. (2017). Those based on time-series and cruise comparisons generally agree with values around −0.003 pH units yr^{-1} (Luchetta et al., 2010; Marcellin Yao et al., 2016; Kapsenberg et al., 2017; Merlivat et al., 2018; Hassoun et al., 2019; Wimart-Rousseau et al., 2021), a rate that is higher than the acidification levels estimated for the surface open ocean (Lauvset et al., 2015), but lower than the reported rate for the MOW in the Strait

[4] https://www.ipcc.ch/srocc/chapter/glossary/.

of Gibraltar, −0.0044 pH units yr^{-1} (Flecha et al., 2015) or −0.009 pH units yr^{-1} along the Lebanese coast (Hassoun et al., 2019). Indeed, the estimation of OA and the corresponding drivers is still an open question in the Mediterranean that needs more sustainable observations with a significant reduction of measurements' uncertainty.

11.4.6 Current biogeochemical monitoring activities with focus on CO_2 variables in the Mediterranean Sea

In the recent decade, biogeochemical monitoring surveys have enormously increased in the Mediterranean Sea and were given better attention by various Mediterranean governmental and private institutions, particularly after the intensification of OA research, thanks to two EU trans-Mediterranean projects, EPOCA[5] and MedSeA.[6] Together with other regional and national studies and initiatives, these efforts showed the actual and potential effects of biogeochemical changes on Mediterranean marine and coastal ecosystems, particularly those related to OA (MerMex Group, 2011; Lacoue-Labarthe et al., 2016; MedECC, 2020). As evidences of OA impacts on key organisms have been published and more institutions have expressed interest in joining forces to better understand OA, there was a clear need to create a platform to facilitate the communication between different research bodies, stakeholders and policymakers in the Mediterranean area. This was made possible through the Global Ocean Acidification Observing Network (GOA-ON), that encouraged the formation of the Ocean Acidification Mediterranean-Hub,[7] a network that is currently gathering more than 70 scientists from 11 Mediterranean countries working on OA, interested in collaborating and willing to share their results and knowledge with nonscientific communities to improve OA literacy and awareness. One of the main challenges to improve biogeochemical research in the Mediterranean Sea relates with reducing the gaps of spatio-temporal data that preclude a better understanding of the carbonate system patterns and trends in unde-sampled areas. The north-south discrepancy in biogeochemical research in the Mediterranean Sea is evidenced by a majority of OA studies published by researchers affiliated to northern shore countries, with very few studies and observations conducted in the southern Mediterranean. Here, major observational gaps stand out, for example, a lack of clear assessment of the terrestrial inputs. Another issue is the lack of long-term studies to better understand the interannual trends of biogeochemical parameters, mainly those related to CO_2 variables in key regions such as the straits. Consequently, the OA Med-Hub is trying to assess the current OA research landscape, to identify the obstacles and gaps in the Mediterranean OA research, and improve the representability of the southern Mediterranean countries

[5] EPOCA was launched in 2008 (https://cordis.europa.eu/project/id/211384).
[6] MedSeA was launched in 2011 (http://www.medsea-project.eu/).
[7] OA Med Hub (http://www.goa-on.org/regional_hubs/mediterranean/about/introduction.php).

in this critical research topic, that is influencing the whole region, and mainly the most vulnerable communities.

To better proceed in biogeochemical monitoring, GOA-ON has established an OA data portal[8] where data-producers are encouraged to report their metadata so their research efforts can be visible to scientists, stakeholders and potential funders. This would facilitate the creation of future collaborations and exchange knowledge and facilities between different Mediterranean institutions. These metadata are visualized via an interactive map to facilitate the search of any OA activity as fixed or ship-based time series, moorings, biogeochemical Argo floats and ships of opportunity (see Chapter 10). Taking into consideration the peculiarities of the Mediterranean biogeochemical features, and its classification as a climate hotspot where many climate change consequences are clearly exacerbating (see Chapter 3), it is necessary to close the gaps of knowledge in some Mediterranean subbasins where biogeochemical studies are rare, mainly in straits, channels, and coastal areas witnessing significant natural variability and direct human pressures.

11.5 Identifying Mediterranean Sea water masses using biogeochemistry

Biogeochemical variables are useful tracers to identify water masses, adding information to the classical potential temperature versus salinity diagrams (TS diagrams, see Chapter 4). Along with temperature and salinity, biogeochemical variables can be introduced into an Optimum Multi Parameter (OMP) water mass analysis (this concept has already been introduced in Chapter 4 as well). However, being nonconservative, their mixing equations should consider a remineralization or biological activity term (this analysis is usually called *extended* OMP, e.g., García-Ibañez et al., 2015). Alternatively, conservative variables, as NO and PO ($NO = DO + RN \times NO_3^-$, $PO = DO + RP \times PO_4^{3-}$, Broecker, 1974; where RN and RP are the stoichiometric ratios between DO and NO_3^- or PO_4^{3-}, respectively) can be introduced in a classical OMP, which could use also silicate concentrations to solve the mixing of several water masses (Álvarez et al., 2014b). Simple OMP analysis have been applied in the Mediterranean Sea, to study the impact of biogeochemical processes on barium (Jullion et al., 2017) or the spreading and modification of intermediate waters (Schroeder et al., 2020).

In the upper 500 m of the Mediterranean, surface and intermediate waters clearly show a pattern related to longitude (Fig. 11.14, left plots): Atlantic Water entering through the Strait of Gibraltar, and identified by a salinity minimum, is also characterized by high DO, low NO_3^-, DOC values around 60 μmol L^{-1}, as well as DIC/TA and pHT_{is} clearly lower than surface waters in the rest of the Mediterranean; in the

[8] http://portal.goa-on.org/.

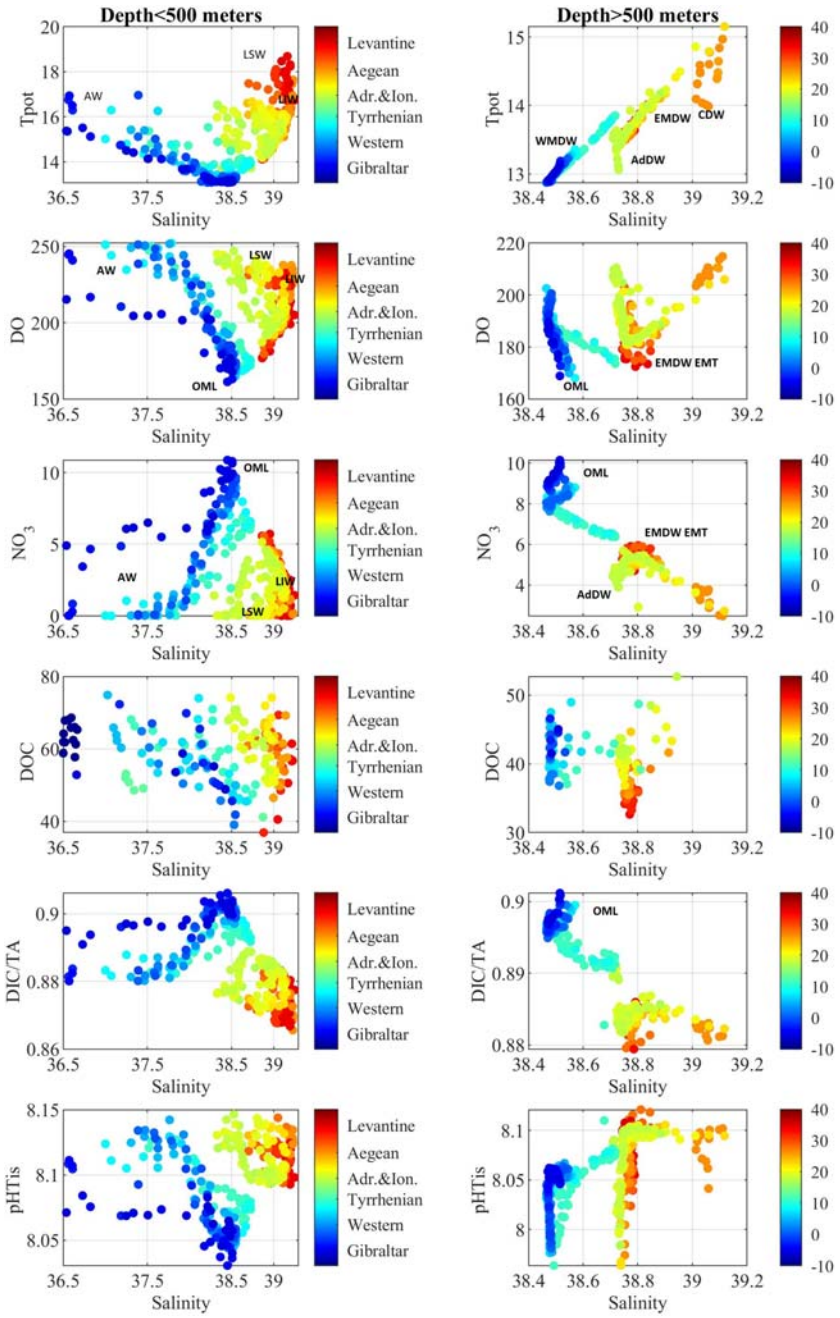

FIGURE 11.14

Property-property plots with salinity as x-axis and potential temperature (Tpot, °C) as y-axis in the first line and several biogeochemical variables in the plots below: dissolved

EMED, the surface water mass is warmer and saltier, with high DO and minimum inorganic nutrient concentrations. The LIW is identified by a salinity maximum at intermediate depths and a hook in the temperature versus salinity diagram (see Chapter 4), and also presents minimum DIC/TA values and very high pHT_{is}. While it moves westward, LIW undergoes mixing and biogeochemical processes, and in the WMED it coincides with the OML, with high NO_3^- and DIC/TA ratio.

Deep waters in the EMED clearly differ from those in the WMED in the TS diagrams (Fig. 11.14 right plots, and Chapter 4). Here Cretan Deep Water (CDW) with very high salinity, high DO, and low NO_3^- and DIC/TA ratio can be identified. The Eastern Mediterranean Deep Water (EMDW) of Aegean Sea origin, produced during the EMT event, can be identified by lower DO values in the Levantine Basin, while in the Ionian Sea post EMT waters with an Adriatic origin present lower DO and NO_3^-. Adriatic Deep Water (AdDW) is high in DO and low in NO_3^-. The Tyrrhenian Sea links the EMED and the WMED with differential and intermediate biogeochemical characteristics. More recent vintages of Western Mediterranean Deep Water (WMDW) are warmer and saltier and also present higher DO values, with very similar nutrients and CO_2 characteristics.

11.6 Future projections and threats to Mediterranean biogeochemistry

All oceans and seas are suffering and will suffer impacts related to changes in the Earth's climate. In this section, the main changes expected for the biogeochemistry of the Mediterranean Sea in the next few decades are summarized, as shown by the latest research available in literature.

11.6.1 Climate change and its impact on the oceans' biogeochemistry and Mediterranean peculiarities

Changes in the climatic conditions of the Earth system will have a profound impact on each of the system's components: atmosphere, ocean and cryosphere. The alterations affecting the marine systems, especially the open ocean, can be analyzed in

oxygen (DO, $\mu mol\ kg^{-1}$), nitrate (NO_3^-, $\mu mol\ kg^{-1}$), dissolved organic carbon (DOC, $\mu mol\ l^{-1}$), DIC to TA (DIC/TA) ratio and pH on the Total scale at in situ conditions. The z-axis shows longitude. Waters shallower (deeper) than 500 m are shown on the left (right). DOC data was taken from the HotMix cruise in April 2014 (Catalá et al., 2018), other biogeochemical variables from the M84/3 cruise in April 2011 (Tanhua et al., 2013b).

terms of modifications of the vertical distribution of physical properties of the water column, where the upper layers will be more impacted (Bindoff et al., 2019). This is particularly important for biogeochemical processes, as most of the primary productivity in the open ocean is driven by the vertical mixing of waters, mainly induced by wind stress, which introduces inorganic nutrients into the upper and lit layer (∼150 m). The dynamics of vertical mixing is extremely complex and one of the key factors modulating it is the vertical distribution of water density (i.e., the stratification of the water column). A reduction of water density occurring principally at the surface, increases stratification (i.e., increases the vertical gradient of density) and makes the water column more stable and more difficult to mix. Density is a function of temperature and salinity that are both linked to the atmosphere-ocean interactions by heat transfer and evaporation/precipitation processes. Thus, changes in the atmospheric conditions (e.g., temperature, humidity, winds) affect the stratification and, hence, the fertilization of the upper layer and its associated biological productivity. The magnitude and even the sign of such changes are, however, largely dependent on the oceanic area being evaluated.

Beside the already described effects mainly affecting the open ocean, the coastal ocean is also subjected to additional impacts related with climate change. Those impacts are mostly mediated through changes in freshwater loads and quality, variations of sea-level and local/regional processes. The Mediterranean Sea is located in the temperate region, almost completely surrounded by land and with limited exchanges with the world's ocean. All these elements make the area particularly sensitive to climate change (Giorgi, 2006) (see Chapter 3). Moreover, given its particular climatic and geographical conditions, the physical vertical structure of the Mediterranean Sea is very peculiar. The negative hydrological budget of the basin is continuously transforming surface and fresh Atlantic waters into saltier and denser Mediterranean Sea waters (see Chapter 4). This process, together with the frequent deep-convection events (see Chapter 7), maintains the antiestuarine circulation through the Strait of Gibraltar and contributes to the extreme oligotrophy of the Mediterranean Sea. Additionally, the high dependency of the Mediterranean ecosystems on the allochthonous nutrient supplies carried by the rivers, add to the peculiar N:P ratio found in this region, which is P-limited. The former elements make the impacts of climate change on the Mediterranean Sea biogeochemistry very peculiar and quite dissimilar compared to the ones observed in the world's ocean.

Most of the works dealing with climate change impacts in the Mediterranean Sea have focused on physical changes (see the review in Table 11.1), while only a handful have dealt with biogeochemical consequences (see review in Table 11.2). Different studies show coherent impacts on the physical drivers, in particular the increase of Sea Surface Temperature (SST), the reduction of Mixed Layer Depth (MLD) (with the exception of one study) and the reduction of the Mediterranean Thermohaline Circulation (MTHC). These changes result in antagonistic effects in terms of oligotrophy versus eutrophy. On one side, the reduction of MLD will reduce the uplift of nutrients, but on the opposite side the weakening of the

Table 11.1 Impacts of global change scenario simulations on key environmental factors affecting biogeochemical processes as derived from state-of-the-art model results. Scenarios considered are based on different hypotheses on atmospheric CO_2 concentration inducing different SST increase. The variables considered are SST, MLD, MTHC, Evaporation Precipitation River RUNOFF balance (E-P-R-B). NWM is the North-Western Mediterranean region. LIW is the Levantine Intermediate Water (200–600 m) and DEEP are deep waters (> 600 m) considered for some indicators.

Scenario	SST (oC)	MLD	MTHC	E-P-R-B	Runoff
HadCM2-SUL experiment[a] [2000–2100]	+1.5	/	Reduction	Increase	/
IPCC A2[b] [2000–2100]	+3.1	−20% Aegean −80% NWM	−40% LIW −80% DEEP	Increase +40%	Decrease in dardanelles
IPCC A2[c] [2000–2100]	+2.6	/	Reduction	Increase	/
IPCC A1b CMCC SXG[d] [2000–50]	+1.5	~0	Reduction	Increase	Decrease
IPCC A1b[e] [2000–50]	+1	/	/	Increase	Decrease
CIRCE[f] [2000–50]	+1.5	/	/	Increase +3% E, −9%P	/
RCP 8.5[g] [2000–50]	+1.0	/	/	/	/
RCP 4.5[h] RCP 8.5[i] [2013–2100]	+1.0 (RCP 4.5) +2.7 (RCP 8.5)	+16% NWM [2030]	/	/	Decrease (latitudinal variations) in 2100
RCP 4.5 RCP 8.5[j] [2010–2100]	+3.0 (RCP 8.5)	Reduction	Reduction	/	/

[a] *Thorpe and Bigg (2000)*.
[b] *Somot et al. (2006)*.
[c] *Somot et al. (2008)*.
[d] *Lazzari et al. (2014)*.
[e] *Dell'Aquila et al. (2012)*.
[f] *Gualdi et al., (2013)*.
[g] *Galli et al., (2017)*.
[h] *Macias et al. (2018a)*.
[i] *Macias et al. (2018b)*.
[j] *Reale et al. (2021)*.

Table 11.2 Impacts of global change scenario simulations on key biogeochemical variables as derived from state-of-the-art model results. Scenarios considered are based on different hypotheses on atmospheric CO_2 concentration, inducing different SST increase. The variables considered are net primary production (NPP), system biomass (BIOMASS), macro-nutrients (NUT) such as phosphates (P) and nitrates, Dissolved Oxygen (DO). Biomass indicators in some works are split in phytoplankton (phyto) and zooplankton (zoo).

Scenario	NPP	Biomass	Nut	DO
IPCC A1b[a] [2000–2100]	+3%	−5%	/	/
RCP 4.5 RCP 8.5[b] [2010–2100]	No net change East-increase west-decrease	/	East-increase wes-decrease	/
SRES A2[c] [2010–2100]	−10%	Phyto [-2%, −30%] Zoo [-8%, −12%]	Increase	/
RCP 4.5[d] [2010–2100]	+7%	Phyto −13% Zoo - 5%	P −2.5% 200–600m	−3% 200–600 m
RCP 8.5[d] [2010–2100]	+17%	Phyto −25% Zoo −10%	P −1.3% 200–600m	−6% 200–600 m

[a] *Lazzari et al. (2014).*
[b] *Macias et al. (2015).*
[c] *Richon et al. (2019).*
[d] *Reale et al., 2021.*

MTHC will reduce the antiestuarine signature of the Mediterranean, reducing the negative nutrient budget at the Strait of Gibraltar (Crispi et al., 2002). The high number of different drivers impacting the system makes it very difficult to add certainty to the biogeochemical scenarios of the Mediterranean Sea. Numerical models are commonly used as tools to perform future projections concerning physical and biogeochemical studies. Different scenarios simulations have been produced (Tables 11.1 and 11.2) according to IPCC projections of atmospheric CO_2 increase and related atmospheric temperature increase: A2 scenario and RCP8.5 assume higher increase in CO_2 and temperature, while A1b and RCP4.5 project a lower CO_2 and warming increase. Cascading effects of such changes on marine systems are studied with multidecadal simulations using hydrodynamical and biogeochemical models where the interaction with the atmospheric scenario is considered. For the same atmospheric scenario, marine ocean models can provide different predictions, due to differences in spatial resolutions, boundary conditions (e.g., different river load change in the future) or different parameterizations. Impacts consistently predicted by different models are considered more robust.

11.6.2 Expected changes of biogeochemical conditions in the Mediterranean Sea

All modeled scenarios predict warmer surface waters in the Mediterranean Sea in the next few decades (see Table 11.1). The rate of warming depends on the climate scenario considered and on the time-horizon. This overall warming will influence the rate of metabolic rates and induce changes in the plankton phenology and community structure, with a potential *tropicalization* of the low-trophic levels in the Mediterranean Sea. A warmer sea will also imply an increase in the evaporation rates which, together with the expected reduction in freshwater supply, will have profound consequences on the vertical stability of the water column. The competition of those two processes (warming and salinity increase) will determine the change in magnitude of fertilization processes of the water column, and the associated ecosystem productivity changes. All models considered indicate a reduction in biomass stocks with possible consequences on both coastal and marine ecosystems (Table 11.2). To complicate things even further, changes in fertilization strength will have different impacts on future levels of surface N and P, as both nutriclines (i.e., the depth at which the vertical gradients of their concentration is maximum) will change. These changes would further impact the whole food web. Present-day modeling tools are not ready to account for those potential changes, and more research efforts are needed in this field.

The expected changes in deep water formation and MTHC will also have consequences on the spatial distribution and intensity of surface currents (e.g., Macias et al., 2018c). Such changes could cause a displacement of present-day productivity hotspots, with cascading consequences for the entire food web and, even, for anthropogenic activities, such as fishing. Finally, being a semienclosed Sea, changes in quantity and quality of freshwater inputs in future decades are going to fundamentally impact the basis of the food webs in the Mediterranean. Such impacts could be either be local (i.e., in the vicinity of rivers' outlets), or happen in offshore waters (i.e., because of the alteration of the vertical stability of the water column).

11.6.3 Regional differences on the effect of climate change in the various Mediterranean subbasins

In addition to the general biogeochemical peculiarities of the Mediterranean, a common pattern found in many of the studies about potential biogeochemical changes in this sea is the presence of strong regional differences (Table 11.2). In particular, the WMED and EMED have been described as showing potentially contrasting trends in primary production (Macias et al., 2015), plankton composition changes (Richon et al., 2019), and major limiting nutrients (Pages et al., 2020). In order to understand those very contrasting trends, it is necessary to consider the very different boundary conditions and water masses distribution in each region (see Chapter 4).

The WMED is largely under the influence of the incoming Atlantic waters through the Strait of Gibraltar. These are light, fresh, and nutrient-poor waters that spread through the upper layer of the Western basin and condition its vertical structure and major horizontal currents. In future scenarios, with higher air

temperature over the Mediterranean, the water column of the WMED is expected to become more stratified, because of the expected surface warming, as a salinization trend is not expected due to the incoming fresh Atlantic waters. This will reduce the vertical mixing in general and, in particular, lower the extent of deep convection events, minimizing the inputs of deep nutrients to the upper water column and, hence, reducing the overall biological productivity.

In the EMED, the vertical structure of the water column different and there is a very limited input of freshwater to the basin and, hence, salinity is the major driver of the vertical stability. In future scenarios, evaporation will most likely increase while riverine discharges are expected to decrease (Macias et al., 2018a). Those two factors might change the vertical salinity distribution, making the water column less stratified and, hence, more prone to mixing. This could have an impact on marine surface biological production with some scenarios indicating a potential increase in the forthcoming decades (Lazzari et al., 2014; Macias et al., 2015).

There are many different smaller subbasins, with particular characteristics that might react in different ways to changes in the atmosphere-ocean interactions. Some of them (e.g., the Adriatic Sea) are largely influenced by riverine discharges, so any future changes in marine biogeochemistry are going to be linked to the freshwater input evolution (both in terms of quantity and quality) (Macías et al., 2018c), while other regions (e.g., Aegean or Alboran Seas) are strongly influenced by exchanges with other seas (Black Sea and Atlantic Ocean, respectively) and the changes of conditions on both sides of the connections.

Additional Resources

- Learn about the Global Ocean Observing System (GOOS, https://www.goosocean.org/) and their Essential Ocean Variables (EOVs, https://www.goosocean.org/index.php?option=com_content&view=article&id=283:essential-ocean-variables&catid=9&Itemid=441)
- Check the International Ocean Carbon Coordination Project (IOCCP, https://www.ioccp.org/), network compiling news, initiatives, data repositories and observational efforts about marine biogeochemistry
- Learn about the Global Ocean Acidification-Observing Network (GOA-ON, http://www.goa-on.org/) and their new UN Ocean Decade program (OARS, http://www.goa-on.org/oars/overview.php), the Ocean Acidification Mediterranean-Hub (OA Med-Hub, http://www.goa-on.org/regional_hubs/mediterranean/about/introduction.php)
- Interact with Ocean Acidification scientists on the Ocean Acidification Information Exchange (OAIE, https://www.oainfoexchange.org/about.html)
- Check how the atmospheric CO_2 is changing every month here: Earth's CO_2 (https://www.co2.earth/) Home Page.
- Check the UNESCO Intergovernmental Oceanographic Commission (IOC, https://ioc.unesco.org/index.php/) initiatives about biogeochemistry, ex, Global Ocean Oxygen Network (GO_2NE, https://en.unesco.org/go2ne), SDG 14.3.1 (https://oa.iode.org/) data portal about CO_2 data
- Compilation of DOM data in the global ocean (https://www.ncei.noaa.gov/access/ocean-carbon-data-system/oceans/ndp_109/ndp109.html): Hansell et al., (2021)
- Interior CO_2 data quality controlled, Global Ocean Data Analysis Project (GLODAP, https://www.glodap.info/), with specific data for the Mediterranean Sea (CARIMED)

References

Álvarez, M., Sanleón-Bartolomé, H., Tanhua, T., Mintrop, L., Luchetta, A., Cantoni, C., Schroeder, K., Civitarese, G., 2014a. The CO_2 system in the Mediterranean Sea: a basin wide perspective. Ocean Sci. 10, 69−92.

Álvarez, M., Brea, S., Mercier, H., Álvarez-Salgado, X.A., 2014b. Mineralization of biogenic materials in the water masses of the South Atlantic Ocean. I: assessment and results of an optimum multiparameter analysis. Prog. Oceanogr. 123, 1−23.

Álvarez, M., Fajar, N.M., Carter, B.R., Guallart, E.F., Pérez, F.F., Woosley, R.J., Murata, A., 2020. global ocean spectrophotometric pH assessment: consistent inconsistencies. Environ. Sci. Technol. 54, 10977−10988.

Álvarez-Salgado, X.A., Otero, J., Flecha, S., Huertas, I.E., 2020. Seasonality of dissolved organic carbon exchange across the strait of Gibraltar. Geophys. Res. Lett. 47 e2020GL089601.

Álvarez, M. et al., The Carbon, Tracers and Ancillary Data in the Mediterranean Sea, CARIMED, Data Synthesis Initiative: Overview and Quality Control Procedures. Earth System Science Data, (in preparation).

Arístegui, J., Duarte, C.M., Agusti, S., Doval, M., Alvarez-Salgado, X.A., Hansell, D.A., 2002. Dissolved organic carbon support of respiration in the dark ocean. Science 298, 1967.

Arrigo, K., 2005. Marine microorganisms and global nutrient cycles. Nature 437, 349−355.

Avril, B., 2002. DOC dynamics in the northwestern Mediterranean Sea (DYFAMED site). Deep. Res. Part II-Topical Stud. Oceanogr. 49, 2163−2182.

Bakker, D.C.E., Pfeil, B., Landa, C.S., Metzl, N., O'Brien, K.M., Olsen, A., Smith, K., Cosca, C., Harasawa, S., Jones, S.D., Nakaoka, S.I., Nojiri, Y., Schuster, U., Steinhoff, T., Sweeney, C., Takahashi, T., Tilbrook, B., Wada, C., Wanninkhof, R., Alin, S.R., Balestrini, C.F., Barbero, L., Bates, N.R., Bianchi, A.A., Bonou, F., Boutin, J., Bozec, Y., Burger, E.F., Cai, W.J., Castle, R.D., Chen, L., Chierici, M., Currie, K., Evans, W., Featherstone, C., Feely, R.A., Fransson, A., Goyet, C., Greenwood, N., Gregor, L., Hankin, S., Hardman-Mountford, N.J., Harlay, J., Hauck, J., Hoppema, M., Humphreys, M.P., Hunt, C.W., Huss, B., Ibánhez, J.S.P., Johannessen, T., Keeling, R., Kitidis, V., Körtzinger, A., Kozyr, A., Krasakopoulou, E., Kuwata, A., Landschützer, P., Lauvset, S.K., Lefèvre, N., Lo Monaco, C., Manke, A., Mathis, J.T., Merlivat, L., Millero, F.J., Monteiro, P.M.S., Munro, D.R., Murata, A., Newberger, T., Omar, A.M., Ono, T., Paterson, K., Pearce, D., Pierrot, D., Robbins, L.L., Saito, S., Salisbury, J., Schlitzer, R., Schneider, B., Schweitzer, R., Sieger, R., Skjelvan, I., Sullivan, K.F., Sutherland, S.C., Sutton, A.J., Tadokoro, K., Telszewski, M., Tuma, M., Van Heuven, S.M.A.C., Vandemark, D., Ward, B., Watson, A.J., Xu, S., 2016. A multi-decade record of high-quality fCO_2 data in version 3 of the Surface Ocean CO_2 Atlas (SOCAT). Earth Syst. Sci. Data 8, 383−413.

Bégovic, M., Copin-Montégut, C., 2002. Processes controlling annual variations in the partial pressure of CO_2 in surface waters of the central northwestern Mediterranean Sea (Dyfamed site). Deep. Res. Part II Top. Stud. Oceanogr. 49, 2031−2047.

Béranger, K., Drillet, Y., Houssais, M.N., Testor, P., Bourdallé-Badie, R., Alhammoud, B., Bozec, A., Mortier, L., Bouruet-Aubertot, P., Crépon, M., 2010. Impact of the spatial distribution of the atmospheric forcing on water mass formation in the Mediterranean Sea. J. Geophys. Res. 115, C12041.

Bindoff, N.L., Cheung, W.W.L., Kairo, J.G., Arístegui, J., Guinder, V.A., Hallberg, R., Hilmi, N., Jiao, N., Karim, M.S., Levin, L., O'Donoghue, S., Purca Cuicapusa, S.R., Rinkevich, B., Suga, T., Tagliabue, A., Williamson, P., 2019. Changing ocean, marine ecosystems, and dependent communities. In: Portner, H.O., Roberts, D.C., Masson-Delmotte, V., Zhai, P., Tignor, M., Poloczanska, E., Mintenbeck, K., Alegría, A., Nicolai, M., Okem, A., Petzold, J., Rama, B., Weyer, N.M. (Eds.), IPCC Special Report on the Ocean and Cryosphere in a Changing Climate. IPCC Special Report on the Ocean and Cryosphere in a Changing Climate. Intergovernmental Panel on Climate Change, Switzerland, pp. 477−587.

Bittig, H.C., Körtzinger, A., 2015. Tackling oxygen optode drift: near- surface and in-air oxygen optode measurements on a float provide an accurate in situ reference. J. Atmos. Ocean. Technol. 32, 1536−1543.

Blough, N.V., Del Vecchio, R., 2002. Chromophoric DOM in the coastal environment. In: Hansell, D.A., Carlson, C.A. (Eds.), Biogeochemistry of Marine Dissolved Organic Matter. Academic Press, San Diego, pp. 509−546.

Brewer, P.G., 2013. A short history of ocean acidification science in the 20th century: a chemist's view. Biogeosciences 10, 7411−7422.

Broecker, W.S., 1974. 'NO' a conservative water-mass tracer. Earth Planet Sci. Lett. 23, 100−107.

Cantoni, C., Luchetta, A., Celio, M., Cozzi, S., Raicich, F., Catalano, G., 2012. Carbonate system variability in the Gulf of trieste (north Adriatic Sea). Estuar. Coast Shelf Sci. 115, 51−62.

Carlson, C.A., Hansell, D.A., Nelson, N.B., Siegel, D.A., Smethie, W.M., Khatiwala, S., Meyers, M.M., Halewood, E., 2010. Dissolved organic carbon export and subsequent remineralization in the mesopelagic and bathypelagic realms of the North Atlantic basin. Deep. Res. Part II 57, 1433−1445.

Catalá, T.S., Álvarez-Salgado, X.A., Otero, J., Iuculano, F., Companys, B., Horstkotte, B., Romera-Castillo, C., Nieto-Cid, M., Latasa, M., Morán, X.A.G., Gasol, J.M., Marrasé, C., Stedmon, C.A., Reche, I., 2016. Drivers of fluorescent dissolved organic matter in the global epipelagic ocean. Limnol. Oceanogr. 61, 1101−1119.

Catalá, T.S., Martínez−Pérez, A.M., Nieto−Cid, M., Álvarez, M., Otero, J., Emelianov, M., Reche, I., Arístegui, J., Álvarez−Salgado, X.A., 2018. Dissolved Organic Matter (DOM) in the open Mediterranean Sea. I. Basin−wide distribution and drivers of chromophoric DOM. Prog. Oceanogr. 165, 35−51.

Catalá, T.S., Rossel, P.E., Álvarez-Gómez, F., Tebben, J., Figueroa, F.L., Dittmar, T., 2020. Antioxidant activity and phenolic content of marine dissolved organic matter and their relation to molecular composition. Front. Mar. Sci. 7, 603447.

Catherman, C., 2021. The World's Only Source of Critical Seawater Samples Could Dry up. Science | AAAS [WWW Document].

Claustre, H., Morel, A., Hooker, S.B., Babin, M., Antoine, D., Oubelkheir, K., Bricaud, A., Leblanc, K., Quéguiner, B., Maritorena, S., 2002. Is desert dust making oligotrophic waters greener? Geophys. Res. Lett. 29, 107−1.

Copin-Montégut, C., Bégovic, M., Merlivat, L., 2004. Variability of the partial pressure of CO_2 on diel to annual time scales in the Northwestern Mediterranean Sea. Mar. Chem. 85, 169−189.

Copin-Montégut, C., 1993. Alkalinity and carbon budgets in the Mediterranean Sea. Global Biogeochem. Cycles 7, 915−925.

Coppola, L., Prieur, L., Taupier-Letage, I., Estournel, C., Testor, P., Lefevre, D., Belamari, S., LeReste, S., Taillandier, V., 2017. Observation of oxygen ventilation into deep waters through targeted deployment of multiple Argo-O_2 floats in the north-western Mediterranean Sea in 2013. J. Geophys. Res. Oceans. 122, 6325−6341.

Coppola, L., Legendre, L., Lefevre, D., Prieur, L., Taillandier, V., Diamond Riquiera, E., 2018. Seasonal and inter-annual variations of dissolved oxygen in the northwestern Mediterranean Sea (DYFAMED site). Prog. Oceanogr. 162, 187−201.

Cossarini, G., Querin, S., Solidoro, C., 2015. The continental shelf carbon pump in the northern Adriatic Sea (Mediterranean Sea): influence of wintertime variability. Ecol. Model. 314, 118−134.

Cossarini, G., Feudale, L., Teruzzi, A., Bolzon, G., Coidessa, G., Solidoro, C., Di Biagio, V., Amadio, C., Lazzari, P., Brosich, A., Salon, S., 2021. High-resolution reanalysis of the Mediterranean Sea biogeochemistry (1999−2019). Front. Mar. Sci. 8, 741486.

Crispi, G., Crise, A., Solidoro, C., 2002. Coupled Mediterranean ecomodel of the phosphorus and nitrogen cycles. J. Mar. Syst. 33−34, 497−521.

Cuss, C.W., Guéguen, C., 2015. Relationships between molecular weight and fluorescence properties for size-fractionated dissolved organic matter from fresh and aged sources. Water Res. 68, 487−497.

Dai, M., Yin, Z., Meng, F., Liu, Q., Cai, W.J., 2012. Spatial distribution of riverine DOC inputs to the ocean: an updated global synthesis. Curr. Opin. Environ. Sustain. 4, 170−178.

De Carlo, E.H., Mousseau, L., Passafiume, O., Drupp, P.S., Gattuso, J.P., 2013. Carbonate chemistry and air-sea CO_2 flux in a NW mediterranean Bay over a four-year period: 2007−2011. Aquat. Geochem. 19, 399−442.

Dell'Aquila, A., Calmanti, S., Ruti, P., Struglia, M.V., Pisacane, G., Carillo, A., Sannino, G., 2012. Effects of seasonal cycle fluctuations in an A1B scenario over the Euro-Mediterranean region. Clim. Res. 52, 135−157.

Deutsch, C., Sarmiento, J.L., Sigman, D.M., Gruber, N., Dunne, J.P., 2007. Spatial coupling of nitrogen inputs and losses in the ocean. Nature 445, 163−167.

Dickson, A.G., 1992. The development of the alkalinity concept in marine chemistry. Mar. Chem. 40, 49−63.

Dickson, A.G., 1993. The measurement of sea water pH. Mar. Chem. 44, 131−142.

Dickson, A.G., 2010. The carbon dioxide system in seawater: equilibrium chemistry and measurements. In: Riebesell, U., Fabry, V.J., Hansson, L., Gattuso, J.P. (Eds.), Guide to Best Practices for Ocean Acidification Research and Data Reporting. Publications Office of the European Union, Luxembourg, pp. 17−40.

Dickson, A.G., Afghan, J.D., Anderson, G.C., 2003. Reference materials for oceanic CO_2 analysis: a method for the certification of total alkalinity. Mar. Chem. 80, 185−197.

Dickson, A.G., Sabine, C.L., Christian, J.R., 2007. Guide to Best Practices for Ocean CO_2 Measurements. North Pacific Marine Science Organization Sidney, British Columbia.

Dickson, A.G., Camões, M.F., Spitzer, P., Fisicaro, P., Stoica, D., Pawlowicz, R., Feistel, R., 2016. Metrological challenges for measurements of key climatological observables. Part 3: seawater pH. Metrologia 53, R26−R39.

Dittmar, T., Stubbins, A., 2014. Treatise on Geochemistry, second ed., pp. 125−156

Dittmar, T., Lennartz, S.T., Buck-Wiese, H., Hansell, D.A., Santinelli, C., Vanni, C., Blasius, B., Hehemann, J.-H., 2021. Enigmatic persistence of dissolved organic matter in the ocean. Nat. Rev. Earth Environ. 1−14.

Djaoudi, K., VanWambeke, F., Barani, A., Hélias-Nunige, S., Sempéré, R., Pulido-Villena, E., 2018. Atmospheric fluxes of soluble organic C, N, and P to the Mediterranean Sea: potential biogeochemical implications in the surface layer. Prog. Oceanogr. 163, 59−69.

Druffel, E.R.M., Williams, P.M., Bauer, J.E., Ertel, J.R., 1992. Cycling of dissolved and particulate organic matter in the open ocean. J. Geophys. Res. Oceans 97, 15639−15659.

Durrieu de Madron, X., Ludwig, W., Civitarese, G., Gacic, M., Ribera d'Alcalà, M., Raimbault, P., Krasakopoulou, E., Goyet, C., 2009. Shelf-slope nutrients and carbon fluxes in the Mediterranean Sea. In: Liu, K.K., Atkinson, L., Quinones, R., Talaue-McManus, L. (Eds.), Carbon and Nutrient Fluxes in Continental Margins. A Global Synthesis, Global Change - the IGBP Series, vol. XII. Springer-Verlag, pp. 364−383.

Durrieu de Madron, X., Houpert, L., Puig, P., Sanchez-Vidal, A., Testor, P., Bosse, A., Estournel, C., Somot, S., Bourrin, F., Bouin, M.N., Beauverger, M., Beguery, L., Calafat, A., Canals, M., Cassou, C., Coppola, L., Dausse, D., D'Ortenzio, F., Font, J., Heussner, S., Kunesch, S., Lefevre, D., Le Goff, H., Martín, J., Mortier, L., Palanques, A., Raimbault, P., 2013. Interaction of dense shelf water cascading and open-sea convection in the northwestern Mediterranean during winter 2012. Geophys. Res. Lett. 40, 1379−1385.

D'Ortenzio, F., Ribera d'Alcala, M., 2009. On the trophic regimes of the Mediterranean Sea: a satellite analysis. Biogeosciences 6, 139−148.

D'Ortenzio, F., Antoine, D., Marullo, S., 2008. Satellite-driven modeling of the upper ocean mixed layer and air-sea CO_2 flux in the Mediterranean Sea. Deep. Res. Part I Oceanogr. Res. Pap. 55, 405−434.

Feely, R.A., Alin, S.R., Newton, J., Sabine, C.L., Warner, M., Devol, A., Krembs, C., Maloy, C., 2010. The combined effects of ocean acidification, mixing, and respiration on pH and carbonate saturation in an urbanized estuary. Estuar. Coast Shelf Sci. 88, 442−449.

Flecha, S., Pérez, F.F., Navarro, G., Ruiz, J., Olivé, I., Rodríguez-Gálvez, S., Costas, E., Huertas, I.E., 2012. Anthropogenic carbon inventory in the Gulf of Cádiz. J. Mar. Syst. 92, 67−75.

Flecha, S., Pérez, F.F., García-Lafuente, J., Sammartino, S., Ríos, A.F., Huertas, I.E., 2015. Trends of pH decrease in the Mediterranean Sea through high frequency observational data: indication of ocean acidification in the basin. Sci. Rep. 51 (5), 1−8.

Fraga, F., Álvarez-Salgado, X.A., 2005. Variación de la alcalinidad durante la fotosíntesis del fitoplancton marino. Cienc. Mar. 31, 627−639.

Friedland, R., Macias, D., Cossarini, G., Daewel, U., Estournel, C., Garcia-Gorriz, E., Grizzetti, B., Grégoire, M., Gustafson, B., Kalaroni, S., Kerimoglu, O., Lazzari, P., Lenhart, H., Lessin, G., Maljutenko, I., Miladinova, S., Müller-Karulis, B., Neumann, T., Parn, O., Pätsch, J., Piroddi, C., Raudsepp, U., Schrum, C., Stegert, C., Stips, A., Tsiaras, K., Ulses, C., Vandenbulcke, L., 2021. Effects of nutrient management scenarios on marine eutrophication indicators: a pan-European, multi-model assessment in support of the marine strategy framework directive. Front. Mar. Sci. 8, 596126.

Galletti, Y., Gonnelli, M., Brogi, S.R., Vestri, S., Santinelli, C., 2019. DOM dynamics in open waters of the Mediterranean Sea: new insights from optical properties. Deep-Sea Res. Part I Oceanogr. Res. Pap. 144, 95−114.

Galletti, Y., Becagli, S., Sarra, A. di, Gonnelli, M., Pulido-Villena, E., Sferlazzo, D.M., Traversi, R., Vestri, S., Santinelli, C., 2020. Atmospheric deposition of organic matter at a remote site in the central Mediterranean Sea: implications for the marine ecosystem. Biogeosciences 17, 3669−3684.

Galli, G., Solidoro, C., Lovato, T., 2017. Marine heat waves hazard 3D maps and the risk for low motility organisms in a warming Mediterranean Sea. Front. Mar. Sci. 4, 136.

García-Ibáñez, M.I., Pardo, P.C., Carracedo, L.I., Mercier, H., Lherminier, P., Ríos, A.F., Pérez, F.F., 2015. Structure, transports and transformations of the water masses in the Atlantic Subpolar Gyre. Prog. Oceanogr. 135, 18−36.

Geider, R.J., La Roche, J., 2002. Redfield revisited: variability of C:N:P in marine microalgae and its biochemical basis. Eur. J. Phycol. 37, 1−17.

Gemayel, E., Hassoun, A.E.R., Benallal, M.A., Goyet, C., Rivaro, P., Abboud-Abi Saab, M., Krasakopoulou, E., Touratier, F., Ziveri, P., 2015. Climatological variations of total alkalinity and total dissolved inorganic carbon in the Mediterranean Sea surface waters. Earth Syst. Dyn. 6, 789−800.

Giorgi, F., 2006. Climate change hot-spots. Geophys. Res. Lett. 33, L08707.

Goyet, C., Bradshaw, A.L., Brewer, P.G., 1991. The carbonate system in the Black Sea. Deep. Res. Part A 38.

Gruber, N., Sarmiento, J.L., Stocker, T.F., 1996. An improved method for detecting anthropogenic CO_2 in the oceans. Global Biogeochem. Cycles 10, 809−837.

Gualdi, S., Somot, S., Li, L., Artale, V., Adani, M., Bellucci, A., Braun, A., Calmanti, S., Carillo, A., Dell'Aquila, A., Déqué, M., Dubois, C., Elizalde, A., Harzallah, A., Jacob, D., L'Hévéder, B., May, W., Oddo, P., Ruti, P., Sanna, A., Sannino, G., Scoccimarro, E., Sevault, F., Navarra, A., 2013. The CIRCE simulations: regional climate change projections with realistic representation of the Mediterranean Sea. Bull. Am. Meteorol. Soc. 94 (1), 65−81.

Guerzoni, S., Chester, R., Dulac, F., Herut, B., Loye-Pilot, M.D., Measures, C., Mignon, C., Molinari, E., Moulin, C., Rossini, P., Saydam, C., Soudine, A., Ziveri, P., 1999. The role of atmospheric deposition in the biogeochemistry of the Mediterranean Sea. Prog. Oceanogr. 44, 147−190.

Hansell, D.A., Carlson, C.A., 2013. Localized refractory dissolved organic carbon sinks in the deep ocean. Global Biogeochem. Cycles 27, 705−710.

Hansell, D., Carlson, C., Repeta, D., Schlitzer, R., 2009. Dissolved organic matter in the ocean: a controversy stimulates new insights. Oceanography 22, 202−211.

Hassoun, A.E.R., Gemayel, E., Krasakopoulou, E., Goyet, C., Abboud-Abi Saab, M., Guglielmi, V., Touratier, F., Falco, C., 2015. Acidification of the Mediterranean Sea from anthropogenic carbon penetration. Deep. Res. Part I Oceanogr. Res. Pap. 102, 1−15.

Hansell, D.A., Carlson, C.A., Amon, R.M.W., Álvarez-Salgado, X.A., Yamashita, Y., Romera-Castillo, C., Bif, M.B. (2021). Compilation of dissolved organic matter (DOM) data obtained from the global ocean surveys from 1994 to 2020. NOAA National Centers for Environmental Information. Dataset. doi.org/10.25921/s4f4-ye35.

Hassoun, A.E.R., Fakhri, M., Raad, N., Abboud-Abi Saab, M., Gemayel, E., De Carlo, E.H., 2019. The carbonate system of the eastern-most Mediterranean Sea, levantine sub-basin: variations and drivers. Deep. Res. Part II Top. Stud. Oceanogr. 164, 54−73.

Herrmann, M., Sevault, F., Beuvier, J., Somot, S., 2010. What induced the exceptional 2005 convection event in the northwestern Mediterranean basin? Answers from a modeling study. J. Geophys. Res. 115, C12051.

Hirose, K., 2007. Metal−organic matter interaction: ecological roles of ligands in oceanic DOM. Appl. Geochem. 22, 1636−1645.

Hood, E.M., Merlivat, L., 2001. Annual to interannual variations of fCO_2 in the northwestern Mediterranean Sea: results from hourly measurements made by CARIOCA buoys, 1995-1997. J. Mar. Res. 59, 113−131.

Huertas, I.E., Ríos, A.F., García-Lafuente, J., Makaoui, A., Rodríguez-Gálvez, S., Sánchez-Román, A., Orbi, A., Ruíz, J., Pérez, F.F., 2009. Anthropogenic and natural CO_2 exchange through the strait of Gibraltar. Biogeosciences 6, 647−662.

Humphreys, M.P., Daniels, C.J., Wolf-Gladrow, D.A., Tyrrell, T., Achterberg, E.P., 2018. On the influence of marine biogeochemical processes over CO_2 exchange between the atmosphere and ocean. Mar. Chem. 199, 1−11.

Humphreys, M.P., Lewis, E.R., Sharp, J.D., Pierrot, D., 2022. PyCO2SYS v1.8: marine carbonate system calculations in Python. Geosci. Model Dev. (GMD) 15, 15−43.

Ingrosso, G., Giani, M., Cibic, T., Karuza, A., Kralj, M., Del Negro, P., 2016. Carbonate chemistry dynamics and biological processes along a river-sea gradient (Gulf of Trieste, northern Adriatic Sea). J. Mar. Syst. 155, 35−49.

Ingrosso, G., Bensi, M., Cardin, V., Giani, M., 2017. Anthropogenic CO2 in a dense water formation area of the Mediterranean Sea. Deep. Res. Part I Oceanogr. Res. Pap. 123, 118−128.

IPCC AR6, 2021. In: Zhai, V.P., Pirani, A., Connors, S.L., Péan, C., Berger, S., Caud, N., Chen, Y., Goldfarb, L., Gomis, M.I., Huang, M., Leitzell, K., Lonnoy, E., Matthews, J.B.R., Maycock, T.K., Waterfield, T., Yelekçi, O., Yu, R., Zhou, B. (Eds.), Climate Change 2021: The Physical Science Basis. Contribution of Working Group I to the Sixth Assessment Report of the Intergovernmental Panel on Climate Change [Masson-Delmotte]. Cambridge University Press.

IPCC, 2014. Climate change 2014: synthesis report. In: Pachauri, R.K., Meyer, L.A. (Eds.), Contribution of Working Groups I, II and III to the Fifth Assessment Report of the Intergovernmental Panel on Climate Change. IPCC), Geneva, p. 151.

IPCC, 2019. Technical summary. In: Pörtner, H.-O., Roberts, D.C., Masson-Delmotte, V., Zhai, P., Tignor, M., Poloczanska, E., et al. (Eds.), IPCC Special Report on the Ocean and Cryosphere in a Changing Climate. IPCC, Geneva.

Johnson, K.S., Needoba, J.A., Riser, S.C., Showers, W.J., 2007. Chemical sensor networks for the aquatic environment. Chem. Rev. 107, 623−640.

Johnson, K.S., Plant, J.N., Riser, S.C., Gilbert, D., 2015. Air oxygen calibration of oxygen optodes on a profiling float array. J. Atmos. Ocean. Technol. 32, 2160−2172.

Jones, V., Meador, T.B., Gogou, A., Migon, C., Penkman, K.E.H., Collins, M.J., Repeta, D.J., 2013. Characterisation and dynamics of dissolved organic matter in the Northwestern Mediterranean Sea. Prog. Oceanogr. 119, 78−89.

Jørgensen, L., Stedmon, C.A., Kragh, T., Markager, S., Middelboe, M., Søndergaard, M., 2011. Global trends in the fluorescence characteristics and distribution of marine dissolved organic matter. Mar. Chem. 126, 139−148.

Jørgensen, L., Stedmon, C.A., Granskog, M.A., Middelboe, M., 2014. Tracing the long-term microbial production of recalcitrant fluorescent dissolved organic matter in seawater. Geophys. Res. Lett. 41, 2481−2488.

Jullion, L., Jacquet, S.H.M., Tanhua, T., 2017. Untangling biogeochemical processes from the impact of ocean circulation: first insight on the Mediterranean dissolved barium dynamics. Global Biogeochem. Cycles 31, 1256−1270.

Kapsenberg, L., Alliouane, S., Gazeau, F., Mousseau, L., Gattuso, J.P., 2017. Coastal ocean acidification and increasing total alkalinity in the northwestern Mediterranean Sea. Ocean Sci. 13, 411−426.

Keraghel, M.A., Louanchi, F., Zerrouki, M., Aït Kaci, M., Aït-Ameur, N., Labaste, M., Legoff, H., Taillandier, V., Harid, R., Mortier, L., 2020. Carbonate system properties and anthropogenic carbon inventory in the Algerian Basin during SOMBA cruise 2014: acidification estimate. Mar. Chem. 221, 103783.

Khatiwala, S., Primeau, F., Holzer, M., 2012. Ventilation of the deep ocean constrained with tracer observations and implications for radiocarbon estimates of ideal mean age. Earth Planet Sci. Lett. 325, 116−125.

Khatiwala, S., Tanhua, T., Mikaloff Fletcher, S., Gerber, M., Doney, S.C., Graven, H.D., Gruber, N., McKinley, G.A., Murata, A., Ríos, A.F., Sabine, C.L., 2013. Global ocean storage of anthropogenic carbon. Biogeosciences 10, 2169−2191.

Kondratyev, S.I., Medvedev, E.V., Konovalov, S.K., 2017. Total Alkalinity and pH in the Black Sea Waters in 2010 − 2011. Morskoy Gidrofiz, zhurnal.

Körtzinger, A., Schimanski, J., Send, U., 2005. High quality oxygen measurements from profiling floats: a promising new technique. J. Atmos. Ocean. Technol. 22 (3), 302−308.

Kouassi, A.M., Zika, R.G., 1992. Light−induced destruction of the absorbance property of dissolved organic matter in seawater. Toxicol. Environ. Chem. 35, 195−211.

Kramer, G.D., Herndl, G.J., 2004. Photo− and bioreactivity of chromophoric dissolved organic matter produced by marine bacterioplankton. Aquat. Microb. Ecol. 36, 239−246.

Krasakopoulou, E., Rapsomanikis, S., Papadopoulos, A., Papathanassiou, E., 2009. Partial pressure and air-sea CO_2 flux in the Aegean Sea during february 2006. Continent. Shelf Res. 29, 1477−1488.

Krasakopoulou, E., Souvermezoglou, E., Goyet, C., 2011. Anthropogenic CO_2 fluxes in the otranto strait (E. Mediterranean) in february 1995. Deep Sea res. Part I oceanogr. Res. Pap. 58, 1103−1114.

Krasakopoulou, E., Souvermezoglou, E., Giannoudi, L., Goyet, C., 2017. Carbonate system parameters and anthropogenic CO_2 in the north Aegean Sea during october 2013. Continent. Shelf Res. 149, 69−81.

Krom, M.D., Herut, B., Mantoura, R.F.C., 2004. Nutrient budget for the Eastern Mediterranean: implications for P limitation. Limnol. Oceanogr. 49, 1582−1592.

Krom, M.D., Emeis, K.C., Van Cappellen, P., 2010. Why is the eastern Mediterranean phosphorus limited? Prog. Oceanogr. 85 (3−4), 236−244.

Krom, M.D., Kress, N., Fanning, K., 2014a. Silica cycling in the ultra-oligotrophic eastern Mediterranean Sea. Biogeosciences 11, 4211−4223.

Krom, M., Kress, N., Berman-Frank, I., Rahav, E., 2014b. Past, present and future patterns in the nutrient chemistry of the eastern mediterranean. In: Goffredo, S., Dubinsky, Z. (Eds.), The Mediterranean Sea. Springer, Dordrecht.

Kujawinski, E.B., 2011. The impact of microbial metabolism on marine dissolved organic matter. Ann. Rev. Mar. Sci 3, 567−599.

Lacoue-Labarthe, T., Nunes, P.A.L.D., Ziveri, P., Cinar, M., Gazeau, F., Hall-Spencer, J.M., Hilmi, N., Moschella, P., Safa, A., Sauzade, D., Turley, C., 2016. Impacts of ocean acidification in a warming Mediterranean Sea: an overview. Reg. Stud. Mar. Sci. 5, 1−11.

Laruelle, G.G., Lauerwald, R., Pfeil, B., Regnier, P., 2014. Regionalized global budget of the CO_2 exchange at the air-water interface in continental shelf seas. Global Biogeochem. Cycles 28, 1199−1214.

Lauvset, S.K., Gruber, N., Landschützer, P., Olsen, A., Tjiputra, J., 2015. Trends and drivers in global surface ocean pH over the past 3 decades. Biogeosciences 12, 1285−1298.

Lauvset, S.K., Lange, N., Tanhua, T., Bittig, H.C., Olsen, A., Kozyr, A., Álvarez, M., Becker, S., Brown, P.J., Carter, B.R., Cotrim Da Cunha, L., Feely, R.A., Van Heuven, S., Hoppema, M., Ishii, M., Jeansson, E., Jutterström, S., Jones, S.D., Karlsen, M.K., Lo Monaco, C., Michaelis, P., Murata, A., Pérez, F.F., Pfeil, B., Schirnick, C., Steinfeldt, R., Suzuki, T., Tilbrook, B., Velo, A., Wanninkhof, R., Woosley, R.J., Key, R.M., 2021. An updated version of the global interior ocean biogeochemical data product, GLODAPv2.2021. Earth Syst. Sci. Data 13, 5565−5589.

Lazzari, P., Mattia, G., Solidoro, C., Salon, S., Crise, A., Zavatarelli, M., Oddo, P., Vichi, M., 2014. Impacts of climate change and environmental management policies on the trophic regimes in the Mediterranean Sea: scenario analyses. J. Mar. Syst. 135, 137−149.

Lee, K., Sabine, C.L., Tanhua, T., Kim, T.W., Feely, R.A., Kim, H.C., 2011. Roles of marginal seas in absorbing and storing fossil fuel CO_2. Energy Environ. Sci. 4, 1133−1146.

Letscher, R., Primeau, F., Moore, J., 2016. Nutrient budgets in the subtropical ocean gyres dominated by lateral transport. Nat. Geosci. 9, 815−819.

Li, P., Tanhua, T., 2020. Recent changes in deep ventilation of the Mediterranean Sea; evidence from long-term transient tracer observations. Front. Mar. Sci. 7, 594.

Lipizer, M., Partescano, E., Rabitti, A., Giorgetti, A., Crise, A., 2014. Qualified temperature, salinity and dissolved oxygen climatologies in a changing Adriatic Sea. Ocean Sci. 10, 771−797.

Louanchi, F., Boudjakdji, M., Nacef, L., 2009. Decadal changes in surface carbon dioxide and related variables in the Mediterranean Sea as inferred from a coupled data-diagnostic model approach. ICES J. Mar. Sci. 66, 1538−1546.

Lovato, T., Vichi, M., 2015. An objective reconstruction of the Mediterranean sea carbonate system. Deep-Sea Res. Part I Oceanogr. Res. Pap. 98, 21−30.

Luchetta, A., Cantoni, C., Catalano, G., 2010. New observations of CO_2-induced acidification in the northern Adriatic Sea over the last quarter century. Chem. Ecol. 26, 1−17.

Ludwig, W., Dumont, E., Meybeck, M., Heussner, S., 2009. River discharges of water and nutrients to the Mediterranean and Black Sea: major drivers for ecosystem changes during past and future decades? Prog. Oceanogr. 80, 199−217.

Macias, D., Garcia-Gorriz, E., Stips, A., 2015. Productivity changes in the Mediterranean Sea for the twenty-first century in response to changes in the regional atmospheric forcing. Front. Mar. Sci. 2, 79.

Macias, D., Stips, A., Garcia-Gorriz, E., Dosio, A., 2018a. Hydrological and biogeochemical response of the Mediterranean Sea to freshwater flow changes for the end of the 21st century. PLoS One 13 (2), e0192174.

Macias, D., Garcia-Gorriz, E., Stips, A., 2018b. Deep winter convection and phytoplankton dynamics in the NW Mediterranean Sea under present climate and future (horizon 2030) scenarios. Sci. Rep. 8, 6626.

Macias, D., Garcia-Gorriz, E., Stips, A., 2018c. Major fertilization sources and mechanisms for Mediterranean Sea coastal ecosystems. Limnol. Oceanogr. 63 (2), 897−914.

Marcellin Yao, K., Marcou, O., Goyet, C., Guglielmi, V., Touratier, F., Savy, J.P., 2016. Time variability of the north-western Mediterranean Sea pH over 1995−2011. Mar. Environ. Res. 116, 51−60.

Margirier, F., Testor, P., Heslop, E., et al., 2020. Abrupt warming and salinification of intermediate waters interplays with decline of deep convection in the Northwestern Mediterranean Sea. Sci. Rep. 10, 20923.

Markaki, Z., Loÿe-Pilot, M.D., Violaki, K., Benyahya, L., Mihalopoulos, N., 2010. Variability of atmospheric deposition of dissolved nitrogen and phosphorus in the Mediterranean and possible link to the anomalous seawater N/P ratio. Mar. Chem. 120, 187−194.

Marsili, L.F., 1725. Histoire Physique de la Mer (Amsterdam: Aux Dépens de la Compagnie).

Martínez-Pérez, A.M., Álvarez-Salgado, X.A., Arístegui, J., Nieto-Cid, M., 2017a. Deep−ocean dissolved organic matter reactivity along the Mediterranean Sea: does size matter? Sci. Rep. 7, 5687.

Martínez-Pérez, A.M., Nieto-Cid, M., Osterholz, H., Catalá, T.S., Reche, I., Dittmar, T., Álvarez-Salgado, X.A., 2017c. Linking optical and molecular signatures of dissolved organic matter in the Mediterranean Sea. Sci. Rep. 7, 3436.

Martínez-Pérez, A.M., Osterholz, H., Nieto-Cid, M., Álvarez, M., Dittmar, T., Álvarez-Salgado, X.A., 2017b. Molecular composition of dissolved organic matter in the Mediterranean Sea. Limnol. Oceanogr. 62, 2699−2712.

Martínez−Pérez, A.M., Catalá, T.S., Nieto−Cid, M., Otero, J., Álvarez, M., Emelianov, M., Reche, I., Álvarez−Salgado, X.A., Arístegui, J., 2019. Dissolved organic matter (DOM) in the open Mediterranean Sea. II: basin−wide distribution and drivers of fluorescent DOM. Prog. Oceanogr. 170, 93−106.

Marty, J.C., Chiavérini, J., 2010. Hydrological changes in the Ligurian Sea (NW Mediterranean, DYFAMED site) during 1995−2007 and biogeochemical consequences. Biogeosciences 7, 2117−2128.

Mavropoulou, A.-M., Vervatis, V., Sofianos, S., 2020. Dissolved oxygen variability in the Mediterranean Sea. J. Mar. Syst. 208, 103348.

McGill, 1969. A budget for dissolved nutrient salts in the Mediterranean Sea. Cah. Oceanogr. 21, 543−554.

Meador, T.B., Gogou, A., Spyres, G., Herndl, G.J., Krasakopoulou, E., Psarra, S., Yokokawa, T., De Corte, D., Zervakis, V., Repeta, D.J., 2010. Biogeochemical relationships between ultrafiltered dissolved organic matter and picoplankton activity in the Eastern Mediterranean Sea. Deep Sea Res. Part II Top. Stud. Oceanogr. 57, 1460−1477.

MedECC, 2020. In: Cramer, W., Guiot, J., Marini, K. (Eds.), Climate and Environmental Change in the Mediterranean Basin, Current Situation and Risks for the Future. First Mediterranean Assessment Report, Union for the Mediterranean, Plan Bleu. UNEP/MAP, Marseille, France, p. 632.

Mentges, A., Feenders, C., Deutsch, C., Blasius, B., Dittmar, T., 2019. Long-term stability of marine dissolved organic carbon emerges from a neutral network of compounds and microbes. Sci. Rep. 9, 17780.

Mentges, A., Deutsch, C., Feenders, C., Lennartz, S.T., Blasius, B., Dittmar, T., 2020. Microbial physiology governs the oceanic distribution of dissolved organic carbon in a scenario of equal degradability. Front. Mar. Sci. 7, 549784.

Merlivat, L., Boutin, J., Antoine, D., Beaumont, L., Golbol, M., Vellucci, V., 2018. Increase of dissolved inorganic carbon and decrease in pH in near-surface waters in the Mediterranean Sea during the past two decades. Biogeosciences 15, 5653−5662.

MerMex Group, Durrieu de Madron, X., et al., 2011. Marine ecosystems' responses to climatic and anthropogenic forcings in the Mediterranean. Prog. Oceanogr. 91, 97−166.

Middelburg, J.J., Soetaert, K., Hagens, M., 2020. Ocean alkalinity, buffering and biogeochemical processes. Rev. Geophys. 58 e2019RG000681.

Millero, F.J., Feistel, R., Wright, D.G., McDougall, T.J., 2008. The composition of standard seawater and the definition of the reference-composition salinity scale. Deep. Res. Part I Oceanogr. Res. Pap. 55, 50−72.

Moon, J.-Y., Lee, K., Tanhua, T., Kress, N., Kim, I.-N., 2016. Temporal nutrient dynamics in the Mediterranean Sea in response to anthropogenic inputs. Geophys. Res. Lett. 43, 5243−5251.

Mopper, K., Kieber, D.J., 2002. In: Hansell, D.A., Carlson, C.A. (Eds.), Photochemistry and the Cycling of Carbon, Sulfur, Nitrogen and Phosphorous in Biogeochemistry of Marine Dissolved Organic Matter, vols 455−507. Academic Press.

Moriarty, J.M., Harris, C.K., Fennel, K., Friedrichs, M.A.M., Xu, K., Rabouille, C., 2017. The roles of resuspension, diffusion and biogeochemical processes on oxygen dynamics offshore of the Rhône River, France: a numerical modeling study. Biogeosciences 14, 1919−1946.

Nelson, N.B., Siegel, D.A., 2013. The global distribution and dynamics of chromophoric dissolved organic matter. Ann. Rev. Mar. Sci 5, 447−476.

Ogawa, H., Amagai, Y., Koike, I., Kaiser, K., Benner, R., 2001. Production of refractory dissolved organic matter by bacteria. Science 292, 917−920.

Orr, J.C., Maier-Reimer, E., Mikolajewicz, U., Monfray, P., Sarmiento, J.L., Toggweiler, J.R., Taylor, N.K., Palmer, J., Gruber, N., Sabine, C.L., Le Quéré, C., Key, R.M., Boutin, J., 2001. Estimates of anthropogenic carbon uptake from four three-dimensional global ocean models. Global Biogeochem. Cycles 15, 43−60.

Orr, J.C., Epitalon, J.M., Gattuso, J.P., 2015. Comparison of ten packages that compute ocean carbonate chemistry. Biogeosciences 12, 1483−1510.

Orr, J.C., Epitalon, J.-M., Dickson, A.G., Gattuso, J.-P., 2018. Routine uncertainty propagation for the marine carbon dioxide system. Mar. Chem. 207, 84−107.

Oschlies, A., Shulz, K., Riebesell, G.U., Schmittner, A., 2008. Simulated 21st century's increase in oceanic suBOX ia by CO_2-enhanced biotic carbon export. Global Biogeochem. Cycles 22, GB4008.

Pagès, R., Baklouti, M., Barrier, N., Ayache, M., Sevault, F., Somot, S., Moutin, T., 2020. Projected effects of climate-induced changes in hydrodynamics on the biogeochemistry of the Mediterranean Sea under the RCP 8.5 regional climate scenario. Front. Mar. Sci. 7, 957.

Palmiéri, J., Orr, J.C., Dutay, J.C., Béranger, K., Schneider, A., Beuvier, J., Somot, S., 2015. Simulated anthropogenic CO_2 storage and acidification of the Mediterranean Sea. Biogeosciences 12, 781−802.

Pantoja, S., Repeta, D.J., Sachs, J.P., Sigman, D.M., 2002. Stable isotope constraints on the nitrogen cycle of the Mediterranean Sea water column. Deep-Sea Res. Pt. I (4), 1609−1621.

Pitta, E., Zeri, C., Tzortziou, M., Rijkenberg, M.J.A., 2019. Transformations of dissolved organic matter in the Marmara Sea traced by its optical signature. J. Mar. Syst. 189, 1−11.

Powley, H.R., Dürr, H.H., Lima, A.T., Krom, M.D., Van Cappellen, P., 2016. Direct discharges of domestic wastewater are a major source of phosphorus and nitrogen to the Mediterranean Sea. Environ. Sci. Technol. 50, 8722−8730.

Powley, H.R., Krom, M.D., Van Cappellen, P., 2017. Understanding the unique biogeochemistry of the Mediterranean Sea: insights from a coupled phosphorus and nitrogen model. Global Biogeochem. Cycles 31, 1010−1031.

Powley, H.R., Krom, M.D., Van Cappellen, P., 2018. Phosphorus and nitrogen trajectories in the Mediterranean Sea (1950−2030): diagnosing basin-wide anthropogenic nutrient enrichment. Prog. Oceanogr. 162, 257−270.

Pujo-Pay, M., Conan, P., Oriol, L., Cornet-Barthaux, V., Falco, C., Ghiglione, J.F., Goyet, C., Moutin, T., Prieur, L., 2011. Integrated survey of elemental stoichiometry (C, N, P) from the western to eastern Mediterranean Sea. Biogeosciences 8, 883−899.

Reale, M., Cossarini, G., Lazzari, P., Lovato, T., Bolzon, G., Masina, S., Solidoro, C., Salon, S., 2021. Acidification, Deoxygenation, Nutrient and Biomasses Decline in a Warming Mediterranean Sea. Biogeosciences Discuss (submitted).

Redfield, A.C., 1958. The biological control of chemical factors in the environment. Am. Sci. 46, 205−221.

Repeta, D.J., 2015. Chemical characterization and cycling of dissolved organic matter. In: Hansell, D.A., Carlson, C.A. (Eds.), Biogeochemistry of Marine Dissolved Organic Matter. Academic Press, Waltham MA, USA, pp. 22−65.

Repeta, D.J., 2021. Unifying chemical and biological perspectives of carbon accumulation in the environment. Proc. Natl. Acad. Sci. U.S.A. 118.

Retelletti Brogi, S., Balestra, C., Casotti, R., Cossarini, G., Galletti, Y., Gonnelli, M., Vestri, S., Santinelli, C., 2020. Time resolved data unveils the complex DOM dynamics in a Mediterranean river. Sci. Total Environ. 733, 139212.

Retelletti Brogi, S., Cossarini, G., Bachi, G., Balestra, C., Camatti, E., Casotti, R., Checcucci, G., Colella, S., Evangelista, V., Falcini, F., Francocci, F., Giorgino, T., Margiotta, F., Ribera d'Alcalà, M., Sprovieri, M., Vestri, S., Santinelli, C., 2022. Evidence of Covid-19 lockdown effects on riverine dissolved organic matter dynamics provides a proof-of-concept for needed regulations of anthropogenic emissions. Sci. Total Environ. 812, 152412.

Revelle, R., Suess, H.E., 1957. Carbon dioxide exchange between atmosphere and ocean and the question of an increase of atmospheric CO_2 during the past decades. Tellus 9, 18−27.

Ribera d'Alcalà, M., Civitarese, G., Conversano, F., Lavezza, R., 2003. Nutrient ratios and fluxes hint at overlooked processes in the Mediterranean Sea. J. Geophys. Res. 108 (C9), 8106.

Richon, C., Dutay, J.-C., Bopp, L., Le Vu, B., Orr, J.C., Somot, S., Dulac, F., 2019. Biogeochemical response of the Mediterranean Sea to the transient SRES-A2 climate change scenario. Biogeosciences 16, 135−165.

Rivaro, P., Messa, R., Massolo, S., Frache, R., 2010. Distributions of carbonate properties along the water column in the Mediterranean Sea: spatial and temporal variations. Mar. Chem. 121, 236−245.

Rodellas, V., Garcia-Orellana, J., Masque, P., Feldman, M., Weinstein, Y., 2015. Submarine groundwater discharge as a major source of nutrients to the Mediterranean Sea. Proc. Natl. Acad. Sci. U.S.A. 112 (13), 3926−3930.

Romera-Castillo, C., Jaffé, R., 2015. Free radical scavenging (antioxidant activity) of natural dissolved organic matter. Mar. Chem. 177, 668−676.

Sanchez-Gomez, E., Somot, S., Josey, S.A., Dubois, C., Elguindi, N., Déqué, M., 2011. Evaluation of Mediterranean Sea water and heat budgets simulated by an ensemble of high resolution regional climate models. Clim. Dynam. 37, 2067−2086.

Sánchez-Pérez, E.D., Pujo-Pay, M., Ortega-Retuerta, E., Conan, P., Peters, F., Marrasé, C., 2020. Mismatched dynamics of dissolved organic carbon and chromophoric dissolved organic matter in the coastal NW Mediterranean Sea. Sci. Total Environ. 746.

Santinelli, C., 2015. DOC in the Mediterranean Sea. In: Hansell, D.A., Carlson, C.A. (Eds.), Biogeochemistry of Marine Dissolved Organic Matter. Academic Press, Waltham MA, USA, pp. 579−608.

Santinelli, C., Nannicini, L., Seritti, A., 2010. DOC dynamics in the meso and bathypelagic layers of the Mediterranean Sea. Deep Sea Res. Part II 57, 1446−1459.

Santinelli, C., Sempéré, R., Van Wambeke, F., Charriere, B., Seritti, A., 2012. Organic carbon dynamics in the Mediterranean Sea: an integrated study. Global Biogeochem. Cycles 26.

Santinelli, C., Hansell, D.A., Ribera d'Alcalà, M., 2013. Influence of stratification on marine dissolved organic carbon (DOC) dynamics: the Mediterranean Sea case. Prog. Oceanogr. 119, 68−77.

Santinelli, C., Follett, C., Retelletti Brogi, S., Xu, L., Repeta, D., 2015. Carbon isotope measurements reveal unexpected cycling of dissolved organic matter in the deep Mediterranean Sea. Mar. Chem. 177, 267−277.

Santinelli, C., Iacono, R., Napolitano, E., Ribera d'Alcalá, M., 2021. Surface transport of DOC acts as a trophic link among Mediterranean sub-basins. Deep Sea Res. Part I 170, 1−18.

Sarmiento, J.L., Gruber, N., 2006. Ocean Biogeochemical Dynamics 503.

Schink, D.R., 1967. Budget for dissolved silica in the Mediterranean Sea. Geochem. Cosmochim. Acta 31, 987−999.

Schneider, A., Tanhua, T., Krtzinger, A., Wallace, D.W.R., 2010. High anthropogenic carbon content in the eastern Mediterranean. J. Geophys. Res. Ocean. 115, C12050.

Schneider, A., Tanhua, T., Roether, W., Steinfeldt, R., 2014. Changes in ventilation of the Mediterranean Sea during the past 25 year. Ocean Sci. 10, 1−16.

Schroeder, K., Ribotti, A., Borghini, M., Sorgente, R., Perilli, A., Gasparini, G.P., 2008. An extensive Mediterranean deep water renewal between 2004 and 2006. Geophys. Res. Lett. 35, L18605.

Schroeder, K., Josey, S.A., Herrmann, M., Grignon, L., Gasparini, G.P., Bryden, H.L., 2010. Abrupt warming and salting of the Western Mediterranean Deep Water after 2005: atmospheric forcings and lateral advection. J. Geophys. Res. 115.

Schroeder, K., Cozzi, S., Belgacem, M., Borghini, M., Cantoni, C., Durante, S., Petrizzo, A., Poiana, A., Chiggiato, J., 2020. Along-path evolution of biogeochemical and carbonate system properties in the intermediate water of the western mediterranean. Front. Mar. Sci. 7, 375.

Sempéré, R., Panagiotopoulos, C., Lafont, R., Marroni, B., Van Wambeke, F., 2002. Total organic carbon dynamics in the Aegean Sea. J. Mar. Syst. 33, 355−364.

Sisma-Ventura, G., Bialik, O.M., Yam, R., Herut, B., Silverman, J., 2017. pCO_2 variability in the surface waters of the ultra-oligotrophic Levantine Sea: exploring the air−sea CO_2 fluxes in a fast warming region. Mar. Chem. 196, 13−23.

Sisma-Ventura, G., Kress, N., Silverman, J., Gertner, Y., Ozer, T., Biton, E., et al., 2021. Post-eastern Mediterranean transient oxygen decline in the deep waters of the southeast Mediterranean Sea supports weakening of ventilation rate. Front. Mar. Sci. 7, 598686.

Smith, R.O., Bryden, H.L., Stansfield, K., 2008. Observations of new western Mediterranean deep water formation using Argo floats 2004−2006. Ocean Sci. 4, 133−149.

Solidoro, C., Cossarini, G., Lazzari, P., Galli, G., Bolzon, G., Somot, S., Salon, S., 2022. Modeling carbon budgets and acidification in the Mediterranean Sea ecosystem under contemporary and future climate. Front. Mar. Sci. 8, 2073.

Somot, S., Sevault, F., Déqué, M., 2006. Transient climate change scenario simulation of the Mediterranean Sea for the 21st century using a high-resolution ocean circulation model. Clim. Dynam. 27 (7−8), 851−879.

Somot, S., Sevault, F., Déqué, M., Crépon, M., 2008. 21st century climate change scenario for the Mediterranean using a coupled Atmosphere-Ocean Regional Climate Model. Global Planet. Change 63 (2−3), 112−126.

Somot, S., Houpert, L., Sevault, F., Testor, P., Bosse, A., Taupier-Letage, I., Bouin, M.-N., Waldman, R., Cassou, C., Sanchez-Gomez, E., Durrieu de Madron, X., Adloff, F., Nabat, P., Herrmann, M., 2016. Characterizing, modelling and understanding the climate

variability of the deep water formation in the North-Western Mediterranean Sea. Clim. Dynam. 51, 1179–1210.

Sørensen, S.P.L., Palitzsch, S., 1909. Über die Messung die Wasserstoffionen konzentration des Meerwassers. Biochem. Z. 24, 387–415.

Stöven, T., Tanhua, T., 2014. Ventilation of the Mediterranean Sea constrained by multiple transient tracer measurements. Ocean Sci. 10, 439–457.

Taillandier, V., D'Ortenzio, F., Antoine, D., 2012. Carbon fluxes in the mixed layer of the Mediterranean Sea in the 1980s and the 2000s. Deep. Res. Part I Oceanogr. Res. Pap. 65, 73–84.

Takahashi, T., Olafsson, J., Goddard, J.G., Chipman, D.W., Sutherland, S.C., 1993. Seasonal variation of CO_2 and nutrients in the high-latitude surface oceans: a comparative study. Global Biogeochem. Cycles 7 (4), 843–878.

Tanhua, T., Hainbucher, D., Schroeder, K., Cardin, V., Álvarez, M., Civitarese, G., 2013a. The Mediterranean Sea system: a review and an introduction to the special issue. Ocean Sci. 9, 789–803.

Tanhua, T., Hainbucher, D., Cardin, V., Álvarez, M., Civitarese, G., McNichol, P., Key, R.M., 2013b. Repeat hydrography in the Mediterranean Sea, data from the meteor cruise 84/3 in 2011. Earth Syst. Sci. Data 5, 289–294.

Testor, P., Bosse, A., Houpert, L., Margirier, F., Mortier, L., Legoff, H., Dausse, D., Labaste, M., Karstensen, J., Hayes, D., Olita, A., Ribotti, A., Schroeder, K., Chiggiato, J., Onken, R., Heslop, E., Mourre, B., D'Ortenzio, F., Mayot, N., Lavigne, H., de Fommervault, O., Coppola, L., Prieur, L., Taillandier, V., Durrieu de Madron, X., Bourrin, F., Many, G., Damien, P., Estournel, C., Marsaleix, P., Taupier-Letage, I., Raimbault, P., Waldman, R., Bouin, M.-N., Giordani, H., Caniaux, G., Somot, S., Ducrocq, V., Conan, P., 2018. Multiscale observations of deep convection in the northwestern Mediterranean Sea during winter 2012–2013 using multiple platforms. J. Geophys. Res.: Oceans 123, 1745–1776.

Thierry, V., Bittig, H., Argo-Team, 2021. Argo Quality Control Manual for Dissolved Oxygen Concentration. https://doi.org/10.13155/46542.

Thorpe, R.B., Bigg, G.R., 2000. Modelling the sensitivity of Mediterranean Outflow to anthropogenically forced climate change. Clim. Dynam. 16, 355–368.

Torres-Valdés, S., Roussenov, V.M., Sanders, R., Reynolds, S., Pan, X., Mather, R., Landolfi, A., Wolff, G.A., Achterberg, E.P., Williams, R.G., 2009. Distribution of dissolved organic nutrients and their effect on export production over the Atlantic Ocean. Global Biogeochem. Cycles 23, GB4019.

Touratier, F., Goyet, C., 2004. Definition, properties, and Atlantic Ocean distribution of the new tracer TrOCA. J. Mar. Syst. 46, 169–179.

Touratier, F., Goyet, C., 2011. Impact of the eastern mediterranean transient on the distribution of anthropogenic CO_2 and first estimate of acidification for the Mediterranean Sea. Deep-Sea Res. Part I Oceanogr. Res. Pap. 58, 1–15.

Touratier, F., Goyet, C., Houpert, L., de Madron, X.D., Lefèvre, D., Stabholz, M., Guglielmi, V., 2016. Role of deep convection on anthropogenic CO_2 sequestration in the Gulf of Lions (northwestern Mediterranean Sea). Deep-Sea Res. Part I Oceanogr. Res. Pap. 113, 33–48.

Turk, D., Malačič, V., Degrandpre, M.D., McGillis, W.R., 2010. Carbon dioxide variability and air-sea fluxes in the northern Adriatic Sea. J. Geophys. Res. Ocean. 115, 10043.

Turley, C., Bianchi, M., Christaki, U., Conan, P., Harris, J.R.W., Psarra, S., Ruddy, G., Stutt, E., Tselepides, A., Van Wambeke, F., 2000. Relationship between primary

producers and bacteria in an oligotrophic sea-the Mediterranean and biogeochemical implications. Mar. Ecol.: Prog. Ser. 193, 11−18.
Ulses, C., Estournel, C., Fourrier, M., Coppola, L., Kessouri, F., Lefèvre, D., Marsaleix, P., 2021. Oxygen budget of the north-western Mediterranean deep- convection region. Biogeosciences 18, 937−960.
Urbini, L., Ingrosso, G., Djakovac, T., Piacentino, S., Giani, M., 2020. Temporal and spatial variability of the CO_2 system in a riverine influenced area of the Mediterranean Sea, the northern adriatic. Front. Mar. Sci. 7, 679.
Vázquez-Rodríguez, M., Touratier, F., Monaco, C.L., Waugh, D.W., Padin, X.A., Bellerby, R.G.J., Goyet, C., Metzl, N., Ríos, A.F., Pérez, F.F., 2009. Anthropogenic carbon distributions in the Atlantic Ocean: data-based estimates from the arctic to the antarctic. Biogeosciences 6, 439−451.
Velaoras, D., Papadopoulos, V.P., Kontoyiannis, H., Cardin, V., Civitarese, G., 2019. Water masses and hydrography during april and june 2016 in the cretan sea and cretan passage (Eastern Mediterranean Sea). Deep Sea Res. Part II Top. Stud. Oceanogr. 164, 25−40.
Wallace, W.J., 1974. The Development of the Chlorinity/Salinity Concept in Oceanography. Elsevier, Amsterdam.
Wang, S., Moore, J.K., Primeau, F.W., Khatiwala, S., 2012. Simulation of anthropogenic CO_2 uptake in the CCSM3.1 ocean circulation-biogeochemical model: comparison with data-based estimates. Biogeosciences 9, 1321−1336.
Wanninkhof, R., 2014. Relationship between wind speed and gas exchange over the ocean revisited. Limnol Oceanogr. Methods 12, 351−362.
Waugh, D.W., Hall, T.M., Mcneil, B.I., Key, R., Matear, R.J., 2006. Anthropogenic CO_2 in the oceans estimated using transit time distributions. Tellus Ser. B Chem. Phys. Meteorol. 58, 376−389.
Williams, R.G., Follows, M.J., 2011. Ocean Dynamics and the Carbon Cycle: Principles and Mechanisms. Cambridge Univ. Press, Cambridge, UK.
Wimart-Rousseau, C., Lajaunie-Salla, K., Marrec, P., Wagener, T., Raimbault, P., Lagadec, V., Lafont, M., Garcia, N., Diaz, F., Pinazo, C., Yohia, C., Garcia, F., Xueref-Remy, I., Blanc, P.E., Armengaud, A., Lefèvre, D., 2020. Temporal variability of the carbonate system and air-sea CO_2 exchanges in a Mediterranean human-impacted coastal site. Estuar. Coast Shelf Sci. 236, 106641.
Wimart-Rousseau, C., Wagener, T., Álvarez, M., Moutin, T., Fourrier, M., Coppola, L., Niclas-Chirurgien, L., Raimbault, P., D'Ortenzio, F., Durrieu de Madron, X., Taillandier, V., Dumas, F., Conan, P., Pujo-Pay, M., Lefèvre, D., 2021. Seasonal and interannual variability of the CO_2 system in the eastern Mediterranean Sea: a case study in the north western Levantine basin. Front. Mar. Sci. 8, 649246.
Winkler, L.W., 1888. Die Bestimmung des im Wasser gelösten Sauerstoffes. Ber. Dtsch. Chem. Ges. 21, 2843−2854.
Wolf-Gladrow, D.A., Zeebe, R.E., Klaas, C., Körtzinger, A., Dickson, A.G., 2007. Total alkalinity: the explicit conservative expression and its application to biogeochemical processes. Mar. Chem. 106, 287−300.
Zakem, E.J., Cael, B.B., Levine, N.M., 2021. A unified theory for organic matter accumulation. Proc. Natl. Acad. Sci. U.S.A. 118.
Zeebe, R., Wolf-Gladrow, D., 2001. CO2 in Seawater: Equilibrium, Kinetics, Isotopes. Elsevier Science.

This page intentionally left blank

CHAPTER

Active geological processes in the Mediterranean Sea

12

Elda Miramontes[1,2], Claudio Pellegrini[3], Daniele Casalbore[4,5], Stephanie Dupré[6]

[1]Faculty of Geosciences, University of Bremen, Bremen, Germany; [2]MARUM-Center for Marine Environmental Sciences, University of Bremen, Bremen, Germany; [3]Consiglio Nazionale delle Ricerche (CNR), Istituto di Scienze Marine (ISMAR), Italy; [4]Dipartimento di Scienze Della Terra, Università di Roma, Sapienza Rome, Italy; [5]Consiglio Nazionale delle Ricerche (CNR), Istituto di Geologia Ambientale e Geoingegneria (IGAG), Rome, Italy; [6]Ifremer, CNRS, Univ Brest, Geo-Ocean Plouzane, France

Learning objectives

In this chapter, you will learn:

- Which sedimentary processes are active in coastal and deep-water environments
- How submarine volcanoes form and which processes contribute to the collapse of their flanks
- How fluid escape forms cold seeps and related deposits
- How sedimentary processes and fluid seepage can become geohazards and affect ecosystems

12.1 General concepts

The basins of the Mediterranean Sea have formed by the convergence between the Africa and the Eurasia plates that began in the Late Cretaceous time (Dercourt et al., 1986). The Mediterranean Sea can be subdivided into the Eastern and Western Mediterranean basins, and are separated by the Sicily Channel (Fig. 12.1). These basins followed a different tectonic evolution, resulting in important contrasts in the dominant geological processes and seafloor morphology between the Eastern and the Western Mediterranean Sea (see Chapter 2 for more details). The Eastern Mediterranean Sea is at present more tectonically active than the Western Mediterranean Sea, with the presence of two subduction zones: the Hellenic subduction zone (south of Greece) and the Calabrian subduction zone (south of Italy), which strongly control the seafloor morphology and the geological processes in these areas.

In contrast, the north-western Mediterranean Sea is a passive margin, with weak tectonic activity at present (Faccenna et al., 2014). This area is strongly shaped by sedimentary processes, with abundant submarine canyons and channels crossing the

Oceanography of the Mediterranean Sea. https://doi.org/10.1016/B978-0-12-823692-5.00010-8

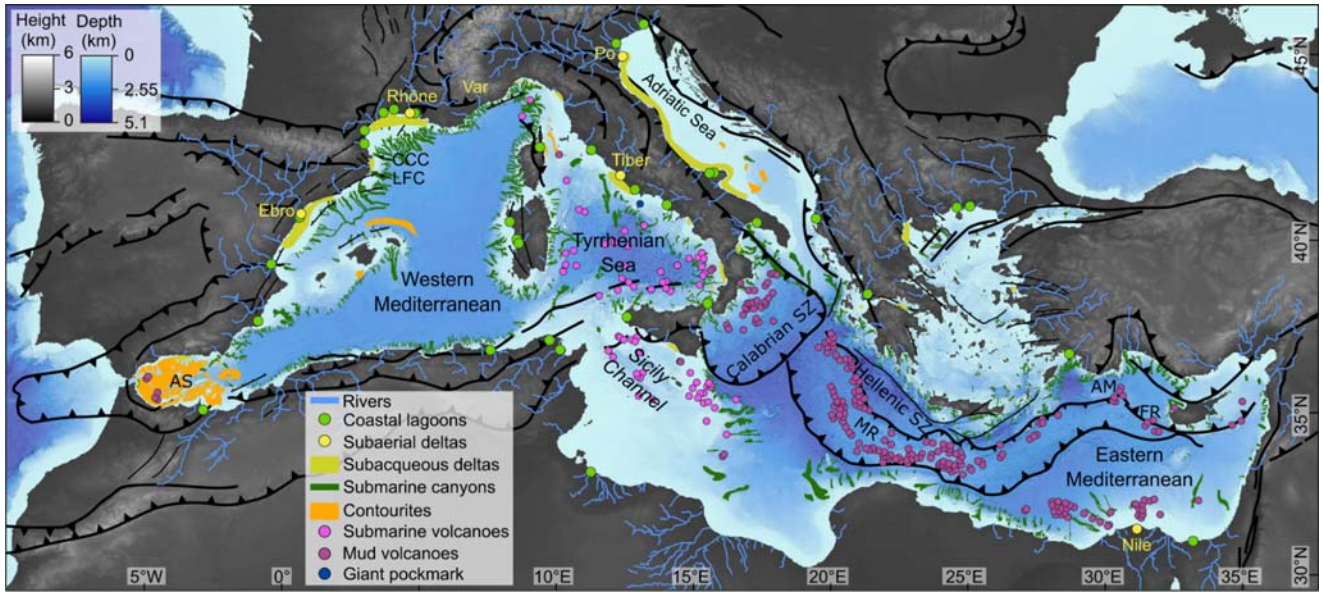

FIGURE 12.1

Map of the Mediterranean Sea showing the location of the main rivers flowing into the Mediterranean Sea (FAO GeoNetwork derived from HydroSHEDS), the main deltas and submarine delta deposits (mud banks; Pellegrini et al., 2015), coastal lagoons (Pérez-Ruzafa et al., 2011; and this study), submarine canyons (Harris et al., 2014), submarine volcanoes (EMODnet Geology), mud volcanoes (modified from Mascle et al. (2014), with additional seep-related sites in the Tyrrhenian Sea from Ingrassia et al. (2015) and Casalbore et al. (2020b)) and contourites (Marineregions.org). Tectonic features are based on Faccenna et al. (2014). *AM*: Anaximander Mountains; *AS*: Alboran Sea; *CCC*: Cap de Creus Canyon; *FR*: Florence Rise; *LFC*: La Fonera Canyon; *MR*: Mediterranean Ridge; *SZ*: subduction zone.

slope and large sedimentary deposits formed by riverine input and currents (Fig. 12.1). In the following subchapters, we present some of the main geological processes that are active at present in the Mediterranean Sea and how they can pose a hazard and affect marine ecosystems. The main aim of this chapter is to show that, although many geological processes evolve over long periods of time, spanning millions of years (e.g., the tectonic processes that resulted in the present-day bathymetry of the Mediterranean Sea), other processes can occur at much higher frequency and thus have a direct interaction with physical, chemical, and (micro)biological processes.

12.2 Sedimentary processes from the coast to the deep sea

12.2.1 Coastal environments

Sediment transport and deposition on coastal environments are affected by river runoff, waves, longshore currents and tides (Pratson et al., 2007). The Mediterranean Sea is a microtidal environment with tidal ranges often below 20 cm (Lonzano and Candela, 1995), although it can reach higher values in the northern Adriatic Sea up to 86 cm (Maicu et al., 2018), and tidal currents can be strong in some areas, reaching for instance up to 2 m s^{-1} in the Messina Strait (Bignami and Saluti, 1990; and references therein). Therefore, coastal sedimentary environments in the Mediterranean are in general not strongly affected by tidal currents, and deltas are formed at the fluvial-marine transition instead of estuaries (Figs. 12.1–12.3). In most of the Mediterranean deltas, sediment accumulation is focused on two coeval and

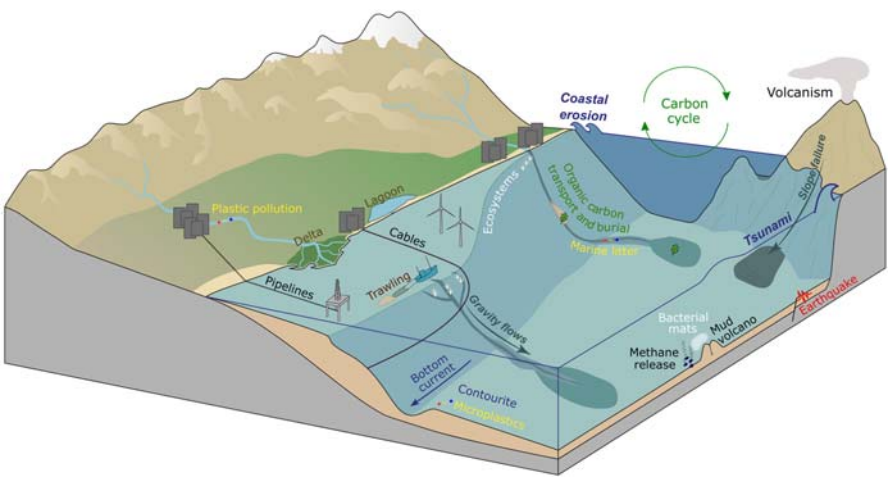

FIGURE 12.2

Schematic representation of the main coastal and marine environments and geological processes and their implications for geohazards and ecosystems.

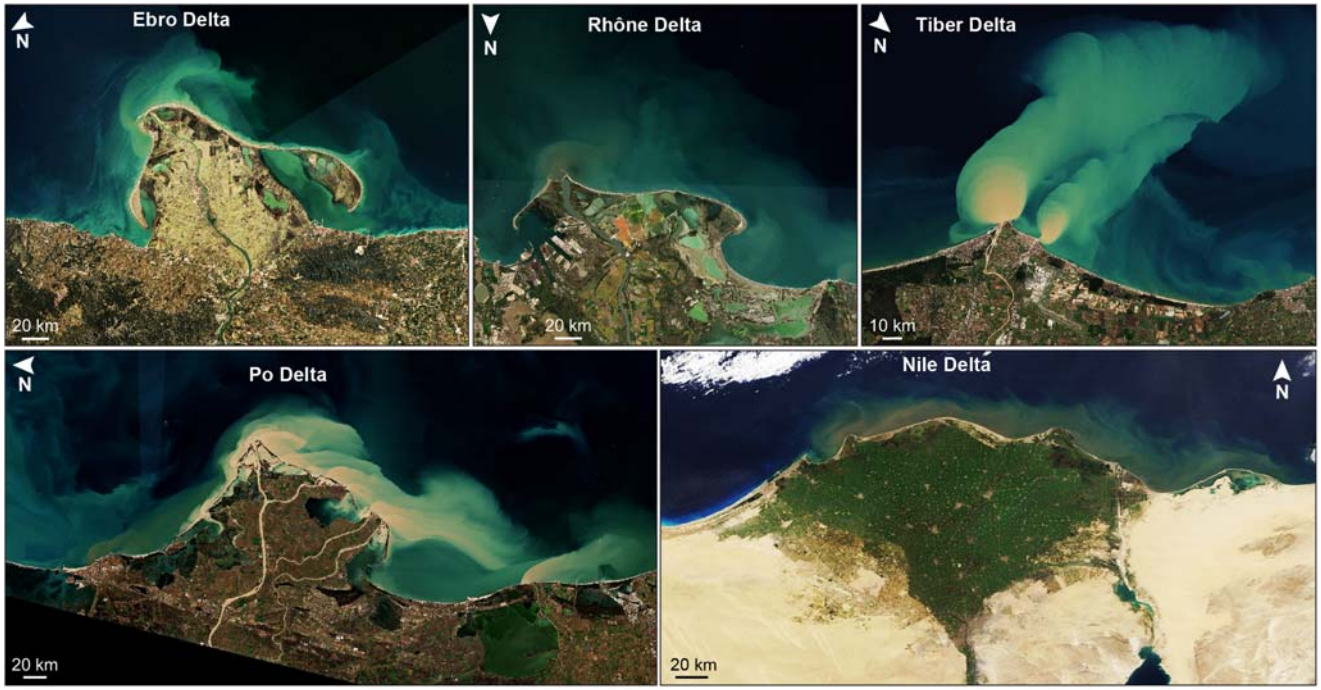

FIGURE 12.3

Satellite images of deltas from the Mediterranean Sea during periods of relative high sediment discharge. The satellite images of the Ebro (February 5, 2020), Rhône (October 4, 2020), Tiber (February 5, 2019), and Po (February 5, 2019) deltas were obtained with Sentinel-2 L2A and processed using the Copernicus Sentinelhub application. The satellite image from the Nile delta (January 18, 2018) was obtained from MODIS Terra using the NASA Worldview application.

laterally continuous sites: the subaerial coastal plain delta and the subaqueous shelf deposits (Hiscott et al., 2002; Cattaneo et al., 2003; Lobo et al., 2006; Fanget et al., 2014; Pellegrini et al., 2016, 2020). The subaerial delta often provides sandy shores, which are strongly shaped by wave action and coastal currents, as suggested by repeated bathymetric surveys at the Po river mouth (e.g., Trincardi et al., 2020). As a result, in plain view, the subaerial delta shows an asymmetrical distribution with main sediment accumulation on the downdrift side compared to the river mouth (Fig. 12.3; Correggiari et al., 2005), determining sand and mud partitioning in the updrift and downdrift of the river mouths, respectively (e.g., Bhattacharya and Giosan, 2003). Besides, subaqueous deltas exhibit thickness distributions that appear strongly asymmetric with respect to their parent deltas, as a function of the interplay between fluvial input and basin hydrodynamics (Korus and Fielding, 2015; and references therein). Because oceanographic processes predominantly redistribute river-borne sediment along the shelf, such clinothems extend continuously for up to hundreds of km along Mediterranean shelves forming lithosomes of 10's of meters thick (yellow polygons in Fig. 12.1). Thus, given the strong longshore currents, the river-borne sediment (especially fine-grained particles) is transported further away from river mouths (Fig. 12.3). Sediment emanates from the mouth of Mediterranean rivers, but on the shelf these contributions are smeared together by waves and currents, making it very difficult to define the sediment provenance.

Besides the main input of large rivers, a significant contribution of river sediments into the Mediterranean Sea is related to short and steep rivers that drain coastal ranges, such as along southern Italy or southern Iberia (Milliman and Syvitski, 1992). Here, small and medium subaqueous deltas formed mainly in relation to the frequent occurrence of flash-flood generated hyperpycnal flows that have a higher density than seawater and thus directly flow downslope, strongly controlling the evolution of these areas (Bárcenas et al., 2015; Casalbore et al., 2011, 2017; Pellegrini et al., 2021).

The circulation also influences the fate of organic particles. Along the shelves, organic matter undergoes physical processes such as transport, deposition, and resuspension several times (Bao et al., 2016; Bianchi et al., 2018; Pellegrini et al., 2021). The resuspension processes are fueled by current-driven mobilization and transport of fine-grained sediments, which become entrained in continuous suspension-deposition loops (Blair and Aller, 2012). Each sedimentary environment along the transit path of organic particles, extending from continental source regions to the eventual sink regions of the marine environment, is characterized by specific balances between import-export exchange fluxes, internal production of new organic-mineral substrates, residence times within local diagenetic conditions (e.g., oxic or anoxic conditions, UV radiation flux), decomposition, and periods of local storage or burial. Overall, these physical processes influence the location and timing of the final deposition and long-term burial of sedimentary organic matter on continental margins governing a fundamental component of the global carbon cycle (Fig. 12.2).

Another important coastal environment in the Mediterranean Sea is lagoons (Fig. 12.1). As a transition environment between land and sea, coastal lagoons comprise organically enriched, relatively enclosed water bodies separated from the sea by narrow barriers with openings allowing limited water exchange (Figs. 12.1 and 12.2). From the geological point of view, natural lagoons are systems where fluvial input is negligible (Boyd et al., 1992). Coastal lagoons can be considered as ephemeral systems that evolve in time into estuaries or open sea, or become infilled (e.g. Boyd et al., 1992; Pellegrini et al., 2017; Campo et al., 2020; Gamberi et al., 2020). Their evolution depends on factors like sea level change, hydrodynamic setting, river sediment supply and preexisting topography (Berné et al., 2007; Ronchi et al., 2018). The Venice Lagoon, located in the northern Adriatic Sea, is the largest lagoon in the Mediterranean region, with a total surface of 550 km^2 (390 km^2 of open lagoon including 40 km^2 of tidal channels, 70 km^2 of salt marshes, and 90 km^2 of fish farms, Madricardo et al., 2019). The Venice Lagoon is characterized by a maze of channels (maximum depth exceeding 15 m), which cut across a large area of shallow waters (average depth of 1 m), fens and salt marshes, and is connected to the Adriatic Sea by three inlets (Fig. 12.4; Madricardo et al., 2017).

FIGURE 12.4

Satellite images of the Venice lagoon (November 24, 2021, obtained with Sentinel-2 L2A and processed using the Copernicus Sentinelhub application) and zoomed-in inset of the city of Venice showing the multibeam bathymetry of the channels (courtesy of Fantina Madricardo).

The water depth of coastal lagoons in the Mediterranean is generally very shallow, in some cases not exceeding 1 m water depth (e.g., Palavasian lagoonal complex, west of the Rhône delta, Gulf of Lion; Sabatier et al., 2010). In other cases, they can be much deeper, for example, maximum depths in the Faro Lagoon (Sicily) can reach up to 30 m (Cosentino and Giacobbe, 2011) and up to 42 m in the Taranto Sea (Ionian Sea; Pastore, 1993).

Some lagoons are hypersaline due to the limited fresh water input and the excess of evaporation. This is the case of the Mar Menor, located in SE Spain, that has a mean depth of 4.4 m and maximum of about 7 m, and is connected with the sea through three inlets. More than 20 ephemeral watercourses flow into Mar Menor, mostly in its southern part. The mean annual rainfall is less than 300 mm yr^{-1} and potential evapotranspiration is close to 900 mm yr^{-1} (García-Pintado et al., 2007). In contrast, other lagoons are composed of brackish waters, such as the Ganzirri and Faro lagoons in Cape Peloro (Sicily, Italy) or the Varano lagoon in the Gargano Promontory (SE Italy) (Spagnoli et al., 2002; Cosentino and Giacobbe, 2011).

12.2.2 Deep-water environments

12.2.2.1 Submarine landslides

Sediment accumulated on the seafloor can become unstable and form submarine landslides even in zones of very gentle slopes (<1 degree) (Field et al., 1982). Slope instability occurs when the applied shear stresses are higher than the shear strength of the sediment. This balance can be affected by earthquakes, presence of gas in the sediment, tectonic movements, differences in sediment properties, and presence of weak sediment layers, among other factors (Huhn et al., 2019). Mass-wasting processes can affect large areas, for instance in the Mediterranean Sea deposits of submarine landslides can have volumes of more than 1000 km^3. Such large events are however infrequent with recurrencies around 40,000 years (Urgeles et al., 2013). Small events are much more frequent and can also pose a hazard for human activities (Sultan et al., 2020; Casalbore et al., 2012).

In 1979, a submarine landslide occurred offshore Nice (southern France). Despite having mobilized a relatively small volume of sediment evacuated from the slope ($8.7 \cdot 10^6$ m^3) compared to other submarine landslides, this event had catastrophic human and economic consequences. The submarine landslide affected part of the extension of the airport of Nice and generated a 2–3 m high tsunami wave (Dan et al., 2007; and references therein). The main factors that control slope instability in this area are groundwater charging, the presence of weak sedimentary layers and liquefiable sediments, high sedimentation rates, anthropogenic activities (e.g., coastal infrastructure) and natural oversteepening (Sultan et al., 2020; and references therein). Time series of multibeam bathymetry of the continental shelf and upper slope offshore Nice showed that landslide scars with volumes of more than 25,000 m^3 are very frequent (<7 years) (Kelner et al., 2016). Mass-wasting processes can thus have a profound and recurrent impact on the seafloor topography.

Submarine landslides are also very common on the flanks of submarine and insular volcanoes (Fig. 12.2). The characteristics and processes controlling these slope failures are explained more in detail in the next Section 12.3.

12.2.2.2 Turbidity currents

Submarine canyons are geological structures that commonly incise continental slopes and act as main conduits of sediment and particle transport from the continent to the deep sea (Figs. 12.1 and 12.2). The main processes responsible for the downslope transfer of sediment are turbidity currents that are gravity-driven flows in which sediment suspension is supported by turbulence. They are capable of transporting and depositing large volumes of sediment. For instance, the amount of sediment carried by a single turbidity current can be over 10 times the annual sediment flux of all the rivers in the world (Talling et al., 2007). Together with sediments, turbidity currents can also transport organic matter (Galy et al., 2007), nutrients (Khripounoff et al., 2012) and microplastics (Kane and Clare, 2019) to deep-marine environments, and they thus play an important role in global carbon cycling and in the development of deep-sea ecosystems. Turbidite systems have often been used as archives for paleoclimatic (Bonneau et al., 2014) and paleoseismological reconstructions (Ratzov et al., 2015). Moreover, turbidity currents are very energetic processes that can reach velocities of several meters per second (Clarke, 2016) and pose a hazard for key submarine infrastructures (e.g., submarine communication cables; Fig. 12.2; Carter et al., 2014).

Some submarine canyons are restricted to the slope and do not reach the coast, such as in the Gulf of Lion (Fig. 12.1). These systems were mainly active during sea-level low-stands, when the shoreline was close to the canyon head, but are at present inactive (see Chapter 2 for more detail). In contrast, in other zones of the Mediterranean Sea, turbidity currents are also formed at present. The Ligurian margin (NW Mediterranean Sea) is characterized by a steep slope, with a very narrow or almost absent continental shelf (Fig. 12.1). Some of the submarine canyons in this area are directly connected to the coast, thus favoring the sediment transfer from the continent to the deep sea (Fig. 12.2). In the Var Canyon, offshore Nice, turbidity currents have been observed with frequencies of one−three per year. The observed turbidity currents lasted 2−5 h, reached peak velocities at the head of the current of more than 85 cm s^{-1} and heights of over 100 m (Fig. 12.5; Khripounoff et al., 2012). Some of the observed turbidity currents were triggered by floods in the Var River, when the river discharge was $\geq$600 m^3 s^{-1} (Khripounoff et al., 2012). When the river discharge is denser than the ambient seawater, it plunges and forms hyperpycnal flows. These flows are relatively thick (over 100 m high) and dilute (0.5−1 g L^{-1}), with peak velocities of 40 cm s^{-1}. Gravity flows can also be formed by slope failure (Talling et al., 2007; Talling, 2014). In these cases, the flows are usually faster (over 85 cm s^{-1}), have higher sediment concentration and can transport sediment further downslope in the system (Mas et al., 2010; Khripounoff et al., 2012). In all the cases, turbidity currents are characterized by a head with higher

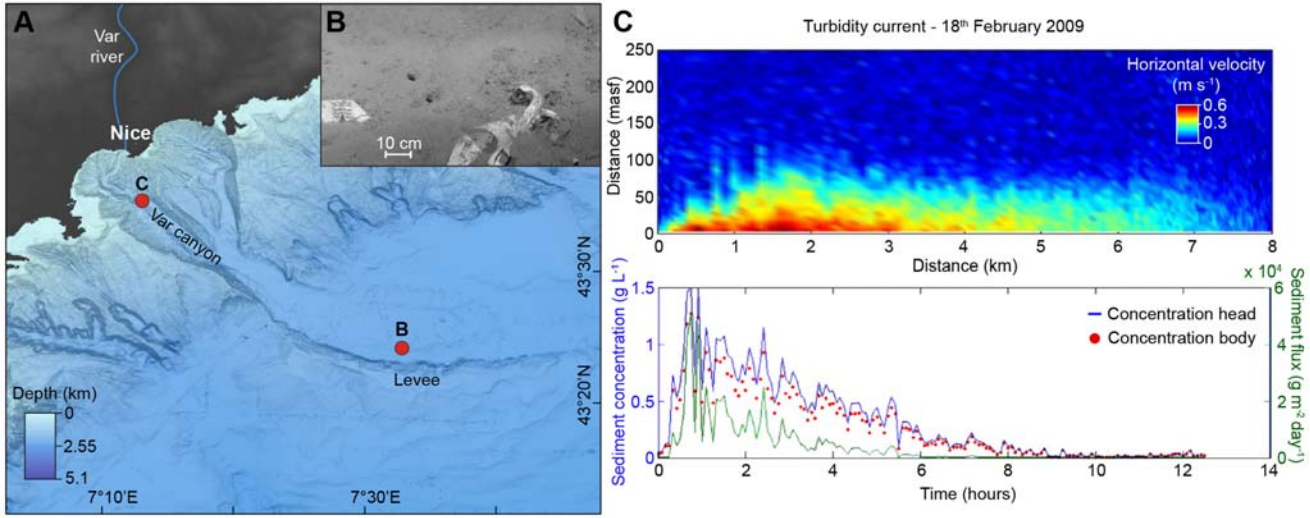

FIGURE 12.5

(A) Bathymetric map of the Var canyon and related turbidite system. (B) Plastic litter at the bottom of the Var canyon at 2200 m depth. (C) Horizontal velocity of a turbidity current measured at 1280 m depth in the Var canyon and estimated sediment concentration and sediment flux.

Modified from (A, C) Khripounoff, A., Crassous, P., Bue, N.L., Dennielou, B., Jacinto, R.S., 2012. Different types of sediment gravity flows detected in the Var submarine canyon (northwestern Mediterranean Sea). Prog. Oceanogr. 106, 138–153. (B) Khripounoff, A., Vangriesheim, A., Crassous, P., Etoubleau, J., 2009. High frequency of sediment gravity flow events in the Var submarine canyon (Mediterranean Sea). Mar. Geol. 263 (1–4), 1–6.

velocity and sediment concentration, followed by a body in which the velocity and the sediment concentration decrease (Fig. 12.5; Khripounoff et al., 2012).

Turbidity currents in the Mediterranean Sea are not only triggered by natural processes, but also by anthropogenic activities. Bottom trawling is a commercial fishing technique that drags heavy fishing gear at the seafloor, strongly affecting benthic ecosystems and seafloor sediments. Trawling makes the seafloor smoother over time, resuspends large amounts of sediment, and triggers turbidity currents (Fig. 12.2; Puig et al., 2012). Moreover, trawling alters the biogeochemical properties of sediments. For instance, the seafloor affected by bottom trawling contains coarser reworked sediments with less organic carbon (Paradis et al., 2021). Trawl-induced turbidity currents were repeatedly observed in La Fonera canyon (NW Mediterranean Sea; Fig. 12.1) during typical working hours and days. These flows are at least 100 thick and reach sediment concentrations up to 236 mg L^{-1} at 5 m above the seafloor (Martín et al., 2014).

12.2.2.3 Near seafloor currents and contourites

Currents flowing near the seafloor (i.e., bottom currents) control sedimentation in many areas of the Mediterranean Sea, generating sedimentary features known as contourites (Fig. 12.2). Contourites were first recognized in the continental rise of the Atlantic Ocean and were considered to be formed by deep geostrophic currents flowing along the bathymetric contours (Heezen et al., 1966). Subsequent studies showed that contourites can actually be found at any depth in the ocean, and even in lakes, and are formed by a wide variety of oceanographic processes that include geostrophic currents, wind-driven currents, dense-shelf water cascading, mesoscale and submesoscale eddies, baroclinic and barotropic tides, and internal waves (Rebesco et al., 2014). All these processes can be in some areas strong enough to generate erosional features such as contourite channels, moats, furrows and scours. The sediment bodies formed by bottom currents are known as contourite drifts (Rebesco et al., 2014).

Contourites can be found in all basins of the Mediterranean Sea, but they are particularly abundant in the Alboran Sea (Fig. 12.1). Contourites related to geostrophic currents are usually elongated sediment bodies parallel to the slope with a mounded morphology that are related to an incision (i.e., moat or contourite channel), where more intense bottom currents are focused (Fig. 12.6A and B; Miramontes et al., 2021). The location and extension of these deposits are strongly controlled by the preexistent topography that induces local changes in the circulation near the seafloor. In the Mediterranean Sea, contourites are commonly related to promontories, islands, seamounts, channels and straits (e.g., Martorelli et al., 2010; Ercilla et al., 2016; Miramontes et al., 2016, 2019; Pellegrini et al., 2016; Rovere et al., 2019; Gauchery et al., 2021a,b). Over the last decades, contourite deposits have increasingly been identified in more shallow-water settings of the Mediterranean Sea, from the base of the slope to the outer shelf: the outer shelf off southwestern Mallorca (Vandorpe et al., 2011), the Corsica Trough (Roveri, 2002; Miramontes et al., 2016), the Sicily Channel (Marani et al., 1993; Verdicchio and

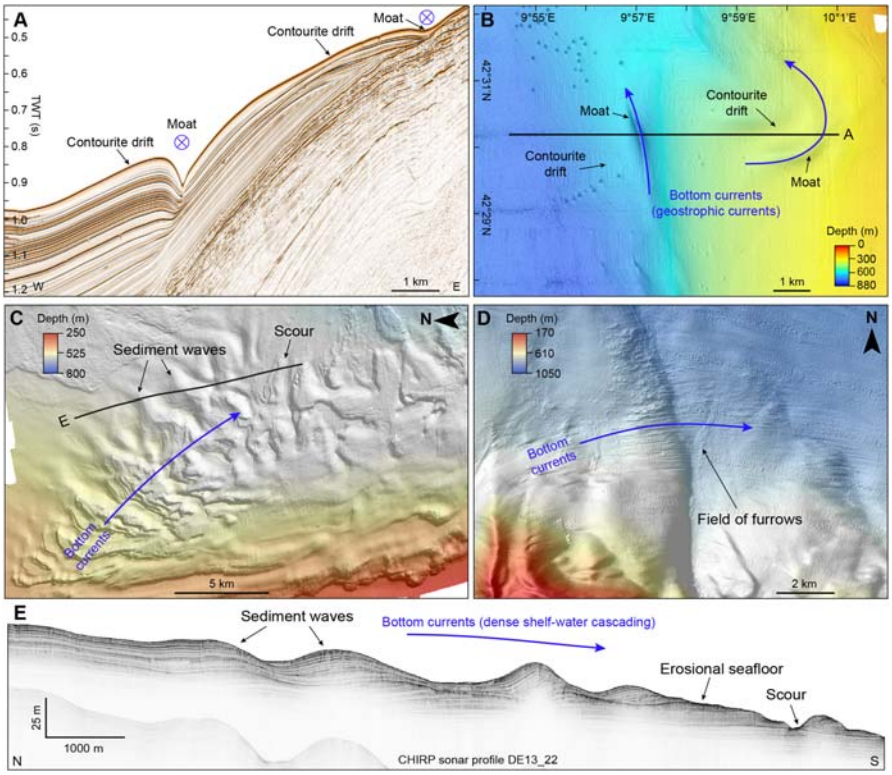

FIGURE 12.6

(A) Multichannel high-resolution seismic reflection profile and (B) multibeam bathymetry showing contourites in the northern Tyrrhenian Sea formed by currents related to the Levantine Intermediate Water. Multibeam bathymetry showing the presence of sediment waves, scours (C), and furrows (D) formed by the interaction of dense-shelf water cascading with the seafloor in the Adriatic Sea. (E) Subbottom profiler image showing the internal architecture of the sediment waves and scours shown in (C).

Modified from (A, B) Miramontes, E., Cattaneo, A., Jouet, G., Thereau, E., Thomas, Y., Rovere, M., Cauquil, E., Trincardi, F., 2016. The Pianosa contourite depositional system (northern Tyrrhenian Sea): drift morphology and Plio-Quaternary stratigraphic evolution. Mar. Geol. 378, 20–42. (C, D, E) Foglini, F., Campiani, E., Trincardi, F., 2016. The reshaping of the South West Adriatic Margin by cascading of dense shelf waters. Mar. Geol. 375, 64–81.

Trincardi, 2008; Martorelli et al., 2011; Gauchery et al., 2021a), the Capo Vaticano slope (Martorelli et al., 2016), and the south-western Adriatic margin (Verdicchio and Trincardi, 2008; Pellegrini et al., 2016). Viana et al. (1998) introduced the term "shallow-water" contourite to describe shelf bottom-current deposits (water depths of 50–300 m) in contexts where the impact of waves and tides is negligible compared to a dominant contour-parallel geostrophic circulation, such as on the

southern Adriatic outer shelf (Rovere et al., 2019) and the Sicilian shelf (Gauchery et al., 2021b). The size of the contourites in the Mediterranean Sea is very variable, they can be only a few km wide and long, and be restricted to local topographic changes (e.g., Martorelli et al., 2010), or they can extend along hundreds of km and be the dominant sedimentary deposit along the whole continental slope, such as in the Alboran Sea (Ercilla et al., 2016) (Fig. 12.1).

Internal waves have also been suggested to play a relevant role in shaping the seafloor of the Mediterranean Sea. Some continental slopes are covered by sediment waves that are mainly composed of mud and migrate upslope with crests parallel to the slope, as observed in the Gulf of Valencia (Western Mediterranean Sea; Ribó et al., 2016) and along the Israeli continental slope (Eastern Mediterranean Sea; Reiche et al., 2018). These authors suggest that the reflection and breaking of near-inertial waves and semidiurnal internal tides on the slope are responsible for the formation of sediment waves. The interaction of barotropic tidal currents with sills at straits (for instance in the Strait of Gibraltar and in the Strait of Messina) forms internal solitary waves at the interface between intermediate and surface waters that can also control sedimentation. In the Alboran Sea, internal solitary waves breaking on the slope have been suggested to favor erosion on the upper continental slope, forming relatively flat surfaces, known as contourite terraces (Ercilla et al., 2016). Internal solitary waves traveling northwards from the Messina Strait are refracted by the seafloor topography and suggested to form a field of asymmetric sand dunes (Droghei et al., 2016).

12.2.2.4 Sedimentation related to dense-shelf water cascading and open-ocean convection

The formation of dense shelf water has been observed at three main sites of the Mediterranean Sea: the Gulf of Lion, the Northern Adriatic Sea and the Northern Aegean Sea (Canals et al., 2009; Chiggiato et al., 2016). These dense waters are formed due to winter cooling and evaporation induced by northerly winds (see Chapter 7 for more details about the physical processes). Other factors favoring the formation of dense shelf water are low river discharges and lateral advection of salinity (Canals et al., 2009; Chiggiato et al., 2016). Once the density threshold is reached, usually during late winter-early spring, the dense shelf waters start sinking and cascade down the slope until they reach hydrostatic equilibrium (Canals et al., 2009). The pathways of cascading dense shelf waters are strongly affected by the seafloor topography. Dense waters formed in the northern part of the Adriatic Sea move southwards along the shelf and the slope, and when they are dense enough, they fill a depression (Jabuka Pit) at 270 m depth (Langone et al., 2016). Submarine canyons are also very important conduits for cascading. In the Adriatic Sea, dense shelf water flux was higher inside the Bari Canyon than in the adjacent slope (Turchetto et al., 2007). In the Gulf of Lion, cascading is in part also focused inside canyons. Cascading events resuspend and transport sediment and associated particles (e.g., organic matter) down-canyon and along the midslope of the western Gulf of Lion (Fig. 12.7; Canals et al., 2009; Palanques et al., 2012). Deep cascading events could

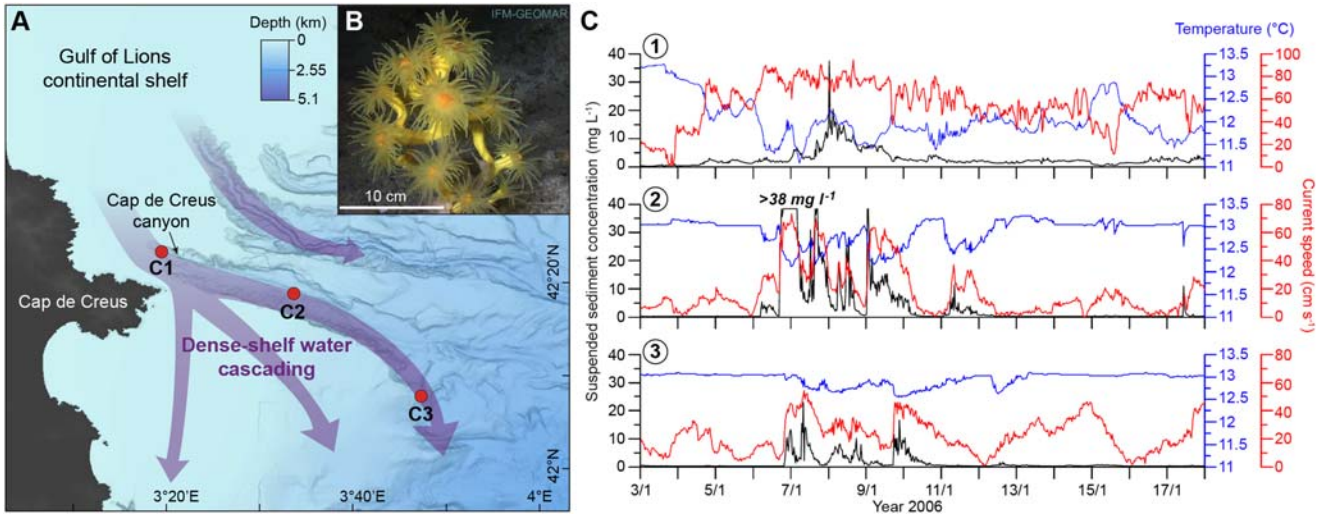

FIGURE 12.7

(A) Bathymetric map of the NW Gulf of Lion showing the main paths of dense-shelf water cascading. (B) Underwater image of a cold water coral (*Dendrophyllia cornigera*) from the Cap de Creus canyon. (C) Time series of temperature, current speed and suspended sediment concentration measured near the seafloor at three mooring sites in the Cap de Creus canyon during a dense shelf water cascading event in January 2006 characterized by a decrease in temperature and an increase in current speed and suspended sediment concentration.

Modified from (B) Lo Iacono, C., Robert, K., Gonzalez-Villanueva, R., Gori, A., Gili, J. M., Orejas, C., 2018. Predicting cold-water coral distribution in the Cap de Creus Canyon (NW Mediterranean): implications for marine conservation planning. Prog. Oceanogr. 169, 169–180. (C) Palanques, A., Puig, P., Durrieu de Madron, X., Sanchez-Vidal, A., Pasqual, C., Martín, J., Calafat, A., Heussner, S., Canals, M., 2012. Sediment transport to the deep canyons and open-slope of the western Gulf of Lions during the 2006 intense cascading and open-sea convection period. Prog. Oceanogr. 106, 1–15.

have been identified in moorings inside and in the vicinity of the Cap de Creus Canyon by a decrease in temperature, an increase in suspended particle concentration and in current speed near the seafloor that reached 95 cm s^{-1} in the upper part of the canyon and 54 cm s^{-1} at 1000 m water depth in the open slope near the canyon (Fig. 12.7; Palanques et al., 2012). In the Gulf of Lion, open-ocean convection occurs by winter heat loss due to strong northern winds, favored by a general circulation with a cyclonic gyre that traps the water in the middle of the basin (Durrieu de Madron et al., 2017). This process is also very important in the resuspension of sediment and formation of large nepheloid layers that reached a thickness of up to 2000 m in the center of the convection zone (Durrieu de Madron et al., 2017).

Even though single cascading events are restricted in time, their recurrency and high intensity induce important changes in the seafloor morphology that can be observed in all the zones affected by this process. Erosional features such as furrows and scours can be often observed in the zones affected by cascading. Furrows are elongated erosional features that are parallel to the flow. In the Adriatic Sea, they have been observed in the open slope (Fig. 12.6; Foglini et al., 2016), while in the Gulf of Lion they are found inside the Cap de Creus Canyon (Lastras et al., 2007). Deep shelf waters in the southwestern part of the Gulf of Lion also generate an erosional channel in the outer part of the shelf (Ribó et al., 2018). When dense shelf waters interact with seafloor escarpments, they often generate incisions dominated by erosion and non-deposition (moats) and associated sediment deposits that are parallel to the slope (contourite drifts). These features have been observed in the Adriatic Sea related to the Dauno Seamount (Pellegrini et al., 2016) and in the southwest Aegean Sea related to the complex seafloor topography between the islands (Bellacicco et al., 2016). The interaction of cascading waters with the seafloor also results in the formation of sediment waves that are mainly composed of mud. They have crests perpendicular to the slope and migrate upstream of the current, and thus in these settings upslope (Fig. 12.6; Foglini et al., 2016; Ribó et al., 2018; Rovere et al., 2019).

12.3 Submarine and insular volcanoes

Submarine and insular volcanoes are commonly characterized by a complex and rapid morphological evolution, resulting from the interplay between volcanism, tectonic, erosive-depositional (also modulated by sea-level fluctuations), and gravity instability processes (e.g., Ramalho et al., 2013; Casalbore, 2018). A large suite of geomorphic features associated with erosive and gravity instability processes commonly dominate the submarine flanks of active volcanic edifices, covering up to 80% of the entire area, as for instance observed in the Aeolian Archipelago (Chiocci and Casalbore, 2017). Because of their rapid growth, volcanic edifices may become unstable and experience failure at any spatial scale, from minor rock falls with volumes of few tens of cubic meters up to catastrophic collapses mobilizing volumes up to thousands of cubic km (Mcguire, 2006). The size of such events

is generally correlated with their recurrence time, ranging from days/months for small rock falls up to hundreds of thousands of years for large events, able to mobilize the entire flank of the edifice. Several preconditioning and triggering factors are responsible for such processes, including unstable volcanic foundation, thermal alteration, dyke intrusion, edifice pore pressure, oversteepening, overloading, vertical movements, unbuttressed flanks, buried faults, earthquakes, and sea-level fluctuations (e.g., Keating and McGuire, 2000; de Vries and Davies, 2015). The largest failure events commonly occur in oceanic islands, such as Hawaiian and Canary Islands (Mitchell et al., 2002 and reference therein), whereas relatively smaller events, with volumes of few or tens of km^3, characterize arc-volcanic settings (Boudon et al., 2007; Coombs et al., 2007).

In the Mediterranean Sea, evidence of large-scale flank collapses has been mainly reported from the Hellenic Arc and active Italian volcanoes. Regarding the first area, submarine studies have revealed a number of volcanic debris avalanche deposits on the external flanks of Antimilos, Santorini and Nisyros volcanoes in the South Aegean Sea (Nomikou et al., 2014). One of the best examples is represented by the 1 km^3 debris avalanche deposit recognized along the south-eastern flank of the Nisyros volcano, and tentatively dated to about 35 ka (Tibaldi et al., 2008).

Regarding the Italian volcanoes, large-scale flank collapses and associated debris avalanches are reported all around Ischia Island (de Alteriis and Violante, 2009), affecting the oversteepened and faulted flanks of Mount Epomeo resurgent block (Buchner, 1986; Della Seta et al., 2012). Among these events, the largest debris avalanche with a mobilized volume of several km^3 of material was recognized along the southern flank of Ischia. The deposit is mostly formed by thousands of giant blocks dispersed over an area of 50 km far from the island (Chiocci and de Alteriis, 2006). The event was dated between 3 and 2.4 ka BP and historically linked to the description of a sudden collapse of a sector of the Ischia Island and associated tsunami waves reported by the Greek writer Strabo in his Geographica (de Alteriis et al., 2010).

Seismic evidence of large-scale instabilities at the Somma-Vesuvio volcano was inferred by Milia et al. (2012; and references therein), with two possible debris avalanches of approximately 3 and 1 km^3 emplaced close to the 22 ka BP Basal Pumice Plinian eruption and the 4.2 ka BP Avellino eruption, respectively (Santacroce et al., 2008).

Repeated flank collapses with volume of approximately 1 km^3 for a single event have been reported along the flanks of Stromboli Volcano through the integration of subaerial and submarine morpho-structural studies (Kokelaar and Romagnoli, 1995; Tibaldi, 2001; Romagnoli et al., 2009). Specifically, the NW flank of Stromboli was affected by multiple collapses in the last 13 ka, the last of them likely occurred during medieval times, forming the Sciara del Fuoco (SdF, hereafter) collapse scar (Fig. 12.8A; Francalanci et al., 2013). Geoarchaeological evidence of Middle-Age tsunamis at Stromboli has been recently reported by Rosi et al. (2019) and tentatively associated with the occurrence of this collapse event. Nowadays, the Sciara

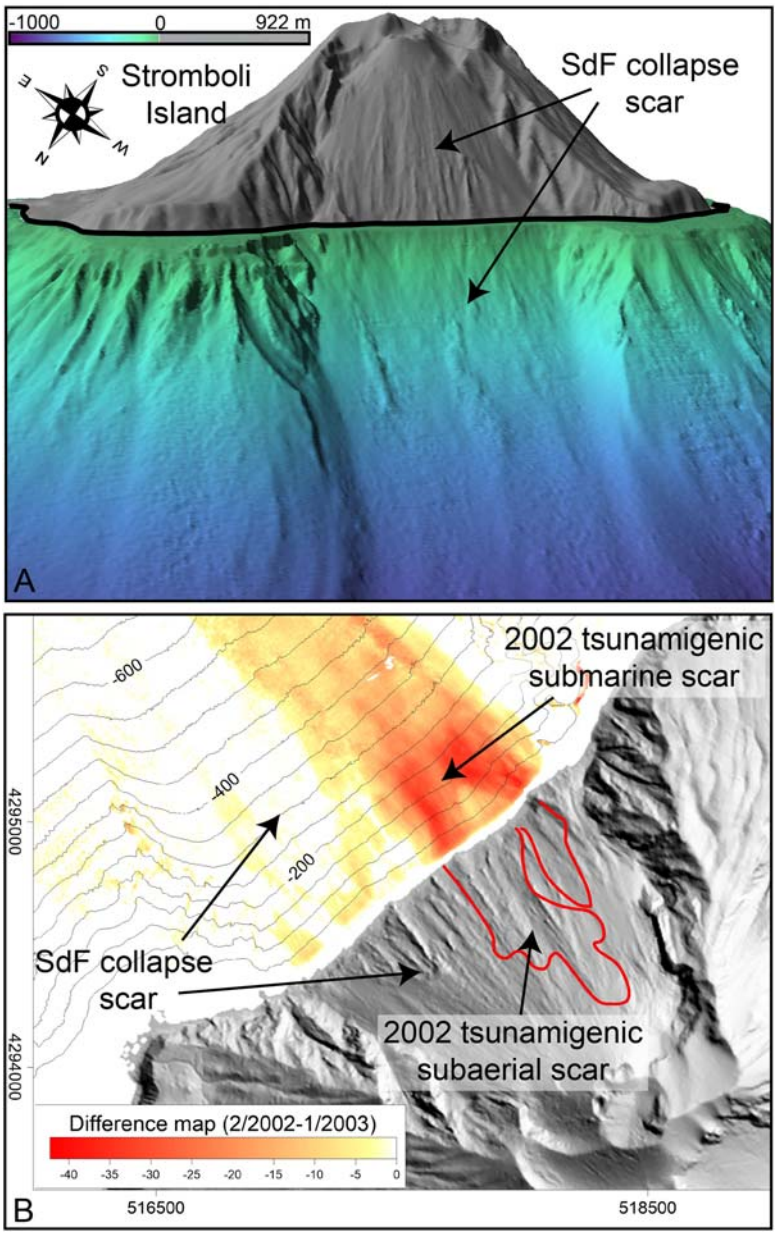

FIGURE 12.8

(A) Perspective image of the Sciara del Fuoco (SdF) collapse scar at Stromboli (for the spatial scale refer to the plan-view of the SdF in Fig. 12.6B). (B) Difference map obtained through the comparison of the pre- and post-30 December 2002 landslide bathymetries at Stromboli, showing the mobilized material during the failure event. The red line draped over the shaded relief of Stromboli Island shows the outline of the tsunamigenic landslide scar affecting the SdF subaerial slope 7 min after the submarine landslide.

del Fuoco collapse scar acts as a preferential conduit for the transport of a large amount of volcanic material produced by persistent Strombolian activity alternated to larger paroxysms and rare effusive eruptions (Barberi et al., 1993). This rapid volcaniclastic infilling coupled with the steepness of the Sciara del Fuoco scar collapse (Fig. 12.8A) are considered responsible for the generation at human timescales (from annual to decennial) of repeated small- and medium-scale submarine landslides (Maramai et al., 2005; Casalbore et al., 2020b). Larger landslide events are able to mobilize volumes up to few tens of millions of cubic meters as reconstructed for the 2002 tsunamigenic landslide occurred at Stromboli in 2002 through a difference map generated by repeated multibeam surveys (Fig. 12.8B; Chiocci et al., 2008). This event generated tsunami waves with maximum run-up values of 10 m around Stromboli coastline, when the island was uninhabited (Tinti et al., 2005).

Another indirect evidence of recent mass-wasting processes affecting the submarine flanks of active insular volcanoes is testified by recognition of crescent-shaped bedforms, interpreted as upper-flow regime bedforms associated with the passage of turbidity currents (e.g., Babonneau et al., 2013). In the Mediterranean Sea, bedforms at different spatial scales (wavelength from tens of meters up to some kilometers) are widespread along most of the Aeolian volcanoes (Casalbore et al., 2014a), as well as around the Santorini caldera in Greece (Bell, 2011). The size of these bedforms is likely related to the magnitude of the flows that formed them, with larger bedforms associated with large-scale flanks or caldera collapses. Differently, small-scale bedforms are recording low magnitude but higher frequency events, as testified by repeated multibeam surveys that evidenced the upslope migration and/or the new formation coaxial trains of these bedforms (Casalbore et al., 2021). It is noteworthy that mass-wasting features and associated bedforms can affect the morphological evolution of insular and submarine volcanoes, even once the volcanic activity ends, as, for instance, observed along the flanks of Ventotene volcano (Casalbore et al., 2016).

Submarine eruptions are commonly unnoticed unless the emitted volcanic materials are able to reach the sea surface (e.g., Ercilla et al., 2021; and reference therein) or generate damages to offshore infrastructures (e.g., Favali et al., 2006). Alternatively, the recognition of submarine eruptions, especially in deep water, is possible only if repeated multibeam surveys and/or hydroacoustic monitoring are performed (e.g., Tepp et al., 2019). Sea water influences eruptions both, indirectly through its hydrostatic pressure by reducing the exsolution and expansion of magmatic volatiles, and directly by thermo-mechanical exchanges between magma and water (e.g., White et al., 2015a,b). Submarine eruptions can be generally grouped in three main categories according to different water depths:

Shallow-water eruptions (<200 m water depth) are commonly characterized by violent explosions, especially when they approach the water−air interface, as for the first time reported at Surtsey in 1963 (Kokelaar, 1986). In the Mediterranean Sea, an example of this kind of eruption occurred in 1650 AD on the summit of Kolumbo submarine volcano (Cantner et al., 2014). This eruption included a first degassing-driven submarine activity manifested as discolored water, followed by intermittent

jets of gas and ash breaching the sea surface from a white ledge. Finally, a small islet was created, with phreatomagmatic activity becoming dominant. This eruption also generated tsunami waves that impacted the east coast of Santorini, with extensive flooding and loss of buildings (Nomikou et al., 2014). Although different mechanisms can be potentially at the origin of this tsunami, the most probable cause has been related to an underwater explosion at water depths between 20 and 150 m (Ulvrova et al., 2016).

Intermediate-water eruption (approximately 300−600 m water depth) are rarely observed, but they can be characterized by a peculiar eruptive style characterized by floating lava balloons or pumice rafting on sea surface, as recently occurred off Terceira Island (Azores) in 1998−2001 (Casas et al., 2018 and reference therein) and El Hierro Island (Canary Islands) in 2011 (Somoza et al., 2017). In the Mediterranean Sea, a similar eruption occurred 5 km off the coast of Pantelleria island (Sicily Channel) in 1891. The eruption was firstly noticed by fishermen for the presence of lava balloons floating on the sea surface and described by Foerstner (1891), Riccò (1892) and Washington (1909). Recent marine studies have identified the small submarine cone responsible for the eruption, whose top is located at around 260 m water depth (Conte et al., 2014; Kelly et al., 2014). Moreover, these submarine studies identified in this area a newly discovered and large submarine volcanic field between 200 and 700 m water depth, made up by several fresh-looking volcanic cones.

Deep-water eruptions are mostly characterized by effusive eruptions, even if this eruptive style can occur at all water depths. Examples of fresh-looking hummocky morphologies associated with submarine eruption of pillow lavas were observed both along the lower flank of Stromboli Volcano (Di Roberto et al., 2008) and shallow-water sectors encompassed between the eastern flanks of Lipari and Vulcano islands in the Aeolian Archipelago (Gamberi, 2001).

Besides eruptive events, hydrothermal activity often characterizes the evolution of insular and submarine volcanoes, altering the surrounding rocks and leading to the development of weak layers that can be used as failure planes by landsliding events. Moreover, these areas are commonly associated with abundant mineralization phenomena and development of peculiar microbial communities and seafloor habitats, as for instance observed along the Aeolian volcanic arc (e.g., Gamberi et al., 1997; Maugeri et al., 2010). In some cases, these events can be a threat for the navigation, as observed during the strong degassing activity occurred offshore the eastern part of Panarea Island in 2002−03, with the generation of large plumes of suspended sediments able to reach the sea surface (Esposito et al., 2006). Underwater surveys performed in this area through scuba dives observed a large exhalative field characterized by 21 main active gas vents and craters, with diameters ranging from meters to tens of meters in diameter. Successive marine geomorphological studies depicted the presence of several craters with diameters ranging from five to over 100 m northwards from the main 2002−03 degassing area (Moneke et al., 2012). This allowed estimating for the Panarea geothermal system a total release of over 70 Mt of CO_2 over 10 ka, suggesting that CO_2 venting at submarine arc volcanoes can significantly contribute to the global atmospheric budget of this

greenhouse gas. These large fluid emissions can also severely impact the surrounding environment, by inducing a strong acidification of seawater which results in the subsequent loss of habitats around the eruption. For example, during the eruption of the submarine Tagoro volcanic cones off El Hierro in 2011, the pH dropped to 5, and the partial pressure of dissolved carbon dioxide increased almost 1000 times (Ercilla et al., 2021; and references therein).

In coastal and insular volcanoes, onland effusive eruptions can extend into the sea, forming lava deltas, whose submarine morphological evolution has been recently monitored through the integration of repeated bathymetric surveys and visual inspections at Stromboli in 2007 and 2014 (Bosman et al., 2014; Casalbore et al., 2021). In other cases, subaerial lava flows were able to extent into the sea as a coherent and thick body for several km down to 800–900 m water depth, as in the case of the 1220 AD Rocche Rosse obsidian-rich lava coulees at Lipari (Forni et al., 2013; Casalbore et al., 2016). Similarly, large subaerial explosive eruption on coastal and insular volcanoes can form pyroclastic flows able to reach the sea, as recently observed during two strong paroxysms occurred at Stromboli in the summer of 2019, causing both significant submarine erosion/landslide and small tsunamis with amplitude of1.5 m (Giordano and De Astis, 2021; Di Traglia, 2022). Dense and fast pyroclastic flows were also considered responsible for the tsunami waves that killed a fisherman during the 1930 eruptive crisis at Stromboli (Maramai et al., 2005). In the Gulf of Naples, a large submarine fan, with an approximately volume of $3 \cdot 10^8$ m^3 has been interpreted as the result of the entry into the sea of pyroclastic density currents occurred during the worldwide famous 79 CE eruption (Milia et al., 2012). During historical time, large explosive eruptions represented a main geohazard for coastal communities in the Mediterranean region, being able to alter social evolution, as testified by the large Minoan eruption of Santorini dated around 1600 BCE (Friedrich, 2013). This eruption produced 78–86 km^3 dense-rock equivalent of volcaniclastic material (Johnston et al., 2014), burying flourishing Bronze Age settlements. It also generated significant tsunami waves, whose deposits were found throughout the Mediterranean basin (Minoura et al., 2000; Goodman-Tchernov et al., 2009).

During explosive eruptions, large amount of volcanic ash can be injected into the atmosphere and deposited as tephras and cryptotephras (i.e., distal layers that have no visible expression and may only be composed of glass shards) in marine basins by winds and oceanic currents. Considering the high number of volcanoes in the Mediterranean Sea and their frequent explosive nature, tephro-stratigraphy studies from marine cores have provided an impressive knowledge on their eruption frequency and geochemical evolution (Siani et al., 2004; Tamburrino et al., 2016; Abbot et al., 2020). Moreover, the study of marine tephras has significant implications for paleo-climatic and paleo-oceanographic reconstructions (Ikehara et al., 2015; Davies, 2015), providing useful insights for correlating marine, continental and cryospheric records (e.g., Newnham et al., 2003; Zanchetta et al., 2011).

12.4 Cold seeps: diversity, distribution and controls

12.4.1 Key-points on submarine cold seeps

In addition to those related to volcanic activity, two main types of fluid are expelled from the seafloor of continental margins: Aquifer groundwater (Micallef et al., 2020) and so-called cold fluids (Judd and Hovland, 2007). Submarine cold seeps are the manifestations of upward migration of overpressured fluids at the seabed from underlying sedimentary strata (Talukder, 2012). The term "cold" refers to fluids that are emitted at the seafloor at low temperatures (generally not exceeding a few tens of °C) compared to warm hydrothermal fluids (200−400°C). Cold seep zones range from shallow water areas (e.g., mud volcano offshore Scoglio d'Africa in the north Tyrrhenian Sea, Casalbore et al., 2020a; pockmark field offshore Israel, Schattner et al., 2012) to the deep sea (e.g., Menes mud volcanoes in the Nile deep-sea fan, Dupré et al., 2014; Milano mud volcano along the Central Mediterranean Ridge, Huguen et al., 2005). The majority of emitted fluids corresponds to gaseous methane, either in the form of gas bubbles or dissolved gas. The methane origin is of either microbial (also called biogenic) or thermogenic, both involve the degradation of organic matter (Whiticar, 1999). Cold seeps occur worldwide in a wide variety of tectonic contexts (both onshore and offshore). It is the case in the Mediterranean Sea where cold seeps are located at both passive and active continental margins, notably along accretionary wedges (Mediterranean Ridge, Calabrian Arc), and in thick sedimentary basin areas (e.g., the deltaic setting of the Nile deep-sea fan) (Fig. 12.1). These fluids migrate upward from the seafloor to form various types of morphological features and substrates of sizes ranging from mm to km (Ceramicola et al., 2018):

(1) mud volcanoes formed by the eruption at the seafloor of sediments coming from clay-rich undercompacted and overpressured formations (Mazzini and Etiope, 2017); the mud volcano deposits are composed of so-called mud breccia (Cita et al., 1981) and incorporate rock fragments of underlying sedimentary formations, namely, clasts (Lykousis et al., 2009; Giresse et al., 2010) (Fig. 12.9);
(2) depressions called "pockmarks" resulting from the collapse of (subsurface) sediments upon the ascent of overpressured fluids (Dimitrov and Woodside, 2003) (Fig. 12.10);
(3) methane-derived authigenic carbonate structures resulting from the precipitation of carbonate via biochemical processes, namely, the anaerobic oxidation of methane (Aloisi et al., 2002) (Fig. 12.11).

Geological and biochemical processes at cold seep sites are strongly coupled. Fluid emission sites are indeed "hotspots" for chemosynthetic fauna and microbial activity. Methane and hydrogen sulfides are used as energy sources by several seep-related biota including microbial mats (e.g., Grünke et al., 2011) and symbiont-bearing invertebrates (e.g., Bivalvia, Polychaeta, Vanreusel et al., 2009; Olu-Le Roy et al., 2004; Sibuet and Olu, 1998).

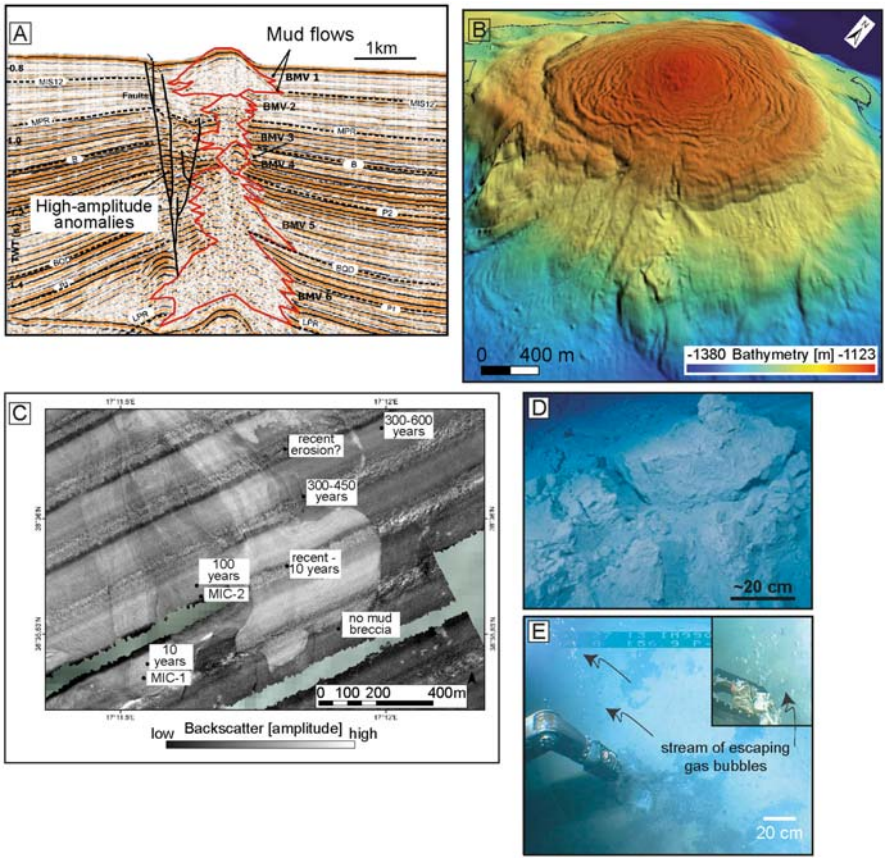

FIGURE 12.9

Mud volcano features: (A) Typical Christmas tree mud volcano structure in seismic data (the Ceuta mud volcano, Alboran Sea, ~550 m water depth) modified from Somoza et al. (2012), attesting to the succession of mud breccia expulsion events interbedded with normal and quieter sedimentation periods. BMV stands for Stacked buried Mud Volcano edifices. (B) Mud volcano seabed morphology of the active Amon mud volcano (Nile deep-sea fan, ~1150 m water depth) illustrated by high-resolution bathymetry (2 m pixel grid) acquired with the AsterX autonomous underwater vehicle (AUV) (Dupré et al., 2008) and displayed in a 3D view (Globe software, Poncelet et al., 2021). (C) Seafloor backscatter facies from high-resolution AUV-acquired multibeam data (300 kHz) of the Venere mud volcano (Ionian Calabrian Margin, ~1600 m water depth) illustrating the relationship between the intensity of the backscatter amplitude and the burial of mud breccia (indicative of the age of the mudflows). (D) and (E) Near-bottom pictures at active mud volcanoes (Nile deep-sea fan) taken on board the Nautile submersible during the NAUTINIL cruise in 2003. (D) A rough topography in the active center of Amon mud volcano (1120 m water depth) with fractured mud breccia blocks. (E) Escaping gas

12.4.2 Diversity of widespread cold seeps

The Mediterranean Sea hosts numerous seeps at the seafloor (Mascle et al., 2014), from its western edge in the back-arc setting of the western Alboran Sea (Somoza et al., 2012) to its eastern edge in the Levantine Basin (Schattner et al., 2012) (Fig. 12.1). Most seeps are, however, located in the eastern Mediterranean Sea, in particular along the accretionary wedge of the Mediterranean Ridge (Robertson et al., 1996) and in the Nile deep-sea fan, the thickest sedimentary edifice in the region (Loncke et al., 2004) (Fig. 12.1). Mediterranean cold seeps cover a wide spectrum (Mascle et al., 2014) from mud volcanoes, pockmarks, brine pools and lakes, gas vents to methane-derived carbonate structures, in association with chemosynthetic fauna and bacterial mats; and in a few places with gas hydrates (Woodside et al., 1998; Lykousis et al., 2009). These different seep-related features may be combined, e.g., with the presence of pockmarks (Dimitrov and Woodside, 2003; Casalbore et al., 2020a), methane-derived authigenic carbonate chimneys (Bayon et al., 2013), brine pools (Huguen et al., 2005), and brine lakes (Dupré et al., 2014) at the surface of mud volcanoes and methane-derived authigenic carbonate structures within pockmarks (Bayon et al., 2009) and brines (Pierre et al., 2014). Gas venting is mainly evidenced in exploratory surveys by water column acoustic data (e.g., from side-scan sonar, Dupré et al., 2010; and multibeam echosounders, Fig. 12.10C; Praeg et al., 2014; Ingrassia et al., 2015). The recent advances, over the last decade, in multibeam technology and computer processing greatly facilitated the detection of seeping sites (Scalabrin and Dupré, 2018).

12.4.3 Mud volcanoes

The majority of submarine mud volcanoes are located in the eastern Mediterranean Sea, in particular along the western (Ionian) and central domains of the Mediterranean Ridge (Robertson et al., 1996; Huguen et al., 2005), and in the Nile deep-sea fan (Loncke et al., 2004; Dupré et al., 2007) (Fig. 12.1). Mud volcanoes are also present along the Calabrian Arc (Ceramicola et al., 2014; Loher et al., 2018), at the Anaximander Mountains (Woodside et al., 1998; Zitter et al., 2005), and to a lesser extent at the Florence Rise (Woodside et al., 2002) (Fig. 12.1). In the Western Mediterranean Sea, most of the mud volcanoes are located in thick sedimentary basins, for instance in back-arc settings, in the Alboran Sea (Somoza et al., 2012) and to a

bubbles at the central dome of Isis mud volcano (990 m water depth) with a smooth seafloor partly covered with dark, reduced sediment patches and bacterial mats.

(C) Modified from Bohrmann, G., Bachmann, K., Buchheister, S., Candoni, O., Ceramicola, S., Loher, M., Meinecke, G., Renken, J., Spiesecke, U., von Wahl, T., Wintersteller, P., (2016) Report and preliminary results of R/V Poseidon Cruise POS499. MARUM. pp. 79, http://nbn-resolving.de/urn:nbn:de:gbv:46-00105556-16. (D, E) Dupré, S., Woodside, J., Klaucke, I., Mascle, J., Foucher, J.-P., 2010. Widespread active seepage activity on the Nile Deep Sea Fan (offshore Egypt) revealed by high-definition geophysical imagery. Mar. Geol. 275 (1–4), 1–19.

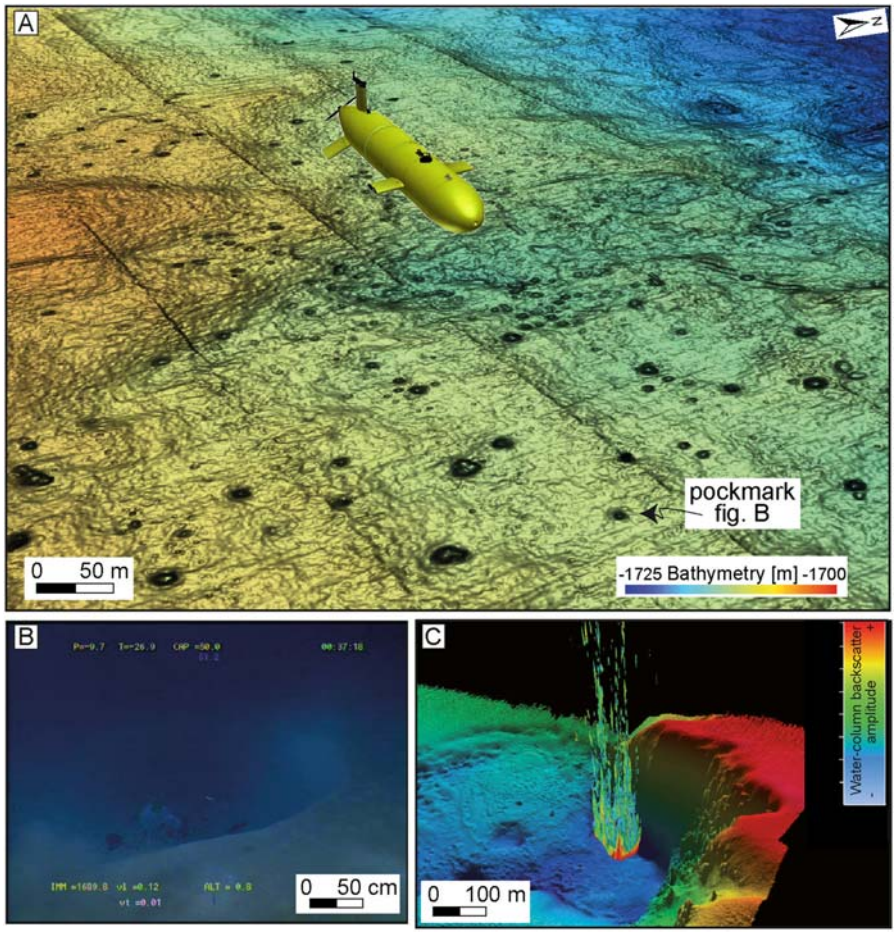

FIGURE 12.10

Pockmark features: (A) Shaded high-resolution bathymetry (1 m pixel grid) of a pockmark field in the Central Province of the Nile deep-sea fan (data from the BIONIL-M70/2 cruise onboard the R/V Meteor, 2006). The data were acquired with the AsterX autonomous underwater vehicle (not to scale in the figure) and are displayed in a 3D view (Globe software, Poncelet et al., 2021). (B) Near-bottom picture of a pockmark, a few meters in diameter, taken by the Victor 6000 remotely operated underwater vehicle (ROV) during the MEDECO2 marine expedition. See location in Fig. 12.9A. (C) Water column acoustic gas-related anomalies above the large-scale (900 m long and 500 m wide) Zannone pockmark (Central Tyrrhenian Sea, around 130 m water depth) acquired with a Kongsberg EM710 multibeam echosounder (70–100 kHz).

(C) Modified from Ingrassia, M., Martorelli, E., Bosman, A., Macelloni, L., Sposato, A., Chiocci, F.L., 2015. The Zannone Giant Pockmark: first evidence of a giant complex seeping structure in shallow-water, central Mediterranean Sea, Italy. Mar. Geol. 363, 38–51.

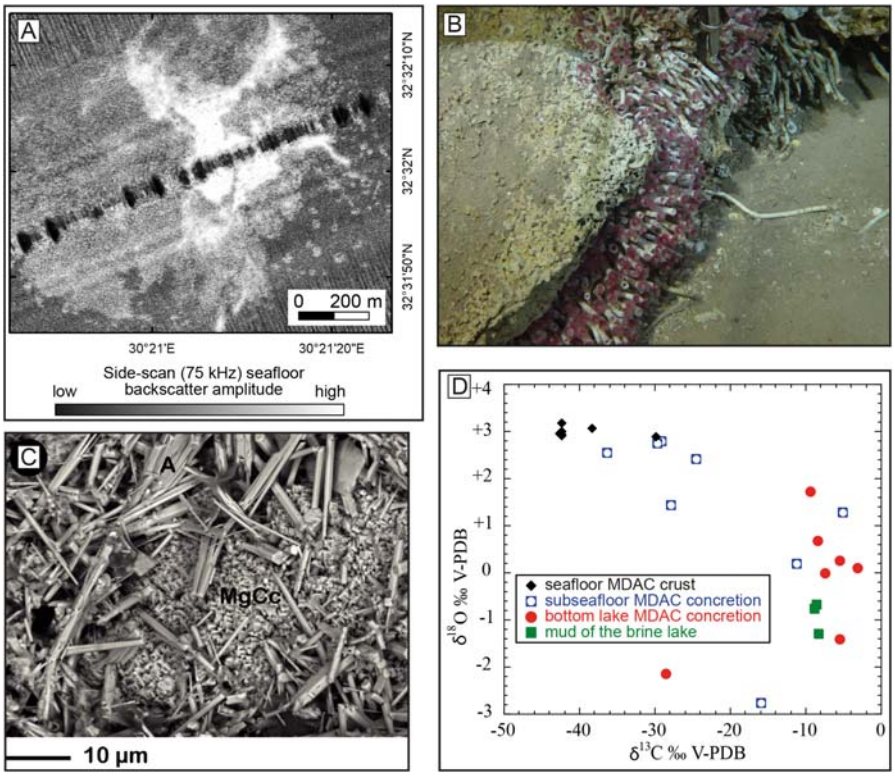

FIGURE 12.11

Methane-derived authigenic carbonate structures: (A) Their high-amplitude seafloor backscatter signatures acquired with a deep-towed side-scan sonar in the Central Nile Province (water depths range from 1715 to 1690 m). (B) Near-bottom picture of an authigenic carbonate crust at the seafloor (Nile deep-sea fan, ~1690 m water depth), taken by the Victor 6000 ROV during the MEDECO2 marine expedition, with Siboglinidae polychaetes (Vanreusel et al., 2009). (C) Scanning electron microscopy photograph of carbonate crust from the Cheops MV (Nile deep-sea fan, 3015 m water depth) with aragonite and Mg-calcite crystals (Pierre et al., 2014). (D) Oxygen and carbon isotopic signatures of methane-derived authigenic carbonate structures and muddy brines at the Cheops mud volcano.

Modified from (A) Dupré, S., Woodside, J., Klaucke, I., Mascle, J., Foucher, J.-P., 2010. Widespread active seepage activity on the Nile Deep Sea Fan (offshore Egypt) revealed by high-definition geophysical imagery. Mar. Geol. 275 (1–4), 1–19. (D) Pierre, C., Bayon, G., Blanc-Valleron, M.-M., Mascle, J., Dupré, S., 2014. Authigenic carbonates related to active seepage of methane-rich hot brines at the Cheops mud volcano, Menes caldera (Nile deep-sea fan, eastern Mediterranean Sea). Geo Mar. Lett. 34 (2–3), 253–267.

lesser extent and number, offshore Italy, in the Tyrrhenian Sea (Casalbore et al., 2020a; Rovere et al., 2014) and at the Sicily Channel (Savini et al., 2009) (Fig. 12.1). Seismic signature of mud volcanoes depends on the amount of gas and frequency of the signal and may correspond to a Christmas-tree-like structure (Fig. 12.9A), a wipe-out column, or a chaotic facies zone. The seafloor morphology of the Mediterranean mud volcanoes are generally slightly conical (e.g., Kazan mud volcano, Lykousis et al., 2009), flat resembling mud pies (Fig. 12.9B) with or without dome(s) (e.g., Isis mud volcano, Dupré et al., 2008) or may correspond to collapsing structures. The seafloor acoustic signatures of mud volcanoes are highly variable depending on the surface roughness (microrelief) and the discontinuities in the subsurface sediments that are insonified by the echosounder. These discontinuities could be related to the presence of authigenic carbonates, rock clasts or shell debris fields. For instance, with a high-frequency signal, areas of outcropping mud breccia backscatter more energy than areas where mud breccia is covered with a thin cover of hemipelagic sediments (e.g., Venere mud volcano, Loher et al., 2018) (Fig. 12.9C). Similarly, areas with a rough mud breccia topography at extrusion centers of mud volcanoes (Fig. 12.9D) have higher backscatter amplitudes than smooth mud breccia surroundings (e.g., Amon mud volcano, Dupré et al., 2010). The activity of mud volcanoes (i.e., mud extrusion, mud flows, fluid escapes) is not necessarily continuous over time through the mud volcano history and alternates with periods of quiescence or dormancy. At many places in the Mediterranean Sea, mud volcanism is inferred to have been initiated during (at least) the Pliocene; for example, 1.2 Ma for Napoli and Milano mud volcanoes from the Olimpi mud volcanoes field in the Central Mediterranean Ridge, 3 Ma for Madonna dello Ionio and Pythagoras mud volcanoes in the Calabrian accretionary prism (Praeg et al., 2009), Mid-Pliocene (~4.2 Ma) for the Ceuta mud volcano in the Alboran Sea (Somoza et al., 2012) and during the Early Pliocene for the Menes mud volcano caldera complex in the western Nile Province (Dupré et al., 2014).

12.4.4 Pockmarks

Pockmarks are numerous at the Mediterranean seafloor, with the main pockmark field located in the Central Nile deep-sea fan (Loncke et al., 2004; Römer et al., 2014) (Fig. 12.9A), as well as, offshore Israel (Schattner et al., 2012) and in the western Alboran Sea (Somoza et al., 2012). Pockmarks of various sizes are also observed in many other places, e.g., along the Mediterranean Ridge and Anaximander Mountains (Dimitrov and Woodside, 2003) and in the Central Adriatic Sea (Geletti et al., 2008; Pellegrini et al., 2018; Rovere et al., 2020). The threshold detection of multibeam is not always suitable to map small-scale pockmarks, giving therefore an incomplete view at the scale of the entire Mediterranean Sea. However, the increasing use of high-resolution multibeam echosounders is most likely going to lead to the discovery of even more pockmarks and seep-related structures, regardless of their size. Many pockmarks at the Mediterranean seafloor are associated with gas saturated sediments and escaping methane bubbles (Dupré et al., 2010; Praeg et al., 2014; Ingrassia et al., 2015; Rovere et al., 2020) (Fig. 12.10B and C).

12.4.5 Methane-derived authigenic carbonate structures

Mud volcanoes and pockmark areas are very often associated with the presence of methane-derived authigenic carbonate structures whether these seep-related sites are currently active (e.g., pockmark fields in the Central Nile Province, Dupré et al., 2010; Praeg et al., 2014; Römer et al., 2014) or correspond to ancient seeping sites (e.g., methane-derived authigenic carbonate chimneys in the Adriatic Sea, Angeletti et al., 2015).

Easily detectable in seafloor backscatter data (e.g., Dupré et al., 2010) (Fig. 12.11A), methane-derived authigenic carbonate structures are key features to identify seep-related areas. These carbonates have different shapes and sizes and may host chemosynthetic fauna (Fig. 12.11B), depending on the methane flux and the duration of methane circulation. Carbonate may precipitate in the form of millimetric to decimetric concretions, nodules, crusts, meter-scale mounds or chimneys, plates and slabs (e.g., Gontharet et al., 2007; Pierre et al., 2014). The dominant mineral phases of these structures are aragonite, Mg-calcite, dolomite and ankerite (e.g., Gontharet et al., 2007; Pierre et al., 2014) (Fig. 12.11C). Their isotopic signatures of $\delta^{13}C$ and $\delta^{18}O$ provide relevant information on the source of the carbon (typically from the anaerobic oxidation of methane, Aloisi et al., 2002) and the fluids in which they precipitated (e.g., in equilibrium with the ambient bottom seawater temperature or with warm fluids, Pierre et al., 2014), respectively (Fig. 12.11D). U/Th dating of methane-derived authigenic carbonate structures at the Amon mud volcano points to precipitation between 12 and 7 kyr ago, a period corresponding to organic-rich sediments (sapropel S1) (Bayon et al., 2013). Anoxic conditions of the bottom seawater associated with these deposits promoted an intense anaerobic microbial activity and consequently the precipitation of the carbonate structures.

12.4.6 Brine seeps

In the parts of the Mediterranean Sea where Messinian salt deposits are present (see Chapter 2 for detailed information about these deposits), expulsions of ascending fluids and mud may be associated with brines. These brines are denser than the ambient seawater and thus accumulate as muddy brines at the seafloor within depressions. These muddy brines are hypersaline, up to 8 times more than ambient seawater (Cheops mud volcano in the western Nile Province, Huguen et al., 2009). This results in a variety of environments, from deep anoxic basins (e.g., the Bannock Basin along the Mediterranean Ridge, Cita, 2006), brine lakes a few hundreds of meters in diameter (Nadir brine lake in the Mediterranean Ridge, Medinaut/Medineth Shipboard Scientific Party 2000; Cheops and Chephren brine lakes in the western Nile Province, Dupré et al., 2014) and meter-scale brine pools (e.g., Napoli mud volcano, Huguen et al., 2005).

12.4.7 Gas hydrates

Although gas hydrate occurrence is suspected from geophysical data and modeling, in particular in the Central Nile Province (Praeg et al., 2017), only a few samples of gas hydrates have been collected in the subsurface of mud volcanoes in the entire Mediterranean Sea so far. It concerns four mud volcanoes located in the Anaximander Mountains (e.g., Amsterdam mud volcano, Woodside et al., 1998; Lykousis et al., 2009).

12.4.8 Processes controlling the formation of gas and its migration

Cold seeps are first necessarily bound to source rocks and overpressured sedimentary layers, for example, the thick early Miocene overpressured shales for the Alboran Sea mud volcanoes (Somoza et al., 2012) and the pre-Messinian mud/fluid sources for the Menes caldera mud volcanoes in the western Nile Province (Dupré et al., 2014). Seepage in the Mediterranean Sea is either associated with thick accretionary wedges (western and central Mediterranean Ridge, Calabrian Arc), thick sedimentary deep-sea fan (offshore Egypt), or thick sedimentary back-arc basins (western Alboran Sea, south-eastern Tyrrhenian Sea). Regardless of the tectonic-sedimentary setting (accretionary prisms, back-arcs, thick depocenters), the location of the mud volcanoes, and more generally cold seeps, is controlled by the upward migration of fluids along faults (e.g., for authigenic carbonate structures at the Amon mud volcano and away from mud volcanoes, Dupré et al., 2010) and in sedimentary weak zones (e.g., for eastern central Nile Province mud volcanoes located above buried Messinian canyons, Dupré et al., 2007). The associated fault networks may be related to thrusting and strike-slip faults in compressive settings (e.g., Central Mediterranean Ridge mud volcanoes, Huguen et al., 2004; San Remo and Kula mud volcanoes in the Anaximander Mountains, Woodside et al., 1998), normal faults (e.g., pockmarks and mud volcanoes in the southern Tyrrhenian Sea, Rovere et al., 2014), and listric faults induced by salt tectonics (e.g., Menes mud volcanoes caldera in the western Nile Province, Huguen et al., 2009). The fault networks may be a combination of deep-seated faults and secondary shallower intrasedimentary faults (e.g., Anaximander mud volcanoes, Zitter et al., 2006; Nile deep-sea fan mud volcanoes, Loncke et al., 2004), these latter being also possibly induced by salt tectonics (Loncke et al., 2004) and sedimentary instabilities (e.g., authigenic carbonate structures in the Central Nile Province, Bayon et al., 2009). In the Mediterranean Sea, the role of Messinian salt is prominent in the occurrence and spatial distribution of cold seeps, in particular of mud volcanoes (Mascle et al., 2014). Most of the mud volcanoes are located in areas where salt layers are thin, absent or have been involved in salt tectonics creating thus favourable pathways for fluids to migrate upward. This results in numerous and widespread cold seeps including mud volcanoes in the Eastern Mediterranean Sea and the absence of seepage in the deep Western Mediterranean Sea (Fig. 12.1).

12.5 Geohazards and ecosystems

12.5.1 Geohazards

The sea, the seafloor, and coastal areas host a large number of human activities that include for instance fishing, shipping, defense, offshore energy (oil and gas exploration and exploitation, and renewable energy), telecommunication, and tourism (Fig. 12.2). Marine geological processes can pose a hazard to these activities and to the related offshore and coastal infrastructures, with potential consequences for human health, economy and environment (Rovere et al., 2020). Major geohazards in the marine realm are earthquakes, volcanic eruptions, gravity-driven sedimentary processes (e.g., submarine landslides and turbidity currents), fluid emissions, migration of bedforms, and tsunamis (mainly formed by fault displacements or submarine landslides) (Fig. 12.2; Chiocci et al., 2011; Ercilla et al., 2021). The use of the seafloor for infrastructure and economic activities is strongly increasing worldwide. Since the first submarine cable was deployed in the 19th century, numerous telecommunication cables connect different continents across the oceans and are responsible for over 95% of the international communications (Carter et al., 2014). Cable breaks induced by sediment gravity flows have occurred in many areas of the world and have provided very valuable information about the characteristics of these sedimentary processes (Carter et al., 2014).

Moderate to large magnitude earthquakes can generate widespread slope instabilities along continental slopes (Goldfinger, 2011). Submarine landslides can transform into turbidity currents by incorporating water and can travel long distances downslope with high velocities. This type of catastrophic event has been observed in different zones of the Mediterranean Sea with important tectonic activity. In 1908, a 7.1-magnitude earthquake affected the Messina Strait, with catastrophic consequences in the cities of Messina and Reggio Calabria. These cities were almost completely destroyed and 195,000 people were reported dead (Pino et al., 2009). This earthquake triggered slope failures and turbidity current that flowed downslope through a canyon in the Ionian Sea and broke two submarine cables (Ryan and Heezen, 1956). Turbidite deposits related to the 1908 earthquake were found at water depths greater than 3800 m in the Ionian Sea together with older turbidite deposits, providing useful paleoseismological insights of this very seismically active area (Polonia et al., 2013). Within minutes after the earthquake, a tsunami with waves up to 12 m reached the coast south of Messina and Reggio Calabria (Pino et al., 2009). In 1783, the seismically triggered M. Pacì landslide (Calabria in Southern Italy) created a local but devastating tsunamis that hit the Marina Grande beach at Scilla town, causing about 1500 casualties (Mazzanti and Bozzano, 2011; and references therein). More recently, in 2003, the Algerian coast was also affected by a 6.8-magnitude earthquake that triggered large turbidity currents and a tsunami that reached the Balearic Islands and the Nice area (Cattaneo et al., 2012; and references therein). The turbidity currents affected an area of more than 150 km at the foot of the slope and in the deep Algerian basin and broke 29 submarine cables,

leaving Algeria without telecommunication during 48 h (Cattaneo et al., 2012). As mentioned in Section 12.3, landslide-generated tsunamis are also reported along the flanks of insular volcanoes, such as in the Aeolian islands where (at least) five tsunamigenic events were reported in the last century (Maramai et al., 2005). The geohazard associated with these events is very high, as testified by the recent collapse that affected the Anak Krakatau in 2018. This event mobilized a few hundreds of 10^6 m^3 of volcanic material, generating tsunami waves with a maximum runup of 13 m along the Sunda Strait that caused over 430 fatalities and 14,000 injured people (Grilli et al., 2019).

In the Mediterranean Sea, a main marine geohazard is also related to retrogressive instabilities (landward migration of slope failures) occurring at the head of shelf-incising canyons that often cut back at very shallow depths (<20 m), few tens or hundreds meters far from the coastline (Chiocci and Casalbore, 2017). These canyons are able to interact with coastal dynamics (intercepting littoral drift or hyperpycnal flows generated at the mouth of narrow and steep water courses, with torrential regime), especially in tectonically controlled margins affected by relevant uplift processes, such as off Liguria, Calabria and Sicily. Particularly, two tsunamigenic landslides recently occurred at the head of the Gioia Canyon (Calabria, Italy) in 1977 (Colantoni et al., 1992; Casalbore et al., 2014b) and Var Canyon (Nice, France) in 1979 (Assier-Rzadkieaicz et al., 2000). In both cases, it is noteworthy that the landslides occurred during or just after human works aimed at building new harbor or airport extensions. The landslide and associated tsunamis caused significant damages to the facing coastal infrastructures and broke underlying submarine cables; in the case of the 1979 Nice landslide, several casualties due to the tsunami waves were reported from the facing Antibes city. Retrogressive erosion of canyon heads has been claimed as a concurrent cause to explain the beach retreat and the locally higher subsidence rates in the eastern part of Lipari (Anzidei et al., 2016; Casalbore et al., 2018), with significant implications for the expected impact of sea level rise at 2100 AD (Anzidei et al., 2017), especially in strongly anthropized and touristically exploited areas, such as the eastern part of Lipari.

From an environmental point of view, submarine canyons also act as preferential conduit for transport of pollutants (e.g., microplastics; Kane and Clare; 2019) and litter in deep-water, as reported by several authors (e.g., Galgani et al., 1996; Tubau et al., 2015) (Figs. 12.2 and 12.5). Litter density in submarine canyons has been reported to be 2−3 times higher than that on adjacent open shelves and slopes (Pham et al., 2014; Pierdomenico et al., 2020). Particularly, one of the highest concentrations of benthic litter in the world was reported from the Messina Strait, with maximum values of about 200 items/10 m (Pierdomenico et al., 2019). Currents control the distribution of microplastics, not only on the sea surface, but also at the seafloor (Liubartseva et al., 2018; Kane et al., 2020). Major hotspots of microplastics, containing up to 1.9 million pieces m^{-2}, have been observed at contourite drifts of the northern Tyrrhenian Sea, demonstrating the important role of bottom currents in the redistribution and final fate of microplastics (Fig. 12.2; Kane et al., 2020).

A recent review of marine geological hazards was performed by Ercilla et al. (2021), evidencing the need of a multidisciplinary approach to better constrain and assess marine geohazards, in which the ocean must be seen as an integrated system including different environments and processes, which can interact and influence each other. The same authors state the importance of a multiscale analysis, mapping, and modeling in order to integrate geological records obtained by seismic profiles and sediment cores with direct deep-sea testing (autonomous underwater vehicles, remotely operated vehicles and cone penetrometer tests) and monitoring systems, such as repeated bathymetric surveys, hydroacoustic systems, arrays of ocean bottom seismometers, moorings, and in situ seafloor observatories.

12.5.2 Ecosystems

Geological processes can generate particular environments (e.g., canyon, seeps, hydrothermal vents, etc) in the Mediterranean Sea that enhance biodiversity, compared to other more homogeneous zones like open slopes, especially for the megafauna (Danovaro et al., 2010). Cold-water corals usually need a hard substrate to be fixed, a constant delivery of organic matter and relatively strong currents that bring organic particles and inhibit sediment deposition on the corals (Lo Iacono et al., 2018). They are therefore often found in the flanks of submarine canyons, where consolidated sediment or rocks outcrop at the seafloor and abundant organic matter is transported downslope (Fig. 12.2 and 12.7B; Lo Iacono et al., 2018). Submarine landslides also favor the settlement of cold-water corals because they create complex seafloor morphologies and expose hard substrates at the seafloor, as observed in the northern Ionian Sea (Savini and Corselli, 2010). Cold-water corals act as ecosystem engineers and create structures that provide a refuge for many species, increasing the biodiversity (Danovaro et al., 2010). They form mounds on geological timescales, by trapping hemipelagic sediments and accumulating bioclasts and coral fragments (Hebbeln et al., 2016). These mounds can reach heights of a few meters to several hundreds of meters, and they thus strongly affect the seafloor morphology and the local hydrodynamic regime, favoring the formation of contourites in their vicinity. Cold-water coral mounds and related contourites are common on the southern slope of the Alboran Sea (Hebbeln et al., 2016).

Fluid escape at cold seeps generates particular geochemical conditions and induces changes in the type of substrate (e.g., precipitation of carbonates, mud flows) that strongly control the development of the living communities. These methane- and sulfur-rich environments are colonized by chemosynthetic communities, often composed of bivalves and siboglinid tube worms with bacterial symbionts, sponges and associated endemic fauna (Danovaro et al., 2010). Mediterranean seeps are rich habitats, especially when compared to other deep-water environments, in particular in the Eastern Mediterranean Sea, where they are mainly found (Danovaro et al., 2010).

Past major geological events in the Mediterranean Sea still have an impact in the living marine ecosystems. During the Messinian salinity crisis (5.96−5.33 Ma ago),

a great part of the Mediterranean Sea was desiccated and evaporites were deposited in the basin floor (Roveri et al., 2014; see more detail about this event in Chapter 2). These evaporitic deposits contribute to the formation of brines that accumulate in some deep basins of the Mediterranean Ridge (3200–3600 m water depth), generating hypersaline anoxic conditions (Danovaro et al., 2010; and references therein). These extreme environments are mainly colonized microbial communities (Bacteria and Archaea) (Danovaro et al., 2010).

In conclusion, the Mediterranean Sea is a region with a complex and varied geology, which is strongly interconnected with climate, physical oceanographic processes, and marine ecosystems. For instance, the circulation in the Mediterranean basins is constrained by the seafloor topography and is especially limited in the straits and sills, which are the result of tectonic processes. At the same time, currents can disperse sediments from rivers alongshore and control sediment deposition and erosion in shallow- and deep-water settings, also affecting the distribution of nutrients and pollutants in the marine system and thus the development of marine ecosystems.

Additional Resources

- EMODnet, https://emodnet.ec.europa.eu/en/portals
- The topographic data set used in this chapter is the GEBCO Compilation Group (2020) GEBCO 2020 Grid (https://doi.org/10.5285/a29c5465-b138-234d-e053-6c86abc040b9) and the bathymetric data set corresponds to the EMODnet Digital Bathymetry (EMODnet Bathymetry Consortium (2018), https://doi.org/10.12770/18ff0d48-b203-4a65-94a9-5fd8b0ec35f6)
- The location of submarine volcanoes used in this chapter was made available by the EMODnet Geology project (http://www.emodnet-geology.eu)
- CIESM, The Mediterranean Science Commission, https://www.ciesm.org/

References

Abbott, P.M., Jensen, B.J.L., Lowe, D.J., Suzuki, T., Veres, D., 2020. Crossing new frontiers: extending tephrochronology as a global geoscientific research tool. J. Quat. Sci. 35, 1–8.

Aloisi, G., Bouloubassi, I., Heijs, S.K., Pancost, R.D., Pierre, C., Damste, J.S.S., Gottschal, J.C., Forney, L.J., Rouchy, J.M., 2002. CH4-consuming microorganisms and the formation of carbonate crusts at cold seeps. Earth Planet Sci. Lett. 203 (1), 195–203.

Angeletti, L., Canese, S., Franchi, F., Montagna, P., Reitner, J., Walliser, E.O., Taviani, M., 2015. The "chimney forest" of the deep Montenegrin margin, south-eastern Adriatic Sea. Mar. Petrol. Geol. 66, 542–554.

Anzidei, M., Bosman, A., Casalbore, D., Tusa, S., La Rocca, R., 2016. New insights on the subsidence of Lipari island (Aeolian islands, southern Italy) from the submerged Roman age pier at Marina Lunga. Quat. Int. 401, 162–173.

Anzidei, M., Bosman, A., Carluccio, R., Casalbore, D., D'Ajello Caracciolo, F., Esposito, A., Nicolosi, I., Pietrantonio, G., Vecchio, A., Carmisciano, C., Chiappini, Chiocci, F.L., Muccini, F., Sepe, V., 2017. Flooding scenarios due to land subsidence and sea-level rise: a case study for Lipari Island (Italy). Terra. Nova 29 (1), 44–51.

Assier-Rzadkieaicz, S., Heinrich, P., Sabatier, P.C., Savoye, B., Bourillet, J.F., 2000. Numerical modelling of a landslide-generated tsunami: the 1979 Nice event. Pure Appl. Geophys. 157 (10), 1707–1727.

Babonneau, N., Delacourt, C., Cancouët, R., Sisavath, E., Bachèlery, P., Mazuel, A., Jorry, S.J., Deschamps, A., Ammann, J., Villeneuve, N., 2013. Direct sediment transfer from land to deep-sea: insights into shallow multibeam bathymetry at La Réunion Island. Mar. Geol. 346, 47–57.

Bao, R., McIntyre, C., Zhao, M., Zhu, C., Kao, S.J., Eglinton, T.I., 2016. Widespread dispersal and aging of organic carbon in shallow marginal seas. Geology 44 (10), 791–794.

Barberi, F., 1993. Volcanic hazard assessment at Stromboli based on review of historical data. Acta Vulcanol. 3, 173–187.

Bárcenas, P., Lobo, F.J., Macías, J., Fernández-Salas, L.M., López-González, N., del Río, V.D., 2015. Submarine deltaic geometries linked to steep, mountainous drainage basins in the northern shelf of the Alboran Sea: filling the gaps in the spectrum of deltaic deposition. Geomorphology 232, 125–144.

Bayon, G., Loncke, L., Dupré, S., Caprais, J.-C., Ducassou, E., Duperron, S., Etoubleau, J., Fouche, J.-P., Fouquet, Y., Gontharet, S., Henderson, G.M., Huguen, C., Klaucke, I., Mascle, J., Migeon, S., Olu-Le Roy, K., Ondréas, H., Pierre, C., Sibuet, M., Stadnitskaia, A., Woodside, J., 2009. Multi-disciplinary investigation of fluid seepage on an unstable margin: the case of the Central Nile deep sea fan. Mar. Geol. 261 (1–4), 92–104.

Bayon, G., Dupré, S., Ponzevera, E., Etoubleau, J., Cheron, S., Pierre, C., Mascle, J., Boetius, A., de Lange, G.J., 2013. Formation of carbonate chimneys in the Mediterranean Sea linked to deep-water oxygen depletion. Nat. Geosci. 6 (9), 755–760.

Bell, K.L.C., 2011. On the Origin of Submarine Sediment Features in the Southern Aegean Sea. Ph.D. thesis. University of Rhode Island.

Bellacicco, M., Anagnostou, C., Falcini, F., Rinaldi, E., Tripsanas, K., Salusti, E., 2016. The 1987 Aegean dense water formation: a streamtube investigation by comparing theoretical model results, satellite, field, and numerical data with contourite distribution. Mar. Geol. 375, 120–133.

Berné, S., Jouet, G., Bassetti, M.A., Dennielou, B., Taviani, M., 2007. Late Glacial to Preboreal sea-level rise recorded by the Rhône deltaic system (NW Mediterranean). Mar. Geol. 245 (1–4), 65–88.

Bhattacharya, J.P., Giosan, L., 2003. Wave-influenced deltas: geomorphological implications for facies reconstruction. Sedimentology 50 (1), 187–210.

Bianchi, T.S., Cui, X., Blair, N.E., Burdige, D.J., Eglinton, T.I., Galy, V., 2018. Centers of organic carbon burial and oxidation at the land-ocean interface. Org. Geochem. 115, 138–155.

Bignami, F., Salusti, E., 1990. Tidal currents and transient phenomena in the Strait of Messina: a review. Phys Oceanogr Sea Straits 95–124.

Blair, N.E., Aller, R.C., 2012. The fate of terrestrial organic carbon in the marine environment. Ann. Rev. Mar. Sci 4, 401–423.

Bohrmann, G., et al., 2016. Report and preliminary results of R/V Poseidon Cruise POS499. Berichte aus dem MARUM und dem Fachbereich Geowissenschaften der Universität Bremen, 311. Universität Bremen, pp. 1–76. http://nbn-resolving.de/urn:nbn:de:gbv:46-00105556-16.

Bonneau, L., Jorry, S.J., Toucanne, S., Silva Jacinto, R., Emmanuel, L., 2014. Millennial-scale response of a western Mediterranean river to late Quaternary climate changes: a view from the deep sea. J. Geol. 122, 687–703.

Bosman, A., Casalbore, D., Romagnoli, C., Chiocci, F.L., 2014. Formation of an 'a'ā lava delta: insights from time-lapse multibeam bathymetry and direct observations during the Stromboli 2007 eruption. Bull. Volcanol. 76 (7), 1–12.

Boudon, G., Le Friant, A., Komorowski, J.C., Deplus, C., Semet, M.P., 2007. Volcano flank instability in the Lesser Antilles Arc: diversity of scale, processes, and temporal recurrence. J. Geophys. Res. Solid Earth 112 (B8).

Boyd, R., Dalrymple, R., Zaitlin, B.A., 1992. Classification of clastic coastal depositional environments. Sediment. Geol. 80 (3–4), 139–150.

Buchner, G., 1986. Eruzioni vulcaniche e fenomeni vulcano-tettonici di età preistorica nell'isola d'Ischia. Pub. Centre J. Berard Naples 7, 145–188.

Campo, B., Bohacs, K.M., Amorosi, A., 2020. Late Quaternary sequence stratigraphy as a tool for groundwater exploration: Lessons from the Po River Basin (northern Italy). AAPG Bulletin 104 (3), 681–710.

Canals, M., Danovaro, R., Heussner, S., Lykousis, V., Puig, P., Trincardi, F., Calafat, A.M., Durrieu de Madron, X., Palanques, A., Sanchez-Vidal, A., 2009. Cascades in Mediterranean submarine grand canyons. Oceanography 22 (1), 26–43.

Cantner, K., Carey, S., Nomikou, P., 2014. Integrated volcanologic and petrologic analysis of the 1650 AD eruption of Kolumbo submarine volcano, Greece. J. Volcanol. Geoth. Res. 269, 28–43.

Carter, L., Gavey, R., Talling, P.J., Liu, J.T., 2014. Insights into submarine geohazards from breaks in subsea telecommunication cables. Oceanography 27 (2), 58–67.

Casalbore, D., 2018. Volcanic islands and seamounts. In: Micallef, A., Krastel, S., Savini (Eds.), Submarine Geomorphology. Springer, Cham, pp. 333–347.

Casalbore, D., Bosman, A., Chiocci, F., 2012. Study of recent small-scale landslides in geologically active marine areas through repeated multibeam surveys: examples from the southern Italy. Submarine mass movements and their consequences 573–582. https://doi.org/10.1007/978-94-007-2162-3_51.

Casalbore, D., Chiocci, F.L., Mugnozza, G.S., Tommasi, P., Sposato, A., 2011. Flash-flood hyperpycnal flows generating shallow-water landslides at Fiumara mouths in Western Messina Strait (Italy). Mar. Geophys. Res. 32 (1–2), 257.

Casalbore, D., Romagnoli, C., Bosman, A., Chiocci, F.L., 2014a. Large-scale seafloor waveforms on the flanks of insular volcanoes (Aeolian Archipelago, Italy), with inferences about their origin. Mar. Geol. 355, 318–329.

Casalbore, D., Bosman, A., Ridente, D., Chiocci, F.L., 2014b. Coastal and submarine landslides in the tectonically-active Tyrrhenian Calabrian margin (Southern Italy): examples and geohazard implications. In: Krastel, S., et al. (Eds.), Submarine Mass Movements and Their Consequences. Springer, Dordrecht, vol. 37, pp. 261–269.

Casalbore, D., Bosman, A., Martorelli, E., Sposato, F.L., Chiocci, F.L., 2016. Mass wasting features on the submarine flanks of Ventotene volcanic edifice (Tyrrhenian Sea, Italy). In: Krastel, S., et al. (Eds.) Submarine Mass Movements and Their Consequences 37. Springer, Dordrecht, pp. 285–293.

Casalbore, D., Ridente, D., Bosman, A., Chiocci, F.L., 2017. Depositional and erosional bedforms in Late Pleistocene-Holocene pro-delta deposits of the Gulf of Patti (southern Tyrrhenian margin, Italy). Mar. Geol. 385, 216–227.

Casalbore, D., Romagnoli, C., Adami, C., Bosman, A., Falese, F., Ricchi, A., Chiocci, F.L., 2018. Submarine depositional terraces at Salina island (Southern Tyrrhenian sea) and implications on the late-quaternary evolution of the insular shelf. Geosciences 8 (1), 20.

Casalbore, D., Ingrassia, M., Pierdomenico, M., Beaubien, S.E., Martorelli, E., Bigi, S., Ivaldi, R., DeMarte, M., Chiocci, F.L., 2020a. Morpho-acoustic characterization of a shallow-water mud volcano offshore Scoglio d'Affrica (Northern Tyrrhenian Sea) responsible for a violent gas outburst in 2017. Mar. Geol. 428, 106277.

Casalbore, D., Passeri, F., Tommasi, P., Verrucci, L., Bosman, A., Romagnoli, C., Chiocci, F.L., 2020b. Small-scale slope instability on the submarine flanks of insular volcanoes: the case-study of the Sciara del Fuoco slope (Stromboli). Int. J. Earth Sci. 109 (8), 2643−2658.

Casalbore, D., Clare, M.A., Pope, E.L., Quartau, R., Bosman, A., Chiocci, F.L., Romagnoli, C., Santos, R., 2021. Bedforms on the submarine flanks of insular volcanoes: new insights gained from high resolution seafloor surveys. Sedimentology 68 (4), 1400−1438.

Casas, D., Pimentel, A., Pacheco, J., Martorelli, E., Sposato, A., Ercilla, G., Alonso, B., Chiocci, F., 2018. Serreta 1998−2001 submarine volcanic eruption, offshore Terceira (Azores): characterization of the vent and inferences about the eruptive dynamics. J. Volcanol. Geoth. Res. 356, 127−140.

Cattaneo, A., Correggiari, A., Langone, L., Trincardi, F., 2003. The late-Holocene Gargano subaqueous delta, Adriatic shelf: sediment pathways and supply fluctuations. Mar. Geol. 193 (1−2), 61−91.

Cattaneo, A., Babonneau, N., Ratzov, G., Dan-Unterseh, G., Yelles, K., Bracène, R., de Lépinay, M., Boudiaf, A., Déverchère, J., 2012. Searching for the seafloor signature of the 21 May 2003 Boumerdès earthquake offshore central Algeria. Nat. Hazards Earth Syst. Sci. 12 (7), 2159−2172.

Ceramicola, S., Praeg, D., Cova, A., Accettella, D., Zecchin, M., 2014. Seafloor distribution and last glacial to postglacial activity of mud volcanoes on the Calabrian accretionary prism, Ionian Sea. Geo Mar. Lett. 34, 111−129.

Ceramicola, S., Dupré, S., Somoza, L., Woodside, J., 2018. Cold seep systems. In: Micallef, A., Krastel, S., Savini, A. (Eds.), Submarine Geomorphology. Springer International Publishing, Cham, pp. 367−387.

Chiggiato, J., Bergamasco, A., Borghini, M., Falcieri, F.M., Falco, P., Langone, L., Miserocchi, S., Russo, A., Schroeder, K., 2016. Dense-water bottom currents in the southern Adriatic Sea in spring 2012. Mar. Geol. 375, 134−145.

Chiocci, F.L., De Alteriis, G., 2006. The Ischia debris avalanche: first clear submarine evidence in the Mediterranean of a volcanic island prehistorical collapse. Terra. Nova 18 (3), 202−209.

Chiocci, F.L., Casalbore, D., 2017. Unexpected fast rate of morphological evolution of geologically-active continental margins during Quaternary: examples from selected areas in the Italian seas. Mar. Petrol. Geol. 82, 154−162.

Chiocci, F.L., Romagnoli, C., Tommasi, P., Bosman, A., 2008. The Stromboli 2002 tsunamigenic submarine slide: characteristics and possible failure mechanisms. J. Geophys. Res. Solid Earth 113 (B10).

Chiocci, F.L., Cattaneo, A., Urgeles, R., 2011. Seafloor mapping for geohazard assessment: state of the art. Mar. Geophys. Res. 32 (1−2), 1−11.

Cita, M.B., 2006. Exhumation of Messinian evaporites in the deep-sea and creation of deep anoxic brine-filled collapsed basins. Sediment. Geol. 188, 357−378.

Cita, M.B., Ryan, W.B.F., Paggi, L., 1981. Prometheus mud breccia; an example of shale diapirism in the Western Mediterranean Ridge. Ann. Geol. Des. Pays Hell. 30, 543−570.
Clarke, J.E.H., 2016. First wide-angle view of channelized turbidity currents links migrating cyclic steps to flow characteristics. Nat. Commun. 7 (1), 1−13.
Colantoni, P., Gennesseaux, M., Vanney, J.R., Ulzega, A., Melegari, G., Trombetta, A., 1992. Processi dinamici del canyon sottomarino di Gioia Tauro (Mare Tirreno). Giorn. Geol. 54 (2), 199−213.
Conte, A.M., Martorelli, E., Calarco, M., Sposato, A., Perinelli, C., Coltelli, M., Chiocci, F.L., 2014. The 1891 submarine eruption offshore Pantelleria Island (Sicily Channel, Italy): identification of the vent and characterization of products and eruptive style. G-cubed 15 (6), 2555−2574.
Coombs, M.L., White, S.M., Scholl, D.W., 2007. Massive edifice failure at Aleutian arc volcanoes. Earth Planet Sci. Lett. 256 (3−4), 403−418.
Correggiari, A., Cattaneo, A., Trincardi, F., 2005. The modern Po Delta system: lobe switching and asymmetric prodelta growth. Mar. Geol. 222, 49−74.
Cosentino, A., Giacobbe, S., 2011. The new potential invader Linopherus canariensis (Polychaeta: Amphinomidae) in a Mediterranean coastal lake: colonization dynamics and morphological remarks. Mar. Pollut. Bull. 62 (2), 236−245.
Dan, G., Sultan, N., Savoye, B., 2007. The 1979 Nice harbour catastrophe revisited: trigger mechanism inferred from geotechnical measurements and numerical modelling. Mar. Geol. 245 (1−4), 40−64.
Danovaro, R., Corinaldesi, C., D'Onghia, G., Galil, B., Gambi, C., Gooday, A.J., Lampadariou, N., Luna, G.M., Morigi, C., Olu, K., Polymnakou, P., Sabbatini, A., Sardà, F., Sibuet, M., Tselepides, A., 2010. Deep-sea biodiversity in the Mediterranean Sea: the known, the unknown, and the unknowable. PLoS One 5 (8), e11832.
Davies, S.M., 2015. Cryptotephras: the revolution in correlation and precision dating. J. Quat. Sci. 30 (2), 114−130.
de Alteriis, G., Violante, C., 2009. Catastrophic landslides off Ischia volcanic island (Italy) during prehistory. Geol. Soc. Spec. Publ. 322 (1), 73−104.
de Alteriis, G., Insinga, D.D., Morabito, S., Morra, V., Chiocci, F.L., Terrasi, F., Lubritto, C., Di Benedetto, C., Pazzanese, M., 2010. Age of submarine debris avalanches and tephrostratigraphy offshore Ischia Island, Tyrrhenian Sea, Italy. Mar. Geol. 278 (1−4), 1−18.
de Vries, B.V.W., Davies, T., 2015. Landslides, debris avalanches, and volcanic gravitational deformation. In: The Encyclopedia of Volcanoes. Academic Press, pp. 665−685.
Della Seta, M., Marotta, E., Orsi, G., de Vita, S., Sansivero, F., Fredi, P., 2012. Slope instability induced by volcano-tectonics as an additional source of hazard in active volcanic areas: the case of Ischia island (Italy). Bull. Volcanol. 74 (1), 79−106.
Dercourt, J., Zonenshain, L.P., Ricou, L.E., Kazmin, V.G., Le Pichon, X., Knipper, A.L., Grandjacquet, C., Sbortshikov, I.M., Geyssant, J., Lepvrier, C., Pechersky, D.H., Boulin, J., Sibuet, J.-C., Savostin, L.A., Sorokhtin, O., Westphal, M., Bazhenov, M.L., Lauer, J.P., Biju-Duval, B., 1986. Geological evolution of the tethys belt from the Atlantic to the pamirs since the lias. Tectonophysics 123 (1−4), 241−315.
Di Roberto, A., Bertagnini, A., Pompilio, M., Gamberi, F., Marani, M.P., Rosi, A.M., 2008. Newly discovered submarine flank eruption at Stromboli volcano (Aeolian Islands, Italy). Geophys. Res. Lett. 35 (16).
Di Traglia, F., et al., 2022. Subaerial-submarine morphological changes at Stromboli volcano (Italy) induced by the 2019−2020 eruptive activity. Geomorphology 400, 108093. https://doi.org/10.1016/j.geomorph.2021.108093.

Dimitrov, L., Woodside, J., 2003. Deep sea pockmark environments in the eastern Mediterranean. Mar. Geol. 195 (1−4), 263−276.

Droghei, R., Falcini, F., Casalbore, D., Martorelli, E., Mosetti, R., Sannino, G., Santoleri, R., Chiocci, F.L., 2016. The role of Internal Solitary Waves on deep-water sedimentary processes: the case of up-slope migrating sediment waves off the Messina Strait. Sci. Rep. 6 (1), 1−8.

Dupré, S., Woodside, J., Foucher, J.-P., de Lange, G., Mascle, J., Boetius, A., Mastalerz, V., Stadnitskaia, A., Ondréas, H., Huguen, C., Harmegnies, F., Gontharet, S., Loncke, L., Deville, E., Niemann, H., Omoregie, E., Olu-Le Roy, K., Fiala-Medioni, A., Dählmann, A., Caprais, J.-C., Prinzhofer, A., Sibuet, M., Pierre, C., Sinninghe Damsté, J., NAUTINIL Scientific Party, 2007. Seafloor geological studies above active gas chimneys off Egypt (central nile deep sea fan). Deep Sea Res. Oceanogr. Res. Pap. 54 (7), 1146−1172.

Dupré, S., Buffet, G., Mascle, J., Foucher, J.-P., Gauger, S., Boetius, A., Marfia, C., the AsterX AUV Team, the Quest ROV Team, the BIONIL Scientific Party, 2008. High-resolution mapping of large gas emitting mud volcanoes on the Egyptian continental margin (Nile Deep Sea Fan) by AUV surveys. Mar. Geophys. Res. 29 (4), 275−290.

Dupré, S., Woodside, J., Klaucke, I., Mascle, J., Foucher, J.-P., 2010. Widespread active seepage activity on the Nile Deep Sea Fan (offshore Egypt) revealed by high-definition geophysical imagery. Mar. Geol. 275 (1−4), 1−19.

Dupré, S., Mascle, J., Foucher, J.-P., Harmegnies, F., Woodside, J., Pierre, C., 2014. Warm brine lakes in craters of active mud volcanoes, Menes caldera off NW Egypt: evidence for deep-rooted thermogenic processes. Geo Mar. Lett. 34 (2−3), 153−168.

Durrieu de Madron, X., Ramondenc, S., Berline, L., Houpert, L., Bosse, A., Martini, S., Guidi, L., Conan, P., Curtil, C., Delsaut, N., Kunesch, S., Ghiglione, J.F., Marsaleix, P., Pujo-Pay, M., Séverin, T., Testor, P., Tamburini, C., the ANTARES collaboration, 2017. Deep sediment resuspension and thick nepheloid layer generation by open-ocean convection. J. Geophys. Res. Oceans 122 (3), 2291−2318.

Ercilla, G., Juan, C., Hernandez-Molina, F.J., Bruno, M., Estrada, F., Alonso, B., Casas, D., Farran, M., Llave, E., García, M., Vázquez, J.T., D'Acremont, E., Gorini, C., Palomino, D., Valencia, J., El Moumni, B., Ammar, A., 2016. Significance of bottom currents in deep-sea morphodynamics: an example from the Alboran Sea. Mar. Geol. 378, 157−170.

Ercilla, G., Casas, D., Alonso, B., Casalbore, D., Galindo-Zaldívar, J., García-Gil, S., Martorelli, E., Vázquez, J.-T., Azpiroz-Zabala, M., DoCouto, D., Estrada, F., Fernández-Puga, M.C., González-Castillo, L., Gónzalez-Vida, J.M., Idárraga-García, J., Juan, C., Macías, J., Madarieta-Txurruka, A., Nespereira, J., Palomino, D., Sánchez-Guillamón, O., Tendero-Salmerón, V., Teixeira, M., Valencia, J., Yenes, M., 2021. Offshore geological hazards: charting the course of progress and future directions. Oceans 2 (2), 393−428.

Esposito, A., Giordano, G., Anzidei, M., 2006. The 2002−2003 submarine gas eruption at Panarea volcano (Aeolian Islands, Italy): volcanology of the seafloor and implications for the hazard scenario. Mar. Geol. 227 (1−2), 119−134.

Faccenna, C., Becker, T.W., Auer, L., Billi, A., Boschi, L., Brun, J.P., Capitanio, A., Funiviello, F., Horvàth, Jolivet, L., Piromallo, C., Royden, L., Rossetti, F., Serpelloni, E., 2014. Mantle dynamics in the mediterranean. Rev. Geophys. 52 (3), 283−332.

Fanget, A.S., Berné, S., Jouet, G., Bassetti, M.A., Dennielou, B., Maillet, G.M., Tondut, M., 2014. Impact of relative sea level and rapid climate changes on the architecture and lithofacies of the Holocene Rhone subaqueous delta (Western Mediterranean Sea). Sediment. Geol. 305, 35–53.

Favali, P., De Santis, A., Anna, G.D., Di Sabatino, B., Sedita, M., Rubino, E., 2006. A new active volcano in the Tyrrhenian Sea? Ann. Geophys. 49 (2–3).

Field, M.E., Gardner, J.V., Jennings, A.E., Edwards, B.D., 1982. Earthquake-induced sediment failures on a 0.25° slope, Klamath River delta, California. Geology 10, 542–546.

Foerstner, H., 1891. Das Gestein der 1891 bei Pantelleria entstandenen Vulcaninsel und seine Beziehungen zu den jüngsten Eruptivgesteinen der Nachbarschaft. Tsch. Min. Petr. Mitth. 12, 510–521.

Foglini, F., Campiani, E., Trincardi, F., 2016. The reshaping of the South West Adriatic Margin by cascading of dense shelf waters. Mar. Geol. 375, 64–81.

Forni, F., Lucchi, F., Peccerillo, A., Tranne, C.A., Rossi, P.L., Frezzotti, M.L., 2013. Stratigraphy and geological evolution of the Lipari volcanic complex (central Aeolian archipelago). Geo. Soc. 37 (1), 213–279.

Francalanci, L., Lucchi, F., Keller, J., De Astis, G., Tranne, C.A., 2013. Eruptive, volcanotectonic and magmatic history of the Stromboli volcano (north-eastern Aeolian archipelago). Geol. Soc. 37 (1), 397–471.

Friedrich, W.L., 2013. The minoan eruption of Santorini around 1613 BC and its consequences. Tagungen des Landesmuseums für Vorgeschichte Halle 9 (2013), 37–48.

Galgani, F., Souplet, A., Cadiou, Y., 1996. Accumulation of debris on the deep sea floor off the French Mediterranean coast. Mar. Ecol. Prog. Ser. 142, 225–234.

Galy, V., France-Lanord, C., Beyssac, O., Faure, P., Kudrass, H., Palhol, F., 2007. Efficient organic carbon burial in the Bengal fan sustained by the Himalayan erosional system. Nature 450, 407–410.

Gamberi, F., 2001. Volcanic facies associations in a modern volcaniclastic apron (Lipari and Vulcano offshore, Aeolian Island Arc). Bull. Volcanol. 63 (4), 264–273.

Gamberi, F., Marani, M., Savelli, C., 1997. Tectonic, volcanic and hydrothermal features of a submarine portion of the Aeolian arc (Tyrrhenian Sea). Mar. Geol. 140 (1–2), 167–181.

Gamberi, F., Pellegrini, C., Dalla Valle, G., Scarponi, D., Bohacs, K., Trincardi, F., 2020. Compound and hybrid clinothems of the last lowstand Mid-Adriatic Deep: Processes, depositional environments, controls and implications for stratigraphic analysis of prograding systems. Basin Research, 32(Clinoforms and Clinothems: Fundamental Elements of Basin Infill) 363–377.

García-Pintado, J., Martínez-Mena, M., Barberá, G.G., Albaladejo, J., Castillo, V.M., 2007. Anthropogenic nutrient sources and loads from a Mediterranean catchment into a coastal lagoon: Mar Menor, Spain. Sci. Total Environ. 373 (1), 220–239.

Gauchery, T., Rovere, M., Pellegrini, C., Cattaneo, A., Campiani, E., Trincardi, F., 2021a. Factors controlling margin instability during the plio-quaternary in the gela basin (Strait of Sicily, Mediterranean sea). Mar. Petrol. Geol. 123, 104767.

Gauchery, T., Rovere, M., Pellegrini, C., Asioli, A., Tesi, T., Cattaneo, A., Trincardi, F., 2021b. Post-LGM multi-proxy sedimentary record of bottom-current variability and downslope sedimentary processes in a contourite drift of the Gela Basin (Strait of Sicily). Mar. Geol. 106564.

Geletti, R., Del Ben, A., Busetti, M., Ramella, R., Volpi, V., 2008. Gas seeps linked to salt structures in the Central Adriatic Sea. Basin Res. 20 (4), 473–487.

Giordano, G., De Astis, G., 2021. The summer 2019 basaltic Vulcanian eruptions (paroxysms) of Stromboli. Bull. Volcanol. 83 (1), 1−27.

Giresse, P., Loncke, L., Huguen, C., Muller, C., Mascle, J., 2010. Nature and origin of sedimentary clasts associated with mud volcanoes in the Nile deep-sea fan. Relationships with fluid venting. Sediment. Geol. 228 (3−4), 229−245.

Goldfinger, C., 2011. Submarine paleoseismology based on turbidite records. Ann. Rev. Mar. Sci 3, 35−66.

Gontharet, S., Pierre, C., Blanc-Valleron, M.M., Rouchy, J.M., Fouquet, Y., Bayon, G., Foucher, J.P., Woodside, J., Mascle, J., 2007. Nature and origin of diagenetic carbonate crusts and concretions from mud volcanoes and pockmarks of the Nile deep-sea fan (eastern Mediterranean Sea). Deep Sea Res. Part II Top. Stud. Oceanogr. 54 (11−13), 1292−1311.

Goodman-Tchernov, B.N., Dey, H.W., Reinhardt, E.G., McCoy, F., Mart, Y., 2009. Tsunami waves generated by the Santorini eruption reached Eastern Mediterranean shores. Geology 37 (10), 943−946.

Grilli, S.T., Tappin, D.R., Carey, S., Watt, S.F., Ward, S.N., Grilli, A.R., Engwell, S.L., Zhang, C., Kirby, J.T., Schambach, L., Muin, M., 2019. Modelling of the tsunami from the December 22, 2018 lateral collapse of Anak Krakatau volcano in the Sunda straits, Indonesia. Sci. Rep. 9 (1), 1−13.

Grünke, S., Felden, J., Lichtschlag, A., Girnth, A.C., De Beer, D., Wenzhöfer, F., Boetius, A., 2011. Niche differentiation among mat-forming, sulfide-oxidizing bacteria at cold seeps of the nile deep sea fan (eastern Mediterranean sea). Geobiology 9 (4), 330−348.

Harris, P.T., Macmillan-Lawler, M., Rupp, J., Baker, E.K., 2014. Geomorphology of the oceans. Mar. Geol. 352, 4−24.

Hebbeln, D., Van Rooij, D., Wienberg, C., 2016. Good neighbours shaped by vigorous currents: cold-water coral mounds and contourites in the North Atlantic. Mar. Geol. 378, 171−185.

Heezen, B.C., Hollister, C.D., Ruddiman, W.F., 1966. Shaping of the continental rise by deep geostrophic contour currents. Science 152 (3721), 502−508.

Hiscott, R.N., Aksu, A.E., Yaşar, D., Kaminski, M.A., Mudie, P.J., Kostylev, V.E., MacDonald, J.C., Isler, F.I., Lord, A.R., 2002. Deltas south of the Bosphorus strait record persistent Black sea outflow to the marmara sea since ∼10 ka. Mar. Geol. 190 (1), 95−118.

Huguen, C., Mascle, J., Chaumillon, E., Kopf, A., Woodside, J., Zitter, T., 2004. Structural setting and tectonic control of mud volcanoes from the central Mediterranean Ridge (eastern Mediterranean). Mar. Geol. 209 (1−4), 245−263.

Huguen, C., Mascle, J., Woodside, J., Zitter, T., Foucher, J.P., 2005. Mud volcanoes and mud domes of the Central Mediterranean Ridge: near-bottom and in situ observations. Deep Sea Res. Oceanogr. Res. Pap. 52 (10), 1911−1931.

Huguen, C., Foucher, J.P., Mascle, J., Ondréas, H., Thouement, M., Gontharet, S., Stadnitskaia, A., Pierre, C., Bayon, G., Loncke, L., Boetius, A., Bouloubassi, I., de Lange, G., Fouquet, Y., Woodside, J., Dupré, S., the NAUTINIL Scientific Party, 2009. Menes caldera, a highly active site of brine seepage in the Eastern Mediterranean sea: "in situ" observations from the NAUTINIL expedition, 2003. Mar. Geol. 261 (1−4), 138−152.

Huhn, K., Arroyo, M., Cattaneo, A., Clare, M.A., Gràcia, E., Harbitz, C.B., Krastel, S., Kopf, A., Finn Løvholt, F., Rovere, M., Strasser, M., Talling, P.J., Urgeles, R., 2019. Modern submarine landslide complexes: a short review. In: Ogata, K., Festa, A., Pini, G.A.

(Eds.), Submarine Landslides: Subaqueous Mass Transport Deposits from Outcrops to Seismic Profiles, Geophysical Monograph Series. Wiley, pp. 181−200.
Ikehara, K., 2015. Marine tephra in the Japan Sea sediments as a tool for paleoceanography and paleoclimatology. Prog. Earth Planet. Sci. 2 (1), 1−14.
Ingrassia, M., Martorelli, E., Bosman, A., Macelloni, L., Sposato, A., Chiocci, F.L., 2015. The Zannone Giant Pockmark: first evidence of a giant complex seeping structure in shallow-water, central Mediterranean Sea, Italy. Mar. Geol. 363, 38−51.
Johnston, E.N., Sparks, R.S.J., Phillips, J.C., Carey, S., 2014. Revised estimates for the volume of the late Bronze age minoan eruption, Santorini, Greece. J. Geol. Soc. 171 (4), 583−590.
Judd, A.G., Hovland, M., 2007. Seabed Fluid Flow. The Impact on Geology, Biology and the Marine Environment. Cambridge University Press, Cambridge, p. 475.
Kane, I.A., Clare, M.A., 2019. Dispersion, accumulation, and the ultimate fate of microplastics in deep-marine environments: a review and future directions. Front. Earth Sci. 7, 80.
Kane, I.A., Clare, M.A., Miramontes, E., Wogelius, R., Rothwell, J.J., Garreau, P., Pohl, F., 2020. Seafloor microplastic hotspots controlled by deep-sea circulation. Science 368 (6495), 1140−1145.
Keating, B.H., McGuire, W.J., 2000. Island edifice failures and associated tsunami hazards. Pure Appl. Geophys. 157 (6), 899−955.
Kelly, J.T., Carey, S., Pistolesi, M., Rosi, M., Croff-Bell, K.L., Roman, C., Marani, M., 2014. Exploration of the 1891 Foerstner submarine vent site (Pantelleria, Italy): insights into the formation of basaltic balloons. Bull. Volcanol. 76 (7), 1−18.
Kelner, M., Migeon, S., Tric, E., Couboulex, F., Dano, A., Lebourg, T., Taboada, A., 2016. Frequency and triggering of small-scale submarine landslides on decadal timescales: analysis of 4D bathymetric data from the continental slope offshore Nice (France). Mar. Geol. 379, 281−297.
Khripounoff, A., Vangriesheim, A., Crassous, P., Etoubleau, J., 2009. High frequency of sediment gravity flow events in the Var submarine canyon (Mediterranean Sea). Mar. Geol. 263 (1−4), 1−6.
Khripounoff, A., Crassous, P., Bue, N.L., Dennielou, B., Jacinto, R.S., 2012. Different types of sediment gravity flows detected in the Var submarine canyon (northwestern Mediterranean Sea). Prog. Oceanogr. 106, 138−153.
Kokelaar, P., 1986. Magma-water interactions in subaqueous and emergent basaltic. Bull. Volcanol. 48 (5), 275−289.
Kokelaar, P., Romagnoli, C., 1995. Sector collapse, sedimentation and clast population evolution at an active island-arc volcano: Stromboli, Italy. Bull. Volcanol. 57 (4), 240−262.
Korus, J.T., Fielding, C.R., 2015. Asymmetry in Holocene river deltas: patterns, controls, and stratigraphic effects. Earth Sci. Rev. 150, 219−242.
Langone, L., Conese, I., Miserocchi, S., Boldrin, A., Bonaldo, D., Carniel, S., Chiggiato, J., Turchetto, M., Borghini, M., Tesi, T., 2016. Dynamics of particles along the western margin of the Southern Adriatic: processes involved in transferring particulate matter to the deep basin. Mar. Geol. 375, 28−43.
Lastras, G., Canals, M., Urgeles, R., Amblas, D., Ivanov, M., Droz, L., Dennielou, B., Fabrés, J., Schoolmeester, T., Akhmetzhanov, A., Orange, D., García-García, A., 2007. A walk down the Cap de Creus canyon, Northwestern Mediterranean Sea: recent processes inferred from morphology and sediment bedforms. Mar. Geol. 246 (2−4), 176−192.
Liubartseva, S., Coppini, G., Lecci, R., Clementi, E., 2018. Tracking plastics in the Mediterranean: 2D Lagrangian model. Mar. Pollut. Bull. 129 (1), 151−162.

Lobo, F.J., Fernández-Salas, L.M., Moreno, I., Sanz, J.L., Maldonado, A., 2006. The sea-floor morphology of a Mediterranean shelf fed by small rivers, northern Alboran Sea margin Cont. Shelf Res 26 (20), 2607–2628.

Loher, M., Ceramicola, S., Wintersteller, P., Meinecke, G., Sahling, H., Bohrmann, G., 2018. Mud volcanism in a canyon: morphodynamic evolution of the active Venere mud volcano and its interplay with Squillace canyon, central mediterranean. G-cubed 19 (2), 356–378.

Lo Iacono, C., Robert, K., Gonzalez-Villanueva, R., Gori, A., Gili, J.M., Orejas, C., 2018. Predicting cold-water coral distribution in the Cap de Creus Canyon (NW Mediterranean): implications for marine conservation planning. Prog. Oceanogr. 169, 169–180.

Loncke, L., Mascle, J., Fanil Scientific Parties, 2004. Mud volcanoes, gas chimneys, pockmarks and mounds in the Nile deep-sea fan (Eastern Mediterranean): geophysical evidences. Mar. Petrol. Geol. 21 (6), 669–689.

Lozano, C.J., Candela, J., 1995. The M (2) tide in the Mediterranean Sea: dynamic analysis and data assimilation. Oceanol. Acta 18 (4), 419–441.

Lykousis, V., Alexandri, S., Woodside, J., de Lange, G., Dählmann, A., Perissoratis, C., Heeschen, K., Ioakim, C., Sakellariou, D., Nomikou, P., Rousakis, G., Casas, D., Ballas, D., Ercilla, G., 2009. Mud volcanoes and gas hydrates in the Anaximander mountains (eastern Mediterranean sea). Mar. Petrol. Geol. 26, 854–872.

Madricardo, F., Foglini, F., Kruss, A., Ferrarin, C., Pizzeghello, N.M., Murri, C., Trincardi, F., 2017. High resolution multibeam and hydrodynamic datasets of tidal channels and inlets of the Venice Lagoon. Sci. Data 4 (1), 1–14.

Madricardo, F., Foglini, F., Campiani, E., Grande, V., Catenacci, E., Petrizzo, A., Kruss, A., Toso, C., Trincardi, F., 2019. Assessing the human footprint on the sea-floor of coastal systems: the case of the Venice Lagoon, Italy. Sci. Rep. 9 (6615). https://doi.org/10.1038/s41598-019-43027-7.

Maicu, F., De Pascalis, F., Ferrarin, C., Umgiesser, G., 2018. Hydrodynamics of the Po river-delta-sea system. J. Geophys. Res.: Oceans 123 (9), 6349–6372.

Maramai, A., Graziani, L., Tinti, S., 2005. Tsunamis in the Aeolian islands (southern Italy): a review. Mar. Geol. 215 (1–2), 11–21.

Marani, M., Argnani, A., Roveri, M., Trincardi, F., 1993. Sediment drifts and erosional surfaces in the central Mediterranean: seismic evidence of bottom-current activity. Sediment. Geol. 82 (1–4), 207–220.

Martín, J., Puig, P., Palanques, A., Ribó, M., 2014. Trawling-induced daily sediment resuspension in the flank of a Mediterranean submarine canyon. Deep Sea Res. Part II Top. Stud. Oceanogr. 104, 174–183.

Martorelli, E., Falcini, F., Salusti, E., Chiocci, F.L., 2010. Analysis and modeling of contourite drifts and contour currents off promontories in the Italian Seas (Mediterranean Sea). Mar. Geol. 278 (1–4), 19–30.

Martorelli, E., Petroni, G., Chiocci, F.L., 2011. Contourites offshore Pantelleria island (Sicily Channel, Mediterranean sea): depositional, erosional and biogenic elements. Geo Mar. Lett. 31 (5–6), 481–493.

Martorelli, E., Bosman, A., Casalbore, D., Falcini, F., 2016. Interaction of down-slope and along-slope processes off Capo Vaticano (southern Tyrrhenian Sea, Italy), with particular reference to contourite-related landslides. Mar. Geol. 378, 43–55.

Mas, V., Mulder, T., Dennielou, B., Schmidt, S., Khripounoff, A., Savoye, B., 2010. Multiscale spatio-temporal variability of sedimentary deposits in the Var turbidite system (North-Western Mediterranean Sea). Mar. Geol. 275 (1–4), 37–52.

Mascle, J., Mary, F., Praeg, D., Brosolo, L., Camera, L., Ceramicola, S., Dupré, S., 2014. Distribution and geological control of mud volcanoes and other fluid/free gas seepage features in the Mediterranean Sea and nearby Gulf of Cadiz. Geo Mar. Lett. 34 (2−3), 89−110.

Maugeri, T.L., Bianconi, G., Canganella, F., Danovaro, R., Gugliandolo, C., Italiano, F., Lentini, V., Manini, E., Nicolaus, B., 2010. Shallow hydrothermal vents in the southern Tyrrhenian Sea. Chem. Ecol. 26 (S1), 285−298.

Mazzanti, P., Bozzano, F., 2011. Revisiting the February 6th 1783 Scilla (Calabria, Italy) landslide and tsunami by numerical simulation. Mar. Geophys. Res. 32 (1), 273−286.

Mazzini, A., Etiope, G., 2017. Mud volcanism: an updated review. Earth Sci. Rev. 168, 81−112.

McGuire, W.J., 2006. Lateral collapse and tsunamigenic potential of marine volcanoes. Geol. Soc. Spec. Publ. 269 (1), 121−140.

Medinaut/Medineth Shipboard Scientific Party, 2000. Linking Mediterranean brine pools and mud volcanism. Eos 81 (51), 625−632.

Micallef, A., Person, M., Berndt, C., Bertoni, C., Cohen, D., Dugan, B., Evans, R., Haroon, A., Hensen, C., Jegen, M., Key, K., Kooi, H., Liebetrau, V., Lofi, J., Mailloux, B.J., Martin-Nagle, R., Michael, H.A., Muller, T., Schmidt, M., Schwalenberg, K., Trembath-Reichert, E., Weymer, B., Zhang, Y.P., Thomas, A.T., 2020. Offshore freshened groundwater in continental margins. Rev. Geophys. 59 (1) e2020RG000706.

Milia, A., Torrente, M.M., Bellucci, F., 2012. A possible link between faulting, cryptodomes and lateral collapses at Vesuvius Volcano (Italy). Global Planet. Change 90, 121−134.

Milliman, J.D., Syvitski, J.P., 1992. Geomorphic/tectonic control of sediment discharge to the ocean: the importance of small mountainous rivers. J. Geol. 100 (5), 525−544.

Minoura, K., Imamura, F., Kuran, U., Nakamura, T., Papadopoulos, G.A., Takahashi, T., Yalciner, A.C., 2000. Discovery of Minoan tsunami deposits. Geology 28 (1), 59−62.

Miramontes, E., Cattaneo, A., Jouet, G., Thereau, E., Thomas, Y., Rovere, M., Cauquil, E., Trincardi, F., 2016. The Pianosa contourite depositional system (northern Tyrrhenian Sea): drift morphology and Plio-Quaternary stratigraphic evolution. Mar. Geol. 378, 20−42.

Miramontes, E., Garreau, P., Caillaud, M., Jouet, G., Pellen, R., Hernández-Molina, F.J., Clare, M., Cattaneo, A., 2019. Contourite distribution and bottom currents in the NW Mediterranean Sea: coupling seafloor geomorphology and hydrodynamic modelling. Geomorphology 333, 43−60.

Miramontes, E., Thiéblemont, A., Babonneau, N., Penven, P., Raisson, F., Droz, L., Jorry, S.J., Fierens, R., Counts, J.W., Wilckens, H., Cattaneo, A., Jouet, G., 2021. Contourite and mixed turbidite-contourite systems in the Mozambique Channel (SW Indian Ocean): link between geometry, sediment characteristics and modelled bottom currents. Mar. Geol. 437, 106502.

Mitchell, N.C., Masson, D.G., Watts, A.B., Gee, M.J., Urgeles, R., 2002. The morphology of the submarine flanks of volcanic ocean islands: a comparative study of the Canary and Hawaiian hotspot islands. J. Volcanol. Geoth. Res. 115 (1−2), 83−107.

Monecke, T., Petersen, S., Hannington, M.D., Anzidei, M., Esposito, A., Giordano, G., Anzidei, M., Esposito, A., Giordano, G., Augustin, N., Melchert, B., Hocking, M., 2012. Explosion craters associated with shallow submarine gas venting off Panarea island, Italy. Bull. Volcanol. 74 (9), 1937−1944.

Newnham, R.M., Eden, D.N., Lowe, D.J., Hendy, C.H., 2003. Rerewhakaaitu Tephra, a land–sea marker for the Last Termination in New Zealand, with implications for global climate change. Quat. Sci. Rev. 22 (2–4), 289–308.

Nomikou, P., Papanikolaou, D., Tibaldi, A., Carey, S., Livanos, I., Bell, K.L.C., Rousakis, G., 2014. The detection of volcanic debris avalanches (VDAs) along the Hellenic Volcanic Arc, through marine geophysical techniques. In: Lamarche, G., et al. (Eds.), Submarine Mass Movements and Their Consequences. Springer, pp. 339–349.

Olu-Le Roy, K., Sibuet, M., Fiala-Médioni, A., Gofas, S., Salas, C., Mariotti, A., Foucher, J.-P., Woodside, J., 2004. Cold seep communities in the deep eastern Mediterranean Sea: composition, symbiosis and spatial distribution on mud volcanoes. Deep Sea Res. Oceanogr. Res. Pap. 51, 1915–1936.

Palanques, A., Puig, P., Durrieu de Madron, X., Sanchez-Vidal, A., Pasqual, C., Martín, J., Calafat, A., Heussner, S., Canals, M., 2012. Sediment transport to the deep canyons and open-slope of the western Gulf of Lions during the 2006 intense cascading and open-sea convection period. Prog. Oceanogr. 106, 1–15.

Paradis, S., Goñi, M., Masqué, P., Durán, R., Arjona-Camas, M., Palanques, A., Puig, P., 2021. Persistence of biogeochemical alterations of deep-sea sediments by bottom trawling. Geophys. Res. Lett. 48 (2) e2020GL091279.

Pastore, M., 1993. Mar Piccolo. Nuova Editrice Apulia, Martina Franca, Taranto.

Pellegrini, C., Bohacs, K. M., Drexler, T. M., Gamberi, F., Rovere, M., & Trincardi, F. (2017, December). Identifying the sequence boundary in over-and under-supplied contexts: the case of the late Pleistocene adriatic continental margin. In *Sequence Stratigraphy: the Future Defined, Proceedings of the 36th Annual Perkins-Rosen Research Conference* (pp. 160–182).

Pellegrini, C., Asioli, A., Bohacs, K.M., Drexler, T.M., Feldman, H.R., Sweet, M.L., Trincardi, F., 2018. The late Pleistocene Po River lowstand wedge in the Adriatic Sea: Controls on architecture variability and sediment partitioning. Mar. Pet. Geol. 96, 16–50.

Pellegrini, C., Maselli, V., Cattaneo, A., Piva, A., Ceregato, A., Trincardi, F., 2015. Anatomy of a compound delta from the post-glacial transgressive record in the Adriatic Sea. Mar. Geol. 362, 43–59.

Pellegrini, C., Maselli, V., Trincardi, F., 2016. Pliocene–Quaternary contourite depositional system along the south-western Adriatic margin: changes in sedimentary stacking pattern and associated bottom currents. Geo Mar. Lett. 36 (1), 67–79.

Pellegrini, C., Patruno, S., Helland-Hansen, W., Steel, R.J., Trincardi, F., 2020. Clinoforms and clinothems: fundamental elements of basin infill. Basin Res. 32, 187–205 (Clinoforms and Clinothems: Fundamental Elements of Basin Infill).

Pellegrini, C., Tesi, T., Schieber, J., Bohacs, K.M., Rovere, M., Asioli, A., Trincardi, F., 2021. Fate of terrigenous organic carbon in muddy clinothems on continental shelves revealed by stratal geometries: insight from the Adriatic sedimentary archive. Global Planet. Change 203, 103539.

Pérez-Ruzafa, A., Marcos, C., Pérez-Ruzafa, I.M., 2011. Mediterranean coastal lagoons in an ecosystem and aquatic resources management context. Phys. Chem. Earth, Parts A/B/C 36 (5–6), 160–166.

Pham, C.K., Ramirez-Llodra, E., Alt, C.H., Amaro, T., Bergmann, M., Canals, M., Company, J.B., Davies, J., Duineveld, G., Galgani, F., Howell, K.L., Veerle, A.I.H., Isidro, E., Jones, D.O.B., Lastras, G., Morato, T., Gomes-Pereira, J.N., Purser, A., Stewart, H., Tojeira, I., Tubau, X., Van Rooij, D., Tyler, P.A., 2014. Marine litter

distribution and density in European seas, from the shelves to deep basins. PLoS One 9 (4) e95839.
Pierdomenico, M., Casalbore, D., Chiocci, F.L., 2019. Massive benthic litter funnelled to deep sea by flash-flood generated hyperpycnal flows. Sci. Rep. 9 (1), 1−10.
Pierdomenico, M., Casalbore, D., Chiocci, F.L., 2020. The key role of canyons in funnelling litter to the deep sea: a study of the Gioia Canyon (Southern Tyrrhenian Sea). Anthropocene 30, 100237.
Pierre, C., Bayon, G., Blanc-Valleron, M.-M., Mascle, J., Dupré, S., 2014. Authigenic carbonates related to active seepage of methane-rich hot brines at the Cheops mud volcano, Menes caldera (Nile deep-sea fan, eastern Mediterranean Sea). Geo Mar. Lett. 34 (2−3), 253−267.
Pino, N.A., Piatanesi, A., Valensise, G., Boschi, E., 2009. The 28 December 1908 Messina Straits earthquake (Mw 7.1): a great earthquake throughout a century of seismology. Seismol Res. Lett. 80 (2), 243−259.
Polonia, A., Bonatti, E., Camerlenghi, A., Lucchi, R.G., Panieri, G., Gasperini, L., 2013. Mediterranean megaturbidite triggered by the AD 365 Crete earthquake and tsunami. Sci. Rep. 3 (1), 1−12.
Poncelet, C., Billant, G., Corre, M.-P., 2021. Globe (GLobal oceanographic bathymetry explorer) software. SEANOE. https://doi.org/10.17882/70460.
Puig, P., Canals, M., Company, J.B., Martín, J., Amblas, D., Lastras, G., Palanques, A., Calafat, A.M., 2012. Ploughing the deep sea floor. Nature 489 (7415), 286−289.
Praeg, D., Ceramicola, S., Barbieri, R., Unnithan, V., Wardell, N., 2009. Tectonically-driven mud volcanism since the late Pliocene on the Calabrian accretionary prism, central Mediterranean Sea. Mar. Petrol. Geol. 26 (9), 1849−1865.
Praeg, D., Ketzer, J., Augustin, A., Migeon, S., Ceramicola, S., Dano, A., Ducassou, E., Dupré, S., Mascle, J., Rodrigues, L., 2014. Fluid seepage in relation to seabed deformation on the central nile deep-sea fan, Part 2: evidence from multibeam and sidescan imagery. In: Krastel, S., Behrmann, J.-H., Völker, D. et al. (Eds.), Submarine Mass Movements and Their Consequences, Vol 37. Advances in Natural and Technological Hazards Research. Springer International Publishing, pp. 141−150.
Praeg, D., Migeon, S., Mascle, J., Unnithan, V., Wardell, N., Geletti, R., Ketzer, J.M., 2017. Geophysical evidence of gas hydrates associated with widespread gas venting on the central nile deep-sea fan, offshore Egypt. In: Paper Presented at the 9th International Conference on Gas Hydrates - ICGH9, Denver, United States, 2017-06-25.
Pratson, L.F., Nittrouer, C.A., Wiberg, P.L., Steckler, M.S., Swenson, J.B., Cacchione, D.A., Karson, J.A., Murray, A.B., Wolinksy, M.A., Gerber, T.P., Mullenbach, B.L., Spinelli, G.A., Fulthorpe, C.S., O'grady, D.B., Parker, G., Driscoll, N.W., Burger, R.L., Paola, C., Orange, D.L., Field, M.E., Friedrichs, C.T., Fedele, J.J., 2007. Seascape evolution on clastic continental shelves and slopes. In: Nittrouer, C.A., Austin, J.A., Field, M.E., Kravitz, J.H., Syvitski, J.P.M., Wiberg, P.L. (Eds.), Continental Margin Sedimentation: From Sediment Transport to Sequence Stratigraphy, vol 37. Special Publications of the International Association, Sedimentol, pp. 340−380.
Ramalho, R.S., Quartau, R., Trenhaile, A.S., Mitchell, N.C., Woodroffe, C.D., Ávila, S.P., 2013. Coastal evolution on volcanic oceanic islands: a complex interplay between volcanism, erosion, sedimentation, sea-level change and biogenic production. Earth Sci. Rev. 127, 140−170.

Ratzov, G., Cattaneo, A., Babonneau, N., Déverchère, J., Yelles, K., Bracene, R., Courboulex, F., 2015. Holocene turbidites record earthquake supercycles at a slow-rate plate boundary. Geology 43 (4), 331−334.

Rebesco, M., Hernández-Molina, F.J., Van Rooij, D., Wåhlin, A., 2014. Contourites and associated sediments controlled by deep-water circulation processes: state-of-the-art and future considerations. Mar. Geol. 352, 111−154.

Reiche, S., Hübscher, C., Brenner, S., Betzler, C., Hall, J.K., 2018. The role of internal waves in the late Quaternary evolution of the Israeli continental slope. Mar. Geol. 406, 177−192.

Ribó, M., Puig, P., Muñoz, A., Iacono, C.L., Masqué, P., Palanques, A., Ballesteros, M.G., 2016. Morphobathymetric analysis of the large fine-grained sediment waves over the Gulf of Valencia continental slope (NW Mediterranean). Geomorphology 253, 22−37.

Ribó, M., Durán, R., Puig, P., Van Rooij, D., Guillén, J., Masqué, P., 2018. Large sediment waves over the Gulf of Roses upper continental slope (NW Mediterranean). Mar. Geol. 399, 84−96.

Riccò, A., 1892. Terremoti, sollevamento ed eruzione sottomarina a Pantelleria nella seconda met a dell'ottobre 1891, Annali dell'Ufficio Centr. Meteorol. e Geodinamico XI, 7−27.

Robertson, A.H.F., Emeis, K.C., Richter, C., Blanc, V.M.M., Bouloubassi, I., Brumsack, H.J., Cramp, A., de Lange, G.J., Di Stefano, E., Flecker, R., Frankel, E., Howell, M.W., Janecek, T.R., Jurado, R.M.J., Kemp, A.E.S., Koizumi, I., Kopf, A., Major, C.O., Mart, Y., Pribnow, D.F.C., Rabaute, A., Roberts, A.P., Rullkoetter, J.H., Sakamoto, T., Spezzaferri, S., Staerker, T.S., Stoner, J.S., Whiting, B.M., Woodside, J.M., Ocean Drilling Program L, Shipboard Scientific Party, College Station, TX, United States, 1996. Mud volcanism on the Mediterranean Ridge. In: Emeis Kay, C., Robertson Alastair, H.F., Richter, C., et al. (Eds.), Proceedings of the Ocean Drilling Program, Initial Reports; Mediterranean I; Covering Leg 160 of the Cruises of the Drilling Vessel JOIDES Resolution, Las Palmas, Gran Canaria, to Naples, Italy, Sites 963-973, 7 March−3 May, 1995., Vol 160. Proceedings of the Ocean Drilling Program, Part A: Initial Reports. Texas A&M University, Ocean Drilling Program, College Station, TX, United States, pp. 521−526.

Romagnoli, C., Kokelaar, P., Casalbore, D., Chiocci, F.L., 2009. Lateral collapses and active sedimentary processes on the northwestern flank of Stromboli volcano, Italy. Mar. Geol. 265 (3−4), 101−119.

Römer, M., Sahling, H., Pape, T., dos Santos Ferreira, C., Wenzhöfer, F., Boetius, A., Bohrmann, G., 2014. Methane fluxes and carbonate deposits at a cold seep area of the central nile deep sea fan, eastern Mediterranean sea. Mar. Geol. 347, 27−42.

Ronchi, L., Fontana, A., Correggiari, A., Asioli, A., 2018. Late Quaternary incised and infilled landforms in the shelf of the northern Adriatic Sea (Italy). Mar. Geol. 405, 47−67.

Rosi, M., Levi, S.T., Pistolesi, M., Bertagnini, A., Brunelli, D., Cannavò, V., Di Renzoni, A., Ferranti, F., Renzulli, A., Yoon, D., 2019. Geoarchaeological evidence of middle-age tsunamis at Stromboli and consequences for the tsunami hazard in the southern Tyrrhenian Sea. Sci. Rep. 9 (1), 1−10.

Rovere, M., Gamberi, F., Mercorella, A., Rashed, H., Gallerani, A., Leidi, E., Marani, M., Funari, V., Pini, G.A., 2014. Venting and seepage systems associated with mud volcanoes and mud diapirs in the southern Tyrrhenian Sea. Mar. Geol. 347, 153−171.

Rovere, M., Pellegrini, C., Chiggiato, J., Campiani, E., Trincardi, F., 2019. Impact of dense bottom water on a continental shelf: an example from the SW Adriatic margin. Mar. Geol. 408, 123−143.

Rovere, M., Mercorella, A., Frapiccini, E., Funari, V., Spagnoli, F., Pellegrini, C., Antoncecchi, I., 2020. Geochemical and geophysical monitoring of hydrocarbon seepage in the Adriatic Sea. Sensors 20 (5), 1504.

Roveri, M., 2002. Sediment drifts of the Corsica channel, northern Tyrrhenian Sea. In: Stow, D.A.V., Pudsey, C.J., Howe, J.H., Faugères, J.C., Viana, A.R. (Eds.), Deep-water Contourite Systems: Modern Drifts and Ancient Series, Seismic and Sedimentary Characteristics, vol 22. Geological Society, London, Memoirs, pp. 191−208.

Roveri, M., Flecker, R., Krijgsman, W., Lofi, J., Lugli, S., Manzi, V., Sierro, F.J., Bertini, A., Camerlenghi, A., De Lange, G., Govers, R., Hilgen, F.J., Hübscher, C., Meijer, P.T., Stoica, M., 2014. The Messinian Salinity Crisis: past and future of a great challenge for marine sciences. Mar. Geol. 352, 25−58.

Ryan, W.B.F., Heezen, B.C., 1965. Ionian Sea submarine canyons and the 1908 Messina turbidity current. Geol. Soc. Am. Bull. 76 (8), 915−932.

Sabatier, P., Dezileau, L., Blanchemanche, P., Siani, G., Condomines, M., Bentaleb, I., Piquès, G., 2010. Holocene variations of radiocarbon reservoir ages in a Mediterranean lagoonal system. Radiocarbon 52 (1), 91−102.

Santacroce, R., Cioni, R., Marianelli, P., Sbrana, A., Sulpizio, R., Zanchetta, G., Donahue, D.J., Joron, J.L., 2008. Age and whole rock−glass compositions of proximal pyroclastics from the major explosive eruptions of Somma-Vesuvius: a review as a tool for distal tephrostratigraphy. J. Volcanol. Geoth. Res. 177 (1), 1−18.

Savini, A., Corselli, C., 2010. High-resolution bathymetry and acoustic geophysical data from Santa maria di Leuca cold water coral province (northern Ionian Sea—Apulian continental slope). Deep Sea Res. Part II Top. Stud. Oceanogr. 57 (5−6), 326−344.

Savini, A., Malinverno, E., Etiope, G., Tessarolo, C., Corselli, C., 2009. Shallow seep-related seafloor features along the Malta plateau (Sicily channel − Mediterranean Sea): morphologies and geo-environmental control of their distribution. Mar. Petrol. Geol. 26 (9), 1831−1848.

Scalabrin, C., Dupré, S., 2018. Water column acoustics: remote detection of gas seeps. In: Ruffine, L., Broseta, D., Desmedt, A. (Eds.), Gas Hydrates, Volume 2: Geoscience Issues and Potential Industrial Applications. Wiley-ISTE, pp. 11−20.

Schattner, U., Lazar, M., Harari, D., Waldmann, N., 2012. Active gas migration systems offshore northern Israel, first evidence from seafloor and subsurface data. Continent. Shelf Res. 48, 167−172.

Siani, G., Sulpizio, R., Paterne, M., Sbrana, A., 2004. Tephrostratigraphy study for the last 18,000 14C years in a deep-sea sediment sequence for the South Adriatic. Quat. Sci. Rev. 23 (23−24), 2485−2500.

Sibuet, M., Olu, K., 1998. Biogeography, biodiversity and fluid dependence of deep-sea cold-seep communities at active and passive margins. Deep Sea Res. Part II Top. Stud. Oceanogr. 45 (1−3), 517−567.

Somoza, L., Medialdea, T., León, R., Ercilla, G., Vázquez, J.T., Farran, M.l., Hernández-Molina, J., González, J., Juan, C., Fernández-Puga, M.C., 2012. Structure of Mud volcano systems and pockmarks in the region of the Ceuta contourite depositional system (western Alborán sea). Mar. Geol. 332−334, 4−26.

Somoza, L., González, F.J., Barker, S.J., Madureira, P., Medialdea, T., de Ignacio, C., Lourenço, N., León, R., Vázquez, J.T., Palomino, D., 2017. Evolution of submarine eruptive activity during the 2011−2012 El Hierro event as documented by hydroacoustic images and remotely operated vehicle observations. G-cubed 18 (8), 3109−3137.

Spagnoli, F., Specchiulli, A., Scirocco, T., Carapella, G., Villani, P., Casolino, G., Schiavone, P., Franchi, M., 2002. The Lago di Varano: hydrologic characteristics and sediment composition. Mar. Ecol. 23, 384–394.

Sultan, N., Garziglia, S., Bompais, X., Woerther, P., Witt, C., Kopf, A., Migeon, S., 2020. Transient groundwater flow through a coastal confined aquifer and its impact on nearshore submarine slope instability. J. Geophys. Res. Earth Surf. 125 (9) e2020JF005654.

Talling, P.J., 2014. On the triggers, resulting flow types and frequencies of subaqueous sediment density flows in different settings. Mar. Geol. 352, 155–182.

Talling, P.J., Wynn, R.B., Masson, D.G., Frenz, M., Cronin, B.T., Schiebel, R., Akhmetzhanov, A.M., Dallmeier-Tiessen, S., Benetti, S., Weaver, P.P.E., Georgiopoulou, A., Zühlsdorff, C., Amy, L.A., 2007. Onset of submarine debris flow deposition far from original giant landslide. Nature 450, 541–544.

Talukder, A.R., 2012. Review of submarine cold seep plumbing systems: leakage to seepage and venting. Terra. Nova 24 (4), 255–272.

Tamburrino, S., Insinga, D.D., Pelosi, N., Kissel, C., Laj, C., Capotondi, L., Sprovieri, M., 2016. Tephrochronology of a ∼70 ka-long marine record in the marsili basin (southern Tyrrhenian Sea). J. Volcanol. Geoth. Res. 327, 23–39.

Tepp, G., Chadwick Jr., W.W., Haney, M.M., Lyons, J.J., Dziak, R.P., Merle, S.G., Butterfield, D.A., Young III, C.W., 2019. Hydroacoustic, seismic, and bathymetric observations of the 2014 submarine eruption at Ahyi seamount, Mariana Arc. G-cubed 20 (7), 3608–3627.

Tibaldi, A., 2001. Multiple sector collapses at Stromboli volcano, Italy: how they work. Bull. Volcanol. 63 (2), 112–125.

Tibaldi, A., Corazzato, C., Kozhurin, A., Lagmay, A.F., Pasquarè, F.A., Ponomareva, V.V., Rust, D., Tormey, D., Vezzoli, L., 2008. Influence of substrate tectonic heritage on the evolution of composite volcanoes: predicting sites of flank eruption, lateral collapse, and erosion. Global Planet. Change 61 (3–4), 151–174.

Tinti, S., Manucci, A., Pagnoni, G., Armigliato, A., Zaniboni, F., 2005. The 30 December 2002 landslide-induced tsunamis in Stromboli: sequence of the events reconstructed from the eyewitness accounts. Nat. Hazards Earth Syst. Sci. 5 (6), 763–775.

Trincardi, F., Amorosi, A., Bosman, A., Correggiari, A., Madricardo, F., Pellegrini, C., 2020. Ephemeral rollover points and clinothem evolution in the modern Po Delta based on repeated bathymetric surveys. Basin Res. 32, 402–418 (Clinoforms and Clinothems: Fundamental Elements of Basin Infill).

Tubau, X., Canals, M., Lastras, G., Rayo, X., Rivera, J., Amblas, D., 2015. Marine litter on the floor of deep submarine canyons of the Northwestern Mediterranean Sea: the role of hydrodynamic processes. Prog. Oceanogr. 134, 379–403.

Turchetto, M., Boldrin, A., Langone, L., Miserocchi, S., Tesi, T., Foglini, F., 2007. Particle transport in the Bari canyon. Mar. Geol. 246, 231–247.

Ulvrova, M., Paris, R., Nomikou, P., Kelfoun, K., Leibrandt, S., Tappin, D.R., McCoy, F.W., 2016. Source of the tsunami generated by the 1650 AD eruption of Kolumbo submarine volcano (Aegean Sea, Greece). J. Volcanol. Geoth. Res. 321, 125–139.

Urgeles, R., Camerlenghi, A., 2013. Submarine landslides of the Mediterranean Sea: trigger mechanisms, dynamics, and frequency-magnitude distribution. J. Geophys. Res. Earth Surf. 118 (4), 2600–2618.

Vandorpe, T.P., Van Rooij, D., Stow, D.A., Henriet, J.P., 2011. Pliocene to Recent shallow-water contourite deposits on the shelf and shelf edge off south-western Mallorca, Spain. Geo Mar. Lett. 31 (5), 391–403.

Vanreusel, A., Andersen, A.C., Boetius, A., Connelly, D., Cunha, M.R., Decker, C., Hilario, A., Kormas, K.A., Maignien, L., Olu, K., Pachiadaki, M., Ritt, B., Rodrigues, C., Sarrazin, J., Tyler, P., Van Gaever, S., Vanneste, H., 2009. Biodiversity of cold seep ecosystems along the European margins. Oceanography 22 (1), 110−127.

Verdicchio, G., Trincardi, F., 2008. Shallow-water contourites. In: Rebesco, M., Camerlenghi, A. (Eds.), Contourites, Vol 60, Developments in Sedimentology. Elsevier, Amsterdam, pp. 409−433.

Viana, A.R., Faugères, J.C., Stow, D.A.V., 1998. Bottom-current-controlled sand deposits—a review of modern shallow-to deep-water environments. Sediment. Geol. 115 (1−4), 53−80.

Washington, H.S., 1909. The submarine eruption of 1831 and 1891 near Pantelleria. Am. J. Sci. 27, 131−150.

Whiticar, M.J., 1999. Carbon and hydrogen isotope systematics of bacterial formation and oxidation of methane. Chem. Geol. 161 (1−3), 291−314.

White, J.D.L., McPhie, J., Soule, S.A., 2015a. Submarine lavas and hyaloclastite. In: Sigurdsson, H., Stix, J., Houghton, B.F., McNutt, S.R., Rymer, H. (Eds.), Encyclopedia of Volcanoes. Academic Press, San Diego, CA, pp. 363−376.

White, J.D.L., Schipper, C.A., Kano, K., 2015b. Submarine explosive eruptions. In: Sigurdsson, H., Stix, J., Houghton, B.F., McNutt, S.R., Rymer, H. (Eds.), Encyclopedia of Volcanoes. Academic Press, San Diego, CA, pp. 553−569.

Woodside, J.M., Ivanov, M.K., Limonov, A.F., 1998. Shallow gas and gas hydrates in the Anaximander Mountains region, eastern Mediterranean Sea. Geol. Soc. Spec. Publ. 137 (1), 177−193.

Woodside, J.M., Mascle, J., Zitter, T.A.C., Limonov, A.F., Ergün, M., Volkonskaia, A., 2002. The florence rise, the western bend of the Cyprus arc. Mar. Geol. 185 (3−4), 177−194.

Zanchetta, G., Sulpizio, R., Roberts, N., Cioni, R., Eastwood, W.J., Siani, G., Caron, B., Paterne, M., Santacroce, R., 2011. Tephrostratigraphy, chronology and climatic events of the Mediterranean basin during the Holocene: an overview. Holocene 21 (1), 33−52.

Zitter, T.A.C., Huguen, C., Woodside, J.M., 2005. Geology of mud volcanoes in the eastern Mediterranean from combined sidescan sonar and submersible surveys. Deep Sea Res. Oceanogr. Res. Pap. 52 (3), 457−475.

Zitter, T.A., Huguen, C., Veen, J.T., Woodside, J.M., 2006. Tectonic control on mud volcanoes and fluid seeps in the Anaximander Mountains, eastern Mediterranean Sea. Spec. Pap. Geol. Soc. Am. 409, 615.

This page intentionally left blank

CHAPTER

The Mediterranean Sea in the Anthropocene

13

Fabio Trincardi[1], Fedra Francocci[2], Claudio Pellegrini[3], Maurizio Ribera d'Alcalà[4,5], Mario Sprovieri[5]

[1]*Consiglio Nazionale delle Ricerche (CNR), Dipartimento di Scienze del Sistema Terra e Tecnologie per l'Ambiente (DSSTTA), Rome, Italy;* [2]*Consiglio Nazionale delle Ricerche (CNR), Istituto per lo studio degli Impatti Antropici e Sostenibilità in ambiente marino (IAS), Rome, Italy;* [3]*Consiglio Nazionale delle Ricerche (CNR), Istituto di Scienze Marine (ISMAR), Italy;* [4]*Stazione Zoologica Anton Dohrn, Napoli, Italy;* [5]*Consiglio Nazionale delle Ricerche (CNR), Istituto per lo studio degli Impatti Antropici e Sostenibilità in ambiente marino (IAS), Campobello di Mazara, Trapani, Italy*

Learning Objectives

In this chapter, you will learn:

- What are the anthropic impacts on the deep seafloor and coastal landscapes in the Mediterranean Basin
- What are the main human impacts on the water budget and the biogeochemistry of nutrients at basin scale
- What are the biogeochemical dynamics of contaminants (organic and inorganic) in the Mediterranean Basin
- What are the characteristics (sources, fluxes, etc.) of plastic input in the Mediterranean

13.1 General concepts

This chapter reflects on how the Mediterranean Sea is evolving in the Anthropocene, discusses the future projections regarding different components of human pressures on the basin, and suggests strategies to keep this area to preserve high levels of biodiversity and ecosystem services also in the future. The key point is that humans have become a crucial driver in the functioning of the entire planet by progressively increasing impacts that, even when developed locally, act and amplify on a global scale. To mention a few, the arrival of humans in new continents was everywhere accompanied by the slaughtering to extinction of several big mammals (Diamond, 1997; Lewis and Maslin, 2018); the maceration of rice and early deforestation through fire have risen the load of green-house gasses since the agricultural revolution more than 8000 years ago (Ruddiman, 2003); the Industrial Revolution of the

Oceanography of the Mediterranean Sea. https://doi.org/10.1016/B978-0-12-823692-5.00013-3

19th century was accompanied by a dramatic increase in the use of energy, mostly from fossil fuels and nuclear reactions, which grew from ~14.6 zetajoules (ZJ) of the entire Holocene (11,700 years) to ~22 ZJ in the last 70 years (Syvitski et al., 2020); the introduction and disposal of new materials, as cement (e.g., Watts, 2019) and plastics (e.g., Ritchie and Roser, 2018), the alteration of biogeochemical (e.g., nitrogen, Hastings et al., 2009) and hydrological (e.g., Wu et al., 2013) cycles, all induced global modification of the land and ocean. Whatever date is taken as the start of the Anthropocene in a geological framework, the last two centuries hosted the most dramatic direct impacts of anthropogenic activities on Earth ecosystems and increased exponentially. A heated debate is going on about the possibility that humans have already crossed some "planetary boundaries," sensu Rockström et al. (2009), that is, values of state variables or fluxes in "planetary life supporting systems" considered essential for human life on the Earth. In this context, Steffen et al. (2015) introduced the term "Great Acceleration" to capture the "holistic, comprehensive and interlinked nature of the post-1950 changes simultaneously sweeping across the socio-economic and biophysical spheres of the Earth System, encompassing far more than climate change." With the onset of the Great Acceleration all socio-economic and earth-system trends began to grow exponentially at global level. When wealthy (OECD) and emerging economies can be differentiated major equity issues appear, as the exploitation of resources and production of goods and consumption is markedly uneven at global scale. Interestingly, however, population growth is peaking in non-OECD countries while the world's economy (GDP), and consumption, is still dominated by the OECD countries. The Earth System indicators continued their long-term, postindustrial rise, although a few display a slowing or apparent stabilization (Steffen et al., 2015). Only beyond the mid-20th century, there is clear evidence for fundamental shifts in the state and functioning of the Earth System that are beyond the range of variability of the Holocene and driven by human activities. Modern societies are now turning their interests more systematically into the ocean in search of biological resources, abiotic resources and space (traffic, platform construction, connection, and dumping sites), and the earth-systems and socio-economic trends that portray this exploitation are exponential and just delayed from those describing the great acceleration (Jouffray et al., 2020).

The extent to which, and by what activities, the Mediterranean Sea has been impacted by the activity of Man, especially considering that it has been one of the earliest regions to be colonized by homo sapiens (Hershkovitz et al., 2018) is discussed in the following subchapters, taking into consideration changes in the water budget, biogeochemical cycles, pollution of coastal zone, loss of sea-floor integrity, alteration of three-dimensional coastal lithosomes. This chapter will focus on the main drivers altering physical, chemical, biological, and geological dynamics at basin scale, based on the most recent literature.

The Mediterranean Sea (Fig. 13.1) is one of the marine regions most impacted by the activity of humans; with a surface extent corresponding only to about 0.7% of the global ocean surface, the Mediterranean retains as much as 7% of the global

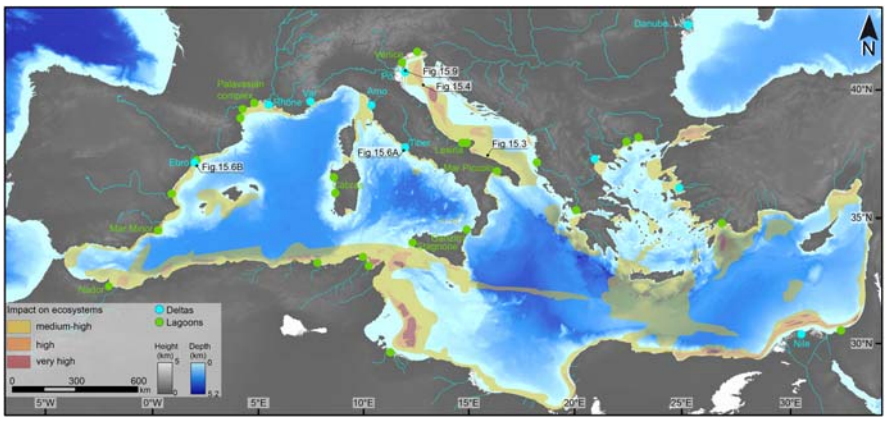

FIGURE 13.1

Location of main rivers, deltas and coastal lagoons in the Mediterranean Sea referred to in this paper (following figures). Polygons denote the main human impacts on marine ecosystems based on multiple drivers that include fishing, ship traffic, pollution, invasive species, oil spills, and coastal population density as documented by Micheli et al. (2013).

mismanaged plastic (Dalberg Advisors, 2019), hundreds of coastal sites polluted by refineries and other chemical plants and is crossed by more than a quarter of the global seaborne traffic. Through history the evolution of Mediterranean coastal systems has been impacted directly, by diversions of rivers, and indirectly, through repeated phases of extensive forest clearance, resulting in a twofold increase of sediment yield to the sea, while, by contrast, the construction of dams resulted in sediment sequestration and reduced sediment yield in the last century. Ecosystems have been dramatically impacted by overfishing, leading to the overexploitation of stocks, the disappearance of most top predators, as well as by the spreading of invasive species brought in through ballast waters or through the Suez Canal. On the other hand, recent publications documented the resilient response of ecosystems to long-term environmental changes highlighting the historically unprecedented nature of the ongoing anthropogenic stressors that are currently shifting coastal regions into novel system states far outside the range of natural variability archived in the fossil record (e.g. Rohling, 2017; Scarponi et al., 2022). The Mediterranean Sea is a semienclosed basin surrounded by three continents and characterized by very rapid ventilation and a relatively short residence time of its water masses (∼70 years) (see Chapter 7), which is of the same order of magnitude as the duration of the Great Acceleration. This implies that the Mediterranean Sea has the potential to react to the anthropogenic pressure but to reflect it in a way not easy to predict. The scheme of 3D ocean dynamics, described in Chapters 4 and 7, strongly and specifically influences the biogeochemistry of elements and inorganic and organic contaminants, interacting with atmosphere, deep-sea, and life. The freshwater input (mainly from the northern

coast, and the Nile to the South) by rivers and the Black Sea play a key role in the Mediterranean Sea because they drive primary productivity at local and regional scales and balance yearly water budget. The Mediterranean area is nowadays a "hot-spot" for climate change and related environmental impacts possibly greater than those in many other places (Fig. 13.2; IPCC, 2021).

A population of 132 million people lives on the 26,000 km of Mediterranean's coast, where also intensive farming and highly diversified industrial activities occur. Land-based activities introduce large volumes of waste-water with extra-nutrients, organic matter, toxicants, emerging contaminants and pathogens, thus representing a primary threat for health, biodiversity and marine ecosystem. Such a highly heterogeneous mixture of natural and anthropogenic forcing, inducing major changes in physical, chemical and socio-economical drivers, respond to an interconnected system of changes at global to regional scales.

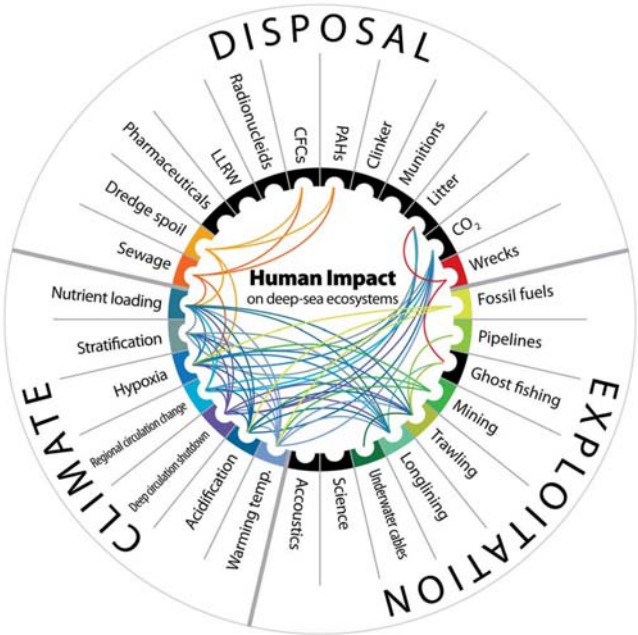

FIGURE 13.2

Infographic on human impacts on deep-sea habitats and faunal communities. Lines are color coded showing the path of interactions among drivers.

From Ramirez-Llodra, E., Tyler, P.A., Baker, M.C., Bergstad, O.A., Clark, M.R., et al., 2011. Man and the last great wilderness: human impact on the deep sea. PLoS One 6, e22588.

13.2 Reduction of seafloor integrity

Three problems limit the knowledge of the seafloor and partially hamper any assessment of human impacts on it: 1. humans do not "see" the seafloor directly, as in the case of any subaerial man-modified landscape, but through essentially geophysical data that decision makers and public are not aquainted with; 2. difficulties arise when trying to return on exactly the same point, for example to compare its status in successive times, depending on difficulties in precisely positioning instruments; 3. the seafloor is usually not considered as a common and, consequently, humans do care very little about any impact they have on this vast environment, encompassing two thirds of the Earth's surface. These are the reasons why mankind is impacting, at places dramatically, the seafloor before even knowing it. In the Mediterranean, like in any other marine environment, anthropogenic impacts can be localized, such as in the case of a dumping site, or extensive like in the case of fish trawling or even basin-scale or global like in the case of fiber-optic connections (Ramirez-Llodra et al., 2010, 2011).

13.2.1 Trawling

Fishing activity by industrial trawlers and dredgers is one of the most impacting human activities on the seafloor. Besides releasing an estimated 1.47 Pg of CO_2 globally, from carbon accumulated in sediments during the first year after trawling, and declining afterward (Sala et al., 2021), they irreversibly damage the benthic habitats. The Mediterranean is one of the world's most overfished regions (Coro et al., 2022) and bottom trawling is extensively adopted on shallow continental shelves and the upper reaches of continental slopes (Puig et al., 2012). Trawling impacts bottom sessile or demersal communities in various ways: by smoothing the sea-floor micromorphology which impact community composition of meiofauna (Pusceddu et al., 2014), and by increasing the resuspension of sediments and their export to deeper water (Palanques et al., 2006; Paradis et al., 2021), in some cases exposing at the seafloor older sediment with much lower organic matter content (Pusceddu et al., 2014). In addition, trawling has a role in redistributing pollutants disposed at seafloor in the case of illegal dumping, by resuspending and smearing them over larger areas, or in the presence of ordnance weapons disposals (Amato et al., 2006). In the last decade, the advent of high-resolution multibeam technologies and the possibility of treating terabytes of backscatter information, pose the basis for a systematic assessment of the impact of trawling on the seafloor (Puig et al., 2012) as seen in the processed backscatter data shown Fig. 13.3, referring to the South Adriatic continental shelf, offshore Apulia. On the continental shelf surrounding Cap de Creus Canyon, Puig et al. (2012) demonstrated how intensive trawling smoothens hard-bottom micromorphology of the seafloor, which in turn represent the key support to benthic biodiversity. In the continental slope of Gulf of Gioia, ROV observations provide clear evidence of the physical damage caused by the trawling gears on soft seafloor on the open slope and canyon margins. Trawling activities over soft bottom

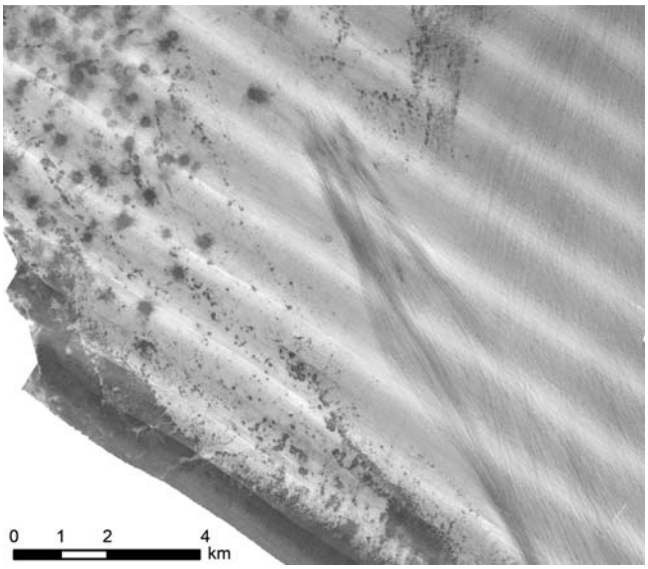

FIGURE 13.3

Backscatter data from hull-mounted multibeam bathymetric data showing the presence of trawl marks on the continental shelf offshore Brindisi, Southern Adriatic basin.

Courtesy of E. Campiani.

habitats has an adverse impact on the distribution and abundance of the main benthic communities resulting in a particularly low abundance of soft-bottom taxa (Pierdomenico et al., 2016). Despite several examples confirm the impact of bottom trawling, the Mediterranean still awaits a systematic quantification of such impact at basin scale.

13.2.2 Ghost fishing

Abandoned, lost, or discarded fishing gears are a major threat for marine fauna in all sea basins, including the Mediterranean and the Black Sea. When floating free or entangled at seafloor, these gears, often called ghost nets, threaten sensitive habitat and pose a risk of entanglement and ingestion to marine wildlife. These gears can remain in a fishing state for years to decades impacting substantially fish communities (Gall and Thompson, 2015; Lively and Good, 2019) and it was estimated that ghost fishing represents a significant component of the total fishing impact but, of course, does not bring any economic value to society. While gears are discarded on purpose anywhere in the Mediterranean, hard seafloor features like cemented beach rocks, drowned on continental shelves during the last postglacial sea-level rise, are preferred sites where trawling gears may get stacked. On Mediterranean scale, the lack of information on the quantification of lost gear and the assessment of impacts other than ghost fishing is critical. Several projects and programs,

however, try to quantify the lost fishing gear and characterize the habitats concerned, like Life Ghost in the North Adriatic, Ghost Med in the French Mediterranean (Ruitton et al., 2019). It is estimated that lost fishing gears kill 10% of eatable species, a major impact on the ecosystem, with no advantage to human economy; beside fish, impacts extend to turtles, mammals, and birds; a secondary positive impact, however, occurs when a gear is at seafloor for long time so to provide a substratum to other species, mostly sessile, an aspect to consider when prioritizing, or not, any removal of the lost gears. In the North Adriatic the problem is further aggravated by cemented coastal deposits that create seafloor reliefs. These reliefs are called *Tegnùe* in the venetian dialect, to signify that they entangle and *keep* the nets and trawling gears in less than 30 m water depth, where a single project (Life Ghost) recognized and removed a total of 362 items by scuba divers (Moschino et al., 2019).

13.2.3 Littering and dumping

The presence of littering is increasing offshore in response to garbage thrown directly in the water by transport, touristic or fishing ships, by tourists in recreational beach areas, or by coastal cities where garbage is particularly poorly managed. A significant amount of litter comes through river transport and, depending on river flow regime, can reach far offshore and very deep on the seafloor. This is the case of macro litter transported by "fiumare" in Calabria and Sicily, in the Central Mediterranean, and leading to a peculiar patchy distribution on the floor of the Messina Strait (Pierdomenico et al., 2019). "Fiumare" are short and steep rivers that seasonally generate hyper-pycnal flows capable of entraining mismanaged litter, often illegally disposed in their thalwegs. Once offshore, floods of this kind generate flows that are denser than ambient water and consequently reach the seafloor, evolving into sedimentary gravity flows, often funneled into gulleys and slope canyons. The energy of the process and the complex path of the flows result in large mounds including hundreds of land-sourced items, mixed to vegetal and coarse-grained debris, including truck tires, pieces of furniture, and bricks. Urbanization of coastal areas and illegal behaviors, are particularly dangerous in the presence of this very efficient source-to-sink sediment-transport underwater drainages. Similar litter hotspots on the sea floor occur offshore several Mediterranean cities (Taviani et al., 2019; Canals et al., 2021).

13.2.4 Direct seafloor modifications

Direct modifications of the seafloor morphology and composition come also from a variety of intentional and nonintentional interventions. The first category includes the construction of pipelines, often detected on multibeam bathymetric images and as acoustic hyperbolae on high-resolution reflection-seismic images; dumping sites, best identified in seafloor back-scatter images (Pierdomenico et al., 2016), and borrowing sites where the sand of drowned beach deposits is extracted and used to contrast coastal erosion of the modern shoreline (Fig. 13.4). Examples of

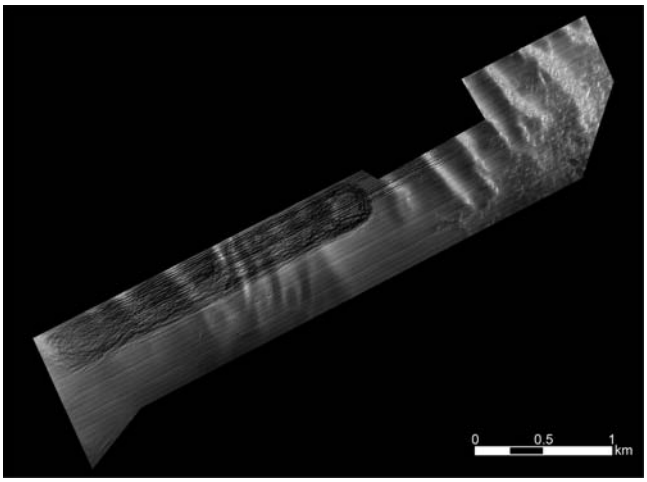

FIGURE 13.4

Example of a borrowing site in the north Adriatic Sea where 450 k m^3 of sand was extracted for beach nourishment. The multibeam bathymetry shows this human fingerprint on the seafloor.

Courtesy of A. Correggiari and A. Remia.

relevant, though nonintentional, and substantially unaware, impacts come from ship traffic, in shallow water environments. Paradigmatic examples of these impacts come from the Venice Lagoon (Madricardo et al., 2019) and include: propeller-wash consisting of meter-scale holes on the seafloor at docking stations where ships like vaporetto maneuver to hold position against the peer typically in 3−5 m water depths and the energy generated by the propeller is capable to resuspend fine-grained sediments from the seafloor; keel marks where boats, and occasionally even large ships, remain stuck ploughing the seafloor for tens to hundreds of meters; anchor "sweeping" occurs when ships hold position outside ports and are particularly prominent when heavy seas tend to move the ship and the anchor drag on the seafloor; periodic dredging is a typical activity in port areas where bottom currents tend to accumulate sediment, shoaling the sea floor.

13.2.5 Ammunitions on the seafloor

A peculiar, and dangerous category of dumped material are the ordnance weapons that in areas of intense bottom boundary layer dynamics can be temporarily buried and repeatedly exhumed (Amato et al., 2006; Alcaro et al., 2012). The Mediterranean has been the theater for massive dumping of obsolete war material. As an example, the shallow land-locked Adriatic basin has received after the end of World War II: 15,551 Yperite aerial bombs, 2533 Ammunition boxes and 20,000 other chemical ordnance (Amato et al., 2006) and thousands of bomblets from cluster

bombs during the Balkan Wars. These bomblets are virtually impossible to detect on geophysical records and can efficiently be transported by bottom-hugging dense-water currents progressively concentrating them in deeper waters (Fig. 13.5). Seventy years after the end of World War II, corrosion of the rusting bombshells on the seabed leads to slow and continuous leakage of chemical warfare agents affecting the marine ecosystem. In other cases, sudden bombshell rupture leads to instantaneous leakage of chemical warfare agents. In addition, in several cases, fishermen are victims of incidents in most cases referred to contamination by yperite and white phosphorous, when fishing accidently corroded bombshells. Direct contact with this agent leaking from the bombs causes severe blistering effects and, in some cases, casualties. It is important to note, also, that metal bomb shells in marine water cannot last more than several decades and that, consequently, their content is destinated to further spread in the environment and impact the trophic chain.

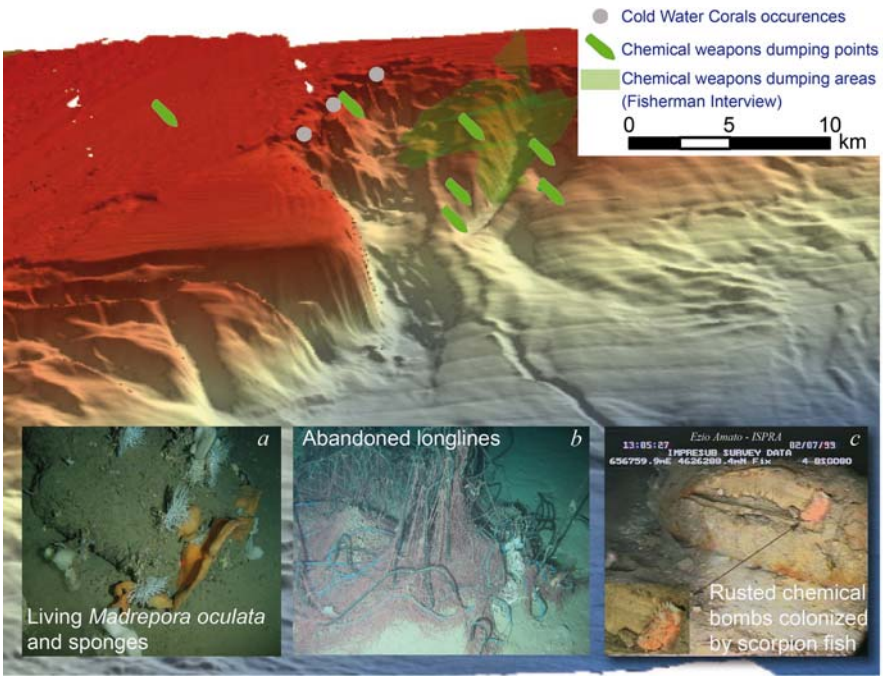

FIGURE 13.5

Location of unexploded ordnance dumping sites in the southern Adriatic Sea, georeferenced and positioned on multibeam bathymetry around Bari canyon.

Courtesy of E. Campiani and F. Foglini. From Amato, E., Alcaro, L., Corsi, I., Della Torre, C., Farchi, C., Focardi, S., Tursi, A., 2006. An integrated ecotoxicological approach to assess the effects of pollutants released by unexploded chemical ordnance dumped in the southern Adriatic (Mediterranean Sea). Mar. Biol. 149 (1), 17–23.

13.3 Modification of coastal lithosomes

Most authors defined the onset of the Anthropocene based on evidence of modifications of the subaerial and coastal landscape, as well as of the seafloor, due to excavations or dumping of materials; other authors relied on the finding of man-made material, such as bricks or plastic debris, in the stratigraphic record observed in section (Zalasiewicz et al., 2008, 2016). This paragraph provides examples of substantial man-induced modification of the three-dimensional shape and distribution of coastal lithosomes, an aspect far less recognized when discussing the Anthropocene.

13.3.1 Deltas

Recent studies have documented that only 23% of worldwide rivers longer than 1000 km flows uninterrupted to the ocean (Grill et al., 2019), nourishing coastal lithosomes. Among coastal lithosomes, river deltas are regions of intense economic activity including agriculture, navigation and trade, fisheries and aquaculture, forestry, hydrocarbon or freshwater production, and manufacturing (Renaud and Kuenzer, 2012; Syvitski et al., 2009, 2022). Urban settlements, industries and natural reserves coexist on deltas such as those of the Ebro, Llobregat, Rhone, Po, Tiber, and Nile rivers. Delta dynamics are primarily governed by riverine sediment supply and reworking by oceanographic processes and controlled over larger time scales by fluctuations in mean sea level (Galloway, 1975). On a global scale, subsidence is a major factor determining flood vulnerability of deltas (Blum and Roberts, 2009; Syvitski et al., 2009; Renaud et al., 2013), expected to be enhanced by future mean sea level rise driven by global warming (Clark et al., 2016).

Humans are globally impacting river sediment transport simultaneously increasing it through land-use change and soil erosion and decreasing it in the coastal zone through sediment retention in anthropogenic channels and reservoirs (Syvitski and Kettner 2011; Giosan et al., 2013; Martín-Vide et al., 2020). For instance, building of reservoirs and fixed embankments (engineered levees) in river catchments for reasons of land reclamation and flood prevention has caused most deltas to become sediment starved (Giosan et al., 2013; Syvitski et al., 2005). The net result is a global reduction in sediment flux to the coast by about 1.4 BT yr^{-1} over prehuman Epoch (Syvitski et al., 2005). Direct manifestations of delta morphological instability include retreat of beaches, riverbank failure, persistent channel incision or aggregation, focused erosion, and local collapses (e.g., Blum and Roberts, 2009; Bosman et al., 2020), and mobility of roll-over point position (Trincardi et al., 2020).

Human activity has impacted on Mediterranean deltas over two millennia. Indeed, internal geometry, sediment partitioning among delta lobes and size of modern deltas have been dramatically altered by human activities (Trincardi et al., 2004; Maselli and Trincardi, 2013; Renaud et al., 2013; Anthony et al., 2014; Day et al., 2019), and are more sensitive to eustatic rise than most other coastal systems due to large areas of near sea level wetlands. A clear example was the diversion of the Po River course at Porto Viro (1600−04 AD) when the Republic of Venice wanted to prevent the infilling of its lagoon, promoting the formation of the modern Po Delta further south leading to a major change in coastal morphology (Nelson, 1970;

Camuffo, 1987; Cencini, 1998; Correggiari et al., 2005a,b; Simeoni and Corbau, 2009). The supply dominated modern Po delta is a composite coastal lithosome certainly shaped by natural processes, but reflecting a primary anthropogenic forcing, as before the Porto Viro cut the delta was a wave-dominated system shifting location along the coast and with limited ability to advance into the open sea. The modern Ebro delta underwent a massive reduction in freshwater and sediment input and over 65% of wetlands in the delta plain have been converted to rice fields (Ibáñez et al., 2010). As the sediment load of the river has been retained by damming, the river sediment discharge has been drastically reduced and erosive processes have become dominant in the Ebro river mouth and delta area (Figs. 13.6 and 13.7). Human impacts have changed input to the Nile delta as well. The Nile delta, particularly after the completion of the High Aswan Dam in 1964 and the ongoing construction of the Grant Ethiopian Renaissance Dam on the Blue Nile, is increasingly suffering from environmental degradation because of reduced sediment and freshwater and the increasing concentration of nutrients, which have negatively impacted the Nile delta coast (Milliman et al., 1989; Stanley and Clemente, 2017). Projections are for increasing salinification and subsidence in the delta. Recent estimations suggest that even under natural levels of sediment yield, the Nile delta would not maintain its extent with a 1-m sea-level rise (Stanley and Clemente, 2017). Along the Rhône River almost all sediment input to the delta plain has been prevented by dikes. Despite this, floods with high sediment concentrations still occur occasionally (Pont et al., 2017).

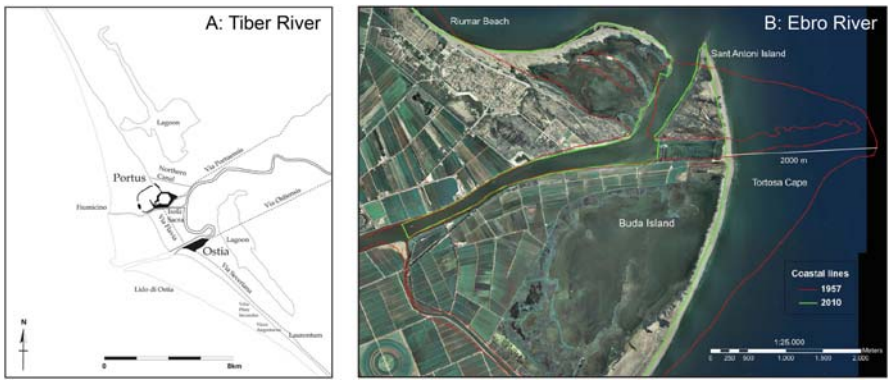

FIGURE 13.6

Examples of human intervention at Mediterranean river mouths. A) the Claudius-Trajan harbor required channels excavation and diversion of Tiber River. B) the trapping of sediment in dams built along the Ebro River and the erosion by wave are the likely cause of the northward shift of the Ebro mouth.

From (Left) Germoni, P., Keay, S., Millett, M., Strutt, K., 2019. Ostia beyond the Tiber: Recent Archaeological Discoveries in the Isola Sacra. 149–168. (Right) Somoza, L., Rodríguez-Santalla, I., 2014. Geology and geomorphological evolution of the Ebro river delta. In: Landscapes and Landforms of Spain. Springer, Dordrecht, pp. 213–227.

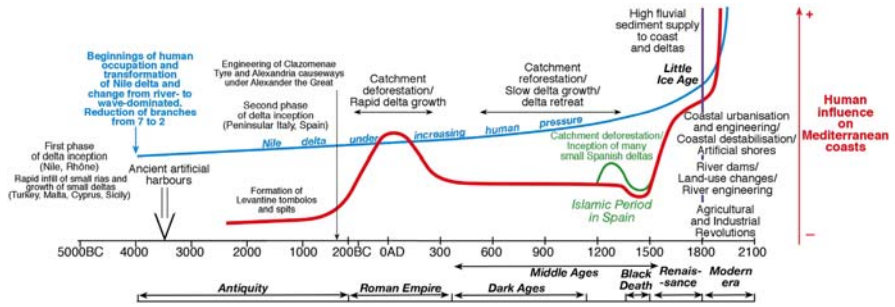

FIGURE 13.7

Synthesis of human-induced impacts on Mediterranean river catchments including ancient harbor development and paleo-engineering, and phases of river delta growth and decay over the last 6000 years. Red line shows the overall human impact on Mediterranean Deltas through time, the blue line denotes the Nile delta pattern, and the green line local changes in Islamic Spain.

From Anthony, E.J., Marriner, N., Morhange, C., 2014. Human influence and the changing geomorphology of Mediterranean deltas and coasts over the last 6000 years: from progradation to destruction phase? Earth Sci. Rev. 139, 336–361.

Even if deltas around the Mediterranean have been transformed to an Anthropocene state during the great acceleration, it can be recognized that human influence dates to before the industrial era (Figs. 13.7 and 13.8). Indeed, besides the natural

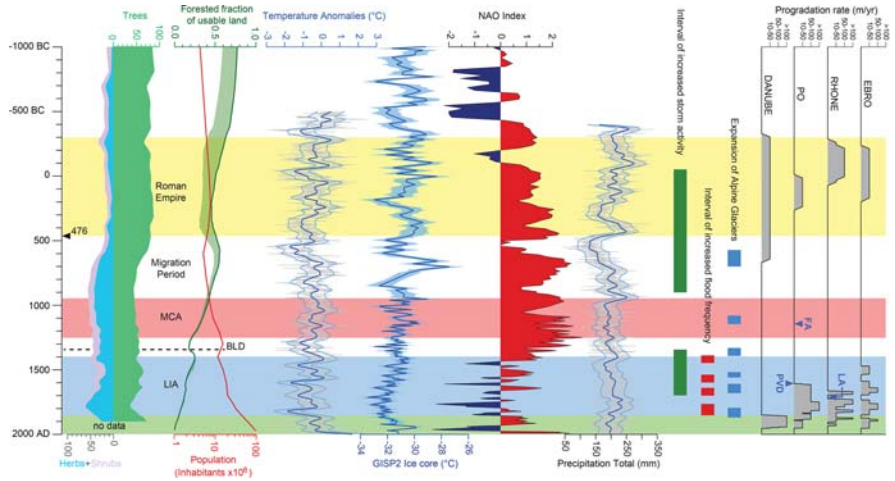

FIGURE 13.8

Reconstruction of human impact on delta lithosomes. Two main growth phases of Mediterranean deltas occurred during the Roman Empire and the Little Ice Age, reflecting forest clearance and land consumption.

From Maselli, V., Trincardi, F., 2013. Man made deltas. Sci. Rep. 3 (1), 1–7.

influence of climate on the Mediterranean sedimentation, humans induced main phases of delta progradation/retreat since the Mid-Holocene (Figs. 13.7 and 13.8; from Anthony et al., 2014 and Maselli and Trincardi, 2013, respectively). These phases of delta construction occurred under contrasting climatic regimes of the Roman period (~2000 cal a BP) and of the Little Ice Age (~500 cal a BP) mainly due to forest clearance in the catchment basins (Maselli and Trincardi, 2013). These growth phases were both followed by phases of delta retreat, driven by two markedly different reasons: after the Romans and during the Migration Period, the demographic fall in response of the barbarian invasions and of the new afforestation let soil erosion in river catchments return to natural background levels; whereas, since the industrial revolution, flow regulation through river dams trapped the sediment along rivers reducing sediment flux to the Mediterranean coasts (Boyer et al., 2005; Vella et al., 2005; Giosan et al., 2006, 2013).

13.3.2 Prodeltas

Most Mediterranean deltas display prominent subaqueous prodeltas, representing the main locus of sediment deposition and a potential archive recording climatic and anthropogenic signals through the last few millennia (Trincardi et al., 2004; Cattaneo et al., 2004; Fanget et al., 2014; Pellegrini et al., 2015; Amorosi et al., 2016; Campo et al., 2020; Scarponi et al., 2022). In the Mediterranean Sea, human pressure has significantly modified timing and distribution of prodelta lithosomes by (i) increasing sediment load through deforestation, mining, agriculture, and road construction (Cattaneo et al., 2004); and (ii) decreasing sediment load through dams, waterway diversions, and riverbank hardening (Syvitski and Kettner, 2011). Changes in sediment load are accompanied by the introduction of new substances through the sedimentary cycle that contaminate waters and near seafloor sediment (Goldman and Jackson, 1986; Amorosi et al., 2014). In the Ebro River the current suspended-sediment flux is significantly lower than before the construction of dams and reservoirs (Palanques et al., 1990), while the concentration of pollutants increases (Palanques et al., 1990). Human-induced erosion episodes in the Rhône Valley, mark the reorganization of the agriculture during the Roman period (~2000 cal a BP; Van der Leeuw, 2005). More recently, the Rhône River became increasingly "anthropogenic" by dyke construction (since 1855 AD) and damming (since 1950 AD), resulting in a dearth of sediment supply to the prodelta leading to the modern wave-dominated morphology (Fanget et al., 2014). The Tiber prodelta lithosomes were markedly influenced by Roman settlement with the building of the city of Ostia and the construction of one of the world's largest harbors (Claudius-Trajan system; Fig. 13.6), during the first and second centuries AD. Romans excavated canals that linked the harbor to the Tyrrhenian Sea eventually governed the loci of main riverine sediment input and episodes of channel avulsion (Belfiore et al., 1987; Bellotti et al., 1994, 2007, 2018; Milli et al., 2013). In addition, historical epigraph documents an episode of dredging of the Tiber talweg suggesting sand extraction and activities associated with aquaculture and salt extraction during

the fourth Century (Paroli, 2005). The river profile continued to change during the 20th century reflecting intensive urbanization of the coastal area that in turn obliterated the natural landscape (Giraudi et al., 2009). In the Adriatic Sea, the integration of foraminifera, pollen, sediment magnetic properties, and stable-isotope analyses helps to identify three main phases of forest clearance ~3600, 2400 and 700 cal a BP, impact on prodelta sedimentation (Oldfield et al., 2003; Piva et al., 2008). Recent analyses on the prodelta deposit documented that the anthropogenic forcing on fluvial discharge is recorded also by subtle changes in prodeltaic stratigraphic architecture (i.e., human impact on strata architecture) determining hotspots (offshore Apennine rivers) of terrestrial organic matter deposition (Pellegrini et al., 2021) in marked phases during the Little Ice Age (1500–1880 CE), and man-made particles of aluminum, stainless steel, and possible smelter slag (i.e., human impact on elemental particles) that were washed into the prodelta during the October 2000 Po-River Flood (Fig. 13.9; Pellegrini et al, in preparation).

13.3.3 Lagoons

In the Mediterranean area, more than 600 lagoons exist (Gaertner-Mazouni and De Wit, 2012), representing one of the most vulnerable ecosystems, particularly exposed to the effects of human and climate change (Lloret et al., 2008; Chapman, 2012). Indeed, lagoons are seldom allowed to evolve naturally and more often are modified by human interventions, typically designed to improve navigability or attempt maintaining a fixed environmental condition (Duck and da Silva, 2012). Lagoons reflect increasing anthropogenic pressures on their watersheds, as they receive freshwater input, rich in organic matter, nutrients and pollutants drained from heavily exploited farmland, urban and industrial settlements. For instance, in the Nador Lagoon (Mediterranean coast of Morocco) iron and steel industry, accompanied by urban sprawling, cause considerable water pollution as well as diminished

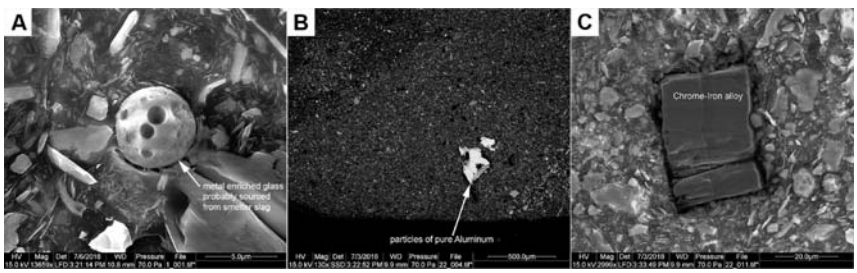

FIGURE 13.9

Cultural artifacts in a sediment core on the subaqueous Po prodelta and derived from a river flood in year 2000. Scanning Electronic Microscope analyses of deposits stabilized in epoxy resins highlighted: (A) Likely smelter slag; (B) Aluminum foil fragments; and (C) particles of Cr–Fe alloy. All these observations witness the pervasive and differentiated impact of human activities in the stratigraphic record.

sediment fluxes (Ruiz et al., 2006). In the Mar Menor (south-east of Spain), the impacts of mining (including sulfur and zinc), agriculture, and urban development in the surroundings to the lagoon are increasing; altogether these impacts promoted physical and chemical disturbances which cause accelerated environmental degradation (Marín-Guirao et al., 2005; Jiménez-Cárceles et al., 2006). In the Cabras lagoon (Sardinia Island, Italy), fish barriers and dams control lagoon hydrodynamics, water exchange, and animal recruitment and colonization (Como et al., 2007). In the Mar Piccolo (Ionian Coast, southern Italy), about 40 $m^3 s^{-1}$ of freshwater are continuously pumped out of the Mar Piccolo and discharged directly offshore, into the Gulf of Taranto for industrial purposes (Bellucci et al., 2016).

In the last decade, until the COVID-19 pandemic, increasing tourism pressure on coastal lagoons led to further land reclamation and fresh-water demand, with an increased deterioration of water quality. The Venice Lagoon is the largest lagoon in the Mediterranean and one of the UNESCO World Cultural and Natural Heritage sites. Human imprints are visible or can be deduced by comparing modern and historical maps (e.g., Carniello et al., 2009; Molinaroli et al., 2009; D'Alpaos, 2010; Sarretta et al., 2010; Madricardo and Donnici, 2014; Madricardo et al., 2020). The morphology and extent of the Venice Lagoon has been strongly influenced by humans since remote times: (i) the islands within the northern Lagoon have been inhabited since Roman times and up to the Medieval Age (Fozzati, 2013); (ii) the city of Venice was one of the largest in Europe with a population of 100,000 inhabitants by the end of the 13th century (Housley et al., 2004); and (iii) the city hosts more than 25 million visitors yearly. The Venice Lagoon represents a paradigmatic case of ecosystem alteration in the Anthropocene, since human activities progressively modified the environment through: the diversion of its major tributaries outside the lagoon to prevent sedimentation in marginal areas (from the 15th to the 17th century); the construction of rigid defenses to protect the barrier islands from storm waves (1740−82); the construction of successive sets of jetties at the inlets (1808−1927); the land reclamation for urban and industrial development (1927−60); the digging of the "Canale dei Petroli" between Malamocco inlet and Marghera refinery area to allow the big oil tankers in the Lagoon in the late 1960s; the subsidence induced by ground water and natural gas extractions (about 10 cm from 1930 to 1970; Trincardi et al., 2016); the stabilization or the construction of artificial salt marshes (since the 1990s); and, lately, the construction of mobile barriers (MOSE) at the inlets for flood protection of Venice (Fig. 13.10). Human footprint is visible on a variety scale of observation on the seafloor: from the presence of litter, namely, fenders, to the formation of scours, induced by propeller wash of water traffic, or by the acceleration of tidal currents around human constructions, typically concrete structures, and keel scars from boat that exit the deep canals and get sucked in the shallows (Madricardo et al., 2017, 2019). A particular area of energetic interaction between tidal dynamics and man-made structures are the engineered inlets of the lagoon, with deep areas of seafloor scouring (Toso et al., 2019; Fogarin et al., 2019).

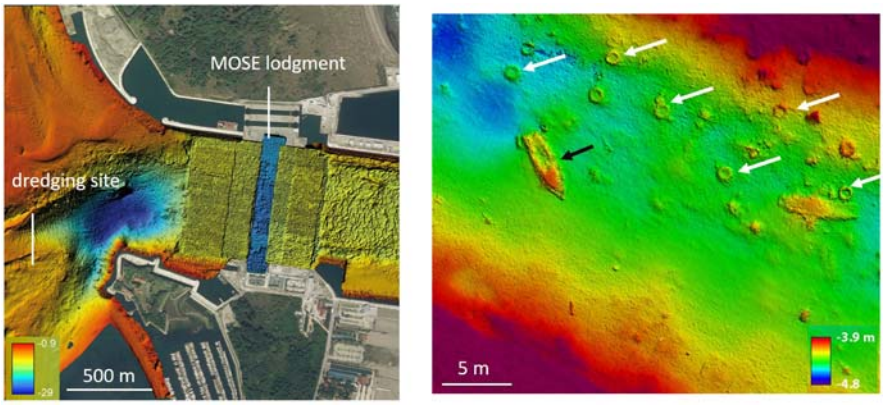

FIGURE 13.10

High resolution multibeam bathymetry maps of the Venice Lagoon. Left: the human modified seafloor of Chioggia inlet showing the lodgment space for MOSE defense barriers. Right: boat-wreck (black arrow) and tires (white arrow) are common on the seafloor. Tires used as fenders for motorboats are thrown in the water when worn and represent the dominant macro-litter on the lagoon seafloor.

Modified after Madricardo, F., Foglini, F., Campiani, E., Grande, V., Catenacci, E., Petrizzo, A., and Trincardi, F., 2019. Assessing the human footprint on the sea-floor of coastal systems: the case of the Venice Lagoon, Italy. Sci. Rep. 9 (1), 1–13.

13.3.4 Ebb and flood tidal deltas

Ebb- and flood tidal deltas are common features at inlets of lagoons regulated by the natural dynamic balance between offshore-directed and onshore-directed sediment flux (Komar, 1996). However, since the 19th century the construction of jetties at the inlets and the dredging of navigable channels, interact with other factors like waves, long-shore, and tidal currents, resulting in modified lagoon morphology and stratigraphy. For instance, rapid and uncontrolled coastal development, together with improperly designed projects, have had a damaging impact on the Egyptian coastal systems where ebb-tide sand shoals formed at the estuary mouth and migrate toward the estuary. The continuous migration of these depositional features threatens the navigation safety and commercial fishing within the Rosetta estuary. The navigation channels, which connect the open sea to the Nile distributaries, are economically relevant for thousands of fishermen and are maintained through frequent dredging activities (Frihy, 2001).

The analysis of historical bathymetric maps of the inlets of the Venice lagoon reveals profound variations because of the strong and persistent efforts to preserve navigable ways through the inlet preventing silting since 1300 CE (Colombo, 1970). The construction of Canale dei Petroli and the transit of large vessels at speeds above eight knots led to the resuspension of increasing volumes of sediment

that are progressively transported outside the lagoon in this ebb-dominated system (Sarretta et al., 2010; Scarpa et al., 2019). In response to this process, all inlets present ebb-tidal delta reaching several meters in thickness in less than a century (Tosi et al., 2009; Fontolan et al., 2012).

In the Marano and Grado Lagoon, land reclamation and seafloor dredging resulted in a substantial reduction in saltmarsh area of 144 ha in the last 50 years. In addition, direct human impact has played a primary role (i) in the marsh-edge retreat of about 0.5−1 m yr^{-1} caused by vessel-generated waves (Fontolan et al., 2012); (ii) in the formation of artificial marshes created by the dumping of sediment (the "pseudo-marshes" documented by Gatto and Marocco, 1992); (iii) in artificial modifications of inlet geometries and jetty fixation that in turn led in changing sediment supply to ebb-tidal delta (Fontolan et al., 2012; Scarpa et al., 2019); and (iv) settling human footprint on the seafloor such as cables, pipelines, mobile barriers, and diffuse littering on the sea-floor (Madricardo et al., 2019). All these anthropogenic actions have a dramatic impact on the lagoon benthos, hydrodynamics and sediment budget (Carniello et al., 2009; Sarretta et al., 2010), that in turn determine timing and place of lithosome deposition.

13.3.5 Drowned coastal barrier islands use as borrow places to extract sands

Inner continental shelf regions have been the most attractive potential sand sources for beach nourishment for decades, however, since nearshore sand availability decreased (Finkl et al., 2007), and nearshore sand bodies tend to be fine grained and mixed with mud and shell fragments (Williams et al., 2012), prospecting for sand resources increasingly moves offshore. Numerous studies have documented that coastal barrier islands, sand ridges, and large-scale bedforms, now lying in tens of meter depths on the shelves of the Mediterranean Sea, formed during intervals of decelerated sea level rise or still stand that punctuated the postglacial eustatic rise. As an example coastal sands formed around the Younger Dryas cold reversal (11.5−12.7 kyr BP), in water depths 50−60 m below the present-day sea level in the Gulf of Lion (Bassetti et al., 2006), on the Murcia shelf (Durán et al., 2017), offshore Corsica (Sømme et al., 2011), along the Tyrrhenian shelf (Chiocci et al., 1991), along the Adriatic shelf (Pellegrini et al., 2015), in the Aegean Sea (Lykousis et al., 2005), and on the shelf of the Levantine margin (Schattner et al., 2010). Hence, coarse-grained shelf deposits formed in marine environment but in shallower waters than today and were preserved by subsequent accelerated sea level rise (e.g., meltwater pulse 1B, Lambeck et al., 2014), which limited their reworking by coastal hydrodynamic processes. Shelf coarse-grained deposits have become of special economic interest where modern sediment supply is absent or limited to a thin veneer, and large sand reservoir can be exploited. Therefore, understanding the distribution of sandy deposits along the continental shelf is becoming crucial for resource management; because these are often preferred borrowing areas for the construction industry, land reclamation and beach nourishment projects (e.g.,

Correggiari et al., 1996; Rovere et al., 2019). Beach nourishment is a soft engineering alternative to hard structures. It is adopted for several purposes including to: (i) protect buildings and infrastructure from wave attack; (ii) improve beaches for recreation; (iii) create new natural environments; and (iv) retain sediment volumes during the ongoing sea level rise. Beach nourishment is changing the Mediterranean coastal landscape leaving also a hidden fingerprint also on the subaqueous landscape.

13.4 Man-made alterations of the Mediterranean hydrological cycle

As discussed in Chapter 4, the hydrological cycle of present Mediterranean Sea is negative, since evaporation (E) exceeds precipitation (P) + runoff (R). All three processes are driven by climate dynamics at both regional and global scale (see Chapters 3, 4, 7 and 9) and are part of hydrological cycle, one of the most complex cycles on the Earth because of the interaction among many abiotic and biotic component (see for an overview, Shiklomanov, 1998; Arnell, 2014). Change in land use by humans alters not only the sediment load (see previous subchapter) but also the water reaching the sea via riverine runoff. Water is withdrawn from rivers to irrigate agriculture to a percentage that can reach 70%−80% of the water intake (Shiklomanov, 1998) while other uses, for example, urban areas with industries, tourism, or uncultivated land have much lower net withdrawal (Shiklomanov, 1998). Forests are also responsible for a significant water withdrawal, however more in the form of diverting potential contribution to runoff to moisture in the air via evapotranspiration (e.g., Arnell, 2014). The other significant human action that modifies, and typically reduces, runoff is the construction of artificial catchment basin of a large suite of sizes. A recent study (Cooley et al., 2021) has assessed that as much as 57% of the water level variability in global water storage, reflects artificial storage. This is another diversion of water within the hydrological cycle from runoff to atmospheric moisture. Excluding changes in the content of reservoirs, the diversion of runoff to atmospheric water may significantly change the fate of water, especially for enclosed basins, since the runoff directly contributes to the fresh water inputs of the basin while atmospheric water vapor may precipitate in areas outside the basin. These processes have been recently reviewed by Lana-Renault et al. (2020) and Fader et al. (2020) for the Mediterranean region. Both studies highlight significant differences between the northern and southern rims of the basin, due to both climatic reasons and different economic development. Overall, more than 70% of water use is for the agriculture which is also the activity with the strongest impact on the reduction of the runoff. This impact is particularly large for irrigated systems, which are increasing in the southern areas where warm climate enhances the withdrawal effect.

The first study showing a clear impact of human activity on the hydrological budget of the basin is likely that by Rohling and Bryden (1992), who linked the

salinity increase of intermediate and deep waters in the basin to the construction of the Aswan dam on the Nile river. A similar effect was observed by Krahmann and Schott (1998) because of the damming of Ebro river in Spain. Modeling studies have also confirmed the possible impact, as a cofactor, of runoff on the circulation patterns of Mediterranean regions (e.g., Skliris and Lascaratos, 2004; Verri et al., 2018). The most extensive analysis of riverine runoff and trends for the Mediterranean and Black seas so far is likely that carried out by Ludwig et al. (2009, 2010), even if limited to data up to 2000. Ludwig and colleagues estimated a total runoff of $\sim$490,109 m^3 yr^{-1}. Considering the possible errors in the estimates, they proposed that the decrease in runoff in the period 1961−2000 could be between 15% and 22%. However, disentangling the impact of climate change, even when anthropogenically driven, and the direct action of Man on land is not an easy task also because most of the analyses focus on the mid-term changes due to climate changes (e.g., Alpert et al., 2013).

An important contribution to this aspect comes from the study by Haddeland et al. (2014). Merging data and results of model simulation the authors made a global assessment of the relative weight of human versus climate impact on water runoff concluding that the weight of human activity on land contributes from 5% to 30%. As for the Mediterranean region, the weight is generally below 5% with the exception of few Spanish areas, where irrigated agriculture withdraws a more significant amount of water.

As discussed above, the impact of the reduction of the runoff by direct human intervention on the freshwater budget of the basin may be overestimated. This also because the runoff varies from one-third to one-fifth of the freshwater contributed by precipitation, which would make the cases of Nile and Ebro rivers mentioned above an extreme scenario in the present Mediterranean Sea. Overall, the water budget of the basin seems to be much more affected by climate dynamics at regional and global scale, than by anthropogenic activity. However, it is worth mentioning that the diversion of rivers, damming and the repeated phases of extensive forest clearance to be replaced by crops, started long ago (e.g., Ruddiman, 2003) especially in the Mediterranean area (Oldfield et al., 2003; Piva et al., 2008; Amorosi et al., 2016). Therefore, in the context of the Anthropocene, as the period of Man driven changes in hydrological cycles, the evolution of Mediterranean to the present state might have been more directly impacted by Man than it is occurring today.

13.5 The load of human activities in changing Mediterranean biogeochemical dynamics

While for the hydrological cycle climate seems to play a dominant role, biogeochemical cycles in the Anthropocene are much more directly affected by human activities. This occurs for two main reasons: (i) Man tend to concentrate population in densely inhabited cities (e.g., West, 2016) with a parallel concentration of material

both in the cities and in more intensively cultivated fields (e.g., Mackenzie et al., 2002); (ii) for some elements, for example, nitrogen (N), Man invented procedures for transforming the element from a very slowly reacting form (N_2) to more reactive oxidized or reduced forms (e.g., Galloway et al., 2003; Gruber et al., 2008). For more than a century those processes have been particularly strong in Europe, producing a significant accumulation in soils and internal waters (e.g., Mackenzie et al., 2002; Sutton et al., 2011) as well as a transfer, via runoff, toward European seas (Grizzetti et al., 2012) and the Mediterranean Sea (e.g., Malagò et al., 2019). In addition to runoff, also atmospheric transport and deposition is a significant term of elemental fluxes to the basin (Kanakidou et al., 2020), which, as mentioned above, relies on both inputs to balance the net export of N and phosphorus (P) at Gibraltar. While the nutrient budget of the Mediterranean Sea has been analyzed quite often in the past (see Chapter 11) all fluxes are generally affected by a certain degree of uncertainty, either for the water transport at the straits and the relative concentrations of the different chemical forms especially of N and P, and for the estimate of the inputs from the boundaries (Atmospheric and Terrestrial Input or ATI, Bethoux, 1989). Ribera d'Alcalà et al. (2003), even considering the possible ranges based on all available data at time, could not derive a consistent balance of the budgets surmising the basin might not be in steady conditions because of changes in ATIs due to change in anthropogenic activities and policies. However, the extent to which stock and changes are related remains elusive. Analyzing the trends in concentrations of N and P, though based on a very small data set, Bethoux (1989) made projections on ATIs and the consequent export production which would have led to hypoxia in few decades. Indeed, this has not been the case (see for the Dyfamed site Coppola et al., 2018) and the reason may be ascribed to the very small data set on which the extrapolations were based. The human impact on Mediterranean N and P biogeochemistry has acted in two opposite directions over the years: Kanakidou et al. (2020), using model simulations, estimated an increase of $\sim$5.6 times and $\sim$1.7 times of the atmospheric input for N and P respectively from 1850 to present. Ludwig et al. (2009), though for a shorter time interval (1960–2000) estimated that the total input to the Mediterranean Sea, by runoff, could have increased by a factor of $>$5. However, while N still remained at elevated levels in 2000, P, after an increase in the 1980–90 decade, dropped to the values of 1960 in year 2000. As for the observed P decrease in rivers, it has been the consequence of the policies of many countries and also of the European Union to reduce the use of phosphorus compounds in detergents and to impose a tight control on P concentration in waste waters. A similar approach has been taken for nitrogen with the Nitrate directive (see Sutton et al., 2011). The estimates by Ludwig (2009), of 1.08 Tg yr^{-1} of N and 0.05 Tg yr^{-1} of P in 1998, have been updated by Malagò et al. (2019), who report for year 2007 inputs by runoff of 1.18 Tg yr^{-1} for N and 0.029 Tg y^{-1} for P. The input increase before year 2000 has been tracked in the intermediate layers of Mediterranean (200–600 m) by Moon et al. (2016). The authors showed similar patterns in the temporal dynamics of N and P in both Mediterranean basins, with N and P concentrations rapidly increasing from 1985 until 2000. In the following years their

concentrations stabilized and then started to decrease. The observed increase was larger in the eastern basin than in the western basin, likely because of greater dependence of nutrient stocks on ATIs. Considering the fast turnover time of Mediterranean intermediate water masses and its antiestuarine dynamics (see Chapter 7) any accumulated N and P would be mostly exported to the Atlantic. However, the increase due to ATIs should have been coupled to a slightly higher export production, but no analysis has been carried out so far on that relatively long-time span, also for the lack of satellite data covering the first decades. On the other hand, considering that runoff enters the basin at the surface along the coasts, a stimulation of algal blooms, that is, what is defined "eutrophication," is the other possible impact. Indeed, the accumulation and persistence of a high phytoplankton biomass is a process more complex than just the result in the increase of the carrying capacity of the system, via nutrient addition. That persistence is a sign of a perturbation in the functioning of the plankton food web, which is what occurs on relatively short time scales also for the intermittency of inputs. However, eutrophication in the Mediterranean is limited to specific coastal areas either close to large rivers, like the Po, or in the vicinity of large cities. The present evidence is that both the North Adriatic, which receives the inputs for Po and other rivers, and the area in front of the river Rhône display for the period 1998–2009 a slight decrease in the annual mean of chlorophyll a (Colella et al., 2016). This seems related to the result of the policies on nutrient input controls, but a more in-depth analysis should be carried out in order to exclude a decrease in the residence time of nutrients due to the general circulation or a reorganization of the food web that might support a more effective transfer to the consumers.

Another key component of Mediterranean biogeochemistry is obviously carbon (C). Chapter 11 provides an extensive analysis of the C cycle in the Mediterranean basin. The C cycle is certainly one of the most perturbed biogeochemical cycles by anthropogenic activity and, also because of this, one the most complex (e.g., Friedlingstein et al., 2021). Due to the high level of economic development and the physiographic characteristics, the Mediterranean basin should also reflect this perturbation. Indeed, despite the export at Gibraltar, a significant accumulation of anthropogenic dissolved inorganic carbon (DIC) has been assessed by Hassoun et al. (2015), who measured an increase in the DIC content of waters below 300 m down to the bottom ranging from 35.2 to 101.9 μmol kg^{-1}, with higher values in the western basin. This oxidized carbon accumulated at depth derives directly from runoff or atmosphere and vertical mixing (see below) and from respiration of particulate organic carbon (POC) and dissolved organic matter (DOM). Discriminating the extent to which the two processes have been altered by anthropogenic activity is not easy, also because dynamics of DOM is quite complex in the basin (e.g., Santinelli et al., 2013, 2021) and data series of significant length are missing. Regnier et al. (2013) inferred the anthropogenic perturbation of carbon transfer from land to ocean by runoff on global scale, by estimating the sources and sinks to inland waters flowing to the sea and along the coastal margins. They estimated a contribution in the order of $\sim$0.1 PgC yr^{-1} corresponding to a 13% increase in respect to

preindustrial times. No such analysis has yet been done for the Mediterranean neither exists, to the best of our knowledge, an updated carbon budget including all the components. As for DOM, which is the second most important component of the C cycle in terms of stocks, the key terms should be the impact of changes in the hydrological cycle, land use and emissions. Santinelli (2015) estimated a total riverine input of DOM in the range of 0.64−0.71 Tg C yr^{-1} while Galletti et al. (2020) estimated a total atmospheric input of DOM of 3.6 Tg C yr^{-1}. Even within the error due to the interpolation of only few land stations, it represents a significant higher value than the contribution by runoff. In addition, as expected for a semienclosed basin by highly inhabited land, the ratio between atmospheric contribution and basin area is two−five time higher than that to the global ocean (Galletti et al., 2020). Intriguingly, the net exchange of CO_2 with the atmosphere, assessed by D'Ortenzio et al. (2008) integrating observations and models, has been slightly negative in the years 1998−2004, meaning that the Mediterranean Sea acted as sink but for an amount in the order 0.24 TgC yr^{-1}, of which only a small fraction (<3%) is the anthropogenic contribution. Very recently Solidoro et al. (2022) published a new estimate of the average net flux of CO_2 from the atmosphere to the basin for the years 2000−09 amounting to 12.2 Tg C yr^{-1}. Assuming again that the anthropogenic fraction is in the order of 3% this would amount to ~0.37 Tg C yr^{-1}. Schneider et al. (2010) estimated in 1.7 PgC the inventory of anthropogenic carbon in the basin, with a net input at Gibraltar of 3.5 Tg C yr^{-1}. For the sake of simplicity and considering the available analyses, we may assume that the 1.7 Pg C accumulation occurred mostly in the last 110 years. This would imply an average anthropogenic input in the order of 15.5 Tg C yr^{-1}, with low values in the first decades and progressively growing values in the last decades. Therefore 15.5 Tg C yr^{-1} should be considered very conservative for the 2000−2009 decade, analyzed by Solidoro et al. (2022). Taking the net input of 3.5 Tg C yr^{-1} at Gibraltar, estimated by Schneider et al. (2010), and the ~0.4 Tg C yr^{-1} estimated by Solidoro et al. (2022), the remaining 11.6 Tg C yr^{-1} should derive form the ATIs. For the runoff component of ATIs, the contribution is mostly in the dissolved forms, since Sadaoui et al. (2018) estimated a removal of 20%−30% of suspended matter and POC from rivers flowing in the Mediterranean, with an particularly strong impact after 1950 (>85% of dams built after that year). As for DIC, Li et al. (2017) reported for the Mediterranean and Black seas a total input of DIC of 12.7 Tg C yr^{-1}, a lower value than the estimate by Solidoro et al. (2022), who report an input 9.2 Tg C yr^{-1} for the Mediterranean proper to which they add 10.1 Tg C yr^{-1} entering the basin from Dardanelles. Only a fraction of the ATIs derives from anthropogenic perturbation. Raymond and Hamilton (2018) estimate a ~50% increase in the riverine DIC load at global scale, which if applied to the Mediterranean, would imply an anthropogenic contribution of ~6.4 Tg C yr^{-1}, which is ~55% of the missing C. With all the caveats of the uncertainty on each of the above quantities, the latter might derive either from the DOM inputs and from an increase in the primary production due to an increase in nutrient fluxes toward the photic zone of the basin. Retelletti Brogi

et al. (2022) showed that the stop due to the pandemics during the months of lockdown reduced by more than 40% the DOM flux in the Arno River. Indeed, this was associated with a stop mostly in the tertiary sector which plays an increasing in a mature phase of industrialization. Therefore, it cannot be applied to the whole industrial phase. On the other hand, we may assume that organic carbon emissions have been strongly increased by anthropogenic activities (see Huang et al., 2015 for a list of sources). Assuming a conservative 20% component in the riverine DOM and attributing 80% of atmospheric DOM deposition to anthropogenic activity would add $\sim$3.0 Tg C yr^{-1} to the inputs (neglecting the DOM component that is removed in coastal processes). As discussed above, it is not easy to assess the variation of primary production in the basin, but all the above suggests on one hand that the carbon dynamics of the Mediterranean basin is significantly affected by other anthropogenically impacted processes than just direct CO_2 uptake and that a more in-depth analysis of the anthropogenic impact is needed, especially for designing future management strategies.

13.6 Dynamic of pollutants in the Mediterranean Sea

The increasing anthropogenic pressures induced by agriculture, overfishing, aquaculture, urbanization, tourism, maritime transport in the Mediterranean Sea, drive relevant inputs of various chemical contaminants (heavy metals, artificial radionuclides, organic compounds such as the group of Persistent Organic Pollutants or POPs, hormones, pharmaceuticals, drugs, etc). The current knowledge on the biogeochemistry, distribution, pathways, and fate of this highly heterogeneous group of pollutants depends on the class of contaminants and their chemical–physical behavior in the environment (mainly at the interfaces of air, sea, organisms and sediments). Specifically, the oligotrophic nature of the open Mediterranean Sea makes it more sensitive to bioaccumulation processes. Indeed, the effects of "dilution" of contaminants by organic carbon are relatively reduced and the rapid turnover at the base of the food webs may represent a key factor for contaminant biomagnification. The highly dynamic coastal community system is nowadays affected by relevant social, economic and environmental changes that are creating unprecedented multilevel pressures.

13.6.1 The European directives (WFD and MSFD)

The quality and status of ecosystems in European coastal waters is monitored under and regulated by the EU Water Framework Directive (WFD; WFD, 2000/60/EC), not yet adequately integrated into the Marine Strategy Framework Directive (MSFD; MSFD Directive, 2008/56/EC) and the Maritime Spatial Planning Directive (MSPD; MSPD Directive, 2014/89/EU). Recent commission reports indicate that $\sim$60% of European surface waters (mainly from coastal areas) do not comply the WFD's standards, while the updated MSFD Environment Report 2020 considers

the good environmental status (GES) of European marine waters by 2020 not achieved. To address the multiple stressors on the marine environment, the MSFD sets the standards conducive to sustainable marine ecosystems and provides the overarching compliance criteria that need to be followed in conducting such economic activities (e.g., Borja et al., 2017; Sprovieri et al., 2021). Specifically, the MSFD is based on an integrative, holistic, ecosystem approach looking at marine environments as ensembles of functional units with complex interactions and fully coupled with the socioeconomic system. The 11 descriptors framing the MSFD explicitly address key traits or processes linked to marine ecosystems, like the perturbations induced by anthropogenic pressures and the persistence of the intrinsic structure or functioning of the systems (Berg et al., 2015; Sprovieri et al., 2021). Once determined, the descriptors should lead to an assessment of the status of the environment and subsequently to the overall qualification of the Environmental Status. Nonetheless, at the current stage, methods to assess the GES appear vague and definition of numerical approaches need further and more robust scientific understanding.

13.6.2 The biogeochemistry of contaminants: geomorphological interferences

The complex biogeochemistry of inorganic and organic contaminants in the marine environment combined to their persistence due to limited potential of degradation produces long-term residence time, long-range potential transport and relevant effects of bioaccumulation and biomagnification in the trophic web (e.g., Lohmann et al., 2007). Pollutants in the marine sediments undergo a combination of chemical (e.g., adsorption/desorption, water/particle exchanges, etc.) and sedimentological processes (e.g., resuspension and redeposition) which make it difficult to track and quantify their spatial and temporal evolution and distribution in the marine environment, in terms of chemical and physical dynamics. Moreover, sediments due to their highly specific interactions primarily with hydrophobic pollutants, determine site-specific distribution modes for organic and inorganic compounds. Indeed, recent investigations demonstrated that many chemical pollutants reach the deep sea (e.g., Storelli et al., 2009; Jamieson et al., 2017) representing, with the reduced physical and chemical dynamics of this environment, a long-term risk with unpredictable effects for the deep ecosystem (Covaci et al., 2008; Froescheis et al., 2000). Besides, the deep-sea ($>$200 m) is still to be considered a pristine environment due to its remoteness from anthropogenic pollution sources. Nonetheless, in continental margins, canyons act as natural conduits of sediments and organic matter from the shelf to the deep basins, providing an efficient physical pathway for transport and accumulation of particles with their associated land-produced contaminants. Also, the role played by canyons in transporting pollutants to the deep sea is enormously reinforced when they are the locations of highly dynamic shelf to basin export processes (e.g., dense shelf water cascading, see Chapter 7; Canals et al., 2009; Chiggiato et al., 2016; Foglini et al., 2016; Pellegrini et al., 2016). Oceanographic currents

and heterogeneous transport mechanisms of solid sediments may result not only in a dilution of the overall amount of pollution, but they are also capable to build local hotspots where oceanographic and morphologic conditions allow the redisposal of fractioned number of contaminants. Thus, a primary control of contaminants transport from land to the deep sea via shelf canyons could represent a systematic process to determine hot spots of pollutants in the deep sea affecting uncontaminated bottom ocean sediments from very far point sources on land. Transport mechanisms by shelf canyons could offer unforeseen fast track system of deep-sea contamination (Pierdomenico et al., 2019). Land and deep sea appear much more connected than previously assumed in a region where coastal pollution represents a crucial threat for larger areas of the Mediterranean Sea.

13.6.3 Heavy metals in seawater, sediments, and organisms

The biogeochemical dynamics of heavy elements (HMs) in the Mediterranean Sea is dominated by atmospheric inputs characterized by a European background signature (natural and anthropogenic) upon which Saharan dust is superimposed (e.g., Guerzoni et al., 1999). The lability of HMs and the enhanced bioavailability in dissolved phase is driven by combined, atmospheric solubilization processes, occurring during aerosol transport (and mainly driven by pH variations) and sources of incoming air mass that primarily characterize the nature of aerosol particles. Dry deposition prevails at basin scale with dominance of particulate deposition mode. Metals of crustal origin are mainly transported and deposited in particulate form, while anthropogenic metals are much more soluble and their biogeochemistry is primarily controlled by wet events (e.g., cadmium Cd, zinc Zn). Once at sea, HMs interact with ions in solution, particulate, and organisms, thus assuming a chemical-physical form (their chemical speciation) that determine their reactivity and kinetic transfer along the trophic web, with the entry point represented by the phytoplankton level. In the Mediterranean basin, atmospheric fluxes (e.g., Migon and Caccia, 1990) are characterized by increasing trends in Cd, Zn and copper (Cu) concentrations, while lead (Pb) tends to decrease following the worldwide banning effect of leaded gasoline. Following the main atmospheric trajectories, under the influence of the highly industrial inputs of the western European regions, dissolved Cd, Cu, and Zn show higher contents in the western Mediterranean. Trace metal profiles (in dissolved phase) in the Mediterranean Sea systematically show higher concentrations in surface waters than those found in open oceanic waters (e.g., Spivack et al., 1983; Copin-Montegut et al., 1986; Sherrell and Boyle, 1988; Morley et al., 1997). These enrichments have been attributed to external sources such as runoff, atmosphere inputs and important vertical mixing and insufficient removal by organisms in the eastern Atlantic (Boyle et al., 1985; Van Geen et al., 1988, 1991; Pino et al., 1990). At sea, Cd shows a fairly homogeneous vertical distribution, but a subsurface rich layer was observed in the Alboran Sea, possibly related to the presence of Western Intermediate Water (see 7) with a strong anthropogenic signature (Riso et al., 2004). Differently, Mn, Co, and Pb show a nearly regular decrease with depth, reflecting classical profiles

already documented in the world ocean (Copin-Montegut et al., 1986). As a general figure, Cd in surface waters ranges between 20 and 40 and 50 and 80 p.m. in the Atlantic and Mediterranean sea (300−350 and 60−110 p.m. in in deeper waters; Statham et al., 1985; Van Geen et al., 1988). Cobalt (Co) in surface waters ranges between 0.037−0.057 nM and 0.084−0.139 nM in the Atlantic and Mediterranean sea (Morley et al., 1997). Cu in surface waters ranges between 0.81−1.13 nM and 1.37−2.27 nM in the Atlantic and Mediterranean sea (0.1−0.5 and 0.15−0.24 nM in deeper waters; Van Geen et al., 1988). Zn in surface waters ranges between 0.8 and 2−18 nM in the Atlantic and Mediterranean sea (1.5−5 nM in deeper waters; Van Geen et al., 1988). Analog patterns emerge also for nickel (Ni), manganese (Mn), iron (Fe) and Pb. Mercury (Hg) shows air−water exchanges; organic matter regeneration processes are the main processes for establishing the vertical distributions and the methylation of this element (methylmercury being the biomagnified and toxic form of this metal) (Cossa and Coquery, 2005).

As reported by Elbaz-Poulichet et al. (2005), the input from rivers constitutes the major source for particulate (and also dissolved) HMs on some continental shelves, particularly for the Rhône and Po rivers. However, at the basin scale, the particulate atmospheric inputs dominate by 2−3 times the Pb, Cd and Cu inputs from rivers. And again, for Hg at the Mediterranean basin scale, Rajar et al. (2007) estimated the annual river inputs to be 65 kmol, while atmospheric deposition was estimated to be twice this amount.

Detailed and specific information about the speciation of the HMs in seawater (the chemical forms that they assume when they interact with the various components in seawater) are extremely limited from the Mediterranean region (Rodriguez et al., 2021, and references therein). This gap of knowledge reduces the possibility to evaluate the real role played by the HMs in affecting the ecosystem health in the Mediterranean Sea. Some bioactive metals are involved in the Redfield model of organic matter synthesis and deep remineralization. They limit the growth of phytoplankton and heterotrophs at low concentrations in seawater, but their potential toxicity may also inhibit development. Potentially toxic metals, even when they have a biological role, are likely to produce environmental harm through their assimilation by planktonic species at high concentrations. Experimental studies (e.g., Wang and Fisher, 1998) concerning the transfer of heavy metals up the food chain and their accumulation in marine organisms have been carried out. In the case of the Mediterranean Sea, field studies have shown significant accumulation in various species, from numerous planktonic and nektonic organisms (Fowler, 1977, 1986; Roméo et al., 1992) up to higher trophic level species at the end of the marine food chain, such as dolphins and whales (Augier et al., 1993; Frodello and Marchand, 2001) with a highly species dependence (Fowler, 1986).

For any given HMs, the concentrations in mixed microplankton samples varied little between regions. Furthermore, the comparison of the levels in microplankton as well as certain individual planktonic species with the data reported for similar species from other oceanic areas suggested that the heavy metals concentrations in open ocean plankton and nekton were no higher in the Mediterranean than

elsewhere at that time. Nonetheless, this evidence needs deeper understanding in terms of bioaccumulation mechanisms in the Mediterranean holigotrophic regime as mentioned before. Furthermore, given that reliable field data on HM concentrations in Mediterranean planktonic species remain sparse, new surveys will be needed to make any sort of state-of-the-art comparison of the levels in the Mediterranean with those in similar species from other regions as well as establishing temporal trends.

In contrast to plankton and other lower trophic level pelagic organisms, more studies are being carried out on the contamination of species under threat, such as cetaceans from the Red List of the International Union for Conservation of Nature. The concentrations of HMs found in whale stomachs suggest that food is responsible for significant metal contamination in whales (Frodello and Marchand, 2001). Hg concentrations in certain Mediterranean fish are twice those found for the same species living in the Atlantic Ocean, and most of the Hg content in the fish muscle is present as methylated species. However, the exact reasons for the higher total Hg levels observed in these Mediterranean fish species remain unclear (Aston and Fowler, 1985). Recent results for fish (Harmelin-Vivien et al., 2009) have confirmed these findings, and the occurrence of higher metal bioaccumulation in planktonic organisms in oligotrophic environments has been suggested. This suggestion that the key cause for the "Med-Hg anomaly" probably originates from the higher bioaccumulation of methyl mercury (MeHg) at the base of the food chain, especially in phyto- and bacterioplankton (Harmelin-Vivien et al., 2009), needs to be rigorously examined, particularly in view of earlier data which indicate that Hg levels in small pelagic organisms from the Mediterranean are no higher than those reported for other areas of the world ocean (Aston and Fowler, 1985; Fowler, 1986). A high Hg methylation rate in the Mediterranean water column has already been suggested (Cossa et al., 1997). Recent results by Heimbürger et al. (2010) show that the mercury methylation within the water column of Ligurian Sea would be favored by microorganisms associated with the degradation of pico- and nanoplankton.

Heavy metals distribution in sediments (e.g., in lagoons, harbors, deep sea) of the Mediterranean Sea (Fig. 13.11) show a highly heterogeneous pattern following the strong variability in anthropogenic sources, physical parameters (e.g., grain size or organic matter content), etc. Wide scale information, mainly from the near-shore coastal areas, can be obtained from monitoring programs based on international expertise that use quantitative biological indicators and/or surface or sediment cores (e.g., GESAMP, ICES, ICEMS, MEDPOL, WFD, MSFD). Hot-spot areas with very high levels of heavy metals were measured in a number of coastal sites, where inputs of contaminants from highly industrialized plants document the effect of the great acceleration of the postsecond world war era (e.g., Salvagio et al., 2016; Traina et al., 2021). The potential impact of these highly polluted zones at regional to basin scale was explored in a few papers and reveals the possible crucial role that climate changes (associated with variation in physical and chemical features of the Mediterranean Sea) could play in the dispersion modes of this class of contaminants.

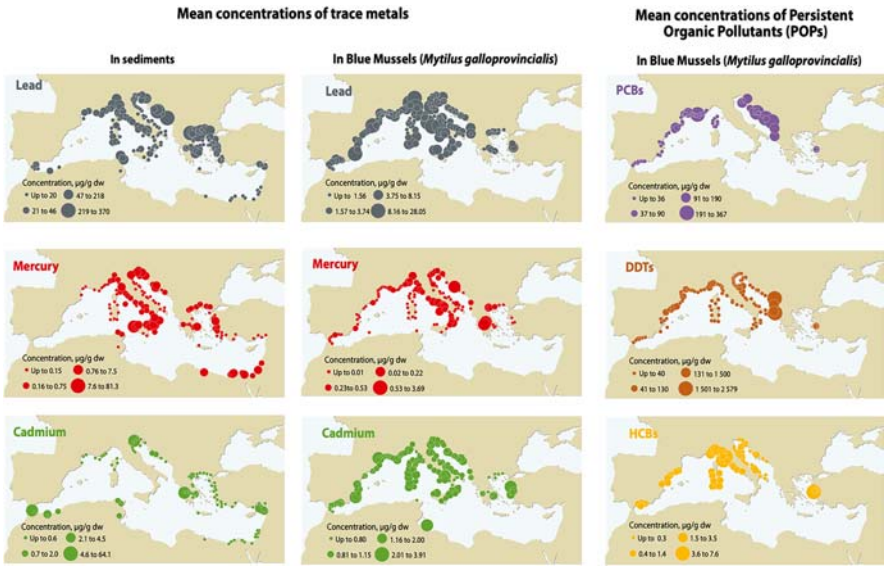

FIGURE 13.11

Distribution of heavy metals and POPs in sediments and biota from the Mediterranean Sea.

From UNEP/MAP: State of the Mediterranean Marine and Coastal Environment, UNEP/MAP—Barcelona Convention, Athens, 2012.

A number of impacts triggered by climate changes could affect the distribution modes and biogeochemical dynamics of heavy metals at Mediterranean scale. Modifications in the water budget could significantly change inputs of heavy metals from land either in the particulate and dissolved form also responding to extreme flushing events. Also, changes in water circulation and stratification with decreasing vertical mixing, will affect the dynamics of HMs, their residence times in the various basins and, following consequent redox potential (Eh) and pH variations, also their speciation and potential toxicity for the trophic web. Changes in summer oxygen concentrations on the shelves may become more numerous, with consequences for the mobilization-remobilization of deposited metals, possible changes in Hg-methylation kinetics and variability (associated to high-frequency Eh variations at the seawater-sediments interface) in HMs release from deep sediments to the seawater. An increase in stratification will permit contaminants to remain in the euphotic zone, increasing their availability for adsorption and uptake by phytoplankton and consequently their transfer within food webs. On the other hand, while oligotrophy favors higher metal bioaccumulation at the base of the trophic web, the possible increase in primary production may constitute a dilution of the elements within the biota. Likewise, industrial processes (e.g., desalination plants) or new uses could determine new sources of heavy metals like Cu or Ni, strictly connected to effects of corrosion. The projected demographic increase in coastal cities could enhance discharges from sewage treatment plants or surface runoff from urbanized soils.

Finally, relatively limited information is available for HMs from marine volcanoes, cold seepage, as well as inputs from large coastal cities, industries and maritime traffic. Lateral advection and vertical mixing dominate vertical profiles of nutrient-like metals (Cd, Cu, Ni, Cr) in the Mediterranean Sea, limiting a direct impact of classical ocean biogeochemical cycling (Achterberg and van Den Berg, 1997).

13.6.4 Organic pollutants in seawater, sediments, and organisms

Organic compounds reaching the ocean may attain dangerous concentration with consequent effects of bioaccumulation and biomagnification processes in the marine food webs. The critical influence of riverine inputs and air masses from northern Europe into the Mediterranean Sea, containing high concentration of organic compounds and, specifically, groups of POPs, represents the main routes of transport at sea. However, very little accurate figures of riverine and atmosphere inputs of POPs to the Mediterranean Sea are nowadays available. High polychlorinated biphenyl (PCB) levels were detected in the Rhône, Po and Ebro river waters and sediments and document industrial waste inputs from chemical treatment plants based in highly industrialized areas on land. As for inorganic contaminants, atmospheric dry/wet deposition and processes of exchanges at the atmosphere−ocean interface dominate the dynamics of POPs at sea. Estimated annual PCBs concentration in the lower troposphere of central Europe are around 800 pg m^{-3}, while 2 times lower concentrations in coastal areas and in the open Mediterranean were measured without evidence of seasonal variation. Conversely, the distribution of polycyclic aromatic hydrocarbons (PAHs), with average concentrations of 2 ng m^{-3}, shows significantly increase in winter (Mandalakis and Stephano, 2002). The biogeochemistry of organic compounds in seawater is strongly connected to dynamics of organic carbon in solution. Thus, primary production and organic carbon in dissolved and particulate form regulate the partition of organic contaminants between surface waters, deep waters and sediments.

Monthly fluxes of PAHs in the deep western Mediterranean basin Bouloubassi et al. (2006) suggest efficient transfers to the deep sea which can be considered as a large sink of chemical contaminants. Analyses of PAHs in dissolved phase show relatively higher concentrations in the southwestern Black Sea and eastern Mediterranean, reflecting heterogeneous inputs, trophic conditions and biogeochemical dynamics (Berrojalbiz et al., 2021), while the highest PCB levels were documented in the northern Mediterranean, where important anthropogenic pressure occurs (Albaigés, 2005). Information from hot-spot areas characterized by important presence of industrial plants shows high levels of PAHs and PCBs in seawater and sediments (e.g., Salvagio Manta et al., 2016; Bonsignore et al., 2020; Tamburrino, et al., 2020). In general, coastal areas, and continental shelves and slopes are dominated by petrogenic PAHs, whereas the deep basins are characterized by high amounts of pyrogenic PAHs accounting for the prevailing dominance of atmospheric inputs (Lipiatou and Albaigés, 1994; Gómez-Gutiérrez et al., 2007). A general decline in

concentrations has been observed over time, more evident for DDTs than for PCBs, while relative scarce information is available for emerging POPs, such as polybrominated diphenyl ethers, or PBDE (D'Agostino et al., 2020).

13.6.5 Emerging pollutants: pharmaceutical products, drugs, etc.

Emerging contaminants represent a wide class of heterogeneous chemicals that are not currently regulated and about which there exist concerns regarding their impact on human or ecological health. Of major interest, for their potential synergistic role in affecting the marine ecosystem health, pharmaceuticals products (PPs) are used in the treatment and prevention of diseases in both humans and animals. They include a wide-ranging group of small biologically active organic molecules, with hydrophilic to moderately lipophilic chemical properties. Consumption of PPs varies considerably from country to country, depending on the specific economic level and organization of the health system and on drug prescription guidelines. After intake, PPs can be partially or totally metabolised in the human body, and a variable fraction of the parent compounds or metabolites is excreted with urine or feces and enter directly the wastewater. Many studies in the Mediterranean seawater and coastal systems, demonstrated that wastewater treatment systems are not able to completely remove PPs (Castiglioni et al., 2006; Kasprzyk-Horden et al., 2009; Jelic et al., 2011; Petrie et al., 2015), thus, the primary way of PPs discharge into the environment is through both raw and treated sewage waters from household or medical facilities. It was well described the occurrence of PPs at trace levels (pg to μg per liter) in hospital wastewaters (Verlicchi et al., 2012), urban wastewaters (Castiglioni et al., 2005, 2018), river waters (Hughes et al., 2013; Osorio et al., 2016), and groundwaters (McEarchran et al., 2016). Studying marine environment is particularly relevant because it receives direct discharges from wastewater treatment plants or even untreated wastewaters and rivers. Several studies recently investigated the presence of PPs in Mediterranean coastal areas (Čelić et al., 2019; Mezzelani et al., 2018; Arpin-Pont et al., 2016; Feo et al., 2021) and assessed the associated potential risk (Desbiolles et al., 2018; Fabbri and Franzellitti, 2016; Feo et al., 2021). Nevertheless, the occurrence, fate, and hazard related to the presence of PPs in the marine environment are still relatively less studied than in wastewater and freshwater. Although the effects of PPs are investigated through safety and toxicology studies before the marketing, their potential risk for the aquatic ecosystem is still not intensely explored. Actually, the presence of PPs in the aquatic environment became of growing concern over the past decades (Fent et al., 2006; Boxall et al., 2005) and in the last years several authors started to investigate PPs concentration in seawater and the potential effects on marine organisms (Erickson, 2002; Alvarez et al., 2014; Gonzalez-Rey and Bebianno, 2014; Arpin-Pont et al., 2016; Moreno-Gonzàlez et al., 2016; Bonefille et al., 2018; Mezzelani et al., 2018). A mandatory monitoring action focuses on distribution, contents, and potential effects on the ecosystem of emerging contaminants (Descriptors eight and nine; among them, PPs and personal care products) in the marine environment. In particular, a number of researches were focused on the

toxic effects of antibiotics on various levels of the marine trophic web (Lalumera et al., 2004), and on the resistance effects in the natural bacterial population (Erickson, 2002; Hernando et al., 2006). Steroids have been also monitored for potential toxic effects on algae and plankton (Erickson, 2002; Hernando et al., 2006), due to their estrogenic properties and consequent effects on reproduction and development processes. Nonetheless, many aspects of the impact of PPs on the marine environment are still at their early stage. The European regulation on this specific issue is limited to a recently established Watch list of substances to be monitored (EU, 2018/840/EU-European Commission, 2018), including for the first time some PPs (hormones, diclofenac, macrolide antibiotics; EU, 2015/495-European Commission, 2015), recently updated with the addition of two antibiotics (amoxicillin, ciprofloxacin) and the exclusion of diclofenac (EU, 2018/840-European Commission, 2018) that will enter the list of priority contaminants.

13.7 Plastisphere in the Mediterranean Sea

Plastic pollution is ubiquitous in the environment: it has been found in soil and freshwater (De Souza Machado et al., 2018; Wong et al., 2020), in remote areas as pristine mountain catchment (French Pyrenees) (Allen et al., 2019) and Polar regions (Peeken et al., 2018), as well as household and food (Correia Prata 2017; Welle and Franz 2018; Weithmann et al., 2018) and, very recently, microplastics were detected in human placentas with potential risk for adverse pregnancy outcomes (Ragusa et al., 2021). As a synergic effect of both natural and economic flows (Francocci et al., 2021), plastic pollution affects mostly the marine environment (Thompson et al., 2009a, b) and extends from the sea surface to the deepest sea, a sink for plastic debris (Woodall et al., 2014; Galgani 2015; Saliu et al., 2018; Lebreton et al., 2019). The dispersal of plastic pollution in the marine environment depends upon the composition, dimension (macro- $>$ 5 mm, micro- $<$ 5 mm, nano- $<$ 100 nm plastics) and density of the plastic particles (van Sebille et al., 2020). Floating plastic debris can cause entanglement of marine species and may be ingested with potential harming effects of the marine biota (Gall and Thompson, 2015); plastic debris can absorb or carry contaminants and microorganisms (Leon et al., 2018; Basili et al., 2020; Prinz and Korez 2020) thus facilitating their transferring across habitats and through the food chain (Cau et al., 2020; Mercogliano et al., 2020; Huerta Lwanga et al., 2017). In addition, plastic fragmentation into microplastics and nanoplastics can allow chemical additives present in plastic items, such as packaging, to move in the environment and bioaccumulate in organisms with adverse effects on human health and biota (Stenmarck et al., 2017). This emerging evidence represents a particular threat, considering that the chemicals potentially associated with plastic packaging, are ranked among the "highest for human health hazards" and "highest for environmental hazards" chemicals (Groh et al., 2019; UNEP 2021).

Plastic pollution has become one of the most pressing environmental issues, as its production increased rapidly during the last 70 years of exponential economic

growth. Plastics revolutionized our society by bringing benefit across all sectors, including the health and food; however, the high incidence of mismanaged plastics waste causes major environmental impacts (Hopewell et al., 2009; Thompson et al., 2009a, b). Plastics enter the marine environment via several pathways directly from land and sea-based activities but also via atmospheric and, to a lesser extent, biological pathways (UNEP 2021, Fig. 13.12).

In 2018, global plastic production almost reached 360 million tons, of which 62million tons in Europe with the employment of over 1.6 million people (PlasticsEurope, 2019). Single-use plastics account for 40% of the plastic produced (PlasticsEurope, 2019) and many of these products, such as plastic bags and wraps, have a short lifespan (Geyer et al., 2017) while they persist in the environment for hundreds of years (Booth, 2017). Those single use and persisting items are also the most common marine litter found in coastal areas, where plastic packaging makes up a considerable portion of collected aquatic litter (Schwarz et al., 2019).

The Mediterranean Sea is recognized as one of the world's most affected regions concerning plastic pollution for the high concentration of microplastics found (Suaria et al., 2016; Alessi et al., 2018; Boucher and Bilard 2020) and potential impact on

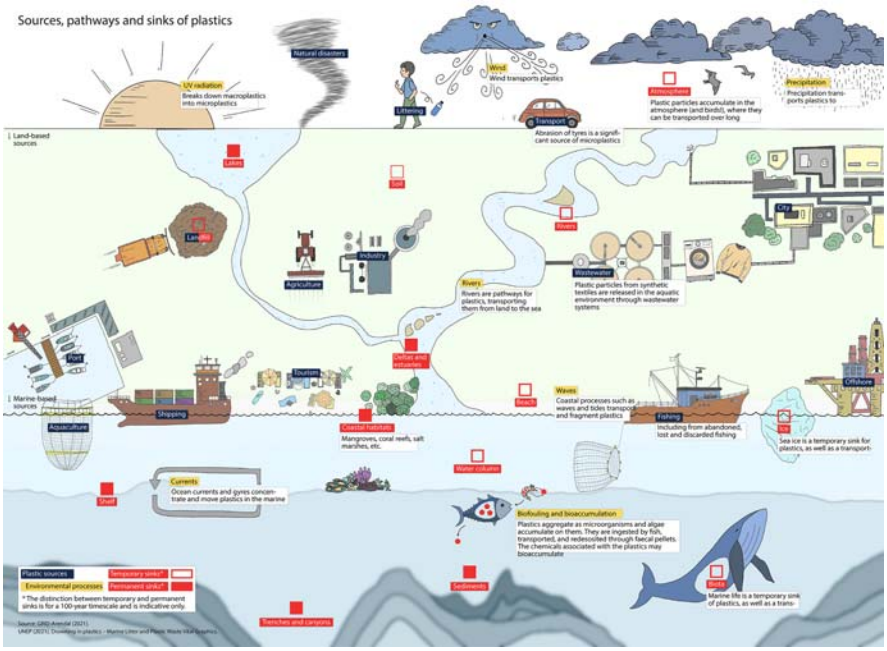

FIGURE 13.12

Sources, pathways and sinks of plastics. Plastic waste leaks into the environment through multiple sources from both sea-based and land-based anthropic activities and flows a variety of pathways.

Source: GRID-Arendal. https://www.grida.no/resources/14896.

the environment and human health. The total plastic accumulated in the Mediterranean is estimated in the order of 1,178,000 tons (ranging from 53,500 to 3,546,700 tons; Boucher and Bilard, 2020). The concentration of microplastics on the water surface reaches more than 64 million floating particles km^{-2} (between 95% and 100% of total floating litter corresponding to a range between 1000 and 3000 tons) (UNEP, 2021). Most plastic tends to accumulate at the seafloor, either in the form of microplastics in the sediments, or as macroplastics scattered on the seafloor (more than 50% of seabed litter; Boucher and Bilard, 2020; UNEP, 2021). An amount of 20,000 items km^{-1} has been estimated to sit on the deep seafloor in the Messina Strait (Pierdomenico et al., 2019), suggesting that the seafloor represents a sink for all materials lost and discarded especially from land-based sources near metropolitan areas on the Mediterranean coasts (Canals et al., 2021).

The annual plastic production of plastic in the Mediterranean region is estimated about 38 million tons; the annual macroplastic leakage (Leak-waste) from waste is estimated at a central value of 216,269 tons yr^{-1} (Boucher and Bilard, 2020), with Egypt, Italy, and Turkey as the main contributors to the overall leakage. The accumulation of floating plastic in the Mediterranean Sea is likely related to the high human pressure (tourism, fishing activities, increasing coastal population) together with the hydrodynamics of this semienclosed basin. The 70% of the Mediterranean population (525 million people) live in urban areas, with an expected increase of an additional 130 million by 2050, especially in the eastern and southern countries (UNEP/MAP and Plan Bleu, 2020.). The Mediterranean populations concentrates within the coastal hydrological basins, thus including hundreds of villages, town and cities that increase the pressure in terms of marine pollution—and plastic uptake—resulting from the discharge of wastewater, contaminants, and mismanaged waste (Boucher and Bilard, 2020). Indeed, according to Boucher and Bilard (2020), coastal cities and towns are responsible for 35% of the total macroplastic leakage, while the remaining 65% is generated inland and carried toward the marine environment by surface run-off.

There is an urgent need to change the consumption, use and disposal pathways for plastic; as the global population continues to increase, plastic waste will continue to grow. Marine plastic pollution in the Mediterranean is having an impact on Mediterranean Blue Economy estimated about €641 million each year, mainly affecting the most important economic sectors such as tourism and fisheries (Dalberg Advisors, WWF 2019). The MSFD (Directive, 2008/56/EC) specifically requires EU Member States to ensure that the marine litter does not affect the coastal and marine environment and highlight the need to act by tackling the problem at its source. To counteract the increase of marine litter, European Member States can also refer to—and adopt—existing EU laws, which include the directive on waste management in ports (EU Directive, 2019/883). According to their national programs, Member States are also adopting measures to improve waste management in the fishing sector, the extended producer responsibility scheme of producers and other actions aimed at limiting the use of single-use plastic products (EU Directive, 2019/904). The EU also provided public support to mitigation actions including fishing for litter

by the European Maritime and Fisheries Fund 2014–2020 (EMFF). The European Commission launched in 2018 "A European strategy for plastics in a Circular Economy" (COM/2018/028 final) setting the scene for a change that with the new Circular Economy Action Plan of 2020 is better focused on addressing the entire life cycle of products, design, processes, consumption, reuse and on the sustainability of the supply chains. The circular economy approach applied to plastic production, use and recycle, represents a major instrument to prevent plastic pollution at the global scale. With this aim, all the member countries of the intergovernmental BlueMed Research and Innovation Initiative for blue jobs and growth in the Mediterranean area, cochaired by the European Commission and the Union for the Mediterranean (UfM), agreed on the urgency to join forces and act together to support the implementation of a common strategy by launching, in 2018, the BlueMed Pilot action on A Healthy Plastic-Free Mediterranean Sea. The Pilot is set up to promote the circulation of good practices and the implementation of economically viable solutions for the prevention, management, and mitigation of the effects of plastic pollution in the marine environment of the Mediterranean region as well as to value the educational component by means of transfer and circulation of knowledge, including by local communities (Francocci et al., 2021).

13.8 Concluding remarks

This chapter aimed at documenting human impacts in the Mediterranean Sea, in response to the "Great Acceleration" of the last 70 years, though humans started altering the dynamics of the region much earlier. Humans are increasingly impacting the oceans through the exploitation of abiotic and biotic resources, accompanied by the increasing use of maritime space to set up the infrastructures needed for transport, energy production, and information. Such uses are likely to increase also in the Mediterranean, where the extremely fragmented political setting (22 countries from three different continents) is not helping in finding shared and coherent solutions to decrease human pressures on the environment and ecosystems. Indeed, a major mapping program should be envisaged to synthesize information on the geographic distribution of human impacts at Mediterranean scale, quantifying how the intensity of every single impact varies in space, and defining where and how such impacts overlap. Where superimposed, such impacts have potential interference and amplification effects that should be assessed and quantified, for example, in the case of intensive trawl fishing across areas of illegal, and not charted, chemical dumping.

The chapter reviewed the large variety of human impacts on the Mediterranean coast, ocean water, and seafloor. Such impacts are pervasive and encompass: (i) changes in composition of seafloor and coastal sediments in response to the spreading of pollutants from land, and/or from coastal tourism, economic activities offshore, accidents, and oil spills; (ii) changes in the morphology of the seafloor in response to the creation of trawl marks, keel marks, propeller-wash holes, anchor

sweeping, or creation of manufactures such as dikes, artificial canals, dams; and (iii) changes in three-dimensional development of coastal deposits (increased presence of ebb-tidal deltas reflecting enhanced sediment resuspension in ebb-dominated lagoons; construction of supply dominated deltas in response to forest clearance and river diversion; prodelta distribution and internal stratal geometries). The knowledge of these three aspects is far from being systematic at the Mediterranean scale and different categories of impact in the same area are seldom put in relation, due to prevailing sectoral, disciplinary approaches. A fourth category of impact, dealt with in other Chapters, includes the changes in water column structure and circulation caused by man-induced global warming through decreased water stratification, weakened dense-water formation and possible phases of water mass stagnation and sapropel formation. Last, dedicated sections reported on anthopric-indices changes in the biogeochemical dynamics of major nutrients, organic/inorganic pollutants (in sediments, seawater and biota), and plastics at Mediterranean scale, with quantitative information on sources and fluxes according to the current knowledge.

Additional Resources

- Directive 2008/56/EC of the European Parliament and of the Council of June 17, 2008 establishing a framework for community action in the field of marine environmental policy (Marine Strategy Framework Directive). https://eur-lex.europa.eu/legal-content/en/ALL/?uri=CELEX%3A32008L0056
- Directive (EU) 2019/883 of the European Parliament and of the Council of April 17, 2019 on port reception facilities for the delivery of waste from ships, amending Directive 2010/65/EU and repealing Directive 2000/59/EC. https://eur-lex.europa.eu/eli/dir/2019/883/oj
- Directive (EU) 2019/904 of the European Parliament and of the Council of June 5, 2019 on the reduction of the impact of certain plastic products on the environment. https://eur-lex.europa.eu/eli/dir/2019/904/oj
- European Commission. 2003. Common implementation strategy for the Water Framework Directive (2000/60/EC). Guidance Document No. 8. Public Participation in Relation to the Water Framework Directive. Office for Official Publications of the European Communities, Luxembourg. https://circabc.europa.eu/sd/a/0fc804ff-5fe6-4874-8e0d-de3e47637a63/Guidance%20No%208%20-%20Public%20participation%20%28WG%202.9%29.pdf
- European Commission, 2015. Commision Implementing Decision (EU) 2015/495 of March 20, 2015 Establishing a Watch List of Substances for Union-Wide Monitoring in the Field of Water Policy Pursuant to Directive 2008/105/EC of the European Parliament and of the Council. https://eur-lex.europa.eu/legal-content/EN/TXT/PDF/?uri=CELEX:32015D0495&from=PT
- European Commission, 2018. Commission Implementing Decision (EU) 2018/840 of June 5, 2018 Establishing a Watch List of Substances for Union-Wide Monitoring in the Field of Water Policy Pursuant to Directive 2008/105/EC of the European Parliament and of the Council and Repealing Commission Implementing Decision (EU) 2015/495. https://eur-lex.europa.eu/eli/dec_impl/2018/840/oj
- BlueMed Research and Innovation Initiative for blue jobs and growth in the Mediterranean area www.bluemed-initiative.eu/
- BlueMed Pilot action on A Healthy Plastic-Free Mediterranean Sea http://www.bluemed-initiative.eu/pilot-action-on-a-healthy-plastic-free-mediterranean-sea/
- Red List of the International Union for Conservation of Nature http://www.iucn.org/

References

Achterberg, E.P., van Den Berg, C.M.G., 1997. Distribution and behavior of some trace metals in the western Mediterranean Sea. Deep Sea Res. Part II 44 (3–4), 675–691.

Albaigés, J., 2005. Persistent organic pollutants in the Mediterranean sea. In: Saliot, A. (Ed.), The Mediterranean Sea. Springer, Berlin, Heidelberg, New York.

Alcaro, L., Torre, C.D., Petochi, T., Sammarini, V., Matiddi, M., Corsi, I., Amato, E., 2012. Studies on environmental effects of underwater chemical munitions in the southern adriatic sea (Mediterranean Sea). Mar. Technol. Soc. J. 46 (3), 10–20.

Alessi, E., Di Carlo, G., 2018. Out of the Plastic Trap: Saving the Mediterranean from Plastic Pollution. WWF Mediterranean Marine Initiative, Rome, Italy, p. 28.

Allen, S., Allen, D., Phoenix, V.R., Le Roux, G., Jiménez, P.D., Simonneau, A., Binet, S., Galop, D., 2019. Atmospheric transport and deposition of microplastics in a remote mountain catchment. Nat. Geosci. 12, 339–344.

Alpert, P., Hemming, D., Jin, F., Kay, G., Kitoh, A., Mariotti, A., 2013. In: Navarra, A., Tubiana, L. (Eds.), Regional Assessment of Climate Change in the Mediterranean, Advances in Global Change Research, vol. 50, pp. 201–239.

Alvarez, D.A., Maruya, K.A., Dodder, N.G., Lao, W., Furlong, E.T., Smalling, K.L., 2014. Occurrence of contaminants of emerging concern along the California coast (2009–10) using passive sampling devices. Mar. Pollut. Bull. 81, 347–354.

Amato, E., Alcaro, L., Corsi, I., Della Torre, C., Farchi, C., Focardi, S., Tursi, A., 2006. An integrated ecotoxicological approach to assess the effects of pollutants released by unexploded chemical ordnance dumped in the southern Adriatic (Mediterranean Sea). Mar. Biol. 149 (1), 17–23.

Amorosi, A., Guermandi, M., Marchi, N., Sammartino, I., 2014. Fingerprinting sedimentary and soil units by their natural metal contents: a new approach to assess metal contamination. Sci. Total Environ. 500, 361–372.

Amorosi, A., Maselli, V., Trincardi, F., 2016. Onshore to offshore anatomy of a late Quaternary source-to-sink system (Po Plain–Adriatic Sea, Italy). Earth Sci. Rev. 153, 212–237.

Anthony, E.J., Marriner, N., Morhange, C., 2014. Human influence and the changing geomorphology of Mediterranean deltas and coasts over the last 6000 years: from progradation to destruction phase? Earth Sci. Rev. 139, 336–361.

Arnell, N.W., 2014. Hydrology and Global Environmental Change. Routledge.

Arpin-Pont, L., Bueno, M.J.M., Gomez, E., Fenet, H., 2016. Occurrence of PPCPs in the marine environment: a review. Environ. Sci. Pollut. Res. 23, 4978–4991.

Aston, S.R., Fowler, S.W., 1985. Mercury in the open Mediterranean: evidence of contamination? Sci. Total Environ. 43, 13–26.

Augier, H., Prak, W.K., Ronneau, C., 1993. Mercury contamination of the striped dolphin *Stenella coeruleoalba* Meyen from the French Mediterranean coasts. Mar. Pollut. Bull. 26, 306–311.

Basili, M., Quero, G.M., Giovannelli, D., Manini, E., Vignaroli, C., Avio, C.G., De Marco, R., Luna, G.M., 2020. Major role of surrounding environment in shaping biofilm community composition on marine plastic debris front. Mar. Sci. 7, 262.

Bassetti, M.A., Jouet, G., Dufois, F., Berné, S., Rabineau, M., Taviani, M., 2006. Sand bodies at the shelf edge in the Gulf of Lions (Western Mediterranean): deglacial history and modern processes. Mar. Geol. 234 (1–4), 93–109.

Belfiore, A., Bellotti, P., Carboni, M.G., Chiari, R., Evangelista, S., Tortora, P., Valeri, P., 1987. Il delta del Tevere: le facies sedimentarie della conoide sommersa. Un'analisi statistica dei caratteri tessiturali, microfaunistici e mineralogici. Boll. Soc. Geol It 106, 425−445.

Bellotti, P., Chiocci, F.L., Milli, S., Tortora, P., Valeri, P., 1994. Sequence stratigraphy and depositional setting of the Tiber delta: integration of high resolution seismics, well logs and archaeological data. J. Sediment. Petrol. B64, 416−432.

Bellotti, P., Calderoni, G., Carboni, M.G., Di Bella, L., Tortora, P., Valeri, P., 2007. Late Quaternary landscape evolution of the Tiber River delta plain (Central Italy): new evidence from pollen data, biostratigraphy and 14C dating. Zeitschrift für Geomprphologie 51 (4), 505−534.

Bellotti, P., Davoli, L., Sadori, L., 2018. Landscape diachronic reconstruction in the Tiber delta during historical time: a holistic approach. Geogr. Fis. Din. Quaternaria 41, 3−21.

Bellucci, L.G., Cassin, D., Giuliani, S., Botter, M., Zonta, R., 2016. Sediment pollution and dynamic in the Mar Piccolo di Taranto (Southern Italy): insight from bottom sediment traps and surficial sediment. Environ. Sci. Pollut. Control Ser. 23 (13), 12554−12565.

Berg, T., Fürhaupter, K., Teixeira, H., Uusitalo, L., Zampoukas, N., 2015. The marine strategy framework directive and the ecosystem-based approach—pitfalls and solutions. Mar. Pollut. Bull. 96, 18−28.

Berrojalbiz, N., Dachs, J., Ojeda, M.J., Valle, M.C., Castro-Jiménez, J., Wollgast, J., Ghiani, M., Hanke, G., Zaldivar, J.M., 2011. Biogeochemical and physical controls on concentrations of polycyclic aromatic hydrocarbons in water and plankton of the Mediterranean and Black Seas. Global Biogeochem. Cycles 25. GB4003.

Bethoux, J.P., 1989. Oxygen consumption, new production, vertical advection and environmental evolution in the Mediterranean Sea. Deep-Sea Res. Part A. Oceanogr. Res. Pap. 36 (5), 769−781.

Blum, M.D., Roberts, H.H., 2009. Drowning of the Mississippi Delta due to insufficient sediment supply and global sea-level rise. Nat. Geosci. 2 (7), 488.

Bonnefille, B., Gomez, E., Alali, M., Rosain, D., Fenet, H., Courant, F., 2018. Metabolomics assessment of the effects of diclofenac exposure on *Mytilus galloprovincialis*: potential effects on osmoregulation and reproduction. Sci. Total Environ. 613−614, 611−618.

Bonsignore, M., Salvagio Manta, D., Barsanti, M., Conte, F., Delbono, I., Horvat, M., Quinci, E.M., Schirone, A., Shlyapnikov, Y., Sprovieri, M., 2020. Mercury isotope signatures in sediments and marine organisms as tracers of historical industrial pollution. Chemosphere 258, 127435.

Booth, A., Kubowicz, S., Beegle-Krause, C., Skancke, J., Nordam, T., Landsem, E., Throne-Holst, M., Jahren, S., 2017. M-918|2017-Unrestricted report microplastic in global and Norwegian marine environments: distributions, degradation mechanisms and transport.

Borja, A., Elliott, M., Uyarra, M.C., Carstensen, J., Mea, M., 2017. Bridging the Gap between Policy and Science in Assessing the Health Status of Marine Ecosystems, second ed. Frontiers Media, Lausanne, Switzerland, p. 548.

Bosman, A., Romagnoli, C., Madricardo, F., Correggiari, A., Remia, A., Zubalich, R., Trincardi, F., 2020. Short-term evolution of Po della Pila delta lobe from time lapse high-resolution multibeam bathymetry (2013−2016). Estuar. Coast. Shelf Sci. 233, 106533.

Boucher, J., Bilard, G., 2020. The Mediterranean: Mare Plasticum. IUCN, Gland, Switzerland x+62 pp.

Bouloubassi, I., Méjanelle, L., Pete, R., Fillaux, J., Lorre, A., Point, V., 2006. PAH transport by sinking particles in the open Mediterranean Sea: a 1 year sediment trap study. Mar. Pollut. Bull. 52, 560−571.

Boxall, A.B.A., Rudd, M.A., Brooks, B.W., Caldwell, D.J., Choi, K., Hickmann, S., Innes, E., Boyer, J., Duvail, C., Le Strat, P., Gensous, B., Tesson, M., 2005. High resolution stratigraphy and evolution of the Rhône delta plain during Postglacial time, from subsurface drilling data bank. Mar. Geol. 222−223, 267−298.

Boyer, J., Duvail, C., Le Strat, P., Gensous, B., Tesson, M., 2005. High resolution stratigraphy and evolution of the Rhône delta plain during Postglacial time, from subsurface drilling data bank. Mar. Geol. 222−223, 267−298.

Boyle, E.A., Chapnick, S.D., Bai, X.X., Spivack, A., 1985. Trace metal enrichments in the Mediterranean Sea. Earth Planet. Sci. Lett. 74 (4), 405−419.

Boyle, E.A., Keigwin, L.D., 1985. Comparison of Atlantic and Pacific paleochemical records for the last 215,000 years: Changes in deep ocean circulation and chemical inventories. Earth Planet. Sci. Lett. 76 (1−2), 135−150.

Campo, B., Bohacs, K.M., Amorosi, A., 2020. Late Quaternary sequence stratigraphy as a tool for groundwater exploration: Lessons from the Po River Basin (northern Italy). AAPG Bulletin 104 (3), 681−710.

Camuffo, D., 1987. Freezing of the Venetian Lagoon since the 9th century AD in comparision to the climate of western Europe and England. Climatic Change 10 (1), 43−66.

Canals, M., Danovaro, R., Heussner, S., Lykousis, V., Puig, P., Trincardi, F., Sanchez-Vidal, A., 2009. Cascades in Mediterranean submarine grand canyons. Oceanography 22 (1), 26−43.

Canals, M., Pham, C.K., Bergmann, M., Gutow, L., Hanke, G., van Sebille, E., Angiolillo, M., Buhl Mortensen, L., Cau, A., Ioakeimidis, C., Kammann, U., Lundsten, L., Papatheodorou, G., Purser, A., Sanchez-Vidal, A., Schulz, M., Vinci, M., Chiba, S., Galgani, F., Langenkämper, D., Möller, T., Nattkemper, T.W., Ruiz, M., Suikkanen, S., Woodall, L., Fakiris, E., Jack, M.E.M., Giorgetti, A., 2021. The quest for seafloor macrolitter: a critical review of background knowledge, current methods and future prospects. Environ. Res. Lett. 16, 023001.

Carniello, L., Defina, A., D'Alpaos, L., 2009. Morphological evolution of the Venice lagoon: evidence from the past and trend for the future. J. Geophys. Res. Earth Surf. 114.

Cattaneo, A., Trincardi, F., Langone, L., Asioli, A., Puig, P., 2004. Clinoform generation on Mediterranean margins. Oceanography 17 (4), 104−117.

Castiglioni, S., Bagnati, R., Calamari, D., Fanelli, R., Zuccato, E., 2005. A multiresidue analytical method using solid-phase extraction and high pressure liquid chromatography tandem mass spectrometry to measure pharmaceuticals of different therapeutic classes in urban wastewaters. J. Chromatogr. A 1092, 206−2015.

Castiglioni, S., Bagnati, R., Fanelli, R., Pomati, F., Calamari, D., Zuccato, E., 2006. Removal of pharmaceuticals in sewage treatment plants in Italy. Environ. Sci. Technol. 40, 357−363.

Castiglioni, S., Davoli, E., Riva, F., Palmiotto, M., Camporini, P., Manenti, A., Zuccato, E., 2018. Mass balance of emerging contaminants in the water cycle of a highly urbanized and industrialized area of Italy. Water Res. 131, 287−298.

Cau, A., Avio, C.G., Dessì, C., Moccia, D., Pusceddu, A., Regoli, F., Cannas, R., Follesa, M.C., 2020. Benthic Crustacean digestion can modulate the environmental fate of microplastics in the deep sea. Environ. Sci. Technol. 54 (8), 4886−4892, 2020 Apr 21.

Čelić, M., Gros, M., Farré, M., Barceló, D., Petrović, M., 2019. Pharmaceuticals as chemical markers of wastewater contamination in the vulnerable area of the Ebro Delta (Spain). Sci. Total Environ. 20 (652), 952−963.

Cencini, C., 1998. Physical processes and human activities in the evolution of the Po delta, Italy. J. Coast Res. 775−793.

Chapman, P.M., 2012. Management of coastal lagoons under climate change. Estuar. Coast Shelf Sci. 110, 32−35.

Chiggiato, J., Bergamasco, A., Borghini, M., Falcieri, F.M., Falco, P., Langone, L., Schroeder, K., 2016. Dense-water bottom currents in the southern Adriatic Sea in spring 2012. Mar. Geol. 375, 134−145.

Chiocci, F.L., Orlando, L., Tortora, P., 1991. Small-scale seismic stratigraphy and paleogeographical evolution of the continental shelf facing the SE Elba Island (northern Tyrrhenian Sea, Italy). J. Sediment. Res. 61 (4), 506−526.

Clark, P.U., Shakun, J.D., Marcott, S.A., Mix, A.C., Eby, M., Kulp, S., Plattner, G.K., 2016. Consequences of twenty-first-century policy for multi-millennial climate and sea-level change. Nat. Clim. Change 6 (4), 360−369.

Colella, S., Falcini, F., Rinaldi, E., Sammartino, M., Santoleri, R., 2016. Mediterranean ocean colour chlorophyll trends. PLoS One 11 (6), e0155756.

Colombo, P., 1970. Osservazioni sul regime di alcuni tratti del litorale occidentale dell'alto Adriatico. In: Scritti in onore del Prof. Guido Ferro, Università di Padova, pp. 23−62.

Como, S., Magni, P., Casu, D., Floris, A., Giordani, G., Natale, S., De Falco, G., 2007. Sediment characteristics and macrofauna distribution along a human-modified inlet in the Gulf of Oristano (Sardinia, Italy). Mar. Pollut. Bull. 54 (6), 733−744.

Cooley, S.W., Ryan, J.C., Smith, L.C., 2021. Human alteration of global surface water storage variability. Nature 591 (7848), 78−81.

Copin-Montegut, G., Courau, P., Nicolas, E., 1986. Distribution and transfer of trace elements in the Western Mediterranean. Mar. Chem. 18 (2), 189−195.

Coppola, L., Legendre, L., Lefevre, D., Prieur, L., Taillandier, V., Riquier, E.D., 2018. Seasonal and inter-annual variations of dissolved oxygen in the northwestern Mediterranean Sea (DYFAMED site). Prog. Oceanogr. 162, 187−201.

Coro, G., Tassetti, A.N., Armelloni, E.N., Pulcinella, J., Ferrà, C., Sprovieri, M., Scarcella, G., 2022. COVID-19 lockdowns reveal the resilience of Adriatic Sea fisheries to forced fishing effort reduction. Sci. Rep. 12 (1), 1−14.

Correggiari, A., Roveri, M., Trincardi, F., 1996. Late pleistocene and Holocene evolution on the North Adriatic Sea. J. Quat. Sci. 9, 697−704.

Correggiari, A., Cattaneo, A., Trincardi, F., 2005a. The modern Po Delta system: lobe switching and asymmetric prodelta growth. Mar. Geol. 222, 49−74.

Correggiari, A., Cattaneo, A., Trincardi, F., 2005b. Depositional patterns in the Late-Holocene Po delta system. In: Bhattacharya, J.P., Giosan, L. (Eds.), Concepts, Models and Examples, vol. 83. SEPM Special Publication, pp. 365−392.

Cossa, D., Coquery, M., 2005. The Mediterranean mercury anomaly, a geochemical or a biological issue. In: Saliot, A. (Ed.), The Mediterranean Sea. Handbook of Environmental Chemistry, vol. 5. Springer, pp. 177−208, p. 413.

Cossa, D., Martin, J.M., Takayanagi, K., Sanjuan, J., 1997. The distribution and cycling of mercury in the western Mediterranean. Deep-Sea Res. Part II 44, 721−740.

Covaci, A., Losada, S., Roosens, L., Vetter, W., Santos, F.J., Neels, H., Storelli, A., Storelli, M.M., 2008. Anthropogenic and naturally occurring organobrominated

compounds in two Deep-Sea fish species from the Mediterranean. Environ. Sci. Technol. 42, 8654−8660.
D'Alpaos, L., 2010. Fatti e Misfatti di Idraulica Lagunare. Istituto Veneto di Scienze, Lettere ed Arti: Venice, Italy, 2010.
D'Agostino, F., Bellante, A., Quinci, E., Gherardi, S., Placenti, F., Sabatino, N., Buffa, G., Avellone, G., Di Stefano, V., Del Core, M., 2020. Persistent and emerging organic pollutants in the marine coastal environment of the Gulf of Milazzo (southern Italy): human health risk assessment. Front. Environ. Sci. 8, 117.
D'Ortenzio, F., Antoine, D., Marullo, S., 2008. Satellite-driven modeling of the upper ocean mixed layer and air−sea CO2 flux in the Mediterranean Sea. Deep-Sea Res. Part I Oceanogr. Res. Pap. 55 (4), 405−434.
Dalberg Advisors, WWF Mediterranean Marine Initiative, 2019. Stop the Flood of Plastic: How Mediterranean Countries Can Save Their Sea. WWF Report. June, 2019.
Day, J.W., Ramachandran, R., Giosan, L., Syvitski, J., Kemp, G.P., 2019. Delta winners and losers in the Anthropocene. In: Coasts and Estuaries. Elsevier, pp. 149−165.
De Souza Machado, A.A., Kloas, W., Zarfl, C., Hempel, S., Rillig, M.C., 2018. Microplastics as an emerging threat to terrestrial ecosystems. Global Change Biol. 24 (4), 1405−1416, 2018 Apr.
Desbiolles, F., Malleret, L., Tiliacos, C., Wong-Wah-Chung, P., Laffont-Schwob, I., 2018. Occurrence and ecotoxicological assessment of pharmaceuticals: is there a risk for the Mediterranean aquatic environment? Sci. Total Environ. 15 (639), 1334−1348.
Diamond, J., 1997. Guns, Germs and Steel: A Short History of Everybody for the Last 13,000 Years. W.W. Norton and Sons.
Duck, R.W., da Silva, J.F., 2012. Coastal lagoons and their evolution: a hydromorphological perspective. Estuar. Coast Shelf Sci. 110, 2−14, 10 September 2012.
Durán, R., Guillén, J., Rivera, J., Lobo, F.J., Muñoz, A., Fernández-Salas, L.M., Acosta, J., 2017. Formation, evolution and present-day activity of offshore sand ridges on a narrow, tideless continental shelf with limited sediment supply. Mar. Geol. 397, 93−107. https://doi.org/10.1016/j.margeo.2017.11.001.
Durán, R., Guillén, J., Rivera, J., Muñoz, A., Lobo, F.J., Fernández-Salas, L.M., Acosta, J., 2017. Subaqueous dunes over sand ridges on the Murcia outer shelf. In: Atlas of Bedforms in the Western Mediterranean. Springer, Cham, pp. 187−192.
Elbaz-Poulichet, F., 2005. River inputs of metals and arsenic. In: Saliot, A. (Ed.), The Mediterranean Sea. Handbook of Environmental Chemistry, vol. 5. Springer, p. 413p. ISSN 1433-6863 (pp. 212−233).
Erickson, B.E., 2002. Analysing the ignored environmental contaminants. Environ. Sci. Technol. 36, 140A−145A.
Fabbri, E., Franzellitti, S., 2016. Human pharmaceuticals in the marine environment: focus on exposure and biological effects in animal species. Environ. Toxicol. Chem. 35 (4), 799−812.
Fader, M., Giupponi, C., Burak, S., Dakhlaoui, H., Koutroulis, A., Lange, M.A., Llasat, M.C., Pulido-Velazquez, D., Sanz-Cobeña, A., 2020. Water. In: Cramer, W., Guiot, J., Marini, K. (Eds.), Climate and Environmental Change in the Mediterranean Basin − Current Situation and Risks for the Future. First Mediterranean Assessment Report, pp. 181−236. Union for the Mediterranean, Plan Bleu, UNEP/MAP, Marseille, France.
Fanget, A.S., Berné, S., Jouet, G., Bassetti, M.A., Dennielou, B., Maillet, G.M., Tondut, M., 2014. Impact of relative sea level and rapid climate changes on the architecture and

lithofacies of the Holocene Rhone subaqueous delta (Western Mediterranean Sea). Sediment. Geol. 305, 35−53.
Fent, K., Weston, A.A., Caminada, D., 2006. Ecotoxicology of human pharmaceuticals. Aquat. Toxicol. 76, 122−159.
Feo, M.L., Bagnati, R., Passoni, A., Riva, F., Salvagio Manta, D., Sprovieri, M., Traina, A., Zuccato, E., Castiglioni, S., 2021. Pharmaceuticals and other contaminants in waters and sediments from Augusta Bay (southern Italy). Sci. Total Environ. 739 (2020), 139827.
Finkl, C.W., Benedet, L., Andrews, J.L., Suthard, B., Locker, S.D., 2007. Sediment ridges on the west Florida inner continental shelf: sand Resources for Beach Nourishment. J. Coast Res. 231, 143−159.
Fogarin, S., Madricardo, F., Zaggia, L., Sigovini, M., Montereale-Gavazzi, G., Kruss, A., Trincardi, F., 2019. Tidal inlets in the Anthropocene: geomorphology and benthic habitats of the Chioggia inlet, Venice lagoon (Italy). Earth Surf. Process. Landforms 44 (11), 2297−2315.
Foglini, F., Campiani, E., Trincardi, F., 2016. The reshaping of the South West Adriatic Margin by cascading of dense shelf waters. Mar. Geol. 375, 64−81.
Fontolan, G., Pillon, S., Bezzi, A., Villalta, R., Lipizer, M., Triches, A., D'Aietti, A., 2012. Human impact and the historical transformation of saltmarshes in the Marano and Grado lagoon, northern Adriatic Sea. Estuar. Coast Shelf Sci. 113, 41−56.
Fowler, S.W., 1977. Trace elements in zooplankton particulate products. Nature 269, 51−53.
Fowler, S.W., 1986. Trace metal monitoring of pelagic organisms from the open Mediterranean Sea. Environ. Monit. Assess. 7, 59−78.
Fozzati, L., 2013. Il primo popolamento della laguna. In: VENEZIA, La Regina del Mare e delle Arti, 30−32 (Biblos, Cittadella).
Francocci, F., Cappelletto, M., Fava, F., Trincardi, F., 2021. The BlueMed Pilot action Healthy plastic-free Mediterranean. Mar. Bull. Geophys. Oceanogr. 62. Supplement N. 3 September 2021.
Friedlingstein, P., Jones, M.W., O'Sullivan, M., Andrew, R.M., Bakker, D.C., Hauck, J., Le Quéré, C., Peters, G.P., Peters, W., Pongratz, J., Sitch, S., Canadell, J.G., Ciais, P., Jackson, R.B., Alin, S.R., Anthoni, P., Bates, N.R., Becker, M., Bellouin, N., Bopp, L., Chau, T.T.T., Chevallier, F., Chini, L.P., Cronin, M., Currie, K.I., Decharme, B., Djeutchouang, L., Dou, X., Evans, W., Feely, R.A., Feng, L., Gasser, T., Gilfillan, D., Gkritzalis, T., Grassi, G., Gregor, L., Gruber, N., Gürses, Ö., Harris, I., Houghton, R.A., Hurtt, G.C., Iida, Y., Ilyina, T., Luijkx, I.T., Jain, A.K., Jones, S.D., Kato, E., Kennedy, D., Goldewijk, K.K., Knauer, J., Korsbakken, J.I., Arne Körtzinger, A., Landschützer, P., Lauvset, S.K., Lefèvre, N., Lienert, S., Liu, J., Marland, G., McGuire, P.C., Melton, J.R., Munro, D.R., Nabel, J.E.M.S., Nakaoka, S.I., Niwa, Y., Ono, T., Pierrot, D., Poulter, B., Rehder, G., Resplandy, L., Robertson, E., Rödenbeck, C., Rosan, T.M., Schwinger, J., Schwingshackl, C., Séférian, R., Sutton, A.J., Sweeney, C., Tanhua, T., Tans, P.P., Tian, H., Tilbrook, B., Tubiello, F., van der Werf, G., Vuichard, N., Wada, C., Wanninkhof, R., Watson, A., Willis, D., Wiltshire, A.J., Yuan, W., Chao Yue, C., Xu Yue, X., Zaehle, S., Zeng, J., 2021. Global carbon budget 2021. Earth Syst. Sci. Data Discuss. 1−191.
Frihy, O.E., 2001. The necessity of environmental impact assessment (EIA) in implementing coastal projects: lessons learned from the Egyptian Mediterranean Coast. Ocean Coast Manag. 44 (7−8), 489−516.
Frodello, J.P., Marchand, B., 2001. Cadmium, copper, lead, and zinc in five toothed whale species of the Mediterranean Sea. Int. J. Toxicol. 20 (6), 339−343.

Froescheis, O., Looser, R., Cailliet, G.M., Jarman, W.M., Ballschmiter, K., 2000. The deep sea as a final global sink of semivolatile persistant organic pollutants? Part I: PCBs in surface and deep-sea dwelling fish in the North and South Atlantic and the Monterey Bay Canyon (California). Chemosphere 40, 661−670.

Gaertner-Mazouni, N., De Wit, R., 2012. Exploring new issues for coastal lagoons monitoring and management. Estuar. Coast Shelf Sci. 114, 1−6.

Galgani, F., 2015. Marine litter, future prospects for research. Front. Mar. Sci. 26.

Gall, S.C., Thompson, R.C., 2015. The impact of debris on marine life. Mar. Pollut. Bull. Volume 92 (Issues 1−2), 170−179, 2015.

Galletti, Y., Becagli, S., Di Sarra, A., Gonnelli, M., Pulido-Villena, E., Sferlazzo, D.M., Rita Traversi, R., Vestri, S., Santinelli, C., 2020. Atmospheric deposition of organic matter at a remote site in the central Mediterranean Sea: implications for the marine ecosystem. Biogeosciences 17 (13), 3669−3684.

Galloway, W.E., 1975. In: Broussard, M.L. (Ed.), Process Framework for Describing the Morphologic and Stratigraphic Evolution of Deltaic Depositional Systems in: Deltas: Models for Exploration. Houston Geological Society, pp. 87−98.

Galloway, J.N., Aber, J.D., Erisman, J.W., Seitzinger, S.P., Howarth, R.W., Cowling, E.B., Cosby, B.J., 2003. The nitrogen cascade. Bioscience 53, 341−356.

Gatto, F., Marocco, R., 1992. Caratteri morfologici ed antropici della Laguna di Grado (Alto Adriatico). Gortania 14, 19e42.

Germoni, P., Keay, S., Millett, M., Strutt, K., 2019. Ostia beyond the Tiber: Recent Archaeological Discoveries in the Isola Sacra, pp. 149−168.

Geyer, R., Jambeck, J.R., Law, K.L., 2017. Production, use, and fate of all plastics ever made. Sci. Adv. 3 (7).

Giosan, L., Donnelly, J.P., Constantinescu, S., Filip, F., Ovejanu, I., Vespremeanu-Stroe, A., Duller, G.A., 2006. Young Danube delta documents stable Black Sea level since the middle Holocene: morphodynamic, paleogeographic, and archaeological implications. Geology 34 (9), 757−760.

Giosan, L., Constantinescu, S., Filip, F., Deng, B., 2013. Maintenance of large deltas through channelization: nature vs. humans in the Danube delta. Anthropocene 1, 35−45.

Giraudi, C., Tata, C., Paroli, L., 2009. Late Holocene evolution of tiber river delta and geoarchaeology of Claudius and trajan harbor. Rome. Geoarchaeology Int. J. 24 (3), 371−382.

Goldman, S.J., Jackson, K.E., 1986. Erosion and Sediment Control Handbook.

Gómez-Gutiérrez, A., Garnacho, E., Bayona, J.M., Albaigés, J., 2007. Assessment of the Mediterranean sediments contamination by persistent organic pollutants. Environ. Pollut. 148, 396−408.

Gonzalez-Rey, M., Bebianno, M.J., 2014. Effects of non-steroidal anti-inflammatory drug (NSAID) diclofenac exposure in mussel *Mytilus galloprovincialis*. Aquat. Toxicol. 148, 221−230.

Grill, G., Lehner, B., Thieme, M., Geenen, B., Tickner, D., Antonelli, F., Zarfl, C., 2019. Mapping the world's free-flowing rivers. Nature 569 (7755), 215−221.

Grizzetti, B., Bouraoui, F., Aloe, A., 2012. Changes of nitrogen and phosphorus loads to European seas. Global Change Biol. 18, 769−782.

Groh, K.J., Backhaus, T., Carney-Almroth, B., Gueke, B., Inostroza, P.A., Lennquist, A., Leslie, H.A., Maffini, M., Slunge, D., Trasande, L., Warhurst, A.M., Muncke, J., 2019. Overview of known plastic packaging-associated chemicals and their hazards. Sci. Total Environ. 651 (15), 3253−3268. Part 2.

Gruber, N., Galloway, J.N., 2008. An Earth-system perspective of the global nitrogen cycle. Nature 451 (7176), 293−296.

Guerzoni, S., Chester, R., Dulac, F., Herut, B., Loÿe-Pilot, M.D., Measures, C., Migon, C., Molinaroli, E., Moulin, C., Rossini, P., Saydam, C., Soudine, A., Ziveri, P., 1999. The role of atmospheric deposition in the biogeochemistry of the Mediterranean Sea. Prog. Oceanogr. 44, 147−190.

Haddeland, I., Heinke, J., Biemans, H., Eisner, S., Flörke, M., Hanasaki, N., Konzmann, M., Ludwig, F., Masaki, Y., Schewe, J., Stacke, T., Tessler, Z.D., Wada, Y., Wisser, D., 2014. Global water resources affected by human interventions and climate change. Proc. Natl. Acad. Sci. Unit. States Am. 111 (9), 3251−3256.

Harmelin-Vivien, M., Cossa, D., Crochet, S., Banaru, D., Letourneur, Y., Mellon-Duval, C., 2009. Difference of mercury bioaccumulation in red mullets from the north- western Mediterranean and Black seas. Mar. Pollut. Bull. 58 (5), 679−685.

Hassoun, A.E.R., Gemayel, E., Krasakopoulou, E., Goyet, C., Abboud-Abi Saab, M., Guglielmi, V., Touratier, F., Falco, C., 2015. Acidification of the Mediterranean Sea from anthropogenic carbon penetration. Deep-Sea Res. Part I Oceanogr. Res. Pap. 102, 1−15.

Hastings, M.G., Jarvis, J.C., Steig, E.J., 2009. Anthropogenic impacts on nitrogen isotopes of ice-core nitrate. Science 324 (5932), 1288-1288.

Heimbürger, L.E., Cossa, D., Marty, J.C., Migon, C., Averty, B., Dufour, A., Ras, J., 2010. Methyl mercury distributions in relation to the presence of nano and picophytoplankton in an oceanic water column (Ligurian Sea, north-western Mediterranean). Geochem. Cosmochim. Acta 74, 4459−5549.

Hernando, M.D., Mezcua, M., Fernandez-Alba, A.R., Barcelò, D., 2006. Environmental risk assessment of pharmaceutical residues in wastewater effluents, surface waters and sediments. Talanta 69, 334−342.

Hershkovitz, I., Weber, G.W., Quam, R., Duval, M., Grün, R., Kinsley, L., Ayalon, A., Bar Matthews, M., Valladas, H., Mercier, N., Arsuaga, J.L., Martinón-Torres, M., Fornai, C., Martín-Francés, L., Rachel Sarig, R., May, H., Krenn, V.A., Rodríguez, L., García, R., Lorenzo, C., Carretero, J.M., Frumkin, A., Shahack-Gross, R., Mayer, D.E.B.Y., Cui, Y., Wu, X., Peled, N., Groman-Yaroslavski, I., Weissbrod, L., Yeshurun, R., Tsatskin, A., Zaidner, Y., Weinstein-Evron, M., 2018. The earliest modern humans outside Africa. Science 359 (6374), 456−459.

Hopewell, J., Dvorak, R., Kosior, E., 2009. Plastics recycling: challenges and opportunities. Philos. Trans. R. Soc. Lond. B Biol. Sci. 364 (1526), 2115−2126.

Housley, A.J., Ammerman, R.A., McClennen, C.E., 2004. That sinking feeling: wetland investigations of the origins of Venice. J. Wetl. Archaeol. 4, 139−153.

Huang, Y., Shen, H., Chen, Y., Zhong, Q., Chen, H., Wang, R., Shen, G., Liu, J., Li, B., Tao, S., 2015. Global organic carbon emissions from primary sources from 1960 to 2009. Atmos. Environ. 122, 505−512.

Huerta Lwanga, E., Mendoza Vega, J., Ku-Quej, V., de los Angeles Chi, J., Sanchez del Cid, L., Chi, C., Segura, G.E., Gertsen, H., Salánki, T., van der Ploeg, M., Koelmans, A.A., Geissen, V., 2017. Field evidence for transfer of plastic debris along a terrestrial food chain. Sci. Rep. 7 (1), 14071.

Hughes, S.R., Kay, P., Brown, L.E., 2013. Global synthesis and critical evaluation of pharmaceuticals data sets collected from river systems. Environ. Sci. Technol. 47, 661−667.

Ibáñez, C., Sharpe, P., Day, J.W., Day, J.N., Prat, N., 2010. Vertical accretion and relative sea level rise in the Ebro delta wetlands. Wetlands 30, 979−988.

IPCC, 2021. In: Masson-Delmotte, V., Zhai, P., Pirani, A., Connors, S.L., Péan, C., Berger, S., Caud, N., Chen, Y., Goldfarb, L., Gomis, M.I., Huang, M., Leitzell, K., Lonnoy, E., Matthews, J.B.R., Maycock, T.K., Waterfield, T., Yelekçi, O., Yu, R., Zhou, B. (Eds.), Climate Change 2021: The Physical Science Basis. Contribution of Working Group I to the Sixth Assessment Report of the Intergovernmental Panel on Climate Change. Cambridge University Press (in press).

Jamieson, A.J., Malkocs, T., Piertney, S.B., Fujii, T., Zhang, Z., 2017. Bioaccumulation of persistent organic pollutants in the 15 relazione-02.04. Technical report, 852 pp 16 deepest ocean fauna. Nat. Ecol. Evol. 1, 1−4.

Jelic, A., Gros, M., Ginebreda, A., Cespedes-Sàncez, R., Ventura, F., Petrovic, M., Barcelò, D., 2011. Occurrence, partition and removal of pharmaceuticals in sewage water and sludge during wastewater treatment. Water Res. 45, 1165−1176.

Jiménez-Cárceles, F.J., Egea, C., Rodriguez-Caparros, A.B., Barbosa, O.A., Delgado, M.J., Ortiz, R., Alvarez-Rogel, J., 2006. Contents of nitrogen, ammonium, phosphorus, pesticides and heavy metals, in a salt marsh in the coast of the Mar Menor lagoon(SE Spain). Fresenius Environ. Bull. 15 (5), 370−378.

Jouffray, J.B., Blasiak, R., Norström, A.V., Österblom, H., Nyström, M., 2020. The blue acceleration: the trajectory of human expansion into the ocean. One Earth 2 (1), 43−54.

Kanakidou, M., Myriokefalitakis, S., Tsagkaraki, M., 2020. Atmospheric inputs of nutrients to the Mediterranean sea. Deep-Sea Res. Part II Top. Stud. Oceanogr. 171, 104606.

Kasprzyk-Horden, B., Dinsdale, R.M., Guwy, A.J., 2009. The removal of pharmaceuticals, personal care products, endocrine disruptors and illicit drugs during wastewater treatment and its impact of the quality of receiving waters. Water Res. 43, 363−380.

Komar, P.D., 1996. Tidal-inlet processes and morphology related to the transport of sediments. J. Coast Res. 23, 23−45.

Krahmann, G., Schott, F., 1998. Longterm increases in Western Mediterranean salinities and temperatures: anthropogenic and climatic sources. Geophys. Res. Lett. 25 (22), 4209−4212.

Lalumera, G.M., Calamari, D., Galli, P., Castiglioni, S., Crosa, G., Fanelli, R., 2004. Preliminary investigation on the environmental occurrence and effects of antibiotics used in aquaculture in Italy. Chemosphere 54, 661−668.

Lambeck, K., Rouby, H., Purcell, A., Sun, Y., Sambridge, M., 2014. sea level and global ice volumes from the last glacial maximum to the Holocene. Proc. Natl. Acad. Sci. USA 111 (43), 15296−15303.

Lana-Renault, N., Morán-Tejeda, E., de las Heras, M.M., Lorenzo-Lacruz, J., López-Moreno, N., 2020. Land-use change and impacts. In: Zribi, M., Brocca, L., Tramblay, Y., Molle, F. (Eds.), Water Resources in the Mediterranean Region. Elsevier, pp. 257−296.

Lebreton, L., Egger, M., Slat, B., 2019. A global mass budget for positively buoyant macroplastic debris in the ocean. Sci. Rep. 9, 12922.

León, V.M., García, I., González, E., Samper, R., Fernández-González, V., Muniategui-Lorenzo, S., 2018. Potential Transfer of Organic Pollutants from Littoral Plastics Debris to the Marine Environment Environmental Pollution, vol. 236, pp. 442−453.

Lewis, S.L., Maslin, M.A., 2018. The Human Planet. Yale University Press.

Li, M., Peng, C., Wang, M., Xue, W., Zhang, K., Wang, K., Shi, G., Zhu, Q., 2017. The carbon flux of global rivers: a re-evaluation of amount and spatial patterns. Ecol. Indicat. 80, 40−51.

Lipiatou, E., Albaigés, J., 1994. Atmospheric deposition of hydrophobic organic chemicals in the northwestern Mediterranean Sea: comparison with the Rhone river input. Mar. Chem. 46 (1−2), 153−164.
Lively, J.A., Good, T.P., 2019. Ghost fishing. In: World Seas: An Environmental Evaluation. Academic Press, pp. 183−196.
Lloret, J., Marin, A., Marin-Guirao, L., 2008. Is lagoon eutrophication likely to be aggravated by global climate change? Estuar. Coast Shelf Sci. 78, 403−412.
Lohmann, R., Breivik, K., Dachs, J., Muir, D., 2007. Global fate of POPs: current and future research directions. Environ. Pollut. 150, 150−165.
Ludwig, W., Dumont, E., Meybeck, M., Heussner, S., 2009. River discharges of water and nutrients to the Mediterranean and Black Sea: major drivers for ecosystem changes during past and future decades? Prog. Oceanogr. 80 (3−4), 199−217.
Ludwig, W., Bouwman, A.F., Dumont, E., Lespinas, F., 2010. Water and nutrient fluxes from major Mediterranean and Black Sea rivers: past and future trends and their implications for the basin-scale budgets. Global Biogeochem. Cycles 24 (4).
Lykousis, V., Karageorgis, A.P., Chronis, G.T., 2005. Delta progradation and sediment fluxes since the last glacial in the thermaikos Gulf and the sporades basin, NW Aegean Sea, Greece. Mar. Geol. 222, 381−397.
Mackenzie, F.T., Ver, L.M., Lerman, A., 2002. Century-scale nitrogen and phosphorus controls of the carbon cycle. Chem. Geol. 190 (1−4), 13−32.
Madricardo, F., Donnici, S., 2014. Mapping past and recent landscape modifications in the Lagoon of Venice through geophysical surveys and historical maps. Anthropocene 6, 86−96.
Madricardo, F., Foglini, F., Kruss, A., Christian Ferrarin, C., Pizzeghello, N.M., Murri, C., Rossi, M., Bajo, M., Bellafiore, D., Campiani, E., Fogarin, S., Grande, V., Janowski, L., Keppel, E., Leidi, E., Lorenzetti, G., Maicu, F., Maselli, V., Mercorella, A., Montereale Gavazzi, G., Minuzzo, T., Pellegrini, C., Petrizzo, A., Prampolini, M., Remia, A., Rizzetto, F., Rovere, M., Sarretta, A., Sigovini, M., Sinapi, L., Umgiesser, G., Trincardi, F., 2017. High resolution multibeam and hydrodynamic datasets of tidal channels and inlets of the Venice Lagoon. Sci. Data 4 (1), 1−14. https://doi.org/10.1038/sdata.2017.121.
Madricardo, F., Foglini, F., Campiani, E., Grande, V., Catenacci, E., Petrizzo, A., Trincardi, F., 2019. Assessing the human footprint on the sea-floor of coastal systems: the case of the Venice Lagoon, Italy. Sci. Rep. 9 (1), 1−13.
Madricardo, F., Ghezzo, M., Nesto, N., Kiver, M., Joseph, W., Faussone, G.C., Moschino, V., 2020. How to deal with seafloor marine litter: an overview of the state-of-the-art and future perspectives. Front. Mar. Sci. 7, 830.
Malagó, A., Bouraoui, F., Grizzetti, B., De Roo, A., 2019. Modelling nutrient fluxes into the Mediterranean sea. J. Hydrol. Reg. Stud. 22, 100592.
Mandalakis, M., Stephano, E.G., 2002. Study of atmospheric PCB concentrations over the eastern Mediterranean Sea. J. Geophys. Res. Atmos. 107 (D23), 4716. https://doi.org/10.1029/2001JD001566.
Marín-Guirao, L., Atucha, A.M., Barba, J.L., López, E.M., Fernández, A.J.G., 2005. Effects of mining wastes on a seagrass ecosystem: metal accumulation and bioavailability, seagrass dynamics and associated community structure. Mar. Environ. Res. 60 (3), 317−337.
Martín-Vide, J.P., Prats-Puntí, A., Ferrer-Boix, C., 2020. What controls the coarse sediment yield to a Mediterranean delta? The case of the Llobregat River (NE Iberian Peninsula). Nat. Hazards Earth Syst. Sci. 20 (12), 3315−3331.

Maselli, V., Trincardi, F., 2013. Man made deltas. Sci. Rep. 3 (1), 1−7.

McEarchran, A.D., Shea, D., Bodnar, W., Guthrie Nichols, E., 2016. Pharmaceuticals occurrence in groundwater and surface waters in forests land-applied with municipal wastewater. Environ. Toxicol. Chem. 35, 898−905.

Mercogliano, R., Avio, C.G., Regoli, F., Anastasio, A., Colavita, G., Santonicola, S., 2020. Occurrence of microplastics in commercial seafood under the perspective of the human food chain. A review. J. Agric. Food Chem. 68 (19), 5296−5301, 2020 May 13.

Mezzelani, M., Gorbi, S., Fattorini, D., D'Errico, G., Consolandi, G., Milan, M., Bargelloni, L., Regoli, F., 2018. Long-term exposure of *Mytilus galloprovincialis* to Diclofenac, Ibuprofen and Ketoprofen: insights into bioavailability, biomarkers and transcriptomic changes. Chemosphere 198, 238−248.

Micheli, F., Halpern, B., Walbridge, S., Ciriaco, S., Ferretti, F., Fraschetti, S., Lewison, R., Nykjaer, L., Rosenberg, A.A., 2013. Cumulative human impacts on Mediterranean and Black sea marine ecosystems: assessing current pressures and opportunities. PLoS One 8, e79889. https://doi.org/10.1371/journal.pone.0079889.

Migon, C., Caccia, J.L., 1990. Separation of anthropogenic and natural emissions of particulate heavy metals in the western Mediterranean atmosphere. Atmos. Environ. 24A, 399−405.

Milli, S., D'Ambrogi, C., Bellotti, P., Calderoni, G., Carboni, M.G., Celant, A., Di Bella, L., Di Rita, F., Frezza, V., Magri, D., Pichezzi, R.M., Ricci, V., 2013. The transition from wave-dominated estuary to wave-dominated delta: the Late Quaternary stratigraphic architecture of Tiber River deltaic succession (Italy). Sediment. Geol. 284−285, 159−180.

Milliman, J.D., Broadus, J., Gable, F., 1989. Environmental and economic implications of rising sea level and subsiding deltas: the Nile and Bengal examples. Ambio 18, 340−345.

Molinaroli, E., Guerzoni, S., Sarretta, A., Masiol, M., Pistolato, M., 2009. Thirty-year changes (1970 to 2000) in bathymetry and sediment texture recorded in the Lagoon of Venice subbasins, Italy. Mar. Geol. 258 (1−4), 115−125.

Moon, J.Y., Lee, K., Tanhua, T., Kress, N., Kim, I.N., 2016. Temporal nutrient dynamics in the Mediterranean Sea in response to anthropogenic inputs. Geophys. Res. Lett. 43 (10), 5243−5251.

Moreno-González, R., Rodríguez-Mozaz, S., Huerta, B., Barceló, D., León, V.M., 2016. Do pharmaceuticals bioaccumulate in marine molluscs and fish from a coastal lagoon? Environ. Res. 146, 282−298.

Morley, N.H., Burton, J.D., Tankere, S.P., Martin, J.M., 1997. Distribution and behaviour of some dissolved trace metals in the western Mediterranean Sea. Deep-Sea Res. 44, 675−691. Ž3 − 4.

Moschino, V., Riccato, F., Fiorin, R., Nesto, N., Picone, M., Boldrin, A., Da Ros, L., 2019. Is derelict fishing gear impacting the biodiversity of the Northern Adriatic Sea? An answer from unique biogenic reefs. Sci. Total Environ. 663, 387−399.

Nelson, B.W., 1970. Hydrography, sediment dispersal and recent historical development of the Po river delta, Italy. In: Morgan, J.P. (Ed.), Deltaic Sedimentation, Modern and Ancient, vol. 15. SEPM Special Publication, pp. 152−184.

Oldfield, F., Asioli, A., Accorsi, C.A., Mercuri, A.M., Juggins, S., Langone, L., Branch, N., 2003. A high resolution late Holocene palaeo environmental record from the central Adriatic Sea. Quat. Sci. Rev. 22 (2−4), 319−342.

Osorio, V., Larranaga, A., Acena, J., Perez, S., 2016. Concentration and risk of pharmaceuticals in freshwater systems are related to the population density and the livestock unit in Iberian Rivers. Sci. Total Environ. 540, 267−277, 16/j.scitotenv.2018.10.290.

Palanques, A., Plana, F., Maldonado, A., 1990. Recent influence of man on the Ebro margin sedimentation system, northwestern Mediterranean Sea. Mar. Geol. 95 (3–4), 247–263.
Palanques, A., Martín, J., Puig, P., Guillén, J., Company, J.B., Sardà, F., 2006. Evidence of sediment gravity flows induced by trawling in the Palamós (Fonera) submarine canyon (northwestern Mediterranean). Deep Sea Res. Oceanogr. Res. Pap. 53 (2), 201–214.
Paradis, S., Lo Iacono, C., Masqué, P., Puig, P., Palanques, A., Russo, T., November 2021. The island Cruise team, 2021. Evidence of large increases in sedimentation rates due to fish trawling in submarine canyons of the Gulf of Palermo (SW Mediterranean). Mar.Pollut. Bull. Volume 172, 112861.
Paroli, L., 2005. History of Past Research at Portus. An Archaeological Survey of the Port of Imperial Rome, London: British School at Rome, pp. 43–59. Portus.
Peeken, I., Primpke, S., Beyer, B., Gütermann, J., Katlein, C., Krumpen, T., Bergmann, M., Hehemann, L., Gerdts, G., 2018. Arctic sea ice is an important temporal sink and means of transport for microplastic. Nat. Commun. 9 (1), 1505.
Pellegrini, C., Maselli, V., Trincardi, F., 2016. Pliocene–Quaternary contourite depositional system along the south-western Adriatic margin: changes in sedimentary stacking pattern and associated bottom currents. Geo-Mar. Lett. 36 (1), 67–79.
Pellegrini, C., Tesi, T., Schieber, J., Bohacs, K.M., Rovere, M., Asioli, A., Trincardi, F., 2021. Fate of terrigenous organic carbon in muddy clinothems on continental shelves revealed by stratal geometries: insight from the Adriatic sedimentary archive. Glob. Planet. Change 103539.
Pellegrini, C., Maselli, V., Cattaneo, A., Piva, A., Ceregato, A., Trincardi, F., 2015. Anatomy of a compound delta from the post-glacial transgressive record in the Adriatic Sea. Mar. Geol. 362, 43–59.
Petrie, B., Barden, R., Kasprzyk-Hordern, B., 2015. A review on emerging contaminants in wastewaters and the environment: current knowledge, understudied areas and recommendations for future monitoring. Water Res. 72, 3–27.
Pierdomenico, M., Martorelli, E., Dominguez-Carrió, C., Gili, J.P., Chiocci, F.L., 2016. Seafloor characterization and benthic megafaunal distribution of an active submarine canyon and surrounding sectors: the case of Gioia Canyon (Southern Tyrrhenian Sea). J. Mar. Syst. 157 (2016), 101–117.
Pierdomenico, M., Casalbore, D., Chiocci, F.L., 2019. Massive benthic litter funnelled to deep sea by flash-flood generated hyperpycnal flows. Sci. Rep. 9, 5330.
Pino, D.R., Jeandel, C., Bethoux, J.P., Minster, J.F., 1990. Are the trace metal cycles balanced in the Mediterranean Sea? Palaeogeogr. Palaeoclimatol. Palaeoecol. 82 (3–4), 369–388.
Piva, A., Asioli, A., Trincardi, F., Schneider, R.R., Vigliotti, L., 2008. Late-holocene climate variability in the Adriatic Sea (central Mediterranean). Holocene 18 (1), 153–167.
PlasticsEurope, 2019. Plastic—the Facts 2019. www.plasticeurope.org.
Pont, D.J., Day, J., Ibáñez, C., 2017. The impact of two large floods (1993–1994) on sediment deposition in the Rhone delta: implications for sustainable management. Sci. Total Environ. 609, 251–262, 31 December 2017.
Prata, J.C., 2017. Airborne microplastics: consequences to human health? Environ. Pollut. 234, 115–126.
Prinz, N., Korez, Š., 2020. Understanding how microplastics affect marine biota on the cellular level is important for assessing ecosystem function: a review. In: Jungblut, S., Liebich, V., Bode-Dalby, M. (Eds.), YOUMARES 9—the Oceans: Our Research, Our Future. Springer, Cham, pp. 101–120.

Puig, P., Canals, M., Company, J.B., Martín, J., Amblas, D., Lastras, G., Palanques, A., Calafat, A.M., 2012. Ploughing the deep-sea floor. Nature 489 (7415), 286–289.

Ramirez-Llodra, E., Brandt, A., Danovaro, R., De Mol, B., Escobar, E., German, C.R., Vecchione, M., 2010. Deep, diverse and definitely different: unique attributes of the world's largest ecosystem. Biogeosciences 7, 2851–2899.

Ramirez-Llodra, E., Tyler, P.A., Baker, M.C., Bergstad, O.A., Clark, M.R., et al., 2011. Man and the last great wilderness: human impact on the deep sea. PLoS One 6, e22588.

Rajar, R., Cetina, M., Horvat, M., Zagar, D., 2007. Mass balance of mercury in the Mediterranean sea. Mar. Chem. 107 (1), 89–102.

Pusceddu, A., Bianchelli, S., Martín, J., Puig, P., Palanques, A., Masqué, P., Danovaro, R., 2014. Chronic and intensive bottom trawling impairs deep-sea biodiversity and ecosystem functioning. Proc. Nat. Acad. Sci. 111 (24), 8861–8866.

Ragusa, A., Svelato, A., Santacroce, C., Catalano, P., Notarstefano, V., Carnevali, O., Papa, F., Rongioletti, M.C.A., Baiocco, F., Draghi, S., D'Amore, E., Rinaldo, D., Matta, M., Giorgini, E., 2021. Plasticenta: first evidence of microplastics in human placenta. Environ. Int. 146, 106274.

Raymond, P.A., Hamilton, S.K., 2018. Anthropogenic influences on riverine fluxes of dissolved inorganic carbon to the oceans. Limnol. Oceanogr. Lett. 3 (3), 143–155.

Regnier, P., Friedlingstein, P., Ciais, P., Mackenzie, F.T., Gruber, N., Janssens, I.A., Laruelle, G.G., Lauerwald, R., luyssaert, S., Andersson, A.J., Arndt, S., Arnosti, C., Borges, A.V., Dale, A.W., Gallego-Sala, A., Yves Goddéris, Y., Goossens, N., Hartmann, J., Heinze, C., Ilvina, C., Joos, F., La Rowe, D.E., Leifeld, J., Meysman, F.J.R., Munhoven, G., Raymond, P.A., Spahni, R., Suntharalingam, P., Thullner, M., 2013. Anthropogenic perturbation of the carbon fluxes from land to ocean. Nat. Geosci. 6 (8), 597–607.

Renaud, F.G., Kuenzer, C., 2012. The Mekong Delta System: Interdisciplinary Analyses of a River Delta. Springer Science and Business Media.

Renaud, F.G., Syvitski, J.P., Sebesvari, Z., Werners, S.E., Kremer, H., Kuenzer, C., Friedrich, J., 2013. Tipping from the Holocene to the Anthropocene: How Threatened are Major World Deltas?.

Retelletti Brogi, S., Cossarini, G., Bachi, G., Balestra, C., Camatti, E., Casotti, R., Checcucci, G., Colella, S., Evangelista, V., Falcini, F., Francocci, F., Giorgino, T., Margiotta, M., Ribera d'Alcalà, M., Sprovieri, M., Vestri, S., Santinelli, C., 2022. Evidence of Covid-19 lockdown effects on riverine dissolved organic matter dynamics provides a proof-of-concept for needed regulations of anthropogenic emissions. Sci. Total Environ. 812, 152412.

Ribera d'Alcalà, M.R., Civitarese, G., Conversano, F., Lavezza, R., 2003. Nutrient ratios and fluxes hint at overlooked processes in the Mediterranean Sea. Journal Geophys. Res. Oceans 108 (C9), 8106.

Ritchie, H., Roser, M., 2018. Plastic Pollution. Published online at Ourworldindata.org. Retrieved from. https://ourworldindata.org/plastic-pollution (Online Resource).

Riso, R.D., Le Corre, P., L'Helguen, S., Morin, P., 2004. On the presence of a cadmium rich subsurface water mass in the western Mediterranean and its influence on the distribution of cadmium in the surface waters. Mar. Chem. 87, 15–22.

Rockström, J., Steffen, W., Noone, K., Persson, A., Chapin III, F.S., Lambin, E.F., Lenton, T.M., Scheffer, M., Folke, C., Schellnhuber, H.J., Nykvist, B., de Wit, C.A., Hughes, T., van der Leeuw, S., Rodhe, H., Sörlin, S., Snyder, P.K., Costanza, R., Svedin, U., Falkenmark, M., Karlberg, L., Corell, R.W., Fabry, V.J., Hansen, J.,

Walker, B., Liverman, D., Richardson, K., Crutzen, P., Foley, J.A., 2009. A safe operating space for humanity. Nature 461, 472−475.

Rodríguez, J.G., Amouroux, I., Belzunce-Segarra, M.J., Bersuder, P., Bolam, T., Caetano, M., Carvalho, I., Correia dos Santos, M.M., Fones, G.R., Gonzalez, J.L., Guesdon, S., Larreta, J., Marras, B., McHugh, B., Menet-Nédélec, F., Menchaca, I., Gabet, V.M., Montero, N., Nolan, M., Regan, F., Robinson, C.D., Rosa, N., Rodrigo Sanz, M., Schintu, M., White, B., Zhang, H., 2021. Assessing variability in the ratio of metal concentrations measured by DGT-type passive samplers and spot sampling in European seawaters. Sci. Total Environ. 783 (2021), 147001.

Rohling, E.J. (2017). The Oceans. In *The Oceans*. Princeton University Press, 2017, https://doi.org/10.1515/9781400888665.

Rohling, E.J., Bryden, H.L., 1992. Man-induced salinity and temperature increase in western Mediterranean deep water. J. Geophys. Res. 97, 11191−11198.

Roméo, M., Gnassia-Barelli, M., Carré, C., 1992. Importance of gelatinous plankton organisms in storage and transfer of trace metals in the northwestern Mediterranean. Mar. Ecol. Prog. Ser. 82, 267−274.

Rovere, M., Pellegrini, C., Chiggiato, J., Campiani, E., Trincardi, F., 2019. Impact of dense bottom water on a continental shelf: an example from the SW Adriatic margin. Mar. Geol. 408, 123−143.

Ruddiman, W.F., 2003. The anthropogenic greenhouse era began thousands of years ago. Clim. Change 61 (3), 261−293.

Ruitton, S., Belloni, B., Marc, C., Boudouresque, C., 2019. Ghost med: assessment of the impact of lost fishing gear in the French Mediterranean sea. In: 3rd Symposium on the Conservation of Coralligenous and Other Calcareous Bio-Constructions.

Ruiz, F., Abad, M., Olıas, M., Galan, E., Gonzalez, I., Aguila, E., Hamoumi, N., Pulido, I., Cantano, M., 2006. The present environmental scenario of the Nador Lagoon (Morocco). Environ. Res. 102 (2), 215−229.

Sadaoui, M., Ludwig, W., Bourrin, F., Romero, E., 2018. The impact of reservoir construction on riverine sediment and carbon fluxes to the Mediterranean Sea. Prog. Oceanogr. 163, 94−111.

Sala, et al., 2021. Protecting the global ocean for biodiversity, food and climate. Nature 592, 397−409.

Saliu, F., Montano, S., Garavaglia, M.G., Lasagni, M., Seveso, D., Galli, P., 2018. Microplastic and charred microplastic in the Faafu Atoll, Maldives. Mar. Pollut. Bull. 136, 464−471.

Salvagio Manta, D., Sprovieri, M., Bonsignore, M., Oliveri, E., Barra, M., Tranchida, G., Giaramita, L., Mazzola, S., 2016. Fluxes and the mass balance of mercury in Augusta Bay (Sicily, southern Italy). Estuar. Coast Shelf Sci. 181 (2016), 134−143.

Santinelli, C., 2015. DOC in the Mediterranean sea. In: Biogeochemistry of Marine Dissolved Organic Matter. Academic Press, pp. 579−608.

Santinelli, C., Hansell, D.A., d'Alcalà, M.R., 2013. Influence of stratification on marine dissolved organic carbon (DOC) dynamics: the Mediterranean Sea case. Prog. Oceanogr. 119, 68−77.

Santinelli, C., Iacono, R., Napolitano, E., d'Alcalá, M.R., 2021. Surface transport of DOC acts as a trophic link among Mediterranean sub-basins. Deep-Sea Res. Part I Oceanogr. Res. Pap. 170, 103493.

Sarretta, A., Pillon, P., Molinaroli, E., Guerzoni, S., Fontolan, G., 2010. Sediment budget in the lagoon of Venice. Italy. Cont. Shelf Res. 30, 934−949.

Scarpa, G.M., Zaggia, L., Manfè, G., et al., 2019. The effects of ship wakes in the Venice Lagoon and implications for the sustainability of shipping in coastal waters. Sci. Rep. 9, 19014. https://doi.org/10.1038/s41598-019-55238-z.

Scarponi, D., Nawrot, R., Azzarone, M., Pellegrini, C., Gamberi, F., Trincardi, F., Kowalewski, M., 2022. Resilient biotic response to long-term climate change in the Adriatic Sea. Glob. Change Biol. https://doi.org/10.1111/gcb.16168.

Schattner, U., Lazar, M., Tibor, G., Ben-Avraham, Z., Makovsky, Y., 2010. Filling up the shelf a sedimentary response to the last post-glacial sea rise. Mar. Geol. 278 (1), 165−176.

Schneider, A., Tanhua, T., Körtzinger, A., Wallace, D.W., 2010. High anthropogenic carbon content in the eastern Mediterranean. J. Geophys. Res. Oceans 115, C12050.

Schwarz, A.E., Ligthart, T.N., Boukris, E., van Harmelen, T., 2019. Sources, transport, and accumulation of different types of plastic litter in aquatic environments: a review study. Mar. Pollut. Bull. 143, 92−100, 2019.

Sherrell, R.M., Boyle, E.A., 1988. Zinc, chromium, vanadium and iron in the Mediterranean Sea. *Deep Sea Research Part A*. Oceanogr. Res. Pap. 35 (8), 1319−1334.

Shiklomanov, I.A., 1998. World Water Resources: A New Appraisal and Assessment for the 21st Century: A Summary of the Monograph World Water Resources. UNESCO.

Simeoni, U., Corbau, C., 2009. A review of the Delta Po evolution (Italy) related to climatic changes and human impacts. Geomorphology 107 (1−2), 64−71.

Skliris, N., Lascaratos, A., 2004. Impacts of the Nile River damming on the thermohaline circulation and water mass characteristics of the Mediterranean Sea. J. Mar. Syst. 52 (1−4), 121−143.

Sømme, T.O., Piper, D.J., Deptuck, M.E., Helland-Hansen, W., 2011. Linking onshore−offshore sediment dispersal in the Golo source-to-sink system (Corsica, France) during the late Quaternary. J. Sediment. Res. 81 (2), 118−137.

Solidoro, C., Cossarini, G., Lazzari, P., Galli, G., Bolzon, G., Somot, S., Salon, S., 2022. Modeling carbon budgets and acidification in the Mediterranean sea ecosystem under contemporary and future climate. Front. Mar. Sci. 8, 781522. https://doi.org/10.3389/fmars.2021.781522.

Somoza, L., Rodríguez-Santalla, I., 2014. Geology and geomorphological evolution of the Ebro river delta. In: Landscapes and Landforms of Spain. Springer, Dordrecht, pp. 213−227.

Spivack, A.J., Huested, S.S., Boyle, E.A., 1983. Copper, nickel and cadmium in the surface waters of the Mediterranean. In: *Trace metals in sea water*. Springer, Boston, MA, pp. 505−512.

Sprovieri, M., Ribera d'Alcalà, M., Roose, P., Drago, A., de Cauwer, K., Falcini, F., Lips, I., Maggi, C., Mauffret, A., Tronczynski, J., Zeri, C., Moretti, P.M., 2021. Science for good environmental status: a European joint action to support marine policy. Sustainability 13 (15), 8664.

Stanley, J.D., Clemente, P.L., 2017. Increased land subsidence and sea-level rise are submerging Egypt's Nile delta coastal margin. GSA Today (Geol. Soc. Am.) 27, 4−11. https://phys.org/news/2017-03-looming-crisis-decreased-fresh-water-egypt.html#jCp.

Statham, P.J., Burton, J., Hydes, D.J., 1985. Cd and Mn in the Alboran Sea and adjacent north Atlantic geochemical implications for Mediterranean. Nature 313, 565−567.

Steffen, W., Richardson, K., Rockström, J., Cornell, S.E., Fetzer, I., Bennett, E.M., Sörlin, S., 2015. Planetary boundaries: guiding human development on a changing planet. Science 347 (6223).

Stenmarck, Å., Elin, L., Belleza, A.F., Busch, N., Larsen, Å., Wahlström, M., 2017. Hazardous Substances in Plastics − Ways to Increase Recycling. Nordic Council of Ministers.

Storelli, M.M., Losada, S., Marcotrigiano, G.O., Roosens, L., Barone, G., Neels, H., Covaci, A., 2009. Polychlorinated biphenyl and organochlorine pesticide contamination signatures in deep-sea fish from the Mediterranean Sea. Environ. Res. 109, 851−856.

Suaria, G., Avio, C., Mineo, A., Lattin, G.L., Magaldi, M.G., Belmonte, G., Moore, C.J., regoli, F., Aliani, S., 2016. The Mediterranean Plastic Soup: synthetic polymers in Mediterranean surface waters. Sci. Rep. 6, 37551.

Sutton, M.A., Howard, C.M., Erisman, J.W., Bleeker, A., Billen, G., Grennfelt, P., Van Grinsven, H., Grizzetti, B., 2011. The European Nitrogen Assessment. Sources, Effects and Policy Perspectives. Cambridge University Press.

Syvitski, J.P., Kettner, A., 2011. Sediment flux and the Anthropocene. Phil. Trans. Math. Phys. Eng. Sci. 369 (1938), 957−975.

Syvitski, J.P., Vörösmarty, C.J., Kettner, A.J., Green, P., 2005. Impact of humans on the flux of terrestrial sediment to the global coastal ocean. Science 308 (5720), 376−380.

Syvitski, J., Kettner, A., Overeem, I., Hutton, E., Hannon, M., Brakenridge, G., Day, J., Vörösmarty, C., Saito, Y., Giosan, L., Nichols, R., 2009. Sinking deltas due to human activities. Nat. Geosci. 2, 681−686.

Syvitski, J., Waters, C.N., Day, J., Milliman, J.D., Summerhayes, C., Steffen, W., Zalasiewicz, J., Cearreta, A., Galuszka, A., Haidas, I., Head, M.J., Leinfelder, R., McNelill, J.R., Poirier, C., Rose, N.L., Shotyk, W., Wagreich, M., Williams, M., 2020. Extraordinary human energy consumption and resultant geological impacts beginning around 1950 CE initiated the proposed Anthropocene Epoch. Commun. Earth Environ. 1 (1), 1−13.

Syvitski, J., Ángel, J.R., Saito, Y., et al., 2022. Earth's sediment cycle during the Anthropocene. Nat. Rev. Earth Environ. 3, 179−196. https://doi.org/10.1038/s43017-021-00253-w.

Tamburrino, S., Passaro, S., Manta, D.S., Quinci, E., Ausili, A., Romano, E., Sprovieri, M., 2020. Re-shaping the "original SIN": a need to re-think sediment management and policy by introducing the "buffer zone" concept. J. Soils Sediments 20 (6), 2563−2572.

Taviani, M., Angeletti, L., Cardone, F., Montagna, P., Danovaro, R., 2019. A unique and threatened deep water coral-bivalve biotope new to the Mediterranean Sea offshore the Naples Megalopolis. Sci. Rep. 9, 3411.

Thompson, R.C., Swan, S.H., Moore, C.J., vom Saal, F.S., 2009a. Our plastic age. Phil. Trans. R. Soc. B 364, 1973−1976, 2009a.

Thompson, R.C., Moore, C., vom Saal, F.S., Swan, S.H., 2009b. Plastics, the environment and human health: current consensus and future trends. Phil. Trans. R. Soc. 2009, B 364, 2153−2166.

Tosi, L., Rizzetto, F., Zecchin, M., Brancolini, G., Baradello, L., 2009. Morphostratigraphic framework of the Venice Lagoon (Italy) by very shallow water VHRS surveys: evidence of radical changes triggered by human-induced river diversions. Geophys. Res. Lett. 36 (9).

Toso, C., Madricardo, F., Molinaroli, E., Fogarin, S., Kruss, A., Petrizzo, A., Trincardi, F., 2019. Tidal inlet seafloor changes induced by recently built hard structures. PLoS One 14 (10), e0223240.

Traina, A., Ausili, A., Bonsignore, M., Fattorjni, D., Gherardi, S., Gorbi, S., Quinci, E., Romano, E., Salvagio Manta, D., Tranchida, G., Regoli, F., Sprovieri, M., 2021.

Organochlorines and Polycyclic Aromatic Hydrocarbons as fingerprint of exposure pathways from marine sediments to biota. Mar. Pollut. Bull. 170, 112676.

Trincardi, F., Cattaneo, A., Correggiari, A., 2004. Mediterranean prodelta systems: natural evolution and human impact investigated by EURODELTA. Oceanography 17 (4), 34−45.

Trincardi, F., Barbanti, A., Bastianini, M., Benetazzo, A., Cavaleri, L., Chiggiato, J., Papa, A., Pomaro, A., Sclavo, M., Tosi, L., Umgiesser, G., 2016. The 1966 flooding of Venice: what time taught us for the future. Oceanography 29 (4), 178−186.

Trincardi, F., Amorosi, A., Bosman, A., Correggiari, A., Madricardo, F., Pellegrini, C., 2020. Ephemeral rollover points and clinothem evolution in the modern Po Delta based on repeated bathymetric surveys. Basin Res. 32, 402−418.

UNEP, 2021. Drowning in Plastics − Marine Litter and Plastic Waste Vital Graphics.

UNEP/MAP, 2012. State of the Mediterranean Marine and Coastal Environment. UNEP/MAP − Barcelona Convention, Athens.

UNEP/MAP, Bleu, P., 2020. State of the Environment and Development in the Mediterranean: Summary for Decision Makers. Nairobi.

Van Geen, A., Rosener, P., Boyle, E.A., 1988. Entrainment of trace metal-enriched Atlantic shelf-waters in the inflow to the Mediterranean Sea. Nature 331, 423−426.

Van Geen, A., Boyle, E.A., Moore, W.S., 1991. Trace metal enrichments in waters of the Gulf of Cadiz, Spain. Geochim.Cosmochim. Acta 55, 2173−2191.

Van der Leeuw, S.E., Archaeomedes Research Team, 2005. Climate, hydrology, land use, and environmental degradation in the lower Rhone Valley during the Roman period. Compt. Rendus Geosci. 337 (1−2), 9−27.

van Sebille, E., Aliani, S., Law, K.L., Maximenko, N., Alsina, J.M., Bagaev, A., Bergmann, M., Chapron, B., Chubarenko, I., Cózar, A., Delandmeter, P., Egger, M., Fox-Kemper, B., Garaba, S.P., Goddijn-Murphy, L., Hardesty, B.D., Hoffman, M.J., Isobe, A., Jongedijk, C.E., Kaandorp, M.L.A., Khatmullina, L., Koelmans, A.A., Kukulka, T., Laufkötter, C., Lebreton, L., Lobelle, D., Maes, C., Martinez-Vicente, V., Morales Maqueda, M.A., Poulain-Zarcos, M., Rodríguez, E., Ryan, P.G., Shanks, A.L., Shim, W.J., Suaria, G., Thiel, M., van den Bremer, T.S., Wichmann, D., 2020. The physical oceanography of the transport of floating marine debris. Environ. Res. Lett. 15, 023003.

Vella, C., Fleury, T.J., Raccasi, G., Provansal, M., Sabatier, F., Bourcier, M., 2005. Evolution of the Rhône delta plain in the Holocene. Mar. Geol. 222, 235−265.

Verlicchi, P., Al Aukidy, M., Galletti, A., Petrovic, M., Barcelò, D., 2012. Hospital effluent: investigation of the concentrations and distribution of pharmaceuticals and environmental risk assessment. Sci. Total Environ. 430, 109−118.

Verri, G., Pinardi, N., Oddo, P., Ciliberti, S.A., Coppini, G., 2018. River runoff influences on the Central Mediterranean overturning circulation. Clim. Dynam. 50, 1675−1703.

Wang, W.X., Fisher, N.S., 1998. Accumulation of trace elements in a marine copepod. Limnol. Oceanogr. 43 (2).

Watts, J., 2019. Concrete: the most destructive material on Earth. Guardian 25, 1−9.

Weithmann, N., Möller, J.N., Löder, M.G., Piehl, S., Laforsch, C., Freitag, R., 2018. Organic fertilizer as a vehicle for the entry of microplastic into the environment. Sci. Adv. 4 (4), eaap8060.

Welle, F., Franz, R., 2018. Microplastic in bottled natural mineral water—literature review and considerations on exposure and risk assessment. Food Addit. Contam. Part A Chem. 35 (12), 2482−2492.

West, G., 2016. Scale: The Universal Laws of Growth, Innovation, Sustainability, and the Pace of Life in Organisms, Cities, Economies, and Companies. Penguin Press.

Williams, S.J., Flocks, J., Jenkins, C., Khalil, S., Moya, J., 2012. Offshore sediment character and sand resource assessment of the northern Gulf of Mexico, Florida to Texas. J. Coast Res. 10060, 30–44.

Wong, J.K.H., Lee, K.K., Tang, K.H.D., Yap, P.S., 2020. Microplastics in the freshwater and terrestrial environments: prevalence, fates, impacts and sustainable solutions, 2020 Jun 1 Sci. Total Environ. 719, 137512. https://doi.org/10.1016/j.scitotenv.2020.137512. Epub 2020 Feb 22. PMID: 32229011.

Woodall, L.C., Sanchez-Vidal, A., Canals, M., Paterson, G.L.J., Coppock, R., Sleight, V., Calafat, A., Rogers, A.D., Narayanaswamy, B.E., Thompson, R.C., 2014. The deep sea is a major sink for microplastic debris. R. Soc. Open Sci. 1, 140317.

Wu, P., Christidis, N., Stott, P., 2013. Anthropogenic impact on Earth's hydrological cycle. Nat. Clim. Change 3 (9), 807–810.

Zalasiewicz, J., Williams, M., Smith, A., Barry, T.L., Coe, A.L., Bown, P.R., Stone, P., 2008. Are we now living in the Anthropocene? GSA Today (Geol. Soc. Am.) 18 (2), 4.

Zalasiewicz, J., Waters, C.N., Do Sul, J.A.I., Corcoran, P.L., Barnosky, A.D., Cearreta, A., Yonan, Y., 2016. The geological cycle of plastics and their use as a stratigraphic indicator of the Anthropocene. Anthropocene 13, 4–17.

This page intentionally left blank

Index

Note: 'Page numbers followed by "f" indicate figures, "t" indicate tables and "b" indicate boxes.'

D

I

L

M

N

T

U

V

W

Z

This page intentionally left blank

OCEANOGRAPHY OF THE MEDITERRANEAN SEA

An Introductory Guide

Provides insights in descriptive oceanography concepts applied to the case of a marginal sea and is thus useful for those starting studying oceanography and the Mediterranean Sea functioning.

Oceanography of the Mediterranean Sea: An Introductory Guide provides a comprehensive but concise introduction to the physical oceanography of one of the most fascinating marginal seas, the Mediterranean Sea. The book is primarily focused on the state-of-the-art understanding of the physical functioning of the Mediterranean Sea, while embracing the fundamentals of associated geological and chemical processes.

Written by multiple scientists active over many years in the Mediterranean marine community, the book provides a broad overview on the information needed to get a robust background on the physical oceanography of the Mediterranean Sea for students in oceanography, climate science, marine geology, and chemistry or scientists unfamiliar with the region.

Key features:

- Provides a comprehensive but concise introduction to the physical oceanography of the Mediterranean Sea
- Presents the existing links between climate, ocean, biogeochemical cycles, and geological evolution at the Mediterranean scale
- Presents clear examples of the Mediterranean region, as well as comparisons with other regions globally

Edited by:

Katrin Schroeder
Senior Scientist, Consiglio Nazionale delle Ricerche-Istituto di Scienze Marine (CNR-ISMAR), Venezia, Italy

Jacopo Chiggiato
Senior Scientist, Consiglio Nazionale delle Ricerche-Istituto di Scienze Marine (CNR-ISMAR), Venezia, Italy

ELSEVIER elsevier.com/books-and-journals

ISBN 978-0-12-823692-5

9 780128 236925